

# PROCEEDINGS OF SPIE



SPIE—The International Society for Optical Engineering

## ***Photon Processing in Microelectronics and Photonics***

**Koji Sugioka  
Malcolm C. Gower  
Richard F. Haglund, Jr.  
Alberto Piqué  
Frank Träger  
Jan J. Dubowski  
Willem Hoving**  
*Chairs/Editors*

**21–24 January 2002  
San Jose, USA**

*Sponsored by*  
SPIE—The International Society for Optical Engineering

*Cosponsored by*  
Air Force Office of Scientific Research (USA)

**DISTRIBUTION STATEMENT A**  
Approved for Public Release  
Distribution Unlimited



**Volume 4637**

**20031028 153**

# REPORT DOCUMENTATION PAGE

AFRL-SR-AR-TR-03-

0415

Public reporting burden for this collection of information is estimated to average 1 hour per response, including the time for reviewing the collection of information, sending comments regarding the collection of information, including suggestions for reducing this burden to Washington Headquarters Service, Directorate for Information Operations and Reports, 1215 Jefferson Davis Highway, Suite 1204, Arlington, VA 22202-4302, and to the Office of Management and Budget, Paperwork Reduction Project (0704-0-88) Washington, DC 20503.

PLEASE DO NOT RETURN YOUR FORM TO THE ABOVE ADDRESS.

1. REPORT DATE (DD-MM-YYYY) 19-08-2002		2. REPORT DATE FINAL TECHNICAL REPORT		3. DATES COVERED (From - To) 01 DEC 01 TO 30 NOV 02	
4. TITLE AND SUBTITLE  PHOTON PROCESSING IN MICROELECTRONICS AND PHOTONICS:  PART A - LASER APPLICATIONS IN MICROELECTRONIC AND OPTOELECTRONIC MANUFACTURING				5a. CONTRACT NUMBER	
				5b. GRANT NUMBER F496200210048	
				5c. PROGRAM ELEMENT NUMBER	
				5d. PROJECT NUMBER	
				5e. TASK NUMBER	
6. AUTHOR(S) Sugioka, Koji Gower, Malcolm C. Haglund Jr., Richard F. Pique, Alberto Trager, Frank Dubowski, Jan J. Hoving, Willem				5f. WORK UNIT NUMBER	
7. PERFORMING ORGANIZATION NAME(S) AND ADDRESS(ES) Society of Photo-Optical Instrumentation Engineers (SPIE) PO Box 10, Bellingham, WA 98227-0010				8. PERFORMING ORGANIZATION REPORT NUMBER  Volume 4637	
9. SPONSORING/MONITORING AGENCY NAME(S) AND ADDRESS(ES) Air Force Office of Scientific Research 801 N. Randolph St., Room 732 Arlington, VA 22203-1977				10. SPONSOR/MONITOR'S ACRONYM(S) AFOSR/NE	
				11. SPONSORING/MONITORING AGENCY REPORT NUMBER	
12. DISTRIBUTION AVAILABILITY STATEMENT Approved for Public Release					
APPROVED FOR PUBLIC RELEASE, DISTRIBUTION UNLIMITED					
13. SUPPLEMENTARY NOTES ISBN 0-8194-4376-X					
14. ABSTRACT This proceedings contains papers on the following topics: Laser processing, Pulsed laser deposition, Surface and thin film treatments, Laser ablation, Laser-matter interaction, Machining and microstructuring, Microsystems and microdevices.					
15. SUBJECT TERMS Microelectronic, Optoelectronic, Laser, Photonics					
16. SECURITY CLASSIFICATION OF:			17. LIMITATION OF ABSTRACT	18. NUMBER OF PAGES	19a. NAME OF RESPONSIBLE PERSON
a. REPORT Non-Classified	b. ABSTRACT	c. THIS PAGE	SAR	597	Janice Gaines Walker
				19b. TELEPHONE NUMBER (Include area code)	(360) 676-3290





# PROCEEDINGS OF SPIE

SPIE—The International Society for Optical Engineering

## ***Photon Processing in Microelectronics and Photonics***

**Koji Sugioka**  
**Malcolm C. Gower**  
**Richard F. Haglund, Jr.**  
**Alberto Piqué**  
**Frank Träger**  
**Jan J. Dubowski**  
**Willem Hoving**  
*Chairs/Editors*

**21–24 January 2002**  
**San Jose, USA**

*Sponsored and Published by*  
SPIE—The International Society for Optical Engineering

*Cosponsored by*  
Air Force Office of Scientific Research (USA)



**Volume 4637**

SPIE is an international technical society dedicated to advancing engineering and scientific applications of optical, photonic, imaging, electronic, and optoelectronic technologies.



The papers appearing in this book compose the proceedings of the technical conference cited on the cover and title page of this volume. They reflect the authors' opinions and are published as presented, in the interests of timely dissemination. Their inclusion in this publication does not necessarily constitute endorsement by the editors or by SPIE. Papers were selected by the conference program committee to be presented in oral or poster format, and were subject to review by volume editors or program committees.

Please use the following format to cite material from this book:

Author(s), "Title of paper," in *Photon Processing in Microelectronics and Photonics*, Koji Sugioka, Malcolm C. Gower, Richard F. Haglund, Jr., Alberto Piqué, Frank Träger, Jan J. Dubowski, Willem Hoving, Editors, Proceedings of SPIE Vol. 4637, page numbers (2002).

ISSN 0277-786X  
ISBN 0-8194-4376-X

Published by  
**SPIE—The International Society for Optical Engineering**  
P.O. Box 10, Bellingham, Washington 98227-0010 USA  
Telephone 1 360/676-3290 (Pacific Time) • Fax 1 360/647-1445  
<http://www.spie.org/>

Copyright© 2002, The Society of Photo-Optical Instrumentation Engineers.

Copying of material in this book for internal or personal use, or for the internal or personal use of specific clients, beyond the fair use provisions granted by the U.S. Copyright Law is authorized by SPIE subject to payment of copying fees. The Transactional Reporting Service base fee for this volume is \$15.00 per article (or portion thereof), which should be paid directly to the Copyright Clearance Center (CCC), 222 Rosewood Drive, Danvers, MA 01923 USA. Payment may also be made electronically through CCC Online at <http://www.directory.net/copyright/>. Other copying for republication, resale, advertising or promotion, or any form of systematic or multiple reproduction of any material in this book is prohibited except with permission in writing from the publisher. The CCC fee code is 0277-786X/02/\$15.00.

Printed in the United States of America.

## In Memory of Dr. Andy Tam

"We dedicate these proceedings to the memory of Dr. Andy Tam who for many years served the laser community represented at these meetings by providing invaluable assistance and unfailingly constructive criticism. He was a true friend and respected colleague to a large number of our community."



# Contents

xiii	Conference Committees
xv	Introduction

## **Part A Laser Applications in Microelectronic and Optoelectronic Manufacturing**

### **SESSION 1 FUNDAMENTALS OF LASER-MATTER INTERACTION**

---

- 1 **Consequences of combined chemical and radiative exposure of solid surfaces (Invited Paper)** [4637-02]  
J. T. Dickinson, M. L. Dawes, K. H. Nwe, S. C. Langford, Washington State Univ. (USA)
- 13 **Onset of laser ablation in  $\text{CaF}_2$  crystal under excimer laser irradiation** [4637-03]  
Y. Kawaguchi, A. Narazaki, T. Sato, H. Niino, A. Yabe, National Institute of Advanced Industrial Science and Technology (Japan)

### **SESSION 2 DIAGNOSTICS AND MECHANISMS OF LASER ABLATION**

---

- 21 **Diagnostics of nanoparticle formation process by laser ablation in a background gas (Invited Paper)** [4637-04]  
T. Okada, Y. Nakata, M. Maeda, Kyushu Univ. (Japan)
- 31 **Ultrafast laser-induced plasma diagnostics with time-spatial-resolved shadow and interferometric techniques** [4637-05]  
S. V. Garnov, A. A. Malyutin, O. G. Tsarkova, V. I. Konov, General Physics Institute (Russia); F. Dausinger, Univ. Stuttgart (Germany)
- 43 **Effects of laser parameters on plume characteristics and ablation rate** [4637-06]  
Z. L. Li, S. Z. Yow, Institute of Materials Research & Engineering (Singapore); L. Lui, National Univ. of Singapore; N. L. Yakovlev, P. M. Moran, Institute of Materials Research & Engineering (Singapore)
- 54 **Modeling of chemical processes in the dynamic expansion for pulsed laser deposition** [4637-07]  
E. W. Kreutz, M. Aden, M. Niessen, A. Husmann, R. Poprawe, RWTH Aachen (Germany)

### **SESSION 3 SURFACE AND THIN FILM TREATMENT**

---

- 64 **General concept of a surface microgeometry reconstruction based on laser technology (Invited Paper)** [4637-08]  
V. P. Veiko, St. Petersburg Institute of Fine Mechanics and Optics (Russia)
- 75 **Laser-induced diffusible resistance: device characterization and process modeling** [4637-09]  
M. Meunier, École Polytechnique de Montréal (Canada) and LTRIM-Technologies (Canada); M. Cadotte, M. Ducharme, École Polytechnique de Montréal (Canada); Y. Gagnon, A. Lacourse, LTRIM-Technologies (Canada)

- 82 **Photoluminescence study of laser-ablated gallium nitride thin films** [4637-10]  
J. M. Wrobel, Univ. of Missouri/Kansas City (USA); E. Płaczek-Popko, Wrocław Univ. of Technology (Poland); J. J. Dubowski, H. Tang, J. B. Webb, National Research Council Canada
- 90 **Excimer ablation of ITO on flexible substrates for large format display applications** [4637-11]  
O. A. Ghandour, D. Constantinide, R. E. Sheets, Tamarack Scientific Co., Inc. (USA)
- 102 **Generation of functional structures by laser pyrolysis of polysilazane** [4637-12]  
H.-J. Krauß, A. Otto, Friedrich-Alexander Univ. Erlangen-Nürnberg (Germany)

#### **SESSION 4 PULSED LASER DEPOSITION**

---

- 111 **Preparation of carbonous nanoparticles for anode electrodes of ultrathin lithium ion rechargeable batteries by laser ablation** [4637-15]  
S. Nishio, K. Tamura, J. Murata, J. Kitahara, A. Matsuzaki, Mi'e Univ. (Japan); M. Okumura, N. Ando, Y. Hato, Kanebo, Ltd. (Japan)
- 119 **Background gas effects on structural properties in thin films deposited by pulsed laser deposition** [4637-16]  
Y. Yamada, N. Suzuki, T. Makino, T. Yoshida, Matsushita Electric Industrial Co., Ltd. (Japan)

#### **SESSION 5 ULTRAFAST LASER PROCESSING I**

---

- 127 **German national femtosecond technology project (FST) (Invited Paper)** [4637-18]  
F. Dausinger, Univ. of Stuttgart (Germany)
- 135 **Laser ablation of nitrogen-solid films by UV ps-laser irradiation: surface modification of materials by fragments in laser ablation plume (Invited Paper)** [4637-19]  
H. Niino, T. Sato, A. Narazaki, Y. Kawaguchi, A. Yabe, National Institute of Advanced Industrial Science and Technology (Japan)
- 148 **TEM investigations of thermal effects on material structure induced by femtosecond and nanosecond laser processing** [4637-21]  
R. Le Harzic, Univ. Jean Monnet (France); S. Valette, École Nationale Supérieure des Mines de St-Etienne (France); N. Huot, E. Audouard, E. Baubeau, C. Jonin, P. Laporte, Univ. Jean Monnet (France)

#### **SESSION 6 ULTRAFAST LASER PROCESSING II**

---

- 159 **Microfabrication by a high-fluence femtosecond exposure: mechanism and applications** [4637-23]  
M. Watanabe, S. Juodkakis, Univ. of Tokushima (Japan); J. Nishii, National Institute of Advanced Industrial Science and Technology (Japan); S. Matsuo, H. Misawa, Univ. of Tokushima (Japan)
- 169 **Processing multilayer systems using femtosecond, picosecond, and nanosecond laser pulses at different wavelengths** [4637-24]  
D. Ashkenasi, Laser- und Medizin-Technologie GmbH (Germany); A. Rosenfeld, Max-Born-Institute (Germany)

- 180 **Development of dicing technique for thin semiconductor substrates with femtosecond laser ablation** [4637-25]  
A. Yokotani, N. Matsuo, K. Kawahara, Y. Kurogi, N. Matsuo, Miyazaki Univ. (Japan);  
T. Ninomiya, H. Sawada, NEC Machinery Corp. (Japan); K. Kurosawa, Miyazaki Univ. (Japan)

---

**SESSION 7 ULTRAFAST LASER PROCESSING III**

---

- 188 **Waveguides produced by ultrashort laser pulses inside glasses and crystals (Invited Paper)** [4637-27]  
S. Nolte, M. Will, Friedrich-Schiller-Univ. Jena (Germany); B. N. Chichkov, Laser Zentrum Hannover e.V. (Germany); A. Tünnermann, Friedrich-Schiller-Univ. Jena (Germany)
- 197 **Fabrication of birefringent microstructures in transparent materials with femtosecond laser pulses** [4637-28]  
W. Watanabe, K. Yamada, D. Kuroda, T. Shinagawa, T. Asano, Osaka Univ. (Japan); J. Nishii, National Institute of Advanced Industrial Science and Technology (Japan); K. Itoh, Osaka Univ. (Japan)
- 204 **Ultrafast laser-induced processing of materials: fundamentals and applications in micromachining** [4637-29]  
T. Y. Choi, A. Chimmalgil, C. P. Grigoropoulos, Univ. of California/Berkeley (USA)
- 212 **Femtosecond laser machining of fluidic microchannels for miniaturized bioanalytical systems** [4637-30]  
A. Ben-Yakar, R. L. Byer, Stanford Univ. (USA)

---

**SESSION 8 F<sub>2</sub> LASER PROCESSING**

---

- 218 **Glass micromachining using the VUV F<sub>2</sub> laser** [4637-32]  
P. E. Dyer, S. M. Maswadi, H. V. Snelling, C. D. Walton, Univ. of Hull (UK)
- 228 **High-resolution F<sub>2</sub>-laser machining of micro-optic components** [4637-33]  
J. Li, P. R. Herman, X. M. Wei, K. P. Chen, Univ. of Toronto (Canada); J. Ihlemann, G. Marowsky, Laser Lab. Göttingen e.V. (Germany); P. Oesterlin, B. Burghardt, MicroLas Lasersystem GmbH (Germany)
- 235 **Laser processing of ion-exchange waveguides in glass** [4637-34]  
S. Ruschin, Tel-Aviv Univ. (Israel); K. Sugioka, RIKEN—The Institute of Physical and Chemical Research (Japan); G. Yarom, Tel-Aviv Univ. (Israel); T. Akane, K. Midorikawa, RIKEN—The Institute of Physical and Chemical Research (Japan)
- 243 **High-efficiency refractive index modification of fused silica by F<sub>2</sub> and KrF excimer laser multiwavelength excitation process** [4637-35]  
K. Obata, RIKEN—The Institute of Physical and Chemical Research (Japan) and Science Univ. of Tokyo (Japan); K. Sugioka, T. Akane, RIKEN—The Institute of Physical and Chemical Research (Japan); K. Toyoda, Science Univ. of Tokyo (Japan); K. Midorikawa, RIKEN—The Institute of Physical and Chemical Research (Japan)
- 251 **F<sub>2</sub>-laser microfabrication of buried waveguide structures in transparent glasses** [4637-36]  
X. M. Wei, K. P. Chen, D. Coric, P. R. Herman, J. Li, Univ. of Toronto (Canada)

---

**SESSION 9      MICROMACHINING AND MICROSTRUCTURING**

---

- 258    **UV laser radiation-induced modifications and microstructuring of glass (Invited Paper)** [4637-37]  
M. Talkenberg, E. W. Kreutz, A. Horn, M. Jacquorie, RWTH Aachen (Germany); R. Poprawe, RWTH Aachen (Germany) and Fraunhofer-Institut für Lasertechnik (Germany)
- 270    **Crack-free laser processing of glass substrate and its mechanisms** [4637-39]  
M. H. Hong, Data Storage Institute (Singapore); K. Sugioka, RIKEN—The Institute of Physical and Chemical Research (Japan); D. J. Wu, L. L. Wong, Y. F. Lu, Data Storage Institute (Singapore); K. Midorikawa, RIKEN—The Institute of Physical and Chemical Research (Japan); T. C. Chong, Data Storage Institute (Singapore)
- 280    **Production of innovative geometries with UV lasers** [4637-40]  
A. Ostendorf, C. Kulik, U. Stute, Laser Zentrum Hannover e.V. (Germany)
- 291    **Microscale bending of brittle materials using pulsed and CW lasers** [4637-41]  
R. X. Zhang, X. Xu, Purdue Univ. (USA)

---

**SESSION 10     MICROSYSTEMS AND MICRODEVICES**

---

- 297    **Development of a 100-gm-class inspector satellite using photostructurable glass/ceramic materials (Invited Paper)** [4637-42]  
A. Huang, W. W. Hansen, S. W. Janson, H. Helvajian, The Aerospace Corp. (USA)
- 305    **Laser micromachining of biofactory-on-a-chip devices (Invited Paper)** [4637-43]  
J. P. H. Burt, A. D. Goater, C. J. Hayden, J. A. Tame, Univ. of Wales Bangor (UK)
- 318    **Laser micromachining of polymeric mold inserts for rapid prototyping of PMMA devices via photomolding** [4637-44]  
W. Pfleging, T. Hanemann, W. Bernauer, M. Torge, Forschungszentrum Karlsruhe (Germany)
- 330    **Bimetallic thermal activated films for microfabrication, photomasks, and data storage** [4637-45]  
Y. Tu, G. H. Chapman, M. V. Sarunic, Simon Fraser Univ. (Canada)

---

**SESSION 11     DIRECT-WRITE PROCESSING**

---

- 341    **Cell-by-cell construction of living tissue (Invited Paper)** [4637-46]  
B. R. Ringeisen, H. Kim, H. D. Young, B. J. Spargo, R. C. Y. Auyeung, A. Piqué, D. B. Chrisey, Naval Research Lab. (USA) P. K. Wu, Southern Oregon Univ. (USA)
- 353    **Direct writing of planar ultracapacitors by laser forward transfer processing** [4637-48]  
C. B. Arnold, R. C. Wartena, B. Pratap, K. E. Swider-Lyons, A. Piqué, Naval Research Lab. (USA)
- 361    **Direct-write of sensor devices by a laser forward transfer technique** [4637-49]  
A. Piqué, D. W. Weir, Naval Research Lab. (USA); P. K. Wu, Southern Oregon Univ. (USA); B. Pratap, C. B. Arnold, B. R. Ringeisen, R. A. McGill, R. C. Y. Auyeung, R. A. Kant, D. B. Chrisey, Naval Research Lab. (USA)

---

**SESSION 12      INNOVATIVE TECHNOLOGY FOR INDUSTRIAL APPLICATIONS**

---

- 369    **Integrated tool for fabrication of electronic components by laser direct write (Invited Paper)** [4637-50]  
S. A. Mathews, C. Zhang, T. Kegresse, D. Liu, Potomac Photonics, Inc. (USA)
- 374    **Laser-based sample preparation for electronic package failure analysis** [4637-51]  
B. M. Frazier, S. A. Mathews, M. T. Duignan, Potomac Photonics, Inc. (USA); L. D. Skoglund, Z. Wang, R. C. Dias, Intel Corp. (USA)
- 378    **Potential of ultrashort laser pulses (<10ps) in future material processing: mode-locked Ti:sapphire vs. q-switch Nd:YAG applications** [4637-83]  
D. Ashkenasi, Laser- und Medizin-Technologie GmbH (Germany)
- 386    **Short-pulse-width micromachining of hard materials using DPSS Nd:YAG lasers** [4637-52]  
M. Heglin, S. V. Govorkov, M. J. Scaggs, H. Theoharidis, T. Schoelzel, Lambda Physik (USA)
- 397    **Laser-assisted manufacture for performance-optimized dielectrically loaded GPS antennas for mobile telephones** [4637-54]  
O. Leisten, Sarantel Ltd. (UK); J. Fieret, I. Stassen, P. T. Rumsby, Exitech Ltd. (UK); P. McEvoy, Y. Vardaxoglou, Loughborough Univ. (UK)

---

**SESSION 13      POSTER SESSION**

---

- 404    **Effect of laser parameters on the exposure and selective etch rate in photostructurable glass** [4637-38]  
F. E. Livingston, W. W. Hansen, A. Huang, H. Helvajian, The Aerospace Corp. (USA)
- 413    **Laser plasma emission of small particles in different gas atmospheres** [4637-55]  
A. A. Andreev, Yokogawa Electric Corp. (Japan) and Institute for Laser Physics (Russia); T. Ueda, M. Wakamatsu, Yokogawa Electric Corp. (Japan)
- 419    **Xe(He,Kr)-I<sub>2</sub>(Cl<sub>2</sub>) glow, barrier and capacitive discharge excilamps** [4637-61]  
V. F. Tarasenko, M. I. Lomaev, D. V. Shitz, V. S. Skakun, Institute of High Current Electronics (Russia)
- 431    **Pulsed laser deposition of silicon dioxide thin films with silicone targets for fabricating waveguide devices** [4637-62]  
M. Okoshi, M. Kuramatsu, N. Inoue, National Defense Academy (Japan)
- 435    **Application and observation of laser-induced forward transfer process** [4637-63]  
Y. Nakata, T. Okada, M. Maeda, Kyushu Univ. (Japan)
- 445    **Pulsed laser ablation of IC packages for device failure analyses** [4637-80]  
M. H. Hong, Data Storage Institute (Singapore); Z. H. Mai, Advanced Micro Devices Pte Ltd. (Singapore); G. X. Chen, Data Storage Institute (Singapore); T. Thiam, Advanced Micro Devices Pte Ltd. (Singapore); W. D. Song, Y. F. Lu, Data Storage Institute (Singapore); C. E. Soh, Advanced Micro Devices Pte Ltd. (Singapore); T. C. Chong, Data Storage Institute (Singapore)



## **Part B    *Laser-Based Packaging in Microelectronics and Photonics***

### **SESSION 14    PHYSICS AND CHEMISTRY OF LASER-BASED PACKAGING**

---

- 453    **Physical and chemical aspects of laser-materials interactions relevant to laser processing (Invited Paper) [4637-64]**  
J. T. Dickinson, Washington State Univ. (USA)
- 465    **Plasma behavior during high-brightness (DPSS) laser-materials interaction (Invited Paper) [4637-66]**  
J. Mazumder, M. Douglass, P. Li, Univ. of Michigan (USA)
- 474    **Laser-material processing: an industrial view of packaging applications (Invited Paper) [4637-65]**  
J. Brannon, IBM Storage Technology Div. (USA)

### **SESSION 15    CUTTING, BENDING, BONDING, AND ANNEALING**

---

- 479    **Water-jet guided laser: possibilities and potential for singulation of electronic packages (Invited Paper) [4637-67]**  
F. R. Wagner, Synova Inc. (Switzerland); A. Spiegel, N. Vago, Budapest Univ. of Technology and Economics (Hungary); B. Richerzhagen, Synova Inc. (Switzerland)
- 487    **Laser joining of glass with silicon [4637-68]**  
R. Witte, H. Herfurth, S. Heinemann, Fraunhofer USA
- 496    **Processing of silicon by Nd:YAG lasers with harmonics generation [4637-70]**  
M. Panzner, J. Kasper, H. Wust, U. Klotzbach, E. Beyer, Fraunhofer Institute of Material and Beam Technology (Germany)

### **SESSION 16    MICROWELDING**

---

- 505    **Laser welding of polymers using high-power diode lasers (Invited Paper) [4637-71]**  
F. G. Bachmann, ROFIN-SINAR Laser GmbH (Germany); U. A. Russek, Fraunhofer-Institute for Laser Technology (Germany)
- 519    **Laser microwelding of electronic components [4637-72]**  
H. K. Tönshoff, K. Körber, C. Kulik, K. Schäfer, Laser Zentrum Hannover e.V. (Germany)
- 528    **Laser welding of plastics transparent to near-infrared radiation [4637-73]**  
K. Sato, Y. Kurosaki, Univ. of Electro-Communications (Japan); T. Saito, I. Satoh, Tokyo Institute of Technology (Japan)
- 537    **Study and process control in laser conduction welding for millisecond-pulse duration range [4637-74]**  
L. Berthe, D. Delage, D. Lepretre, L. Bacinello, W. Knapp, Coopération Laser Franco-Allemande (France); N. Dumont, Laser Cheval (France); F. Durand, SMH Automation (Switzerland)
- 545    **SHADOW: a new welding technique [4637-75]**  
T. Kramer, A. M. Olowinsky, Fraunhofer-Institut für Lasertechnik (Germany); F. Durand, SMH Automation (Switzerland)

- 555 **Laser penetration spike welding: a welding tool enabling novel process and design opportunities** [4637-82]  
D. K. Dijken, W. Hoving, Philips Ctr. for Industrial Technology (Netherlands);  
J. Th. M. De Hosson, Univ. of Groningen (Netherlands)

---

**SESSION 17 OVERVIEW AND PROSPECTS OF LASER-BASED PACKAGING**

---

- 561 **Overview and future prospects of the use of lasers for packaging by the microelectronics and photonics industry in Japan (Invited Paper)** [4637-76]  
K. Washio, H. Kouta, NEC Corp. (Japan)
- 571 **Laser beam microwelding in the watch industry** [4637-77]  
A. Olowinsky, T. Kramer, Fraunhofer-Institut für Lasertechnik (Germany); F. Durand, SMH Automation (Switzerland)
- 581 **Laser applications in integrated circuit packaging** [4637-78]  
Y. F. Lu, W. D. Song, Z. M. Ren, C. W. An, K. D. Ye, D. M. Liu, W. J. Wang, M. H. Hong, T. C. Chong, National Univ. of Singapore and Data Storage Institute (Singapore)
- 593 *Addendum*  
595 *Author Index*

## Conference Committees

### Part A Laser Applications in Microelectronic and Optoelectronic Manufacturing

#### *Conference Chairs*

**Koji Sugioka**, RIKEN—The Institute of Physical and Chemical Research (Japan)  
**Malcolm C. Gower**, Exitech Ltd. (UK)  
**Richard F. Haglund, Jr.**, Vanderbilt University (USA)  
**Alberto Piqué**, Naval Research Laboratory (USA)  
**Frank Träger**, Universität Kassel (Germany)

#### *International Advisory Committee*

**Jan J. Dubowski**, National Research Council Canada  
**Peter E. Dyer**, University of Hull (UK)  
**Henry Helvajian**, The Aerospace Corporation (USA)  
**Ernst W. Kreutz**, RWTH Aachen (Germany)  
**Jyotirmoy Mazumder**, University of Michigan (USA)

#### *Program Committee*

**Douglas B. Chrissey**, Naval Research Laboratory (USA)  
**Ronald M. Gilgenbach**, University of Michigan (USA)  
**Arnold Gillner**, Fraunhofer Institut für Lasertechnik (Germany)  
**Andrew S. Holmes**, Imperial College of Science, Technology and Medicine (UK)  
**Willem Hoving**, Philips Center for Industrial Technology (Netherlands)  
**Koji Ikuta**, Nagoya University (Japan)  
**Richard B. Jackman**, University College London (UK)  
**Hiroshi M. Masuhara**, Osaka University (Japan)  
**Kouichi Murakami**, University of Tsukuba (Japan)  
**Robert J. Nemanich**, North Carolina State University (USA)  
**Satoru Nishio**, Mie University (Japan)  
**Andreas Ostendorf**, Laser Zentrum Hannover e.V. (Germany)  
**Wilhelm Pfleging**, Forschungszentrum Karlsruhe GmbH (Germany)  
**Richard F. Wood**, Oak Ridge National Laboratory (USA)

#### *Session Chairs*

- 1 Fundamentals of Laser-Matter Interaction  
**Tatsuo Okada**, Kyushu University (Japan)
- 2 Diagnostics and Mechanisms of Laser Ablation  
**Craig B. Arnold**, Naval Research Laboratory (USA)
- 3 Surface and Thin Film Treatment  
**Koji Sugioka**, RIKEN—Institute of Physical and Chemical Research (Japan)

- 4 Pulsed Laser Deposition  
**Ernst W. Kreutz**, RWTH Aachen (Germany)
- 5 Ultrafast Laser Processing I  
**Jan J. Dubowski**, National Research Council Canada
- 6 Ultrafast Laser Processing II  
**Friedrich Dausinger**, Universität Stuttgart (Germany)
- 7 Ultrafast Laser Processing III  
**Andreas Ostendorf**, Laser Zentrum Hannover e.V. (Germany)
- 8 F<sub>2</sub> Laser Processing  
**Malcolm C. Gower**, Exitech Ltd. (UK)
- 9 Micromachining and Microstructuring  
**Wilhelm Pfleging**, Forschungszentrum Karlsruhe GmbH (Germany)
- 10 Microsystems and Microdevices  
**Alberto Piqué**, Naval Research Laboratory (USA)
- 11 Direct Write Processing  
**Henry Helvajian**, The Aerospace Corporation (USA)
- 12 Innovative Technology for Industrial Applications  
**Frank Träger**, Universität Kassel (Germany)

## **Part B Laser-Based Packaging in Microelectronics and Photonics**

### *Conference Chairs*

**Jan J. Dubowski**, National Research Council Canada  
**Willem Hoving**, Philips Center for Industrial Technology (Netherlands)

### *Program Committee*

**Ruediger Hack**, JDS Uniphase (USA)  
**Yong F. Lu**, Data Storage Institute (Singapore)  
**Kurt Mann**, Haas-Laser GmbH (Germany)  
**Andreas Ostendorf**, Laser Zentrum Hannover e.V. (Germany)  
**Manfred Rahe**, Lambda Physik AG (Germany)  
**Hans-Peter Schwob**, Lasag Industrial Lasers (Switzerland)

## Introduction

Laser materials processing is one of the key technologies in the 21st century which will enable the synthesis of advanced materials by controlled modification of the material properties and precision microfabrication of the material shape. Laser-based techniques can be applied to process a variety of materials, from soft materials like bio tissues and polymers to hard materials like diamond and glass. In addition, recent progress in using ultrashort-pulse lasers has realized the feasibility for embedded modification and microfabrication of transparent materials via a nonlinear absorption process. Embedded materials processing is difficult to accomplish by other materials processing technologies. As a result, lasers are finding use in various fields, not only in microelectronic and optoelectronic manufacturing, but also in MEMS and microsystem fabrication.

The proceedings on Photon Processing in Microelectronics and Photonics 2002 consists of reports presented at two conferences:

I. Laser Applications in Microelectronic and Optoelectronic Manufacturing (LAMOM-VII)

II. Laser-Based Packaging in Microelectronics and Photonics (LPMP)

These conferences were held 21-23 January and 24 January, respectively, as part of LASE 2002 at Photonics West in San Jose, California, USA.

The LAMOM conference series was established in 1995 and is now considered an annual event. The aim of this conference is to provide a forum for discussion of both the fundamental aspects of laser materials processing and the practical applications of lasers in the manufacturing process of microelectronic, optoelectronic, and microsystem devices. The success of this conference is evident by the growing number of participants. The LAMOM conference has really become an important conference combining elements of fundamental and applications interest.

LAMOM-VII comprised 12 oral sessions plus a poster session which included papers on fundamentals of laser-matter interaction, diagnostics, and mechanisms of laser ablation, surface and thin film treatment, pulsed laser deposition, ultrafast laser processing,  $F_2$  laser processing, micromachining and microstructuring, microsystems and microdevices, direct write processing, and innovative technology for industrial applications. In particular, the topic on ultrafast laser processing had three sessions, which reflects the current high level of interest. More than 60 oral and poster papers including 13 invited papers were presented from the USA, Japan, Germany, Canada, Russia, Singapore, UK, France, and Israel. The LPMP conference comprised four oral sessions and a poster session. One of the main themes at this meeting was laser microwelding, which reflects the strong potential of this aspect of laser-based technology in contributing to packaging in modern microelectronics and photonics.

We would like to thank the members of the program committee, the invited speakers, and presenters of contributed papers, and all those who attended for their contribution to the success of LAMOM-VII and LPMP. We also thank the SPIE staff for helping in organizing this conference.

Finally, we respectfully acknowledge the U.S. Air Force Office of Scientific Research (Dr. Howard Schlossberg, in particular) for the continued financial support provided to many prior LAMOM meetings including LAMOM-VII.

**Koji Sugioka**  
**Jan J. Dubowski**  
**Willem Hoving**

## Consequences of combined chemical and radiative exposure of solid surfaces

J. T. Dickinson, M. L. Dawes, Khin Hla Nwe, and S. C. Langford

Surface Dynamics Laboratory, Physics Department  
Washington State University, Pullman, WA 99164-2814

### ABSTRACT

We present studies of the consequences of simultaneous exposure of inorganic single crystals to radiation and water. The first case consists of a biomineral namely  $\text{CaHPO}_4 \cdot 2\text{H}_2\text{O}$  (brushite) which is a wide band gap, hydrated inorganic single crystal. We examine the laser induced ion and neutral emissions accompanying 248-nm excimer laser radiation. Both types of emission are several orders of magnitude higher following exposure to 2 keV electrons at current densities of  $200 \mu\text{A}/\text{cm}^2$  and doses of  $10^2$ - $10^3 \text{ mC}/\text{cm}^2$ . We show that the enhancements in emission are strongly correlated with e-beam induced morphology changes (including recrystallization) on this unusual surface. We then examine similar effects on "dry" crystals such as NaCl and  $\text{NaNO}_3$  which are exposed to  $10^{-5} \text{ Pa}$  partial pressures of  $\text{H}_2\text{O}$ . Again dramatic enhancements in radiation induced emissions are exhibited along with the generation of unique morphological structures with nanometer scale dimensions.

**Keywords:** laser desorption, defects, hydrated single crystal, biomineral, surface modification, electron stimulated desorption, water vapor, nanostructures

### 1. INTRODUCTION

When two stimuli are applied to a system simultaneously one always has the possibility of a synergism, i.e., where the total result is greater than the sum of the individual effects. We have shown in the past that such synergisms arise when we combine exposure of materials to mechanical stress and electron beam irradiation,<sup>1,2</sup> chemical exposure and e-beam irradiation,<sup>3-6</sup> electron and laser beams,<sup>8-10</sup> and mechanical and chemical stimulation,<sup>11-14</sup> all of which are cloaked in what we sometimes call our "one-two punch". Here we would like to examine the possible role water can play in changing rates of radiation induced desorption and decomposition on single crystals. For soluble inorganic materials, water can be considered somewhat aggressive in that when sorbed on such a surface, the oriented dipoles of the water can exert forces on lattice ions/atoms and lower their binding energies. This is particularly effective at defect sites such as steps and kinks because these structures correspond to lower coordination (therefore lower binding energy) and water can better surround (solvate) the ions at these sites. This results again on stronger forces and lowered binding energies. In addition, many defects on ionic crystals are chemically active and promote dissociation of the water leading to sorbed H and OH. Examples are  $\text{MgO}$ <sup>15</sup> and  $\text{TiO}_2$ <sup>16</sup> where anion vacancies are shown to dominate the reactions.

Very little work has been done on the influence of electron and laser irradiation on inorganic crystalline materials that contain waters of hydration. Such structures are common in the environment as well as in a number of biologically derived materials. The surfaces of such crystals can be dramatically altered by UV and electron irradiation. Single crystal  $\text{CaHPO}_4 \cdot 2\text{H}_2\text{O}$  (brushite) is a wide band gap, UV transparent, inorganic phosphate biomineral with applications in dentistry, medical implants, and prosthetic devices, as well as serving as a possible target material for laser surface modification and pulsed laser deposition of biocompatible materials. Here we compare mass-selected measurements of laser-desorbed ions and neutral molecules from as-grown or as-cleaved surface with measures from electron-irradiated surfaces (2 keV electrons at current densities of  $\sim 200 \mu\text{A}/\text{cm}^2$  and doses of  $\sim 10^2$ - $10^3 \text{ mC}/\text{cm}^2$ ). As-cleaved brushite crystals

are transparent and quite resistant damage by 30-ns pulses of 5 eV photons (KrF excimer laser, 248 nm). However, prior exposure to the electron beam creates defects that dramatically increase the surface-laser interaction and the resulting ionic and neutral products.

Likewise, little work has been done on the influence of background water present during irradiation of ionic crystals with electron and laser beams. We present our results of such irradiation in background pressures of water  $\sim 10^{-5}$  Pa. Strong synergisms are revealed and we suspect that water vapor is enhancing defect moderated emission processes.

## 2. EXPERIMENT

Single crystals of monoclinic brushite were grown from aqueous solutions of  $\text{Ca}(\text{NO}_3)_2$  and  $\text{NH}_4(\text{H}_2\text{PO}_4)$  by slow diffusion in dilute nitric acid (pH 2-4) at room temperature<sup>17</sup>. The resulting plate-like crystals were stored in saturated solution and exposed to air only when mounted in the vacuum chamber. As-grown crystals and crystals cleaved minutes before placing in the vacuum system showed very similar emissions. All work on brushite was carried out at a nominal crystal temperature of 25 °C. Melt grown single crystals of  $\text{NaNO}_3$  grown in our laboratory after heating to 315 °C in air 99.0% pure  $\text{NaNO}_3$  powder (melt point: 306.8 °C) and then slowly, over a period of several days, cool it back down to room temperature. Transmission measurements obtained using a Lambda 900, Perkin Elmer UV/VIS/NIR spectrometer, and a 400  $\mu\text{m}$  thick melt grown  $\text{NaNO}_3$  single crystal, as well as x-ray and ultraviolet photoelectron emission experiments<sup>18</sup> resulted in spectra similar to those reported in the literature.<sup>19-23</sup> Optical grade, high purity NaCl crystals were purchased from Optovac, Inc. Both the  $\text{NaNO}_3$  and NaCl crystals were cleaved in air before mounting in the vacuum system. The cleavage process is known to generate significant densities of surface defects including vacancies, steps, and kinks. The sample holder was capable of heating the crystals to temperatures as high as 900 K.

The electron source was a Varian Model 981-2455 Auger electron gun operated at an electron kinetic energy of 2 keV and a current density of 100-200  $\mu\text{A}/\text{cm}^2$ . A Lambda Physik LEXtra 200 provided 30-ns pulses of excimer laser radiation at 248 nm (KrF). The laser intensity was controlled with a MICROLAS Laser system variable attenuator. The laser beam was focused by a quartz lens (focal length 35 cm) onto the sample at an angle of 20° with respect to the surface normal. Experiments were performed in a system with a background pressure of  $10^{-10}$  Torr. The emitted particles during both electron and laser beam irradiation were detected with a UTI 100C Quadrupole Mass Spectrometer (QMS) mounted with its axis along the surface normal. The QMS mass filter was tuned to a specific mass/charge ratio and the output detected as a function of time. Neutral particles were ionized by electron impact in the QMS ionizer operated at 70 eV and 2 mA emission. The resulting ions were drawn into the mass filter section, mass selected, and detected with a Channeltron Electron Multiplier (CEM). Measurements of mass selected ion emission were made by grounding the electron optics at the entrance of the QMS (ionizer filaments, grids, and the focus plate). The CEM output was amplified by an Ortec Model 474 timing filter amplifier (< 10 ns rise time), and then discriminated and counted by an EG&G Model 914P Multiple-Channel Scaler.

For the laser desorption of ions, time-of-flight (TOF) curves were fit to Gaussian energy distributions with one or occasionally two peaks, which, when transformed into TOF-space, take the form:

$$I(t) = \frac{Amd^2}{t^3} \exp\left[-\frac{\left(E - \frac{md^2}{2t^2}\right)^2}{2\sigma^2}\right] \quad (1)$$

where  $d$  is the distance between the sample surface and the CEM (28 cm),  $m$  is the ion mass,  $t$  is the ion time of flight;  $E$  is the mean kinetic energy,  $\sigma$  is the standard deviation of the kinetic energy distribution; and  $A$  is a constant.



For neutral particles emitted in thermal equilibrium from a surface at a temperature  $T$ , the time required to reach the QMS ionizer is described by a "half-range" Maxwell-Boltzmann distribution. After accounting for the time required for ions generated in the QMS ionizer to pass through the mass filter, this distribution takes the form:

$$I(t) = \frac{\alpha m^2 d^2}{2\pi(kT)^2 t^4} \int_{\Delta V} r_x \exp\left[\frac{-mr^2}{2kt^2}\right] dV \quad (2)$$

where  $\alpha$  is the ionizer efficiency,  $m$  is the particle mass, and  $k$  is the Boltzmann constant. The integral is performed over the volume of the ionizer,  $\Delta V$ , where  $r$  is the position vector (with origin at the sample) and  $r_x$  is the component of the position vector normal to the sample surface. Fits were performed only on the first 500  $\mu$ s of data to avoid signals due to particles which have bounced off vacuum system walls. With a beam block between the sample and QMS ionizer, detectable signals due to particles reaching the detector via indirect paths were not observed during the first 500  $\mu$ s after the laser pulse. To minimize the contribution of ion emissions to the neutral signals at high fluences, a negatively biased needle between two positively biased (or grounded) grids was positioned in front of the QMS ionizer for some measurements.

### 3. RESULTS AND DISCUSSION

**Brushite: Laser induced ion emissions.**  $\text{Ca}^+$  is the principal cation observed from as-cleaved samples, followed by  $\text{CaO}^+$ , and  $\text{PO}^+$ . Electron irradiated surfaces yielded these same ions, but several orders of magnitude more intense; in addition, electron-irradiated surfaces also yielded  $\text{P}^+$ . Figure 1 compares the fluence dependence of the  $\text{Ca}^+$ ,  $\text{CaO}^+$ ,  $\text{PO}^+$  emission intensities from as-cleaved samples with those from the same samples after exposure to electron doses of approximately 0.43 C/cm<sup>2</sup>. All signals show highly non-linear behaviors, with slopes (on log-log plots) ranging from 4 to 10. Somewhat lower slopes are observed after electron irradiation. As reported previously for a number of ionic crystals<sup>24</sup> and for brushite,<sup>10</sup> the laser desorption of positive ions is best described as a multiple photon process (a sequence of excitations)<sup>24-26</sup>. In this scenario, a sorbed adion is launched when a nearby electron trap is emptied, leading to the Coulomb repulsion necessary to push the ion away. For adion-trap separations on the order of one lattice spacing, we estimate that 1 to 2 charges must be removed from the trap to account for the observed ion energies. Defect complexes are required to account for the emission of molecular ions.  $\text{P}^+$  emission [Fig. 1(d)] is detected only from electron irradiated surfaces.

The  $\text{Ca}^+$  intensities from all samples are characteristically orders of magnitude higher than that of  $\text{CaO}^+$ ,  $\text{PO}^+$ , and  $\text{P}^+$ . Typical mean kinetic energies for electron-irradiated brushite are:  $\text{Ca}^+$ : 6 eV;  $\text{CaO}^+$ : 1 eV;  $\text{PO}^+$  3-4 eV and  $\text{P}^+$ : 5-6 eV. Thus the average ion kinetic energy often exceeds the 5 eV photon energy. Molecular ion emissions<sup>27</sup> from a number of ionic crystals (e.g.,  $\text{MgO}$ ,  $\text{NaCl}$ , and  $\text{NaNO}_3$ ) show non-linear fluence dependencies; further, the polyatomic ions display distinctly lower kinetic energies than the atomic cations. These measurements were made at fluences low enough to ensure that the observed ions are emitted directly from the surface and are not produced by ionization of neutral particles.

**Effect of electron irradiation on the surface.** Brushite has a layered structure consisting of alternating layers of  $\text{CaHPO}_4$  and  $\text{H}_2\text{O}$ .<sup>28</sup> These layers are parallel to the cleavage plane, allowing near-surface water to diffuse to the surface under vacuum conditions. Electron-induced heating generates subsurface voids due to the expansion of water vapor. These cavities serve as incubation sites for efflorescence<sup>29-34</sup> and recrystallization, resulting in the growth of tiny platelets and feathery structures. The rapid formation of these recrystallized structures is expected to yield high defect densities.

Previous FTIR and XPS observations<sup>10,35</sup> indicate that electron-irradiated surfaces are principally composed of pyrophosphate ( $\text{P}_2\text{O}_7^{4-}$ ); exposed voids are typically composed of recrystallized phosphate,  $\text{PO}_4^{3-}$ , in contrast to both  $\text{HPO}_4^{3-}$  and  $\text{P}_2\text{O}_7^{4-}$ . Large delaminated areas are observed in SEM images of electron irradiated surface, as shown in Fig. 2. Similar structures are observed on the surfaces of brushite crystals

heated to 100 °C in air in an oven<sup>36</sup>. Images taken at higher magnifications [Fig. 2(b) and 2(c)] show that many of these exposed voids are lined with small plate-like crystals.

These rough, defect-laden surfaces are expected to absorb strongly at the laser wavelength and yield intense emission. The formation of  $P_2O_7^{4-}$  on the  $HPO_4^{2-}$  sublattice should result in high densities of anion defects, such as  $HPO_4^{2-}$  vacancies. These vacancies are similar to F-centers in the alkaline earth oxides.  $P_2O_7^{4-}$  vacancies on damaged brushite surfaces are potentially more efficient electron traps than  $HPO_4^{2-}$  vacancies, being able to trap up to twice as many electrons.  $P_2O_7^{4-}$  vacancies and related complex anion defects would serve as sorption and emission sites, significantly reducing the observed "threshold fluences" for ion emission from electron-irradiated surfaces.

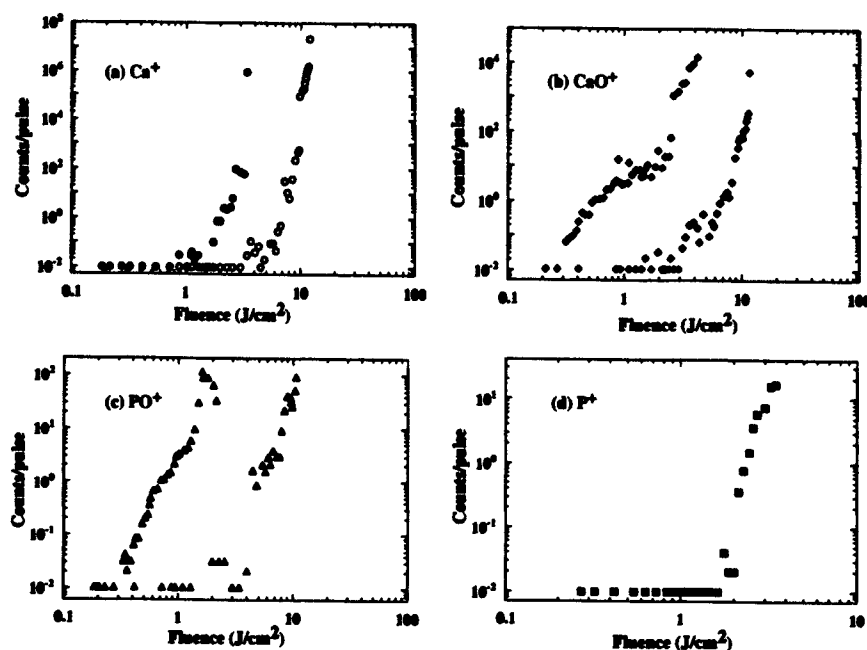


Fig. 1. Fluence dependence of the intensities of the principal ion emissions from as-cleaved brushite: (a)  $Ca^+$ , (b)  $CaO^+$ , (c)  $PO^+$ , and (d)  $P^+$ , before (*open symbols*) and after (*filled symbols*) electron irradiation.

In addition to thermally-induced changes, electron irradiation produces additional chemical effects. The production of  $P^+$  and  $P^0$  from electron-irradiated surfaces, and their absence from as-grown and as-cleaved surfaces, is strong evidence for chemical reduction of surface species. The high electron and excitation densities near the surface during electron irradiation would naturally provide a strongly reducing chemical environment. A reducing environment may also enhance of  $P_2O_7^{4-}$  production, with the attendant emission of  $O_2$ . ( $P_2O_7^{4-}$  can also be produced by simple heating.)

**UV laser induced neutral emission.** One might expect water to be a major neutral product from hydrated crystals. Following any reasonable pumpdown, however, the  $H_2O$  signals accompanying laser irradiation at 248 nm laser are barely detectable. The dehydration of the near surface region of the crystal is clearly evident in the background mass spectrum. Thus the surface is presumably transformed to  $CaHPO_4$ ; this transformation is supported by XPS measurements on evacuated brushite samples.<sup>35</sup> Laser-induced neutral emissions on the resulting surfaces are difficult to observe in the absence of electron- or laser-induced damage. These samples do show weak neutral  $O_2$  and some neutral Ca. The latter signal typically depletes with repeated laser pulses at modest fluences, indicating that the associated defect sites are destroyed faster than they are created by the laser.

After electron irradiation at doses of 0.1-2.8 C/cm<sup>2</sup>, laser irradiation produces neutral Ca, CaO,  $O_2$ ,  $PO_2$ , PO, and P emissions. Typical TOF curves for these emissions, before and after electron irradiation, are

shown in Fig. 3. Electron doses and laser fluences were not exactly the same for each species; at this stage we are most interested in determining if the electron beam influenced the emission intensities which it clearly does.

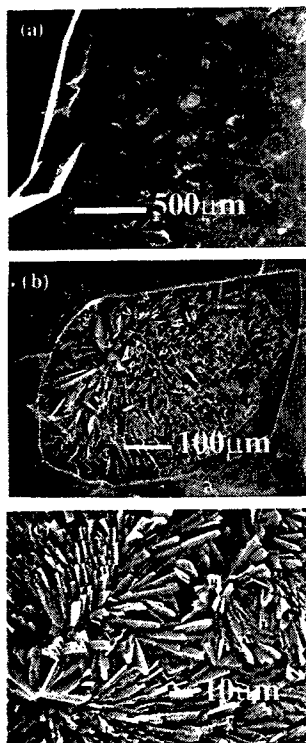


Fig. 2. SEM micrographs of an electron-irradiated surface: (a) Entire irradiated region, (b) close up of exposed interior material, (c) view of recrystallized material at a still higher magnification. These rough regions are "hot-spots" for both ion and neutral emissions due to high defect densities.

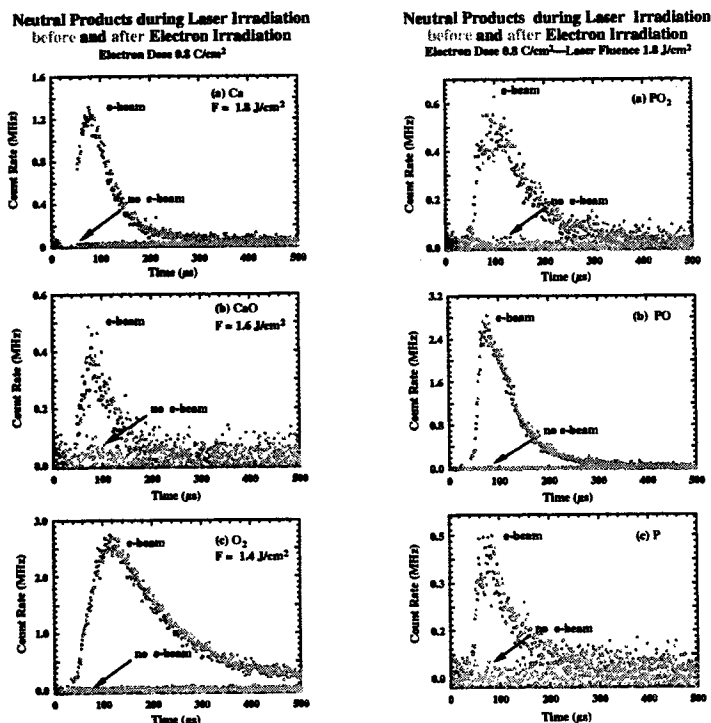


Fig. 3. Neutral emission time-of-flight curves before and after electron irradiation: (a) Ca, (b) CaO, (c) O<sub>2</sub>, (d) PO<sub>2</sub>, and (e) P. Basically, at this fluence, no NE is seen without electron bombardment.

Electron irradiation increases O<sub>2</sub> and Ca signals more than an order of magnitude (at the same laser fluence). For a given laser fluences, the electron dose required to achieve reasonable neutral Ca signals is

nearly an order of magnitude higher than for the other species. The TOF curves (really, "time-of-arrival") for Ca, CaO, PO, and PO<sub>2</sub> are well fit by Maxwell-Boltzmann distributions. Atomic P emission curves are generally too small for reliable curve fitting. Curve fits for the four significant neutral emissions are shown in Fig. 4, along with the resulting "best fit" temperatures. We wish to emphasize that on all ionic crystals studied to date in our laboratory, the neutral products all exhibit thermal behavior at wavelengths corresponding to photon energies below the bandgap. Defects are the only reasonable absorbers to initiate such a process.

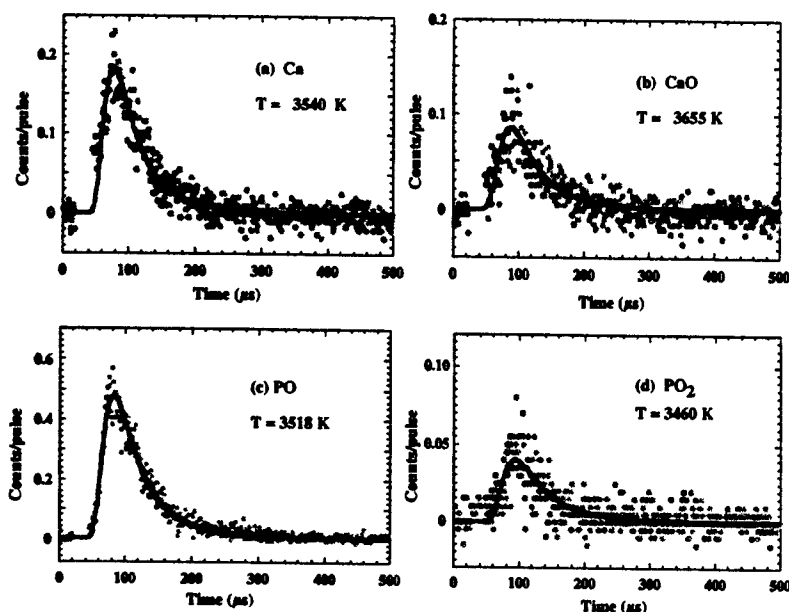


Fig. 4. Neutral product time-of-flight signals from the same site and laser fluence for (a) Ca, (b) CaO, (c) PO, and (d) PO<sub>2</sub>. Note that all of the best fit Maxwell-Boltzmann distributions correspond to similar temperatures.

Obviously, the temperature rise and fall accompanying the laser pulse is not constant in time. If, however, the emission mechanism is thermal, the highest temperatures dominate, so that the range of temperatures (and time) of significant emission is rather narrow. Consequently, the time of flight curves will correspond to a  $\delta$ -function in time and a single temperature. The good agreement among the four temperatures shown here is consistent with thermal desorption from surfaces with well defined temperatures.

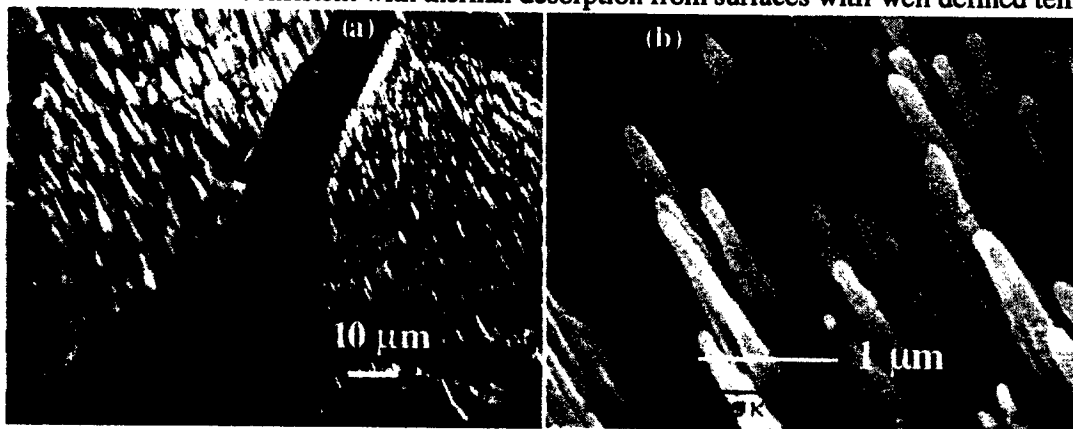


Fig. 5. Cones formed by extensive irradiation of brushite cleavage surfaces by 2 keV electrons (dose = 2.5 C/cm<sup>2</sup>). The arrays of cones tend to occur in rows along surface crystallographic directions and the cones point in the direction of the incident electron beam. They often have lengths of several microns and end in radii ~100 nm or less.

**More extensive electron beam exposure.** By extending the time of exposure to the electron beam to several minutes we found that the brushite surface became even rougher. Close examination of this surface showed us that in parts of the surface where structures were in poor thermal contact with the main crystal body (overhangs of the craters and the platelets grown in the cavities), high aspect ratio cones were generated. Typical images of these structures are shown in Figure 5. The cones are often 2-5 microns in length and end with tips with radii on the order of 100 nm or less. An important aspect of the mechanism for this cone formation is revealed at places where one platelet on the surface partially shields another from the electron beam. Such a region is seen in Fig. 6. In the shadow, the original surface can be seen unaffected by the beam. As one goes out from the shadow, the current density increases continuously. The entire exposed region is recessed relative to the unexposed region and the cones are seen to be highest in the weaker beam and lower in the region receiving the full current density. This proves conclusively that it is an etching process as opposed to a growth process.

The heating of these structures that are poorly attached to the bulk of the crystal is also an important part of the mechanism. We hypothesized that the major etching mechanism is a thermally assisted electronic process, namely electron stimulated desorption/decomposition (ESD).<sup>37-39</sup> With our mass spectrometer (MS), we were able to measure the neutral gaseous products generated during irradiation and found in decreasing order of intensity:  $O_2$ , P, PO,  $PO_2$ , Ca, and  $PO_3$ . Assuming cosine angular distributions for all of the emissions, the MS data could be quantified and integrated to provide a total loss of material during the beam exposure. Estimates of the material volume lost were made from the SEM photographs, such as those above. Comparing these two measurements confirmed that the gasification of the sample accounted for the material missing.

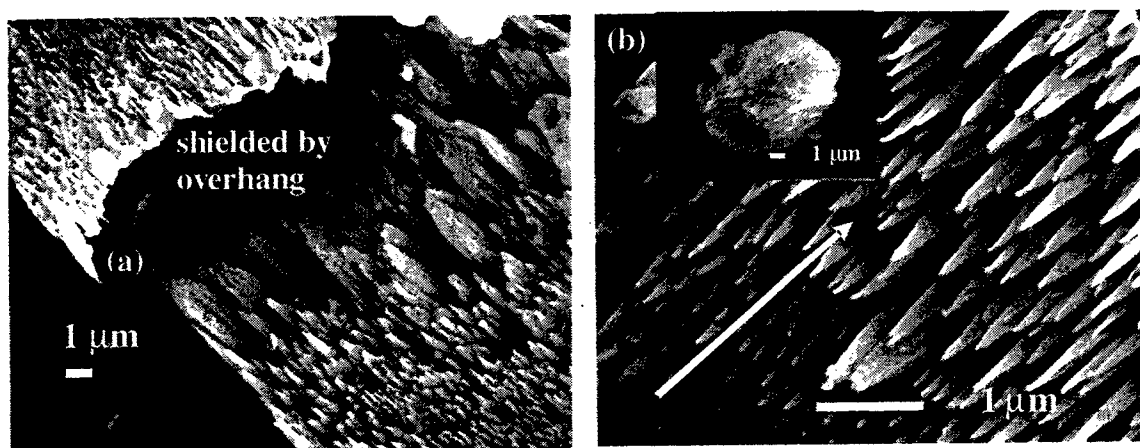


Fig. 6. (a) Cones generated on two overhanging platelets on bulk brushite. The bottom sheet is shielded from the electron beam by the overhang above showing that cone formation is an erosion process rather than a growth process. (b) Cone formation on a small flake of brushite (insert shows an irradiated flake 15 microns in diameter) attached to a heater. Irradiation was carried out at 550 C; the dose (and therefore the time) required to produce cones was  $\sim 1/100$  of that required on the bulk brushite surface.

To confirm that heating was indeed important, we mounted small flakes of brushite on a sample holder that could be heated to 700 C. Fig. 6(b) shows the resulting cone formation on such a flake ( $\sim 15$  microns in diameter). The dose used to generate these cones was far smaller,  $\sim 1/100^{\text{th}}$  that of what was needed on the bulk brushite surface. This is due to a dramatic increase in the rates of ESD at externally provided elevated temperatures. For simpler substrates such as alkali halides this thermal aspect is understood (see below). For brushite we are not yet sure what the thermally activated step is that determines this behavior. Nevertheless, this simple experiment shows that steady state heating leads to enhanced rates of cone formation. Note that again the direction of the cone orientation is towards the incident electron beam.

The XPS and FTIR studies mentioned above suggest that the outer regions of these structures are reduced, tending towards dehydrated pyrophosphate. This material is more robust and is likely to be more resistant to decomposition. Furthermore, this happens first on the outer most surfaces where more electron density is received.

From the above observations we propose the following scenario for cone formation:

- Initially, ESD on nearly perfect substrate begins the formation of point defects; aggregation of such defects initiates a roughening of the surface.
- Through anion decomposition, the material towards the top is more resistant to decomposition and can form capstones that will cause strong heterogeneity in etch rates favoring cone formation.
- Preferential etching occurs in the depressed regions; charging of the top parts of the emerging cones could also help channel electrons down into the regions around the cones. Obviously, the direction of the incoming electrons sets the preferred regions that get etched the fastest, thus the directionality of the cones.

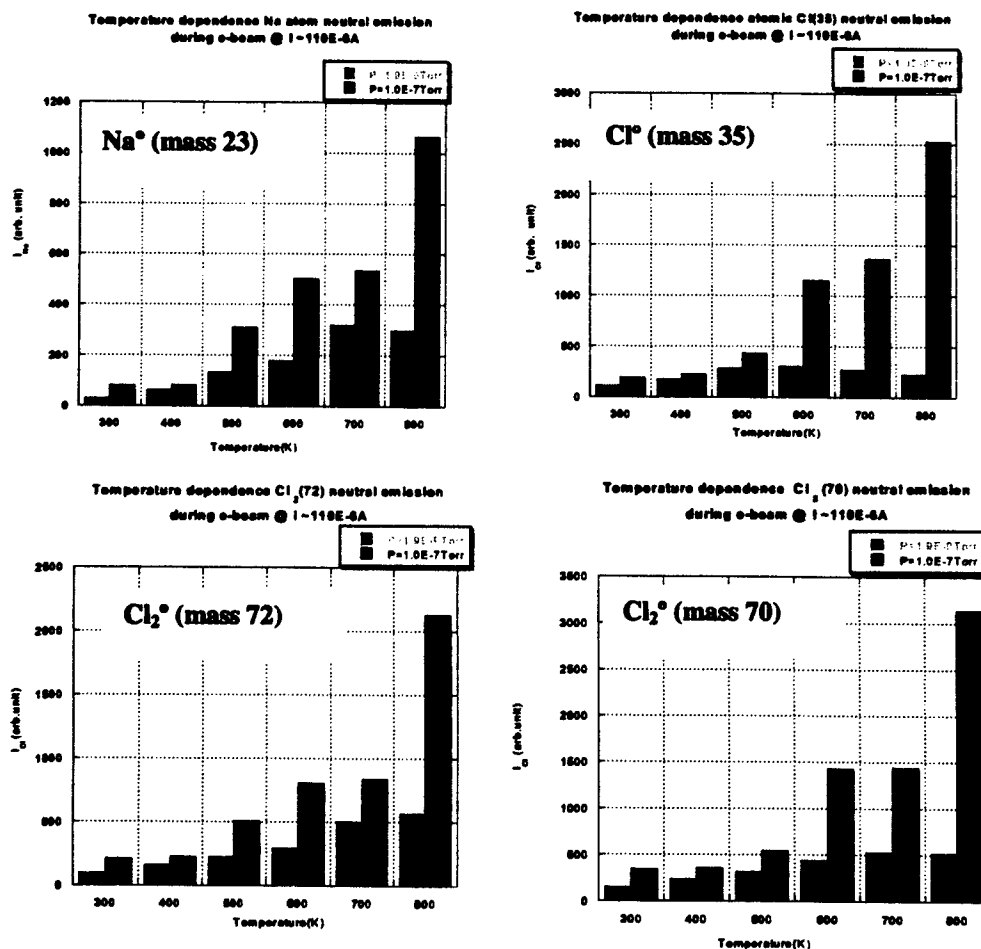


Fig. 7 The emission intensities of the neutral species seen from cleaved NaCl in  $\sim 10^{-7}$  Pa background and in  $10^{-5}$  Pa water vapor for temperatures ranging from 300–800 C. The presence of water can enhance the yields by as much as a factor of 6. The other isotope of chlorine (mass 36) shows similar results to mass 35.

**Adding Water Vapor to “Dry Crystals” Does it enhance radiation induced decomposition?** We now consider the influence of background water in the vapor phase during irradiation of two inorganic crystals not containing hydrated water, NaCl and NaNO<sub>3</sub>. During electron beam irradiation at 10<sup>-7</sup> Pa vs. 10<sup>-5</sup> Pa partial pressure H<sub>2</sub>O, significant increases in the ESD yields for these two materials was observed in the presence of water vapor. Because heating brushite was so effective in enhancing phosphate decomposition, we also varied the temperature of the crystals. From the temperature dependence we can use Arrhenius plots to determine an activation energy ( $E_a$ ), for each of the products. The fits are surprisingly consistent and yield the *same value for all of the products*, namely 0.075 ± 0.01 eV. Similar measurements of intensity, “wet” and “dry” and vs. temperature have been carried out for the e-beam products from NaNO<sub>3</sub> and for 248 nm laser irradiation of both NaCl and NaNO<sub>3</sub>. For illustration, in Fig. 8 we show the Arrhenius plots for the laser induced neutral emissions at 60 mJ/cm<sup>2</sup> fluence on NaCl—for all products and both wet and dry we obtain the same activation energy as with electrons: 0.075 eV. The NaNO<sub>3</sub> activation energies are also constant for all detected products and averages slightly higher than for NaCl, namely 0.09 eV ± 0.01 eV. We have been able to identify from the literature a process that corresponds to the measured  $E_a$  for NaCl, namely a thermally activated step in F-center formation. The latter consists of electronic excitation in the alkali halides in general and NaCl in particular has been especially well studied. (See Ref. [40] and references therein.) A self-trapped exciton at a Cl<sup>-</sup> site can decay to form an F-center/H-center pair (anion vacancy adjacent to a Cl<sub>2</sub><sup>-</sup> center) when the Cl<sup>•</sup> at the exciton site hops to a nearest neighbor Cl<sup>-</sup> site. This hop is thermally activated, with an activation energy of 0.07 eV—consistent with the 0.075 ± 0.01 eV activation energies observed here.

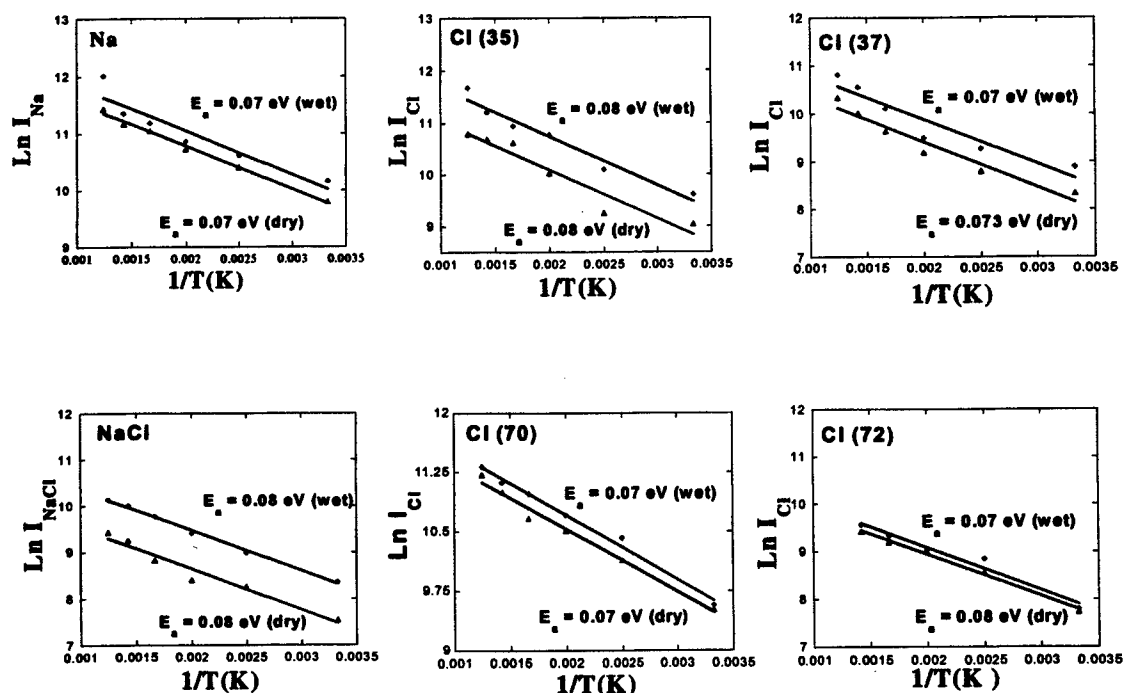


Fig. 8. Arrhenius Plots for the neutral species from 248 nm laser irradiated NaCl(100); Fluence was 60 mJ/cm<sup>2</sup>.

Finally, we show an example in Fig. 9 of the rich topography generated on NaNO<sub>3</sub> by extensive electron beam irradiation in a background of 10<sup>-5</sup> Pa water vapor. This surface is highly light absorbing due to its extremely high tortuosity (light cannot make it back out!). We call it our “stealth surface”. Even when gold coated, the measured reflectivity in the electron irradiated region is near zero from 500 nm down below 200 nm (see Fig. 10).

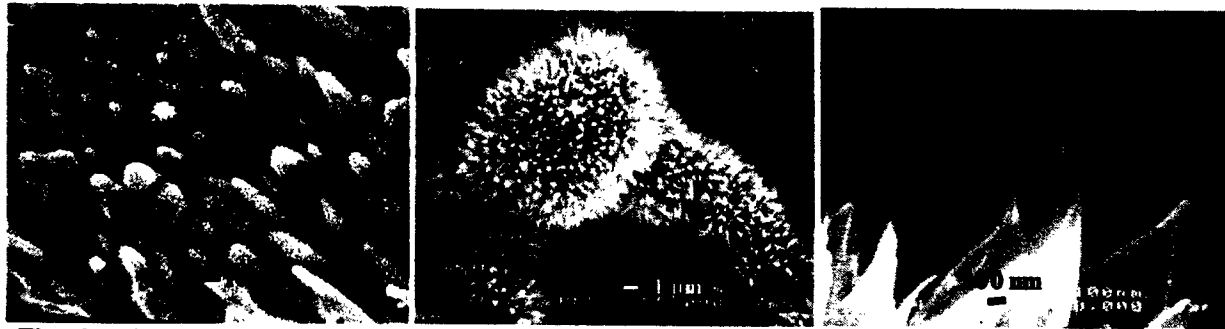
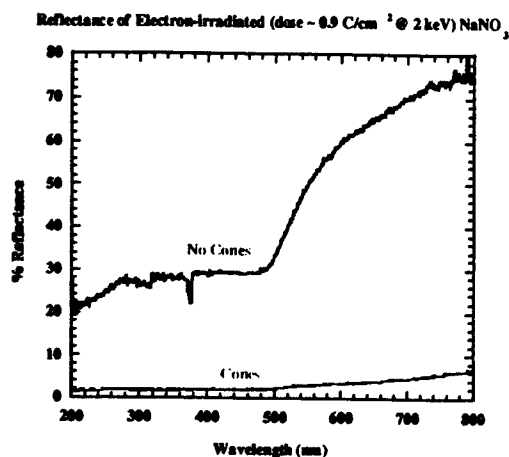


Fig. 9. SEM images of the e-beam irradiated  $\text{NaNO}_3$  surfaces showing the diverse structures generated by 2 keV electrons (dose  $\sim 0.9 \text{ C/cm}^2$ ) in  $2 \times 10^{-5} \text{ Pa}$  partial pressure of water vapor.



## White Light Image



— 1 mm

Fig. 10. Reflectivity vs. wavelength of the surface (gold coated) corresponding to the surfaces shown in Fig. 9. A white light image of the surface is shown also—the black spot is the e-beam irradiated region.

## 4. CONCLUSION

We have shown how systems containing water of hydration ( $\text{CaHPO}_4 \cdot 2\text{H}_2\text{O}$ ) or those with an affinity for water ( $\text{NaNO}_3$ ,  $\text{NaCl}$ ) result in unique interactions with electron and laser radiation. For brushite, the waters of hydration strongly influence the formation of voids via thermally induced segregation of water resulting in fracture of the lattice. These voids form incubators for effluorescence-driven recrystallization. Further e-beam irradiation leads to nanometer scale cone formation through extensive ESD driven erosion. "Dry" (non-hydrated) crystals with some affinity for water show dramatic increases in sensitivity to both e-beam and laser irradiation at relatively low ( $10^{-5} \text{ Pa}$ ) partial pressures of water vapor. Simultaneously heating the crystal enhances this process for both types of radiation and exhibits the same activation energies ( $E_a$ ) for all the products detected. In the case of  $\text{NaCl}$ , the value of 0.75 eV corresponds closely to the energy required for thermally assisted F Center formation. Structures observed on these non-hydrated crystals are noteworthy and span a size range from several microns down to a few nm. Accordingly, they form strong optical absorbers in the visible and near UV. We anticipate in general to observe interesting consequences from continued studies of combined exposure of surfaces to radiation and slightly aggressive chemicals.



## Acknowledgments

We thank Loren Cramer, WSU, for help in the laboratory and Wayne Hess, Pacific Northwest Laboratory and Richard Haglund, Vanderbilt University for helpful discussions. This work is supported by the U.S. Department of Energy under Grant DE-FG03-98ER14864 and by the National Science Foundation KDI Grant DMR-9980015.

## REFERENCES

1. J. T. Dickinson, L. C. Jensen, and M. L. Klakken, "Electron beam induced fracture of Kevlar single fibers," *J. Vac. Sci. Technol. A* **4**, 1501 (1986).
2. J. T. Dickinson, K. Tonyali, M. L. Klakken, and L. C. Jensen, "Crack Initiation and Crack Growth in Polymers Induced by Electron Bombardment," *J. Vac. Sci. Technol. A* **5**, 1076 (1987).
3. J. T. Dickinson, M. A. Loudiana, and A. Schmid, in *Adhesion, Sealants and Coatings for Space and Health Environments*, edited by L. H. Lee (Plenum Press, New York, 1987), p. 467-475.
4. M. Guardalben, A. Schmid, M. Loudiana, and J. T. Dickinson, "Photothermal analysis of synergistic radiation effects in ThF<sub>4</sub> optical thin films," *Phys. Rev. B* **35**, 4026 (1987).
5. S. C. Langford, J. T. Dickinson, and L. C. Jensen, "Simultaneous measurements of the electron and photon emission accompanying fracture of single-crystal MgO," *J. Appl. Phys.* **62**, 1437-1449 (1987).
6. M. A. Loudiana, J. T. Dickinson, A. Schmid, and E. J. Ashley, "Electron enhanced sorption of fluorine by silver surfaces," *Appl. Surf. Sci.* **28**, 311 (1987).
7. J. T. Dickinson, "Surface Interactions Relevant to Space Station Contamination Problems," Report No. 3002 (1988).
8. J. T. Dickinson, S. C. Langford, L. C. Jensen, P. A. Eschbach, L. R. Pederson, and D. R. Baer, "Consequences of simultaneous exposure of inorganic solids to excimer laser light and an electron beam," *J. Appl. Phys.* **68**, 1831-1836 (1990).
9. J. T. Dickinson, J.-J. Shin, and S. C. Langford, "Laser-induced emission of neutral atoms and molecules from electron-irradiated NaNO<sub>3</sub>," *Appl. Surf. Sci.* **96-98**, 326-331 (1996).
10. M. Dawes, S. C. Langford, and J. T. Dickinson, "Laser desorption of positive ions from a model hydrated inorganic crystal(CaHPO<sub>4</sub>·2H<sub>2</sub>O) by 248 nm irradiation," *Appl. Surf. Sci.* **127-129**, 81-87 (1998).
11. S. Nakahara, S. C. Langford, and J. T. Dickinson, "Surface force microscope observations of corrosive tribological wear on single crystal NaNO<sub>3</sub> exposed to moist air," *Tribology Lett.* **1**, 277-300 (1995).
12. N.-S. Park, M.-W. Kim, S. C. Langford, and J. T. Dickinson, "Tribological enhancement of CaCO<sub>3</sub> dissolution during scanning force microscopy," *Langmuir* **12**, 4599-4604 (1996).
13. R. F. Hariadi, S. C. Langford, and J. T. Dickinson, "Atomic force microscope observations of particle detachment from substrates: the role of water vapor in tribological debonding," *J. Appl. Phys.* **86**, 4885-4891 (1999).
14. L. Scudiero, S. C. Langford, and J. T. Dickinson, "Scanning force microscope observations of corrosive wear on single-crystal Brushite (CaHPO<sub>4</sub>·2H<sub>2</sub>O) in aqueous solution," *Tribology Lett.* **6**, 41-55 (1999).
15. M. J. Stirniman, C. Huang, R. S. Smith, S. A. Joyce, and B. D. Kay, "The Adsorption and desorption of water on single crystal Mg(100): The role of surface defects," *J. Chem. Phys.* **105**, 1295 (1996).
16. R. Schaub, P. Thostrup, N. Lopez, E. Lægsgaard, I. Stensgaard, J. K. Nørskov, and F. Besenbacher, "Oxygen Vacancies as Active Sites for Water Dissociation on Rutile TiO<sub>2</sub> (110)," *Phys. Rev. Lett.* **87**, 266104 (2001).

17. R. Z. LeGeros and J. P. LeGeros, "Brushite crystals grown by diffusion in silica gel and in solution," *J. Crystal Growth* **13/14**, 476-480 (1972).
18. C. Bandis, L. Scudiero, S. C. Langford, and J. T. Dickinson, "Photoelectron emission studies of cleaved and excimer laser irradiated single-crystal surfaces of  $\text{NaNO}_3$  and  $\text{NaNO}_2$ ," *Surf. Sci.* **442**, 413-419 (1999).
19. S. Aduru, S. Contarini, and J. W. Rabalais, "Electron-, x-ray-, and ion-stimulated decomposition of nitrate salts," *J. Phys. Chem.* **90**, 1683-1691 (1986).
20. H. Yamashita and R. Kato, "Vacuum ultraviolet absorption in alkali-nitrites and alkali-nitrates," *J. Phys. Soc. Jpn.* **29**, 1557-1561 (1970).
21. H. Yamashita, "Optical properties of sodium nitrate in the vacuum ultraviolet region," *J. Phys. Soc. Jpn.* **33**, 1407-1414 (1972).
22. M. Kamada and R. Kato, "Temperature dependence of UV absorptions in  $\text{KNO}_3$  and  $\text{NaNO}_3$ ," *J. Phys. Soc. Japan* **35**, 1561 (1973).
23. V. N. Voitsekhovskii, V. P. Nikolaeva, L. I. Venevtseva, and E. A. Sidorova, "Optical-quality sodium nitrate crystals grown from aqueous solution," *Sov. Phys. Crystallogr.* **30**, 360 (1985).
24. J. T. Dickinson, in *Experimental Methods in Physical Sciences; Vol. 30*, edited by J. C. Miller and R. F. Haglund (Academic Press, New York, 1998), p. 139-172.
25. J. T. Dickinson, S. C. Langford, J. J. Shin, and D. L. Doering, "Positive ion emission from excimer laser excited  $\text{MgO}$  surfaces," *Phys. Rev. Lett.* **73**, 2630-2633 (1994).
26. D. R. Ermer, J.-J. Shin, S. C. Langford, K. W. Hipps, and J. T. Dickinson, "Interaction of wide bandgap single crystals with 248 nm excimer laser radiation. IV. Positive ion emission from  $\text{MgO}$  and  $\text{NaNO}_3$ ," *J. Appl. Phys.* **80**, 6452-6466 (1996).
27. S. Kano, S. C. Langford, and J. T. Dickinson, "Interaction of wide band gap single crystals with 248 nm excimer laser irradiation. VIII. Laser desorption of molecular ions from  $\text{MgO}$ ," *J. Appl. Phys.* **89**, 2950-2957 (2001).
28. C. A. Beevers, "The crystal structure of dicalcium phosphate dihydrate:  $\text{CaHPO}_4 \cdot 2\text{H}_2\text{O}$ ," *Acta Cryst.* **11**, 273-277 (1958).
29. L. Backbier and J. Rousseau, "Analytical study of salt migration and efflorescence in a medieval cathedral," *Anal. Chim. Acta* **283**, 855-867 (1993).
30. L. T. Gibson, B. G. Cooksey, D. Littlejohn, and N. H. Tennent, "Characterisation of an unusual crystalline efflorescence on an Egyptian limestone relief," *Anal. Chim. Acta* **337**, 151-164 (1997).
31. E. Ordonez and J. Twilley, in *Anal. Chem.; Vol. 69* (1997), p. 416A-422A.
32. A. G. Verduch, V. Sanz, J. V. Agramunt, and V. Beltrán, "New method of assessing efflorescence," *Am. Ceram. Soc. Bull.* **75**, 60-64 (1996).
33. T. Vickers and M. Moukwa, "Evaluation of test methods and environmental conditions to promote efflorescence formation under laboratory conditions," *J. Testing Eval.* **24**, 80-83 (1996).
34. P. Zanetta and M. Facchini, "Local correlation of laser speckle applied to the study of salt efflorescence on stone surfaces," *Optics Commun.* **104**, 35-38 (1993).
35. J. T. Dickinson, S. C. Langford, C. Bandis, M. L. Dawes, and Y. Kawaguchi, "Consequences of combining laser irradiation with other stimuli on laser desorption and ablation from wide bandgap insulators," *Appl. Surf. Sci.* **154-155**, 291-304 (2000).
36. Y. Kawaguchi, M. L. Dawes, S. C. Langford, and J. T. Dickinson, "Effect of heat treatment on UV laser induced positive ion desorption in  $\text{CaHPO}_4 \cdot 2\text{H}_2\text{O}$ ," *Appl. Phys. A* **69**, S621-S624 (1999).
37. M. L. Knotek and P. J. Feibelman, "Ion desorption by core-hole auger decay," *Phys. Rev. Lett.* **40**, 964-967 (1978).
38. R. Gomer, in *Desorption Induced by Electronic Transitions DIET I*, edited by N. H. Tolk, M. M. Traum, J. C. Tully, and T. E. Madey (Springer-Verlag, Berlin, 1983), p. 40.
39. R. D. Ramsier and J. T. Yates, "Electron-stimulated desorption: Principles and applications," *Surf. Sci. Rep.* **12**, 246-378 (1991).
40. N. Itoh and M. Stoneham, *Materials Modification by Electronic Excitation* (Cambridge University, Cambridge, UK, 2000).

# Onset of laser ablation in $\text{CaF}_2$ crystal under excimer laser irradiation

Yoshizo Kawaguchi<sup>a,\*</sup>, Aiko Narazaki<sup>a</sup>, Tadatake Sato<sup>a</sup>, Hiroyuki Niino<sup>a</sup>, and Akira Yabe<sup>a</sup>

<sup>a</sup> Photoreaction Control Research Center (PCRC),  
National Institute of Advanced Industrial Science and Technology (AIST)  
Tsukuba Central 5, Higashi 1-1-1, Tsukuba, Ibaraki 305-8565, Japan

## ABSTRACT

With the widespread application of excimer lasers for micro-processing, optically transparent materials in the UV region have become more important as optical components. The transparent materials currently available commercially are silica glass and fluoride crystals,  $\text{CaF}_2$  and  $\text{MgF}_2$ . The resistance of these materials against cumulative irradiation of excimer lasers is required from the viewpoint of application, and it is important to clarify the mechanism of the optical damage on these materials. In this paper, we report the onset of laser ablation, that is, the initiation of optical breakdown and plume formation, in  $\text{CaF}_2$  crystal under cumulative irradiation of an ArF excimer laser. When the laser fluence is below the ablation threshold, a blue luminescence due to self-trapped exciton is observed from the whole laser-irradiated region. When the fluence is increased near the threshold, successive irradiation finally causes a bright, localized luminescence due to the initiation of laser ablation. SEM images of the laser-damaged region show two features: (1) a small bump with pits of the order of  $0.1\ \mu\text{m}$  formed by UV laser absorption and following local heating, (2) small cracks with triangular fragments caused by mechanical stress under local heating.

Keywords:  $\text{CaF}_2$ , laser ablation, optical breakdown, ArF excimer laser, defect

## 1. INTRODUCTION

UV lasers are widely applied to manufacturing processes in micron to sub-micron dimensions. In photolithography, because the resolution of the patterning is proportional to the wavelength of the light source, a light source with shorter wavelength is required. Now a KrF laser ( $\lambda = 248\ \text{nm}$ ) is utilized to a photolithography system, and the usage of an ArF laser ( $\lambda = 193\ \text{nm}$ ) and  $\text{F}_2$  laser ( $\lambda = 157\ \text{nm}$ ) is scheduled on the road map of the ULSI manufacturing processes. The importance of optical materials with high transmission at DUV and VUV wavelengths such as silica glass and fluoride crystals increases for optical components, a photo-mask and an illumination and projection lens optics. Though these optical materials have high transparency, they cannot avoid the optical damage by cumulative irradiation of UV laser beams when the laser fluence is even below the damage threshold, which is known as incubation effect.<sup>1</sup> In order to improve the resistance of optical components to UV laser irradiation, it is very important to investigate the interaction between the UV laser and optical materials and to clarify the mechanism of optical breakdown and the onset of laser ablation.<sup>1-17</sup>

In the previous papers, we investigated the optical breakdown of NaCl crystal<sup>2-3</sup> and silica glass<sup>6-7</sup> under irradiation of KrF laser beams. In this paper, the onset of optical breakdown and laser ablation on the surface of  $\text{CaF}_2$  single crystal with the irradiation of ArF laser beams is investigated. The bandgap of the  $\text{CaF}_2$  is 12.2 eV, and  $\text{CaF}_2$  shows high transparency in the DUV and VUV region. Optical components made of  $\text{CaF}_2$  are widely utilized with a combination of those of silica glass in the DUV region because two optical materials with different refractive indices are necessary to compensate for color aberration. Moreover,  $\text{CaF}_2$  is the most important optical material for  $\text{F}_2$  laser optics. Thus, the irradiation effect of UV and VUV beams on  $\text{CaF}_2$  has attracted much interest.<sup>8-14</sup>

---

\* Correspondence: E-mail: y-kawaguchi@aist.go.jp; Telephone: +81-298-61-4564; Fax: +81-298-61-4560.

## 2. EXPERIMENTAL

UV grade  $\text{CaF}_2$  crystals were obtained from Ohyo Koken Kogyo Co. The purity is 99.5 % and the nominal impurity contents observed by ICP mass spectroscopy are shown in Table 1. The (111) surfaces of the crystals were polished to the optical quality.

The experimental setup is shown in Fig. 1. Samples were mounted in room air for the optical experiment. A pulsed UV beam at  $\lambda = 193 \text{ nm}$  was generated with an ArF excimer laser (Lambda Physik Compex102) whose pulse width was 20 ns. The laser beam was passed through a variable attenuator (Showa Optonics V193-II) for controlling the pulse energy, and focused on the sample with a fused silica lens at an angle of about  $20^\circ$  relative to the sample normal. Because the laser beam was focused tight on the back surface of the transparent sample, optical breakdown and resulting laser ablation occurred from the back surface, and the luminescence was observed from the backside. A spot size of the laser beam was obtained by observing the burned pattern on the sample when the single laser pulse was irradiated with a fluence much higher than the ablation threshold.

Time-resolved luminescence spectra were measured with a gated image-intensified CCD camera (ICCD, Roper

Al	Ba	Fe	Mg	Sr
24	1	5	6	150

Table 1 Nominal impurity contents detected by ICP mass spectroscopy (in wt. ppm).

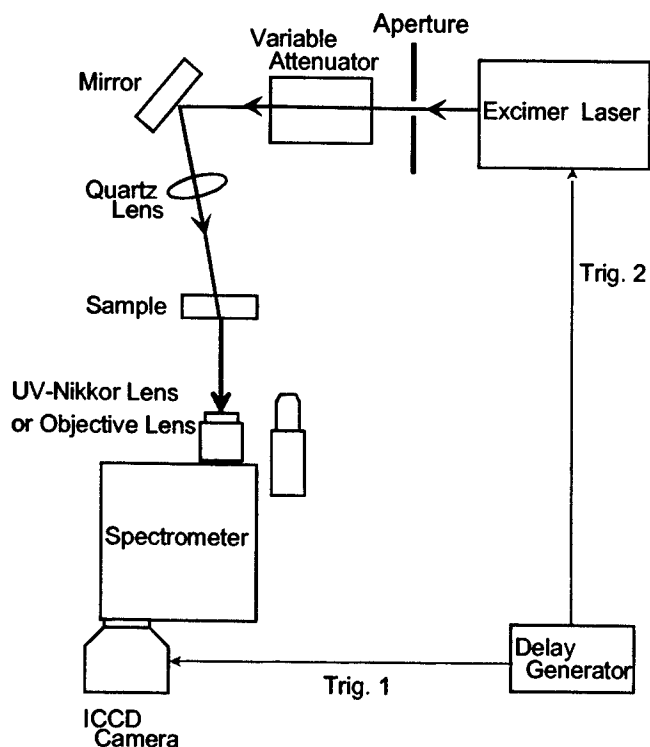


Fig. 1 Experimental setup.

Scientific IMAX-512-T) attached to a spectrometer (Acton SpectroPro 150,  $f = 15$  cm). The grating with 150 grooves  $\text{mm}^{-1}$  was used to acquire spectra with a wide wavelength range. The sensitivity of the acquisition system was not corrected. The emission was focused with an UV-Nikkor lens (Nikon) mounted in front of the entrance slit of the spectrometer. A delay generator (Stanford Research DG-535) was used to trigger the laser and the ICCD camera with an adjusted timing. For the measurement of luminescence images, the UV-Nikkor lens was replaced with an objective lens for higher magnification, and the image was acquired with the ICCD camera. The working distance was about 6 cm. After the laser experiment, the samples were Au coated and the laser-damaged regions were observed with a secondary electron microscope (SEM).

### 3. RESULTS AND DISCUSSION

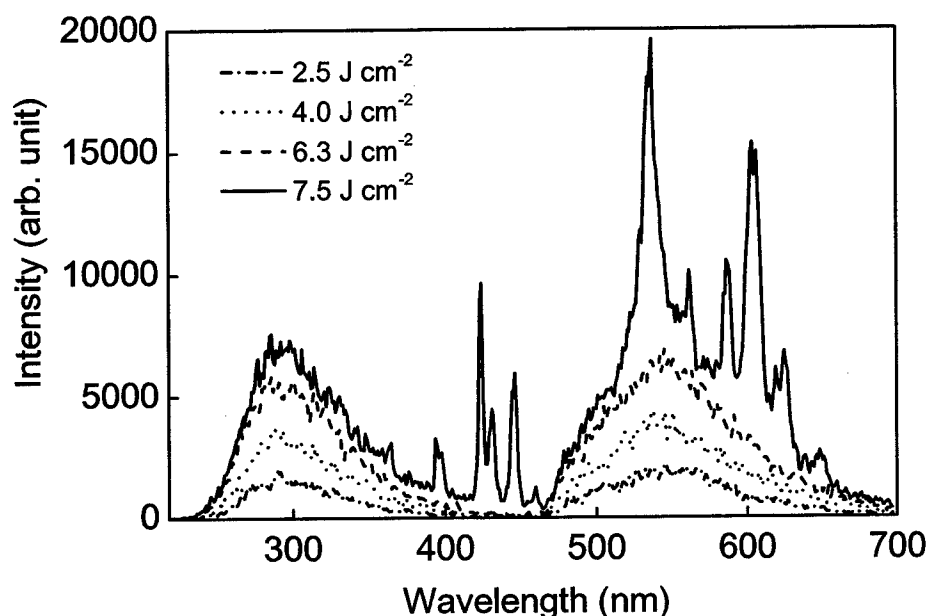


Fig. 2 Fluence dependence of luminescence spectra in  $\text{CaF}_2$  single crystal under ArF laser irradiation.

Figure 2 shows fluence dependence of luminescence spectra in  $\text{CaF}_2$  under irradiation of ArF laser pulses. The ICCD camera was triggered 50 ns after the rise of the laser pulse, and the acquisition time was set to 100 ns. When the fluence is below ablation threshold, a broad, blue emission band centered at 290 nm appears and grows with the increment of the fluence. Another broad, red emission band is an artifact, the second order line of the blue band. Time-resolved measurement shows that the blue band decayed in the order of microseconds. This emission band can be assigned to relaxation luminescence of the self-trapped exciton (STE).<sup>13, 14</sup> By band-to-band excitation, an electron-hole pair is created, and the strong interaction of the electron-hole pair results in the STE formation. Because the bandgap of  $\text{CaF}_2$  is 12.2 eV, at least two photons of  $\lambda = 193$  nm, *i. e.*  $h\nu = 6.4$  eV, are necessary for the band-to-band excitation and STE formation. The possibilities are (1) two-photon absorption and (2) defect-mediated two-step absorption. The blue emission band due to STE was not observed by KrF laser irradiation. This is because the photon energy of the KrF beam is 5.0 eV, and the energy of the two photons is still below the bandgap, 12.2 eV, and the efficiency of the three-photon process is negligibly small under nanosecond laser excitation.

When the fluence is increased above the threshold, a localized luminescence starts to be observed with the naked eye, and several sharp lines are overlapped to the broad STE emission band in the emission spectra, characteristic of a plasma associated with the surface optical breakdown.<sup>2, 3, 6, 7</sup> The sharp lines situated at 424, 431, 446, 459, 535, 560

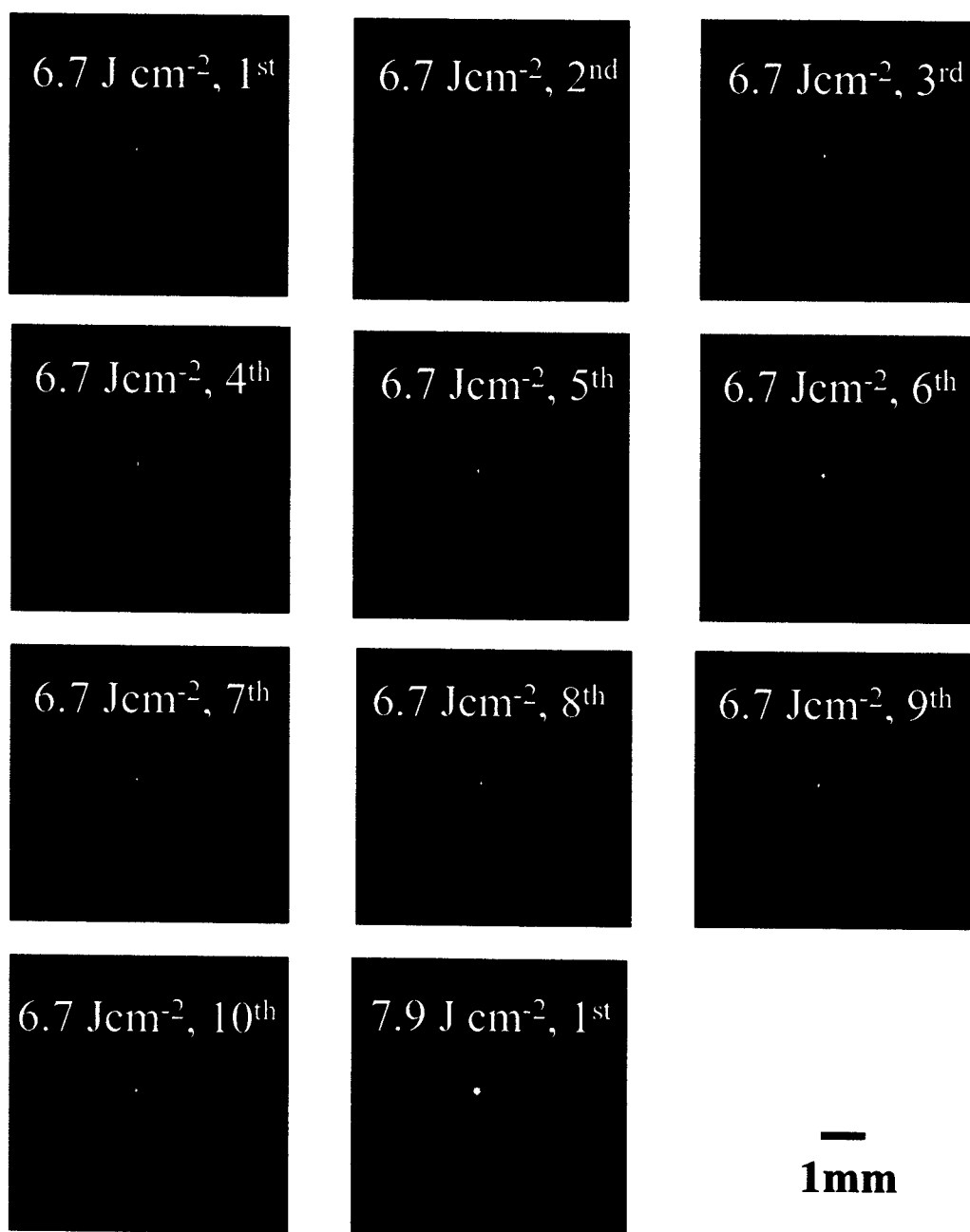


Fig. 3 Luminescence images of  $\text{CaF}_2$  by successive irradiation of ten ArF laser pulses at  $6.7 \text{ J cm}^{-2}$  and another pulse at  $7.9 \text{ J cm}^{-2}$ .

and  $647 \text{ nm}$  are assigned to the excited neutral Ca atom luminescence, and the line at  $624 \text{ nm}$  is due to excited neutral F atom.<sup>18</sup> These atomic lines are generated by the collisions between the electrons and ground state Ca and F atoms in the plume.<sup>15, 16</sup> The line luminescence intensity increases rapidly with the progress of the optical damage on the  $\text{CaF}_2$  surface. Time-resolved measurement shows that the line luminescence decays in the order of several microseconds, similar to the case of NaCl and silica glass. This means that the expansion and cooling of the plasma in  $\text{CaF}_2$  takes several microseconds in the atmospheric conditions.

Next, imaging of the luminescence under cumulative irradiation of the ArF laser pulses was executed. Up to ten laser pulses were irradiated, and luminescence image for each irradiation was acquired. Then, the fluence was increased and the same procedure was repeated until the optical breakdown was observed. The ICCD camera was triggered 100 ns after the rise of the laser pulse, and the acquisition time was set to 100 ns. The result is shown in Fig. 3. The image of the bulk luminescence, a blue emission due to STE is observed from the ArF-laser-irradiated region. Besides, when the fluence is increased to  $6.7 \text{ J cm}^{-2}$ , a localized luminescence due to plume appears on the first pulse, disappears on the second pulse, and reappears and continues from the third pulse. Appearance and disappearance of the localized luminescence was also observed in NaCl and silica glass under KrF laser irradiation,<sup>2, 3, 6, 7</sup> though the increase of the localized luminescence intensity by successive irradiation is much slower in  $\text{CaF}_2$  crystal. We attribute the localized luminescence to micro-plasmas formed when near-surface defective regions are strongly excited by the laser, and micro-plume formation apparently removes defective material and possibly reconstructs nearby atoms on the surface region, resulting in the depletion of the emitting sites. Further irradiation of one more laser pulse at  $7.9 \text{ J cm}^{-2}$  generates much brighter, localized emission due to plume, the onset of strong laser ablation. Figure 4 shows the SEM images of the laser-damaged region in Fig. 3 with different magnifications. There exist many fragments of several

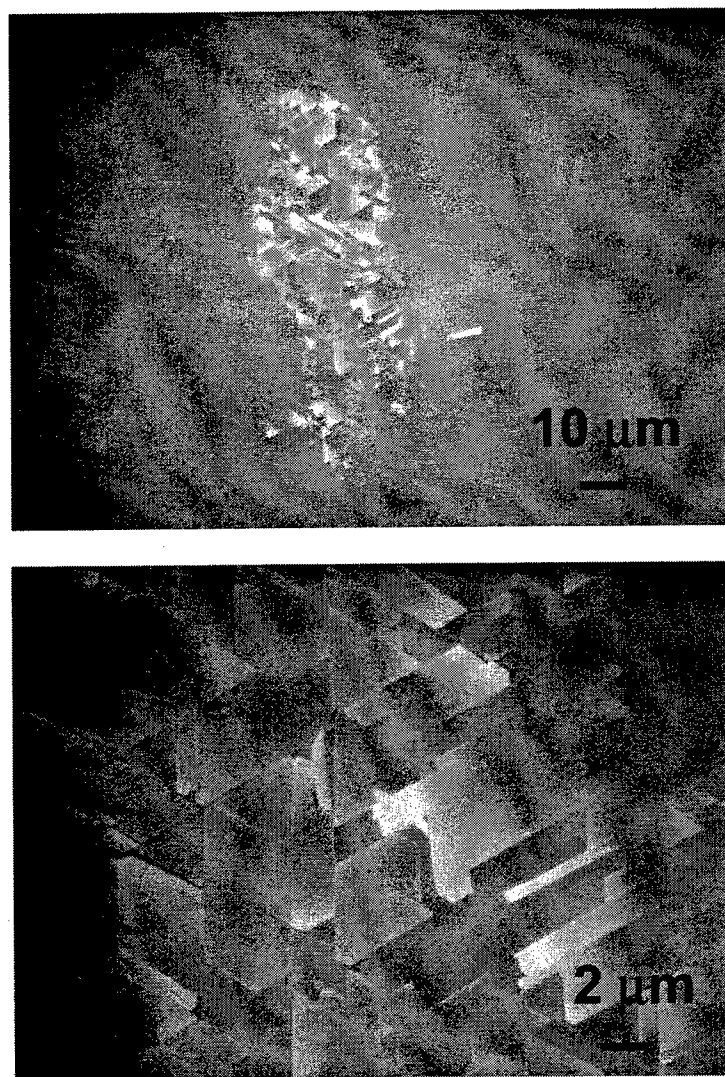


Fig. 4 SEM images of the laser-damaged region in Fig. 3.

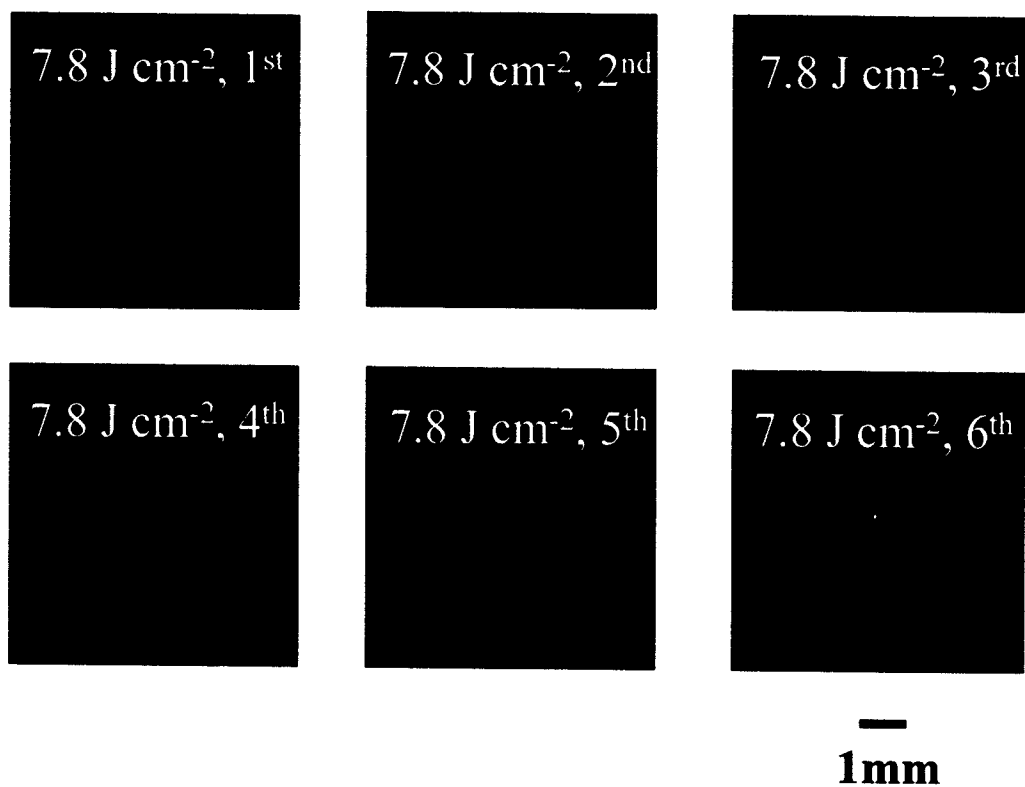


Fig. 5 Luminescence images of  $\text{CaF}_2$  by successive irradiation of six ArF laser pulses at  $7.8 \text{ J cm}^{-2}$ .

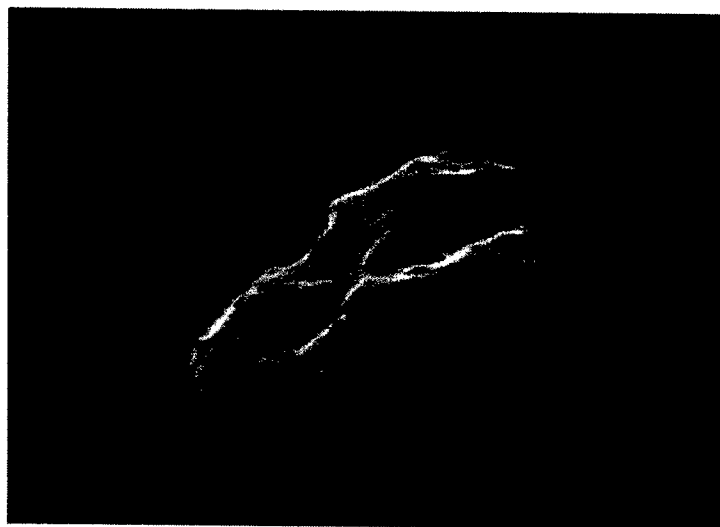


Fig. 6 SEM image of the laser-damaged region corresponding to localized luminescence in Fig. 5.

micrometers with a triangular shape. This structure was also observed when the  $\text{CaF}_2$  surface was severely damaged by successive irradiation of KrF laser pulses, and E. Matthias's group also reported the same structure on the damaged



surface by single-shot irradiation of KrF laser pulse with a fluence much higher than the damage threshold.<sup>9-11</sup> By UV laser absorption and following local heating, large mechanical stress is induced and causes fracture along the crystallographic axes, and the spallation of the surface layer occurs.

Figure 5 shows luminescence images acquired by sequential irradiation of six ArF laser pulses at  $7.8 \text{ J cm}^{-2}$ . On the sixth pulse, a localized luminescence due to micro-plume is observed. Figure 6 shows the SEM image of the laser-damaged region corresponding to the localized luminescence. Because no more irradiation was executed after the appearance of the first localized luminescence, the damage on the surface was not severe. A round bump of several micrometers with wrinkles is observed, and there are several small pits of the order of hundred nanometers around the bump. The former should be due to thermal expansion of the locally heated area by UV laser absorption, and the small pits should be caused by vaporization of particles near the surface region by local heating, similar to the case of silica glass under irradiation of KrF laser beams. The laser damage initiates with a small bump due to thermal expansion, and still further UV irradiation enhances thermal stress and finally causes fracture along the crystallographic axes, and resulting spallation of the surface layer as shown in Fig. 4.

#### 4. CONCLUSION

When a pulsed beam of the ArF excimer laser is irradiated cumulatively to a polished (111) surface of  $\text{CaF}_2$  single crystal, in addition to a blue photoluminescence due to relaxation of the STE, a localized luminescence due to laser ablation in the surface region occurs. The localized luminescence shows line spectra of Ca and F atoms, excited by collision with electrons in the plume. At the onset of optical breakdown on the surface, the laser-damaged surface shows a small bump with several pits of the order of  $0.1 \text{ }\mu\text{m}$ , reflecting the effect of local heating by UV laser absorption. In case of severe damage with successive irradiation after the onset of optical breakdown, a large damaged area is observed with many triangular fragments of several micrometers, caused by the mechanical stress and spallation of the surface layer by local heating.

#### ACKNOWLEDGMENT

We are deeply indebted to Ryozo Kurosaki of AIST for his help in SEM observation.

#### REFERENCES

1. R. W. Webb, L. C. Jensen, S. C. Langford, and J. T. Dickinson, "Interactions of wide band-gap single crystals with 248 nm excimer laser radiation. I.  $\text{MgO}$ ", *J. Appl. Phys.* **74**, pp. 2323-2337, 1987.
2. J. T. Dickinson, Y. Kawaguchi, M. L. Dawes, and S. C. Langford, "Onset of laser plume formation at 248 nm on cleaved single crystal  $\text{NaCl}$ : Evidence for highly localized emissions", *Proc. of SPIE* **3935**, pp. 38-46, 2000.
3. Y. Kawaguchi, M. L. Dawes, S. C. Langford, and J. T. Dickinson, "Interaction of wide bandgap single crystals with 248 nm excimer laser irradiation. VII. Localized plasma formation on  $\text{NaCl}$  single crystal surfaces", *J. Appl. Phys.* **89**, pp. 2370-2378, 2001.
4. K. Yoshida, H. Yoshida, T. Kamimura, and N. Kuzuu, "Laser-induced bulk damage of various types of silica glasses with fundamental and higher harmonics of Nd:YAG laser", *Jpn. J. Appl. Phys.* **37**, pp. 1882-1883, 1998.
5. N. Kuzuu, K. Yoshida, H. Yoshida, T. Kamimura, and N. Kamisugi, "Laser-induced bulk damage in various types of vitreous silica at 1024, 532, 355, and 266 nm: evidence of different damage mechanisms between 266-nm and longer wavelengths", *Appl. Opt.* **38**, pp. 2510-2515, 1999.
6. Y. Kawaguchi, S. C. Langford and J. T. Dickinson, "Plume formation and optical breakdown on KrF excimer laser irradiated silica glass, *Proc. of SPIE* **4274**, pp. 258-265 2001.

7. Y. Kawaguchi, A. Narazaki, T. Sato, H. Niino, A. Yabe, S. C. Langford, J. T. Dickinson: The onset of optical breakdown in KrF-laser-irradiated silica glass (submitted to *Appl. Surf. Sci.*).
8. J. Reif, S. Petzoldt, A. P. Elg, and E. Matthias, "The role of defects in laser surface damage thresholds of fluoride crystals", *Appl. Phys. A* **49**, pp. 199-204, 1989.
9. H. Johansen, S. Gogoll, E. Stenzel, M. Reichling, and E. Matthias, "SEM-analysis of fracture features formed in excimer-laser induced surface damage in  $\text{CaF}_2$ ", *Radiat. Effects and Defects Solids* **139**, pp. 151-156, 1995.
10. S. Gogoll, E. Stenzel, M. Reichling, H. Johansen, and E. Matthias, "Laser damage of  $\text{CaF}_2$  (111) surfaces at 248 nm", *Appl. Surf. Sci.* **96-98**, pp. 332-340, 1996.
11. M. Reichling, J. Sils, H. Johansen, and E. Matthias, "Nanosecond UV laser damage and ablation from fluoride crystals polished by different techniques", *Appl. Phys. A* **69**, pp. S743-S747 (1999).
12. M. Mizoguchi, H. Hosono, H. Kawazoe, and T. Ogawa, "Generation of optical absorption bands in  $\text{CaF}_2$  single crystals by ArF excimer laser irradiation: Effect of yttrium impurity", *J. Vac. Sci. Technol. A* **16**, pp. 3052-3057, 1998.
13. M. Mizoguchi, H. Hosono, H. Kawazoe, and T. Ogawa, "Time-resolved photoluminescence for diagnosis of resistance to ArF excimer laser damage to  $\text{CaF}_2$  single crystals", *J. Opt. Soc. Am. B* **16**, pp. 1153-1159, 1999.
14. V. Denks, A. Maaroos, V. Nagirnyi, T. Savikhina, and V. Vassiltsenko, "Excitonic processes in pure and doped  $\text{CaF}_2$ ", *J. Phys. Condens. Matter* **11**, pp. 3115-3125 (1999).
15. D. R. Elmer, S. C. Langford, and J. T. Dickinson, "Interaction of wide band gap single crystals with 248 nm excimer laser radiation. V. The role of photoelectronic processes in the formation of a fluorescent plume from  $\text{MgO}$ ", *J. Appl. Phys.* **81**, pp. 1495-1504, 1997.
16. J. T. Dickinson, D. R. Elmer, J.-J. Shin, and S. C. Langford, "Mechanisms of laser desorption of positive ions and plume formation on ionic crystals", *Appl. Surf. Sci.* **127-129**, pp. 7-20, 1998.
17. J. T. Dickinson, L. C. Jensen, R. L. Webb, M. L. Dawes, and S. C. Langford, "Interactions of wide band gap single crystals with 248 nm excimer laser radiation. III. The role of cleavage-induced defects in  $\text{MgO}$ ", *J. Appl. Phys.* **74**, pp. 3758-3767, 1993.
18. D. R. Lide, *CRC Handbook of Chemistry and Physics*, 81th ed. (CRC Press, Washington, D. C., 2000)

# Diagnostics of nanoparticle formation process by laser ablation in a background gas

Tatsuo Okada, Yoshiki Nakata, Mitsuo Maeda  
Kyushu University, Faculty of Information Science and Electrical Engineering,  
Fukuoka 812-8581, Japan

## ABSTRACT

We have developed a new visualization technique named as re-decomposition laser-induced fluorescence (ReD-LIF), in order to investigate the dynamics of clusters, which are difficult to be visualized by any other means. In the ReD-LIF technique, clusters or nano-particles synthesized in the laser ablation plume are decomposed by laser irradiation and the atoms generated by the decomposition are visualized by LIF. This technique is very sensitive than the other visualization technique, because we can use the sensitive LIF technique. Decomposition of nano-particles by the laser irradiation is considered theoretically and the characteristics of ReD-LIF technique are compared with other visualization techniques such as laser-induced fluorescence (LIF) and Rayleigh scattering. The ReD-LIF technique has been applied for the visualization of the Si nano-particle synthesis process. Based on the results, the particle dynamics in the ablation plume generated in the background gas during Si nano-particle synthesis are described besides the basic characteristics of the ReD-LIF signal.

**Keywords:** Nano-particles, laser ablation, imaging, decomposition, laser-induced fluorescence, Rayleigh scattering

## 1. INTRODUCTION

Laser ablation in a background gas has been widely used to synthesize the nanoparticle [1,2] and nano-composite thin films [3,4]. In order to understand the synthesis process of the nano-particles, the particle dynamics in the laser ablation plume has been extensively studied experimentally or theoretically. Muramoto et al. applied imaging spectroscopic techniques based on laser-induced fluorescence (LIF) and Rayleigh scattering (RS) for the visualization of the particle behavior in the ablation plume during Si nano particle synthesis. They found that Si atoms started to disappear in the central part of the plume 0.1-0.2 ms after ablation in 10 Torr He and the Si dimmers were observed at the same stage [6,7]. Murakami et al. tried to detect Si nanoparticles by X-ray absorption spectroscopy [8]. More recently Geohegan et al. applied photoluminescence technique (PL) to image Si nanoparticles that were synthesized and suspended in the plume [9]. They found as reported by Muramoto et al. that on-set times for nanoparticle formation after pulsed laser ablation were 0.15-0.2 ms in 10 Torr He and 3 ms in 1 Torr Ar. Makimura et al. also observed the growing Si nanoparticles in time period of 0.6-1.0 ms after ablation by a newly developed plasma emission from laser-decomposed nanoparticles [10].

On the other hand, Luk'yanchuk and Marine claimed based on a theoretical consideration that the nanoparticles are formed around a few  $\mu$ s after ablation [11], and pointed out the limitations in the measurements of small nanoparticles in the earlier stage of the condensation. For instance, RS is not so sensitive to detect the nanoparticles of less than 1 nm in diameter, because the RS signal depends on the 6<sup>th</sup> power of the diameter. Therefore, the on-set time for nanoparticle formation can not be discussed based on RS data. Thus, there are two or three orders of discrepancy in the on-set time for nanoparticle formation after laser ablation in a background gas. In order to clarify the onset of the clustering, it is essential to develop a new sensitive method which can detect the onset of the clustering.

In this paper, we describe the development of a new imaging technique, named as ReD-LIF (Re-Decomposition laser-induced fluorescence), for the visualization of nanoparticles (hereafter we call them as clusters), which are difficult to be visualized by RS and LIF. First, we consider the response of the nano-particles irradiated by a laser beam and estimate the laser energy required for the decomposition of the particles, then the ReD-LIF technique has been applied to the diagnostics of the formation process of Si nanoparticles and the results are compared with the previous LIF and RS results. The particle dynamics during nanoparticle formation under various conditions are discussed based on the imaging ReD-LIF diagnostics.

## 2. REDECOMPOSITION LASER-INDUCED FLUORESCENCE

A new imaging technique for clusters, named as re-decomposition LIF (ReD-LIF), has been developed. In Red-LIF, clusters formed in the ablation plume are re-decomposed by a laser beam, and then the atoms generated by the re-decomposition of the clusters are visualized by an imaging LIF technique. That is, the spatial distributions of clusters are visualized by imaging those atoms that are generated from clusters. In this section, we consider the detection of clusters or nano-particles by various methods.

### 2.1 Decomposition of particles

When the particles with diameter of  $d_p$  are irradiated by a laser beam, the following relationship can be established based on the energy conservation [12].

$$\sigma_a I(t) - \pi d_p^2 \Lambda (T - T_0) - \frac{(\Delta H)}{M} \frac{dm}{dt} + \pi d_p^2 \int \Phi(\lambda) M(T, \lambda) d\lambda + \frac{\pi d_p^3}{6} \rho C_t \frac{dT}{dt} \quad (1)$$

$\sigma_a$  is the absorption cross section of the particles and  $I(t)$  is the pulse shape of the power flux of the laser beam. The left hand side of Eq. (1) stands for the heating of the particle by the laser beam. The first term in the right hand side of Eq. (1) is the cooling by the thermal conduction to the surrounding gas, the second term is the loss due to the melting and evaporation, the third term is the radiation cooling by the black body radiation and the fourth term is the heating of the particle itself.  $\Lambda$  is the generalized thermal conduction constant.  $T$  and  $T_0$  are the temperatures of the particle and the surrounding gas, respectively.  $\Delta H$  is the specific energy for evaporation and melting.  $M$  is the molecular weight,  $dm/dt$  is the decrease of mass by evaporation,  $\Phi(\lambda)$  is the emissivity,  $M(T, \lambda)$  is the irradiance of the black body radiation,  $\rho$  and  $C_t$  are the density and the specific heat, respectively.

From eq. (1), we can estimate an laser energy  $E_v$  which is required to completely vaporize the particle, assuming that the heat conduction and the thermal radiation can be neglected during the vaporization process. Since  $dm/dt = \pi d_p^3 / 6$ ,  $E_v$  is given by

$$E_v \geq \frac{\pi d_p^3 \rho}{6 \sigma_a} \left\{ C(T_v - T_0) + \frac{\Delta H}{M} \right\} \quad (2)$$

$\sigma_a$  is approximately given by

$$\sigma_a = \frac{\pi^2 d_p^3}{\lambda_l \ell} \ln \left[ \frac{n^2 - 1}{n^2 + 2} \right] \quad (3)$$

where  $\lambda_l$  is the wavelength of the laser beam and  $n$  is the complex refractive index [13]. Inserting the numerical constants for Si in Eqs. (2) and (3), we obtain  $E_v \approx 30 \text{ mJ/cm}^2$  and independent of the diameter in our present rough estimation. For the smaller clusters of less than 10 nm in diameter, however, melting and vaporization temperatures decrease as the particle becomes smaller [14,15]. Therefore, less energy may be sufficient for those particles compared to that given Eq. (2).

### 2.2 Evaluation of signals for particle

Next let's evaluate the signal intensities which are expected for the different detection schemes. The detection schemes used widely for nano-particle measurements are the Rayleigh scattering and the laser-induced incandescence (LII). In the Rayleigh scattering, the total scattering energy is proportional to  $\sigma_s N_p E_0$ , where  $\sigma_s$  is the scattering cross section,  $N_p$  is the number density of the nano-particles and  $E_0$  is the energy flux of the probe laser.  $\sigma_s$  is simplified as [13]

$$\sigma_s = \frac{2}{3} \frac{\pi^5 d_p^6}{\lambda} \left| \frac{n^2 - 1}{n^2 + 1} \right|^2 \quad (4)$$

In the case of laser ablation, furthermore, the total density of atoms which builds up the nano-particle is kept constant. Therefore, the following relation can be derived for the atomic number density and the particle number density. That is

$$N_p = \frac{N}{n} = \frac{6MN}{\pi \rho N_A d_p^3} \quad (5)$$

where  $N$  is the atomic number density,  $N_A$  is Avogadro number and  $n$  is the number of atoms which are contained in the particle. Thus the Rayleigh signal intensity  $\Phi_R$  is proportional to the following equation, in neglecting the spatial distribution of the scattered light.

$$\Phi_R = \frac{4\pi^4 d_p^3 M N E_0}{\lambda^4 N_A \rho} \left| \frac{n^2 - 1}{n^2 + 2} \right|^2 \quad (6)$$

In order to evaluate the LII signal, the temporal change of the particle temperature should be analyzed based on Eq. (1). However, we simply analyze the upper most value of the ILL signal. The total black body radiation power  $\Phi_{ILL}$  is given by

$$\Phi_{ILL} = \varepsilon \sigma_{SB} T^4 \pi d_p^2 \Delta t = \varepsilon \sigma_{SB} \frac{1}{C^4} \left( \frac{6E_0 \sigma_a}{\pi d_p^3 \rho} - \frac{\Delta H}{M} \right) 4\pi d_p^2 \Delta t \quad (7)$$

where  $\varepsilon$  is the emissivity of the particle and is approximated by  $4\sigma_s/\pi d_p^2$ ,  $\sigma_{SB}$  is the Stephan-Boltzmann constant,  $T$  is the peak temperature which is obtained from Eq. (2) and  $\Delta t$  is the observation time period. As mentioned above, eq. (7) gives the upper most value, since only the limited band width is observed and time averaged temperature is lower than that used in Eq. (7).

In ReD-LIF, on the other hand, the total signal is equal to that of laser-induced fluorescence from the atomic density of  $N$ , assuming the particles are fully decomposed. Under saturated excitation condition for LIF, the total fluorescence signal  $\Phi_F$  is simply given by

$$\Phi_F = f N h \nu / 2 \quad (8)$$

Where  $f$  is the fraction of the atomic number density in the lower energy sub-level  $h\nu$  is the photon energy at the observation wavelength. We assumed that half of the atoms in the sub-level are excited due to the saturated excitation. Eqs. (6), (7) and (8) were evaluated using the physical parameters of Si and  $E_0 = 30 \text{ mJ/cm}^2$ .

The results are summarized in Fig. 1. ReD-LIF signal is basically independent of the particle size under full decomposition. ILL signal is also independent of the particle size under the present simplified model and a constant probe laser fluence. Rayleigh scattered signal is proportional to the third power of the particle diameter. The scattering cross section itself is proportional to the six power of the diameter as shown in Eq. (4), but the present result is due to the constriction that the number of atoms is kept constant. Thus ReD-LIF signal is the most sensitive method, especially for smaller particles.

### 3. DETECTION OF PARTICLE BY RED-LIF

#### 3.1 Experimental setup

The experimental setup used for a ReD-LIF imaging of laser ablation plume is depicted in Fig. 2 and almost similar to that of LIF and RS imagings [6,7]. In this study, a Si wafer was ablated by a KrF laser in a variety of background gases.

In the case of LIF imaging, the generated Si atoms were excited via the  $3p^3P_1 - 4s^3P_2$  transition at 250.69 nm with a sheeted probe laser beam, which was delivered from a frequency-doubled optical parametric oscillator (OPO). The fluorescence from the excited Si atoms was captured by an image-intensified and time-gated CCD camera and stored in a computer. Using the same setup as LIF imaging, Rayleigh scattered image from nanoparticles were observable.

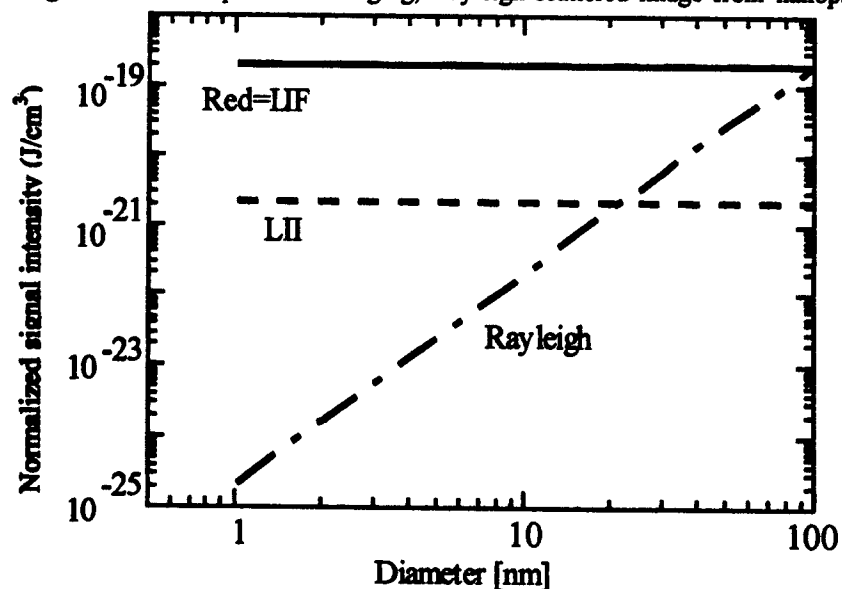


Fig. 1 Signal level from different detection schemes of ReD-LIF, Rayleigh scattering and laser induced incandescence.

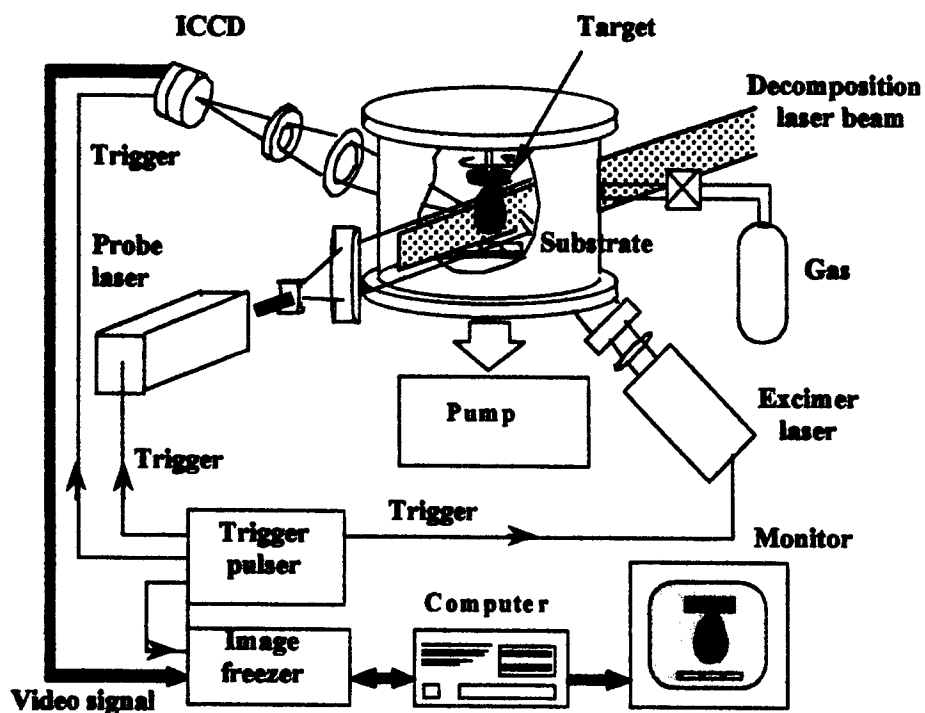


Fig. 2 Experimental setup for ReD-LIF imaging.

The time evolutions of Si atomic plume and nanoparticles were measured by changing the delay time between the KrF laser and the OPO laser.

In the case of ReD-LIF, the plume was irradiated by a sheeted decomposition laser beam from a XeCl laser and the Si atoms generated by the decomposition of clusters were detected by a photo-multiplier tube or visualized by the LIF imaging system as described above. It was confirmed that the time delay between the decomposition and the LIF imaging was less than 10  $\mu$ s, the spatial distribution of visualized Si atoms was equivalent to that of clusters [16]. The temporal behavior of clusters was observed by changing the delay time between the KrF laser for ablation and the XeCl laser for decomposition, while keeping the delay time between the XeCl laser and OPO laser for LIF at 10  $\mu$ s.

### 3.2 Detection of nano-particles by ReD-LIF

Red-LIF signals were measured as a function of decomposition laser fluence, as shown in Fig. 3. In this case, Si nano-particles formed in a He background gas at 10 Torr was decomposed by a XeCl excimer laser beam 1 ms after ablation and the generated Si atoms were detected by LIF. Under these experimental conditions, nano-particles could also be detected by Rayleigh scattering caused by the probe laser beam for LIF. The Rayleigh signal level is indicated in Fig. 3 as a dotted line. When the fluence of the decomposition laser was below 10  $\text{mJ}/\text{cm}^2$ , only the Rayleigh scattered signal was observed. The ReD-LIF signal became observable when the fluence of the decomposition laser increased above 10  $\text{mJ}/\text{cm}^2$ . Above 200  $\text{mJ}/\text{cm}^2$ , the ReD-LIF signal was tending to saturate, indicating that the nano-particles were fully decomposed. Although this value is larger than the value of 30 mJ as estimated in Sec. 2.1, this may be because of the thermal loss term of the heat conduction that was neglected in eq. (2).

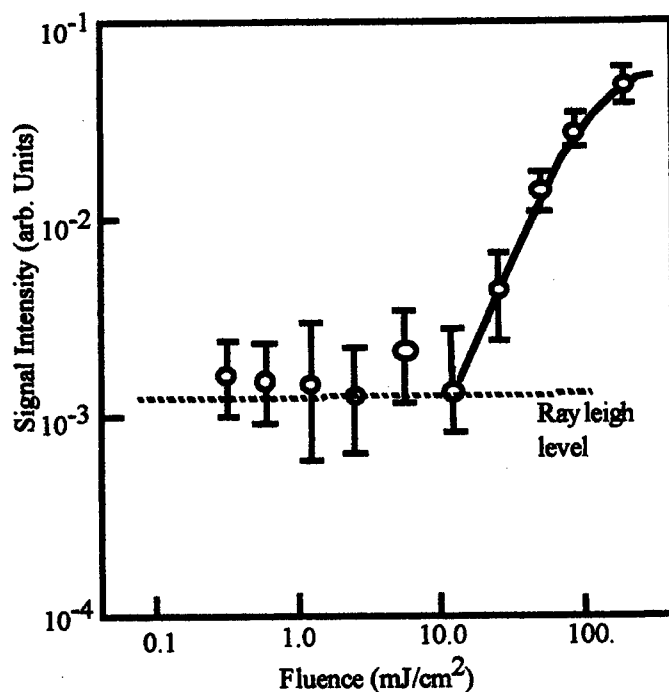


Fig. 3 ReD-LIF signals as a function of the fluence of the decomposition laser.

### 3. Imaging ReD-LIF

In order to demonstrate the ability of the ReD-LIF technique, the initial stage of the condensation of Si atoms in the laser ablation plume was visualized by the conventional LIF and the newly developed ReD-LIF techniques. The ablation was performed in a He background gas at 10 Torr. Spatial distributions of Si atoms and clusters at different moments after ablation were visualized by LIF in Fig. 4 (a) and by ReD-LIF in Fig. 4 (b). In each picture, the Si target

was placed at the top and the KrF excimer laser hit the target from the downward. The scales on the left-hand side indicate the distance from the target surface. The numbers shown in pictures indicate the time after ablation in seconds when LIF imaging or the decomposition was performed. In Fig. 4, images from 20  $\mu$ s to 300  $\mu$ s after ablation are presented. During this time stage, the shock propagation is already finished and the diffusion is dominant.

In LIF images, it can be seen that Si started to disappear around 200  $\mu$ s after ablation in central part of the plume and also near the target surface. This dark hole grew gradually with time and spread over whole plume. At 1.3 ms after ablation, Si atoms almost disappeared and the Rayleigh scattered images of well-grown nano-particles became observable, as already reported in [4]. In ReD-LIF images, similar images as observed by LIF were observed until 240  $\mu$ s after ablation. However, at 250  $\mu$ s after ablation, Si atoms generated by decomposition became observable in the dark hole where Si disappeared in LIF images, indicating the presence of clusters. Signals from the decomposed Si atoms became strong, clearly indicating the growth of clusters. It has been clearly demonstrated that the ReD-LIF

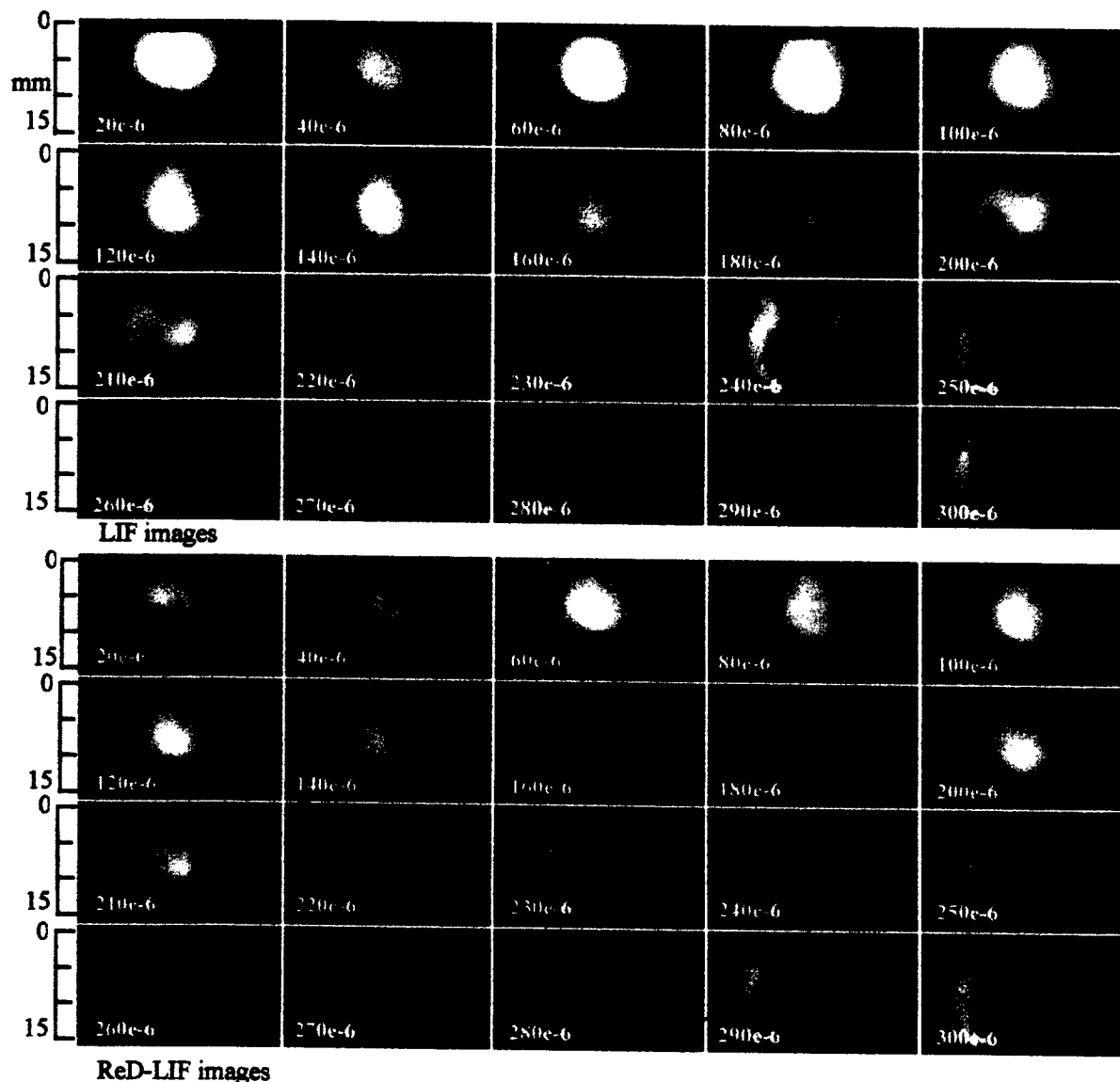


Fig. 4 LIF imaging (upper) and ReD-LIF imaging (lower) of Si plume in 10 Torr He. It can be seen in LIF images that Si started to disappear around 200  $\mu$ s after ablation in central part of the plume. In ReD-LIF images Si atoms generated by decomposition can be observed in the hole where Si disappeared in LIF images, indicating the presence of clusters.



technique can visualize the small nano-particles which could not be visualized by any other method.

It is very interesting to know how small clusters can be visualized by the ReD-LIF imaging. Unfortunately, we have no direct experimental result. According to the previous experimental results, where  $\text{Si}_2$  molecules produced by the clustering of Si atoms were detected under similar experimental conditions,  $\text{Si}_2$  density started to increase around 200  $\mu\text{s}$  after ablation. After it was peaked at 260  $\mu\text{s}$  after ablation,  $\text{Si}_2$  signal rapidly decreased within 30  $\mu\text{s}$  and almost disappeared 300  $\mu\text{s}$  after ablation. This indicates that  $\text{Si}_2$  molecules are converted into larger Si-containing molecules by the cascaded clustering reaction with a growth time of several tens of microseconds. In Figs. 4 (a) and (b), Si atoms started to decrease 200  $\mu\text{s}$  after ablation and this is well corresponding to the time history of the appearance of  $\text{Si}_2$  molecules. In ReD-LIF, on the other hand, no difference was observed compared with LIF images until the clusters became observable at 250  $\mu\text{s}$  after ablation. Therefore, it is obvious that ReD-LIF can not visualize  $\text{Si}_2$  molecules, but can visualize the molecules produced by the cascaded clustering of  $\text{Si}_2$ , those may be produced by  $\text{Si} + \text{Si}_2 + \text{M} \rightarrow \text{Si}_3 + \text{M}$  or  $\text{Si}_2 + \text{Si}_2 + \text{M} \rightarrow \text{Si}_4 + \text{M}$  where M is the third collision partner. The reason why ReD-LIF cannot detect  $\text{Si}_2$  molecules is as follows. The resonance absorption line of  $\text{Si}_2$  molecules is too sharp to be accidentally excited by the XeCl laser which was used to decompose the clusters in the present experiment. However, the absorption line of  $\text{Si}_3$  is already diffusive so that it became possible to excite the clusters accidentally by the XeCl laser. Furthermore the absorption spectra were almost continuum in the visible and ultra-violet spectral regions for  $\text{Si}_n$  ( $n > 21$ ) [17]. In conclusion, we believe that ReD-LIF with a XeCl laser as a decomposition laser could visualize the Si containing molecules of larger than  $\text{Si}_3$  or  $\text{Si}_4$ .

## 5. APPLICATION OF RED-LIF

Using the ReD-LIF technique, we can observe the clusters in the laser ablation plume from an initial stage of clustering. In this section, the initial stage of the clustering process in different background gas is visualized by ReD-LIF. Figure 5 shows the temporal behavior of the Si ablation plume in an Ar background gas of 10 Torr. The

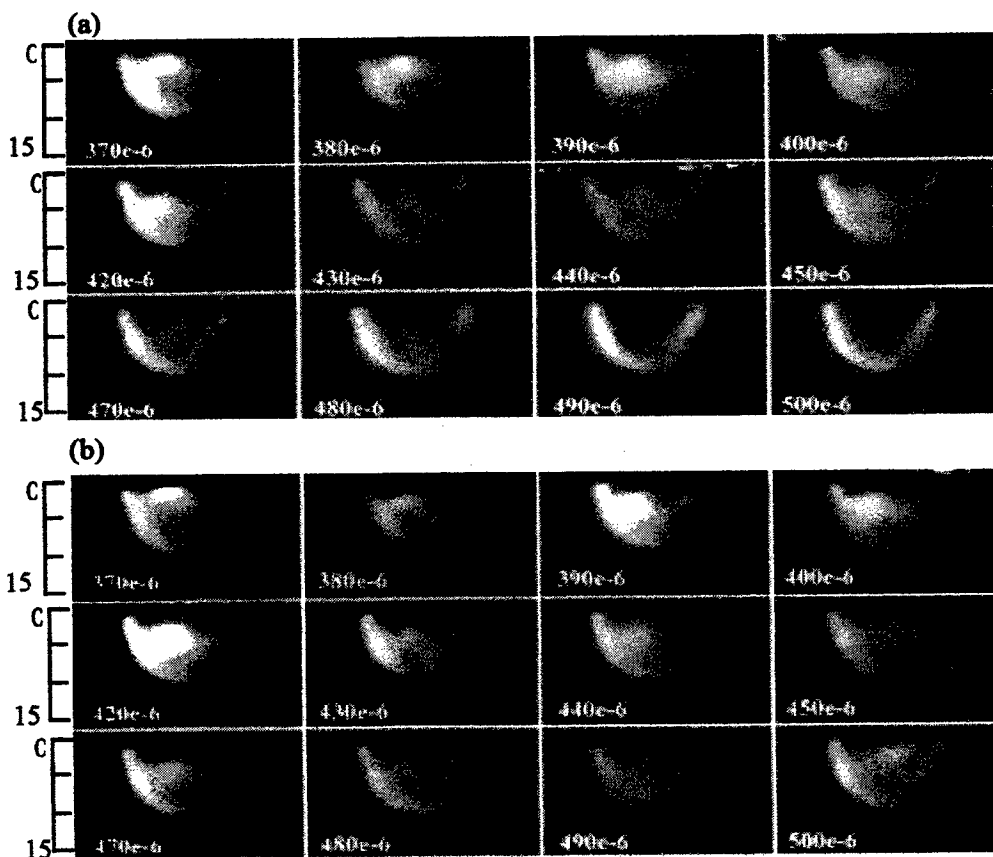


Fig. 5 Si plume in 10 Torr Ar background gas. (a) LIF and (b) ReD-LIF. The delay time is given at the bottom of each picture. Scales on the left hand side is in mm.

arrangement of the figure is the same as that in Fig. 4. The conventional LIF images are shown in (a) and the ReD-LIF in (b). In an Ar background gas, the onset time of the clustering is started around 300  $\mu$ s after ablation and is delayed compared to that in He gas. The clustering started near the target surface in contrast with the case in He where the clustering started in the center of the plume, as shown in Fig. 4.

Figures 6 (a) and (b) show the behavior of Si atoms and the clusters in a Ne background gas at 10 Torr. The clustering behavior was very similar to that in an Ar background gas. The clustering started at about 300  $\mu$ s after ablation and near the target surface. The clustering behavior in a N<sub>2</sub> background gas is shown in Figs. 7 (a) and (b). In a N<sub>2</sub> background gas, the clustering was largely delayed than in rare gases and started at about 800 ns after ablation. The reason is not clear, but the reactivity between Si and N<sub>2</sub> could have introduced a different way of clustering. In the case of O<sub>2</sub> background gas, Si atoms disappeared quickly due to rapid oxidation.

Based on the ReD-LIF imaging in different background gases [18], the on-set time of the cluster formation and the appearance time of ReD-LIF signal are summarized in Table I. The growth rate from Si<sub>2</sub> molecules to Si<sub>3</sub> or Si<sub>4</sub> molecules can be estimated as a time delay between the on-set time of the cluster formation and the appearance time of ReD-LIF signal. In the case of rare gases, the on-set time and the growth rate is faster in a He background gas than in Ne and Ar background gases. We believe that this is due to the lower viscosity of He gas than those of Ar and Ne. It is thought that the gas flow into the plume along the target surface accelerates the clustering.

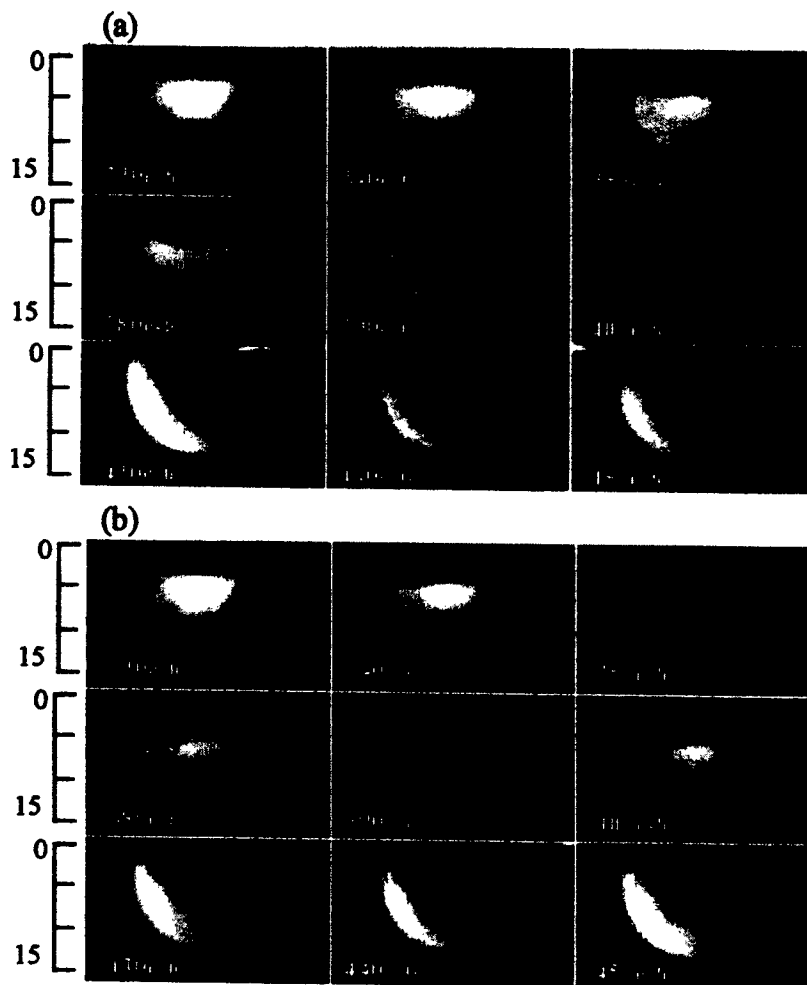


Fig. 6 Si plume in 10 Torr Ne background gas. (a) LIF and (b) ReD-LIF. The delay time is given at the bottom of each picture. Scales on the left hand side is in mm.

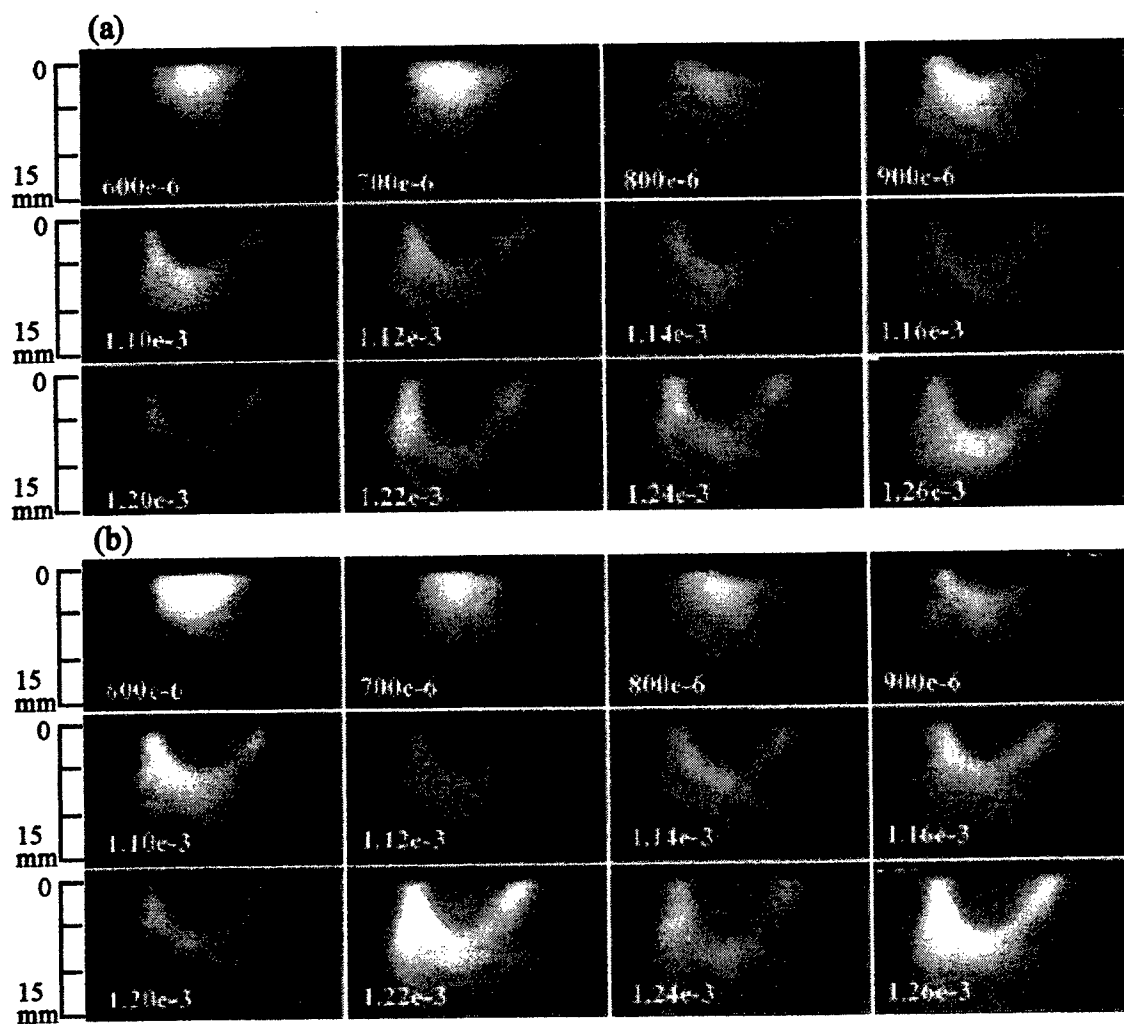


Fig. 7 Si plume in 10 Torr  $N_2$  background gas. (a) LIF and (b) ReD-LIF. The delay time is given at the bottom of each picture. Scales on the left hand side is in mm.

Table I On-set time of the cluster formation and the appearance time of ReD-LIF signal in various background gases.

Background Gas (10 Torr)	On-set time of clustering	Appearance of ReD-LIF Signal ( Clusters $> Si_n$ $n=3$ )
He	0.2 ms	0.25 ms
Ne	0.27 ms	0.41 ms
Ar	0.3 ms	0.44 ms
N2	0.7 ms	1.22 ms

#### 4. CONCLUSION

We have developed a new visualization technique named as re-decomposition laser-induced fluorescence (ReD-LIF), in order to investigate the dynamics of clusters, which are difficult to be visualized by any other means. The sensitivity of the ReD-LIF technique was theoretically compared with the other methods such as Rayleigh scattering and laser-induced incandescence. The results show that the ReD-LIF technique is the most sensitive for the smaller clusters and only the fluence of several tens of  $\text{mJ}/\text{cm}^2$  is enough to decompose the nano-particles. The ReD-LIF technique has been applied for the visualization of Si nano-particle synthesis process in a laser ablation plume. It is believed that the ReD-LIF technique is as sensitive as to detect the Si containing molecules of larger than  $\text{Si}_3$  or  $\text{Si}_4$ . The present technique could be applied to other processing systems like dust formation in a plasma and to other nano-particles which contain the atoms that can be observed by LIF.

#### REFERENCES

1. E. Wera, A. A. Seraphijn, L. A. Chiu, C. Zhou and K. D. Kolenbrander, *Appl. Phys. Lett.* **64**, 1821 (1994).
2. T. Yoshida, S. Takeyama, Y. Yamada and K. Mutoh, *Appl. Phys. Lett.* **68**, 4780 (1999).
3. R. Sema and C. N. Afonso, *Appl. Phys. Lett.* **69**, 1541 (1996).
4. S. Ohtsuka, T. Tsunemoto, H. Nagata and S. Tanaka, *Appl. Phys. Lett.* **61**, 2953 (1992).
5. L. Patrone, D. Nelson, V. I. Safarov, S. Giorgio, M. Sentis and W. Marine, *Appl. Phys. A* **69**, S217 (1999).
6. J. Muramoto, Y. Nakata, T. Okada and M. Maeda, *Jpn. J. Appl. Phys.* **36**, L563 (1997).
7. J. Muramoto, Y. Nakata, T. Okada and M. Maeda, *Appl. Surf. Sci.* **127-129**, 373 (1998).
8. K. Murakami, T. Makimura, N. Ono, T. Sakuramoto, A. Miyashita and O. Yoda, *Appl. Surf. Sci.* **127-129**, 368 (1998).
9. D. B. Geohegan, A. A. Puretzky, G. Duscher and S. J. Pennycook, *Appl. Phys. Lett.* **72**, 2983 (1998).
10. T. Makimura, T. Mizuta and K. Murakami, *Appl. Phys. Lett.* **76**, 1401 (2000).
11. B. Luk'yanchuk and W. Marine, *Proc. SPIE* **3885**(1999)182.
12. L. A. Melton, *Appl. Phys.* **23**, 2201(1984).
13. H. C. van de Hulst, *Light Scattering by Small Particles*, p.71, Dover Publication, Inc., New York, 1981.
14. M. Wautelet, *J. Phys. D* **24**, 343 (1991).
15. A. N. Goldstein, *Appl. Phys. A* **62**, 33 (1996).
16. J. Muramoto, T. Inmaru, Y. Nakata, T. Okada and M. Maeda, *Appl. Phys. Lett.* **75**, 751 (1999).
17. K. -D. Rinnen and M. L. Mandich: *Phys. Rev. Lett.* **69**, 1823 (1992).
18. Y. Nakata, J. Muramoto, T. Okada and M. Maeda, *J. Appl. Phys.* (2002)in press.

# Ultrafast laser-induced plasma diagnostics with time-spatial-resolved shadow and interferometric techniques

S.V. Garnov<sup>\*a</sup>, A.A. Malyutin<sup>a</sup>, O.G. Tsarkova<sup>a</sup>, V.I. Konov<sup>a</sup>, F. Dausinger<sup>b</sup>

<sup>a</sup>General Physics Institute of Russian Academy of Science, Moscow, Russia;

<sup>b</sup>Institut für Strahlwerkzeuge, Universität Stuttgart, Stuttgart, Germany

## ABSTRACT

The experimental studies of laser-induced plasma accompanying the laser ablation of materials have been conducted with the developed shadow-interferometric technique. High intensity single picosecond pulses of YAP:Nd laser ( $\lambda=1078$  nm) were applied to ablate tested samples and time-delayed probing pulses of second harmonic ( $\lambda=539$  nm) illuminating the interaction area were used to make snap-shots of the expanded plasma plume. Both shadow and interferometric images of hot plasma were captured simultaneously with a CCD camera providing  $\approx 1.5$  micron spatial and  $\approx 10$  ps temporal resolution of the investigated processes. By varying the intensity of ablating pulses (in the range of  $5 \cdot 10^{13}$ – $5 \cdot 10^{14}$  W/cm<sup>2</sup>) and the time-delay of probing pulses (in the ps range) it was possible to study a highly inhomogeneous small-scaled plasma density and refractive index distribution within the plume. The longer (nano-subnanosecond) time-delays allowed study of laser-initiated shock wave expansion in the surrounding atmosphere. A special attention was paid to the plasma formation arising at a through-hole laser drilling process. The strong influence of laser breakdown of the ambient gas (air) and laser-ignited explosion of clusters of ablated material on the efficiency of the drilling process was observed. In particular, it was shown that the cluster explosion can efficiently block the laser radiation resulting in decreasing the ablation rate. A computer modeling of optical visualization of small-scale plasma objects has been conducted. The analysis of the experimental and numerical results has revealed a number of characteristic features of plasma images that should be taken into account at the qualitative and quantitative evaluations of the plasma parameters.

**Keywords:** laser ablation, picosecond pulses, laser plasma, interferometry, shadowgraphy

## 1. INTRODUCTION

For years, the role of plasma in laser ablation of materials is the topic being widely discussed. Arising in the vicinity of laser-matter interaction area dense and hot plasma strongly influences the laser ablation process. On one side, it can effectively absorb and reflect the incident laser radiation and thus reduce the total amount of laser energy delivered to and deposited in the ablated target that decreases the efficiency of laser processing<sup>1</sup>. On the other side, the hot temperature plasma itself being a source of heat, short wavelength electromagnetic radiation and shock waves (arising both in the ambient atmosphere and in the material body) can efficiently affect the processed material causing its surface etching and local structural and chemical modifications<sup>2</sup>. The latter can result in a noticeable change in physical properties of the solids including such as optical absorptivity, thermal conductivity and mechanical resistance that, in turn, can promote the further laser processing by increasing the ablation rate (material removal efficiency). Especially important role plasma plays in laser ablation of solids with ultrashort, picosecond and femtosecond pulses. Here the strong laser fields can easily produce high-density plasma emitting EUV and x-ray radiation of up to several keV-quanta energy<sup>3</sup>. Well known and widely discussed in the past arguments for advantages of femtosecond laser pulses in material processing, from the point of view processing quality and efficiency, such as the negligible role of plasma in laser radiation screening and the possibility to reduce a thermal-affected zone to a few tenth of micron, have not been experimentally confirmed in general. Instead, as was turned out, in a number of cases both the efficiency of the laser processing and the quality of the structures produced with the femtosecond pulses could be even worse than those for the longer (e.g. picosecond and nanosecond) laser pulses<sup>4,5</sup>. And the source of that seems mainly results from the plasma formation. Therefore, it is quite obvious that the study of plasma and the accompanying phenomena is the issue of the day as for the fundamental science, as for the practice. Among the others, the optical methods of laser plasma investigations are widely and successfully used. These methods are based mainly on a time-resolved ("pump-probe") shadowgraphy<sup>6,7</sup> and interferometry<sup>8-11</sup>. In particular, they provide

\* garnov@kapella.gpi.ru; phone (095)1328146, General Physics Institute, 38 Vavilov street, Moscow, 119991, Russia.

information on plasma and blast waves dynamics including the characteristic speed of gas-dynamic expansion and the plasma density spatial distribution. Being used in the studies of relatively simple plasma objects such as a laser-ignited gas plasma with the pronounced cylindrical symmetry the developed optical (interferometric) methods allow one to obtain the valid quantitative data of plasma parameters with ultrafast (pico-femtosecond) time resolution at tens of micron spatial resolution<sup>10,11</sup>. However, for the plasmas with non-symmetrical small-scale (few microns) density distributions the applicability of the optical measurements and the validity of the data obtained become controversial. It commonly occurs, for instance, at laser ablation of solids when strongly inhomogeneous plasma is produced near the surface of ablated material. Nonetheless, even in these conditions the optical methods allow one as to reveal the characteristic features of plasma, as to estimate and describe qualitatively (and, in some cases, quantitatively) the parameters of the object<sup>6,7,9</sup>. In this paper we present an advanced method of ultrafast optical diagnostic of small-scale laser-plasma objects and the results of laser material ablation studies performed with this method. The distinctive feature of the developed technique consists in the simultaneous recording of shadowgraphic and interferometric images of the plasma<sup>12</sup> in combination with the picosecond temporal and micron spatial resolutions.

## 2. EXPERIMENTAL SETUP

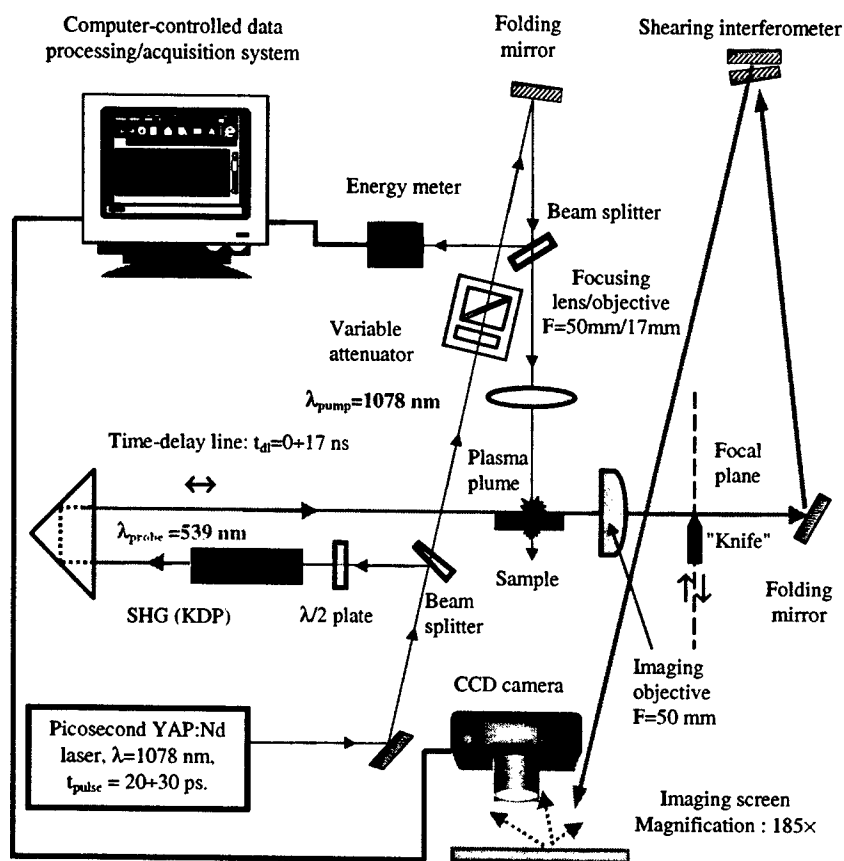


Fig.1. The principal scheme of the experimental setup.

The principal scheme of the experimental arrangement is shown in fig.1. A single picosecond pulse emitted by the YAP:Nd laser ( $\lambda_{\text{pump}}=1078$  nm;  $t_{\text{pulse}}=20+30$  ps;  $1+10$  Hz repetition rate) is split by a glass wedge into two unequal parts in proportion 1:10. The high-energy (up to 3 mJ) pumping pulse is focused with either a 50 mm focal length lens or a microscope objective (plan, 9X, NA=0.2) to ablate the tested material (stainless steel, ceramics etc.) and to create plasma onto a target surface or in the air. The incident beam diameter onto the focusing lens is 3 mm ( $1/e^2$ ) and the focused beam waist diameter is 20 or 6 microns (calculated values). The low-energy pulse is converted to the second harmonic ( $\lambda_{\text{probe}}=539$  nm) and the "green" probing pulse is sent to a variable time-delay line. By varying the time-delay between the exciting and probing (backlighting) pulses in the range 0+17 ns it is possible to record the plasma plume spatial expansion with the picosecond time resolution. The delayed probing pulse travels (at the right angle to the pump beam) through the plasma-filled zone and

undergoes spatially inhomogeneous phase and amplitude modulation. The modulation takes place only in a fairly small central area of the collimated probing beam comparing to its whole cross-section (a few square millimeters) because typical sizes of expanding plasma and the accompanying blast wave are from several to a few hundreds of microns for the considered pico-nanosecond time-scale. After passing through the plasma the probing pulse is collected with an imaging objective (50 mm focal length aspherical lens) and directed to a shearing interferometer. The reflected from the interferometer probing radiation creates the spatially separated interferometric and shadow (or schlieren) images of the plasma onto a view screen. The images are captured with a CCD camera. To record the schlieren (dark-field) images of the plasma, which are known to be most sensitive to the smallest perturbation of the phase of probing radiation, an opaque screen – a sharp blade (“knife”) or a 100 micron steel wire – are placed in the back focal plane of the imaging objective. The view screen is placed 4 meters away from the object that allows to obtain an 185X magnification of the plasma and to achieve a 1.5-micron spatial resolution.

In our experiments we assembled and employed a shearing interferometer consisting of two reflecting flat mirrors separated by an air gap<sup>12</sup>. The principal scheme of the interferometer is shown in fig.2.

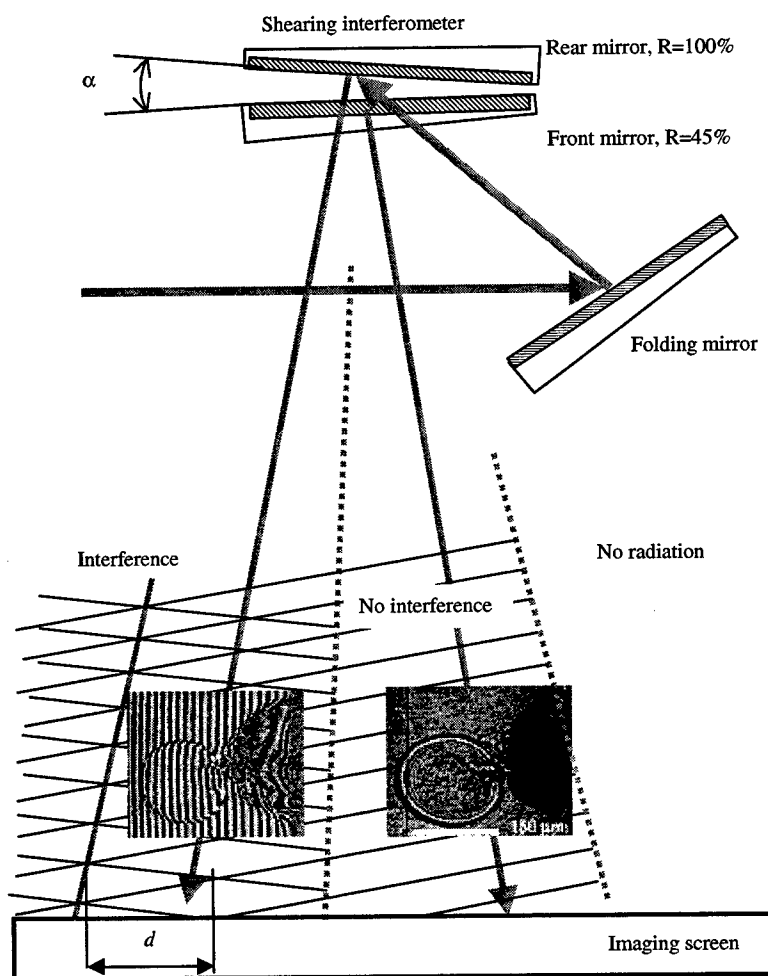


Fig.2. The shearing interferometer principal scheme.

For the interferometer reflecting surfaces are not parallel to each other, the beams reflected by front ( $R=45\%$ ) and rear ( $R=100\%$ ) mirrors are interfering in space forming the interference (fringed) image of the plasma object onto the imaging screen. By varying the angle between the interferometer mirrors  $\alpha$  it is possible to change the period of the interference fringes  $d$  and, as a result, to vary the spatial resolution and the phase sensitivity of measurements. Besides, as was mentioned above, due to the spatial separation of the reflected beams in the shearing interferometer the simultaneous recording of both the interferometric and shadow (or schlieren) images of plasma is accomplished. As it is seen in the fig.2, the interference

occurs only in the area where two beams are overlapped – in the left part of the screen, while in the right part only one beam (that is reflected by the front interferometer mirror) is present and thus no interference takes place. Note that this border appears due to the blocking of the part of the probing beam traveling below the specimen surface (*see* fig.1) by the opaque specimen body (or by a special screen).

The photo in fig.3 demonstrates the image of a reference test object. The distance between vertical dark lines (grooves etched onto a glass substrate) is equal to 10 microns that corresponds to 32 pixels of the electronic image. The thickness of a single groove is estimated to be 1.5 microns that is equal to 5 pixels. Hence, the geometrical spatial resolution in terms of image pixel number is about 3.3 pixel/micron. Fig.4 demonstrates the spatial resolution of the interferometric measurements done in the experiments. The distance between the nearest fringes (one-lambda fringe shift) is 2.6 microns i.e. the interferometric resolution (determined as a half-lambda fringe shift) is 1.3 microns.



Fig.3. The shadow image of a reference test object. Geometrical spatial resolution is 3.3 pixel/micron.

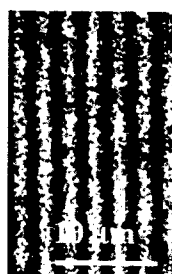


Fig.4. The fragment of an interferogram. Interferometric spatial resolution is 1.3 μm.

### 3. EXPERIMENTAL RESULTS

#### 3.1 Shadowgraphy of plasma and shock waves at picosecond laser micro-ablation and through-hole drilling

Temporal behavior of laser-initiated plasma plumes and shock waves arising at laser micro-ablation and through-hole drilling in a 100-micron thick stainless steel plates was investigated with the developed experimental setup. In the experiments the intensity of ablating laser pulses was  $I \approx (4+8) \cdot 10^{13} \text{ W/cm}^2$ . The time-delay between ablating and probing pulses ( $t_{\text{probe}} \approx 15 \text{ ps}$ ) was varied in the range  $t_{\text{dl}} = 0+53 \text{ ps}$ . Besides that, the long 10 ns and 17 ns time-delays were set to demonstrate the transformation of a plasma plume to a "pure" shock wave. A quite high intensity value of ablating pulses was chosen to reveal the details of produced plumes.

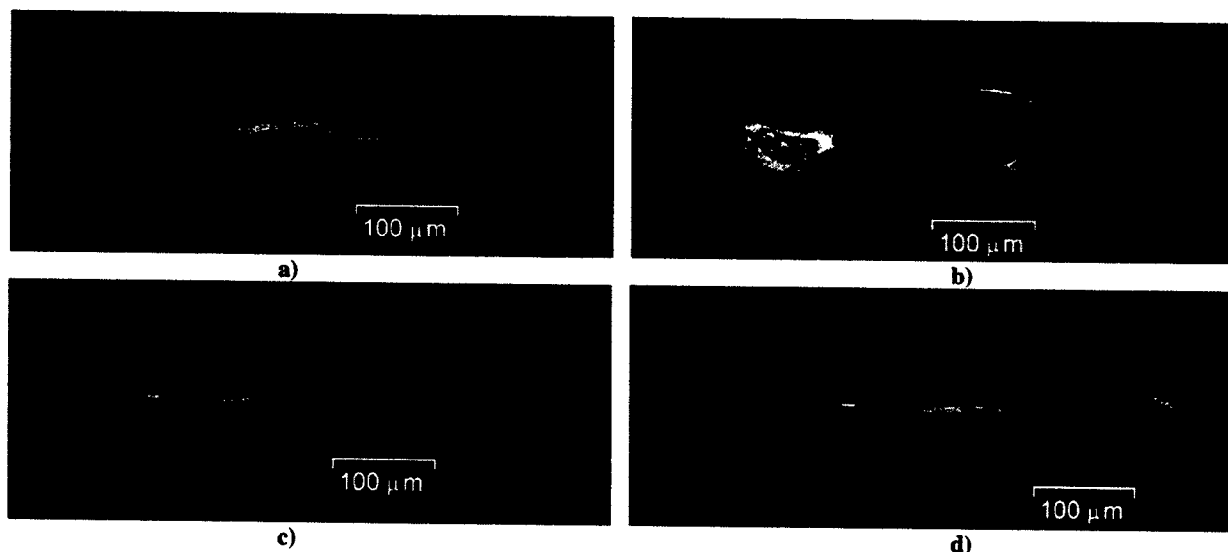


Fig.5. The dark-field images of plasma-plumes consequently changing with the laser shot-number during the drilling process: a) first shot; b) after 24 shots; c) 47 shots; d) 216 shots.  $I \approx 8 \cdot 10^{13} \text{ W/cm}^2$ ,  $t_{\text{dl}} \approx 53 \text{ ps}$ . Fig.5b demonstrates a laser-ignited explosion of the dust particle in the air.

The schlieren images presented in figs.5a-d show how the plasma-plume is changing with the pulse number during the process: beginning from the first shot (a) to the last one (# 216) corresponding to the final stage of the through hole formation. The time-delay is fixed at 53 ps. It should be pointed out that the "zero"-point of the time-delay corresponds to



the absence of any visible "bright spot" in the recorded dark-field image of plasma-affected-zone – i.e. the absence of any plasma image at all. It means that the probing pulse has been almost passed through the interaction area and has not been disturbed yet by arising plasma and only its tail (rear part) could slightly illuminate it. Because of high sensitivity of the schlieren technique the arising uncertainty in zero time-delay determination (which is quite typical for any kind of pump-probe experiments) can be reduced to a possible minimum value. For our experiments we estimate it as  $1/5+1/4$  of the full probing pulse width. Thus, the last digit indicated in the figures for the time-delay "53 ps" just means the value corresponding to the translation stage revolution counter numbers. (Note, that being determined in this manner, the zero time-delay actually fixes the moment of plasma appearance but not the peak position of the exciting laser pulse and depends on its intensity. The zero-point coincides with the peak of the exciting pulse when the peak intensity is equal to the threshold of plasma formation, and it is gradually shifted to the leading front of the pulse when the peak intensity is increased.) The pictures presented in figs.6a-b demonstrate the plasma plumes produced at the same time-delay ( $t_{dl} \approx 53\text{ps}$ ) but at two-times low laser intensity –  $I \approx 4 \cdot 10^{13} \text{ W/cm}^2$ .

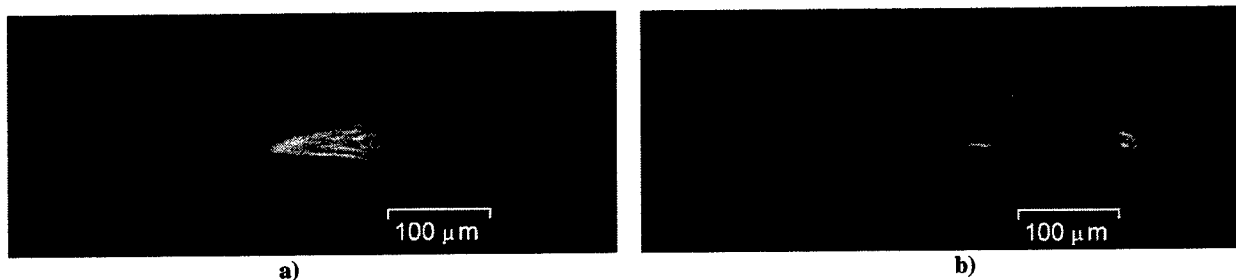


Fig.6. The dark-field images of plasma-plumes produced at  $I \approx 4 \cdot 10^{13} \text{ W/cm}^2$ . a) first shot; b) after 169 shots.  $t_{dl} \approx 53\text{ps}$ .

As it is clearly seen from the pictures, the shape of plasma is noticeably modified during the hole deepening – its transverse size gradually decreases, whereas the length is kept approximately the same. The residual plume of a small diameter is mostly due to the laser breakdown arising in the vicinity of the focal area. (The focal point of the applied 50 mm focal length lens was set at the rear surface of the drilled plate.) The pictures exhibit a complicated small-scale spatial structure resulted from the inhomogeneous plasma density distribution and the other peculiarities of laser-interaction zone. One of them is the laser-initiated explosion of clusters – small-scale particles free-flying in the air. The picture presented in fig.5b clearly illustrates how the laser-initiated explosion of a cluster (a dust particle in the air) can affect "the delivery" of laser radiation to the ablated area. Namely, due to the cluster explosion the most part of laser pulse energy is deposited in and/or reflected from the high-density laser-ignited plasma far from processed surface. As it follows from the far smaller size of plasma-plume arising at the target surface, only a small part of the laser pulse energy is delivered to the target. (Based on the average size of the plume one can qualitatively estimate the relative value of laser energy delivered to the target. For instance, one can compare the pictures presented in fig.5a and fig.6a obtained at the same time-delay but at two-times low ablating intensity.) Not only a single dust particle free-flying in the air and occasionally crossing the laser beam-waist, but also those small-size pieces of ablated material, which has been produced by previous laser pulses and were not able to leave the surroundings, can cause the partial blocking of laser radiation. Such situation can appear even at a relatively low repetition rate of a few Hz. It illustrates the photos shown in the fig.7 obtained at the same experimental conditions (after the hole was drilled through), but at 2 Hz repetition rate.

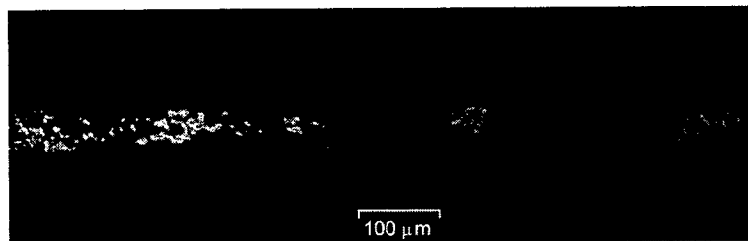


Fig.7. Laser-ignited explosion of clusters created by previous laser pulse(s). 2 Hz repetition rate.  $I \approx 7 \cdot 10^{13} \text{ W/cm}^2$ ,  $t_{dl} \approx 53\text{ps}$ .

As to the pictures presented in figs.5a-d, they were recorded 5 to 10 seconds after the previous shot, when debris of the processed material left the interaction area. It worth to mention that the spatial area where the clusters are exploded can extend up to the distance 800-1000 microns along the beam axis (see fig.7). With the consequent laser "cleaning" of the hole and the reduction of the total quantity of ablated material removed per pulse, the cluster explosion becomes less pronounced.

A part of the experiments was made with long, nanosecond time-delays. Fig.8 shows the shape of blast waves arising at both sides of a 100 micron steel plate drilled through. Because the channel is still in the process of drilling – in the stage of the so-called output widening - the source of shock wave is more intensive at the rear surface and the speed of wave expansion here is about two-times faster. Fig.9 shows the shapes of the shock wave and the plasma-plume arising near the target surface when two laser pulses of the equal energy separated by 10 ns interval ablate the material. The probing pulses follow each of ablating pulses with time-delay 40 ps. To make this experiment we adjusted the pulse slicer to extract two successive pulses from the train. The aim of the experiment was to reveal a possible influence of blast waves resulting from multi-pulse ablation of material. By comparing of the results presented in fig.9 and fig.6a (ablation with a single pulse of the same energy) one can conclude that there is no pronounced influence of the blast wave produced by the first laser pulse onto the shape of the plasma-plume produced by the second pulse: the shapes and the sizes of plumes are quite similar.

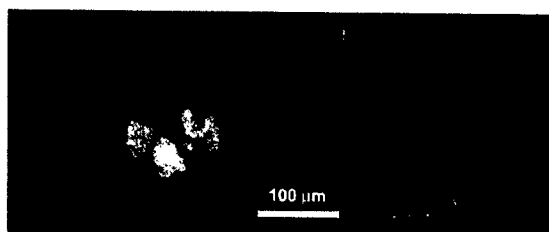


Fig.8. The shock wave expansion at a through hole drilling. hole is still in the process of drilling – widening of the output.  $I \cong 5 \cdot 10^{13} \text{ W/cm}^2$ ,  $t_{dl} \cong 17 \text{ ns}$ .



Fig.9. The shock wave and the plasma-plume. The produced with two time-delayed by 10 ns laser pulses of the equal energy.  $I \cong 4 \cdot 10^{13} \text{ W/cm}^2$ ,  $t_{dl} \cong 40 \text{ ps}$ .

### 3.2. Interferometry of plasma plumes and shock waves arisen at picosecond laser micro-ablation

As an example, the combined interferometric and shadow photographs of plasma objects produced onto the surface of a stainless steel sample are shown in fig. 10.

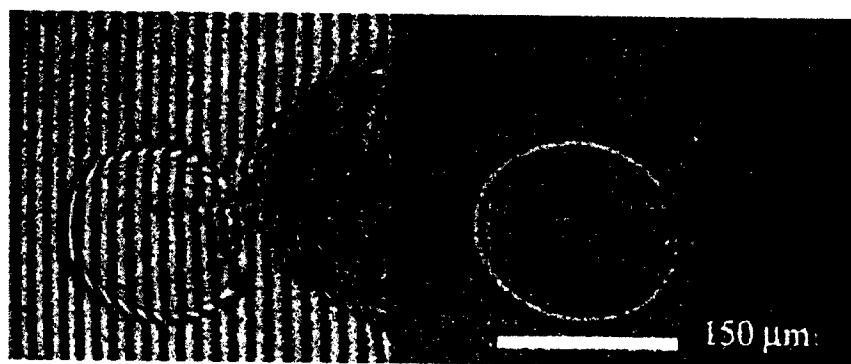


Fig.10. The captured simultaneously interferometric and shadow (bright-field) images of plasma plume arisen near the ablated surface of a stainless steel sample and the spherical blast wave (resulted from a cluster explosion in the air) both produced by a single picosecond laser pulse of  $I_0 \sim 10^{13} \text{ W/cm}^2$ . Time-delay is 3 ns.

The figure exhibits several features characterizing the later stages of the surface ablation and the cluster explosion. It was obtained at 3 ns time-delay between ablating and probing pulses. Two objects can be seen in the image: one is a spherical, highly transparent "bubble" - the spherical shock wave resulted from a dust particle (cluster) explosion in the air; another one is a rather absorbing "hemisphere" contacting with the ablated surface – the result of laser pulse interaction with the steel specimen. The hemisphere is filled with dense plasma and ablated material debris. The left part of the photo is the interferometric image - the result of the interference of two beams successively reflected from the front and the rear interferometer mirrors. Both beams bear the amplitude and phase information about the tested object and thus both of them create the object images separated in space. The beam reflected from the front mirror forms the image in the central part of the screen while that reflected from the rear mirror forms the image in its left part. Because the right part of the screen is illuminated by one beam only, the formed image is the common shadow picture of plasma. (Worth mentioning that the plasma object can be visualized without any additional screens in the optical scheme even if the  $F$ -numbers of the imaging lens is rather small  $F \approx 2-3$ ). The image created by the second beam is also the shadow image. However this image is superimposed onto the part of the first beam that serves as the reference beam to form the interferometric fringes. Thus, both the shadow and interferometric images of the plasma are formed. The shape of the fringes crossing the image represents

the phase shift of the probing radiation passed through the plasma and maps the spatial distribution of the plasma refractive index.

As seen in fig.10, the interferometric fringes across the spherical object are almost straight and nearly equidistant. Fringe displacement does not exceed one period that corresponds to the phase shift of one  $\lambda$  (for 539 nm). The straight equidistant interferometric fringes across the spherical object imply the phase shift independent on the radial coordinate (measured from the sphere center) for the most part of the sphere. This is possible only if the  $n(r)$  dependence is to be a smooth function in the central part of the sphere and a sharply rising function in the vicinity of the shell (similar dependencies are given in fig.17). Moreover, as it follows from the direction of fringe bending (taking into account the geometry of the experimental arrangements) the sign of the phase shift is the negative one, i.e. the phase velocity of light inside the "bubble" is higher than that in the surrounding atmosphere (air at normal conditions). In other words, the refractive index inside the sphere is less than that in the air ( $n_0=1.00023$ ). This is possible only if the plasma filling the sphere contains a large number of free electrons.

As to the hemispherical object the interferometric fringes crossing it are far more arched and also are strongly irregular ("interlaced"). In the area where both objects are contacting each other the fringe irregularities can be observed inside the spherical object too. At the periphery of the hemisphere the displacement of the fringes exceeds  $4\lambda$ . The strong arching of fringes and irregularities in the interferometric image are indicating a strongly inhomogeneous spatial distribution of the dense plasma arising near the ablated surface. Note that the direction of the fringe bending also demonstrates the negative phase shift – the presence of high dense free electron plasma inside the hemisphere. In spite of the complicated picture of the interferometric image that hardly can be unambiguously decoded and interpreted quantitatively we see that it provides us with at least qualitative data describing the plasma plume. In other words the interferometric image clearly demonstrates the obvious advantage of interferometric studies of high density plasma plumes. It is essentially more informative than the shadow image of the hemisphere, which looks as a dark, almost nontransparent object exhibiting no pronounced spatial substructure.

Fig.10 was obtained at a relatively long time-delay between pumping and probing pulses ( $t_{dl}=3$  ns) when a typical size of plasma object exceeds hundreds of microns. On the time scale of the backlighting pulse equal to  $t_{probe} \approx 15$  ps the plasma can be considered as static, "frozen" object. On the other side, figs.11a,b presented below show the earlier stages of plasma evolution. These photos were obtained at time-delay 40 ps. Fig.11a shows the plasma plume striation that is a characteristic feature for the beginning of the material ablation. The corresponding interferogram (fig.11b) exhibit the fringe blurring in the outer part of plasma plume.

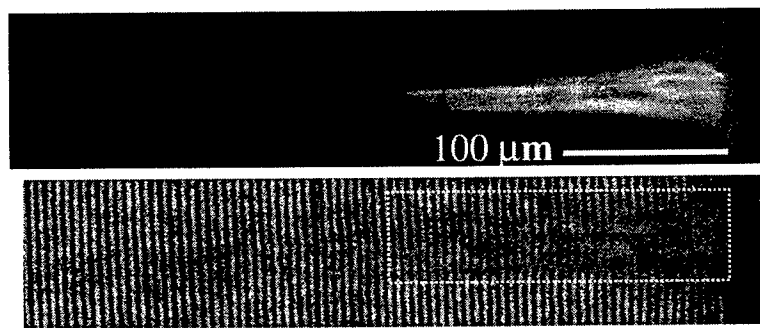


Fig.11. The interferometric and dark-field images of plasma plume arisen near the ablated surface.  $I \approx 7 \cdot 10^{13} \text{ W/cm}^2$ ,  $t_{dl}=40\text{ps}$ .

The fringes almost vanish in the area extending to about  $50+100$  micron above the treated surface. The image smearing and the total disappearance of fringes resulted from ultrafast nonstationary (on a time-scale of  $t_{probe} \approx 15$  ps) processes of plasma formation and plasma expansion in space. The period of fast perturbations lasts for a few tens of picoseconds. As it was observed the fringes become more pronounced and sharp and cover most part of the plasma plume at time delays longer than 53 ps. Only in the area directly contacting with the ablated surface where the electron density seems to reach maximum value, the fringes are not resolved till the  $t_{dl}=3$  ns. The latter is similar to that shown in the fig.10 for the hemispherical plasma formation.

### 3.3. Credibility limits of interferometric and shadowgraphic methods

The plasma created either onto a solid target or in the air passes two distinct stages: (a) the stage of laser energy deposition (laser-driven plasma) lasting for  $20+30$  ps (the pumping laser pulse duration), and (b) the stage of plasma "free" expansion. On the stage (a) the probe beam radiation is strongly refracted, scattered and also noticeably absorbed by plasma. Both the

detailed balance of the mentioned effects as well as the evaluation of other plasma parameters on this stage is the most interesting but quite difficult task. One of the reasons is the small plasma size (few to tens of microns) that requires the corresponding micron (or even sub-micron) spatial resolution. In this case the ultrafast non-stationary and non-local perturbation processes occurring in laser-driven plasma require both the shorter wavelength of probing radiation, and the faster (femtosecond) exposure times. With the experimental arrangement we have at the present time, this stage of plasma evolution can be studied rather qualitatively than quantitatively. On the stage (b), when the pumping laser pulse is terminated, the plasma, with respect to the probe pulse radiation, behaves like a weakly absorbing and slowly expanding in space ("quasi-frozen") phase object. The plasma size is of the order of a few tens of microns. Thus with the spatial resolution we have at hand ( $\sim 1.3 \mu\text{m}$ ) both the shadowgraphy and the interferometry can be used not only for a qualitative but for the quantitative measurements also. The quantitative versions of both methods are based on a classical relationship for the phase shift  $d\Phi$  of the probing beam (Abel integral):

$$d\Phi(h) = \frac{2\pi}{\lambda} \int_h^R \frac{(n(r)-1)rdr}{\sqrt{r^2 - h^2}} \quad (1)$$

that assumes weak refraction inside the object, i.e. the heights of the probing ray  $h$  (measured from the object geometrical axis) at the ray entrance and the ray exit should coincide. This imposes some limitations onto the procedure of retrieving the refractive index dependence  $n(r)$  from the experimentally measured data  $d\Phi(h)$ . To understand which details of the recorded shadowgraphic and interferometric pictures refer to the object under study and which are artifacts of the imaging system we have performed the additional experiments and numerical modeling. The modeling was made using the code FRESNEL that has been developed earlier in General Physics Institute for the calculations of the laser beam propagation in various optical systems. The program operates within the frameworks of paraxial approximation using special algorithm of the automatic scale adjustment to minimize the aliasing effect<sup>13</sup>. In the current study most calculations were done on a grid of  $2048 \times 2048$  sampling points.

First let us consider the details of the shadow image shown in fig.10 - the spherical blast wave expanding in the air. Three pronounced details are visible: (a) the circular interference (diffraction) pattern with the period decreasing to the center of the plasma bubble, (b) the black rim surrounding the bubble, (c) about the same average luminosity inside and outside of the bubble. The modeling of the plasma bubble aiming to reveal these experimentally observed features was done first with a flat phase object (phase screen) in the scheme shown in the fig.12. The phase screen was given by its radius ( $R_{\text{obj}} = 35 \mu\text{m}$ ), total phase shift ( $\Phi = 1 \cdot \lambda$ ), and by the scale of the phase variation at the screen edge ( $\delta$ ). The imaging lens was given by its focal length ( $F$ ), clear aperture size ( $D$ ), and magnification ( $M = 100 + 200$ ).

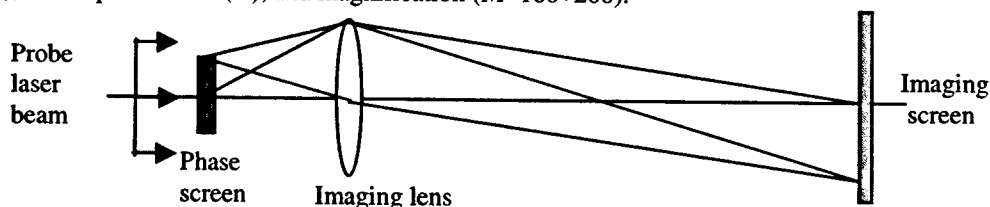


Fig.12. The schematic plot of plasma visualization optical scheme used in the computer modeling.

Fig.13a shows the intensity variation across the image for various values of  $\delta/2R_{\text{obj}}$ . These results are more or less obvious. First, we should note that depending on  $\delta/2R_{\text{obj}}$  the edge of the phase object can be visualized without any special means (the "knife" is absent in the scheme in fig.12). This fact and the equality of the surrounding luminosity with that inside the object image are known for the phase object with abrupt edges<sup>14</sup>. The visualization occurs because the aperture of the imaging lens "removes" the higher spatial frequencies associated with the light refracted/diffracted on the phase object edge. If the edge size is very small ( $\delta/2R_{\text{obj}} \ll 1$ ) the energy "removed" is low (i.e. the lens spatial resolution is not sufficient) and the edge is not visible (the contrast is low). For a large enough  $\delta/2R_{\text{obj}}$  the edge is not visible again for it is weakly refracting object - all the light comes through the lens.

One can notice that the period of the ring structure for the curves in the fig.13a does not depend on  $\delta/2R_{\text{obj}}$ . But this again is the artifact of our optical scheme. If we change  $F/D$  we shall see (figs.13b,c) that the period varies  $\propto F/D$ . Moreover the number of the rings relates with the number of Fresnel zones  $N_r$  on the radius of the phase screen visible from the rim of the lens aperture:

$$N_r = \frac{1}{\lambda} \left( \sqrt{F^2 + (D/2)^2} - \sqrt{F^2 + (D/2 - R_{\text{obj}})^2} \right). \quad (2)$$

E.g. for  $R_{obj}=35\text{ }\mu\text{m}$  and  $F/D=5$  we get  $N_r=6.43$ , while for  $F/D=2.5$  :  $N_r=12.69$  that is almost precisely coincides with the results of numerical modeling in figs.13b,c. If the relation (2) is valid for our case (the coincidence is not occasional) than we can assume that for an apodized lens the interference should vanish or be weakened. The numerical modeling confirms this as it is shown in the fig.13d for the apodizing scale  $d_a/D=0.25$ . As one can see in the fig.10 the interference period is changing across the radius of the plasma bubble while the period in the figs.13b,c is constant. The discrepancy can be ascribed to oversimplification made by replacement of the real spherical object by a flat phase screen. (The displacement of the center for the interference rings from the bubble axis most probably can be accounted for the non-ideal shape of the bubble.)

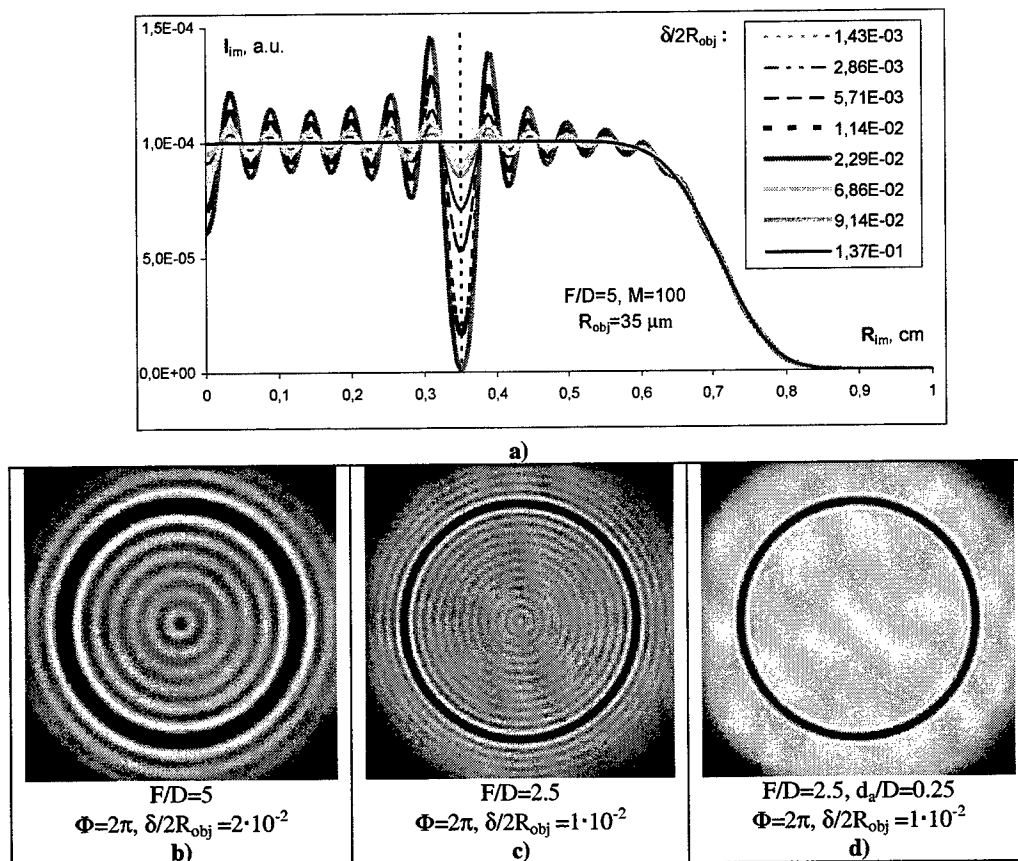


Fig.13. The results of the computer modeling of plasma phase objects.

There exists one more possibility to explain the features of the fig.10. This is the defocusing of the imaging objective with respect to the center of plasma bubble. The conducted numerical modeling of the defocusing with the phase screen shows that the effects resembling those observed experimentally do exist. The results of calculations and the recorded images of plasma produced in the air (laser spark) with short focal distance objective ( $F=17.8\text{ cm}$ ,  $I \approx 5 \cdot 10^{14}\text{ W/cm}^2$ ;  $t_{dl}=1\text{ ns}$ ) are shown in fig.14. As seen, the "positive" defocusing results in the interference with the similar dependence of the period versus radius (bottom of the figure). Note, that the experiments (done with picosecond laser spark) do not verify the numerical modeling calculations in all details – the diffraction pattern outside the plasma boundary has not been ever observed at defocusing  $\pm 100\text{ }\mu\text{m}$ . It demands additional experimental and theoretical studies to be performed.

### 3.4. Temporal evolution of refractive index spatial profile of the picosecond laser spark in air

The inherent complexity of plasma plumes arisen at laser ablation of materials and mainly the pronounced inhomogeneity and asymmetry of plasma density spatial distribution do prevents the routine procedure of refractive index retrieval to be unambiguously applied. Moreover, the observed experimentally and confirmed by the computer modeling characteristic features of plasma images such as a diffraction ring structure that can result from both the intrinsic (actual plasma properties) and extrinsic (aberrations of imaging system) reasons, additionally distort the original information on plasma physical parameters and essentially complicate the problem. In this connection it seemed reasonable at first to verify the applicability

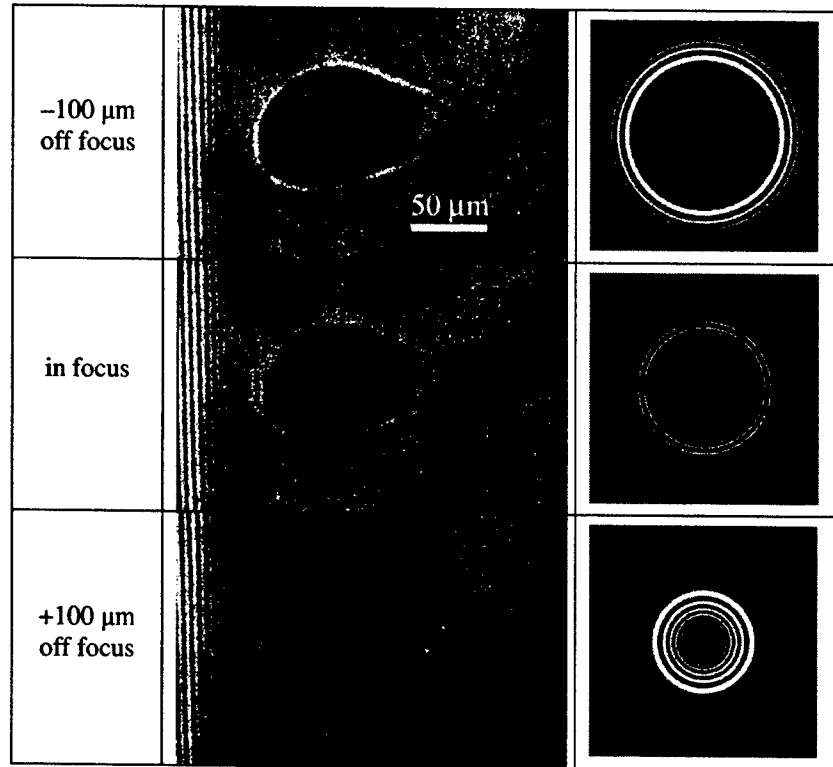


Fig. 14. The results of computer modeling of a plasma phase object - laser spark in the air. ( $I \approx 5 \cdot 10^{14} \text{ W/cm}^2$ ;  $t_d = 1 \text{ ns}$ )

of the developed plasma diagnostic method with a reference test object with more or less known and reproducible parameters. The most simple phase reference object that can be easily produced in an experiment is the common laser spark in the air. The reproducible and cylindrically symmetric picosecond laser spark allowed us to demonstrate the validity of the developed optical system and technique in retrieving the refractive index spatial profiles of the plasma at different moments of time starting from a few picoseconds after plasma ignition till 3 ns. To create a stable plasma object a short focal length objective ( $F=17.8 \text{ mm}$ ) was used and the pump laser pulse energy of about 2 mJ was applied. Therefore the peak intensity in the focal point was as high as  $I \approx 5 \cdot 10^{14} \text{ W/cm}^2$ . The recorded interferograms are shown in figs. 15a-b.

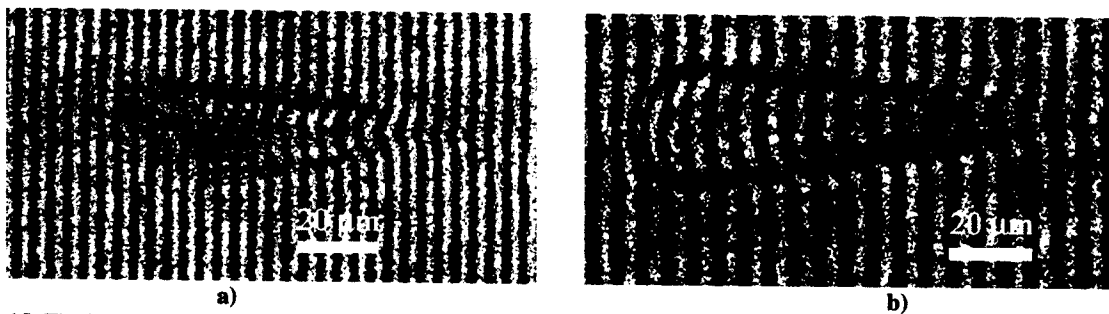


Fig. 15. The interferometric images of laser spark in the air: a) time delay = 40 ps; b) time delay = 105 ps.  $I \approx 5 \cdot 10^{14} \text{ W/cm}^2$ .

These interferograms allow us to retrieve the refractive index spatial profiles of the plasma by applying the simplest inverse Abel transform procedure<sup>10,11</sup>. Assuming a cylindrical symmetry of the plasma (at least in its central part) we can obtain the radial distribution of the refractive index just by measuring the interferometric fringe profile  $\Delta(r)$  – the fringe shift as a function of the radial coordinate ( $\Delta(r) \equiv \Delta(h)$ ), and assigning it to the phase shift of the probing wave -  $d\Phi(h)$ . Then, we retrieve the refractive index  $n(r)$  from the system :

$$\Delta(h) = \frac{2}{\lambda} \int_h^R \frac{(n(r)-1)rdr}{\sqrt{r^2 - h^2}}, \quad n(r) \equiv n(h) = 1 - \frac{\lambda}{\pi} \int_h^R \left( \frac{d\Delta}{du} \right) \frac{1}{\sqrt{u - h^2}} du, \quad \text{where } u=r^2. \quad (3)$$

It is worthy of note that at the periphery of the plasma near the blast wave front the interferometric fringes do not replicate exactly the wave phase shift radial distribution, so that this simplest inverse Abel transform algorithm does not allow one to retrieve correctly the phase shift of the probing wave and thus to obtain the reliable information on the refractive index spatial distribution. A 2D numerical algorithm should be applied in this case. The results of the 2D phase shift retrieving are shown in figs.16a,b, where the numerically calculated and the recorded plasma images are in a quite good coincidence.

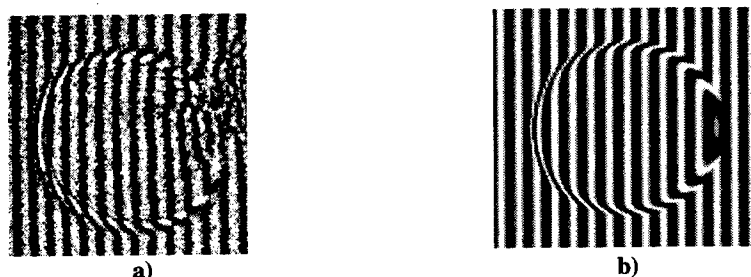


Fig.16. The recorded (a) and retrieved (b) with 2D algorithm interferometric images of laser plasma (see fig.10 for the details).

Nonetheless the retrieved with the system (3) refractive index values in the central part of plasma (far from the blast wave front) are correct and meaningful. Also, any small-scale variations in a fringe shape (less than about half-lambda) are hardly can be attributed to the physical fringe bending, but to a noise (image pixelization) or to "parasitic" diffraction rings originating due to imaging optics imperfections. The latter are partially seen in fig.15b where a "saw-like" modulation of the fringes in the center of the plasma plume is the result of the diffraction rings and the interferometric grid overlapping. Therefore, to retrieve refractive index correctly, one should properly smooth the recorded fringes before performing the Abel inversion procedure.

The retrieved refractive index radial profiles of laser spark are presented in fig.17 and the corresponding blast wave radius time dependence is shown in fig.18. Worth mentioning that the refractive index drops well below  $n_0=1.00023$  inside the object demonstrating the presence of high density free electron plasma. Simple estimations show that the equivalent electron concentration in the center of the plasma exceeds  $\sim 10^{20} \text{ cm}^{-3}$  at the early stages of the laser spark expansion and gradually decreases to  $\sim 10^{18} \text{ cm}^{-3}$  during several nanoseconds.

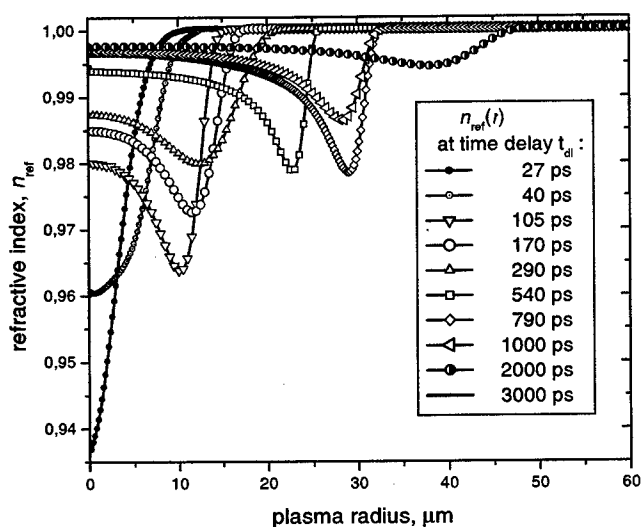


Fig.17. The laser plasma refractive index radial distributions of laser spark in the air.  $I \cong 5 \cdot 10^{14} \text{ W/cm}^2$ .

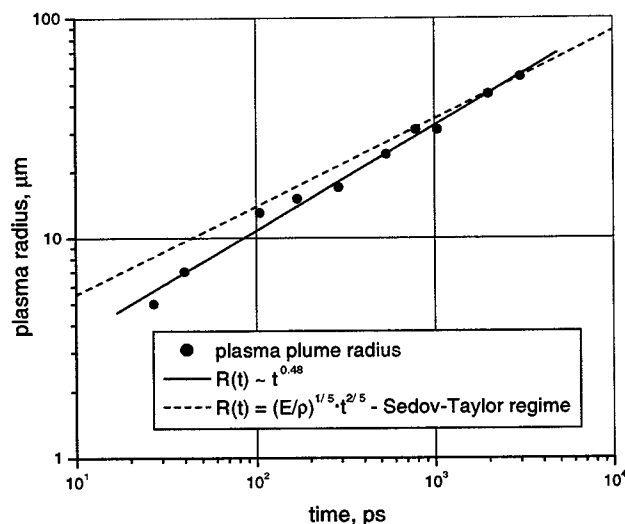


Fig.18. The laser plasma (blast wave) radius time dependence. Laser spark in the air.  $I \cong 5 \cdot 10^{14} \text{ W/cm}^2$ .

#### 4. CONCLUSIONS

To summarize the obtained results we can conclude that the developed shadow and interferometric technique allows one to study the spatial distribution and temporal behavior of laser plasma arising at laser micro ablation of materials. To the

best of our knowledge this technique was applied for the first time to the study of laser ablation on the picosecond time scale.

The computer modeling and analysis of the shadowgraphs and interferometric plasma images obtained with the coherent laser backlighting has demonstrated that the visualization of small-size plasma objects is accompanied by many artifacts that can prevent quantitative evaluations of the plasma parameters. Nonetheless, such measurements can be done if a reliable calibration of the imaging optical system is performed with an appropriate test objects with the well-defined parameters. The advantages of the developed interferometric technique such as the achieved is 1.3 microns spatial resolution of the interferometric measurements allow us to retrieve the refractive index spatial profiles of the simplest plasma object – laser spark in the air - at different moments of time starting from a few picoseconds after plasma ignition till several nanoseconds by applying the simplest inverse Abel transform procedure or the developed 2D computer algorithm. It is shown that the refractive index drops well below  $n_0=1.00023$  inside the laser spark demonstrating the presence of high dense free electron plasma. The equivalent electron concentration in the center of the plasma during few tens of picoseconds after plasma initiation reaches  $\sim 10^{20} \text{ cm}^{-3}$ .

### ACKNOWLEDGMENTS

The authors express their thanks to Dr. Yu.S. Kas'yanov for helpful discussions throughout this work and I.S. Yatskovsky for the permanent technical support.

This work was performed under the BMBF Project "Präzise Materialbearbeitung mit Ultrakurzpuls-Strahlquellen" ("PRIMUS").

### REFERENCES

1. S.V. Garnov, S.M. Klimentov, V.I. Konov, T.V. Kononenko, F. Dausinger, "Characteristics of plasma screening in ablation shaping of deep channels by high-intensity laser radiation," *Quantum Electronics*, **28**(1), pp.42-45, 1998.
2. T.V. Kononenko, S.V. Garnov, S.M. Klimentov, V.I. Konov, E.N. Loubnin, F. Dausinger, A. Raiber, C. Taut, "Laser ablation of metals and ceramics in picosecond-nanosecond pulsewidth in the presence of different ambient atmospheres," *Applied Surface Science*, **109-110**, pp. 48-51, 1997.
3. Y.L. Shao, T. Ditmire, J.W.G. Tisch, E. Springate, J.P. Marangos, M.H.R. Hutchinson, "Multi-keV electron generation in the interaction of intense laser pulses with Xe clusters," *Phys. Rev. Lett.*, **77**(16), pp.3343-3346, 1996.
4. F. Dausinger, T. Abeln, D. Breitling, J. Radtke, V. Konov, S. Garnov, S. Klimentov, T. Kononenko, O. Tsarkova, "Drilling of ceramics with short-pulsed solid-state lasers," *LaserOpto*, **31**(3), pp.78-85, 1999 (in German).
5. T.V. Kononenko, V.I. Konov, S.V. Garnov, R. Danielius, A. Piskarskas, G. Tamoshauskas, F. Dausinger, "Comparative study of the ablation of materials by femtosecond and pico- or nanosecond laser pulses," *Quantum electronics*, **29**(8), pp.724-728, 1999.
6. S. Ariga, R. Sigel, "Picosecond microphotography as a diagnostic method for laser produced plasmas," *Z. Naturforsch.*, **31a**, pp. 697-706, 1976.
7. O. Willi, P.T. Rumsby, S. Sartang, "Optical probe observation of nonuniformities in laser-produced plasmas," *IEEE J. of Quant. Elect.*, **QE-17**(9), pp.1909-1917, 1981.
8. N.G. Vlasov, S.V. Korchazhkin, R.B. Matsonashvili, V.M. Petryakov, S.S. Sobolev, S.F. Chalkin, "Picosecond interferometry of laser plasma," *Optika i Spektroskopiya*, **59**(4), pp. 934-937, 1985(in Russian).
9. D. Breitling, H. Schittenhelm, P. Berger, F. Dausinger, H. Hugel, "Shadowgraphic and interferometric investigations on Nd:YAG laser-induced vapor/plasma plumes for different processing wavelengths," *Appl. Phys.A*, **69**, pp. S505-S508, 1999.
10. T. Ditmire, E.T. Gumbrell, R.A. Smith, A. Djaoui, M.H.R. Hutchinson, "Time-resolved study of nonlocal electron heat transport in high temperature plasmas," *Phys. Rev. Lett.*, **80**(4), pp.720-723, 1998.
11. M.J. Edwards, A.J. MacKinnon, J. Zweiback, K. Shigemori, D. Ryutov, A.M. Rubenchik, K.A. Keilty, E. Liang, B.A. Remington, T. Ditmire, "Investigation of ultrafast laser-driven radiative blast waves," *Phys. Rev. Lett.*, **87**(8), 2001.
12. G.S. Sarkisov, "Air-wedge shearing interferometer for diagnostic of electron density in a dense plasma," *Priboru i tehnika eksperimenta*, **5**, pp. 110-114, 1996 (in Russian).
13. I.V. Epatko, A.A. Malyutin, R.V. Serov, D.A. Solov'ev, A.D. Chulkin, "New algorithm for numerical simulation of the propagation of laser radiation," *Quantum Electronics*, **28** (8), pp. 697-702, 1998.
14. M.E. Barnett, N.P. Turner, "Phase information in the coherent imaging of abrupt edges," *Optics Communications*, **96**, pp. 27-35, 1993.



# Effects of laser parameters on plume characteristics and ablation rate

Zhongli LI, Soh Zeom YOW, Lena LUI\*, Nikolai L. YAKOVLEV and Peter M. MORAN  
Institute of Materials Research & Engineering, Singapore 117602

\* Department Physics, National University of Singapore, Singapore 120332

## Abstract:

Laser ablation of polyimide and polycarbonate by 3<sup>rd</sup> harmonic Nd-YAG laser is studied using secondary ion mass spectrometry (SIMS) and confocal microscopy. The ablated debris were collected on an H-terminated Si substrate and then analysed using SIMS. Mass resolved images of collected debris showed near-hemispherical distribution of hydrocarbon, nitrogen containing and oxygen containing compounds with radius up to 0.7 mm. Ablation in different gases (air, N<sub>2</sub>, He) revealed that the nitrogen and oxygen containing compounds are formed because of a reaction of the hot plume with air in the course of thermal dissociation of O<sub>2</sub> and oxygen-assisted dissociation of N<sub>2</sub>. The shape and size of the microvia were measured using confocal microscopy through a polished edge of the polymer target. The via drilled in pulse-by-pulse ablation (PBPA) was found to be deeper than that drilled in continuous ablation (CA) with the same number of pulses. This is due to shading of the laser light by the plume from the preceding pulse. In result, explosive boiling occurs during PBPA, while normal vaporisation dominates during CA. Several mechanisms of etching of side walls are discussed.

**Keywords:** TOF-SIMS, plume attenuation, ablation rate, deep hole drilling

## 1. Introduction

Pulsed lasers are widely used for industrial processes, for example microvia drilling in the electronic packaging industry. When the laser power is above the materials ablation threshold, material ejection occurs within nanoseconds of the beginning of the laser pulse. This forms a plume/plasma above the target surface<sup>1</sup>. There have been extensive experimental and theoretical investigations of the formation, laser energy absorption and laser light scattering effects of plumes formed from single laser pulses<sup>1, 2, 3, 4, 5, 6</sup>. Callies *et al.*<sup>1</sup> use high-speed Schlieren photography and shadowgraphy to investigate the gas dynamics above a copper target. Based on their observations they define five discontinuities within the gas. The first discontinuity is a shock wave propagating through the gas surrounding the target. Closely following the first discontinuity there is a second one that they identify as the "ionization front", behind which the air is ionized. The third discontinuity is called the "contact front". This separates the shocked air and the ablated material vapor and plasma.

In a previous paper<sup>2</sup> we used a hydrogen terminated silicon surface to "catch" the debris within the plume. Subsequent analysis using time of flight secondary ion mass spectrometry (TOF-SIMS) of the silicon surface revealed spatial distributions of various components of the plume. The results confirmed that the oxygen and nitrogen in air around the ablation site dissociate due to the ablation process. Also shown in that paper is that dissociation of nitrogen occurs only in the presence of oxygen. This was demonstrated by changing the atmospheres surrounding the target material. In air, strong, well-defined distributions of both nitrogen containing compounds (NCCs) and oxygen containing compounds (OCCs) were found. While in nitrogen only trace amounts of NCCs and OCCs – which could be attributed to the oxygen and nitrogen contained within the polymer itself - were found.

In the present paper we experimentally investigate the ablation of certain polymers (polyimide and polycarbonate) by a 355 nm third harmonic Nd-YAG laser. We first present a TOF-SIMS analysis of the ablation debris using the method introduced in Li *et al.*<sup>2</sup>. The measured distributions of the NCCs and OCCs are used to measure the extent of the contact front. We use the Zeldovich two-step mechanism to explain the dissociation of nitrogen in air and subsequent formation of NCCs.

In the second part of the paper we report results of multi-pulse ablation of holes of various depths. We relate the TOF-SIMS results to phenomena seen in multi-pulse hole formation. Even though many industrial applications use multiple pulses for drilling deep holes, few reports of detailed multi-pulse laser ablation studies exist<sup>7, 8</sup>. During multi-pulse ablation the plume from one pulse may affect subsequent pulses. Our results show that even at repetition rates as low as 1kHz these effects are important when drilling deep holes. As the laser repetition rate is increased and as the ablated hole becomes deeper, plume interactions with subsequent pulses become increasingly important. Further results are presented that suggest material compliance or constraint may play a role in deep hole ablation rates.

## 2. Experimental

An ESI Microvia Drill M5200 was used in this study. This Q-switched third harmonic Nd : YAG laser produces a 355 nm wavelength beam with a Gaussian energy distribution. The laser was focused onto the target surface to a spot size of radius 25  $\mu\text{m}$  at  $1/\text{e}^2$  density. The maximum average laser power is 2 W and repetition rates can be varied from 1-20 kHz. The experimental setup for capturing plumes for SIMS investigations is shown schematically in Fig. 1(a). A hydrogen terminated silicon substrate was placed on the target, and was vertically aligned in the direction of the laser beam. The silicon substrate was placed 50  $\mu\text{m}$  away from beam center. Debris from the plume deposited onto the silicon substrate. It was then analyzed using a time-of-flight secondary ion mass spectrometer (TOF-SIMS) built by ION-TOF GmbH. The pulsed primary 10 keV  $\text{Ar}^+$  ion beam was scanned over the area of interest and secondary ion mass spectra of the sputtered fragments were collected from each point. The principle of the TOF detector is that all ionized fragments are collected after each primary ion pulse. This provides high sensitivity so that a mass spectrum can be obtained after sputtering of less than one molecular layer. The mass resolution is 8000 - enough to distinguish different fragments, e.g.  $\text{SiH}^+$ ,  $\text{OCH}^+$ ,  $\text{C}_2\text{H}_5^+$ , within one integer mass. The data were reconstructed as mass resolved images (MRI), representing the distributions of the sputtered fragments over the scan area. Polyimide (Kapton HN, a PMDA-ODA chemistry polyimide from Dupont Chemicals) was used as the target for all TOF-SIMS data presented here.

The ablation rate studies were carried out using polyimide films and transparent polycarbonate sheets. 75  $\mu\text{m}$  polyimide films were used to investigate ablation rates for shallow holes ( $<100\mu\text{m}$ ). 5mm polycarbonate sheets were used to study ablation of deep holes ( $>100\mu\text{m}$ ). The experiments were carried out using two methods: continuous ablation (CA) and pulse-by-pulse ablation (PBPA). Continuous ablation is defined as ablation due to continuous pulsing of the laser at various frequencies (repetition rates) between 1 kHz and 15kHz. In the case of PBPA, the interval between consecutive pulses was between 8 and 30 seconds. In all cases (CA and PBPA) the first 20 laser pulses were suppressed, i.e. the machine was programmed not to deliver them to the target surface. The 21<sup>st</sup> pulse was allowed to hit the target. This was done in order to reduce variations between pulses that are common during the first pulses of a laser. The machine was also programmed to shut off if the average pulse energy changed by more than 10% during ablation.

For the deep hole ablation studies, the edge of the polycarbonate target was polished prior to laser ablation. The laser was focused onto a spot 400  $\mu\text{m}$  from the edge of the target, as shown in Fig. 1(b). The laser-drilled hole was directly examined through the polished edge using confocal and optical microscopy. An Olympus Flouview300 confocal microscope and Nikon MM-40 measuring microscope were used.

### 3. Results and discussion

#### 3.1 Plume investigation by TOF-SIMS

Typical mass resolved images of a plume collected on a hydrogen-terminated silicon substrate are shown in Fig. 2. The mass spectra from the sample consist of hydrocarbon compounds (HCCs), nitrogen containing compounds (NCCs) and oxygen containing compounds (OCCs) originating from the plume and silicon containing compounds from the substrate. Figures 2 (a), (b) and (c) show images of all NCCs, OCCs and HCCs, respectively, from the same plume. This plume was deposited during ablation of polyimide in an air environment. The laser was set at a repetition rate of 5kHz and the fluence was 48.9 J/cm<sup>2</sup>. Debris from 6 pulses was collected in order to increase the amount of material on the sample. The ablated area of the target was directly in front of the middle of the bottom edge of the area shown.

The MRIs are hemispherical in accordance with isotropic propagation of the plume reported in ref. [1]. The distributions all have well-defined edges. The radius of the distributions does not depend on the number of pulses, so the debris from each pulse are frozen on the substrate and only stack up in thickness after each pulse. The radius of NCCs distribution is consistently slightly smaller than that of HCCs and OCCs distributions, see Fig. 2. The reasons for this are explained below.

SIMS analysis of the plumes deposited in different atmospheres<sup>2</sup> – air, helium and nitrogen – revealed significantly different MRIs. In contrast to ablation in air where the amount of NCCs and OCCs comparable with HCCs, ablation in He and N<sub>2</sub> gives the usual amounts of HCCs but only trace amounts of NCCs and OCCs. It is believed that the OCC and NCC traces seen in MRIs for ablation within H and N<sub>2</sub> are from the material itself (polyimide contains small amounts of oxygen and nitrogen within its chemical structure). SIMS analysis of plumes from polycarbonate targets showed similar results. The marked difference in the amount of OCCs and NCCs between the air environment and the nitrogen or helium environments indicates that the majority of the oxygen and nitrogen must have come from the air.

Nitrogen molecules have high dissociation energy and no dissociation occurs in an N<sub>2</sub> environment, as revealed by the lack of NCCs. However the presence of oxygen in air enables nitrogen dissociation at elevated temperatures due to the two processes - the first process is thermal dissociation of oxygen molecule in air. The second process is the atomic oxygen oxidizing the atmospheric nitrogen by Zeldovich two-step mechanism<sup>9</sup> - see reactions (1) and (2) below:



During this reaction nitrogen atoms are released and are able to combine with the molecules surrounding them (in our case ablated vapor molecules). They are also able to assist in further oxygen dissociation (reaction 2). According to Hill *et al*<sup>10</sup>, the Zeldovich reactions are highly dependent on temperature, residence time and atomic oxygen concentration. Reaction (1) is regarded as the rate-determining step due to its high activation energy and hence renders the Zeldovich mechanism highly sensitive to temperature. The minimum temperature required for nitrogen dissociation due to oxygen was observed<sup>10</sup> to be 1800 K. The temperature of debris at the beginning of the ablation was estimated to be much higher than this value (27600 K, at 10 ns)<sup>1</sup>, but as the plume expands, the contact front between the debris and air cools down (3600 K at 100 ns)<sup>1</sup>. At some point, it becomes colder than the threshold of the Zeldovich reaction, hence NCCs are no longer formed and the edge of their distribution occurs, Fig 2(a). However, direct oxidation of the ablated material vapor is still able to occur under these conditions and OCCs continue to be formed until the contact front itself stops expanding. Consequently the OCCs cover a slightly larger area than the NCCs, see Fig. 2b. Where the contact front stops expanding, also defines the limit of HCCs, thus their radius is similar to that of OCCs. Images taken by Callies *et al*<sup>1</sup> show the contact front stopping (and even retreating slightly) at distances of about 300 μm from the target. This is in good agreement with measured OCC and HCC distributions even though the laser conditions and target material differ significantly between the experiments. We have found that the radii of the NCC, OCC and HCC compounds are highly dependent on parameters such as laser fluence (results not presented here).

### 3.2 Ablation of shallow holes

The number of pulses taken to go through a 75  $\mu\text{m}$  polyimide film is plotted against laser fluence in Fig. 3. As mentioned previously, in PBPA experiments the laser was set running at a given repetition rate and only the 21st pulse was delivered to the target. The figure shows curves for a repetition rate of 5kHz. There is a significant difference between the CA and PBPA ablation rates, with PBPA ablation always being faster. Although data from other frequencies were obtained, they are not presented here. This is due to the fact that the laser's pulse profile changes considerably at different repetition rates making their respective ablation rates difficult to compare for our purposes. However the trend, PBPA ablation being faster than CA ablation is the same for all repetition rates tested (between 1kHz and 20kHz). Furthermore the difference between CA and PBPA ablation rates increases dramatically as the repetition rate is increased. This observation suggests that, for ablation within a hole, the plume generated from one pulse is able to shield ablation due to subsequent pulses. Using a 1078nm laser to drill holes in steel substrates, Kononenko *et al*<sup>8</sup> present evidence that the ablated particles from preceding pulses caused laser-induced sparking of the atmosphere (air) when hit by subsequent pulses. The air breakdown due to the laser induced sparking caused significant shielding of their laser and also resulted in sidewall etching. The etching caused more material to be vaporized, increasing the amount of vaporized particles within the hole. They were able to observe these effects even when using ultrashort pulses at repetition rate of 1 kHz. In order to examine this shielding phenomenon in more detail we used polycarbonate targets as described below.

### 3.3 Hole evolution studies

Polycarbonate targets were used for all hole evolution investigations presented here. Polycarbonate is transparent and therefore facilitates easy observation of ablated holes without any cross sectioning. Furthermore polycarbonate is readily available in thick sheets ( $>200\mu\text{m}$ ) whereas polyimide (Kapton HN) is not. In all experiments the repetition rate was fixed at 1kHz in order to reduce the thermal effects on the polycarbonate target. The laser fluence was fixed at 30.57 J/cm<sup>2</sup>. Figure 4 shows typical CA ablated holes in polycarbonate, using the experimental configuration depicted in Fig. 1(b). Comparing the series of images in Fig. 4(a), CA, with those shown in Fig. 4(b), PBPA, a number of differences are readily apparent. Blunt lump-like structures protruding perpendicular from the hole direction can be seen developing as early as 10 pulses for PBPA ablation. They are not evident for CA ablation until about 200 pulses – note the smooth sides of the 50-pulse CA hole, compared with the rough 50-pulse PBPA hole. These structures are most likely due to sidewall etching by the plasma contained within the hole. The PBPA holes are able to fill with air in between pulses and, as shown by the TOF-SIMS results, dissociation of both oxygen and nitrogen within the hole will occur with every pulse. This hot plasma is able to etch the sidewalls very rapidly. In the case of CA ablation however, pulses follow rapidly after each other. As the hole grows it is likely that the air within the holes is not able to replace itself between pulses. the oxygen, which comprises of only 16 % in air soon becomes depleted. Thereafter the Zeldovich mechanism cannot occur and the remaining nitrogen (~78% of air) is not ionized. This reduces the heat and etching capabilities of the plasma, and the lump structures are not formed as readily. After 200 pulses lump structure formation can be seen within the CA holes (~300 $\mu\text{m}$  deep), and this effect is more pronounced after 500 pulses. We suggest that in deep CA holes so much material vapor is trapped in the hole that subsequent pulses are strongly absorbed and each pulse re-ionizes the material vapor. Consequently the material vapor not only shields the ablation site, but also etches the wall, causing even more sidewall material to vaporize and draw into the hole.

A second clear difference between the PBPA and CA holes is the amount of thermal damage around the hole. CA holes show significant thermal damage whereas PBPA holes do not. This is expected since the PBPA target has time to cool down between pulses. Consequently it is likely that the CA pulses "see" a very different target material than the PBPA pulses do. The CA pulses hit a target material that is hot and probably partially molten (large molten droplets are always seen around CA holes but only fine droplets are found around PBPA holes, see Fig. 5). This material will have different physical properties (such as absorption coefficients). It is also likely to appear "softer" during CA ablation. Figure 6 shows an interesting phenomenon related to the softness or "constraint" of a material. In this experiment CA holes were drilled at various distances from the edge of the target, i.e. instead of the 400  $\mu\text{m}$  marked in Fig. 1(b) the distance was changed. As can be seen from Fig. 6, holes drilled closer to the edge of the target were deeper. The edge of the target was seen to bulge out around the ablation site. The amount of bulging increased as the hole became nearer to the edge. The amount of constraint on the material around the hole is clearly

decreased when the hole is closer to the edge. This allows the hole to become deeper under the same drilling conditions.

In addition to this the governing ablation mechanism within CA and PBPA holes may be very different. It has been argued<sup>11, 12</sup> that as the laser fluence increases, the ablation mechanism changes from "normal vaporization" to "explosive boiling" (or phase explosion). Normal vaporization occurs at the extreme outer surface of a molten layer. Explosive boiling extends to a depth of the laser light absorption length and is due to a rapid transition from superheated liquid to a mixture of vapor and small liquid droplets from the surface. In the case of PBPA it is likely that explosive boiling occurs, resulting in the fine droplets seen around the PBPA holes. However, in the case of CA, the material vapor trapped in the hole shields subsequent laser pulses and reduces the energy deposited onto the ablation surface. The absorbed laser energy may be insufficient for explosive boiling to occur, and normal vaporization may dominate the ablation process. As materials evaporate from the ablated site, due to momentum conservation, species removal from surface causes a recoil pressure. The recoil pressure is of the order of the saturated vapor pressure and acts on the non-ablated material resulting in molten layer ejection in the form of large droplets<sup>13</sup>. This mechanism may be partially responsible for the large droplets of material seen around the edges of CA holes. Clearly the fact that CA ablation causes greater thermal damage to the material on the sidewall would also assist in this since there would be more molten /soften material to be etched.

Figure 7(a) shows the ablation depth plotted against number of pulses for PBPA and CA ablation. In the case of PBPA, ablation depth increases linearly with the number of pulses. In the case of CA, the ablation depth increases consistently with the first 60 pulses, mimicking the PBPA ablation rate. However, after about 50 pulses (~200 $\mu$ m) the CA ablation rate decreases significantly and the PBPA and CA curves diverge. This suggests that once the CA hole becomes deeper than about 200 $\mu$ m material vapor shielding begins to dominate. This relationship is clearly dependent on the target material, aspect ratio of the hole, the repetition rate and laser wavelength of the laser. Dissociation of oxygen and nitrogen in the is likely to occur only at a distance from ablation floor where sufficient air is available in the CA holes since, as mentioned before, they will become oxygen starved deeper in the hole. This dissociation of oxygen and nitrogen in the CA holes may be caused by laser-induced sparking<sup>8</sup> or by the hot vapor of each pulse reaching its first supply of oxygen. The diameter of the hole opening is plotted against the number of pulses in Fig. 7(b). It is found that the hole opening increases with number of pulses in both CA and PBPA cases. The CA hole opening increases to around 50  $\mu$ m, whereas the PBPA stabilizes around 40  $\mu$ m after 50 pulses.

Figure 8 shows the CA ablation depth and hole opening diameter as a function of the number of pulses. After about 500 pulses the opening diameter stabilizes at around 70  $\mu$ m. The ablation depth curve shows at least two distinct regions. Up to about 200 pulses the average ablation rate is about 2.45  $\mu$ m per pulse. Thereafter, until more than 1000 pulses the average ablation rate drops to about 0.83  $\mu$ m per pulse.

#### 4. Conclusions

A study of polymer ablation by a 355nm pulse laser is presented. A new method of using SIMS to analyze chemical composition of debris is used. Confocal microscopy was used to determine the shape of holes drilled by continuous pulsed laser ablation (CA) and pulse-by-pulse ablation (PBPA) and to measure corresponding ablation rates.

For TOF-SIMS analysis, the debris was collected on a substrate placed near the hole and parallel to the laser beam. Mass resolved images of the collected materials show hemispherical shape of the plume with a distinct edge. The radius of plume was found to depend on the laser pulse energy, repetition rate and gas in which the plume expanded. The plume consisted of nitrogen containing, oxygen containing and hydrocarbon compounds when ablation in air. Ablation in N<sub>2</sub> and He gave traces of nitrogen and oxygen containing compounds. This was explained by the Zeldovich two-step mechanism when thermal dissociation of oxygen molecules in air enables release of atomic nitrogen, which is then able to combine with ablated molecules at the front of the plume.

In the case of continuous ablation (CA) in deep hole, oxygen, which comprises only 16% of air, may become rapidly depleted within. With the depletion of oxygen, dissociation of the remaining nitrogen (which comprises 78% of fresh air) is no longer possible and no ionization of the air occurs. This means that, at least while the hole is fairly shallow, sidewall etching within CA holes is suppressed (at the hole opening oxygen is available and rapid etching will still occur). However, as the hole becomes deeper, sufficient material vapor becomes trapped within it so as to cause significant absorption of incoming radiation from subsequent pulses. This incoming radiation continually re-ionizes the material vapor allowing it to etch the sidewalls effectively.

In pulse-by-pulse ablation (PBPA) the interval between pulses is very long (many seconds). Air enters the hole between pulses. Since there is always a ready supply of oxygen, dissociation of oxygen and nitrogen within the air occurs with each pulse. This causes significant etching of the sidewalls within the hole even for relatively shallow holes.

Due to the different shielding mechanisms within CA and PBPA holes, different ablation mechanisms may dominate each case. It is likely that normal vaporization dominates CA ablation, while PBPA is dominated by explosive boiling. Other factors such as material constraint and changing absorption properties of the material may affect the ablation rates.

Multi-pulse ablation of deep holes within polymers is highly complex and further studies are needed in order to improve our understanding of this important industrial process.

## References

- <sup>1</sup> G. Callies, P. Berger and H. Hugel, "Time-resolved observation of gas-dynamic discontinuities arising during excimer laser ablation and their interpretation", *J. Phys. D* **28**, 794-806, 1995.
- <sup>2</sup> Z.L. Li, S.Z. Yow, L. Lui, N. L. Yakovlev, P.M. Moran, "TOF-SIMS Investigation of Plume Induced by Nd-YAG Laser", to be submitted to *Appl. Phys. A*.
- <sup>3</sup> P. Solana, P. Kapadia, J.M Dowden and P.J. Marsden, "An analytical model for the laser drilling of metals with absorption within the vapor", *J. Phys. D* **32**, pp. 942-952, 1999
- <sup>4</sup> S. Sankaranarayanan, H. Emminger and A. Kar, "Energy loss in the plasma during laser drilling", *J. Phys. D* **32**, pp.1605-1611, 1999
- <sup>5</sup> H. Schmidt, J. Ihlemann, B. Wolff-Rottke, K. Luther and J. Troe, "Ultraviolet laser ablation of polymers: spot size, pulse duration and plume attenuation effects explained", *J. Appl. Phys.* **83**(10), pp. 5458-5468, 1998
- <sup>6</sup> K.H. Song, X. Xu, "Mechanisms of absorption in pulsed excimer laser-induced plasma", *Appl. Phys. A* **65**, pp. 477-485, 1997
- <sup>7</sup> E.G. Gamaly, A.V. Rode, A. Perrone, A. Zocco, "Mechanisms of ablation-rate decrease in multiple-pulse laser ablation", *Appl. Phys. A* **73**, pp. 143-149, 2001
- <sup>8</sup> T.V. Kononenko, S. M. Klimentov, V. I. Konov, P. A. Pivovaro, S. V. Garnov, F. Dausinger, and D. Breitling, "Propagation of short-pulsed laser radiation and stages of ablative deep channel formation", *SPIE Proc.* **4274**, 2001
- <sup>9</sup> Zeldovich Ya. B, "The oxidation of nitrogen in combustion and explosions" *Acta Physicochimica URSS* (1946) 577-628
- <sup>10</sup> S.C. Hill, L. Douglas Smoot: "Modeling of nitrogen oxides formation and destruction in combustion systems" *Progress in Energy and Combustion Science* **26**, 17-458, 2000
- <sup>11</sup> A. Miotello and R. Kelly, "Critical assessment of thermal models for laser sputtering at high fluences", *Appl. Phys. Lett.* **67** (24), 3535, 1995
- <sup>12</sup> N.M Bulgakova, A.V. Bulgakov, "Pulsed laser ablation of solids: transition from normal vaporization to phase explosion", *Appl. Phys. A* **73**, 199, 2001
- <sup>13</sup> D. Bauerle, *Laser Processing and Chemistry*, **204**, Springer, New York, 2000

Fig. 1 Experimental setup

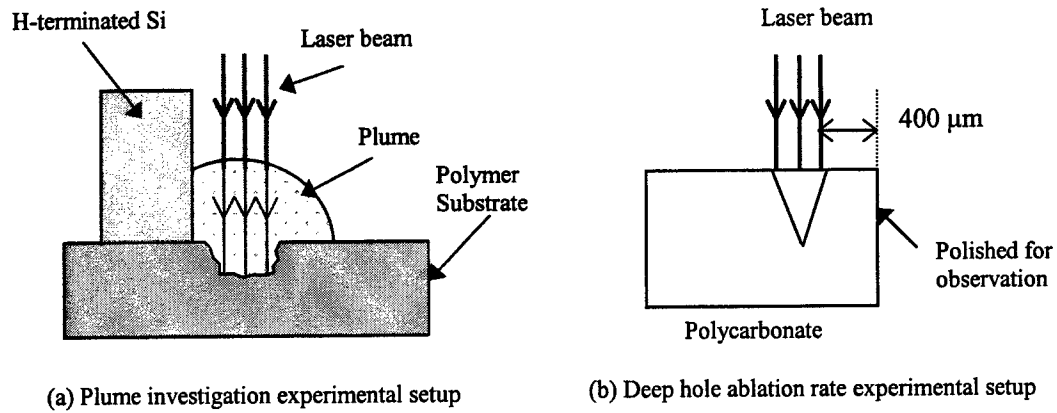


Fig. 2 TOF-SIMS plume images of polyimide (1mm x 1mm scan):

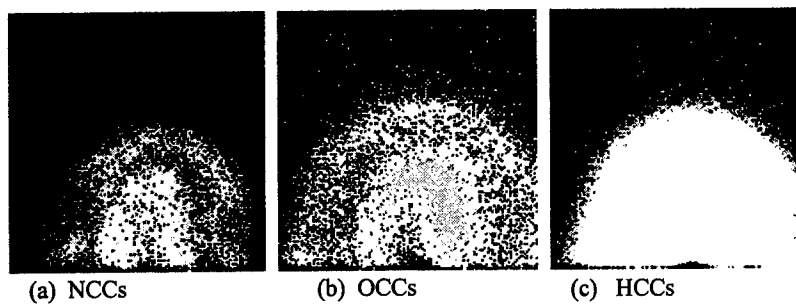


Fig. 3 Number of pulses go through 75  $\mu\text{m}$  polyimide film as a function of fluence

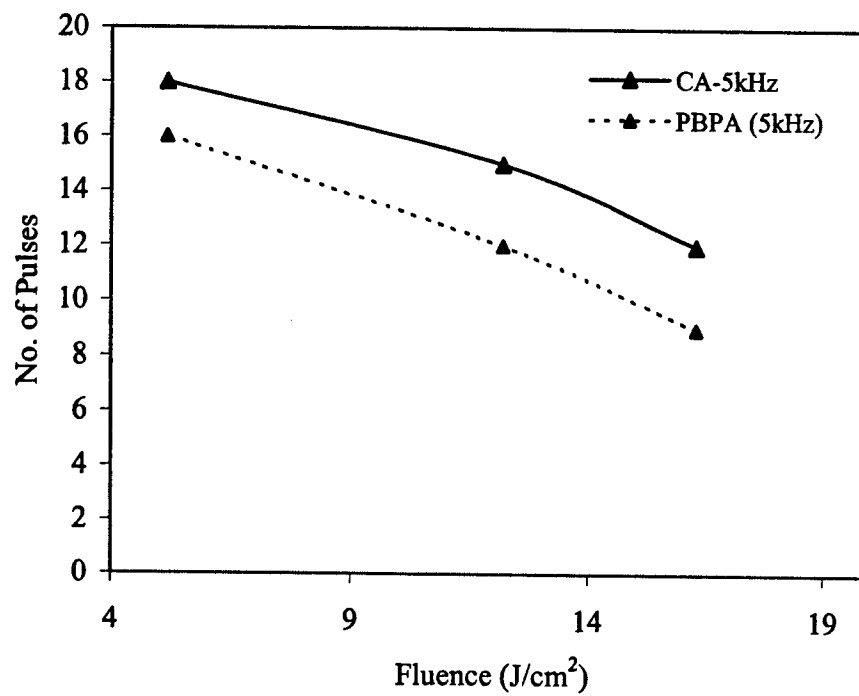




Fig. 4 Confocal microscope images of polycarbonate

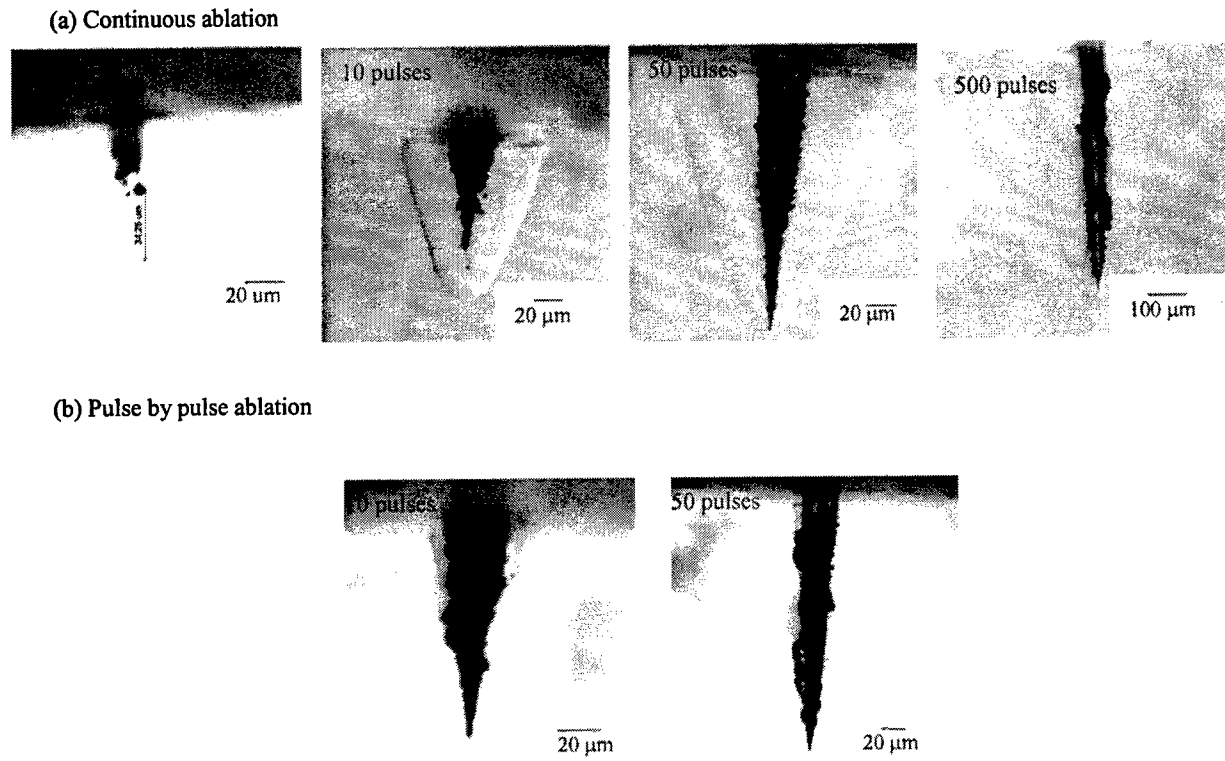


Fig. 5 Top view of ablated hole

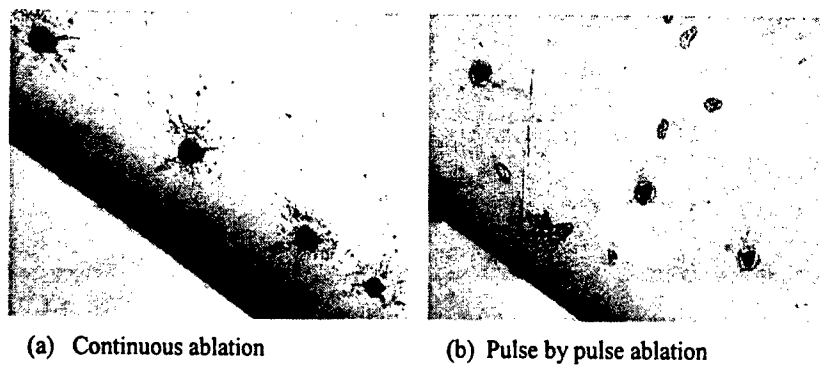


Fig. 6 Effects of material constrain on ablation rate

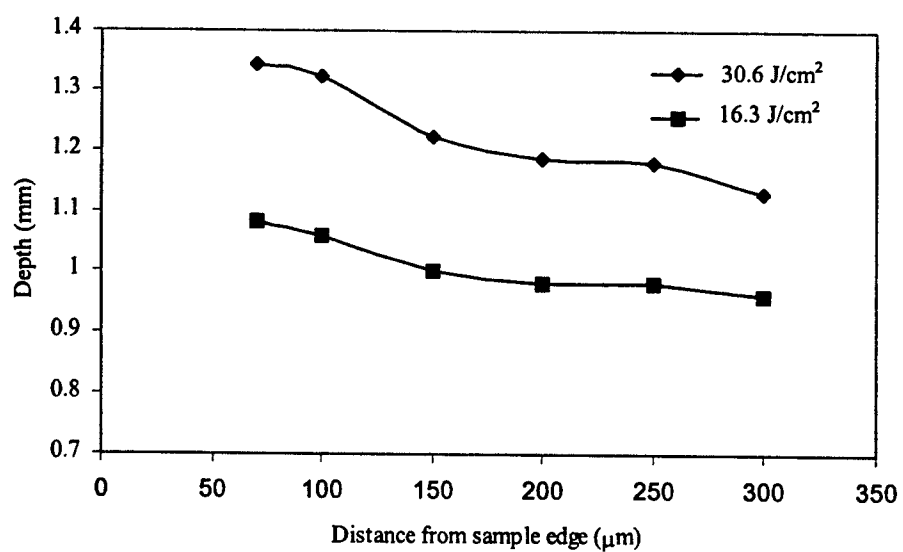


Fig. 7 Ablation depth (a) and opening (b) as a function of number of pulses at initial ablation

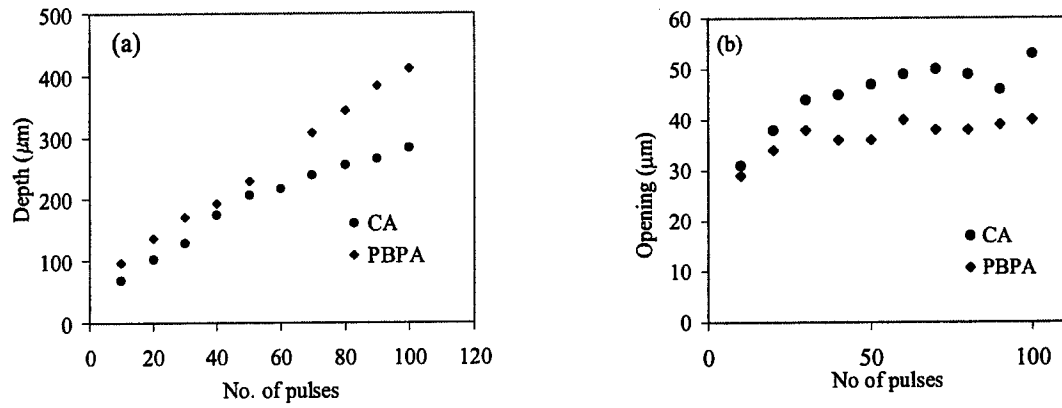
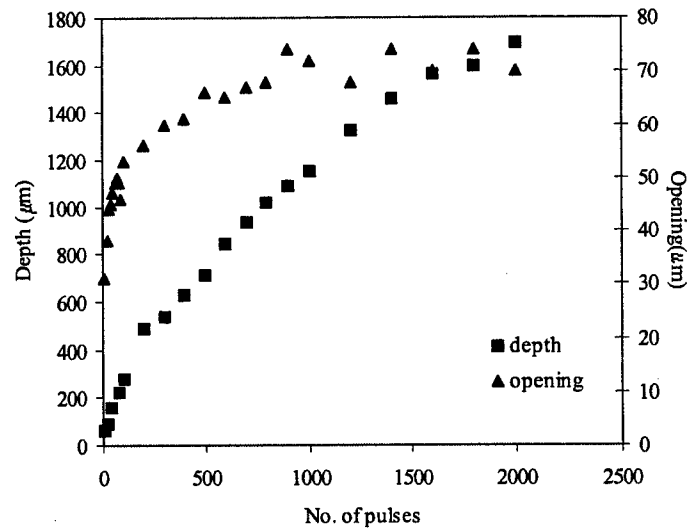


Fig. 8 Depth and opening as a function of number of pulses at deeper hole (CA)



# Modelling of chemical processes in the dynamic expansion for pulsed laser deposition

E. W. Kreutz<sup>a,\*</sup>, M. Aden<sup>a,b</sup>, M. Niessen<sup>a,c</sup>, A. Husmann<sup>a,d</sup>, R. Poprawe<sup>a,e</sup>

<sup>a</sup>Lehrstuhl für Lasertechnik, Rheinisch-Westfälische Technische Hochschule Aachen,  
Steinbachstraße 15, 52074 Aachen, Germany

<sup>b</sup>Present address: Fraunhofer-Institut für Lasertechnik, Steinbachstraße 15, 52074 Aachen, Germany

<sup>c</sup>Present address: Lehrstuhl für Mathematik und Institut für Reine und Angewandte Mathematik,  
Rheinisch-Westfälische Technische Hochschule Aachen, Templergraben 55, 52062 Aachen,  
Germany

<sup>d</sup>Present address: ORGA Kartensysteme GmbH, Am Hoppenhof 33, 33104 Paderborn, Germany

<sup>e</sup>Fraunhofer-Institut für Lasertechnik, Steinbachstraße 15, 52074 Aachen, Germany

## ABSTRACT

The material transfer from the target to the substrate involved in pulsed laser deposition is described with respect to chemical reactions in the processing gas atmosphere in order to derive the laser parameters and the processing variables necessary for the deposition of thin films with application-adapted properties. The heating and removal are described by the conversion of the optical energy into internal energy followed by a phase transition from the condensed to the gaseous state. The delivered energy becomes distributed into different channels of decomposition in accordance to the temperature. The dynamics of the volatile species is calculated by the use of non-dissipative continuum mechanical equations of the conservation laws of mass, momentum, and energy. The flow field patterns of the gas phase (density, velocity and pressure) during the material transfer of the polymers PE, PP and PMMA and the ceramic  $\text{Al}_2\text{O}_3$  are calculated. The modelling calculations are directed towards the spatial and temporal dependence of the total and partial pressures either of the materials to be processed or of the processing gas species. The mathematical models are applied to the polymers PE, PP, and PMMA and to the ceramic  $\text{Al}_2\text{O}_3$  following the chemical composition in thermodynamic equilibrium. The main emphasis of the calculations is to derive parameters and processing variables for pulsed laser film deposition in the case of other material properties.

**Keywords:** Pulsed laser deposition, dynamics, polymers, PE, PP, PMMA, ceramics,  $\text{Al}_2\text{O}_3$

## 1. INTRODUCTION

Pulsed laser deposition (PLD)<sup>1</sup> is conceptually a relatively simple technique, which consists of various consecutive processes separated in space and time: energy coupling to the target material, removal of the material from the target, transfer of the target material as melt, vapor, and/or plasma to the substrate via the processing gas phase, and the growth of thin films on the substrate. The outstanding properties during PLD of thin films include their reproducibility, accurate stoichiometry, single phase purity and/or crystal orientation. On the other hand, hybrid PLD<sup>2</sup> using additionally rf-excited electrical fields allows the particle excitation of the processing gas and the ion bombardment of the growing films due to self-biasing of the substrate electrode with subsequent acceleration of the processing gas ions to the substrate. In comparison with techniques using ion guns as the source of the energetic species, the use of a low pressure gas discharge has the advantage of easy process scaling for industrial applications.

In addition to excimer lasers, Nd:YAG lasers, and  $\text{CO}_2$  TEA lasers, as the most frequently ones in PLD, ps- and fs-lasers<sup>3,4</sup> are used in the last years, and recently the use of a fast axial rf-excited Q-switch  $\text{CO}_2$  cw-laser with a maximum

\* [contact.kreutz@llt.rwth-aachen.de](mailto:contact.kreutz@llt.rwth-aachen.de); phone 49 241 89 06-146; fax 49 241 89 06-112; <http://www.llt.rwth-aachen.de>;  
Lehrstuhl für Lasertechnik, Rheinisch-Westfälische Technische Hochschule Aachen, Steinbachstraße 15, 52074 Aachen, Germany

average output power of 5 kW has been demonstrated for the deposition of ceramics.<sup>5</sup> Q-switching is done with a mechanical unit based on a rotating chopper disc with slit-shaped apertures. The repetition rate is in the range of 150 to 3800 Hz, the pulse duration in the range 300 ns up to some  $\mu$ s, the maximum pulse energy 220 mJ, the peak power 220 kW and the maximum average output power 1050 W, depending on the Q-switch parameters and on the temporal synchronization of the Q-switch, and the rf-excitation of the laser medium. The deposition rate is higher for smaller pulse durations according to the material removal rate. The maximum deposition rate is 200 pm/pulse, that 1  $\mu$ m/s, for example, can be achieved at 4 kHz repetition rate.

After more than a decade of steady increasing basic research and development pulsed laser deposition is now entering industrial applications and will share the market with the existing PVD technologies like thermal evaporation and the sputtering processes. Due to relatively costly laser systems first applications have been films, that are difficult to deposit with desired composition and structure using conventional technologies like multicomponent ceramics (e. g.  $\text{YBa}_2\text{Cu}_3\text{O}_7$  for SQUIDS,  $\text{SrBi}_2\text{Ta}_2\text{O}_9$  or  $\text{PbZr}_{0.52}\text{Ti}_{0.48}\text{O}_3$  for memory and sensor applications) or thin film deposition with restrictive boundary conditions like need for low deposition temperatures (e. g. back end processing on CMOS structures or hard coatings on polymer surfaces). PLD also can produce diamond-like coatings<sup>6</sup> that make a surface nearly diamond-hard, or the process can apply high-temperature superconducting thin films to pave the way for practical superconducting devices. The technique also has the potential to radically enhance other devices, including electroluminescent displays and micro-optics. Microwave dielectric thin films, for example, possess an overwhelming advantage over bulk materials in several aspects, including lower operation voltage, faster response, feasibility for epitaxial growth, and most of all a non-linear relationship in dielectric properties, which increases the tunability. Therefore, applications of these thin films as planar capacitors, coplanar waveguides, tunable phase shifters, tunable mixers, and tunable filters have been extensively investigated. Among the microwave dielectrics,  $\text{Bi}_2\text{O}_3\text{-ZnO-Nb}_2\text{O}_5$  series materials exhibit excellent properties such as high dielectric constant and low dielectric loss, an adjustable temperature coefficient of the resonance frequency, and the low firing temperature necessary for sintering. The same desirable microwave dielectric properties are expected in thin film form. PLD<sup>7</sup> compared with other thin film deposition techniques such as rf-sputtering, sol-gel, MOCVD processes, can synthesize the multicomponent materials at a rapid rate with precise control of composition. PLD, for example, is adopted for synthesizing  $\text{Bi}_2(\text{Zn}_{1/3}\text{Nb}_{2/3})_2\text{O}_7$  microwave dielectric thin films.

Despite the simple technique the underlying process control in PLD has to be quite sensitive<sup>8</sup> and consequently complex in measuring many processing parameters. When producing a diamond-like coating, for example, the target is graphite, and the chamber is evacuated to about  $10^{-5}$  Pa. This allows the plasma ions to achieve energies up to 1.5 keV and leads to their adherence to the surface in a diamond-like crystal with a hardness of 60 – 70 GPa. Creation of these high energies requires minimum laser intensity of roughly  $10^{11}$  W/cm<sup>2</sup> for 1064-nm infrared light and  $10^8$  W/cm<sup>2</sup> for 193- or 248-nm ultraviolet (UV) radiation. The UV light has an advantage in its ability to reduce splashing of microparticles ejected from the target surface, because light in this wavelength range removes the material in large part by photon sputtering instead of thermal removal. For diamond growth, the substrate surface also must stay cool, which means coating rates are limited to about 0.01 – 0.02 nm, per pulse, with substrate distances of 5 or 10 cm. In addition, when an ambient gas such as oxygen is used to deposit oxides, process complexity grows because contact with the gas rapidly decelerates the plasma flow. The ionization energy of the plasma transfers to the kinetic energy of the gas, which reaches supersonic velocity and develops into a shock wave. The interaction of this shock wave with the substrate limits deposition rates for oxides to about 0,1 nm per pulse, or approximately one complete atomic layer.

According to the capabilities of PLD and due to large number of processing variables to be controlled during deposition modelling of the overall process, especially of the chemical parameters, is most helpful in order to be able to extrapolate, for example, from the processing windows or to scale to other sets of parameters, respectively, for a given material. The chemistry of the gas phase greatly influences the transfer of the target material and the film deposition by interaction with the gaseous particles, which open both the deposition of arbitrary materials and the generation of various film structures. Therefore, models will be described for the laser-induced removal and the dynamics of the volatile species of the polymers PE, PP and PMMA and the ceramic  $\text{Al}_2\text{O}_3$  following the volume-heating of the irradiated materials due to the absorption of laser radiation within the optical penetration depth and a phase transition from the condensed to the gaseous state of the material. The flow field pattern of the gas phase (density, velocity, and pressure) during the material transfer including the dynamics of the volatile species is calculated by the use of non-dissipative continuum mechanical equations of the conservation laws of mass, momentum, and energy. The properties

to be calculated are the total pressure and the partial pressures either of the material to be processed or of the processing gas species including their spatial and temporal behaviour during pulsed laser deposition. The main emphasis of the calculations is to avoid time consuming trial and error film deposition in the case of other material properties, laser parameters, and processing variables. In relation to experimental results of film deposition the results of the calculations are expected to improve the film deposition with high reproducibility, flexibility and homogeneity according to the tailoring of their properties adapted to the requirements of applications.

## 2. LASER-INDUCED MATERIAL REMOVAL

The laser radiation penetrating the material is absorbed within the optical penetration depth with conversion of the optical energy absorbed into internal energy depending on the photon - matter - interaction. Within the interaction zone and the surrounding volume the temperature may rise above melting temperature, vaporization temperature, and/or degradation temperature. Since the materials are composed by elements, which may form different molecules and complexes in the gaseous state, the materials may be removed as melt (droplets), clusters, vapor, and/or plasma, with the vapor and plasma composed of elements, ions, molecules, and complexes. Disregarding the droplets whose formation becomes less probable with decreasing pulse duration of the laser radiation and the clusters the gaseous phase consists mainly in atoms, ions, molecules, and complexes with the composition and the stoichiometry depending on the temperature and pressure. The material undergoes a phase transition or degradation from a condensed to a volatile phase if sufficient optical energy is converted into other internal energy channels.

## 3. GASDYNAMICS OF POLYMERS

### 3.1 The model

The stoichiometry of the polymers in the gas phase-following the photon-matter-interaction with subsequent conversion of the optical energy into internal energy in the interaction zone and the surrounding volume (Section 2)-is not known apriori. As a consequence the energy  $e_d$  necessary for the degradation of a monomer in smaller molecules or atoms might change during the removal process according to the pressure and temperature in the gas phase. The energy

$$e_d(T) = \Delta h_{P, M} + \Delta h(T) + C_{v, DP}T \quad (1)$$

$C_{v, DP}$ : heat capacity of the degradation products

depends on the enthalpy difference for the polymer-monomer cracking  $\Delta h_{P, M}$ , the enthalpy differences for creating smaller molecules  $\Delta h(T)$ , and the internal energy of the gas phase  $C_{v, DP}T$ . The energy density of degradation

$$E_d = e_d \cdot n_{Mono} \quad (2)$$

is proportional to the density of monomers  $n_{Mono}$  in the polymer.

The energy density  $E$  in the polymer, due to the absorption of laser radiation and internal heat fluxes, is determined by the conservation equation of energy

$$\frac{\partial E}{\partial t} + v_p \nabla E = \alpha I(z, r, t) + \nabla (K \nabla T). \quad (3)$$

$v_p$ : velocity of material removal,

$\alpha$ : absorption coefficient,

$I$ : power density of the laser radiation,

$K$ : thermal conductivity,

$z, r$ : coordinates,

$t$ : time.

The degradation of the polymer starts if its vapor pressure at a certain temperature  $T_{ini} = T_{ini}(P)$  exceeds the pressure of the undisturbed processing gas (ambient gas). The corresponding energy density  $E(z = 0, t = t_{ini})$  at the surface of the polymer equals the energy density (Eqn. 2) of degradation  $E_d(T_{ini})$ .

Following the well-known formalism for the degradation of polymers written in terms of a reaction<sup>9</sup> the degradation of PE<sup>10</sup>, for example, is described by



$\Theta_i$ : stoichiometric coefficients of the species  $i$  (molecule or atom) of the gas phase depending on the temperature and pressure.

Using the partial pressures of reaction channels with each channel conserving the stoichiometry of the monomer and the stoichiometry coefficients of molecule/element in the reaction channel, the description changes from the unknown stoichiometric coefficients to the normalized partial pressure of a reaction channel yielding in the calculation of the pressure of the gas phase according to the law of mass action.<sup>9</sup> The formalism is described in more detail elsewhere.<sup>11</sup> So the stoichiometry and the vapor pressure are in mutual interaction depending both on the temperature. Therefore, the degradation energy per monomer (Eqn. 1) depends on the vapor pressure and temperature.

The temperature is given by

$$T(z, t) = \begin{cases} \frac{E}{n_{mono} C_v} & \text{if } E \leq n_{Mono} C_v T_{ini} \\ T_{ini} & \text{if } n_{Mono} C_v T_{ini} < E \leq E_{ini} \\ E = E_z(T) & \text{if } E_{ini} < E \end{cases} \quad (5)$$

$C_v$ : heat capacity of the polymer.

In the first step of heating it is assumed, that an increase of the energy is proportional to an increase of the temperature, as long as the temperature is below the degradation temperature  $T_{ini}$ . In the second step the energy exceeds the first level ( $E > n_{Mono} C_v T_{ini}$ ) and it is assumed that the excess energy is used for rising the internal energy at a constant temperature  $T_{ini}$ . In the last step, where the energy exceeds the initial degradation energy  $E_d(T_{ini})$ , the temperature is obtained by solving the implicit equation  $E = E_d(T)$ .

To calculate the gasdynamical properties of the gas phase at the surface of the irradiated polymer the conservation equations of mass, momentum, and energy across the surface have to be solved. The physical meaning of the dependence of the degradation process on the pressure  $P$  of the gas phase (or at least on any property of the gas phase) is that the process of material removal depends on the physical state of the ambient or processing gas. So to close the corresponding system of equations one has to introduce the state equations of the vapor/gas phase. The dynamics of the vapor/gas phase will be given by the conservation equations of mass, momentum, and energy taking the thermophysical properties from the literature.<sup>12, 13, 14</sup>

### 3.2 Results and discussion

For polypropylen (PP) the vapor pressure as a function of temperature increases (Fig. 1) as for polypropylen (PE) and polymethylmethacrylat (PMMA).<sup>11</sup> The fractions of monomers in the vapor phase decrease with increasing temperature, because they are decomposed into smaller molecules or atoms (Figure 1) since PP degrades into its monomers at high temperatures.

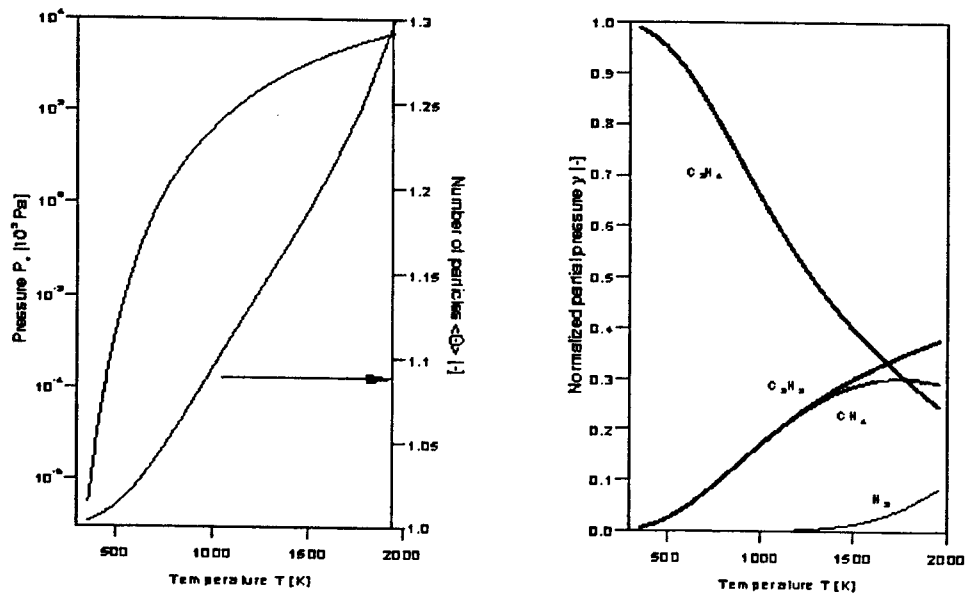


Fig. 1: Vapor pressure  $P_s$  of PE and the normalized partial pressures  $P_i$  (normalized to  $P_s$ ) as a function of temperature.

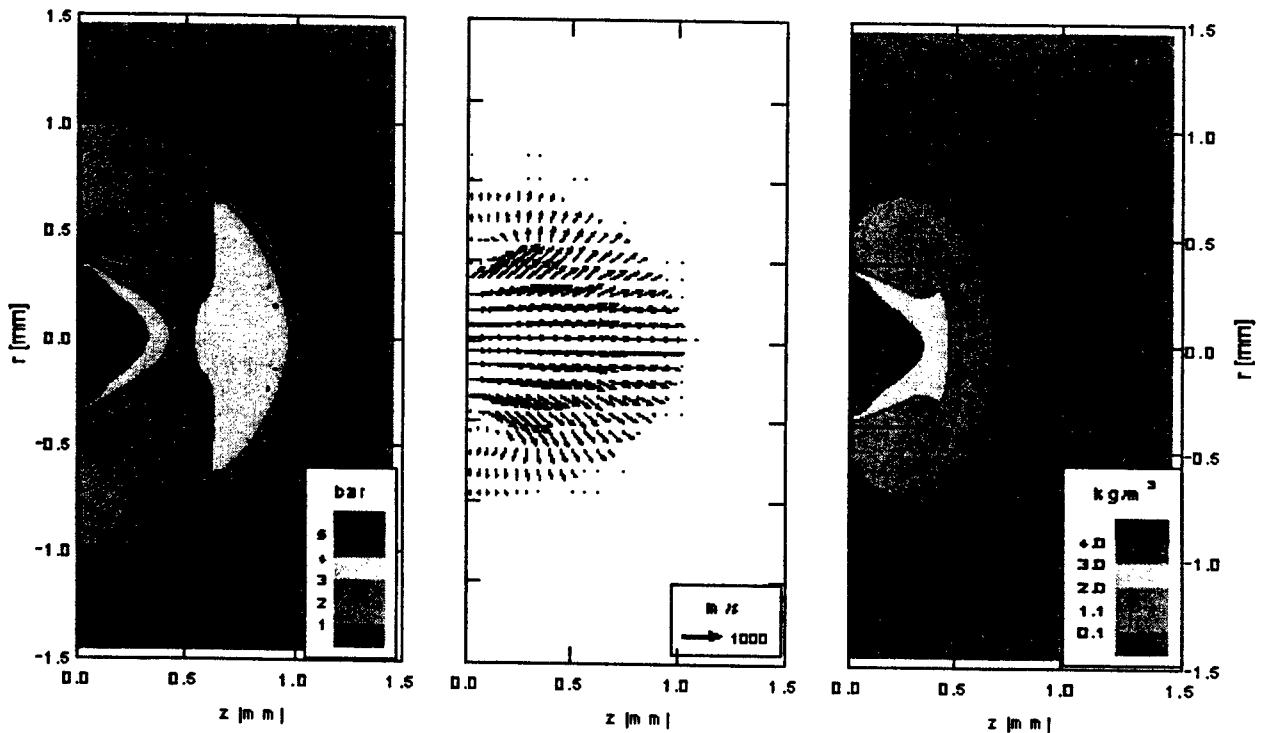


Fig. 2: Pressure distribution (left), velocity field (middle), and mass density (right) of the removed material 600 ns after the beginning of the laser pulse for PE (absorption coefficient  $\alpha = 1.6 \cdot 10^5 \text{ m}^{-1}$ ; fluence  $\epsilon = 3 \text{ J/cm}^2$ , pulse duration  $\tau_{FWHM} \approx 30 \text{ ns}$ , wavelength  $\lambda = 248 \text{ nm}$ , beam radius  $r_0 = 400 \mu\text{m}$ , pressure of the nitrogen



As seen from the pressure distribution (Figure 2) and results reported<sup>11</sup> the distance of the shock front from the surface is approximately 1 mm, so the velocity of the shock front is smallest for PP and largest for PMMA. This corresponds to the maximum vapor pressure, which is largest for PMMA. Due to the gradients of the pressure the velocity has also the largest values for PMMA. The different expansion behaviour is attributed to the different values of the optical penetration depth. PMMA has the smallest one and so the power density within the polymer is the highest one compared to PE and PP leading to a higher temperature and therefore, to a higher pressure at the surface of the polymer. A further difference in the expansion behaviour is, that for PMMA and PE the maximum pressure is in the vicinity of the shock front, where for PP it is near the surface. This corresponds to the down stream behaviour at the surface. The magnitude of the velocity for PMMA is virtually zero, for PP it is of considerable magnitude. This means that for PP the material removal is still working creating highest density<sup>11</sup> and pressure at the surface of the irradiated polymer. For PMMA the removal is terminated and the surplus of pressure is removed due to the expansion.

## 4. GASDYNAMICS OF CERAMICS

### 4.1. Properties of gases in thermodynamic equilibrium

All thermodynamic properties of a gas can be obtained from one of the generalized thermodynamic potentials expressed as a function of appropriate variables, for example  $F(T, \rho)$ , where  $F$  is the free energy density depending on temperature  $T$  and density  $\rho$ . The internal energy  $\epsilon^{(int)}$  of a gas is in general made up of contributions which correspond to the different degrees of freedom of a gas, as for example, translational motion, rotation and vibration of the molecules, or electronic excitation of the atoms and molecules. There are also contributions which correspond to molecular dissociation, chemical reactions, and ionisation. The most rigorous and consistent method for finding the thermodynamic functions is the method of partition functions, based on statistical mechanics. A detailed description can be found in the literature. According to statistical mechanics the partition function  $Q$  of a system consisting of  $N$  particles with possible energy levels  $\epsilon_n$  is given by

$$Q = \sum_n e^{-\frac{\epsilon_n}{kT}} \quad (6)$$

Considering a mixture of perfect gases consisting of several kinds of  $N_\alpha$  molecules and atoms, the partition function can be factored into a product of co-factors, each corresponding to particles of one kind

$$Q = \prod_\alpha \frac{Q_\alpha^{N_\alpha}}{N_\alpha!} \quad (7)$$

Here  $Q_\alpha$  are the partition functions of type  $\alpha$ . The free energy density  $F$  and the specific internal energy  $e^{(int)}$  of such a system are given by

$$F = \sum_\alpha F_\alpha = - \sum_\alpha c_\alpha K T \left\{ \ln \left( \frac{Q_\alpha}{c_\alpha N_\alpha V} \right) + 1 \right\}, \quad (8)$$

$$e^{(int)} = \sum_\alpha e_\alpha^{(int)} = \sum_\alpha R_\alpha T^2 \left\{ \frac{\partial \ln Q_\alpha}{\partial T} \right\}. \quad (9)$$

Where  $c_\alpha = n_\alpha/N_A$  denotes the concentration and  $R_\alpha$  the specific gas constant. Here  $n_\alpha$  is the particle density and  $N_A$  the Avogadro constant. The specific internal energy i. e. the caloric equation of state gives  $e^{(int)} = e^{(int)}(p, T)$ .<sup>14</sup> This is in contrast to the situation of a non-reacting perfect gas, where  $e^{(int)} = e^{(int)}(T)$ . The thermal equation of state for a mixture of perfect gases is given by

$$p = \sum_{\alpha} \rho_{\alpha} R_{\alpha} T. \quad (10)$$

Neglecting any interaction between electronic, vibrational, and rotational states, and considering molecules as rigid rotators and the vibrations as harmonic, the degrees of freedom are independent. The partition functions can be factorized

$$Q_{\alpha} = Q_{\alpha}^{(tr)} Q_{\alpha}^{(el)} Q_{\alpha}^{(rot)} Q_{\alpha}^{(vib)} Q_{\alpha}^{(0)}. \quad (11)$$

Here  $Q_{\alpha}^{(m)}$  denotes the partition function of the degree of freedom  $m$  and  $m = 0$  denotes the ground state. The ground state energy of atoms is set to zero, the ground state energy of molecules is set to the dissociation energy and the ground state energy of ions is set to the ionisation energy. The partition functions  $Q_{\alpha}^{(m)}$  are given by

$$Q_{\alpha}^{(m)} = \sum_{k=0}^{k=k_{\max}} g_{\alpha(k)} e^{-\frac{\epsilon_{\alpha(k)}^{(m)}}{KT}}, \quad (12)$$

where  $g_{\alpha(k)}$  is the statistical weight of energy level  $k$  of degree of freedom  $m$ . The explicit expressions for the partition functions and internal energies are taken from the literature including the coupling between rotational and vibrational excitations.

#### 4.2 Chemical composition of gases in thermodynamic equilibrium

The chemical composition of a mixture of gases can change due to chemical reactions, dissociation and ionisation. In thermodynamic equilibrium from a macroscopic point of view there are a constant energy distribution and a constant chemical composition. Therefore, time dependent variations of the concentrations  $c_{\alpha}$  vanish. In order to calculate the chemical composition it is necessary to determine the gas components and the involved reaction mechanisms, e. g. chemical reactions, dissociation, or ionisation. Let the chemical composition of a mixture of gases be determined through  $R$  reactions ( $r = 1, \dots, R$ ), with  $r'$  forward and  $r''$  backward reactions. In thermodynamic equilibrium the free energy density  $F$  has a minimum at constant temperature and particle number. The necessary condition for a minimum of the free energy with respect to the concentration is

$$dF = \sum_{\alpha} \left( \frac{\partial F}{\partial c_{\alpha}} \right)_{T, c_{\beta \neq \alpha}} dc_{\alpha} = 0. \quad (13)$$

All concentrations  $c_{\alpha}$  are determined through reaction equations given by

$$dc_{\alpha} = \sum_{r=1}^R \left( \nu_{\alpha}^{(r'')} - \nu_{\alpha}^{(r')} \right) d\lambda_r. \quad (14)$$

Here  $d\lambda_r$  is the reaction increment and

$$\nu_{\alpha}^{(r'')} - \nu_{\alpha}^{(r')}$$

are the stoichiometric coefficients. The stoichiometric coefficients determine how many particles participate as educt or as product in the reactions. A minimum of the free energy exists if all coefficients of the reaction increments vanish,

$$\sum_{\alpha} \left( \nu_{\alpha}^{(r')} - \nu_{\alpha}^{(r'')} \right) \left( \frac{\partial F}{\partial c_{\alpha}} \right)_{T, c_{\beta \neq \alpha}} = 0. \quad (15)$$

Equ. 15 represents a system of equations describing the reactions. Performing the differentiation of the free energy with respect to the concentrations the law of mass action

$$\prod_{\alpha} c_{\alpha}^{\left( \nu_{\alpha}^{(r')} - \nu_{\alpha}^{(r'')} \right)} = \prod_{\alpha} \left( \frac{Q_{\alpha}}{N_A V} \right)^{\left( \nu_{\alpha}^{(r')} - \nu_{\alpha}^{(r'')} \right)} = K_r^c(T) \quad (16)$$

is obtained. The equilibrium constants (Equ. 16) determined by the partition functions  $Q_{\alpha}$  depend only on the temperature. In order to calculate the equilibrium composition the elementary composition of the mixture must be specified. The concentrations of the atoms  $c_s$  ( $s = 1, \dots, S$ ) are expressed in terms of the concentrations of the components

$$c_s = \sum_{\alpha} d_{s,\alpha} c_{\alpha}, \quad (17)$$

where  $d_{s,\alpha}$  determines how many atoms of an element  $s$  are bound in a mixture component  $\alpha$ . Due to the mass conservation of elements the concentrations  $c_s$  are invariant with respect to the reactions. The concentrations  $c_s$  and thus the elementary composition of the mixture are specified by reference mole fractions  $y_{\alpha}^{(ref)}$ . The mole fractions are defined by  $y_{\alpha} = c_{\alpha} / c$  with  $c = \sum_{\alpha} c_{\alpha}$ . The constraints for the concentrations are given by

$$c_s = \sum_{\alpha} d_{s,\alpha} c_{\alpha} = c \sum_{\alpha} d_{s,\alpha} y_{\alpha}^{(ref)}. \quad (18)$$

For a gas mixture consisting of  $N$  components up to now there are  $R + S$  equations.  $R$  equations (Equ. 16) for all the possible reactions and  $S$  equations (Equ. 18) given by the mass conservation of elements. Using the  $S$  equations given by the mass conservation of elements the reaction mechanism must be specified by  $R^* = N - S$  independent reactions. This set of  $N$  nonlinear equations can be solved with a Newton-Raphson method. Once the composition of the mixture of gases is calculated the thermal equation of state  $p = p(\rho, T)$  and the caloric equation of state  $e = e(\rho, T)$  are known, too. For the solution of the Euler equations the pressure  $p = p(\rho, e)$  and the velocity of sound  $c = c(\rho, e)$  can be precalculated and expressed by curve fits in the  $\rho, e$  plan (Section 4.3).

#### 4.3 Composition of an gas mixture in equilibrium with $Al_2O_3$

The composition of the gas mixture above an  $Al_2O_3$  target evaporating into vacuum has been investigated by spectroscopic and mass-spectrometric methods. The identified components are O,  $O_2$ , Al,  $Al_2$ , AlO,  $AlO_2$ ,  $Al_2O$  and  $Al_2O_3$ . The elementary composition for a gas mixture consisting of these components is specified through the reference mole fractions

$$y_{Al_2O_2}^{(ref)} = 0.666\dots, y_{O_2}^{(ref)} = 0.333\dots, y_{\alpha}^{(ref)} = 0 \quad \forall \alpha \neq Al_2O_2, O_2. \quad (19)$$

If the temperature and the density or the pressure are given the equilibrium composition can be calculated using the mass conservation of elements yielding equations for Al, O and  $e^-$  and the following reactions

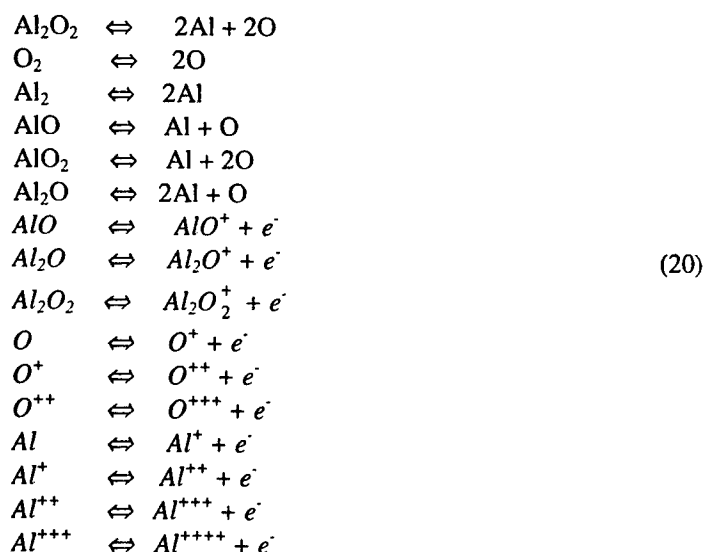


Fig. 3 shows the mole fractions  $y_\alpha$  as a function of the temperature within a temperature range between 1000 K and 50000 K for a pressure of 1 bar. The mole fractions of the molecule  $\text{Al}_2\text{O}$  and of all positive charged molecules are below  $2 \cdot 10^{-2}$ . Below 2000 K only the molecules  $\text{Al}_2\text{O}_2$  are existing. These molecules dissociate with increasing temperature. Within a temperature range between 3000 K and 4000 K maxima of the molecules  $\text{Al}_2\text{O}$  and  $\text{AlO}$  are present. With increasing temperature these molecules dissociate into their atomic components. The ionisation of Al and O occurs above 5000 K and higher ionisation levels can be seen above 12000 K. Each ionisation level contributes to an stepwise increase of the mole fraction  $y_e$  of the electrons.

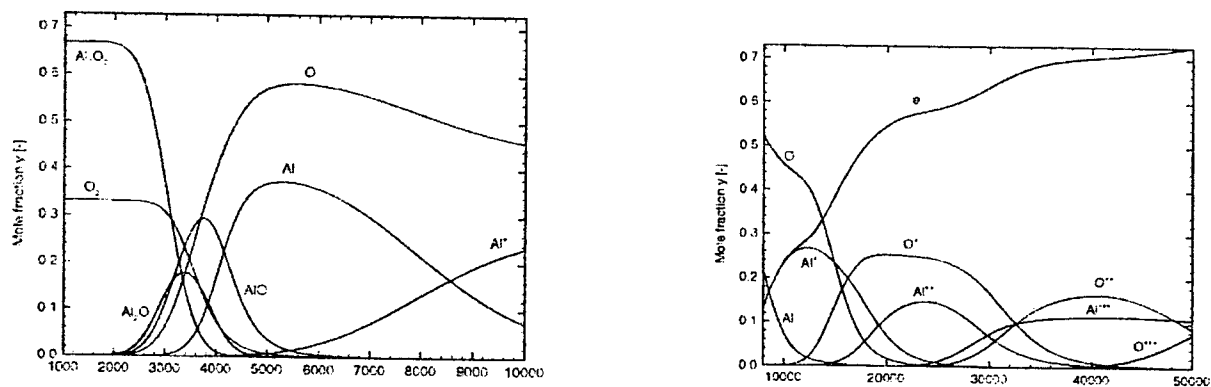


Fig. 3: Mole fractions  $y_\alpha$  of various species in the gaseous phase at 1 bar for the laser-induced removal of  $\text{Al}_2\text{O}_3$  in the temperature range  $10^3$  to  $10^4$  K (left) and  $8 \times 10^3$  to  $5 \times 10^4$  K (right).

## 5. CONCLUSION

The modelling of chemical processes during pulsed laser deposition describes the processes of material removal of the polymers PE, PP, and PMMA and the ceramic  $\text{Al}_2\text{O}_3$  in terms of a reaction depending on the dynamical state of the gas phase of the volatile species. The processing energy is distributed into different channels of decomposition resulting in changes of the chemical composition of the gas phase with subsequent changes of its flow field and temperature. Since any state of the gas phase requires a certain decomposition of the materials into molecules or atoms, as feedback the energy of degradation changes during the removal process and consequently the dynamics of the gaseous phase that in micro-machining, for example, the slope of the depth of material removal as a function of the fluence decreases with increasing fluence.

## ACKNOWLEDGEMENT

The authors would like to thank Bundesministerium für Bildung und Forschung, Germany for financial support within the framework "Strömungsmechanik des Plasmatransfers bei der Ablation mit UV-Laserstrahlung" and "Verfahrensbedingter Materialabtrag und Transfer Lasererzeugter Partikelströme". The authors are very grateful to Mrs. I. Stein for their cooperation in typing the manuscript.

## REFERENCES

1. D. B. Chrisey and G. K. Huber, Eds. *Pulsed Laser Deposition of Thin Films*, Wiley-Interscience, New York, 1994.
2. T. Klotzbücher, M. Scherge, M. Mergens, D. A. Wesener, and E. W. Kreutz, "Deposition of carbon nitride thin films in a hybrid RF-PLD-technique," *Surf. Coat. Technol.* **98**, 1072 - 1078, 1998.
3. E. Millon, O. Albert, J. C. Loulergue, J. Etchepare, D. Hulin, W. Seiler, and J. Perrière, "Growth of heteroepitaxial ZnO thin films by femtosecond pulsed-laser deposition," *J. Appl. Phys.* **88**, 6937 - 6939, 2000.
4. Z. Zhang, P. A. VanRompay, J. A. Nees, R. Clarke, X. Pan, and P. P. Pronko, "Nitride film deposition by femtosecond and nanosecond laser ablation in low-pressure nitrogen discharge gas," *Appl. Surf. Sci.* **154 - 155**, 165 - 171, 2000.
5. A. Husmann, M. Nießen, F. Grumbel, E. W. Kreutz, and R. Poprawe, "Scaling of a Q-switch  $\text{CO}_2$  laser for pulsed laser deposition," *SPIE Proc. Series* **3343**, pp. 759 - 768, 1998.
6. Y. Yamagata, A. Sharma, J. Narayan, R. M. Mayo, J. W. Newman, and K. Ebihara, "Optical emission study of ablation plasma plume in the preparation of diamond-like carbon films by KrF excimer laser," *J. Appl. Phys.* **86**, pp. 4154 - 4159, 1999.
7. Hsiu-Fung Cheng, Yi-Chun Chen, and I.-Nan Lin, "Frequency response of microwave dielectric  $\text{Bi}_2(\text{Zn}_{1/3}\text{Nb}_{2/3})_2\text{O}_7$  thin films laser deposited on indium-tin oxide coated glass," *J. Appl. Phys.* **87**, pp. 479 - 483, 2000.
8. E. J. Lerner, "Pulsed lasers target industrial coatings," *Laser Focus World* **35 (12)**, pp. 79 - 81, 1999.
9. P. W. Atkins, *Physical Chemistry*, Oxford University Press, London, 1986.
10. P. Andre, "Composition and thermodynamic properties of ablated species of PMMA, PA 6 - 6, PETP and PE," *J. Phys. D: Appl. Phys.* **29**, pp. 1963 - 1973, 1995.
11. M. Aden, D. A. Wesner, E. W. Kreutz, R. Poprawe, "Model of laser-induced material removal of polymers and gasdynamics," *SPIE Proc. Series* **3343**, pp. 505 - 514, 1998.
12. A. Franck and K. Biederbick, *Kunststoff-Kompendium*, Vogel-Buchverlag, Würzburg 1984.
13. M. W. Chase et al., "JANAF Thermochemical Tables Third Edition Part I, Al-Co", *J. Phys. Chem. Reference Data* **14**, Supplement No. 1, 1985.
14. T. E. Daubert et al., *Physical and Thermodynamic Properties of pure Chemicals*, Design Institute for Physical Property Data, American Institute of Chemical Engineers, Hemisphere Publ. Co., New York, 1997.

# General concept of a surface microgeometry reconstruction based on laser technology

Vadim P. VEIKO

Laser Applications Engineering and Applied Ecology Department,  
St.Petersburg Federal Institute of Fine Mechanics (Technical University)  
14 Sablinskaya str., 197101, St.Petersburg, Russia  
E-mail: veiko@lastech.ifmo.ru  
Phone/Fax: +7.812.2333406

**Keywords:** microgeometry, laser technology, roughness, ablation, microstructuring.

## ABSTRACT

Surface of solids play a leading role in any process of interaction between solids, solids-liquids, solids-gases and solids-plasma. Microgeometry (roughness) is a key parameter of the solids surface which influence a lot mechanical, optical, electronic, chemical, thermal and other characteristics.

Nowadays the laser-based technologies is a great challenge to improve a surface microgeometry (SM) quality and controllability.

Different laser-based surface processing are considered:

- surface microstructuring and control of roughness by laser ablation,
- surface microstructuring based on creation of surface electromagnetic waves (SEW) and surface periodic structures (SPS),
- surface smoothing and microstructuring based on laser heating till melting and further phenomena in a melted phase.

Some examples of laser applications to improve optical, tribological and other surface characteristic are considered and analyzed.

Future prospects of this field are discussed.

## 1. INTRODUCTION

Life generally is an interaction of surrounding bodies, medias and fields. And the interface dividing them is the place where phenomena of interaction act. All subjects of living and unliving nature as well as artificial objects have surfaces are never absolutely smooth. The surface is always rough to some degree. The degree of roughness strongly influences the workability of any machine, device etc. The roughness of a surface is the first factor which meets any blow, friction, crush, or action of a liquid, vapor, gas or plasma. Mechanical, but also physical properties (such as optical, acoustical, electrical, magnetic, thermal etc) of solids are affected by roughness to a high degree.

Different phenomena of the interaction of solid with other medias — solids, liquids, gases which are highly influenced by roughness have been investigated in the Laboratory of Surface Quality IFMO for many years. The list of the most important phenomena of solid surface interaction is presented in Table 1, and service characteristics of interacted surfaces are in Table 2<sup>1</sup>. A general view of some optimal microreliefs of surfaces is given in Fig. 1.

The roughness standard covers the region of deviations about the ideal surface from 320  $\mu\text{m}$  (1<sup>st</sup> class of cleanliness) through 0.05  $\mu\text{m}$  (14<sup>st</sup> class of cleanliness). Because of the important role of a surface quality, many methods have been suggested and investigated to control a surface roughness, among them mechanical, chemical and thermal.

There is no time and place to analyze every of them, but mechanical methods lead generally to an appearance of mechanical defects to some degree. Chemical methods are good for smoothing but are very limited for microstructuring of surfaces because of the need of many stencils.

That is why the development of new methods for control of surface roughness is very important always, especially in the age of nanodevices, nanoparticles, nanotribology, etc., when the size of some details are comparable with the roughness.

On the other hand, the latest progress in the laser technique makes to be possible a strongly controllable laser modification of surface topology due to the following reasons:

- 1) a choice of various wavelengths (especially deep UV and non-linear absorption at femtosecond pulses) provides extremely high absorption ( $\alpha$ ) and, correspondingly, a very small penetration depth  $\delta = 1/\alpha$ , (where  $\alpha$  — Bouger coefficient) of the light,
- 2) ultrashort laser pulses (less than  $10^{-9}$  s such as  $10^{-12}$  s,  $10^{-15}$  s and even less) along with the small  $\delta$  make possible a strictly dozed ablation of material and strong decrease of the heat transfer from the irradiated zone,
- 3) development of focusing—scanning, mask—projection and combined optical techniques allows to realize very well localized surface microstructures at large areas of treatment,

Table 1. Different sorts of surface interaction of solid

Interaction with solid	Interaction with liquid	Interaction with gas
<b>Mechanical</b>		
Rolling and sliding friction	Streamlining by liquids	Streamlining by gases
Static and dynamic loading		
<b>Chemical</b>		
Catalysis, adhesion	Wet ability, corrosion	Adsorption, corrosion
<b>Electromagnetic</b>		
Reflection and refraction of electromagnetic waves	Reflection and refraction of electromagnetic waves	Reflection and refraction of electromagnetic waves
<b>Electrostatic</b>		
Electrical conductivity	Galvanic effects	Electron emission
Electrization	Electrization	Electrization
<b>Thermal</b>		
Heat transfer	Thermal contact	Heat reflection

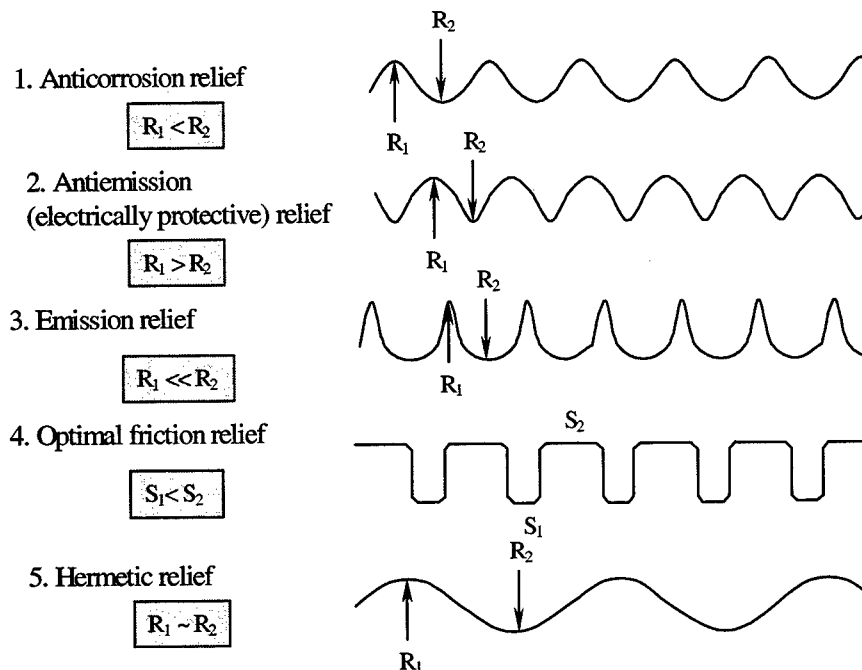


Fig. 1. Some optimal surface reliefs.

Table 2. Relationships between service characteristics and geometric microrelief parameters

Service characteristics		R <sub>a</sub>	R <sub>z</sub>	R <sub>max</sub>	S	F <sub>bs</sub>	k <sub>filling</sub>	β	r	F <sub>real</sub>	L <sub>real</sub>	N	r		Roughness	σ R <sub>z</sub>	r'
													R <sub>max</sub>				
Mechanical																	
Wear resistance		+	+	+	+	+	+	+	+	+	+	+	+	+	+	+	
Friction coefficient		+	+	+	+	+	+	+	+	+	+	+	+	+	+	+	
Fatigue strength		+	+	+											+	+	+
Fit strength		+	+	+		+	+		+			+					+
Hydro-aero mechanical																	
Tightness of hydraulic sealings		+	+	+	+	+	+	+	+	+	+	+	+	+	+	+	+
Streamlining by liquids/gases		+	+	+	+			+	+					+	+		+
Chemical																	
Corrosion strength		+	+	+	+		+		+					+	+		+
Strength and quality of galvanic coatings		+	+	+	+			+	+					+	+		
Electrical																	
Electric strength		+	+	+			+	+	+					+	+	+	+
Electrical conductivity		+	+	+	+		+				+			+	+		
Optical																	
Reflection of light		+	+	+	+	+	+		+			+	+	+	+	+	+
Reflection of IR radiation(heat-reflection)		+	+	+		+	+	+	+			+	+	+	+	+	+
Other																	
Ability to removal the dust		+	+	+	+			+	+							+	+
Surface cleaning during vacuumization		+	+	+			+	+	+					+		+	
Properties of thin films		+	+	+	+	+	+		+			+					
Adhesion of coatings																	

Symbols: R<sub>a</sub> – the normal deflection of profile, R<sub>z</sub> - the height of irregularities that determined through ten pointes, R<sub>max</sub>- the greatest height of irregularities, S – the average pitch of roughness by peaks, F<sub>bs</sub> – the square of base surface, k<sub>filling</sub> – the coefficient of profile filling, β- the angle of inclination of side walls of irregularities, r- the peaks nonhomogeneity of peaks height radius of irregularities, F<sub>real</sub> - the total square of real surface, L<sub>real</sub> - the length of real profile, N –the number of peaks per unit of surface, σ<sub>Rz</sub>- coefficient of nonhomogeneity of peaks height, r' – the valley radius of irregularities.

Symbols:  $R_a$  - the normal deflection of profile,  $R_z$  - the height of irregularities that determined through ten points,  $R_{max}$  - the greatest height of irregularities,  $S$  - the average pitch of roughness by peaks,  $F_{bs}$  - the square of base surface,  $k_{filling}$  - the coefficient of profile filling,  $\beta$  - the angle of inclination of side walls of irregularities,  $r$  - the peaks nonhomogeneity of height radius of irregularities,  $F_{real}$  - the total square of real surface,  $L_{real}$  - the length of real profile,  $N$  - the number of peaks per unit of surface,  $\sigma R_z$  - coefficient of nonhomogeneity of peaks height,  $r'$  - the valley radius of irregularities.



4) modern achievements in laser-matter interaction investigations allow to realize a broad range of surface modification processes from structuring to smoothing.

Nowadays the area of laser-based surface modification attracts more and more attention of different research groups. At least here should be mentioned M.Gower et al.<sup>2</sup>, V.I.Konov et al.<sup>3</sup>, H.Weber et al.<sup>4</sup>, V.P.Veiko et al.<sup>5</sup>, C.M.Geiger et al.<sup>6</sup>, I.Myamoto et al.<sup>7</sup>, A.C.Tam et al.<sup>8</sup>, J.Jiang et al.<sup>9</sup> and others (look below).

Thus it looks like it would be just the time to summarize results which have been received already in this field for better understanding future directions and steps.

## 2. LASER-BASED METHODS FOR SURFACE MICROGEOMETRY MODIFICATION (LSM)

The laser-based surface microstructuring has the following main directions:

1. Creation of new micro- and nano-devices for microoptics, photonics, microfluidics, micromechanics, microelectronics etc.

2. Modification of surface structure to improve various service characteristics: tribological performance, emission ability, wet ability etc.

In my opinion when the first direction successfully develops in many areas the second one only makes first steps. At the same time it has a big potential for the laser technology to increase influence on this very broad market — from mechanical pairs through space apparatus (satellites protection) etc.

There are different ways to modify the surface relief by laser action on to a solid. Let us analyze the most important of them:

1. Surface microstructuring based on local evaporation-ablation of a matter.
2. Control of roughness based on evaporation-ablation — laser polishing.
3. Surface microstructuring based on creation of surface electromagnetic waves (SEW) and surface periodic structures (SPS).
4. Microstructuring based on LASER-LIGA.
5. Surface smoothing based on the laser heating to a melting point and further phenomena in a melted phase.
6. Surface microstructuring based on a laser heating.

### 2.1. LSM based on laser ablation

Laser ablation is the most suitable process for a surface microstructuring and for a roughness control. In this case we mean evaporation under ablation because it is the most controllable (in depth, at least) mechanism of ablation. This is well known, universal, relatively high productive and simple method.

For this purpose it is possible to use any laser, which allows to obtain the power density  $q_{th}$  about<sup>10</sup>

$$q_{th} = \frac{2kT_{ev}\sqrt{\pi}}{A\sqrt{a\tau}} \approx 10^8 \frac{W}{cm^2} \quad (1)$$

where  $T_{ev}$  is evaporation temperature,  $k$  — thermoconductivity and  $a$  — thermodiffusivity coefficients,  $A$  — absorption of light,  $\tau$  — pulse duration (action time), which is enough for evaporation of any materials. At typical parameters of a microrelief structure  $r_0 \sim 10 \mu m$  it takes the laser with power  $P \geq qS \sim 10^4 W$ .

*Let us note, that pulse-repetition (PR) lasers are much better for microstructuring than continuous waves (CW) lasers. CW lasers are not optimal for the surface microstructuring because they produce relatively large and difficult to control heat-affected zone (for melting, oxidizing, recrystallization etc) with the size  $r_{np} \sim \sqrt{\alpha\tau}$ , where  $\tau$  in this case depends on the scanning speed,  $V_{sc}$  as  $\tau \sim r_0/V_{sc}$ . For example at  $V_{sc} \sim 1 cm/s$   $\tau \sim 10^{-2} s$  for metals which is strongly limits parameters of microstructures.*

*Beside of that a CW laser is not optimal for microstructuring because of energy losses. The relationship of PR and CW laser power when it reaches the same temperature can be calculated by the formula as,<sup>10</sup>:*

$$\overline{P_{PP}} / P_{CW} = f \tau r_0 / \sqrt{\alpha \tau}$$

At  $f = 10^3 \text{ Hz}$ ,  $\tau = 10^{-3} \text{ s}$ ,  $r_0 = 10^{-2} \text{ cm}$  —  $\overline{P_{PP}} / P_{CW} \sim 1$ , but quickly goes down with the decrease of  $\tau$  and for short pulses PR laser is much more effective than CW.

The thickness of an evaporated layer  $h_{ev}$  at the given power density depends on the pulse duration  $\tau$ . It can be easily estimated in the case (which is close to experimental conditions the shorter the better the laser pulse) when the whole energy goes to evaporation of the material (heat losses are negligible)

$$h_{ev} = V_{ev} \cdot \tau = \frac{q}{L_{ev}} \tau \quad (2)$$

where  $V_{ev}$  — the speed of evaporation — speed of a solid–gas interface motion,  $L_{ev}$  — specific energy of evaporation.

Typical values for  $h_{ev}$  at  $q \sim 10^8 \text{ W/cm}^2$  ( $V_{ev} = 2 \cdot 10^3 \text{ cm/s}$ ) for steel (when screening effect is negligible which is true for a surface microstructuring with a short pulses) is given at the Table 3.

Table 3. Thickness of evaporated layer  $h_{ev}$  under laser action with the various pulse duration  $\tau$

$\tau, \text{ s}$	$10^{-6}$	$10^{-9}$	$10^{-12}$
$h_{ev}, \text{ m}$	$2 \cdot 10^{-5}$	$2 \cdot 10^{-8}$	$2 \cdot 10^{-11}$

One can see the excellent controllability of the high parameters of a roughness are under the short laser pulses.

When a pulse laser is used no any visible limitation for the degree of structuring of surface while reasonable for machine– and instrument–building industry about light wavelength ( $\sim 0.5 \mu\text{m}$ ).

But it may take a lot of time to produce very complicated structures. That is why for industrial microstructuring it is necessary to use laser with high enough pulse repetition rate.

The next limitation for lasers is the wavelength of radiation primarily from pure energetic reasons, absorption coefficient (look formula (1)).

The most suitable lasers for surface microstructuring are presented at the Table 4.

Table 4. Parameters of laser for LMS by evaporation

Laser	Parameters				Comment: tentative matter for LSM
	$\lambda, \mu\text{m}$	$\tau, \text{ s}$	$f, \text{ Hz}$	Average power, W	
Excimer lasers	0,157 0,193 0,218 0,308	$\sim 10^{-9}$	$10^2$	100	non–metals, composites, plastics
Q-switching YAG:Nd laser	1,06 0,53	$\sim 10^{-8}$ $\sim 10^{-7}$	$10^4$	20	Metals
Pulsed $\text{CO}_2$ –laser	10,6	$\sim 10^{-6}$ $\sim 10^{-4}$	$10^3$	200	Glasses, plastics, composites, metals
Laser on vapor of Cu	0,51 0,57	$\sim 10^{-8}$	$10^4$	20	Metals

A focused laser beam as projected through the mask (so called projection method)<sup>10</sup> can be applied for LSM. The role of focusing will be discussed in the next section.

A laser beam in opposite to a mechanical tool do not wear out, and in difference from chemical methods permits more easy localization of area of processing.

Photographs of surfaces microstructured by laser radiation are presented in Fig. 2.

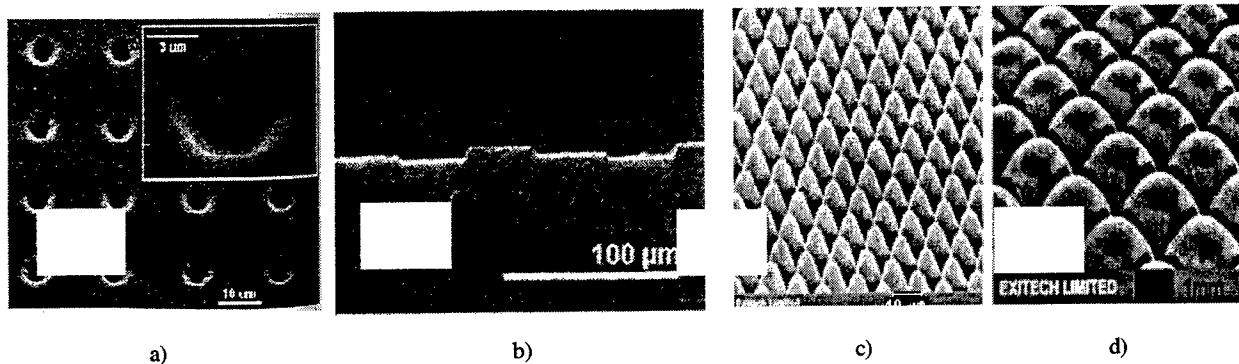


Fig. 2. Microstructures produced on different surfaces by a laser evaporation:

- a — REM image of a structured steel surface for improving tribological performance (Q-switched Nd-YAG laser)<sup>4</sup>,  
b — part of the surface profile of the diamond four-level cylindrical Fresnell lens (KrF-laser)<sup>12</sup>; c, d — microoptical surfaces fabricated by KrF-laser micromachining and orthogonal mask-dragging: c) cesium iodide far-infrared optical crystal, d) polycarbonate<sup>13</sup>.

## 2.2. Laser control of roughness

This method is also based on laser evaporation and permits to control the height and depth of roughness based on correct focusing of laser beam<sup>14</sup>. During treatment with divergent beam—power density at selected level  $h$  of roughness corresponds to a threshold  $q_{th}$  (formula 1), that is why below  $h$   $q$  is not enough to ablate material. Result is the roughness height decrease as shown in Fig. 3, a. Having a good control of focal plane position, it is possible to decrease the roughness to desirable degree. The most controlled situation is for sublimating (evaporating from solid phase) materials like diamond. Konov et al.<sup>3</sup> demonstrated the excellent quality of laser polishing for thick diamond coatings (see Fig. 3, b, c).

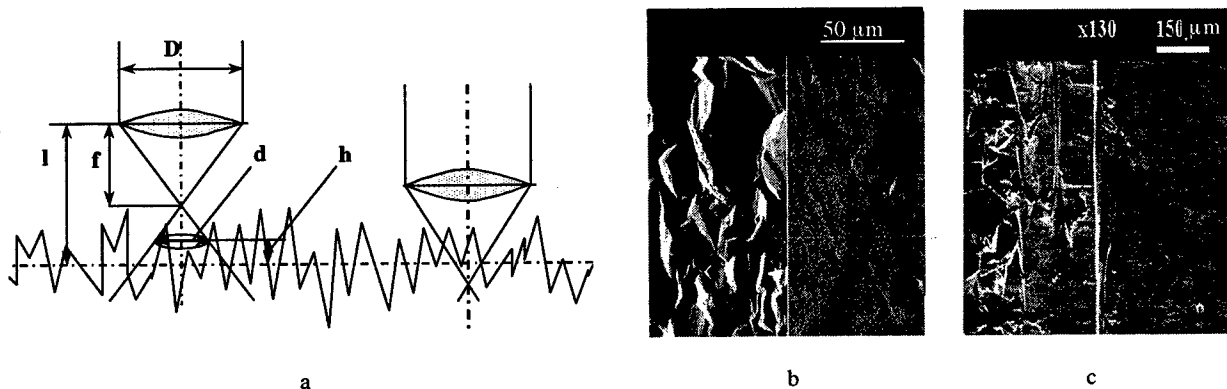


Fig. 3. Scheme of laser-based control of roughness (a)<sup>14</sup> and resulting SEM-images of thick diamond films before and after the laser polishing by Cu-vapor (b) and ArF (c) lasers<sup>3</sup>.

One can observe the opposite situation for a processing in a coincident beam. The power density is greater in valleys of the relief than on peaks and the height of the relief becomes more.

The final height of the relief depends only on the numerical aperture of an optical system NA, distance between the lens and surface  $l$  and the accuracy of its position, and, of course, from the material and laser power  $P$ :

$$h_n = (1-f) - \frac{NA}{2} \sqrt{\frac{P}{q_n}} \quad (3)$$

In case of metals which evaporates from the melt, the situation is more complicated because of much more phenomena involved in the process of surface modification, such as melting, thermocapillary flowing, viscosity friction at heating and cooling etc.

This way of a surface processing allows to control only height parameters of roughness but is not able to change distribution of them on the surface.

### 2.3. LMS based on surface electromagnetic waves (SEW) and surface periodic structures (SPS)

At some special conditions surface electromagnetic waves inevitably appear to fulfill the law of energy conservation at the surface of solids. Most important condition of SEW generation is that one of two contacted media should have negative dielectric permeability (negative polarizability). In the visible region metals and sometimes semiconductors have such parameters and that why one calls them "surface-active media". A polarized light and an inclined incidence are also necessary to produce running SEW which can interfere with an incident light. Such kind of interaction produces new intensity distribution modulated by a parameter of the resonance grating. The resonance parameter is always exists on the real surface in the spatial spectrum of random surface roughness.

The modulated intensity distribution at high enough value can cause corresponding spatially inhomogeneous heating, melting, evaporation and other concomitant to heating phenomena and finally produces the SPS.

Direct physical mechanisms of the SPS formation in different conditions may be evaporation, melting, thermal deformations etc. Many phenomena play their roles in this process, such as inhomogeneous recoil vapors pressure, thermocapillary effect, thermochemical reaction, generating surface defects etc. Anyway, an SPS appears at the surface after its cooling in the shape of some microstructure (Fig. 4).

The SPS formation has an universal character. It is being observed on metals, semiconductors and dielectrics in a wide range of wavelengths (from IR to UV spectral region), durations and intensities of the incident laser radiation (from a continuous one with flux density of  $q \sim 100$  W/cm<sup>2</sup> to picosecond pulses of  $q \sim 10^9$  W/cm<sup>2</sup>). Such structures are usually oriented in a certain way toward the projection of the light-wave electric vector on the surface and have a period of the order of the incident radiation wavelength  $\lambda$ .

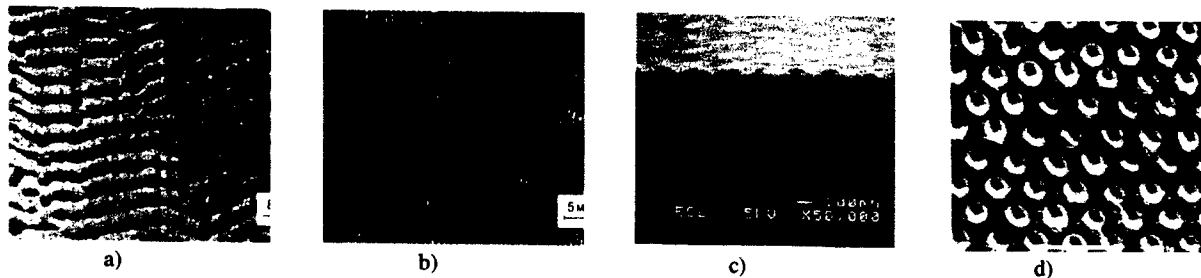


Fig. 4. Periodic structures at different surfaces fabricated under laser irradiation by different wave-length  $\lambda$ , pulse duration  $\tau$ .  
a — Si, Nd-YAG-laser,  $\lambda = 1.06$   $\mu$ m,  $\tau = 1$   $\mu$ s, 1 pulse,  $q = 0.7$   $\mu$ W/cm<sup>2</sup>; b — stainless steel, Nd-YAG-laser,  $\lambda = 1.06$   $\mu$ m,  $\tau = 30$  ns, 40 pulses,  $q = 30$  mW/cm<sup>2</sup>; c — SEM-photographs of biharmonic relief structure with period 0.21  $\mu$ m, fabricated on n-InP material using combine holographic and SEW-techniques<sup>16</sup>; d — W, single crystal surface ( $\theta = 10^\circ$ ), SEM-image, Q-switched Nd-YAG-laser,  $\lambda = 1.06$   $\mu$ m,  $q = 26$   $\mu$ W/cm<sup>2</sup><sup>17</sup>.

A lot of papers in recent years are devoted to formation of the SPS (look for example fundamental work<sup>15</sup>). But relationships between topological parameters of generated regular microstructures and laser radiation characteristics are highly complicated and still not completely studied. Besides of that, the SPS parameters depend on the properties and statement of the irradiated material, but these relationships are not completely clear. All these limitations do not permit to

use this method in industry right now, but known theoretical and experimental results give possibility to recommend SEW-SPS method to structure the surfaces of the nearest future confidently. Some promising results has been demonstrated in fabrication of prototypes of diffraction gratings<sup>16</sup>, Fig 4, c, cathodes of emission devices<sup>17</sup>, Fig. 4, d etc.

## 2.4. Laser-Liga based microstructuring

One interesting case of surface microstructuring is Laser-Liga process described in<sup>18</sup>. It consists of two laser-assisted processes in combination with an intermediate step of electroplating (Fig. 5, a).

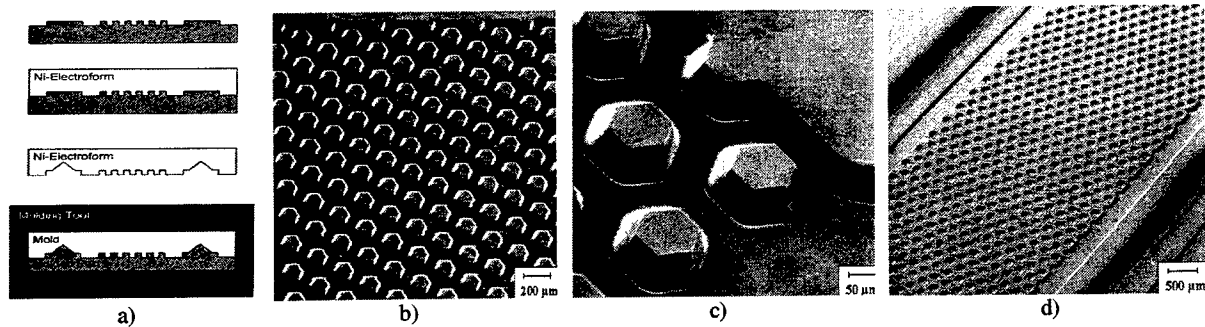


Fig. 5. Principle of Laser-Liga based combine method<sup>16</sup> — a, part of a large area microstructure in polycarbonate — b, detailed view of the same part — c, electroplated insert of the master with additional structures machined by laser-assisted thermochemical etching — d<sup>18</sup>.

- firstly, a polycarbonate substrate was microstructured by KrF excimer laser photoablation (photochemical dry etching) in a dynamic projection scheme. It enables the transfer of structures having dimensions much larger than the laser beam section by synchronized scanning of the mask and the substrate,
- secondly, by electroforming of nickel the polymeric master converts into a metallic form,
- thirdly, additional structures are micromachined by the laser-assisted thermochemical etching. The direct processing of the workpiece is resulted in high accuracy microstructuring with smooth surfaces  $R_a < 0.5 \mu\text{m}$  and without any debris or thermal influence on the material properties.
- fourthly, the finished metallic mold can be used for a fabrication of similar plastic microparts, for example, by the injection molding.

As an example, microstructures at polycarbonate surface for microfluidic devices are presented in Fig. 5, b, c, d. Fig. 5, b, c show a part and a detailed view of a 10x20 mm<sup>2</sup> sized microstructure in polycarbonate achieved by using the technology of synchronous scanning. The depth of the structure is 60  $\mu\text{m}$  and the angle of the walls approximately 15 degrees.

## 2.5 Laser smoothing in a liquid (viscous-flowing) phase

This method is based on heating of material to the temperature when responsible for surface quality processes take place in a melted (softened) phase. The best results in this way can be achieved for glass surfaces.

*In opposite to glasses for metals active polycrystallization during cooling impedes the creation of a smooth surface. In case of metals it is possible to eliminate the crystallization having a very high speed of cooling. In fact it can be realized when a very thin metal film is heated by ultrashort laser pulses. In these conditions "metallic glasses" with typically glazing smooth surface appears in irradiated zone. Formation of large areas of metallic glasses is still a problem of boundaries of irradiated spots.*

The physical idea of a laser smoothing of glass surfaces is similar to a fire polishing of glass: laser irradiation should provide heating till the temperature of softening when viscosity of glass does not disturb a surface tension to realize the tendency to minimal free (surface) energy and correspondingly minimal surface size.

Two most difficult problems appear in this case: hydrodynamic wave at a softened surface and thermomechanical residue stresses in a glass sample during and after the cooling. These problems have been investigated in our laboratory<sup>5</sup>.

Briefly the first problem can be solved by an optimal choice of beam size and scanning speed. For example, scanning speed  $V_{sc}$  should be less than hydrodynamic wave speed  $V_h$ :  $V_{sc} \leq V_h$ , where  $V_h \sim k \frac{dT}{dz}$ ,  $\frac{dT}{dz}$  — temperature gradient in a softened zone in a direction of scanning,  $k$  depends on viscosity, temperature coefficient of viscosity and thickness of the softened zone. In this case laser beam produces smooth area driving irregularities to the side of a sample in similar manner to a cleaning of semiconductors from impurities by a zone melting.

The problem of thermomechanical stresses can also be overcome by optimal choice of laser beam cross-section, pre- and postheating etc. The positive results have been demonstrated for mini- and microoptics (Fig. 6)<sup>5</sup> and even for macrooptics<sup>19</sup>.

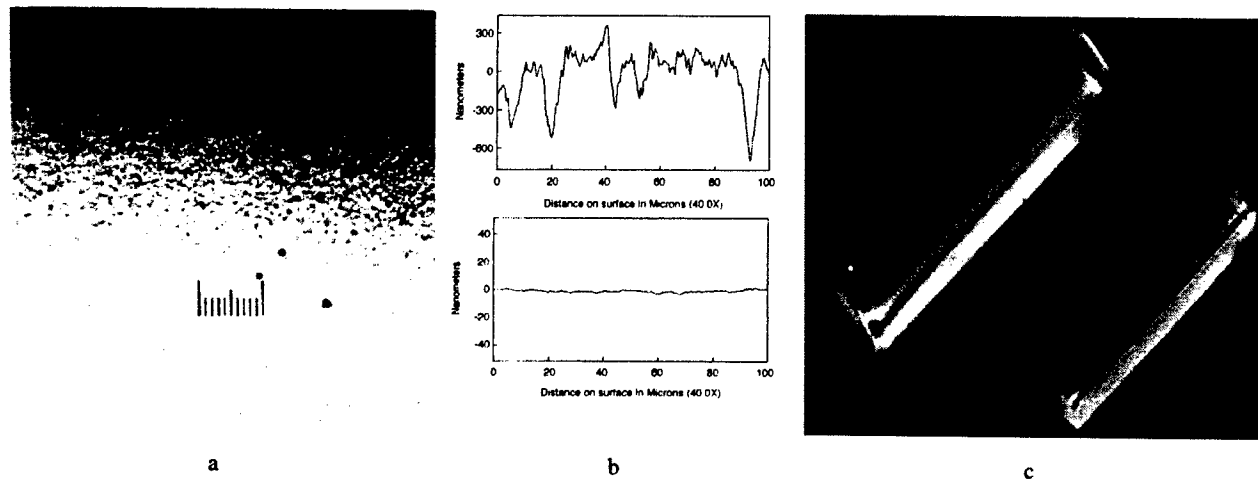


Fig. 6. Laser polishing of glass: electron micrographs of B-270 glass after mechanical polishing (a, up) and after additional laser polishing (a, down), the transition region between irradiated and non-irradiated area is shown; corresponding measured profiles after mechanical (b, up) and laser (b, down) treatment of glass samples<sup>19</sup>; c) aspherical cylindrical lens after laser profiling and polishing<sup>5</sup>.

## 2.6. Surface microstructuring by soft laser heating

As in the last section (2.5), a soft laser heating is a regime where no any ablation of the material takes place. In a glass and glass-like materials (porous glasses, glass-ceramics etc) different phenomena one can observe which can lead to the fine surface microstructuring. At first it is of interest for microoptics<sup>20</sup> because along with the structuring (profiling), a high quality of the structured surface is provided due to the action of the surface tension (Fig. 7).

Let us point here only two possibilities.

1. Laser densification of porous glasses cause the shrinkage of irradiated in a softened phase zone and the profile of the surface is defined by intensity distribution. The general view of the shrinkage zone during laser densification of porous glass under CO<sub>2</sub>-laser irradiation is represented in Fig. 7, a and a microoptical raster produced by the laser densification of glasses is shown in Fig. 7, b.

2. Laser amorphization of a glass-ceramics has a different nature — it is a change of phase state from a polycrystalline to an amorphous one which accompanies changes in specific volumes  $V_{cr}$  and  $V_{am}$ . The crystalline phase is packed more densely and the amorphous one of less density and  $V_{am}/V_{cr} < 1$ .

The final profile of an irradiated surface of ZnSiO<sub>4</sub>-2PbO-BaO<sub>3</sub>ZnO glass-ceramic and a general view of the corresponding lens raster by consequent light spots (CO<sub>2</sub>-laser) is shown in Fig. 7, c, d.

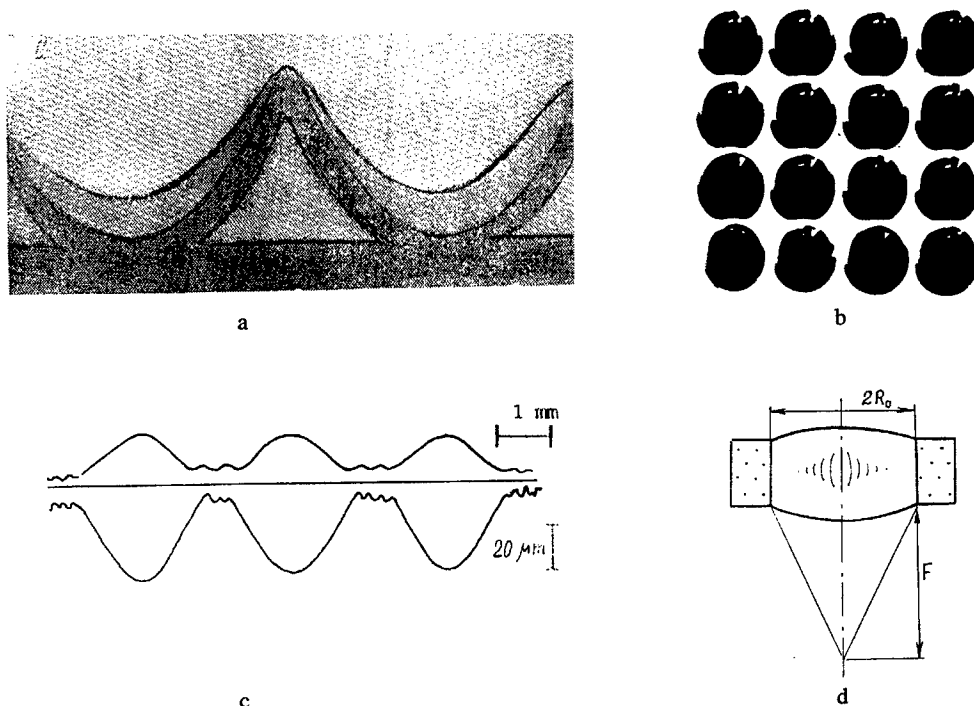


Fig. 7. Surface microstructuring by soft laser heating. a, b — laser densification of porous glass: a — a general view of the zone of the shrinkage, b — the microoptical raster produced under a  $\text{CO}_2$ -laser irradiation<sup>20</sup>. c, d — laser amorphisation of glass-ceramics: c — the profile of the zone irradiated by consequent light pulses, d — a general view of the lens<sup>21</sup>.

### 3. CONCLUDING REMARKS

A number of important problems could be solved by the creation of a special surface microreliefs. For example, as it is well known regular hexagonal microrelief has a minimal free energy, what provides its maximal stability under any external action — mechanical, chemical thermal etc. Such kind of surfaces improves the anti-seizing properties and corrosion strength, increases the contact rigidity, fatigue strength, slider resistivity, tightness of stable junctions and their hydrodensity; reduces adhesion and seizure with rubber during prolonged rubber-metal sealing; improves the quality of a galvanic covering; speeds up a surface cleaning under vacuum conditions; reduces irradiation in the outer space; provides normal friction conditions in vacuum; increases the reflecting capacity; etc.

It is worth to note that the nature also pays attention to the surface relief and regular hexagonal structures are the most popular. Some examples of them are shown in Fig. 8<sup>22</sup>.

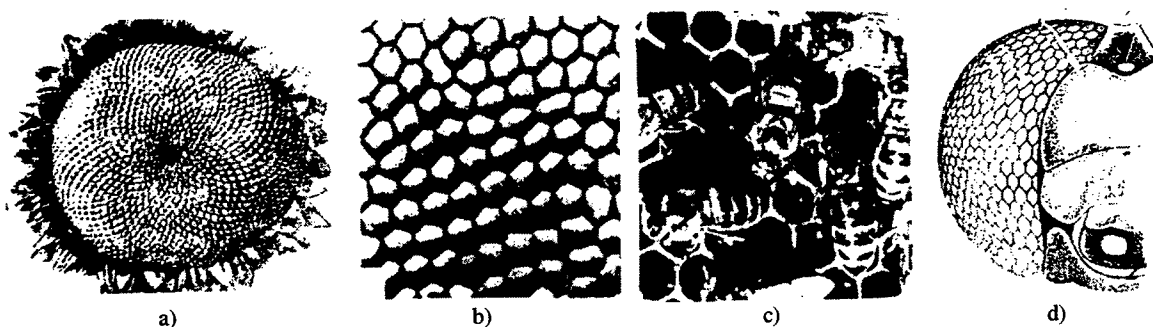


Fig. 8. Natural analogues to regular microreliefs: a — sunflower, b — metal melt, c — honeycombs, d — faceted eye<sup>20</sup>.

It seems to me that possibilities of laser-based surface topology reconstruction put us to the edge of a new jump in a surface science and technology.

#### 4. ACKNOWLEDGEMENTS

I am very grateful to Yu. Kouzmin and H. Huber which help me to find some materials and to S. Dyshlovenko and S. Sarnakov for the help in preparing this paper.

#### 5. REFERENCES

1. Yu. G. Shneider. Service characteristics of workpieces with regular microrelief. 2nd ed., Machine-building, Leningrad, 1982.
2. D. W. Thomas, C. Foulkes-Williams, P. T. Rumsby, M. C. Gower. Surface modification of polymers and ceramics induced by excimer laser irradiation. In "Laser ablation of Electronic Materials", ed. E. Fogarassy, S. Lazare. Elsevier Sci. Pub., p. 221, 1992.
3. S. M. Pimenov, V. V. Kononenko, V. I. Konov et al. Laser polishing of diamond plates. *Applied Physics A*, 69 (1), p. 81, 1999.
4. G. Dumitry, V. Romano, H. P. Weber et al. Laser microstructuring of surface for improving of their tribological performance. *Proceedings SPIE*, v. 4157, Laser-Assisted Microtechnology 2000, p. 105, 2001.
5. V. P. Veiko, A. T. Shakola, V. A. Chuiko et al. Aspherization of cylindrical lenses by laser irradiation. *Proceedings SPIE*, v. 2687, Miniaturized Systems with Microoptics and Micromechanics, p. 156-166, 1996.
6. S. Roth, M. Geiger. Novel technique for high-quality microstructuring with excimer lasers. *Proceedings SPIE*, v. 3933, Laser Applications in Microelectronic and Optoelectronic Manufacturing, p. 338, 2000.
7. E. Ohmura, R. Murayama, I. Myamoto. Thermohydrodynamics analysis on the mechanism of bump formation in laser texturing. *Proceedings SPIE*, v. 4088, Laser Precision Microfabrication, p. 244, 2000.
8. A. C. Tam, C. C. Poon, L. Crawforth et al. New laser curvature adjust technique for fine adjustment of the crown and cambers of magnetic head sliders. *Insight Publisher by Int. Disk Drive Equipment and materials Ass., USA*, p. 8-12, May/June 2000.
9. J. Jiang, Y. He, Y. Yan et al. Research on laser texturing and surface quality control. *Proceedings SPIE*, v. 4088, Laser Precision Microfabrication, p. 240, 2000.
10. S. M. Metev, V. P. Veiko. Laser assisted microtechnology. Springer-Verlag, Heidelberg, 1994 (first edition), 1998 (second edition).
11. V. P. Veiko. Overview of laser microprocessing: fundamentals, practical applications and future prospects. *Proceedings SPIE*, v. 4088, Laser Precision Microfabrication, p. 9, 2000.
12. V. I. Konov, V. V. Kononenko, S. M. Pimenov et al. Excimer laser micromachining for fabrication of diamond diffractive optical elements. *Proceedings SPIE*, v. 3933, Laser Applications in Microelectronic and Optoelectronic Manufacturing, p. 322, 2000.
13. M. Gower. Excimer laser microfabrication and micromachining. *Proceedings SPIE*, v. 4088, Laser Precision Microfabrication, p. 124, 2000.
14. V. P. Veiko, E. A. Touchkova. The method for laser machining of materials. Russian patent, N 1107431 from 08.04.84.
15. A. M. Bonch-Bruевич, M. N. Libenson. Laser-Induced Surface Polaritons and Optical Breakdown. In book "Nonlinear Electromagnetic Surface Phenomena", ch. 10, p. 561-609, Elsevier Sci. Publishers B. V., North Holland, 1991, The Netherlands.
16. V. Ya. Panchenko, A. I. Khudobenko and V. N. Seminogov. Laser maskless formation of submicron periodic relief gratings on  $A_3B_5$  semiconductor wafers by combination of holographic and surface electromagnetic waves generation methods. *Proceedings SPIE*, v. 2703, Laser Applications in Microelectronic and Optoelectronic, p. 579, 1996.
17. Y. Kawakami and E. Ozawa. Non-lithographic coherent array of ultrafine particles on an irradiated material using Nd:YAG laser - Influence of the laser fluence on the microstructure -. *Proceedings SPIE*, v. 4088, Laser Precision Microfabrication, p. 228, 2000.
18. G. Sepold, A. Stephen, T. Lilienkamp and S. Metev. Precise laser-assisted 3-D microstructuring of metals and alloys. *Proceedings SPIE*, v. 4426, Second International Symposium on Laser Precision Microfabrication, 2001 (in print).
19. F. Laquarta, N. Lupon and J. Armengol. Optical glass polishing by controlled laser surface-heat treatment. *Applied Optics*, v. 33, N27, p. 6508, 1994.
20. V. P. Veiko. Laser technology of microoptical components with gradient index refraction. *Proceedings SPIE*, v. 1352, Laser Surface Microprocessing, p. 92, 1989.
21. V. P. Veiko, K. G. Predko, V. N. Volkov, P. A. Skiba. Laser formation of microoptical elements based on glass ceramics materials. *Proceedings SPIE*, v. 1751, Miniature and microoptics, p. 361, 1992.
22. Yu. G. Shneider. Surface control on precision components. *Precision engineering*, v. 6, N4, p. 219, 1984.



# LASER INDUCED DIFFUSIBLE RESISTANCE: DEVICE CHARACTERIZATION AND PROCESS MODELING

M. Meunier<sup>\*a,b</sup>, M. Cadotte<sup>a</sup>, M. Ducharme<sup>a</sup>, Y. Gagnon<sup>b</sup>, and A. Lacourse<sup>b</sup>

<sup>a</sup> École Polytechnique de Montréal, Département de Génie Physique, Case Postale 6079, Succursale.  
Centre-ville, Montréal (Québec), Canada, H3C 3A7

<sup>b</sup> LTRIM-Technologies, 440 Blvd Armand Frappier, suite 140, Laval, Québec, Canada, H7V 4B4

## ABSTRACT

Highly accurate resistances can be made by iteratively laser inducing diffusion of dopants from the drain and source of a gateless field effect transistor into the channel, thereby forming an electrical link between two adjacent p-n junction diodes. We show that the current-voltage characteristics of these new microdevices are linear at low voltages and sublinear at higher voltages where carrier mobility is affected by the presence of high fields. A process model is proposed involving the calculation of the laser melted region in which the dopant diffusion occurs. Experimental results are well described by the proposed model.

**Keywords:** Laser trimming, microelectronics, resistance

## INTRODUCTION

Due to the inevitable fabrication process variabilities, microelectronics circuit functionality are very often altered, resulting in chips off specifications or useless. Because of the intrinsic characteristics of digital microelectronics, which essentially consists of low (or 0) and high (or 1) voltages, they can be built more robust to these fabrication variabilities than analog circuits for which high accurate components are required. To keep pace with the rapid growth of digital microelectronics, trimming techniques have to be used to accurately adjust some microdevices' characteristics for analog microelectronics. We have recently proposed a new laser technique to finely tune analog microelectronics circuits which presents the advantages of being very accurate, using very small die area, and being easily integrated into any actual CMOS process without additional steps [1,2]. A patent disclosing the detailed device structure and creation method has been recently accepted [3].

In this paper, after reviewing the principle of the technique, we present the electronic characterization and the modeling of these new microdevices and show that they present excellent current-voltage linear behavior at usual microelectronics voltages. Furthermore, process modeling based on the laser induced silicon melted region calculation is detailed and successfully compared to experimental results.

## PRINCIPLE OF THE LASER TRIMMING METHOD

The laser trimming technique, which has been described previously [1,2] is performed on a device structure consisting of a MOSFET, without the gate, fabricated by a conventional CMOS process. For an n-type resistor, the device structure consist of two highly doped regions, separated by 2L and formed by implantation into a p-well, resulting into two p-n junctions facing each other. Before performing laser trimming, the only current that can flow through the device is the p-n junctions leakage current, resulting essentially in an open circuit. Focusing a laser beam on the gap region between the two junctions causes melting of the silicon, resulting in dopant diffusion from the highly doped regions to the lightly-doped gap region. Upon removal of the laser light, the silicon solidifies and freezes in place, leaving the diffused dopants in a new special distribution forming an electrical link between the highly doped regions. This laser-diffused link constitutes the trimmed resistor. Tight control of process parameters is necessary to create efficiently these laser diffusible links while avoiding damage to adjacent devices and structures. These parameters are the laser spot size, the pulse duration, the laser power, the number of laser expositions and the position of the laser spot relative to the device. By varying the parameters between each laser intervention, one can accurately control the tuning of the device. The laser system consisting of the laser, the necessary optics to focus the beam on the microelectronics chip and a X-Y-Z computer controlled positioner has been described previously [1,2].

*\*meunier@phys.polymtl.ca, phone: 514-340-4711 ext 4971*

## DEVICE CHARACTERIZATION

Figure 1 shows some typical microdevices that have been tuned with the laser. These circuits, which have no specific electronic functionality other than testing the devices, consist essentially of arrays of gateless MOSFET's with a source to drain distance of  $1.7\mu\text{m}$ . Figure 1 (a) has been taken by an optical microscope and shows that the top interdielectrics layers are almost not affected by the laser. Figure 1 (b) shows an image taken by a Focus Ion Beam (FEI Company). The two black spots represent holes which have been deliberately made with the laser to cut electrical links. Again, the laser process for making a diffusible resistance has essentially no effect on the interdielectrics. Figure 2 shows images produced with an Atomic Force Microscope (AFM) and a Scanning Capacitance Microscope (SCM) (Digital Instruments, Dimension 3100 model) of a laser diffused resistance, where all outer dielectric layers have been removed by an HF etch. Five laser pulses with a beam waste of  $0.9\mu\text{m}$  were used in this experiment and the laser parameters were maintained at a duration of  $1\mu\text{s}$  and a laser power of  $0.75\text{W}$  incident on the surface of the chip (estimated at  $0.65\text{ W}$  on the silicon surface). While the AFM image reveals no significant deformation of the p-well, the SCM image shows clearly that dopants, represented by a dark gray, have diffused from the two  $n^+$  regions into the p-channel. The diffused region is about  $1.1 \pm 0.2\mu\text{m}$  in diameter.

Figure 1 (a)  
Optical microscope image  
of a laser induced  
modification of the device.  
The interdielectrics are  
essentially unaffected.

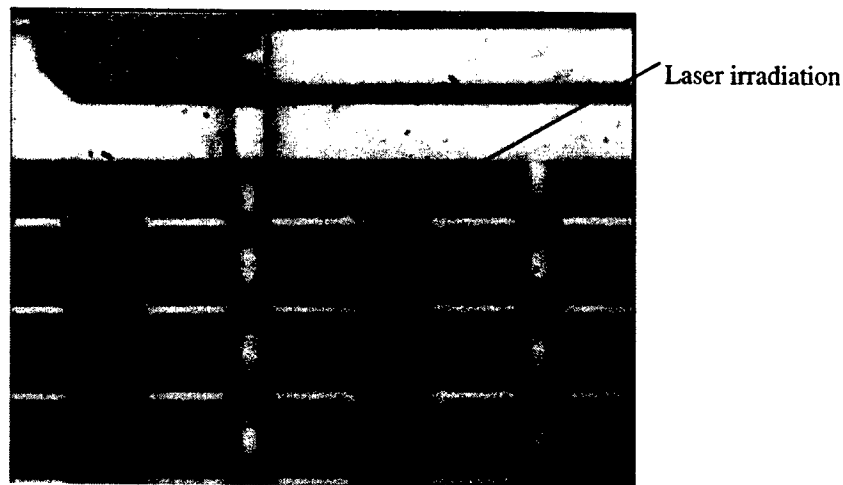


Figure 1 (b)  
Focus ion beam image of a  
laser induced diffusible  
resistance. The two black  
spots on the left are due to  
two deliberate laser cuts. In  
the middle, three laser  
irradiations were performed  
on the microdevices. The  
interdielectrics layers are  
essentially unaffected.

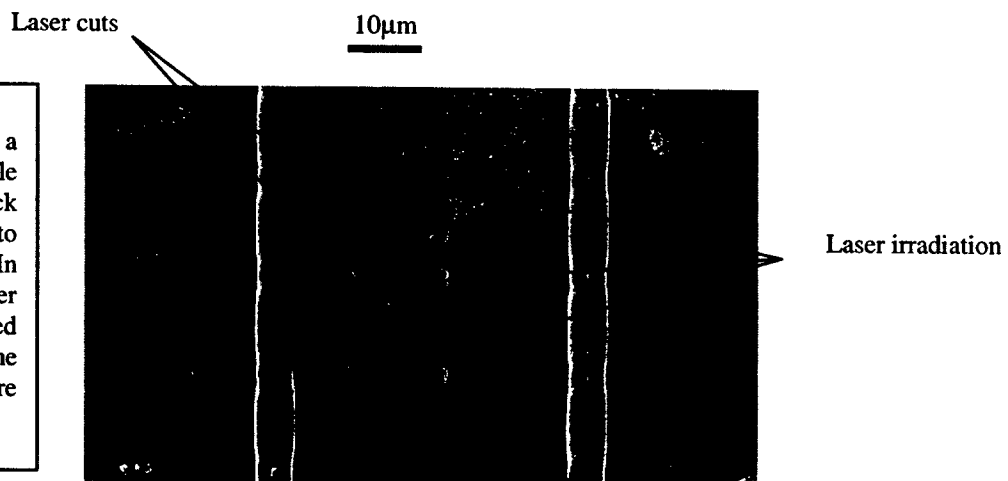


Figure 1 Images of laser induced diffusible resistances

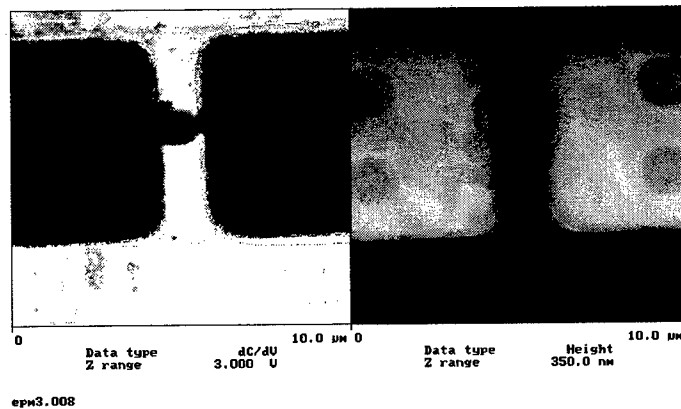
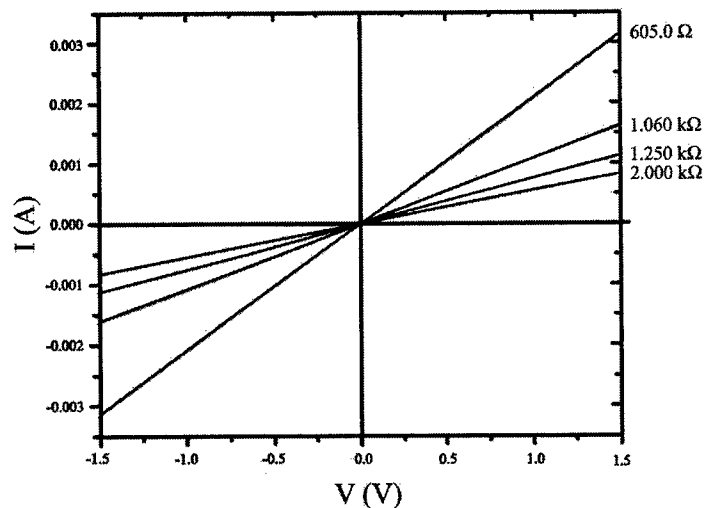
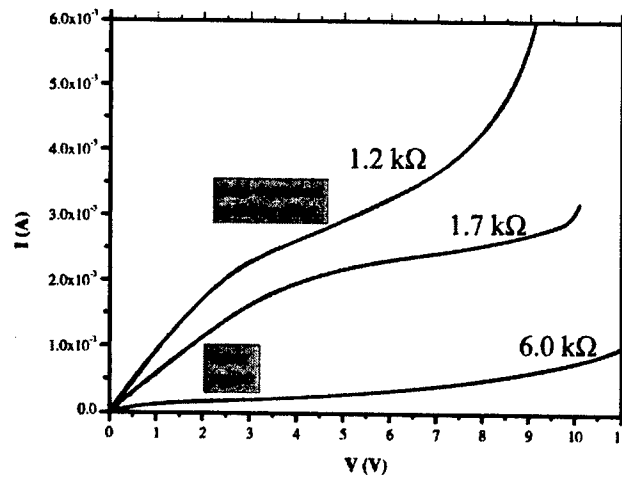


Figure 2 : SCM image (left) and corresponding AFM image (right) of a laser induced diffusible resistance. The n-channel is clearly visible on the SCM image whereas topography (AFM) reveals no significant deformation of the p-well. (The distance between the source and the drain is  $1.7\mu\text{m}$ )

Current-voltage (I-V) characteristics have been measured using a Hewlett Packard 4155A semiconductor parameter analyzer. The current-voltage curves of typical laser diffusible resistances are presented in Figure 3. Lower resistance devices (lower than few  $\text{k}\Omega$ ) present an excellent linearity over the range of voltages normally used in microelectronics ( $\pm 1.5\text{V}$ ), while higher resistance devices show non-linear effects and a relatively small ( $-0.3\text{V}$  to  $0.3\text{V}$ ) linear region. In Figure 3(b), I-V characteristics are plotted up to relatively large applied voltages. They show a non-linear behavior primarily related to the carrier velocity saturation at moderate fields and to an avalanche effect at high fields, reducing the resistance which permits a greater current to flow into the device.



(a)



(b)

Figure 3: Current-voltage characteristics of three laser diffusible resistances at (a) low voltages ( $< 1.5\text{V}$ ) and (b) at high voltages

In order to more deeply understand these I-V characteristics, these created devices can easily be associated to a  $n^+-v-n^+$  diode where the laser diffused region acts as the  $n$ -doped region [4]. At low applied voltages, a 1D finite element analysis shows that a monotonous electric field is created throughout the  $v$  region generating a drift carrier current, resulting in a linear I-V curve. As the applied voltage increases, a more intense electric field, as large as  $5\text{kV/cm}$ , is applied on the carriers, especially near the junctions where the presence of space charges adds to the magnitude of the field. The bending of the I-V is attributed to the saturation of the carriers velocity at these higher fields. To verify this, a 2D finite element quasi-stationary analysis has been carried out with the computer program ISE TCAD [5], using the doping level dependant mobility model of Masetti et al.[6] and the velocity saturation model of Canali et al [7]. As shown in figure 4, simulation calculations are in very good agreement with experimental results when a uniform dopant concentration of  $1.5 \times 10^{18} \text{ cm}^{-3}$  is assumed. The theoretical analysis is being pursued on the I-V characteristics at even higher fields, especially after the current saturation, where space-charge-limited currents are expected to be important.

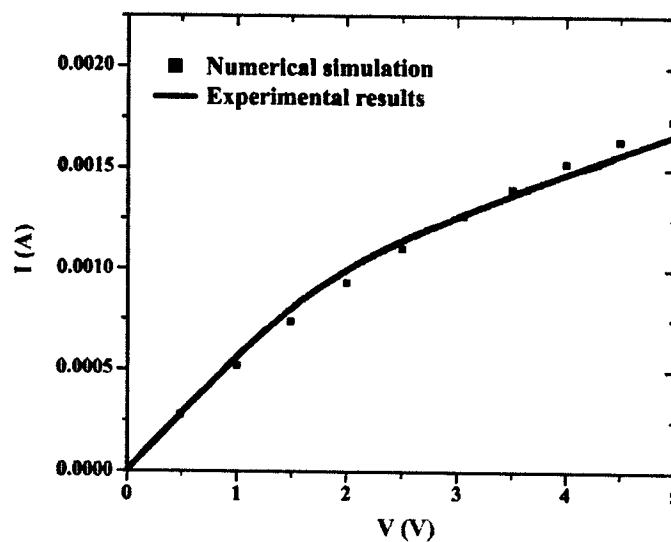


Figure 4: 2D simulation of the I-V characteristics of a laser diffusible resistance of  $1.802 \text{ k}\Omega$

## PROCESS CHARACTERIZATION AND MODELING

Modeling this process involves a time-dependent three-dimensional (3D) calculation of the temperature due to the laser irradiation [8], followed by a dopant distribution calculation using Fick's law. A simple model must include the effects of the laser power, beam waist and exposure time as well as the geometric characteristics of the initial structure. Device characteristics can then be evaluated by solving the three differential coupled equations to obtain the 3D distributions of electron and hole concentrations, as well as the electric field in the device presenting a non-uniform dopant distribution. In addition, modeling must also include the possibility of varying the laser beam location and power from pulse to pulse to obtain the desired device characteristics.

Some insight on process modeling can be obtained by using careful approximations. We consider the effect of a focused laser beam incident on a n+-p-n+ silicon structure, resulting in the diffusion of dopants into silicon. Because the diffusion coefficient of dopants in liquid Si is almost seven orders of magnitude higher than that of crystalline Si, we assume that only dopants in the silicon melt diffuse [9]. During the laser pulse, the silicon melt dimension increases and then decreases as the pulse ends. Therefore, we propose that only the maximum melted region (as denoted by  $r_{\text{melt}}$  on the Si surface) has to be determined in the temperature calculation; the dopants located outside this region are assumed to be immobile. As the pulse duration  $t$  gets longer, dopants with a diffusion coefficient  $D_d$  will have more time to diffuse over a length of

$$r_D = 2\sqrt{D_d t} \quad (1)$$

in the entire melted region, yielding a more uniform dopant distribution. For instance, Arsenic, the major dopant in the n+ regions of the investigated structures, presents diffusion constants between  $D_d = 3.3 \times 10^{-4} \text{ cm}^2/\text{s}$  and  $6.8 \times 10^{-3} \text{ cm}^2/\text{s}$  corresponding respectively to the fusion temperature ( $T=1683\text{K}$ ) and to a reasonable temperature of molten Si ( $T=3000\text{K}$ ) [9]. Equation (1) gives in these conditions:

$$r_D (\mu\text{m}) = 0.36\sqrt{t(\mu\text{s})} \quad \text{for } T=1683 \text{ K} \quad (2)$$

$$\text{and} \quad r_D (\mu\text{m}) = 1.65\sqrt{t(\mu\text{s})} \quad \text{for } T=3000 \text{ K} \quad (3)$$

suggesting that laser pulses of the order of a microsecond are required for uniform dopant distribution over a fraction of a micrometer.

To calculate the maximum melted region one has to solve the basic energy balance equation including the laser source term as well as the conduction, convection and radiation heat losses. Since the radiation term is essentially negligible compared to the conduction term and since, in a first approximation, we can neglect convection because the pulse melting time is lower than few  $\mu\text{s}$ , the energy balance equation can be written as [8]:

$$\rho c \frac{\partial T}{\partial t} = \nabla \cdot [\kappa \nabla T] + S(x, y, z, t) \quad (4)$$

where  $\rho$ ,  $c$ ,  $\kappa$  denote density, specific heat and thermal conductivity, respectively. The heat source  $S$  is given by:

$$S(x, y, z, t) = [1-R] Q(x, y) f(z) g(t), \quad (5)$$

$$Q(x, y) = \frac{P}{\pi w^2} \exp\left[-\frac{x^2 + y^2}{w^2}\right], \quad (6)$$

$$f(z) = \alpha e^{-\alpha z} \quad (7)$$

where  $R$  is the surface reflectivity,  $P$  the incident power,  $w$  the 1/e laser spot radius,  $\alpha$  the optical absorption coefficient and  $g(t)$  the temporal laser profile (in this case we assume a rectangular pulse). Temperature dependent thermal conductivity can be eliminated from equation (4) using a Kirchhoff transform [10]:

$$\Theta(T) = \int_{T_0}^T \frac{\kappa(T')}{\kappa(T_0)} dT' \quad (8)$$

where  $\Theta(T)$  is called the linear temperature and  $T_0$  is the initial temperature. The heat equation is then solved using Green's function method [11]. The solution has been calculated by Cohen et al [12] and is given by:

$$\Theta(x, y, z, t) = \frac{(1-R)P\alpha}{2\pi^{3/2}\kappa(T_0)} \int_0^{\sqrt{4Dt}} d\xi I(z, \xi) \frac{\exp[-(x^2 + y^2) / (\xi^2 + w^2)]}{\xi^2 + w^2} \quad (9)$$

$$I(z, \xi) = \frac{\sqrt{\pi}}{2} \xi \exp(\alpha^2 \xi^2 / 4) \left[ e^{-\alpha z} \left( 1 - \operatorname{erfc} \left( \frac{\alpha \xi}{2} - \frac{z}{\xi} \right) \right) + e^{\alpha z} \left( 1 - \operatorname{erfc} \left( \frac{\alpha \xi}{2} + \frac{z}{\xi} \right) \right) \right]$$

where  $\operatorname{erfc}()$  is the complementary error function,  $D$  is the thermal diffusivity and

$$\xi = \sqrt{4D(t-t')} \quad (10)$$

As it is, equation (9) does not take into account the temperature dependence of Si properties or latent heat of fusion. However, by using an adiabatic approximation [13], it is possible to partially consider these in the calculation. The temporal integral of equation (8) is subdivided into small time segments, each lasting  $\Delta t_i$ . These segments cumulatively add up to give the total temperature at the designated time. Each segment depends on the total temperature reached by the preceding segment. In this way, silicon properties can be adjusted to the temperature reached after each segment. The time intervals  $\Delta t_i$  are chosen so as to limit the temperature only to rise a few Kelvins. The main drawback to this method is that the properties of Si depend on temperature which in turn depends on time and position. The adiabatic approximation takes care of the temperature variation with time, but not with position. As for latent heat of fusion ( $L$ ), it is taken into account with the use of an energetic criterion [14]. If the fusion temperature ( $T_f$ ) of silicon is reached, subsequent temperature increases are converted into enthalpy:

$$H = \int_{T_f}^T (\rho c)_{T_f} dT' \quad (11)$$

where  $\rho c$  is evaluated at  $T_f$ . As long as the energy accumulated is less than the latent heat of fusion, the material is considered still in the melt transition. When  $H \geq L$ , the liquid phase is reached and subsequent temperature rise calculations return to normal (albeit with liquid silicon properties).

While our calculation approach using equation (9) is basically not rigorous, it is expected to be more accurate than using equation (9) without temperature dependent properties, as it will be shown when calculations are compared to experimental results. As an example, for the conditions given in figure 2, the model using constant silicon properties predicted that the silicon would not melt, which is obviously not the case. However, our approach gives a calculated radius of  $0.5\mu\text{m}$ , which is very close to the observed dopant diffused area of  $0.55 \pm 0.1\mu\text{m}$  seen in Figure 2.

Another way to compare experimental and theoretical calculations is to determine the conditions which give a fixed melted radius. This can be done in the following manner. Before laser irradiation, the resistance of the microdevice has essentially an infinite value. According to the proposed model, process parameters must be such that the melted region must reach the source and the drain before the dopants begin to diffuse into the channel. For a determined laser power, a minimum pulse width is required to diffuse sufficient dopants to produce a resistance. We have performed measurements on microdevices with a  $1.7\mu\text{m}$  source to drain distance and for source and drain initial concentrations of  $5 \times 10^{19} \text{ cm}^{-3}$ . Figure 6 shows experimental results to produce a resistance of a finite value (readable on the multimeter, i.e. between  $10^7$  and  $10^8 \Omega$ ) with only one laser irradiation. Note that to obtain  $10^8 \Omega$  on the multimeter, a silicon resistivity of  $10^3 \Omega\text{cm}$  is needed corresponding to a dopant concentration as low as  $10^{13} \text{ cm}^{-3}$  in the channel on the average [15]. Even at the shortest pulse width of  $0.07 \mu\text{s}$  (at few Watts on figure 6), we estimate using equation (3) that this time is long enough to assure sufficient dopant diffusion to be observed at the multimeter. The dashed line on figure 5 corresponds to the calculated time and power for a melted radius of  $0.85\mu\text{m}$  (half the distance source to drain) using equation (9). The full line corresponds to our calculation taking into consideration all silicon properties dependence with temperature. The agreement between the results and our calculation (full line) is very good and furthermore supports the proposed model that the diffusion into the melted region is the main mechanism controlling the process.

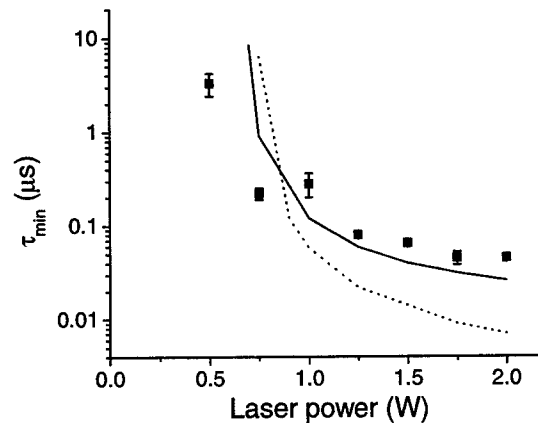


Fig. 5: Minimum time needed to create a resistance of finite value (i.e. between  $10^7$  and  $10^8 \Omega$ ) as a function of laser power for one laser irradiation. Small squares are experimental results and lines are calculated from the model with (full line) and without (dotted line) latent heat of fusion and thermally dependent Si properties.

## CONCLUSIONS

Highly accurate resistances compatible with CMOS technology can be easily made by laser inducing dopant diffusion. These new microdevices have very linear I-V curves at the usual microelectronics operating voltages and present non-linear behavior due to carrier velocity saturation followed by avalanche effects. We clearly showed that the process is based on the dopant diffusion into the melted silicon and our calculations are in good agreements with experimental results.

## ACKNOWLEDGMENTS

The authors are grateful to J.P. Lévesque and Hugo St-Pierre for technical assistance and Yvon Savaria for stimulating discussions. The authors wish to thank Digital Instruments and FEI Company for AFM-SCM and FIB measurements respectively.

## REFERENCES

- [1] M. Meunier, Y. Gagnon, Y. Savaria, A. Lacourse and M. Cadotte, Proc. of SPIE, **4274**, 384 (2001)
- [2] M. Meunier, Y. Gagnon, Y. Savaria, A. Lacourse and M. Cadotte, accepted in Applied Surface Science, (2001)
- [3] Y. Gagnon, M. Meunier, Y. Savaria, , "Method and Apparatus for Iteratively Selectively Tuning the Impedance of Integrated Semiconductor Devices Using a Focused Heating Source", US Patents **6,329,272** and PCT # 06042-002-WO-1 by LTRIM Technologies Inc. (2001)
- [4] A. Van Der Ziel, "Space-Charge-Limited Solid-State Diode", Semiconductors and Semimetals, Ch.3 (1980)
- [5] ISE TCAD 7.0, ISE Integrated Systems Engineering, AG, Switzerland, [www.ise.com](http://www.ise.com)
- [6] G. Masetti, M. Severi, and S. Solmi, "Modeling of Carrier Mobility Against Carrier Concentration in Arsenic-, Phosphorus- and Boron-Doped Silicon", IEEE Trans. Electron Devices, **ED-30**, 764-769 (1983)
- [7] C. Canali, G. Majni, R. Minder, and G. Ottaviani, "Electron and hole drift velocity measurements in silicon and their empirical relation to electric field and temperature", IEEE Trans. ED, pp. 1045-1047 (1975)
- [8] D. Bäuerle, Laser Processing and Chemistry, 3rd ed., Springer, Berlin (2000)
- [9] H. Koda, Jap. J. Appl. Phys., **2**, 212 (1963)
- [10] H.S. Carslaw and J.C. Jaeger, "Conduction of Heat in Solids", Clarendon Press, Oxford (1988).
- [11] E. Butkov, "Mathematical Physics", Addison-Wesley, Reading (1968)
- [12] S.S. Cohen, P.W. Wyatt, G.H. Chapman and J.M. Canter, IEEE Trans. Electron Devices **35**, 1533 (1988)
- [13] D.M. Kim, R.R. Shah and D.L. Crosthwait, J. Appl. Phys **51**, 3121 (1980)
- [14] J.E. Moody and R.H. Hendel, J. Appl. Phys. **53**, 4364 (1982)
- [15] see for example, Robert F. Pierret, "Advanced Semiconductor Fundamentals", Modular Series on Solid State Devices, volume VI (1989)

# A photoluminescence study of laser ablated gallium nitride thin films

Jerzy M. Wrobel<sup>a</sup>, Ewa Płaczek-Popko<sup>b</sup>, Jan J. Dubowski<sup>c</sup>, Haipeng Tang<sup>c</sup>, and James B. Webb<sup>c</sup>

<sup>a</sup> University of Missouri – KC, Department of Physics, Kansas City, MO, 64110 USA

<sup>b</sup> Wroclaw University of Technology, Institute of Physics, Wroclaw, Poland

<sup>c</sup> National Research Council of Canada, Institute for Microstructural Sciences,  
Ottawa, Ontario K1A 0R6, Canada

## ABSTRACT

Photoluminescence analysis has been implemented to investigate the crystalline properties of Gallium Nitride layers ablated with an XeCl excimer laser. The measurements were carried out on craters up to 1  $\mu\text{m}$  deep, which corresponded to almost half the thickness of the deposited film. The craters were etched in an air environment with laser fluences in the range of 99-231  $\text{mJ}/\text{cm}^2$ . In the 350-1200 nm spectral range, the near-band-edge emission, and the donor-acceptor pair recombination were identified. All spectra were dominated by the excitonic recombination. The analysis revealed that during the ablation, the full width at half maximum of the donor-bound luminescence line remained almost independent of both the depth of the crater and of the laser fluence. Also, the donor-acceptor pair recombination, which manifests its presence through a weak yellow luminescence observed in the vicinity of the 600 nm wavelength, has been consistently observed in the spectra. A relative decrease in the excitonic emission indicated that a thin layer of altered material with lower crystalline quality was formed at the surface of the ablated material.

**Keywords:** Gallium nitride (GaN), laser ablation, photoluminescence

## 1. INTRODUCTION

Over the last decade, the development of short wavelength light-emitting diodes and diode lasers in gallium nitride (GaN) based materials<sup>1</sup> stimulated a significant increase in the amount of research being done on this material. Blue and blue-green light-emitting diodes in GaN structures<sup>2-3</sup> were reported for the first time in 1993 soon followed by the announcement of successful fabrication of blue semiconductor lasers<sup>4</sup> and UV detectors.<sup>5</sup> In addition, electronic devices, such as metal-semiconductor field-effect transistors<sup>6</sup> and high-mobility transistors,<sup>7</sup> were made in GaN.

Various materials, such as SiC, Si, GaAs, MgO, and ZnO, have been used as the substrates for the epitaxy<sup>8</sup> but so far, despite a large lattice mismatch, sapphire ( $\text{Al}_2\text{O}_3$ ) is most frequently selected as the substrate of choice for epitaxy of GaN. Application of an AlN buffer layer between the sapphire substrate and GaN layer relaxes the mismatch related stress.<sup>9</sup>

A wider application of GaN in optoelectronics requires improved methods of processing this material. The high resistance of GaN to chemical processing leads to consideration of alternate methods. So far the removal of material by wet-etching techniques was usually achieved by implementing photoelectrical effects,<sup>10-12</sup> which complicated the process due to the necessity of making electrical contacts, and limited the selection of the substrates to conductive materials. Recently, peroxydisulfide ions ( $\text{K}_2\text{S}_2\text{O}_8$ ) have been applied for UV enhanced wet etching without the necessity of an electric field.<sup>13-14</sup> The advantage of wet etching is the possibility of forming undercut profiles which can be used for liftoff and transfers of GaN structures between alternative substrates.<sup>15</sup> A number of dry etching methods such as plasma



etching,<sup>16-19</sup> or ion etching<sup>20-22</sup>, have been implemented for processing of GaN. Typically, the rates in both wet and dry etching techniques are up to 50 nm/min, however the etched surfaces usually require additional treatment in order to improve surface morphology. Higher etch rates (~100 nm/pulse) have been demonstrated by laser ablation.<sup>23-27</sup> In addition, it has been demonstrated that under certain irradiation conditions the surface morphology of ablated GaN films can be made smoother than that of the as-grown material.<sup>23-24, 26-28</sup> Laser ablation has also been used to transfer thick GaN films onto Si substrates.<sup>29</sup> This approach was further developed to successfully transfer a 2- $\mu$ m thick GaN film on a (001) Si wafer.<sup>30</sup>

Despite the simplicity of direct laser ablation and its potential for patterning of GaN films with submicron resolution, no systematic investigation of this approach has been documented in the literature. One of the most important parameters that could determine the usefulness of this technique concerns the extent of damage induced at the surface and on the walls of the ablated structures. The purpose of this work was to use photoluminescence to assess the extent of structural damage in GaN films that were patterned by laser ablation in an air environment.

## 2. EXPERIMENTAL DETAILS

The investigated film was fabricated by ammonia-molecular beam epitaxy.<sup>31</sup> A 2- $\mu$ m-thick film was grown on a (0001) sapphire substrate with a 20 nm thick aluminum nitride (AlN) buffer layer, which relaxed induced stress resulting from the mismatch between GaN and sapphire.

The wafer was ablated with 10 ns pulses of an XeCl excimer laser operating at 308 nm. Details of the ablation setup have been published elsewhere.<sup>28</sup> A series of craters, 375  $\mu$ m in diameter, have been etched using laser fluence varied between 99 mJ/cm<sup>2</sup> and 231 mJ/cm<sup>2</sup>. A uniform fluence distribution profile within the crater was achieved by projecting a circular aperture illuminated with a homogenized laser beam. The process was carried in the atmospheric air environment. Following the irradiation, an excess of gallium, which formed on the surface, was chemically etched in a 50% solution of HCl in water. The craters were up to ~1  $\mu$ m deep, as determined by a stylus scanner (DEKTAK).

Low temperature photoluminescence studies have been performed in a Janis Supravertemp cryostat at 20 K. Photoluminescence was stimulated with an Omnichrome T2056-MA03 Helium-Cadmium laser operating at 325 nm. The beam was focused to a spot about 50  $\mu$ m in diameter resulting in an excitation intensity of about 20 W/cm<sup>2</sup>. A 0.75 m Jobin-Yvon HR 640 monochromator with a nitrogen-cooled photon counting system was used to collect the spectra.

## 3. RESULTS AND DISCUSSION

As seen in Figure 1, the photoluminescence spectrum of the as grown GaN layer used for the studies was dominated by excitonic emission. The strongest line ( $D^0BX$ ), observed at 3562 Å (3.4807 eV), is associated with recombination of a donor-bound exciton. This line typically occurs at temperatures below 50 K<sup>32</sup> and is considered to be a signature of quality in n-type GaN.<sup>33</sup> The intensity of this line, the relative intensity, and the full width at half maximum (FWHM), are generally used to evaluate the crystalline quality of the material. In the unprocessed areas of the samples studied here, the full width at half maximum of the  $D^0BX$  line is about 9 meV. In the near-band-edge emission, a barely noticeable shoulder on the low-energy side of the  $D^0BX$  line can be seen. A curve fitting procedure, shown in Figure 2a, to two Gaussian/Lorentzian peaks leads to the location of the second peak consistent with the acceptor bound excitonic recombination ( $A^0BX$ ) in GaN. As seen in Figure 2b, the exact fit requires three peaks in the near-band-edge emission. The presence of three peaks is additionally justified by the spectra obtained in the processed regions. Up to four LO-phonon replicas of the excitonic line, separated by about 93 meV, have also been seen in the spectra. The separation is consistent with the reported LO phonon energy. In the regions of the layer not affected by the ablation, the maximum intensity of the defect-related, "yellow" emission was about thousand times lower than the excitonic emission.

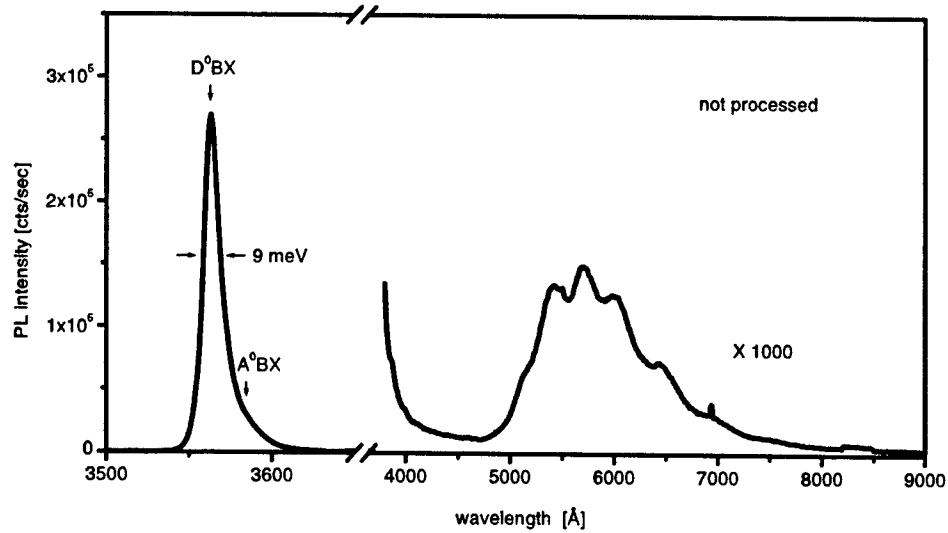


Figure 1. The photoluminescence spectrum of the unprocessed GaN layer. Spectrum collected at a temperature of 20 K, with a 20 W/cm<sup>2</sup> excitation at 325 nm from a CW cadmium laser.

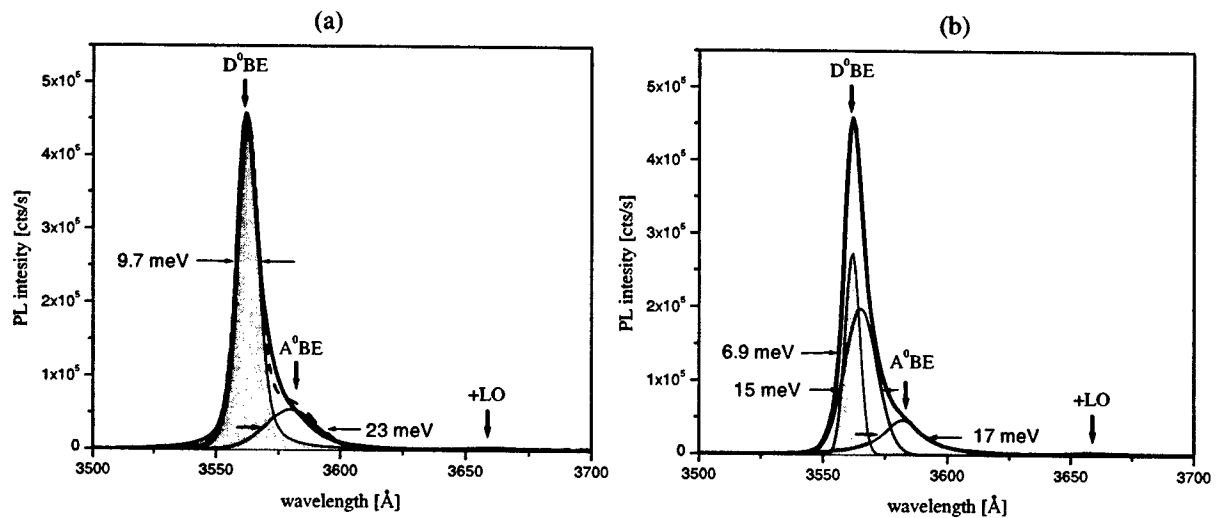


Figure 2. (a) Two- and (b) three-peak fit of the PL spectra to the Gaussian/Lorentzian distribution functions. The thick solid lines represent the collected spectra and the broken lines are the best fits. The separate peaks are marked with thin solid lines. The D<sup>0</sup>BX line is shaded.

In order to evaluate the crystal quality of the material in the laser-processed craters, the characteristics of the near-band-edge (excitonic) emission were analyzed in this work. The spectra from a sequence of craters, ablated with  $N = 1, 2, 4$ , and 40 pulses at  $132 \text{ mJ/cm}^2$ , are shown in Figure 3. The depth,  $d$ , of each crater is also indicated in the figure. All the spectra have been collected under very similar conditions and are normalized to the strongest line. The labels along the vertical axis allow one to compare the actual values of the PL intensity. In order to isolate the contribution of the  $D^0BX$  to excitonic emission, a curve-fitting algorithm has been used for each data set. A minimum number of Gaussian/Lorentzian peaks have been chosen to exactly fit the intensity distribution of the near-band-edge region. In each case, no more than three peaks were required for the fit. For each peak the wavelength, the intensity and the width were adjustable parameters.

The shaded peak, in each frame of the stack, corresponds to the  $D^0BX$  recombination. With an accuracy of  $0.5 \text{ \AA}$ , the fit always resulted in the same value for the position of the line at  $3563 \text{ \AA}$  ( $3.480.0 \text{ eV}$ ). In Figure 3, it can be seen that the ablation also has no effect on the width of the line. However, even a single laser pulse lowers the intensity by almost two orders. After a few pulses, the number of laser pulses has practically no effect on the intensity of the excitonic line. In this case, the intensity of the  $D^0BX$  recombination after forty pulses is even greater than after four pulses. Most likely the increase was associated with an experimental error rather than having any significant meaning.

The remaining emission in the near-band-edge region shows another discernable pattern, which can be seen in Figure 3. One can clearly recognize that with the increase of the number of pulses, this emission moves away from the  $D^0BX$ . The best-fit analysis always results in an additional two peaks for this emission. Considering their FWHM (about  $20 \text{ meV}$ ) they appear at fixed locations in the  $3573 - 3583 \text{ \AA}$  and  $3590 - 3595 \text{ \AA}$  ranges, respectively. The second peak corresponds to the commonly observed  $A^0BX$  recombination, occurring at  $3592 \text{ \AA}$  ( $3.4167 \text{ eV}$ ), which as mentioned earlier, was present in the unprocessed region of the layer. It appears that the third line is the least sensitive to a single pulse ablation, but after repetitive ablation it eventually disappears from the spectrum. Further studies would be required to associate this line precisely with a particular recombination process. It was also found that after the first laser shot, the shape of the "yellow" emission, and its intensity relative to the near- band-edge emission were practically independent of the number of pulses.

A set of commonly used parameters obtained from photoluminescence spectra indicating the change in the crystal quality of the ablated surface is listed in Table 1. The first row in the table refers to a spot in the close vicinity of the crater ablated with 40 pulses at  $132 \text{ mJ/cm}^2$ . The corresponding spectrum is shown in Figure 1. Except for the FWHM of the  $D^0BX$  line, the parameters indicate the deterioration of crystalline properties of the ablated surface within the first few pulses. The following pulses appear to have no effect on the further surface damage. A steady state condition of the

Table 1. The values of commonly used quality related parameters for GaN ablated at  $132 \text{ mJ/cm}^2$  laser fluence.

number of pulses	$D^0BX$ maximum [cts/sec]	fraction of $D^0BX$ in excitonic emission	ratio of excitonic to "yellow" intensity	FWHM [meV]
0	$3.0 \cdot 10^5$	0.56	390	7.4
1	$4.1 \cdot 10^3$	0.06	31	6.5
2	$4.2 \cdot 10^3$	0.04	55	6.8
4	$5.4 \cdot 10^3$	0.09	23	7.7
40	$8.5 \cdot 10^3$	0.31	21	8.8

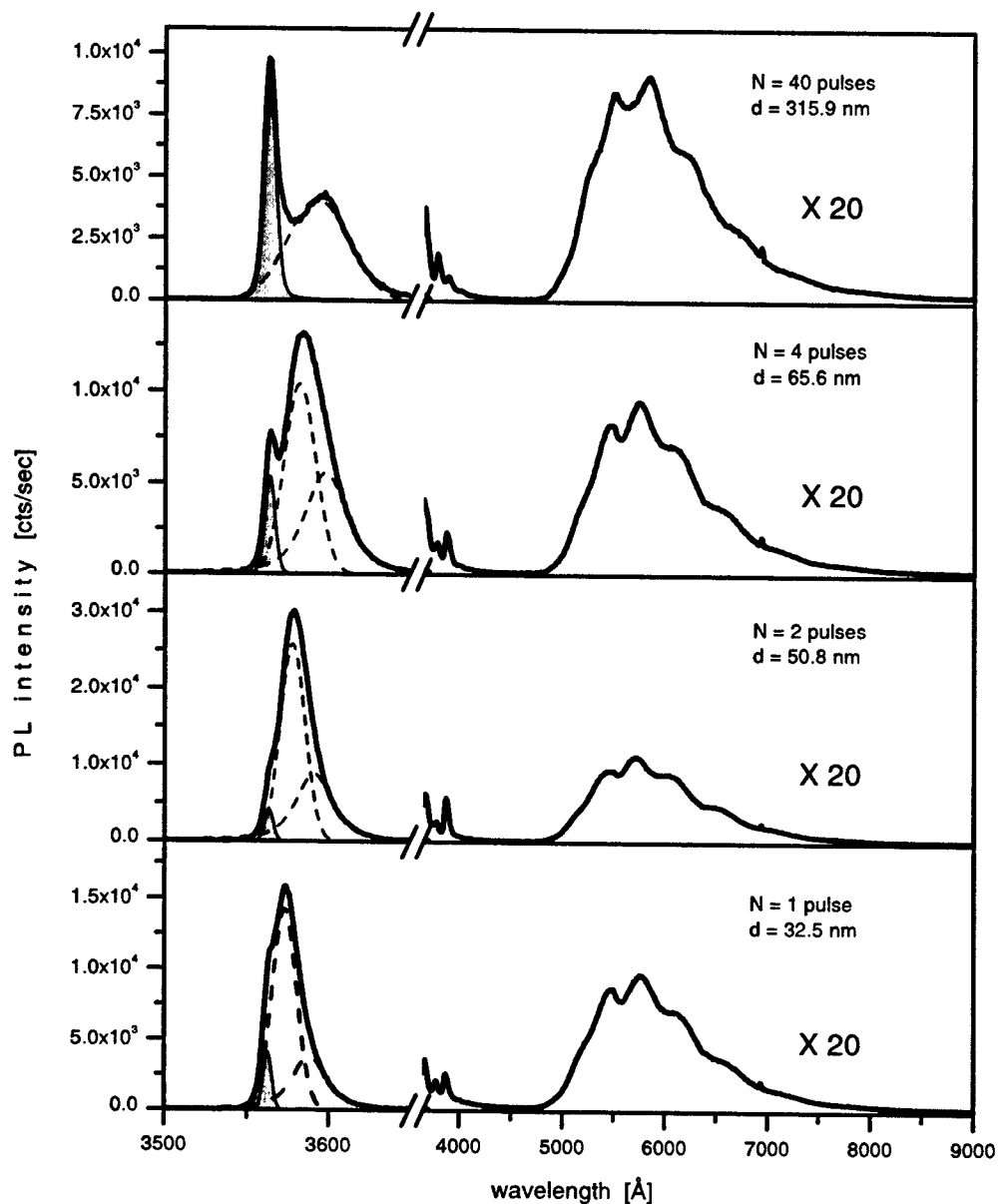


Figure 3. The effect of the total number of laser pulses on the near-band-edge photoluminescence in a GaN epitaxial layer ablated at  $132 \text{ mJ/cm}^2$  laser fluence. The number of pulses  $N$  as well as the depth  $d$  of the crater is indicated in the upper right hand corner of each graph.

surfaces ablated is achieved. This kind of pattern is observed for all the laser fluences used and it could be explained by the presence of a defective or chemically altered layer on the surface of laser ablated GaN. (It is quite feasible that the laser-induced chemical alteration of the irradiated surface, in addition to its decomposition, takes place during processing in an air environment.) Such a layer would be characterized by the absence of the  $D^0BX$  line in the near-band-edge photoluminescence and a relatively strong "yellow" emission. Simultaneously, the absorption of the layer would only allow the observation of a weak  $D^0BX$  line originating from the unaltered material below it. These effects were stronger at higher fluences, suggesting that the laser-induced damage is proportional to the laser fluence used for the ablation.

All the spectra discussed above have been collected at the center of the craters. The uniformity of the craters has also been investigated and the representative results are shown in Figure 4. The PL system allowed one to select the investigated region with high accuracy. It was possible to move the spot continuously along the crater while the diameter of the spot constituted about 1/8 of the crater's diameter. Significant differences have been observed in the near-band-edge emission, however the "yellow" luminescence was identical in both locations.

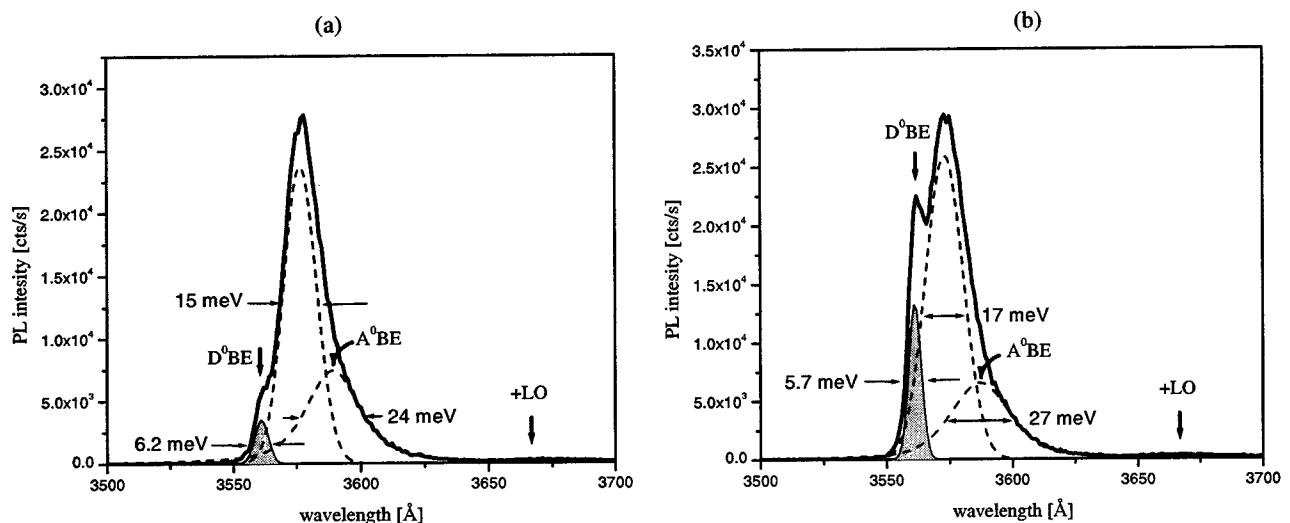


Figure 4. Uniformity of the crater ablated with a single pulse at  $231 \text{ mJ/cm}^2$ . Spectra collected at the center (a) and half the radius from the center (b) of the crater.

The center region of each crater experienced qualitatively more damage than the side region as indicated by both the reduced overall PL intensity and the decreased contribution of the  $D^0BX$  to the near-edge-emission. A possible mechanism responsible for such behavior could be associated with the higher efficiency of heat dissipation at spots further away from the center of the crater, due to the lateral heat transport. It should be pointed out that the thermal conductivity of sapphire, which is about four times lower than that of GaN, obstructs dissipation of heat in the direction perpendicular to the layer.<sup>34-35</sup>

PL spectra in the vicinity of a crater ablated with the highest number of pulses (40) at the highest fluence ( $231 \text{ mJ/cm}^2$ ) have been collected in order to observe thermally induced deterioration of the layer in the unprocessed region. Photoluminescence from the region at the edge of the crater (within  $50 \mu\text{m}$ ) are identical to those collected at regions where thermal effects have been excluded ( $1 \text{ mm}$  from the edge). It appears that ablation in air could be efficiently used for formation of GaN mesa structures. However, patterning of this material without damage in the processed area probably would require an atmosphere of a reactive gas, which would allow for lower laser fluences required for processing. Low-fluence laser etching has been demonstrated for GaInAs and InP.<sup>28</sup>

#### 4. CONCLUSIONS

Excimer laser ablation at 308 nm of GaN thin film deposited on sapphire has been carried out in air. The evolution of the crystalline quality with the number of laser pulses has been determined using low temperature photoluminescence. Within the investigated range of fluence (99-231 mJ/cm<sup>2</sup>), the first pulse results in the highest deterioration of the crystalline properties of the ablated layer. After the first few pulses, further ablation has little effect. The photoluminescence analysis suggests the existence of a thin damaged layer on the surface of laser-ablated material. The nature of damage is not exactly clear, but it appears that it is dominated by the alteration of the material crystalline properties with possible chemical changes. The thickness of the damaged layer, under which the material is unaltered, was found to be proportional to the laser fluence.

The radial dependency of the crystalline quality is observed in the craters. Most damage occurs in the center of the craters, which could be explained by nonuniform lateral heat dissipation. No thermally induced decrease in crystalline quality around the craters was found within the resolution (50  $\mu$ m) of this experiment. It appears that ablation in an atmosphere of a reactive gas, which would require lower laser fluences, could be necessary for patterning of this material without damage or significantly reduced thickness of the damaged layer in the processed regions. The ability to carry out patterning in an air environment is the potentially attractive approach for some applications only. An accurate analysis is still required to determine the microscopic extent of laser-induced lateral damage for the ablation conditions applied in this work.

#### ACKNOWLEDGMENTS

The photoluminescence experiments have been funded from a grant awarded by the University of Missouri Research Board. The authors wish to acknowledge its support of this project.

#### REFERENCES

1. S. Nakamura and G. Fasol, *"The Blues Laser Diode, GaN Based light Emitters and Lasers"*, Springer, Berlin 1997.
2. S. Nakamura, M. Senoh, and T. Mukai, "p-GaN/N-InGaN/N-GaN double heterostructure blue-light-emitting diodes", *Japanese Journal of Applied Physics, Part 2-Letters*, **32**, pp. L8-11, 1993.
3. B. Goldenberg, J.D. Zook, and R.J. Ulmer, "Ultraviolet and violet light-emitting GaN diodes grown by low-pressure metalorganic chemical vapor deposition", *Applied Physics Letters*, **62**, pp. 381-383, 1993.
4. S. Nakamura, M. Senoh, S. Nagahama, N. Iwasa, T. Yamada, T. Matsushita, Y. Sugimoto, and H. Kiyoku, "Room-temperature continuous-wave operation of InGaN multi-quantum-well structure laser diodes with a lifetime of 27 hours", *Applied Physics Letters*, vol. 70, pp. 1417-1419, 1997.
5. G. Parish, S. Keller, P. Kozodoy, J.P. Ibbetson, H. Marchand, P.T. Fini, S.B. Fleischer, S.P. DenBaars, U.K. Mishra, and E.J. Tarsa, "High-performance (Al,Ga)N-based solar-blind ultraviolet p-i-n detectors on laterally epitaxially overgrown GaN", *Applied Physics Letters*, **75**, pp. 247-249, 1999.
6. S. Yoshida and J. Suzuki, "Reliability of metal semiconductor field-effect transistor using GaN at high temperature", *Journal of Applied Physics*, **84**, pp. 2940-2942, 1998.
7. N.X. Nguyen, B.P. Keller, S. Keller, Y.-F. Wu, M. Le, C. Nguyen, S.P. Denbaas, U.K. Mishra, and D. Grider, "GaN/AlGaIn MODFET with 80 GHz  $f_{max}$  and > 100 V gate-drain breakdown voltage", *Electronics Letters*, **33**, pp. 334-335, 1997.
8. S. Strite and H. Morcoç, "GaN, AlN, and InN: a review", *Journal of Vacuum Science & Technology B*, **10**, pp. 1237-1266, 1992.
9. T. Paskova, E. Valcheva, J. Birch, S. Tungasmita, P.-O. Å. Persson, P.P. Paskov, S. Evtimova, M. Abrashev, and B. Monemar, "Defect and stress relaxation in HVPE-GaN films using high temperature reactively sputtered AlN buffer", *Journal of Crystal Growth*, **230**, pp. 381-386, 2001.
10. C. Youtsey, I. Adesida, and G. Bulman, "Highly anisotropic photoenhanced wet etching of n-type GaN", *Applied Physics Letters*, **71**, pp. 2151-2153, 1997.
11. C. Youtsey, G. Bulman, and I. Adesida, "Dopant-selective photoenhanced wet etching of GaN", *Journal of Electronic Materials*, **27**, pp. 282-287, 1998.

12. C. Youtsey, I. Adesida, L.T. Romano, and G. Bulman, "Smooth n-type GaN surfaces by photoenhanced wet etching" *Applied Physics Letters*, **72**, pp. 560-562, 1998.
13. J.A. Bardwell, I.G. Foulds, J.B. Webb, H. Tang, J. Fraser, S. Moisa, and S.J. Rolfe, "A simple wet etch for GaN", *Journal of Electronic Materials*, **28**, pp. L24-26 1999.
14. J.A. Bardwell, J.B. Webb, H. Tang, J. Fraser, and S. Moisa, "Ultraviolet photoenhanced wet etching of GaN in  $K_2S_2O_8$  solution", *Journal of Applied Physics*, **89**, pp. 4142-4149, 2001.
15. A.R. Stonas, T. Margalith, S.P. DenBaars, L.A. Coldren, and E.L. Hu, "Development of selective lateral photoelectrochemical etching of InGaN/GaN for lift-off applications", *Applied Physics Letters*, **78**, pp. 1945-1947, 2001.
16. S.J. Pearton, R.J. Shul, G.F. McLane, and C. Constantine, "Dry etching of III-V nitrides", *Gallium Nitride and Related Materials*. First International Symposium. Mater. Res. Soc., pp. 717-722, Pittsburgh, PA, USA, 1996.
17. S.A. Smith, C.A. Wolden, M.D. Bremser, A.D. Hanser, R.F. Davis, and W.V. Lampert, "High rate and selective etching of GaN, AlGaIn, and AlN using an inductively coupled plasma", *Applied Physics Letters*, **71**, pp. 3631-3633, 1997.
18. H.P. Gillis, D.A. Choutov, K.P. Martin, S.J. Pearton, and C.R. Abernathy, "Low energy electron-enhanced etching of GaN/Si in hydrogen direct current plasma", *Journal of the Electrochemical Society*, **143**, pp. L251-253, 1996.
19. R.J. Shul, G.B. McClellan, S.A. Casalnuovo, D.J. Rieger, S.J. Pearton, C. Constantine, C. Barratt, R.F. Karlicek Jr., C. Tran, and M. Schurman, "Inductively coupled plasma etching of GaN", *Applied Physics Letters*, **69**, pp. 1119-1121, 1996.
20. D. Basak, M. Verdú, M.T. Montojo, M.A. Sánchez-Garcia, F.J. Sánchez, E. Muñoz, and E. Calleja, "Reactive ion etching of GaN layers using  $SF_6$ ", *Semiconductor Science & Technology*, **12**, pp. 1654-1657, 1997.
21. J.B. Fedison, T.P. Chow, H. Lu, and I.B. Bhat, "Reactive ion etching of GaN in  $BCl_3/N_2$  plasmas", *Journal of the Electrochemical Society*, vol.144, pp. L221-224, 1997.
22. H. Lee, D.B. Oberman, and J.S. Harris, Jr., "Reactive ion etching of GaN using  $CHF_3/Ar$  and  $C_2F_4/Ar$  plasmas", *Applied Physics Letters*, **67**, pp. 1754-1756, 1995.
23. T. Akane, K. Sugioka, and K. Midorikawa, "High-speed etching of hexagonal GaN by laser ablation and successive chemical treatment", *Applied Physics A*, **A69**, suppl., pp. 309-313, 1999.
24. T. Akane, K. Sugioka, H. Ogino, H. Takai, and K. Midorikawa, "KrF excimer laser induced ablation-planarization of GaN surface", *Applied Surface Science*, **148**, pp. 133-136, 1999.
25. M.K. Kelly, O. Ambacher, R. Dimitrov, R. Handschuh, and M. Stutzmann, "Optical process for liftoff of group III-nitride films", *Physica Status Solidi A*, **159**, pp. R3-4, 1997.
26. H. Chen, R.D. Vispute, V. Talyansky, R. Enck, S.B. Ogale, T. Dahmas, S. Choopun, R.P. Sharma, T. Venkatesan, A.A. Iliadis, L.G. Salamanca-Riba, and K.A. Jones, "Pulsed laser etching of GaN and AlN films", *Nitride Semiconductors Symposium. Mater. Res. Soc.*, pp. 1015-1020, Warrendale, PA, USA, 1998.
27. J.J. Dubowski, S. Moisa, B. Komorowski, H. Tang, and J.B. Webb, "Laser polishing of GaN", *Proceedings of SPIE*, **4274**, pp. 442-447, 2001.
28. J.J. Dubowski, M. Julier, G.I. Sproule, and B. Mason, "Laser-assisted dry etching ablation for microstructuring of III-V semiconductors", *Advanced Laser Processing of Materials - Fundamentals and Applications*. Pittsburgh, PA, USA, Symposium. Mater. Res. Soc. pp. 509-518, 1996.
29. W.S. Wong, A.B. Wengrow, Y. Cho, A. Salleo, N.J. Quitoriano, N.W. Cheung, and T. Sands, "Integration of GaN thin films with dissimilar substrate materials by Pd-In metal bonding and laser lift-off", *Journal of Electronic Materials*, vol. 28, pp. 1409-1413, 1999.
30. unpublished: J.J. Dubowski, J. Bardwell, H. Tang and J.B. Webb, 2001.
31. H. Tang and J.B. Webb, "Growth of high mobility GaN by ammonia-molecular beam epitaxy", *Applied Physics Letters*, **74**, pp. 2373-2374, 1999.
32. J.P. Bergman, C. Harris, B. Monemar, H. Amano, and I. Akasaki, "Exciton lifetimes in GaN", *Gallium Nitride and Related Materials*, Pittsburgh, PA, USA, First International Symposium. Mater. Res. Soc. pp. 709-714, 1996.
33. R. Dingle, D.D. Sell, S.E. Stokowski, and M. Ilegems, "Absorption, reflectance and luminescence of GaN epitaxial layers", *Physical Review B*, **4**, pp. 1211-1218, 1971.
34. D.P. White, "A comparison of the effect of radiation on the thermal conductivity of sapphire at low and high temperatures", *Journal of Nuclear Materials*, **219**, pp. 165-168, 1995.
35. E.K. Sichel and J.I. Pankove, "Thermal conductivity of GaN, 25-360K", *Journal of Physics & Chemistry of Solids*, **38**, pp. 330, 1977.

# Excimer ablation of ITO on flexible substrates for large format display applications

Osman A. Ghandour\*, Dan Constantinide, and Ron Sheets  
Tamarack Scientific Co., Inc.

## ABSTRACT

Excimer-based ablative patterning of Indium Tin Oxide (ITO) thin film on flexible substrates has been evaluated for large format display applications. In display package manufacturing, excimer-based ITO ablation can provide a great advantage over conventional photolithographic processing. It can eliminate many steps from the manufacturing cycle, resulting in significant cost reduction. Flexible substrate display packaging is desirable for at least two reasons. It allows roll-to-roll low cost, large volume manufacturing. Its low weight provides for an easy scale up to larger format displays. A XeCl excimer, 1x, amplitude mask pattern projection, scan-and-repeat system was utilized in the evaluation work. The mask pattern had line groupings of line-widths varying from 8 to 30  $\mu\text{m}$  with line length of 44 mm. Lines from all the groupings were simultaneously ablated in 150 nm-thick ITO layer on a flexible 100  $\mu\text{m}$  thick Polyethylene terephthalate (PET) substrate using scanning with optimized dwell duration of 10 pulses and optimized fluence level of 350  $\text{mJ}/\text{cm}^2$ . Lines ablated with mask line groupings of line-width greater than or equal to 11  $\mu\text{m}$  showed complete electrical isolation indicating complete ITO removal. Scanning Electron Microscopy (SEM) showed the presence of a slight curling effect at ablated line edges. The effect was studied as a function of wavelength and imaging resolution. A  $\text{CO}_2$  snow cleaning method was evaluated for removing the extruding curled material.

**Keywords:** excimer, display, ITO, flexible substrates, ablation, pattern projection, scan-and-repeat, fluence gradient, SEM, large format, cost reduction.

## 1. INTRODUCTION

Recently, liquid crystal displays with flexible plastic substrates have become very attractive for replacing glass-based liquid crystal displays. Plastic substrate displays offer many advantages including low weight, durability and easy scale up to large format. Their flexibility permits varying the device shape to optimize visibility and suppress reflections. It also allows low cost, large volume roll-to-roll production. Furthermore, their thin construction, not achievable with glass substrates, provides wide viewing angles<sup>1</sup>. These display devices are suitable for many highly demanded existing and future product applications including pagers, personal digital assistants (PDA's), smart cards, cell phones, and the future "electronic paper"<sup>2</sup>.

Plastic substrates used in display device construction are coated with thin films of conductive electrode material that is transparent in the visible spectral range. Commonly used substrate materials include Polycarbonate (PC), Polyarylate (PAR), Polyestersulfone (PES), Polyimide (PI), Polyethylene terephthalate (PET), and Polyolefin.<sup>1</sup> Indium Tin Oxide (ITO) thin film is widely used as transparent conductive electrode<sup>3</sup>. Prior to ITO coating, a barrier layer of  $\text{SiO}_2$ ,  $\text{Ta}_2\text{O}_5$ , or organic film is sputtered on the substrate. ITO is then coated on top of the barrier layer by a sputtering method or the like<sup>4</sup>. The barrier layer protects the plastic substrate against gas and water permeation as well as against reacting with the liquid crystal at high temperatures<sup>1</sup>.

Typically, the plastic substrate is 100-200  $\mu\text{m}$  thick, the ITO layer is 100-150 nm thick, and the barrier layer is 1-4  $\mu\text{m}$  thick. Two substrates coated with ITO are overlaid with a very thin spacing of 1-20  $\mu\text{m}$  in between<sup>4</sup>. The spacing is filled with liquid crystal and sealed off using UV-cure resin<sup>4</sup>. The ITO layer on both substrates faces the liquid crystal in between. The ITO layer on one or both substrates is photolithographically patterned in strips 250-300  $\mu\text{m}$  wide with separation lines of width  $\sim 20 \mu\text{m}$ . Hence, when the two substrates are overlaid, a collection of pixels is formed. The pixels can be individually addressed and turned on and off. The photolithographic ITO layer patterning step may constitute a bottleneck in high volume, low cost device manufacturing. A high throughput, direct patterning process would help remove this bottleneck. Q-switched Nd:YAG laser-based systems have been used to pattern the ITO



layer<sup>5</sup>. These systems use single spot scanning in a direct write configuration. The required amount of ITO to be removed during large format device patterning is large. This makes these systems appropriate for prototyping but too slow for low cost, large volume production<sup>6</sup>. Production of such large format devices at low cost and large volume can be realized using an excimer-based, mask pattern projection, ablation technique<sup>6</sup>.

The advantage of using the excimer-based ablation technique for ITO film patterning instead of conventional photolithography can be illustrated in the process flow diagram shown in figure 1. Using conventional photolithography, the ITO layer is patterned as per the following procedure: resist coating, soft bake, exposure, development, post-development hard bake, etching, and resist stripping. On the other hand using excimer ablation, the ITO layer can be patterned directly in one step. However, a cleaning step may be required after the excimer-based direct patterning. As shown in the flow diagram, the excimer-based patterning method eliminates at least 5 steps from the display device ITO patterning step. Hence, this method can potentially reduce the overall manufacturing cost and improve yield.

## 2. EXPERIMENTAL SET-UP

### 2.1 Experimental system general features

This paper describes the evaluation of an excimer-based technique used for patterning display device ITO layers on PET substrates. The system used in this technique is an excimer-based 1x, mask pattern projection, scan-and-repeat system. The excimer source is Xenon Chloride (XeCl) with 308 nm wavelength. Figure 2 shows a photograph of Tamarack model 330 system resembling the experimental system used in the evaluation. The figure shows a close-up view of the system mask, lens, and substrate stage area<sup>7</sup>. A diamond-shaped beam with a side length of 10 mm is shaped and homogenized by a standard Tamarack beam delivery sub-system. The beam impinges on a mask containing a desired pattern. A 1x Dyson lens transfers the mask pattern onto the workpiece surface. The mask and the workpiece are scanned as one unit relative to the beam<sup>8</sup>. This allows the patterning of large format devices without being limited by lens field size. Using readily available masks of size 177.8 mm x 177.8 mm allows patterning of devices with size up to 150 mm x 150 mm.

### 2.2 Process and material specific features

Lines patterned during this work are 44 mm long with various line widths ranging from 11 to 30  $\mu\text{m}$ . Patterned ITO strips have width values of 150  $\mu\text{m}$  or 375  $\mu\text{m}$ . Optimal ITO layer removal was obtained using 350  $\text{mJ}/\text{cm}^2$  and 10 pulses at 10 Hz repetition rate. Under these conditions, the ITO material within the lines was completely removed without causing any damage to the underlying layers. The PET substrate is 100  $\mu\text{m}$  thick. The ITO layer and the barrier layer have a thickness of 0.15 and 4  $\mu\text{m}$ , respectively. The system is equipped with  $\sim 0.05$  NA, 1x Dyson projection lens with transmission coefficient of  $\sim 85\%$  and an aluminum-on-quartz amplitude mask with transmission coefficient of  $\sim 92\%$ . Hence, to obtain the optimal fluence level of 350  $\text{mJ}/\text{cm}^2$  at the substrate plane, a fluence level of  $\sim 450 \text{ mJ}/\text{cm}^2$  would be required at the mask plane. Unfortunately, aluminum-based masks have a damage threshold of  $\sim 200 \text{ mJ}/\text{cm}^2$ <sup>9</sup>. Thus, the aluminum-based mask was used with care when exposed to 450  $\text{mJ}/\text{cm}^2$  fluence level. Experiments were run in short duration using low laser repetition rates of 10-50 Hz. Production conditions, however, entail runs of long duration at high repetition rates. In this case, an aluminum-based mask may suffer significant damage. However, a dielectric-on-quartz amplitude mask with reported damage threshold of 800  $\text{mJ}/\text{cm}^2$  can be successfully utilized under production conditions<sup>10</sup>. Figure 3 shows a schematic of the aluminum-based mask utilized in the experiments. The mask consists of many line groupings. Each grouping has a certain line width and strip width. The line widths used here are 8, 9, 11, 15, 16, 20, 25, and 30  $\mu\text{m}$ . Some groupings have a strip width of 150  $\mu\text{m}$  and others have a strip width of 375  $\mu\text{m}$ . The total number of lines within a grouping is either 17 or 23 lines. For clarity purpose, the schematic in figure 3 shows a detailed view of only a part of one line grouping.

## 3. DATA AND DISCUSSIONS

### 3.1 Test for complete ITO layer removal

The above-mentioned system was used under the optimized conditions to simultaneously ablate lines from all the mask groupings in the ITO layer. A multi-meter was used to perform conductivity testing on each grouping and determine complete electrical isolation, which in turn indicates complete ITO removal. Lines in each grouping of the

mask were designed in such a way that upon ablating the ITO layer, ITO strips are formed in an interlaced comb test pattern. As illustrated in figure 3, ITO strips of each grouping were shorted together at one end and connected to one multi-meter probe. At the other end, a pad connecting the ITO strips interlacing with the above-mentioned ones in the same grouping was connected to the other multi-meter probe. Resistance was then measured. Complete electrical isolation between the strips of one grouping was indicated by a large measured resistance value  $> 40 \text{ M}\Omega$ . Based on this test, it was determined that under the optimal conditions, ITO removal was complete within lines of width as small as  $12.5 \text{ }\mu\text{m}$  produced by mask lines with width of  $11 \text{ }\mu\text{m}$ . This result was confirmed using EDX (Energy Dispersive X-ray Spectroscopy) analysis performed in certain locations within lines of each grouping.

### 3.2 Edge quality of ITO removal lines

Electrical isolation resulting from complete ITO removal is required for successful display device operation. Therefore, our excimer-based technique was successful in patterning display device ITO layers with lines of width  $\geq 12.5 \text{ }\mu\text{m}$  and length of  $44 \text{ mm}$ . However, the technique produced a non-desirable effect at the edges of the ablated lines. Specifically, the ITO material at the ablated line edge extruded beyond the surface of the ITO layer. As determined by SEM, the extruding material was shaped as a curl; hence it will be referred to in this paper as curling. A typical curled region had an extrusion height of  $1\text{-}1.5 \text{ }\mu\text{m}$  and a width of  $1\text{-}4 \text{ }\mu\text{m}$ . Figure 4(a) shows a SEM top-view of a collection of lines ablated by  $11 \text{ }\mu\text{m}$  wide mask lines using the optimal conditions. Figure 4(b) shows a close up SEM top-view of a location within one of the lines. Figure 4(c) shows a SEM cross-sectional view of another line within the collection with line width of  $12.5 \text{ }\mu\text{m}$ , curled material regime width of  $1.4 \text{ }\mu\text{m}$ , and curled material height of  $1.2 \text{ }\mu\text{m}$ . We believe that this line edge curling is due to a thermal effect, taking place at the ablation zone edge. We propose that this curling phenomenon is inherent in the mechanism of excimer-based ITO thin film removal from PET substrate.

### 3.3 Mechanism of the removal process

A few recent publications have attempted to explain the mechanism of similar laser-based thin film metal or oxide removal from plastic and other types of substrates. For example, Koo et al. discuss a mechanism of removing copper film of thickness  $250 \text{ }\text{\AA}$  from  $1 \text{ mm}$  thick flexible glass reinforced epoxy<sup>11</sup>. A Q-switched Nd:YAG laser source operating at  $1.06 \text{ }\mu\text{m}$  wavelength was directed to a  $50 \text{ }\mu\text{m}$  spot onto the metal film. According to the authors, the laser beam heats portions of the film and underlying substrate. The heated substrate portion at the film-substrate interface is vaporized. Vapors are entrapped inducing an explosion, which removes the portion of thin film coating from the substrate. Because of the extremely high vaporization temperature of the copper film,  $1083^\circ \text{C}$ , a direct metal film vaporization mechanism would require large laser intensity threshold, which can damage the underlying heat-sensitive substrate. Therefore, it is more feasible to raise the substrate temperature to its vaporization level (e.g.  $200^\circ \text{C}$  for glass reinforced epoxy) and achieve thin film metal removal via the explosion mechanism explained above.

In another example, Rumsby et al. discuss a mechanism for UV excimer-based removal of thin metal or oxide film from flexible and other types of substrates<sup>6</sup>. According to the authors, the incident laser pulse is only partially absorbed by the film so that a small part of the energy reaches the film-substrate interface. The authors explain that the discontinuity at the interface produces high electric field gradients, which cause the thin film to be ejected from the surface at high speed. Ablation threshold is lower for thinner film. They also state that since the metal film is shocked from the surface and not directly cut, the edge quality of the patterned area is dependent upon the quality of the coated thin film layer. The finer the grain structures the better the quality of the edge. In addition, the authors state that for some metals there is evidence suggesting that the material may be removed, at least partially, in molten form.

Again, the process discussed in this paper is an excimer-based mask pattern projection process used to directly remove a thin ITO film deposited on a thin  $\text{SiO}_2$  barrier layer that is deposited on a flexible PET substrate. We propose that three different mechanisms take place simultaneously during the removal process. These mechanisms are ablative removal, melt induced removal, and heat induced softening at the edge of removal region followed by shrinking and curling. Following is a detailed discussion of the proposed mechanisms.

Forouhi et al. have experimentally determined the extinction coefficient  $k$  of ITO film on quartz substrate over a wide spectral range<sup>3</sup>. The determined extinction coefficient  $k$  is  $0.1539$  and  $0.5$  at  $308 \text{ nm}$  and  $248 \text{ nm}$  wavelength, respectively. Since the optical properties of ITO films, including  $k$ , are highly dependent on deposition parameters, our specific ITO film may have a slightly different  $k$ . However, it can be assumed with some approximation that our ITO

film has the same extinction coefficient values mentioned above. These values are then plugged in equation (1), below, and the corresponding ITO film absorption coefficients are calculated<sup>12</sup>.

$$\alpha = (4 \cdot \pi \cdot k) / \lambda \quad (1)$$

where  $\alpha$  is the absorption coefficient, and  $\lambda$  is the operating wavelength.

Based on the calculation, our ITO film has an absorption coefficient  $\alpha \approx 6.279 \times 10^4 \text{ cm}^{-1}$  and  $2.5335 \times 10^5 \text{ cm}^{-1}$  at 308 nm and 248 nm wavelength, respectively. Polyimide material has an absorption coefficient  $\alpha \approx 1.2 \times 10^5 \text{ cm}^{-1}$  and  $2.8 \times 10^5 \text{ cm}^{-1}$  at 308 nm and 248 nm wavelength, respectively<sup>13</sup>. Notice that the calculated values of the ITO film absorption coefficient are relatively close to those of polyimide at 308 nm and 248 nm wavelengths. Hence, similar to polyimide material, the ITO material can be excimer ablated at these wavelengths when using a fluence level above a certain threshold.

The system aerial image (i.e. image at the substrate plane) has critical line width with a certain fluence level and a fluence gradient at the edge<sup>14</sup>. The gradient slope depends on the system imaging quality represented by many parameters including resolution. The better the image quality the higher the gradient slope, resulting in a narrower gradient regime. Conventionally known ablation is obtained at fluence levels higher than the ablation threshold within the critical line width and within the higher portion of the edge fluence gradient. As the fluence decreases along the gradient it becomes low enough to fall below the ablation threshold but high enough to cause laser induced melting. At even lower fluence levels along the gradient, we obtain heat induced softening of the ITO material. The melting point of ITO material is around 1900 °C. Hence, the melting and softening mechanisms occurring during this process suggest that the temperature of the ITO material, in some localized regions, rises to a level that is in the neighborhood of the melting point. However, no damage is caused to the heat sensitive substrate due to the transient nature of the mechanisms occurring on nanoseconds time scale. The excimer short pulse width of ~ 34 nsec coupled with high absorption coefficients ( $0.6279 \times 10^5 \text{ cm}^{-1}$  at 308 nm and  $2.5335 \times 10^5 \text{ cm}^{-1}$  at 248 nm) confine the extreme heating which causes melting and softening to the thin ITO layer. Furthermore, the 4  $\mu\text{m}$ -thick  $\text{SiO}_2$  layer serves as a thermal barrier to protect the heat sensitive PET substrate during the excimer-based removal process<sup>15</sup>. Such ultra-fast thermal mechanisms were reported and studied in great detail for silicon on sapphire in a Ph. D. dissertation by M. O. Thompson of Cornell University<sup>16</sup>. The molten material is mostly removed by ejection due to the shock wave caused by the excimer short pulse-width and the, moderately, high fluence. ITO layer curling takes place within the heat induced softening regime at the edge of the ablated line. In this regime, the laser induces an ultrafast temperature rise sufficient to soften the material and cause it to expand. Upon cooling, the material shrinks causing curling and cracking as shown in figure 4 (b). The figure also shows bead-like features at the end of the curled layer indicating melting. This melting takes place between the ablation regime within the critical line width and the heat induced softening/curling regime at the line edge<sup>15</sup>.

Better image quality (i.e. better resolution) will result in higher gradient slope reducing the width of the edge heat induced softening/curling regime. This, as will be seen below, results in much reduced material curling at the ablated line edge. The 1x Dyson lens utilized in our evaluation runs has a relatively poor image quality due to the low NA of ~ 0.05 with resolution of ~ 6.2  $\mu\text{m}$ . Hence, lines ablated during the runs have a very pronounced edge curling as shown in figure 4. Figure 4(b) shows that the width of the curled region on either side can reach about 4  $\mu\text{m}$ . A cross-sectional view of the ablated line, shown in figure 4(c), clearly shows the existence of curling with curled material height of ~ 1.2  $\mu\text{m}$ . It will be seen later in this paper, that edge curling was observed even after a single pulse. Thus, within the pulse duration, the laser, simultaneously, drives the three proposed mechanisms: ablation, melting and heat induced softening. The shock wave removes the ablated material and most of the molten material by ejection and causes the heat-softened ITO material to extrude upwards and subsequently curl upon cooling.

### 3.4 Edge quality (curling) as a function of wavelength and imaging quality

The effect of wavelength and imaging quality on the curling phenomenon was tested using two other Tamarack experimental imaging systems operating at 308 nm and 248 nm wavelengths. The systems, used in a stationary mode (i.e. no scanning), were equipped with 5x reduction projection lenses. The lenses have a good imaging quality with NA = 0.1 for the 308 nm 5x reduction lens and NA = 0.08 for the 248 nm 5x reduction lens, resulting in a resolution value of

~ 3.1  $\mu\text{m}$  for both. Both 5x systems were optimized for ablating line features in the ITO layer. SEM and conductivity testing were utilized to determine optimal conditions for complete ITO removal without damaging the underlying layers. The optimal ablation conditions for the 5x system operating at 308 nm wavelength were the same as determined for the 1x Dyson 308 nm system used in the evaluation work (i.e. 350  $\text{mJ}/\text{cm}^2$ , 10 pulses, and 10 Hz). The optimal conditions for the 5x 248 nm system were 163  $\text{mJ}/\text{cm}^2$ , 10 pulses, and 10 Hz.

Initially the curling effect was examined after 1 pulse using each system under the above-mentioned optimal fluence and repetition rate conditions. Figure 5(a) shows SEM cross-sectional view for an edge of a feature ablated using the 308 nm 5x-reduction system under the optimal fluence level with duration of 1 pulse. Figure 5(b) shows a SEM cross-sectional view for an edge of a feature ablated using the 248 nm 5x-reduction system under the optimal fluence level with duration of 1 pulse. Notice that the curling effect is evident even after a single pulse, indicating that the laser induced mechanisms, responsible for edge curling, do take place within a single pulse as proposed in the mechanism section above. Also, notice that ITO layer edge curling is more pronounced at 308 nm wavelength confirming that the edge curling effect is thermally driven. Thermal effects are more pronounced at longer wavelengths.

Subsequently, the effect of resolution was studied. In this study, both of the 5x 3.1  $\mu\text{m}$  resolution systems were used to ablate lines in the ITO layer under their particular optimized conditions. At 308 nm wavelength, we can compare ablated line edge quality (curling) produced by the 5x 3.1  $\mu\text{m}$  resolution system to the one produced by the 1x Dyson 6.2  $\mu\text{m}$  resolution system, both running under the same conditions. Figure 6(a) shows a SEM cross-sectional view of a line ablated in ITO using the 308 nm 5x-reduction system with line width of ~ 3  $\mu\text{m}$ . Notice that the curling effect still exists as produced with the 308 nm 1x Dyson system. However, curling is dramatically reduced. The width of the curled region at either edge of the line is 0.6-0.8  $\mu\text{m}$  as opposed to 1.2-4  $\mu\text{m}$  produced by 1x Dyson system. The curled extrusion height is ~ 0.7  $\mu\text{m}$  as opposed to 1.2  $\mu\text{m}$  produced by 1x Dyson lens system. Figure 6(b) shows a SEM cross-sectional view of a line ablated in ITO using the 248 nm 5x-reduction system with line width of ~ 2.6  $\mu\text{m}$ . The curling effect is also evident but, again, with a much narrower dimension than produced by the 308nm 1x Dyson system. The width of the curled region on either side is 0.5  $\mu\text{m}$  and its height is ~ 1.18  $\mu\text{m}$ . This study shows that better imaging quality (i.e. better resolution) dramatically reduces the non-desirable curling effect. In addition, better imaging quality allows successful excimer-based patterning of lines with very small line-widths of 2.6-3  $\mu\text{m}$ .

### 3.5 Effect of edge curling on device performance and evaluation of a curled material removal process

The curled ITO material extruding beyond the ITO layer top surface can have adverse effects on the performance of the display device. The material can intrude into the liquid crystal layer causing discontinuity within a displayed pixel. Also, during device construction, the loosely held curled material may break free and contaminate the liquid crystal. Therefore, it is important to remove the curled material on the edge of ablated features. A preliminary evaluation for curled material removal by  $\text{CO}_2$  snow-based cleaning process was performed. The process is based on directing a  $\text{CO}_2$  snow jet on a sample surface. The jet, incident on the surface at a certain angle, is scanned uniformly to remove any contamination particles and the extruding curled material<sup>17</sup>.

Samples ablated by the various systems mentioned in this paper were exposed to  $\text{CO}_2$  snow jet to test its effectiveness in removing the curled material. Figure 7(a) shows a SEM cross-sectional view of a line ablated with the 308 nm 1x Dyson lens system using the optimized conditions. The line width, before  $\text{CO}_2$  snow cleaning, is 12.5  $\mu\text{m}$ . The curled region on either side of the line has a width of ~1.4  $\mu\text{m}$  and a height of ~ 1.2  $\mu\text{m}$ . Figure 7(b) shows a SEM cross-sectional view of the same line after  $\text{CO}_2$  snow cleaning. The line width is ~ 15.3  $\mu\text{m}$  and the curled material is completely removed. Figure 8(a) shows a SEM cross-sectional view of a line ablated with the 308 nm 5x-reduction system, using the optimized conditions. The line width, before  $\text{CO}_2$  snow cleaning, is ~ 3  $\mu\text{m}$ . The curled region on either side of the line has a width of 0.6-0.8  $\mu\text{m}$  and a height of ~ 0.6  $\mu\text{m}$ . Figure 8(b) shows a SEM cross-sectional view of the same line after  $\text{CO}_2$  snow cleaning. The line width is ~ 5.4  $\mu\text{m}$  and the curled material is completely removed. Figure 9(a) shows a SEM cross-sectional view of a line ablated with the 248 nm 5x-reduction system under the optimized conditions. The line width, before  $\text{CO}_2$  snow cleaning, is 2.6  $\mu\text{m}$ . The curled region on either side of the line has a width of 0.5  $\mu\text{m}$  with a height of 1.2  $\mu\text{m}$ . Fig. 9(b) shows a SEM cross-sectional view of the same line after  $\text{CO}_2$  snow cleaning. The line width is ~ 3.9  $\mu\text{m}$  and the curled material is completely removed.

In all of the above-mentioned cases, the CO<sub>2</sub> snow cleaning method successfully removed the curled material. However, as shown in figure 10, the ablated line edge has a jagged appearance after cleaning. This is due to unwanted excessive peeling in some locations. The excessive peeling is attributed to the aggressive conditions (angle, flow, etc.) of CO<sub>2</sub> snow jet used in the preliminary cleaning evaluation. As demonstrated above, cross-sectional SEM analysis of cleaned lines showed no residue of curled material or de-lamination at the edges. Hence, the aggressiveness of the cleaning process can be reduced to minimize the jagged line edge appearance while still achieving complete removal of the curled material. Therefore, it is necessary to perform further optimization of the cleaning process.

#### 4. SUMMARY

In summary, we have evaluated excimer-based ablative patterning of large format display device thin film ITO. The ITO film is sputtered on thin film SiO<sub>2</sub> that is deposited on flexible PET substrate. The evaluation was performed using a 308 nm excimer-based mask pattern projection system. Ablation conditions were optimized at a fluence level of 350 mJ/cm<sup>2</sup> and a pulse count of 10 pulses, using 10 Hz repetition rate. The system relies on a scan-and-repeat method to pattern-ablate existing large format display devices with lines of length 44 mm and width as small as 12.5 µm. It is also capable of pattern-ablating devices of larger formats up to 150 mm x 150 mm, if required. Ablated line edge quality suffers slightly due to a thermally induced curling effect. It was shown that improvement of the system imaging quality could significantly reduce the curling effect and allow patterning of lines with width as small as 2.6 µm. In addition, a CO<sub>2</sub> snow-based process for removing extruding curled material was preliminarily evaluated. The process proved promising, however, further optimization is required.

#### ACKNOWLEDGMENTS

The authors would like to thank Peter Chow of Tamarack Scientific Company for his efforts in helping set up and perform some of the experiments.

#### REFERENCES

1. E. Lueder, "Liquid Crystal Displays with Plastic Substrates", *Conference on Liquid Crystal Materials, Devices, and Applications*, Robert Shasidhar, Proc. SPIE 3297, 64-72, SPIE, 1998.
2. P. Mach, S. J. Rodriguez, R. Nortrup, P. Wiltzius, and J. A. Rogers, "Monolithically Integrated, Flexible Display of Polymer-dispersed Liquid Crystal Driven by Rubber-stamped Organic Thin-film Transistors", *Appl. Phys. Lett.*, **78**, 3592-3594, 2001.
3. A. R. Forouhi, G. G. Li, and I. Bloomer, "Optical Characterization of ITO Films Used in Flat Panel Displays", Susan K. Jones, Proc. SPIE 2725, 471-475, SPIE, 1996.
4. I. Kenji Nishiguchi, K. Maskazu Okada, S. Kiyofumi Hashimoto, U.S. Patent No. 6,226,067.
5. S. C. Tam, Y. H. Chen, H. Y. Zheng, and W. L. Chen, "Scribing of ITO-Coatings Using a Q-Switched Nd:YAG Laser", *Microelectronic Packaging and Laser Processing*, Yong Khim Swee, Hong Yu Zheng, Ray T. Chen, Proc. SPIE 3184, 186-194, SPIE, 1997.
6. P. Rumsby, E. Harvey, D. Thomas, and N. Rizvi, "Excimer Laser Patterning of Thick and Thin Films for High Density Packaging", *Microelectronic Packaging and Laser Processing*, Yong Khim Swee, Hong Yu Zheng, Ray T. Chen, Proc. SPIE 3184, 176-185, SPIE, 1997.
7. Tamarack Scientific Co., Inc., product brochure on Excimer Laser Ablation Systems.
8. Ronald E. Sheets, "Scanning projection for large-area lithography", *Microlithography World (feature paper)*, PennWell Publishing Company, 1996.
9. S. J. Kirch, J. R. Lankard, J. J. Ritsko, K. A. Smith, J. L. Speidell, and J. T. Yeh, U.S. Patent No. 4,923,772.
10. R. S. Patel, T. F. Redmond, C. Tessler, D. Tudryn, and D. Pulaski, "Laser Via Ablation Technology for MCM-D Fabrication at IBM Microelectronics", *The International Journal of Microcircuits and Electronic Packaging*, Volume 18, Number 3, 266-274, Third Quarter 1995.
11. J. C. Koo, V. J. Zaleckas, U. S. Patent No. 4,081,653.
12. W. W. Duley, *UV Lasers: Effects & Applications in Materials Science*, Chapter 2, Cambridge University Press, Cambridge, 1996.

13. Y. S. Liu, H. S. Cole, H. R. Philipp, and R. Guida, "Photo-etching of Polymers with Excimer Lasers", *Lasers in Microlithography*, Daniel J. Ehrlich, Proc. SPIE 774, 133-137, SPIE, Santa Clara, 1987.
14. James R. Sheats, Bruce W. Smith, *Microlithography Science and Technology*, Chapter 4, Marcel Dekker, Inc., New York, 1998.
15. P. M. Smith, P. G. Carey, and T. W. Sigmon, "Excimer laser crystallization and doping of silicon films on plastic substrates", *Appl. Phys. Lett.*, **70**, 342-344, 1997.
16. M. O. Thompson, "Liquid-Solid Interface Dynamics During Pulsed Laser Melting of Silicon-on-Sapphire", Ph. D. thesis, Cornell University, 1984.
17. ATS Eco-Snow Systems, Inc., product brochure.

\*oghandour@tamsci.com; fax 1 (909) 817-0640; <http://www.tamsci.com>; Tamarack Scientific Company, 220 Klug Circle, Corona, CA, USA, 92880

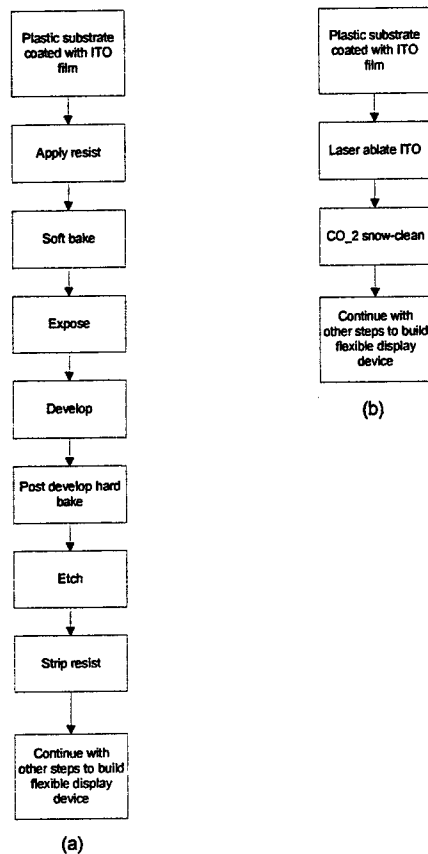


Fig. 1: Process flow diagram for patterning of ITO-on plastic substrate.

- (a) Conventional Photolithography.
- (b) Excimer-based ablative patterning.

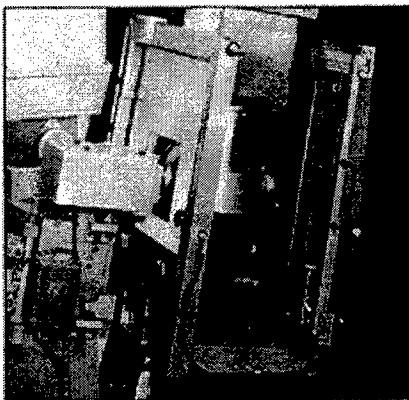


Fig. 2: Tamarack Model 330 system. Close-up view of system mask, lens, and substrate stage.

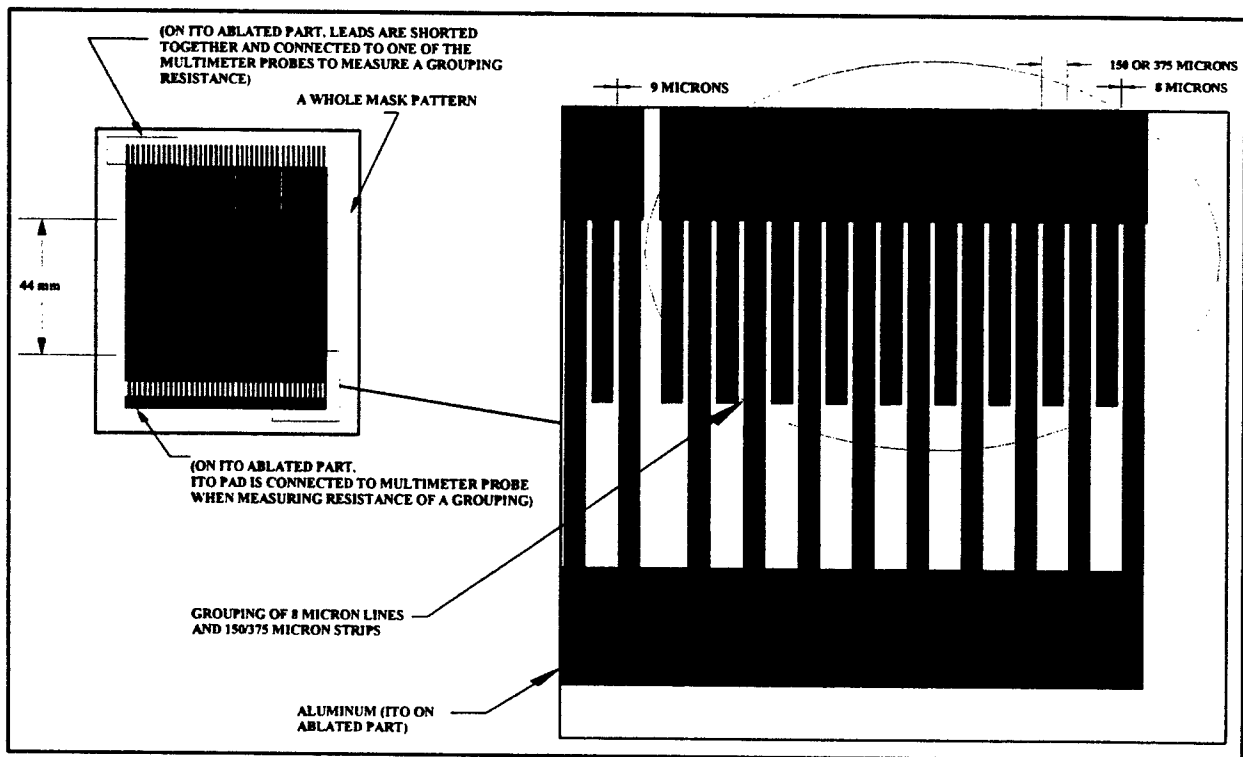
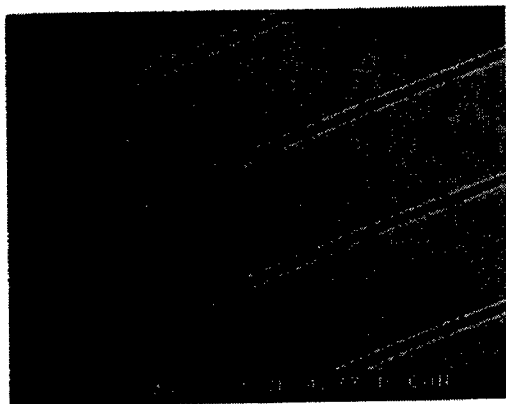
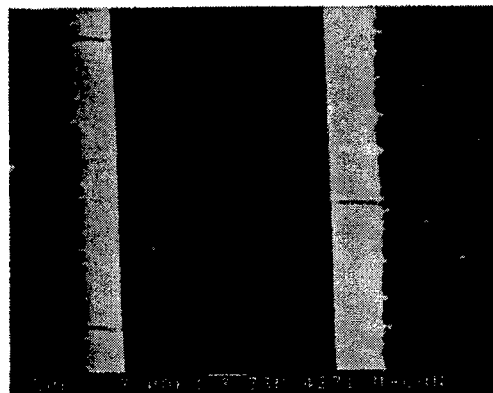


Fig. 3: Schematic of Aluminum-on-Quartz mask utilized in excimer-based ablative ITO patterning (not to scale). Comments in brackets illustrate conductivity measurement on pattern-ablated ITO part, which is approximately a 1x reproduction of the mask pattern.

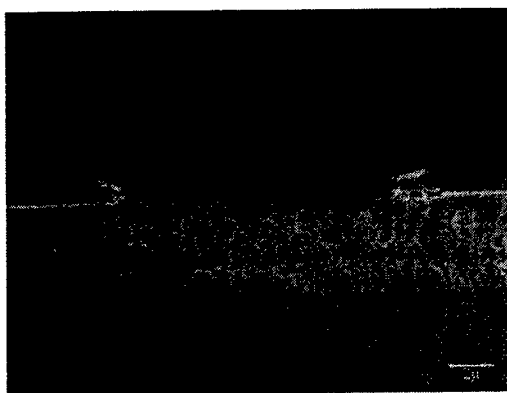




(a)

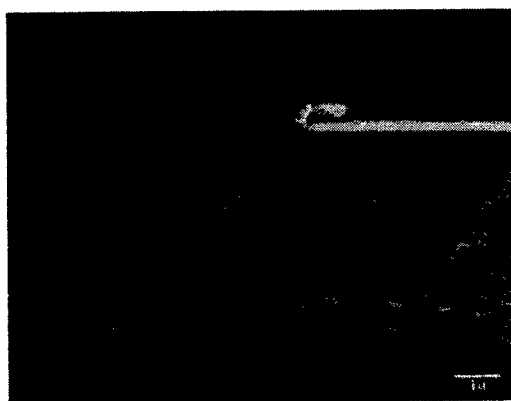


(b)

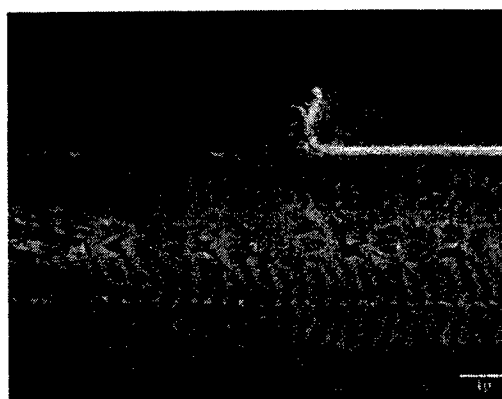


(c)

Fig. 4: (a) SEM top view of a grouping of lines ablated by excimer in ITO layer using 11  $\mu\text{m}$  wide mask lines, 1x Dyson system, resolution  $\sim 6.2 \mu\text{m}$ , 308 nm, 350  $\text{mJ}/\text{cm}^2$ , 10 pulses, 10 Hz. (b) SEM top view of a single line out of the grouping mentioned above. (c) Ablated line SEM cross-sectional view. Line width = 12.5  $\mu\text{m}$ , curled material width  $\sim 1.4 \mu\text{m}$ , curled material height  $\sim 1.2 \mu\text{m}$ .



(a)

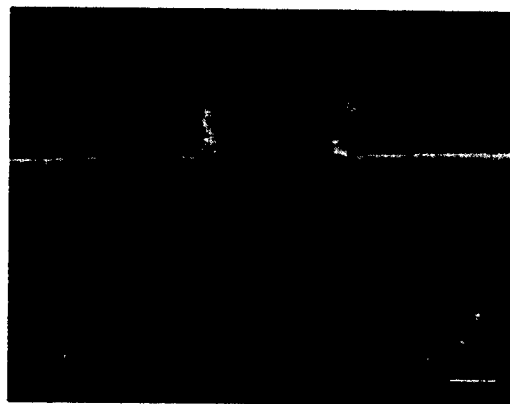


(b)

Fig. 5: (a) SEM cross-sectional view of an ablated feature edge. Feature ablated in ITO using 5x-reduction stationary system, resolution  $\sim 3.1 \mu\text{m}$ , 308 nm, 350  $\text{mJ}/\text{cm}^2$ , 1 pulse, 10 Hz. (b) SEM cross-sectional view of an ablated feature edge. Feature ablated in ITO using 5x-reduction stationary systems, resolution  $\sim 3.1 \mu\text{m}$ , 248 nm, 163  $\text{mJ}/\text{cm}^2$ , 1 pulse, 10 Hz.

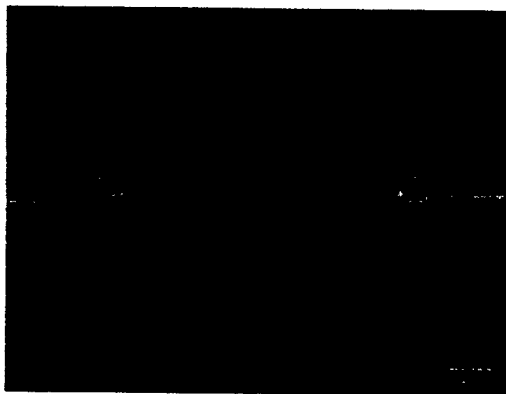


(a)

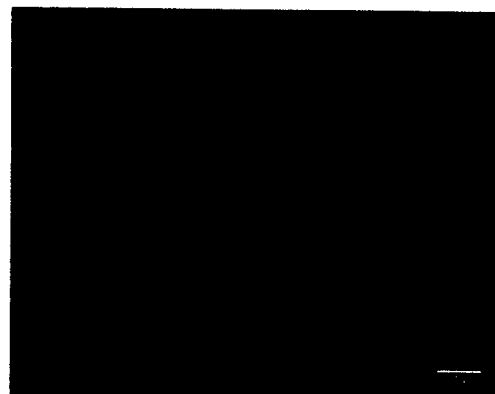


(b)

Fig. 6: (a) SEM cross-sectional view of line ablated using stationary 308 nm 5x-reduction system with resolution  $\sim 3.1 \mu\text{m}$  at  $350 \text{ mJ/cm}^2$ , 10 pulses, 10 Hz. Line width =  $3 \mu\text{m}$ , curled region width =  $0.6\text{--}0.8 \mu\text{m}$ , curled region height =  $0.65 \mu\text{m}$ . (b) SEM cross-sectional view of line ablated using stationary 248 nm 5x-reduction system with resolution  $\sim 3.1 \mu\text{m}$  at  $163 \text{ mJ/cm}^2$ , 10 pulses, 10 Hz. Line width =  $2.6 \mu\text{m}$ , curled region width =  $0.5 \mu\text{m}$ , curled region height =  $1.18 \mu\text{m}$ .



(a)

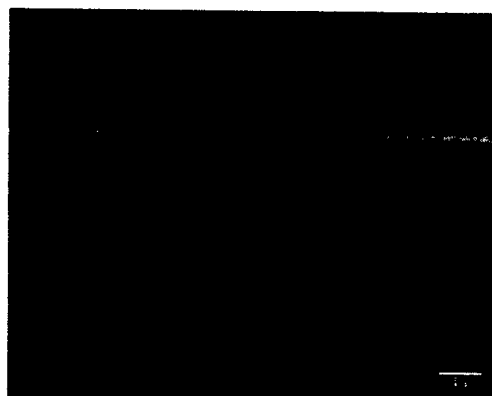


(b)

Fig. 7: (a) SEM cross-sectional view of ablated line before  $\text{CO}_2$  snow cleaning. Line was ablated using  $11 \mu\text{m}$  wide mask lines, the 1x Dyson system, 308 nm,  $350 \text{ mJ/cm}^2$ , 10 pulses, 10 Hz. Line width =  $12.5 \mu\text{m}$ , curled material width  $\sim 1.4 \mu\text{m}$ , curled material height  $\sim 1.2 \mu\text{m}$ . (b) SEM cross-sectional view of same line after  $\text{CO}_2$  snow cleaning. Line width  $15.2 \mu\text{m}$ .

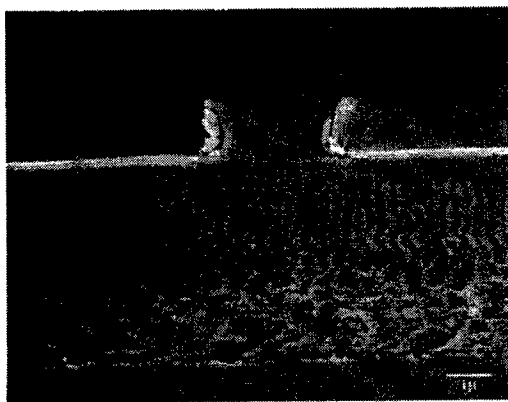


(a)

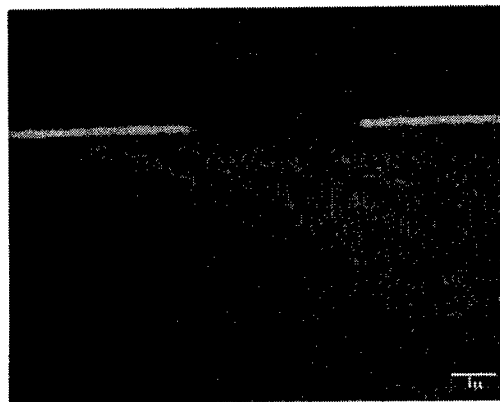


(b)

Fig. 8: (a) SEM cross-sectional view of ablated line before  $\text{CO}_2$  snow cleaning. Line was ablated using the stationary 308 nm 5x reduction system at  $350 \text{ mJ/cm}^2$ , 10 pulses, 10 Hz. Line width =  $3 \mu\text{m}$ , curled region width =  $0.6\text{--}0.8 \mu\text{m}$ , curled region height =  $0.653 \mu\text{m}$ . (b) SEM cross-sectional view of same line after  $\text{CO}_2$  snow cleaning. Line width =  $5.4 \mu\text{m}$ .



(a)



(b)

Fig. 9: (a) SEM cross-sectional view of ablated line before CO<sub>2</sub> snow cleaning. Line was ablated using the stationary 248 nm 5x reduction system at 163 mJ/cm<sup>2</sup>, 10 pulses, 10 Hz. Line width = 2.6 μm, curled region width = 0.5 μm. Curled region height = 1.18 μm. (b) SEM cross-sectional view of same line after CO<sub>2</sub> snow cleaning. Line width = 3.9 μm.

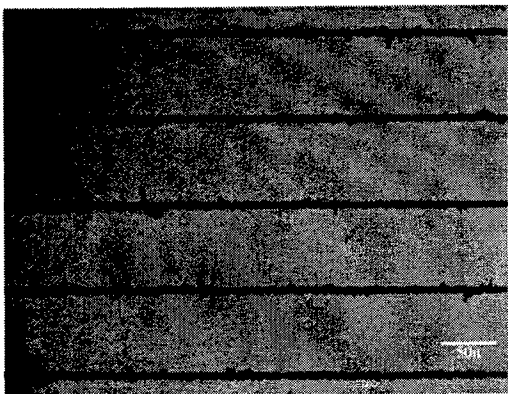


Fig. 10: SEM top view of typical ITO ablated sample after CO<sub>2</sub> snow cleaning.

# Generation of functional structures by laser pyrolysis of polysilazane

Hans-Joachim Krauß\*, Andreas Otto

Chair of Manufacturing Technology, Univ. of Erlangen-Nuremberg, 91058 Erlangen, Germany

## ABSTRACT

The pyrolysis of polysilazanes by laser power represents an innovative technique for the generation of ceramic-like coatings and structures. The dissolved polysilazane can be easily applied by painting techniques such as dipping or spraying. In the following pyrolysis the polysilazane layer transforms into an amorphous ceramic-like coating. The laser power is absorbed in the precursor layer, which leads to the latter's ceramisation without damaging the substrate by thermal load. While plane laser pyrolysis creates a protective coating, selective pyrolysis creates a raised and adherent ceramic-like structure that remains after the unexposed polymer layer has been removed. The flexibility of a writing laser system in conjunction with a suitable handling system makes it possible to inscribe any kind of two-dimensional structure on nearly any complexly shaped part. Some of the chemical, magnetic, and electrical structure properties can be adjusted by the pyrolysis parameters and special types of filler particles. Especially the possibility to control electric conductivity should make it possible to create structured dielectric films or planar resistors, inductors or capacitors, which are basically written on the surface of the part. Because of their ceramic nature the structures are resistant against high temperatures and corrosive media. Thus, this new additive structuring technique could finally strike a new path in creating corrosion resistant high-temperature sensors and control systems.

**Keywords:** laser pyrolysis, polysilazane, surface treatment, additive structuring, functional structures

## 1. INTRODUCTION

In this paper, pyrolysis means the transformation of special polymers (so-called precursors) into ceramic materials by heating. As powder, solution, or melt they can be processed into fibers, coatings, or compact parts. Especially the generation of ceramic coatings and structures is of interest because in conjunction with such innovative technologies as laser material processing it offers a powerful alternative to conventional coating techniques.<sup>1,2,3</sup> Normally, the pyrolysis of the preformed precursor is done in a furnace under protective atmosphere. Because of the loss of mass during the transition of the polymer to the ceramic state a corresponding loss in volume occurs. This can lead to unwanted cracks especially when thick layers and parts are pyrolysed. Filling powders are used to avoid this problem.<sup>4,5</sup> The filler powders can also give the pyrolysed part a special function.

Polysiloxane polymers (SiCO polymer) are often used as precursor material because they are cheap and stable in air. Polysilazanes (SiCN polymer), in contrast, are expensive and normally unstable in air so that they can only be used for special applications. Nevertheless, in both their polymer and their ceramic state, polysilazanes show a much better adhesion to almost any kind of substrate than polysiloxanes do.<sup>6</sup> Furthermore, a new specially modified polysilazane called ABSE was developed that shows a very low air sensitivity so that it can be applied and pyrolysed in air.<sup>7</sup> The high cost of the ABSE precursor compared with conventional polysiloxanes is put into perspective when, as in this project, only thin precursor layers are needed.

Temperatures above 700°C are needed to ceramize the ABSE polymer. This limits the generation of coatings and structures to high-melting materials such as CMCs (Ceramic Matrix Composites). For the coating of low-melting substrates, e.g. aluminum or magnesium, the laser is a suitable instrument for pyrolysis. The laser power is absorbed in the coating so that it is heated and transforms into a ceramic layer. The substrate, however, stays "cold"; i.e. it is not damaged by the laser beam. Another advantage of laser pyrolysis is the flexibility of the process. With the help of a writing laser system the precursor can be pyrolysed only selectively. Thus, it is possible to write a ceramic pattern on nearly any complexly shaped part.

---

\* j.krauss@blz.org; phone +49 9131 97790-22; fax +49 9131 97790-11; <http://www.lft.uni-erlangen.de>;

Chair of Manufacturing Technology, University of Erlangen-Nuremberg, Egerlandstrasse 11, 91058 Erlangen, Germany

## 2. LASER PYROLYSIS OF POLYSILAZANE

### 2.1 Pyrolysis with a CO<sub>2</sub> laser

Pyrolysis of an ABSE coating with the CO<sub>2</sub> laser always leads to a crack structure with a clod size typically between 50  $\mu\text{m}$  and 100  $\mu\text{m}$ . Fig. 1 shows the cracks in an ABSE layer on aluminum after treatment with a CO<sub>2</sub> laser.

The cross-section on the left side in Fig. 2 shows the internal structure of the ABSE layer on a C-fiber-reinforced epoxy pyrolysed with the CO<sub>2</sub> laser. It is easy to see that the surface is formed by individual ceramic-like clods about 10  $\mu\text{m}$  thick. Below the clods there is a thick layer of crack-free - since not pyrolysed - ABSE precursor. The substrate shows no thermal effect from the laser treatment. Transmission measurements demonstrate that the ABSE polysilazane absorbs the radiation of the CO<sub>2</sub> laser to an extremely high degree.<sup>3</sup> Therefore, nearly all of the laser's energy is absorbed in the surface of the coating and leads to a superficial ceramization of the ABSE, whereas the deeper zones of the coating remain in the polymer state.<sup>8</sup> The right-hand side of Fig. 2 shows the universal hardness ( $H_{U, \text{korr}}$ ) over the shown cross-section.

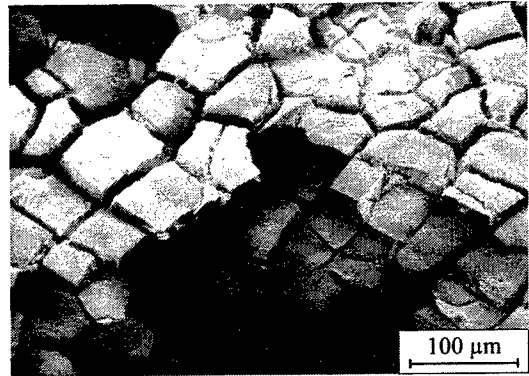


Fig. 1: Crack structure in an ABSE coating ceramized by a CO<sub>2</sub> laser

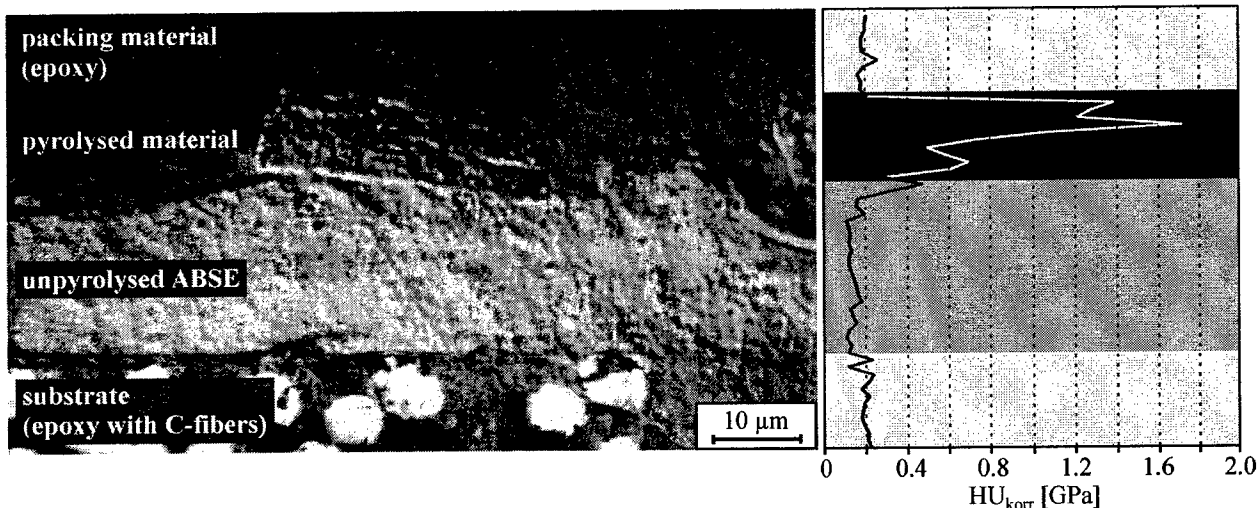


Fig. 2: Cross-section of an ABSE layer on a fiber-reinforced epoxy and the corresponding progression of hardness; the pyrolysis is done by a CO<sub>2</sub> laser

The hardness of the clods is about seven times (1.4 GPa) that of the epoxy substrate (0.2 GPa). This could mean a great potential for the wear protection of weak plastic surfaces; unfortunately, the adhesiveness of the ceramized clods on the unpyrolysed layer is not very good: the clods can be scratched off by a hard subject. Furthermore, corrosive liquids or gases could invade through the cracks and corrode the unpyrolysed precursor and finally the substrate. Thus, at present the cracked coating surface prevents the utilization of the described CO<sub>2</sub> laser-assisted coating technique for wear or corrosion protection in practical applications.

### 2.2 Pyrolysis with a Nd:YAG laser

The situation changes when using a Nd:YAG laser. On the left-hand side, Fig. 3 shows the ABSE layer on an aluminum substrate after having been exposed by the laser three times. The resultant coating shows a good adhesiveness (measured by a cross cutting test<sup>9</sup>) and its surface exhibits a droplet structure. This may be a result of the forming and melting of silicon oxide modifications. The surface seems crack-free but not free of pores. The cross-section shows that a continuous, unfragmented layer is formed. This result differs clearly from the surface morphology obtained by CO<sub>2</sub> laser pyrolysis. This difference could be explained by the unequal absorption behavior of the two laser wavelengths

within the ABSE layer. As explained above, the CO<sub>2</sub> laser radiation is completely absorbed in the ABSE layer within a distance of only a few micrometers, which leads to the fragmented coating structure shown. The Nd:YAG laser radiation, in contrast, is absorbed in the whole volume of the layer, since ABSE shows a medial absorption for this type of laser radiation.<sup>10</sup> This leads to a "smooth" pyrolysis without crack formation.

On the right-hand side, Fig. 3 shows the distribution of the universal hardness measured on the surface of the coating. It can be seen that the maximum of the distribution lies around a hardness value of 3.6 GPa, i.e. a hardness of the pyrolysed layer that is more than 3 times that of the aluminum substrate (1.1 GPa, vertical line).

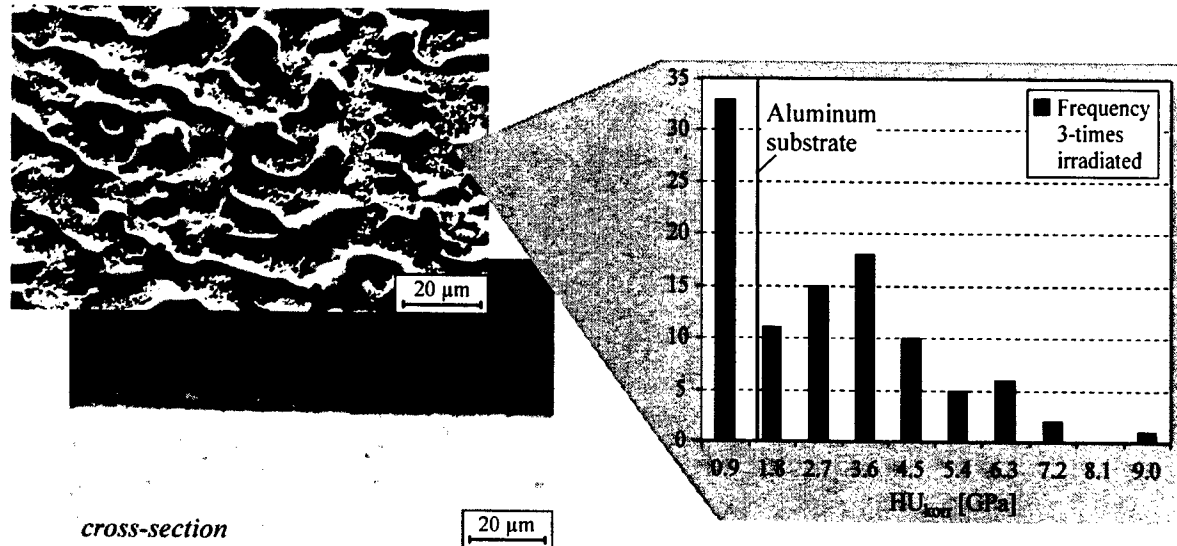


Fig. 3: Topography and cross-section of an ABSE layer on aluminum pyrolysed by a Nd:YAG laser; frequency distribution of the hardness measured on the coating surface

### 3. SELECTIVE LASER PYROLYSIS

#### 3.1 Experimental procedure

For the coating of substrates by polysilazane, the ABSE precursor is dissolved in octane. Because of the good results in previous studies Al<sub>2</sub>O<sub>3</sub> powder is mixed into the solution, which is then applied to Al<sub>2</sub>O<sub>3</sub> substrates by dip coating or with the help of a doctor roll.<sup>10</sup> After the solvent has evaporated, ceramic-like structures are generated by selective laser pyrolysis. In order to create micro-sized structures, it is necessary to use a laser system with a well-focusable beam. While for plane laser pyrolysis a wide beam (defocusing) suffices to radiate an area as large as possible, selective laser pyrolysis has to be done preferably in or near the focus of the beam, depending on the desired width of the structure. A beam diameter smaller than 50 μm is useful to create thin lines. Because of the small spot size a few watts of laser power are enough to pyrolyse the ABSE precursor. For pyrolysis, the guidance system of the laser should be a scanner system as shown in Fig. 4. The guidance of the beam by mirrors, which are moved very fast by galvanometers, allows scanning velocities up to 5 m/sec. with a positioning precision better than 10 μm. In this project, pyrolysis is done with an argon ion laser ( $\lambda = 514.5$  nm, *Coherent, Innova Sabre 15/3 DBW*) with a beam diameter of about 33 μm and a maximum power of 14 W and a Nd:YAG laser ( $\lambda = 1064$  nm, *Haas-Laser, VMCI*) with a spot size of about 45 μm and a maximum power of 7 W. Both laser

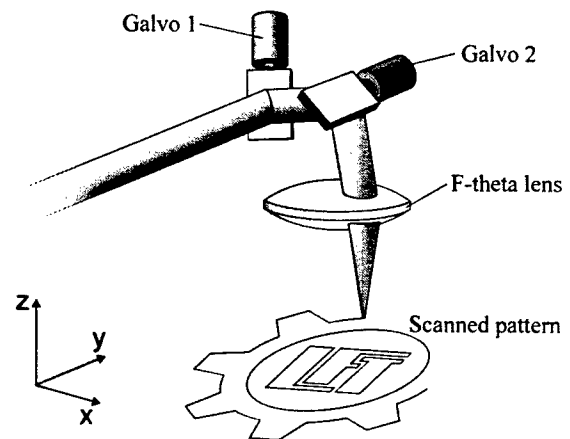


Fig. 4: Optical setup of a laser system adapted for micro structuring

work in cw-mode. For the structuring experiments, the model pattern in Fig. 4 (toothed wheel with writing) is chosen to show the potential of the technique by means of different criteria. The pattern shows both straight and bent lines, different angles, and lines that run parallel with different spacing.

### 3.2 Uncovering the structure

The radiation of the ABSE coating is done only selectively. Thus, the unexposed polymer layer could be removed after the structuring process by dissolving it e.g. in acetone. The cleaning procedure is very successful when done in an ultrasonic bath: the unpyrolysed precursor is already removed after a few seconds. Fig. 5a shows the un-cleaned structure generated with an argon ion laser slightly out of its focus (beam diameter on the surface of the coating is about 100  $\mu\text{m}$ ). After cleaning, the unexposed polymer is removed and the ceramized part of the structure remains (Fig. 5b). The dark rims of the structures in Fig. 5a are the heat-affected zone. This is the non-irradiated but thermally affected precursor, which frames the directly illuminated and ceramized core of the structure. Often, parts of the heat-affected zone remain after cleaning in acetone. Because of their poor mechanical properties these relicts can be removed completely by enforcing the cleaning process using a brush.

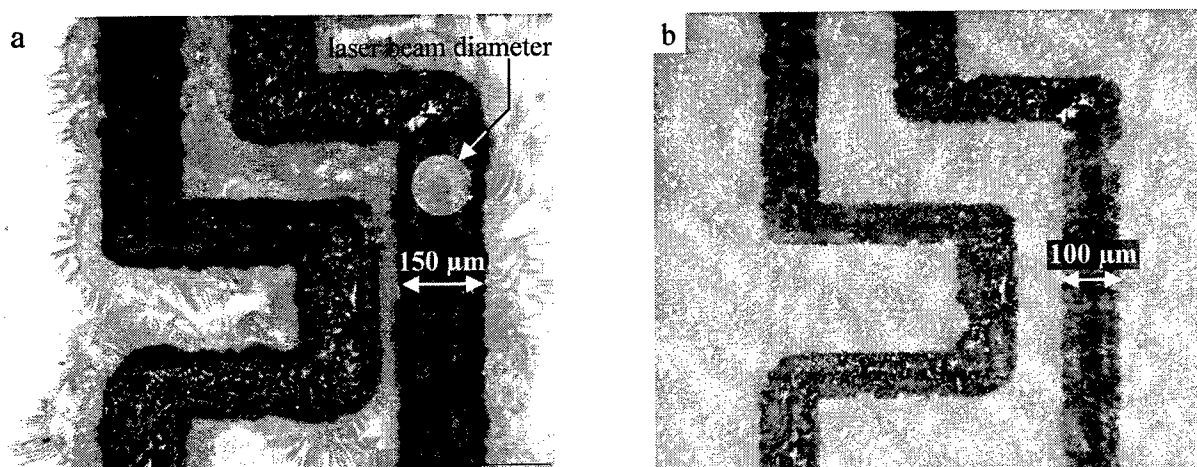


Fig. 5: Excavating a ceramic structure generated with an argon ion-laser on an  $\text{Al}_2\text{O}_3$  substrate. a. structure before excavating; b. structure after cleaning with acetone in an ultrasonic bath and with a brush

Fig. 5a shows how the heat-affected zone ranges beyond the generated structure widely into the unexposed layer. Parallel to the temperature gradient that establishes during pyrolysis, the precursor goes through all states from complete ceramisation to cross-linked and finally unaffected polymer. While the polymer in the region of the laser beam is ceramized and thus indicates a good corrosion and wear resistance, the coating in the heat-affected zone shows insufficient toughness and can be removed easily.

### 3.3 Characterization of the structures

The generated microstructures are investigated using materialographical methods. Because of its low depth of focus, the light microscope is used only for a superficial examination of the pyrolysis result. For a more detailed investigation the scanning electron microscope (SEM) is better suited. The quantitative analysis of the structure is done with a confocal microscope, which allows a contact-less topography measurement. Fig. 6 shows a light-microscopic overview of the structure pyrolysed with the argon ion laser on an  $\text{Al}_2\text{O}_3$  plate, a topographic map, and a detailed SEM picture. The topographic map demonstrates that a raised structure with a height of about 3  $\mu\text{m}$  was produced. The SEM picture shows the structure in detail.

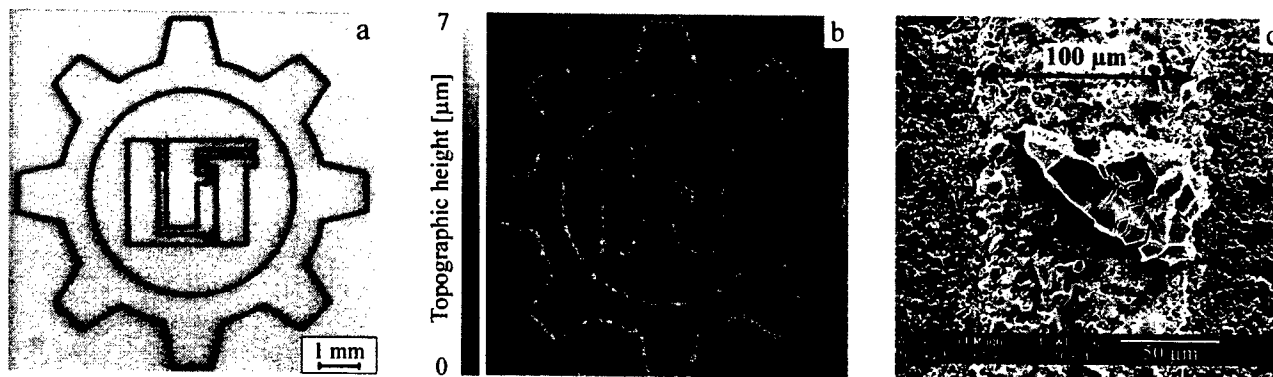


Fig. 6: Ceramic-like structures on  $\text{Al}_2\text{O}_3$  substrate, generated with an argon ion laser. a. light-microscopic picture; b. topographic map; c. detailed SEM picture

It can be seen that the structure is crack-free but interspersed with small pores. There are sporadic remains of probably unpyrolysed coating material covering the structure. Fig. 6c shows such a remain. The ABSE precursor filled with  $\text{Al}_2\text{O}_3$  powder obviously is highly transparent to the green light of the argon ion laser. This leads to an absorption of laser power at the layer-substrate contact area; thus, this region is heated and pyrolysis takes place there. The polymer located above this region is blasted off by the pyrolysis gases and volume shrinkage. Finally, a ceramized layer remains that is only a few microns thick. This effect indicates that the starting thickness of the coating probably has only little influence on the final structure height. Further investigations with other precursor-filler systems are necessary to get more information about the mechanism of laser pyrolysis and finally to create also higher structures.

Laser structuring is also done with a Nd:YAG laser. Fig. 7 shows light-microscopic pictures and corresponding topographic maps of structures with different sizes generated with the Nd:YAG laser on  $\text{Al}_2\text{O}_3$  substrates.

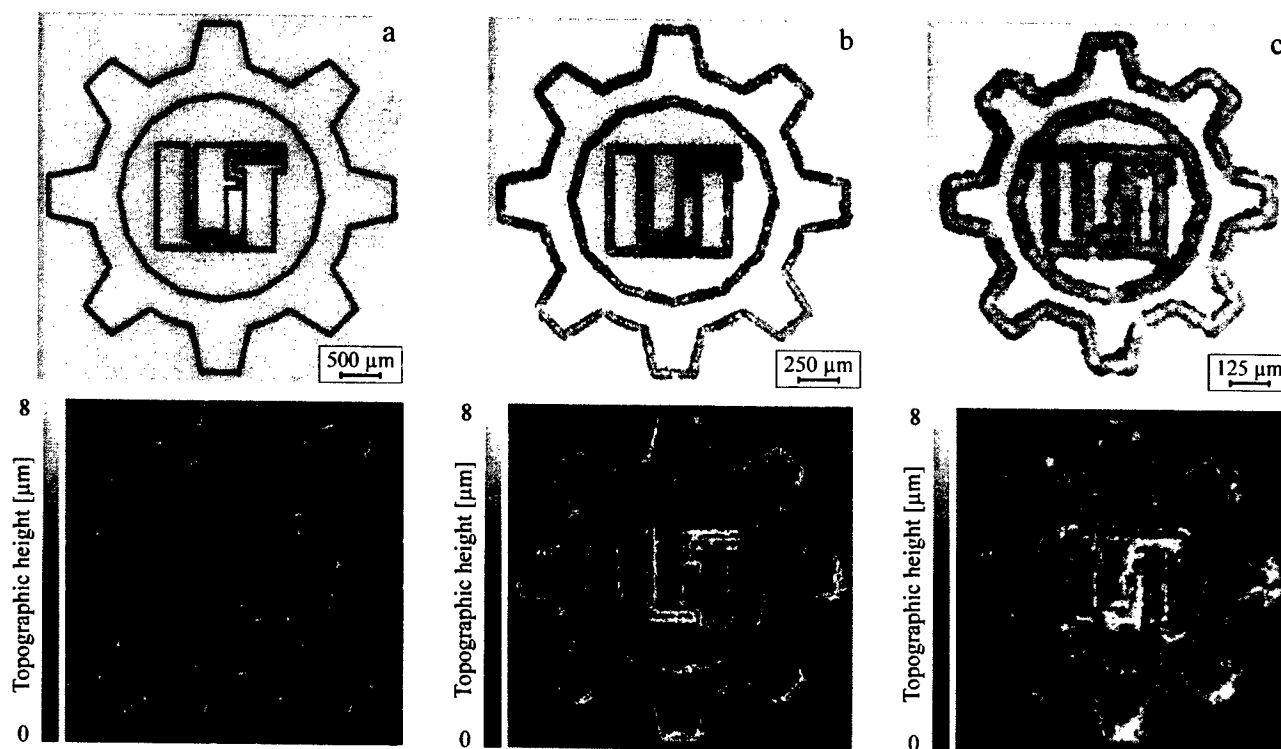


Fig. 7: Differently sized ceramic-like structures on  $\text{Al}_2\text{O}_3$  substrates, generated with a Nd:YAG laser; light-microscopic pictures and corresponding topographic maps. a. Structure diameter  $d_a = 5,17$  mm; b. Structure diameter  $d_b = 2,26$  mm; c. Structure diameter  $d_c = 1,08$  mm



The structures' height is about  $4\text{ }\mu\text{m}$  and their width around  $70\text{ }\mu\text{m}$ . Whereas in the model structure in Fig. 7a all lines are separated, the structure in Fig. 7b shows a borderline case: the internal lines of the writing touch each other but are still recognizable as independent lines. Fig. 7c finally shows these lines conflating. The generation of such fine, closely spaced lines as separated structure elements requires a better-focusable laser. Future work should show, if this can be realized with a fiber laser, which has a spot size of about  $10\text{ }\mu\text{m}$ . Fig. 8 shows SEM pictures of the structures from Fig. 7. The structure lines are almost crack-free and have only few pores. Their surface roughness is less than that of the substrate.

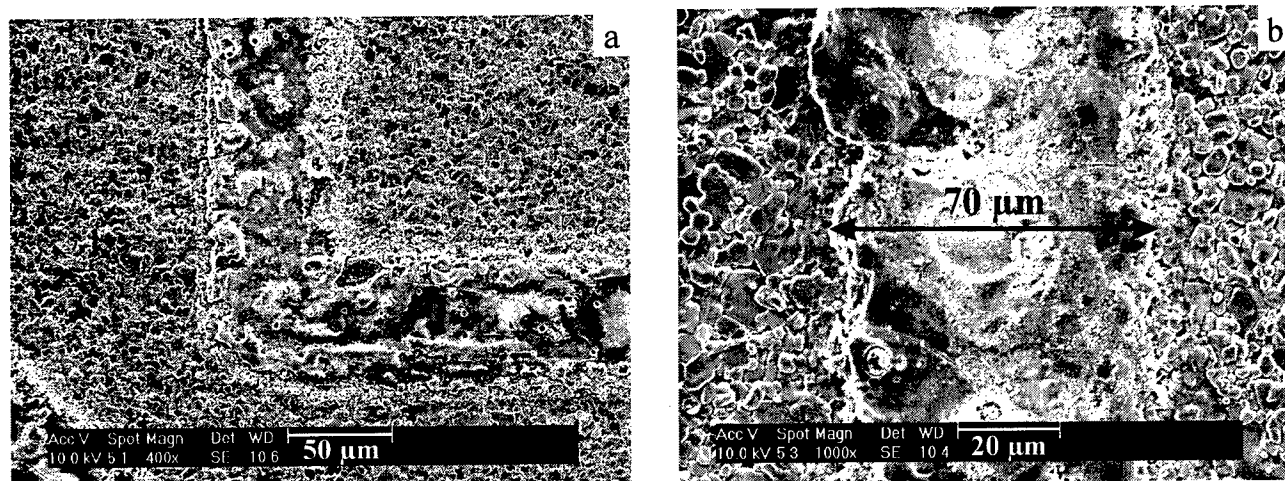


Fig. 8: Ceramic-like structure lines on  $\text{Al}_2\text{O}_3$  substrates, generated with the Nd:YAG laser; detailed SEM pictures of the structures from Fig. 7

At  $70\text{ }\mu\text{m}$  the line width is about 60 % bigger than the spot size of the laser beam ( $45\text{ }\mu\text{m}$ ). The heat insertion in the surrounding precursor layer by heat conduction obviously is high enough for pyrolysis to take place outside the irradiated area. New irradiation strategies, e.g. the use of a pulsed laser or increasing the scanning velocity, should probably make it possible to reduce the heat-affected zone and generate smaller lines with the same laser system.

### 3.4 Abrasion resistance of the structures

An important criterion to estimate the practical usability of the structures is their abrasion wear behavior. Therefore, a simple testing machine, pictured in Fig. 9, was built.

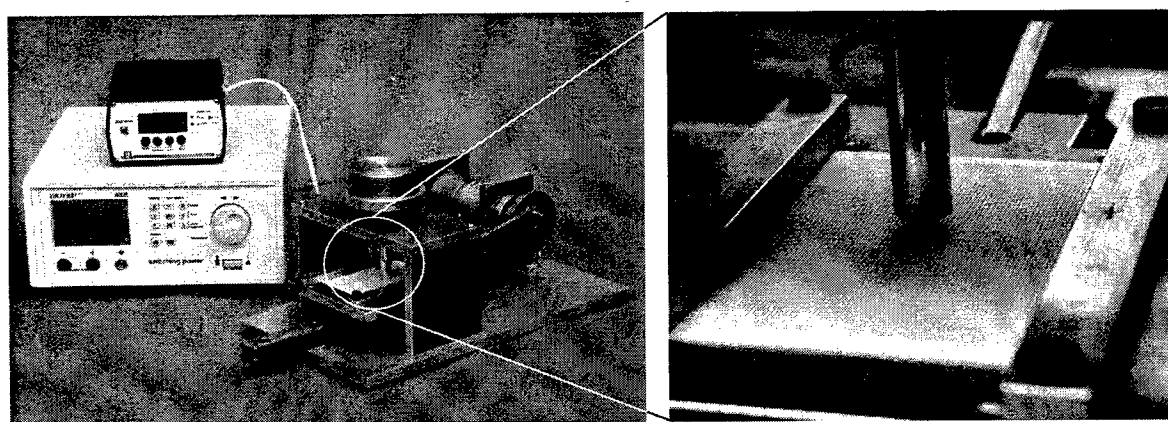
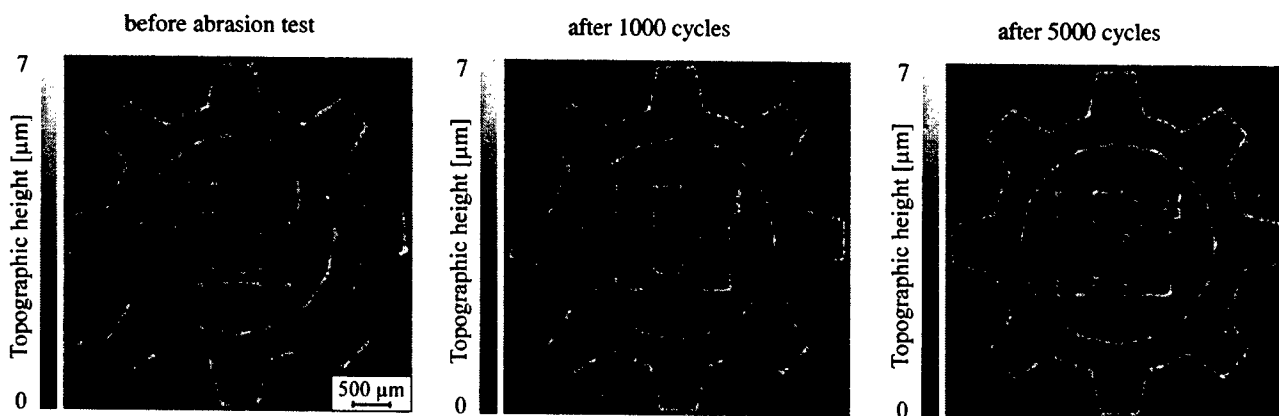


Fig. 9: Abrasion tester: device for the investigation of the abrasion resistance of the generated ceramic structures (according to DIN 58196-4<sup>11)</sup>)

This wear tester helps to investigate the resistance of the structure against abrasion according to DIN 58196-4 using a rubber.<sup>11</sup> The sample is clamped on a board, which is assembled on a linear guide and driven forward and backward by an electro motor. This motion presses a rubber against the sample with a load of 10 N and strains the structure.

Fig. 10 shows topographic maps and detailed light-microscopic pictures of structures generated with a Nd:YAG laser and exposed to abrasion by the wear tester described above. The left-hand side shows the initial state. The structure height is about 4  $\mu\text{m}$ . The center picture describes the situation after 1000 cycles and the right-hand side the situation after 5000 cycles.

a. Topographic maps:



b. Detailed light-microscopic pictures:

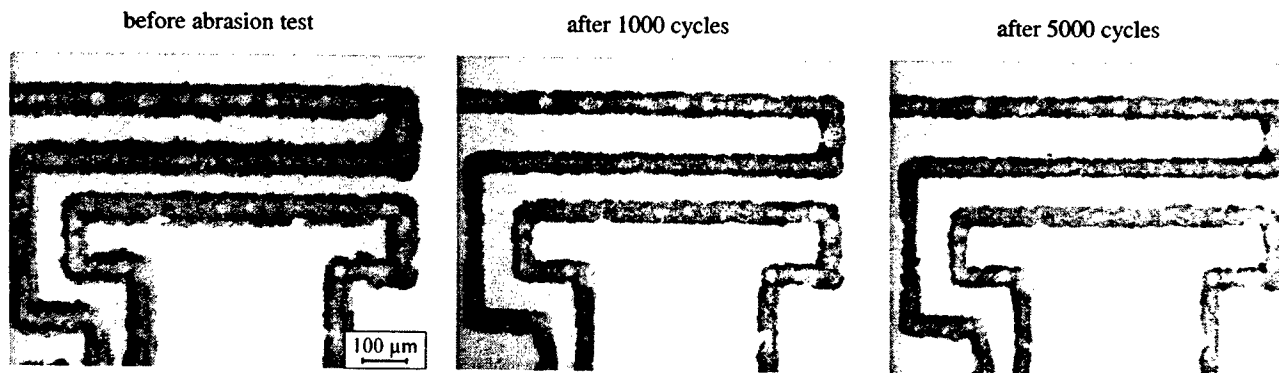


Fig. 10: Ceramic-like structures on  $\text{Al}_2\text{O}_3$  generated with the Nd:YAG laser: abrasion test with a rubber. a. topographic maps; b. detailed light-microscopic pictures

The topographic maps demonstrate that the abrasion stress does not recognizably decrease the structure height. Even after 5000 cycles the structure is as high as at the beginning. Only the irregular rims of the structure present at the beginning, which are part of the heat-affected zone, are removed by the wear test as can be seen in the light-microscopic picture taken after 1000 cycles. This reduces the structure width from about 80  $\mu\text{m}$  to 50  $\mu\text{m}$ , the area that had been directly irradiated by the laser. The new edges of the structure seem to be smoother. Even 4000 more cycles do not lead to important change in the structure. Obviously, a quasi-stationary condition is achieved after a certain number of cycles, in which the structure shows no more wear under the given conditions.

#### 4. FUNCTIONALIZATION OF THE STRUCTURES

The addition of suitable filler powders to the precursor solution makes it possible to give the pyrolysed structures special functions. This should facilitate the use of laser-pyrolysed structures e.g. as embedded components (resistors, inductors or capacitors) in ceramic multi-layers or as sensor elements. In addition, laser pyrolysis could be a suitable method for the generation of structured dielectric layers. In conjunction with photo-structurable metal pastes for the conducting paths it should be possible to produce complexly shaped multi-ply circuits. This not only simplifies the manufacturing process of ceramic multi-layers but also lowers tool costs, since this technology does not need punch cutters for the generation of vias between the single circuit levels. The exposure process with a writing laser system requires no forms or masks. To change the circuit layout it is sufficient to adjust the CAD data. Thus, the described process shows a maximum of flexibility.

To give the structure electric conductivity, an electrically conducting powder needs to be added. Fig. 11 shows the influence of graphite filler on the specific electric resistance of a structure generated on an  $\text{Al}_2\text{O}_3$  substrate with a Nd:YAG laser. As little as 0.5 Vol.-% of graphite content are enough to reduce the specific resistance of the structure line from above  $10^{12} \Omega\text{m}$  (good insulator) to around  $6 \cdot 10^{-2} \Omega\text{m}$  (equal to semi-conductors). If the content of the graphite filler is increased to 40 Vol.-% the specific resistance shows an exponential decrease of factor 100 to a value of about  $6 \cdot 10^{-4} \Omega\text{m}$ . Further investigation with metal powders (e.g. copper) should show if the resistance can be reduced further. Other filler materials should also be tested in order to generate other structure functions. In this context it is of particular interest to create chemically active structures with e.g. catalytic properties. It also needs to be investigated how the use of different filler types and a larger amount of filler powder affect the mechanical properties of the structures, especially their adhesiveness and abrasion resistance.

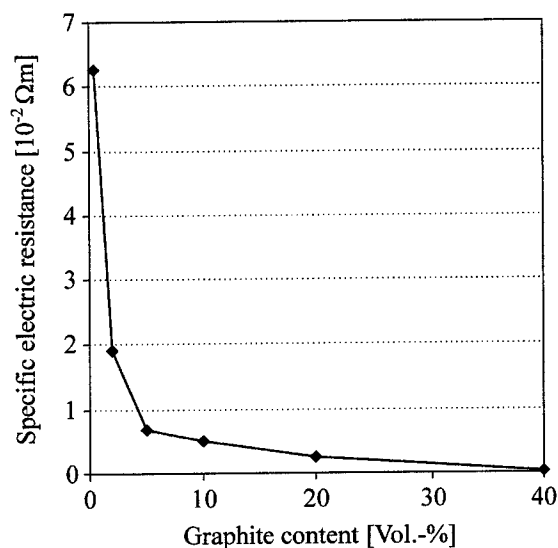


Fig. 11: Specific electric resistance of a structure pyrolysed with a Nd:YAG laser on  $\text{Al}_2\text{O}_3$  substrate as a function of the graphite powder content

#### 5. CONCLUSION

The exposure of the used polysilazane ABSE with a  $\text{CO}_2$  laser showed that pyrolysis of the precursor is feasible. Unfortunately, it has not been possible to generate un-cracked layers because of the absorption of the laser radiation in the surface of the polymer coating and the shrinkage during its pyrolysis. The situation changes when a Nd:YAG laser is used. Because of a "smoother" absorption of the laser power - i.e. the absorption takes place over the whole volume of the precursor layer - the pyrolysis does not crack the coating. Micro-hardness measurements show a medial surface hardness three times as high as the hardness of the aluminum substrate.

When a writing laser system is used, raised and adherent ceramic-like structures can be generated by selectively exposing the precursor and removing the unexposed polymer with a solvent. The structure height is about  $4 \mu\text{m}$ , its width depends on the spot size of the laser beam and the laser parameters. Heat conduction creates a heat-affected zone, which makes the structure wider than the laser beam diameter. Because of its insufficient degree of ceramisation, the heat-affected zone is removed by mechanical stress. Tests with an abrasive wear tester have shown that the heat-affected zone can be removed easily but the ceramized core of the structure lines remains without a reduction in height. In order to utilize the structures for industrial applications, it is necessary to functionalize them. Therefore, graphite powder is mixed to the precursor solution in order to generate electric conductivity. Without graphite filler, the pyrolysed structures show the specific resistance of a good insulator (above  $10^{12} \Omega\text{m}$ ). But as little as 0.5 Vol.-% of graphite reduces the resistance to about  $6 \cdot 10^{-2} \Omega\text{m}$ . If the graphite content is increased up to 40 Vol.-% the resistance is again reduced by factor 100.

## ACKNOWLEDGEMENTS

Financial support for this research was given by the *Bayerische Forschungsstiftung* within the "*Bayerischer Forschungsverbund für Oberflächentechnik*" (*FOROB II*), project number 1.3, and by the *Deutsche Forschungsgemeinschaft (DFG)* within the *Schwerpunktprogramm "Mikromechanische Produktionstechnik 2000"*, project number OT 172/3-1. The authors wish to thank Dr. rer. nat. G. Motz and Mr. Th. Kabelitz of the *Institute for Materials Research (IMA I)*, *University of Bayreuth*, for their supply of ABSE precursor and their extensive and helpful work within this research project. Thanks also go to Mr. M. Bork, Mr. R. Eck, Mr. M. Horn and Mr. A. Schießl, *Chair of Manufacturing Technology, University of Erlangen-Nuremberg*, for their kind support within this research project.

## REFERENCES

1. G. Motz, G. Ziegler, H.-J. Krauß, and M. Geiger, "Eigenschaften und Anwendungen polymerer und keramikartiger Schichten auf Polysilazanbasis", *DGM-Proc. Verbundwerkstoffe und Werkstoffverbunde*, K. Schulte, and K.U. Kainer, pp. 749-753, Hamburg, 1999.
2. G. Motz, G. Ziegler, H.-J. Krauß, and M. Geiger, "Neue keramikartige Schichten: Herstellung, Charakterisierung und Anwendung", *DKG-Jahrestagung 1999*, pp. 97-99, Freiberg, 1999.
3. M. Geiger, G. Ziegler, H.-J. Krauß, G. Motz, and U. Engel, "Generation of ceramic coatings by laser pyrolysis of organo-metallic polymers", *Proc. 1st Int. Conf. on "THE" Coatings in Manufacturing Engineering*, K.-D. Bouzakis, H.-K. Toenshoff, and M. Geiger, pp. 333-342, Ziti Editions, Thessaloniki (Greece), 1999.
4. P. Greil, and M. Seibold, "Active filler controlled pyrolysis (AFCOP) - a novel fabrication route to ceramic composite materials", *Ceram. Trans.* **19**, pp. 43ff, 1991.
5. P. Greil, "Near net shape manufacturing of ceramics", *Materials Chemistry and Physics* **61**, pp. 64-68, 1999.
6. G. Motz, and G. Ziegler, "Herstellung polymerer und keramischer Schichten über modifizierte Polysilazane", *Proc. Werkstoffwoche 98, Symp. 9, Vol. 7*, pp. 667-672, München, 1998.
7. J. Hacker, G. Motz, and G. Ziegler, "Synthesis and Characterisation of Novel Preceramic Polymers for SiCN-Fibres", *Proc. 6th Conf. & Exhibition of the Europ. Ceram. Soc.*, Vol. 2, pp. 391-392, IOM Communications Ltd, Brighton (UK), 1999.
8. H.-J. Krauß, G. Motz, M. Geiger, and G. Ziegler, 2. *Ergebnisbericht des bayerischen Forschungsverbundes für Oberflächentechnik – FOROB II*, pp. 71-98, Erlangen, 2000.
9. DIN EN ISO 2409, *Lacke und Anstrichstoffe – Gitterschnittprüfung*, Beuth Verlag, Berlin, 1994.
10. H.-J. Krauß, G. Motz, M. Geiger, and G. Ziegler, *Abschlußbericht des bayerischen Forschungsverbundes für Oberflächentechnik – FOROB II*, pp. 51-87, Erlangen, 2001.
11. DIN 58196-4, *Dünne Schichten für die Optik – Teil 4: Prüfung der Beständigkeit gegen Abrieb mit einem Radiergummi*, Beuth Verlag, Berlin, 1996.

# Preparation of carbonous nano-particles for anode electrodes of ultra thin lithium ion rechargeable batteries by laser ablation

Satoru Nishio<sup>\*a</sup>, Kazuyuki Tamura<sup>a</sup>, Jun Murata<sup>a</sup>, Junko Kitahara<sup>a</sup>, Akiyoshi Matsuzaki<sup>a</sup>, Motoyoshi Okumura<sup>b</sup>, Nobuo Ando<sup>b</sup>, and Yukinori Hato<sup>b</sup>

<sup>a</sup>Faculty of Engineering, Mie University; <sup>b</sup>Kanebo, LTD.

## ABSTRACT

Carbonous nano-particles basically consisting of polyperinaphthalene (PPN), one of the low dimensional conducting polymers, are prepared on substrates at various temperatures by excimer laser ablation of 3, 4, 9, 10-perylenetetracarboxylic dianhydride (PTCDA) using a 308nm(XeCl) pulsed excimer laser beam. Particles deposited on the substrates are applied to anode electrodes for ultra thin rechargeable Li ion batteries. Substrate temperature dependence of effective capacitance of lithium ions at first cycle are investigated. In addition, in-situ Raman spectroscopy of the particles under lithium ion doping and undoping is performed to elucidate the storage mechanism of lithium ion at cis-polyacetylene-type edge (phenanthrene-edge) of PPN structure. Reversible change of the spectrum in the region related C-H bending of PPN structure in lithium doping and undoping process supports a lithium insertion mechanism proposed by Zheng et al. where lithium atoms bind on the hydrogen-terminated edge of hexagonal carbon fragments.

**Keywords:** carbonous nano-particles, polyperinaphthalene, excimer laser ablation, anode electrodes, ultra thin rechargeable lithium ion batteries, in-situ Raman spectroscopy

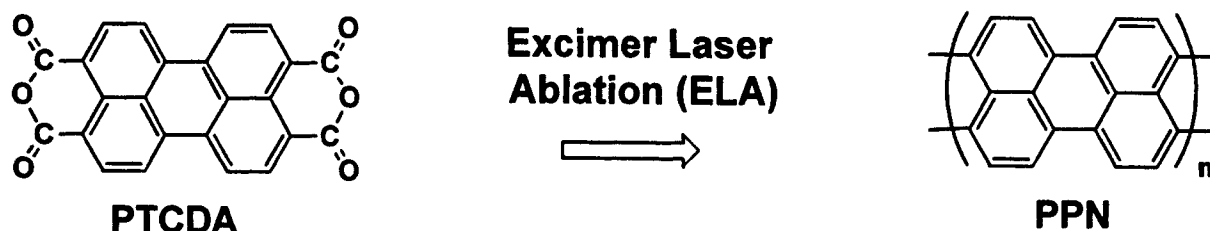
## 1. INTRODUCTION

Ultra thin lithium ion rechargeable batteries come to public notice for the purpose of application to future memory backup power supply for IC cards and microelectronic devices. So, it is desirable to develop the method to prepare thin film cathode and anode electrodes with high capacity.

Recently, a series of amorphous carbon materials with hydrogen named polycyclic aromatic hydrocarbons (PAHs) have attracted a great deal of public attention as the anode electrodes of rechargeable lithium ion batteries because of their higher capacities and potentials against the positive electrode.<sup>1,2</sup> Numerous attempts have been made to elucidate the lithium doping mechanism and enhance the lithium storage capability. Dahn et al.<sup>3</sup> pointed out that in carbons that contain substantial amounts of hydrogen, the maximum amount of lithium that could be inserted was proportional to the hydrogen content, which suggested that the lithium binds somehow in the vicinity of the H atoms. Zheng et al.<sup>4</sup> that high capacities and hysteresis were due to lithium bonded covalently with carbon atoms at the periphery with cis-polyacetylene-type structure (phenanthrene-edge). However, structural intricacy of carbonaceous materials makes it difficult to understand the lithium doping mechanism.

Along this trend, in order to clarify the lithium ion insertion mechanism and apply to anode electrode for ultra thin lithium ion rechargeable batteries, we have tried to prepare thin films of PAH, the structure of which can be specified. We have already succeeded to prepare films consisting of polyperinaphthalene (PPN) nano-particles by excimer laser ablation (ELA) of 3, 4, 9, 10-perylenetetracarboxylic dianhydride (PTCDA) with excimer laser beams under careful control of ablation conditions.<sup>5-7</sup> (See scheme I) PPN is a member of the group of polymers consisting of condensed aromatic rings, called the one-dimensional graphite family. This material is promising because of their intrinsic high conductivity and stability against oxidation. According to the theoretical studies, the electronic structure of PPN or its related compounds suggests that this material will be intrinsically conductive or semiconductive due to its small band gap and dopant-philic nature and that it is expected to form novel organic electronic devices making good use of such a characteristic band

\*nishio@chem.mie-u.ac.jp; phone +81 59 231 9424; fax +81 59 231 9471; <http://laser.chem.mie-u.ac.jp>; Faculty of Engineering, Mie University, 1515 Kamihama-cho, Tsu, Mie, Japan 514-8507; \*\*n.ando@fbr.kanebo.co.jp; phone +81 835 25 6836; fax +81 835 25 6819; Kanebo, LTD., 3-1, Kanebo-cho, Hofu, Yamaguchi, Japan 747-0823



Scheme I

structure.<sup>8,9</sup> In addition, as Wang et al. pointed out, PPN is promising as an anode electrodes of lithium ion rechargeable batteries because this material is surrounded by the phenanthrene-edge.<sup>10</sup> We demonstrated that in-situ Raman spectroscopy of PPN nano-particles under lithium doping and undoping process was quite useful to make clear the lithium ion insertion mechanism<sup>11</sup>. Furthermore a trial piece of thin lithium ion rechargeable battery with the films was fabricated to appraise performance of the films as anode thin electrodes for ultra thin rechargeable lithium ion batteries.

In this study, dependence of effective capacitance of lithium ions at first cycle on substrate temperature in deposition are investigated. Furthermore, in-situ Raman spectroscopy of the particles under lithium ion doping and undoping are performed to elucidate the storage mechanism of lithium ion at phenanthrene-edge of PPN structure.

## 2. EXPERIMENTAL

### 2.1. Film preparation by ELA and their characterization

The experimental setup is shown in Fig. 1. PTCDA was compressed into pellet to use as a target. Laser ablation of PTCDA was performed for 2-3 hours in a reaction chamber evacuated below  $10^{-3}$  Torr with a 308 nm (XeCl) pulsed beam of an excimer laser at a repetition rate of 5 Hz. Deposited films were prepared on quartz or KBr substrates located at a distance of 3-4 cm from the target. The substrate temperature ( $T_s$ ) was controlled with a heater at 200, 300, 400 and 500°C.

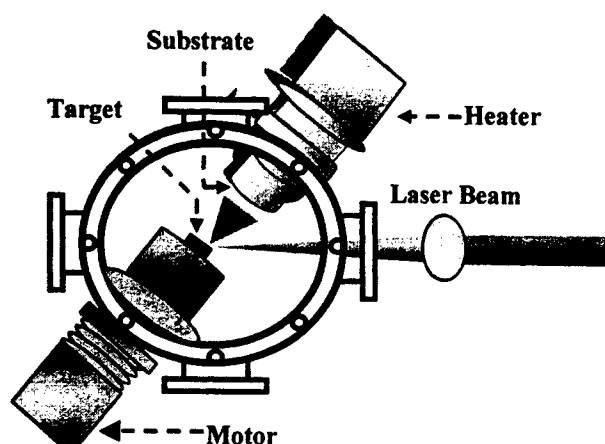


Figure 1: (a) Schematic representation of the experimental set up.

(b) The reaction chamber for preparation of PPN.

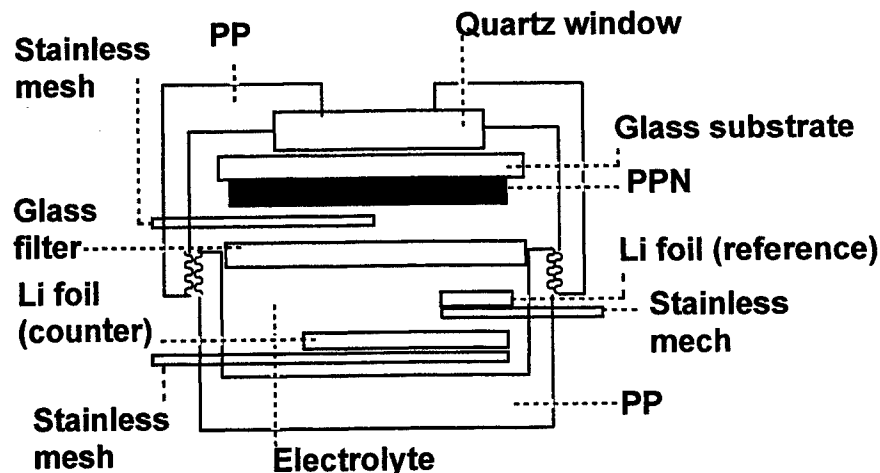


Figure 2: Schematic representation of the cell assembly for lithium ion doping.

The laser beam was focused on the PTCDA target with a quartz lens. The fluence of the laser beam was fixed at  $0.25 \text{ Jcm}^{-2}\text{pulse}^{-1}$ . The target was spun with a motor, preventing a laser beam from concentrating on a fixed spot. Structure and electric properties of the deposited nano-particles were investigated by scanning electron microscopy (SEM), FT-IR, Raman, and electric conductivity measurements.

## 2.2. Electrochemical doping of the nano-particles prepared by ELA with lithium ion

For the nano-particles deposited by ELA of PTCDA on Cu or glass substrates at  $T_s = 200, 300, 400$  and  $500^\circ\text{C}$  ( $1 \mu\text{m}$  in thickness and  $1 \text{ cm} \times 1 \text{ cm}$  in area), electrochemical doping with lithium ions was performed. Lithium metal foils were used as counter and reference electrodes.  $1\text{M LiCF}_3\text{SO}_4$  or  $\text{LiClO}_4$  in propylene carbonate (PC) was applied for electrolyte. Each electrode was separated with a glass filter. After the films were rinsed with tetrahydrofuran (THF) and dried in Ar atmosphere, the cells were fabricated in a dry box filled with Ar.

Electrochemical properties of the nano-particles were investigated by charge-discharge cycling tests. The electrochemical measurements were carried out at  $25^\circ\text{C}$ . In-situ Raman spectroscopy was performed for doping of the nano-particles with lithium ions at several doping levels in the initial charge and discharge cycle. Schematic representation of a special cell fabricated for in-situ Raman spectroscopy is shown in Fig. 2. For in-situ Raman spectroscopy, a dispersive Raman spectrometer T64000 (Jobin Yvon) was used. A beam at  $488\text{nm}$  was applied for the excitation.

## 3. RESULTS AND DISCUSSION

### 3.1. Preparation PPN nano-particles by ELA of PTCDA

In this study, nano-particles were deposited by ELA of PTCDA at a wavelength and a fluence of  $308 \text{ nm}$  and  $0.25 \text{ Jcm}^{-2}\text{pulse}^{-1}$ , respectively, as reported before<sup>5,6</sup>. As for substrate temperature,  $400$  and  $500^\circ\text{C}$  were applied as well as  $200$  and  $300^\circ\text{C}$ , in order to investigate the substrate temperature dependence of the molecular structure in higher temperature region than that we reported before.

SEM image of a deposited film prepared by ELA at  $T_s$  of  $300^\circ\text{C}$  is shown in Fig. 3. The film consists of nano-particles. FT-IR spectra for the nano-particles prepared on KBr substrates at  $T_s$  of  $200, 300, 400$  and  $500^\circ\text{C}$  are shown in Fig. 4 together with that for a PTCDA film by vacuum evaporation. In the spectrum for the PTCDA evaporated film, peaks at  $1750, 1780, 1300 \text{ cm}^{-1}$  are related to the side groups of the PTCDA monomer and a peak at  $1600 \text{ cm}^{-1}$  is related to condensed aromatic ring of perylene skeleton in the monomer. Peaks intensities related to the side groups of PTCDA decrease with increasing substrate temperature, indicating the elimination of the side groups of PTCDA monomers. Raman spectra of the nano-particles prepared on substrates at  $T_s$  of  $300, 400$  and  $500^\circ\text{C}$  by ELA are shown on Fig. 5 together with that for a PTCDA film by vacuum evaporation. In each Raman spectrum, peaks at  $1400 \text{ cm}^{-1}$  and  $1296 \text{ cm}^{-1}$  due to in-plane

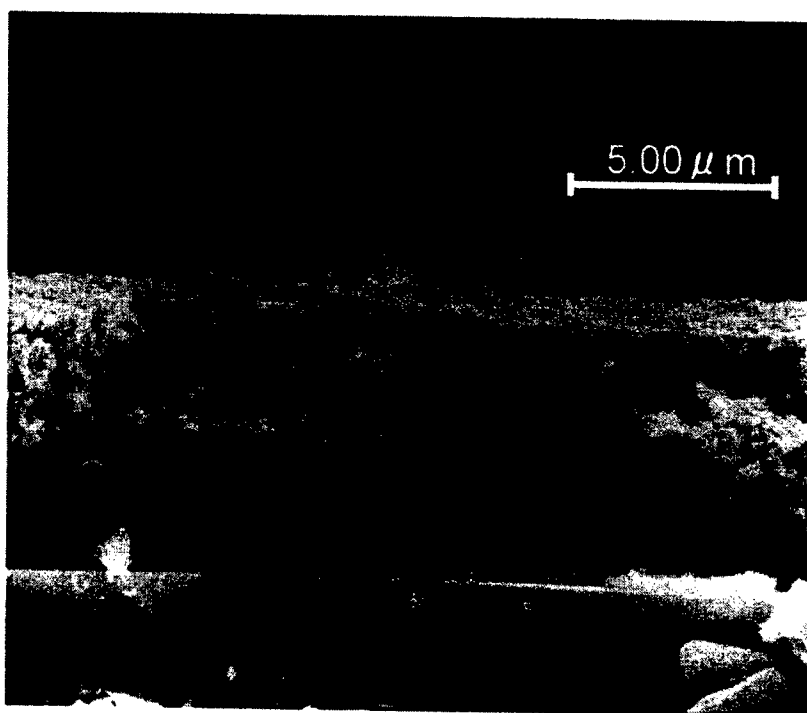


Figure 3: SEM image of a film consisting of PPN nano particle prepared by ELA of PTCDA at 300°C.

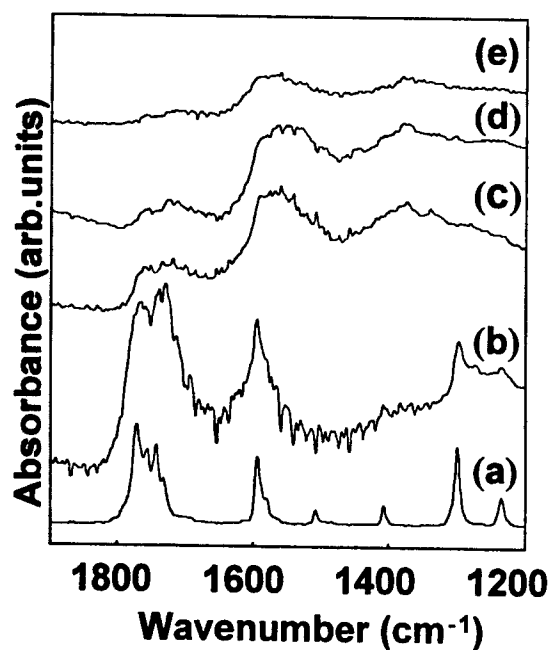


Figure 4: FT-IR spectra for the nano particles prepared KBr substrates at  $T_s$  of (b)200, (c)300, (d)400 and (e)500°C by ELA of PTCDA together with (a)that for a PTCDA film by vacuum evaporation.

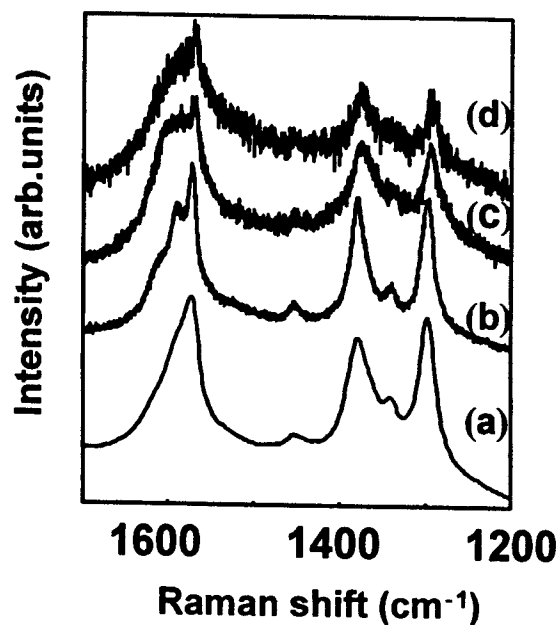


Figure 5: Raman spectra of the nano-particles prepared on substrates at  $T_s$  of (b) 300, (c)400 and (d)500°C by ELA of PTCDA together with (a)that for a PTCDA film by vacuum evaporation.



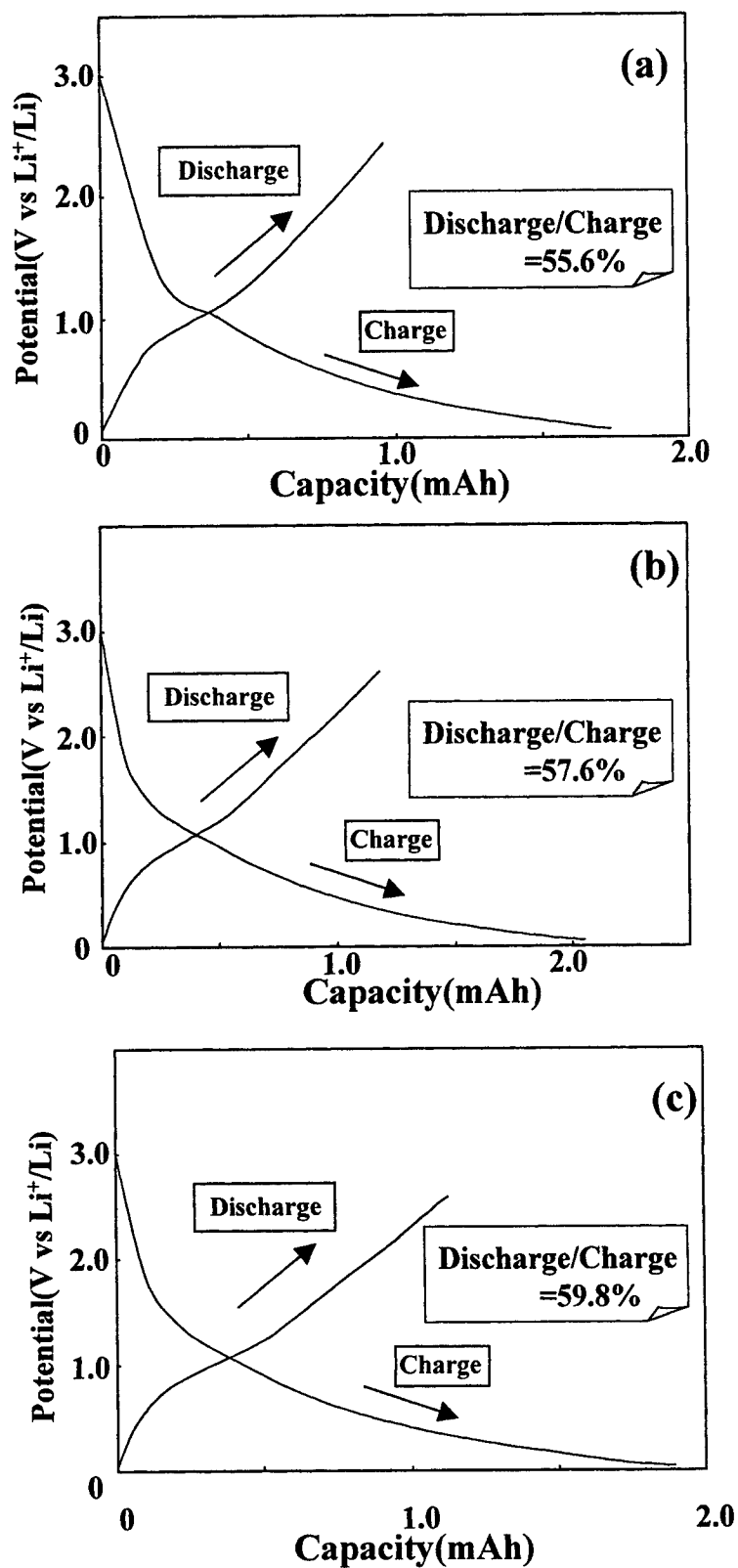


Figure 6: Charge-discharge curves at the first cycle for the PPN electrode prepared by ELA at  $T_s$  of (a)200, (b)300 and (c)400°C .

C-H bending as well as peak at  $1600\text{cm}^{-1}$  due to aromatic rings are observed, meaning that the perylene structure is basically preserved, though the former two peaks are broadened and their intensity decreased gradually. Although every film by ELA at  $T_s$  below  $200^\circ\text{C}$  possessed the electric conductivity around  $10^{-5}\text{Scm}^{-1}$  at room temperature, drastic increase in conductivity at  $T_s$  around  $200^\circ\text{C}$  could be observed. These suggest that  $\pi$ -conjugated system develops for the film at  $T_s$  above  $200^\circ\text{C}$  owing to polymerization with elimination of side groups of PTCDA, resulting in increase of electric conductivity. The conductivity came up to  $10^{-1}\text{Scm}^{-1}$  for the film prepared at  $T_s$  at more than  $300^\circ\text{C}$ .

These results together with that from FT-IR measurement as described above, convince us of partial formation of PPN structure in the film prepared at  $T_s$  of 300 and  $400^\circ\text{C}$ . Actually, the Raman spectrum for this film was nearly similar to that for PPN prepared with vapor polymerization method by Murakami et al.<sup>12</sup> Considering from these results, although structural defects such as carbon radicals were detected to some extent, it is safely be said that this film basically consists of polyperinaphthalene (PPN) structure. Nano-particles prepared at  $500^\circ\text{C}$  may partially possess PPN structure, but component of amorphous carbon may be included because of elimination of hydrogen atoms binding at phenanthrene-edge of PPN.

### 3.2. Electrochemical doping of lithium ion into PPN nano particles

#### 3.2.1. Substrate temperature dependence of charge-discharge profile at first cycle

In order to clarify substrate temperature dependence of doping/undoping behavior of lithium ion at the first cycle, charge (lithium doping)-discharge (lithium undoping) profile was investigated for the nano-particles prepared at different substrate temperature. Figure 6 shows charge-discharge curves at the first cycle for the PPN electrode prepared by ELA at  $T_s$  of 200, 300 and  $400^\circ\text{C}$ . The whole profile is not so different between them. Efficiencies defined by charge (doping) amount/discharge (undoping) amount for the electrode prepared at 200, 300 and  $400^\circ\text{C}$  are 55.6, 57.6 and 59.8%, respectively, increasing gradually with substrate temperature.

#### 3.2.2. In-situ Raman spectroscopy of doping of PPN nano particles with lithium ion

In-situ Raman spectroscopy of doping and undoping with lithium ion was performed for the PPN nano particles. Figure 7 shows the spectra for the nano particles at various levels in doping and undoping processes, respectively. As the doping level increases, it is observed that the peaks at  $1360\text{cm}^{-1}$  characteristic to amorphous carbon and  $1296\text{cm}^{-1}$  assigned to C-H in-plane bending mode gradually decrease their intensities as well as broadening of the peak at  $1600\text{cm}^{-1}$ . The intensities of the two peaks at 1360 and  $1296\text{cm}^{-1}$  are increased again when lithium ions are undoped. These results suggest that lithium ions interact reversibly not only with condensed aromatic rings of perylene skeleton but also with carbon atoms at phenanthrene-edge, supporting a lithium insertion mechanism proposed by Zheng et al.<sup>4</sup> where lithium atoms bind on the hydrogen-terminated edged of hexagonal carbon fragments.

## 4. CONCLUSION

Carbonous nano-particles basically consisting of polyperinaphthalene (PPN), one of the low dimensional conducting polymers, were prepared on substrates at various temperatures by excimer laser ablation of 3, 4, 9, 10-perylenetetracarboxylic dianhydride (PTCDA) using a 308nm(XeCl) pulsed excimer laser beam. Particles deposited on the substrates were applied for anode electrodes for ultra thin rechargeable Li ion batteries. Substrate temperature dependence of effective capacitance of lithium ions at first cycle was also investigated. Efficiencies defined by charge(doping) amount/discharge(undoping) amount for the electrode prepared at 200, 300 and  $400^\circ\text{C}$  were 55.6, 57.6 and 59.8%, respectively, increasing gradually with substrate temperature. In-situ Raman spectroscopy of the particles under lithium ion doping and undoping were performed to elucidate the storage mechanism of lithium ion at cis-polyacetylene-type edge (phenanthrene-edge) of PPN structure. Reversible spectra change of the region related C-H bending of PPN structure in lithium doping and undoping process supports a lithium insertion mechanism proposed by Zheng et al. where lithium atoms bind on the hydrogen-terminated edged of hexagonal carbon fragments.

## ACKNOWLEDGEMENTS

This work is supported by a Grant Program of Research Foundation for the Electrotechnology of Chubu.

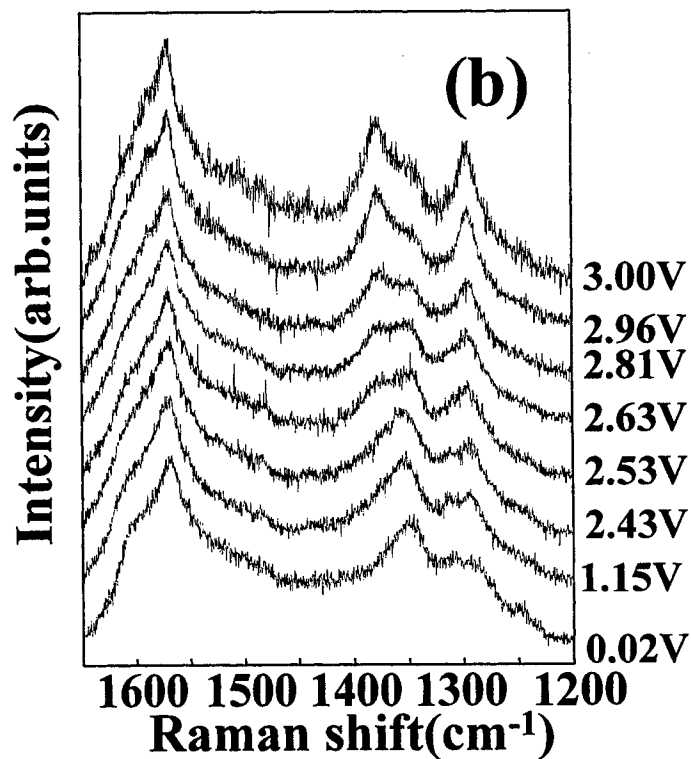
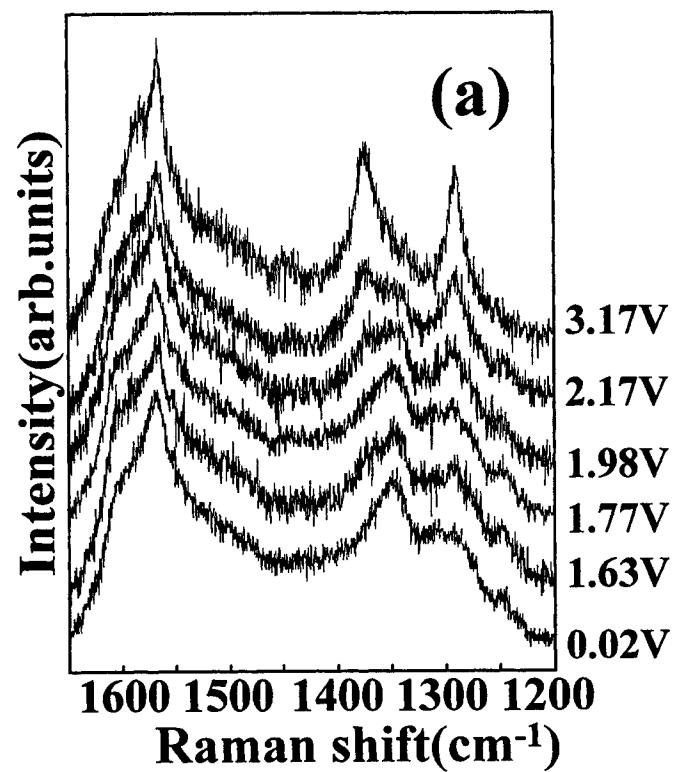


Figure 7: In-situ Raman spectra for the PPN electrode at various doping levels. (a) Lithium doping and (b) undoping.

## REFERENCES

1. P. Novak, K. Muller, K. S. V. Santhanam, and O. Hass, "Electrochemically Active Polymers for Rechargeable Batteries," *Chem. Rev.*, 97, pp. 207-281, 1997.
2. M. Wakihara, and O. Yamamoto (Eds.), *Lithium Ion Batteries-Fundamentals and Performance*, Kodansha, Tokyo, 1998.
3. J. R. Dahn, T. Zheng, Y. Liu, and J. S. Xue, "Mechanism for Lithium Insertion in Carbonaceous Materials," *Science*, 270, pp. 590-593, 1995.
4. T. Zheng, W. R. McKinnon, and J. R. Dahn, "Hysteresis during Lithium Insertion in Hydrogen-Containing Carbons," *J. Electrochem. Soc.*, 143, pp. 2137-2145, 1996.
5. S. Nishio, R. Mase, T. Oba, A. Matsuzaki, and H. Sato, "Preparation of Amorphous Organic Semiconductor Thin Films with Polyperinaphthalene Structure on Temperature-Controlled Substrates by Excimer Laser Ablation of 3,4,9,10-Perylenetetracarboxylic Dianhydride," *Appl. Surf. Sci.*, 127-129, pp. 589-594, 1998.
6. S. Nishio, H. Sato, and T. Yamabe, "Control of Structure and Electric Properties of Amorphous Organic Semiconductive Thin Films Prepared by Excimer Laser Ablation," *Appl. Phys.*, A69, pp. S711-S714, 1999.
7. S. Nishio, S. Kuriki, Y. Tsujine, A. Matsuzaki, H. Sato, N. Ando, Y. Hato, and K. Tanaka, "Characterization of polyperinaphthalenic organic semiconductor thin films prepared by excimer laser ablation and application to anode electrodes for ultra thin rechargeable Li ion batteries," *Proc. SPIE*, 3933, pp. 487-495, 2000.
8. J. L. Bredas, and R. H. Baughman, "Theoretical study of the electronic properties and crystal structure of poly(perinaphthalene): On the origin of high observed conductivities," *J. Chem. Phys.*, 83, pp. 1316-1322, 1985.
9. K. Tanaka, S. Yamanaka, K. Ueda, S. Takeda, and T. Yamabe, "Design of Polymers with Metallic Properties: Substituted Polyperylene and poly(p-phenylene)," *Synth. Met.*, 20, pp. 333-345, 1987.
10. S. Wang, S. Yata, J. Nagano, Y. Okano, H. Kinoshita, H. Kikuta, and T. Yamabe, "A New Carbonaceous Material with Large Capacity and High Efficiency for Rechargeable Li-Ion Batteries," *J. Electrochem. Soc.*, 147, pp. 2498-2502, 2000.
11. S. Nishio, K. Tamura, Y. Tsujine, T. Fukao, J. Murata, M. Nakano, A. Matsuzaki, H. Sato, N. Ando, and Y. Hato, "Characterization of polyperinaphthalenic organic semiconductor thin films prepared by excimer laser ablation and application to anode electrodes for ultra thin rechargeable Li ion batteries", *Proc. SPIE*, 4274, pp266-277.
12. M. Murakami, S. Iijima, and S. Yoshimura, "Morphology and structure of a one-dimensional graphite polymer, Poly-peri-naphthalene," *J. Appl. Phys.*, 60, pp. 3856-3863, 1986.

# Background gas effects on structural properties in thin films deposited by pulsed laser deposition

Yuka Yamada, Nobuyasu Suzuki, Toshiharu Makino, Takehito Yoshida  
Advanced Technology Research Laboratories, Matsushita Electric Industrial Co., Ltd.  
3-10-1 Higashimita, Tama-ku, Kawasaki 214-8501, Japan

## ABSTRACT

Pulsed laser deposition (PLD) in background gases is a promising method of preparing multicomponent functional thin films, because interactions between the ablated species and the background gases promote not only physical collisions but also chemical reactions, and affect the characteristics of the deposited films. The properties of indium oxide ( $\text{In}_2\text{O}_3$ ) thin films prepared by PLD in background gases were characterized in relation to the background gas pressures. Transparent crystalline  $\text{In}_2\text{O}_3$  thin films could be obtained at background gas pressures above 1.0 Torr on unheated glass substrates. This result can be accounted for by the background gas effects. The stoichiometric  $\text{In}_2\text{O}_3$  nuclei should be formed in the nonequilibrium high-pressure and high-temperature region generated by the shock front excited by the pulsed laser. Microstructures of the deposited thin films were also investigated using a cross-sectional transmission electron microscope. Initially, amorphous-like layers with a thickness of about 50 nm were formed on the substrates. Subsequently, strongly textured crystalline columns grew on the amorphous-like layers. We discuss the mechanism of thin film growth in PLD.

**Keywords:** pulsed laser deposition, background gas, indium oxide, shock front, thin film growth, stoichiometry, columnar structure, surface migration

## 1. INTRODUCTION

Functional multicomponent oxides are widely used in optical and electronic device applications. Transparent conducting oxide films are favorable for electrodes of devices such as flat panel displays, solar cells, and heat mirrors.<sup>1,2</sup> Ferroelectric films are of great interest in the fields of nonvolatile random access memory, surface-acoustic wave devices, and optical modulators.<sup>3</sup> Multicomponent oxide functional films have been deposited by various methods, including chemical vapor deposition, physical vapor deposition and the sol-gel method.<sup>1-3</sup> Vapor-phase thin film deposition is suitable for microelectronic device applications. However, oxygen gas introduction<sup>4-7</sup> and substrate heating<sup>6,8</sup> or post-annealing<sup>9,10</sup> are required for oxygen compensation or crystallization. These constraints make wider applications difficult, since they limit the choice of substrate materials. In particular, there is high demand for transparent conducting oxide films formed on organic or compound semiconductor substrates, which are generally incompatible with a high-temperature oxide deposition process.

Pulsed laser deposition (PLD) has emerged as one of the simplest and most versatile methods for the deposition of thin films of a wide variety of materials.<sup>11,12</sup> A major advantage of PLD is that the plume generated by laser ablation of the target can contain almost the same constituents as the target even though the melting points of constituent materials differ greatly. In particular, reactive PLD in oxidizing gases is one of the promising methods of preparing multicomponent oxide functional films,<sup>11-13</sup> and has been applied to the deposition of transparent conducting oxide films.<sup>14-16</sup> On the other hand, PLD in pure inert background gas is effective for nanocrystallite formation when utilizing the physical collision of ablated species with atoms of the inert background gas.<sup>17-19</sup> When we apply this method to multicomponent oxide film formation, interactions between ablated species and background gases result in not only physical collisions but also chemical reaction control.<sup>20</sup> Therefore, the interactions affect the properties of the deposited films.

In this investigation, we study the influence of the background gases on the properties of the deposited film. We adopt PLD in background gases for the deposition of indium oxide ( $\text{In}_2\text{O}_3$ ) thin films without substrate heating. The optical, electrical and structural properties of the deposited films are characterized in relation to the background gas

pressures. Consequently, transparent crystalline  $\text{In}_2\text{O}_3$  thin films are obtained on unheated glass substrates. Furthermore, we discuss the mechanism of thin film growth in PLD.

## 2. EXPERIMENTAL PROCEDURE

Indium oxide thin films were prepared by pulsed laser ablation of a sintered  $\text{In}_2\text{O}_3$  target in background gases at a constant pressure. A schematic diagram of the PLD apparatus used in this study is shown in Fig. 1. The targets were formed by sintering pure (4N)  $\text{In}_2\text{O}_3$  powders into 2-inch-diameter disks. After the vacuum chamber was evacuated to a base pressure of  $1.0 \times 10^{-8}$  Torr, a pure (6N) helium (He) gas or a  $\text{He}/\text{O}_2$  (1 %) gas mixture was introduced into the chamber and maintained at a constant pressure using a differential evacuation system. The background gas pressure was varied from 0.25 Torr to 5.0 Torr, as the dominant experimental parameter. An argon-fluoride (ArF) excimer laser beam (wavelength: 193 nm, energy density:  $1.0 \text{ J}/(\text{cm}^2 \cdot \text{pulse})$ , pulse duration: 12 ns, repetition rate: 10 Hz) was focused onto a  $3 \times 1 \text{ mm}^2$  rectangular spot at the surface of the target. Then, a plume of ejected species was created, which extended almost perpendicular to the target surface. The target was rotated at 8 rpm. Silicon (Si) or fused silica ( $\text{SiO}_2$ ) substrates without heating were positioned at a distance of 30 mm normal to the target.

The deposited film thickness was measured using a stylus profilometer. Optical transmission spectra of the films were measured in the wavelength range of 200–2500 nm. The spectra were normalized by the transmission of the substrate. The electrical resistivity of the films was determined by a standard four-point probe method. Crystal structures of the films were characterized by X-ray ( $\text{CuK}\alpha$  line) diffraction and selected-area electron diffraction. The film textures were observed using a scanning electron microscope (SEM) and a high-resolution transmission electron microscope (HRTEM).

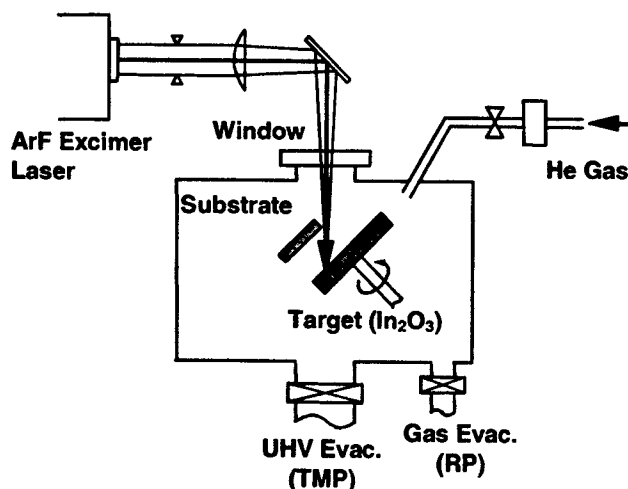


Fig. 1. Schematic diagram of preparation system of  $\text{In}_2\text{O}_3$  thin films using pulsed laser ablation in background gases.

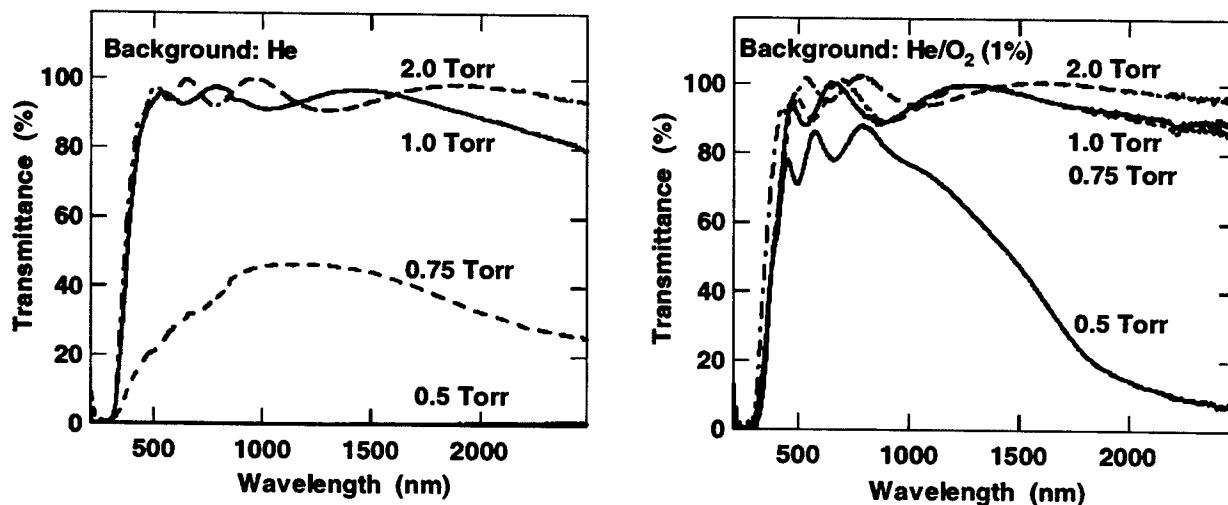


Fig. 2. Optical transmission spectra for films deposited at different He and  $\text{He}/\text{O}_2$  (1 %) gas pressures. The transmittance increases with increasing background gas pressure.

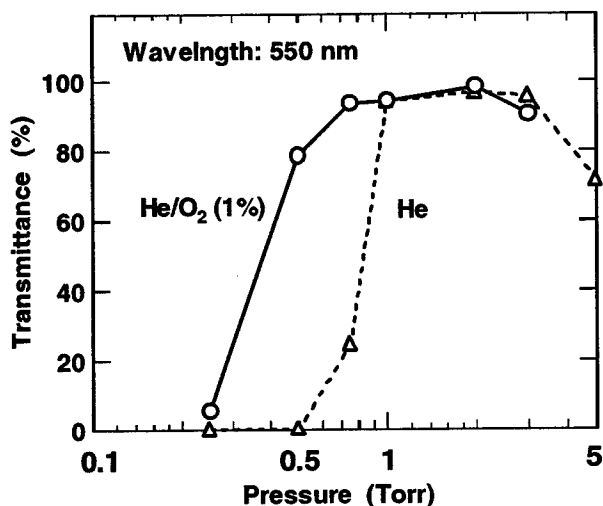


Fig. 3. Transmittance at a wavelength of 550 nm as a function of background gas pressure, in the case of pure He gas (○) and He/O<sub>2</sub> (1 %) gas mixture (△). In pure He gas, the transmittance abruptly increases, while the increase is relatively gradual in the He/O<sub>2</sub> gas mixture.

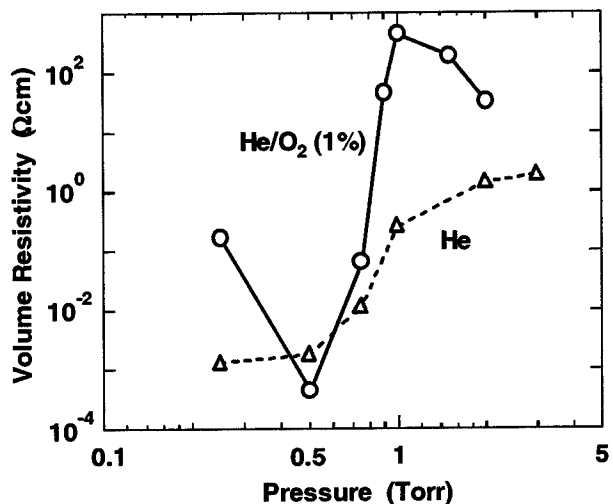


Fig. 4. Volume resistivity as a function of background gas pressure, in the case of pure He gas (○) and He/O<sub>2</sub> (1 %) gas mixture (△). In the He/O<sub>2</sub> gas mixture, the resistivity can be controlled in a wide range of  $5 \times 10^{-4} - 5 \times 10^2 \Omega\text{cm}$ , with visible transmittance of more than 80 %.

### 3. EXPERIMENTAL RESULTS

#### 3.1. Optical and electrical properties

Figure 2 shows the optical transmission spectra for the films deposited at different He and He/O<sub>2</sub> gas pressures. Film thicknesses were around 300 nm. The transmittance increases with increasing background gas pressure.

The visible transmittances at a wavelength of 550 nm are shown in Fig. 3 as a function of background gas pressure. Open circles and triangles represent the results for the films deposited in pure He gas and a He/O<sub>2</sub> gas mixture, respectively. In pure He gas, the transmittance abruptly increases in the pressure range of 0.5 to 1.0 Torr. On the other hand, in the He/O<sub>2</sub> gas mixture, the increase in transmission is relatively gradual between 0.25 and 1.0 Torr. The transmittance of about 80 % can be obtained at 0.5 Torr in the He/O<sub>2</sub> gas mixture but only above 1.0 Torr in pure He gas.

The volume resistivities of the deposited films are shown in Fig. 4 as a function of background gas pressure. Open circles and triangles represent the results for the films deposited in pure He gas and a He/O<sub>2</sub> gas mixture, respectively. In pure He gas, the films deposited below 0.5 Torr show the volume resistivity of an order of  $10^{-3} \Omega\text{cm}$ , and the resistivity increases monotonically with increasing He pressure. On the other hand, in the He/O<sub>2</sub> gas mixture, the films deposited at 0.5 Torr have the lowest resistivity of  $5 \times 10^{-4} \Omega\text{cm}$ . It has been reported that an optimal gas pressure for obtaining low resistivity exists in thin film formation in an atmosphere of oxygen gas.<sup>4,21</sup> Furthermore, the resistivity can be controlled in a wide range of  $5 \times 10^{-4} - 5 \times 10^2 \Omega\text{cm}$  by varying the background gas pressures, with visible transmittance of more than 80 %.

#### 3.2. Structural properties

Figure 5 shows the X-ray diffraction spectra of the films deposited at different He gas pressures. The films deposited at He pressures below 0.5 Torr show only one broad peak at around  $33^\circ$ . The maximum position corresponds to the (101) plane spacing of metallic indium, although the broadness is presumably caused by amorphous-like or coalesced microcrystalline structures. On the other hand, the films deposited at He pressures of 1.0 and 2.0 Torr show sharp peaks at  $31^\circ$ ,  $35^\circ$ ,  $38^\circ$  and  $51^\circ$ , which correspond to the cubic bixbyite structure of In<sub>2</sub>O<sub>3</sub> crystals with (222), (400), (411), and (440) orientations, respectively. In particular, strong preferred orientation is observed in the (400) plane, even though it

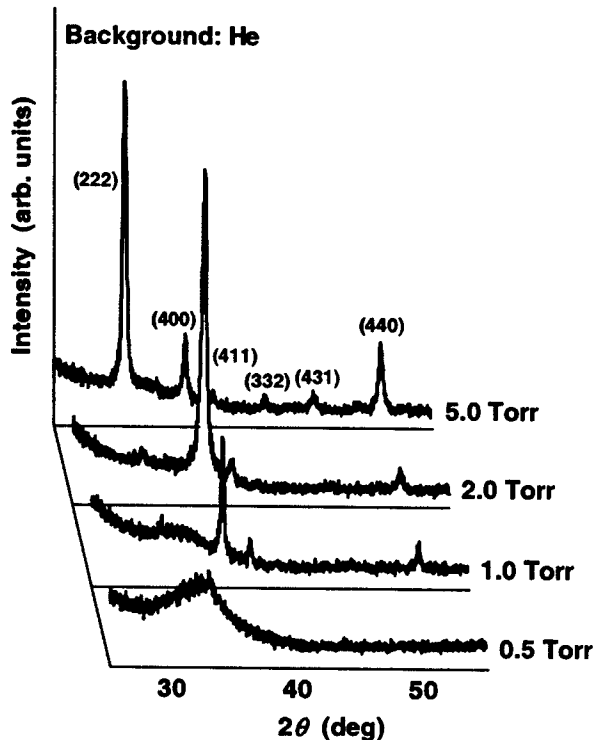


Fig. 5. X-ray diffraction spectra of films deposited at different He gas pressures. Films deposited below 0.5 Torr show only one broad peak corresponding to metallic indium. Films deposited above 1.0 Torr show sharp peaks corresponding to a cubic bixbyite structure of  $\text{In}_2\text{O}_3$  crystals. At 1.0 and 2.0 Torr, strong preferred orientation is observed in the (400) plane, even though the film was deposited on fused silica substrates without heating.

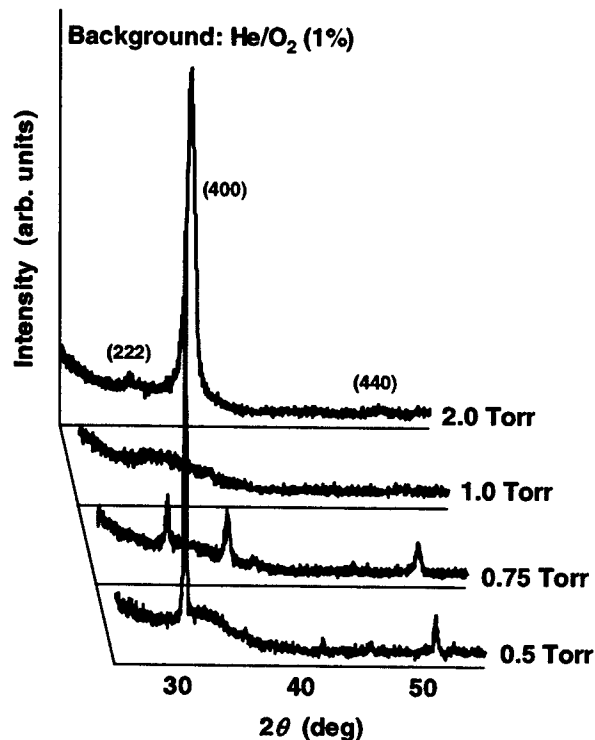


Fig. 6. X-ray diffraction spectra of films deposited at different  $\text{He}/\text{O}_2$  (1 %) gas pressures. Films deposited at 0.5 Torr show a sharp peak corresponding to the cubic bixbyite structure of  $\text{In}_2\text{O}_3$  crystals with (222) orientation. Films deposited at 2.0 Torr show strong preferred orientation in the (400) plane. This result indicates that the orientations of the deposited films depend strongly on the background gas pressures.

was deposited on  $\text{SiO}_2$  substrates without heating. Furthermore, the film deposited at a He pressure of 5.0 Torr shows six sharp peaks, the intensity ratios of which are the same as those of standard powders. This indicates that the films have random orientation.

From Rutherford backscattering spectroscopy (RBS) measurements, the In/O atomic concentration ratios of the deposited films were evaluated.<sup>20</sup> It was clarified that stoichiometric  $\text{In}_2\text{O}_3$  films were obtained at 2.0 Torr; in contrast, oxygen-deficient films were deposited below 0.5 Torr.

Surface morphology of the deposited films was observed by SEM.<sup>20</sup> The films deposited at He pressures below 0.5 Torr consist of fine particles of less than 20 nm, and some larger particles. In the films deposited at He pressures of 1.0 and 2.0 Torr, ordered structures of the 100 nm order were observed. Furthermore, the film deposited at a He pressure of 5.0 Torr consists of aggregated crystallites.

Figure 6 shows the X-ray diffraction spectra of the films deposited at different  $\text{He}/\text{O}_2$  (1 %) gas pressures. The films deposited at a gas pressure of 0.5 Torr show a sharp peak at  $31^\circ$ , which corresponds to the cubic bixbyite structure of  $\text{In}_2\text{O}_3$  crystals with (222) orientation. On the other hand, the films deposited at a gas pressure of 2.0 Torr show strong preferred orientation in the (400) plane. This result indicates that the orientations of the deposited films depend strongly on the background gas pressures.

Figure 7 shows cross-sectional SEM images of the films deposited at  $\text{He}/\text{O}_2$  gas pressures of (a) 2.0 Torr, (b) 1.0 Torr and (c) 0.5 Torr. In Fig. 7(a), we observe a crystalline layer with prominent columnar texture in the thickness direction. The textures of the deposited films weaken with decreasing background gas pressures. This result corresponds to the difference in the crystal structures of the deposited films, as shown in Fig. 6.



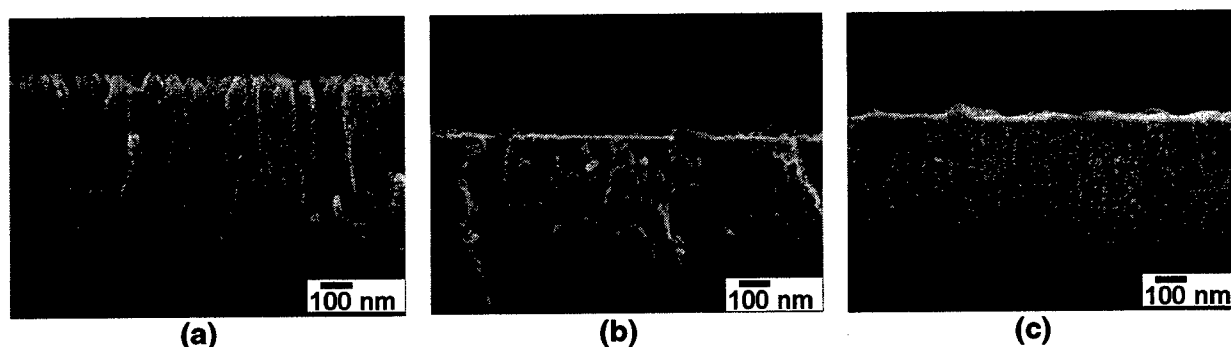


Fig. 7. Cross-sectional SEM images of the films deposited at background He/O<sub>2</sub> gas pressures of (a) 2.0 Torr, (b) 1.0 Torr, and (c) 0.5 Torr. In (a), we observe a crystalline layer with prominent columnar texture. The texture of the deposited films weakens with decreasing background gas pressure.

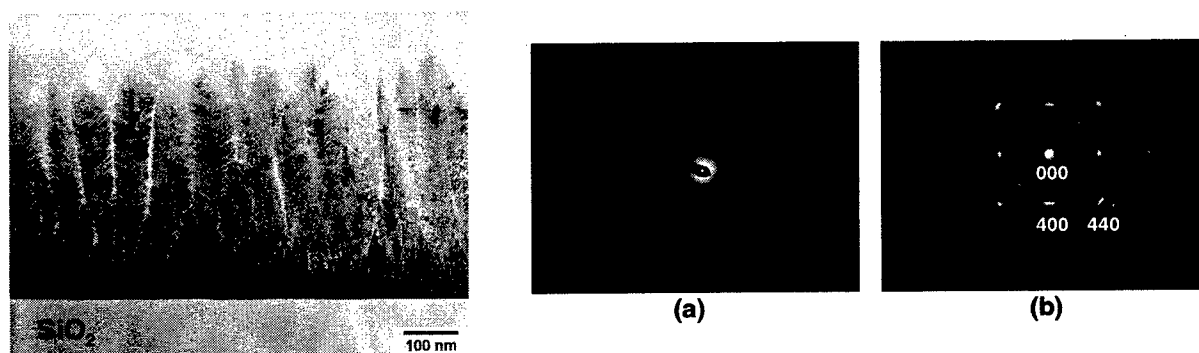


Fig. 8. Cross-sectional HRTEM image of the films deposited at background He/O<sub>2</sub> gas pressure of 2.0 Torr. Crystallinity of the film was transformed to strongly textured columns on the 50 nm low-contrast layer.

Fig. 9. Electron diffraction patterns of (a) low-contrast layer and (b) strongly columnar layer in Fig. 8. The low-contrast layer has an amorphous-like structure which shows a halo pattern. The strongly columnar layer shows strong preferred orientation in the (400) plane.

Figure 8 shows a bright-field cross-sectional HRTEM image of the film deposited at a He/O<sub>2</sub> gas pressure of 2.0 Torr. Initially, a low-contrast layer with a thickness of about 50 nm was deposited on the SiO<sub>2</sub> substrate. Subsequently, a crystalline layer with strong columnar texture was formed on the low-contrast layer.

The crystal structure of each layer was characterized by selected-area electron diffraction. Figures 9(a) and 9(b) show the electron diffraction patterns of the bottom low-contrast layer and the upper crystalline layer, respectively. The bottom layer is an amorphous-like structure which exhibits a halo pattern. The upper layer shows strong preferred orientation in the (400) plane.

## 4. DISCUSSION

### 4.1. Dependence of film properties on background gas pressure

It is known that the properties of In<sub>2</sub>O<sub>3</sub> films depend on the oxygen content.<sup>4</sup> Oxygen deficiency leads to darkening of the films due to suboxide formation<sup>4,22</sup> or precipitation of In metal.<sup>7</sup> Although PLD is promising for use in the deposition of complex materials with congruent transfer of the target composition,<sup>11,12</sup> oxygen, which has high vapor pressure, easily outdiffuses in vacuum.<sup>13</sup> This also occurs at low He gas pressures below 1.0 Torr in this study. When

the  $\text{In}_2\text{O}_3$  thin films were deposited in the  $\text{He}/\text{O}_2$  gas mixture, transparent films were obtained in the lower pressure region. This is because the oxygen deficiency is compensated by  $\text{O}_2$  in the background gas.

In the case of high background gas pressure, stoichiometric crystalline  $\text{In}_2\text{O}_3$  films are obtained, even without oxygen addition. This result can be attributed to the background gas pressure effects.<sup>20</sup> Atoms and ions ejected from the target initially travel with inherent velocities. At high background gas pressure, these velocities tend to equilibrate due to the large number of collisions with the ambient gas atoms.<sup>23</sup> This results in the spatial confinement of the ablated species, which leads to the suppression of the outdiffusion of oxygen. This effect is essential, particularly for PLD in pure He gas, because oxygen from the target itself dominates the oxygen content of the deposited films.

Furthermore, in pulsed laser ablation into a higher pressure background gas, a shock front is generated as a result of collisions between the ablated species and the ambient gas.<sup>24</sup> In general, the shock wave compresses the background gas, thereby increasing its pressure and temperature. The increase in pressure promotes  $\text{In}_2\text{O}_3$  formation because it brings about reductions in volume and mole number. The increase in temperature can thermally enhance reactions between the ablated species. However, too high a temperature retards  $\text{In}_2\text{O}_3$  formation, because the free energy of  $\text{In}_2\text{O}_3$  formation increases with increasing temperature.<sup>25</sup> During the propagation of the shock front, both pressure and temperature decrease with increasing distance from the target surface.<sup>24</sup> Also, the free energy of formation decreases with decreasing temperature. Consequently, stoichiometric  $\text{In}_2\text{O}_3$  films can be formed through "the facilitated oxidation region" in the vapor phase, where both high pressure and a sufficiently low value of the free energy of formation are realized.

#### 4.2. Mechanism of crystal growth in PLD

It is well known that  $\text{In}_2\text{O}_3$  films deposited on unheated glass substrates tend to be amorphous.<sup>7,16</sup> In contrast, crystalline  $\text{In}_2\text{O}_3$  films are obtained on unheated  $\text{SiO}_2$  substrates in this study. With respect to orientation,  $\text{In}_2\text{O}_3$  films deposited at background gas pressures above 1.0 Torr show strong preferred orientation. Next, we will discuss the influence of the shock wave on crystal growth in PLD.

In the films formed by sputtering at a substrate temperature of  $400^\circ\text{C}$ , a  $\langle 100 \rangle$  preferred orientation and a columnar texture have also been observed.<sup>9,26</sup> The microstructure of the sputter-deposited films is consistent with the zone model<sup>27</sup> in which the microstructure of sputter-deposited metal thin films is a function of the substrate temperature. The sputter process conditions with the substrate temperature of  $400^\circ\text{C}$  correspond to the zone where surface and self-diffusion become active and the structure of films consists of columnar grains. Furthermore, Shigesato and Paine proposed a model for describing the columnar structure as a result of energetic ion (several tens of eV) bombardment of the growth surface and consequent perturbation of the atom attachment template.<sup>26</sup>

However, in this study, the substrates are unheated, and the kinetic energies of the ablated species should be low compared with the energetic ions in sputtering, after collision with the background gases.<sup>23,28</sup> Thus, in PLD in background gases, the columnar texture should be obtained as a result of surface excitation by the shock wave as follows.

As mentioned in the above section, in the case of PLD in a higher pressure background gas,  $\text{In}_2\text{O}_3$  nuclei are formed in "the facilitated oxidation region" in the vapor phase. Initially, the  $\text{In}_2\text{O}_3$  nuclei formed in the vapor phase are randomly deposited on the  $\text{SiO}_2$  substrate as a thin amorphous-like buffer layer with a thickness of about 50 nm. Subsequently, strongly textured crystalline columns should be formed due to the enhancement of surface migration by the excitation of the substrate surface by the shock front. Consequently, the film is selectively grown in the  $\langle 100 \rangle$  direction and the prominent columnar structure shown in Fig. 8 is obtained. Furthermore, since the effect of surface excitation by the shock front depends on the background gas pressure, the texture of the deposited films should depend on the gas pressure, as shown in Fig. 7.

### 5. CONCLUSIONS

Stoichiometric crystalline  $\text{In}_2\text{O}_3$  thin films with visible transmittances of more than 80 % were prepared by PLD in background gases on unheated  $\text{SiO}_2$  substrates. This result can be accounted for by the background gas effects. Stoichiometric  $\text{In}_2\text{O}_3$  nuclei should be formed in the nonequilibrium high-pressure and high-temperature region generated by the shock front excited by the pulsed laser. Furthermore, the mechanism of thin film growth in PLD was analyzed. Initially, the  $\text{In}_2\text{O}_3$  nuclei formed in the vapor phase are randomly deposited on the substrates in the form of a thin amorphous-like buffer layer. Subsequently, strongly textured crystalline columns grow due to the enhancement of surface migration by the excitation of the substrate surface by the shock front. This technique offers great promise for

future applications which require the deposition of multicomponent oxide functional films on substrates thermally unstable and/or sensitive to an oxidizing ambient.

## ACKNOWLEDGMENTS

This work was conducted with the program "Advanced Photon Processing and Measurement Technologies" of the Agency of Industrial Science and Technology, the Ministry of Economy, Trade and Industry, consigned to the R&D Institute for Photonics Engineering (RIPE) from the New Energy and Industrial Technology Development Organization (NEDO).

## REFERENCES

1. J. L. Vossen, "Transparent conducting films", *Phys. Thin Films* **9**, pp. 1-71, 1977.
2. K. L. Chopra, S. Major, and D. K. Pandya, "Transparent conductors – a status review", *Thin Solid Films* **102**, pp. 1-46, 1983.
3. C. Paz de Araujo, J. F. Scott, and G. W. Taylor, Eds., *Ferroelectric Thin Films: Synthesis and Basic Properties*, Gordon and Breach Publishers, Amsterdam, 1996.
4. J. C. C. Fan, F. J. Bachner, and G. H. Foley, "Effect of O<sub>2</sub> pressure during deposition on properties of rf-sputtered Sn-doped In<sub>2</sub>O<sub>3</sub> films", *Appl. Phys. Lett.* **31**, pp. 773-775, 1977.
5. M. Buchanan, J. B. Webb, and D. F. Williams, "Preparation of conducting and transparent thin films of tin-doped indium oxide by magnetron sputtering", *Appl. Phys. Lett.* **37**, pp. 213-215, 1980.
6. M. Mizuhashi, "Electrical properties of vacuum-deposited indium oxide and indium tin oxide films", *Thin Solid Films* **70**, pp. 91-100, 1980.
7. W. Qin, R. P. Howson, M. Akizuki, J. Matsuo, G. Takaoka, and I. Yamada, "Indium oxide film formation by O<sub>2</sub> cluster ion-assisted deposition", *Mater. Chem. Phys.* **54**, pp. 258-261, 1998.
8. J. C. C. Fan and F. J. Bachner, "Properties of Sn-doped In<sub>2</sub>O<sub>3</sub> films prepared by RF sputtering", *J. Electrochem. Soc.* **122**, pp. 1719-1724, 1975.
9. K. Itoyama, "Properties of Sn-doped indium oxide prepared by high rate and low temperature RF sputtering", *Jpn. J. Appl. Phys.* **17**, pp. 1191-1196, 1978.
10. M. Mizuhashi, "Electrical properties of post-oxidized In<sub>2</sub>O<sub>3</sub>:Sn films", *Thin Solid Films* **76**, pp. 97-105, 1981.
11. D. B. Chrisey and G. K. Hubler, Eds., *Pulsed Laser Deposition of Thin Films*, John Wiley & Sons, New York, 1994.
12. D. H. Lowndes, D. B. Geohegan, A. A. Puretzky, D. P. Norton, and C. M. Rouleau, "Synthesis of novel thin-film materials by pulsed laser deposition", *Science* **273**, pp. 898-903, 1996.
13. A. Gupta, "Gas-phase oxidation chemistry during pulsed laser deposition of YBa<sub>2</sub>Cu<sub>3</sub>O<sub>7-δ</sub> films", *J. Appl. Phys.* **73**, pp. 7877-7886, 1993.
14. C. M. Dai, C. S. Su, and D. S. Chuu, "Growth of highly oriented tin oxide thin films by laser evaporation deposition", *Appl. Phys. Lett.* **57**, pp. 1879-1881, 1990.
15. E. J. Tarsa, J. H. English, and J. S. Speck, "Pulsed laser deposition of oriented In<sub>2</sub>O<sub>3</sub> on (001) InAs, MgO, and yttria-stabilized zirconia", *Appl. Phys. Lett.* **62**, pp. 2332-2334, 1993.
16. J. P. Zheng and H. S. Kwok, "Preparation of indium tin oxide films at room temperature by pulsed laser deposition", *Thin Solid Films* **232**, pp. 99-104, 1993.
17. T. Yoshida, S. Takeyama, Y. Yamada, and K. Mutoh, "Nanometer-sized silicon crystallites prepared by excimer laser ablation in constant pressure inert gas", *Appl. Phys. Lett.* **68**, pp. 1772-1774, 1996.
18. D. B. Geohegan, A. A. Puretzky, G. Duscher, and S. J. Pennycook, "Time-resolved imaging of gas phase nanoparticle synthesis by laser ablation", *Appl. Phys. Lett.* **72**, pp. 2987-2989, 1998.
19. N. Suzuki, T. Makino, Y. Yamada, T. Yoshida, and S. Onari, "Structures and optical properties of silicon nanocrystallites prepared by pulsed-laser ablation in inert background gas", *Appl. Phys. Lett.* **76**, pp. 1389-1391, 2000.
20. Y. Yamada, N. Suzuki, T. Makino, and T. Yoshida, "Stoichiometric Indium Oxide Thin Films Prepared by Pulsed Laser Deposition in Pure Inert Background Gas", *J. Vac. Sci. & Technol. A*, **18**, pp. 83-86, 2000.

21. J. P. Zheng and H. S. Kwok, "Low resistivity indium tin oxide films by pulsed laser deposition", *Appl. Phys. Lett.* **63**, pp. 1-3, 1993.
22. S. Ishibashi, Y. Higuchi, Y. Ota, and K. Nakamura, "Low resistivity indium-tin oxide transparent conductive films. II. Effect of sputtering voltage on electrical property of films", *J. Vac. Sci. Technol.* **A8**, pp. 1403-1406, 1990.
23. J. P. Zheng, Q. Y. Ying, S. Witanachchi, Z. Q. Huang, D. T. Shaw, and H. S. Kwok, "Role of the oxygen atomic beam in low-temperature growth of superconducting films by laser deposition", *Appl. Phys. Lett.* **54**, pp. 954-956, 1989.
24. D. Bauerle, Ed., *Laser Processing and Chemistry*, Third Ed., Springer-Verlag, Berlin, 2000.
25. K. A. Klinedinst and D. A. Stevenson, "The determination of the standard Gibbs energies of formation of indium oxides from e.m.f. measurements using a solid oxide electrolyte technique", *J. Chem. Thermodynamics* **5**, pp. 21-29, 1973.
26. Y. Shigesato and D. C. Paine, "A microstructural study of low resistivity tin-doped indium oxide prepared by d.c. magnetron sputtering", *Thin Solid Films* **238**, pp. 44-50, 1994.
27. J. A. Thornton and D. W. Hoffman, "Stress-related effects in thin films", *Thin Solid Films* **171**, pp. 5-31, 1989.
28. P. E. Dyer, A. Issa, and P. H. Key, "Dynamics of excimer laser ablation of superconductors in an oxygen environment", *Appl. Phys. Lett.* **57**, pp. 186-188, 1990.

# German National Femtosecond Technology Project (FST)

Friedrich Dausinger\*  
Institut für Strahlwerkzeuge, University of Stuttgart

## ABSTRACT

The German federal government started the funding of a national project intended to exploit the potential of femtosecond technology. In a foregoing competition five research consortia had been successful and have started now together with an adjoin research consortium their investigations in the following fields:

- micro-machining of technical materials for microstructuring and drilling,
- medical therapy in: ophtalmology, dentistry, neurology and ear surgery,
- metrology,
- laser safety,
- x-ray generation.

Lasers, systems and technologies required in these potential fields of applications will be investigated. The program aims at industrial success and is dominated by industrial partners, therefore. The more fundamntal research is done in university institutes and research centers.

**Keywords:** Femtosecond lasers, micro-machining, ablation, medical therapy, metrology, x-ray generation

## 1. INTRODUCTION

Femtosecond technology with its ultrashort light pulses forms an innovative laser technology, which can be used for multiple technical application e.g. in industrial manufacturing, information and communication technologies, environmental technology or life sciences (medicine, biology, chemistry). It offers completely new possibilities for minimal invasive materials processing.

The most striking feature of the new technology is the extreme shortness of the laser pulses ranging from about 10 fs ( $10^{-14}$ s) to 10 ps ( $10^{-11}$ s). To give an example: Within 100 fs the light travels only as far as a fraction of the diameter of a human hair. For comparison: Within one second the light can surround the earth about 7.5 times. When interacting with material, the pulse duration is shorter than the minimum time (several ps) required for heating the material. The consequence of this is that the material remains cold during pulses with fs-duration which leads to the expectation of ultra high precision and minimised heat load.

Another predominant feature of ultrashort pulses is their extremely high intensity. At a pulse width of 100 fs and a focal area of  $100 \mu\text{m}^2$  a pulse energy of 1 mJ yields an intensity value of  $10^{16} \text{ W/cm}^2$ , for example. With such high intensities multi-photon effects are achieved easily, allowing e.g. materials treatment inside of transparent materials like glass or the human eye cornea.

## 2. GERMAN NATIONAL PROJECT FEMTOSECOND TECHNOLOGY (FST)

To promote the potential of FS technology and its industrial application German companies and research institutions formed cooperations in the framework of the national project 'FEMTOSECOND TECHNOLOGY (FST)'

The structure of the FST program is shown in table 1. It consists of five participating project clusters **PRIMUS**, **FESMET**, **MUSKL**, **FLIM** and **SAFEST** as well as of the associated project cluster **GEPULAM**. In total 24 companies and 22 research institutes are involved as full members. Additionally a number of institutions in Eastern Europe and Israel contribute as subcontractors. The program is funded by the Federal Ministry of Education and Research with nearly 30 millions of Euro. An equivalent amount is spent by industrial partners. The VDI-Technologiezentrum in Düsseldorf acts as project agency.

---

\*[dausinger@ifsw.uni-stuttgart.de](mailto:dausinger@ifsw.uni-stuttgart.de); phone +49 (0)711 685-6844; fax +49 (0)711 685-7244; <http://www.ifsw.uni-stuttgart.de>; Institut für Strahlwerkzeuge, University of Stuttgart, Pfaffenwaldring 43, 70569 Stuttgart

The project clusters are focusing on the areas shown in table 2:

**Table 1** Scheme of the FST project

<b>National Project FEMTOSECOND - Technology</b> General coordination: Prof. Dr. F. Dausinger, FGSW					
<b>PRIMUS</b> Precise Material Processing with Ultrashort Pulsed Lasers  Coordination Dr. G. Schmitz, Bosch  13 Partner (9 companies / 5 institutes)	<b>MUSKL</b> Medical Ultrashort Pulsed Laser System  Coordination Dr. M. Dick, Asclepion Meditec  8 partner (4 companies / 4 institutes)	<b>FLIM</b> Femtosecond Lasers in Medical Surgery  Coordination Dr. F. Löffel, 20/10 PERFECT VISION  4 partner (2 companies / 2 institutes)	<b>FESMET</b> Fundamentals of Broadband Short Pulsed Lasers for Interferometry  Coordination Prof. Dr. R. Menzel, Universität Potsdam  8 partner (6 companies / 2 institutes)	<b>SAFEST</b> Safety for Applications of Femtosecond Laser Technology  Coordination Dr. W. Kautek, BAM  8 partner (3 companies / 5 institutes)	<b>GEPULAM*</b> Triggered, Ultrashort-Pulsed X-ray Point Sources for Analytics and Medical Technology  Coordination Dr. G. Korn, Max-Born-Institut  4 partner (4 institutes)

\*associated project

The cooperation between the different project clusters is encouraged by annual meetings of all partners and working groups discussing topics of common interest like laser design, beam quality and laser-material interaction. Inside the clusters general meetings and workgroup meetings take place at least every six months.

In the following a short discription of the project clusters will be given. Further information are available via internet from <http://www.fgs.w.uni-stuttgart.de/fst/>.

**Table 2** Focal points of the participating FST cluster projects

Application field	Project
Precise Materials	PRIMUS
Metrology	FESMET / GEPULAM
Medical Therapy	MUSKL / FLIM
Laser Safety	SAFEST
X-Ray Generation	GEPULAM

### 3. PRECISE MATERIALS PROCESSING WITH ULTRASHORT-PULSED LASERS (PRIMUS)

Objective of the project cluster PRIMUS is to economically utilise the Femtosecond Technology for ablative production processes of highest precision. This will be achieved by simultaneous research, development and testing (with feed back):

- of new, direct diode pumped laser source concepts completely based on solid state materials, suitable for industrial use, with which the necessary properties of use can be achieved,
- of adequate systems technique,
- of methods for beam characterisation,

- of effective processing strategies.

The main future applications the project targets at are drilling of deep holes with aspect greater than 10 and surface structures for tribological purposes. Robust, suitable for industrial use and efficient turn-key ultrashort-pulse lasers with the following features will be developed:

- Pulse energy up to 5 mJ,
- Pulse duration < 10 ps,
- Repetition rate up to 10 kHz,
- Beam quality  $M2 < 2$ ,
- Wavelength  $\sim 1 \mu\text{m}$ .

Three different approaches will be studied:

- A thin disc design using Yb:YAG,
- A rod design using Nd:YVO,
- A fibre design using Yb-fibres.

#### 4. MEDICAL ULTRASHORT-SHORT PULSED LASER SYSTEM (MUSKL)

Ultrashort pulsed laser systems with pulse duration significantly less than one picosecond have an enormous potential for the use as beam sources for medical treatment of biological hard and soft tissues. The as well spatially (focussing) as temporally (pulse duration) highly compressed light pulses allow for making finest cuts in the tissue with a precision in the range of the size of the focus ( $\sim 1 \mu\text{m}$ ). At intensities of about  $10^{13} \text{ W/cm}^2$  that can be achieved already at low pulse energies of some  $\mu\text{J}$  due to the energy compression, the tissue gets ionised in the laser focus. The plasma spark produced thereby disintegrates the cohesion of the tissue locally. If several laser pulses are directed successively on neighbouring positions (scanning), linear and two dimensional cuts as well as three dimensional ablations can be made. Tissue that is not situated inside the laser focus is subject to a much lower thermal, mechanical and acoustical damage as would occur through laser treatment with longer pulse duration (ps, ns,  $\mu\text{s}$ ).

The specific properties of the femtosecond laser pulses allow for completely novel ways of treatment or can improve or simplify significantly conventional treatment techniques. The localised impact of the femtosecond laser pulses satisfies the specifications for minimal invasive treatment. Due to universal cutting effect irrespective of material hardness and composition, the femtosecond laser source is regarded as a highly versatile tool in medicine.

Within the cluster MusKL possibilities for utilisation at ear bones, teeth and eyes (cornea) where the femtosecond technology (FST) is promising significant improvements, are investigated.

#### 5. FEMTOSECOND LASERS IN MEDICAL SURGERY (FLIM)

The project cluster FLIM is doing basic investigation of applications of the femtosecond technology in surgery. FLIM has set up the following objectives:

- Realisation and investigation of a compact and stable femtosecond medical laser for use in surgery,
- Fundamental studies about the use of femtosecond laser pulses in minimal invasive refractive cornea surgery,
- Fundamental investigation of the use of fs-laser pulses in functional neuro surgery.

Ultrashort laser pulses offer the advantage by production of a microplasma through a non linear absorption process to do ablation directly inside a tissue or a liquid environment. This cutting and ablation processing is extremely precise. These extraordinary interaction properties of the femtosecond laser pulses shall be evaluated for the use in novel refractive methods in cornea surgery and for minimal invasive functional neuro surgery. Simultaneously a femtosecond laser source, suitable for use in a hospital is to be investigated, that satisfies the specifications for medical lasers. E.g. it has to be extremely stable and of low maintenance.

## **6. FUNDAMENTALS OF BROADBAND SHORT PULSED LASERS FOR INTERFEROMETRY (FESMET)**

Objective of this project cluster is the investigation of interferometrical measuring procedures based on novel, cheap short pulse laser sources with high bandwidth and beam quality. As such lasers are not available, at the moment, the first task is to develop them. Two different approaches are investigated by two involved laser manufacturers. The next step is the realisation of a new measurement procedure using three-dimensional surface information. Finally the method will be tested with large scale work pieces like turbine blades of industrial partners.

## **7. SAFETY FOR APPLICATIONS OF FEMTOSECOND-LASER-TECHNOLOGY (SAFEST)**

The femtosecond technology (FST) leads to complex safety-relevant issues with regard to the operation of laser beam sources. It is of special interest, whether the knowledge of hazards and dangers, and corresponding safety measures of conventional laser radiation can be transferred to the femtosecond technology. This applies in particular to fs-radiation interactions with human tissue as well as with laser protective materials, due to nonlinear effects in the ultrashort time regime.

The main objectives of the envisioned joint project can be subdivided as follows:

- Systematic collection of experimental data and of available knowledge of other working groups on beam-material interactions between fs-laser radiation and human tissue (eye and skin). Verifying, determining and completing minimum visible lesion values (MVL) and maximum permissible exposure threshold values (MPE) for all types of relevant human tissues (eye, cornea, skin). Elaborating and verifying the influence of pulse duration and repetition rates on threshold values.
- Providing threshold values of maximum permissible exposure (MPE), as well as the accessible exposure limit (AEL) for FST laser installations with emission duration in the range between 5 fs and 10 ps.
- Qualifying measuring and testing methods and providing referential methods for the characterisation of irradiation values in the fs-range.
- Systematic elaboration of beam-material interactions on technical materials for safety equipment, and specification of material requirements for suitable safety equipment, e.g. laser protective eyewear, laser protective shields, laser protective curtains, etc.
- Data base for new regulations in the field of FST and to complement or extend existing regulations and standards.
- Suggestions to standardisation organisations and their working groups.

## **8. TRIGGERED ULTRASHORT-PULSED X-RAY POINT SOURCES FOR ANALYTIC AND MEDICAL TECHNOLOGY (GEPULAM)**

Incoherent X-ray radiation can be produced by illuminating target materials with extremely high intensity beams as delivered by FST lasers. The advantages of this method compared to the classical one using tubes are:

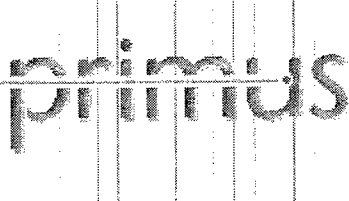
- Small diameter of radiation source ("point" source),
- Short duration of emission,
- High brilliance.

Additionally coherent XUV radiation with spatially concentrated emission is obtained as high harmonics of the ultrashort laser pulse.

The object of the project cluster GEPULAM is to make available suitable lasers for X-ray production and to examine possible application for this new type of X-ray source. These are expected in the fields of on-line control of semiconductor production and medical diagnostic with minimal damage.



**Table 3** Objectives and participants of the PRIMUS project cluster

<b>Project cluster PRIMUS</b> <b>Precise Materials processing with Ultrashort Pulsed Lasers</b>		
<b>Objectives:</b>	<ul style="list-style-type: none"> <li>➤ Understanding of fundamental interaction mechanisms</li> <li>➤ Processing strategies for high precision and efficient materials processing</li> <li>➤ System components for FST</li> <li>➤ Compact, low maintenance (turn-key) and low cost ultrashort-pulsed lasers</li> <li>➤ Beam characterisation methods</li> </ul>	
<b>Coordination:</b>	<p>Dr. Godehard Schmitz, Robert Bosch GmbH,  Postfach 30 02 40, D-70442 Stuttgart</p> <p>Tel.: 0711 / 811-8616, Fax: 0711 / 811-1640, <a href="mailto:godehard.schmitz@de.bosch.com">godehard.schmitz@de.bosch.com</a></p>	
<b>Partners:</b>	<ul style="list-style-type: none"> <li>➤ DaimlerChrysler AG</li> <li>➤ Forschungsgesellschaft für Strahlwerkzeuge (FGSW)</li> <li>➤ Gehring GmbH &amp; Co.</li> <li>➤ HAAS-LASER GmbH &amp; Co. KG</li> <li>➤ Inst. für Laserphysik (ILP), Universität Hamburg</li> <li>➤ Inst. für Strahlwerkzeuge der Universität Stuttgart (IFSW)</li> <li>➤ Kugler GmbH</li> <li>➤ Laserzentrum Hannover e.V. (LZH)</li> <li>➤ Layertec-optische Beschichtungen GmbH</li> <li>➤ Robert Bosch GmbH</li> <li>➤ Vollmer Werke Maschinenfabrik GmbH</li> <li>➤ Zentrum für Lasertechnik und Diagnostik, Universität Kaiserslautern</li> <li>➤ Institut für Optik und Quantenelektronik, Universität Jena</li> </ul>	

**Table 4** Objectives and participants of the FESMET project cluster

<b>Project cluster FESMET</b> Fundamentals of Broadband Short Pulsed Lasers for Interferometry	
<b>Objectives:</b>	<ul style="list-style-type: none"> <li>➤ Realization of two novel short pulse laser sources</li> <li>➤ Realization of a new analysis method for comparing three dimensional surface data</li> <li>➤ Demonstrator of a measuring system for determination of the three dimensional shape of technical surfaces</li> </ul>
<b>Coordination:</b>	Prof. Dr. Ralf Menzel, Universität Potsdam Inst. F. Experimentalphysik, Lehrstuhl für Photonik Tel.: 0331 / 977-1104, Fax: 0331 / 977-1134, <a href="mailto:menzel@rz.uni-potsdam.de">menzel@rz.uni-potsdam.de</a>
<b>Partners:</b>	<ul style="list-style-type: none"> <li>➤ Jenoptik Laser, Optik, Systeme GmbH</li> <li>➤ Lehrstuhl für Photonik, Universität Potsdam</li> <li>➤ Lehrstuhl für Optik, Universität Erlangen-Nürnberg</li> <li>➤ Polytec GmbH</li> <li>➤ Rolls Royce Deutschland</li> <li>➤ Robert Bosch GmbH</li> <li>➤ Spektrum Laser-Entwicklungs- und Vertriebs-GmbH</li> <li>➤ WISenT GmbH</li> </ul>


**Table 5** Objectives and participants of the GEPULAM project cluster

## Project cluster GEPULAM\*


Triggered Ultrashort pulsed X-ray Point-sources for Analytic and Medical Technology

<b>Objectives:</b>	<ul style="list-style-type: none"> <li>➤ Study and development of femtosecond laser systems for generation of X-ray radiation with maximized photon flux</li> <li>➤ Effective conversion of FS laser radiation into X-ray radiation</li> <li>➤ Evaluation of applications in the different fields (medical technology, analytic nuclear technology)</li> </ul>
<b>Coordination:</b>	Dr. Heinrich Schwörer Institut für Optik und Quantenelektronik, Friedrich Schiller Universität Max-Wien-Platz 1, 07743 Jena Tel.: 03641-947219; E-Mail: <a href="mailto:schworerer@ioq.uni-jena.de">schworerer@ioq.uni-jena.de</a>
<b>Partners:</b>	<ul style="list-style-type: none"> <li>➤ Max-Born-Institut (MBI), Berlin</li> <li>➤ Fraunhofer Institut für Lasertechnik (FHG-ILT), Aachen</li> <li>➤ Friedrich-Schiller-Universität Jena (FSU)</li> <li>➤ Physikalisches Institut, Westfälische Wilhelms-Universität Münster</li> </ul>


**Table 6 Objectives and participants of the MUSKL project cluster**

<b>Project cluster MusKL</b> Medical ultrashort-pulsed laser system		
<b>Objectives:</b>	<ul style="list-style-type: none"> <li>➤ Realisation of compact laser sources for medical application</li> <li>➤ Dentistry: building up of a system for diagnosis and therapy of caries by use of spectroscopic control</li> <li>➤ Ear surgery: treatment of auditory canal by use of ultrashort laser pulses during surgery</li> <li>➤ Ophthalmology: intrastromal refractive cornea surgery (<i>fs-LASIK</i>)</li> </ul>	
<b>Coordination:</b>	Dr. Manfred Dick, Asclepion-Meditec AG Prüssingstr. 41, D-07739 Jena Tel.: 03641 / 65-3957, Fax: 03641 / 65-3815, <a href="mailto:md@asclepion.com">md@asclepion.com</a>	
<b>Partners:</b>	<ul style="list-style-type: none"> <li>➤ Asclepion-Meditec AG, Jena</li> <li>➤ Dr. med.dent. Anton Kasenbacher, Traunstein</li> <li>➤ Laserforum e.V. Köln</li> <li>➤ Laserzentrum Hannover e.V. (LZH)</li> <li>➤ MABEL-Mannheim Biomedical Engineering Laboratories Fakultät für Klinische Medizin Mannheim</li> <li>➤ Medizinische Hochschule Hannover, Klinik für HNO-Heilkunde</li> <li>➤ Poliklinik für Zahnärztliche Prothetik, J.W.Goethe-Universität Frankfurt/Main</li> <li>➤ Soliton Laser- und Meßtechnik GmbH, Gilching</li> <li>➤ W&amp;H Dentalwerk Bürmoos</li> </ul>	

**Table 7 Objectives and participants of the FLIM project cluster**

<b>Project cluster FLIM</b> Femtosecond <u>L</u> asers <u>i</u> n <u>M</u> edical Surgery		
<b>Objectives:</b>	<ul style="list-style-type: none"> <li>➤ Femtosecond medical laser source: diode pumped Nd:glass laser system</li> <li>➤ Method for refractive fs-laser cornea surgery</li> <li>➤ Precise femtosecond laser ablation for functional neuro surgery</li> </ul>	
<b>Coordination:</b>	Dr. Frieder Lösel, 20/10 Perfect Vision Optische Geräte GmbH Waldhofer Str. 100, D-69123 Heidelberg Tel.: 06221 / 82813-10, Fax: 06221 / 82813-21, <a href="mailto:loesel@2010pv.com">loesel@2010pv.com</a>	
<b>Partners:</b>	<ul style="list-style-type: none"> <li>➤ 20/10 PERFECT VISION Optische Geräte GmbH, Heidelberg</li> <li>➤ Kirchhoff-Institut für Physik, Heidelberg</li> <li>➤ Klinik für Stereotaxie und Funktionelle Neurochirurgie der Universität Köln</li> <li>➤ MRC Systems GmbH, Heidelberg</li> </ul>	

**Table 8** Objectives and participants of the SAFEST project cluster

<b>Project cluster SAFEST</b> <b>Safety for Applications of FS-Laser Technology</b>		
<b>Objectives:</b>	<ul style="list-style-type: none"> <li>➤ Comprehensive acquisition of data on interaction of fs-laser radiation with human tissue</li> <li>➤ Comprehensive acquisition of data on interaction of fs-laser radiation with laser protective equipment as well as qualification of safety measurements</li> <li>➤ Qualification of the measurement and testing procedures and equipment for fs-laser radiation and possible secondary radiation</li> <li>➤ Implementing the results into a data matrix and transferring them into standards and regulations</li> </ul>	
<b>Coordination:</b>	<p>PD Dr. Wolfgang Kautek, Labor für Dünnschichttechnologien          Bundesanstalt für Materialforschung und -prüfung (BAM)          Unter den Eichen 87, D-12200 Berlin</p> <p>Tel.: 030 / 8104-1822, Fax: 030 / 8104-1822, <a href="mailto:Wolfgang.Kautek@bam.de">Wolfgang.Kautek@bam.de</a></p>	
<b>Partners:</b>	<ul style="list-style-type: none"> <li>➤ Bundesanstalt für Materialforschung und -prüfung (BAM), Berlin</li> <li>➤ Berufsgenossenschaft Feinmechanik und Elektrotechnik (BGFE), Köln</li> <li>➤ Femtolasers Produktions GmbH (FEMTO), Wien</li> <li>➤ Gehör-, Lärm- und Arbeitsschutz GMBH (GELA), Heusenstamm</li> <li>➤ Landeskrankenanstalten Salzburg (LKH)</li> <li>➤ Laser Zentrum Hannover e.V. (LZH)</li> <li>➤ Physikalisch-Technische Bundesanstalt (PTB), Braunschweig</li> <li>➤ Rupp + Hubrach Inferoptics / Laserschutz GmbH (RH), Bamberg</li> </ul>	

# Laser Ablation of Nitrogen-Solid Films by UV ps-Laser Irradiation: Surface Modification of Materials by Fragments in Laser-Ablation Plume

Hiroyuki Niino<sup>\*</sup>, Tadatake Sato, Aiko Narazaki, Yoshizo Kawaguchi and Akira Yabe  
Photoreaction Control Research Center (PCRC)  
National Institute of Advanced Industrial Science and Technology (AIST)

## ABSTRACT

Laser ablation of nitrogen solid film deposited on a copper plate at 10 K was investigated by the irradiation of a picosecond UV laser at 263 nm in vacuum. Photo-dissociation of nitrogen molecule in the solid film was confirmed by the optical emissions, which were ascribed to atomic nitrogen, during the laser irradiation at the fluence of  $5 \text{ J} \cdot \text{cm}^{-2} \cdot \text{pulse}^{-1}$ . This photolysis was discussed by the comparison with laser-induced breakdown of nitrogen gas. At the fluence over ca.  $10 \text{ J} \cdot \text{cm}^{-2} \cdot \text{pulse}^{-1}$ , the ablation of the frozen nitrogen film was observed. Employing the ablation plume including a reactive species such as nitrogen atoms, the surface reaction of a graphite (highly oriented pyrolytic graphite (HOPG)) plate and silicon wafer was studied. XPS analysis indicated that nitrides were formed on the surfaces by the treatment. The ps-laser ablation of nitrogen solid film provides a novel technique for surface modification of materials.

**Keywords:** Laser ablation, Cryogenic temperature, Nitrogen-solid film, picosecond UV laser, Emission spectroscopy, Plume reactivity, Reactive species, Surface modification

## 1. INTRODUCTION

Ablative photodecomposition of materials with pulsed lasers has been shown to be useful for etching, surface modification, and thin film deposition.<sup>1,2</sup> One aspect of the ablation process which has been studied extensively is the fact that the fragments emitted explosively from the surface of solid materials include large amounts of reactive intermediates such as radicals and ions.<sup>3-7</sup> This suggests the possibility for utilizing the reactive intermediates in a novel method for the chemical modification of material surfaces, as this method can produce a pulsed beam of intermediates with a higher density compared to the pulsed super sonic method.<sup>8</sup> In our previous reports,<sup>9-11</sup> we investigated the chemical reactivity of the intermediates produced by the ablation of a solid film of a photoreactive organic molecule in an argon matrix at 10 K.

From the viewpoint of new applications in laser ablation techniques, we have investigated the laser ablation of nitrogen solid films induced by UV picosecond (ps) laser irradiation at cryogenic temperature. Chemically activated nitrogen species are quite useful for fabricating a nitride material applied into electronics and optics.<sup>12-16</sup> However, molecular nitrogen is an inert compound, and has no single-photon absorption band in UV, visible, and IR region.<sup>17-21</sup> For such a transparent molecule, multi-photon excitation by short-pulsed laser irradiation with high intensity would be an effective technique to form the excited states of molecules.<sup>22-25</sup>

In this paper, we monitored the photolysis of nitrogen solid film by UV-visible optical emission spectroscopy. The mechanism of this process was discussed from the comparison with laser-induced breakdown of nitrogen gas. Moreover, chemical modification of graphite and silicon surface was carried out by exposure to a plume from ablated nitrogen solid, and confirmed by X-ray photoelectron spectroscopy (XPS).

---

<sup>\*</sup>Email: niino.hiro@aist.go.jp; phone: +81-298-61-4562; fax: +81-298-61-4560; <http://unit.aist.go.jp/pcrc/laserpro/index.htm>  
Photoreaction Control Research Center (PCRC), National Institute of Advanced Industrial Science and Technology (AIST),  
Tsukuba Central 5, 1-1-1 Higashi, Tsukuba, Ibaraki 305-8565 JAPAN

## 2. LASER ABLATION AT CRYOGENIC TEMPERATURE

Table I shows the list of the papers in the field of laser ablation at cryogenic temperature. Although there are not many papers published in these areas, the target materials have widely expanded into polymers, organic materials, inorganic materials, and inert gases. Plume diagnoses using time-of-flight mass spectrometry are mainly investigated to elucidate the mechanism of laser ablation process.

Table 1 Laser ablation at cryogenic temperature

Target	Lasers <sup>a)</sup>	Temperature	Substrate	Analysis, investigation <sup>b)</sup>	Ref paper
<i>Polymer</i>					
PMMA <sup>c)</sup>	ns-ArF,KrF excimer	90, 293K	Cold finger	Etching rate, Temperature effect	26
PET, PEN <sup>c)</sup>	ns-KrF excimer	83K	Cold finger	ESR, Chemical reactivity with monomers	27
<i>Organic materials</i>					
CH <sub>2</sub> I <sub>2</sub>	ns-XeCl excimer	90K	Sapphire, Ag	TOF-MS, yields	28
Benzene	ns-CO <sub>2</sub>	liq. N <sub>2</sub>	NaCl	TOF-QMS, kinetic energy	29
Aniline in CO <sub>2</sub>	ns-YAG (1064nm)	liq. N <sub>2</sub>		TOF-QMS, RE2PI	30
Phenylazide	ns-KrF excimer	10K	Ag, CsI, Sapphire	Optical emission, plume image	10
Phenylazide in Ar	ns-KrF excimer	10K	Ag, CsI	IR, emission, surface reaction of polymer	9
Phenylazide in C <sub>6</sub> F <sub>14</sub>	ns-KrF excimer	84K	Sapphire	Emission, surface reaction of polymer	11
Chlorobenzene	ns-KrF excimer	liq. N <sub>2</sub>	SiO <sub>2</sub>	TOF-QMS, yields, kinetic energy	31
Toluene, C <sub>6</sub> H <sub>5</sub> Cl	ns-KrF excimer	liq. N <sub>2</sub>	SiO <sub>2</sub>	TOF-QMS, yields vs. fluence	32
CH <sub>2</sub> Cl <sub>2</sub> , C <sub>6</sub> H <sub>12</sub>	ns-ArF,KrF excimer	liq. N <sub>2</sub>	SiO <sub>2</sub>	TOF-QMS, yields vs. fluence	33
Acetylene	ns-ArF excimer	liq. N <sub>2</sub>	Cu	PLD of diamond-like carbon	34
Acetone	fs-Ti:Al <sub>2</sub> O <sub>3</sub> (790nm)	liq. N <sub>2</sub>	Stainless steel	PLD of diamond-like carbon	35
CH <sub>4</sub>	ns-YAG (532nm)	16K	Si(100)	PLD of SiC	36
CH <sub>4</sub> , CO <sub>2</sub>	ns-KrF excimer	12K	Graphite	PLD of diamond-like carbon	37
Al(CH <sub>3</sub> ) <sub>3</sub>	ns-ArF excimer	110K	SiO <sub>2</sub>	TOF-QMS, kinetic energy	4
Zn(CH <sub>3</sub> ) <sub>2</sub> , In(CH <sub>3</sub> ) <sub>3</sub> , Ga(CH <sub>3</sub> ) <sub>3</sub> , Sn(CH <sub>3</sub> ) <sub>4</sub>	ns-ArF excimer	100K	SiO <sub>2</sub>	TOF-QMS, kinetic energy	38
tryptophan, tyrosine in ethanol+glycerol	ns-CO <sub>2</sub>	liq. N <sub>2</sub>	Cold finger	TOF-MS, REMPI-MS	39
<i>Inorganic materials</i>					
NO <sub>2</sub> (N <sub>2</sub> O <sub>4</sub> )	ns-XeCl excimer	liq. N <sub>2</sub>	Sapphire	TOF-QMS, kinetic energy	40
NO	ns-ArF excimer	30K	MgF <sub>2</sub>	TOF-QMS, 1+1 MPI, kinetic energy	41
NO	ns-ArF excimer	25K	SiO <sub>2</sub> , MgF <sub>2</sub>	TOF-QMS, kinetic energy	42
NH <sub>3</sub> in H <sub>2</sub> O	ns-ArF,KrF excimer	77K	SiO <sub>2</sub>	TOF-QMS, kinetic energy	43
TiO, CrO, CoO in Ar + O <sub>2</sub>	ns-XeCl excimer	10K	Cu	TOF-MS, ion detection	44
O <sub>3</sub>	ns-KrF excimer	30-60K	Sapphire	TOF-QMS, kinetic energy, oxidation	45
O <sub>3</sub> + N <sub>2</sub> O	ns-KrF excimer	30K	Sapphire	oxidation and nitridation of Si	46
Cl <sub>2</sub>	ns-ArF excimer	25-110K	SiO <sub>2</sub>	TOF-QMS, kinetic energy	47
Cl <sub>2</sub> , CH <sub>3</sub> Cl	ns-ArF,XeF excimer	100K	Si(100), SiO <sub>2</sub>	TOF-QMS, kinetic energy	48
Cl <sub>2</sub>	ns-YAG (355nm)	20K	SiO <sub>2</sub>	Etching of Si(100)	49
Cl <sub>2</sub>	ns-YAG (355nm)	20K	SiO <sub>2</sub>	TOF-QMS, sattering from Si(100)	50
Cl <sub>2</sub> in Xe	ns-YAG (355nm)	20K	SiO <sub>2</sub>	TOF-QMS, kinetic energy	51
Cl <sub>2</sub> , ICl	ns-YAG (266,355,532 nm)	18K	SiO <sub>2</sub>	TOF-QMS, kinetic energy	52
XeF <sub>2</sub>	ns-YAG (266nm)	20K	SiO <sub>2</sub>	TOF-QMS, kinetic energy	53

Table 1 (continued)

Target	Lasers <sup>a)</sup>	Temperature	Substrate	Analysis, investigation <sup>b)</sup>	Ref.
<i>Inorganic materials</i>					
N <sub>2</sub> , H <sub>2</sub> O	ns-N <sub>2</sub>	He Cryostat	Ag	Quartz-crystal microbalance	54
N <sub>2</sub>	ps-YLF (263nm)	10K	Cu	Emission, surface reaction of graphite	55
N <sub>2</sub>	ns-ArF, KrF excimer	10K	Nb	Emission, co-ablation with Nb	24
N <sub>2</sub>	ns-ArF, KrF excimer	10K	Nb, BN	PLD of NbN, BN	25
Ar	ns-dye (228,281,283nm)	5-70K	CaF <sub>2</sub>	Mass, etching rate	56

<sup>a)</sup> ArF laser ( $\lambda=193$  nm), KrF laser ( $\lambda=248$  nm), XeCl laser ( $\lambda=308$  nm), XeF laser ( $\lambda=351$  nm), N<sub>2</sub> laser ( $\lambda=337$  nm), CO<sub>2</sub> laser ( $\lambda=10.6$   $\mu$ m), ns-: nanosecond, ps-: picosecond, fs-: femtosecond

<sup>b)</sup> TOF-QMS: Time-of-flight quadrupole mass spectrometry, RE2PI: resonance-enhanced 2-photon ionization,

PLD: Pulsed laser deposition, REMPI: resonance-enhanced multiphoton ionization

<sup>c)</sup> PMMA: polymethylmethacrylate, PET: poly(ethylene terephthalate), PEN: poly(ethylene naphthalate)

### 3. EXPERIMENTAL

To prepare a solid film of nitrogen, nitrogen gas (>99.9995 %) was deposited on a copper plate at 10 K in a vacuum chamber ( $10^{-4}$  Pa), as shown in Figure 1. Thickness of the film on the plate was approximately 3 nm. The deposited film was irradiated with a UV ps-laser at the wavelength of 263 nm in vacuum (fourth harmonic wavelength (FHG) of Nd:YLF laser (Continuum, YFP-79CU);  $\tau = 8$  ps, intensity= 1.5 mJ pulse<sup>-1</sup>, repetition rate=10 Hz). Since the second harmonic wavelengths of the Nd:YLF laser beam was very close to an emission band of a photoproduct in the solid film, four dichroic mirrors were employed to reduce the contamination of the wavelengths at 526.5 nm. The laser beam was focused with an achromats quartz lens in air.

Optical emission spectrum of photoproducts in the nitrogen solid was measured in the region between UV and visible wavelength with an ICCD camera system (Princeton Instruments, I-MAX) with a 105-mm Nikon telephoto lens (UV-Nikkor). The emission was detected without a time-gated function on the ICCD through a monochromator (Acton Research Co., SP-150) having diffraction gratings of 1200 grooves·mm<sup>-1</sup> (resolution: < 0.5nm). In the detection of emission from solid-nitrogen, a glass filter (cut-off: 290nm) was used to eliminate scattering of the excitation laser beam on the film. The spectrum tube of nitrogen (Electro-Technic Products, Inc.; Model SP200, power supply: 5000 V) was used for detecting emission from discharged nitrogen gas.

A plate of highly oriented pyrolytic graphite (HOPG; Veeco ZYH Grade) and silicon wafer at room temperature (RT) was used as targets for exposure to the plume beam at a distance of ca. 2 cm from the cryogenic nitrogen solid. The surface of the modified HOPG plate was analyzed by XPS (Perkin Elmer Co., PHI-5600ci; X-ray: monochromatic Al-K $\alpha$ ). Photoelectron from the HOPG surfaces on the XPS measurement was detected at the angle of 75°. The atomic ratio of the sample surfaces was estimated from the peak areas of XPS spectra recorded by fine scanning.

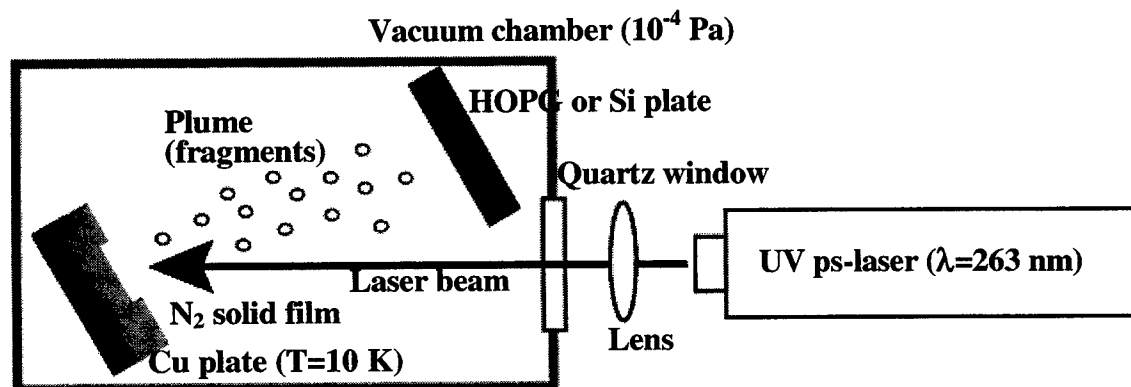


Fig. 1 Schematic drawing of experimental apparatus.

## 4. RESULTS AND DISCUSSION

### 4.1 PHOTOLYSIS OF CRYOGENIC NITROGEN SOLID

The optical emission spectra of the nitrogen gas and solid, which were excited by electron discharge and ps-pulsed laser irradiation are shown in Figure 2. Figure 2(a) shows the emission spectrum from a spectroscopic discharged tube of nitrogen gas. All the emission peaks in the region between 300 nm and 450 nm were ascribed to the second positive system of excited neutral molecular nitrogen (transition:  $C^3\Pi_u \rightarrow B^3\Pi_g$ ). Emissions from the first positive system of excited  $N_2$  ( $B^3\Pi_g \rightarrow A^3\Sigma_u^+$ ) were also detected between 500 nm and 900 nm. These two systems are typical emission from a nitrogen gas, which was excited by electron impact in a discharge tube.<sup>57</sup>

At the breakdown of nitrogen gas (pressure: 200 Torr) irradiated by a focused laser beam of a ps-Nd:YLF laser with a fluence of ca.  $20 \text{ J}\cdot\text{cm}^{-2}\cdot\text{pulse}^{-1}$  at 263 nm, a unique spectrum was obtained as shown in Fig.2(b). These detectable peaks in the spectrum are corresponding to the emissions from both the excited  $N_2$  (second positive system) and atomic nitrogen. Several major peaks between 400 nm and 900 nm were assigned to atomic N and  $N^+$  (868 nm:  $N(^4D \rightarrow ^4P)$ , 821 nm:  $N(^4P \rightarrow ^4P)$ , 746 nm:  $N(^4S \rightarrow ^4P)$ , 568 nm:  $N^+(^3D \rightarrow ^3P)$ , 500 nm:  $N^+(^3P \rightarrow ^3S \text{ or } ^3F \rightarrow ^3D)$ , 463 nm:  $N^+(^3P \rightarrow ^3P)$ , 444 nm:  $N^+(^1D \rightarrow ^1P)$ ).<sup>58</sup> Formation of atomic nitrogen in the breakdown with an intense laser beam was explained by a Coulomb explosion of photo-ionized nitrogen molecule, so that excited species of atomic N and  $N^+$  were produced in the multiple-fragmentation process of a nitrogen molecule.<sup>59-62</sup> In addition, electrons having a high kinetic energy released from an ionized  $N_2$  molecule during the laser irradiation would cause formation of the second positive system of excited  $N_2$ . It was concluded that the laser-induced breakdown of nitrogen gas involved the formation of ionized species.

On the other hand, when a cryogenic nitrogen solid film deposited on a copper plate at 10 K was irradiated with the ps-laser with a fluence of  $5 \text{ J}\cdot\text{cm}^{-2}\cdot\text{pulse}^{-1}$ , new optical emission bands appeared. Figure 2(c) shows the emission spectrum in the range between 270 nm and 700 nm. The intense peak at 523.3 nm was ascribed to  $\alpha$  emission ( $^2D \rightarrow ^4S$ ) of atomic neutral nitrogen.<sup>63-70</sup> The peak at 594.8 nm was a vibrational satellite ( $\alpha'$  emission) lines which correspond to the simultaneous  $0 \rightarrow 1$  transition in molecular nitrogen with the atomic  $^2D \rightarrow ^4S$  emission. In the region between 280 nm and 400 nm, very weak emissions from the electronically excited nitrogen molecule (Vegard-Kaplan system;  $A^3\Sigma_u^+(v'=0,1) \rightarrow X^1\Sigma_g^+(v''=6-11)$ ) were observed.<sup>71,72</sup>

In addition,  $\delta$  emission (transition:  $^2P \rightarrow ^2D$ ) of atomic nitrogen was observed at 1047 nm.<sup>63</sup> The peak at 856 nm is a vibrational satellite ( $\delta'$  emission) line which corresponds to the simultaneous  $1 \rightarrow 0$  transition in molecular nitrogen with the atomic  $^2P \rightarrow ^2D$  emission. Moreover,  $\beta$  emissions of excited atomic oxygen (transition:  $^1S \rightarrow ^1D$ ) were observed between 550 nm and 570 nm on the solid film.<sup>67-70</sup> Since the concentration of oxygen atom was estimated to be less than 0.002% from calculations using a factor in the literature,<sup>73,74</sup> these emissions were originated from negligible contamination of oxygen molecule in the nitrogen gas cylinder. These phenomena indicated that excited molecular and atomic nitrogen were produced in the solid film by the laser irradiation.



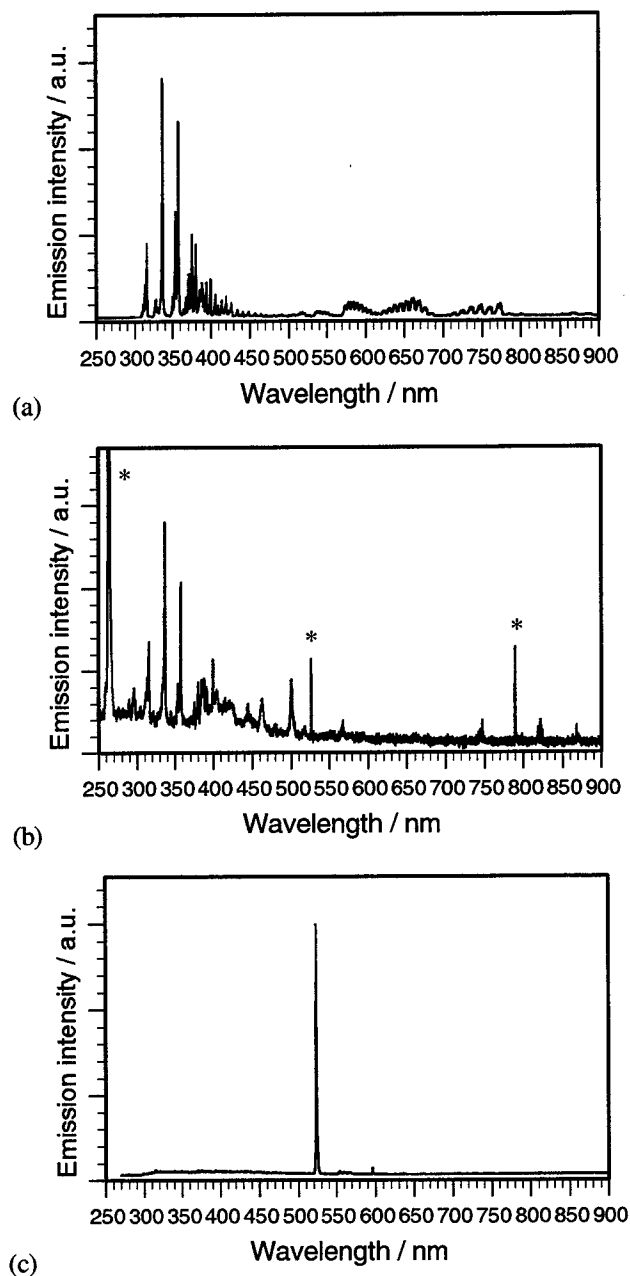


Fig. 2 Optical emission spectra of nitrogen from (a) a discharge tube, (b) a optical breakdown using ps-laser at 263 nm ( $N_2$ : 200 Torr) Asterisk in the Figure corresponds to scattering of the laser beam, (c) a nitrogen solid film upon irradiation of a ps-Nd:YLF laser at 263 nm with  $5 \text{ J cm}^{-2} \text{ pulse}^{-1}$ .

In the solid film, major optical emissions of nitrogen during the laser irradiation were corresponded to neutral atomic nitrogen. These results suggested that neutral atomic nitrogen was dominantly produced and trapped in the cryogenic solid film in the photo-dissociation of a nitrogen molecule. Trapping of N atom in the solid was evidenced by thermo-luminescence during annealing of the laser-irradiated solid film.<sup>75</sup> Figure 3 shows a clear emission peak at 523 nm, which was assigned to  $\alpha$  emission of atomic nitrogen, indicating that the atomic nitrogen formed by the photolysis was trapped without recombination in the nitrogen solid. ESR measurements of nitrogen solids after an electric high frequency discharge treatment indicated that atomic nitrogen was dominantly trapped at a substitutional site which was

the center of one of the twelve neighboring nitrogen molecules,<sup>64,65</sup> and that a limiting concentration of matrix isolated atoms was estimated to be a few percents.<sup>66</sup>

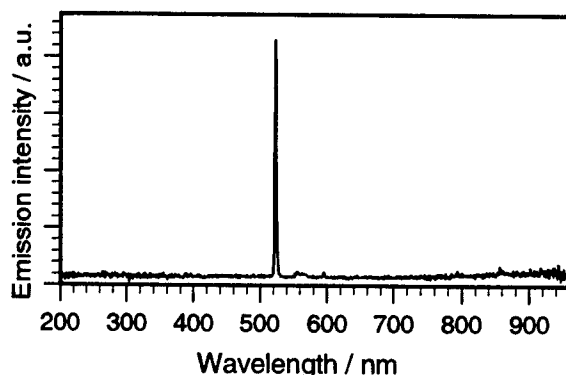


Fig. 3 Thermo-luminescence spectrum of a nitrogen solid film at annealing after ps-laser irradiation at 263 nm (temperature: ca. 15-25K).

Emission intensity of these lines was dependent on the laser fluence. Figure 4 indicated  $\alpha$  emission intensity of nitrogen atom as plotted by laser fluence. The slope of the intensities on logarithm scale was estimated to be 2.86 from a calculation of curve fitting, suggesting that nitrogen molecules were dissociated to the atom under multi-photon process. The value of 2.86 suggests that three-photon process was dominant for the decomposition. It is worth noting that Koda and coworkers have reported that, at the irradiation of a nanosecond KrF excimer laser at 248 nm (photon energy: 5.0 eV), the increase rate of the  $\alpha$  emission was experimentally dependent on the 2.8th power of the laser fluence.<sup>22</sup> Our observation was in good agreement with the case of ns-laser irradiation. Moreover, since total energies of two and three photon at 263 nm are ca. 9.4 and 14.1 eV, respectively, the photo-dissociation of molecular nitrogen would require over 10 eV of photon energy.

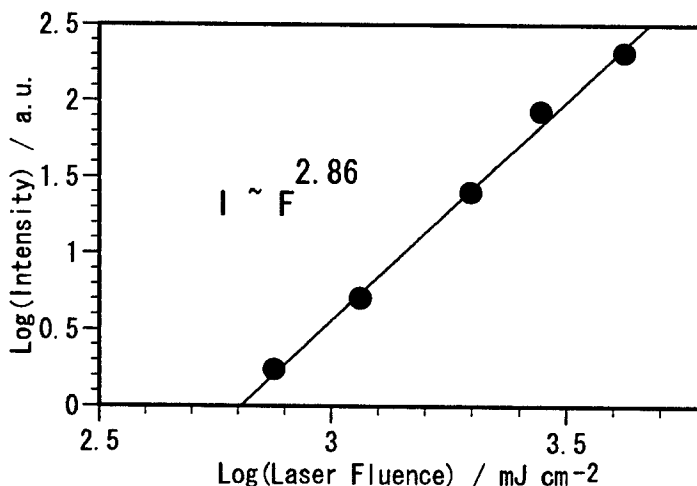


Fig.4 Emission intensity of  $\alpha$  emission at 523.3 nm upon the irradiation of the ps-laser at 263 nm.

Figure 5 displays potential energy diagram for nitrogen in the gas phase.<sup>76,77</sup> It was suggested that the excitation of molecular nitrogen by three-photons at 263 nm mainly induces the transition from the ground state  $X^1\Sigma_g^+$  to an excited state  $b^1\Pi_u$ . Since the potential curves of  $b^1\Pi_u$  and  $^7\Sigma_u$  states cross, excited molecular nitrogen on  $b^1\Pi_u$  state could dissociated to atomic nitrogen through  $^7\Sigma_u$  states by intersystem crossing. In addition, the potential curve of an excited state  $^5\Sigma_g^+$ , which is another dissociation potential to atomic nitrogen, intersects potential curves of several excited states in the range around 10 eV. These dissociation potentials indicates that inactivation process of the photo-excited molecular nitrogen was led the decomposition. Figure 5 also shows that two nitrogen atoms on the ground state  $^4S$

recombine to produce a nitrogen molecule on vibrational excited states of  $A^3\Sigma_u^+$  and  $X^1\Sigma_g^+$ . As our observation indicates that atomic nitrogen trapped into solid nitrogen film, dissociation process of photo-excited molecular nitrogen would have a channel to obstruct the recombination in the cryogenic nitrogen solid. It is concluded that molecular nitrogen, which was excited by multi-photon absorption, would decompose to atomic nitrogen through a high-lying excited state.

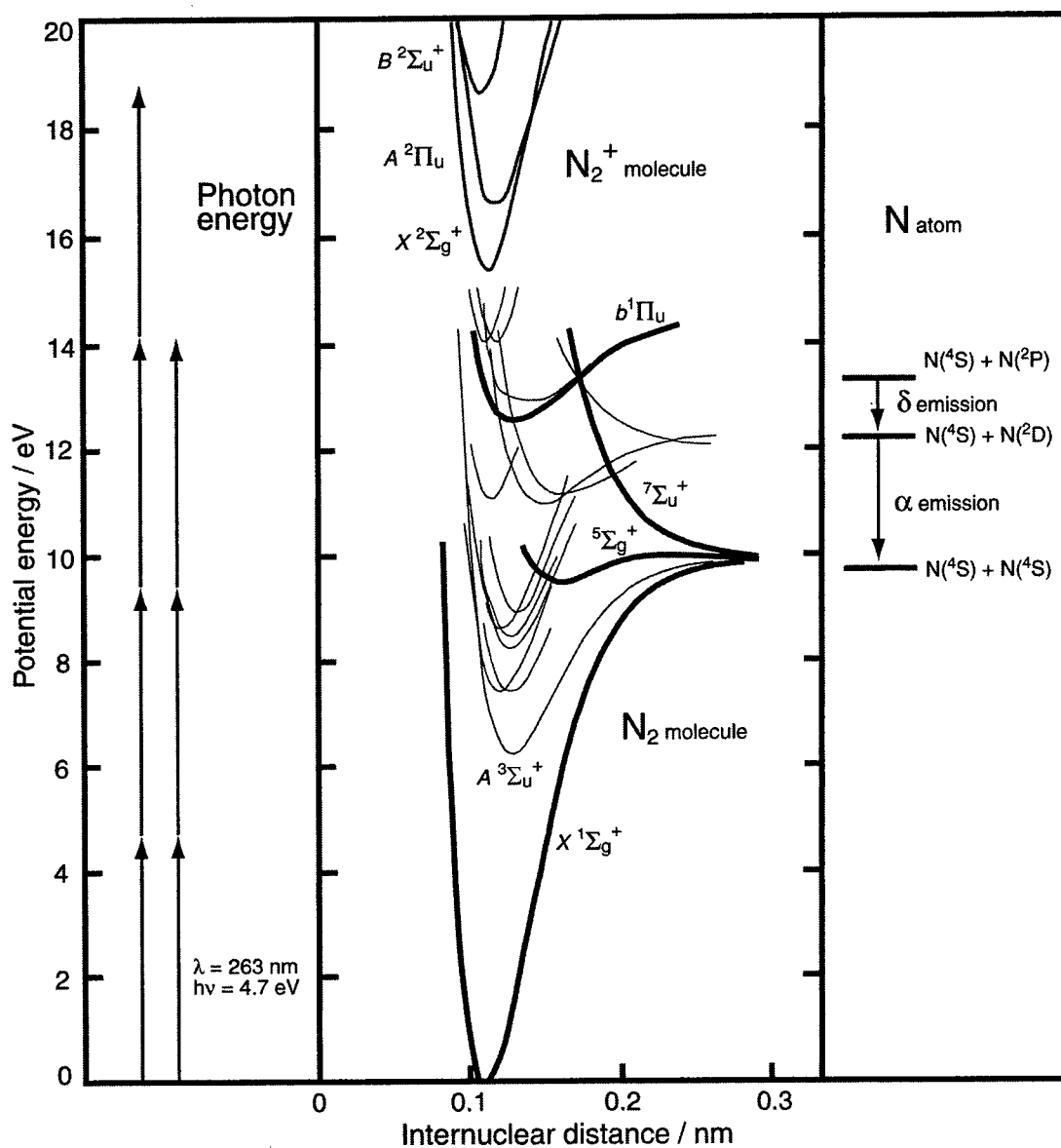


Fig. 5 Potential energy diagram for nitrogen in the gas phase (see ref. 76).

## 4.2 LASER ABLATION OF NITROGEN SOLID FILM

Upon the laser irradiation at fluence of  $10 \text{ J cm}^{-2} \text{ pulse}^{-1}$ , the nitrogen film was ablated on the plate. Figure 6 shows optical photograph of laser-irradiated area after the ablation. An etched hole was observed in the picture that was taken from the angle of ca. 45 degree. It has been reported that a thin nitrogen solid film on a metal plate was evaporated upon the irradiation of a pulsed laser by thermal energy transfer from metal plate to nitrogen solid layer.<sup>54</sup> However, since the thickness of nitrogen solid was used to be ca. 3mm to avoid thermal effects from copper plate, ablation in our system was observed on the surface layer of the nitrogen thick film. The etching rate for the ablation was several micrometers per a laser shot.

When the fluence of  $10 \text{ J cm}^{-2} \text{ pulse}^{-1}$ , was applied onto the nitrogen solid, not only three-photons process but also four-photons process would be possible. The excitation of molecular nitrogen by four photons at 263 nm mainly produces single-ionized molecular nitrogen ( $\text{N}_2^+$ ), as shown in Fig. 5. Upon the laser irradiation, the formation of a large amount of ionized species on the surface of the film was expected to cause coulomb explosion, which induced ablation process on the surface. Since nitrogen solid film is transparent for single photon absorption at the wavelength of 263 nm, multi-photon process would be require for the ablation process.

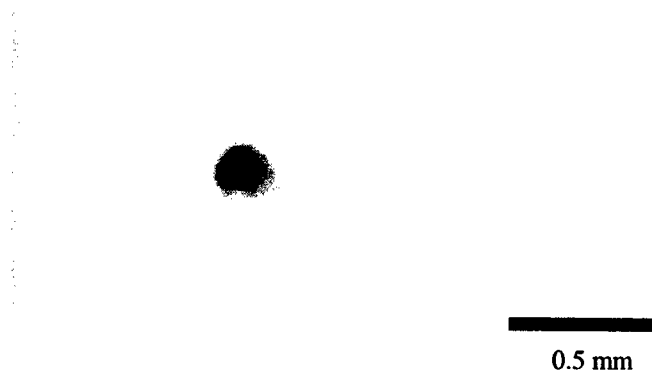


Fig. 6 Optical photograph of the ablated area on solid nitrogen upon ps-laser irradiation.

The chemical reactions of a HOPG and silicon surface with the reactive intermediates in the plume produced by the ablation of nitrogen solid film were studied from the viewpoints of surface modification of the solid material. After treatment with the plume formed by the laser irradiation at  $10 \text{ J cm}^{-2} \text{ pulse}^{-1}$  for 5 min, a new  $\text{N}_{1s}$  peak was observed in XPS spectra of the HOPG and silicon surface, as shown in Fig. 7. On the fine scanning spectrum, a new  $\text{N}_{1s}$  peak at 399.4 eV of the HOPG spectrum was observed, indicating that the nitrogen atoms ejected by the ablation were immobilized through chemical bonds onto the HOPG surface, because the nitrogen molecules physisorbed on HOPG surface had a binding energy at a peak of 403.9 eV,<sup>78</sup> which was much larger than that obtained in our measurements. These data suggested that nitrogen atoms were not bonded in a molecular configuration. Atomic ratio of  $\text{N}_{1s}/\text{C}_{1s}$  was estimated to be 0.23 by comparison with the peak areas of fine scanning spectra at  $\text{C}_{1s}$  and  $\text{N}_{1s}$  regions.

Atomic ratio of  $\text{N}_{1s}/\text{C}_{1s}$  was dependent on the detection angle of XPS. Nitrogen content increased as decrease in the angle  $\theta$ , indicating that nitrogen was dominantly localized on the top of surface layers of HOPG. The ratio at the surface was estimated by extrapolation to be  $\text{N}_{1s}/\text{C}_{1s} = 0.3$ . Moreover, immobilized amount of nitrogen on HOPG surface simply increased as increase in the laser treatment time up to 5 min. However, saturation of the amount was observed at the treatment between 5 min and 15 min. These results suggested that our method of nitride formation on HOPG surface produced different products from that by nitrogen discharge plasma treatment of HOPG<sup>12,13</sup> and by laser ablation of graphite in nitrogen atmosphere.<sup>14</sup>

Alvares and co-workers reported that a critical value of nitrogen concentration  $[\text{N}]/[\text{N}+\text{C}] \sim 15\% - 20\%$  for structural change was theoretically and experimentally observed in carbon materials having random nitrogen substitution.<sup>79,80</sup> At

a concentration lower than the critical value, amorphous carbon-nitrogen alloys consist of a graphite-like layer structure. Above the critical value, the alloys were changed to a non-planar structure with cyano-species ( $-\text{CN}$ ). As the HOPG surface treated with the nitrogen-plume included a planar structure having a maximum ratio  $[\text{N}]/[\text{N}+\text{C}] \sim 23\%$  on the basis of XPS and AFM measurements, our method was a highly effective modification of graphite surface layer to incorporate nitrogen.

In the case of the laser-treated silicon wafer, new  $\text{N}_{1s}$  peaks at 398 eV and 400 eV were detected on the surface. These peaks were ascribed to the formation of a nitride on the surface, and the atomic ratio of  $\text{N}_{1s}/\text{Si}_{2p}$  was estimated to be 0.54. These atomic ratios determined by XPS suggested that carbon nitride ( $\text{C}_3\text{N}_4$ ) and silicon nitride ( $\text{Si}_3\text{N}_4$ ) would be partly produced in the surface layer of the HOPG and silicon plate. This technique provides an effective method to form a nitride on materials surfaces.

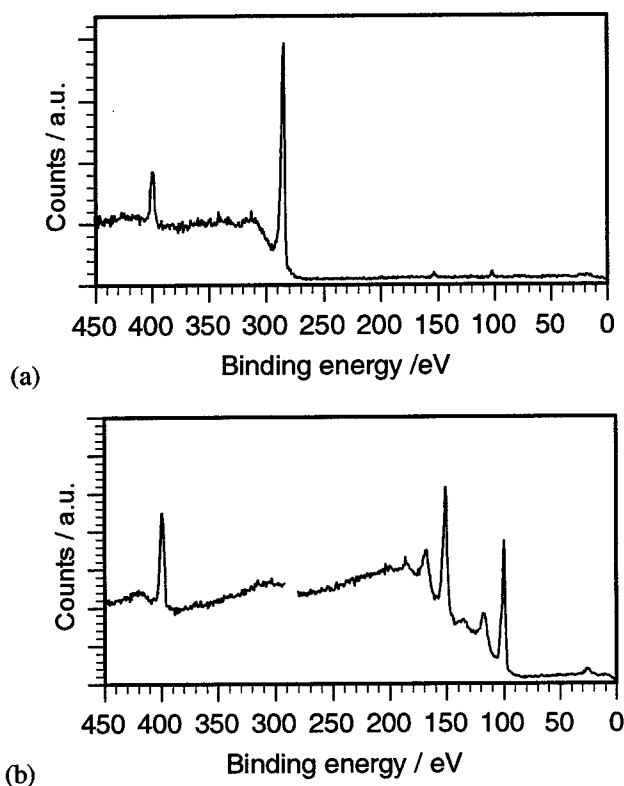


Fig. 7 XPS spectra recorded with a survey scan of the surface of HOPG (a) and silicon (b) plate after the nitrogen-plume treatment.

## 5. CONCLUSION

We demonstrated a new technique using the ablation of nitrogen induced by UV ps-laser irradiation. Multi-photon excitation of a cryogenic nitrogen solid film produced atomic nitrogen, which was trapped in the film. The mechanism of multi-photon processes was discussed on the basis of the excitation of molecular nitrogen. By using the reactive nitrogen plume, a new chemical surface modification technique was developed, which will be useful for fabricating nitride thin films in future electronic and optical applications.

## REFERENCES

1. D. Bäuerle, *Laser Processing and Chemistry*, 2nd Edn., Springer-Verlag, Berlin, pp.191-228, 1996.
2. R. Srinivasan and B. Braren, "Ultraviolet laser ablation of organic polymers", *Chem. Rev.*, **89**, pp.1303-1316, 1989.
3. Y. Tsuboi, K. Hatanaka, H. Fukumura, and H. Masuhara, "The 248 nm Excimer Laser Ablation of Liquid Benzene Derivatives: A Relation between Ablation Threshold and Molecular Photochemical Reactivity", *J. Phys. Chem.*, **98**, pp.11238-11241, 1994.
4. M. Kobayashi, A. Sato, Y. Tanaka, H. Shinohara, and H. Sato, "Photodissociation of multilayered trimethylaluminum adsorbed on a cryogenic substrate: a time-of-flight mass-spectrometric study", *Appl. Organomet. Chem.*, **7**, pp.303-309, 1993.
5. H. Niino and A. Yabe, "Positively charged surface potential of polymer films after excimer laser ablation: application to selective-area electroless plating on the ablated films", *Appl. Phys. Lett.*, **60**, pp.2697-2699, 1992.
6. H. Niino and A. Yabe, "Excimer laser polymer ablation: formation of positively charged surfaces and its application into the metalization of polymer films", *Appl. Surf. Sci.*, **69**, pp.1-6, 1993.
7. H. Niino, T. Imura, T. Ohana, C. Nagai and A. Yabe, "ESR study and surface reaction of laser-ablated polymer films", *Chem. Lett.*, pp.1341-1344, 1994.
8. D. Weber, A. Baronavski, T. Heavner, and C. Gordon III, "Synthetic applications of molecular beams", *J. Chem. Soc., Chem. Commun.*, pp.912-913, 1987.
9. H. Niino and A. Yabe, "Laser ablation of phenylazide in an argon matrix: direct observation and chemical reactivity of ablated fragments", *Appl. Phys.*, **A69**, pp.605-610, 1996.
10. H. Niino, T. Sato, A. Yabe, "Direct observation of fragments in laser ablation of phenylazide at a cryogenic temperature", *Appl. Phys.*, **A69**, pp.S145-S148, 1999.
11. H. Niino, Y. Koga, A. Yabe, "Surface reaction of organic materials by laser ablation of matrix-isolated photoreactive aromatic azido compound", *J. Photochem. Photobiol. A: Chem.*, **106**, pp.9-13, 1997.
12. S. Muhl, J. M. Mendez, "A review of the preparation of carbon nitride films", *Diamond and Related Mater.*, **8**, pp. 1809-1830, 1999.
13. C. Ronning, H. Feldermann, R. Merk, H. Hofsass, P. Reinke, J. U. Thiele, "Carbon nitride deposited using energetic species: A review on XPS studies", *Phys. Rev.*, **B58**, pp. 2207-2215, 1998.
14. C. M. Niu, Y. Z. Lu, C. M. Lieber, "EXPERIMENTAL REALIZATION OF THE COVALENT SOLID CARBON NITRIDE", *Science*, **261**, pp. 334-337, 1993.
15. A. Y. Liu, M. L. Cohen, "PREDICTION OF NEW LOW COMPRESSIBILITY SOLIDS", *Science*, **245**, pp. 841-842, 1989.
16. D. Marton, K. J. Boyd, A. H. Albayati, S. S. Todorov, J. W. Rablais, "CARBON NITRIDE DEPOSITED USING ENERGETIC SPECIES - A<sub>2</sub>-PHASE SYSTEM", *Phys. Rev. Lett.*, **73**, pp. 118-121, 1994.
17. R. W. B. Pearse and A. G. Gaydon, *The identification of molecular spectra*, 4th Edn., John Wiley & Sons, New York, pp.217-229, 1976.
18. Y. Tanaka, M. Ogawa, and A. S. Jursa, "Forbidden Absorption-band systems of N<sub>2</sub> in the vacuum-ultraviolet region", *J. Chem. Phys.*, **40**, pp.3690-3700, 1964.
19. R. A. H. Buxton and W. W. Duley, "Reflection spectrum of solid nitrogen in the vacuum ultraviolet", *Phys. Rev. Lett.*, **25**, pp.801-803, 1970.
20. E. Boursey, J.-Y. Roncin, "Experimental deperturbation of the  $b^1\Pi_u \leftarrow X^1\Sigma_g^+$  transition of N<sub>2</sub> in the solid state, pure and trapped in Ne and CF<sub>4</sub> matrices at low temperature", *Phys. Rev. Lett.*, **26**, pp.308-311, 1971.
21. R. Haensel, E. E. Koch, N. Kosuch, U. Nielsen, M. Skibowski, "Vacuum ultraviolet reflectivity of solid nitrogen and oxygen", *Chem. Phys. Lett.*, **9**, pp.548-550, 1971.
22. H. Kajihara, F. Okada, and S. Koda, "Multi-photon induced atomic nitrogen production in a low-temperature nitrogen crystal", *Chem. Phys.*, **186**, pp.395-400, 1994.
23. K. Takizawa, A. Takami, and S. Koda, "Decay kinetics of N(<sup>2</sup>P or <sup>2</sup>D) + N<sub>2</sub>(X<sup>1</sup>Σ<sub>g</sub><sup>+</sup>, v") in low temperature solid nitrogen", *J. Phys. Chem.*, **104**, pp.3693-3697, 2000.
24. Y. Hiroshima, T. Ishiguro, and K. Esaki, "Formation of a frozen nitrogen target and characterization for the application of pulsed laser deposition", *Jpn. J. Appl. Phys.*, **36**, pp.798-804, 1997.
25. Y. Hiroshima, T. Ishiguro, and K. Esaki, "Applications of pulsed excimer laser deposition with a frozen nitrogen target to deposition of NbN and BN films", *Jpn. J. Appl. Phys.*, **36**, pp. 2267-2271, 1997.
26. B. Braren and D. Seeger, "Low temperature UV laser etching of PMMA: on the mechanism of ablative photodecomposition (APD)", *J. Polym. Sci.: Polym. Lett. Ed.*, **24**, pp.371-376, 1986.

27. (a) H. Niino, T. Imura, T. Ohana, C. Nagai and A. Yabe, "ESR study and surface reaction of laser-ablated polymer films", *Chem. Lett.*, **1994** pp.1341-1344, 1994,  
 (b) H. Niino, T. Imura, C. Nagai, and A. Yabe, "Surface reaction of laser-ablated polyester films with vinyl derivatives", *J. Photopolym. Sci. Technol.*, **8**, pp.461-468, 1995.
28. (a) K.Domen and T.J.Chuang, "Electronically excited photodissociation and desorption of adsorbates: diiodomethane on aluminum oxide and silver surfaces", *Phys. Rev. Lett.*, **59**, pp.1484-1487, 1987,  
 (b) T.J.Chuang, K.Domen, "Electronically excited photodissociation and desorption of molecules on surfaces ", *J. Vac. Sci. Technol.*, **A5**, 473, 1987,  
 (c) K.Domen and T.J.Chuang, "Laser induced photodissociation and desorption. I. Diiodomethane adsorbed on aluminum oxide", *J. Chem. Phys.*, **90**, pp. 3318-3331, 1989,  
 (d) K.Domen, T.J.Chuang, "Laser-induced photodissociation and desorption. II. Diiodomethane adsorbed on silver", *J. Chem. Phys.*, **90**, pp.3332-3338, 1989,  
 (e) A. Modl, K. Domen, and T. J. Chuang, *Chem. Phys. Lett.*, **154**, pp.187-192, 1989.
29. R.Braun, P.Hess, "Time-of-flight investigation of infrared laser-induced multilayer desorption of benzene", *J. Chem. Phys.*, **99**, pp.8330-8340 (1993).
30. V.A.Elokhin, A.N.Krutchinskii, S.E.Ryabov, "Vibrational cooling of aniline molecules by laser evaporation from a cryogenic matrix ", *Chem Phys. Lett.*, **170**, pp.193-196, 1990.
31. (a) S. Georgiou, A. Koubenakis, M. Syrrou, and P. Kontoleta, " The importance of the plume ejection time for the fragmentation yields observed in the UV ablation of molecular van der Waals films. Ablation of chlorobenzene films at 248 nm ", *Chem. Phys. Lett.*, **270**, pp.491-499, 1997,  
 (b) A. Koubenakis, J. Labrakis, and S. Georgiou, "Reactivity characteristics in the UV ablation of molecular van der Waals solids", *J. Chem. Soc., Faraday Trans.*, **94**, pp.3427-3432, 1998,  
 (c) S. Georgiou, A. Koubenakis, J. Labrakis, and M. Lassithiotaki, " Photoproduct desorption dynamics in the UV ablation of model molecular solids: Ablation of chlorobenzene films at 248 nm ", *Appl. Surf. Sci.*, **127-129**, pp.122-127, 1998,  
 (d) S. Georgiou, A. Koubenakis, J. Labrakis, and M. Lassithiotaki, "Formation and desorption dynamics of photoproducts in the ablation of van der Waals films of chlorobenzene at 248 nm", *J. Chem. Phys.*, **109**, pp.8591-8600, 1998,  
 (e) S. Georgiou, C. Kosmidis, A. Koubenakis, W. J. Jia, K. W. D. Ledingham, " Translational characteristics in the ablation of chlorobenzene van der Waals solids at 248 nm ", *Phys. Chem. Chem. Phys.*, **1**, pp.5339-5344, 1999.
32. (a) S. Georgiou and A. Koubenakis, " A comparative study of the desorption efficiencies in the UV irradiation of molecular van der Waals films above and below the ablation threshold ", *Appl. Phys.*, **A69**, pp.S637-S641, 1999,  
 (b) S. Georgiou, A. Koubenakis, P. Kontoleta, M. Syrrou, "A comparative study of the UV laser ablation of van der Waals films of benzene derivatives", *Laser Chem.*, **17**, pp.73-95, 1997.
33. S. Georgiou, A. Koubenakis, P. Kontoleta, and M. Syrrou, "Induction and memory effects in the UV laser ablation of weakly absorbing van der Waals films", *Chem. Phys. Lett.*, **260**, pp.166-172, 1996.
34. M.Hanabusa and K.Tsujihara, "Diamond-like carbon films deposited by laser ablation using frozen acetylene targets", *J. Appl. Phys.*, **78**, pp.4267-4269, 1995.
35. (a) M. Okoshi , S. Higuchi, and M. Hanabusa, "Femtosecond laser ablation of frozen acetone for deposition of diamond-like carbon films", *J. Appl. Phys.*, **86**, pp.1768-1770, 1999,  
 (b) M. Okoshi , S. Higuchi, and M. Hanabusa, "Deposition of diamond-like carbon films by femtosecond laser ablation using frozen acetone targets", *Appl. Surf. Sci.*, **154-155**, 376-381, 2000,  
 (c) M. Okoshi , S. Higuchi, and M. Hanabusa, "Synthesis of microcrystals from frozen acetone irradiated by a femtosecond laser", *Jpn. J. Appl. Phys.*, **40**, pp.4926-4927, 2001.
36. T. Ishiguro, T. Shoji, and H. Inada, "Synthesis of C-N and Si-C films by pulsed laser ablation with frozen N<sub>2</sub> and CH<sub>4</sub> targets ", *Appl. Phys.*, **A69**, pp.S149-S152, 1999.
37. T. Ishiguro, K.Esaki, and Y. Hiroshima, "Synthesis of carbon films using pulsed laser deposition method with frozen CH<sub>4</sub> and CO<sub>2</sub> targets", *Appl. Surf. Sci.*, **127-129**, pp.553-558, 1998.
38. M.Kawasaki, N.Nishi, "Laser photodissociation of organometallic compounds on a cryosubstrate", *Appl. Organomet. Chem.*, **5**, pp.247-255, 1991.
39. M.E.Belov, S.S.Alimpiev, V.V.Mlynsky, S.M. Nikiforov, P.J.Derrick, "Laser-ablation of organic-molecules from frozen matrices", *Rapid Commun. Mass Spectro.*, **9**, p.1431, 1995.
40. S.Sekine, S.Ichimura, H.Shimizu, H.Hashizume, "Excimer-laser ablation of cryogenic NO<sub>2</sub> films", *Jpn. J. Appl. Phys.*, **33**, pp.L387-L389, 1994.

41. L.M.Cousins, R.J.Levis, S.R.Leone, "Translational and internal state distributions of NO produced in the 193 nm explosive vaporization of cryogenic NO films: Rotationally cold translationally fast NO molecules", *J. Chem. Phys.*, **91**, pp.5731-5742, 1989.
42. L. M. Cousins and S. R. Leone, "Production of 0.1-3 eV reactive molecules by laser vaporization of condensed molecular films - a potential source for beam-surface interactions", *J. Mater. Res.*, **3**, pp.1158-1168, 1988.
43. N. Nishi, H. Shinohara, and T. Okuyama, "Photodetachment, photodissociation, and photochemistry of surface molecules of icy solids containing nh<sub>3</sub> and pure H<sub>2</sub>O ices", *J. Chem. Phys.*, **80**, pp.3898-3910, 1984.
44. L. Andrews, A. Rohrbacher, C. M. Laperle, and R. E. Continetti, "Laser Desorption/Ionization of Transition Metal Atoms and Oxides from Solid Argon", *J. Phys. Chem. A*, **104**, pp.8173-8177, 2000.
45. (a) T. Nishiguchi, Y. Morikawa, M. Miyamoto, H. Nonaka, and S. Ichimura, "Hyperthermal O<sub>3</sub> beam produced by laser ablation of solid-ozone film", *Jpn. J. Appl. Phys.*, **39**, pp.L1200-L1202, 2000,  
(b) T. Nishiguchi, Y. Morikawa, M. Miyamoto, H. Nonaka, and S. Ichimura, "Enhanced oxidation of silicon using a collimated hyperthermal ozone beam", *Appl. Phys. Lett.*, **79**, pp.382-384, 2001.
46. T. Nishiguchi, Y. Morikawa, M. Miyamoto, H. Nonaka, and S. Ichimura, "Hyperthermal beam for oxidation and nitridation produced by laser evaporation of mixed O<sub>3</sub>/N<sub>2</sub>O cryogenic film", *Jpn. J. Appl. Phys.*, **40**, pp.L897-L899, 2001.
47. L. M. Cousins and S. R. Leone, "Time-of-flight measurements of hyperthermal chlorine molecules produced by UV laser vaporization of cryogenic chlorine films", *Chem. Phys. Lett.*, **155**, pp.162-167, 1989.
48. M. Kawasaki, H. Sato, and N. Nishi, "Laser photodissociation of chlorine and methyl chloride on low-temperature silicon substrates", *J. Appl. Phys.*, **65**, pp.792-798, 1989.
49. F. X. Campos, G. C. Weaver, C. J. Waltman, and S. R. Leone, "Enhanced etching of Si(100) by neutral chlorine beams with kinetic energies up to 6 eV", *J. Vac. Sci. Technol.*, **B10**, pp.2217-2221, 1992.
50. G. C. Weaver and S. R. Leone, "Scattering of Cl<sub>2</sub> beams from Si(100) for kinetic energies up to 2.6 eV-implications for sticking coefficients and reaction-product formation", *Surf. Sci.*, **328**, pp.197-214, 1995.
51. F. X. Campos, C. J. Waltman, and S. R. Leone, "Laser vaporization time-of-flight studies of cryogenic chlorine/xenon films", *Chem. Phys. Lett.*, **201**, pp.399-403, 1993.
52. G. C. Weaver and S. R. Leone, "Fragmentation and Recombination of Molecules during Laser Vaporization of Cryogenic Films", *J. Phys. Chem.*, **100**, pp.4188-4192, 1996.
53. R. J. Levis, C. J. Waltman, L. M. Cousins, R. G. Copeland, and S. R. Leone, "A hyperthermal (0.1-4 eV) F atom beam source suitable for surface etching investigations", *J. Vac. Sci. Technol.*, **A8**, pp.3118-3122, 1990.
54. O. Ellegaard and J. Schou, "Ablation of volatile films by laser heating of substrates", *J. Appl. Phys.*, **83**, pp.1078-1086, 1998.
55. (a) H. Niino, T. Sato, and A. Yabe, "Laser ablation of solid films at a cryogenic temperature", *Proc. SPIE*, **3933**, p.174-181, 2000,  
(b) H. Niino, T. Sato, and A. Yabe, "Laser Ablation of Solid-Nitrogen Films at a Cryogenic Temperature", *Proc. SPIE*, **4279**, pp.232-239, 2001.
56. G. Schilling, W. E. Ernst, N. Schwentner, "Nonlinear laser-ablation from solid rare-gas films", *Appl. Phys.*, **B58**, pp.267-271, 1994.
57. D. W. Turner, C. Backer, A. D. Baker, C. R. Brundle, *Molecular photoelectron spectroscopy: A Handbook of He 584A spectra*, John Wiley & Sons, Lpndon and New York, 1970.
58. NIST Atomic Spectra Database: [http://physics.nist.gov/cgi-bin/AtData/main\\_asd](http://physics.nist.gov/cgi-bin/AtData/main_asd)
59. C. Cornaggia, "Small polyatomic molecules in intense laser fields", *Molecules and clusters in intense laser fields*, J. Posthumus Ed. (Cambridge University Press, Cambridge, 2001) pp.84-.
60. K. Codling and L.J.Frasinski, "Molecules in intense laser fields: an experimental viewpoint", *Atoms and molecules in intense fields*, L.S.Cederbaum, K.C.Kulander, N.H.March, Eds. (Springer, Berlin, 1997) pp.1-26.
61. K. Boyer, T. S. Luk, J. C. Solem, and C. K. Rhodes, "KINETIC-ENERGY DISTRIBUTIONS OF IONIC FRAGMENTS PRODUCED BY SUBPICOSECOND MULTIPHOTON IONIZATION OF N<sub>2</sub>", *Phys. Rev.*, **A39**, pp. 1186-1192, 1989.
62. K. Codling, C. Cornaggia, L. J. Frasinski, P. A. Hatherly, J. Morellec, and D. Normand, "CHARGE-SYMMETRICAL FRAGMENTATION OF DIATOMIC-MOLECULES IN INTENSE PICOSECOND LASER FIELDS", *J. Phys. B: At. Mol. Opt. Phys.*, **24**, pp. L593-, 1991.
63. P. L. Kunsch and K. Dressler, "Calculation of dynamically induced electronic trasitions of matrix-isolated atomic nitrogen", *J. Chem. Phys.*, **68**, pp.2550-2561, 1978.



64. O. Oehler, D. A. Smith, and K. Dressler, "Luminescence spectra of solid nitrogen excited by electron impact", *J. Chem. Phys.*, **66**, pp.2097-2107, 1977.
65. K. Dressler, O. Oehler, and D. A. Smith, "Measurement of slow vibrational relaxation and fast vibrational energy transfer in solid N<sub>2</sub>", *Phys. Rev. Lett.*, **34**, pp.1364-1367, 1975.
66. M. Peyron and H. P. Broida, "Spectra emitted from solid nitrogen condensed at very low temperatures from a gas discharge", *J. Chem. Phys.*, **30**, pp.139-150, 1959.
67. R. J. Sayer, R. H. Prince, and W. W. Duley, "Luminescence of N atom in solid N<sub>2</sub> stimulated by low energy electrons", *Proc. R. Soc. Lond.*, **A365**, pp.235-251, 1979.
68. R.E.Boltnev, E.B.Gordon, V.V.Khmelenko, I.N.Krushinskaya, M.V.Martynenko, A.A.Pelmenev, E.A.Popov, and A.F.Shestakov, "Luminescence of nitrogen and neon atoms isolated solid helium", *Chem. Phys.*, **189**, pp. 367-382, 1994.
69. D.M.Lindsay, "ESR spectra of atomic nitrogen in an N<sub>2</sub> matrix", *J. Chem. Phys.*, **81**, pp. 3356-3358, 1984.
70. L.A.Wall, D.W.Brown, R.E.Florin, "Atoms and free radicals by  $\gamma$ -irradiation at 4.2 K", *J. Phys. Chem.*, **63**, pp.1762-1769, 1959.
71. D. S. Tinti and G. W. Robinson, "Spectroscopic evidence for slow vibrational and electronic relaxation in solids. The Vegard-kaplan and second positive systems of N<sub>2</sub> in solid rare gases", *J. Chem. Phys.*, **49**, pp.3229-3245, 1968.
72. B. Buijsse and W. J. vander Zande, "The predissociation mechanisms of the  $e\ ^1\Pi_u$  and the  $b\ ^1\Sigma^+_u$  states of N<sub>2</sub>", *J. Chem. Phys.*, **107**, pp. 9447-9456, 1997.
73. R.J.Sayer, R.H.Prince, W.W.Duley, "Luminescence of O atoms in solid N<sub>2</sub> stimulated by low energy electrons", *Proc. R. Soc. Lond.*, **A373**, pp.477-490 (1981).
74. P.H.Krupenie, "The spectrum of molecular oxygen", *J. Phys. Chem.*, **1**, pp.423-534, 1972.
75. B. Brocklehurst and G. C. Pimentel, "Thermoluminescence of solid nitrogen after electron bombardment at 4.2 K", *J. Chem. Phys.*, **36**, pp.2040-2046, 1962.
76. O. Ellegaard, J. Schou, B. Stenum, H. Sorensen, R. Pedrys, B. Warczak, D. J. Oostra, A. Haring, and A. E. de Vries, "Sputtering of solid nitrogen and oxygen by keV hydrogen ions", *Surf. Sci.*, **302**, pp.371-384, 1994.
77. A.Lofthus and P.H.Krupenie, "The spectrum of molecular nitrogen", *J. Phys. Chem. Ref. Data*, **6**, pp.113-307, 1977.
78. H.Tillborg, A.Nilsson, B.Hernnaes, N.Martensson, "X-ray and UV photoemission studies of mono-, bi-, and multilayers of physisorbed molecules: O<sub>2</sub> and N<sub>2</sub> on graphite", *Surf. Sci.*, **295**, pp.1-12, 1993.
79. F.Alvarez, M.C. dos Santos, and P.Hammer, "Identification of structural changes in carbon-nitrogen alloys by studying the dependence of the plasmon energy on nitrogen concentration", *Appl. Phys. Lett.*, **73**, pp.3521-3523, 1998.
80. M.C. dos Santos, P.Hammer, "Nitrogen substitution of carbon in graphite: structure evolution toward molecular forms", *Phys. Rev.*, **B58**, pp.13918-13924, 1998.

# TEM investigations of thermal effects on material structure induced by femtosecond and nanosecond laser processing

R. Le Harzic<sup>a1</sup>, S. Valette<sup>b</sup>, N. Huot<sup>a</sup>, E. Audouard<sup>a</sup>, E. Baubeau<sup>a</sup>, C. Jonin<sup>a</sup> and P. Laporte<sup>a</sup>

<sup>a</sup>Laboratoire Traitement du signal et Instrumentation (TSI)

Universite Jean Monnet, UMR CNRS 5516

23, rue du docteur Paul Michelon, 42023 Saint Etienne cedex 2, France

<sup>b</sup>Ecole Nationale Supérieure des Mines de Saint-Etienne, centre SMS,  
158, Cours Fauriel, 42023 Saint-Etienne cedex 2, France

## ABSTRACT

Holes drilled in Aluminum using nanosecond and femtosecond laser pulses are characterized by Transmission Electronic Microscopy (TEM). Hence we present a method for quantifying the dimensions of the heat affected zone (HAZ) surrounding micro-holes by analyzing the grain size evolution. Drilled samples investigations are performed after electrolytic thinning down to 100 nm.

The experiments require a real time imaging system to shot close to the located thinner zone with an accuracy in the  $\mu\text{m}$  range. Thin Al samples are drilled both in nanosecond and femtosecond regimes using the same pulse number and the same Ti-Sapphire laser source (1 kHz, 800 nm). The regeneratively amplified ultra-short pulses (150 fs) are utilized at a low fluence regime (typically 0.01-0.5 mJ/pulse), while the longer pulses (ns) are obtained from the regenerative amplifier without oscillator seeding (0.5 mJ,  $\tau \sim 7-8$  ns).

The main conclusion is that a 40  $\mu\text{m}$  wide HAZ is induced by nanosecond pulses, whereas the femtosecond regime does not produce any TEM observable HAZ. It has to be noticed that the width of the femtosecond HAZ is roughly less than 2  $\mu\text{m}$ , which is our observation limit.

**Keywords:** femtosecond, micromachining, microcutting, non thermal interaction, HAZ, TEM.

## 1. INTRODUCTION

Due to recent progress in ultrashort laser sources, fundamental and technological fields have been investigated. In the sub-picosecond time duration range, very precise processing of materials can be achieved<sup>1-4,11</sup>. It has been shown that physical phenomena occurring during laser-matter interaction were drastically different for the nanosecond regime compared to the sub-picosecond one<sup>5</sup>. Among these phenomena, the paper focuses on thermal effects during hole drilling or cutting. These thermal effects are due to the heat diffusion process and lead to a heat affected zone (HAZ) near the domain irradiated by the laser beam. In the nanosecond regime, a width of 10  $\mu\text{m}$  to 1 mm is usually observed for the HAZ, whereas in the femtosecond case, the penetration length of thermal diffusion in the material is very limited, leading to a very small HAZ. Studies of the thermal effects in the femtosecond regime are mainly theoretical and concern the diffusion length along the beam axis. The femtosecond regime is thus often considered as HAZ free, since the HAZ is very difficult to observe and quantify with conventional optics or microscopy techniques. In further sections some qualitative analysis are obtained with classical optical microscopy, scanning electronic microscopy (SEM) and optical profilometry. These techniques give a good estimation of surface quality, roughness or material

<sup>1</sup> ronan.leharzic@univ-st-etienne.fr  
<http://www.univ-st-etienne.fr/tsi>



To allow a low energy regime (typically 0.01 to 0.5 mJ/pulse), laser pulses are obtained without the two-pass amplifier. Additional attenuation is then provided by a half-wave plate combined with a polarizer. An external electronic clock device which controls the voltage applied to the Pockels cell of the amplifier 1, also enables a single shot mode running. The samples are mounted on a three-motorized-axes system with 0.5  $\mu\text{m}$  accuracy. Focusing objectives of 50 mm, 25 mm or 10 mm focal lengths are used to obtain micro-holes with a less than 100  $\mu\text{m}$  diameter.

The drilling process is monitored in real time thanks to an incoherent imaging system which consists in a He-Ne laser illuminating a rotating diffusing plate. Speckle effects observed on the CCD camera are then averaged. The resolution of the imaging device is less than 5  $\mu\text{m}$ , which is widely enough compared to typical micro-holes dimensions. A Fresnel reflection of the same He-Ne laser on a beam sampler is used as an alignment guide for the whole set-up. Precise focusing of the 633 nm He-Ne alignment beam on the sample is reached when speckles observed through an additional diffusive plate situated off-axis close to the sample are as large as possible. Axial chromatism between 633 nm and 800 nm (e.g. 120  $\mu\text{m}$  for the 25 mm focal length lens) is then corrected experimentally with one of the three motorized axes.

Experiments are performed both at the focal point and at the image point of an aperture placed before the objective as depicted in figure 2. Image-point processing has several advantages : spurious conical drilling effects are reduced and the hole's borders are sharper. The main drawback is high loss rate due to spatial amplitude filtering.

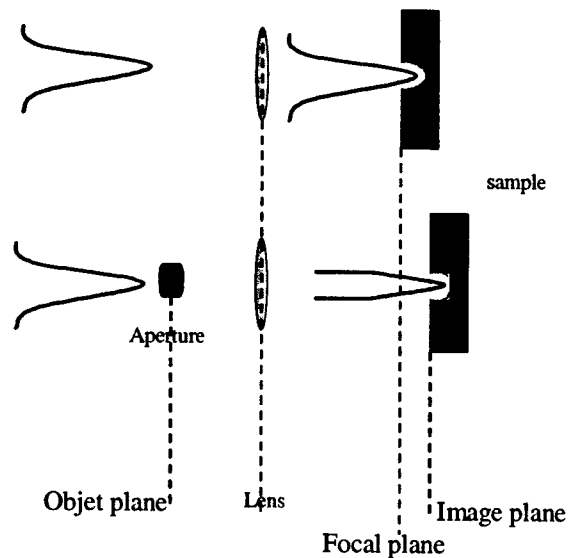


**Figure 2** : Schematic understanding of material processing at the focal plane or at the image plane

### 3. CLASSICAL CHARACTERIZATIONS OF THERMAL EFFECTS.

#### 3.1. Optical profilometry.

Surface topography after microdrilling, microcutting and microetching can be precisely analysed by optical profilometry.

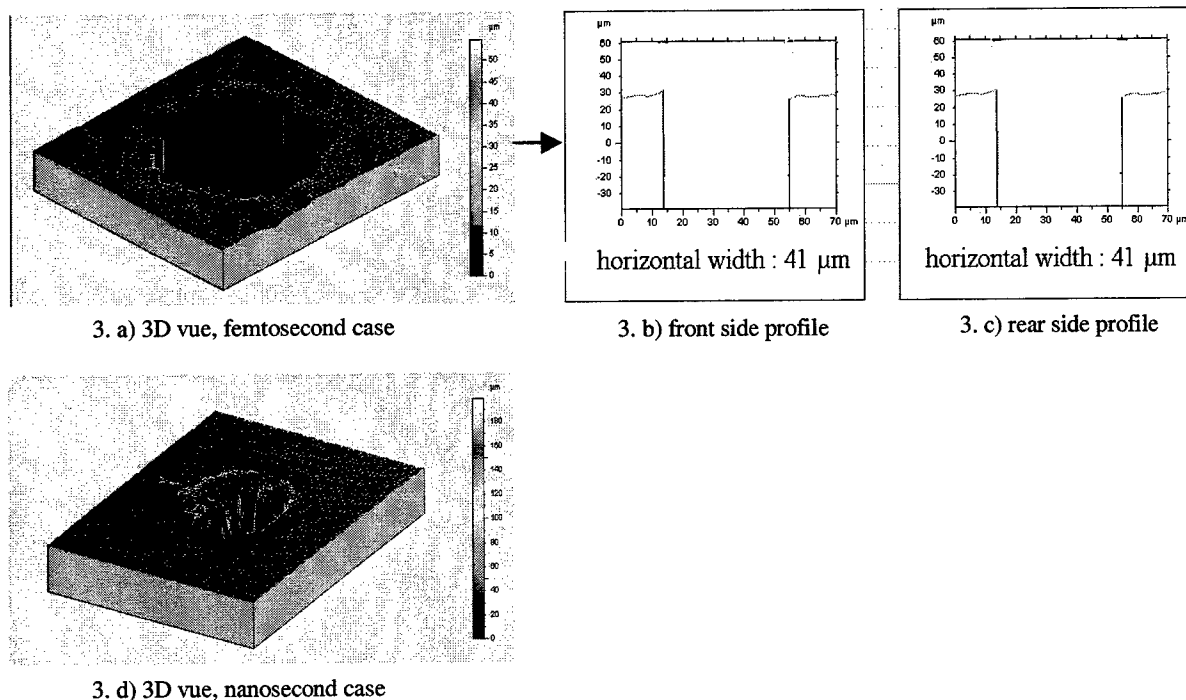


**Figure 3 :** Optical profilometry investigations of holes drilled in a 50  $\mu\text{m}$  thick Al sample in a) femtosecond mode, d) nanosecond mode.

Micro-holes were performed on a 50  $\mu\text{m}$  thick aluminum sample. Experiments are performed at the image point of a 3.5 mm aperture placed 1.35 m before the 10 mm focal length objective. This was achieved at 1 kHz, 800 nm, 150 fs and with a fluence of 2 J/cm<sup>2</sup> in the femtosecond mode. The accuracy of our experimental procedure was demonstrated by controlling the diameter and conicity (widths at the rear and front side are equal, fig 3. b) and 3. c)) with optical profilometry. The second main interest is the evaluation of the roughness and "wall" quality of the microdrilling. No removal matter or stress of the material are observed, the roughness is weak around the micro-hole. That's not the case in the nanosecond mode (fig. 3.d)), where quite significant removal matter close to the micro-hole is present. This hole was drilled at the same wavelength, 1 kHz, 8 ns and with a fluence of 5 J/cm<sup>2</sup>.

Optical profilometry is the first step of an accurate characterization of microdrilled samples.

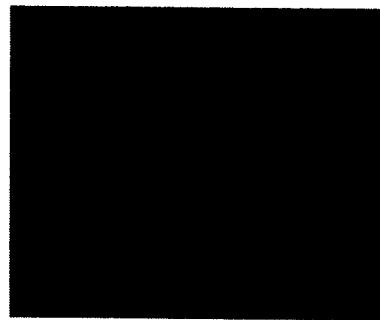
#### 3.2. Optical microscopy and scanning electronic microscopy (SEM)

##### 3.2.1. Microdrilling

Optical microscopy and scanning electronic microscopy give an overview of the micromachining quality, it can show differences of roughness or material removal with ultra-short laser pulses in compared to nanosecond case as illustrated in figures 4. a) and 4. b).



4. a) nanosecond



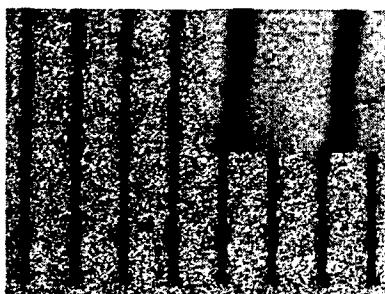
4. b) femtosecond

**Figure 4 :** SEM image of 50  $\mu\text{m}$  holes drilled in a 100  $\mu\text{m}$  thick copper sample .

It has to be noticed that the fluence was  $6 \text{ J/cm}^2$  in both case presented in the fig. 4, and that the drilling is performed at 1 kHz and at the same wavelength, 800 nm. These conditions are obviously not the best for drilling with ns pulses, but it allows to put in evidence the difference between the two regimes.

### 3.2.2. Microcutting

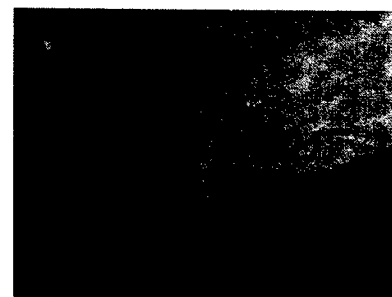
For a beam diameter in the range of ten micrometers, a high repetition rate and a very low fluence, at high speed displacement of the motorized translations are necessary for precise micromachining or microcutting. A grid on a gold foil of 20  $\mu\text{m}$  thickness has been performed at 800 nm, at a repetition rate of 100 kHz and at a fluence of about  $1 \text{ J/cm}^2$ . A 20 mm/s scan speed of the motorized stage was used to obtain the grooves with widths of 15  $\mu\text{m}$  and spaced out from 50  $\mu\text{m}$ . The obtained result is depicted in figure 5.



5. a)



5. b)



5. c)

**Figure 5 :** a) top view (optical microscope, x10 and x50 top right) of a grid on a 20  $\mu\text{m}$  thick gold foil, the width of the grooves is 15  $\mu\text{m}$  and distanced from 50  $\mu\text{m}$  ; b) top view (SEM) of the groove ; c) SEM image of the microcutting quality of the edge.

Microcutting with ultra-short laser pulses for such an accurate work is very efficient. As shown by the SEM images, a great edge straightness is obtained, no collateral damages occur and the redeposit matter is reduced. Such a quality in micromachining is hardly to obtain without any assist gas. For comparison results are presented in fig 6 for microcutting with nanosecond pulses ( $10 \text{ J/cm}^2$ , 800 nm, 1 kHz, 8 ns). Properties material modification, melting and resolidification occur without assist gas. The difference on thermal properties on material processing by femtosecond or nanosecond pulses is evidenced at atmospheric pressure.

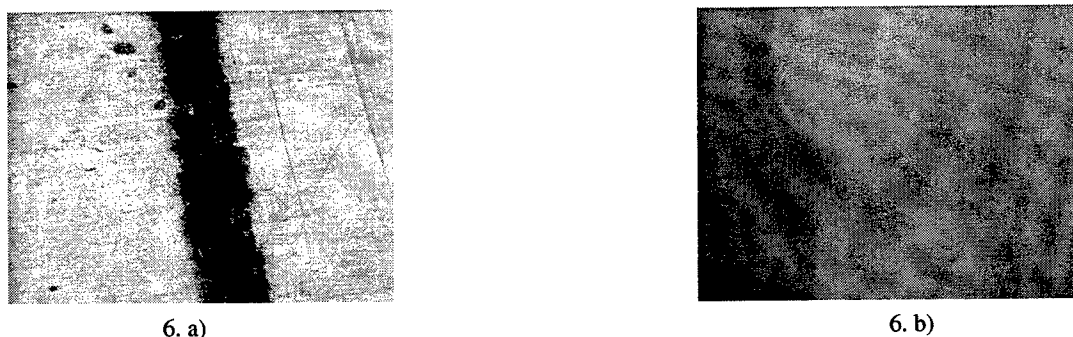


**Figure 6 :** a) top view (optical microscope, x10) of a groove on a  $20 \mu\text{m}$  thick copper foil, the central width of the grooves is  $50 \mu\text{m}$  ( $10 \text{ J/cm}^2$ , 800 nm, 1 kHz, 8 ns) ; b) SEM image of the microcutting quality of the edge.

#### 4. CHARACTERIZATION OF HAZ USING TRANSMISSION ELECTRONIC MICROSCOPY.

Femtosecond ablation in metals near the plasma energy threshold can be described using the two temperature model (TTM)<sup>5-8,12,13</sup>. In this model, we consider that the free electrons are in thermal equilibrium at a temperature  $T_e$  greater than the temperature of the lattice  $T_l$ . The evolution of  $T_e$  and  $T_l$  are then described by two coupled heat diffusion equations. The key parameter is the electron/phonon coupling constant, namely  $g$ , which determines the electron-phonon energy transfer time  $\tau_e$ , and then the limit between thermal and non-thermal processes. This coupling value has been widely studied, in copper for instance,  $g=10^{16} \text{ W/m}^3/\text{K}^5$ , and the electron-phonon relaxation time is found to be 4 ps. If the time width of the laser pulse is greater than  $\tau_e$ , part of the energy is lost into the lattice. Hence, the material is thermally affected, the efficiency of the ablation is reduced and since ejected matter interact with the laser. Whereas in the femtosecond regime the energy is temporally concentrated (lower than  $\tau_e$ ), then the thermally diffused energy is very reduced and the HAZ is minimum. The HAZ size is found to be few hundreds of nanometers in the case of metals in the beam direction<sup>7</sup>.

A new method to quantify the Heat Affected Zone by a measurement of the transverse microstructural changes no more at the surface but inside the material is possible using Transmission Electronic Microscopy (TEM).

##### 4.1. Experimental procedure.

The experimental procedure proposed here is based on a laser drilling of samples previously prepared for TEM analysis. The thickness of the samples is reduced down to 500 nm, before the experiments. This allows a local study of the effects produced by a finite number of low fluence laser pulses. In this study, 1000 pulses were produced in one second with fluences of  $2 \text{ J/cm}^2$  and  $5 \text{ J/cm}^2$  respectively for the femtosecond and the nanosecond cases, these fluences were chosen above the ablation threshold fluences in both cases.

The thickness of the samples was reduced by an electrolytic process. Metallic disks of about 3mm in diameter were used. The process was stopped automatically when light was detected through the sample. It turns out that a randomly shaped hole is always present in the middle of the sample. Throughout this paper, this hole will be referred to as the "middle hole". The final shape of the sample is depicted in figure 7, whereas the middle part of it is zoomed in figure 8.

The thickness of the area observed by a CM 200 TEM operated at 200 kV used in this study has to be less than 500 nm. This area is thus located in the vicinity of the middle hole, namely at a maximum distance of 40 to 100  $\mu\text{m}$ , depending on the quality of the thinning down. In order to observe the local effects induced by laser drilling, the produced holes have to cross this area. Positioning of the target sample was achieved by using the real-time imaging device described in section 2.

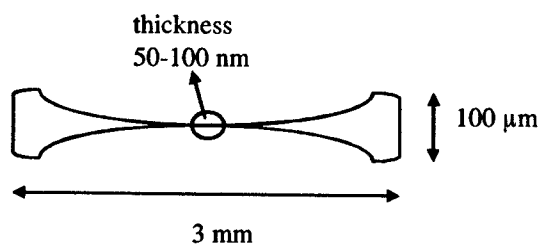


**Figure 7 :** Side-view schematic of the thinned samples

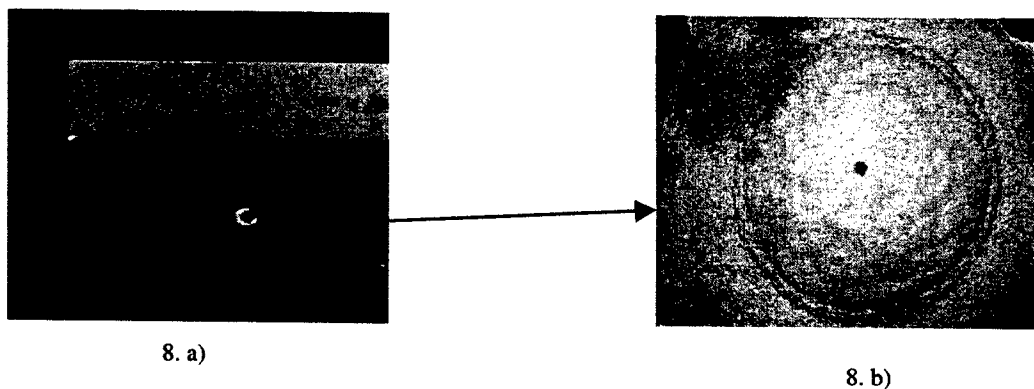


**Figure 8 :** a) 3 mm Al disc ; b) Top view ( $\times 5$ , optical microscope) of a Al thinned sample. A  $\sim 100 \mu\text{m}$  thinning-down hole is present in the middle of the sample. The target has to be drilled by the fs and ns pulses laser at a maximum distance of 80  $\mu\text{m}$  from the middle hole to allow an efficient TEM analysis.



## 4.2. Results

In order to obtain a quantitative estimation of the HAZ width, we focused on the evolution of the grain size between the middle and the laser drilled holes in both pulse duration regime. In the nanosecond pulse duration case we shot the Al sample at 70  $\mu\text{m}$  from the middle hole (figure 9) and at 35  $\mu\text{m}$  for the femtosecond case (figure 10).

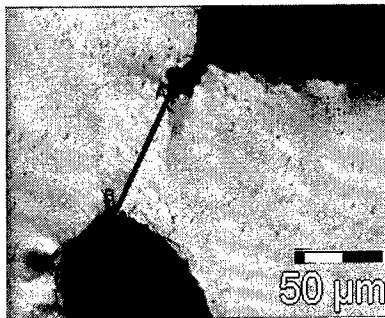


**Figure 9 :** optical microscope top-view (x50), showing the middle hole (point A) and the laser hole drilled in nanosecond regime (point B).

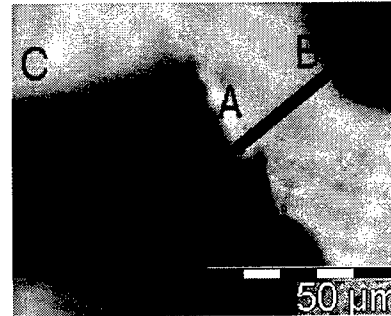


**Figure 10 :** optical microscope top-view (x100), showing the middle hole (point A) and the laser hole drilled in femtosecond regime (point B).

An example of Magnified (x 8500) images obtained by TEM is shown in figure 11, this image was treated by an average statistical method to obtain the local grain size. The average grain number is about 50 per image. Several images were analyzed between point A ("middle" hole border) and point B (laser hole border).



**Figure 11 :** image of the grains obtained by TEM (x 8500)

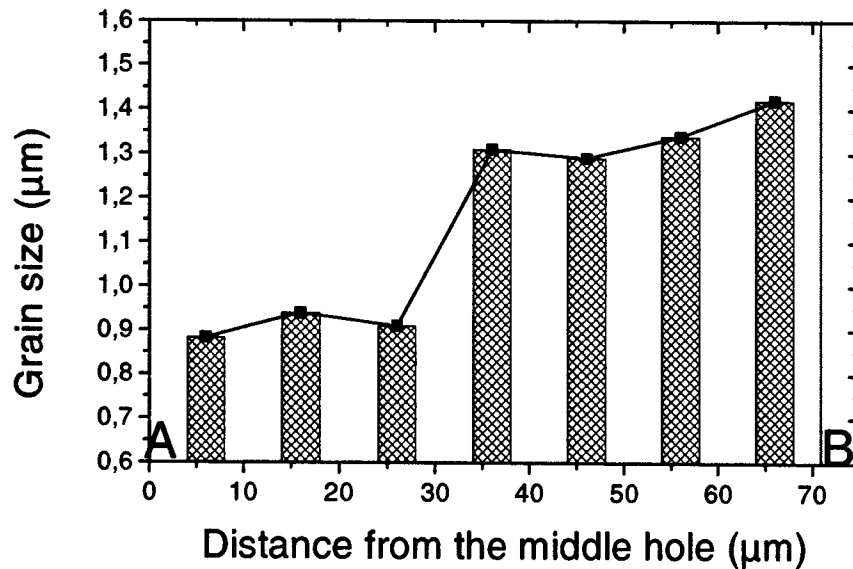


**Figure 12 :** Evolution of the grain size in the Al sample drilled with nanosecond pulses

Figure 12 displays the evolution of the grain size in the sample which is drilled with nanosecond pulses. Two regions can be observed. In the vicinity of the middle hole, up to 35  $\mu\text{m}$  from it, the grain size is approximately 0.9 to 1.0 micrometer which is the initial grain size of the sample. The second region, near the laser hole, is characterized by a grain growth. In this region, the grain size increases up to 1.3-1.4 micrometers (cf : fig 9). The transition between these two regions provides an estimation of the size of the Heat Affected Zone. In the nanosecond regime, the HAZ is then about 40  $\mu\text{m}$  width.

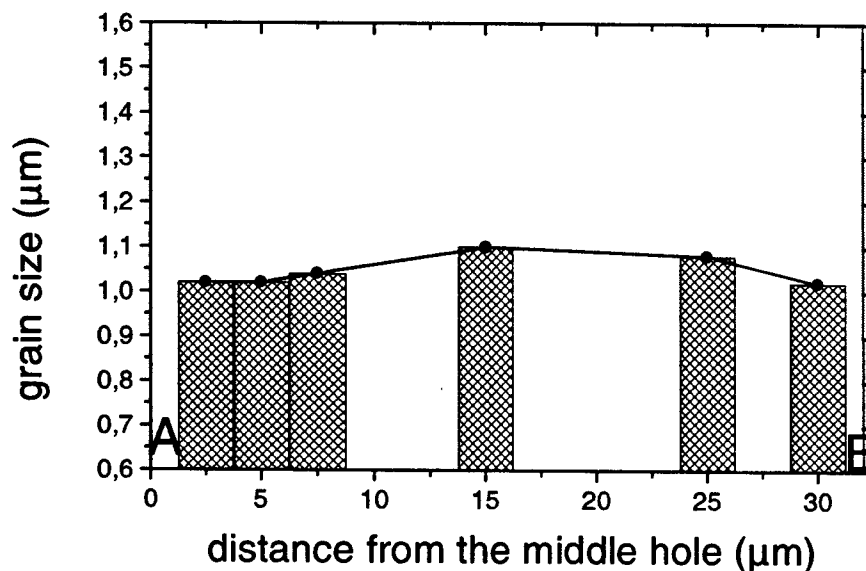


**Figure 13 :** Evolution of the grain size in the Al sample drilled with femtosecond pulses

Figure 13 represents the grain size evolution between the middle hole (point A) and the laser hole (point B) in the case of femtosecond pulses. In this case, only one region can be identified, with a constant averaged grain size of about 1  $\mu\text{m}$ . Since the distance between points A and B is only 35  $\mu\text{m}$ , the grain size was also determined at point C, which is located far from the laser holes (cf : fig 10). A 1  $\mu\text{m}$  grain size was also obtained at this point. As a result, we can say that the size of the HAZ is less than 2  $\mu\text{m}$  in the femtosecond regime. This value corresponds to the nearest position from the laser hole border that could be experimentally analyzed.

In a previous work using TEM technique, the width of the HAZ was found to be independent of the pulse duration (from 50 ns to 200 fs)<sup>9</sup>, and reached a value of 5 to 10  $\mu\text{m}$ . It should be noticed here that these results were obtained with very different experimental conditions (very high fluences, thick samples...).

## 5. CONCLUSION

The experimental procedure presented in this paper emphasizes differences in the HAZ size obtained with nanosecond and femtosecond regimes, which was evidenced by many theoretical investigations. Classical tools like optical profilometry, optical microscopy or scanning electronic microscopy allow only qualitative observation concerning thermal effects and micromachining quality. These classical techniques are used to control and improve experimental machining processes, but a precise measurement of the HAZ is not possible. Transmission electronic microscopy appears to be of great interest to fill this gap by studying the transverse microstructural changes not only at the surface but inside the material. In our experimental conditions, a 40  $\mu\text{m}$  HAZ is found in an Al sample with nanosecond pulses and no HAZ is detected in femtosecond pulses case limited by the 2  $\mu\text{m}$  spatial resolution of the analysis. To improve and perhaps measure the width of the HAZ in the femtosecond regime, we have to reach the nm scale. Some theoretical suggest a diffusion length of a few hundreds of nanometers in the case of metals. A thermal model is currently being developed to describe the radial heat diffusion in the sample, and thus explain the differences between nanosecond and femtosecond regimes. Such works are under progress.

## ACKNOWLEDGMENTS

The authors thank the European Community (FEDER funds 1997/1999) and the " Conseil général de la Loire en Rhône-Alpes " for financial support.

## REFERENCES

- <sup>1</sup> X. Zhu, "A new method for determining critical pulse width in laser material processing", *Applied surface science*, **167**, pp 230-242, 2000.
2. C. Momma, B.N. Chichkov, B. Wellegehausen, "Short-pulse laser ablation of solid targets", *Optics communications*, **129**, pp. 135-142, 1996.
3. B. N. Chichkov, C. Momma, A. Tunnermann, "Femtosecond, picosecond and nanosecond laser ablation of solids", *Applied physics. A*, **63**, pp. 109-115, 1996.
4. S. Nolte, C. Momma, H. Welling, "Ablation of metals by ultrashort laser pulses", *Journal of the optical society of america. B*, **14**, pp. 2716-2728, 1997.
5. P.B. Corkum, F. Brunel, N. K. Sherman, "Thermal response of metals to ultrashort-pulse laser excitation ", *Physical review letters*, **61**, pp. 2886-2889, 1988.
6. N.K. Sherman, F. Brunel, P.B. Corkum, "Transient response of metals to ultrashort pulse excitation ", *Optical engineering*, **28**, pp. 1114-1121, 1989.
7. S.-S Wellershoff, J. Hohlfeld, J. Güdde, E. Matthias, "The role of electron-phonon coupling in femtosecond laser damage of metals", *Appl. Phys. A*, **69**, pp. 99-107, 1999.
8. A.P. Kanavin, I.V. Smetanin, A. Tunnermann, "Heat transport in metals irradiated by ultrashort laser pulses", *Physical review B*, **57**, pp. 14698-14703, 1998.
9. A. Luft, U. Franz, A. Emsermann, J. Kaspar, "A study of thermal and mechanical defects on materials induced by pulsed laser drilling", *Appl. phys A*, **63**, pp. 93-101, 1996.
10. P. S. Perry, "Laser Surface Treatment of Metals", Draper C.W. and Mazzoldi, P. (eds.), Dordrecht, Netherlands, pp. 57, 1986.

11. X.Zhu, A. Naumov, D.Villeneuve, P. Corkum, "Influence of laser parameters and material properties on micro drilling with femtosecond laser pulses ", *Applied Physics A*, **69**, pp. 1-5, 1999.
12. S.I. Anisimov, B.L. Kapeliovich, T. L. Perel'man, "Electron emission from metal surfaces exposed to ultrashort laser pulses", *Sov. Phys.-JETP*, **39**, pp. 375-377, 1974.
13. M. I. Kaganov, I. M. Lifshitz, L. V. Tanatarov, "Relaxation between electrons and the crystalline lattice", *Sov. Phys.-JETP*, **4**, pp. 173-178, 1957.

# Microfabrication by a High Fluence Femtosecond Exposure: Mechanism and Applications

Mitsuru Watanabe,<sup>a</sup> Saulius Juodkazis,<sup>a</sup> Junji Nishii,<sup>b</sup> Shigeki Matsuo,<sup>a</sup> and Hiroaki Misawa<sup>a</sup>

<sup>a</sup>Department of Ecosystem Engineering, The University of Tokushima,  
2-1 Minamijyosanjima, Tokushima 770-8506, Japan

<sup>b</sup>AIST Kansai, Ikeda, Osaka 563-8577, Japan

## ABSTRACT

We report the observation of 3/2-frequency generation during an Optically-induced failure of silica under femtosecond laser pulse irradiation. The origin of 3/2-frequency generation is due to a two-plasmon decay instability, which occurs at the quarter critical density of free charge carriers. We observed this emission during the optical damaging of glasses by tightly focused (numerical aperture of the objective lens was 0.5-1.35) femtosecond laser pulses. The pulse duration at the irradiation spot was about 0.35 ps, the energy 25-250 nJ, and the damage was recorded in a single shot event inside the glass. The emission at about 530 nm was only present in the spectra measured during an optical damage by 795 nm irradiation with the pulse energy 9 times and more higher than the threshold.

We observed a new phenomenon applicable for microstructuring of glass. The high energy fs pulses (50-200  $\mu$ J) were focused by a plano-convex lens (focal length 2-10 cm) on the exit surface of a glass plate. The surface was ablated and the ablation was transferred into a volume of glass by translation of a "plasma spark". The length of such a channels can be up to few-cm and with a diameter of tens-of-micrometers. The mechanism and application of high-fluence fs fabrication in dielectrics is discussed.

**Keywords:** direct laser writing, dielectric breakdown, two plasmon decay instability, silica, light-induced damage threshold, microfabrication

## 1. INTRODUCTION

Microstructuring and microfabrication of materials by ultra-short 100-400 fs ( $1 \text{ fs} = 10^{-15} \text{ s}$ ) pulses find new fields of application, especially, where three-dimensional (3D) freedom of fabrication inside transparent solid<sup>1</sup> or liquid<sup>2</sup> material is necessary. At the same time, a full understanding of laser light-material interaction is still missing in the case of fs exposure. 3D microstructuring is elucidated even less than the ablation due to an inherent difficulty to apply such techniques as mass spectrometry and time-of-flight methods, which have been proven to be essential in the ablation studies.

Light induced damage threshold (LIDT) for a 3D microstructuring is usually defined as the light intensity (or fluence) necessary to generate critical density of electrons,  $N_{cr}$ .<sup>3</sup> The maximum free charge carriers concentration to be reached by optical excitation is defined by the plasmon frequency as  $\omega_{pl} = \sqrt{4\pi N_{cr} e^2 / (m_e m^*)}$ , where  $e$  is the electron charge,  $m^*$  and  $m_e$  are the gravity and effective mass of electron, respectively. When plasmon frequency is equal to that of laser irradiation, the material reflects the laser light (the reflection coefficient  $R \rightarrow 1$ ). This is true for the ideal case of homogeneous plasma and at right angle incidence. However, in the case on non-homogeneous plasma and in the presence of longitudinal light field along its propagation, as it is in the case of oblique incidence of  $p$ -polarization (or at tight focusing), the light energy can be further delivered to the plasma region. In fact, namely this principle is used in experiments on laser induced nuclear fusion experiments where longitudinal energy transfer from light to matter is implemented.

Definition of LIDT via  $N_{cr}$ , however, does not describe the nature of the phenomenon of *dielectric (optical) breakdown*, which is a total photoionization of focal volume via non-linear absorption processes. Technically LIDT can be defined as the intensity/fluence at which residual structural modifications of material is introduced. Obviously, this criterion of LIDT determination is dependent on the measurement technique used to examine the modification.

---

Author information for correspondence:

S.J.: E-mail address: saulius@eco.tokushima-u.ac.jp.

H.M.: Corresponding author. E-mail address: misawa@eco.tokushima-u.ac.jp. (fax: (+81) 88 656 7598)

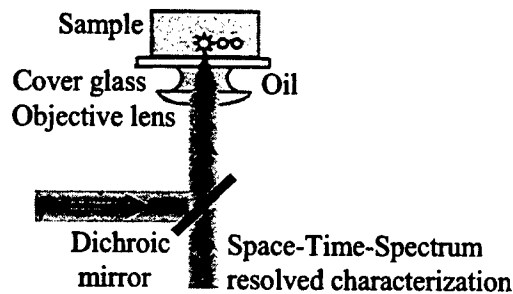


**Figure 1.** Principal setup of fabrication and characterization using a high numerical aperture,  $NA > 1$ , objective lens.

Here we describe an experiment aimed at fs microstructuring by fluencies corresponding to free carrier densities lower than  $N_{cr}$ . We examined a light emission from the irradiation spot during dielectric breakdown for a characterization of the breakdown. Also, the fabrication by a plasma spark scanned inside the glass is demonstrated. This technique allowed microstructuring on a mm-to-cm length scale.

## 2. EXPERIMENTAL

Fs-fabrication was carried out by amplified 150 fs pulses obtained from laser setup, which consists of Ti:sapphire *Tsunami* oscillator and regenerative (chirped pulse) amplifier *Spitfire*, both from *Spectra Physics*. The output power was about 500 mW at 1 kHz repetition rate. This radiation was delivered to sample under fabrication by focusing with (i) plano-convex lens or (ii) microscope (Fig. 1). The pulse energy at irradiation point was calculated and is specified where it applies. For a optical damaging with two consecutive fs-pulses we used an Mach-Zehnder-type interferometer setup to split and to combine coaxially two fs-pulses of perpendicular polarizations.<sup>4</sup> Microstructuring of transparent dielectric materials by fs-pulses using simple plano-convex lens focusing requires typically 20 – 200  $\mu\text{J}/\text{pulse}$  energies, while the microstructuring in the microscope needs just 10 – 100 nJ/pulse. More details on the setup can be found elsewhere.<sup>1</sup> We used silica (purified to have OH and Cl contamination lower than 100 ppm) and borosilicate glass BK7 for our experiments.

Spectral characterization of light emission from the irradiation spot (Fig. 1) observed at fluencies below and above that of dielectric breakdown was carried out by *Oriel* spectrometer, which was set to a side port of a microscope. In such a geometry (Fig. 1), the window for spectral observation was limited by the transmission of a dichroic mirror in the microscope (spectral profile is given in Fig. 2). Structural modifications of exposed glass were tested by their response to wet etching in BHF (49%HF with 100% $\text{NH}_4\text{F}$ ) water solutions.

## 3. RESULTS AND DISCUSSION

In this section we will, first, explore the possibility of microstructuring of silica at the irradiation intensities, which correspond to a free carrier plasma density  $N_{cr}/4$ , second, we will compare surface ablation with 3D optical damaging by the fabricated damage sizes, and, third, we will introduce a novel mechanism of microstructuring of glass by an ablation front, which was scanned into the bulk of sample, the “plasma spark” method. Fabricated channels were characterized by optical cross-polarized imaging and wet etching.

### 3.1. Generation of $3/2$ -frequency during dielectric breakdown

In order to reduce cost of fs-fabrication the attempts are made to decrease the LIDT of fabrication by, either, modification of glass by the doping of absorptive agents<sup>5</sup> or by quasi-cw exposure to fs pulses as it was demonstrated in the case of a waveguide recording in silica. The motivation is to avoid the use of regenerative amplifier, which increases the cost and complexity of microfabrication setup. This prompted us to examine the possibility to microstructure glass by irradiation, which correspond to the free carrier plasma densities less than  $N_{cr}$ . If such a microstructuring would be possible, the measurement of light emission spectrum observed during dielectric breakdown (or at a fluence below it) is expected to be a good tool to evaluate the density of electrons in plasma. Indeed, the presence of, so called,  $3/2\omega$  frequency should indicate the free carrier density of just  $N_{cr}/4$ .

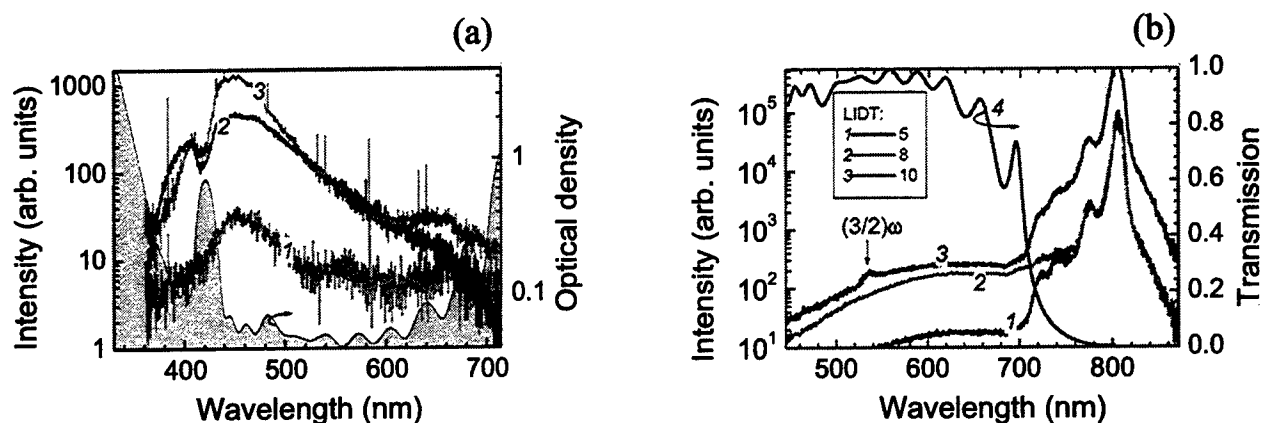


**Figure 2.** (a) Radiation spectra observed during an optical breakdown of silica by sub-ps pulses at different fluencies (background subtracted): by one pulse of  $0.5LIDT$  (1), at damaging by the two pulses separated by 30 ps  $LIDT(2) = 0.7 \times LIDT + 0.2 \times LIDT$  (2), and by one pulse at  $1LIDT$  (3). The transmission spectrum of microscope is given by a gray profile (right axis). Optical damage was made inside silica, pulse duration at the irradiation point was 0.35 ps for one-pulse and 0.45 ps for two-pulses irradiation, the wavelength 795 nm. (b) Spectra of light emission of optical breakdown from a focal point in silica at different fs-irradiation fluencies at 800 nm wavelength. The emission at  $3/2\omega$  (around 530 nm) is shown by arrow. Spectral profile of registration path in microscope is given on the right axis.

Strictly speaking the light emission below and above LIDT should be distinguished. At lower fluencies, below the LIDT, the emission is called white light continuum (WLC) or super-continuum (ps<sup>6,7</sup>; fs<sup>8,9</sup>), while at a dielectric breakdown the emission is caused by thermal plasma radiation (PR). Phenomenon of WLC can occur in a wide variety of transparent condensed media<sup>8,10</sup> and in gases.<sup>9</sup> The general characteristics of the femtosecond continuum are as follows: its spectral width depends on the medium in which is generated,<sup>11</sup> its spectrum is modulated,<sup>6</sup> its polarization is in the same direction as the polarization of the input pulse,<sup>11</sup> and its anti-Stokes frequency components lag temporally its Stokes components.<sup>8,12</sup> The fs-continuum exhibits a smaller beam divergence than the ps-continuum.<sup>9</sup> It is found that its anomalous divergence does not imply the absence of strong self-focusing but is rather due to a self-guiding mechanism that involves the Kerr effect.

Especially intriguing is the mechanism that determines its spectral width. Among the various mechanisms that have been suggested so far, we find self-phase modulation (SPM),<sup>6,8,13</sup> ionization-enhanced SPM,<sup>14</sup> and four-wave mixing.<sup>6,15</sup> It is at present generally believed that the main mechanism in fs-continuum generation is SPM enhanced by self-steepening of the pulse.<sup>7,13</sup> A shortcoming of this model is its prediction of a broader continuum in media with higher Kerr nonlinearity, a trend that is not observed<sup>7</sup> (the bandgap dependence dominates - large bandgap implies lower Kerr effect).

Experiments have shown that the power threshold for continuum generation coincides with the calculated critical power for self-focusing.<sup>9,16</sup> This is not surprising, considering that the onset of catastrophic self-focusing at critical power leads to a drastic increase in intensity, which can enhance SPM. This coincidence also suggests an intimate connection between the WLC and the mechanism that stops catastrophic self-focusing. Such a connection was first proposed by Bloembergen<sup>14</sup> to explain the ps-continuum. In his model, self-focusing is stopped by avalanche ionization; the appearance of free electrons enhances SPM and results in the continuum. A similar mechanism can be envisaged for fs-continuum generation in condensed media. In this case, an important mechanism of free-electron generation is multiphoton excitation (MPE).<sup>17</sup>

Figure 2 shows light emission collected from an irradiation spot inside silica at different fluencies (setup of experiment is given in Fig. 1). Transmission window of the microscope optics is given in (Fig. 2(a)) and, in fact, was limiting spectrally the emission, which was extending from UV-to-IR<sup>18</sup> under the direct measurement (not in microscope). An interesting result was that at the fluence of  $0.5LIDT$  the emission band around 470 nm was present. However, at the lower fluencies no WLC emission was observed in one or two-pulse experiments (for a time

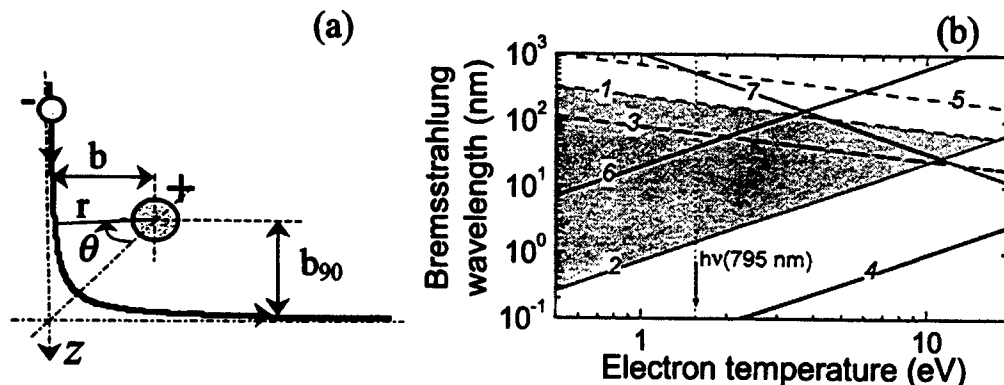


**Figure 3.** (a) Geometry of electron-ion collision. The impact distance is  $b$ , the right angle scattering length is  $b_{90}$ . (b) Approximate spectral extent of *bremsstrahlung* vs. free electron temperature for linear (1, 3, 5) and parabolic (2, 4, 6) electron collisions. The impact distance expressed in Si-O bond length is:  $b = 1$  (1, 2), 0.34 - (3, 4), and 3 - (5, 6). The line 7 marks the frequency where spectra due to linear collisions is overridden by that from parabolic ones. The gray region marks the main spectral content of radiation at impact distance  $b = 1$ .

separation between pulses 0-20 ps). This implies that microstructuring at fluencies, which correspond to a free carrier concentration (FCC) below  $N_{cr}$  is not possible.

Only at extremely high fluencies over 9LIDT we detected a weak emission of  $(3/2)\omega$  (Fig. 2(b)). Spectra in Fig. 2(b) were numerically deconvoluted from the transmission profile of microscope transmission (curve 4). This emission is a signature of parametric instability, known as  $3/2$ -frequency generation or two-plasmon decay (TPD).<sup>19</sup> This laser plasma instability occurs at a quarter critical density  $N = N_{ec}/4$ , which corresponds to the plasma wave at a plasmon frequency,  $\omega_p = \omega/2$ , where  $\omega$  is the cyclic frequency of laser irradiation. The impulse of the laser light scattered from such a plasma excitation,  $\mathbf{k}_s$ , can be matched by two plasma waves. As a result of impulse matching  $\mathbf{k}_s = \mathbf{k}_p + \mathbf{k}_p$ , the laser scattered light will possess the frequency component at  $3\omega/2$ . Also, the higher harmonic generation at half-harmonic frequencies  $\omega = (n+1)\omega$  is expected; here  $n$  is the integer. It was demonstrated that  $(3/2)\omega$  emission has a threshold at  $1 \times 10^{14} \text{ W/cm}^2$  in BK7 type glass (K8 in Russian nomenclature) and it depends on the driving pulse intensity,  $I_0$ , as  $I_{(3/2)\omega} \propto I_0^{3/2} T_e^{3/2}$ ,<sup>20</sup> where  $T_e$  is the electron temperature in plasma. In our case the  $3\omega/2$  emission corresponds to a 530 nm wavelength light, which was submerged into the broad emission band, the origin of which will be discussed below. Threshold intensity for  $(3/2)\omega$  emission in silica we found at  $1.6 \times 10^{14} \text{ W/cm}^2$ . It is worth to note that the  $0.1 \text{ PW/cm}^2$  light intensity is corresponding to the electron quiver (oscillating) energy of 6 eV for a linear polarization at  $0.8 \mu\text{m}$  wavelength according to the following scaling dependence<sup>21</sup>:

$$E_{osc}[\text{eV}] = 9.3(1 + \alpha^2) \frac{I}{10^{14}[\text{W/cm}^2]} (\lambda[\mu\text{m}])^2 \quad (1)$$

where  $\alpha = 1$  or  $0$  for the circular and linear polarizations, respectively. Threshold emission at  $(3/2)\omega$  corresponds to a 9.6 eV quiver energy, which almost perfectly coincides with the bandgap of silica at 9-10 eV.

The possible explanation of spectrally broad radiation can be understood in the frame of a free moving electron in the Coulomb field of an ion, what is known as the *classical bremsstrahlung* (German word for "braking radiation"). This is the most probable source of light emission since there is a poor compliance of silica luminescence bands with experimentally observed spectra during optical damage. Spectrally broad XUV-to-infrared radiation is expected from a free electron passing the ion due to its "braking". The hyperbola path of free electron in spherical coordinates  $r, \theta$  is given by formulas:<sup>22</sup>

$$r = \frac{b^2}{b_{90}(1 + \epsilon \cos \theta)}; \quad b_{90} = \frac{Ze^2}{4\pi\epsilon_0 m^* v^2}; \quad \epsilon = \sqrt{1 + \left(\frac{b}{b_{90}}\right)^2}, \quad (2)$$

where  $b$  is the impact distance,  $b_{90}$  is the distance at  $\theta = -\pi/2$  scattering,  $v$  is the velocity of an electron, and  $\epsilon$  is the eccentricity (Fig. 3(a)). The *bremsstrahlung* radiation is a direct consequence of an acceleration (or deceleration)



of charged particle; the radiated energy,  $W$ , per unit angular frequency is given by:<sup>22</sup>

$$\frac{dW}{d\omega} = \frac{e^2}{6\pi^2\epsilon_0 c^3} \left| \int_{-\infty}^{\infty} \dot{v} e^{i\omega t} dt \right|^2, \quad (3)$$

where  $\dot{v}$  is the acceleration of an electron. Spectral content of *bremsstrahlung* depends on the type of electron-ion collision. At first, let us consider free-free type encounters, where the incoming electron is not captured into an available electronic shell of an ion and is free after the collision. There are two types of collisions: the linear ones, when  $b \ll b_{90}$  and the parabolic at  $b \gg b_{90}$ , here  $b_{90}$  is the electron-ion distance at right angle scattering. The short wavelength edge of spectra for these two types of collisions is plotted in Fig. 3(b) for the different impact distance  $b$  as a function of electron energy. The value of  $b$  is expressed in terms of Si-O bond length (1.62 Å) to evaluate the possible radiation spectrum in silica. The distance of  $0.34 \times 1.62$  Å is, for example, the distance traveled by a free electron during the half of optical cycle at 795 nm wavelength (Fig. 3(b) lines 3,4). The radiation spectrum at this value of  $b$  could be considered as a light-induced "friction" of an electron with the ion, from which the electron was freed. At large value of  $3 \times 1.62$  Å the electron is moving in the field of an atom from the neighboring SiO<sub>3</sub> tetrahedron. Figure 3(b) qualitatively shows the extent of spectrum expected in the case of *bremsstrahlung*. As one can see the most blue-shifted spectrum is expected from parabolic collisions. The line 7 (Fig. 3(b)) demarks the spectrum caused by the linear collisions from that of parabolic ones and is given by  $v/b_{90}$ . At the electron energies larger than 1 eV the *bremsstrahlung* is expected to be caused mainly by parabolic electron-ion encounters due to the increased probability of inelastic scattering at the large electron energies.

The model of *bremsstrahlung* radiation qualitatively well explains the origin of continuum (in which part it is applicable to WLC and PR is still needs investigation). This is particularly appealing explanation for a continuum emission observed from the focal point of the size comparable with the wavelength, because in this case the length of light propagation in the photomodified region is extremely small, on the order of the Rayleigh distance, and there is no plausible explanation of spectral broadening due to the optical nonlinear effects (e. g. self-phase modulation (SPM) the longitudinal Kerr  $\chi^{(3)}$  effect), which could explain a spectral broadening of spectrum up to UV region for the laser wavelength of 795 nm.

Light emission during optical breakdown has a number of components, which can be separated by their time decays and characteristic emission bands. For example, a shock-compressed lime-glass at 110 GPa has an emission peak at 490 nm, which corresponds to a 5700 K temperature.<sup>23</sup> One could expect a contribution of fractoluminescence (FL)<sup>24,25</sup> to a radiation spectrum of optical damage in silica. The emission band at 650 nm in Fig. 2(a) could be actually caused by the FL as it was observed in similar low-OH-content silica.<sup>25</sup> This band is attributable to a non-bridging oxygen hole center (NBOHC). Typical time scale of FL is from  $\mu$ s-to-ms. Finally, a photo-luminescence (PL) is always present in a recorded spectrum of optical damage and can be distinguished by the corresponding bands. Usually, a long lasting PL spectrum of glass is spectrally similar to a FL. Apart of FL, which occurs during the crack formation and propagation as a result of recombination of excited state of defects or atoms (ions, molecules), the sonoluminescence<sup>26</sup> (SL) is expected to occur as well. This is a "milder" response of material to the optically driven shock wave propagating in solid media. The cause of SL is the recombination of separated charges during dislocation movement. Similar mechanism is applicable to the amorphous material such as silica and is expected to occur during the dielectric breakdown induced by sub-ps pulses.<sup>27</sup> SL might originate on the extended area as compared with the size of focal point of irradiation. Spectral form-factors of SL and FL are similar, what is caused by their origin on the recombination of charges separated on the defect sites. Also, the spiking emission from the atomic, ionic, and molecular species are usually present.

### 3.2. Power dependence of laser ablation of silica

For a Gaussian pulse/beam the ablation threshold can be determined from the following dependence:

$$A_{th} = A_0 \exp(-(D/w)^2), \quad (4)$$

where  $D$  is the diameter of crater,  $w$  is the diameter of beam at  $1/e$ -level, and  $A_{th}$  with  $A_0$  stands respectively for threshold and amplitude of the incident light expressed in terms of energy, fluence (energy density), or intensity. Figure 4 shows the data on laser ablation plotted along with predictions calculated by eqn. 4. The diameter of crater measured by atomic force microscopy (AFM) was found following eqn. 4 in terms of fluence (Fig. 4(b)) much better than in terms of pulse energy (Fig. 4(a)). It was found that surface ablation took also place at pulse energies

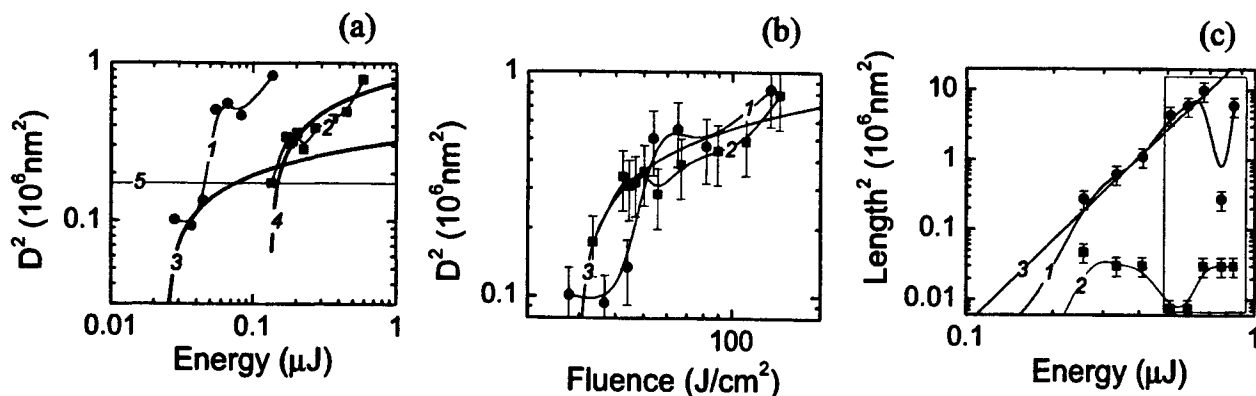


**Figure 4.** The dependence of the ablation crater diameter,  $D$ , on incident pulse energy (a) and fluence (b) for an ablation by a single pulse at  $\lambda = 400$  nm (1) and at 800 nm (2). Curves 3 and 4 are plotted by eqn. 4 with  $w = 1.1\lambda$ . Curve 5 depicts an *in situ* observable LIDT in optical transmission microscope. Curve 3 in (b) was plotted by eqn. 4 with  $w = 0.92\lambda$ . The values of  $D$  were measured by AFM.

(c) Axial (1) and lateral (2) lengths of a voxel (an optical damage site) evaluated from optical microscopy (diffraction limit subtracted). Line 3 depicts a dependence  $\text{Length} \propto \text{Energy}^2$ . Curves are plotted to guide the eye.

lower than the detection limit in microscope observation, which is given by line 5 in Fig. 4(a). The fact that the damage fluence for  $D = 0.1 - 0.4 \mu\text{m}$  was slightly larger at  $\lambda = 400$  nm than that at 800 nm can be explained by the established dependence for surface damage intensity  $I_{\text{damage}} \propto 1/\sqrt{\text{SpotArea}}$ .<sup>28</sup> This dependence describes, in fact, the importance of diffraction losses in the case of tight focusing into spot size with diameter close to  $\lambda$ . Recently, we reported similar LIDT dependence for an in-volume microstructuring of silica<sup>29</sup> found at tight focusing by  $NA = 1.35$  objective lens, when the wavelength of fs pulses was changed from 400 nm to 800 nm.

We imaged the voxel (an optical damage site) in an optical microscope and the axial and lateral sizes were found not obeying eqn. 4 (Fig. 4(c)), as it was in the case of surface ablation (Fig. 4(a-b)). Instead, the axial length was found following  $\propto \text{Energy}^2$  dependence for the voxels fabricated by an objective lens with  $NA = 1.35$  till the cracking point marked by a boxed region in Fig. 4(c). The lateral size was not considerably changing with the pulse energy. Figure 4(c) shows data presented in the form comparable with the surface ablation given in Fig. 4(a-b). This observation can be explained by the focal intensity distribution of a Gaussian pulse, which decays laterally as  $\exp(-\text{radius})$ , while axially as  $z^{-2}$ , where  $z$  is the distance from the focus. This eventually defines a focal region as a cylinder, what was observed experimentally examining voxels.

This shows that the spatial intensity distribution of the pulse are defining the feature sizes in both surface ablation and 3D microstructuring.

### 3.3. 3D fabrication by ablation: the "plasma spark" method

Here we introduce a new method of microstructuring of transparent solid materials by fs pulses. Fs-pulses are focused on the exit plane of the sample using plano-convex lens of focal length  $f = 20 - 100$  mm. The amplitude of the electric field,  $E$ , on the exit plane is larger by a factor  $2n/(n+1)$  as that on the entrance plane, here  $n$  is the refractive index of sample. If we disregard the absorption and reflection of the sample, which is low for transparent dielectrics in visible-to-near-infra-red spectral region, the enhancement up to 20% can be obtained for typical glasses (silica-based or polymers) with  $n = 1.5$ . The nature of enhancement is in the phase of reflected light, which undergo a phase shift of  $\pi$  for the entrance plane, since the light travels from the lower into the higher refractive index material. At the exit plane, there is no phase shift. This causes the total E-field at the entrance surface to be, usually, lower than that on the exit. When the intensity of ablation at the rear plane is reached, the ablation plume is visible (Fig. 5). The ablation front was scanned slowly, typically at  $5-20 \mu\text{m/s}$  inside the sample. This fabrication could be called microstructuring by "plasma spark".

This method is different from microstructuring by self-focusing,<sup>30</sup> where the waist of the beam is at the entrance surface. Moreover, self-focusing would not allow to make microstructuring just a the surface, since a close presence

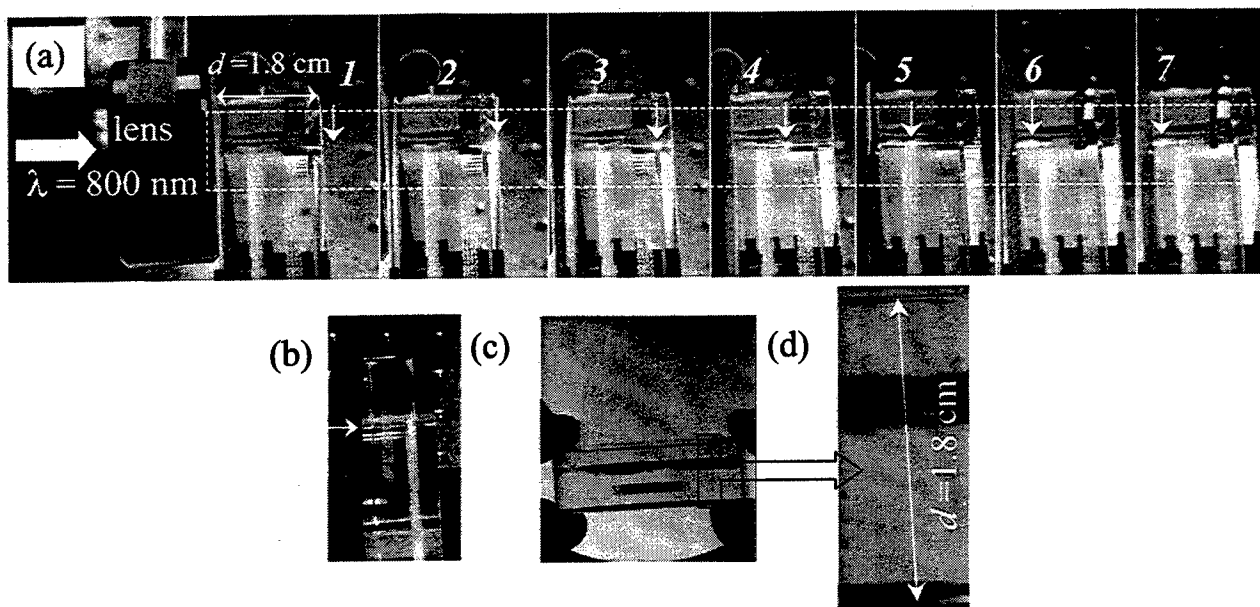


**Figure 5.** (a) Series of images (1-7) during “plasma spark” scanning throughout a 1.8 cm thick BK7 glass sample. Image 1 correspond to a focus location (pointed to by an arrow) just beneath the exit plane (a starting point for fabrication); 2 - at the exit and entrance planes, respectively. (b) Fabricated channel was imaged in the scattering light of introduced laser beam at 532 nm. (c) Image of the coloration of glass along the fabricated channel. (d) Close-up look at the coloration region of channel.

of the boundary disturbs the necessary conditions for self-focusing as we found in our experiments.

We applied this principle for a large-scale ( $10^1 - 10^4 \mu\text{m}$ ) 3D microfabrication of borosilicate glass, technical grade of BK7. The fabrication of a channel was photographed and is shown in Fig. 5(a). Series 1  $\rightarrow$  7 of images shows the translation of a “plasma spark”, which location is pointed to by an arrow. The bluish light emission at  $\simeq 365 \text{ nm}$  observed to the left of an arrow (Fig. 5(a)) is caused by photoluminescence (PL) of L-centers, which defines an absorption edge of silicate glasses at 213 nm (5.8 eV).<sup>31</sup> This type of PL emission is only present for an intrinsic absorption of glass. Orange light seen to the right of arrows (Fig. 5(a)) is a signature of the light, caused by a “plasma spark”, which was scattered on the walls of the just fabricated micro-channel. Similar results of microfabrication were obtained in the case of plastic acrylic glass.

An post-fabrication observation showed that a channel of 80 – 100  $\mu\text{m}$  in diameter was fabricated throughout almost 2 cm length of glass as shown in Fig. 5(b). Coloration of BK7 glass along the channel was clearly seen (Fig. 5(c-d)). This type of color center formation with absorption bands centered at 310 nm (4.0 eV), 440 nm (2.82 eV), and 640 nm (1.94 eV) is known to appear only at exposures to a light corresponding to the bandgap or shorter wavelengths absorption (including ionizing  $\gamma$ - and X-rays), also, to the absorption of high energy particles (electrons, neutrons,  $\alpha$ -particles). These color centers can be annealed at 100 – 200°C (a coloration disappears).

It was found that the optically damaged regions in borosilicate glass BK7 are etched much slower in BHF solution. This is, most probably, caused by the densification of glass around the channel. Even a presence of the defects, which had caused the coloration of glass, was not in favor of faster etching. However in pure silica, the etching contrast of optically damaged and fresh silica was such, that the 3D-channel fabrication was possible as we reported earlier.<sup>32</sup> The difference could be explained by the internal stress distribution around the damaged spots as presented in Fig. 6 by cross-polarized imaging along the channel. The stress was found highly localized around the channel in pure silica and was distributed much wider in the case of borosilicate glass. Further studies are planned to elucidate this mechanism.

Presence of densification under optical damaging with fs-pulses was also inferred from Raman scattering data. To assess the structural modifications of silica the Raman spectrum was measured from a sample optically damaged by

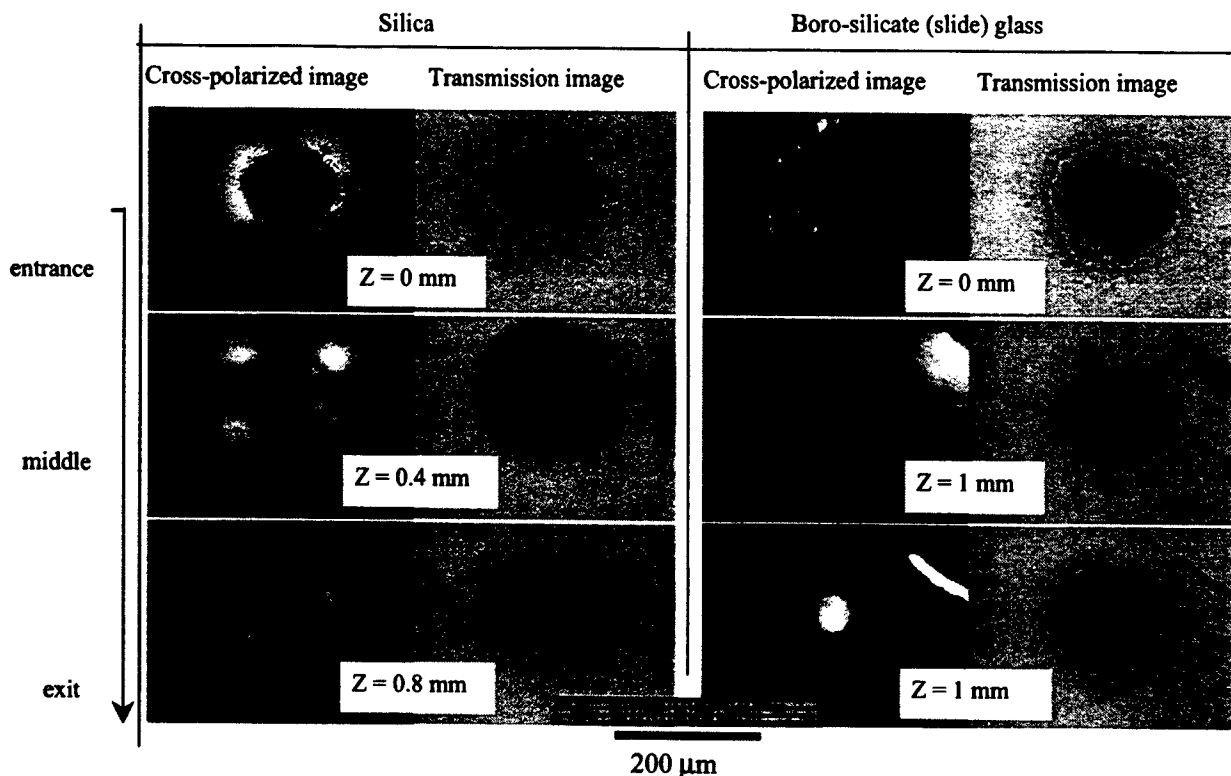


**Figure 6.** Cross-polarized and transmission images of optically damaged channels in silica (*Sumitomo*) and boro-silicate slide glass (*Matsunami*). Focusing was made on the exit plane using a plano-convex lens with focal length of  $f = 25$  mm. Then, the ablation plasma was transferred into the sample by translation along the beam propagation with approximate velocity of 0.2 mm/s. Laser power was 280 mW at 1 kHz repetition rate. The wavelength was 800 nm.

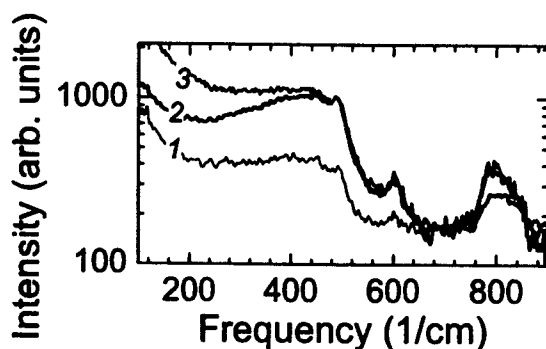


**Figure 7.** Raman spectra of silica before (1 for VH and 2 for VV polarization) and after (3 VH-pol.) optical damaging. Fluorescence background subtracted.

a single shot irradiation per voxel. Four layers of voxels with an average inter-voxel distance of 3  $\mu\text{m}$  was recorded in a 150  $\mu\text{m}$ -thick silica plate on the area of  $4 \times 4$  mm<sup>2</sup>. The spectra from damaged and fresh material are plotted in Fig. 7 (VV and VH denotes vertical-vertical and vertical-horizontal polarizations of illumination-detection setup, respectively). The band  $D_1$  at 495  $\text{cm}^{-1}$  is related to the regular puckered 4-ring structure vibrations and the  $D_2$  band at 606  $\text{cm}^{-1}$  is due to planar 3-ring vibrations, and 800  $\text{cm}^{-1}$  band is due to collective, network, vibrations.<sup>33</sup> One can see, that the 4-ring structure vibrations have been decreased in intensity by a factor of 1.47 in comparison

with those of 3-membered rings, while the network vibrations were left almost unchanged. This points out that the bond breaking was taking place during optical damaging in favor of more dense 3-membered ring structures.

In the case of silica, the LIDT energy for 3D microstructuring was 24 nJ at a 50  $\mu\text{m}$  depth. We can evaluate the corresponding total Si-O bond energy stored in the irradiated volume. Si-O bond energy is 432 kJ/mol and mass density of silica is 2.2 g/cm<sup>3</sup>. The volume of focus can be approximated by the volume of cylinder, which height is twice the Rayleigh length,  $2z_0$ , and the radius of a base is the waist of the beam  $w_0$ . This gives the energy stored in Si-O bonding in the focal region to be 7.6 nJ. It means, when the chemical bonding energy comprises 29% of that in the light field, the LIDT is reached in silica. This is just a bit larger than the Lindeman melting criterion,  $x$ . For the most of materials  $0.20 \leq x \leq 0.25$ , what means that the melting starts when the time average deviation of an atom's position in respect to its equilibrium state comprises a value  $x$  of the interatomic distance.

#### 4. CONCLUSIONS

We found that emission of  $3/2\omega$  radiation was observed in silica at irradiation intensity higher than  $1.6 \times 10^{14} \text{ W/cm}^2$ . Spectrally broad band emission observed at fluencies around optical breakdown can be qualitatively explained by classical *bremsstrahlung*. Large scale mm-to-cm 3D microstructuring of transparent materials can be achieved by using a novel, "plasma spark" method, which was successfully applied for microstructuring of silica, borosilicate, and acrylic glasses.

#### ACKNOWLEDGMENTS

This work was in part supported by the Satellite Venture Business Laboratory of the University of Tokushima. The authors are grateful for BK7 glass samples to Dr. O. Efimov. The discussions with Dr. A. Rode, Dr. M. Richardson and Dr. D. Ashkenasi are highly appreciated. We would like to acknowledge a collaboration with Dr. N. Novomlntsev for the Raman scattering measurements.

#### REFERENCES

1. M. Watanabe, H. Sun, S. Juodkazis, T. Takahashi, S. Matsuo, Y. Suzuki, J. Nishii, and H. Misawa, "Three-dimensional optical data storage in vitreous silica," *Jpn. J. Appl. Phys.* **37**(12B), pp. L1527-L1530, 1998.
2. M. Miwa, S. Juodkazis, T. Kawakami, S. Matsuo, and H. Misawa, "Femtosecond two-photon stereo-lithography," *Appl. Phys. A* **73**, pp. 561-566, 2001.
3. C. Quiox, G. Grillon, A. Antonetti, J.-P. Geindre, P. Audeberet, and J.-C. Gauthier, "Time-resolved studies of short pulse laser-produced plasmas in silicon dioxide near breakdown threshold," *Eur. Phys. J. AP* **5**, pp. 163-169, 1999.
4. S. Juodkazis, A. Marcinkevicius, M. Watanabe, V. Mizeikis, S. Matsuo, and H. Misawa, "Sub-picosecond optical damaging of silica: time resolved measurements of light induced damage threshold," in *Proc. SPIE vol. 4347, Laser-induced damage in optical materials: 2000*, G. J. Exarhos, A. H. Guenther, M. R. Kozlowski, K. L. Lewis, and M. J. Soileau, eds., pp. 212-222, 2001.
5. K. Yamasaki, S. Juodkazis, T. Lippert, M. Watanabe, S. Matsuo, and H. Misawa, "Dielectric breakdown of rubber materials by femtosecond irradiation," *Appl. Phys. A*, 2002. (In press).
6. R. R. Alfano and S. L. Shapiro, "Emission in the region 4000 to 7000  $\text{\AA}$  via four-photon coupling in glass," *Phys. Rev. Lett.* **24**, p. 584, 1970.
7. R. R. Alfano, *The Supercontinuum laser source*, Springer-Verlag, New York, (1989).
8. R. L. Fork, C. V. Shank, C. Hirlimann, R. Yen, and W. J. Tomlinson, "Femtosecond white-light continuum pulses," *Opt. Lett.* **8**, p. 1, 1983.
9. P. B. Corkum, C. Rolland, and T. Srinivasan-Rao, "Supercontinuum generation in gasses," *Phys. Rev. Lett.* **57**(18), pp. 2268-2271, 1986.
10. A. Brodeur, F. A. Ilkov, and S. L. Chin, "Beam filamentation and the white light continuum divergence," *Opt. Comm.* **129**, p. 193, 1996.
11. Q. Z. Wang, P. P. Ho, and R. R. Alfano in *ref. 6*, pp. 39-90.
12. Q. X. Li, T. Jimbo, P. P. Ho, and R. R. Alfano, "Temporal distribution of picosecond super-continuum generated in a liquid measured by a streak camera," *Appl. Opt.* **25**, p. 1869, 1986.
13. G. Y. Yang and Y. R. Shen, "Spectral broadening of ultrashort pulses in a nonlinear medium," *Opt. Lett.* **9**(11), p. 510, 1984.
14. N. Bloembergen, "Influence of electron plasma formation on superbroadening in light filaments," *Opt. Comm.* **8**(4), p. 285, 1973.
15. A. Penzkofer, "Parametrically generated spectra and optical breakdown in H<sub>2</sub>O and NaCl," *Opt. Comm.* **11**(3), p. 275, 1974.

16. F. A. Ilkov, L. S. Hkova, and S. L. Chin, "Supercontinuum generation versus optical-breakdown in CO<sub>2</sub> gas," *Opt. Lett.* **18**, p. 681, 1993.
17. Q. Feng, J. V. Moloney, A. C. Newell, E. M. Wright, K. Cook, P. K. Kennedy, D. X. Hammer, B. A. Rockwell, and C. R. Thompson, "Theory and simulation on the threshold of water breakdown induced by focused ultrashort laser pulses," *IEEE J. Quantum Electron.* **33**(2), p. 127, 1997.
18. H. Misawa, S. Juodkazis, S. Matsuo, V. Mizeikis, and A. Marcinkevicius, "Advantages and shortcomings of femtosecond laser microfabrication," in *Proc. 2002 Japan-USA Symp. on Flexible Automation*, 2002. (In press).
19. *Plasmas and Fluids*, Series: Physics through the 1990s, National Academy Press, Washington, D. C. Panel on the Physics of Plasmas and Fluids and Physics Survey Committee and Board on Physics and Astronomy and Commission on Physical Sciences, Mathematics, Resources and National Research Council, 1986.
20. A. A. Babin, A. M. Kiselev, K. I. Pravdenko, A. M. Sergeev, A. N. Stepanov, and E. A. Khazanov, "Experimental investigation of the influence of subterawatt femtosecond laser radiation on transparent insulators at axicon focusing," *Physics-Uspeski* **42**(1), pp. 74-77, 1998.
21. E. G. Gamaly, A. V. Rode, V. T. Tikhonchuk, and B. Luther-Davies, "Ablation of solids by femtosecond lasers: ablation mechanism and ablation thresholds for metals and dielectrics," *Phys. Plasmas*, 2002. (In press).
22. I. H. Hutchinson, *Principles of Plasma Diagnostics*, Cambridge University Press, New York, 1987.
23. T. Kobayashi, T. Sekine, O. V. Fat'yanov, E. Takazawa, and Q. Y. Zhu, "Radiation temperatures of soda-lime glass in its shock-compressed liquid state," *J. Appl. Phys.* **83**(3), pp. 1711-1718, 1998.
24. Y. Kawaguchi, "Time-resolved fractoluminescence spectra of silica glass in a vacuum and nitrogen atmosphere," *Phys. Rev. B* **52**, pp. 9224-9228, 1995.
25. Y. Kawaguchi, "OH-content dependence of fractoluminescence spectra in silica glass," *Phys. Rev. B* **54**, pp. 9721-9725, 1996.
26. I. V. Ostrovskii, O. A. Korotchenko, T. Goto, and H. G. Grimmeiss, "Sonoluminescence and acoustically driven optical phenomena in solids and solid-gas interfaces," *Phys. Rep.* **311**(1), pp. 1-46, 1999.
27. X. Wang and X. Xu, "Thermoelastic wave induced by pulsed laser heating," *Appl. Phys. A* **73**, pp. 107-114, 2001.
28. W. Koechner, *Solid-state laser engineering*, Springer, Berlin, Heidelberg, 1999.
29. S. Juodkazis, M. Horiyama, M. Miwa, M. Watanabe, A. Marcinkevicius, V. Mizeikis, S. Matsuo, and H. Misawa, "Stereolithography and 3D microstructuring of transparent materials by femtosecond laser irradiation," in *Proc. SPIE of Int. Conf. on Laser and Laser Information Technologies (ILLA 2001)*, 23 - 25 June 2001, Vladmir, Russia., 2002. (In press).
30. D. Ashkenasi, H. Varel, A. Rosenfeld, S. Henz, J. Herrmann, and E. E. B. Campbell, "Application of self-focusing of ps laser pulses for three-dimensional microstructuring of transparent materials," *Appl. Phys. Lett.* **72**(12), pp. 1442-1444, 1998.
31. L. B. Glebov, "Optical absorption and ionization of silicate glasses," in *Proc. SPIE vol. 4347, Laser-induced damage in optical materials: 2000*, G. J. Exarhos, A. H. Guenther, M. R. Kozlowski, K. L. Lewis, and M. J. Soileau, eds., pp. 343-356, 2001.
32. A. Marcinkevicius, S. Juodkazis, M. Watanabe, M. Miwa, S. Matsuo, H. Misawa, and J. Nishii, "Femtosecond laser-assisted three-dimensional microfabrication in silica," *Opt. Lett.* **26**(5), pp. 277-279, 2001.
33. R. A. Barrio, F. L. Galeener, E. Martinez, and R. J. Elliott, "Regular ring dynamics in AX<sub>2</sub> tetrahedral glasses," *Phys. Rev. B* **48**(21), pp. 15672-15689, 1993.

# Processing of multi-layer systems using femtosecond, picosecond, and nanosecond laser pulses at different wavelengths

David Ashkenasi<sup>\*a</sup>, Arkadi Rosenfeld<sup>\*\*b</sup>

<sup>a</sup>Laser- und Medizin-Technologie GmbH, Berlin, Germany;

<sup>b</sup>Max Born Institut, Berlin, Germany

## ABSTRACT

We performed ablation studies on multi-layer systems at different wavelength – pulse duration combinations. The multi-layer systems of interest, 150 nm thin indium tin oxide (ITO), 200 nm thin polyaniline (PANI) on 1  $\mu$ m thick photo resist, and 280 nm PPV/pedot layer-combination on 150 nm thin ITO are optically transparent and used for a variety of industrial applications. One important goal of the study was to determine the possible process window for a complete removal of only the top layer, leaving the remaining layer basically unharmed. The investigations were conducted with the following wavelength – pulse duration combinations: 800 nm and 180 fs, 800 nm and 5 ps, 266 nm and 150 fs, 266 nm and 5 ns, 532 nm and 5 ns. We generated micro dots, lines and areas to determine the damage threshold, the processing quality and the processing speed for the specified application of selective layer removal. The structures were analyzed by means of optical and atomic force microscopy. In some cases, we observed a strong pulse duration dependence in the ablation threshold, an indication for the observed difficulties using laser pulses in the ns range. Comparative studies at different wavelengths demonstrate that laser pulses in the UV are not necessarily always a first choice to achieve a precise removal of the optically transparent top layer.

**Keywords:** laser processing, damage threshold, ultra-short pulses, multi-layer, transparent thin films

## 1. INTRODUCTION

Micro-structuring of transparent conductive materials, such as thin indium tin oxide (ITO) films, is generally carried out by wet etching, requiring photolithography. As a parallel process, wet etching offers high process yields. However, the performance of wet etching critically depends on the properties of the material to be etched, i.e. crystallinity and microstructure. This imposes stringent limitations, which are enhanced for multi-layer systems, where only the top layer should be processed. Plasma etching also demonstrates similar disadvantageous in these cases. Therefore, direct-write laser patterning without the need of photolithography may offer an alternative and/or complementary solution.<sup>1,2</sup>

The availability of ultra short, sub-ps, pulsed lasers has stimulated a growing interest in exploiting the enhanced flexibility of femtosecond technology for micro-machining. Ultra short laser pulses offer a variety of advantages for precision micro-fabrication. Due to lower energetic thresholds for sub-picosecond ablation and the controllability of individual laser pulses (e.g. by laser pulse duration) the amount of energy deposited into the processed sample can be minimized and highly localized. This leads to a reduction of unwanted thermal effects, a minimization of energy diffusion, that may be exploited for the selective removal of thin transparent films. Main goal of this study is to determine possible wavelength and pulse duration dependencies at laser processing of three different model systems of transparent thin films. This included a first-time determination of a laser process window for PANI on photo-resist and PPV/pedot on ITO.

---

Corresponding author: \* [d.ashkenasi@lmtb.de](mailto:d.ashkenasi@lmtb.de); phone: +49 30 67053-6; fax: +49 30 67053-500; <http://www.lmtb.de>; Fabeckstr. 60-62, D-14195 Berlin, Germany; \*\* [rosenfeld@mbi-berlin.de](mailto:rosenfeld@mbi-berlin.de); phone: +49 30 6392-1214; fax: +49 30 6392-1229; <http://www.mbi-berlin.de>; Max Born Str. 2a, D-12489 Berlin, Germany.

## 2. EXPERIMENT

The experimental setup for the investigations on laser processing of three transparent multi-layer systems (I-III) is shown schematically in Figure 1a and 1b. Table 1 compiles the laser parameters of the laser systems (A-E) and optical configurations used in the experiments. In order to vary the pulse energy on the target different methods have been chosen. In the case of system A and B the variation was accomplished by means of an attenuator. To reduce the pulse energy of system C the frequency triplication crystal was detuned. For the matter of system D neutral density filters were positioned in the beam path to reduce the irradiation of the target. In the case of system E a change of the q-switch delay setting lead to a variation of the pulse energy. The shutter was used for single laser shot control, i.e.  $N$  on 1 damage threshold studies, where  $N$  specifies the number of shots placed on the same spot under identical conditions at a repetition rate of 1-10 Hz. Best form fused silica lenses with a focal length of either 75 and 150 mm (see Table 1) focused the laser beam on the multi-layer samples, that are specified in Fig. 1b. In addition, the low-power cw He-Ne laser light illuminated the region of interest on the sample to monitor possible changes in surface roughness during the (multi) pulsed processing. In situ inspection was achieved by enlarged visualization of the (pulsed laser activated) surface by combination of far field microscope, CCD-camera and video monitor. This allowed for an on-line estimation of the damage threshold, which were determined with higher precision using ex situ methods, as discussed in the next section.

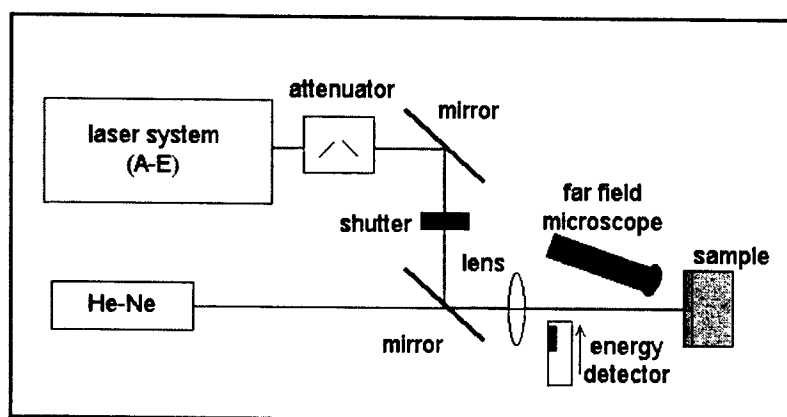


**Fig. 1: a)** Schematic illustration of the experimental set-up for the laser structuring studies on transparent multiplayer samples with stray-light monitoring of the sample surface with a far field microscope device. The dielectric mirrors were chosen appropriately for the different wavelengths 800 nm, 532 nm and 266 nm, in connection with the laser systems used (see also Table 1).

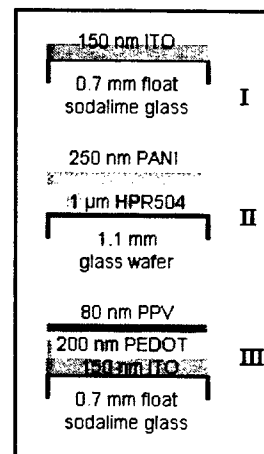


**Fig. 1: b)** Schematic illustration of the three different multi-layer systems (sample type I-III) on glass substrate.

The samples, schematically depicted in Fig. 1b, are I: 150 nm thin indium tin oxide (ITO) on 0.7 mm float glass, II: 200 nm thin polyaniline (PANI) on 1  $\mu$ m thick photo-resist (HPR504) on 1.1 mm thick glass wafer, and III: 80 nm PPV on 200 nm pedot on 150 nm ITO on 0.7 mm float glass. The sample fabrication was supervised and characterized at the Philips Centre for Industrial Technology.

The technical importance and electrical properties of these layers will be not discussed in the frame of this paper. We focus our study primary on the principle questions concerning laser processing and selective removal of transparent thin layers, using samples I-III as model systems. The optical properties, specifically reflectivity and transmission, of our single and multi-layer samples were determined experimentally between 250 and 1100 nm using a Perkin Elmer UV/VIS spectrometer Lambda 12. In order to determine the reflectivity the samples were illuminated under an angle of 8 degrees. The reflected light was integrated in an Ulbricht ball. The amount of the reflected light was compared to a reference measurement carried out with a labsphere SPS-99-010 reference plate. In order to get absolute reflection values the relative reflection values were multiplied with the known reflection spectrum of the reference plate. Table 2 compiles the reflectivity  $R$  and the calculated absorption  $A$  each for the glass substrate, ITO on glass, PANI on glass, photo-resist on glass, and finally PPV/pedot on ITO on glass for the UV, green and IR light used in our experiments.



Following interesting notes can be made based on the results in Table 2, which is of importance for the further discussion in section 3:

- ITO on glass demonstrates a pronounced increase in linear absorption from 532 to 800 nm, especially compared to the glass substrate alone.
- PPV/pedot on ITO on glass shows a significant absorption at 532 nm and 800 nm, compared to ITO on glass, where at 532 nm the layer can be characterized as transparent.
- PANI on glass has a high absorption of 55 % at 800 nm compared to photo-resist on glass of < 1 % (no significant change to glass substrate alone). The difference in absorption for the PANI on glass compared to photo-resist on glass is less dramatic at 532 nm. At 266 nm the situation is practically identical for both layer systems (and for the glass substrate).

	system A	system B	system C	system D	system E
laser	Oscillator: Spectra Physics Ampilfier: Quantronix		Multi pass amp.**	Continuum I-10	
laser type	Ti:Sapphire	Ti:Sapphire	Ti:Sapphire	freq. doubled Nd:YAG	freq. quadr. Nd:YAG
wavelength [nm]	800	800	266	532	266
pulse duration	180 fs	5.1 ps	150 fs	5 ns	5 ns
pulse repetition rate [Hz]	100*	100*	10	10	10
Applied single pulse energy [ $\mu$ J]	$\leq 3.6^*$	$\leq 12.6^*$	$\leq 10$	$\leq 400$	$\leq 90$
focal length [mm]	75	75	150	150	150
1/e <sup>2</sup> focus size [ $\mu$ m]	29x39 elliptical	29x39 elliptical	59x118 elliptical	140x171 elliptical	68x86 elliptical
measured beam size on target [ $\mu$ m <sup>2</sup> ]	880 $\pm$ 80	880 $\pm$ 80	5500 $\pm$ 500	19000 $\pm$ 1000	4700 $\pm$ 300
depth of focus	>> thickness of multi-layer stack				
	* used in the experiment: alternatively 1 mJ/pulse at 1 kHz is possible				
	** developed at the Max Born Institute, Berlin, Germany				

**Table 1:** Experimental parameters of the ultra-short pulse (system A-C) and short pulse (system D+E) solid state lasers

Choosing the adequate wavelength is important but not necessarily sufficient to reach a satisfying machining result. If the thermal penetration depth exceeds the layer thickness of the top layer, its removal may also lead to the damage of the underlying layers. In this case we were interested if shorter pulses might offer remedy. Thanks to the substantially smaller thermal penetration depth of such ultra short laser pulses there is a potential, that even layers in the order of 100 nm thickness can be removed at high quality. The peak intensity of fs laser pulses is sufficient to induce non-linear absorption mechanisms that can significantly increase the density of free electrons up to a critical value for optical breakdown. Material that is ultimately transparent for a certain wavelength starts absorbing fs pulsed laser radiation at precisely that wavelength. In addition, it is interesting to compare the processing results of fs laser pulses at the wavelength of 800 nm and at 266 nm (UV), to determine if wavelength dependencies are actually less significant for ultra short laser pulses, as often claimed. Utilizing the five different wavelength – pulse duration combination we address the problem of precise localization of laser energy and the influence of combined linear and non-linear channels of photon absorption in the material.

	glass (1.1 mm)		ITO (150 nm) on glass (1.1 mm)		PPV/pedot (280 nm) on ITO (150 nm) on glass (0.7 mm)		PANI (200 nm) on glass (1.1 mm)		photo-resist (1 $\mu$ m) on glass (1.1 mm)	
wavelength	R [%]	A [%]	R [%]	A [%]	R [%]	A [%]	R [%]	A [%]	R [%]	A [%]
266 nm	10	90	40	60	10	90	10	90	15	85
532 nm	8	<<1	8	<1	18	10	7	25	7	18
800 nm	8	<<1	8	7	8	18	2	55	11	<1
"naked eye" impression	<i>neutral, transparent</i>		<i>very light grey, transparent</i>		<i>light yellow, transparent</i>		<i>yellow-green, transparent (PANI on photo-resist on glass)</i>			

**Table 2:** Optical properties compiled for different single and multi-layer systems given at the wavelengths 266, 532 and 800 nm and compared to the glass substrate. Also compiled is the "naked eye" impression of the multi-layer systems. The absorption  $A$  was calculated using following equation:  $A = 100 - R - T$ , where  $R$  and  $T$  is the experimentally obtained reflectivity and transmission in %, respectively.

### 3. RESULTS AND DISCUSSION

Characteristic for a process are threshold fluence values that define the inception of a certain occurrence. For laser ablation processes the most important threshold values are:

- A visible modification or roughening on the surface = damage threshold,
- Re-solidification of a liquid phase = melting threshold, and
- A loss of material inside the irradiated region = ablation threshold.

When functional conductive layers are structured there are mainly two methods to judge the result of the patterning process:

- Analyzing the surface topography of the irradiated area gives information on the geometrical quality of the generated structure. The ablation depth tells whether enough material been removed. The bottom roughness of the of the ablated zone related to the structure depth as well as the amount of debris lets one draw conclusions with regard to the suitability of the chosen process parameters.
- On the basis of local electrical resistance measurements it can be determined whether the patterned sample fulfills the given specifications.

Within this study only the surface topography of the laser structured patterns has been inspected, mainly for following reasons:

- The resistance between two points separated by a trench depends on the width of the trench and on how thoroughly the conductive layer has been removed. A high resistance requires therefore the ability to remove the conducting layer completely. To what extend this has been achieved can be determined by analyzing the shape of the irradiated area.
- The experiments carried out served mainly to determine which wavelength - pulse duration combinations is best suited to process the three sample layer systems. Based on the findings further experiments planned will determine the capability of the laser structuring process of the most promising wavelength - pulse duration combination based on functional design and performance.

Three inspection techniques have been applied in order to analyze the topography of the processed samples. To get an overview which parameter settings resulted in a modification or (partial) ablation of the targets they have been visually inspected with an optical microscope. For further information with regard to the topography of the irradiated spots atomic force microscope scans have been made for selected structures. This technique is appropriate for micro structures with lateral dimensions in the order of several  $\mu\text{m}$ . To get a broader view on the machining results, the laser processed areas of  $300\mu\text{m} \times 300\mu\text{m}$  have been scanned with an optical profiler.

The threshold values have been determined by surface inspection with aid of optical microscopy and atomic force microscopy. In addition, for a number of processed pockets at different laser fluence above the obvious threshold we determined the modified area. The size of the (visible) modification should follow the laser intensity distribution, provided the threshold level remains constant. A semi-logarithmic plot of the modified area versus laser fluence leads to an expected linear dependency for a Gaussian spatial intensity profile on the surface (at least for laser shot numbers  $N < 20 - 30$  and at modest fluence above threshold). The intersection of the linear fit with the energy axis yields threshold values that were in all cases in the expected fluence interval from former in situ stray light observations and rigorous ex situ microscopic inspections.<sup>3,4</sup> Table 3 compiles the single and multiple-shot damage threshold values in  $\text{mJ}/\text{cm}^2$  for the three different multi-layer samples at the five wavelength – pulse duration combinations. The characteristic threshold results of the individual multi-layer cases and possible implications for industrial processing are discussed in the following sub-sections 3.1 to 3.3.

wavelength / pulse duration combination	damage threshold [ $\text{mJ}/\text{cm}^2$ ]					
	I: ITO		II: PANI on photo-resist		III: PPV/pedot on ITO	
	$N = 1$	$N = 1000$	$N = 1$	$N = 1000$	$N = 1$	$N = 1000$
532 nm / 5 ns	$680 \pm 50$	$480 \pm 50$	$150 \pm 35$	$120 \pm 35$	$200 \pm 50$	$190 \pm 50$
266 nm / 5 ns	$380 \pm 50$	$330 \pm 50$	$180 \pm 35$	$150 \pm 35$	$170 \pm 35$	$90 \pm 35$
800 nm / 5 ps	$750 \pm 35$	$550 \pm 35$	$16 \pm 3$	$14 \pm 3$	$82 \pm 5$	$82 \pm 5$
800 nm / 0.2 ps	$235 \pm 25$	$180 \pm 25$	$16 \pm 3$	$16 \pm 3$	$51 \pm 5$	$43 \pm 5$
266 nm / 0.2 ps	$82 \pm 5$	$60 \pm 5$	$13 \pm 3$	$10 \pm 2$	$18 \pm 3$	$11 \pm 3$

**Table 3:** Single ( $N=1$  laser shot) and multiple ( $N=1000$  laser shots on identical area) damage threshold for the top layer of the three different multi-layer systems: **I:** ITO (on glass), **II:** PANI (on photo-resist), and **III:** PPV/Pedot combination (on ITO on glass) determined at five different wavelength-pulse duration combinations

### 3.1. ITO on glass

Comparing the damage threshold results for ITO on glass at 800 nm in Table 3, we observe an at least 3 fold increase in the threshold from 0.2 and 5 ps. To receive a better impression on possible pulse duration dependencies at laser wavelength 800 nm we performed additional threshold studies in the pulse duration interval between 0.2 and 5 ps. Fig. 2 illustrates the continuous increase in threshold with increasing pulse duration, a tendency observed at higher fluence level also for transparent dielectrics, e.g. glass or fused silica.<sup>5</sup> Specifically in the case of ITO (on glass), the results in Fig. 2 may be explained by a strong optical penetration depth due to the minor linear absorption coefficient at 800 nm. Additional localization of laser energy utilizing non-linear effects such as multi-photon absorption is more efficient at reduced pulse durations. The damage threshold for ultra short laser pulses at 800 nm is below one-third of that for the glass substrate (polished and uncoated). This ensures a wide fluence processing window for the removal of ITO from the glass substrate. When we compare the obtained damage threshold values for all of the 5 selected wavelength – pulse duration combinations the following can be concluded: 1. for all chosen material combinations the threshold fluence decreases with increasing number of laser pulses, 2. the threshold fluence decreases with the laser wavelength within the investigated range, and 3. the threshold fluence decreases with the laser pulse duration within the investigated range.

Atomic force microscope investigations of an array of pockets (or spots) - machined with different pulse energies and number of shots using 180 fs or 5 ps pulses at a wavelength of 800 nm - show the following: At a fluence of  $< 2 \text{ J/cm}^2$  the first shot roughens the surface. The second shot initiates the ablation, the 3<sup>rd</sup>-10<sup>th</sup> shot removes the remaining ITO from the glass surface. From AFM profile analysis we observe linear increase of ablated volume with increasing fluence. In other words applying ultra short laser pulses at 800 nm enables a partial removal of the 150 nm thin ITO layer, and this highly reproducible. Fig. 3 depicts an AFM analysis of ITO on glass processed with ultra short laser pulses at 800 nm. The fairly well-defined edges of the resulting 150 nm deep pocket (or spot) is outlined by a rim with thin wall ca. 30 nm high. We observe even a slight improvement in quality using sub-ps laser pulses at equal wavelength.

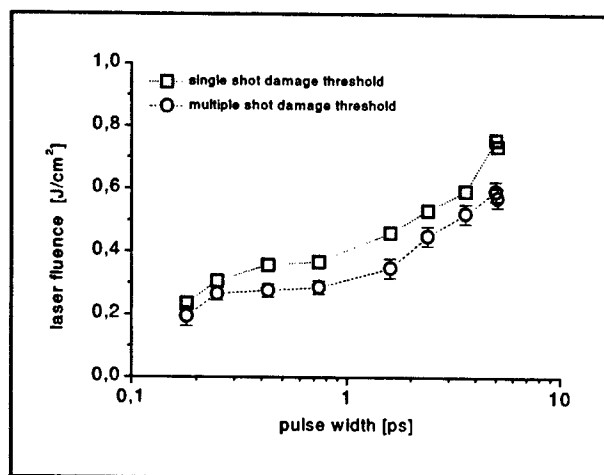


**Fig. 2:** Single and multiple shot damage threshold for ITO on glass at 800 nm as a function of laser pulse width.

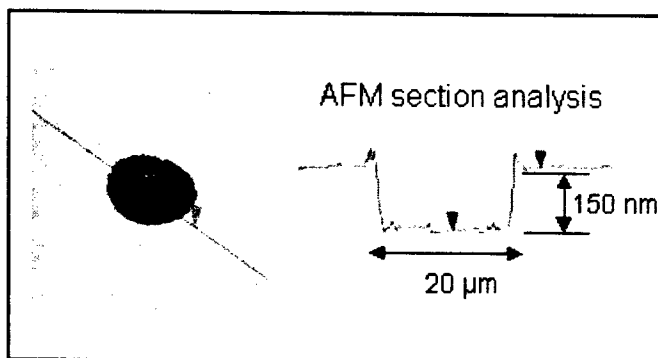


**Fig. 3:** AFM analysis of a laser-induced micro pocket after removal ITO layer using 10 laser pulses at the wavelength of 800 nm, the pulse width of 3.6 ps and a single laser pulse fluence of ca.  $1 \text{ J/cm}^2$ . The depth profile in the cross section (right) illustrates the quality of removal.

The damage threshold for ITO on glass for fs laser pulses in the UV is much lower than in the IR, see Table 3. It was expected that the combined linear and non-linear increase in absorption and, hence, theoretical reduction in optical penetration depth could improve the processing quality. For ITO on glass, however, the higher intensity stability of the ultra short laser pulses at 800 nm proved to be more important for this type of processing. Concerning the ns processing at 532 nm and 266 nm, in both cases the ITO layer could be removed from the glass substrate without damaging the glass. However, at ns processing we observed much debris around the processed area. Also, the rim surrounding the ns laser processed pockets, lines and areas is wider and higher, therefore of poorer quality as in ultra short pulse laser processing. In addition, processing at 266 nm and 5 ns more care has to be taken in the choice of laser fluence to avoid any multiple shot damage of the glass substrate. The fairly low threshold at 266 nm and 5 ns compared to ultra short laser pulses in the IR may be explained by phonon absorption at the glass-ITO interface, contributing to a thermal ablation process. This can be underlined by the fact that opposite to the ultra short laser pulses at 800 nm, a partial removal of ITO with laser light at 266 nm was not obtainable. This situation changed at 5 ns and 532 nm, where at modest laser fluence of  $530 \text{ mJ/cm}^2$  between the single and multiple shot threshold, also partial removal of 100 nm ITO was observed. In this case photon absorption in the glass is negligible and has little or no influence on the layer removal.

Based on the analysis (optical microscope, AFM and optical surface profiler) of the laser irradiated areas we conclude, that the material removal mechanism for all five wavelength - pulse duration combinations is (mainly) of thermal origin. Whether the UV ultra-short pulses also trigger a photochemical process is presently unclear and can not be answered without introducing additional in situ experimental techniques.

For ITO on glass we also performed processing experiments using only the oscillator system of the fs laser system. Focusing the fs laser pulses to a diameter below  $3 \mu\text{m}$  at a single pulse energy of only 10 nJ at a repetition rate of 80 MHz, we obtained a complete and very precise removal of ITO from the glass substrate at fluence levels around only  $100 \text{ mJ/cm}^2$ . This drop in processing threshold - compared to the 100 Hz application - seems to have its origin in the

reduced diffusion rate at 80 MHz processing, underlying our assumption of a predominate thermal activation in the material removal of ITO with fs laser pulses. However, to avoid any misunderstanding, the high peak power of the low-energy fs laser pulses is an absolute necessity to achieve a minimal free-electron plasma density as precursor for additional (thermal) photon absorption on the surface (or inside) the transparent layer. This case of localized energy accumulation is comparable to the fs high repetition laser-induced plasma reactions and modifications reported in bulk glass and fused silica at single pulse energies below 100 nJ.<sup>6</sup>

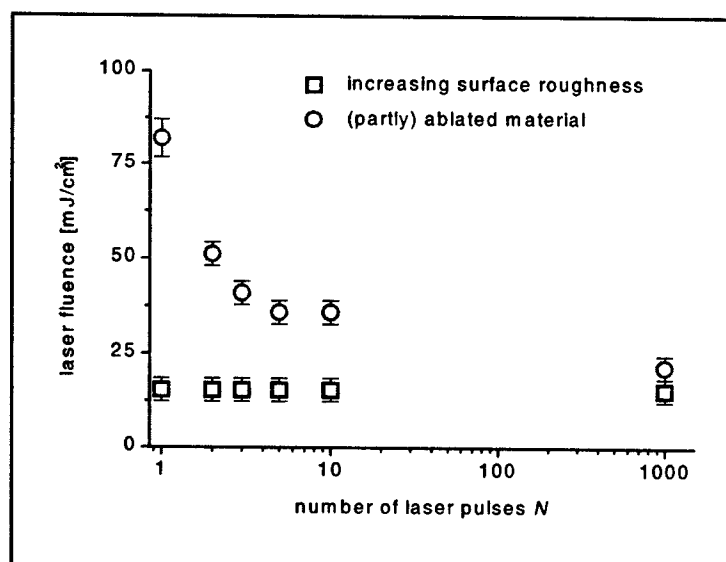
### 3.2. PANI on photo-resist

Figure 4 depicts the threshold fluence for modification (damage) and ablation of PANI on photo-resist at laser wavelength of 800 nm and a pulse duration of 0.2 ps. The former appears to be independent of the number of laser pulses. Contrary the ablation threshold drops sharply between 1 and ten laser pulses. As the laser fluence is reduced below 20 mJ/cm<sup>2</sup> (1/4 of the single shot threshold fluence for ablation) no ablation is observed even at a very high number of laser pulses. Laser pulses with a fluence in an interval between the single shot fluence for ablation and the damage threshold for modification lead to a roughening of the surface and, hence, to an increase of absorption at 800 nm and to a lower threshold for ablation. The damage and ablation threshold for 800 nm and 5 ps laser pulses show an almost identical behavior. In opposite to the ITO on glass substrate, threshold values are far less dependent on the pulse duration in the fs and ps range. Concerning the 5 ns laser pulses at 532 and 266 nm, we obtained a pronounced 10 fold increase in damage threshold for the PANI layer on photo-resist on glass. Actually, this difference in threshold between fs/ps and ns laser pulses is surprising, taking the absorption properties into account. However, the combination of linear absorption at 800 nm and non-linear ionization channels using ultra short pulses leads obviously to a very efficient photon energy input into the PANI layer.

Fig. 5 depicts six processing examples of PANI on photo-resist on glass using ultra-short laser pulses at 0.2 ps and 800 nm. The top left laser-induced modification at 44 mJ/cm<sup>2</sup> and  $N = 1$  laser shot demonstrates a first roughening of the surface in an fluence level between the damage and ablation threshold. After the second laser shot at 44 mJ/cm<sup>2</sup> (top middle of Fig. 5) the roughening seems more complete. The third shot at that fluence finally leads to a (partial) ablation of the PANI layer (dark center in the top right picture of Fig. 5), leaving the photo-resist unharmed. This assumption is verified by our AFM profile analysis of these structures. The size of the laser-induced modifications at this modest fluence level remain inside the average laser spot diameter of ca. 35  $\mu$ m. At a slightly higher fluence of 50 mJ/cm<sup>2</sup> the single-shot processing enhances the roughening in size and depth (middle left picture of Fig. 5), without actually removing the top layer. Selective removal with  $N = 1$  laser shot is achieved at 100 mJ/cm<sup>2</sup>, more precisely in the center region of the focused laser beam (bottom left picture of Fig. 5). In the picture bottom right of Fig. 5 we present an example of complete removal of the PANI layer after 10 laser shots at 300 mJ/cm<sup>2</sup>, as illustrated by the transition from a dark to a light optical impression in the center of illumination. The photo-resist film was not ablated even partially and the mean roughness of the processed surface remains in its original stage after processing in the fluence range up to 500 mJ/cm<sup>2</sup>. This is confirmed by AFM analysis and optical profiler measurements. However, one can observe a well-defined dark rim as boundary between the unaffected region and the ablated zone, yielding a with laser fluence increasing elevation from 10 to 50 nm. This effect may be reduced by introducing a "top-hat" profile in the processing beam, instead of a Gaussian intensity distribution. The modifications are surprisingly reproducible, considering the significant changes obtainable by slight adjustments in the laser fluence. Also, the results for the wavelength - pulse duration combination 800 nm and 5 ps are equivalent to the fs case, with a tendency of reduced quality near the rim. In the near IR region fs laser pulses appear to be superior to the ps pulses with regard to the quality of the irradiated area as well as the ablation efficiency.

In contrast to the removal of ITO on glass the wavelength is much more crucial when it comes to the ablation of PANI on photo-resist on glass. The machining result is strongly wavelength dependent regardless of the pulse duration. Analysis of the depth profiles for the processed multi-layer system II – PANI on photo-resist on glass – demonstrate clearly, that in UV laser processing at 266 nm both layers, PANI and photo-resist, are removed. We were unable to control any selective removal of PANI on photo-resist at 266 nm, independent of the pulse duration. This is perhaps a surprising result, we expected at least for the wavelength – pulse duration combination 266 nm and 0.2 ps a higher selectivity due to the stronger potential of energy localization in a very thin surface region (as in the skin depth for metals). However, the photo-resist underneath the PANI is highly sensitive to ultraviolet radiation. The ablation of

PANI is associated with roughening and partial removal of the layer, leading to local sites of possible transmission of photon energy into the resist layer. Therefore, even minor fluence levels in the UV can cause partial damage in the photo-resist. At a wavelength of 800 nm and to some part also at 532 nm, this optical penetration is not severe, since at least linear absorption in photo-resist is not expected from the data in Table 2. However, at 266 nm a layer discrimination of photon penetration is less probable and even fs laser pulses are inadequate to solve the problem in the UV. The selectivity is in this case strongly wavelength related. The laser pulse duration regulates the thermal diffusion surrounding the volume of optical penetration. Therefore, processing with ultra short laser pulses at 800 nm reduces the thermal penetration depth to a minimum, ensuring the selective removal of PANI.



**Fig. 4:** Laser-induced damage (squares) and ablation (circles) threshold of PANI (on photo-resist on glass) at a wavelength of 800 nm and a pulse width of 0.2 ps as a function of number of laser shots  $N$  per location.

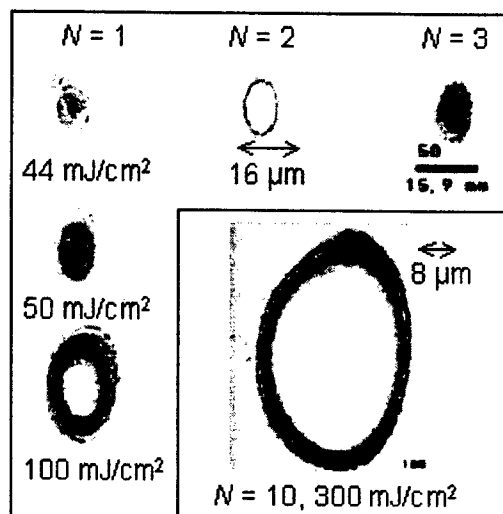


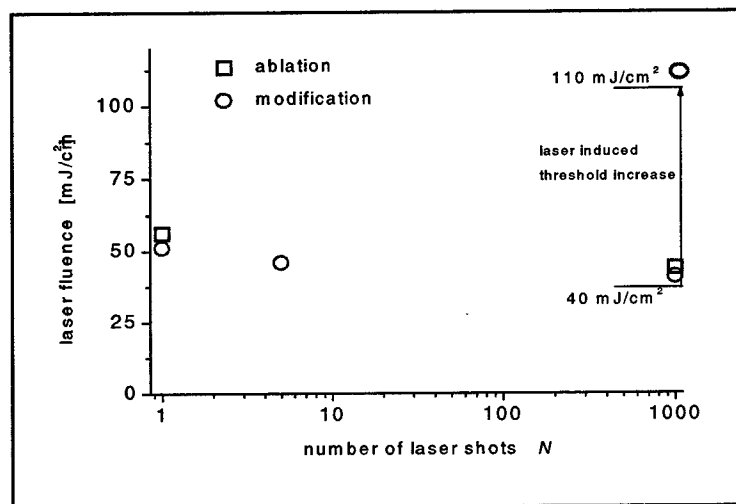
**Fig. 5:** Optical microscope pictures of laser-induced modifications on the multi-layer system II: PANI on photo-resist on glass using fs laser pulses at 800 nm.  $N$ : number of laser shots. The laser fluence of 44 mJ/cm² was used to generate the top three modifications.

As perhaps expected from the absorption coefficient for the two layers at 532 nm compiled in Table 2, green laser light does also allow for a selective removal of the PANI layer without considerably damaging the underlying photo-resist. This is observed especially in a fluence interval of 100 to 300 mJ/cm², slightly above the damage and near the ablation threshold for this wavelength – pulse duration combination. Although the optical microscope pictures give an impression of a well-defined removal, depth profile analysis using AFM and optical profiler technique reveal an elevation of residuals at the rim of several 100 nm. In many cases we also obtained an unwanted partial removal of the photo-resist and an increase in the mean roughness, indicating that the selective removal of PANI is more difficult to control at the wavelength – pulse duration 532 nm and 5 ns. The increase in thermal diffusion at 5 ns laser pulse duration is probably responsible for the difficulties encountered. Additional experiments using 800 nm or 1.06 µm around 5 ns pulse duration are planned to evaluate this assumption more closely.

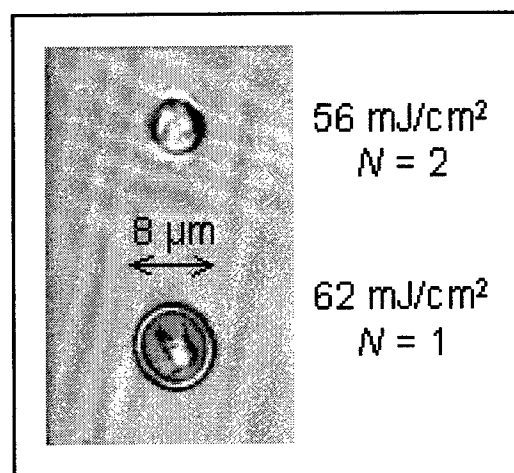
### 3.3. PPV/Pedot on ITO on glass

Figure 6 illustrates the threshold fluence for modification (damage) and for single shot ablation of the layer combination PPV/pedot on ITO (on glass) at laser wavelength of 800 nm and a pulse duration of 0.2 ps. The damage and ablation threshold are practically identical after  $N = 2$  laser shots. Using ultra short laser pulses the damage threshold demonstrates only minor shot-number dependencies, similar to the PANI case. A substantial decrease of the threshold value between single and 100 shots occurs only at 266 nm at 0.2 ps and also at 5 ns pulse duration. As indicated in Fig. 6, the treatment of the this multi-layer system III with multiple ultra short laser pulses ( $N > 1000$ ) at wavelength of 800 nm and a processing fluence of <40 mJ/cm² (beneath the multi-shot damage threshold) leads to an increased resistance against subsequent laser exposure. The process responsible for this surprising laser-induced increase in the

damage threshold from 40 mJ/cm<sup>2</sup> to over 100 mJ/cm<sup>2</sup> is presently unclear. Following additional notes can be made: The threshold fluence decreases with the laser wavelength within the investigated range. Compared to the wavelength the pulse duration has a far stronger influence on the threshold fluence within the investigated range. At 266 nm the use of fs pulses instead of ns pulses results in a significant drop of the damage threshold fluence (almost one order of magnitude). Compared to ITO the threshold fluence for modification is much lower. The ratio is between 2 and 10, depending on the chosen wavelength – pulse duration combination. Especially pronounced are the fairly low threshold levels at 800 nm for 0.2 and 5 ps, which are at least 5 times lower than for sample I: ITO on glass. The increasing linear absorption at 800 nm for the sample III: PPV/pedot on ITO on glass may contribute to the decreasing threshold. However, the ablation process in the sample III seems to differ considerably from the case sample I: ITO on glass, which is probably the main reason for the reduction in threshold.



**Fig. 6:** Laser-induced damage (circles) and ablation (squares) threshold of PPV/Pedot (on ITO on glass) at a wavelength of 800 and a pulse width of 0.2 ps as a function of number of laser shots  $N$  per location. Note the enhancement in the threshold for  $N = 1000$  (larger circle) after low fluence (35 - 40 mJ/cm<sup>2</sup>) illumination of identical location.



**Fig. 7:** Optical microscope pictures of laser-induced modifications on the multi-layer system III: PPV/Pedot on ITO on glass at a laser pulse width of 0.2 ps and at a wavelength of 800 nm.  $N$ : number of

Fig. 7 depicts optical microscope pictures of laser-induced damage sights on the sample system III: PPV/pedot on ITO (on glass) using ultra-short laser pulses of 0.2 ps at 800 nm. The laser fluence for  $N = 2$  shots (top) and single-shot is closely above damage threshold. Based on the surface inspection a discrimination between damage and ablation is very difficult. In the initial stage of laser processing the PPV/pedot layer is rather peeled off than actually ablated from the surface. This can be seen quite clearly in the lower picture of Fig. 7. The threshold and processing results for the wavelength – pulse duration combination 800 nm and 5 ps are very similar. The penetration of laser energy in the interface region PPV/pedot and ITO seems to be responsible for the processing. Clearly, the damage threshold of ITO on glass alone is much higher, however, it is unclear, in which way the additional layer may enhance the deposition rate at the interface. The examples in Fig. 7 reveal a stress related process, perhaps based on thermal expansion or other thermally related effects, such as the pressure of a gas bubble developing between the PPV/pedot and ITO layer.

For additional assessments on the possible “ablation” process, Fig. 8 presents optical microscope pictures of laser-induced damage sights on the sample system III: PPV/pedot on ITO (on glass) using ultra-short laser pulses of 0.2 ps at 266 nm. In the example of top left in Fig. 8 one receives the impression of a laser-induced “tear-off” or peeling procedure of the top layer combination PPV/pedot from the ITO layer underneath. This flag-like feature was reproducible at this fluence level of 80 mJ/cm<sup>2</sup> and  $N = 2$  shots. Additional laser shots reduces the size of dangling features, they remain, however, visible near the rim. In situ monitoring demonstrated a smoke-like impression even several seconds after the ultra short laser pulse (at 266 and 800 nm) has acted on the surface, revealing a sub-layer material release, probably vapor. In the two top examples processed at 55 mJ/cm<sup>2</sup> one can observe the development of the laser-induced layer peeling procedure. In the sub-surface region, probably at the interface PPV/pedot and ITO, the

stabilized modification is causing a darkening in the optical microscope picture. With the second laser shot the center region changes again, leading to the impression, that the top layers PPV/pedot lost contact to the ITO layer underneath. Additional laser shots enhance the size and contrast of the inner circle until a sudden burst initiates the peeling of the top layer, locally corresponding to the original single laser shot induced sub-surface modification.

As indicated earlier, UV laser processing shows signs of incubation during multi-shot illumination. The results in the "ablation" of PPV/pedot on ITO at a fairly low fluence level  $< 15 \text{ mJ/cm}^2$  and after  $N = 100$  laser shots differ significantly from the previously discussed case, as illustrated in the lower examples in Fig. 8. Although we observe a similar sub-surface modification, the PPV/pedot damage consists of many sub-micron sights of partial and complete removal. Outside of problems facing some residuals of the top layer combination near the rim, multi-shot fs laser processing at 266 nm at a fluence level of  $40 \text{ mJ/cm}^2$  selectively removes the PPV/pedot layer combination. The ablation depth remains at ca. 250 nm, so that the ITO layer seems unharmed. Using 5 ns laser pulses at 266 nm, the processing results at fluence levels around  $150 \text{ mJ/cm}^2$  are similarly acceptable, with the exception that ITO layer is in many cases at least partially damaged or ablated. The processing with ns laser pulses at 266 nm compared to the fs case is more difficult to control and less reproducible. Above  $600 \text{ mJ/cm}^2$  at 266 nm and 5 ns the ITO layer is also completely removed (without damaging the glass substrate).

For 5 ns laser pulses at 532 nm the processing results are even less acceptable. We observed a small processing window at a fluence level around  $500 \text{ mJ/cm}^2$ , at which selective removal of the combined PPV/pedot layer from the ITO is to some extent possible. However, there are many large residuals inside the laser processed area and near the rim, some several  $\mu\text{m}$  long. AFM analysis of the laser processed regions with using 532 nm at 5 ns was very difficult due to several dangling left-others of the PPV/pedot layer.

For all wavelength pulse duration combinations we observe the following results for sample layer system III: In order to remove the top layer completely to generate grooves and larger areas a very high pulse overlap ( $\approx 90\%$ ) has to be chosen. An 2/3 pulse overlap results in partial ablation. Laser processing of the PPV/pedot layer is indirect, the effect of the laser energy deposition is visible at the interface between PPV/pedot and ITO and not directly at the PPV/pedot layer. This demonstrates how important the localization of laser energy for high quality processing is.

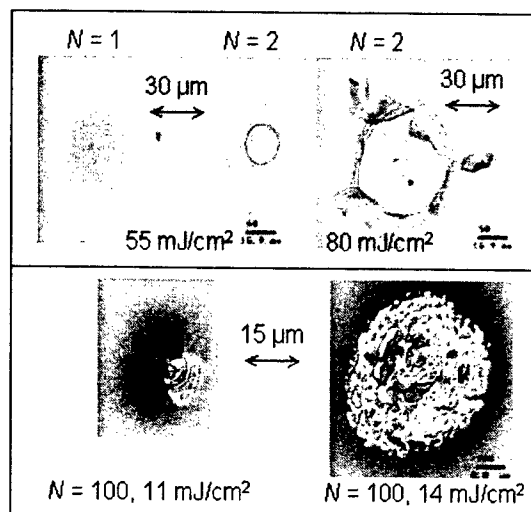


**Fig. 8:** Optical microscope pictures of laser-induced modifications on the multi-layer system III: PPV/Pedot on ITO on glass at a laser pulse width of 0.2 ps and at a wavelength of 266 nm.  $N$ : number of laser shots.



#### 4. CONCLUSION

The laser processing investigation at certain wavelength - pulse duration combinations for multi-layer systems such as 150 nm thin indium tin oxide (ITO), 200 nm thin polyaniline (PANI) on 1  $\mu\text{m}$  thick photo resist, and 280 nm PPV/pedot layer-combination on 150 nm thin ITO demonstrated, that focused laser light can be a feasible tool for selective layer removal even for these optically transparent materials. The applicability of ultra short laser pulses at 800 nm for micro-machining of the top layer alone has been demonstrated for ITO on glass, PANI on photo-resist on glass, and to some extent also for PPV/pedot on ITO on glass, considering the remaining problem involving flag-like residuals at the rim. The low threshold levels observed using ultra short laser pulses at 800 nm allow for laser processing at single shot energies of only 10 nJ with beam spot sizes between 3  $\mu\text{m}$  (ITO) and 6  $\mu\text{m}$  (PANI). Turn-key and stand-alone oscillator systems for the generation of high repetition, ultra-short laser pulses at sufficient average power for adequate processing speeds are just recently made available for this kind of application.

In cases, where the optical penetration depth is discriminated by strong differences in linear absorption, selectivity can be achieved by the choice of wavelength, so that also ns pulses, e.g. at 532 nm, may lead to acceptable results concerning micro-machining of the top layer. However, the thermal penetration depth exceeds the optical absorption depth, especially for longer pulse durations. This is demonstrated in the tendency of increasing partial damage of the lower layer and in some cases unacceptable elevation of the rim after processing with ns laser pulses. The combination 0.2 ps pulse duration and 266 nm does not necessarily guarantee the localization of photon energy in the top (thin) layer alone. Laser-induced layer removal based on surface roughening or non-isotropic ablation as a pre-cursor can attribute to a enhanced energy penetration in the lower substrate. This may be a great problem if the absorption coefficient for the lower layer at the processing wavelength is significant, independent of the pulse duration.

In short, we observe the following laser-induced processes: thermal ablation for ITO, sub-surface modification and incubation for PANI, and vapor related expansion and stress-related peeling for PPV/pedot. Concerning an evaluation of the technical feasibility on laser processing of transparent multi-layer systems this study is too preliminary. Additional experimental investigations are necessary to decide on future implementations. However, we hope to have outlined in this paper that transparent thin multi-layer systems serve as most interesting model systems for additional fundamental studies on laser interaction mechanism and photon absorption.

#### ACKNOWLEDGMENT

Special thanks are expressed to M.C. Mueller for the aid in the 3D analysis of the structures and the useful discussions.

#### REFERENCES

1. O. Yavas, C. Ochiai, M. Takai, "Substrate-assisted laser patterning of indium tin oxide films", *Appl. Phys. A* **69** [Supl.], pp. 875-878, 1999.
2. R. Haight, D. Hayden, P. Longo, T. Neary, A. Wagner, "MARS: Femtosecond laser mask advanced repair system in manufacturing", *J. Vac. Sci. Technol. B* **17**(6) pp. 3137-3142, 1999.
3. D. Ashkenasi, A. Rosenfeld, H. Varel, M. Wöhner, E.E.B. Campbell, "Laser processing of sapphire with picosecond and sub-picosecond pulses", *Appl. Surf. Sci.* **120**, pp. 65-80, 1997.
4. A. Rosenfeld, M. Lorenz, R. Stoian, D. Ashkenasi, „ Ultrashort-laser-pulse damage of transparent materials and role of incubation“, *Appl. Phys. A* **69** [Supl.], pp. 373-376, 1999.
5. H. Varel, D. Ashkenasi, A. Rosenfeld, R. Herrmann, F. Noack and E.E.B. Campbell, "Laser-induced damage in  $\text{SiO}_2$  and  $\text{CaF}_2$  with picosecond and femtosecond laser pulses", *Appl. Phys. A* **62**, 293-294 (1996).
6. C.B. Schaffer, A. Brodeur, J.F. Garcia, and E. Mazur, "Micromachining bulk glass using femtosecond laser pulses with nanojoule energy", *Opt. Lett.* **26**, pp. 93-95 (2001).

# Development of Dicing Technique for Thin Semiconductor Substrates with Femtosecond Laser Ablation

Atsushi Yokotani<sup>a</sup>, Naoyuki Matsuo<sup>a</sup>, Kosuke Kawahara<sup>a</sup>, Yasunobu Kurogi<sup>a</sup>, Norihide Matsuo<sup>a</sup>,  
Takahumi Ninomiya<sup>b</sup>, Hiroshi Sawada<sup>b</sup>, Kou Kurosawa<sup>a</sup>

<sup>a</sup>Department of Electrical and Electronic Engineering, Miyazaki University,  
1-1 Gakuen Kibanadai-Nishi, Miyazaki, 889-2192, Japan.

<sup>b</sup>NEC Machinery Corporation 85, Minami Yamada-cho, Kusatsu, Shiga, 525-8511, Japan.

## ABSTRACT

Recently, the semiconductor substrates for integrated circuits (ICs) have been required to become as thin as 50  $\mu\text{m}$ , because the many electronic devices are strongly demanded to be miniaturized and light-weighted. Machining of such thin substrates with conventional dicing techniques is very difficult. Therefore, we have proposed to process them using femtosecond laser ablation, expecting advantage of efficient etching without undesirable mechanical and thermal damages such as cracking and melting is expected. In this work, we have investigated the influence of the laser conditions such as pulse duration and fluence on the cutting depth and diameter in order to develop a new photo-dicing technique for very thin ICs. Within the range of pulse energy used in the present experiments, the dependence of the pulse duration did not seem to be significant. It was also found that the lower energy of the laser pulses, the smaller and the deeper, i.e., the sharper holes were formed. The typical cutting depth and diameter for 0.20 mJ/pulse and 5 shots were 17  $\mu\text{m}$  and 40  $\mu\text{m}$ , respectively. These values are very promising for the practical dicing applications.

**Keywords :** femtosecond laser, laser ablation, laser scanning microscope, processing efficiency

## 1. INTRODUCTION

Recently, the semiconductor substrates for integrated circuits (ICs) have been required to become thinner, because the many electronic devices are strongly demanded to be miniaturized and light-weighted. The thickness of the semiconductor substrates generally used now is about 600 ~ 800  $\mu\text{m}$ . For the near future, one expects the thickness of less than 50  $\mu\text{m}$ . Consequently, the mechanical strength of the substrates is getting worse, machining of such thin substrates using conventional dicing techniques such as machining with diamond cutter is very difficult. So, we proposed to develop a processing technique with laser ablation [23, 24]. However, use of nanosecond laser such as Nd:YAG laser for this purpose had been results in undesirable mechanical and thermal damages such as cracking and melting. On the other hand, recent researches on laser ablation using femtosecond laser pulses have become taken much attention for micromachining because of the advantages of efficient etching without such damages [1-22]. Such innovative researches and developments have the background that very intense ultrashort laser pulses have become utilized easily with commercially available laser systems. We have already reported that the ablation induced by the femtosecond laser irradiation is very promising for photomachining of Si substrates such as cutting and drilling [23, 24]. In this paper, we have prepared the Si wafers with 50  $\mu\text{m}$  thick, and investigated the influence of the laser conditions such as pulse duration and fluence on the cutting depth and diameter in order to develop a new photo-dicing technique for fabrication of very thin ICs.

## 2. EXPERIMENTAL

Figure 1 shows a schematic block diagram of a laser system used in this work. A mode-locked Ti:sapphire laser operated at 770 nm pumped by a cw argon ion laser was used for generation of seed pulses to the subsequent

regenerative amplification. The modulation frequency was 82 MHz and the duration of a single pulse was approximately 80 fs. The laser final condition obtained from this system was as follows: the energy was 0.13 ~ 0.50 mJ/pulse, the frequency, 10 Hz, and the pulse duration, 100 ~ 500 fs. The energy and the pulse duration were measured just before the irradiation of the each sample with a laser power meter (407A, Spectra Physics Lasers) and a single shot autocorrelator (SSA-F, Spectra Physics Lasers), respectively.

Figure 2 shows a schematic drawing of the processing unit. A plano-convex lens with a nominal focal length of 100 mm was used. A mechanical shutter inserted at the upstream of the lens in the laser path controlled the shot numbers irradiated on the sample. The minimum spot size at the focal point was about 50  $\mu\text{m}$ . The samples used in this work were specially prepared Si wafers with a thickness of 50  $\mu\text{m}$ , which had been obtained by very careful grinding and etching of conventional Si wafers. Through the range of the energy used in this work, air breakdown has not been observed at the focal point. The processed surface was observed and characterized with a scanning electron microscope (SEM) and a laser scanning microscope (LSM).

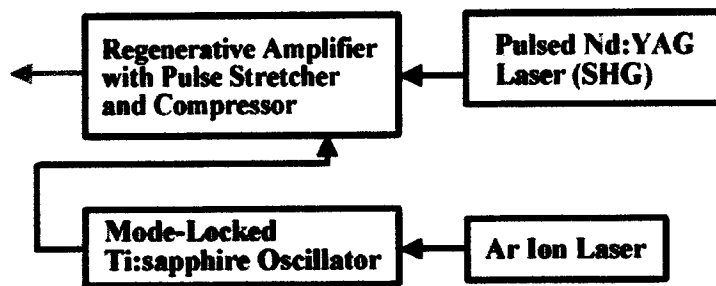


Figure 1: Schematic block diagram of the femtosecond laser system.

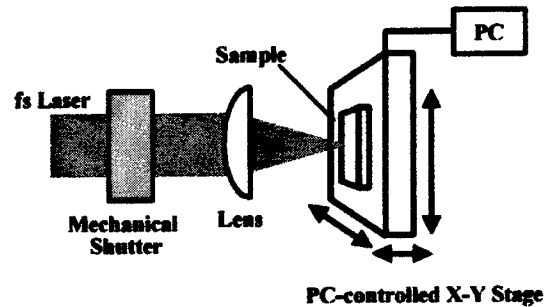


Figure 2: Schematic drawing of the processing unit.

### 3. RESULTS AND DISCUSSIONS

#### 3.1 The comparison of the cutting grooves

Figure 3 shows the results of the cutting of Si wafers. (a) shows the results from the femtosecond laser (0.30 mJ/pulse, 10 Hz, 800nm and 5.5  $\mu\text{m/s}$ ). (b) shows the results from a nanosecond laser (532 nm, 15 ns) irradiation with almost the same conditions (0.30 mJ/pulse, 10 Hz and 5.5  $\mu\text{m/s}$ ). Cracking and melting appeared in (b), clearly. Such damages were successfully suppressed in (a) compared with the case of (b). The difference between these two results is due to the fact that energy deposition by laser irradiation is faster than energy escaping by thermal diffusion in the case of the femtosecond laser, while the energy is escaping during the irradiation in the case of the nanosecond laser [24]. Consequently, very clean traces were successfully engraved by the femtosecond laser.

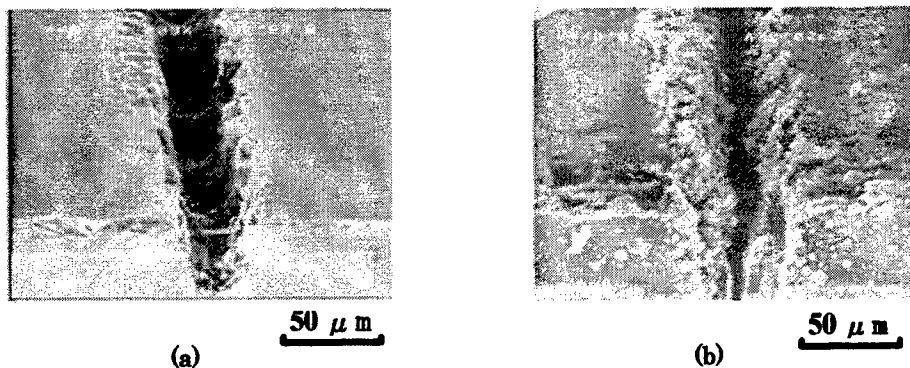


Figure 3: SEM photographs of processed portion of Si wafer.

Next, the influence of the scan rate on the depth of the grooves was characterized. Assuming the removed volume increases proportionally to the totally irradiated laser energy or shot numbers while the width of grooves is constant, the depth should be inversely proportional to the scan rate. In this experiment, the scan rate was changed from 5.5 to 111  $\mu\text{m/s}$ . The results are shown in Fig. 4. The ordinate stands for the reciprocal of the depth estimated from SEM photographs in logarithmic scale. As the abscissa in Fig. 4 is the scan rate in logarithmic scale, the slope of the plots should become unity, if the above assumption is correct. In Fig. 4, data of other samples were also plotted for comparison. The principal properties of these materials are summarized in Table 1. As a result, this relationship is found to be maintained in the range from approximately 20 to 111  $\mu\text{m/s}$  for all samples. This fact means that the scan rate of less than 20  $\mu\text{m/s}$  is excessively slow for the practical efficient material processing.

Table 1: Physical properties of the sample materials which were plotted in Fig. 4.

Materials	Specific Heat $C$ (cal/g·K)	Thermal Conductivity $\kappa$ (W/m·K)	Melting Point $T_m$ (K)	Density $\rho$ (g/cm <sup>3</sup> )
PMMA	0.385	0.17	373	1.19
Silica Glass	0.17	1.4	2073	2.22
Si	20.0	148	1683	2.34
Al	24.3	237	937	2.69
Cu	24.5	398	1357	8.93

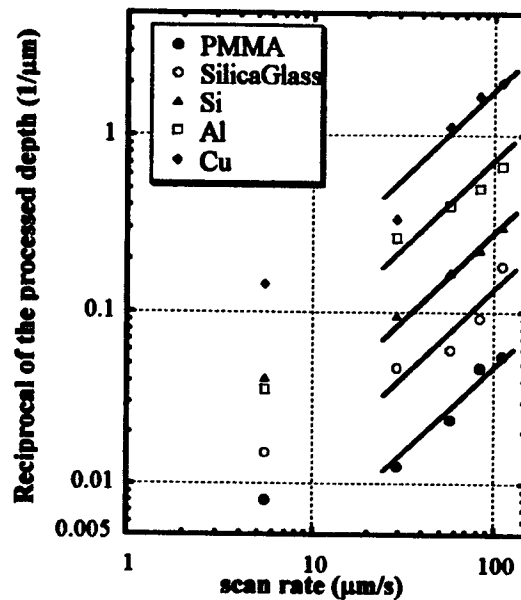


Figure 4: The depth of the processed grooves versus the scan rate of the samples.

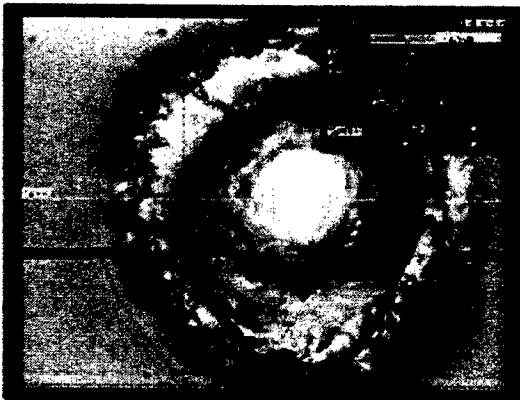


Figure 5: Typical laser scanning microscopic image.

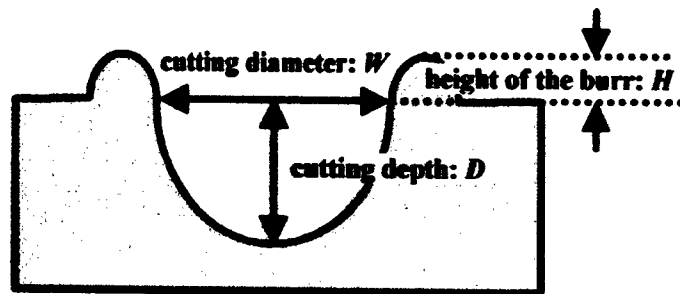


Figure 6: A schematic drawing of the cross section of the typical ablation trace.

### 3. 2 Influence of the laser conditions

#### 3. 2. 1 Measurement of cutting diameter, cutting depth and height of the burr by the LSM

Morphological studies were performed for the ablation trace that had been formed by irradiation of the focused laser without scanning the stage in order to investigate to find the optimal laser condition for the machining. Figure 5 shows a typical laser scanning microscopic image which were formed by 5 shots of laser irradiation. Because the Si wafer with 50  $\mu\text{m}$  thick was penetrated by 15 to 25 shots of irradiation, all following observations were carried out for the ablation

traces which had been formed by 5-shot irradiation. Figure 6 illustrates a schematic drawing of the cross section of the typical ablation trace which were obtained by 3-dimensional analysis of the image shown in Fig. 5. We defined the cutting diameter  $W$  [ $\mu\text{m}$ ], cutting depth  $D$  [ $\mu\text{m}$ ] and height of the burr  $H$  [ $\mu\text{m}$ ] as shown in Fig. 6.

Figure 7 shows the dependence of the  $D$  and the  $H$  on the distance between the lens and the sample when it was irradiated at 0.13 mJ/pulse and 300 fs. The  $H$  became the minimum at a distance where the  $D$  became the minimum. We defined this distance as the length which give the best focus condition. Of course, the  $H$  is expected to be as small as possible in the application point of view for the micromachining, so the following analyses have been carried out for the data which have been taken at the best focus conditions.

Figure 8 shows the dependence of the best focus condition on the energy of the irradiated laser. The best focal distance changed with the laser energy. Comparing the data taken for 200 fs-0.16 mJ/pulse and 200 fs-0.28 mJ/pulse, the larger the energy, the shorter the distance. Besides, the best focal distance for 200 fs-0.16 mJ/pulse was corresponded to that for 400 fs-0.28 mJ/pulse. From these facts, we considered that this change of the distance was caused by the nonlinear refractive changes of the BK-7 glass which the lens was made of by the very high peak power of the laser. Taking this into account, we adjusted the lens-sample distance to be the best focus condition with the accuracy of  $\pm 0.1$  mm for each experiment.

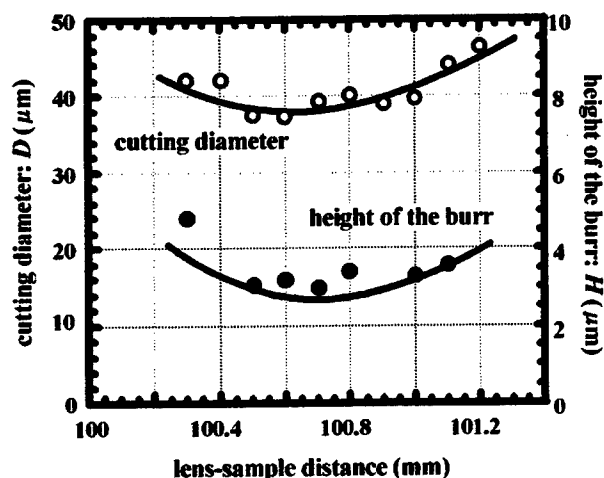


Figure 7: The dependence of the  $D$  and the  $H$  on the lens-sample distance.

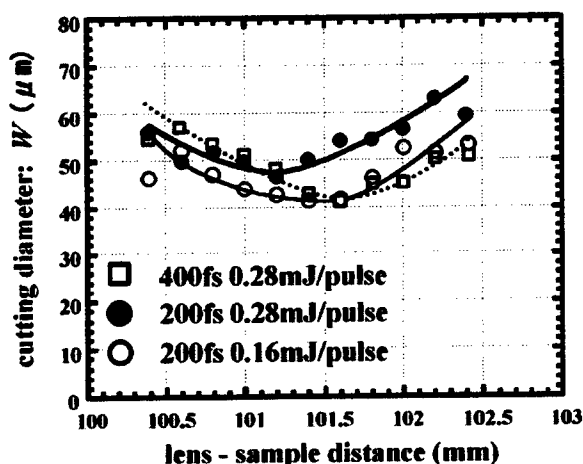


Figure 8: The dependence of the best focus condition on the energy.

### 3. 2. 2 Influence of the pulse duration and the energy on the cutting diameter

Figure 9 shows the relation between the measured  $W$  and the pulse energy. In Fig. 9, the pulse duration used in this experiment was divided into 3 groups and indicated by different shapes of the plot (solid circle: 100~150 fs, solid triangle: 151~250 fs, open square: 251~500 fs). Within the range of the pulse duration used in the present experiments, the dependence on the pulse duration did not seem to play an important role for the determination of the  $W$ . Within the range of pulse energy (0.13~0.50 mJ/pulse), the higher the energy of the laser pulses, the larger holes were formed. Consequently, it was found that the  $W$  was almost proportional to the laser energy within this range of the energy and the pulse duration. Below a energy of approximately 0.08 mJ/pulse, clear holes were not formed. We considered this level of the energy is corresponded to the threshold of the laser ablation for the laser conditions and the sample used in this work.

### 3. 2. 3 Influence of the energy on the cutting depth

Figure 10 shows the relation between the measured  $D$  and the pulse energy. In Fig. 10, the same plotting style as Fig. 9 for the pulse duration was used. Also for the discussion of the  $D$ , the pulse duration did not seem to be important. Within the range of the pulse energy from 0.20 to 0.50 mJ/pulse, results that the lower energy of the laser pulses formed the deeper holes have been obtained. In this region, the lower pulse energy provided the smaller and the deeper, i.e.,

the sharper holes. This tendency is very different from the results carried out with nanosecond laser ablation in which the larger energy provides the deeper holes. On the other hand, within the pulse energy below 0.20 mJ/pulse, the smaller the energy, the shallower the  $D$ . This means a energy which gives the maximum cutting speed can be found a energy of around 0.20 mJ/pulse.

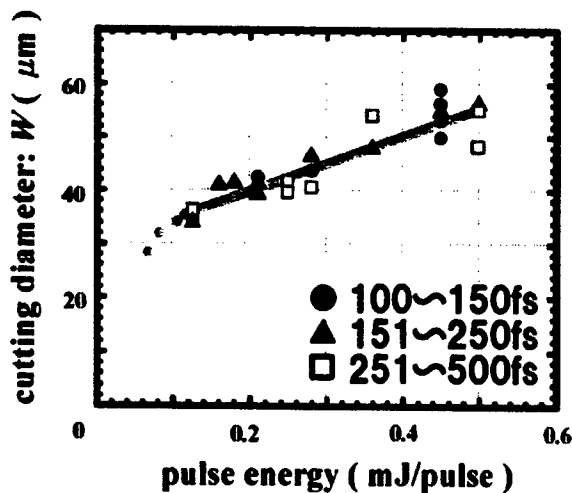


Figure 9: The relation between the  $W$  and the pulse energy.

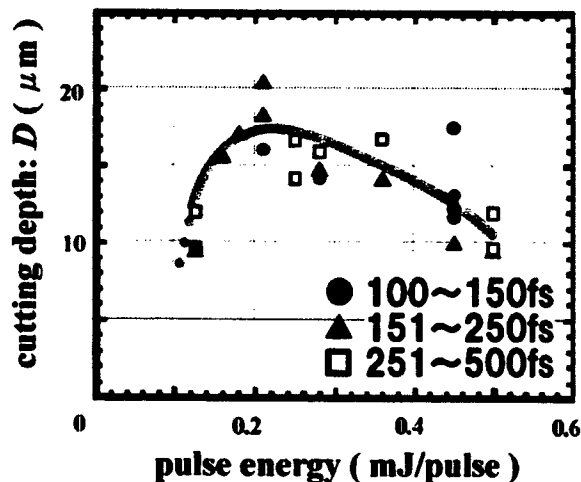


Figure 10: The relation between the  $D$  and the pulse energy.

### 3. 2. 4 Influence of the energy on the height of the burr

Figure 11 shows the relation between the measured  $H$  and the pulse energy. The obtained data were so ramble that we couldn't find the certain tendency about the relation between these. Although we consider that the discussion about the reason of this rambling will be work for the future, at least we can say that the  $H$  can be controlled at most less than 5  $\mu\text{m}$ . Figure 12 ((a) and (b)) shows the images of a hole which has the smallest  $H$  through the present experiments taken with the LSM and the SEM, respectively. Especially in Fig 12 (b), it is clearly observed that a clean hole without any cracking can be successfully formed for the Si substrate of which thickness is as thin as 50  $\mu\text{m}$ .

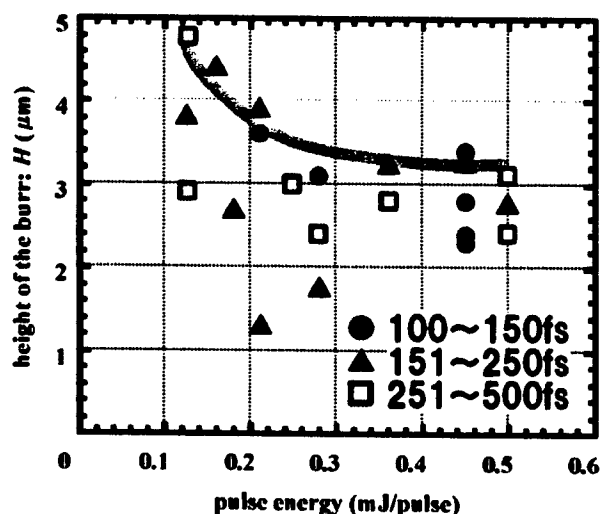
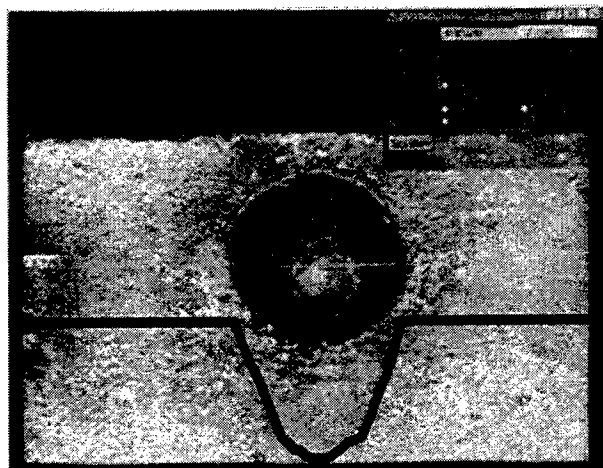
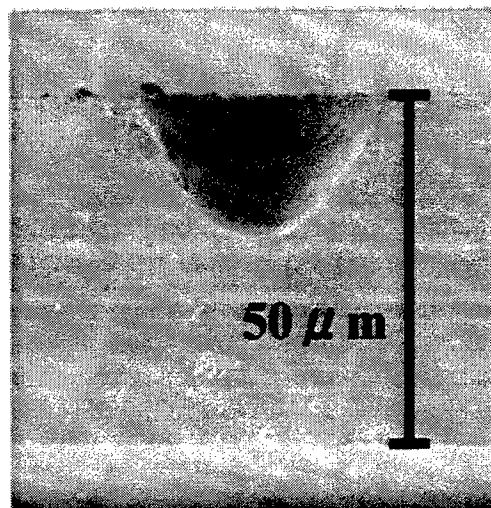


Figure 11: The relation between the  $H$  and the pulse energy.



(a)



(b)

Figure 12: The images of a hole taken with the LSM (a) and the SEM (b).

### 3. 2. 5 Estimation of the efficiency

We have estimated the processing efficiency from the energy-expending point of view. We defined the processing efficiency  $\eta$  as follows:

$$\eta = (E_B V \rho / n E_L) \times 100 \quad [\%],$$

where  $E_B$  is the binding energy between atoms in the Si substrates (16.2 kJ/g),  $V$  the removed volume,  $\rho$  the density of Si,  $n$  the shot numbers and  $E_L$  the laser energy. The numerator  $E_B V \rho$  stands for the total energy which is supplied by the laser beam. Figure 13 shows the relation between  $\eta$  and the pulse energy. The results in Fig. 13 are similar to the tendency about  $D$  in Fig. 10, whereas it is completely different tendency about  $W$  in Fig. 9. The efficiency  $\eta$  indicated the maximum at a energy around 0.18 mJ/pulse. We consider that the energy range from 0.18 to 0.20 mJ/pulse in which both the  $D$  and  $\eta$  become nearly the maximum should provide the optimal machining condition for the dicing thin Si substrates by femtosecond lasers.

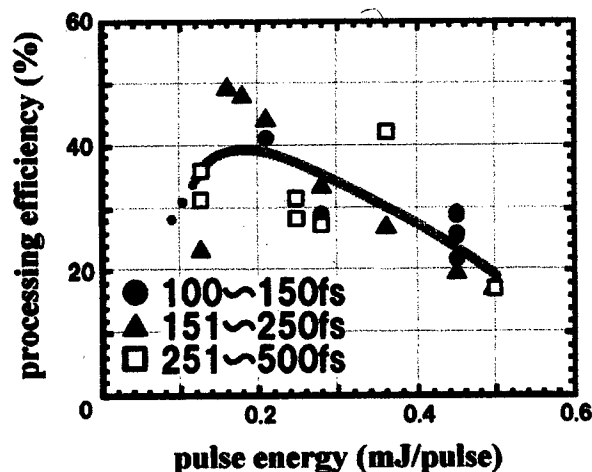


Figure 13: The relation between the  $\eta$  and the pulse energy.

#### 4. SUMMARY AND CONCLUSIONS

We have developed the cutting technique for Si wafer of which thickness is 50  $\mu\text{m}$  utilizing the femtosecond laser ablation. We have investigated the influence of the laser conditions such as pulse duration and fluence. The principal conclusions for the range of pulse duration and energy used in this experiment may be summarized thus:

- 1) The dependence of the pulse duration did not seem to be significant.
- 2) The cutting diameter is nearly proportional to the pulse energy and the depth reaches to the maximum (approximately 4  $\mu\text{m}/\text{pulse}$ ) at a pulse energy of around 0.20 mJ/pulse.
- 3) The height of the burr could be controlled at most 5  $\mu\text{m}$ .
- 4) The processing efficiency indicates the maximum at a pulse energy of around 0.18 mJ/pulse.

From these, we can conclude that the energy around (0.18–0.20 mJ/pulse) should be the optimal machining condition for dicing very thin Si substrates by femtosecond lasers. These results are very promising for the practical applications.

#### REFERENCES

- [1] R. Srinivasan, E. Sytcliffe and B. Bararen, "Ablation and Etching of Polymethylmethacrylate by Very Short (160 fs) Ultraviolet (308 nm) Laser Pulses", *Appl. Phys. Lett.*, **51**, p.1285, 1987.
- [2] S. Küper and M. Stuke, "Femtosecond UV Excimer Laser Ablation", *Appl. Phys.*, **B 44**, p.199, 1987.
- [3] S. R. Cain, F. C. Burns, C. E. Otis and B. Bararen, "Photothermal Description of Polymer Ablation: Absorption Behavior and Degradation Time Scales", *J. Appl. Phys.*, **72**, p.5172, 1992.
- [4] H. Kumagai, K. Midorikawa, K. Toyoda, S. Nakamura, T. Okamoto and M. Obara, "Ablation of Polymer Film by a Femtosecond High-Peak-Power Ti:sapphire Laser at 798 nm", *Appl. Phys. Lett.*, **65**, p.1850, 1994.
- [5] Z. Bor, R. Racz, G. Szabo, D. Xenakis, C. Kalpouzos and C. Fotakis, "Femtosecond Transient Reflection from Polymer Surfaces during Femtosecond UV Photoablation", *Appl. Phys.*, **A 60**, p.365, 1995.
- [6] S. Küper and M. Stuke, "Ablation of Polytetrafluorethylene (Teflon) with Femtosecond UV Eximer Laser Pulses", *Appl. Phys. Lett.*, **54**, p.4, 1989.
- [7] S. Preuss, M. Spath, Y. Zhang and M. Stuke, "Time Resolved Dynamics of Subpicosecond Laser Ablation", *Appl. Phys. Lett.*, **62**, p.3049, 1993.
- [8] S. Nakamura, K. Midorikawa, H. Kumagai, M. Obara and K. Toyoda, "Effect of Pulse Duration on Ablation Characteristics of Tetrafluoroethylene Hexafluoropropylene Copolymer Film Using Ti:Sapphire Laser", *Jpn. J. Appl. Phys.*, **35**, p.101, 1996.
- [9] J. Ihlemann, B. Wolff and P. Simon, "Nanosecond and Femtosecond Excimer Laser Ablation of Fused Silica", *Appl. Phys.*, **A54**, p.363, 1992.
- [10] B. Wolff-Rottke, J. Ihlemann, H. Schmit and A. Scholl, "Influence of the Laser-Spot Diameter on Photo-Ablation Rates", *Appl. Phys.*, **A60**, p.13, 1995.
- [11] B. C. Stuart, M. D. Feit, A. M. Rubenchik, B. W. Shore and M. D. Perry, "Laser-Induced Damage in Dielectrics with Nanosecond to Subpicosecond Pulses", *Phys. Rev. Lett.*, **74**, p.2248, 1995.
- [12] J. Ihlemann, A. Scholl, H. Schmit and B. Wolff-Rottke, "Nanosecond and Femtosecond Excimer-Laser Ablation of Oxide Ceramics", *Appl. Phys.*, **A60**, p.411, 1995.
- [13] E. N. Glezer and E. Mazur, "Ultrafast-Laser Driven Micro-Explosions in Transparent Materials", *Appl. Phys. Lett.*, **71**, p.882, 1997.
- [14] M. Samoc, A. Samoc, B. Luther-Davies, Z. Bao, L. Yu, B. Hsieh and U. Scherf, "Femtosecond Z-scan and Degenerate Four-wave Mixing Measurements of Real and Imaginary Parts of the Third-order Nonlinearity of Soluble Conjugated Polymers", *J. Opt. Soc. Am.*, **B 15**, p.817, 1998.
- [15] D. Ashkenasi, M. Lorenz, R. Stoian and A. Rosenfeld, "Surface Damage Threshold and Structuring of Dielectrics Using Femtosecond Laser Pulses: the Role of Incubation", *Appl. Surface. Sci.*, **150**, p.101, 1999.
- [16] I. L. Shumay and U. Höfer, "Phase Transformations of an InSb Surface Induced by Strong Femtosecond Laser Pulses", *Phys. Rev.*, **B 53**, p.878, 1996.
- [17] J. Sun, J. P. Longtin and P. M. Norris, "Ultrafast Laser Micromachining of Silica Aerogels", *J. Non-Cry. Sol.*, **281**, p.39, 2001.
- [18] K. Kumagai, M. Okoshi and M. Hanabusa, "Micromachining Transparent Materials by Femtosecond Laser", *Rev. Laser Eng.*, **27**, p.773, 1999.
- [19] Makoto Murai, Tomokazu Sano and Isamu Miyamoto: *Proc. 51st Symp. on Laser Precision Microfabrication*, p.44,



Wako city, 2000.

- [20] B. N. Chichkov, C. Momma, S. Nolte, F. von Alvensleben and A. Tünnermann, "Femtosecond, Picosecond and Nanosecond Laser Ablation of Solids", *Appl. Phys.*, **A 63**, p.109, 1996.
- [21] S. Küper and M. Stuke, "Femtosecond UV Excimer Laser Ablation", *Appl. Phys.*, **B 44**, p.199, 1987.
- [22] E. Ohmura and I. Miyamoto, "Molecular Dynamics Simulation of Laser Ablation Phenomina", *Rev. Laser Eng.*, **26**, p.800, 1998.
- [23] K. Kawahara, Y. Kurogi, N. Matsuo, H. Sawada, A. Yokotani and K. Kurosawa, "Morphological Characterization of Various Kinds of Materials in Femtosecond-Laser Micromachining", *Proc. 2nd Int. Symp. On Laser Precision Microfabrication*, Singapore, 2001, in press.
- [24] K. Kawahara, Y. Kurogi, N. Matsuo, H. Sawada, A. Yokotani and K. Kurosawa, "Development of Laser Turning Using Femtosecond Laser Ablation", *Proc. 2nd Int. Symp. On Laser Precision Microfabrication*, Singapore, 2001, in press.

## Waveguides produced by ultra-short laser pulses inside glasses and crystals

Stefan Nolte<sup>\*a</sup>, Matthias Will<sup>\*a</sup>, Boris N. Chichkov<sup>\*\*b</sup>, and Andreas Tünnermann<sup>\*a</sup>

<sup>a</sup>Institute of Applied Physics, University Jena; <sup>b</sup>Laser Zentrum Hannover e.V.

### ABSTRACT

Using tightly focused femtosecond laser pulses waveguides are fabricated inside glasses and crystalline materials. The guiding and attenuation properties at different wavelengths as well as the micromorphology of the irradiated samples are studied. We demonstrate the fabrication of single- and multimode waveguides with damping losses well below 1 dB/cm in fused silica. In crystalline quartz we found that the irradiated area has become amorphous due to the absorption of the laser radiation. In this case waveguiding is observed in a stress-induced region surrounding the irradiated, amorphous area.

**Keywords:** waveguides, integrated optics devices, microstructuring, ultrafast lasers, ultrafast laser processing

### 1. INTRODUCTION

The fabrication of optical waveguides and waveguide arrays in different glasses and crystals is required for many applications in integrated optics. At present, such structures are usually fabricated by ionic diffusion or exchange into a transparent substrate, by laser irradiation of special photorefractive materials, or by lithographic methods. Although these processes are well established, their use is in general limited to the production of two-dimensional photonic structures at the surface of the samples.

Recently, it has been demonstrated that optical waveguides can be directly written by ultrashort laser pulses.<sup>1,2</sup> When tightly focused into the bulk of a transparent solid, femtosecond laser pulses can produce a permanent refractive index modification inside a small focal volume. The laser energy is absorbed in the focal volume by multiphoton and avalanche absorption, leading to optical breakdown and microplasma formation.<sup>3-5</sup> The evolution of this microplasma induces structural and refractive index changes in the focal region. Possible mechanisms responsible for the refractive index modifications (which are still under discussion) are induced stress,<sup>6</sup> local density changes<sup>2</sup> and the formation of color centers.<sup>1</sup> In any case, this technique seems to be universal and allows to perform three-dimensional refractive index patterning. Buried optical waveguides and more complicate three-dimensional photonic structures can be fabricated in practically all transparent materials by moving the sample with respect to the laser beam.

Technological applications of this novel direct femtosecond laser-writing technique can spur new and innovative developments in integrated optics, optical communications, and optical data storage. Among the structures which have already been demonstrated are optical waveguides,<sup>1,2,7,8</sup> beam splitters,<sup>6</sup> X-couplers,<sup>9</sup> directional couplers,<sup>10</sup> stacked waveguides and waveguide arrays,<sup>9</sup> 3-dimensional data storage,<sup>11</sup> transmission gratings,<sup>12</sup> and long-period fiber gratings.<sup>13</sup>

To date there are two different processing techniques under investigation. When a high-repetition rate laser system with repetition rates in the MHz-range is used, localized melting due to the accumulative heating of several following pulses occurs.<sup>8</sup> In this case the time between successive pulses is not long enough to allow the deposited heat to diffuse away before the next pulse arrives. In consequence, the material is locally melted and resolidifies when the laser beam is moved to another place. The heating and cooling rates are dependent not only on pulse energy and pulse duration but also on the repetition rate and the scanning speed of the laser beam.

The second processing technique is based on a low repetition rate laser system (e.g. 1 kHz). In this case a single laser pulse is responsible for the material modifications and the time between the pulses is much longer than the deposited energy needs to dissipate. Although the scanning speed and the repetition rate do have an influence on the amount of the

modification in this case too, the induced changes are single pulse effects and the actual time between the pulses is unimportant.

In this paper we report on our recent advances in fabricating waveguides using low-repetition rate femtosecond lasers. The properties of waveguides fabricated in glasses and crystals and their dependence on the production laser parameters will be discussed.

## 2. EXPERIMENTAL

For the fabrication of optical waveguides we used a commercial low-repetition rate Ti:sapphire femtosecond laser system (1 mJ, 120 fs, 1 kHz, Spectra-Physics, Spitfire). Laser pulses at 800 nm with an energy of a few  $\mu\text{J}$  were focused by a 10x microscope objective with a numerical aperture of  $NA = 0.25$  and a focal length of  $f = 15.6$  mm into the transparent samples approximately 500  $\mu\text{m}$  below the surface. The samples could be moved perpendicular to the laser beam axis as shown in Fig. 1 by a computer controlled three-axis positioning system (Physik Instrumente, M-126.DG) with a maximum velocity of 1.5 mm/s. The third axis was used for controlling the focal position inside the target (depth). Using this setup, waveguides as long as 2.5 cm have been written, which was limited only by the travel range of the positioning system.

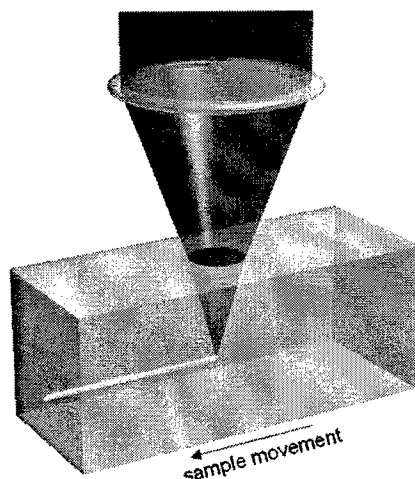


**Fig. 1:** Schematic of the experimental setup.

To measure the near-field intensity distribution of the light guided in the fabricated waveguides, we used laser radiation of an Ar-ion laser (1 mW) at 514 nm and of a 2 mW laser diode at 1.54  $\mu\text{m}$  coupled into a single mode fiber with  $NA = 0.11$  (mode field diameter 3-4  $\mu\text{m}$ ). In order to couple the laser radiation into the fabricated waveguides, the fiber was brought into contact with the polished sample surface. The near-field distribution of the guided mode was obtained by imaging the back-side of the fabricated waveguide onto a CCD-camera. By careful adjustment of the fiber-waveguide coupling, single propagation modes could be excited.

Direct measurements of the refractive index profile were performed using a commercial refractive-near-field (RNF) profilometer (Rinck elektronik, Germany). Absolute values of the refractive index were obtained by repeating measurements with a reference sample and an immersion fluid having well-known refractive indices. Although the RNF measurements were performed at a wavelength of 635 nm, we assume that the measured relative changes are approximately the same for other wavelengths as well.

In addition, the waveguides fabricated in crystalline material were analyzed with respect to their morphological structure using x-ray topography and transmission electron microscopy (TEM).

The transversal and longitudinal structure sizes produced by Gaussian femtosecond laser pulses focused close beneath the sample surface can be estimated from the well-known expressions

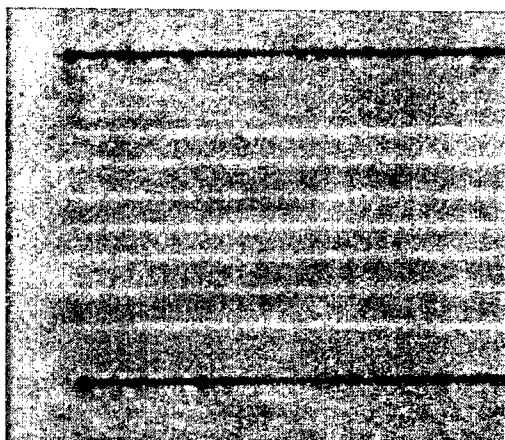
$$w_0 = M^2 f \lambda / \pi w_s, \quad b = 2 M^2 f^2 \lambda / \pi w_s^2, \quad (1)$$

where  $w_0$  is the radius of the focal spot,  $w_s$  is the initial beam radius, and  $b$  is the confocal parameter. In our case ( $\lambda = 800$  nm,  $M^2 = 1.6$ , and  $w_s / f \approx NA = 0.25$ ), Eq. (1) provides the following estimates for the transversal  $2w_0 \approx 3.2$   $\mu$ m and longitudinal  $b \approx 13$   $\mu$ m structure sizes. The actual dimensions might differ slightly from that predicted by Eq. (1). When the laser beam is focused at different depths inside the sample, one must take into account the spherical aberration. This will have an effect not only on structure size but also on the required energy to induce the modifications. Deep inside the sample the focus size will grow due to spherical aberration (for the axial rays the focus is located closer to the sample surface than for the peripheral rays). Therefore, the laser pulse energy which is required for a structural modification and also the structure size will grow with increasing depth of the focal position inside the sample. This behavior has been observed in recent experiments on the formation of voids in silica glass.<sup>14</sup>

While the influence of the spherical aberration would lead to slightly larger structures (although this effect is small due to the relatively low  $NA$  of the objective used), the actual structure dimensions could be smaller, since the simultaneous absorption of several photons at  $\lambda = 800$  nm is required to induce structural modifications (e.g. at least five photons are required in fused silica). These modifications appear above a certain irradiation threshold which depends on the laser intensity and the number of pulses. Close to this threshold only the central part of the laser pulse with the highest intensity can induce structural modifications inside a small fraction of the focal volume determined by Eq. (1).

### 3. WAVEGUIDES IN GLASS

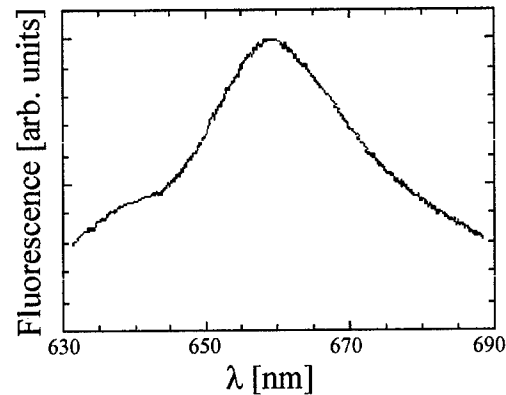
Fig. 2 shows a polarization contrast optical microscope image (top view) of several waveguides written in fused silica. While the waveguides (bright) are hardly visible, they can be easily distinguished from the traces of micro-destructions (dark), where a higher pulse energy was used to mark the irradiated area.



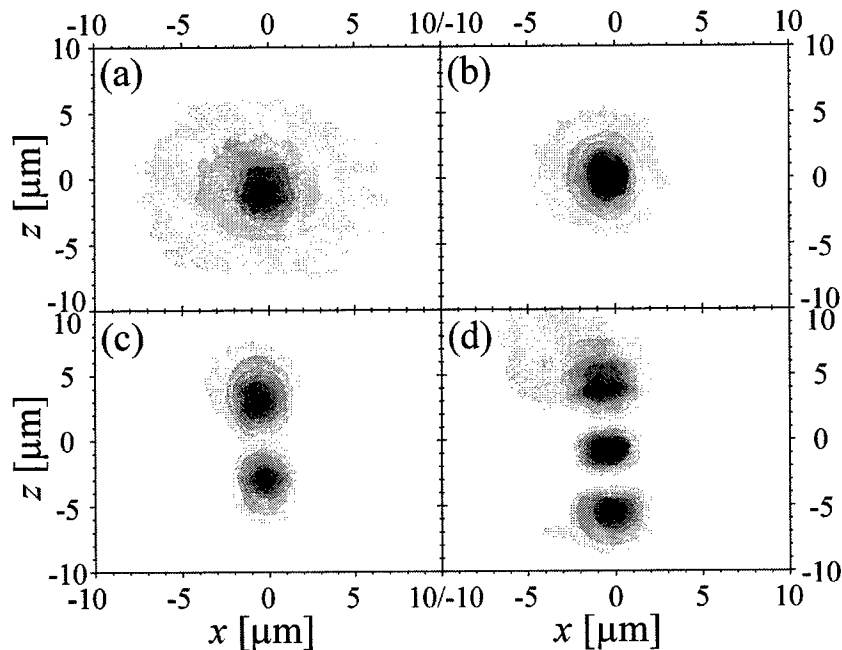
**Fig. 2:** Polarization contrast optical microscope image of waveguides written in fused silica with femtosecond laser pulses.

The induced refractive index modifications are very stable. We observed that the waveguiding properties were preserved after heating the samples up to 500 °C for several hours. In contrast, the characteristic fluorescence of color centers excited at ~600 nm (see Fig. 3), which are known to be formed during the waveguide fabrication process,<sup>1</sup> disappears, when the sample is heated to ~400 °C. After this annealing process no fluorescence emission is observable anymore, while the near-field distribution of the guided light hasn't changed. These observations allow to conclude that

the refractive index modifications in fused silica and the waveguiding properties are not determined by the generation of color centers.



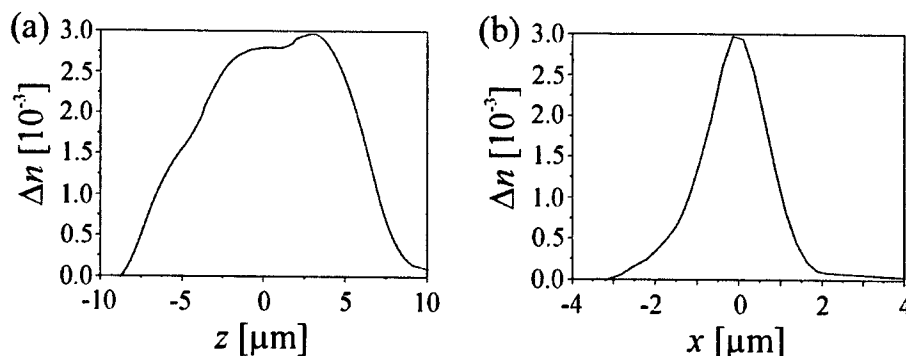
**Fig. 3:** Fluorescence of the produced waveguide (color centers) excited at 594 nm.



**Fig. 4:** Influence of the writing speed on the waveguiding properties at a wavelength of 514 nm. Only the highest order guided modes are shown for a writing speed of (a) 1000  $\mu\text{m/s}$ , (b) 500  $\mu\text{m/s}$ , (c) 80  $\mu\text{m/s}$ , and (d) 25  $\mu\text{m/s}$ .

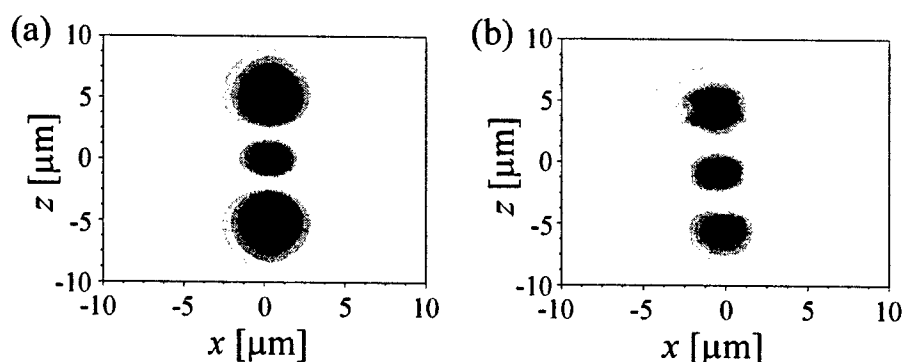
The waveguiding properties are not only dependent on the laser parameters but also on the writing speed (i.e. different spatial overlap of successive pulses in the sample). A lower writing speed and, thus, a higher number of pulses results in a stronger increase of the refractive index change. As a consequence, the near-field distribution is different. In Fig. 4 the measured near-field intensity distributions of waveguides written at different writing speeds is shown. In all cases the highest order mode for 514-nm laser radiation that is guided in these structures is shown. At writing speeds of 1000  $\mu\text{m/s}$  (Fig. 4a) and 500  $\mu\text{m/s}$  (Fig. 4b) the femtosecond laser induced refractive index changes are small and only single mode operation can be observed. When the writing speed is decreased down to 80  $\mu\text{m/s}$  (Fig. 4c) and 25  $\mu\text{m/s}$  (Fig. 4d) the refractive index increase is high enough that higher order modes are guided (in the horizontal axis the

waveguides are still single mode due to the smaller diameter in this direction compared to the vertical axis). RNF measurements yielded a refractive index increase of about  $\Delta n \approx 5 \cdot 10^{-4}$  for a writing speed of 1000  $\mu\text{m/s}$ . In case of the slow writing speed (25  $\mu\text{m/s}$ ) the measured refractive index increase amounts to  $\Delta n = 3 \cdot 10^{-3}$ . These values are in good agreement with previous observations.<sup>6</sup>



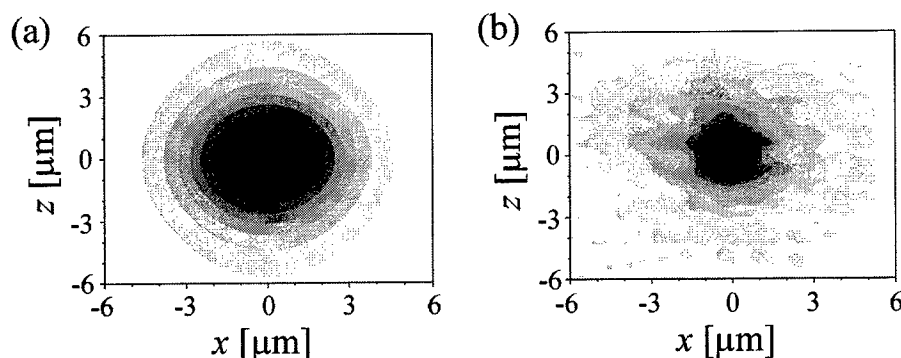
**Fig. 5:** Measured refractive index profiles ((a) longitudinal and (b) transversal) of the waveguide written at 25  $\mu\text{m/s}$ .

Fig. 5 shows a RNF measurement of the waveguide written at a speed of 25  $\mu\text{m/s}$ . The longitudinal (Fig. 5a) and transversal (Fig. 5b) profiles show approximately a gaussian shape and are in good agreement with the estimated structure sizes based on Eq. (1). Based on these measurements (approximated by Gaussian distributions) the modes that guide light of a certain wavelength can be identified. The field distribution of the guided modes was calculated using the commercial program BeamPROP 4.0 (RSoft, Inc.). This program is based on a finite difference beam propagation method which is used for the solution of the Helmholtz equation in the paraxial approximation. The calculated intensity distribution for the highest order guided mode at a wavelength of 514 nm is shown in Fig. 6(a). For comparison, the measured near-field intensity profile of the highest order mode guided in the corresponding waveguide is shown in Fig. 6(b). The measured and calculated intensity distributions are in a very good agreement.



**Fig. 6:** Comparison of (a) calculated and (b) measured guided light intensity distributions at 514 nm for the waveguide written at 25  $\mu\text{m/s}$ . For the calculations the measured refractive index profile of Fig. 5 was used.

Single mode operation can be achieved even in the waveguides produced at a writing speed of 25  $\mu\text{m/s}$  when a longer radiation wavelength is used, e.g. 1.54  $\mu\text{m}$ , which is important for optical communications. The calculated and measured near-field intensity distributions for this wavelength are shown in Fig. 7. The calculations are again based on the measured refractive index profiles shown in Fig. 5.



**Fig. 7:** Comparison of (a) calculated and (b) measured guided light intensity distributions at  $1.54\ \mu\text{m}$  for the waveguide written at  $25\ \mu\text{m/s}$ . At this wavelength the produced waveguide is single-mode in agreement with the calculations.

The fabricated waveguides show losses significantly lower than  $1\ \text{dB/cm}$  at a wavelength of  $514\ \text{nm}$ . This value has been determined by measuring the transmission after different waveguide lengths by cutting back the sample. This allows to subtract the coupling losses. The measured damping value has been confirmed by measuring the exponential decay of the straylight along the waveguide with a CCD camera.

#### 4. WAVEGUIDES IN CRYSTALS

The femtosecond direct writing technique is not only suited for the fabrication of waveguides in glass but also in crystalline materials. Fig. 8 shows a polarization contrast optical microscope image of a cross-cut through a waveguide in crystalline  $\alpha$ -quartz, which has been produced with the same setup as used for the fused silica samples but at a slightly higher pulse energy ( $14\ \mu\text{J}$ , writing velocity  $0.1\ \text{mm/s}$ ).

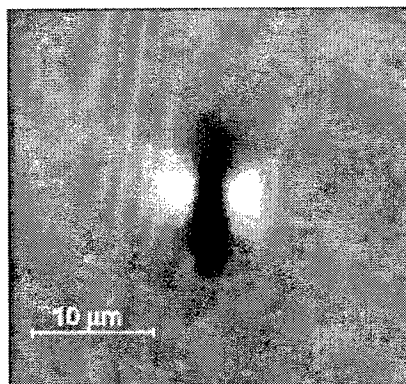


**Fig. 8:** Polarization contrast optical microscope image of a waveguide (end view) written in crystalline  $\alpha$ -quartz with femtosecond laser pulses.

Fig. 8 shows two different features. The dark, central area corresponds to the focal area, where the laser radiation was absorbed (the laser beam was incident from the top of the image), resulting in increased scattering losses. This dark area is surrounded by two bright regions indicating a refractive index change. The maximum refractive index increase  $\Delta n$  in these regions was estimated from interferometric analysis to be  $\Delta n \approx 0.01$ .

Due to the created refractive index profile light can be guided. Fig. 9 shows a near-field intensity distribution of  $514\text{-nm}$  radiation. The light is guided not in the central part, but in the bright areas visible in Fig. 8. Note that the near-field

distribution does not show a higher order mode comparable to Fig. 6b (in that case the peaks would have to be oriented along the other axis since the Rayleigh-length is larger than the beam diameter).

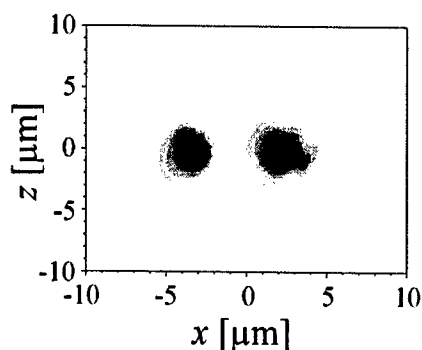


**Fig. 9:** Near-field distribution of 514 nm radiation guided in the waveguide produced by femtosecond laser pulses in crystalline  $\alpha$ -quartz.

This is confirmed by transmission electron microscopy (TEM) studies of the modified area. For that purpose thin slices have been cut from the laser irradiated crystals parallel to the beam direction, perpendicular to the written waveguide. These slices were thinned using mechanical polishing, dimpling and ion milling.

Figure 10 shows a cross-sectional TEM image of the modified region. The irradiated area has an elliptical shape with a width of about  $1\ \mu\text{m}$  and a height of approximately  $10\ \mu\text{m}$ . It can be divided into three parts according to their different contrasts. Region I has a high density of defects but the material is still crystalline. The central part II is amorphous, and region III corresponds to a crystalline area with strong strain contrast.

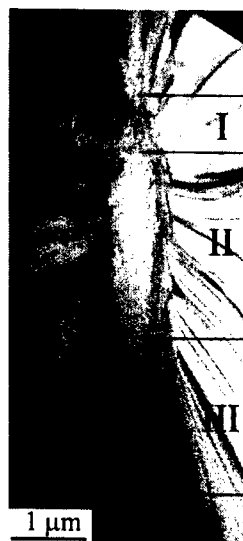


**Fig. 10:** Cross-sectional TEM image of a waveguide written with femtosecond laser pulses. Region I has a defective crystalline structure, region II is amorphous, region III shows a complex strain contrast of the crystalline matrix.

The focal area that has been irradiated is surrounded by a region showing high internal strains in the matrix. This can be deduced from the numerous bending contours present in this area. Since it is very reasonable that this strong strain field is responsible for the refractive index increase, we simulated the strain field by the finite element method (FEM) using



the code ANSYS. As input we used an expanding ellipse with the a diameter ratio of 1:10 embedded in a crystalline quartz matrix.

A two-dimensional solution was obtained within isotropic elastic approximations using the elastic constants of fused silica ( $E = 72$  Gpa,  $\nu = 0.17$ )<sup>15</sup>. The inner phase was simulated with a fictive thermal expansion coefficient  $\alpha$  of 0.06 and a fictive temperature change  $\Delta T$  of unity. The value  $\alpha \Delta T$  reflects the length change from crystalline to amorphous quartz according to the density change of the bulk quartz matrix during amorphization.<sup>16</sup> Figure 11 displays the hydrostatic pressure distribution, given by the trace of the strain tensor, according to the FEM results. Since the simulation does not reflect the actual behavior of the inner part, the solution is not valid inside the irradiated, ellipsoidal region. Two maxima of the strain distribution are clearly visible on both sides of the central ellipse. These maxima reflect a local increase in the material density, to which the refractive index is proportional in a first approximation. These results of the simulation are in agreement with the polarization contrast microscope image (Fig. 8).

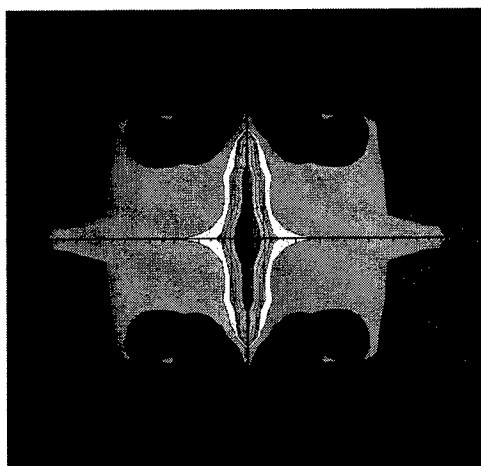


**Fig. 11:** Distribution of the hydrostatic pressure in the quartz matrix after irradiation with femtosecond laser pulses (expansion of the central, elliptical area) according to the FEM calculations. The solution is not valid in the central area.

The results of the TEM analysis are confirmed by x-ray topography measurements. These measurements yield a strongly disturbed core with an area of approximately  $1 \times 10 \mu\text{m}^2$  (in agreement with the TEM analysis). After a short transition zone of  $\sim 50$  nm, this central core is surrounded by a deformed crystalline lattice.

The measured losses of the waveguides in crystalline quartz are lower than 5 dB/cm. This is significantly higher than in glass, which is probably due to the disturbed central area. However, the produced refractive index changes are very stable. They remain present even after thermal annealing at  $1200^\circ\text{C}$  for several hours.

## 5. CONCLUSION

In conclusion, optical waveguides have been fabricated by femtosecond laser pulses inside glasses and crystalline quartz. In fused silica we demonstrated refractive index changes up to  $\Delta n = 3 \cdot 10^{-3}$  and waveguides with losses below 1 dB/cm. It has been shown that by changing only one parameter (the writing speed) it is possible to produce waveguides with a controllable mode number. For a laser wavelength of 514 nm both single mode and multimode waveguides with a controllable mode number have been fabricated. At the telecommunication wavelength of  $1.54 \mu\text{m}$  all fabricated waveguides showed single-mode operation. In both cases the measured near-field intensity distributions were in good agreement with simulations based on the measured refractive index profiles.

In crystalline  $\alpha$ -quartz refractive index changes of up to  $\Delta n \approx 0.01$  have been realized, which were stable up to temperatures above  $1200^\circ\text{C}$ . Based on these modifications waveguides with losses below 5 dB/cm have been produced.

Micromorphological TEM and x-ray analyses have revealed that the irradiated quartz has lost its crystalline structure and was transformed into amorphous material. Due to the amorphization the material expanded and produced strong strains in the surrounding matrix, which are responsible for the refractive index increase. This has been confirmed by FEM simulations. The light is in this case not guided in the irradiated area but in the surrounding modified region, which is still crystalline.

## ACKNOWLEDGEMENTS

We gratefully acknowledge the assistance of T. Gorelik and U. Glatzel for the TEM investigations and the simulation of the strain field and F. Wunderlich and K. Goetz in preparing the x-ray analysis. This work was supported by the Deutsche Forschungsgemeinschaft (SFB 196).

## REFERENCES

1. K. M. Davies, K. Miura, N. Sugimoto, and K. Hirao, "Writing waveguides in glass with a femtosecond laser," *Opt. Lett.* **21**, 1729-1731 (1996).
2. K. Miura, J. Qiu, H. Inouye, T. Mitsuyu, and K. Hirao, "Photowritten optical waveguides in various glasses with ultrashort pulse laser," *Appl. Phys. Lett.* **71**, 3329-3331 (1997).
3. D. Du, X. Liu, G. Korn, J. Squier, and G. Mourou, "Laser-induced breakdown by impact ionization in SiO<sub>2</sub> with pulse widths from 7 ns to 150 fs," *Appl. Phys. Lett.* **64**, 3071-3073 (1994).
4. B. C. Stuart, M. D. Feit, S. Herman, A. M. Rubenchik, B. W. Shore, and M. D. Perry, "Optical ablation by high-power short-pulse lasers," *J. Opt. Soc. Am. B* **13**, 459-468 (1996).
5. M. Lenzner, J. Krüger, S. Sartania, Z. Cheng, Ch. Spielmann, G. Mourou, W. Kautek, and F. Krausz, "Femtosecond optical breakdown in dielectrics," *Phys. Rev. Lett.* **80**, 4076-4079 (1998).
6. D. Homoelle, S. Wielandy, A. L. Gaeta, N. F. Borrelli, and C. Smith, "Infrared photosensitivity in silica glasses exposed to femtosecond laser pulses," *Opt. Lett.* **24**, 1311-1313 (1999).
7. F. Korte, S. Adams, A. Egbert, C. Fallnich, A. Ostendorf, S. Nolte, M. Will, J.-P. Ruske, B. N. Chichkov, and A. Tünnermann, "Sub-diffraction limited structuring of solid targets with femtosecond laser pulses," *Opt. Express* **7**, 41-49 (2000).
8. C. B. Schaffer, A. Brodeur, J. F. Garcia, and E. Mazur, "Micromachining bulk glass by use of femtosecond laser pulses with nanojoule energy," *Opt. Lett.* **26**, 93-95 (2001).
9. K. Minoshima, A. M. Kowalevich, I. Hartl, E. P. Ippen, and J.G. Fujimoto, "Photonic device fabrication in glass by use of nonlinear materials processing with a femtosecond laser oscillator," *Opt. Lett.* **26**, 1516-1518, (2001).
10. A. M. Streltsov and N. F. Borrelli, "Fabrication and analysis of a directional coupler written in glass by nanojoule femtosecond laser pulses," *Opt. Lett.* **26**, 42-43 (2001).
11. E. N. Glezer, M. Milosavljevic, L. Huang, R. J. Finlay, T.-H. Her, J. P. Callan, and E. Mazur, "Three-dimensional optical storage inside transparent materials," *Opt. Lett.* **21**, 2023-2025 (1996).
12. L. Sudrie, M. Franco, B. Prade, and A. Mysyrowicz, "Writing of permanent birefringent microlayers in bulk fused silica with femtosecond laser pulses," *Opt. Commun.* **171**, 279-284 (1999).
13. Y. Kondo, K. Nouchi, T. Mitsuyu, M. Watanabe, P. G. Kazansky, and K. Hirao, "Fabrication of long-period fiber gratings by focused irradiation of infrared femtosecond laser pulses," *Opt. Lett.* **24**, 646-648 (1999).
14. W. Watanabe, T. Toma, K. Yamada, J. Nishii, K. Hayashi, and K. Itoh, "Optical seizing and merging of voids in silica glass with infrared femtosecond laser pulses," *Opt. Lett.* **25**, 1669-1671 (2000).
15. N. P. Bansal, R. H. Doremus, *Handbook of Glass Properties*, Academic Press, Orlando (1986).
16. F. Harbsmeier, W. Bolse, "Ion beam induced amorphization in  $\alpha$  quartz," *J. Appl. Phys.* **83**, 4049-4054 (1998).

\* [nolte@iap.uni-jena.de](mailto:nolte@iap.uni-jena.de); phone +49 3641 657656; fax +49 3641 657680; <http://iapnt.iap.uni-jena.de>; Institute of Applied Physics, Friedrich-Schiller-University Jena, Max-Wien-Platz 1, 07743 Jena, Germany; \*\* [ch@lzh.de](mailto:ch@lzh.de); phone +49 511 2788316; fax +49 511 2788100; <http://www.lzh.de>; Laser Zentrum Hannover e.V., Hollerithallee 8, 30419 Hannover, Germany

# Fabrication of birefringent microstructures in transparent materials with femtosecond laser pulses

Wataru Watanabe\*<sup>a</sup>, Kazuhiro Yamada\*<sup>a</sup>, Daisuke Kuroda\*<sup>a</sup>, Taishi Shinagawa\*<sup>a</sup>, Taishi Asano\*<sup>a</sup>, Junji Nishii\*\*<sup>b</sup>, and Kazuyoshi Itoh\*\*\*<sup>c</sup>

<sup>a</sup> Department of Applied Physics, Graduate School of Engineering, Osaka University;

<sup>b</sup> Photonics Research Institute, Kansai Center, National Institute of Advanced Industrial Science and Technology;

<sup>c</sup> Department of Material and Life Science, Graduate School of Engineering, Osaka University

## ABSTRACT

When femtosecond laser pulses are tightly focused inside the bulk of transparent materials, the intensity in a focal volume becomes high enough to produce submicrometer-scale structural modifications. The modifications has been applied to fabricate three-dimensional photonic structures. Tightly-focused femtosecond laser pulses create voids, which are surrounded by densified material. In this paper we show that the shapes of voids can be controlled by the spatial profile of incident laser pulses. We also show that the diffraction intensities due to the fabricated arrays of voids depend on the polarization-states of the readout beam. Finally we demonstrate that irradiation of femtosecond laser pulses moves a void inside calcium fluoride and silica glass without any mechanical translations of the optical system. *In situ* observation revealed that a void moves towards incident direction of laser pulses as long as 2 micron.

Keywords: ultrashort laser pulses, nonlinear optics, micromachining, birefringence, glass

## 1. INTRODUCTION

When a femtosecond laser pulse is focused inside the bulk of a transparent material, the intensity in a focal volume becomes high enough to produce permanent structural modifications. This three-dimensional modifications has been utilized as optical data storage,<sup>1-3</sup> waveguides,<sup>4-7</sup> gratings,<sup>8,9</sup> couplers,<sup>10,11</sup> and hole drilling<sup>12</sup> inside a wide variety of transparent materials including glasses, crystals, and plastics. Submicrometer-damages are produced by tightly-focusing femtosecond laser pulses with high numerical-aperture (NA) lenses. The damages were demonstrated to be cavities or voids surrounded by densified

\*w-wata@ap.eng.osaka-u.ac.jp; phone 81 6 6879 7326; fax 81 6 6879- 7295; <http://optinfo.ap.eng.osaka-u.ac.jp/>; Department of Applied Physics, Graduate School of Engineering, Osaka University, 2-1 Yamadaoka, Suita, Osaka 565-0871, Japan

\*\*junji.nishii@aist.go.jp ; phone 81 727-51-9543; fax 81 727-51-9637; Photonics Research Institute, Kansai Center, National Institute of Advanced Industrial Science and Technology, 1-8-31, Midorigaoka, Ikeda, Osaka 563-8577, Japan

\*\*\*itoh@ap.eng.osaka-u.ac.jp; phone 81 6 6879 7850; fax 81 6 6879- 7295; <http://optinfo.ap.eng.osaka-u.ac.jp/>; Department of Material and Life Science, Graduate School of Engineering, Osaka University, 2-1 Yamadaoka, Suita, Osaka 565-0871, Japan

material.<sup>1,2</sup> In this paper we show that the shapes of voids can be controlled by the spatial profile of incident laser pulses. We also show that the diffraction intensities due to the fabricated arrays of voids depend on the polarization-states of the readout beam. We have recently demonstrated the optical movement of a void and merger of two voids along the optical axis by the translation of the focal spot of a focusing lens.<sup>3</sup> We show that the void continues to move inside calcium fluoride and silica glass during irradiation of femtosecond laser pulses without any mechanical translations of optical components.<sup>13</sup> *In situ* observation revealed that a void moves towards incident direction of laser pulses as long as 2 micron by a train of successive laser pulses. We also move a void along perpendicular direction to the beam propagation axis by translation of the focal volume of a focusing lens.

## 2. EXPERIMENTAL SETUP

The experiments were performed with a regeneratively amplified Ti:sapphire laser system (Spectra-Physics, Inc., Hurricane), which produces 130-fs, 800-nm pulses at 1 kHz. Figure 1 shows a schematic of the experimental setup. The beam was magnified by the help of a concave lens L1 with a focal length  $f$  of negative 60 mm and an achromatic convex lens L2 ( $f = 300$  mm). The central part of the beam was truncated by an aperture (diameter; 5 mm) to give uniform spatial profile. The pulse energy was controlled by a half-wave plate and a polarizer. The linearly polarized laser pulses were tightly focused by a high-NA microscope objective (NA, 0.55) to localize structural changes. The four-sides of the samples were optically polished to obtain sideview of bulk modifications. To visualize the structural change *in situ*, optical images of the voids were observed from the direction perpendicular to the optical axis by a transilluminated optical microscope.

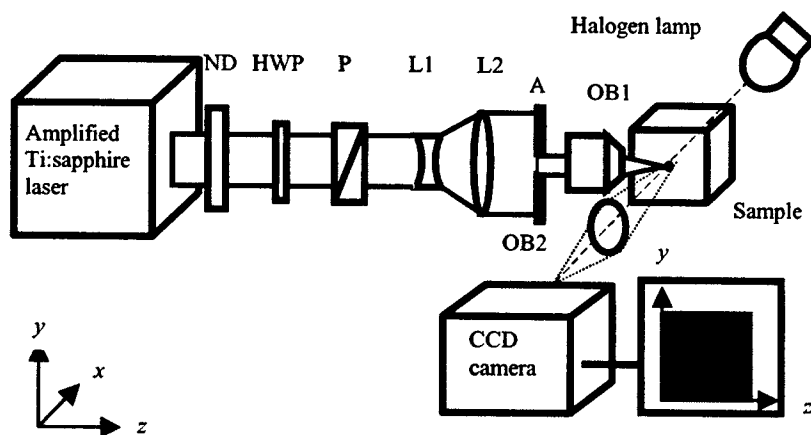


Fig. 1: Schematic of experimental setup for creation by femtosecond laser pulses and in situ observation of voids. ND, HWP, and P denote neutral density filter, half-wave plate, and polarizer, respectively. OB1 and OB2 indicate objective lenses. L1 and L2 indicate lenses.

## 3. SHAPE OF VOIDS AND POLARIZATINAL DEPENDENCE

### 3.1 Shapes of voids by focusing spatially-controlled beam

We investigate how the spatial profiles of incident laser pulses affect to the shapes of voids. Rectangular masks were placed in front of OB1 to give spatially controlled beam. The central part of the beam passed

through the mask which was shown in Figs. 2 (a) or (b). The laser pulses were focused at the depth of the sample of 300  $\mu\text{m}$  in silica glass. The shape of mask was rectangular and its size was 4 mm x 0.8 mm. The pulse energy was 0.8  $\mu\text{J}/\text{pulse}$  in front of the mask. Eight successive pulses were normally launched during the exposure time of 1/125 s. After we fabricated the voids, the surface of the sample was polished down until the surface level was at the level of the voids and was observed under a scanning-electron microscope (SEM). Figures 2 (c) and (d) show photographs of SEM images of fabricated voids with mask (a) and (b), respectively. When we used the mask of Fig. 2 (a), the shape of voids was elongated along  $y$  axis. On the other hand, when we used the mask of Fig. 2 (b), the shape of voids was elongated along  $x$  axis. The shapes of the voids can be controlled by those of masks.

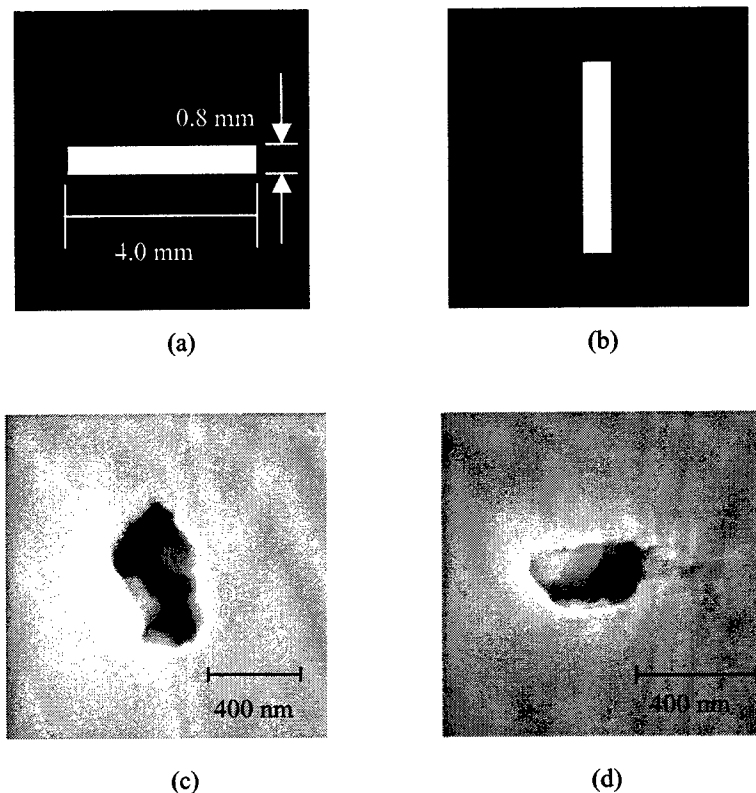


Fig 2: (a), (b) Rectangular masks placed in front of the focusing objective to control spatial profile of the focusing beam. (c), (d) SEM images of fabricated voids with mask (a) and (b), respectively.

### 3.2 Fabrication of two-dimensional array of voids and polarizational dependence of diffraction intensity

We fabricated a periodic structure and investigated the dependence of diffraction intensities on the polarization-state of readout beam. The fabrication of an array of voids was performed by displacing the sample in the  $xy$  plane perpendicular to the laser propagation axis by steps of 5  $\mu\text{m}$ . We fabricated 100 x 100 voids at the depth of 200  $\mu\text{m}$  through the mask which was shown in Fig. 2(b). Figure 3 shows an optical image of the two-dimensional array of voids. The image was observed under illumination by halogen lamp. The shapes voids elongated along  $x$  axis. Two-dimensional array of voids forms a periodic diffraction pattern. Figure 4 shows a far-field diffraction pattern of a cw-He-Ne laser beam at the wavelength of 633 nm

transmitted through the array of voids embedded in silica glass. The central undiffracted beam is blocked. The diffraction pattern is distorted by spherical aberration of the rear surface of the sample.

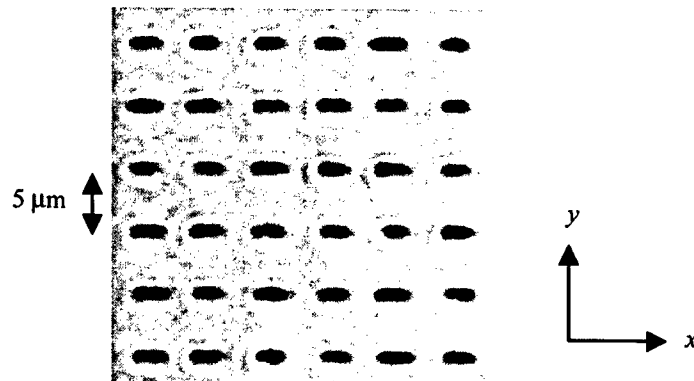


Fig.3: Optical image of two-dimensional array of voids. The voids were elongated along x axis.



Fig.4: Far-field diffraction pattern of a He-Ne laser beam transmitted through the array of voids written in silica glass.

The diffraction intensities due to the grating were measured. Figure 5 shows that the intensities of the beams diffracted along  $y$  axis were plotted as a function of polarizational angle of readout beam. The He-Ne laser beam was linearly polarized by a polarizer and the polarization of the beam was rotated by a half-wave plate. The original of direction of electric field or polarization position angle was set to be  $+x$ -axis and a polarization position angle was measured with the anti-clock-wise angle from the original. Diffraction intensities of first order to fourth order sinusoidally vary with the polarizational angle. Diffraction intensity with  $x$ -polarized beam is twice as large as that with  $y$ -polarized beam. The diffraction intensities due to the fabricated arrays of voids depend on the polarization-states of the readout beam.

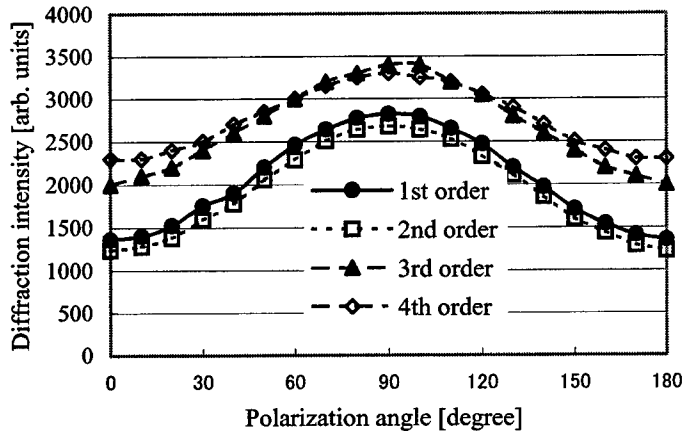


Fig. 5: Diffraction intensities due to the fabricated arrays of voids depend on the polarization-states of the readout beam.

### 3.3 Etching experiments

After we fabricated the voids without any masks in silica glass, the sample was polished down until the surface level was at the level of the voids. The sample was etched with 5 mol-% during 1 minutes. Figure 6 shows a photograph of a SEM image before and after etching. The modified region was with a diameter of 1 micron after etching, which may correspond to the compacted region around the void. We also found the several cracks running outer ward from the void. These cracks imply the presence of strong expansion due to compaction of the glass.

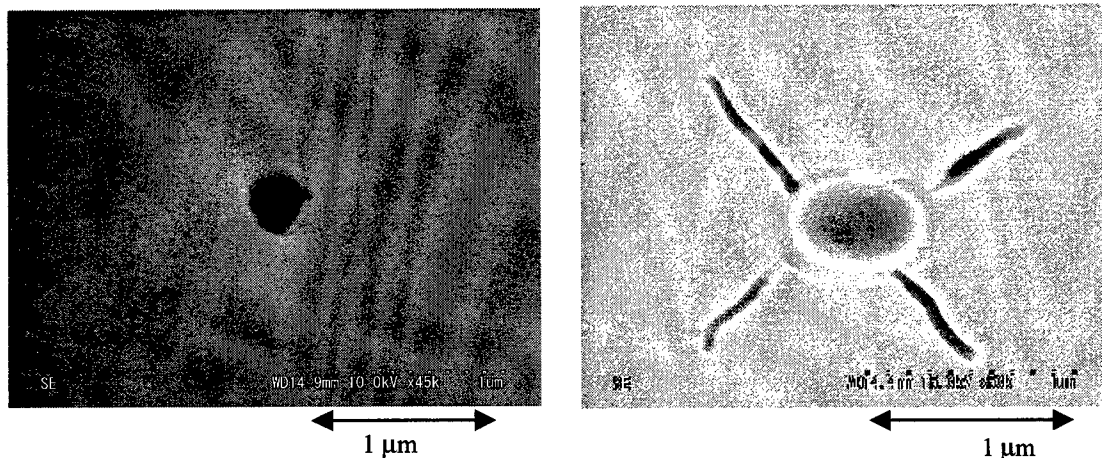


Fig. 6: SEM images before and after etching The sample was etched with 5 mol-% during 1 minutes.

## 4. MOVEMENT OF VOIDS UNDER SUCCESSIVE IRRADIATION OF LASER PULSES

We have recently demonstrated the optical movement of a void and merger of two voids along the optical axis by the translation of the focal spot of a focusing lens.<sup>3</sup> We show that the void continues to move inside calcium fluoride and silica glass during irradiation of femtosecond laser pulses without any mechanical

translations of optical components.<sup>13</sup> We will show in the following the experiments with 3-mm-thick plate of calcium fluoride at room temperature, however, similar effects were also observed for amorphous silica glass. We investigated the movement of voids by changing the number of laser shots under fixed pulse energy. We operated the laser system at a repetition rate of 1 Hz. We created voids in the bulk calcium fluoride at a depth of 200  $\mu\text{m}$  beneath the surface. The energy threshold for the observable permanent structural change was 386 nJ/pulse by a single shot. The number of laser shots was varied from 1 shot to 5 shots. As the number of laser shots increased, the void moved toward  $-z$  direction and the optical images of the void became darker. *In situ* observation showed that the laser pulses began to flash around the void after creation of the void. We showed that the void moved approximately by 2  $\mu\text{m}$  in the  $z$  direction by successive irradiation of laser pulses without any mechanical translations. This direction of movement coincides with the translation of a void reported by our group.<sup>3</sup> As we increased the number of laser shots more than five pulses, the shape of void seemed to be elongated along  $z$  direction and then the second void was visible around the original location of first void. We investigated the distance of movement with respect to the incident energy.

The minimum possible spacing between two adjacent voids was 3  $\mu\text{m}$  and 7  $\mu\text{m}$  in  $y$  axis and  $z$  axis, respectively. This is because the focal area where the intensity is high is considered to be cylindrical. We could move two separated voids simultaneously. After creation of a void, another void was created with a spacing of 5  $\mu\text{m}$ . We set the focal point of the focusing lens in the middle of two voids. Then we irradiated laser pulses. Two voids move toward  $-z$  direction at the same time shot by shot.

So far we only moved the void in the  $-z$  direction. We succeeded in lateral movement of a void along the axis perpendicular to the beam propagation axis for the first time. Figures 7 show optical images of movement of voids observed in the  $yz$  plane under illumination by unpolarized halogen lamp. The black region in the image corresponds to the void. The beam propagation direction of the femtosecond laser pulses ( $+z$  direction) was left to right in the plane of the image. We created several voids and set the focal point of the objective lens in the upper left in the figure. Then we created a void (Fig. 7 (a)). We translated the focal point of the focusing objective to the  $+y$  direction by 1  $\mu\text{m}$  and irradiated laser pulses. The void hopped upward in the figure. We repeated the procedure (Fig. 7 (b)-(d)). The void moves by 2  $\mu\text{m}$  along the direction perpendicular to optical axis.

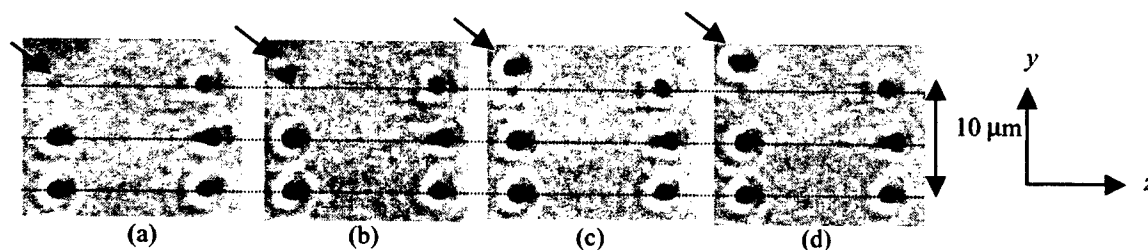


Fig. 7: Lateral movement of a void perpendicular to the beam propagation axis.

The movement of the void is attributed to the repetition of localized melting and resolidification by irradiation of successive laser pulses. The physical characteristics of the surrounding region and the trajectory after the movement of the void may change due to the structural transition caused by the breaking of bonds in the materials followed by melting and resolidification. Details of material changes are still open for question.

## CONCLUSIONS

We showed that the shapes of voids can be controlled by the spatial profile of incident laser pulses. We also show that the diffraction intensities due to the fabricated arrays of voids depend on the polarization-states of the readout beam. We demonstrated the observation that a void moves under irradiation of femtosecond laser



pulses inside calcium fluoride and silica glass. *In situ* observation revealed that the void moved towards incident direction of laser pulses as long as 2 micron by successive laser pulses without any mechanical translations of optical systems. We demonstrated lateral movement of a void along the axis perpendicular to the beam propagation axis. Studies of movement of voids may lead to applications to the devices of optical information-processing and communication such as the rewritable, three-dimensional, and high-speed optical storage and reconfigurable micro-structures inside transparent materials. The present study also suggests that one allows to fabricate micro birefringent structures inside silica glass.

### ACKNOWLEDGEMENTS

The experiments reported in this paper were conducted at the Venture Business Laboratory, Osaka University.

### REFERENCES

1. E. N. Glezer, M. Milosavljevic, L. Huang, R. J. Finlay, T.-H. Her, J. P. Callan, and E. Mazur, *Opt. Lett.* **21**, pp. 2023-2025, 1996.
2. E. N. Glezer and E. Mazur, *Appl. Phys. Lett.* **71**, pp. 882-884, 1997.
3. W. Watanabe, T. Toma, K. Yamada, J. Nishii, K. Hayashi, and K. Itoh, *Opt. Lett.* **25**, pp. 1669-1671, 2000.
4. K. M. Davis, K. Miura, N. Sugimoto, and K. Hirao, *Opt. Lett.* **21**, pp. 1729-1731, 1996.
5. K. Miura, J. Qiu, H. Inouye, T. Mitsuyu, and K. Hirao, *Appl. Phys. Lett.* **71**, pp. 3329-3331, 1997.
6. K. Yamada, T. Toma, W. Watanabe, J. Nishii, and K. Itoh, *Opt. Lett.* **26**, pp. 19-21, 2001.
7. C. B. Schaffer, A. Brodeur, J. F. Garca, and E. Mazur, *Opt. Lett.* **26**, pp. 93-95, 2001.
8. L. Sudrie, M. Franco, B. Prade, A. Mysyrowicz, *Opt. Commun.* **171**, pp. 279-284, 1999.
9. T. Toma, Y. Furuya, W. Watanabe, J. Nishii, K. Hayashi, and K. Itoh, *Opt. Rev.* **7**, pp. 14-17, 2000.
10. D. Homoelle, W. Wielandy, A. L. Gaeta, E. F. Borrelli, and C. Smith, *Opt. Lett.* **24**, pp. 1311-1313, 1999.
11. A. M. Streltsov and N.F. Borrelli, *Opt. Lett.* **26**, pp. 42-44, 2001.
12. Y. Li, K. Itoh, W. Watanabe, K. Yamada, D. Kuroda, J. Nishii, and Y. Jiang, *Opt. Lett.* **27**, pp. 1912-1914, 2001.
13. W. Watanabe and K. Itoh, *Science*, submitted.

# Ultra-fast laser-induced processing of materials: fundamentals and applications in micromachining

Tae Y. Choi, Anant Chimmalgi and Constantine P. Grigoropoulos  
Department of Mechanical Engineering, University of California, Berkeley

## ABSTRACT

Fundamental questions arise regarding the possibility and nature of melting and the ensuing mechanism of ablation in femtosecond laser processing of materials. A comprehensive experimental study is presented to address these issues in depth and detail. The mechanisms of ultra-fast (femtosecond) laser-induced phase-transformations during the laser interactions with materials have been investigated by time-resolved pump-and-probe imaging in both vacuum and ambient environment. The temporal delay between the pump and probe pulses is set by a precision translation stage up to about 500 ps and then extended to the nanosecond regime by an optical fiber assembly. Ejection of material in the form of nanoparticles is observed at several picoseconds after the main (pump) pulse. The ignition of surface-initiated plasma into the ambient air immediately following the pump pulse and the ejection of ablated material in the picosecond and nanosecond time scales have been probed by high-resolution, ultra-fast shadowgraphy. To further dissect the origin and evolution of the ablation process, a double pulse experiment has been implemented, whereby both the pump and probe pulses are split into two components each separated by variable temporal delays. A diffractive optical element is used to fabricate micro-channels in silicon wafers.

**Key words:** Femtosecond laser, ablation, pump-and-probe, double beam, diffractive optical element

## 1. INTRODUCTION

### 1.1 Femtosecond laser source

Ultra-short laser pulses impart extremely high intensities and provide precise laser-ablation thresholds at substantially reduced laser energy densities. Thorough knowledge of the short-pulse laser interaction with the target material is essential for controlling the resulting modification of the target topography. Pulsed lasers are attractive for one-step micro-machining of sensitive microstructures and micro-electro-mechanical system (MEMS) components. The use of ultra-short pulses with correspondingly high laser intensities reduces the extent of the heat penetration into the target and facilitates the instantaneous material expulsion. This enables high aspect ratio cuts and features, free of debris and lateral damage<sup>1-3</sup>. Therefore, the ablation process is extremely stable and reproducible. As a result, the produced structure size is not limited by thermal or mechanical damage, i.e., melting, formation of burr and cracks, etc. Thus, the minimal achievable structure size is limited only by diffraction to the order of the wavelength<sup>4</sup>.

### 1.2 Femtosecond laser interaction with solids

Femtosecond time-resolved experiments upon ultra-fast irradiation have shown the existence of a high-reflectivity phase for laser fluences exceeding a critical threshold<sup>5</sup>. Yet, many fundamental questions remain concerning the physical origin of the vaporization process under the extreme non-equilibrium conditions imposed by femtosecond laser irradiation<sup>6</sup>. The possibility and role of explosive vaporization in the ultra-short pulse regime are unclear. Liquid expulsion in the form of droplets could account for enhanced ablation rate<sup>7</sup>. However, the recoil pressure, the triggering of molten liquid surface instability, and the subsequent liquid phase decomposition are not well understood.

### 1.3 Diffractive optical elements

Diffractive optical elements (DOE) could be valuable optics for micromachining. The most useful equation for understanding DOE can be written by assuming first order diffraction and normal incidence as follows.

$$\sin \theta = \frac{\lambda}{d} \quad (1)$$

where  $\theta$  is diffracting angle,  $\lambda$  is wavelength of the incoming light, and  $d$  is the period of the gratings. If we hold the period  $d$  constant in one dimension across the aperture, for instance, a linear phase grating can be obtained to steer the incoming beam. If hundreds of gratings with different periods in one dimension across an aperture are superposed, complex intensity shapes can be produced from any incoming beam. The design of complex extended images is then computationally intensive. A uniform rectangle intensity pattern can be used for rectangular channel fabrication. Micro-fluidic channels used for biological applications and micro heat exchangers can be fabricated using this procedure.

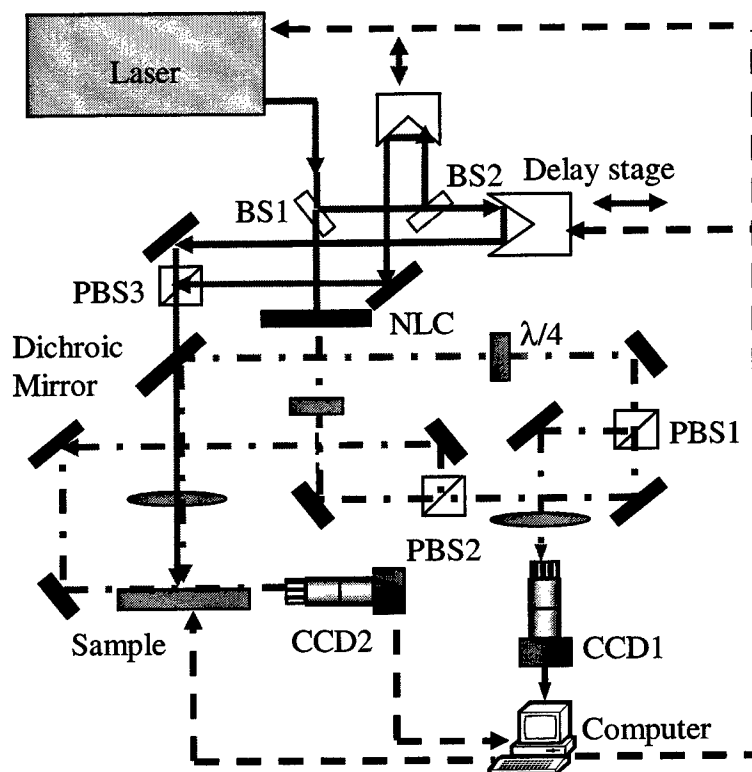


Fig. 1 Schematic diagram of experiment

This paper presents an experimental study on the interaction of femtosecond laser pulses with crystalline silicon semiconductor wafers. The ablative material removal process is monitored by utilizing ultra-fast pump-and-probe imaging supplemented by a fiber optic technique. Two pump beams and two probe beams are used for observing plasma dynamics as well as shockwave propagation in ambient environment. The two pump beams have a fixed delay time ranging from 1 to 50 ps to more deeply explore the explosive ablation mechanism. Further, a diffractive optical element is used for fabrication of micro-fluidic channels.

## 2. EXPERIMENT

### 2.1 Experimental apparatus

A detailed schematic of the experimental apparatus is shown in Fig. 1. A femtosecond mode-locked seed beam of 14 nm bandwidth, pulse energies in the nanojoule range and repetition rate of 80 MHz is emitted from a Ti:sapphire oscillator pumped by a diode laser. A pulsed Nd:YLF operating at the repetition rate of 1 kHz pumps the seed beam through a regenerative amplifier. Using the chirped pulse amplification technique, ultra-short pulses are generated with a FWHM pulse width of about 83 fs, 800 nm wavelength and 1 mJ maximum pulse energy. Fluctuations of the beam energy were measured to be within 1 % of mean value.

During the present experiment, single pulses were used at variable pulse energies of 0.034 mJ ~ 0.36 mJ focused onto about a 100  $\mu\text{m}$ -diameter spot. This corresponds to energy fluences of 0.42 ~ 4.6 J/cm<sup>2</sup>. The collinear scheme was applied to facilitate alignment of the two split beams (pump and probe beam, both normal to the sample), and was ensured by passing them through two identical iris apertures. Split by the polarizing beam splitter, the second probe beam was used to take the shadowgraph viewed from the side. The position of the focal waist and the focal spot size of the pump beam were determined by the knife-edge technique<sup>8</sup>.

## 2.2 Detailed description of beam path

The pump and probe beam paths are indicated by the solid and dotted lines, respectively. A 10 % portion of the fundamental 800 nm beam (probe beam) served to generate a frequency-doubled ( $\lambda=400$  nm) beam through the nonlinear crystal (NLC). The remaining 90% of the original beam (pump beam) was utilized to heat up the sample. The pump beam was horizontally (P) polarized before hitting NLC. The NLC changes the polarization to vertical (S). A half-waveplate ( $\lambda/2$ ) then changes the polarization back to P so that it can pass through the polarizing beam splitters (PBS1 and PBS2), which transmits P-polarized and reflects S-polarized light. The beam is then converted to circularly polarized by a quarter waveplate ( $\lambda/4$ ). The dichroic mirror (DM) reflects the frequency-doubled beam but transmits the pump beam. The probe beam arrives at the sample at specified delay time after the irradiation by the pump beam. A micrometer stage is employed to set this time delay. The accuracy of the pump-and-probe experiment depends on precise alignment of the heating and interrogating beams. Errors introduced by misalignment of the two beams were thoroughly examined as suggested by Capinski and Maris<sup>9</sup>. In the present experiment, the axes of the probe beams in and out of the delay stage were aligned parallel to the stage travel direction. No shift of the probe beam intensity distribution was detected up to about 100 ps.

The reflected probe beam was directed through the  $\lambda/4$  waveplate so that its polarization was converted to S and after passing through the polarizing beamsplitter (PBS) formed an image of the heated target area at the focal plane of a 250 mm lens. The image was relayed via an interference filter centered at 400 nm, a 100x microscope objective and a 10x eyepiece to a CCD camera. The camera was connected to a digital image acquisition board of a personal computer. The board was triggered by a delay pulse generator that also synchronized the firing of the femtosecond laser pulse. The acquired digitized image was then processed by software to extract the gray scale intensity distribution.

Reflected by PBS1, the second probe beam was used to take shadowgraphs of the ablation process in conjunction with a super long working distance objective lens and a CCD camera. The plasma thickness in this case can be estimated to be a few micrometers at an elapsed time of a few tens of picoseconds. Hence, alignment of the lens with respect to the workpiece placement is critical to this experiment. Sample rotation and tilt were thoroughly examined so that the single shot measurement can have reasonable consistency. For shock wave propagation measurement at longer time delay, optical fiber was used. Beam coupling into the fiber optical component is critical for obtaining the smooth Gaussian profile.

## 3. RESULTS AND DISCUSSION

### 3.1 Plasma dynamics

Time-resolved surface images taken at various time steps reveal many physical phenomena as shown in Fig. 2. The plasma annealing mechanism<sup>10</sup> is monitored by the enhanced reflectivity recorded in the early stage of the heating process ( $t < 2\text{-}3$  ps), indicating presence of a dense electron-hole plasma or a non-thermal liquid phase. The post-analyzed absolute reflectivity data at the center in Fig. 3 reveal this mechanism is active up to 2 or 3 ps. Diffusion and recombination of electron-hole pairs lead to lower reflectivity between 2 and 4 ps. This process seems to last longer for the higher energy fluences due to denser electron hole plasma. Additionally, the reflectivity drops more sharply for the higher fluences as shown in Fig. 3 (a). Based on the measured reflectivity, it can be stated that material ablation starts at around 10 ps. It should be noted, however, that energetic electrons overcoming work function can escape from the target. Consequently, the electric field created by the charge separation between the escaping electrons and parent ions effectively pulls ions out of the target.

Side-view shadowgraphs in Fig. 4 provide direct visualization of plasma development supporting this argument. Gradual darkening of the central portion of the irradiated area was observed for longer elapsed times due to the emergence of a very thin layer consisting of a mixture of nanometer-sized scattering particles in the proximity of the sample surface.

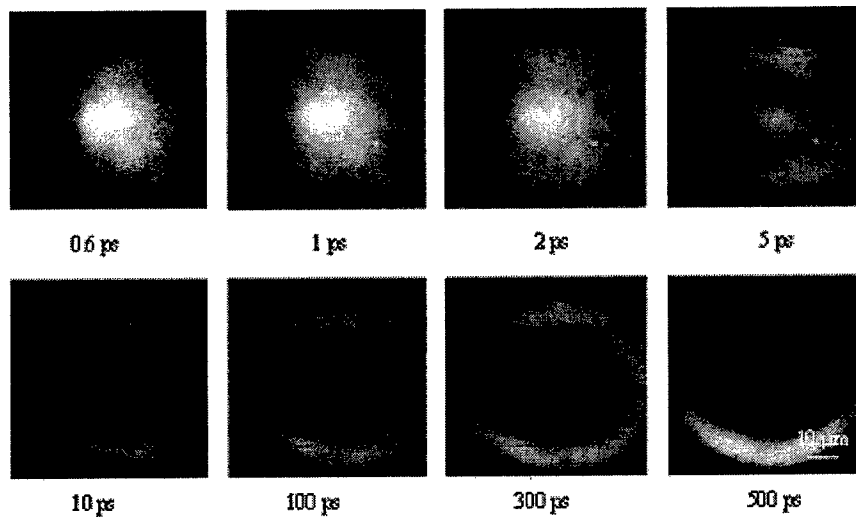


Fig. 2 Time-resolved surface images @ fluence of  $1.5 \text{ J/cm}^2$

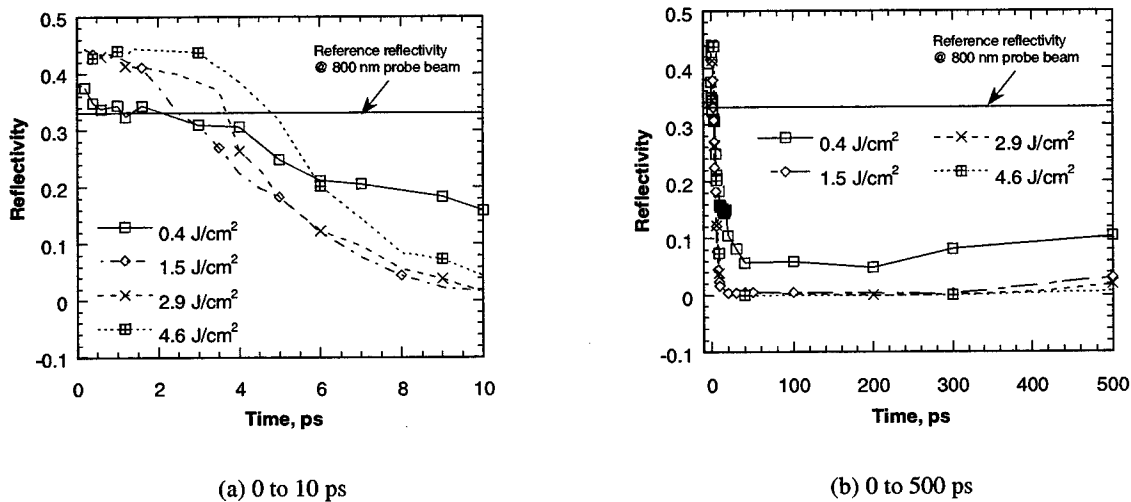


Fig. 3 Time resolved surface reflectivity @ fluence of  $1.5 \text{ J/cm}^2$

The side view picture at 10 ps does not differ significantly from the initial image (a) and does not show the dark protrusion depicted in (c), (d), and (e). The dark spot extruded from the sample has been observed at around 50 ps in case of the side view images. Figures 4(d) and 5(e) reveal a distinct curved front moving towards the sample, implying discontinuity of electron density and therefore of the refractive index. Such density jumps induced by rarefaction pressure waves have been predicted theoretically<sup>11</sup>.

### 3.2 Shock wave formation and propagation

Shockwave propagation and material ablation for single beam irradiation at longer pump-to-probe elapsed times are shown in Fig. 5. Spherical shock wave front shape is eminent at 18.2 ns. While the initial shock wave propagation is remarkably fast, the much slower ablation front becomes visible beyond 29.8 ns. Under the assumption of a perfect gas with constant specific heats and density, the explosion liberates extremely high energy density in a small volume during a short time interval. A shock wave is then launched into the ambient gas emanating from the point of energy release. The self similar solution for the instantaneous point source explosion is of the form<sup>12</sup>.

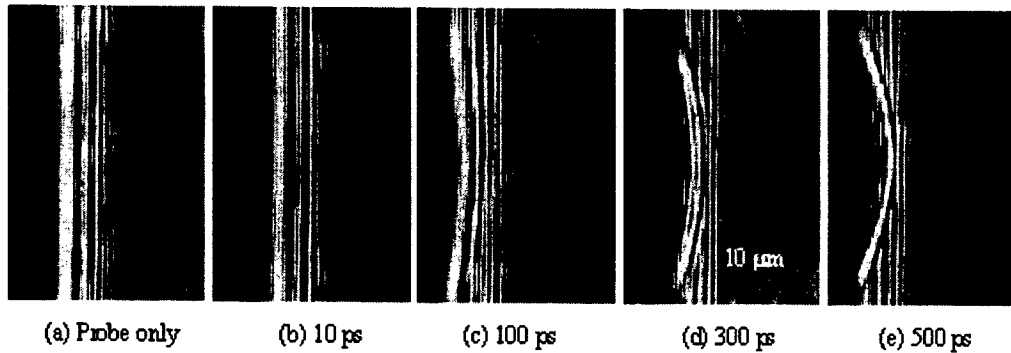


Fig. 4 Side viewed images @ fluence of 1.5 J/cm<sup>2</sup>

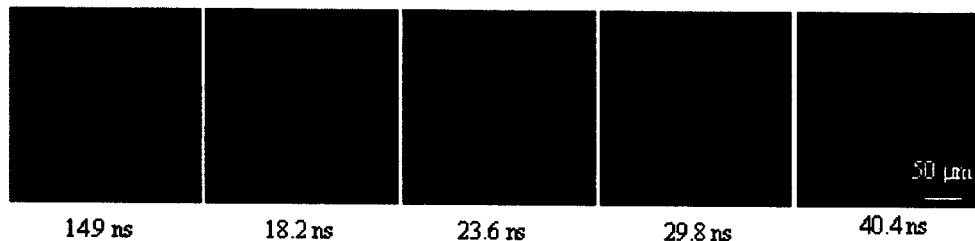


Fig. 5 Shock wave propagation

$$\varepsilon_s = R \left( \frac{\rho}{Et^2} \right)^{1/5} \quad (2)$$

where  $\varepsilon_s$  is a constant close to unity,  $E$  is the energy released at  $R=0$  and  $t=0$ ,  $t$  is the elapsed time, and  $\rho$  is the density of undisturbed air. From the measured  $R$  and  $t$ , the energy released,  $E$ , was estimated to be 7.9  $\mu\text{J}$  for  $F=1.0 \text{ J/cm}^2$  and 20.4  $\mu\text{J}$  for  $F=1.5 \text{ J/cm}^2$ . This is about 15 % and 26 % of absorbed energy considering 34 % of reflection on the silicon surface (The incident laser energy is 81 and 120  $\mu\text{J}$ , respectively.).

### 3.3 Double beam irradiation

Figure 6 shows successive images taken at various probing times, while the delay time between the two pump beams is fixed. Two sets of images look similar in terms of shock wave propagation. Indeed, the shock travels with nearly the same speed, while the released energy is about 33  $\mu\text{J}$ . Compared with the single beam, the double beam ablated plasma is stronger and faster. However, the ablation front emerging from the irradiated surface is barely visible at  $t=40.4 \text{ ns}$ , contrasted with the corresponding image for single beam ablation. In summary, the plume pushes the ambient harder but at the same time, the recoil pressure launched by the first pump beam, together the plasma generated by the second pump beam affect the plasma distribution.

Von der Linde and Sokolowski-Tinten estimated the elapsed time for the formation of expansion layer to be around 40 ps<sup>13</sup>. X-ray diffraction with femtosecond time resolution could also detect non-thermal melting of semiconductor materials<sup>14-16</sup>. In fact, Cavalleri et al. observed thermal liquid layer of germanium at the time of 6 ps, expanding up to about 100 ps<sup>16</sup>. As time progresses beyond 1-5 ps after the pump beam irradiation, the surface condition is significantly altered so that there could be more absorption (surface roughness induced by material ablation). Another source of increased coupling of the second pump beam onto the sample could be caused by the depletion of the dense surface plasma, so that the reflection loss of the beam can be reduced as was demonstrated in the literature<sup>17</sup>. However, it should be noted that the released shock wave energies for both cases are the same. This implies that the absorbed energy by the second pump beam at longer time delays is deposited on a 'hot' target surface. Hence, the surface morphology condition

does not change enough within the tens of picoseconds pump-to-pump temporal interval to affect the subsequent plasma expansion and shock wave propagation. On the other hand, more material is ejected from the sample when the second pump shines on the sample at longer time delay.

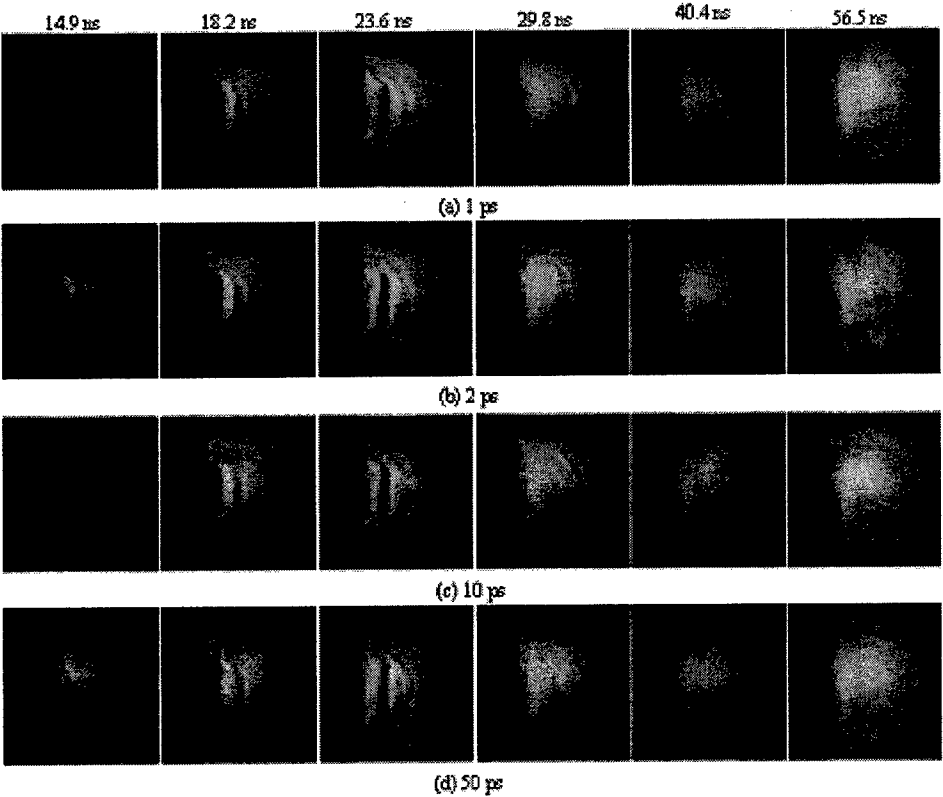


Fig. 6 Shock wave propagation upon double beam irradiance at delay between the pump beams



Fig. 7 Square-like intensity pattern generated by DOE

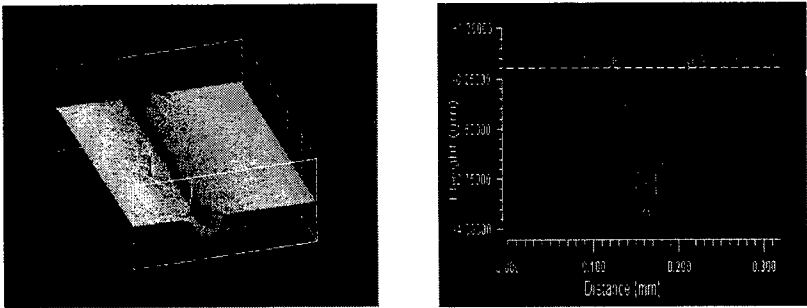


Fig. 8 Microchannel fabricated by DOE

### 3.4 Micro-channel fabrication using DOE

Fig. 7 is a simple square-like intensity pattern generated by transmitting the incoming laser beam through a diffractive optical element (DOE) for micro-channeling applications. The damage on the irradiated sample traces the similar pattern but somewhat intense damage was detected at the center area. Using this shaped and modified beam, one can machine micro-channels as shown in Fig. 8. The channel length is 1 mm. A program transferring the sample stage repeatedly (back and forth with 3 mm/sec) was adapted. Laser energy fluence can be estimated to be about  $0.77 \text{ J/cm}^2$  based on the damaged area. The crater profile has maximum depth at the center caused by the focusing of the higher intensity. However, no elevation of the crater edge has been observed as is typical in micromachining utilizing refractive optics. With DOE, we can eliminate the intermediate focal plane causing self-focusing and filamentation of the incoming beam. This can be advantageous in terms of machining quality as revealed in Fig. 8.

## 4. CONCLUSION

Pump-and-probe techniques employing beam delivery via fiber-optic lines in both collinear and side view schemes were performed to accomplish ultra-fast time-resolved microscopy of femtosecond laser-induced ablation of crystalline silicon in both single and double beam configuration. The imaging with the time-delayed frequency-doubled probe beam had a temporal resolution of 80 fs. The results showed a highly reflecting phase indicating creation of near-solid density plasma or a non-thermal molten phase within 2 ps after the pump beam incidence on the sample surface. Earlier studies demonstrated substantial emission of both charged particles and neutrals possessing high kinetic energies in the keV range but the exact timing of ejection of particles is unclear. However, time-resolved shadowgraphs of the shock wave propagation indicate that the faster initial plasma component is followed by a slower 'thermal' contribution. A diffractive optical element was used to fabricate micro-channels in silicon wafers.

## ACKNOWLEDGEMENT

Support to this work by the Department of Energy, Office of Basic Energy Sciences, Engineering Research Program, under Grant DE-FG03-95ER14562 is gratefully acknowledged.

## REFERENCES

1. C. Momma, S. Nolte, G. Kamlage, F. von Alvensleben, A. Tunnermann, "Beam Delivery of Femtosecond Laser Radiation by Diffractive Optical Elements," *Applied Physics A*, **67**, pp. 517-520, 1998.
2. P. Pronko, S. Dutta, J. Squier, J. Rudd, D. Du, G. Mourou, "Machining of Sub-micron Holes using a Femtosecond Laser at 800 nm," *Optics Communications*, **114**, pp. 106-110, 1995.
3. M. Wu, "Micromachining for Optical and Optoelectronic Systems," *Proceedings of the IEEE*, **85**, pp. 1833-1856, 1997.
4. F. Korte, S. Nolte, B.N. Chichkov, T. Bauer, G. Kamlage, T. Wagner, C. Fallnich, and H. Welling, "Far-field and near-field material processing with femtosecond laser pulses," *Appl. Phys. A*, **69**, pp. S7-S11, 1999.
5. D. Reitze, X. Wang, H. Ahn, and M. Downer, "Femtosecond Laser Melting of Graphite," *Physical Review B*, **40**, pp. 11986-11989, 1989.
6. K. Sokolowski-Tinten, J. Bialkowski, A. Cavalleri, D. von der Linde, A. Oparin, J. Meyer-ten-Vehn, and S. Anisimov, "Transient States of Matter During Laser Ablation," *Physical Review Letters*, **81**, pp. 224-227, 1998.
7. M. Downer, R. Fork, and C. Shank, "Femtosecond Imaging of Melting and Evaporation at a Photoexcited Silicon Surface," *Journal of Optical Society of America B*, **2**, pp. 595-599, 1985.
8. W. W. Duley, *Laser Processing and Analysis of Materials*, Plenum Press, New York, 1983.
9. W. Capinski and H. Maris, "Improved Apparatus for Picosecond Pump-and Probe Optical Measurements," *Review of Scientific Instruments*, **67**, pp. 2720-2726, 1996.
10. J. Van Vechten, R. Tsu, and F. Saris, "Nonthermal pulsed laser annealing of Si, plasma annealing," *Physics Letters A*, **74A**, pp. 422-426, 1979.
11. L. Wickens, J. Allen, P. Rumsby, "Ion emission from laser-produced plasmas with two electron temperatures," *Physical Review Letters*, **41**, pp. 243-246, 1978.
12. Y. Zel'dovich, and Y. Raizer, *Physics of shock waves and high-temperature hydrodynamic phenomena*, Academic Press, New York and London, 1966.



13. D. von der Linde and K. Sokolowski-Tinten, "The physical mechanisms of short-pulse laser ablation," *Appl. Surf. Sci.* **154-155**, pp. 1-10 (2000).
14. C. W. Siders, A. Cavalleri, K. Sokolowski-Tinten, C. S. Toth, T. Guo, M. Kammler, M. Horn von Hoegen, K. R. Wilson, D. von der Linde, and C. P. J. Barty, "Detection of nonthermal melting by ultrafast X-ray diffraction," *Science* **286**, pp. 1340-2 (1999).
15. C. Rose-Petruck, R. Jimenez, T. Guo, A. Cavalleri, C. W. Siders, F. Raksi, J. A. Squier, B. C. Walker, K. R. Wilson, and C. P. J. Barty, "Picosecond-milliangstrom lattice dynamics measured by ultrafast X-ray diffraction," *Nature* **398**, pp. 310-2, 1999.
16. A. Cavalleri, C. W. Siders, F. L. H. Brown, D. M. Leitner, C. Toth, J. A. Squier, C. P. J. Barty, and K. R. Wilson, "Anharmonic lattice dynamics in germanium measured with ultrafast X-ray diffraction," *Phys. Rev. Lett.*, **85** pp. 586-9, 2000.
17. K. Sokolowski-Tinten and D. von der Linde, "Generation of dense electron-hole plasmas in silicon," *Phys. Rev. B*, **61**, 2643-50, 2000.

# Femtosecond laser machining of fluidic microchannels for miniaturized bioanalytical systems

Adela Ben-Yakar<sup>a</sup> and Robert L. Byer<sup>b,1</sup>

<sup>a</sup>Postdoctoral Fellow, Applied Physics Department, Stanford University, Stanford, CA, USA

<sup>b</sup>Professor, Stanford University, Stanford, CA, USA

## ABSTRACT

Femtosecond laser ablation of borosilicate (Borofloat<sup>TM</sup>) glass has been studied to machine fluidic micro-channel geometries (high aspect ratio and variable depth) not possible through traditional micro-lithographic techniques. Utilizing a 1 kHz repetition rate femtosecond laser system (Positive Light, Spitfire) and a long-working distance 5x objective lens, groove patterns 10  $\mu\text{m}$  wide and as deep as 30  $\mu\text{m}$  have been produced. The experiments were performed in air and the samples were cleaned after the ablation with sodium hydroxide dissolved in water to remove the debris. The substrates were mounted on a computer controlled x-y translation stage. The quality of the micro-channels showed dependency on the scanning speed of the sample. The surrounding area of the channels was smooth at scanning rates greater than 400  $\mu\text{m/s}$  and smaller than 10  $\mu\text{m/s}$ . Whereas, cracks appeared around the channels at scanning rates between 200 to 50  $\mu\text{m/s}$ . Surface morphology is studied using optical, electron and atomic force microscopies. For a quantitative evaluation of ablation threshold and ablation rates, single-shot experiments in vacuum were performed. We found that the damage threshold for borosilicate glass is around 1.7 J/cm<sup>2</sup>. With single pulse laser fluence of 30 J/cm<sup>2</sup>, a 600 nm deep crater could be ablated. A ring, higher than the surface, appeared around the craters and was most probably created by adiabatic compression of glass due to the high-pressure plasma generated in the early stages of the process.

**Keywords:** Ultrafast lasers, micromachining, borosilicate glass, damage threshold, ablation rate, optical penetration depth, micro-channels, microfluidics

## 1. INTRODUCTION

The advent of lasers with sub-picosecond pulse durations and millijoule output power has opened new opportunities for precision laser machining of metals, dielectrics, and biological materials. The rapid coupling of energy allows material removal before significant heating occurs, resulting in extremely precise and controllable processing with nearly undetectable collateral damage

At Stanford University, we have recently established a new ultrafast laser laboratory with the hardware necessary to carry out studies of ultrafast laser/material interactions and applications to machining of a variety of materials. In this paper, the initial studies on the use of laser machining of borosilicate glass to generate fluidic micro-channel geometries are presented. Because of the isotropic nature of wet chemical etching, only shallow channels can be produced using these photolithographic techniques. However, fabrication of deeper channels has a number of important practical advantages. Deeper channels provide an increased path length for optical detection that yields a linear increase in signal. An ultrashort pulse laser can machine high aspect ratio channels on borosilicate glass to be used in the development of miniaturized bioanalytical systems.

<sup>1</sup> Further author information: (Send correspondence to Adela Ben-Yakar)

Adela Ben-Yakar: E-mail: [adela@stanford.edu](mailto:adela@stanford.edu), Telephone: 1 650 723 0161

Robert L. Byer: E-mail: [rbyer@stanford.edu](mailto:rbyer@stanford.edu), Telephone: 1 650 723 0226

Address: Stanford University, Applied Physics Department, Ginzton Lab, 450 Via Palou, Stanford CA 94305-4085

The paper summarizes the measurements of damage threshold and ablation rate of borosilicate glass when machined with femtosecond laser pulses and the influence of scanning rate on the machining process of micro-channels for miniaturized bioanalytical systems. Surface morphology of grooves machined with femtosecond pulse laser is analyzed using optical, electron and atomic force microscopies.

## 2. EXPERIMENTAL APPROACH

The experimental facility for ultrafast laser microfabrication consists of two parts: 1) the laser system, 2) a microscope for beam delivery to the sample. A kHz repetition rate Ti:sapphire amplifier system (Positive Light, "Spitfire") is used to generate ultrashort pulse lasers with output energies up to 0.9 J per pulse at 780 nm. The chirped-pulse amplification (CPA) technique used in the amplification system allows us to vary the pulse duration from 200 fs up to 20 ps. The pulse duration is measured by means of a single-shot, second harmonic generation autocorrelator. For the current experiments, 300fs duration pulses are used.

The laser fluence on the target can be precisely varied from 10 nJ to 0.9 J using two energy attenuators. Each energy attenuator involves a half-wave plate that rotates the polarization of the laser beam and a cube beam splitter in which the intensity of the transmitted light depends on its polarization. The attenuated laser-pulse energies are measured by a pyroelectric detector. The output of the laser system is linearly polarized. A fast mechanical shutter is used to select the desired number of pulses for the ablation experiments.

The laser beam is delivered to the surface by a long working distance objective lens (Mitutoyo, 5x) attached to the microscope. To obtain a homogeneous and well-defined distribution on the target, a circular aperture (5mm in diameter) is placed in the beam path just before the objective lens. In the surface plane, a Gaussian spatial beam profile with a radius ( $1/e^2$ ) of  $\omega_0=5.8 \mu\text{m}$  is obtained. The same microscope can be used to inspect in-situ the irradiated surface during the ablation process.

For micro-structuring, the substrates are mounted on a computer controlled x-y translation stage of the microscope. The surface of the sample is positioned to be perpendicular to the direction of the incident beam. The borosilicate glass substrates (Borofloat™ 1.1 mm thick, Precision Glass and Optics, Ltd.) used in the current experiments are cleaned ultrasonically with alcohol before the experiments and with a 0.5 Molar sodium oxide (NaOH) solution after the ablation to remove debris.

Figure 1 shows a picture of the microscope with objective lenses for beam focusing and the vacuum chamber mounted on the x-y translation stage. A Lab-VIEW program controls both the laser energy by rotating the half-wave plate and the position of x-y stage for machining of micro-channels (grooves).

The laser ablated borosilicate glass surface is analyzed by optical and scanning electron microscopes for its morphology and by an atomic force microscope (AFM) for the measurement of the profile, that is, the size and depth of the machined surface. AFM is an excellent tool to investigate craters with small depths ( $< 6 \mu\text{m}$ ). From these measurements a quantitative evaluation of the crater depth, the ablated volume and the crater profiles is possible.

In this work, the effects of variety of parameters such as laser fluence, pulse repetition rate, and speed of scanning rate on the quality of micro-channels were studied.

## 3. RESULTS AND DISCUSSION

Figure 2 shows a comparison between nanosecond and femtosecond pulse laser ablation of borosilicate glass in air. Thermal effects, which dominate the long pulse laser ablation, cause cracks with non-reproducible machining quality. Ablation of borosilicate glass with an ultrashort laser pulse is, in contrary to the processing with long pulse lasers, free of thermal diffusion providing a precise and reproducible processing ability. These results demonstrate that for high quality machining of glass substrates ultrashort pulse lasers are needed.

In the following sections the properties of the single shot laser ablation of borosilicate glass will be first discussed. Second, the damage threshold and ablation rate data will be presented. The third part will summarize the properties of the micro-machined channels (grooves).

### 3.1. Properties of Single Shot Craters

AFM studies were performed to examine the properties of craters generated using a single laser pulse in vacuum with different energies. Figure 3 presents three examples of AFM images of craters ablated with laser pulse energies of 13.6,

18.8, and 30  $\mu\text{J}$ . These AFM pictures depict no cracks around the ablated crater and that the dimensions of the craters increase with increasing laser energy. These images also show the existence of a white ring around the ablated crater from which thin strips of melted material are extending away. Three-dimensional representation of AFM data shows that the height of these features around the crater is higher than the surface. The ring formation might be attributed to an adiabatic compression of glass due to high-pressure plasma generated in the very early stages of the ablation process. The plasma starts to expand within 10 ps above the surface having enough time to compress the material around though with negligible heat diffusion. The thin strips expanding away from the crater might be the result of the recasting of ablated material that could not escape from the surface and melted back.

### 3.2. Ablation Rate

To determine the threshold fluence of borosilicate glass ablation, we plotted the ablated depth  $h$  of single-shot craters as a function of laser fluence  $F_0$  (Fig. 4). To precisely measure the ablation threshold, namely, to avoid nonlinear beam distortion in air the experiments were performed in a vacuum chamber at a pressure below  $10^{-4}$  mbar. The linear relation between the depth and the logarithm of the laser fluence can clearly be observed in Fig. 4. This logarithmic dependence of the ablation depth on the laser pulse fluence was demonstrated in early studies<sup>1</sup> for the ablation of metal targets with femtosecond laser pulses and can be described by

$$h = \kappa \ln \left( \frac{F_0}{F_{th}} \right), \quad (1)$$

where  $\kappa$  can be interpreted as the "effective optical penetration depth" as expected from the Beer's law<sup>2</sup>. The slope of the linear fit yields the optical penetration depth. A value of  $\kappa = 221$  nm was obtained for borosilicate glass. The extrapolation of the fit to  $h=0$  resulted in a damage threshold of  $F_{th} = 1.7$  J/cm<sup>2</sup>. This result is consistent with earlier studies<sup>3,4</sup> where a multi-shot damage threshold of  $F_{th}$  ( $N=50$ , 300fs) =  $1.7 \pm 0.4$  J/cm<sup>2</sup> was found.

### 3.2. Machining of Microchannels

Micro-channels on the surface of borosilicate sample were machined by moving the sample with a certain speed relative to the stationary-pulsed laser beam. The speed at which the samples are moved is called the scanning rate. Figure 5 shows optical images of channels machined at different scanning rates at 200 Hz pulse repetition rate. These experiments were performed in air at laser fluence of  $F_0 = 28$  J/cm<sup>2</sup>.

A minimum number of overlapping laser pulses was required to create a continuous channel. At scanning rates below 400  $\mu\text{m/s}$  an effectively continuous overlap of multiple laser pulses was reached, leading to ablation depth of several microns. The ablation depth of micro-channels depends on the number of overlapped laser pulses  $N_{eff}$ , which can be defined as:

$$N_{eff} = \frac{D \cdot RR}{SR}, \quad (2)$$

where  $D$  is the diameter of a single pulse crater,  $RR$  is the repetition rate of the laser system and  $SR$  is the scanning rate at which the samples are moved. Assuming 10  $\mu\text{m}$  for the diameter of a single pulse crater, the minimum number of pulses required to obtain an effectively continuous channel was  $N_{eff} = 5$  (scanning rate of 400  $\mu\text{m/s}$  at 200 Hz repetition rate.)

The quality of the microchannels was found to be a strong function of the scanning rate or in other words overlapping number of pulses. As Fig. 5 indicates, at intermediate speeds ( $SR = 200$ -50  $\mu\text{m/s}$ ), cracks along the sidewalls of channels are obtained when the laser repetition rate is at 200 Hz. At speeds lower and higher than these intermediate values cracks could be eliminated. Uniform and highly reproducible channels are achieved at  $SR > 400$   $\mu\text{m/s}$  and  $SR < 50$   $\mu\text{m/s}$ .

### ACKNOWLEDGMENTS

The authors gratefully acknowledge the contributions of Professor Herbert Looser to this investigation. The work has been supported by TRW research fund.

### REFERENCES

1. S. Preuss, A. Demchuk, M. Stuke, "Sub-picosecond UV laser ablation of metals," *Appl. Phys. A* **61**, pp. 33, 1995.

2. J. Bonse, J. M. Wrobel, J. Krüger, and W. Kautek, "Ultrashort-pulse laser ablation of indium phosphide in air," *Appl. Phys. A* **72**, pp. 89-94, 2001.
3. W. Kautek, J. Krüger, M. Lenzner, S. Sartania, C. Spielmann, and F. Krausz, "Laser ablation of dielectrics with pulse durations between 20 fs and 3 ps," *Appl. Phys. Lett.* **69** (21), pp. 3146-3148, 1996.
4. M. Lenzner, J. Krüger, S. Sartania, Z. Cheng, Ch. Spielmann, G. Mourou, W. Kautek, and F. Krausz, "Femtosecond optical breakdown in dielectrics," *Phys. Rev. Lett.* **80** (18), pp. 4076-4079, 1998.

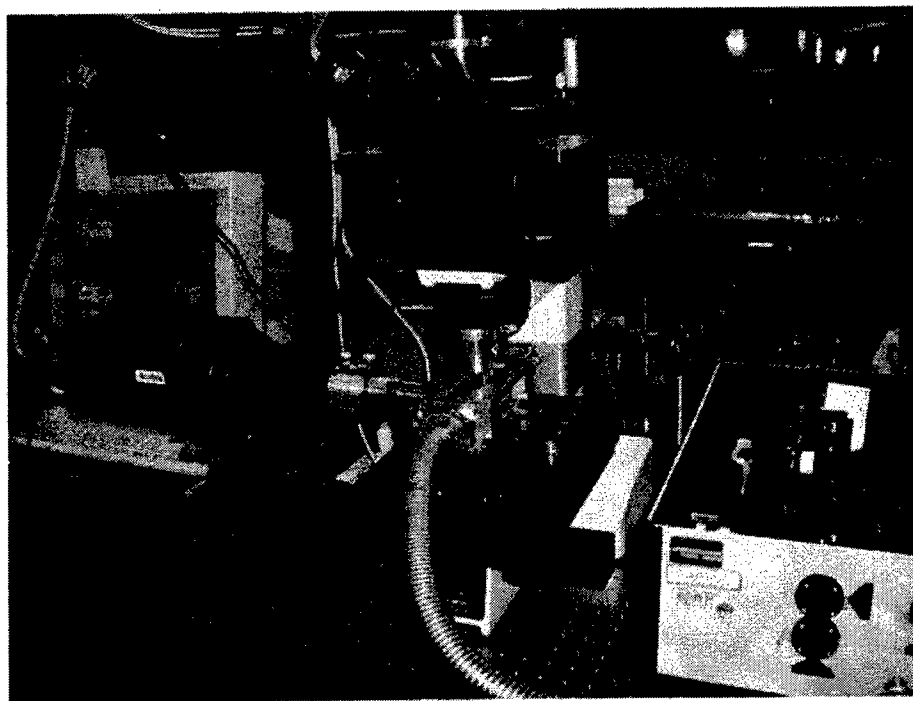
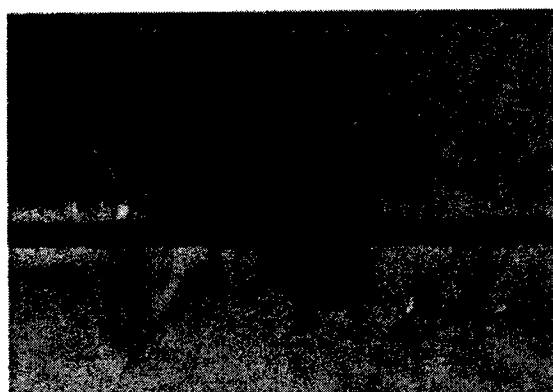


Figure 1. A picture of the experimental facility.

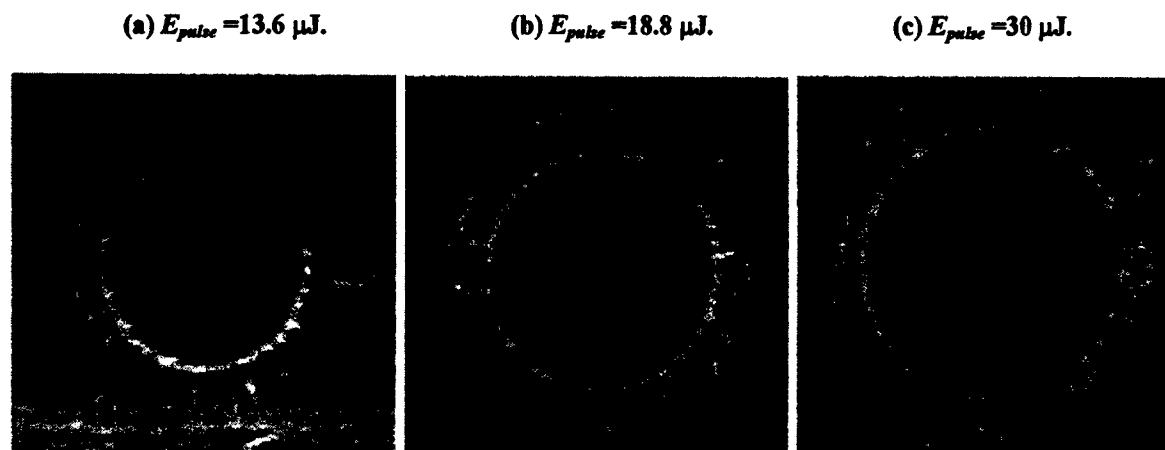
(a)  $\tau=10$  ns.



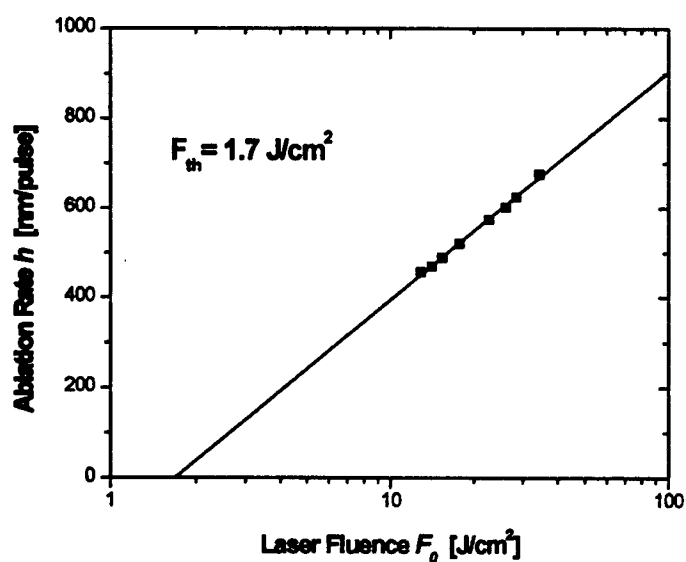
(b)  $\tau=300$  fs.



Figure 2. Comparison of ns and fs-pulse laser machining of borosilicate glass at  $\lambda=780$  nm.



**Figure 3.** Samples of atomic force microscopy images demonstrating the properties of single shot craters for different laser pulse energies.



**Figure 4.** Plot of ablated depth of borosilicate glass as a function of the laser fluence.

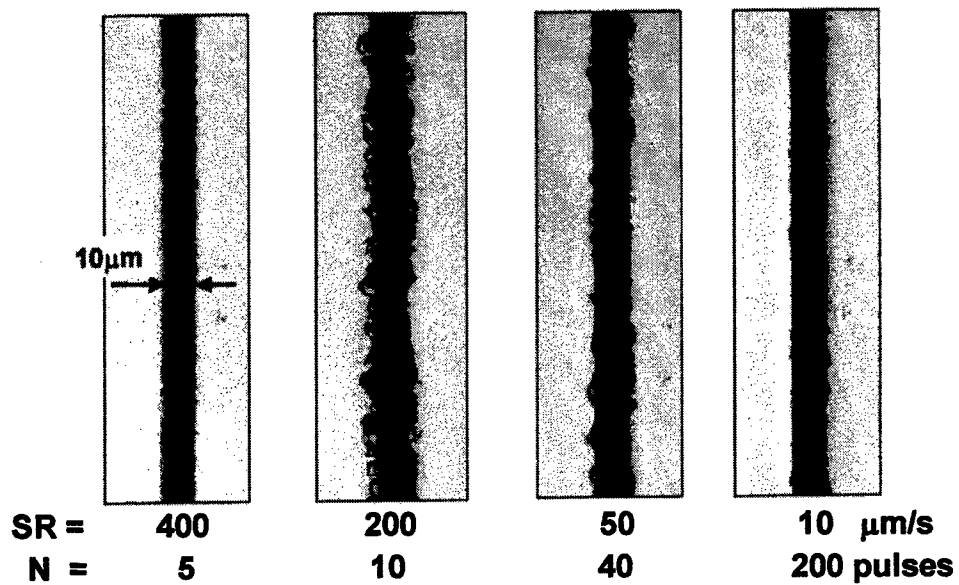


**Figure 5.** Effect of the scanning rate in machining of continuous micro-channels. Laser repetition rate was 200 Hz. Laser pulse energy was  $E_{pulse}=29 \mu\text{J}$  ( $F_0=27.5 \text{ J/cm}^2$ .)

# Glass Micromachining Using the VUV F<sub>2</sub> Laser

Peter E. Dyer, Saher M. Maswadi, Howard V. Snelling and Christopher D. Walton  
Department of Physics, University of Hull, Hull, HU6 7RX, UK.

## ABSTRACT

Theoretical and experimental studies of the surface quality in 157nm F<sub>2</sub> laser-ablated glasses are reported. Limitations set by statistical fluctuations in the multi-mode beam and by stationary beam non-uniformity are explored together with materials issues such as laser-induced surface cracking. Experimental work on ablating polymethylmethacrylate (PMMA), used as a low threshold medium for recording of the VUV beam, and soda lime glass are described. Use is made of the probe beam deflection technique to determine ablation thresholds, and a variety of methods adopted for characterising and assessing the quality of ablated surfaces e.g. scanning-electron microscopy, mechanical and optical interference profiling and atomic force microscopy. Preliminary roughness measurements are compared with theoretical expectations and the implication for glass micromachining with the F<sub>2</sub> laser discussed.

**KEYWORDS:** VUV, F<sub>2</sub> Laser, Micromachining, Glass, Ablation, Surface Roughness.

## 1. INTRODUCTION

The possibility of using laser micromachining to fabricate components in glass is of interest for optoelectronic and micro-device applications. The relatively low absorption coefficient of glasses, even in the deep UV, coupled with complex issues such as melting and induced stress, are limiting factors and, to date, results obtained are generally poor compared with UV laser polymer ablation. Resolution and ultimate surface quality attainable are important, especially for many perceived micro-optic components, and the 157nm VUV F<sub>2</sub> laser offers one possible route to improving this. Most glasses exhibit strong absorption at 157nm and even fused silica which is relatively transparent can be ablated with good precision through what is thought to be photo-induced surface absorption [1]. Previous work on UV and VUV laser ablation of glasses [1-4] is relatively sparse compared with polymers although progress is now starting to be made on understanding the benefits and limitations of this approach to micromachining.

Here we describe a theoretical study of the surface quality that might be realized in F<sub>2</sub> laser-ablated glasses and report some preliminary experimental work related to this. Theoretical consideration is given to the fundamental limitation set by spatially varying statistical fluctuations in the multi-mode beam, practical aspects related to stationary beam non-uniformity and to material issues such as laser induced surface cracking. Experimental work has been carried out using the 157nm laser to ablate polymethylmethacrylate (PMMA), which served as a low threshold medium for testing laser-induced roughness against theory, and soda lime glass which has previously been investigated at much longer laser wavelengths [5]. The probe beam deflection technique was used for in situ threshold measurements, and a variety of methods adopted for characterising and assessing the quality of ablated surfaces. The latter included scanning-electron microscopy, DekTak and optical interference profiling and atomic force microscopy.

## 2. THEORETICAL CONSIDERATIONS OF ABLATION UNIFORMITY

### 2.1 Multimode beam fluctuations

Consideration is first given to beam fluctuations that can arise in highly multi-mode lasers and set a 'fundamental' limitation on attainable spatial uniformity. As is well known, free-running F<sub>2</sub> and excimer lasers operate with emission linewidths and resonator Fresnel numbers that are large and, as a consequence, produce output on a vast number of electromagnetic modes ( $> 10^6$ ) characterised by distinct transverse field distributions and frequencies. This property is attractive for certain applications as the many modes when superimposed can produce very good spatial uniformity but with a low degree of coherence, greatly reducing speckle effects [6]. In general the modes will have random relative



phases on a pulse-to-pulse basis and interference among them can lead to small scale-size fluctuations in the local fluence. Those modes lying within a sufficiently small frequency interval that their coherence time exceeds the laser pulse duration will add coherently producing a stationary contribution to the output during the pulse. This contribution, however, varies from pulse-to-pulse if the mode phasing is random. When averaged across all such mode groups within the lasing linewidth the output should approximate to a Gaussian probability distribution for the fluence of the form:

$$dp/dF = (2\pi)^{-1/2} \sigma^{-1} \exp(\{F - \langle F \rangle\}^2 / 2\sigma^2) \quad (1)$$

where  $dp$  is the probability that the fluence  $F$  will lie in the range  $F, F+dF$  and  $\langle F \rangle$  is the mean fluence. The standard deviation of the distribution is given by  $\sigma = \langle F \rangle (\tau_c / f\tau_p)^{1/2}$  where  $\tau_p$  is the laser pulse duration and  $\tau_c = 1/\Delta\nu$  is the laser coherence time,  $\Delta\nu$  being the laser linewidth.  $f=1$  for a polarised beam and 2 for an unpolarised beam.

The coherence area  $A_c$  determines the transverse spatial extent over which the output beam retains coherence. For a rectangular beam this is given approximately by  $A_c = \lambda^2 / \Delta\phi\Delta\theta$  where  $\Delta\phi$  and  $\Delta\theta$  are the full-width beam divergence angles in its long and short dimensions. The coherence fluctuations described by equation 1, will thus be uncorrelated and random between different coherence 'patches' in the beam.

The effect of these fluctuations can now be assessed for a material that has an assumed removal rate per pulse,  $x$ , of the form:

$$x = k^{-1} \ln(F/F_T) \quad (2)$$

Here  $k$  is the effective absorption coefficient at the laser wavelength and  $F_T$  is the fluence at the ablation threshold. Equation 2 has been found to be approximately applicable for many laser-material systems over a limited fluence range and has the advantage of analytical simplicity.

Suppose now that the surface is exposed to  $m$  laser pulses at an average fluence  $\langle F \rangle$ . It follows from equations 1 and 2 that the ablation depth  $D$  will have an uncertainty between different coherent patches that can be determined from:

$$D = mk^{-1} \ln(\{\langle F \rangle \pm \sigma/m^{1/2}\} / F_T) \quad (3)$$

as  $\sigma/m^{1/2}$  is the standard error i.e. standard deviation of the mean. Assuming  $\langle F \rangle$  is large compared to  $\sigma/m^{1/2}$ , equation 3 can be expanded as:

$$D = \langle D \rangle \pm m^{1/2} \sigma / \{k\langle F \rangle\} \quad (4)$$

where  $\langle D \rangle = m k^{-1} \ln(\langle F \rangle / F_T)$  is the mean depth of material removal. Equation 4 shows that the spatially varying fluence leads to an uncertainty in the ablation depth. Although the *relative* uncertainty in depth, given by  $(m^{1/2} \sigma / \{k\langle F \rangle\}) / \langle D \rangle$ , decreases with number of pulses as  $m^{-1/2}$ , a residual roughness is imposed on the surface of magnitude  $r = m^{1/2} \sigma / \{k\langle F \rangle\}$  that *increases* as  $m^{1/2}$ .

Evaluating  $\sigma$  in equation 1 using a recent estimate for the linewidth of  $\sim 10$  GHz (0.82 pm) for the main 157.63 nm transition of the  $F_2$  laser [7] and  $\tau_p = 11$  ns, we obtain estimates of  $\sigma/\langle F \rangle = 9.5\%$  for a polarised beam ( $f=1$ ) and 6.7% for an unpolarised beam ( $f=2$ ). The  $F_2$  laser has 'mode speckle' fluctuations that are predicted to be significantly larger than, for example, the free-running ArF or KrF laser on account of its much smaller linewidth.

If the surface roughness factor,  $r$ , is expressed in terms of  $D$ , we obtain:

$$r = (D/[k \ln\{\langle F \rangle / F_T\}])^{1/2} \sigma / \langle F \rangle \quad (5)$$

This indicates that when it is desirable to minimise roughness it is advantageous to have a high absorption coefficient and to operate at well above the ablation threshold. In this respect the  $F_2$  laser has an evident benefit for processing glasses and, indeed, other non-metallic materials, as  $k$  can be large in the VUV with correspondingly low thresholds, permitting 'well-above threshold' ablation. Even so the roughness induced by 'mode speckle' can be significant. Taking, for example,  $k=4 \times 10^5 \text{ cm}^{-1}$ ,  $F_T = 150 \text{ mJ/cm}^2$  and  $F = 800 \text{ mJ/cm}^2$  for the ablation of a glass at 157 nm and  $\sigma/\langle F \rangle = 6.7\%$ , leads to a roughness of  $r = 82 \text{ nm}$  for  $D = 100 \mu\text{m}$ . At this level, scattering could be problematic if ablation was used to configure optical surfaces to this depth.

In the foregoing it is assumed that either the direct output beam or an optical system with a point-spread-function (width =  $\omega_p$ ) that is small in comparison to the characteristic dimensions of the coherence patch at the image is used. In these cases imaging is 'coherent' whereas if the magnification satisfies  $M \ll \omega_p/A_c^{1/2}$  imaging can be classed as incoherent [8], resulting in the mixing of several or more adjacent (and uncorrelated) coherence patches. This effects a reduction in the roughness factor  $r$  by a approximate factor of  $\{MA_c^{1/2}/\omega_p\}^{1/2}$ . As an example, we take a value of  $A_c \sim 25 \times 50 \mu\text{m}^2$  at an object mask and a diffraction-limited imaging lens with f-number  $f\# = 10$ . In this case  $\omega_p = 2\lambda f\# = 3.14 \mu\text{m}$  for  $\lambda = 0.157 \mu\text{m}$  and to satisfy  $\omega_p \geq MA_c^{1/2}$  requires  $M \leq 0.088$  i.e. a demagnification of more than 11. For a demagnification of  $30\times$  we find  $\{MA_c^{1/2}/\omega_p\}^{1/2} = 0.61$ , so that even with relatively large demagnification only a small advantage accrues.

## 2.2 Stationary Beam Non-Uniformity

It is of interest to examine how stationary beam non-uniformity influences the ablation depth i.e. differences in  $\langle F \rangle$  that remain fixed from pulse-to-pulse. Suppose a nominally flat-topped beam has a residual fluence variation of  $|dF| \ll \langle F \rangle$ . Then, from equation 2, we find that the difference in the depth of material ablated when exposed to  $m$  pulses at fluence  $\langle F \rangle$  and at  $\langle F \rangle \pm dF$  is:

$$\delta D = m dF / (\langle F \rangle k) = D (dF / \langle F \rangle) / \ln\{\langle F \rangle / F_T\} \quad (6)$$

Note that unlike equation 5, the depth variation ('roughness') is now independent of  $k$  and linearly dependent on  $D$ . It is again, however, advantageous to work at a high fluence above threshold. Taking  $dF/\langle F \rangle = 1\%$  and the parameters for glass used above ( $F_T = 150 \text{ mJ/cm}^2$ ,  $F = 800 \text{ mJ/cm}^2$  and  $D = 100 \mu\text{m}$ ), we find  $\delta D = 597 \text{ nm}$ . Stationary beam non-uniformity even at a level as low as 1% can evidently produce significant differences in ablation depth and it is likely that random variations of this magnitude could easily be introduced by imperfections in beam delivery components. This would pose a significant problem if fabricating precision optical surfaces by ablation and points to the need for excellent beam homogenisation. Stationary non-uniformity may also arise from coherence effects in contact [8,9] and projection [8] imaging and can be problematic for the  $F_2$  laser because of its narrow linewidth and long coherence length.

## 3. MATERIAL CONSIDERATIONS

To ablate a glass through a predominantly vapour removal phase it is necessary to elevate the surface to a high temperature. Consequently under short pulse laser irradiation a surface layer of the glass will inevitably be cycled through a low viscosity, effectively molten, state. Rapid quenching of this layer through conduction cooling can then lead to strain-freezing [5] and the formation of residual tensile stress in the surface. In certain cases this is sufficiently large to produce failure by micro-cracking, a feature that is exploited in laser marking [5]. It is unacceptable, however, in glass micro-machining applications because of its deleterious effect on the optical as well as mechanical properties of micro-components.

Analysis of strain-freezing in laser heated surfaces [5] gives the residual tensile stress,  $\Sigma$ , as:

$$\Sigma = E\alpha\Delta T_m/(1-\nu) \quad (7)$$

where  $E$  is the Young's modulus,  $\alpha$  is the linear thermal expansion coefficient and  $\nu$  is the Poisson ratio for the glass.  $\Delta T_m$  is the difference between the temperature at which strain freezing occurs and the initial sample temperature. For glasses irradiated in the deep UV or VUV the effective beam penetration depth defined by surface states or by the bulk absorption coefficient can be very small. The layer of glass subjected to a substantial temperature rise is then restricted to the larger of the effective beam absorption depth or the thermal diffusion depth  $(\kappa\tau_p)^{1/2}$  where  $\kappa$  is the thermal diffusivity. The short duration of the  $F_2$  laser pulse and large effective absorption coefficient restrict the thickness,  $h$ , of the low viscosity, and subsequently strain-frozen layer, to below  $\sim 500$  nm. Under these conditions cooling is rapid and strain-freezing [5] occurs at an estimated  $\Delta T_m \approx 900$ -1000 K. For soda lime glass with  $E = 70$  GPa,  $\nu = 0.3$  and  $\alpha = 8 \times 10^{-6}$  /K, this produces a residual tensile stress of  $\Sigma \approx 7 - 8 \times 10^8$  Pa (equation 7). Whether this stress is sufficient to cause failure by crack propagation is a complex issue and dependent on several factors. We note, however, that as the critical stress for crack propagation in thin film scales as  $h^{-1/2}$  [10] the very shallow heat-affected zones produced by  $F_2$  (and possibly ArF) lasers should be advantageous for crack-free glass micro-machining.

It is known from other studies [1] that high quality ablation of weakly absorbing glasses such as fused silica is also possible with the  $F_2$  laser. In this case it is likely that surface-mediated rather than bulk absorption plays a dominant role. The low thermal expansivity of fused silica results in much lower residual stress and, as confirmed by experimental observation [1], failure by cracking does not appear to be a problem.

Other possible 'material' effects that may influence the surface quality of ablated glasses include the relaxation of intrinsic stress in the surface region of an incompletely annealed substrate, and the formation of cone-like structures by particulates shielding of the beam. Both effects have been extensively reported for polymer ablation [11].

#### 4. EXPERIMENTAL TECHNIQUES

Experiments on ablation were carried out using a Lambda Physik LPF 202  $F_2$  laser producing output energy of up to 35mJ at a pulse repetition rate  $\leq 20$ Hz. The full beam energy was determined using a large area joulemeter calibrated for the VUV (Molelectron, Type J25 HR). The laser pulse duration was measured to be 11ns (full-width at half-maximum) using a fast time-response photoemissive detector [12]. Based on focal spot-size measurements made at a distance of  $\sim 0.4$ m from the laser output mirror using a 110 mm focal length  $CaF_2$  lens the full angle beam divergence was  $\sim 8$ mrad  $\times 3$  mrad. The characteristic spatial coherence area of the  $10 \times 24$  mm<sup>2</sup> beam was thus estimated to be  $A_c = 20 \times 52$   $\mu\text{m}^2$ .

To determine the level of beam fluctuations occurring within a coherence patch, a GaP photodiode with a high impedance amplifier was used as a sensitive pulse-integrating joulemeter. This was fitted with a 12.5 $\mu\text{m}$  diameter pinhole aperture to ensure that the beam sampled an area significantly smaller than  $A_c$ . The GaP detector was placed in the direct beam and its signal recorded for a series of pulses. Each individual measurement was normalised by the total laser output energy for the same pulse, sampled using a beam splitter and the Molelectron joulemeter. This normalisation procedure thus eliminated contributions from pulse-to-pulse fluctuations in the total output energy.

Samples of PMMA (Goodfellows Limited, Clinical Grade CQ) and standard soda lime glass ( $\sim 70\%$   $SiO_2$ , 15%  $Na_2O$ , 10%  $CaO$  and a few per cent  $MgO$ ,  $BaO$  and  $Al_2O_3$ ) were used as the ablation targets. PMMA was selected as a suitable medium for recording beam non-uniformity following a series of experiments on various materials (e.g. polyimide, polyethylene terephthalate, gelatin sheets). It was found to have a low ablation threshold and relative freedom from spurious microstructure formation. Soda lime glass was studied because of its ready availability in the form of flat samples (e.g. as microscope slides) and because its ablation characteristics have been investigated in some detail with long wavelength lasers [5]. The targets were mounted on a stepper motor driven stage that allowed

precision adjustment of their position. Exposure took place in an evacuable chamber (base pressure =  $10^{-5}$  mbar) that was back-filled with high purity Ar to a pressure of typically 300mbar. The chamber was connected to the laser by means of a 2m long tube.

A laser probe beam deflection technique was used for in-situ investigation of ablation [13]. For this purpose glass windows on the chamber allowed a HeNe laser beam to pass parallel to the surface of the sample and at a variable height above it. The output beam was directed to a silicon quadrant detector, wired as two pairs, which provided sensitive measurement of the deflection produced by an acoustic wave or ablation products traversing the beam.

The surfaces of ablated samples were investigated using scanning-electron-microscopy (SEM), atomic-force-microscopy (AFM) and a Wyko optical profilometer (Model RS-2) used in phase scan imaging mode. A mechanical stylus (DekTak) was also employed.

## 5. RESULTS

### 5.1 PMMA

Probe beam deflection measurements were made on PMMA exposed at various  $F_2$  laser fluences. With the probe beam located 1mm above the sample surface it was possible to observe the deflection signature of a fast-propagating acoustic wave and that produced by the slower moving ablation products. From the onset fluence of the product signal an ablation threshold  $F_T = 20 \pm 5 \text{ mJ/cm}^2$  was obtained for PMMA, which is similar to that deduced for other polymers [14] and photoresists [15, 16] ablated at 157nm. Assuming the applicability of equation 2, the effective absorption coefficient was calculated as  $k = 1.7 \times 10^5/\text{cm}$ , based on the measured threshold and ablation depths recorded at known fluence. This is in reasonable agreement with a low irradiance value of  $\sim 1 \times 10^5/\text{cm}$  for PMMA extrapolated from the data in [17].

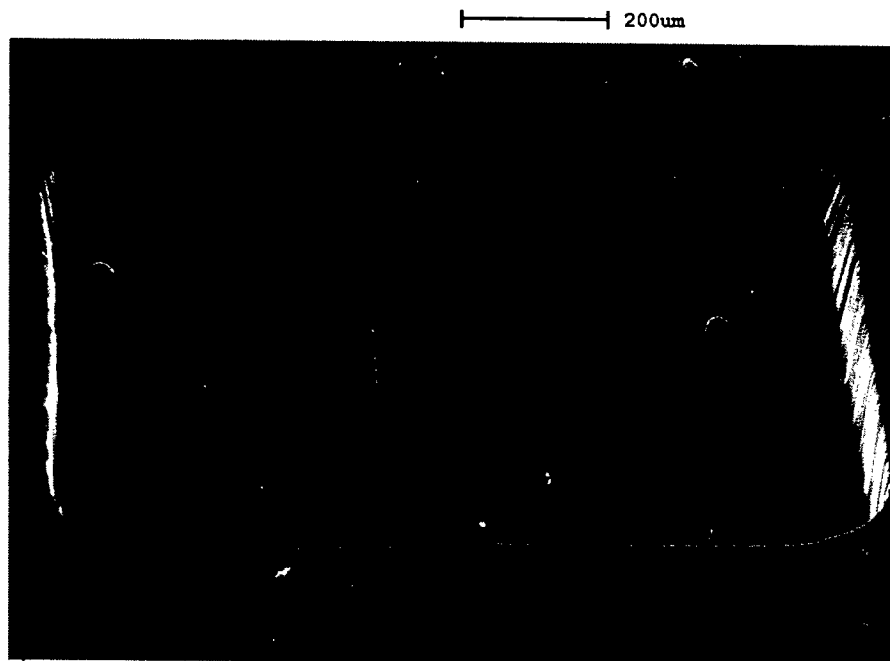


**Figure 1.** Scanning electron micrograph of polymethylmethacrylate (PMMA) ablated in vacuum (pressure =  $10^{-4}$  mbar) using 1000 pulses from the  $F_2$  laser. The fluence varies from the front to the rear of the site and has an average value of  $80 \text{ mJ cm}^{-2}$ .

An example of the ablated surface of PMMA produced by exposure to 1000 pulses at an average fluence of  $80\text{mJ/cm}^2$  from the  $\text{F}_2$  laser beam is shown in figure 1. Here the beam was weakly focused onto a rectangular mask in contact with the surface. This SEM reveals several interesting features. Firstly, the ablated surface at this scale is predominantly smooth. There is, however, a factor-of-two difference in the ablation depth of the near and far sides of the crater indicating a relatively large variation in fluence across the beam. Secondly, several steep-walled cones can be seen extending to the same depth as the crater suggesting they are initiated by particulate contamination on the surface. The relative freedom from cones of other heights also suggests that debris formation/re-deposition from the ablation products is not a major factor with PMMA, unlike for some other polymers [14] where high densities of cones with varying depth appear under  $\text{F}_2$  laser exposure. The cone walls are steeper at the front of the crater where the fluence is higher which is consistent with theoretical expectation [14]. Based on the measured cone apex half-angle the fluence on the near side of the crater is calculated as  $\sim 130\text{mJ/cm}^2$  compared with  $\sim 70\text{mJ/cm}^2$  at the rear. The rounded features also evident in figure 1 likely arise from cones that have either broken or lost their particulate shield and hence have been smoothed by repeated pulse exposure.

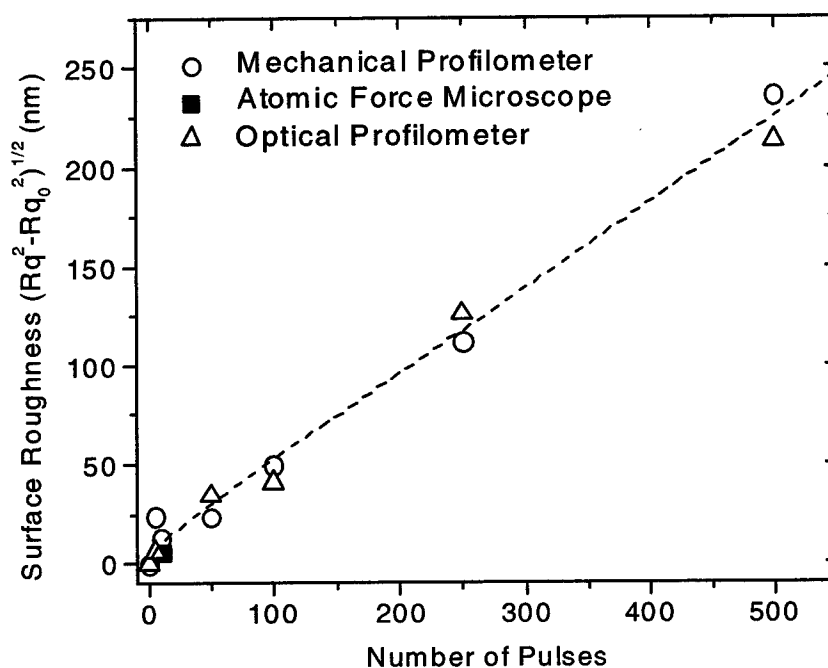


**Figure 2.** Surface roughness of  $\text{F}_2$  laser ablated PMMA versus number of laser pulses. Measured  $R_q$  is corrected for that of the unexposed sample  $R_{q_0}$  by plotting  $(R_q^2 - R_{q_0}^2)^{1/2}$ . Optical (Wyko) and mechanical (DekTak) profilometer measurements were used to record  $R_q$ . One result for peak-to-peak roughness obtained using Atomic Force Microscopy (AFM) is also shown. The dashed line is a fit based on beam fluctuations and stationary non-uniformity (see text).

Roughness measurements made on essentially cone-free PMMA surfaces using a Wyko optical profilometer and a DekTak mechanical profilometer are shown in figure 2. Here  $(R_q^2 - R_{q_0}^2)^{1/2}$  where  $R_q$  is the measured roughness and  $R_{q_0} = 6\text{nm}$  is that for the unirradiated surface is plotted as a function of the number of exposure pulses. One datum point obtained using an AFM is also included. There is a generally good agreement between measurements made using the different techniques and a clear trend of roughness increasing with number of pulses is evident.

To quantify the magnitude of beam fluctuations experimentally, the GaP detector was placed in the direct beam of the  $F_2$  laser and its normalised output recorded over 100 pulses. From these data a value of  $\sigma/\langle F \rangle = 5.1\%$  was obtained, close to that predicted for an unpolarised multimode  $F_2$  laser beam (see section 2.1 above). This gave a roughness factor (equation 4) of  $r = m^{1/2} \sigma / \{k \langle F \rangle\} = 3.0 \times m^{1/2}$  (nm) where an effective absorption coefficient of  $k = 1.7 \times 10^5/\text{cm}$  is used for PMMA. As seen in figure 2 the data diverge from this dependence at low  $m$  and then follow more closely a linear behaviour. Assuming multimode and stationary fluctuations combine in quadrature, a fit of the form  $(9m + 0.18m^2)^{1/2}$  was made to the data in figure 2. Using equation 6 this implies that a contribution of  $dF/\langle F \rangle = 0.73\%$  from small-scale stationary beam non-uniformity. It can tentatively be concluded that though roughness arising from 'mode speckle' may be contributory, the dominant effect at larger pulse numbers is a result of (random) stationary variations in beam fluence. More detailed investigation are required to confirm this or otherwise.

## 5.2 Soda Lime Glass

The threshold fluence for ablation of soda lime glass was derived from probe beam deflection measurements made over a range of fluences. In the sub-threshold regime the signature had the form of a short duration bipolar pulse (figure 3a) that can be attributed to an acoustic wave, generated by surface heating, passing over the beam. This disturbance was found to propagate from the surface at an average speed of 312 m/s which is close to the sound speed for Ar. Above threshold, the rapid acoustic deflection was followed by a slower and broader signature associated with ablation products driven from the surface (figure 3b). The propagation speed of the 'products' was much lower than for the acoustic wave e.g.  $\sim 5\text{m/s}$  at  $250\text{mJ}/\text{cm}^2$ . From plots of the amplitude of the product signal versus fluence (figure 3c), a threshold of  $F_T = 150 \pm 10\text{mJ}/\text{cm}^2$  for the soda lime glass was derived based on the appearance of the 'product' signal.

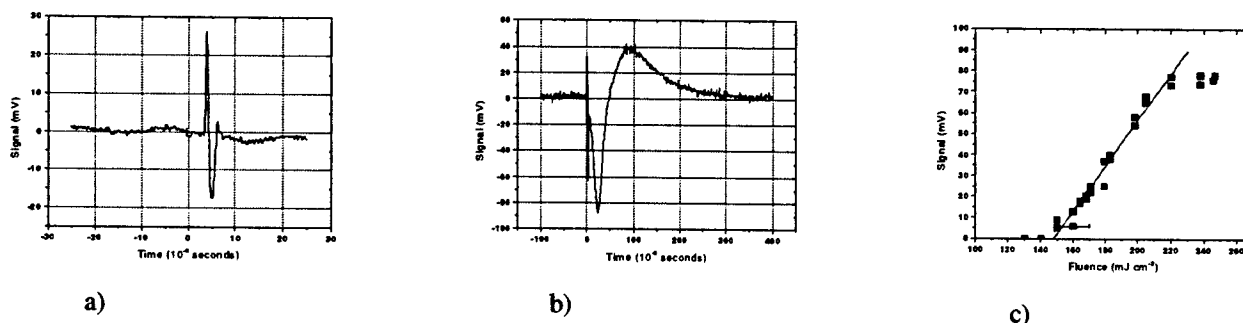


**Figure 3.** Probe beam deflection measurements for soda lime glass. (a) Acoustic signature, laser fluence  $100\text{ mJ cm}^{-2}$ , (b) Ablation product signature at a laser fluence of  $250\text{ mJ cm}^{-2}$  and (c) Determination of ablation threshold from product signal recorded in the fluence range  $130\text{ mJ cm}^{-2}$  and  $250\text{ mJ cm}^{-2}$ . Measurements were carried out in 300 mbar high purity (99.9995) Argon.

The depth of glass removed in samples subjected to multiple pulse exposure above threshold was measured using an optical microscope ( $\pm 2\mu\text{m}$  depth resolution), and used to calculate the average removal rate per pulse. Using these data and the measured threshold fluence in equation 2, gave  $k = 4.8 \times 10^5/\text{cm}$  for the effective absorption coefficient. This can be compared with a value of  $\sim 1.4 \times 10^4/\text{cm}$  derived from  $F_2$  laser transmission measurements made at low irradiance on specially prepared samples of the glass (thickness  $5 \pm 1\mu\text{m}$ ).

An estimate of the surface temperature,  $T_s$ , at the ablation threshold can be made by neglecting thermal diffusion during the short laser pulse and assuming absorbed laser energy is transformed to heat. This leads to:

$$T_S = T_R + (1-R) k F_T / C \quad (8)$$

where  $R \approx 0.05$  is the surface reflection coefficient at 157nm,  $C$  is the volume specific heat of the glass and  $T_R = 300\text{K}$  is its initial temperature. Using the low irradiance absorption coefficient of  $k = 1.4 \times 10^4/\text{cm}$  and  $F_T = 150\text{mJ}/\text{cm}^2$  we find  $T_S = 1500 \pm 200\text{K}$  at threshold. This is relatively close to but somewhat lower than the temperature at which pure silica glass (no fluxing agent) is known to decompose. Given uncertainties in the various parameters, and the possibility that the low irradiance absorption coefficient is an underestimate because of averaging over localised surface-absorbing states, it does not seem unreasonable to associate this threshold with the onset of significant thermal vaporization. The removal rate would then be governed by kinetic-limited surface vaporisation [18], rather than bulk absorption, explaining the high value of the effective absorption coefficient.

SEM investigations of micro-features produced in soda lime glass over a range of exposure conditions revealed no evidence of crack formation on or adjacent to the ablation site. As the above calculations suggest that the surface temperature reaches at least 1500 K, which is higher than the inception temperature for micro-cracking with the  $\text{CO}_2$  laser [5], this points to the strain-frozen layer being restricted to a small depth under 157nm irradiation (see section 3). Figure 4 shows an enlarged SEM view of the centre of a cross-shaped feature formed by 1000 pulses from the  $\text{F}_2$  laser at  $1600 \text{ mJ}/\text{cm}^2$ . The base of the pattern shows no signs of cracking and is macroscopically smooth although a small quantity of particulate debris is evident. It was noted, however, that a very substantial quantity of ablated material was deposited just outside of the ablation site under both vacuum and Ar back-filled conditions.

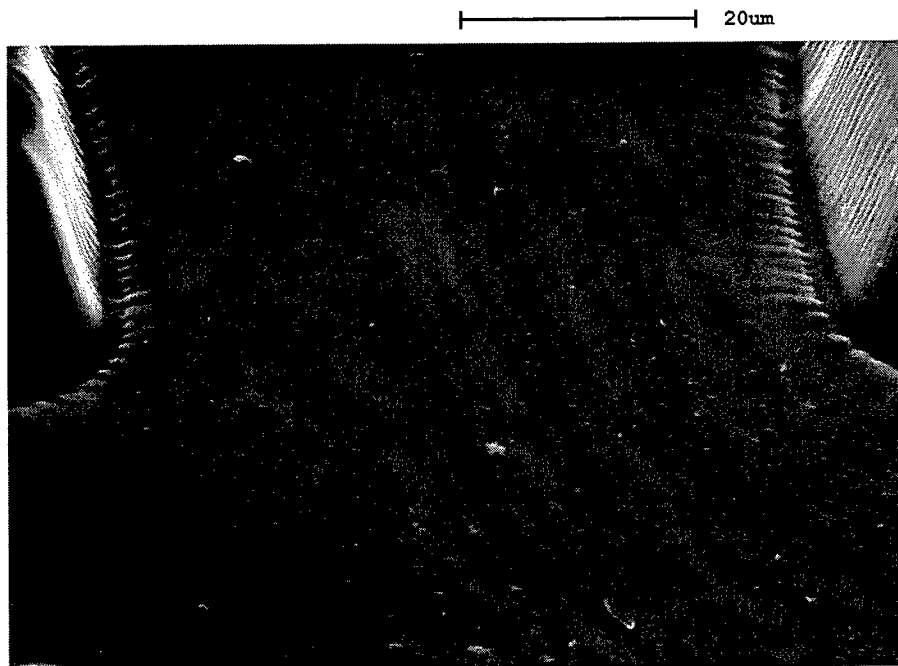


**Figure 4.** Scanning electron micrograph of central section of a feature produced by  $\text{F}_2$  laser ablation of soda lime glass. Projection imaging with 16x reduction was used (fluence of  $1600\text{mJ cm}^{-2}$ , 1000 laser pulses, pressure of  $\sim 10^{-4}$  mbar). The surface is macroscopically smooth and devoid of cracks but has low levels of particulate debris.

This is seen in figure 5a where a fine grid has been micro-machined in the glass surface under vacuum. Here, extensive coverage by what appears to be a film of deposited glass can be seen around the site, whereas this is absent in figure 5b

where ablation took place through a sacrificial coating (Opti-Clean™) that was subsequently peeled off. It should be noted that the definition quality of these grids is largely limited by the optical resolution of the simple single-element imaging lens used ( $\sim 3\mu\text{m}$ ,  $f\# = 10$ ).

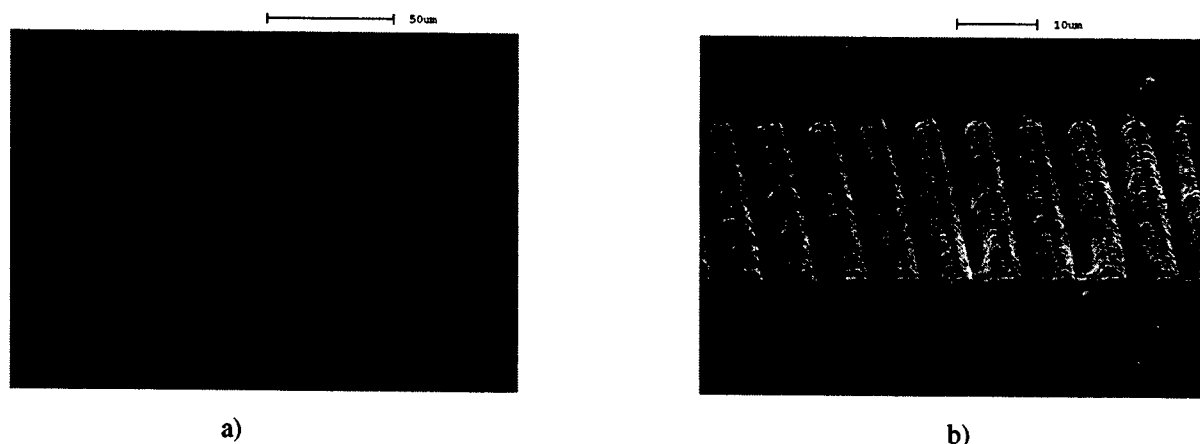


**Figure 5.** Scanning electron micrographs of a grid produced in soda lime glass by  $F_2$  laser ablation. A mask projection arrangement with a single element lens was used with a  $13\times$  optical reduction. Ablation was carried out in vacuum at a fluence of  $370\text{ mJ cm}^{-2}$ . a) Low magnification SEM showing deposited debris in the vicinity of the ablated area when bare surface exposed. b) Magnified view of feature when ablation took place with a protective coating that was subsequently peeled away after exposure. In this case the surroundings of the site are debris-free although the walls of the bars exhibit enhanced microstructure, apparently, induced by the presence of the coating.

AFM imaging of the ablated glass showed that the as-received surface roughness of  $R_q \approx 30\text{nm}$  increased to  $115\text{nm}$  as a result of exposure to 500 pulses at  $800\text{ mJ/cm}^2$  from the  $F_2$  laser. For comparison, a calculation combining mode fluctuations and stationary beam non-uniformity, assuming  $dF/\langle F \rangle = 0.73\%$  as derived from the PMMA results and  $k = 4.8 \times 10^5/\text{cm}$  for the glass, gave a net roughness of  $80\text{ nm}$ . This is in reasonable agreement with the induced roughness of  $(115^2 - 30^2)^{1/2} = 111\text{nm}$ . It should also be noted that some uncertainty arises in making these comparisons because the AFM roughness includes surface particulates not accounted for in the model.

## 6. CONCLUSION

We have outlined possible effects that will limit the ultimate surface quality of glasses that are micro-machined using the VUV  $F_2$  laser. Roughness attributable to pulse-to-pulse 'mode speckle' fluctuations and stationary beam non-uniformity are predicted to increase with number of pulses,  $m$ , with dependencies of  $m^{1/2}$  and  $m$  respectively. Preliminary studies confirm roughness increases with  $m$ , but disentangling the data to ascertain the importance of each contribution is difficult and requires further work. Likewise there is a need to confirm, or otherwise, the prediction that a smoother surface should be obtained with higher 'above threshold' processing. If so, then given the relatively low output energy of the  $F_2$  laser and the need for beam homogenization (e.g. by optical trains or spatial filtering means) which is inevitably lossy, we are restricted to addressing small area formats by single pulse ablation. Taking an energy of  $30\text{ mJ}$  and what is probably a realistic overall optical loss of  $50\%$ , would restrict the area to  $0.0125\text{cm}^2$  ( $\sim 1 \times 1\text{mm}^2$ ) for a glass ablated at  $F/F_T = 8$  with  $F_T = 150\text{ mJ/cm}^2$ . To process larger areas requires rastering the beam, bringing the possibility of shaping the surface by programmed ablation but additional demands from the need to ensure seam-free overlap of multiple sites. The good degree of depth control provided by the strong absorption of  $157\text{nm}$  radiation in glasses (e.g. sub- $100\text{ nm/pulse}$  for soda lime glass) makes feasible the precise micro-machining of profiles. An additional advantage is the absence of micro-cracking, even in soda lime glass which has a high thermal expansivity



and is prone to surface crazing at longer laser wavelengths. This is attributed to reduced thickness of the strain-frozen layer.

It is finally noted that debris deposition appears to be particularly extensive for the soda lime glass investigated here and could be problematic in terms of ultimate machining quality. Further work is required to investigate this in a range of glasses.

### ACKNOWLEDGEMENTS

We acknowledge the support provided through an EPSRC ROPA award (GR/N22502) and the EU programme on Hard Photon Processing (HARP). SMM acknowledges the support of an EPSRC research assistantship. We are also indebted to Ms V Corfield of Cambridge University for carrying out the Wyko surface profiling, and Dr A Lee of the Chemistry department at Hull University and Dr Zhao of the Physics department at Salford University for providing AFM results. Thanks also go to Paul Monk for his excellent technical support and T Sinclair for the electron microscopy.

### REFERENCES

- [1] P. R. Herman, K. Beckley, B. Jackson, K. Kurosawa, D. Moore, T. Yamanishi and J. Yang, *Proc SPIE*, **2992**, pp. 86-95, 1997.
- [2] B. Braren and R. Srinivasan, *J Vac Sci*, **B6**, pp. 537-541, 1988.
- [3] S. R. Jackson, W. J. Metheringham and P. E. Dyer, *Appl Surf Sci*, **86**, pp. 223-227, 1995.
- [4] C. Buerhop, B. Blumenthal, and R. Weissmann, N. Lutz and S. Biermann, *Appl Surf Sci*, **46**, pp. 430-4, 1990.
- [5] G. Allcock, P. E. Dyer, G. Elliner and H. V. Snelling, *J Appl Phys*, **78**, pp. 7295-7303 1995.
- [6] K. Jain, 'Laser Applications in Semiconductor Microlithography', *Lasers and Applications*, pp. 49-56, Sept 1983.
- [7] C. J. Sansonetti, J. Reader and K. Vogler, *Appl Opt*, **40**, pp. 1974-1978, 2001.
- [8] M. Rothschild and D. J. Ehrlich, *J Vac Sci Technol*, **B6**, pp. 1-17, 1988.
- [9] P. E. Dyer and J. Sidhu, *J Opt Soc Am*, **B3**, pp. 792-795, 1986.
- [10] A. Atkinson and R. M. Guppy, *J Mat Sci*, **26**, pp. 3869-73, 1991.
- [11] P. E. Dyer 'Laser ablation of Polymers' in *Photochemical Processing of Electronic Materials*, Ed I. W. Boyd and R. B. Jackman, Academic London 1992.
- [12] P. E. Dyer, H. V. Snelling and C. D. Walton accepted for publication in *Measurement Science and Technology* 2001.
- [13] J. A. Sell, D. M. Heffelfinger, P. Ventzek and R. M. Gilgenbach, *Appl Phys Lett*, **55**, pp. 2435-2437, 1989.
- [14] P. E. Dyer, S D Jenkins and J Sidhu, *Appl Phys Lett*, **52**, pp. 1880-1882, 1988.
- [15] D. Henderson, J. C. White, H. G. Craighead and I. Adesida, *Appl Phys Lett*, **46**, 900- 902 1985.
- [16] G. M. Davis and M. C. Gower *Appl Phys Lett*, **50**, pp. 1286-1288, 1987.
- [17] H. R. Phillip, H. S. Cole, Y. S. Liu and T. A. Sitnik, *Appl Phys Lett*, **48** 192- 4 1986.
- [18] R. Kelly and R. W. Dreyfus, *Nucl Instr Meth* **B32**, p. 341, 1988.

# High-Resolution F<sub>2</sub>-Laser Machining of Micro-Optic Components

Jianzhao Li\*, Peter R. Herman, Midori Wei, Kevin P. Chen  
Department of Electrical and Computer Engineering, University of Toronto,  
10 King's College Rd., Toronto, ON, M5S 3G4, Canada

Jürgen Ihlemann, Gerd Marowsky  
Laser Laboratorium Göttingen, Hans-Adolf-Krebs-Weg 1, 37077 Göttingen, Germany

Peter Oesterlin and Berthold Burghardt  
MicroLas Lasersystem GMBH, Robert-Bosch-Breite 10, 37079 Göttingen, Germany

## ABSTRACT

The F<sub>2</sub>-laser Nanofabrication Facility at the University of Toronto delivers high-fluence 157-nm radiation at high resolution to microfabricate high-finesse silica-based optical components. The 7.9-eV photons drive strong material interactions near the band-edge states of fused silica and related glasses that help avoid microcrack formation, a common limitation of longer wavelength lasers. The strong interactions provide for small and smooth excisions, offering depth control on a scale of tens of nanometers. A 157-nm beam homogenization system and a 25× Schwarzschild lens provided a uniform ( $\pm 5\%$ ) on-target fluence of 9 J/cm<sup>2</sup> in a 0.25 mm × 0.25 mm field. Larger work area was enabled by synchronously driving the projection mask and target motion stages. The 0.4 NA lens supported the formation of high-aspect channel walls and surface-relief features as small as ~500 nm. Both mask projection and direct writing technique were employed. The novel aspects of the optical beam delivery system are presented together with results on fabricating microchannels, cutting optical fiber, fabricating surface relief grating and cylindrical lens. The results demonstrate broad application directions for fabricating telecommunication devices, general optical and photonic components, and biological devices.

**Keywords:** F<sub>2</sub> laser, high-resolution, ablation, micromachining, microfabrication, micro-optic component

## 1. INTRODUCTION

The F<sub>2</sub> laser has become a commercially reliable source providing high-power laser light at a record short wavelength of 157 nm. Radiation at this forefront provides two distinct advantages over ultraviolet excimer and other longer-wavelength lasers in processing materials: a large photon energy of 7.9 eV drives strong absorption in almost all solid materials including ultraviolet-transparent glasses, and the short 157-nm wavelength is focusable to a diffraction-limited spots of ~100-nm to define the smallest features of any laser process. This combination together with a short pulse duration of ~15 ns affords precise control in smoothly ablating fine features in 'difficult' materials such as transparent glasses and polymers. The F<sub>2</sub>-laser lithography development effort[1-3] has recently made available new high quality optical materials and dielectric coatings for 157-nm radiation that provides further incentive for pursuing this F<sub>2</sub>-laser micromachining direction.

Materials processing by F<sub>2</sub>-laser radiation has been investigated for more than a decade across a wide range of organic and inorganic materials[4,5] such as polymers,[2,6] sapphire,[7] and semiconductor materials[8]. Our group has targeted fused silica and germanosilicate glasses materials for applications in

\* jzli@ecf.utoronto.ca; <http://www.ecf.utoronto.ca/~hermanp>

surface microstructuring and imprinting of buried refractive index structures that serve telecommunication and general optical component applications.[5,9] While such research has pointed to many promising application directions, further technology development is required before  $F_2$ -lasers become indispensable tools in material processing. Supporting this direction is the availability of new optical tool systems[2,3] that deliver high-fluence 157-nm radiation while also overcoming the challenge of strong 157-nm absorption in air and most optical materials.

Our group is developing the world's first  $F_2$ -laser micromachining system for high-resolution and high-fluence fabrication of photonic components.[3] This paper updates our progress on this novel  $F_2$ -laser processing system, describes the system resolution for micromachining of glasses, and overviews progress in several application directions in micro-optic fabrication. The modulation transfer function is presented for micromachining of glass, and specific examples of excising glass trenches, cleaving optical fibers, machining surface-relief phase masks, and shaping micro-lenses are described.

## 2. HIGH-FLUENCE $F_2$ -LASER MICROFABRICATION SYSTEM

The  $F_2$ -laser processing system consists of a commercial laser (Lambda Physik, LPF 220i), a MicroLas Lasersystems 157-nm optical system, and a high-resolution micromachining station, as described previously.[3] The laser provides ~25 mJ single-pulse energy with ~15 ns pulse duration (FWHM) and 1-200 Hz repetition rate. A narrow spectral linewidth of <5 pm and transverse coherence length of several hundred microns offers sufficient finesse for interferometric applications. The horizontal and vertical beam divergence is ~3 mrad and ~1 mrad, respectively. A recirculating chiller (Thermo NESLAB) heats the laser water coolant (~35°C) for boosting and stabilizing the laser energy.

The  $F_2$ -laser microfabrication system is shown in Figure 1. The optical delivery system was assembled inside a 2.5-m long airtight aluminum enclosure with further detail provided in Ref [3]. Dielectric-coated  $CaF_2$  optical mounts were mounted on a single base-rail to facilitate changes between medium and high-resolution beam imaging configurations. The high-resolution configuration employs beam-shaping optics, a mask, and a 25 $\times$  Schwarzschild objective lens with 0.4 NA. The  $F_2$ -laser beam was first expanded vertically by two prisms, and then homogenized by 4 sets of 9  $\times$  9 cylindrical lens arrays, to produce a uniform (<  $\pm 5\%$ ) illumination field of 6 mm  $\times$  6 mm with 24 mJ/cm<sup>2</sup> fluence at the mask plane. The prism expanders also served to create a central gap in the energy profile that avoided the normal incidence obscuration by the Schwarzschild's objective. The objective provided a uniform fluence of up to 9 J/cm<sup>2</sup> across the complete target image plane of 250  $\mu$ m  $\times$  250  $\mu$ m, which was more than sufficient to ablate silica-based glasses. The fluence was adjustable over a 10-70% range when using an angle-tuned dielectric-coated attenuator. The theoretical diffraction-limited resolution was ~250 nm.

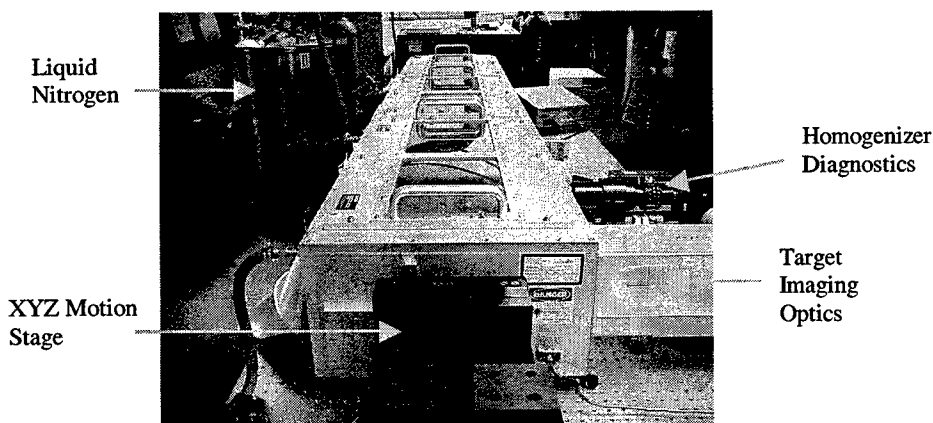


Figure 1. Photograph of the  $F_2$ -laser (background) and the 157-nm optical delivery system (foreground) for high-resolution and high-fluence microfabrication.

The 157-nm optical system employed several beam diagnostics. A movable 157-nm reflection mirror redirected the laser beam to a vacuum-ultraviolet (VUV) fluorescent plate, positioned in a plane equivalent

to the mask plane, to facilitate alignment of the homogenizing optics and to monitor degradation of optical components. A second CCD camera and visible-light vision system was aligned to share the VUV Schwarzschild lens for precise registration of the patterned F<sub>2</sub>-laser light with the sample surface. Sample positioning was controlled by computer-driven linear stages having 50-nm resolution and 100-nm repeatability. Synchronous motion control of the mask and target sample extended the sample work area beyond the 250- $\mu\text{m} \times 250\text{-}\mu\text{m}$  target field.

Absorption of 157-nm light by ambient air was overcome by flushing the full optical beam path with high-purity N<sub>2</sub> gas evaporated from a liquid nitrogen dewar. The 157-nm attenuation across the full 3-m beam path was <30% with O<sub>2</sub> and H<sub>2</sub>O impurity levels of less than 4 ppm and 3.5 ppm, respectively, as monitored with a gas sensor (Cambridge Sensotec, Rapidox 2000). A gas-flow nozzle was positioned between the sample and the Schwarzschild lens to direct transparent nitrogen to the working sample and thereby facilitate the rapid exchange of the samples without opening and flushing the optical tool system. The full optical system, diagnostics, and precision motor drives floated on an optical table to isolate acoustic noise and improve prospects for micromachining on the nano-scale.

### 3. MODULATION TRANSFER FUNCTION: HIGH-FLUENCE ABLATION

The micromachining resolution for silica glass was assessed for the Schwarzschild lens by ablating soda-lime glass microscope slides (Corning 2947) with single pulses of 157-nm light, patterned by a custom chrome-coated CaF<sub>2</sub> transmission mask. The chrome coating consisted of open rectangular bars with various periods as shown in Figure 2 (left). The modulation transfer function is normally obtained as a function of the line-and-space frequency (lines per millimeter) from the expression[10]

$$Mod = \frac{I_{max} - I_{min}}{I_{max} + I_{min}}, \quad (1)$$

where  $I_{max}$  and  $I_{min}$  refer to the maximum and minimum light intensity projected on the sample surface by the mask and lens system. For the present purpose, time-integrated intensity values were inferred from the maximum and minimum ablation depths patterned in the glass by the patterned F<sub>2</sub> laser light. The laser ablation rate  $D$  (depth per pulse) is related to the laser fluence  $F$  by

$$D = \frac{1}{\alpha_{eff}} \ln \left( \frac{F}{F_{th}} \right), \quad (2)$$

where  $\alpha_{eff}$  is the effective absorption coefficient ( $\sim 170,000 \text{ cm}^{-1}$  for fused silica) and  $F_{th}$  is the ablation threshold fluence ( $\sim 1 \text{ J/cm}^2$  for fused silica).[5] The time-integrated intensity values (i.e.  $F$ ) were therefore obtained from the simple scaling relationship,  $I \propto \exp(D\alpha_{eff})$ , to provide values for  $Mod$  in Eq. 1.

The modulated ablation depths,  $D_{max}$  and  $D_{min}$ , were measured by atomic force microscopy (AFM), and the modulation transfer function was calculated and plotted as shown in Figure 2(b). The resolution of the optical system is  $\sim 1 \mu\text{m}$  (line and space), with smallest observed features of  $\sim 600 \text{ nm}$ . These values do not meet the theoretical 250-nm diffraction limit of the Schwarzschild lens. The imperfections in the surface figure and alignment of the Schwarzschild may account for a 2-fold decrease in resolution. Additional factors also contributing are thermal transport during the 15-ns laser pulse, the flow of surface melt, and the ablation plume dynamics. Higher resolution features are anticipated for polymer materials, which have lower values of thermal diffusivity and less melt-phase dynamics than for silica-based glasses. Further work is in progress to improve the resolution of micromachined glasses.

### 4. MICRO-OPTICS MICROMACHINING DIRECTIONS

The controlled fabrication of glass microstructures such as gratings, microvias and microchannels with smooth morphology is of widespread interest for medical, biological, and photonic integrated-circuit

applications.[11-13]. The present high-fluence  $F_2$ -laser micromachining system is being applied in several such directions to define processing windows amenable to high-resolution micromachining.

Rectangular and V-shaped microgrooves of 4 – 40  $\mu\text{m}$  width were excised in glass microscope slides (Corning 2947) at 5 – 9  $\text{J}/\text{cm}^2$  fluence using free-standing metal foils as projection masks. Figure 3 shows optical microscope edge-views of two glass microchannels. The rectangular channel in Figure 3(a) was machined with a high on-target fluence of  $\sim 9 \text{ J}/\text{cm}^2$  per pulse, using 200 laser pulses at a pulse repetition rate of 10 Hz. The 30- $\mu\text{m}$  wide by  $\sim 35\text{-}\mu\text{m}$  deep channel has vertical walls without microcracks. In contrast, the 10- $\mu\text{m}$  wide V-channel in Figure 3(b) yielded  $25^\circ$  wall angles. The taper arises from a reduced fluence of  $\sim 3 \text{ J}/\text{cm}^2$  and a smaller 100-pulse exposure. The observed wall angle,  $\gamma$ , coarsely follows the empirical relation,[4]  $\gamma = \sin^{-1}(F_{th}/F)$ , for a  $F_{th}$  value of  $1.0 \text{ J}/\text{cm}^2$  for fused silica. The combination of high and variable fluence, large numerical optic ( $\text{NA} = 0.4$ ), and micropositioning tools offers wide latitude in fabricating custom microstructure shapes with controllable surface morphology.

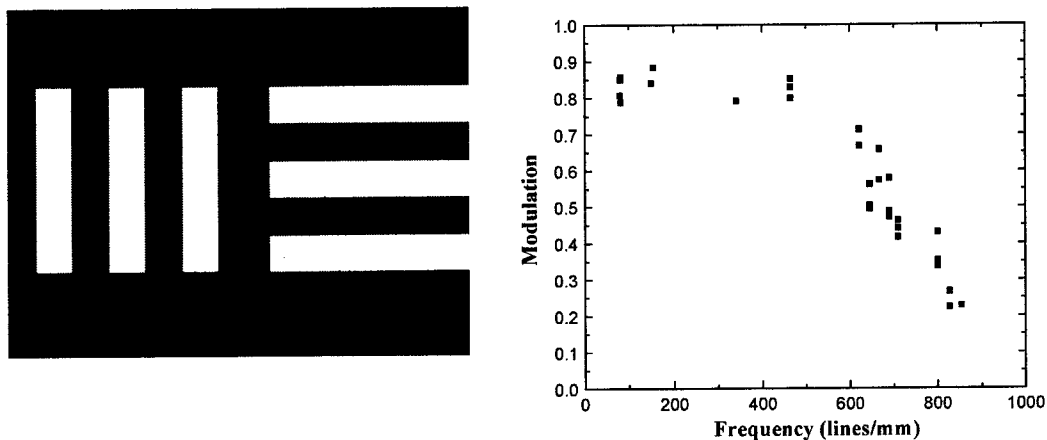


Figure 2. Basic bar pattern of the projection mask (left) used to infer the Modulation Transfer Function (right) of the 157-nm optical imaging system. The visibility of ablation profiles excised in silica glasses were obtained as a function of the spatial frequency.

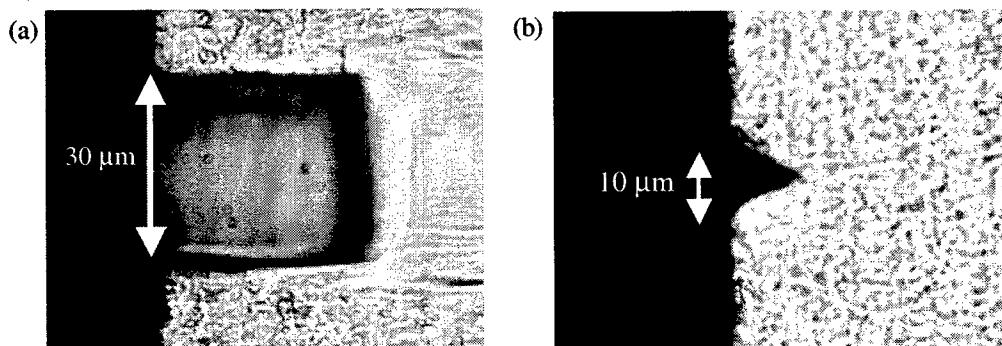


Figure 3. Optical microscope end-view of microscope glass slides (Corning 2947) in which steep-walled rectangular (a) and V-grooved (b) microchannels were excised by  $F_2$ -laser ablation. The V-groove has  $25^\circ$  wall angles.

The vertical walls in Figure 3(a) are attractive in glass cutting applications such as required in cleaving optical fibers and dicing planar lightwave circuits. The  $F_2$  laser offers smooth and orthogonal end surfaces without microcrack generation. A standard single-mode optical communication fiber (Corning SMF-28) was *cleaved* with single-pulse fluence of  $9 \text{ J}/\text{cm}^2$  over a 2-min. exposure at 10 Hz. A 750- $\mu\text{m}$  metal slit served as a projection mask to provide a 30- $\mu\text{m}$  x 180- $\mu\text{m}$  cutting beam on the 125- $\mu\text{m}$  diameter glass fiber. The polymer jacket was stripped and the glass fiber cleaned with methanol prior to laser cutting. Figure 4(a) illustrates the side view image of the cut fiber while Figure 4(b) shows an AFM image of the fiber end,

obtained near the central 9- $\mu\text{m}$  diameter waveguide core. The RMS and arithmetic roughness over the probe area are 50 nm and 40 nm, respectively, less than 3% of the telecommunication wavelength. The ripples on the surface originate with defects on the slit edge used as a projection mask and can therefore be improved by use of a higher quality mask. Faster fiber cleaving times of several seconds are anticipated with higher repetition rate of 100 Hz.

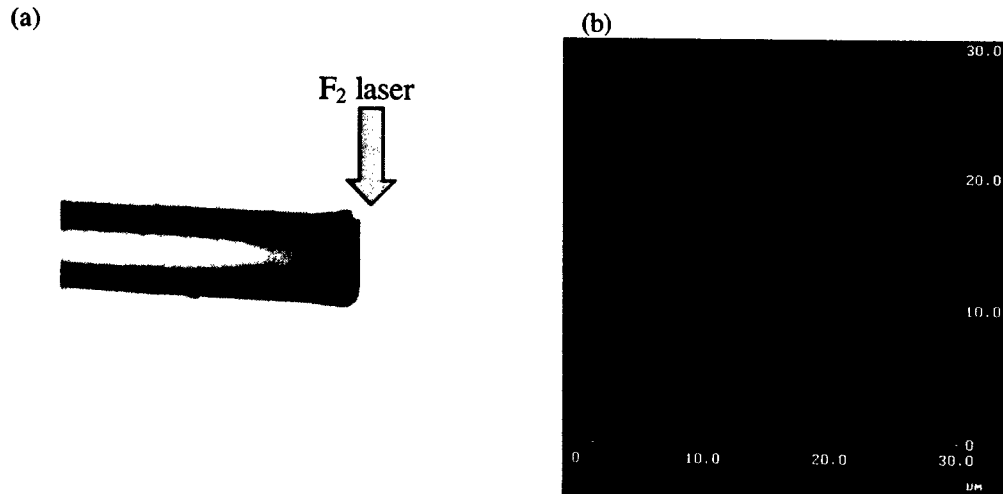


Figure 4. Optical microscope side-view (a) of a single-mode optical fiber (Corning SMF-28) cleaved with the  $F_2$ -laser micromachining system. The fiber diameter is 125  $\mu\text{m}$ . (b) AFM image of the laser-cut fiber end at the center core region. The arithmetic and root-mean-square surface roughness are 40 nm and 50 nm, respectively.

Surface relief gratings were formed on a glass slide (Corning 2947) across the full 250-nm  $\times$  250-nm optics field of the high-resolution  $F_2$  laser processing system. The 157-nm homogenization optics was essential in forming a uniform grating relief across the full field. An AFM image (a) and the cross-sectional profile (b) of grating are shown in Figure 5. A laser-cut metal foil served as the transmission amplitude mask (50- $\mu\text{m}$  period and 50% open). An on-target fluence of  $\sim 3 \text{ J/cm}^2$  and 30 pulse exposure were applied for the sample in Figure 5, where a 2- $\mu\text{m}$  period grating with a 300-nm (peak-to-peak) modulation depth are clearly discernable. Laser processing parameters are under investigation for micromachining sub-micron features with high aspect-ratio troughs that support the fabrication of fused silica phasemasks and other diffractive optical elements.

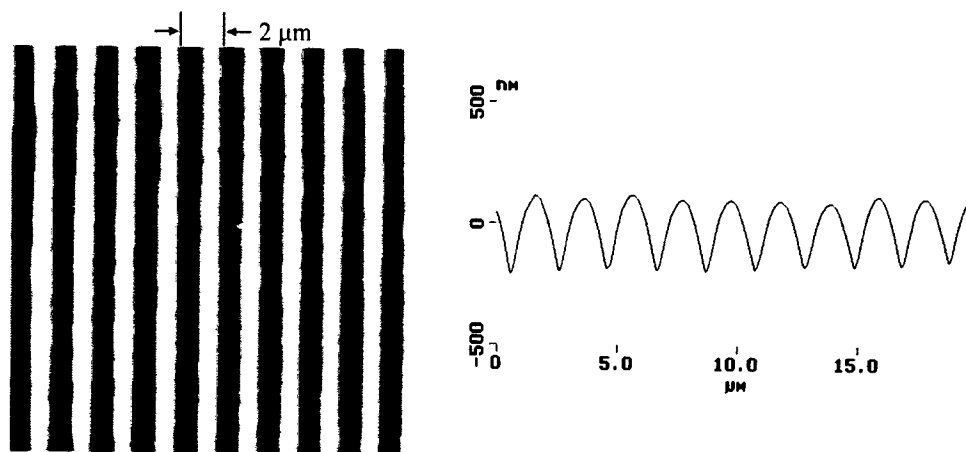


Figure 5. AFM image (a) and topographical profile (b) of a surface-relief grating (phase mask) of 2- $\mu\text{m}$  period formed on glass by  $F_2$ -laser ablation.

Surface relief structures on optical materials can also be formed by velocity scanning of the sample while continuously ablating the surface with a shaped laser beam. The surface relief is controlled by the dwell time. Figure 6 shows a SEM image of a cylindrical microlens fabricated by velocity scanning of a glass slide (suprasil fused silica) under a uniform  $12\text{-}\mu\text{m} \times 160\text{-}\mu\text{m}$  laser beam (image of a  $300\text{-}\mu\text{m} \times 4\text{-mm}$  rectangular mask). The laser-generated cylindrical lens was  $640\text{ }\mu\text{m} \times 160\text{ }\mu\text{m}$  in area. Several defects are present due to rough edges on the projection mask and poor quality motion stages used during this first trial. Optical quality microlens surfaces are anticipated with the use of better quality masks and new motion stages.

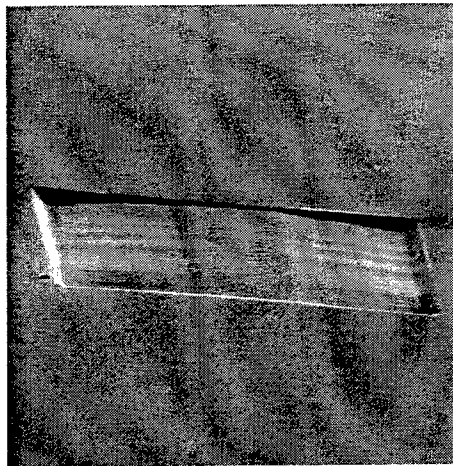


Figure 6. SEM image of a micro-cylindrical lens ( $640\text{ }\mu\text{m} \times 160\text{ }\mu\text{m}$ ) fabricated on a glass slide (suprasil fused silica) with the  $F_2$ -laser micromachining system by velocity scanning of the target.

## 5. SUMMARY

A high-resolution and high-fluence  $F_2$ -laser microfabrication system developed by University of Toronto and MicroLas Lasersystem has been described. A variety of micromachining demonstrations on glass samples was provided that point to new directions of applying this novel system to fabricate and process micro-optic components.

## 6. ACKNOWLEDGMENTS

The authors gratefully acknowledge support from the Natural Science and Engineering Research Council of Canada, the Canadian Institute of Photonics Innovation, and Photonics Research Ontario.

## REFERENCES

1. <http://www.sematech.org>
2. P. Gruenewald, J. Cashmore, J. Fieret, and M. Gower, *High-resolution 157nm laser micromachining of polymers*, in *Laser Appl. in Microelectronic and Optoelectronic Manuf.*, (SPIE 4274, 2001) p. 158.
3. P. R. Herman, K. P. Chen, M. Wei, J. Zhang, J. Ihlemann, D. Schafer, G. Marowsky, P. Oesterlin, and B. Burghardt, *F<sub>2</sub>-lasers: high-resolution optical processing system for shaping photonic components*, in *Laser Appl. in Microelectronic and Optoelectronic Manuf. V*, (SPIE 4274, 2001) p. 149.
4. D. Basting, ed. *Excimer laser technology: laser sources, optics, systems and applications*, (Lambda Physik, Göttingen, 2001) p. 155.
5. P. R. Herman, K. Beckley, B. Jackson, K. Kurosawa, D. Moore, T. Yamanishi, and J. Yang, *Processing applications with the 157-nm fluorine excimer laser*, in *Excimer Lasers, Optics, and Applications*, (SPIE 2992, 1997) p. 86.

6. M. Lapczynska and M. Stuke, *Rapid prototype fabrication of smooth microreactor channel systems in PMMA by VUV laser ablation at 157 nm for applications in genome analysis and biotechnology*, (Mat. Res. Symp. **526**, 1998) p. 143.
7. A. Ostendorf, *157 nm excimer laser radiation for precision machining of innovative materials*, in *3<sup>rd</sup> International UV Laser Symposium for 157 nm Applications*, (Lambda Physik, 2000).
8. A. Ostendorf, T. Bauer, T. Temme, and T. Wagner, *Short-pulse and short-wavelength ablation of semiconductor materials*, in *Laser Appl. in Microelectronic and Optoelectronic Manuf. V*, (SPIE **4274**, 2001) p. 116.
9. J. Zhang, P. R. Herman, C. Lauer, K. P. Chen, and M. Wei, *157-nm laser-induced modification of fused-silica glasses*, in *Laser Appl. in Microelectronic and Optoelectronic Manuf. V*, (SPIE **4274**, 2001) p. 125.
10. W. J. Smith, *Modern optical engineering: the design of optical systems*, 2nd Ed., (McGraw-Hill, NY, 1990).
11. A. T. Woolley and R. A. Mathies, *Ultra-high-speed DNA fragment separations using microfabricated capillary array electrophoresis chips*, Natl. Acad. Sci, USA, **91** (1994) p. 11348.
12. C. Backhouse, M. Caamano, F. Oaks, E. Nordman, A. Carrillo, B. Johnson, and S. Bay, *DNA sequencing in a monolithic microchannel device*, Electrophoresis, **21** (2000) p. 150.
13. G. C. Bjorklund, *Packaging requirements for integrated optics components*, (SPIE **4290**, 2001) p. 94.



# Laser processing of ion-exchange waveguides in glass

**S. Ruschin**

*Department of Electrical Engineering-Physical Electronics, Tel-Aviv University, 69978 Ramat-Aviv, Israel.*

**K. Sugioka**

*RIKEN, Institute of Physical and Chemical Research, Wako, Saitama 351-01, Japan*

**G. Yarom**

*Department of Electrical Engineering-Physical Electronics, Tel-Aviv University, 69978 Ramat-Aviv, Israel.*

**T. Akane and K. Midorikawa**

*RIKEN, Institute of Physical and Chemical Research, Wako, Saitama 351-01, Japan*

## Abstract

Using lasers at different wavelengths, the optical and geometrical properties of waveguides can be affected via photochemical, thermo-chemical and diffusion effects. In this paper we review several of these options and show experimental results. Among others, we report on refractive index modification and buried waveguide formation by UV-VUV laser irradiation and on controlled tapering of channel waveguides by thermal laser treatment.

**Keywords:** waveguides, integrated optics, laser microfabrication

## 1. Introduction

Ion-exchanged waveguides in glasses are attractive regarding many applications in telecommunications and sensing. One special feature of them is that their properties can be modified post-fabrication by laser irradiation. Our purpose was to rely on well-developed techniques of Ag-Na ion exchange to form planar and channel waveguides and subsequently modify them by means of direct laser treatment. Common type of glasses with high Sodium contents makes one of the most commonly available and inexpensive types of optical substrates. Their use is therefore highly attractive in applications of wave-guided optical devices where low cost is an advantageous requirement. Application examples include passive optical communication devices for low-end and massive consumption and wave-guide bio-sensors. Many of these glasses have in addition, a well-developed technology for waveguide fabrication based on ion exchange<sup>1</sup>. Within this research effort we pursue to explore technologies concerning the utilization of laser processing that are relevant to waveguide applications. We recall that pure conventional thermal annealing of Ag-Na ion exchange planar waveguides causes a decrease in refractive index and enlargement of the waveguide's cross-section, due to a dominant diffusion effect.

The use of laser radiation in order to modify properties of waveguides prepared in different technologies has been reported in the literature<sup>2-4</sup>. In this article we report experiments of two kinds. In the first one, by means of laser treatment by short pulses in the UV-VUV range, we observed an increase effect in the refractive index, leaving the waveguide's size unchanged. Several pulsed lasers were used as irradiation source ( $\lambda=157\text{nm}$ ,  $198\text{nm}$  and  $248\text{nm}$ ). In the first case we irradiated

ion-exchanged waveguides by visible and mid-infrared CW laser. By this localized thermal treatment, we achieved large (up to 50%) reduction in the refractive index in conjunction to an enlargement in the mode-field size. This effect was applied in order to accomplish controlled tapering of planar and channel waveguides. In another application, we observed buried waveguide formation by VUV laser irradiation.

## 2. Tapering of channel waveguides by continuous visible laser irradiation.

In these experiments the irradiation was continuous and the application in mind was to taper channel waveguides at the input and output ports in order to fit their mode size to suitable interfacing elements like optical fibers, diode lasers and detectors. The utilization of thermal methods for this purpose is reported in the literature based on induced temperature gradients. The method reported here of applying laser irradiation has the advantages of direct and easy control of the amount of energy deposited and fairly good localization the treated area. This last feature would be advantageous in the compactization of an Integrated Optical device where tapering is desirable. Soda-lime silica glass and Corning 0211 samples of commercial grade were used in this study. The chemical composition ( % ) according to manufacturers for soda-lime glass was: 72.0 SiO<sub>2</sub>, 14.0 Na<sub>2</sub>O, 0.6 K<sub>2</sub>O, 7.1 CaO, 4.0 MgO, 1.9 Al<sub>2</sub>O<sub>3</sub>, 0.1 Fe<sub>2</sub>O<sub>3</sub>, 0.3 SO<sub>3</sub>, while for Corning 0211 the composition was: 64.0 SiO<sub>2</sub>, 7.0 Na<sub>2</sub>O, 7.0 K<sub>2</sub>O, 9.0 B<sub>2</sub>O<sub>3</sub>, 3.0 Al<sub>2</sub>O<sub>3</sub>, 7.0 ZnO, 3.0TiO<sub>2</sub>. Ion-exchange was carried out in a mixture of (AgNO<sub>3</sub>)<sub>0.05</sub>:(KNO<sub>3</sub>)<sub>0.5</sub>:(NaNO<sub>3</sub>)<sub>0.5</sub> heated to a temperature range of 270-315C. In all cases the ion-exchange time was 1.5hr. The procedure furnished planar multimode waveguides of  $\Delta n \sim 0.09$  and depth of about 4 $\mu$ m. Irradiation was accomplished by means of a frequency-doubled Nd-YAG laser ( $\lambda=532$ nm). At this wavelength, the glasses are basically transparent. To enhance absorption, the samples were coated by a thin black polyurethane layer.

In order to optimize the irradiation process, slab-type waveguides were chosen first. Samples were irradiated for 45 minutes by laser radiation at powers of 2W, 2.25W and 2.5W. The black polyurethane layer could withstand well theses power levels. At the highest power, the sample started to show apparent darkening of ion exchanged region, hinting Ag<sup>+</sup> reduction and eventually metal segregation. The slab waveguides were analyzed by means of a Metricon 2010 prism-coupler analyzer. Figure 1 shows changes in waveguide thickness as a function of time for irradiation at 2.25W.

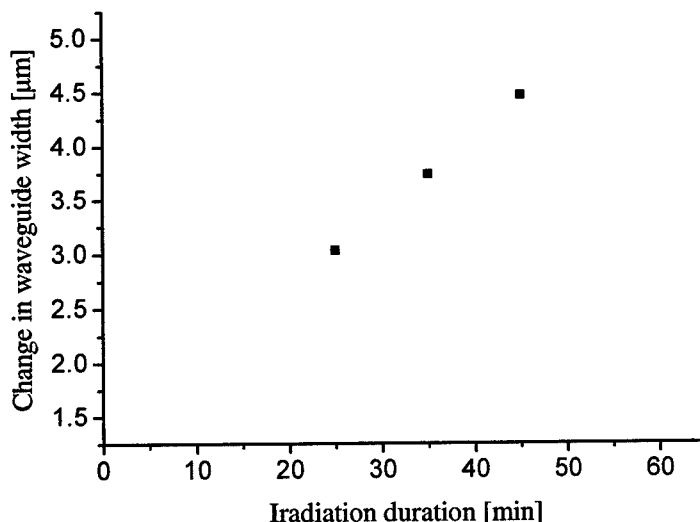


Figure 1: Change in waveguide thickness as a function of time for irradiation at 2.25W

Detailed measurements on the samples showed no significant enlargement of the waveguides' thickness in non-irradiated portions of the waveguides.

In order to evaluate the temperature at which the tapering of the waveguides took place, we applied two different methods. First, the heat transfer equation was solved for the glass material chosen (soda-lime silica) using implicit finite-difference method. The solution showed quasi-homogeneous heating at the relevant depths to temperatures of 290°C, 372°C and 403°C for irradiation at 2.0W, 2.25W and 2.5W respectively. The second method of evaluation was the controlled heating of the entire samples inside an oven at temperatures within those calculated ranges, resulting in similar thickening of the waveguides.

Channel waveguides were fabricated in order to investigate lateral tapering effect by laser irradiation.. The photolithography mask contained straight waveguides of widths in the range of 2.5 $\mu\text{m}$ -3  $\mu\text{m}$ . The silver-source melt was identical to that of the one used for planar waveguides, but this time, the processing temperature was lowered to 270°C and exchange time was set to 25min. These parameters ensured formation of single-mode waveguides. Irradiation took place at a power level of 2.25W and a laser beam of 3.5mm diameter. This size ensures that all the contiguous waveguides selected for measurement undergo similar thermal treatment conditions. The center of the beam was placed at the edge of the sample in order to be able to measure the largest possible tapering effect. Mode spot-sizes were measured by a near-field imaging setup, at a wavelength of 790nm of radiation fed by a SMF at the untreated end of each channel waveguide. Figure 2 shows lateral and depth cross-sections of the TE basic mode at the exit facet.

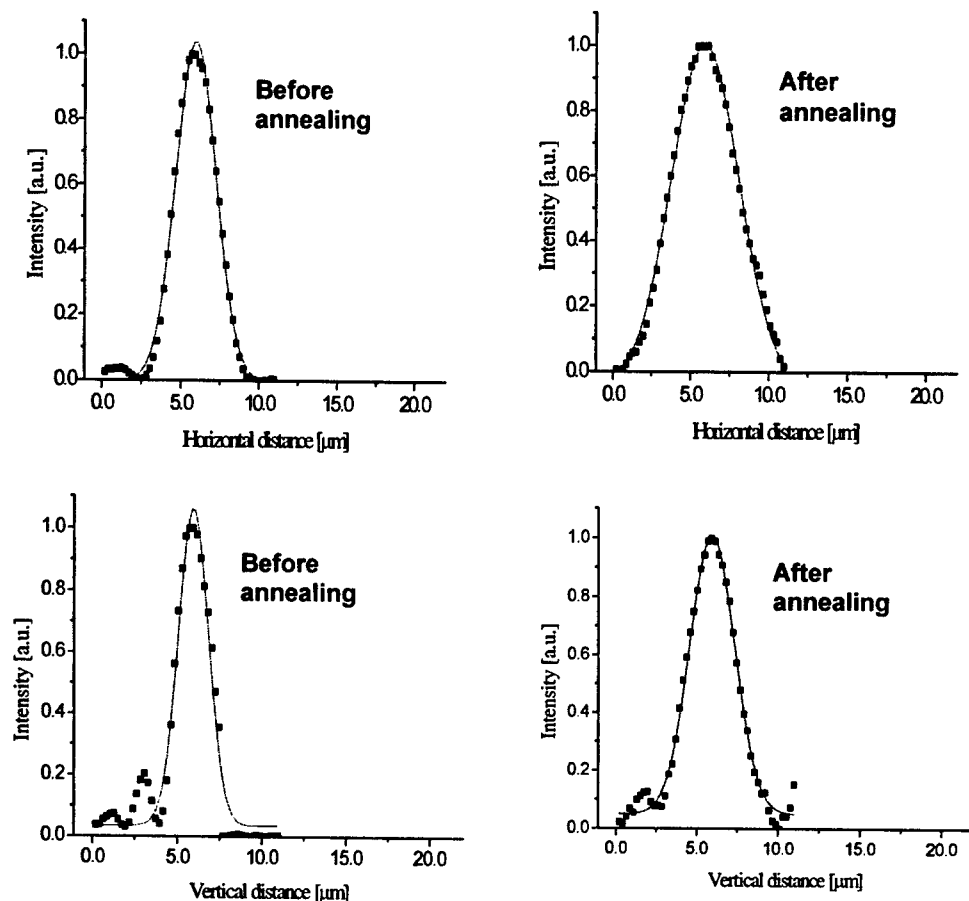


Figure 2. Cross-sections of modes at exit facet before and after laser annealing. Upper graphs show lateral cross-sections and lower graphs depth cross-sections.

As seen, the effect of mode widening by means of laser annealing is considerable in all cases. On the average the widening amounted 73% and 47% in the lateral and depth dimensions respectively.

A last check of the effect of laser irradiation on the dimensions of the waveguides was performed by SEM imaging, and are shown in Figure 3. The density of back-scattered electrons is an indication of  $\text{Ag}^+$  ion concentration. Both effects, namely the widening of channels and the dilution of silver are apparent in the figure. Measurements from the SEM scan show widening from 3.2 μm and 4.6 μm before annealing to 5.8 μm and 6.2 μm after annealing, respectively.

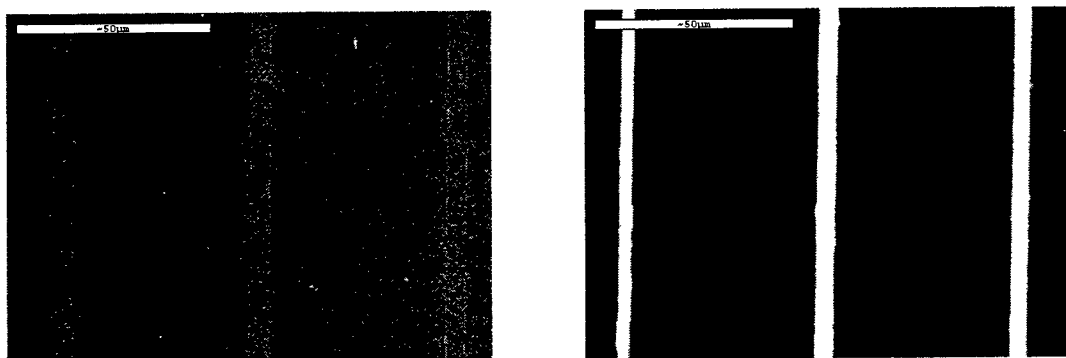


Figure 3: SEM pictures of waveguides before (right) and after annealing (left)

We can summarize from all the observations above that widening of the order of 60% and up is attainable in channel waveguides by laser irradiation at moderate power levels.

### 3. Modification of refractive index in ion-exchanged glasses by vacuum-ultraviolet pulse laser irradiation

The objective of the experiments reported in this section was to explore the possibility of modifying the refractive index of already existing planar waveguides by pure irradiation of laser light in the vacuum ultraviolet range. The relatively high absorption coefficient of the type of glass used, in the near UV, leads to the expectation that available UV sources like excimers or higher harmonics of Nd:YAG laser, would be effective in processing the glass. The influence of this irradiation will induce structural modification at moderate irradiation power, and surface relief modification and ablation at higher levels of irradiation. The first type of process is likely to lead to refractive index modification for waveguide formation,<sup>2,5</sup> and the second one to a controlled etching process<sup>6</sup> that would be useful in fabrication of gratings and rib-type structures. Applications of this technology should not be limited to waveguide devices, but may be useful also in other applications like phase gratings, holography and diffractive optical elements. Our purpose again was to rely on well-developed techniques of  $\text{Ag}^+ - \text{Na}^+$  ion exchange to form planar waveguides and subsequently modify them by means of direct laser irradiation.

Literature reports exist on UV sensitization of glass materials by incorporating silver ions, into bulk material.<sup>7</sup> More recently, Tsunemoto and Koyama<sup>8</sup> reported on relief gratings fabricated by laser irradiation, where the glass surface was pretreated by Ag molten salt.

Although several excimer laser wavelength were attempted, best results were obtained by using an  $F_2$  laser ( $\lambda=157\text{nm}$ , Lambda-Physik Model LPF105) as irradiation source. Laser pulse duration was 20 nsecs and energies were in the 20-30mJ range. Radiation outcoming from the laser was focused by means of a  $MgF_2$  lens of 10cm focal length. The lens and sample were enclosed in an oxygen-free environment. The effect of laser irradiation on ion-exchanged waveguides was monitored as a function of laser fluence and number of laser pulse shots. Laser fluence was varied by positioning the sample at various distances away from the focal spot. For distances closer than 3cm to the focus, ablation effects were apparent. Most of our measurements took place in the 4-5.5cm range. Absence of ablation and surface smoothness for reported samples was verified by surface profilometer down to a resolution of 5nm.

The optical modes in the slab wave-guide and their effective indexes were measured using a Metricon Model 2010 Prism Coupler, based on He-Ne laser (632.8nm). Three measurements were taken at each position. The apparatus furnishes effective indices from which the entire refractive index can be retrieved. 7-8 modes in each polarization were typically measured. The optical absorption spectra of the glass samples either after ion exchange or after ion exchange followed by irradiation, were measured in the range of 200-700nm using Hewlett Packard 8452A diode array Spectrophotometer.

Figure 4 shows the effective index as a function of the number of pulses for the first and the third modes. The samples here were based on 0.5mm thick Corning 0211 substrates pretreated by  $Ag^+$  ion-exchange.

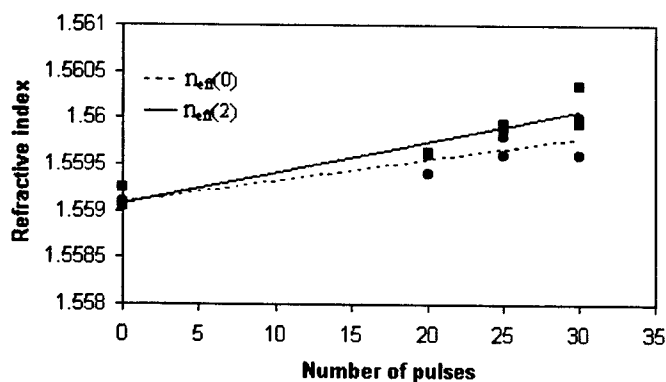


**Fig.4** Change in effective index of the first and third guided modes (full and dotted lines respectively) as a function of number of irradiated pulses. Note that in all cases the third mode changed more than the first one

Straight lines in Figure 4, correspond to linear regression best fit, and the intercept of the lines close to the origin indicate a cumulative effect as a function on number of pulses. The order of magnitude of the UV induced increments is of  $2 \times 10^{-3}$ . Observe that the slope of the third mode is higher than the slope corresponding to the first one, hinting that the highest change of refractive index induced by the VUV laser is attained below the surface of sample. The irradiation fluence corresponding to

a single pulse was of  $55\text{mJ/cm}^2$ . The waveguide index profiles were reconstructed on the basis of measured modal effective indices by means of an inverse WKB procedure.<sup>9</sup> According to literature the graded index profiles corresponding to ion-exchange waveguides follow either Gauss or Erfc shapes.<sup>1</sup> In our case Gauss gave much better fits. Figure 5 shows a graph of the difference between the refractive index profiles before and after VUV irradiation. A maximum is attained here at depth of  $\sim 5\mu\text{m}$ . This sample was irradiated by 10 pulses from  $\text{F}_2$  laser. The effect of a buried maximum was common to all examined samples.

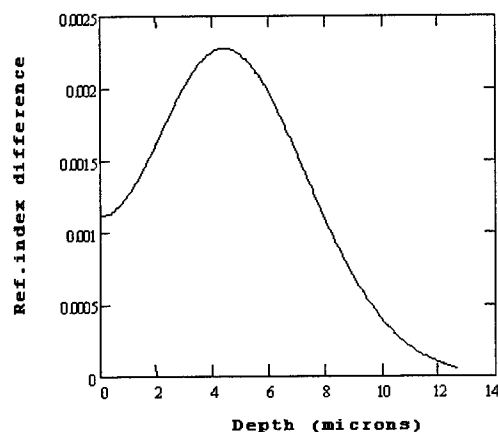


**Fig.5** Profile of refractive index difference in Ag/Na ion-exchanged samples, before and after irradiation by  $\text{F}_2$  laser

Two main mechanisms are accepted to be responsible for further changes in the refractive index of waveguides produced by exchange of Na and Ag ions from melt. Both of them are present when these waveguides are thermally annealed. One of them

is the reduction of  $\text{Ag}^+$  ions into neutral atoms, while further heating causes aggregation of silver atoms<sup>10</sup>. The second effect is thermal diffusion of both atoms and ions into the bulk. This last effect causes inevitably a decrease in refractive index. From a Kramers-Kronig type of argument one would expect an *increase* in refractive

index from the first mechanism, namely the  $\text{Ag}^+ \rightarrow \text{Ag}^0$  reaction, since the absorption bands are shifted toward longer wavelengths. This increase however has not been observed in conventional heat-treatment experiments, since it is covered by the effect of diffusion, which is dominant. The VUV laser irradiation method reported here, due to the short pulse duration, eliminates almost completely thermal diffusion, allowing the sole effect of Ag reduction to manifest. Indeed, reconstructed refractive index profiles show almost no change in penetration depth after laser treatment. Samples were irradiated also by lasers at longer wavelengths (248nm and 193nm), giving rise to weaker effects for the same power irradiation conditions.

### Concluding remarks

We presented here two techniques for the modification of refractive index profiles in ion-exchanged waveguides in glass. Both methods are based on laser treatment of the waveguides surroundings.

The first one is based on visible-NIR CW radiation and induces a localized thermal effect given rise of a wider index profile together with lowering of the maximum index. This effect is attributed purely to thermal diffusion. The second method is accomplished by irradiation of short VUV laser pulses. Here the short time of interaction excludes practically diffusion effects but induces an increase in index due to  $\text{Ag}^+$  ion reduction. Both methods therefore complement each other and should be useful in fabrication of waveguided devices requiring tight control of parameters.

**Acknowledgements:** This research was founded partly by the Israel-Japan Collaboration Program-Israel Ministry of Science. The authors also thank Dr. K. Obata for help in irradiation experiments.

#### References:

- <sup>1</sup> S.I. Najafi, *Introduction to glass integrated optics* (Artech House, Boston, 1992).
- <sup>2</sup> J. Zhang, K. Sugioka, S. Wada, H. Tashiro, K. Toyoda, and S. Ruschin, *IEEE J. Select. Top. Quant. Electron.* **3**, 789 (1997).
- <sup>3</sup> Herman PR. Chen KP. Corkum PB. Naumov A. Ng S. Zhang J. *Proc. SPIE* **4088**, 345 (2000)
- <sup>4</sup> Zauner DA. Hubner J. Malone KJ. Kristensen M, *Electron. Lett.* **34**, 780 (1998).
- <sup>5</sup> X.C. Long, and S.R.J. Brueck, *Appl. Phys. Lett.* **74**, 2110 (1999).
- <sup>6</sup> K. Sugioka, S. Wada, H. Tashiro, and K. Toyoda, *Appl. Phys. Lett.* **65**, 1510 (1994).
- <sup>7</sup> O.M. Efimov, L.B. Glebov, L.N. Glebova, K.C. Richardson, and V.I. Smirnov, *Appl. Optics.* **38**, 619 (1999).
- <sup>8</sup> K. Tsunetomo and T. Koyama, *Optics Letters.* **22**, 411 (1997).
- <sup>9</sup> A.H. Hartog and M.J. Adams, *Optical and Quantum Electron.* **9**, 223 (1977).
- <sup>10</sup> A.A. Ahmed, and E.W. Abd Allah, *J.Am.Ceram.Soc.* **78**, 2777 (1995).
- <sup>11</sup> A. Mahapatra and JM. Connors. *Optics Letters*, **13**, 169, (1988).



# High-efficiency refractive index modification of fused silica by F<sub>2</sub> and KrF excimer laser multiwavelength excitation process

Kotaro Obata<sup>1,2</sup>, Koji Sugioka<sup>1</sup>, Toshimitsu Akane<sup>1</sup>, Koichi Toyoda<sup>2</sup>, and Katsumi Midorikawa<sup>1</sup>

<sup>1</sup>RIKEN (The Institute of Physical and Chemical Research),

2-1 Hirosawa, Wako, Saitama 351-0198, Japan

<sup>2</sup>Science University of Tokyo, Yamazaki 2641, Noda, Chiba 278-8510, Japan

## ABSTRACT

Novel materials processing by a multiwavelength excitation process using F<sub>2</sub> and KrF excimer lasers for high-efficiency and high-speed refractive index modification of fused silica is demonstrated. We find that this process is essentially superior to single-wavelength F<sub>2</sub> laser processing. The multiwavelength excitation process achieves twice of diffraction efficiency compared with that of single F<sub>2</sub> laser irradiation sample at the same number of total photons supplied to the sample. This high-efficiency and high-speed modification is realized within  $\pm 50$  ns of the delay time of each laser beam irradiation. In addition, the refractive index change of the multiwavelength sample was increased by  $8.2 \times 10^{-3}$ , which is 1.78 times larger than that of single wavelength F<sub>2</sub> laser irradiation sample at same irradiation time. This superiority of the multiwavelength excitation process is attributed to resonance photoionization-like process based on excited state absorption in fused silica.

**Keywords:** F<sub>2</sub> laser, excimer laser, multiwavelength excitation process, resonance photoionization-like process, excited-state absorption, fused silica, refractive index, modification, diffraction efficiency, optoelectronics

## 1. Introduction

Refractive index modification of fused silica and related silicate glass is one of the key technologies for manufacturing integrated optics and optoelectronic integrated circuits [1-3]. The conventional technique for the refractive index modification involves introduction of dopants by either ion-implantation or ion-exchange [4,5]. Alternative way using laser processing can avoid impurity incorporation and make direct patterning without a resist process possible, so that it conquers disadvantage of former technique. However, the refractive index modification of fused silica by laser beam is quite difficult due to its excellent transmittance in a wide wavelength range from ultraviolet (UV) to infrared (IR). Therefore, germanium-doped silica glass (germanosilicate) is commonly used for the refractive index modification by UV excimer laser irradiation [6]. Recently, a vacuum ultraviolet (VUV) laser has shown great potential as a tool for refractive index modification of pure fused silica [7-10]. However, VUV laser process currently presents some drawbacks for practical use such as small pulse energy, expensive optics, instability and unreliability.

To overcome these problems, we have developed a VUV-UV multiwavelength excitation process, in which F<sub>2</sub> laser with relatively small laser fluence and KrF excimer laser with large laser fluence are simultaneously irradiated to

---

\*Corresponding author

e-mail: ksugioka@postman.riken.go.jp, FAX +81-48-462-4682 (RIKEN)

the samples. This process achieved high-quality ablation of fused silica similarly to single-wavelength ablation using  $F_2$  laser [11-13]. In addition, this process has some advantages over single-wavelength  $F_2$  laser ablation. That is, 1) the small fluence of  $F_2$  laser reduces the photon cost of using the high-fluence  $F_2$  laser in the latter process, and therefore, 2) the processing area and throughput increase. Additionally, 3) since the ablation proceeds via the KrF excimer laser, the necessity for the expensive  $F_2$  laser optics and projection system is eliminated, and a conventional excimer laser mask projection system can be utilized for micropatterning. The ablation mechanism can be attributed to excited-state absorption (ESA) [14]. Namely, electrons are first excited from the valence band to the defect levels located slightly below the conduction band by  $F_2$  laser, and then the electrons trapped at the defect levels are further excited over vacuum level by simultaneously irradiating with the KrF excimer laser. This cascade excitation process leads to bond scission in fused silica and finally causes effective ablation.

In this study, we apply the multiwavelength excitation process for high-efficiency and high-speed refractive index modification of fused silica. From the results, we prove the essential superiority of this process compared with single-wavelength  $F_2$  laser processing. This superiority, which is a new finding in materials processing, is attributed to a resonance photoionization-like process based on excited-state absorption (ESA), and may be applicable for various kinds of laser processing.

## 2. Experimental procedure

The experimental setup for refractive index modification of fused silica by the multiwavelength excitation process using  $F_2$  and KrF excimer lasers is shown in Fig.1. This setup is almost similar to that used for ablation [11]. UV-grade fused silica (VIOSIL, thickness of 0.525 mm, Shin-Etsu Chemical Co., Ltd.) substrates were used in this experiment. Before the fused silica substrate was introduced into the chamber, ultrasonic cleaning with acetone and ethanol, followed by a DI water rinse, each for 5 min, was carried out. The chamber was filled with dry nitrogen gas at 1 atm to prevent absorption of the  $F_2$  laser beam from oxygen. The fused silica substrates were simultaneously irradiated by  $F_2$  ( $\lambda=157$

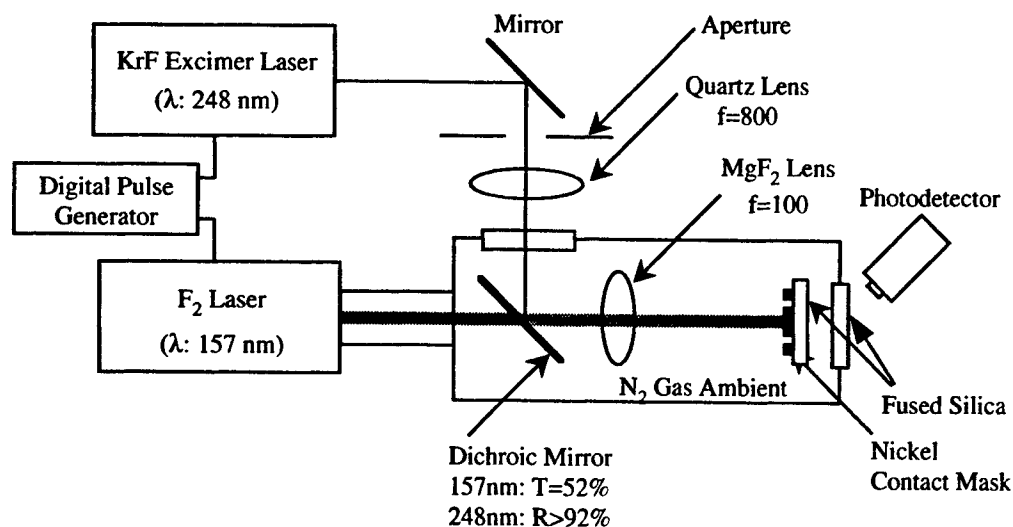


Figure 1. Schematic illustration of experimental setup for refractive index modification of fused silica by the multiwavelength excitation process using  $F_2$  and KrF excimer lasers.

nm,  $\tau=20$  ns) and KrF excimer ( $\lambda=248$  nm,  $\tau=23$  ns) lasers. For co-axial irradiation of  $F_2$  and KrF excimer laser beams, a special dichroic mirror composed of multilayer of dielectric thin films on an  $MgF_2$  substrate was used. This mirror transmits 52 % of the  $F_2$  laser and reflects more than 92 % of the KrF excimer laser. To detect each laser pulse arriving at the sample surface, fluorescence from the modified fused silica was observed using a photodetector, and then the irradiation timing of each laser beam was adjusted by a digital pulse generator (Stanford DG 535). In this setup, the irradiation timing was controlled within about 1 ns. Both of the laser beams behind the dichroic mirror were focused by an  $MgF_2$  lens onto the surface of fused silica through a contact mask with a 70  $\mu\text{m}$  line and space pattern made of stainless steel. To investigate the index modification efficiency, the diffraction efficiency of the modified samples was defined by comparing the powers of a first-order beam with that of a zeroth-order beam using a He-Ne laser.

### 3. Results and discussion

Figure 2 shows the dependence of the diffraction efficiency on irradiation time for  $F_2$ -KrF multiwavelength and single-wavelength  $F_2$  laser irradiation. The fluences of  $F_2$  and KrF excimer lasers are set at 200 and 120  $\text{mJ}/\text{cm}^2$ , respectively, where each laser pulse has almost the same photon number. Repetition rate of each laser is set at 1 Hz. In this figure, the laser beams were irradiated under conditions where no compaction took place in the fused silica for easy determination of diffraction efficiency. The surfaces of the fused silica after laser irradiation were observed by an atomic force microscope (AFM). The AFM images indicated that all samples maintained very smooth surfaces without compaction or ablation. This surface smoothness was also confirmed by a surface profiler ( $\alpha$ -Step: KLA Tencor, Co., Ltd.). Diffraction efficiency of both samples linearly increases with increasing irradiation time. At an irradiation time of 60 min, the diffraction efficiency of the multiwavelength sample becomes 0.37 %, which is 4.1 times larger than the value of 0.09 % obtained for the single-wavelength  $F_2$  laser irradiation sample. Thus, the multiwavelength excitation process enhanced

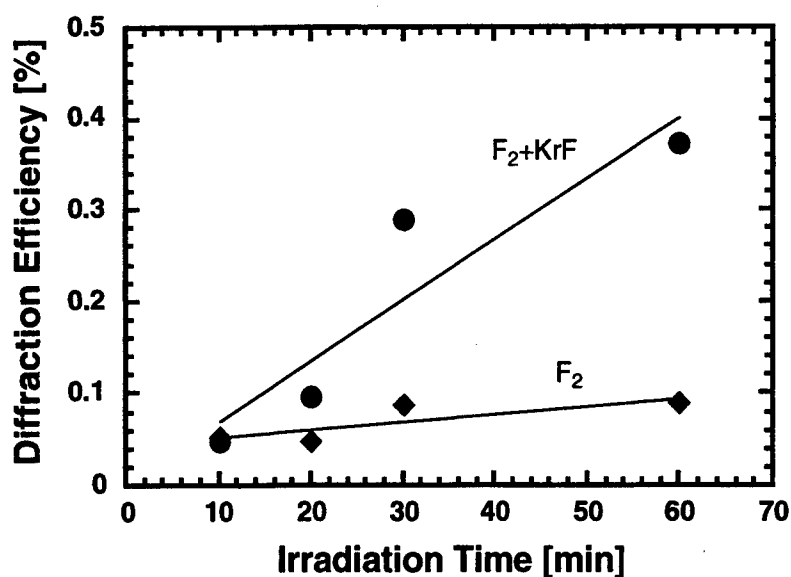


Figure 2. Dependence of the diffraction efficiency on irradiation time for  $F_2$ -KrF multiwavelength and single  $F_2$  laser irradiation at the repetition rate of 1 Hz. The fluences of  $F_2$  and KrF excimer lasers are set at 200 and 120  $\text{mJ}/\text{cm}^2$ , respectively.

increase of diffraction efficiency at the same irradiation time compared with single-wavelength  $F_2$  laser irradiation process. In other words, the multiwavelength excitation process achieves specific diffraction efficiency in a much shorter irradiation time. Of course, the irradiation time for achieving the specific efficiency can be shortened by increasing the repetition rate (note that the repetition rate is kept constant at 1 Hz in the present experiments), and the diffraction efficiency can be increased by increasing the irradiation time, i.e., the number of laser pulses.

Zhang et al. reported that diffraction efficiency is a function of both the number of laser pulses and the laser fluence [10]. From a more detailed discussion in their experiment, the diffraction efficiency could be determined by merely the total number of photons supplied to the samples. Here, we re-draw Fig. 2 focusing on the dependence of diffraction efficiency on the total number of photons, and present the results in Fig. 3. In the case of multiwavelength irradiation, the total number of photons means the sum of the photon numbers for both  $F_2$  and KrF excimer lasers. The diffraction efficiency of the multiwavelength irradiated samples shows a much more rapid increase with an increase in the total number of photons than that of single-wavelength  $F_2$  laser irradiated samples. The diffraction efficiency of the multiwavelength irradiated sample is almost twice that in the case of the  $F_2$  laser at the total photon number of  $10^{21} \text{ cm}^{-2}$ . It is noted that the multiwavelength irradiation samples are supplied half number of  $F_2$  laser photons compared with that of single-wavelength  $F_2$  laser irradiation sample at same total photon samples. Thus,  $F_2$ -KrF excimer laser multiwavelength excitation process achieved much high-efficient modification of fused silica.

This high-efficient enhancement of diffraction efficiency may be attributed to a resonance photoionization-like process based on the ESA. The mechanism can be understood easily based on the band structure of fused silica shown in Fig. 4. In the case of single-wavelength  $F_2$  laser irradiation, electrons are first excited from the valence band to native defect levels, which are ascribed to impurities and defects, located slightly below the conduction band. (Direct excitation from valence band to conduction band is impossible since the band gap of fused silica (9.0 eV) is larger than

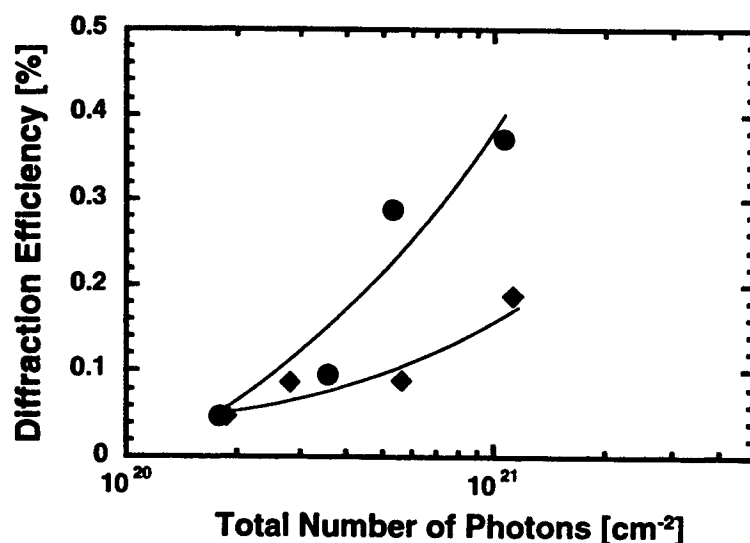


Figure 3 Dependence of the diffraction efficiency on the total number of photons for  $F_2$ -KrF multiwavelength and single  $F_2$  laser irradiation samples which used in Fig. 1. The total number of photons means product of photon number in a single pulse and pulse number. In the case of multiwavelength irradiation, it corresponds to sum of the photon numbers for both  $F_2$  and KrF excimer lasers.

the photon energy of  $F_2$  laser (7.9 eV.) A fraction of excited electrons are further excited beyond the vacuum level by additional  $F_2$  laser photons in the same pulse, but some of them are relaxed due to the much smaller relaxation rate (1.7 ns) than the pulse duration of each laser (20-23 ns) [14]. On the other hand, in the case of the multiwavelength excitation process, the electrons excited by  $F_2$  laser are efficiently excited beyond the vacuum level by simultaneously irradiated KrF excimer laser beam since KrF excimer laser is absorbed only by the excited-state electrons. This resonance photoionization-like process leads to much more efficient photoionization or photodissociation, resulting in greater refractive index change.

To carry out high-speed and high-efficiency modification by multiwavelength excitation process, irradiation timing of each  $F_2$  and KrF excimer laser beam is the one of the most important factors. Figure 5 shows variation of diffraction efficiency as a function of the delay time of  $F_2$  laser irradiation to KrF excimer laser irradiation. The delay time in a minus range corresponds to  $F_2$  laser irradiation followed by KrF excimer laser irradiation. The laser fluences of  $F_2$  and KrF excimer lasers are 140 and 90 mJ/cm<sup>2</sup>, respectively, where each laser pulse has almost the same photon number. The repetition rate of each laser pulse is 10 Hz. At the delay time of 0 ns, which correspond to simultaneous irradiation of  $F_2$  and KrF excimer lasers, diffraction efficiency achieves about 3 times larger than that of single-wavelength  $F_2$  laser irradiation sample. This high-efficiency and high-speed modification is realized between  $\pm 50$  ns of the delay time of each laser beam irradiation. Therefore, resonance ionization-like process based on excited-state absorption is obvious at this range. While, relaxation rate of excited electrons has been estimated to 1.7 ns, which is much shorter than the present range mentioned above [14]. One of the reasons is ascribed to much longer pulse duration of 20 ns (FWHM) for  $F_2$  laser and 23 ns (FWHM) for KrF excimer laser than the relaxation rate. Another reason may be due to jitter of each Pulse ( $\sim \pm 10$  ns).

In the case of the multiwavelength excitation process for effective refractive index modification, another important factor is KrF excimer laser fluence. Figure 6 shows the dependence of diffraction efficiency on the irradiation at two different KrF excimer laser fluences of 120 and 300 mJ/cm<sup>2</sup>. In this experiment, KrF excimer laser fluence of 120

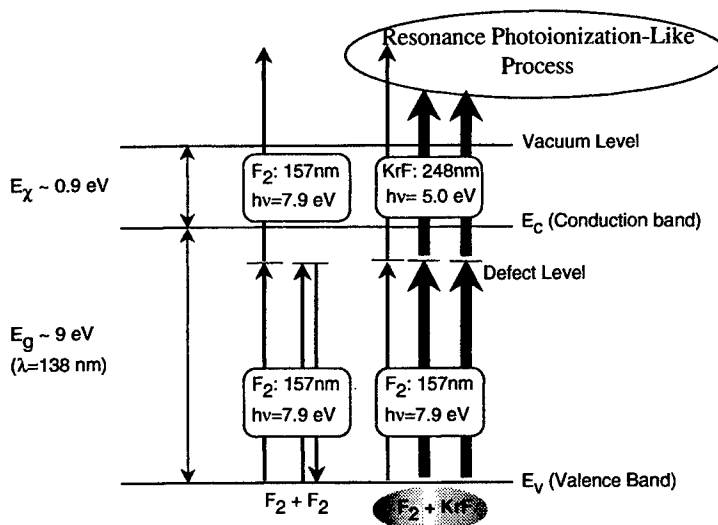


Figure 4 Band structure of fused silica and the excitation process of electrons by  $F_2$ -KrF multiwavelength and single-wavelength  $F_2$  laser irradiation.

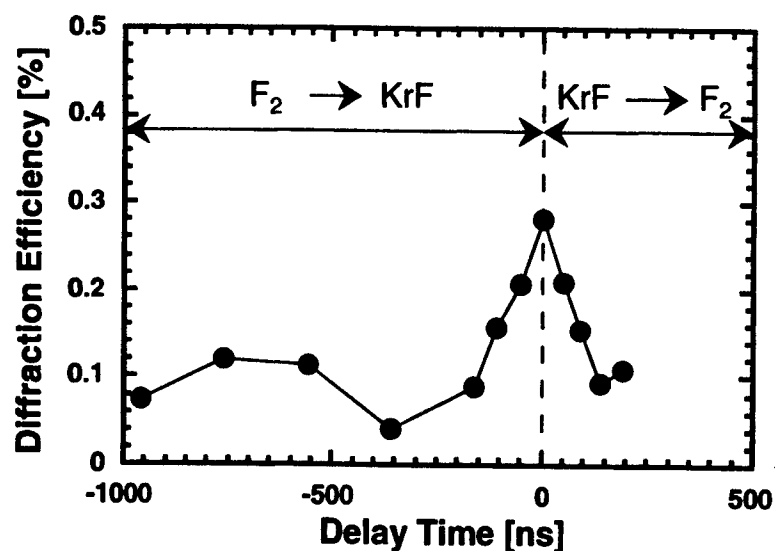


Figure 5 Dependence of the diffraction efficiency on delay time of KrF excimer laser irradiation. Laser beams are irradiated for 10 min at 10 Hz. The fluences of  $F_2$  and KrF excimer lasers are set at 140 and 90 mJ/cm<sup>2</sup>, respectively.

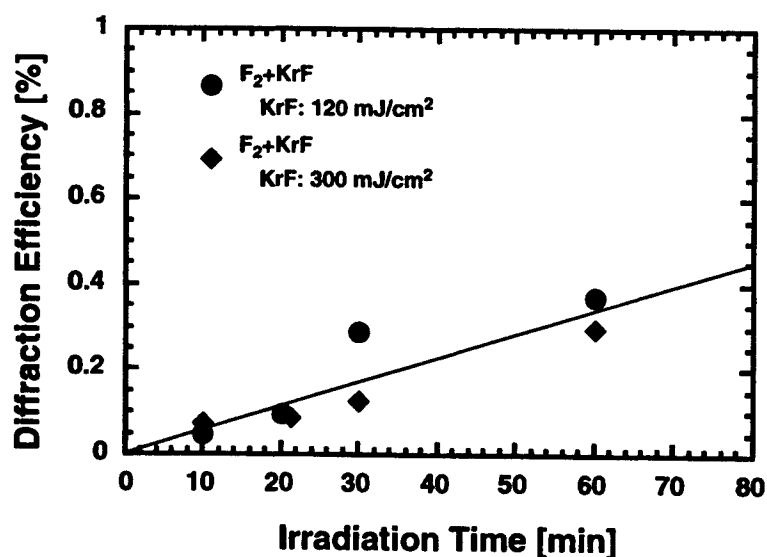


Figure 6 Dependence of the diffraction efficiency on the irradiation time at the  $F_2$  laser fluence of 200 mJ/cm<sup>2</sup>. KrF excimer laser is simultaneously irradiated at two different laser fluence of 120 (= same photon number as that in an  $F_2$  laser pulse) and 300 mJ/cm<sup>2</sup>. The repetition rate of laser irradiation is 1 Hz.

mJ/cm<sup>2</sup> has almost the same number of photons as that of  $F_2$  laser fluence of 200 mJ/cm<sup>2</sup>, whereas that of 300 mJ/cm<sup>2</sup> corresponds to approximately 2.5 times larger photon numbers. The repetition rate of each laser is 1 Hz. Diffraction efficiency increases with increasing pulse number independent of KrF excimer laser fluence. This result indicates that supply of excess photons of KrF excimer laser does not influence the diffraction efficiency increase and much photon are wasted.

Therefore, the ratio of the photons supplied from each laser beam is important for effective modification of fused silica. To determine the most efficient rate, variation of the diffraction efficiency on the ratio of photon number in KrF excimer laser beam to that in  $F_2$  laser beam is investigated as shown in Fig. 7. The ratio of photon numbers ( $KrF/F_2$ ) of 1 means that  $F_2$  and KrF excimer laser beams processing same number of photons are irradiated to the sample. The diffraction efficiency monotonously increase with increasing the ratio up to 0.65. However, at more than 0.65, diffraction efficiency tends to the saturation. This result supports the resonance photoionization-like process discussed before. In the multiwavelength excitation process,  $F_2$  laser photons first excite the electrons from valence band to the defect level, and a fraction of the excited electrons are further excited from defect level over vacuum level similarly to the case of single  $F_2$  laser irradiation. Residual excited electrons absorb KrF excimer laser photons. Therefore, the diffraction efficiency increases with increasing KrF excimer laser photon number up to the critical ratio of 0.65. At this critical ratio, all of the residual excited electrons couple with KrF excimer laser photons. When the photons of KrF excimer laser beyond the critical ratio are supplied, the excess photon has no partner for the coupling. Consequently, the diffraction efficiency is saturated beyond the critical ratio. Thus, the ratio of 0.65 between  $F_2$  and KrF excimer laser photons is most effective for modification of fused silica by  $F_2$ -KrF multiwavelength excitation process.

Finally, we checked the refractive indices at the surfaces of the sample modified by  $F_2$ -KrF multiwavelength and single-wavelength  $F_2$  laser irradiation without the contact mask by ellipsometry. The  $F_2$  and KrF excimer laser fluence are 75 and 50 mJ/cm<sup>2</sup> respectively and irradiation time is set at 90 min at 40 Hz. The increase of the refractive index of the multiwavelength sample becomes  $8.2 \times 10^{-3}$ , which is 1.78 times larger than that of  $4.6 \times 10^{-3}$  obtained for the single-wavelength irradiation sample.

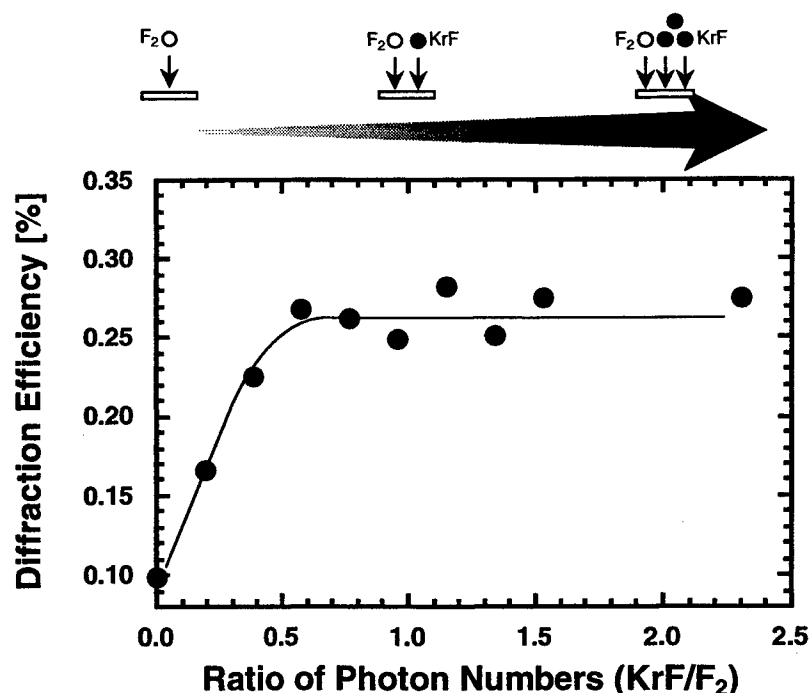


Figure 7 Variation of the diffraction efficiency on the ratio of photon number in KrF excimer laser beam to that in  $F_2$  laser beam. Laser beams are irradiated for 10 min at 10 Hz. The fluence of  $F_2$  laser is set at 200 mJ/cm<sup>2</sup>.

#### 4. Conclusion

By the multiwavelength excitation process using  $F_2$  and KrF excimer lasers, high-efficiency and high-speed refractive index modification of fused silica has been realized. Diffraction efficiency obtained by the multiwavelength excitation process reached more than twice than that by single-wavelength irradiation of  $F_2$  laser at the same total number of photons supplied to the samples. This high-efficient process strongly depended on delay time of each laser beam irradiation as well as the ratio of KrF excimer and  $F_2$  laser photon numbers. 3 times larger diffraction efficiency of compared with single- $F_2$  laser irradiation was obtained within the delay time of  $\pm 50$  ns. The most effective ratio of supplied photon of KrF excimer and  $F_2$  lasers is estimated to be 0.65. Excess supply of photons from the KrF excimer laser did not contribute to this process, resulting in waste of energy. Furthermore, the increase of refractive index change of the multiwavelength irradiation sample achieved 1.78 times larger than that of the single-wavelength sample. These favorable and unique features of the multiwavelength excitation process are caused by the resonance photoionization-like process based on the excited state absorption. Thus, we conclude that the multiwavelength excitation process by co-axial irradiation using  $F_2$  and KrF excimer lasers is highly attractive for high-efficiency and high-speed refractive index modification of fused silica and its practical application.

#### Acknowledgments

The authors would like to thank K. Watanabe for his help with AFM observation, and J. Zhang for helpful discussions of the refractive index modification experiments. K. Obata was supported by a grant from the Junior Research Associate (JRA) program of RIKEN.

#### References

- [1] K. O. Hill, B. Malo, F. Bilodeau, D. C. Johnson, and J. Albert, *Appl. Phys. Lett.* **62**, 1035 (1993).
- [2] K. Tsunetomo and T. Koyama, *Opt. Lett.* **22**, 411 (1997)
- [3] Y. Hibino, M. Abe, T. Tanaka, A. Himeno, J. Albert, D. C. Johnson, and K. O. Hill, *Electron. Lett.* **35**, 1844 (1999).
- [4] M. Verhaegen, J. L. Brebner, L. B. Allard, and J. Albert: *Appl. Phys. Lett.* **68**, 3084 (1996)
- [5] C. Montero, C. Gomez-Reino, and J. L. Brebner: *Opt. Lett.* **24**, 1487 (1999)
- [6] J. Albert, B. Malo, K. O. Hill, F. Bilodeau, and D. C. Johnson: *Appl. Phys. Lett.* **67**, 3529 (1995)
- [7] J. Zhang, K. Sugioka, S. Wada, H. Tashiro, and K. Toyoda, *IEEE J. Quantum Electron. IEEE J. Select. Top. Quant. Electron.* **3**, 789 (1997).
- [8] K. Sugioka, J. Zhang, S. Ruschin, S. Wada, H. Tashiro, and K. Toyoda, *Appl. Surf. Sci.* **127-129**, 843 (1998).
- [9] P. R. Herman, K. P. Chen, P. Corkum, A. Naumov, S. Ng, and J. Zhang, *Proc. SPIE* **4088**, 345 (2000).
- [10] J. Zhang, P. R. Herman, C. Lauer, K. P. Chen, and M. Wei, *Proc. SPIE* **4274**, 125 (2001).
- [11] K. Obata, K. Sugioka, T. Akane, N. Aoki, K. Toyoda, and K. Midorikawa, *Appl. Phys. A* **73**, 755 (2001).
- [12] J. Zhang, K. Sugioka, T. Takahashi, K. Toyoda, and K. Midorikawa, *Appl. Phys. A* **71**, 23 (2000).
- [13] P. R. Herman, R. S. Marjoribanks, A. Oetli, K. Chen, I. Kononov, and S. Ness: *Appl. Surf. Sci.* **154-155**, 577 (2000).
- [14] K. Sugioka, S. Wada, Y. Ohnuma, A. Nakamura, H. Tashiro, and K. Toyoda, *Appl. Phys. Lett.* **67**, 2789 (1995).



# F<sub>2</sub>-Laser Microfabrication of Buried Waveguide Structures in Transparent Glasses

X. Midori Wei\*, Kevin P. Chen, Dragan Coric, Peter R. Herman, and Jianzhao Li

Department of Electrical and Computer Engineering, University of Toronto,  
10 King's College Rd., Toronto, ON, M5S 3G4, Canada

## ABSTRACT

Buried optical waveguides have been fabricated directly in pure bulk fused silica with a novel high-resolution 157-nm optical processing system. Refractive index changes of  $>10^{-4}$  were induced within the small focal volume ( $\sim 6\text{-}\mu\text{m}$  dia.) of large numerical-aperture optics (0.4), removing the need for ultrafast laser interactions. Single-mode guiding was inferred from Gaussian-like near-field and far-field intensity distributions of 635-nm guided light. The results demonstrate a useful extension of writing buried three dimensional refractive index structures inside glasses with nanosecond duration ultraviolet lasers.

**Key words:** F<sub>2</sub> laser, photosensitivity, direct writing, buried waveguides, fused silica

## 1. INTRODUCTION

More than a decade of research has been directed towards the study and application of ultraviolet (UV) and vacuum ultraviolet (VUV) lasers in shaping refractive index structures in silica-based glasses such as optical fibers and planar optical circuits.[1] UV lasers (193-250 nm) are routinely applied today to fabricate fiber Bragg gratings and long period gratings of commercial importance to the photonics industry.[1,2] Current development efforts are aimed at UV-laser trimming of arrayed-waveguide grating wavelength-division demultiplexers[3] and direct writing of photonic devices such as waveguides, splitters, and couplers.[4,5] In all cases, the UV laser light is either shaped, masked, or focused to induce refractive index patterns solely within buried photosensitive waveguide layers, restricting the patterning to one- or two-dimensional structures. Ultrafast lasers have been applied [6] as an alternative means to induce three-dimensional structures within bulk glasses by driving nonlinear absorption mechanisms within the focal volume of a tightly focused beam.

In the present paper, we demonstrate that high numerical aperture optics (NA = 0.4) are sufficient to concentrate UV-laser photosensitivity responses within a tight focal volume inside fused silica without the need for ultrafast interaction physics. The short-wavelength F<sub>2</sub> laser has substantial advantage over other UV laser sources in this regard, by driving efficient one-photon processes (at 7.9 eV) that access near band-edge defect states in fused silica.[7-9] The 157-nm interactions smoothly excise fine surface structures in ablation or efficiently induce refractive index structures in photosensitivity, with minimal collateral damage and free of microcrack formation.

In UV-laser damage studies of fused silica at 193, 213, and 248 nm wavelengths, [10] only very small refractive-index-changes of  $\sim 10^{-5}$  were noted after large  $\sim 350\text{ kJ/cm}^2$  doses. The underlying multi-photon absorption mechanisms are weak in contrast to 157-nm F<sub>2</sub>-laser irradiation, which generated volume phase gratings in fused silica having 19% efficiency in first order following a modest  $20\text{-kJ/cm}^2$  dose.[9] A refractive index change of  $4.5 \times 10^{-4}$  was noted within a moderate penetration depth of  $\sim 1\text{ mm}$ . A single-photon photosensitivity mechanism was inferred, and the F<sub>2</sub>-laser-induced refractive index change remained stable over several weeks and appeared permanent. Much stronger 157-nm photosensitivity mechanisms are noted in germanium-doped silica glasses[11] such as found in the core of standard telecommunication fiber and in planar optical circuits. Strong long period gratings were formed rapidly in hydrogen-enhanced fiber using only  $5\text{-J/cm}^2$  fluence of 157 nm light.[12] Highly stable and strong photosensitivity responses could be locked into hydrogen-soaked waveguides by pre-treatment

midori@ecf.utoronto.ca; <http://www.ecf.utoronto.ca/~hermanp>

with F<sub>2</sub>-laser light.[11,13] Refractive index changes in the range of  $10^{-4}$  to  $10^{-3}$  were easily generated, which is practically useful for writing Bragg or volume gratings.

In this paper, the strong photosensitivity responses of record short wavelength F<sub>2</sub>-laser light was combined with large 0.4-NA Schwarzschild optics to drive refractive index changes below the surface of bulk fused silica. Refractive index changes of  $\sim 10^{-4}$  were generated within the beam's focal volume ( $\sim 6\text{-}\mu\text{m}$  diameter) without damage to the glass surface. A 157-nm optical penetration depth of  $\sim 1\text{-mm}$  provided sufficient latitude for marking glasses and printing buried waveguides. This represents the first formation known to the authors of buried 3D structures by a long-pulse duration UV laser source. Processing windows for avoiding cracks and writing optical waveguides are assessed. The buried waveguide structures represent an important extension for nanosecond-duration ultraviolet laser sources, since only ultrafast lasers have been successful to date in writing buried structures inside bulk glasses.[6] The results suggest new possibilities for F<sub>2</sub>-laser microfabrication of photonic components.

## 2. EXPERIMENTAL PROCESSING SYSTEM

A novel high-resolution 157-nm optical processing system has been developed at the University of Toronto for fabrication of micro-optical glass components in telecommunication, photonic, and biophotonic applications, as described in Ref. [8]. In brief, a commercial F<sub>2</sub> laser (Lambda Physik, LPF 220i) was integrated with a high-resolution optical system for 157-nm light as shown schematically in Figure 1. The F<sub>2</sub> laser provided  $\sim 25\text{-mJ}$  pulses of 15-ns duration at 1 – 200-Hz repetition rate. Beam grooming optics, mounted on a stable aluminum rail, consisted of a dielectric attenuator, prism telescope expander, cylindrical lens arrays and lenses for beam homogenization, and a 0.4 NA Schwarzschild lens with 25 $\times$  demagnification. All optics were anti-reflection-coated CaF<sub>2</sub> for high transparency ( $\sim 96\text{--}98\%$ ) at 157-nm wavelength. The homogenizer-lens assembly distributed uniform fluence ( $\pm 5\%$ ) across the  $6\text{ mm} \times 6\text{ mm}$  mask plane, which was projected in turn by a Schwarzschild lens onto a  $240\text{ }\mu\text{m} \times 240\text{ }\mu\text{m}$  target plane to provide variable fluence doses of up to  $\sim 9\text{ J/cm}^2$  per pulse. Free-standing metal foil masks defined 150 to 1000- $\mu\text{m}$  diameter beams that were imaged with 25 $\times$  demagnification to positions 100 to 450- $\mu\text{m}$  deep inside highly-polished fused silica samples of  $20\text{ mm} \times 10\text{ mm} \times 5\text{ mm}$  size.

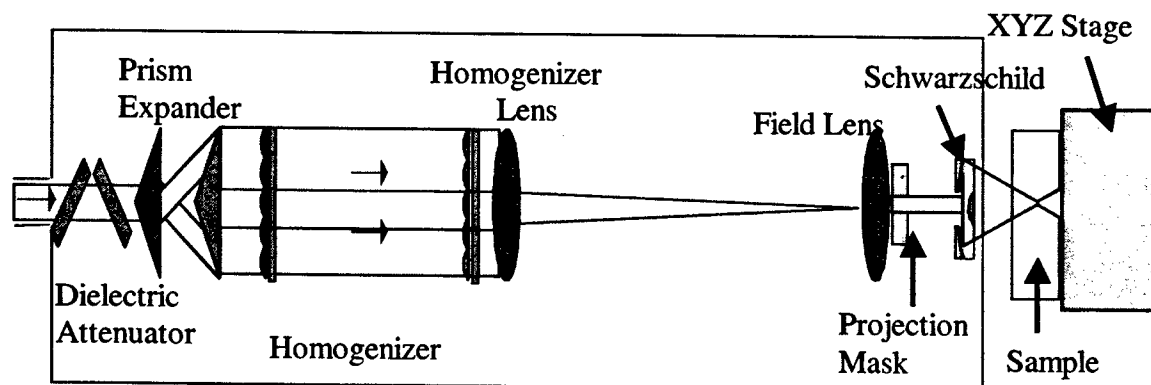


Fig. 1 Schematic of the high-resolution Schwarzschild configuration of the F<sub>2</sub>-laser optical processing system.

The 3-m long aluminum-processing chamber and beam tubes were flushed with ultra-pure nitrogen gas ( $<1\text{ ppm O}_2$ ) bled from a liquid dewar in order to provide a high transparency path for the 157-nm radiation. A nozzle located between the Schwarzschild lens and the target sample directed a 1 – 2-mm long transparent stream of nitrogen gas to the glass sample. In this way, samples could be conveniently mounted on precise computer-controlled xyz-motion stages in an air ambient outside of the optical processing chamber. For the present experiment, samples were driven at velocities of  $0.5\text{--}2.5\text{ }\mu\text{m/s}$  to control the total laser exposure.

Both static and scanning exposures of fused silica were examined in order to assess laser-processing windows for forming refractive index structures devoid of microcracks and other damage. A single-pulse fluence of  $7.1 \text{ J/cm}^2$  was applied in all cases, which exceeded the  $1\text{-J/cm}^2$  threshold fluence for surface ablation of fused silica.[7] Such large fluence was tolerated internally within the glass without notable damage. An accumulated fluence of  $10 - 15 \text{ kJ/cm}^2$  was targeted for generating refractive index changes above  $10^{-4}$  as based on a previous  $\text{F}_2$ -laser fused silica study.[9] Such index change is sufficient for forming single-mode waveguides and can be generated at scan speeds of  $\sim 1 \text{ }\mu\text{m/s}$  for a focal spot of  $10 \text{ }\mu\text{m} \times 20 \text{ }\mu\text{m}$  and a  $5 \text{ J/cm}^2$  single-pulse fluence. Waveguides were formed in a side-writing geometry as shown in Figure 2. Samples were scanned surface-to-surface to form waveguides across the full glass length.

Laser-treated samples were backlit and viewed with a high-resolution optical microscope to assess the size and structure of the laser modified zone. Laser diode light at  $635 \text{ nm}$  or HeNe laser light at  $633 \text{ nm}$  were launched in standard telecommunication fiber, butt-coupled into the laser-formed waveguides, and observed in both near and far field from the waveguide exit with a CCD camera and a  $20\times$  microscope objective.

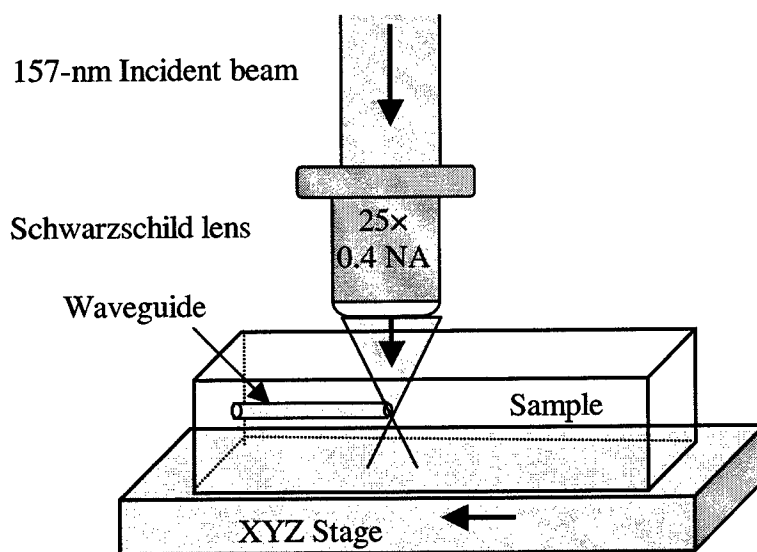


Fig. 2 Side-writing arrangement for forming buried single-mode waveguides in fused silica glass blocks.

### 3. RESULTS AND DISCUSSION

Static  $157\text{-nm}$  exposure of fused silica was first applied with various focal spot sizes of  $6 - 40\text{-}\mu\text{m}$  diameter. Surface ablation and micro-cracking due to radiation damage and thermal shocks could be induced under prolonged exposure when the laser beam was imaged near the first surface of the glass sample. Such gross damage was avoided when the focal spot was moved  $\sim 400\text{-}\mu\text{m}$  into the interior of the glass. Under internal focusing, the laser-induced refractive index contrast became visible under an optical microscope as shown in Figure 3. Microcracks were not observable by the optical microscope for high exposure conditions of 15 min, 20 min, and 30 min (left to right) corresponding to total exposures of 640, 850, and  $1,300 \text{ kJ/cm}^2$  at a single pulse fluence of  $7.1 \text{ J/cm}^2$ . The  $40\text{-}\mu\text{m}$ -diameter modification zone was consistent with the  $25\times$  demagnification of the  $1\text{-mm}$  diameter mask, and appeared insensitive to the total laser dose as also noted for waveguide fabrication with ultrafast lasers.[14] The static-exposure study revealed a large laser-processing window for generating buried refractive index structures without microcrack formation. In contrast, processing windows for ultrafast lasers are much narrower due to

material-damage limits at high fluence and a large fluence threshold for driving nonlinear absorption mechanisms in transparent glasses.[15]



Fig 3. Optical image in backlighting of fused silica following static exposure by 157 nm laser light at 640, 850, and 1,300 kJ/cm<sup>2</sup> doses, from left to right. The refractive index contrast is confined within a 40-μm diameter focal spot as viewed parallel to the laser axis.

Fused silica samples were transversely scanned during the laser exposure to form buried waveguide structures or ablated surface channels, defined according to the relative position of the focal spot and the fused silica surface. A smaller 6-μm diameter focal spot size was used to form waveguides slightly smaller than that in standard telecommunication fiber. Close matching of the core size and refractive index profile reduces insertion loss and supports single-mode guiding. Figure 4(a) shows typical buried waveguides written across the full 5-mm width of the sample using total exposures of 6.3 kJ/cm<sup>2</sup> (top) and 5 kJ/cm<sup>2</sup> (bottom) at 2.0 μm/s and 2.5 μm/s scan speeds, respectively. Figure 4(b) shows surface channels ablated under similar exposure conditions. The images revealed ~6-μm wide waveguides and channels, in agreement with the 6-μm laser spot size. The waveguide width appeared little affected by the laser fluence or the sample translation speed.

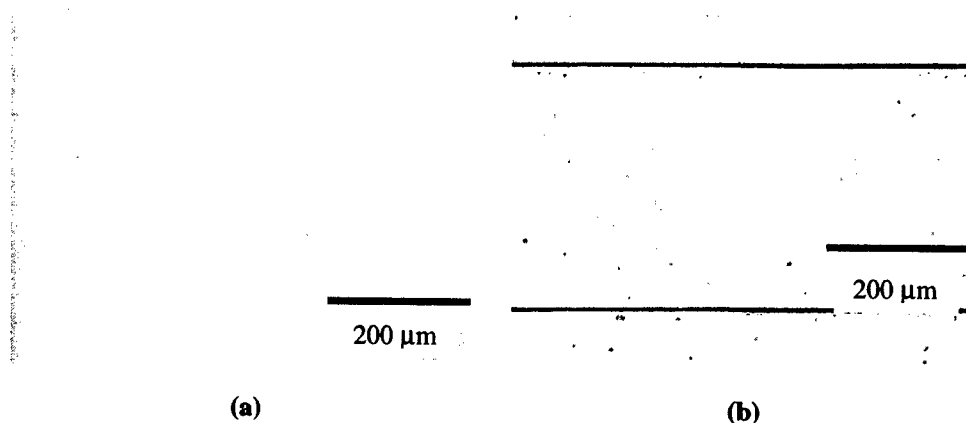


Fig. 4 Optical images of fused silica showing buried waveguide structures (a) and ablated surface channels (b) formed by scanning the F<sub>2</sub>-laser focal spot within the bulk glass and on the glass surface, respectively.

Visible laser light was readily launched by fiber-butt coupling and guided by the laser-generated waveguides. Stable and smooth motion drives were essential during waveguide writing to reduce losses as noted by the brightness of scattered waveguide light. Pronounced waveguide losses were noted for large F<sub>2</sub>-laser exposures of 50 kJ/cm<sup>2</sup> when scanned at 0.28 μm/s. An estimate of the refractive index change,  $\Delta n$ , was obtained from the  $NA = (2n\Delta n)^{1/2}$  of He-Ne laser light emerging from the output facet of the waveguide. A  $\Delta n$  value of  $\sim 1 \times 10^{-4}$  was

observed, which is in a good agreement with a value of  $\sim 2 \times 10^{-4}$  inferred from volume gratings generated by a similar  $15\text{-kJ/cm}^2$  radiation dose.[9] The buried waveguides were stable at room temperature, showing no measurable degradation three months after the initial exposure.

Near-field intensity profiles of 635-nm light exiting the 5-mm long and 6- $\mu\text{m}$  diameter waveguides are shown in Figure 5. The inset figure reveals a highly symmetric single-mode intensity profile of 6.4- $\mu\text{m}$  diameter (FWHM), closely matching the diameter of the focused  $F_2$  laser. The high symmetry was possible because of the small depth-of-focus of the 0.4-NA Schwarzschild optics. The three data sets in Figure 5 were obtained from waveguides exposed to an accumulated fluence of  $2.5\text{ kJ/cm}^2$  (squares),  $5.0\text{ J/cm}^2$  (circles), and  $10\text{ J/cm}^2$  (triangles), yielding modal diameters of  $11.5\text{ }\mu\text{m}$ ,  $6.4\text{ }\mu\text{m}$ , and  $5.2\text{ }\mu\text{m}$  (FWHM), respectively. The data are well represented by the Gaussian curves in each case, indicating single mode propagation. Single mode-guiding is expected for the small  $\sim 10^{-4}$  refractive index change in the 6- $\mu\text{m}$  diameter cylindrical waveguide. The trend of decreasing mode size with increasing laser dose (and lower scanning speed) is consistent with an increasing refractive index change without changes to the diameter of the refractive index profile.

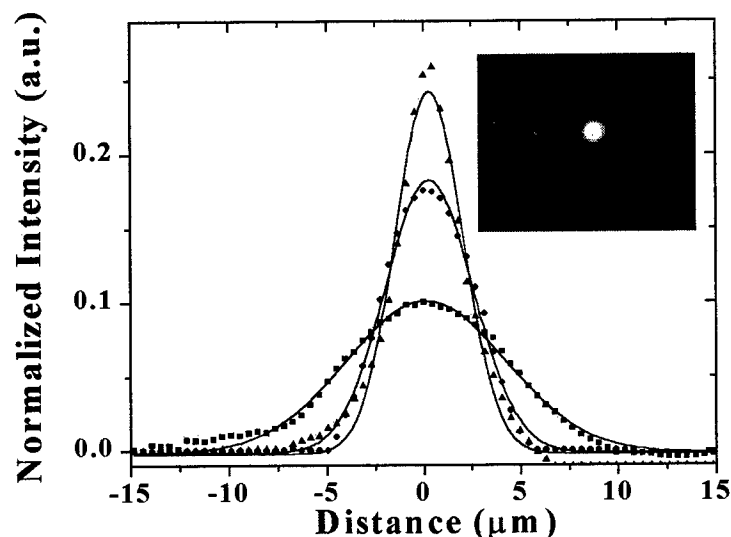


Fig. 5 Near-field intensity profiles of the guided 633-nm light in waveguides formed at  $10\text{ kJ/cm}^2$  (triangles),  $5.0\text{ J/cm}^2$  (circles), and  $2.5\text{ J/cm}^2$  (squares) fluence, respectively. The inset figure shows a CCD camera image of the near-field profile for data denoted by the triangles.

The far-field intensity profile of guided 635-nm light is shown in Fig. 6 for a 6- $\mu\text{m}$  diameter waveguide formed at  $14\text{-J/cm}^2$  dose and  $1.0\text{-}\mu\text{m/s}$  scanning speed. The Gaussian-like shape is also indicative of single-mode propagation. The rings arise from interference between the waveguide light and uncoupled light from the fiber launch. Further refinements in the beam shaping optics will improve the symmetry of the waveguide mode and reduce overall insertion losses in coupling with standard optical communication fiber.

The present results are the first known demonstration of controlling the writing of glass waveguide structures in three-dimension with the beam focus, eliminating the conventional requirement of ultrafast-laser interaction physics. Large NA optics were shown to compensate for single-photon photosensitivity mechanisms that would normally induce refractive index changes beginning at the surface of the optical sample. Record short wavelength  $F_2$  laser light and the special optical tools offered a flexible approach in developing new application directions in fabricating, trimming, and tuning photonic components in three dimensions directly inside fused silica bulk materials. Such principles are presently well demonstrated for ultrafast lasers that rely on carefully tuned non-linear absorption processes in a focused laser beam. The  $F_2$ -laser has the advantage of a broader processing window, which

accommodates a lower laser-interaction intensity to avoid the substantial heating, shock, micro-void formation, and microcrack generation normally associated with ultrafast-laser interactions. Optical diffraction limits also favor the patterning of much smaller features with 157-nm light than with longer wavelength ultrafast lasers. Further contrasts with ultrafast laser waveguide writing are described in a separate conference paper.[15]

The general principles of waveguide writing demonstrated here for  $F_2$  lasers are generally extensible to longer wavelength UV lasers for glasses appropriately designed with strong photosensitivity response and modest UV transparency. Faster waveguide writing speeds than the  $\sim 1\text{-}\mu\text{m/s}$  applied here are an important goal before practical application of  $F_2$ -laser photonics fabrication can be realized. To this end, our group is exploring photosensitivity enhancement techniques and other writing geometries that fully utilize the large output power of the  $F_2$  laser.



Fig. 6 Far-field intensity image of 635-nm light exiting from the  $F_2$ -laser laser formed waveguide. Single mode propagation is inferred from a near-Gaussian profile. The output beam has 28-mrad divergence (FWHM).

#### 4. SUMMARY

Single-mode buried channel waveguides have been fabricated inside fused silica with a high-resolution 157-nm  $F_2$ -laser optical system. A large 0.4 NA Schwarzschild lens was critical in concentrating single-photon photosensitivity responses tightly within a small  $\sim 6\text{-}\mu\text{m}$  diameter focal volume of the laser beam. Waveguides showed a high degree of cylindrical symmetry and modest refractive-index changes of  $\sim 10^{-4}$  were observed for a fluence exposure of  $10\text{ kJ/cm}^2$ . Motorized x-y-z translation stages will fully extend such refractive index structuring into three dimensions, representing an important extension from the 1-D and 2-D structures presently fabricated with nanosecond-duration UV-laser sources. Buried 3-D structures were previously only formed with ultrafast lasers, and the present results point to new manufacturing directions for  $F_2$ -laser fabrication of photonic components.

#### ACKNOWLEDGMENTS

The authors gratefully acknowledge support from the Natural Science and Engineering Research Council of Canada, the Canadian Foundation for Innovation, the Ontario Innovation Trust, and the Canadian Institute of Photonics Innovation.

## REFERENCES

1. R. Kashyap, *Fiber Bragg Gratings*, (Academic Press, NY, 1999).
2. A. M. Vengsakar, P. J. Lemaire, J. B. Judkins, V. Bhatia, T. Erdogan, and J. E. Sipe, *Long-period fiber gratings as band-rejection filter*, J. Lightwave Technol., **14** (1996) p. 58-65.
3. D. A. Zauner, J. Hubner, K. J. Malone, and M. Kristensen, *UV trimming of arrayed-waveguide grating wavelength division demultiplexers*, Electronics Lett., **34** (1998) p. 780-781.
4. M. Svalgaard, C. V. Poulsen, A. Bjarklev, and O. Poulsen, *Direct UV-writing of buried single mode channel waveguides in Ge-doped silica films*, Electron. Lett., **30** (1994) p. 1401-1403.
5. M. Svalgaard, *Direct writing of planar waveguide power splitters and directional couplers using a focused ultraviolet laser beam*, Electronics Lett., **33** (1997) p. 1694-1695.
6. K. M. Davis, K. Miura, N. Sugimoto, and K. Hirao, *Writing waveguides in glass with a femtosecond laser*, Opt. Letts., **21** (1996) p. 1729-1731.
7. P. R. Herman, K. Beckley, B. Jackson, K. Kurosawa, D. Moore, T. Yamanishi, and J. Yang, *Processing applications with the 157-nm fluorine excimer laser*, in *Excimer Lasers, Optics, and Applications*, (SPIE **2992**, 1997) p. 86-95.
8. P. R. Herman, K. P. Chen, M. Wei, J. Zhang, J. Ihlemann, D. Schafer, G. Marowsky, P. Oesterlin, and B. Burghardt, *F<sub>2</sub>-lasers: high-resolution optical processing system for shaping photonic components*, in *Laser Appl. in Microelectronic and Optoelectronic Manuf. V*, (SPIE **4274**, 2001) p. 149-157.
9. J. Zhang, P. R. Herman, C. Lauer, K. P. Chen, and M. Wei, *157-nm laser-induced modification of fused-silica glasses*, in *Laser Appl. in Microelectronic and Optoelectronic Manuf. V*, (SPIE **4274**, 2001) p. 125-132.
10. M. Rothschild, D. J. Ehrlich, and D. C. Shaver, *Appl. Phys. Lett.*, **55** (1989) p. 1276.
11. K. P. Chen, P. R. Herman, D. Coric, J. Li, M. Wei, R. Taylor, and C. Hnatovsky, *F<sub>2</sub>-laser photosensitivity applications in germanosilicate fiber and planar waveguides*, in *Integrated Optics: Devices, Materials, and Technologies*, (SPIE **4640**, 2002)
12. K. P. Chen, P. R. Herman, R. Tam, and J. Zhang, *Rapid long-period grating formation in hydrogen-loaded fibre with 157nm F<sub>2</sub>-laser radiation*, Electronics Lett., **36** (2000) p. 2000-2001.
13. K. P. Chen, P. R. Herman, and R. Tam, *Strong fiber Bragg grating fabrication by hybrid 157-nm and 248-nm laser exposure*, Photonics Tech. Letts., (to appear Feb. 2002) p.
14. K. Miura, J. Qiu, H. Inouye, and T. Mitsuyu, *Appl. Phys. Lett.*, **71** (1997) p. 3329-3331.
15. D. Coric, P. R. Herman, K. P. Chen, M. Wei, P. Corkum, R. Bhardwaj, and D. Rayner, *Contrasts in writing photonic structures with ultrafast and ultraviolet lasers*, in *Optical Devices for Fiber Communication III*, (SPIE **4638**, 2002) in press.

## UV laser radiation-induced modifications and microstructuring of glass

Marc Talkenberg<sup>\*a</sup>, Ernst W. Kreutz<sup>\*\*a</sup>, Alexander Horn<sup>a</sup>, Michael Jacquorie<sup>a</sup>, Reinhart Poprawe<sup>a,b</sup>

<sup>a</sup>Lehrstuhl für Lasertechnik, Rheinisch-Westfälische Technische Hochschule,  
Steinbachstraße 15, 52074 Aachen, Germany

<sup>b</sup>Fraunhofer-Institut für Lasertechnik, Steinbachstraße 15, 52074 Aachen, Germany

### ABSTRACT

Modifications and microstructures are generated on the surface and in the volume of silicate glasses using pulsed UV laser radiation of small pulse length. During the interaction of pulsed excimer laser radiation (193 nm/20 ns, 248 nm/20 ns, 308 nm/40 ns, 351 nm/20 ns) and frequency-trippled Nd:YAG laser radiation (355 nm/10 ns) with intensities below the removal-threshold of the cerium- and silver-doped multi-component silicate glass absorption centers in the UV are induced. Subsequent thermal treatment and wet chemical etching results in crystallisation of the laser-illuminated absorbing region and in the fabrication of microstructures on the surface. Processing of sodalime- and boro-silicate glass with pulsed ArF excimer laser radiation (193 nm/20 ns) and frequency-doubled Nd:YAG laser radiation (532 nm, 1064 nm/40 ps) with intensities above the removal-threshold leads to microstructures including the generation of microcracks on the surface and in the bulk. The dynamics and the transmission of the expanding plasma and changes in the refractive index of the glass are investigated with Speckle photography using the pump and probe method. The determination of plasma emission and crack generation is carried out using high speed- and Nomarski photography. Morphological and chemical properties of the debris generated under defined processing gas atmospheres are investigated with REM, white light interferometry, XPS and EPMA. Induced absorption and changes of the crystalline-phase are probed using optical-spectroscopy and XRD as well REM. On the basis of these investigations the processes of the generation of induced absorption centers and crystallisation on the one hand and the generation of cracks and debris on the other hand as well as the quality of the produced microstructures is discussed.

**Keywords:** microstructuring, laser irradiation, UV absorption, excimer laser radiation, microreaction technology, photosensitive glass, soda lime glass

### 1. INTRODUCTION

The interaction of laser radiation with dielectric materials has been investigated since the beginning of laser material processing. Puzzling effects of optical breakdown, avalanche ionization, multiphoton ionization or laser-induced absorption center formation especially in glasses claim for research until now. Glass is a material of major technological interest for design, production and application of microsystems for numerous applications in chemistry, pharmacy, medicine and biotechnology (e.g. micromixers, microreaction chambers) as well as in integrated optics (e.g. waveguides, active and passive optical devices and Bragg-gratings). Selected optical glass combines high optical transmission in the UV to IR with low material production costs. However, the processing of undoped and doped glasses using laser radiation is limited by laser radiation induced modifications on the surface and in the volume such as the generation of absorption centers or the formation of cracks, for example.

The focus here is on modification of photosensitive glass after illumination to UV-laser radiation with fluences below the material removal threshold and on microstructuring of optical soda lime glass above the material removal threshold with respect to the formation of laser radiation induced cracks on the surface and in the volume of the glass.

\* [contact.talkenberg@l1t.rwth-aachen.de](mailto:contact.talkenberg@l1t.rwth-aachen.de); phone: 0049 241 8906 205; fax: 0049 241 8906 121; <http://www.l1t.rwth-aachen.de/>; Lehrstuhl für Lasertechnik, Rheinisch-Westfälische Technische Hochschule, Steinbachstraße 15, D-52074 Aachen, Germany; \*\* [t.kreutz@l1t.rwth-aachen.de](mailto:t.kreutz@l1t.rwth-aachen.de); phone: 0049 241 8906 146; fax: 0049 241 8906 121; <http://www.l1t.rwth-aachen.de/>; Lehrstuhl für Lasertechnik, Rheinisch Westfälische Technische Hochschule, Steinbachstraße 15, D-52074 Aachen, Germany



Rare-earth-ion-doped crystals and glasses are ideal candidates as materials for tunable UV-solid-state lasers and scintillators due to broad  $4f \leftrightarrow 5d$ -fluorescence emission-bands<sup>1</sup>. The  $4f \leftrightarrow 5d$  transitions have high cross-sections because they are both electric-dipole and spin-allowed. However, due to a high probability of excited state absorption (ESA) and non-radiative decay as well as photoionisation, and color center-formation rare-earth doped glasses and crystals show rather poor laser-performance characteristics such as small efficiency and repetition rate as well as high laser thresholds when pumped with laser radiation below the surface damage threshold.<sup>2,3</sup> Oscillator-strengths and quantum efficiencies as well as the positions of the maximum and their halfwidths of the  $4f \leftrightarrow 5d$ -absorption-and emission-bands of the rare-earth-ions are experimentally well-known and theoretically investigated for a multitude of glasses and crystals.<sup>4,5,6</sup> Since the  $4f$  and  $5d$  states have opposite parity, a two-photon transition is electric-dipole-forbidden. Significant crystal-fields can lift the parity-selection rule leading to a mixing of the  $5d$ -energy levels and to a two-photon-absorption in  $Ce^{3+}$ -doped  $CeF_2$ -crystals.<sup>7</sup> The ionisation of the  $Ce^{3+}$ -Ion due to photo-excitation in the region of the  $4f$ - $5d$ -absorption-bands can be explained by the degeneration of excited  $5d$ -states with the electronic-states of the conductivity band of the glass or the crystal.<sup>8</sup> Capture of the quasi-free electron by  $Ce^{4+}$ -ions can lead to the subsequent generation of extrinsic (impurity) hole centers (HC) such as  $(Ce^{3+})^+$  or impurity electron color centers (CC) such as  $(Ce^{4+})^-$  in Ce-doped glasses. The spectroscopic properties of the HCs and CCs are known for a few silicate glasses.<sup>9</sup> The generation of HCs and CCs in crystals and glasses are characterized by significant oscillator-strengths ( $f = 0,1-1,0$ ) which are larger by a factor of ten compared to the  $5d$ - $4f$ -fluorescence transitions.<sup>10</sup> In lithium aluminosilicate and sodium zinc aluminosilicate glass doped with cerium (Ce) and silver (Ag) holographic modifications were generated by illumination of UV laser radiation followed by thermal treatment.<sup>11</sup> In a photo-thermal process (UV-illumination and thermal treatment) colloidal silver ( $xAg^0 \rightarrow (Ag^0)_x$ ) as well as dielectric microcrystals (e.g. Lithium metasilicate) are generated in the bulk of the glass.<sup>12</sup> The nucleation and growth kinetics of silver particles as well as the crystallization kinetics of the crystals in photosensitive glass have been investigated in detail experimentally and theoretically.<sup>13,14</sup> Using pulsed IR-femtosecond laser radiation the generation of linear microstructures in the bulk of photosensitive Ce-and Ag-doped lithium aluminosilicate glass due to multiphoton absorption without subsequent tempering was recently demonstrated.<sup>15,16</sup>

Using a simple model<sup>17</sup> the optical changes caused by illumination with UV laser radiation in Ce-and Ag-doped lithium aluminosilicate glass can be described within a two-step-process. The photoionisation of the donor  $Ce^{3+}$  in the electronic ground state configuration  $[Xe] 4f^2 F_{5/2, 7/2}$  leads to a  $Ce^{4+}$ -Ion with a photoelectron in the conduction-band of the glass-matrix (first step). Absorption of the electron by ionic silver  $Ag^{1+}$  due to heat treatment leads to atomic silver  $Ag^0$  (second step). The photon energy required for ionisation of the  $Ce^{3+}$ -donor in silicate glass is  $>3.5$  eV.<sup>18,19</sup> The optical bandgap energy of 4,8 eV for the non-illuminated glass is determined using a standard-procedure.<sup>20</sup> Illumination of Ce-and Ag-doped photosensitive glass with UV-photons by laser radiation can lead to the generation of defect centers and to positive as well as negative changes in induced absorption in the deep UV spectral range. For a proper understanding of the photochemical processes underlying the defect generation, it is important to know the change of the valence-states and the concentrations of the polyvalent ions during exposure to UV-laser radiation. Besides it is important to take not only the acceptor Ag but also the acceptors Sn and Sb into account. Since the polyvalent acceptors  $Ag^{1+}$ ,  $Sn^{4+}$  and  $Sb^{5+}$  are isoelectronic with the electronic configuration  $[Xe] 4d^{10}$  the dominant photochemical-processes such as UV-absorption and re-charging of the polyvalent ions are expected to be multistage and cooperative in nature. This is probably the reason that the physical processes in multicomponent photosensitive glasses are still less understood.

Microstructuring of glass with pulsed excimer lasers ( $\lambda_L = 193$  nm (ArF) and  $\lambda_L = 248$  nm (KrF)) with fluences above the material removal threshold yields structure sizes down to the 1  $\mu m$  range with material removal rates  $> 1 \mu m/pulse$ <sup>21</sup> and shows generation of precise geometric surface structures. Mask projection with homogenized power density distribution allows processing of surface areas ( $cm^2$ -scale) without the need of manipulating the workpiece. Depending on the laser parameters, the generation of cracks and spallation of the glass surface, as one of the main problems with microstructuring of glass, could be avoided.<sup>22</sup> The material removal process of glass in thermal regime is based on melting and subsequent vaporisation. Photon energies of excimer laser radiation (ArF: 6.4 eV/KrF: 5.0 eV) are not sufficient to sublime the glass with binding energies and optical band gap energies in the range of 7-9 eV.<sup>23</sup> Debris on the edges of the microstructures is produced due to solidification of molten glass droplets, which are carried along with the vapor/plasma during the material removal process, leading to deposits of vapor/plasma particles depending on processing parameters such as processing gas pressure.

## 2. EXPERIMENTAL

The photosensitive glass 74,29 SiO<sub>2</sub> 11,61 Li<sub>2</sub>O 7,2 Al<sub>2</sub>O<sub>3</sub> 2,74 Na<sub>2</sub>O 4,16 K<sub>2</sub>O 0,18 AgNO<sub>3</sub> 0,4 Sb<sub>2</sub>O<sub>3</sub> 0,07 SnO 0,065 CeCl<sub>3</sub> (raw materials in wt %) under investigation was melted four hours at 1550 C in a platinum furnace and annealed under controlled conditions in a high-grade steel cylinder. The solid-glass was sawn and polished to optical quality. The substrates are 20 mm long, 5 mm broad and 1 mm thick. The glass-substrates were illuminated using pulsed excimer laser radiation (XeF/351 nm, XeCl/308 nm, KrF/248 nm, ArF/193 nm) with pulse length  $\tau_L = 30, 40, 20$  and  $20$  ns and pulsed  $3\omega$ Nd:YAG-laser radiation (355 nm, pulse length  $\tau_L = 10$  ns) below the surface damage threshold. For illumination the substrates were translated with constant velocity on a x-y-stage perpendicular to the laser beam. The excimer laser radiation was imaged with a mask (circular-hole with diameter 1 mm) on the glass surface by large working distance objectives (working distance: 15 cm, demagnification 10:1). For  $3\omega$ Nd:YAG-laser radiation the focus of the radiation was outside the glass surface. The diameter of the laser radiation on the glass surface varied between 80 and 100  $\mu$ m. The overlap in x-and y-direction of the laser beam between successive pulses of the laser radiation was 0,1.

For modification the surface damage thresholds were determined by viewing the surface for a given pulse number after illumination using optical microscopy. The surface damage threshold is given by the fluence interval for no observable modification and the on-set of visible surface damage. For investigations on induced absorption the transmittivity of the non-illuminated and of the glass in the spectral range of 230-2500 nm were measured with optical spectroscopy for vertical incidence of non-coherent and low-intensity radiation. The absorption coefficient for non-illuminated and illuminated glass was calculated taking reflections on the surface as well as internal dispersion into account.

The method for production of optical soda lime glass (74 SiO<sub>2</sub> 16 Na<sub>2</sub>O 12 CaO 4 K<sub>2</sub>O 6 MgO, 3 Al<sub>2</sub>O<sub>3</sub>) is the float process. A ribbon of molten glass is fed across a bath of heated liquid, usually molten tin, in a carefully controlled processing atmosphere. The side of the glass ribbon in contact to the molten tin is called bathside, whereas the opposite side of the glass ribbon is called fireside. The samples of optical soda lime glass (dimensions: 1 cm  $\times$  1 cm  $\times$  0.1 cm) are mounted onto a high precision (accuracy of position 2  $\mu$ m along a length of 2 cm) x-y-z-translation stage in a process gas chamber. Pulsed ArF excimer laser radiation ( $\lambda_L = 193$  nm,  $\tau_L = 20$  ns) and KrF excimer laser radiation ( $\lambda_L = 248$  nm,  $\tau_L = 25$  ns) is imaged by rectangular masks onto the sample surface by large working distance objectives (working distance: 13 cm, demagnification 8:1). The sapphire entrance window is protected against the reactive processing gas atmosphere by He purging gas.

XPS measurements (surface sensitive up to measuring depths < 10 nm) for investigations on chemical composition on bathside and fireside of the glass samples are carried out. Investigations on geometries of the microstructures, structure depth and debris height and width are made by optical microscopy and white light interferometry. Transmittivity and reflectivity in the spectral range of 350-2500 nm were measured with optical spectroscopy at vertical incidence of radiation.

## 3. RESULTS AND DISCUSSION

### 3.1 Photosensitive glass

#### Transmittivity

Fig. 1 displays the transmittivity as a function of wavelength from UV to IR for non-illuminated photosensitive glass. The non-illuminated glass is transparent ( $T > 0,9$ ) from 350 to 3250 nm, showing two absorption edges with no observable structure in the IR at 2750 nm and around 300 nm in the UV. The IR-transmittivity for wavelengths > 2750 nm is ascribed to vibration-modes of hydroxyl groups in the glass-network. Fig. 2 shows the transmittivity as a function of wavelength between 200-400 nm. Bars indicate the wavelengths of the laser radiation used for illumination. The absorption-band at 300 nm is assigned to the well known 4f-5d-absorption of Ce<sup>3+</sup>.

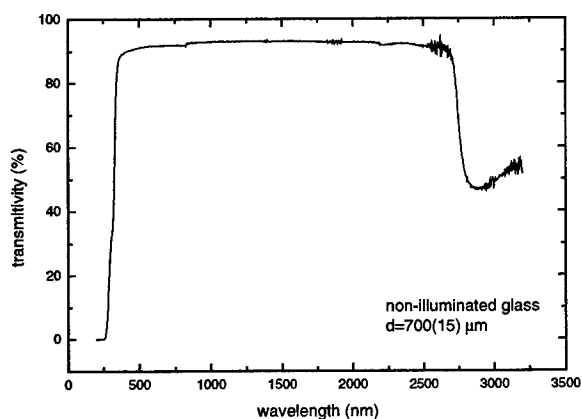


Fig. 1: Transmittivity of photosensitive glass (thickness  $d = 700(15) \mu\text{m}$ ).

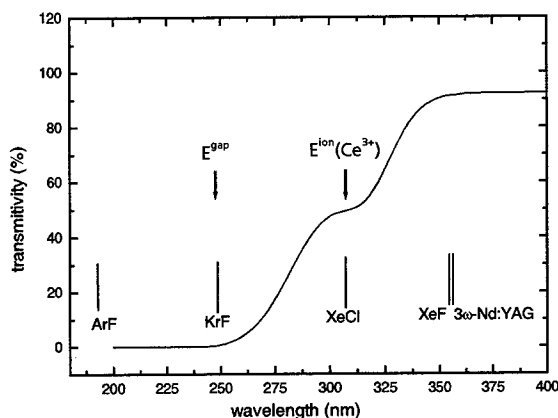


Fig. 2: UV-transmittivity of photosensitive glass, bars indicate the laser-wavelength used for illumination, arrows indicate the energy  $E^{\text{ion}}(\text{Ce}^{3+})$  for  $\text{Ce}^{3+}$ -ionisation and the energy  $E^{\text{gap}}$  of the optical band gap.

### Surface damage thresholds

For ns-laser radiation there is significant transfer of optical energy from the laser radiation excited electrons to the lattice on the time scale of the laser pulse duration. Optical energy is coupled into the glass and is transported out of the focal volume by thermal diffusion. Surface damage occurs when the temperature of the glass in the illuminated region is greater than the temperature for melting or fracture. Thus, the surface damage threshold is determined by the relative rate of energy deposition to thermal diffusion.

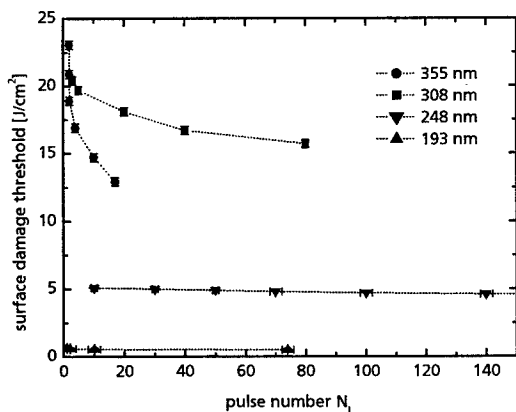


Fig. 3: Surface damage threshold as a function of pulse number  $N_L$  ( $3\omega\text{Nd:YAG} / \lambda = 355 \text{ nm} / \tau_L = 10 \text{ ns}$ ,  $\text{XeCl} / \lambda = 308 \text{ nm} / \tau_L = 40 \text{ ns}$ ,  $\text{KrF} / \lambda = 248 \text{ nm} / \tau_L = 20 \text{ ns}$ ,  $\text{ArF} / \lambda = 193 \text{ nm} / \tau_L = 20 \text{ ns}$ , repetition rate  $\nu_L = 1 \text{ Hz}$ ).

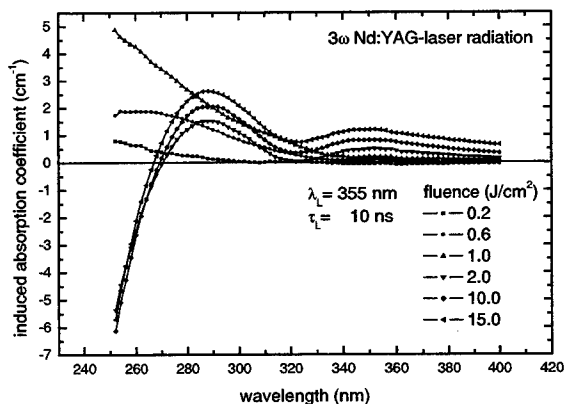


Fig. 4: Induced absorption coefficient as a function of wavelength (laser wavelength  $\lambda_L = 355 \text{ nm}$ , pulselength  $\tau_L = 10 \text{ ns}$ , repetition rate  $\nu_L = 100 \text{ Hz}$ , illuminated area  $A = 5 \times 20 \text{ mm}^2$ , overlap  $O$  of laserbeam between successive pulses = 0.1).

Fig. 3 displays the surface damage thresholds as a function of pulse number for pulsed laser radiation of wavelengths 355 nm ( $3\omega$ Nd:YAG), 308 nm (XeCl), 248 nm (KrF), and 193 nm (ArF). The surface damage threshold for ArF laser radiation is  $0.5 \text{ J/cm}^2$  and constant for pulse number  $N_L < 80$ . The surface damage threshold for KrF-laser radiation is  $5 \text{ J/cm}^2$  for pulse number  $N_L < 2000$ . For pulse number  $N_L > 2000$  a slight shift ( $< 10\%$ ) of the surface damage threshold as a function of pulse number is observed. The surface damage thresholds for  $3\omega$ Nd:YAG and XeCl-laser radiation are a non-linear and monotonous decreasing function of pulse number  $N_L$ . For  $3\omega$ Nd:YAG and pulse number  $N_L < 20$  the surface damage threshold is found to be  $12 \text{ J/cm}^2$ . For XeCl laser radiation and pulse number  $N_L < 100$  the surface damage threshold is  $15 \text{ J/cm}^2$ . The change of the surface damage threshold for ns-laser radiation as a function of pulse number can be explained qualitatively by incubation and accumulation processes of absorption centers induced by the pulsed UV-laser radiation. The ionisation of  $\text{Ce}^{3+}$ -Ions with laser-photons  $> 3.5 \text{ eV}$  leads to an increase in electron concentration in the conduction band of the glass matrix.

A fraction of the conduction-band electrons will be captured by polyvalent ions such as  $\text{Ag}^{1+}$ ,  $\text{Sn}^{4+/5+}$  or  $\text{Sb}^{5+/6+}$  leading to atomic silver  $\text{Ag}^0$ ,  $\text{Sn}^{3+/4+}$  and  $\text{Sb}^{4+/5+}$ . Another fraction of electrons will be used for the generation of CC or HC-defect centers with a binding energies similar to the  $\text{Ce}^{3+}$  or  $\text{Ce}^{4+}$ -ions. The generation of new electronic states within the optical band gap will lead to a significant change of the spectral absorption cross section between successive laser pulses. The change in the concentration of the polyvalent ions  $\text{Ag}^0$ ,  $\text{Sn}^{3+}$  and  $\text{Sb}^{4+}$  will increase with pulse number and will finally saturate depending on the concentration of the polyvalent ions in the non-illuminated glass and on fluence. The change of the surface damage threshold will eventually decrease as a function of pulse number.

### Induced absorption

The permanent changes of the absorption coefficient for the illuminated glasses using  $3\omega$ Nd:YAG, XeCl and KrF-laser radiation as a function of fluence is shown and the absorption coefficient of the non-illuminated glass is subtracted (Fig. 4, 5, and 6). Because of the small transmittivity ( $T < 0,15$ ) in the spectral range 200-250 nm of the non-illuminated glasses the induced absorption coefficient for  $\lambda < 250 \text{ nm}$  is not displayed. The absorption coefficient of the photosensitive glass changes in amount and sign during illumination with laser radiation as a function of photon energy and fluence.

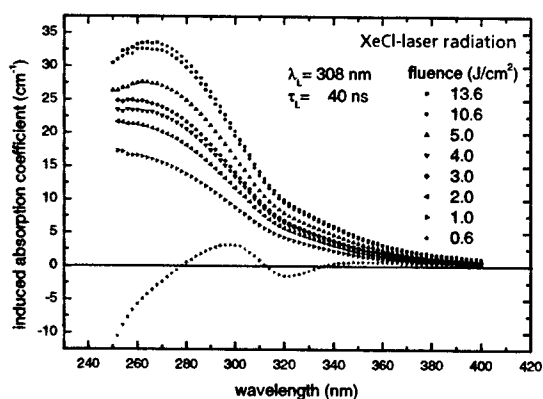


Fig. 5: Induced absorption coefficient as a function of wavelength (wavelength  $\lambda_L = 308 \text{ nm}$ , pulslength  $\tau_L = 40 \text{ ns}$ , repetition rate  $\nu_L = 20 \text{ Hz}$ , illuminated area  $A = 5 \times 20 \text{ mm}^2$ , overlap  $O$  of laserbeam between successive pulses  $= 0.1$ ).

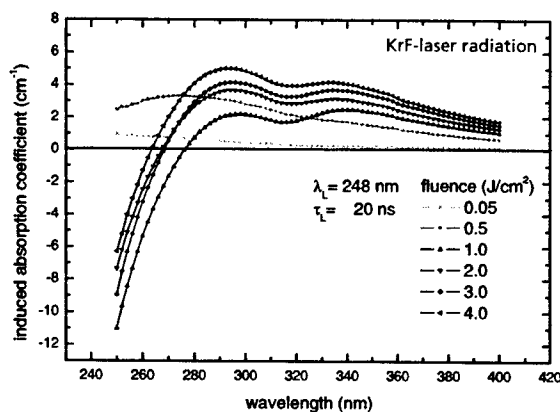


Fig. 6: Induced absorption coefficient as a function of wavelength (wavelength  $\lambda_L = 248 \text{ nm}$ , pulslength  $\tau_L = 20 \text{ ns}$ , repetition rate  $\nu_L = 20 \text{ Hz}$ , illuminated area  $A = 5 \times 20 \text{ mm}^2$ ,

Fig. 4 displays the induced absorption coefficient for illumination with  $3\omega\text{Nd}:\text{YAG}$  laser radiation. For fluence  $< 0.8 \text{ J/cm}^2$  the absorption coefficient is positive ( $< 5 \text{ cm}^{-1}$ ) and a linear monotonous function of the fluence. For fluence  $> 2 \text{ J/cm}^2$  the change in absorption coefficient is positive as well as negative ( $< -6 \text{ J/cm}^2$ ) with two pronounced maxima at 290 nm (4.6 eV) and 350 nm (3.5 eV). The amount of induced absorption coefficient at 290 nm and at 350 nm is an increasing function of fluence. The induced absorption band is distributed in the optical band gap and located 0.2 eV and 1.3 eV below the edge of the conduction band.

Fig. 5 displays the induced absorption coefficient for illumination with XeCl-laser radiation. For a fluence of  $0.6 \text{ J/cm}^2$  the induced absorption coefficient is minimal and negative ( $< 2 \text{ cm}^{-1}$ ) at 320 nm with a maximum around 300 nm ( $< 5 \text{ J/cm}^2$ ). For  $\lambda < 280 \text{ nm}$  an induced absorption coefficient of  $< -10 \text{ J/cm}^2$  is found. For fluences  $> 0.6$  to  $10 \text{ J/cm}^2$  one pronounced maximum ( $+ 33 \text{ cm}^{-1}$ ) is observed at 270 nm (4.6 eV) with a full width at half maximum of  $> 70 \text{ nm}$ . The absorption coefficient at 270 nm (4.6 eV) is a increasing function fluence and seems to saturate between 10 and  $13 \text{ J/cm}^2$ . The induced absorption band for XeCl-laser radiation is located near the edge of the conduction band and seems to have a significant overlapp with the conduction band.

Fig. 6 shows the induced absorption coefficient for illumination with KrF-laser radiation. The spectral dependence of the induced absorption coefficient for KrF-laser radiation is the same compared to  $3\omega\text{Nd}:\text{YAG}$ -laser radiation. Two pronounced positive maxima at 290 nm (4.3 eV) and 330 nm (3.7 eV) which are not as well separated than for  $3\omega\text{Nd}:\text{YAG}$ -laser radiation illumination and a negative change for  $\lambda < 280 \text{ nm}$  is observed. For fluence  $< 0.5 \text{ J/cm}^2$  the induced absorption coefficient is positive with an amplitude  $< 4 \text{ cm}^{-1}$ . For fluence  $> 0.5 \text{ J/cm}^2$  the induced absorption coefficient is positive and with two maxima  $< 5 \text{ cm}^{-1}$  at 290 nm and  $< 4 \text{ cm}^{-1}$  at 330 nm. The induced absorption coefficient at 290 nm and at 330 nm is an increasing function of fluence. For  $\lambda < 280 \text{ nm}$  the induced absorption coefficient is negative ( $< -10 \text{ J/cm}^2$ ) as for  $3\omega\text{Nd}:\text{YAG}$ -laser radiation. The induced absorption band is located in the optical bandgap 0.5 eV and 1.1 eV below the edge of the conduction band.

The generation for extrinsic defect centers is only possible for a photon energy  $h\nu$  greater than the optical inter-band energy  $E_{\text{gap}}$  of the glass-matrix. Intrinsic defect centers in the glass such as  $\text{Ce}^{3+}$ -ions can lead to electronic energy levels located in the optical band gap. The generation of extrinsic defect centers is then possible with a photon energy  $h\nu \leq E_{\text{gap}}$ . The density of electronic states for amorphous materials as a function of energy can be written in the form  $G_V(E) \propto E^p$  for the conduction-band and  $G_L(E) \propto (E - E_{\text{gap}})^q$  for the valence-band.<sup>24</sup> This assumption is expected to hold not only for chalcogenide- and fluorid glass but also for silicate glass.<sup>25</sup> When the shape density of electronic states is parabolic ( $p = q = 1/2$ ) the energy-dependence of the absorption-coefficient  $\alpha$  can be written as  $\alpha h\nu = C(h\nu - E_{\text{gap}})^2$ ,  $C$  is a constant. The energy of the optical band  $E_{\text{gap}}$  in this model is the difference between the valence and conduction band localization edges.  $E_{\text{gap}}$  of the photosensitive glass is found to be 4.8 eV with extrapolation. With the assumption of linear absorption processes a direct inter-band excitation with UV-laser radiation of the energy  $h\nu \geq E_{\text{gap}}$  creating excitons is only possible for KrF ( $h\nu = 5 \text{ eV}$ ) and ArF ( $h\nu = 6.4 \text{ eV}$ ) laser radiation. Since defect center generation is observed for XeCl and for  $3\omega\text{Nd}:\text{YAG}$  laser radiation with photon energy  $h\nu \leq E_{\text{gap}}$  the ionic-ground of the  $\text{Ce}^{3+}$ -ion is located within the optical bandgap of the glass-matrix. Since the highest induced absorption ( $< 35 \text{ cm}^{-1}$ ) is observed with 4.0 eV-photons from XeCl-laser radiation 0.2 eV below the optical bandgap (4.8 eV) the dominating process for illumination with XeCl-laser radiation seems to be photoionisation  $\text{Ce}^{3+} + h\nu \rightarrow \text{Ce}^{4+} + e^-$ . The pronounced maximum  $< 35 \text{ cm}^{-1}$  of induced absorption observed around 4.6 eV can be assigned to the creation of  $\text{Ce}^{4+}$ -ions due to resonant photoionisation of the  $\text{Ce}^{3+}$ -ions.<sup>26</sup> The two maxima of induced absorption at 290 nm (4.3 eV) and 350 nm (3.5 eV) as observed with  $3\omega\text{Nd}:\text{YAG}$ - and KrF-laser radiation for photon-densities  $> 1 \text{ J/cm}^2$  can be assigned to the generation of two extrinsic (impurity) hole centers such as  $(\text{Ce}^{3+})^+$  or impurity electron color centers such as  $(\text{Ce}^{4+})^-$  with binding energies comparable and higher to the  $\text{Ce}^{3+}$ -ionisation energy threshold ( $> 3.5 \text{ eV}$ ). The observation of comparatively small induced absorption of  $< 3 \text{ cm}^{-1}$  around 4.3 eV with 3.5 eV-photons from  $3\omega\text{Nd}:\text{YAG}$ -laser radiation and with 5.0 eV photons from KrF-laser radiation showing similar induced-absorption spectra can be understood by a significant radiative relaxation-rate during non-resonant excitation instead of a non-radiative relaxation to the  $\text{Ce}^{3+}$ -ground state or photoionisation generating  $\text{Ce}^{4+}$  ions at 4.6 eV.

### 3.2 Soda lime glass

#### Material removal rate

The material removal rates on the fireside for processing with excimer laser radiation at a wavelength of  $\lambda_L = 193$  nm are below 100 nm/pulse for fluences  $< 2.05$  J/cm<sup>2</sup> (Fig. 7). The removal threshold is estimated by extrapolation of the material removal functions for processed areas of  $A = 0.01$  mm<sup>2</sup> and  $A = 1.5$  mm<sup>2</sup> to a value of 0.49 J/cm<sup>2</sup>. The material removal rate is depending on the size of the processed area. Possible reasons for the increase of the material removal rate with decreasing processed area are Fresnel diffraction at the mask, plasma absorption, and reflexion on the generated flanks of the structure.

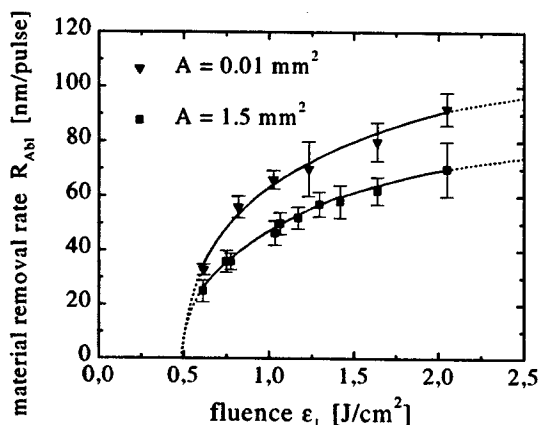


Fig. 7: Material removal rate on the fireside as a function of fluence for different processed areas  $A$  (wavelength  $\lambda_L = 193$  nm, repetition rate  $\nu_L = 1$  Hz, number of pulses  $N_L = 50$ ).

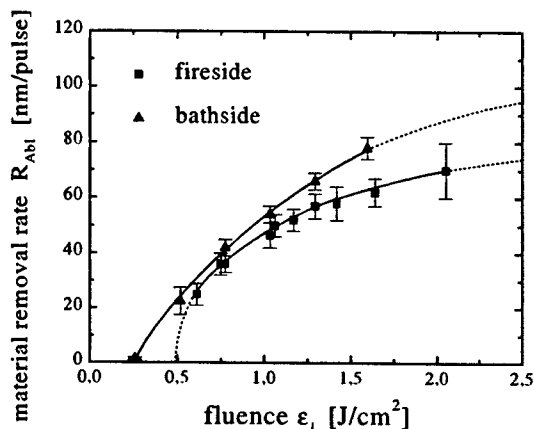


Fig. 8: Material removal rate on fireside and bathside as a function of fluence (wavelength  $\lambda_L = 193$  nm, repetition rate  $\nu_L = 1$  Hz, processed area  $A = 1.5$  mm<sup>2</sup>, number of pulses  $N_L = 50$ ).

Fig. 8 shows higher material removal rate on the bathside compared to fireside. XPS measurements indicate a small amount of tin at the surface of the bathside in contrast to the fireside. The absorption of laser radiation on the bathside may be increased by the tin particles as additional absorption centres. As a consequence, structural modifications in the glass may occur, probably leading to generation of color centers as additional absorption centers for excimer laser radiation. Different absorption mechanisms and related material removal rates for fireside and bathside can be estimated.

For processing with excimer laser radiation at a wavelength of  $\lambda_L = 248$  nm, no material removal on the fireside occurs up to fluences  $\leq 5.2$  J/cm<sup>2</sup>. At least, the processed glass surface becomes slightly opaque. On the bathside, material removal is measured for fluences  $> 1.5$  J/cm<sup>2</sup>, as a result of additional absorption in the detected tin at the bathside surface. Material removal rates up to 200 nm/pulse are reached for a fluence of 5.2 J/cm<sup>2</sup> (Fig. 9). Higher material removal rates for processing with 248 nm excimer laser radiation could be assigned to different absorption mechanisms in soda lime glass compared to 193 nm excimer laser radiation.

Fig. 10 shows a steep increase in material removal rate for processing at  $\lambda_L = 193$  nm with the pulse number  $N_L < 10$ . For  $N_L > 10$  a slightly decreasing material removal rate is observed down to a steady state at pulse numbers  $N_L \approx 500$ . For processing the bathside with excimer laser radiation at  $\lambda_L = 248$  nm a decrease of the material removal rate with an increasing pulse number is observed for  $N_L \geq 1$  (Fig. 9). For a fluence of 5.2 J/cm<sup>2</sup> a steady state material removal rate value is reached for  $N_L > 100$  whereas for a smaller fluence of 4.0 J/cm<sup>2</sup> the steady state is reached for  $N_L > 500$ . The steep increase of the material removal rate for small pulse number at a wavelength of  $\lambda_L = 193$  nm may be explained by the generation of color centers in glass.<sup>27</sup> The investigations show that sub-band gap excimer laser radiation can induce

color centers with a two photon-absorption process for fluences  $> 100 \text{ mJ/cm}^2$ . The color centers function as absorption centers for incident laser radiation during subsequent pulses. The generation rate for color centers, like E'-centers, non-bridging oxygen hole centers (NOBHC) and peroxy radicals, depends on properties of the glass, photon energy and fluence. For  $N_L > 10$  the density of color centers probably saturates (Fig. 10).

A different absorption mechanism for excimer laser radiation at 248 nm (Fig. 9), probably including the generation of a different type of color center, is shown for soda lime glass compared to excimer laser radiation at  $\lambda_L = 193 \text{ nm}$  (Fig. 10). Related to the generation of different color centers, saturation of the color center density may be achieved by the first pulse of excimer laser radiation at  $\lambda_L = 248 \text{ nm}$ . In this case no increase of the material removal rate within the subsequent pulses is expected (Fig. 9) like it is observed for excimer laser radiation at  $\lambda_L = 193 \text{ nm}$  (Fig. 10).

The decrease of the material removal rate for a higher pulse number can be explained by the vapor/plasma absorption.<sup>11</sup> For small pulse number the vapor/plasma expansion is mainly 3-dimensional, compared to the axis of symmetry by the incident laser radiation. Increase of the structure depth leads to a more 1-dimensional vapor/plasma expansion in axial direction, in combination with an increase of the optical density of the vapor/plasma for incident laser radiation. The transmission of the expanding vapor/plasma and the resulting material removal rate decreases up to a certain structure depth, at which the whole vapor/plasma expands approximately in axial direction. Values for vapor/plasma absorption and material removal rate reach saturation. The certain structure depth of  $7.5\text{--}12.8 \text{ }\mu\text{m}$  (calculated from material removal rates and pulse number in Fig. 9) related to the saturation of the material removal rate is reached by processing at a fluence of  $5.2 \text{ J/cm}^2$  with less numbers of pulses than at processing with a fluence of  $4.0 \text{ J/cm}^2$  (Fig. 9).

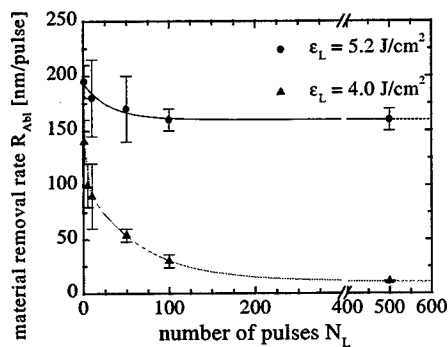


Fig. 9: Material removal rate on the bath side as a function of the pulse number wavelength  $\lambda_L = 248 \text{ nm}$ , repetition rate  $\nu_L = 1 \text{ Hz}$ , processed area  $A = 0.01 \text{ mm}^2$ .

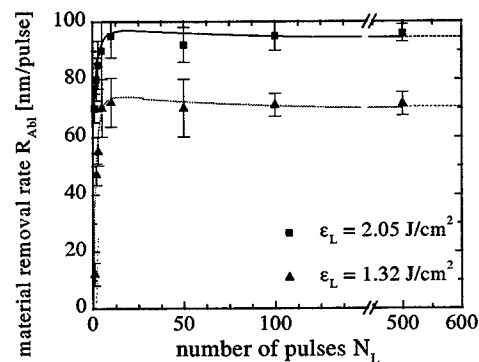


Fig. 10: Material removal rate as a function of the pulse number (wavelength  $\lambda_L = 193 \text{ nm}$ , repetition rate  $\nu_L = 1 \text{ Hz}$ , processed area  $A = 0.01 \text{ mm}^2$ ).

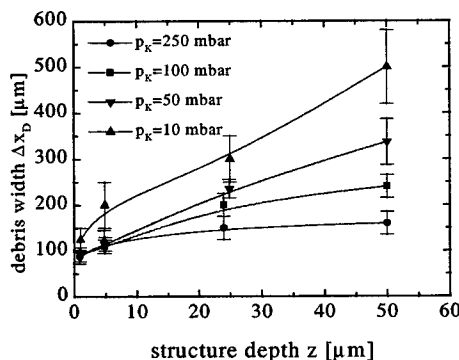


Fig. 11: Debris width as a function of structure depth (wavelength  $\lambda_L = 193 \text{ nm}$ , repetition rate  $\nu_L = 1 \text{ Hz}$ , fluence  $\epsilon_L = 2.05 \text{ J/cm}^2$ , processed area  $A = 0.01 \text{ mm}^2$ , processing gas: He).

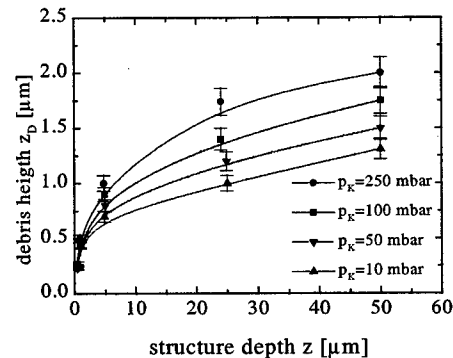


Fig. 12: Debris height as a function of structure depth (wavelength  $\lambda_L = 193 \text{ nm}$ , repetition rate  $\nu_L = 1 \text{ Hz}$ , fluence  $\epsilon_L = 2.05 \text{ J/cm}^2$ , processed area  $A = 0.01 \text{ mm}^2$ , processing gas: He).

## Generation of debris at different processing gas atmospheres

Fig. 11 shows a lateral increase of debris generation at structure edges and on the surface of the samples with increase of the pulse number and structure depth, respectively. When a microstructure begins to be produced in the glass, the expanding vapor/plasma builds up a pressure that causes a flow towards the exit aperture of the microstructure. The flow can carry along some of the molten material, solidifying and deposits along the edges of the microstructure at the sample surface. Collision processes of expanding vapor/plasma particles with the ambient processing gas particles leads to re-deposition of the vapor/plasma particles as debris on the sample surface. The mean free path for collision of the vapor/plasma particles strongly depends on the pressure of the processing gas atmosphere. The decrease of the mean free path with increasing processing gas pressure leads to high debris generation at areas near to the microstructure as shown for He processing gas atmospheres (Fig. 6). Debris width  $\Delta x_D$  (Fig. 6) is defined as the radial distance between structure edge and debris boundary for debris heights  $> 200$  nm.

Transfer of kinetic energy of the expanding vapor/plasma particles to processing gas particles, caused by collision processes, is correlated to heating of the processing gas atmosphere depending on heat capacity and thermal conductivity of the processing gas. He as inert processing gas with higher values of heat capacity and thermal conductivity, compared to mixed processing gas atmospheres of He/F<sub>2</sub>, yields higher losses of kinetic energy of the expanding vapor/plasma particles.

## Mechanical induced stress

Laser processing of glass using laser radiation with a fluence above the material removal threshold is dominated by a photo-thermal-induced phase-transition (solid-fluid-vapor). During plasma formation a combination of material-vapour and plasma expands over the surface and causes an momentum onto the surface. A shock-wave in the substrate is generated and stress in the substrate is induced producing cracks and conchoidal fracture induced at micro-cracks in the surface (Fig13 and Fig. 14). Length and depth of the cracks depend on the fluence of the laser radiation. The value of the pressure surge depends on the material properties and on the on the fluence of the laser radiation.

Based on a model for laser induced material removal<sup>28,29</sup> the time development of the pressure P on the surface is calculated taking into account the chemical decomposition of the solid glass-monomers into atoms and molecules of the form  $[0,74 \text{ SiO}_2, 0,12 \text{ Na}_2\text{O}, 0,14 \text{ CaO}] \rightarrow [p_1 \text{ Si}, p_2 \text{ SiO}, p_3 \text{ O}_2, p_4 \text{ Na}, p_5 \text{ O}, p_6 \text{ CaO}, p_7 \text{ Ca}]$  for soda lime glass,  $p_i$  being the partial pressures. The pressure is a monotonous function of temperature and reaches 2000 K at 1 bar. At a temperature of 2000 K and a pressure of  $10^{-4}$  bar the vapor is composed mainly of SiO<sub>2</sub>, Na and Ca. The energy of decomposition amounts from 8 to 12 eV.

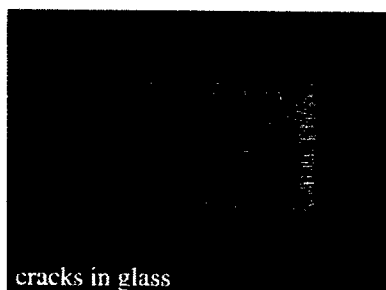


Fig. 13: Laser-induced cracks in glass (wavelength  $\lambda_L = 193$  nm, fluence  $\epsilon_L = 3.0 \text{ J/cm}^2$ , pulse number  $N_L = 50$ , repetition rate  $\nu_L = 1 \text{ Hz}$ ).

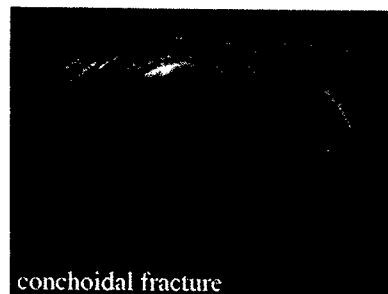


Fig. 14: Laser-induced conchoidal fracture in glass (wavelength  $\lambda_L = 193$  nm, fluence  $\epsilon_L = 3.0 \text{ J/cm}^2$ , pulse number  $N_L = 50$ , repetition rate  $\nu_L = 1 \text{ Hz}$ ).



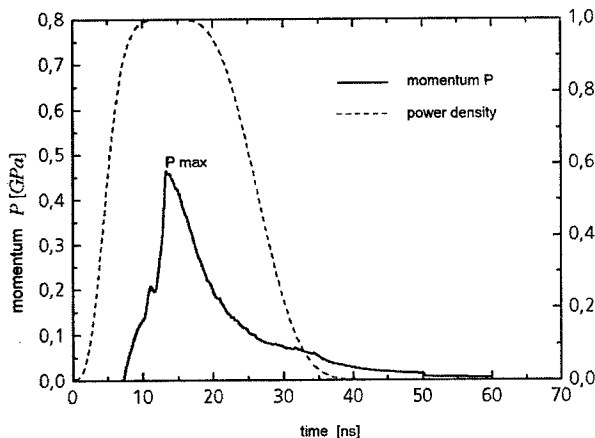


Fig. 15: Laser-induced momentum of the vapor/plasma on the surface of soda lime glass (wavelength  $\lambda_L = 193$  nm, fluence  $\epsilon_L = 3.0$  J/cm<sup>2</sup>, pulse duration  $\tau = 20$  ns, pulse number  $N_L = 1$ ).

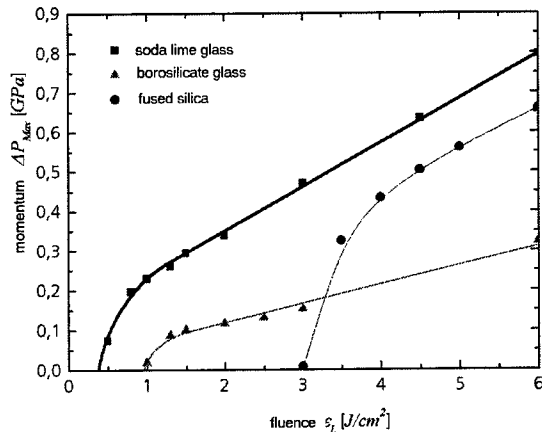


Fig. 16: Laser-induced maximal momentum of the material-vapor-plasma on the surface as a function of fluence  $\epsilon_L$  (wavelength  $\lambda_L = 193$  nm, pulse duration  $\tau = 20$  ns, pulse number  $N_L = 1$ ).

Fig. 15 shows the calculated momentum as a function of time for soda lime glass. In a first step the glass substrate is heated due to laser radiation after the beginning ( $t=0$  ns) of the laser pulse. After 7 ns the decomposition of the solid glass starts until the first dip at  $t = 11$  ns is reached. At  $t = 14$  ns an absolute maximum of the momentum  $< 0.5$  GPa due to plasma formation is reached. The maximum momentum as a function of fluence for soda lime, borosilicate glass, and fused silica is shown in Fig. 16. For the investigated glasses and fluences a maximum pressure 0.8 GPa is obtained.

#### 4. CONCLUSIONS

The surface damage threshold for photosensitive glass as a function of pulse number are measured for pulsed ns-laser radiation of wavelengths 355 nm ( $3\omega\text{Nd:YAG}$ ), 308 nm (XeCl), 248 nm (KrF), and 193 nm (ArF). For KrF and ArF laser radiation the surface damage threshold is independent of pulse number ( $N_L < 150$ ). For  $3\omega\text{Nd:YAG}$  and XeCl laser radiation the change of the surface damage threshold as a function of pulse number ( $N_L < 100$ ) is due to incubation processes and accumulation of absorption centers. The changes of the absorption coefficient as a function of fluence are presented after illumination of photosensitive glass with pulsed laser radiation of wavelengths 355 nm ( $3\omega\text{Nd:YAG}$ ), 308 nm (XeCl) and 248 nm (KrF). The energy  $E^{\text{gap}}$  of the optical band gap of the non-illuminated photosensitive glass is 4.8 eV (260 nm). The absorption coefficient for illuminated glass changes in amount and sign as a function of wavelength and fluence of the laser radiation. For  $3\omega\text{Nd:YAG}$  and KrF laser radiation non-resonant with the absorption cross section of the  $\text{Ce}^{3+}$ -ions (310 nm) two positive maxima at 290 nm and 350 nm of the induced absorption coefficient are found. The corresponding absorption bands are assigned to extrinsic (impurity) hole centers such as  $(\text{Ce}^{3+})^+$  or impurity electron color centers such as  $(\text{Ce}^{4+})^-$  and located in the optical band gap. For XeCl laser radiation resonant with the absorption cross section of the  $\text{Ce}^{3+}$ -ions one positive maximum of induced absorption at 270 nm is found. The corresponding absorption band is assigned to resonant  $\text{Ce}^{3+} \rightarrow \text{Ce}^{4+}$  photoionisation and located near the energy of the optical band gap.

Production of rectangular test structures in soda lime glass by means of microstructuring with excimer laser radiation showed the process capabilities of laser technology in view to the production of prototypes for microreaction technology, e.g. microchannels for micromixers or microreaction chambers. Increase of material removal rate with decrease of microstructure dimensions and the differences in processing bathside or fireside of soda lime glass are presented. Different characteristics of the material removal rate as a function of pulse numbers related to different absorption mechanisms for excimer laser radiation at  $\lambda_L = 193$  nm compared to  $\lambda_L = 248$  nm are shown. Material removal rates for processing at  $\lambda_L = 193$  nm of  $< 100$  nm/pulse at a fluence of  $2.05$  J/cm<sup>2</sup> are measured compared to

material removal rates  $< 200$  nm/pulse at a fluence of  $5.2 \text{ J/cm}^2$  for processing at  $\lambda_L = 248$  nm. Microstructuring of soda lime glass with mask projection using ArF excimer laser radiation, yielding wall angles of up to 70 degrees for a depth of  $\geq 50 \text{ }\mu\text{m}$  and a width of  $\geq 100 \text{ }\mu\text{m}$ , has to be preferred concerning the accuracy of the produced rectangular microstructure geometries. Contact mask processing with  $\text{cm}^2$ -scale spot size of homogenized laser radiation generates channel-like structures with a width of  $>100 \text{ }\mu\text{m}$ , depth of  $50\text{-}100\text{ }\mu\text{m}$  and a length of  $>1 \text{ cm}$  at processing times of  $> 75\text{ s}$ .

The laser-induced momentum on the surface as a function of time was calculated for laser processing of soda lime glass above the material removal threshold for wavelength  $\lambda_L = 193 \text{ nm}$ , fluence  $\epsilon_L = 3.0 \text{ J/cm}^2$ , pulse duration  $\tau = 20 \text{ ns}$  and pulse number  $N_L = 1$ . At  $t = 14 \text{ ns}$  an absolute maximum of the momentum  $< 0.5 \text{ GPa}$  is reached. The maximum momentum as a function of fluence for soda lime, borosilicate glass, and fused silica was calculated. For the investigated glasses and fluences a maximum pressure  $0.8 \text{ GPa}$  is obtained. The results indicate the formation of cracks due to plasma formation.

### ACKNOWLEDGEMENTS

We thank Prof. Dr. D. Hülsenberg, Dr.-Ing. A. Harnisch and Dipl.-Ing. U. Brokmann for providing the photosensitive glass substrates and for helpful discussions. This work was supported by the Deutsche Forschungsgemeinschaft (DFG) under project numbers Hu 560/14-2 and Po 591/10-2.

### REFERENCES

1. S. Kück, "Laser-related spectroscopy of ion-doped crystals for tuneable solid-state lasers", *Applied Physics B* **72**, pp. 551-562, 2001.
2. D. J. Ehrlich, P. F. Moulton, and R. M. Osgood Jr, "Optically pumped Ce:LaF<sub>3</sub> laser at 286 nm", *Optics Letters*, pp. 339-341, 1980.
3. D. S. Hamilton, K. S. Lim, "Optical gain and loss studies in Ce<sup>3+</sup>:YLiF<sub>4</sub>", *J. Opt. Soc. Am. B*, pp. 1401-1406, 1989.
4. G. H. Dieke, *Spectra and Energy Levels of Rare Earth Ions in Crystals*, Wiley, New York, 1968.
5. P. Dorenbos, "The  $4f^n-4f^{n-1} \rightarrow 5d$  transitions of the trivalent lanthanides in halogenides and chalcogenides", *J. Luminescence* **91**, pp. 91-106, 2000.
6. P. Dorenbos, "The 5d level positions of the trivalent lanthanides in inorganic compounds", *J. Luminescence* **91**, pp. 155-176, 2000.
7. G. J. Pogatschnik, D. S. Hamilton, "Excited-State photoionisation of Ce<sup>3+</sup> ions in Ce<sup>3+</sup>:CaF<sub>2</sub>", *Phys. Rev. B* **36**, pp. 8251-8257, 1987.
8. V. I. Arbutov, "Photostimulated electron transfer between coactivator ions in alkali silicate glasses", *J. Non Crystalline Solids* **253**, pp. 37-49, 1999.
9. J. Stroud, "Color centers in cerium-containing silicate glass", *J. Chem. Phys.* **37**, pp. 836-841, 1962.
10. A. J. Bayramian, "Ce:LiSrAlF<sub>6</sub> laser performance with antisolatorant pump beam", *J. Luminescence* **69**, pp. 85-94, 1996.
11. O. M. Efimov, "High-efficiency Bragg gratings in photo-thermorefractive glass", *Applied Optics* **38**, pp. 619-625, 1999.
12. S. D. Stookey, "Full color photosensitive glass", *J. Appl. Phys.* **49**, pp. 5114-5123, 1978.
13. U. Kreibitz, "Small Silver Particles in Photosensitive Glass: Their Nucleation and Growth", *Appl. Phys.* **10**, pp. 255-264, 1976.

14. G. A. Sycheva, "Nucleation kinetics of lithium metasilicate in photosensitive lithium aluminosilicate glass", *Glass Physics and Chemistry* **25**, pp. 501-511, 1999.
15. Y. Kondo, "Three-dimensional microscopic crystallisation in photosensitive glass by femtosecond laser pulses at nonresonant wavelength", *Jpn. J. Appl. Phys.* **37**, pp. L94-L96, 1998.
16. Y. Kondo, "Three-dimensional arrays of crystallites within glass by using non-resonant femtosecond pulses", *J. Non Cryst. Sol.* **253**, pp. 143-156, 1999.
17. S. D. Stookey, "Photosensitive Glass", *Industrial and Engineering Chemistry* **41**, pp. 856-861, 1949.
18. J. Stroud, "Photoionisation of  $Ce^{3+}$  in glass", *J. Chem. Phys.* **35**, pp. 844-850, 1961.
19. V. I. Arbuzov, "Photostimulated electron transfer between coactivator ions in alkali silicate glasses", *J. Non Cryst. Solids* **253**, pp. 37-49, 1999.
20. J. Tauc, *Optical Properties of Amorphous Semiconductors*, p. 159, Plenum, New York, 1974.
21. H. Hornberger and R. Weißmann, "Machining of silica glasses using excimer laser radiation", *Glastechn. Ber. Glass Sci. Technol.* **69**, pp. 44-49, 1996.
22. B. Braren and R. Srinivasan, "Controlled etching of silicate glasses by pulsed ultraviolet laser radiation", *J. Vac. Sci. Technol. B* **6**, pp. 537-541, 1988.
23. P.R. Herman, K. Beckley, B. Jackson, K. Kurosawa, D. Moore, T. Yamanishi and J. Yang, "Processing applications with the 157-nm fluorine excimer laser", *EXCIMER LASERS, OPTICS AND APPLICATIONS, SPIE Proc.* **2992**, pp. 86-95, 1997.
24. S. R. Elliot, *Physics of Amorphous Materials*, Longman, New York, 1983
25. H. S. Nalwa (Ed.), *Handbook of Advanced Electronic and Photonic Materials and Devices*, Chapter 2, 2001, pp. 47-85
26. J. Stroud, "Photoionisation of  $Ce^{3+}$  in glass", *J. Chem. Phys.* **35**, pp. 844-850, 1961.
27. G.C. Escher, "KrF laser induced color centers in commercial fused silicas", *EXCIMER BEAM APPLICATIONS, SPIE Proc.* **998**, pp. 30-7, 1988.
28. M. Aden, E. Beyer, G. Herziger, and H. Kunze, "Laser-induced vaporisation of a metal surface", *J. Phys. D: Appl. Phys.* **25**, pp. 57-65, 1992.
29. M. Aden, E. W. Kreutz, and A. Voss, "Laser-induced plasma formation during pulsed laser deposition", *J. Phys. D: Appl. Phys.* **26**, pp. 1545-53, 1993.

# Crack-Free Laser Processing of Glass Substrate and Its Mechanisms

M. H. Hong<sup>\*a</sup>, K. Sugioka<sup>b</sup>, D.J. Wu<sup>a</sup>, L.L. Wong<sup>a</sup>, Y.F. Lu<sup>a</sup>, K. Midorikawa<sup>b</sup> and T.C. Chong<sup>a</sup>

<sup>a</sup> Laser Microprocessing Group, Data Storage Institute, DSI Building,  
5 Engineering Drive 1, Singapore 117608

<sup>b</sup> RIKEN-The Institute of Physical and Chemical Research, Wako, Saitama 351-01, Japan

## ABSTRACT

Laser-induced-plasma-assisted ablation (LIPAA) for crack-free laser processing of glass substrate is investigated. Different from laser breakdown at high laser fluence, a pulsed green laser is used to achieve the glass processing in air at much lower laser fluence. Laser beam goes through the substrate first and then irradiates on a solid target behind. For laser fluence above target ablation threshold, plasma generated from target ablation flies forward at a high speed. At a small target-to-substrate distance, there are strong interactions among laser light, target plasma and glass substrate at its rear side surface. With the target materials deposition on the glass surface or even doping into the glass substrate, light absorption characteristic at the rear side surface is modified. The laser processing result is closely related to target-to-substrate distance, laser scanning speed and its repetition rate. Color marking, glass metallization and structuring can be achieved with the fine tune of the laser processing parameters.

**Keywords:** LIPAA, glass microfabrication, non-crack and color marking

## 1. INTRODUCTION

In modern Photonics and liquid crystal display (LCD) industries, glass substrate plays a more and more important role due to its high hardness, high thermal stability and high transparency in visible wavelength region. There are many functional microstructures fabricated on the glass substrate, such as phase shift mask, optical waveguide, v-groove and UV optics [1,2]. However, it is a long time challenge for the industries to achieve the high quality glass microfabrication, especially with the laser processing. The first issue is that the glass substrate is transparent to most of industrial laser sources. For these laser sources, very high laser fluence is required to induce the glass substrate breakdown for the surface microprocessing. There are many microcracks formed along the laser processing lines, which is not expected for the industries. Many researches were reported to use ultrashort pulse lasers (femto-second laser) or ultrashort wavelength lasers ( $F_2$  or VUV Raman lasers) for the glass microfabrication [3-6]. Though the femto-second laser also causes the glass substrate breakdown, it can obtain the fine microstructures on or inside the transparent substrate due to its very short pulse duration, which limits the heat effect to the laser spot surrounding area. Since the glass can absorb the VUV laser light,  $F_2$  laser can ablate away the glass substrate materials easily for the high quality microfabrication. The other issue is how to find the optimal laser means to meet the industrial requirement for a low cost, flexible, fast speed and reliable processing in the manufacturing environment. For the current femto-second and VUV laser technology, they have many challenges faced during the commercialization for the industrial applications, such as high photon cost, poor beam quality and complicated setup. K. Sugioka et al. proposed a highly potential laser ablation scheme for transparent hard materials microfabrication by UV and visible laser irradiation [7, 8]. With an aid of laser-induced plasma from a metal target ablation, fused quartz can be drilled through or patterned. The process is called the laser-induced-plasma-assisted ablation (LIPAA). Plasma optical signal diagnostics and analyses show that the quartz ablation is highly dynamic. In a time scale of nanoseconds, there are target ablation with plasma generation and complicated interactions among target plasma, incident laser beam and quartz substrate [9, 10]. The glass ablation

\*dsihmh@dsi.nus.edu.sg; Phone 65-8748707; fax 65-7771349; <http://www.dsi.nus.edu.sg>; DSI Building, 5, Engineering Drive 1, Singapore 117608

quality is closely related to laser fluence and target-to-substrate distance. Recently, we extended the LIPAA applications to 532 nm diode-pumped-solid-state (DPSS) Nd:YAG laser. This laser source shows excellent operation reliability, low cost and is widely applied in the microelectronics industry for the via hole drilling on printed circuit board (PCB). With the flexible software configuration and fast scanning of the laser beam by a galvanometer, crack-free and color printing of characters, logos and pictures was obtained on the transparent glass substrates with the use of different target materials [11]. In this paper, we will report more LIPAA applications for the DPSS Nd:YAG laser crack-free processing on the glass substrate. Glass metallization and ablation profile on the laser processing parameters (target-to-substrate distance, laser scanning speed and repetition rate) will be investigated for the better control of the microfabrication results.

## 2. EXPERIMENTAL SETUP

Figure 1 shows experimental setup of LIPAA for the crack-free laser processing of glass substrate. A 532 nm diode-pumped solid state Nd:YAG laser (Lightwave, Series 210) is used as light source. Laser beam goes through a mirror to change the light path, following through a beam attenuator to tune laser energy. Laser beam is reflected by a galvanometer, which can scan the laser beam on the target surface at a high speed with the fast rotating of the attached X & Y mirrors. The theta-lens of the galvanometer can ensure the focal plane of the laser beam during the scanning to be on the target surface. Its focal length is 10 cm and it can achieve a 60 x 60 mm scanning region on the target surface with the same focusing plane. The galvanometer is controlled by a PC through the software MarkPro. The PC is also sent out the trigger signal to control the laser shutter in real time. In order to get the laser marking of characters and logos, software CorelDRAW and AutoCAD are used to design the drawing and then convert the related drawing files into HPGL Plotter (PLT) files for the galvanometer controlling. To obtain the pictures printing on the glass, the image BMP files are first converted to the drawing vector files and then exported as a PLT file to control the laser scanning. The glass microfabricated results are observed under a high magnification microscope. For the LIPAA of the glass microfabrication, proper arrangement of the solid target and glass substrate is very important. The solid target is put behind the glass substrate. Distance between the target and substrate is adjusted by a micrometer. Laser fluence for the LIPAA is controlled inside a fluence window from the target ablation threshold to the glass ablation threshold. With this setting, the glass substrate is not damaged when the green laser light goes through it first. When the laser beam reaches the solid target, laser light absorption by the target materials induces the target ablation. Target plasma flies toward the glass substrate at a high speed (up to  $10^4$  m/s). Since the LIPAA is carried out in the ambient air, target plasma collides

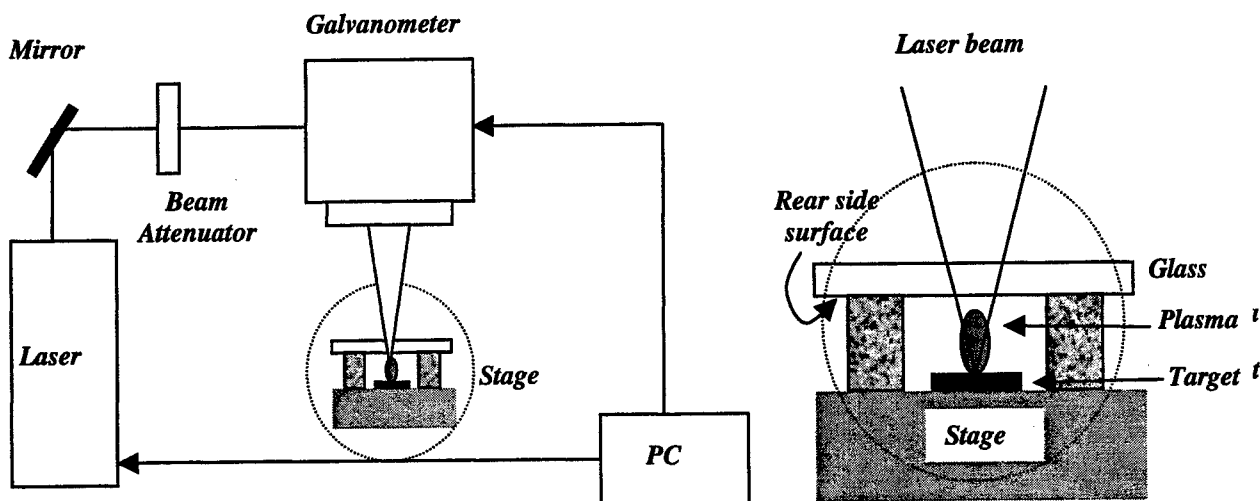


Figure 1 Experimental setup of LIPAA for the crack-free laser processing of glass substrate and configuration of target and glass positions.

with the air molecules and loses its kinetic energy. If the target-to-substrate distance is very large, it cannot reach the rear side surface of the glass substrate. There is no LIPAA effect. However, at a short target-to-substrate distance, the target plasma will arrive at the glass rear side surface during its dynamics. There are complicated interactions among the target plasma, glass materials and incident laser light. It will finally result in both the target materials deposition on the glass rear side surface and glass materials removal. Laser fluence can also be tuned by changing the target position relative to the theta-lens. Besides the target-to-substrate distance, laser scanning speed and pulse repetition rate are two important parameters for the high quality of glass microfabrication results. They can be properly set by the PC controller. Glass metallization is characterized by the metal film resistivity, which is measured by the 4-point probe method. Glass surface morphology was analyzed by an Alpha-Step 200 profilometer (Tencor Instruments) to get the information on the depth and width of the ablated crater.

### 3. RESULTS AND DISCUSSION

#### 3.1 LIPAA for crack-free laser processing on glass substrate:

Figure 2 shows the microscopic images of the characters "DSI" printed by the laser on the glass substrate with the LIPAA in air. Copper is the target material. The laser scanning speed is 10 mm/s, pulse repetition rate 1000 Hz and target-to-substrate distance 0.1 mm. It took only dozens of seconds to finish the printing. From the enlarged corner image in the central low part of character "S", it can be found that there are no microcracks along the 100  $\mu\text{m}$  wide laser lines. However, the glass substrate materials are removed inside the laser lines, which can be confirmed from the tuning of the microscopy focusing to get clear views of the ablated and non-ablated glass surfaces. The surface profiler measurement carried out later also proved the removal of the glass materials inside the laser lines. It shows that the LIPAA can be used to remove the glass materials with the good edge quality. Therefore, this technique can be applied to form different microstructures on the glass substrate with the proper software design to control the laser beam scanning geometry. Meanwhile, it can also be observed from the image that there are copper materials deposited along the laser lines. The total width of the copper line is around 300  $\mu\text{m}$ . This copper thin film is very difficult to be removed by the mechanical scrubbing. It shows that the LIPAA can be used as a new technique to form the glass metallization or metal plating on the glass substrate in air. There is one point, which needs to be taken into account is that the laser processing is in air, the deposited film is actually the metal oxide thin film and the film resistivity will be higher than the pure metal film. It is due to the chemical reaction of the high temperature metal plasma with oxygen molecules in air. With the LIPAA inside the good vacuum, the pure metal film can be obtained.

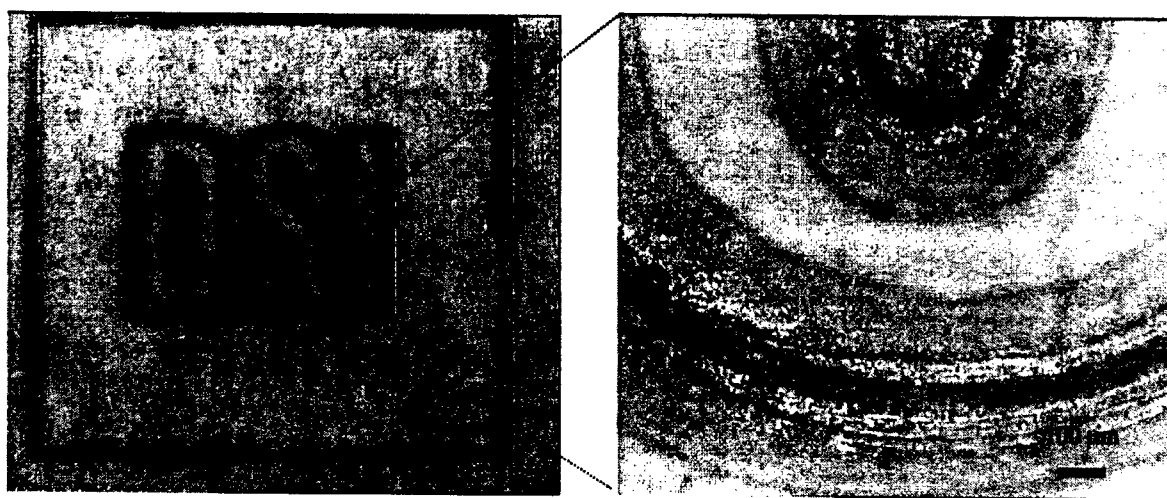


Figure 2 Microscopic images of the characters "DSI" printing on the glass substrate with the LIPAA in air. Copper is the target material.

Figure 3 (a) shows microscopic image of different color and tone Chinese characters printing on the glass substrate with the LIPAA in air. It is clear that each stroke of the Chinese characters is very smooth. It demonstrates the flexibility of the LIPAA in the characters printing. Different target materials can result in different color characters printed, for example, copper for red color and SiC for black color. By changing the laser fluence and target-to-substrate distance, different tones of the printing are obtained due to different target materials deposited on the glass substrate. Figure 3 (b) shows the characters "EMRS 2001" engraved on the glass substrate with the LIPAA after the surface cleaning to remove the target materials deposited inside and along the laser lines. It is clear that the characters are clearly engraved on the glass surface. There are not microcracks along the laser lines, especially along the curve laser lines. Furthermore, there is no big difference in the light transmission between the ablated and non-ablated glass surfaces. It brings in a high potential to fabricate the microstructures on the glass surface with the simple modification of the laser scanning geometry. LIPAA experiment shows that the high quality glass processing (edge, width and depth) is closely related to the laser processing parameters, which will be discussed in the later part of this paper.

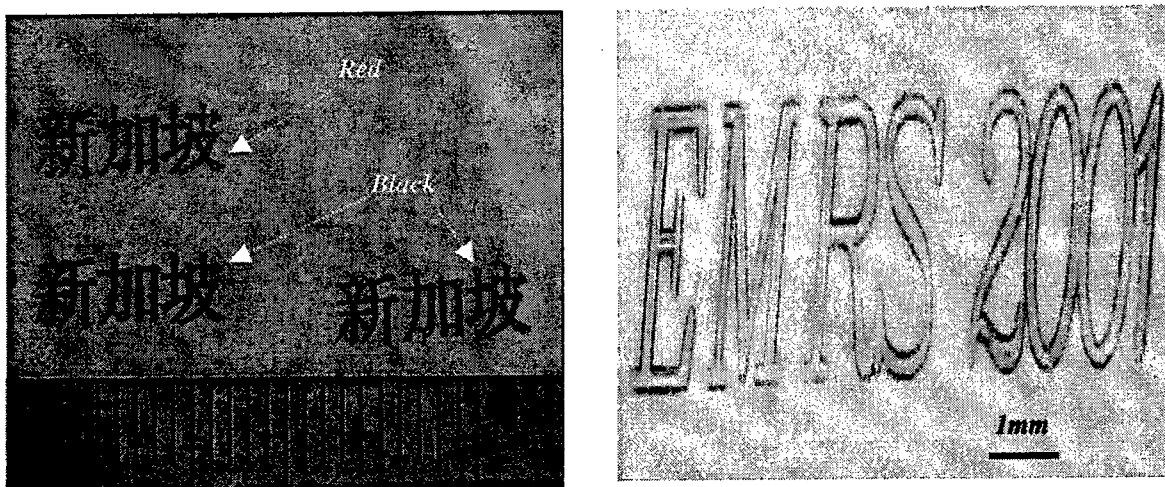


Figure 3 Microscopic images of different color Chinese characters printing on the glass substrate (a) and characters "EMRS 2001" engraved on the glass substrate after the surface cleaning with the LIPAA in air.

Figure 4 (a) shows the SEM image of the copper particles deposited on the glass substrate during the LIPAA in air. It can be observed that the copper particle size is ranging from 300 nm to 12  $\mu\text{m}$ . LIPAA is also one of the metal target ablation. It was reported that carbon and tungsten oxide nanoparticle with the size less than 10 nm could be generated during the laser ablation of the targets in air. The particle size depends on the laser fluence. With the fine tune of the laser parameters, the LIPAA can be used to obtain target nanoparticles on the glass surface. With some equipment setup, the LIPAA in a good vacuum can be applied to form nanostructuring on the glass surface with the nanodeposition of the target nanoparticles generated in the ablation. This is one of the new applications of the LIPAA in the near future. The other new applications of the LIPAA would be the laser doping of the transparent substrate. Figure 4 (b) shows microscopic image of the glass substrate after the copper particle removal. It can be seen that the glass surface was modified after the LIPAA with some copper particle ranging from 300 nm to 2  $\mu\text{m}$  embedded inside the glass. This is why the LIPAA can be used to achieve glass ablation. Due to the interactions among target plasma, laser light and glass substrate, the target materials are doped inside the glass substrate, which modifies the glass light absorption characteristics and results in the glass processing. Since the target particle size and distribution reaching to glass surface can be controlled with the laser parameters, the finer glass surface modification with the surface roughness less than a micron can be easily obtained for the higher quality laser processing. It may also open a space for the LIPAA to get a metallic glass with the metal particle doping into the glass substrate. LIPAA application is not limited only in the visible

laser light. It can be extended to IR light. For example, CO<sub>2</sub> laser is transparent to Si. LIPAA may be applied to dope target materials into the Si substrate to form short junction device due to short heat diffusion length during the short laser pulse. We will report the LIPAA applications in these two areas soon.

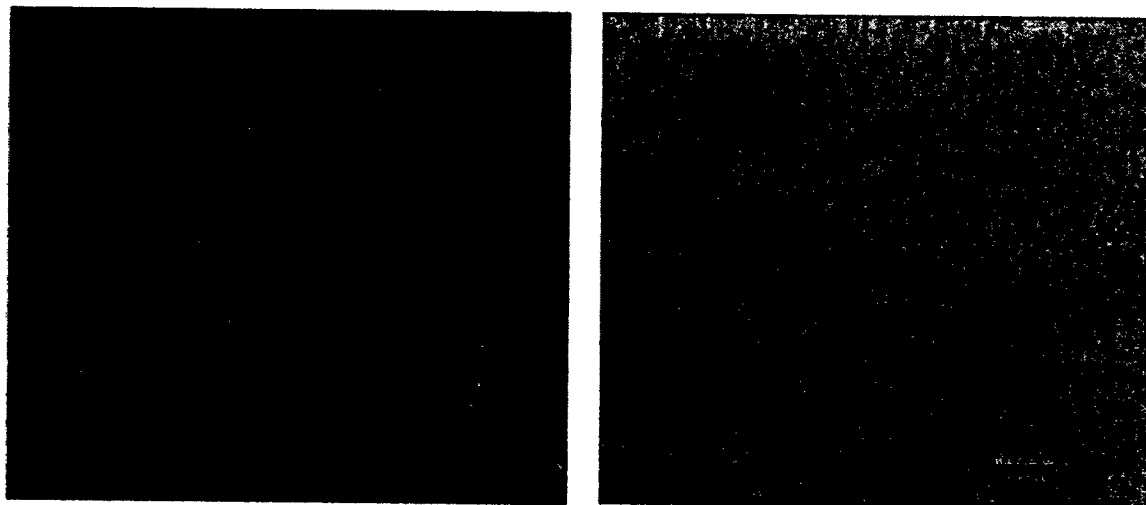


Figure 4 (a) SEM image of the copper particles deposited on the glass substrate during the LIPAA in air and (b) microscopic image of the glass substrate after the copper particle removal.

### 3.2 LIPAA for glass structuring:

Figure 5 shows the curves of ablation depth and width versus target-to-substrate distance during the LIPAA in air with the scanning speed of 10 mm/s and repetition rate of 1000 Hz. Al is the target material. It can be found that the ablation depth decreases while ablation width increases with target-to-substrate distance. During the laser ablation at a fixed

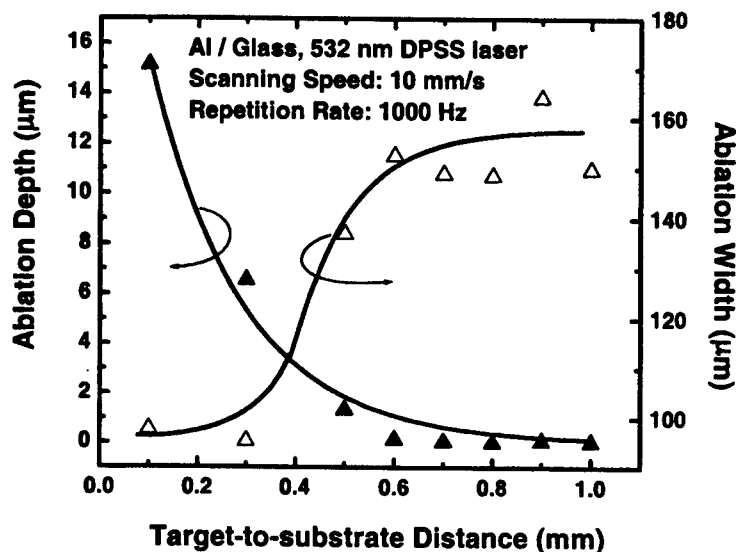


Figure 5 Ablation depth and width versus target-to-substrate distance during the LIPAA in air with the scanning speed of 10 mm/s and repetition rate of 1000 Hz. Al is the target material.



pulse repetition rate and target position, the laser fluence is a constant with the same target plasma generated. As the distance increases, the target plasma takes a longer time to reach the glass surface with a lower kinetic energy. Therefore, the plasma-assisted laser ablation becomes weaker with the smaller ablation rate. Since the plasma has more time to expand before it reaches the glass substrate, its size becomes bigger, which offers a bigger ablated crater. Figure 6 presents the dependence of ablation depth and width on laser scanning speed during the LIPAA in air with the target-to-substrate distance of 0.1 mm and repetition rate of 1000 Hz. Cr is the target material. It can be observed that the ablation depth decreases while ablation width increases slightly with scanning speed. Since the target-to-substrate, repetition rate and target position are fixed, the laser ablation, target plasma and its interactions with the glass substrate are the same. The higher scanning speed means less laser pulses overlapped together during the laser beam moving, which reduces the chances for the LIPAA for the glass processing. Therefore, the ablation depth decreases. The higher ablation width at a higher scanning speed may be due to the less interaction among the neighboring laser-induced target plasmas, which provides more free space for the target plasma to expand.

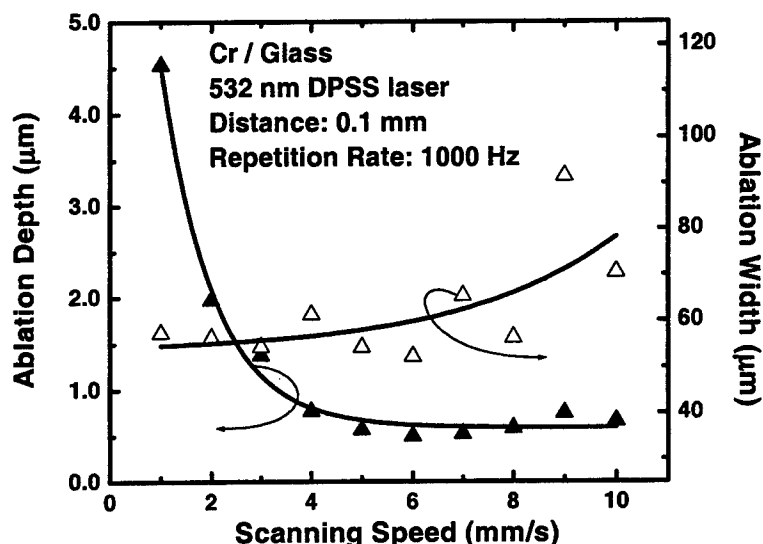


Figure 6 Ablation depth and width versus scanning speed during the LIPAA in air with the target-to-substrate distance of 0.1 mm and repetition rate of 1000 Hz. Cr is the target material.

Figure 7 shows ablation depth and width as a function of repetition rate during the LIPAA in air with the target-to-substrate distance of 0.1 mm and scanning speed of 1 mm/s. Ti is the target material. It is clear that both the ablation depth and width increase as the repetition rate increases up to 2000 Hz and then they tend to decrease as the repetition rate increases further. For a better explanation of this phenomenon, laser output pulse energy as a function of repetition rate for the 532 nm DPSS Nd:YAG laser was measured and the curve is shown in Fig. 8. Different from the excimer laser and lamp-pumped Nd:YAG laser, the laser pulse energy is different at different repetition rates. The pulse energy is a constant for the repetition rate up to 1000 Hz and then reduces as the repetition rate increases. Variation of the repetition rate leads to the change of both laser pulse energy (different plasma generation) and the number of laser pulses for the LIPAA. At the low repetition rate (less than 1000 Hz), the plasma is the same since the laser pulse energy, distance, scanning speed and target position are fixed. Higher repetition rate offers more laser pulses for the LIPAA, which leads to the higher ablation depth and width. As the repetition rate increases higher than 1000 Hz, the plasma becomes weaker due to lower laser pulse energy, which tends to decrease ablation rate and width. It balances with the increase of the ablation rate and width due to more laser pulses for the LIPAA, which leads to the maximum laser ablation at the repetition rate of 2000 Hz. As the repetition rate increases further, the plasma becomes much weaker and may not have enough kinetic energy to take part in the LIPAA. Therefore, the ablation is weaker with the lower ablation rate and width.

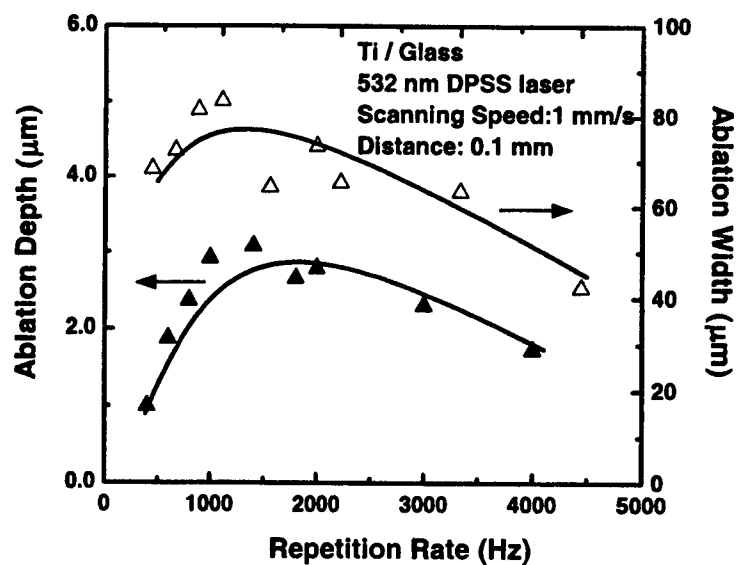


Figure 7 Ablation depth and width versus repetition rate during the LIPAA in air with the target-to-substrate distance of 0.1 mm and scanning speed of 1 mm/s. Ti is the target material.

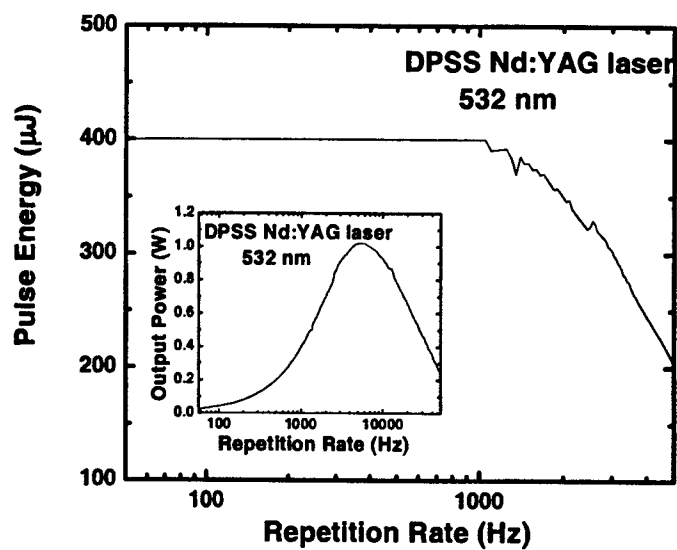


Figure 8 Output laser pulse energy as a function of repetition rate for the 532 nm DPSS Nd:YAG laser.

### 3.3 LIPAA for glass metallization:

To study the metal film conductivity, the LIPAA was applied to form a rectangle in the size of 5 mm x 10 mm on the glass substrate for the 4-point probe measurement. Since the film is actually the metal oxide film and the film thickness varies greatly, the value of the resistivity measured can only be used as a reference. The objective is to study how the laser parameters influence on the metal film conductivity as a hint for the further research.

Figure 9 shows the dependence of resistivity versus scanning speed during the LIPAA in air with the target-to-substrate distance of 0.1 mm and repetition rate of 1000 Hz. Cr is the target material. It can be found that the resistivity increases with the scanning speed. It is due to less laser pulse overlapping at a higher scanning speed, which causes the less metal particles deposition on the glass substrate and higher resistivity. Figure 10 presents the curve of resistivity versus target-to-substrate distance during the LIPAA in air with the scanning speed of 10 mm/s and repetition rate of 1000 Hz. Al is the target material. It is clear that the resistivity increases as the target-to-substrate distance. This is because at the higher distance between the target and glass substrate, the target plasma takes a longer time to reach the glass substrate with the lower kinetic energy. Some big and low kinetic energy target plasma species will lose the chance to reach the glass substrate to contribute the metal film conductivity, which results in the higher resistivity at a higher distance.

Since both the laser pulse number and laser output pulse energy change with the repetition rate, variation of the resistivity with the repetition rate would be more complicated, as shown in Fig. 11. It can be found that the resistivity reduces as the repetition rate increases up to 2000 Hz. It is attributed to the more target materials ablated at a higher laser fluence and more laser pulses. However as the repetition rate increases further, the laser pulse energy reduces with the less target materials deposition. It leads to the high resistivity and balances with the more laser pulses to deposit more target materials on the glass substrate. This brings about the lowest resistivity and best conductivity of the metal film. As the repetition rate keeps increasing, the target plasma becomes much weaker and leads to little target materials deposition even though the more laser pulse irradiation.

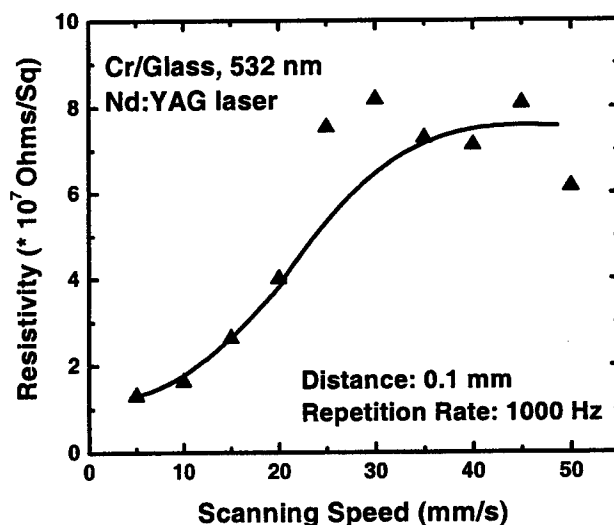


Figure 9 Resistivity versus scanning speed during the LIPAA in air with the target-to-substrate distance of 0.1 mm and repetition rate of 1000 Hz. Cr is the target material.

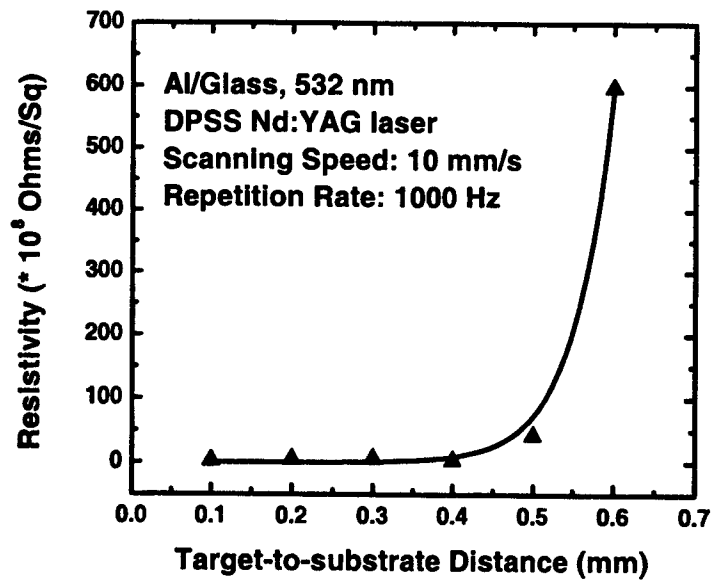


Figure 10 Resistivity versus target-to-substrate distance during the LIPAA in air with the scanning speed of 10 mm/s and repetition rate of 1000 Hz. Al is the target material.

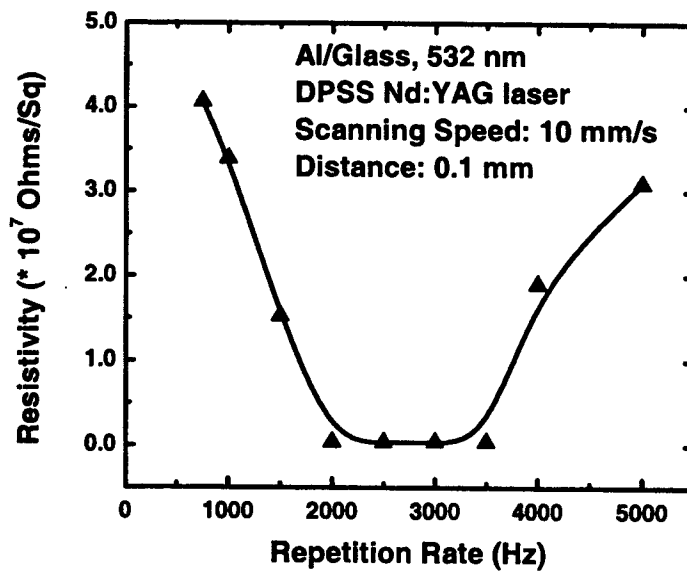


Figure 11 Resistivity versus repetition rate during the LIPAA in air with the target-to-substrate distance of 0.1 mm and scanning speed of 10 mm/s. Al is the target material.

#### 4. CONCLUSIONS

A 532-nm diode-pumped solid state Nd:YAG laser-induced-plasma-assisted ablation was used to achieve the crack-free laser processing of glass substrate. With the laser fluence in a region from the target ablation threshold to the glass ablation threshold, the laser light goes through the glass substrate first and then induces the target ablation. The target plasma flies towards the glass substrate at a high speed. At a short target-to-substrate distance, there are the complicated interactions among the target plasma, incident laser light and glass substrate at the rear side surface of the substrate. It results in both the target materials deposition and glass materials removal. It is concluded from the experiment results that: (1) ablation depth and metal film conductivity decrease while ablation width increases with target-to-substrate distance; (2) ablation depth and metal film conductivity also decrease while ablation width increases slightly with scanning speed; and (3) ablation depth, width and metal film conductivity increase with the repetition rate up to 2000 Hz and then decrease with the further increase of the repetition rate. With the proper tuning of laser beam scanning speed, pulse repetition rate and target-to-substrate distance, high quality of glass microfabrication can be obtained. With different target materials, different colors and different tones of laser printing on the glass substrate can be achieved. The potential applications of the LIPAA technique in the device doping and nanoparticle generation and nanostructuring are also discussed.

#### REFERENCES

1. K.O. Hill, B. Malo, F. Bilodeau, D.C. Jhonson and J. Albert, "Bragg gratings fabricated in monomode photosensitive optical fiber by UV exposure through a phase mask", *Appl. Phys. Lett.* **62**, pp. 1035-1037, 1993.
2. K.M. Davis, K. Miura, N. Sguimoto and K. Hiro, "Writing waveguides in glass with a femto-second laser", *Opt. Lett.* **21**, pp. 1729-1933, 1996.
3. P.R. Herman, K. Beckley, B. Jackson, D. Moore and T. Yamanishi, "Processing applications with the 157-nm fluorine excimer laser", *SPIE* **2992**, pp. 86-97, 1997.
4. K. Sugioka, S. Wada, H. Tashiro, K. Toyada and A. Nakamura, "Novel ablation of fused quartz by pre-irradiation of vacuum-ultraviolet laser beams followed by fourth harmonics irradiation of Nd:YAG laser", *Appl. Phys. Lett.* **65**, pp. 1510-1512, 1994.
5. E. Dupont, X. Zhu, S. Chiu, M. Buchanan, M. Gao, H.C. Liu, and P.B. Corkum, "In situ repair of optoelectronic devices with femto-second laser pulses", *Semicond. Sci. Technol.* **15**, pp. L15-L18, 2000.
6. K. Hirao, and K. Miura, "Writing waveguides and gratings in silica and related materials by a femto-second laser", *J. Non-Crys. Soli.* **239**, pp. 91-95, 1998.
7. K. Sugioka, J. Zhang and K. Midorikawa, "Hybrid laser processing of micromachining for hard materials", *SPIE* **3822**, pp. 6-17, 1999.
8. J. Zhang, K. Sugioka, and K. Midorikawa, "Direct fabrication of microgratings in fused quartz by laser-induced-plasma-assisted ablation with a KrF excimer laser", *Opt. Lett.* **23**, pp.1486-1490, 1998.
9. M.H. Hong, K. Sugioka, Y.F. Lu and K. Midorikawa, "Optical diagnostics in laser-induced plasma-assisted ablation of fused quartz", *SPIE* **4088**, pp. 359-362, 2000.
10. M.H. Hong, K. Sugioka, Y.F. Lu, K. Midorikawa, and T.C. Chong, "Laser microfabrication of Transparent hard materials and its signal diagnostics", *Appl. Sur. Sci.* (in press).
11. M. H. Hong, K. Sugioka, D.J. Wu, L.L. Wong, Y.F. Lu' K. Midorikawa, T.C. Chong, "Laser-induced-plasma-assisted ablation for glass microfabrication", *SPIE* **4595**, pp. 138-146, 2001.

# PRODUCTION OF INNOVATIVE GEOMETRIES WITH UV LASERS

Andreas Ostendorf, Christian Kulik and Uwe Stute

Laser Zentrum Hannover e.V., Hollerithallee 8, D-30419 Hannover, Germany

## ABSTRACT

Excimer lasers are proven tools to machine 2½-D microstructures with variable lateral dimensions. Therefore developed techniques are limited in the vertical dimension since material is removed along the optical axis perpendicular to the target plane.

This paper presents 3-D structures produced with such UV-lasers. In contrast to optical set-ups for machining 2½-D structures, this approach tilts the target plane and ablates material underneath the target superficies. The tilting angle adds two major difficulties to laser machining: the distortion of the image on the target and the alteration of the ablation cross section. These two difficulties were studied in experiments with different tilting angles  $\beta_L$  between target plane and optical axis of the laser. The impact of  $\beta_L$  was identified on the achieved geometry of 3-D structures. A first theoretical approximation integrates the material reflectance and the target cross-section in order to give an estimation of the influence of further effects within the ablation process.

This theoretical analysis is a starting point for producing undercutting structures and can additionally be applied to changeable shaped surfaces. Such complex 3-D structures have the potential to be used in micro-tribology as well as in micro guidance systems and are estimated being an important step in micro-mechanics.

## INTRODUCTION

Due to the increasing market of systems using micro-components, micro-electronic and more recently micro-mechanical components, the use of laser machining increases with this evolution. Excimer lasers are well adapted tools when chemical resistant materials such as polymers, ceramics or glass are required to be structured with high quality [BÜT91; ALV99, MOM95]. Developments of micro-structures in silicon have been carried out for the semiconductor industry and many of these developments can nowadays be adapted to different materials by lasers machining. A further advantage of laser machining is the flexibility of the set-up thus little and medium series can be produced with acceptable costs.

Excimer lasers have a quasi top hat beam profile. This can especially be used with mask techniques to ablate areas and to obtain high surface quality. Functional surfaces with nearly optical quality can directly be structured with optimized arrangements for the single pulse ablations (ablation strategies) [OST99a, OST99b]. Further developments in ablation strategies have improved efficiency and minimized working time by optimization and automation of pulse shaping [TÖN99a]. In consequence the demand of short processing time and high surfaces quality can be fulfilled by excimer lasers. The recent implementation of F<sub>2</sub> laser extends the wavelength to be used down to 157 nm. Since then, further innovative materials with high binding energies (e.g. PTFE, fused silica) can be machined with a sub-micron accuracy [TÖN00, OST00] and increase the high potential by adding a high number of applications.

All described techniques only permit to machine 2 ½ D structures in plane surfaces. Many aspects of laser machining are actually studied to enable the production of real 3 D functional parts. In this context undercutting structures and machining of pre-treated surface topologies are of major interest. Such structures are already used or supposed to be introduced soon in micro-mechanical systems, medical implementation techniques and telecommunication systems. In this context, UV-excimer laser are particularly competitive with their high flexibility. The high surface quality of excimer machined work pieces was studied and demonstrated [OST99a, OST99b, TÖN98, TÖN99d]. Therefore these effects can be excluded from this study and the analysis focuses on effects induced by the tilting angle  $\beta_L$ . The flexible handling of succeeding pulses allows fine structuring of complex surfaces and undercutting structures by the NC-system and the laser control. Hence, the techniques will be cost efficient for individual work pieces, small and medium series.

A further step to exploit the study of machining tilted surfaces is the treatment of pre-formed parts which get their final shape by excimer laser machining.

## 1. MACHINING TECHNIQUE TO PRODUCE 3-D STRUCTURES

This paper presents the manufacturing technique to produce 3-D structures with a KrF-excimer laser at 248 nm. In contrast to optical set-ups for machining 2½-D structures, this approach tilts the target plane and ablates material underneath the target surfaces. The arrangement of the laser ablation by pulsed laser radiation is illustrated in Figure 1a. In the study the mask technique was used to ablate an area being the projection (demagnification: 1:40) of a mask [ALV99]. The tilting of the target is also illustrated in Figure 1b.

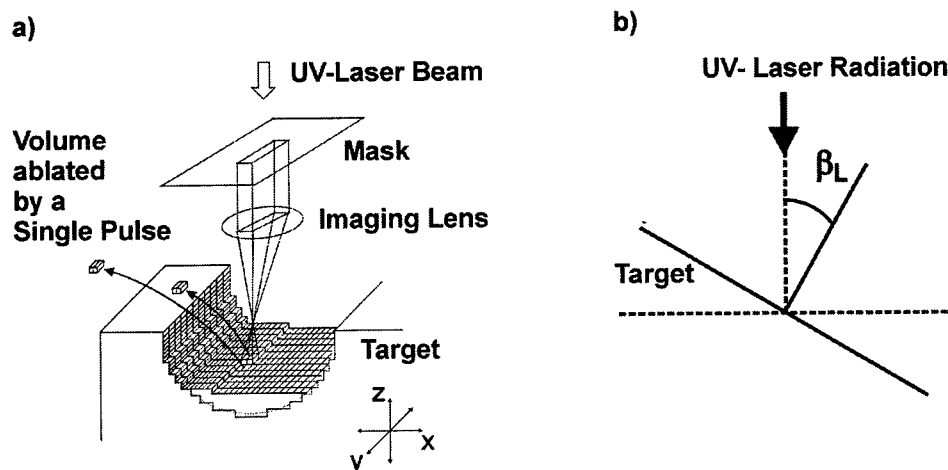


Figure 1: Arrangement excimer laser machining:  
a) Schema of ablation with single pulses b) Schema of the target rotation

The study was carried out with a Lambda Physics excimer laser series 4000. The technical specifications of the laser are given together with the process parameters in the following table.

Laser characteristics		Process parameter	
Wavelength	$\lambda_L = 248 \text{ nm}$	N.A.	0.56
Beam profile	$d_x = 11 \text{ mm}$ $d_y = 30 \text{ mm}$	Mask size	$D_x = 3 \text{ mm}$ $D_y = 6 \text{ mm}$
Divergence	$\Theta_x = 1.5 \text{ mrad}$ $\Theta_y = 4.5 \text{ mrad}$	Magnification	1:40
Max. repetition rate	$f_{p,\max} = 250 \text{ Hz}$	Rep. rate	$f_p = 50 \text{ Hz}$
Pulse duration	$\tau_p = 20 \text{ ns}$	Energy fluence	$15 \text{ J/cm}^2 \text{ (A-997)}$ $20 \text{ J/cm}^2 \text{ (F2)}$

Tabelle 1: Laser characteristics and process parameters

The tilting angle  $\beta_L$  of the target was realized with a rotation axis mounted on the linear axes of the machining center. The accuracy of the rotation axis is better than  $0.06^\circ$  with a reproducibility of less than  $0.0035^\circ$ . To reach a high number of applications, two materials (F2-glass and A997-ceramic) with high technical relevance were chosen for the experiments.

## 2. ANALYSIS OF UNDERCUTTING 3-D STRUCTURES

To perform a systematic analysis, the geometry of undercutting structures was parametrized. The analysis focuses on the effects induced by the tilting angle  $\beta_L$ , which is as well illustrated in the drawing in Figure 2 as the set of parameters to describe the entire geometry.

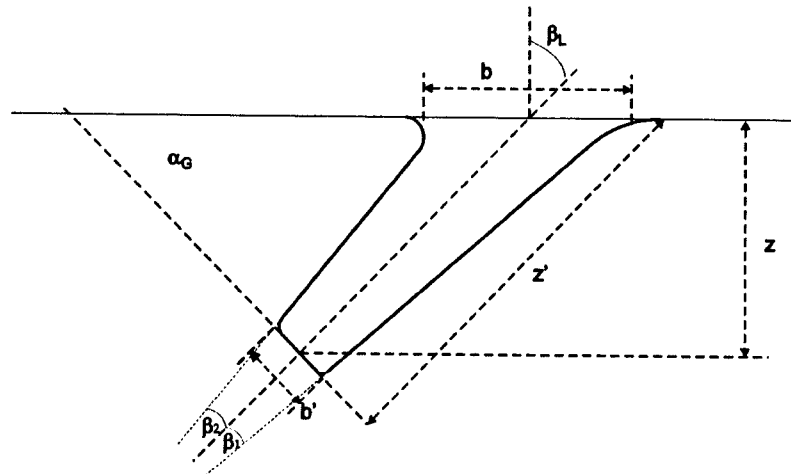


Figure 2: Model of an excimer machined undercutting structure

Geometrical measurements on undercutting structures can not be carried out from the surface e.g. with a microscope or with optical or acoustical sensors. Therefore, the polish of the cross section was used to analyze the machined

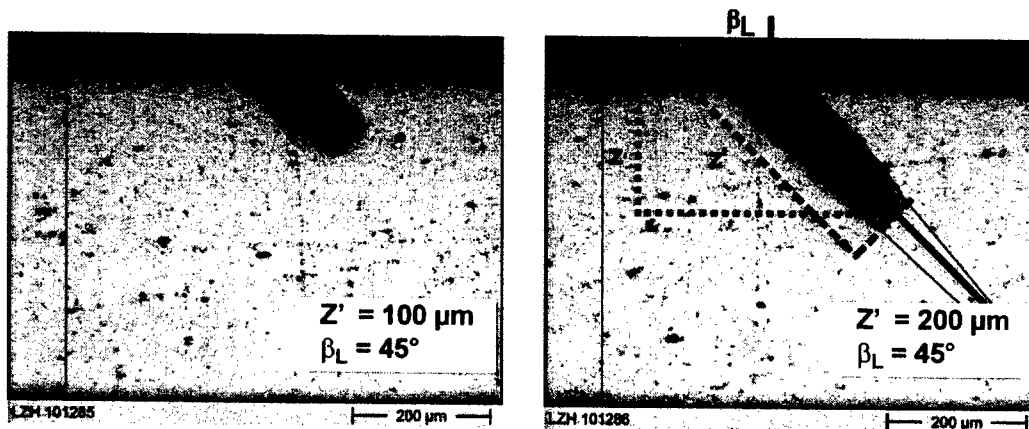


Figure 3: Polish of cross section of undercutting structures in F2

structures. An example to illustrate the analysis from the digitized images is given in Figure 3.

In order to obtain parameters which can be compared to those used to describe 2D structures, the definition of the ablation rate must be detailed. The ablation rate  $a_p$  is a parameter of major interest defined by ratio of the depth  $z$  and the number of pulses  $N$  applied. In order to quantify the ablation depth when  $\beta_L \neq 0^\circ$ , the depth  $z'$  has to be used instead of  $z$  and the averaged ablation rate becomes:

$$a_p(\beta_L) \equiv \frac{z'}{N}$$

In a first step the ablation rate  $a_p$  has been determined for a ceramic (A997) and a glass (F2). In Figure 4, the determined  $a_p$  is illustrated for different tilting angles  $\beta_L$  as a function of  $N$ .



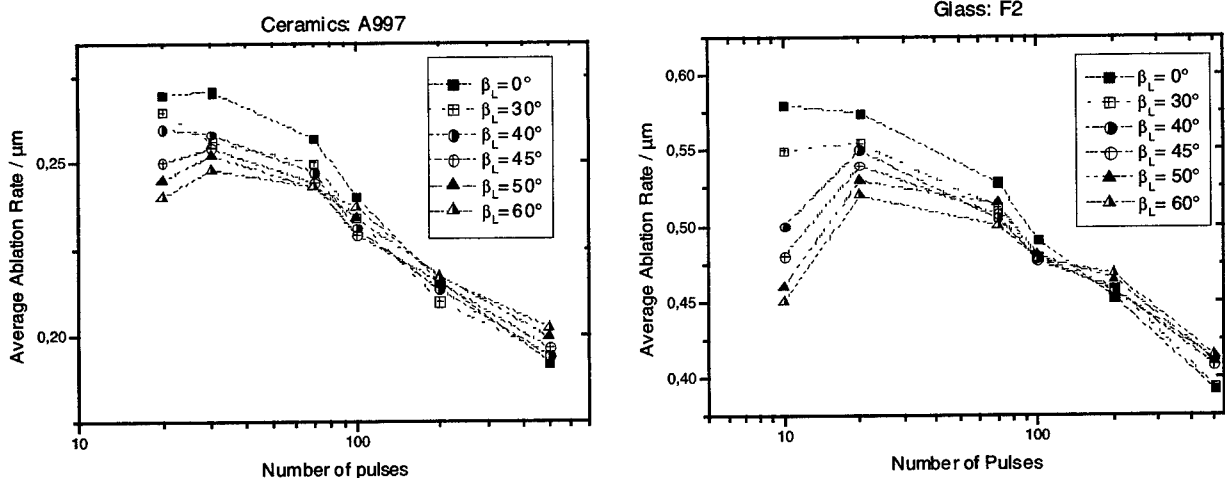


Figure 4: Dependency of the average ablation rate of two materials from number of pulses

A decreasing  $a_p$  for an increasing  $N$  was observed for both materials at any angle, when the numbers of pulses  $N$  exceeds 50. Other studies have already reported such a tendency for 2D structures and are often attributed to geometrical and plasma induced obstruction [RIN00]. The aspect ratio and the material determine the ablation rate and the depth, which can be obtained. The observation for both materials, that  $a_p$  is independent of the tilting angle  $\beta_L$  when  $N > 50$ , is considered to be due to obstruction of the laser radiation.

#### Analysis of the ablation rate by the cosine law

In contrast to deep ablations, an angle dependency was observed for little numbers of pulses. In the first step a parallel laser beam will be analyzed. The intensity of such a laser beam is inversely proportional to the illuminated area, which increases by tilting a target. The illuminated surface  $A_T$  is described by the cosine law related to tilting the target by  $\beta_L$  and the laser beam cross section  $A_L$ :

$$A_T = \frac{A_L}{\cos(\beta_L)}$$

Collimated radiation on a tilted target has thus an intensity, which must obey the cosine law and in consequence the intensity  $I_T$  on the target can be deduced from the laser intensity  $I_L$ .

$$I_T = I_L \cos(\beta_L)$$

Normalizing the cosine law using the approximation that the ablation rate  $a_p$  is directly proportion to the intensity on the target, the theoretical dependence of  $a_p$  from the tilting angle  $\beta_L$  can be computed. These dependency is illustrated in Figure 5 together with experimental results for a low numbers of pulses and different tilting angles.

It can be stated for both materials, that only with low pulse numbers a significant influence of  $\beta_L$  in the experimental data is observed. The observation made with these data correspond to the conclusions made from the data presented in Figure 4.

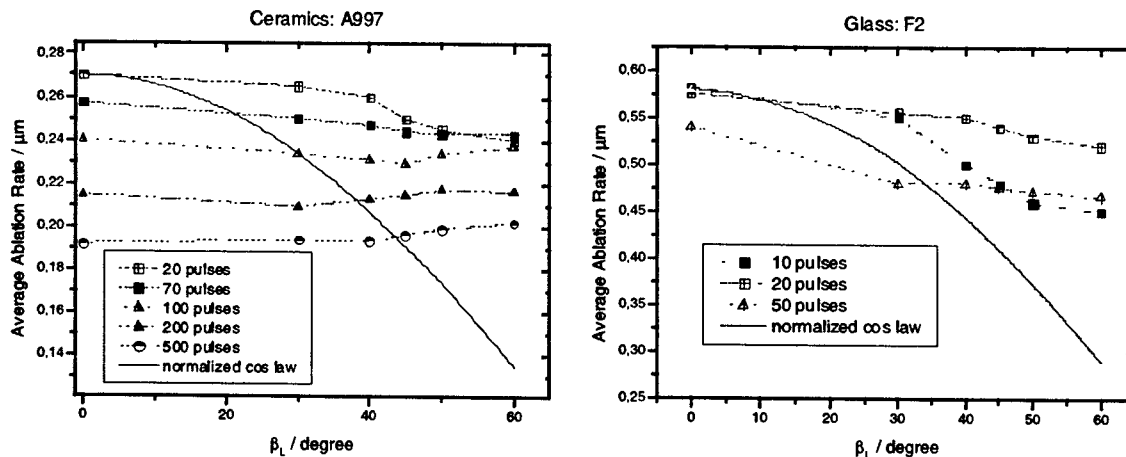


Figure 5: Dependency of the average ablation rate of two materials from the tilting angle  $\beta_L$

The experimental data do not follow the cosine law, so the assumption of a collimated laser beam may not be valid. A more realistic description of the laser beam will be introduced after an analysis of the ground angle and the consequences of the divergence of the beam will then be computed.

#### Analysis of the ground angle

To study the influence of the first pulses on the structuring tilted surfaces, the polish of cross section was investigated; the angle between the target surface and the surface on the ground of the ablated structure  $\alpha_G$  (see Figure 2) was determined. To avoid statistical uncertainties e.g. due to energy fluctuations of the laser, a high number of pulses must be applied. Either few pulses can be used to produce many samples or as it has been done for efficiency reasons, many pulses are applied to machine a few samples. Samples with  $N > 100$  were investigated. Along with the number of pulses  $N$  the tilting angle  $\beta_L$  was varied. A series of polished cross sections with the measured ground angles  $\alpha_G$  is illustrated in Figure 6. In this figure  $\beta_L$  was set to  $45^\circ$ .

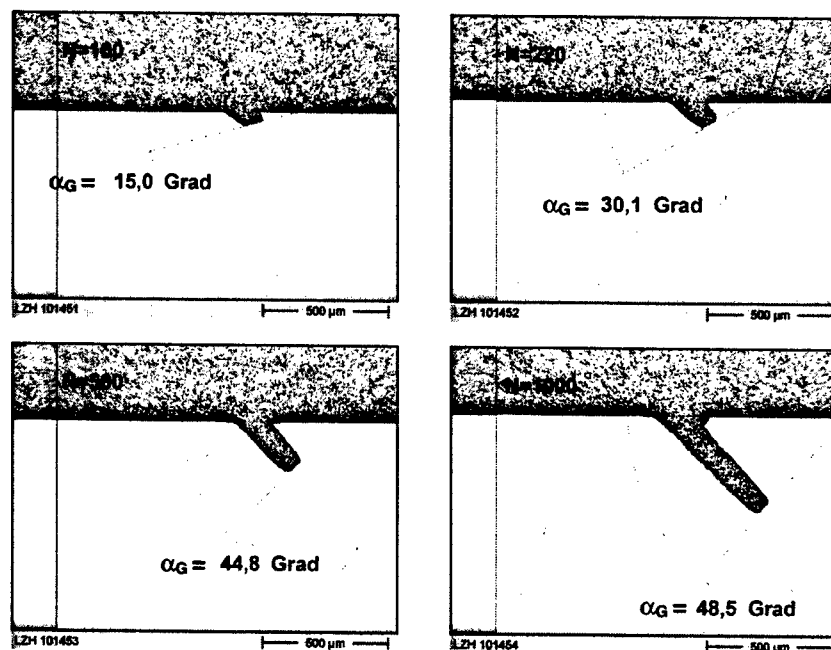


Figure 6: Variation of the ground angle in F2 for different number of pulses and a fixed tilting angle  $\beta_L = 45^\circ$

In this series the ground angle  $\alpha_G$  increases from  $15^\circ$  to  $48.5^\circ$  with an increasing depth  $z'$ . The angles  $\alpha_G$  were determined with an error of less than  $1^\circ$ . This tendency was also observed for different tilting angles  $\beta_L$  and is illustrated in Figure 9. A tilting of the ground angle is measured for the three angles  $\beta_L$ . The volume is not ablated in the same manner along the optical axis. Combining this observation with the results of the ablation rate, it can be concluded that laser radiation hitting a target under a tilting angle  $\beta_L$  ablates the material stronger on one side. This phenomena occurs even at low pulse numbers  $N \ll 50$ .

#### Analysis of the ground angle: intensity approximation due to the caustic of the laser beam

The distortion of the image on the target is a major difficulty in laser machining induced by the tilting angle. The previous considerations concerning the alteration of the ablation cross section were based on a beam hitting the target with nearly parallel angles of incidence over the beam cross section. In the following, the analysis is expanded to the caustic of the imaging optics.

The beam shaping is made with a field lens having a focal length of  $f_{FL} = 2000$  mm, placed at a distance of 2020 mm in front of the imaging lens. With the mask size on the y-axis  $D_Y = 6$  mm, the numerical aperture was calculated to be  $N.A. = 0.56$ . With the focal length of the imaging lens, the rays on the caustic of the beam hit a target with  $\beta_L = 0^\circ$  at an angle of  $\alpha_{BL} = 34.4^\circ$ . For a tilted target this angle has to be subtracted on the one side and added on the other side. The caustic in relation to the tilting angle is illustrated in Figure 7.

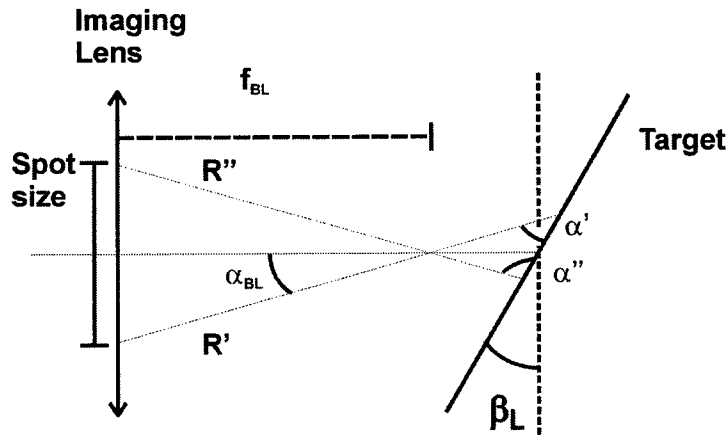


Figure 7: Influence of the target tilting on the angles of incidence on the target

For a ground angle  $\alpha_G = 0^\circ$ , the two angles ( $\alpha'$ ,  $\alpha''$ ) delimiting the range of the angles of incidence can be calculated from the target tilting  $\beta_L$  and the caustics angle  $\alpha_{BL}$ :

$$\alpha' = 90^\circ - \beta_L - \alpha_{BL} \quad \alpha'' = 90^\circ - \beta_L + \alpha_{BL}$$

Target tilting combined with geometrical optics in mask techniques induced in the experimental values a height difference  $\Delta_H$  at the two edges of the image as illustrated in Figure 9. The used approximation attributes the ablation rate and hence this height difference to the variation in the intensity. At the edges of the ablated volume, this variation in the intensity on the target is related to the angles ( $\alpha'$ ,  $\alpha''$ ) by the cosine law

$$I_T(\alpha') = I_L \cos(90^\circ - \alpha') \quad I_T(\alpha'') = I_L \cos(90^\circ - \alpha'')$$

Using the ablation rate  $a_p$  on the optical axis of the laser radiation, the height difference  $\Delta_H$  can be computed for the individual pulses based on the caustic and the cosine law. The height  $\Delta_H$  related to  $\beta_L$  becomes:

$$\begin{aligned} \Delta_H(\beta_L) &= a_p(\beta_L, N) \{ \cos(90^\circ - \alpha'') - \cos(90^\circ - \alpha') \} \\ &= a_p(\beta_L, N) \{ \cos(\beta_L - \alpha_{BL}) - \cos(\beta_L + \alpha_{BL}) \} \end{aligned}$$

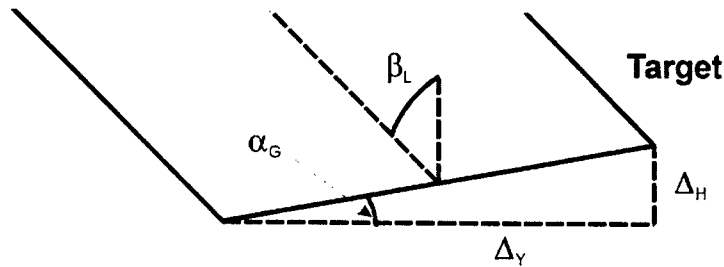


Figure 8: The height difference  $\Delta_L$  and the ground angles  $\alpha_G$  for an ablated structure

The ground angle of the first pulse can be computed with  $\Delta_H$  and the projected image diameter  $\Delta_Y$  according to Figure 8 by

$$\alpha_G(N=1, \beta_L) = \arctan\left\{\frac{\Delta_H}{\Delta_Y}\right\}$$

Where the projected image diameter  $\Delta_Y$  can be derived from the measured image diameter of  $\Delta_{Y,IM} = 150 \mu\text{m}$  and the tilting angle  $\beta_L$  by

$$\Delta_Y = \Delta_{Y,IM} / \cos(\beta_L)$$

With these parameters, an estimation of  $\alpha_G$  can be carried out taking a fixed ablation rate  $a_p(N=20, \beta_L = 45^\circ) = 550 \mu\text{m}$  taken from the data presented in Figure 4: An iteration has to be applied for computing the ground angle  $\alpha_G(N)$  at arbitrary pulse numbers  $N$ . Therefore the equation to calculate the height difference  $\Delta_H(N)$  has to be extended by the using the ground angle  $\alpha_G(N-1)$  of the preceding pulse:

$$\Delta_H(\beta_L, N) = a_p(\beta_L, N) \{ \cos(\beta_L - \alpha_G(N-1) - \alpha_{BL}) - \cos(\beta_L - \alpha_G(N-1) + \alpha_{BL}) \}$$

To test this iteration the ground angle values were computed and compared with the results for F2 with 3 different tilting angles  $\beta_L$  (Figure 9).

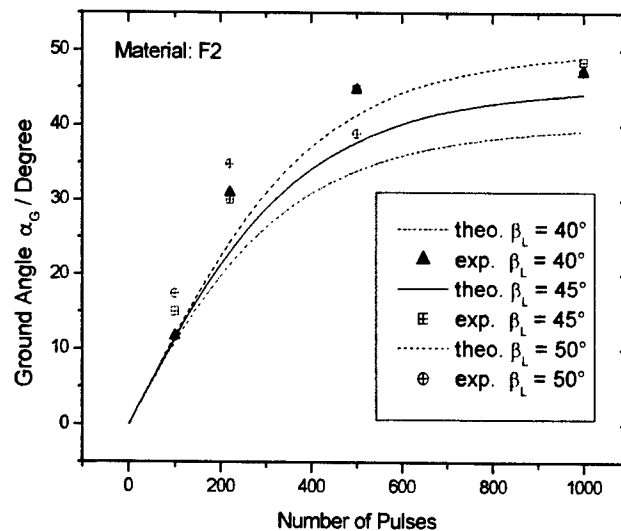


Figure 9: The ground angle  $\alpha_G$  of drilled structures in F2; theoretical values and measured data for different number of pulses  $N$  and tilting angle  $\beta_L$

Based on the theoretical results, it can be stated, that the ground angles determined in the experimental data is strongly related to the numerical aperture, although these angles are underestimated. Since the approximation does not integrate reflection, which increases with the angle of incidence, an improvement for further modeling is expected by a more detailed description of an angular dependent ablation rate.

### 3. FIRST INNOVATIVE GEOMETRY WITH ITS APPLICATIONS PRODUCED WITH THE NEW TECHNIQUE

3-D structures have been produced to demonstrate prospective advances in microsystems technology which can be achieved with undercutting structures. Two demonstrators have been selected: a free standing needle, which can be used as a vibration element in actuator or sensor technology and a micro-cavity for enhancements in the tribologic functional parts.

The micro needle based system can already be machined by selective wet edging in silicon. With new laser machining such structures in piezo-electrical ceramics are of major interest, since they can directly be integrated in electronic devices.

In tribology, micro-cavities can store lubricant and reduce wear due to friction. These 2D structures are already used e.g. in the automotive industry [ABE 01] nevertheless 3D cavities are advantageous when the cavity can not be refilled during the life time of mobile components. Especially in micro systems, lubrication must mostly be carried out before the assembly of the components. In order to demonstrate the machining of an example, a 3D micro cavity was produced and will be described below.

#### Micro needle based system

The vibrating part of a typical sensor is usually a detached triangle over a length in the order of some millimeters. The detached volume acts as an inert mass and must therefore be precisely adjusted to the target resonance frequency. The dimensions of the programmed geometry are given in Figure 9.

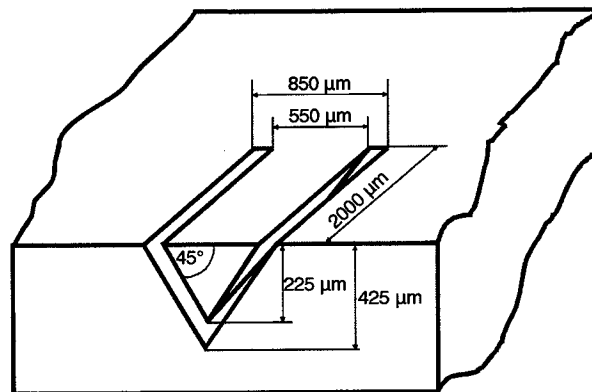


Figure 10: Model Machining of a free standing needle

The structures were machined in the two investigated materials (ceramics and glass). The achieved structures are given in Figure 11. The surface quality of the structure is considered to be sufficient for this application, when machined in A997. Studies on 2D structures recently revealed, that the process parameters for F2 can be improved by ablating with a lower pulse energy at shorter wavelengths e.g. with 157 nm.

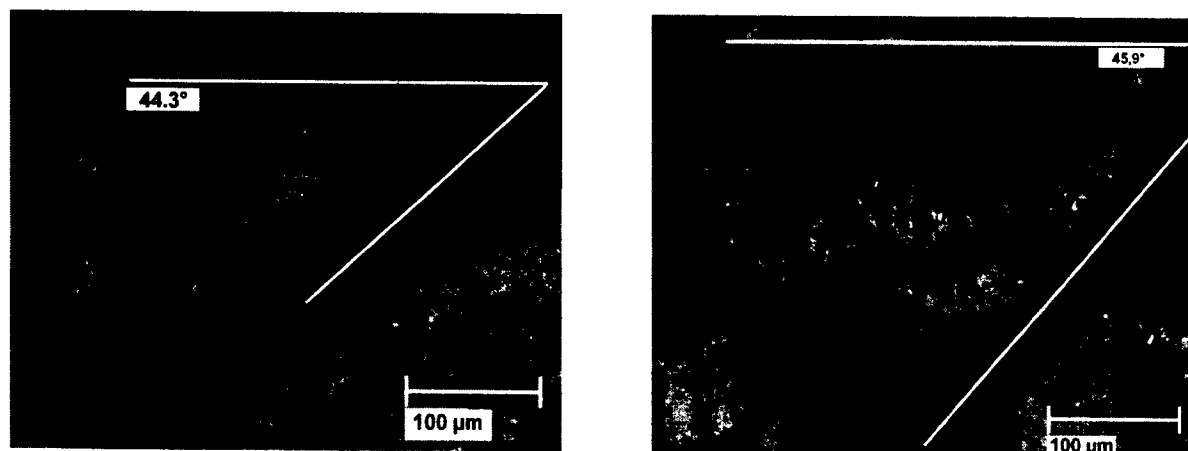


Figure 11: Machining of a needle by use of undercuttings: on the left A-997, on the right :F2

### Micro-cavities in tribology

The machined micro-cavities were planned to be symmetrical with a ground composed by drilling channels with different tilting angles. The depth of these channel was planned to be on a spherical surface as shown in the drawing in Figure 12a) with the machined structure in the ceramic. The sequence to drill into the target is marked by numbers from 1 to 9. The structure was machined by drilling each time as far as possible away from the drilling made before: first drilled along the two borders (No. 1 & 2 in Figure 12a) and then in the middle of the structure. After the first drilling, the number of pulses must carefully be adjusted for the succeeding ablations to obtain depths being all on a spherical surface.

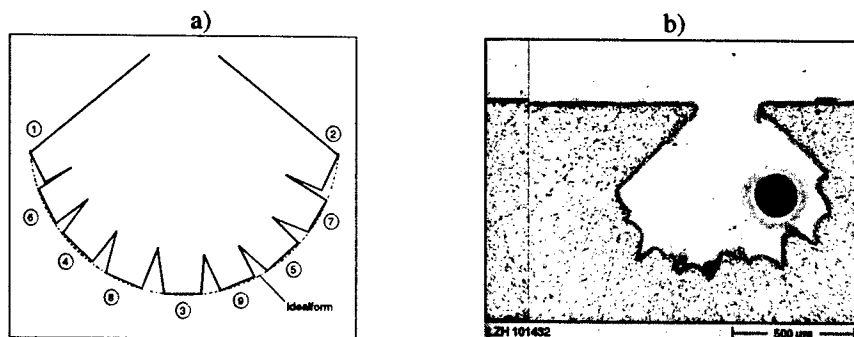


Figure 12: Machining of a buried cavity: a) Model with the numbered drilling sequence b) Machined in ceramics (A997)

The achieved cavity in ceramics (Figure 12a) showed well defined borders and flank angles. Although the difficulty to adjust the pulse number for the channels led to a less defined ground surface, the averaged depth of the cavity was sufficient for a potential storage of lubricant and demonstrates well the potential of such a undercutting structure.

### Outlook

Further developments will optimize the reachable surface quality of 3D structures. This optimization is a important step towards further applications such as individual reworking of medical implementation products. Furthermore, an adaptation of the theory and machining with other wavelength such as 193 nm and 157 nm will be performed. With those solutions the 3D-structuring of innovative materials such as PTFE and fused silica will be possible.

## CONCLUSION

Machining of undercutting structures in ceramics and glass was described and analyzed. The influence of the tilting angle  $\beta_L$  on the structures geometry was investigated in a fundamental study. For a low number of pulses, the ablation rate  $a_p$  and the ground angle  $\alpha_G$  were influenced by  $\beta_L$  due to the numerical aperture of the machine working with the applied mask technique.

Undercutting structures are usually machined with a high number of laser pulses since they normally exceed depths of more than 12-20  $\mu\text{m}$ . This means for an industrial use of this technique that the influence of tilting angles on the ablation rate and on the ground angle is of less importance. The potential of undercutting structures has been demonstrated for a sensor and a tribologic application. With the great variety of materials which can be machined with excimer lasers, this technique is expected to be important for specialized applications in microsystems.

This study leads also to new potential applications for structures with little depth exploiting the numerical aperture of the system. A defined angle between the surface and the machined structure can be adjusted by the geometry of the laser beam caustic.

## ACKNOWLEDGEMENT

The authors would like to thank the DFG for financial support (Proj. No. OS 188 / 1-1).

## REFERENCES

- [ABE 01] ABELN T., KLINK U.: Laserstrukturieren zur Verbesserung von tribologischen Eigenschaften von Oberflächen, Stuttgarter Laser Tage 2001
- [ALV99] ALVENSLEBEN, F. VON; KÖRBER, K.; SCHÄFER, K.: Maskentechniken in der Lasermaterialbearbeitung. In: Feinwerktechnik, Mikrotechnik, Mikroelektronik. Jahrg. 107, November 1999
- [BÜT91] BÜTTGENBACH, S.: Mikromechanik, Einführung in Technologie und Anwendung, Teubner Studienbücher, Stuttgart 1991
- [MOM95] MOMMSEN, J.: Verfahren des automatisierten Mikroabtrags mit Excimerlasern, Dr.-Ing. Diss., TU Hannover, 1995
- [OST99a] OSTENDORF, A.; STAMM, U.; RUMSBY, P. ET AL.: LZH e.V.; Lambda Physik; Exitech Ltd.; REOSC; Relais Electroniques Deutsch: New Machining Technique for Optical Components using Photoablation (MATOC). Publishable Final Summary. Project No. BE 95/1202 im Auftrag der Europ. Commission, 1999
- [OST99b] OSTENDORF, A. ET AL.: Produktionsverfahren für die flexible Mikrostrukturierung passiver optischer Bauteile. Abschlussbericht FZKA-PFT 198, Laser Zentrum Hannover e.V., Projektträgerschaft Forschungszentrum Karlsruhe, 1999
- [OST00] OSTENDORF, A.: Untersuchungen zum Präzisionsabtrag mit VUV-Laserstrahlung und ultrakurzen Laserpulsen. Dr.-Ing. Diss., TU Hannover, 2000
- [PFL00] PFLEGING, W. ET AL.: Lasergestützte Entwicklung von mikrostrukturierten Komponenten und Abformwerkzeugen. In: 4. Statuskolloquium des Programms Mikrosystemtechnik, Forschungszentrum Karlsruhe, 2000
- [RIN00] RINKE M.: Glasbearbeitung mit ArF-Laserstrahlung. Dr.-Ing. Diss., TU Hannover, 2000

- [TÖN97] TÖNSHOFF, H.K.; OVERMEYER, L.; OSTENDORF, A.: General machining concept for producing micro-optics with high power UV-lasers. In: Conference on Excimer lasers, optics and applications, Proceedings of SPIE, San Jose, 1997
- [TÖN98] TÖNSHOFF, H.K. ET AL: Comparison of 3-D surfaces produced by 248 nm- and 193-Excimer Laser Radiation. In: Proceedings of SPIE, Intelligent Systems and Advanced Manufacturing, Boston, 1998
- [TÖN99a] TÖNSHOFF, H.K. ET AL: Optimierung der Bearbeitungszeit für die Mikrostrukturierung mit gepulsten UV-Lasern. In: LaserOpto, April 1999
- [TÖN99b] TÖNSHOFF, H.K.; A. OSTENDORF, WILLMANN, G. ET AL: Precision Machining using UV and Ultrashort Pulse Lasers. In: Proceedings of SPIE, Design, Test and Microfabrication of MEMS and MOEMS, Paris, 1999
- [TÖN99c] TÖNSHOFF, H.K.; VON ALVENSLEBEN, F.; KULIK, C.: Advanced 3D-CAD-Interface for Micro Machining with Excimer Lasers. In: Proceedings of SPIE, Design, Test and Microfabrication of MEMS and MOEMS, Paris, 1999
- [TÖN99d] TÖNSHOFF, H.K., ET AL: Machining Concepts for three-dimensional Micro-Structuring with pulsed UV-Lasers. In: Proceedings of Microengineering, Stuttgart 1999
- [TÖN00] TÖNSHOFF, H.K.; F. VON ALVENSLEBEN, F.; OSTENDORF, A. ET AL: 3-D micro structuring with F2-Lasers. In: EOS / SPIE Symposion on Applied Photonics, Glasgow, Scotland 2000
- [WAI99] WAIS, J.; PLAMANN, C.; CZARSKE, C.: Rapid fabrication of robust phase transmission gratings in optical glass by excimer laser ablation. In: LaserOpto, January 1999
- [WEN99] WENDA, BECK, HÜNTRUPP ET AL: Möglichkeiten und Grenzen der Mikrozerspanung. In: F&M Feinwerktechnik, Mikrotechnik, Mikroelektronik, Heft 11/99, Carl Hanser Verlag, München, 1999



# Microscale Bending of Brittle Materials using Pulsed and CW Lasers

Richard X. Zhang, Xianfan Xu\*  
School of Mechanical Engineering  
Purdue University  
West Lafayette, IN 47907

## ABSTRACT

This work demonstrated using pulsed and CW lasers for microscale bending of brittle materials, including glass, ceramic, and silicon. Based on the absorption characteristics of these materials, different types of lasers were used for achieving bending. Experimental studies were conducted to find out relations between bending angles and laser operation parameters.

**Keywords:** Laser bending, brittle materials, thermal stress, pulsed laser, CW laser

## 1. INTRODUCTION

Laser bending or laser forming is a newly developed, flexible technique to modify the curvature of sheet metals or hard materials. There are several mechanisms causing laser bending, which are determined by the thermophysical properties and geometry of the specimen, and laser processing parameters. Common laser bending mechanisms include the temperature gradient mechanism and the buckling mechanism [1]. For the temperature gradient mechanism, only the surface layer is heated (thus there is a temperature gradient with the highest temperature at the surface), the residual stress and strain are concentrated in the near surface region. The residual strain is compressive, causing the specimen to bend toward the laser beam. This type of bending is preferred when a consistent bending direction is required. If laser heating is uniform across the thickness of the specimen, the specimen will bend just like a beam under compression. In this case, bending is caused by the buckling mechanism and the bending direction depends on the pre-curvature and the initial stress of the specimen.

Applications of laser bending include ship construction [2], removing welding distortion and straightening car body parts [3], and rapid prototyping [4, 5]. Laser bending was also studied for micro-machining of brittle materials, which is very difficult to be machined by traditional techniques due to its sensitivity to machining damage. Chen et al. [6] studied high precision laser bending for ceramic computer components. They achieved a bending precision of sub-microradian, far exceeding those obtained by any other method.

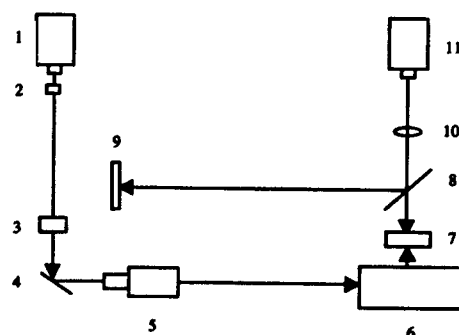
The purpose of this work is to study laser bending technique for brittle materials, including glass, ceramic, and silicon. Three types of lasers, i.e., a Nd:VA pulsed laser, a fiber CW laser and a CO<sub>2</sub> CW laser are used to bend different materials. The amount of bending with different laser powers and laser scanning velocities is obtained and compared.

## 2. EXPERIMENTAL

Figure 1 illustrates the experimental setup for performing laser bending as well as for measuring the bending angle. The irradiation laser beam is expanded by a beam expander and then focused onto the target using a focus lens. One end of the target is clamped. The focused laser beam scans the specimen surface along the y-axis (Fig. 1) using a digital control scanning system. A He-Ne laser beam is focused at the free end of the specimen to measure the bending angle in the z direction. The reflected He-Ne laser beam is received by a position sensitive detector (PSD) with 1  $\mu$ m sensitivity in position measurement. The accuracy of the bending angle measurement is about  $\pm 1.5 \mu$ rad when the distance between the specimen and the PSD is set to 750 mm in the experiment. After laser scanning, the

\* xxu@ecn.purdue.edu; <http://widget.ecn.purdue.edu/~xxu>; phone (765) 494-5639; fax (765) 494-0539

specimen bends toward the laser beam, causing the reflected He-Ne laser beam to move across the PSD. The position change of He-Ne laser beam can be converted to the bending angle of the specimen using geometrical calculations. The whole apparatus is set on a vibration-isolation table.



1. Laser, 2. shutter, 3. polarizing beamsplitter, 4. mirror  
5. beam expander, 6. x-y scanner, 7. specimen, 8. beam splitter  
9. position sensitive detector, 10. lens, 11. He-Ne laser  
Fig. 1: Experimental setup

The operation parameters of three lasers are shown in Table 1. The CO<sub>2</sub> laser and the fiber laser are run at the CW mode, and the Nd:VA laser is run at the pulsed mode. The laser beam diameter is measured using the knife edge technique. SiO<sub>2</sub> glass, ceramic (Al<sub>2</sub>O<sub>3</sub>/T/C) and silicon sheets are used as test specimens. Before the laser treatment, the samples are polished and cleaned with acetone. The parameters of the specimens are summarized in Table 2.

Table 1: Parameters of pulsed laser and CW laser

	CO <sub>2</sub> laser	Nd:VA laser	Fiber laser
Laser wavelength	10.6 $\mu\text{m}$	1.06 $\mu\text{m}$	1.10 $\mu\text{m}$
Laser pulse full width	---	120 ns	---
Laser pulse repetition	---	22 kHz	---
Laser maximum power	10.0 W	1.6 W	9.0 W
Laser beam diameter	100-150 $\mu\text{m}$	50-60 $\mu\text{m}$	60-70 $\mu\text{m}$

Table 2: Specimen parameters

Specimen material	Glass	Ceramic	Silicon
Specimen length	10.0 mm	10.0 mm	8.0 mm
Specimen width	2.0 mm	1.25 mm	1.50 mm
Specimen thickness	0.15 mm	0.35 mm	0.20 mm

### 3. RESULTS AND DISCUSSIONS

Different lasers and laser bending processes are chosen for different materials. This is mainly because the materials have different optical absorption characteristics. Glass is transparent to laser beam of wavelength 1.06  $\mu\text{m}$ , therefore, neither the Nd:VA laser nor the fiber laser can bend the glass. On the other hand, glass can be bent by a CO<sub>2</sub> laser of 10.6  $\mu\text{m}$  wavelength. The optical absorption depth of SiO<sub>2</sub> glass at  $\lambda=10.6 \mu\text{m}$  is around 0.5  $\mu\text{m}$  [7]. Ceramic specimens can also be bent by the CO<sub>2</sub> laser. Figure 2 shows bending angle of glass and ceramic specimens as a function of the power of the CO<sub>2</sub> laser at the scanning velocity of 0.2 mm/s. It can be seen that the bending angle increases when the input laser power increases. For the glass specimen, a bending angle of 102  $\mu\text{rad}$  is obtained when the laser power is 0.28 W. The glass surface is melted when the laser power is higher than 0.28 W. It is also found that a bending angle on the order of 1 degree can be obtained by using higher laser powers (>0.28 W) and multiple scanning. For ceramic bending, as shown in Fig. 2b, the maximum bending angle is 33.28  $\mu\text{rad}$  when the laser power is 0.76 W. It is observed that the inverse bending, i.e., away from the laser beam, will happen when the laser power is increased to higher than 0.9 W.

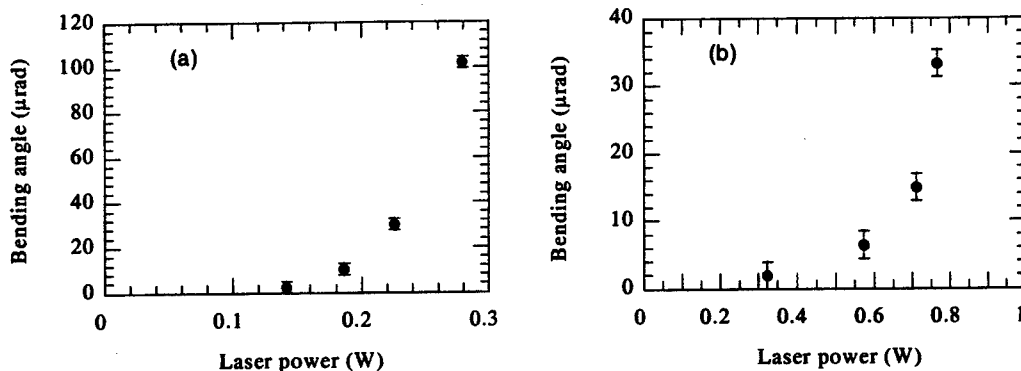
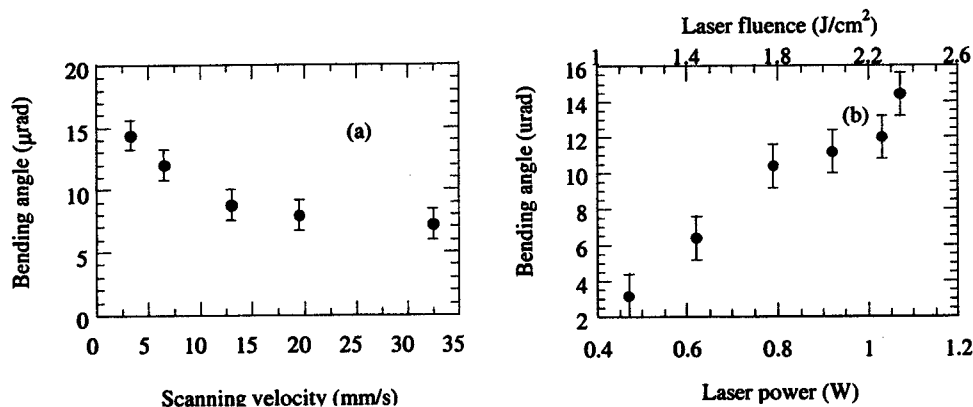


Fig. 2: CO<sub>2</sub> laser bending of (a) SiO<sub>2</sub> glass, (b) ceramic as a function of laser power (scanning velocity=0.2 mm/s)

Bending angles of ceramic specimens are also obtained using the laser of wavelength 1.06  $\mu\text{m}$  at various laser processing. Results obtained by the Nd:VA pulsed laser and the fiber CW laser are shown in Fig. 3 and Fig. 4, respectively. As expected, it is seen from Fig. 3a and Fig. 4a that the bending angle decreases with an increase in the scanning velocity, and from Fig. 3b and Fig. 4b that the bending angle increases when the input laser power increases. For the pulsed laser at the power of 1.1 W, the scanning velocity should be kept below 35 mm/s in order to get a bending angle of about 5  $\mu\text{rad}$  or larger. For the CW laser at the power of 5 W, the corresponding scanning velocity is about 400 mm/s. During CW laser bending, it is found that if the scanning velocity is 26 mm/s or lower at the laser power of 5 W, the bending mechanism changes from the temperature gradient mechanism to the buckling mechanism and the specimen bends away from the laser beam. This is because energy deposited from the laser diffuses through the thickness of the specimen when scanning of the CW laser beam slows down. On the other hand, the specimen always bends toward the laser beam during pulsed laser bending owing to the high temperature gradient near the surface obtained during pulsed laser bending.

Figures 3c and 4c indicate that for both pulsed laser and CW laser, scanning over the specimen surface repetitively would increase the total bending angle, but the amount of additional bending angle decreases with the number of scanning lines. For the pulsed laser, the bending angle obtained by the second laser scan drops to about 25% of the angle obtained by the first scan and no additional bending occurs after 4 scans. For the CW laser, the bending angle of the second scan is about 70% of the first scan, and no additional bending occurs after 6 scans.



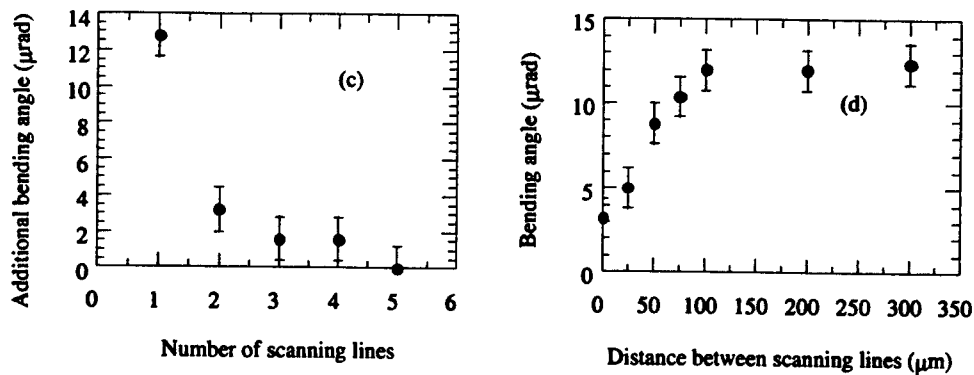


Fig. 3: Pulsed laser bending of ceramics as a function of (a) scanning velocity (laser power =1.1 W), (b) laser power (scanning velocity=3.25 mm/s), (c) number of laser scanning lines, (d) distance between adjacent scanning lines (laser power=1.1 W, scanning velocity=3.25 mm/s for c and d).

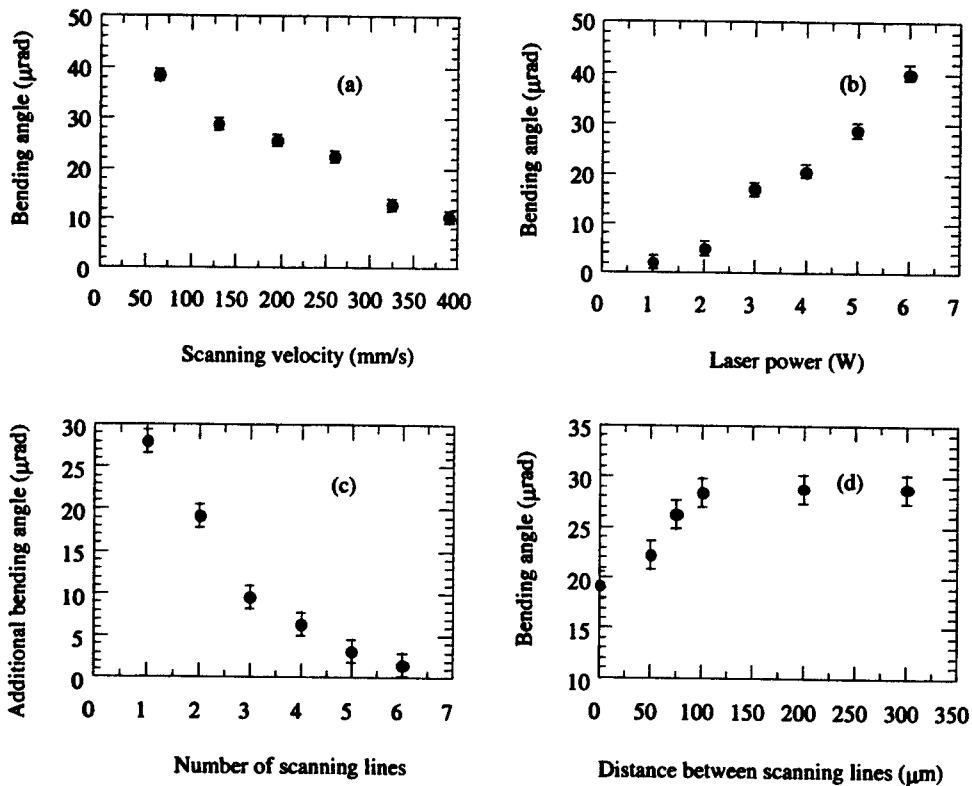


Fig. 4: CW laser bending of ceramic as a function of (a) scanning velocity (laser power=5.0 W), (b) laser power (scanning velocity=130 mm/s), (c) number of laser scanning lines, (d) distance between adjacent scanning lines (laser power=5.0 W, scanning velocity=130 mm/s for c and d).

The amount of bending induced by the pulsed laser and the CW laser is compared while keeping the same laser generated stress-affected zone. The size of the stress-affected zone is determined in experiment as the separation distance above which any two adjacent scans do not influence each other. The bending angle as a function of the separation distance between two scans is measured. As shown in Fig. 3d and Fig. 4d, when the scanning velocity of the 1.1 W pulsed laser is set at 3.25 mm/s and the scanning velocity of the 5 W CW laser is set at 130 mm/s, the stress affected zone in both cases is 100 micrometers. However, the resulting bending angles are different, the bending angle obtained with the CW laser is about twice of that obtained from the pulsed laser.

The main reason for the CW laser to cause more bending compared to the pulsed laser is the longer thermal penetration depth obtained in CW laser bending. In pulsed laser bending, the peak power and the peak temperature are higher, therefore, the top surface layer is sputtered. The thermally affected depth is on the order of one micrometer. On the other hand, in CW laser bending, the peak power and the peak temperature are lower. The molten material is not all sputtered, and is accumulated on the surface after resolidification. The thermal penetration depth is on the order of one hundred microns, resulting in a larger stress affected region and more bending.

Unlike SiO<sub>2</sub> glass, silicon cannot be bent using the CO<sub>2</sub> laser. This is because its optical absorption depth at  $\lambda=10.6$   $\mu\text{m}$  is about 12 mm [7], which is sixty times of the silicon thickness (0.2 mm). This long absorption depth cannot create a sharp temperature gradient in silicon specimens to cause bending. The silicon optical absorption depth at  $\lambda=1.06$   $\mu\text{m}$  is about 0.25 mm [7], thus silicon can be bent using the Nd:VA laser and the fiber laser. Figures 5a and 5b show the bending angle of silicon specimens as a function of the power of the pulsed Nd:VA laser and the CW fiber laser, respectively. Comparing Fig. 5b with Fig. 4b, it can be seen that the bending angles of silicon are less than half of the bending angles of ceramic specimens at most of laser power levels, due to the longer absorption depth and the faster heat diffusion process in silicon.

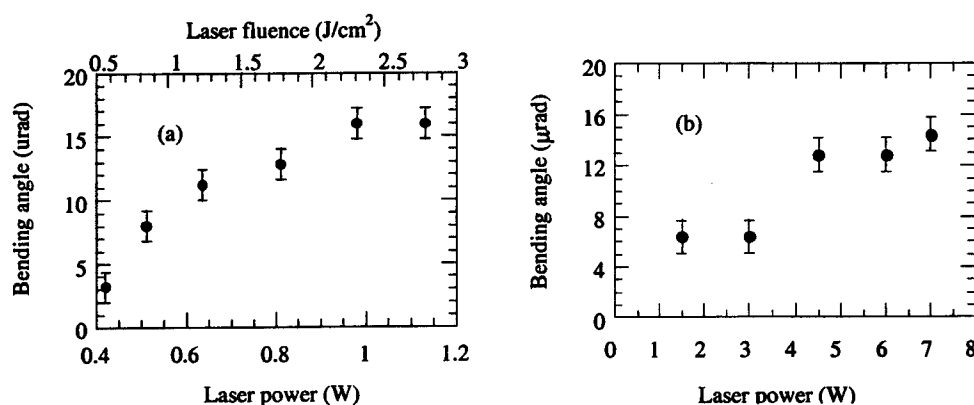


Fig. 5: Bending angle of silicon as a function of laser power at scanning velocity 3.25 mm/s for (a) pulsed Nd:VA laser, (b) CW fiber laser

#### 4. CONCLUSIONS

This work demonstrated using CO<sub>2</sub> laser, Nd:VA pulsed laser, and fiber CW laser for microscale bending of brittle materials, including glass, ceramics, and silicon specimens. Experimental studies were conducted to find out relations between bending angles and laser operation parameters. The glass specimen can only be bent using CO<sub>2</sub> laser and a bending angle on the order of 1 degree may be obtained using high laser power and multiple scanning. Bending results of ceramic and silicon obtained by different lasers were compared. It was found that when the laser generated stress-affected zone was kept same, the CW fiber laser produced more bending than the pulsed Nd:VA laser did. However, the Nd:VA pulsed laser caused much less surface composition change and thermomechanical damage to the specimens.

#### ACKNOWLEDGMENTS

Support to this work by the National Science Foundation is gratefully acknowledgement. The authors also thank SDL, Inc. for providing the CW fiber laser system.

## REFERENCES

1. Geiger, M., and Vollertsen, F., "The Mechanisms of Laser Forming," *Annals of the CIRP*, **42**, pp. 301-304, 1993.
2. Scully, K., "Laser Line Heating," *J. Ship Production*, **3**, pp. 237-246, 1987.
3. Geiger, M., Vollertsen, F., and G. Deinzer, "Flexible Straightening of Car body Shells by Laser Forming," *SAE paper 930279*, pp. 37-44, 1993.
4. Arnet, H., and Vollertsen, F., "Extending Laser Bending for the Generation of Convex Shapes," *Proc. Instn. Mech. Engrs.*, **209**, pp. 433-442, 1995.
5. Vollertsen, F., Komel, I., and Kals, R., "The Laser Bending of Steel Foils for Microparts by the Buckling Mechanism-A Model," *Modelling and Simul. Mater. Sci. Eng.*, **3**, pp. 107-109, 1995.
6. Chen, G., Xu, X., Poon, C.C., and Tam, A.C., "Laser-assisted Microscale Deformation of Stainless Steels and Ceramics," *Optical Engineering*, **37**, pp. 2837-2842, 1998.
7. CRC handbook of chemistry and physics: a ready-reference book of chemical and physical data, editor-in-chief, David R. Lide, Boca Rato, CRC Press, 2000.

## Development of a 100 gm Class Inspector Satellite Using Photostructurable Glass/Ceramic Materials

A. Huang, W. W. Hansen, S. W. Janson and H. Helvajian\*

Center for Microtechnology  
The Aerospace Corporation  
Los Angeles, California, USA

### ABSTRACT

A pulsed UV laser volumetric direct-write patterning technique has been used to fabricate the structural members and key fluidic distribution systems of a miniature 100 gm mass spacecraft called the Co-Orbital Satellite Assistant (COSA). A photostructurable glass ceramic material enables this photo-fabrication process. The COSA is a miniature space vehicle designed to assist its host ship by serving as a maneuverable external viewing platform. Using orbital dynamics simulation software, a minimum  $\Delta V$  solution has been found that allows a COSA vehicle to eject from the host and maneuver into an observation orbit about the host vehicle. The results of the simulation show that a cold gas propulsion system can adequately support the mission given a total fuel volume of 5 cm<sup>3</sup>. A prototype COSA with dimensions of 50 x 50 x 50 mm has been fabricated and assembled for simulation experiments on an air table. The vehicle is fashioned out of 7 laser patterned wafers, electronics boards and a battery. The patterned wafers include an integrated 2-axis propulsion system, a fuel tank and a propellant distribution system. The electronics portion of the COSA vehicle includes a wireless communication system, 2 microcontrollers for systems control and MEMS gyros for relative attitude determination. The COSA vehicle is designed to be mass producible and scalable.

Keywords: laser microfabrication, 3D fabrication, nanosatellite, picosatellite, volumetric patterning, photostructurable glass ceramic

### 1. INTRODUCTION

Future space systems will incorporate architectures that rely heavily on distributed sensing, analysis and functionality for both spacecraft and systems of spacecraft. Microelectromechanical systems (MEMS) or microsystems play an important role in reducing the size of spacecraft systems and/or enhancing their functionality. The same can be said for the fabrication of the overall satellite which, depending on the mission, can be reduced in size to that of a nanosatellite (1-to-10 kg mass) or smaller. Studies show that a one kilogram satellite can be used in missions of long duration.<sup>1</sup> However, far more space missions can only be realized with spacecraft of more traditional size and weight. These larger spacecraft, including the NASA Shuttle and the International Space Station (ISS), will require periodic inspection of external systems during routine maintenance, or emergency inspection during critical malfunctions such as a failed solar array deployment. To assist these larger space systems, The Aerospace Corporation is developing a miniature inspector satellite of the ~100 gm class that is designed to be pre-fueled and stowed on board a "mother" ship. When needed, the miniature satellite is deployed and controlled via the mother ship communications system. The miniature satellite is put into an appropriate co-orbit around the mother ship and commences inspection. Upon mission completion, the satellite is not retrieved but either put into an earth de-orbit maneuver or for non earth orbit missions is jettisoned away from the mother ship. To make this mission viable, the Co-Orbiting Satellite Assistant (COSA) must be designed to be mass producible to make it an expendable unit. It must be highly integrated to increase reliability and reduce cost, and it must have some autonomous behavior to insure that close encounters with the mother ship do not result in a collision. If a COSA can be made small and lightweight, many COSAs could be stored on board without incurring a large mass

---

\* Author to whom correspondence should be addressed: [henry.helvajian@aero.org](mailto:henry.helvajian@aero.org); phone 1-310-336-7621; fax 1 310-563-3175; M2:241, The Aerospace Corporation, PO Box 92956, Los Angeles, California 90009, USA

penalty and these units could be used to assist in a multitude of operations such as providing visual inspections and assisting in the calibration of onboard antennas.

## 2. SYSTEMS ENGINEERING & MISSION FEASIBILITY

A systems engineering study was performed to both identify technology goals and to identify a minimum energy Co-orbit that could be achieved with the limited fuel ( $\sim 5\text{cm}^3$ ) expected on board a COSA. To make the COSA mass producible and expendable, we considered materials for the structure that could be processed with large flexibility. Both plastics and glass materials fulfill this requirement with glass having the additional advantage of higher strength and feasibility of implementing on-board photonics. To make the design expandable, we chose a modular layer design philosophy. We required integral microelectronics and MEMS either within the structural layer or within a layer that could be easily mated with an electronics multi chip module "board". The major functional subsystems of the COSA are a short range wireless communication system, a propulsion system for attitude control, MEMS rate gyros, MEMS accelerometers, and a horizon sensor for short term navigation between host satellite position updates. Table 1 below lists the major subsystems of the COSA laboratory prototype design. The choice of components is primarily driven by the requirement to keep the total mass (including fuel) near 100gm and the desire to maintain a volume less than  $50 \times 50 \times 50 \text{ mm}^3$ . Additional add-on systems for the laboratory prototype COSA would be a camera or an electronic or photonic calibration source.

Table 1: COSA subsystem components and their function

COSA Critical Subsystem Components	Function
MEMS pressure sensor and signal conditioner	Fuel pressure measurement
433.92 MHz FM receiver @9600 bps OOK	Wireless communications (uplink)
Thermocouple (Type K) with ice point compensator	Fuel temperature measurement
Five solenoid valves (3-way)	Thruster control
315MHz FM transmitter @ 4500 bps OOK	Down link channel
Two microcontrollers (Pickstic3_2K/PIC16F628)/ 4ADC channels	COSA control
MEMS gyro	Inertial attitude determination
Two Lithium ion batteries ( 7.2V @ 1.1 Watts)	Power source
Nichrome heater (0.3 – 3 W)	Fuel pressure control

The COSA mission requires precision thrusting that maneuvers the daughter satellite into a co-orbital observation trajectory about the mother ship. Thrusting results in a change in velocity ( $\Delta V_i$ ) that alters the previous COSA orbit. Minimum propellant usage, corresponding to minimum  $\Delta V = \Sigma(\Delta V_i)$ , requires a COSA phasing trajectory where the released COSA initially gets a tangential  $\Delta V$  in the opposing direction of the host vehicle flight path, followed by a similar  $\Delta V$  maneuver in the opposite direction after one-half of an orbital period. This results in the COSA being placed in the same orbit, but behind, the host vehicle. A second series of maneuvers places the COSA in an inclined observation trajectory about the host vehicle. Figure 1 shows the COSA, the host vehicle, and several potential observation orbits. The phasing orbit is also shown. For a 700 km altitude 99 minute earth orbit, the orbital simulations show that the phasing orbit requires a  $\Delta V$  of 3 mm/s while the total  $\Delta V$  for reaching an observation orbit is 180 mm/s. Using first order kinetic equations of motion,  $F\delta t = m(\Delta V)$ , where  $F$  is the force,  $m$  is the mass and  $\delta t$  and  $\Delta V$  represent the impulse duration and change in velocity respectively, a 1 mN thruster firing for 1 sec would generate a  $\Delta V$  of 10 mm/s for a 100 gm mass vehicle. These results suggest that a 1 mN class propulsion system could fulfill the mission requirements if sufficient fuel could be stored on board the COSA. A potential fuel candidate for space applications is butane or ammonia. For the laboratory tests we use 1,1,1,3,3,3 hexafluoropropane (Dupont; HFC – 236fa, 30 PSIG at room temperature and pressure) and fuel volume of  $5.6 \text{ cm}^3$ .



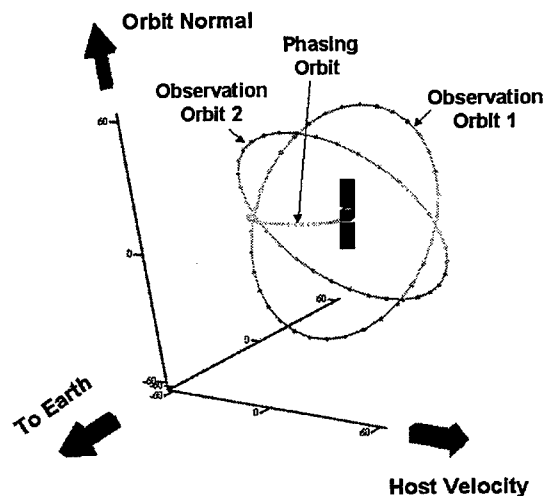


Figure 1: COSA observation trajectories around host vehicle.

There are different types of propulsion systems that could be integrated into a COSA. Specific impulse, defined as thrust divided by propellant mass flow rate, is a figure-of-merit for propulsion systems and a direct measure of propellant efficiency. Cold gas thruster systems typically have the lowest specific impulse of any practical thruster, typically between 40 and 80 seconds. Other propulsion approaches such as ion or pulsed plasma propulsion offer drastically increased specific impulse (thousands of seconds), but entail additional system and fabrication complexities. Due to the low velocity increment requirements for the COSA mission, however, cold gas thrusters impose less than a 1% propellant mass fraction used per maneuver where the propellant mass fraction is defined as the propellant consumed divided by the total spacecraft mass (with propellant). Figure 2 shows the required propellant mass fraction as a function of velocity increment  $\Delta V$  for a number of different specific impulses. These curves show that a  $\Delta V$  of 1 m/s is easily obtained using propellant mass fractions below 1% even for a low specific impulse (about 25 seconds) cold gas thruster. The total  $\Delta V$  required for positioning of the COSA into an observational orbit is  $<0.19$  m/s.

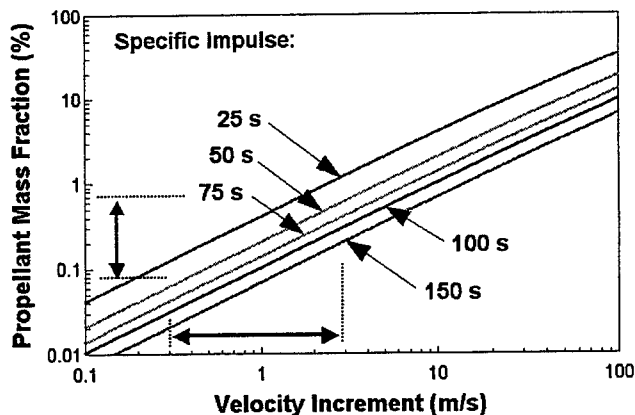


Figure 2: Propellant requirements to achieve a necessary velocity increment per maneuver.

Our orbital simulations show that a COSA observational mission around the host vehicle is technically feasible for a 100 gm COSA vehicle containing 5 cm<sup>3</sup> volume of fuel. The question is whether a COSA vehicle could be fabricated and assembled within the mass requirement.

### 3. Material Processing and Systems Assembly

Laser direct-write (LDW) material processing techniques were implemented for the fabrication of the COSA component wafers. The reasons are twofold. First, LDW material processing permits rapid prototyping of COSA component designs because it is a maskless processing approach. Second, LDW easily permits the fabrication of true 3 dimensional (3D) structures, e.g., nozzles, for efficient use of the limited on board propellant. Even though LDW has these unique advantages, it is an inherently slow process because of its serial nature. Fabricating the patterned wafers that make up the COSA by laser ablation would not be cost-effective because expensive laser photons are used to remove matter. In addition, laser ablation may not be feasible given that high aspect ratio (>25) millimeter deep trenches are required. A more economic and viable solution would be to consider merging the advantages of batch processing (parallel processing, wafer scale uniformity, low cost) with that of LDW (maskless processing, true 3D fabrication). This could be done in materials where a selective photosensitivity leads to enhanced chemical reactivity. The result of merging these processes permits the slow/serial operations such as LDW to be used only for material patterning with 3D control while batch operations (e.g. chemical etching) are used for actually removing the exposed material. This philosophy is commonly implemented in photoresist material but the mechanical properties of photoresists are not adequate for the COSA application.

Alternative materials, the photostructurable glass/ceramic materials<sup>2</sup> or photocerams, better meet the COSA strength requirements. These materials commonly function via a three step process: illumination, ceramization, and preferential isotropic etching step<sup>3</sup>. In Foturan<sup>TM</sup>, manufactured by Schott Corporation, the photosensitive character arises from trapped Ce<sup>3+</sup> (admixture CeO<sub>2</sub>) and Ag<sup>+</sup> (admixture Ag<sub>2</sub>O) ions that are stabilized by Sb<sub>2</sub>O<sub>3</sub> in a lithium aluminosilicate mixture host<sup>4</sup>. Using the conventional linear absorption model, Ce<sup>3+</sup> can be photoionized to form Ce<sup>4+</sup> plus a free electron at incident photon energies near 3.97 eV (318 nm). The free electron neutralizes a nearby Ag<sup>+</sup> ion (i.e. Ag<sup>+</sup> + e<sup>-</sup> → Ag<sup>0</sup>) leaving a latent image of the absorption event. In the ceramization step, migration and local clustering of the Ag<sup>0</sup> nuclei lead to formation of lithium silicate crystals. In a 5% solution of HF these crystals etch 20-to-40 times faster than the unexposed amorphous material. Glass/ceramic composites can be prepared where the hardness is greater than fused quartz, granite, and high-carbon stainless steel and more closer to that of tempered steel. The Foturan material has a Knopp hardness of 4600 – 5200 N/mm<sup>2</sup> and a modulus of rupture that ranges between 60-150 N/mm<sup>2</sup>. These materials can be manufactured with no porosity to any size and can be shaped using traditional glass forming techniques. In addition, photocerams can be processed to contain very complex patterns by UV lithographic techniques<sup>5</sup>.

The Aerospace Corporation has added a number of refinements to the general processing of photocerams<sup>6</sup>. These include the use of pulsed UV lasers instead of a UV lamp to enable direct-write operations and 3D fabrication, the use of various UV wavelengths to control the penetration depth within the bulk material, and the metered control of the laser fluence (J/cm<sup>2</sup>) and power (#shots/sec) to enable fabrication of embedded structures<sup>7</sup> or to enhance, with site-specificity, the chemical etching rate<sup>8</sup>. With additional controls and characterization in the ceramization and chemical etching steps, we have been able to fabricate numerous microstructures that are relevant for COSA. By design, the COSA is a 7 layer sandwich structure comprising of individually patterned wafers using 100 mm diameter Foturan wafers. However, each COSA layer has dimensions of 50 x 50 mm. We were able to save a dicing/cutting operation by using the laser to pattern a 50 x 50 mm perimeter pattern. By controlling the laser dose and setting the pattern profile, it is possible to chemically etch the required fluidic patterns on the layer and to release the 50 x 50 coupon simultaneously from the larger substrate. Figure 3 (left) shows the CAD layers used in the fabrication of the COSA wafers, while the Figure 3 (right) describes the function of each layer. Substrates of 1 and 2 mm thickness were used. It should be possible to reduce the number of layers from 7 to 4 by (1) using a 4 mm thick substrate to combine the two 2 mm fuel tank layers (4 mm thick wafers not currently available from the manufacturer), (2) further integrating the "valve" layer and the "nozzle/flow channel plate" and (3) integrating the "heater/TC" layer with fuel tank. The pattern on each wafer/coupon consisted of numerous layers of CAD files where each CAD file grouped pattern segments that had to be

exposed at a particular wavelength or laser power setting. For each wafer/coupon all the CAD layers could be run sequentially.

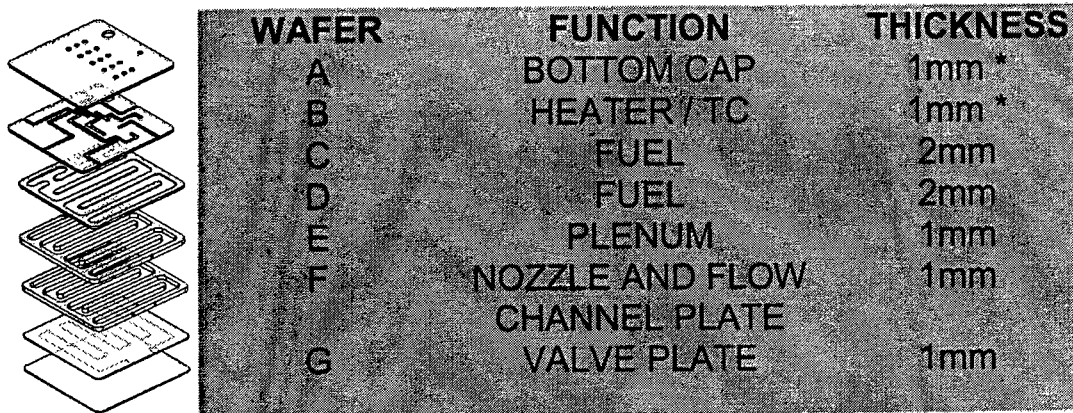


Figure 3: Computer assisted drawings (CAD) of the 7 COSA wafers, dimension 50 x 50 x 8 mm (left). Wafer characteristics with wafer A as the bottom (left). Asterisks identify wafers to be thinned from the original thickness to save more mass.

The LDW patterning steps were performed on a computer controlled XYZ stepper with total precision of better than 5 microns. A solid state diode pumped Nd-Yag laser(Continuum HPO1000) was focused through a 10X UV microscope objective (OFR LMU -10x-248 - with an  $f^{\#}$  of 5) and onto the photoceram substrate. The substrate was held by a vacuum chuck and its planarity could be measured and corrected by a white light interferometer (WYKO NT 2000) which is integral to the LDW exposure tool. The laser power could be continuously monitored via a calibrated beam splitter and a power meter (Molelectron XXX). The laser spot size on the target surface and the total incident power depended on the pattern "drawn". On the average a spot size of 5 -20  $\mu\text{m}$  and power of 2 - 15 mW (2 $\mu\text{J}$  - 15 $\mu\text{J}$  per pulse) was used. Other fabrication attributes of the COSA are shown below.

- Seven wafer stack of patterned layers (total photoceram dimension 50 x 50 x 8 mm)
- Electronics/battery/microvalves make the total dimension (50 x 50 x 50 mm)
- Pattern registration (<50  $\mu\text{m}$ ) on a 50 x 50 mm footprint
- Via holes connecting multiple wafers
- Plenum wafer has 1200 shaped holes and microstructures for liquid/gas separation
- Micro channel fluid paths through 6 wafers
- Patterns contain both 2D and 3D structures
- Six integrated thruster nozzles in nozzle and flow channel wafer
- Processed using 3 UV laser wavelengths (248 nm, 266nm, 355nm)
- Processed using multiple CAD layer patterning
- Exposure processing speed 1 - 2 mm /s
- Typical on target laser power 2 - 15 mW at 1KHz laser repetition rate

Table 2 shows the measured processing times for each processed wafer divided into Exposure, Bake and Etch operations. The total time for fabricating all the wafers is roughly 75 hours. However, both the Bake and Etch operations are batch processes - i.e. more than one wafer can be baked/etched at one time and therefore are not considered a rate limiting step. On the other hand, the Exposure step is a serial operation and its duration is dependent on the pattern generator motor speed and laser power. However, considering that the Exposure process is fundamentally a non-thermal excitation process it should be possible to significantly reduce the Exposure step duration by a subsequent increase in the laser power and scanning speed. A thermally initiated process would have the requirement of a minimum residence time to permit deposition of sufficient quantity of heat. A non-thermally initiated system is not so constrained. We use scanning velocities of 1-2mm/sec and mW power levels, but much higher speed (e.g. m/sec) stepper motors are

currently available and galvanometer based scanners offer even faster scanning capabilities. Finally, we have noted that with the Bake protocol used nearly half of the time expended is in the cooling phase. It should therefore be possible to reduce the four hour segment by at least one hour. The chemical etching step cannot be much altered. This is because the fundamental chemical etching rate is roughly  $20\text{ }\mu\text{m}/\text{min}$  for segments that have absorbed the maximum dose. Given that many of the microstructures in Wafers A-G are at least 1 mm high ( C and D wafers being 2 mm thick), there is a minimum time for material removal ( $\sim 50$  minutes for 1mm thick samples). This minimum etch time only applies if the pattern can be etched without encountering the limitation of chemical transport to the etch front. However, in many of the patterns there are significant chemical transport issues. We have employed the use of high pressure sprays to more efficiently drive the etchant to within deep holes and crevices.

Table 2: COSA wafer processing times (hours:minutes), delineated by LDW (serial) and batch (parallel)

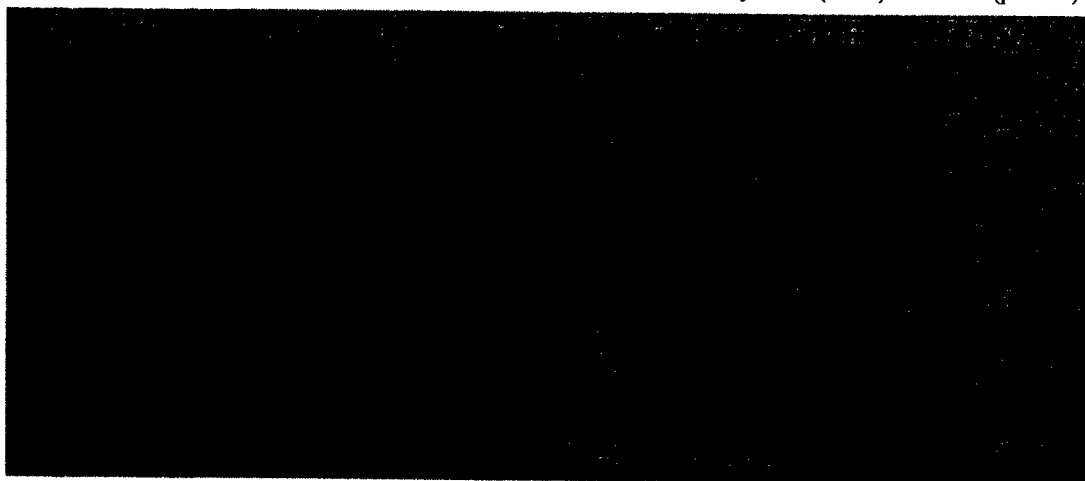


Figure 4 shows the processed COSA wafers after the Bake step (right hand image) and after the final Chemical Etching step (left hand image). Also shown are two of the five miniature commercial solenoid valves (LEE Corp. LHDA 0523112H) used in the COSA (foreground left image). In the right image, six of the wafers are shown stacked to delineate detail of the circuitous fluidic channel pattern. The dark regions will be removed by the chemical etching process. It is difficult to detail much of the patterned microstructures because of the large aspect ratio and the lack of access to a large depth-of-field microscope. However, Figures 5 and 6 show expanded views of the integrated supersonic nozzle region (Figure 5) and a section of the plenum wafer and the liquid-to-gas transfer interface (Figure 6).



Figure 4: The fabricated and etched wafers with two microvalves shown (left). Six of the seven wafers are stacked to show registration, the plenum wafer is not included as it would obstruct the view to layers below.

There are a number of immediate conclusions one can draw from analyzing Figures 4 –6. First, the LDW volumetric exposure process using commercial solid state pumped Nd-Yag lasers is sufficiently robust to permit long exposure processing that includes complex patterns and intricate microstructures. The running of a multi-hour “job”, unattended, only becomes acceptable because the pattern transfer process and the laser systems control can be automated. Second, as a result of using a chemical etching process to remove the material, the processed surface is inherently smoother than that typically measured from laser-ablated material processing. We have measured surface roughness on the order of 1-2 microns without using additional annealing operations. This roughness is directly related to the photoactive dopant density in the photoceram, a parameter which we cannot control but can be modified by the photoceram manufacturer. Third, because the laser is used in the exposure step and not for material removal, there is no laser-induced residual stress in the material, or more importantly, in the standing microstructures as one might find in laser ablation patterning.

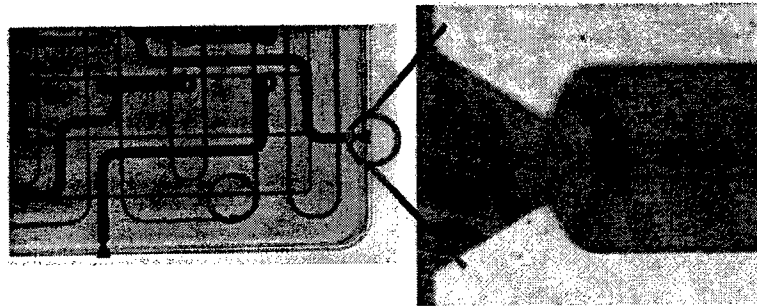


Figure 5: Expanded view of the integrated supersonic nozzle region for the laser patterned and baked COSA wafers. The nozzle exit port is 1300  $\mu\text{m}$  with a throat dimension of 470  $\mu\text{m}$ . The nozzle is 260  $\mu\text{m}$  deep.

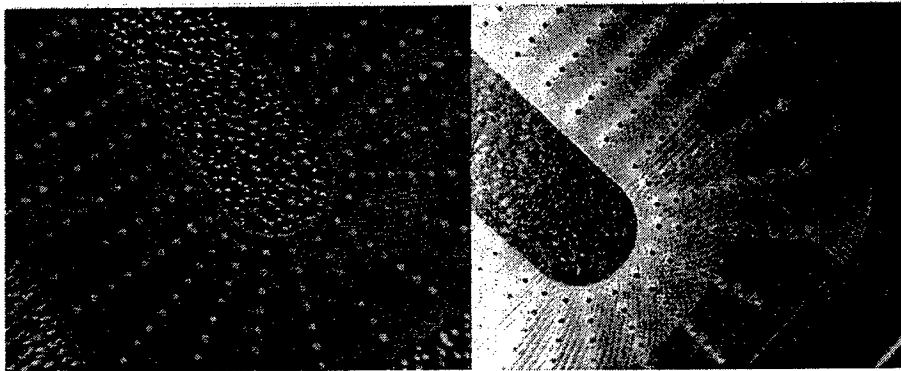


Figure 6: Optical microscope image of a section of the plenum wafer. Left image after Bake step, Right image after chemical etch treatment. Holes are 100  $\mu\text{m}$  in diameter.

#### 4. Conclusions

A laser volume patterning technique has been applied in the development of a miniature satellite for a COSA type mission. Orbital dynamics simulations show that a 100 gm class COSA can be placed in an observation orbit around the host vehicle. The laser processing technique used merges the best aspects of both LDW and batch processing. The LDW is used only to expose the material and can do this with volumetric precision, while the batch processing steps, defined by the bake and chemical etching, are implemented for the actual material removal operation. Key to this "merged" processing approach is the material which can be photoactivated at low laser powers. The data show that nearly 75 hours were required to process all the COSA wafers. Of that time nearly 30 hours were relegated to the serial LDW operations. If a higher velocity stepper motors (m/sec) or a combination of multiple galvanometric pattern generator systems were to be implemented, it should be possible to see at least a factor of 30 reduction in the exposure operations to just one hour. This 30-fold reduction in the exposure duration cycle would also require a concomitant increase in the laser power by a factor of 30. Our current operational power levels of 2 – 15 mW would have to increase to 60 – 900 mW of UV laser light. Current commercial diode pumped solid state lasers now routinely put out Watts of UV light. Finally, the processing approach, as implemented, is scalable to larger size COSA vehicles and because the substrate material is fundamentally a glass, it could be preformed to any shape and size prior to laser patterning.

Current COSA development is continuing with a Lucite™ mock-up of the COSA for electronics and controls testing. A set of photoceram wafers have been fabricated. The first prototype COSA vehicle with photoceram wafers will use a multilayer printed circuit board and glass-to-glass bonding techniques to fuse the photoceram wafers. Further development involves electronics integration into the glass with conducting lines written either via laser direct write chemical vapor deposition or via a variant of the Laser Plasma Assisted Ablation (LIPAA) technique<sup>9</sup>. Larger frame COSA for more demanding missions are in design.

#### ACKNOWLEDGMENTS

This project was sponsored by The Aerospace Corporation Corporate Research Initiative Program. The authors would like to acknowledge the valuable discussions with Drs. Pete Fuqua, Dave Taylor and Frank Livingston.

#### REFERENCES

- <sup>1</sup> S. Janson "Silicon Satellites for 21<sup>st</sup> Century Missions, Proceedings of The 2<sup>nd</sup> International Conference on Integrated MicroNanotechnology for Space Applications, 11-15 April 1999, Pasadena Ca. Pg. 535.
- <sup>2</sup> A. Berzhnoi, "Glass-Ceramics and Photosittals" Plenum Press (New York, 1970).
- <sup>3</sup> A. Berzhnoi, "Glass-Ceramics and Photosittals" Plenum Press (New York, 1970).
- <sup>4</sup> D. Hulsenberg, R. Brunsch, K. Schmidt, F. Reinhold, "Micromechanische Bearbeitung von Fotoempfindlichem Glas" Silikattechnik, Vol. 41, (1990) 364; T.R. Dietrich, W. Ehrfeld, M. Lacher, M. Krämer, B. Speit, "Fabrication Technologies for Microsystems Utilizing Photoetchable Glass", Microelectronic Engineering 30 (1996) 497-504
- <sup>5</sup> Foturan – a Material for Microtechnology, Schott Glaswerke publication, Optics Division ([www.mikroglas.com](http://www.mikroglas.com))
- <sup>6</sup> W. W. Hansen, S. W. Janson and H. Helvajian " Direct-Write UV Laser Microfabrication of 3D Structures in Lithium Aluminosilicate Glass" Proc. of SPIE Vol. 2991, pg. 104, 1997.
- <sup>7</sup> P. D. Fuqua, D. P. Taylor, H. Helvajian, W. W. Hansen, and M. H. Abraham, " UV Direct-Write Approach for Formation of Embedded Structures in Photostructurable Glass/Ceramics" in *Materials Development for Direct-Write Technologies*, D. B. Chrisey, D. R. Gamota, H. Helvajian and D. P. Taylor, Mat. Res. Soc. Symp. Proc., p.79, Vol. 624, 2000.
- <sup>8</sup> F. E. Livingston\*, W. W. Hansen and H. Helvajian, Effect of Laser Parameters on the Exposure and Selective Etch Rate in Photostructurable Glass, SPIE Proceedings Laser Applications in Microelectronic and Optoelectronic Manufacturing VII, 2002.
- <sup>9</sup> Z. Zhang, K. Sugioka, K. Midorikawa, " Micromachining of glass materials by laser-induced plasma-assisted ablation (LIPAA) using conventional nanosecond laser.

## Laser Micromachining of Biofactory-on-a-Chip Devices

Julian P. H. Burt, Andrew D. Goater, Christopher J. Hayden and John A. Tame  
Institute of Bioelectronic and Molecular Microsystems, University of Wales, Bangor, Dean Street,  
Bangor, Gwynedd, LL57 1UT United Kingdom

### ABSTRACT

Excimer laser micromachining provides a flexible means for the manufacture and rapid prototyping of miniaturised systems such as Biofactory-on-a-Chip devices. Biofactories are miniaturised diagnostic devices capable of characterising, manipulating, separating and sorting suspensions of particles such as biological cells. Such systems operate by exploiting the electrical properties of microparticles and controlling particle movement in AC non-uniform stationary and moving electric fields. Applications of Biofactory devices are diverse and include, among others, the healthcare, pharmaceutical, chemical processing, environmental monitoring and food diagnostic markets. To achieve such characterisation and separation, Biofactory devices employ Laboratory-on-a-Chip type components such as complex multilayer microelectrode arrays, microfluidic channels, manifold systems and on-chip detection systems. Here we discuss the manufacturing requirements of Biofactory devices and describe the use of different excimer laser micromachining methods both in stand-alone processes and also in conjunction with conventional fabrication processes such as photolithography and thermal moulding. Particular attention is given to the production of large area multilayer microelectrode arrays and the manufacture of complex cross-section microfluidic channel systems for use in sample distribution and device interfacing.

**Keywords:** Excimer, Laser, Micromachining, Biofactory, Laboratory-on-a-Chip

### INTRODUCTION

In recent years microfabricated devices, or microsystems, have found applications in areas as diverse as the aerospace, automotive, environmental, healthcare, pharmaceuticals, chemical processing, biotechnological and food industries. A major area of expansion for microsystems technology has been in the areas of chemical and biochemical analysis that play a routine part of many industries. These microsystems, known generally as Laboratory-on-a-Chip devices, offer many advantages over conventional laboratory apparatus. The small internal volumes of such devices can lead to reduced reagent and sample costs whilst at the same time benefiting from faster reaction times. In addition, the small internal dimensions of these devices allows accurate control of environmental parameters such as temperature and pressure. The integrated nature of Laboratory-on-a-Chip devices allows multiple processes to be carried out within a single device giving rise to increased ability to automate complex analytical and production processes. Whilst a single device may be limited in the reagent volumes it can process, the small physical dimensions of Laboratory-on-a-Chip devices provide the possibility of employing many devices operated in parallel arrays to provide the production throughput of conventional apparatus. Additionally, with judicious choices of construction materials and manufacturing processes, such devices can also offer the advantages of lost-cost, single use disposable units to ensure process quality control and to eliminate concerns of inter-process contamination.

Laboratory-on-a-Chip devices have employed a wide range of techniques to provide on-chip processing. Many of these techniques can be considered as macroscopic technologies that are miniaturized to provide additional functionality. Examples of such devices are those that employ techniques such as capillary electrophoresis for separations or labelling processes for identification. In these devices the reduced physical dimensions of Laboratory-on-a-Chip devices allow, in the case of capillary electrophoresis, increased separation resolution or, for labelling methods, increased signal to noise ratios during detection. An increasingly important group of Laboratory-on-a-Chip devices are those that employ processes that function optimally in miniature systems. Biofactory-on-a-Chip devices are an exemplar of such devices

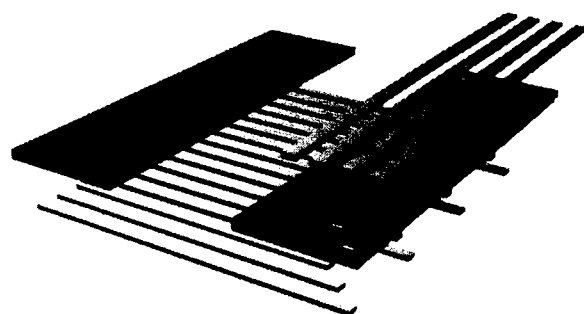
and are capable of performing a wide range of complex diagnostic tasks in a single, miniaturised, low-cost package. Such devices have the advantage of being automated systems capable of the rapid analysis of small volume samples and have applications in the fields such as medical and single cell diagnostics, chemical detection, water quality control and food analysis. The phenomena utilised in Biofactory-on-a-Chip devices exploit the dielectric properties of particles and the electric field induced motion caused by the following AC electrokinetic processes:

- (1) Dielectrophoresis (DEP), the translational motion induced when particles are exposed to stationary, non-uniform, electric fields.
- (2) Electrorotation (ROT), the rotational motion induced in particles when exposed to rotating electric fields.
- (3) Travelling Wave Dielectrophoresis (TWD), the translational motion induced when particles are exposed to travelling electric fields.

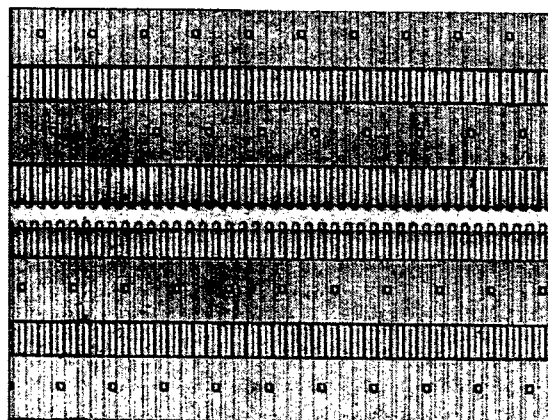
For these AC electrokinetic phenomena to operate, the geometries of strong AC electric fields need to be accurately controlled over dimensions of the same order as the size of the particles to be processed. The combination of the required electric field strengths and geometric control make exploiting such phenomena problematic on a macroscopic scale. The background theories of these AC electrokinetic processes and perceived biotechnological applications are described elsewhere<sup>1,2</sup>. Here, we discuss the design and manufacturing issues of Biofactory on-a-Chip type devices. To illustrate the manufacturing processes, examples have been taken from a recently completed device for the detection and viability analysis of parasites known to contaminate water supplies.

### EXAMPLE BIOFACTORY-ON-A-CHIP DEVICE

Central to the Biofactory concept is the use linear arrays of electric field producing electrodes allowing particles to be transported around Biofactory devices using travelling wave dielectrophoresis<sup>3</sup>. The speed and direction of travel is dependent on the dielectric properties of the particles and the suspending medium along with the frequency and strength of the travelling electric field. Figure 1a shows an illustration of the multilayer construction of such electrode arrays. Field producing electrodes form the lowest layer and are partially covered with a thin insulator. The insulator is patterned with an array of via holes that expose the underlying electrodes in defined regions. A series of four bus-bars form the top layer of the structure and are positioned to allow every fourth field-producing electrode to be connected together, with adjacent field producing electrodes being connected to adjacent bus-bars. Energising the



(A)



(B)

**Figure 1.** (A) Illustration of multilayer electrode arrays used in the construction of Biofactory devices. (B) A multilayer electrode array for the transport and selective trapping of particles in Biofactory devices.



Bus-bars with quadrature sinusoidal voltages produces a travelling electric field along the length of the electrode array. The use of a multilayer structure for such electrodes allows arbitrary length electrode arrays to be constructed whilst requiring only four external electrical connections.

Figure 2 shows an image of an unencapsulated example Biofactory-on-a-Chip device for the detection and viability analysis of oocysts of the water borne parasites *Cryptosporidium parvum* and *Giardia lamblia*. The presence of such parasites, even in very low concentrations, in drinking water has led to outbreaks of human infection that occurs as self-limiting diarrhoea in healthy adults but may lead to death in infants and immuno compromised people. Since these oocysts do not multiply outside their hosts, conventional microbiological procedures are not applicable for their detection. The Biofactory device shown in figure 1 can be considered in two sections. The first section, forming the upper half of figure 1, is an array of external electrical connections to allow control of the Biofactory device. These connections are arranged in blocks of four electrodes allowing the individual sections of the device to be energised independently using quadrature sinusoidal voltages. The nine blocks of four electrodes signify that this device contains nine independently controllable regions. The second section of the device covers the lower half of figure 1. Here a series of conveyor tracks can be seen forming a network of analysis tools. A raw water sample, filtered to both remove large debris and concentrate particulates is fed into inlet port A1. At the same time, a sample of latex beads coated in an antibody targeted to a specific microorganism is fed into inlet port A2. Water sample particles travel along TWD conveyor electrode arrays or 'tracks', similar to B, through the junction structure, C and arrive at a dielectrophoretic particle trap, D. Latex beads travel along conveyor track, B, and also arrive at the trap D. At this point, antibodies on the latex beads will react with any of their targeted microorganisms if present. The result of this is the binding of latex beads to the microorganism to form a complex particle. This complex particle will have different electrical properties to the unreacted microorganisms and so will move along conveyor tracks with a different velocity. Energising the conveyor track to the right of the dielectrophoretic trap causes all particles to move along the track. Energising different junction branches within the device allows unreacted latex beads to be directed back to dielectrophoretic trap whilst unreacted microorganisms can be directed to one of the outlet ports A3 or A5. Bead/microorganism complexes are directed to the electroration analysis unit, E, where the microorganism complexes are made to rotate under the influence of a rotating electric field. Observation of the speed and direction of rotation for a range of electric field frequencies, allows microorganism presence and viability to be detected. Finally, analysed complexes can be removed from the device through outlet port A4. Therefore, through the appropriate application of electric fields and detection of rotation, it is a simple matter to enumerate the number of a specific organism present as well as calculate their viability.

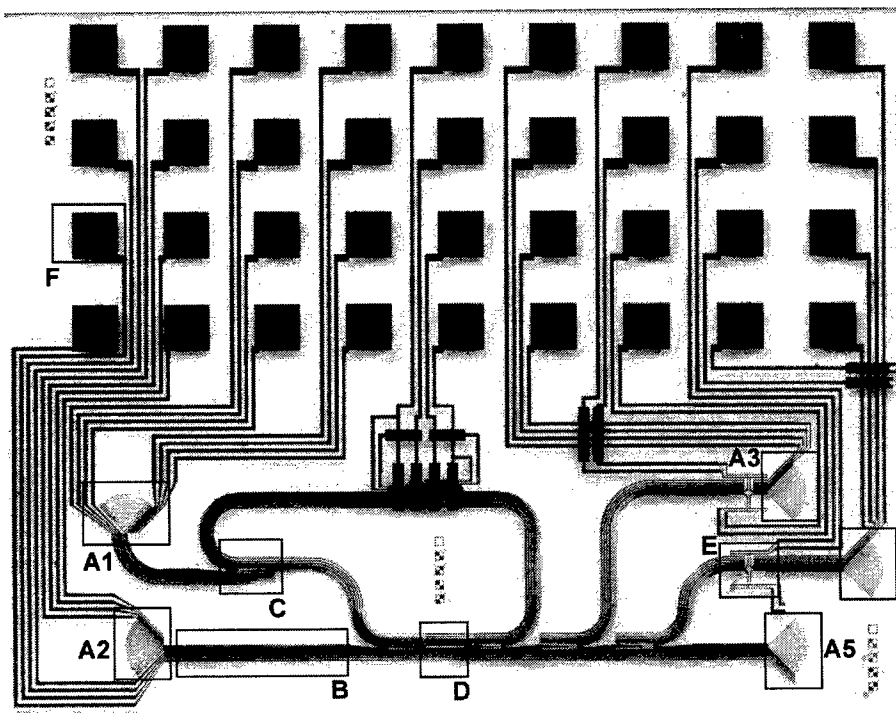


**Figure 2.** Image of an example Biofactory-on-a-Chip device. Six key elements are employed in the device.

- A Inlet/outlet ports.
- B Travelling wave dielectrophoresis conveyor tracks.
- C TWD conveyor track junctions.
- D Dielectrophoretic particle trap units.
- E Electroration analysis units.
- F External electrical connection contacts.

## MATERIALS AND METHODS

### MATERIALS

A diverse range of materials has been used for the fabrication of Laboratory-on-a-Chip devices. In Biofactories, the choice of materials is governed by the device's application area. In general, Biofactories are intended to be used as low-cost, single or low usage, devices. As such, chosen materials must have low volume costs and be applicable to simple, inexpensive, large scale manufacturing processes. Being essentially planar devices, Biofactories are fabricated as a series of thin layers on a supporting substrate. This substrate must be rigid and optically clear to allow observation of processing within the Biofactory. In current work, thin glass substrates have been employed although it is also possible to use transparent polymers such as polycarbonate and PMMA. Microelectrode arrays within Biofactory devices must be capable of providing controlled electric fields in a diverse range of sample media. Therefore, electrode arrays are primarily constructed from inert metals such as thin, thermally evaporated, gold films typically 100nm thick. To assist in adhesion to different substrates, a 5nm seed layer of chrome is often deposited prior to gold deposition<sup>4</sup>. The insulating material used between the field producing electrodes and bus-bars in multilayer electrodes is a critical part of Biofactory devices. Current work employs a series of different insulators depending on the Biofactory application. For the majority of devices, polyimide films are used to isolate different conducting layers within devices. These films are deposited by spin coating followed by a series of patterning and baking stages to produce robust isolating layers. Other Biofactory devices have made use of the photosensitive epoxy resist SU-8. An important feature of SU-8 is its ability, under correct conditions, to produce contact type bonds between layers of SU-8<sup>5</sup>. This is particularly useful when encapsulation layers are fabricated from SU-8. Encapsulation layers are used to define microfluidic channels over the microelectrodes arrays and so confine analysis samples to defined areas of the Biofactory devices. A wide range of materials can be used for this stage. For low-cost development work, the popular mouldable elastomer polydimethylsiloxane (PDMS) has been successfully used. For untreated, clean surfaces, PDMS forms a weak, releasable, bond on contact with materials such as glass and so allows fluidic distribution systems to be evaluated on a single standard electrode array. More permanent bonding of encapsulation layers has employed thermoplastic polymers such as polycarbonate. Fluidic channel structures are thermally embossed into polymer sheets and bonded to the electrode bearing substrate using a range of adhesives. The advantage of such encapsulation layers is the ability to mould external inlet and outlet ports into the encapsulation layer allowing easy interconnection with other laboratory equipment.

### EXCIMER LASER ABLATION

A key factor in developing Biofactory-on-a-Chip technology is the ability to employ a wide range of low-cost production processes in the bulk production of such devices. Examples of this include photolithography for the patterning of microelectrode arrays and thermal embossing or injection moulding for the production of encapsulation layers. However, in the design stage there is a need to employ flexible microfabrication processes that allow rapid development of devices whilst interfacing directly with final production processes. Excimer laser ablation and laser based micromachining is an ideal method for this design stage. Thin metal films can be patterned directly by laser ablation without the need for the multistep processes of mask preparation, resist coating, exposure, developing, etching and resist removal involved in photolithography. At the same time, to interface with bulk production using photolithography, an excimer laser can also be used as a highly controllable, deep ultra violet (UV) light source for high-resolution photolithographic patterning. In addition, excimer lasers are ideal for the accurate patterning of polymers both in thin film form and as bulk materials. In this way, both the insulation layers used in multilayer electrodes and encapsulation layers used to control sample position can be directly machined using excimer lasers.

The laser system used for this work was an Exitech Series 8000 microfabrication workstation (Exitech Ltd, Oxford, UK) incorporating a Lambda Physik Compex 110 excimer laser configurable for operation at either 248nm or 193nm. In this system, beam delivery optics contain beam shaping and homogenisation components to create a uniform intensity beam at the plane of a mask held on a CNC controlled XY stage. The double 6x6 (36 element) homogeniser arrays produced a 12mm x 12mm uniform illumination at the mask plane with an intensity variation of  $\pm 5\%$  RMS. A projection lens was used to transfer the pattern on the mask to a workpiece mounted on precision, air-bearing, XY stages. The demagnification factors of the projection lenses allow low-resolution mask patterns to be used to produce

high-resolution structures on the workpiece. Demagnification factors of 4x, 10x and 30x provided workpiece fluences of  $1.5 \text{ Jcm}^{-2}$ ,  $5 \text{ Jcm}^{-2}$  and  $60 \text{ Jcm}^{-2}$  respectively.

The main workpiece XY air-bearing stages (Aerotech inc. ATS80020) employed brushless linear servomotors giving 200mm x 200mm travel with 100nm resolution. Mask stages (Aerotech Inc. ATS34030) also used brushless servo drives to give 300mm x 300mm travel with 100nm resolution. Additional stages provided workpiece elevation and rotation control at similar resolutions. All stages were controlled through standard CNC control programming. Stages and beam delivery optics were mounted in a single enclosure with a damped frame to reduce vibrational coupling between the mask and workpiece stage sets. To reduce errors due to thermal expansion of the mechanical systems, the laser machining workstation was housed in a temperature controlled ( $\pm 1^\circ\text{C}$ ) semi-clean environment.

The stages of the laser micromachining workstation were controlled by two PC-based motion controllers (Aerotech Inc. Unidex 500), one of which was coupled to a laser-firing interface. The flexibility of this control system allowed the system to operate in one of two modes. Serial write mode projected the beam through a fixed mask aperture and moved the workpiece stages to serially write a pattern onto a workpiece sample. Control of stage movement was achieved either through CNC program commands or directly from graphical computer design files using a CAD/CAM software interface (AlphaCAM, Licom Systems Ltd UK). In this mode, the maximum ablation area was defined by the beam width and the write rate was limited by the laser repetition rate ( $100 \text{ pulses sec}^{-1}$ ) and the number of laser pulses required to produce the pattern. The second mode of operation employed the synchronised movement of both mask and workpiece stage sets. In this scanning mode, large area mask patterns could be transferred onto a workpiece at a rate that depended mainly on the number of laser pulses required to pattern a workpiece area equivalent in dimensions to the unapertured beam.

To achieve accurate laser machining, high quality masks were required. For long-term, frequent use applications such as beam aperturing, conventional 4" chrome-on-quartz plates were used. These were commercially produced using electron beam based lithography and could sustain mask beam fluences of up to  $0.1 \text{ Jcm}^{-2}$  without damage. Such masks, whilst providing excellent quality, suffer from a high individual cost and relatively long production and delivery times. To allow rapid development of Biofactory concepts, low-cost, limited lifetime, masks were also used produced using the laser micromachining workstation. These masks exploited the fact that most polymers are strong absorbers of deep ultra violet radiation at 248 nm and 193 nm. Masks were produced by spin coating a quartz plate with a thin layer of photoresist and then directly ablating the resist with an apertured beam. Mask patterns were drawn using a low-cost CAD package (Autosketch, Autodesk Inc.) and serial laser writing of the mask pattern was controlled through the CAD/CAM interface provided by AlphaCAM. Using a  $1\mu\text{m}$  thick resist layer (Shipley 1818) these masks could be patterned at a resolution of  $0.8 \mu\text{m}$ . Since this limitation appeared to be governed by the resolution of the projection lens used in the writing process, the masks produced, when placed in the mask stages, allowed the system to operate at its full resolution. Resist based masks were capable of sustaining higher initial beam fluences than conventional chrome masks. However, after prolonged use at fluences greater than approximately  $0.05 \text{ Jcm}^{-2}$ , gradual degradation of the mask pattern was observed. Durability of the masks could be improved by adjusting baking the resist and the addition of a thin evaporated chrome film over the resist prior to ablating the mask pattern.

## BIOFACTORY DEVELOPMENT

### MICROELECTRODE ARRAYS

Microelectrodes are essential for the operation of any Laboratory-on-a-Chip device employing AC electrokinetic processes. In Biofactory devices, the movement, separation and characterisation of biological particles is achieved using electrode arrays that impart travelling wave dielectrophoretic or electrorotational movement in bioparticles. An important factor to note is that in Biofactory devices, particles are made to move directly rather than as a result of general fluid motion. To produce controlled motion of particles in a Biofactory device linear, multilayer, electrode arrays that form travelling wave dielectrophoresis conveyor tracks are required. An example travelling wave conveyor track is shown in figure 1. Field producing electrodes are formed on the first layer of the multilayer structure whilst bus-bar connecting electrodes are fabricated on a second, insulating, layer with interconnecting via holes to allow every

fourth electrode to be connected together. Since these electrode arrays are typically used to create AC electric fields in conducting aqueous media, and hence, in total, must be able to carry up to 100mA of electrical current, the reliable production of such arrays poses two challenges. First, the rapid production of the field producing electrodes, typically 10 $\mu$ m in width, using laser micromachining and the second, the production of reliable interconnecting via holes in the insulating layer.

Several methods were investigated for the production of field producing electrodes. The first of these was direct, single pulse, ablation of thin, evaporated, chrome-gold films on a glass substrate using scanning mode ablation through a large area mask<sup>6</sup>. Using a wavelength of 248nm and a fluence of 200 mJcm<sup>-2</sup> electrode structures with widths >25 $\mu$ m were successfully produced. However, for smaller electrodes with widths of the order of 10 $\mu$ m, poor edge quality was observed. The laser ablation of metal films is a complex process involving a combination of the rapid thermal expansion and melting of the metal film and a shock wave associated with the delivery of high energies in the short, typically 20ns, laser pulse. In the case of fine electrodes, the shock wave caused the lifting of the thin chrome-gold metal film from the glass substrate. To provide additional mechanical rigidity to the metal film and to damp shock wave effects, a second approach was to coat the metal film with a thin, baked, polyimide layer. Electrodes were then formed by ablating through both the polyimide and the gold film prior to the chemical removal of the polyimide. Using this method, improved edge definition was observed. Figure 3 shows a series of 5 $\mu$ m wide electrodes on a glass substrate produced using this improved direct ablation process.

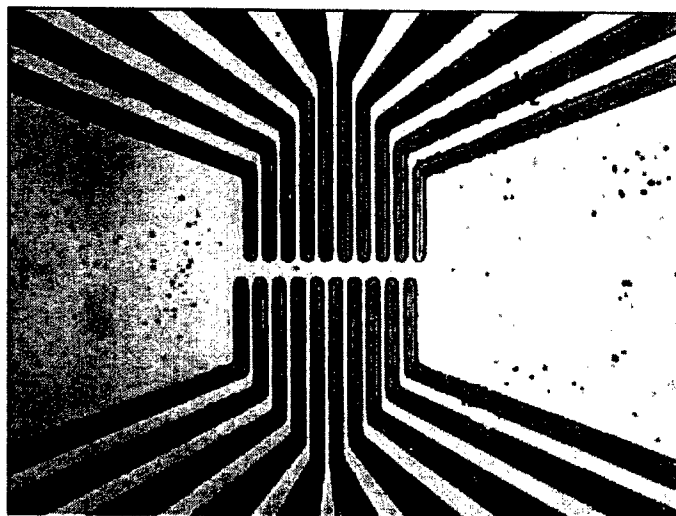


**Figure 3.** An example of laser patterned microelectrodes for travelling wave dielectrophoresis.

Also visible in figure 3 is a significant amount of debris caused by the recasting of material from the ablation process. This debris is an undesirable by-product of clearing large areas of unwanted metalisation. This form of debris can largely be removed by rinsing in a solvent such as propanol. A better approach to high-resolution electrode manufacture is to avoid debris contamination all together. This was achieved using a third production technique that employed the excimer laser workstation as a deep ultra violet exposure source. In this case, the thin chrome-gold film was coated with a 248nm resist (UVIII, Chestech Ltd UK) which was exposed using synchronised scanning of the mask and workpiece stages with a fluence of 15 mJcm<sup>-2</sup>. Following development of the resist the exposed gold and chrome was etched to produce high quality electrode arrays. Electrodes produced using this process achieved a resolution of 1.25 $\mu$ m being limited by the optical resolution of the 4x demagnification projection lens used to transfer the mask pattern to the workpiece.

Having established a reliable method of producing microelectrodes capable of producing strong AC electric fields, a method for producing reliable inter-layer electrical connections was investigated. The insulator used to separate the field producing electrodes from the busbar electrodes was a spin coatable polyimide (Dupont) that produced a 3 $\mu$ m thick film over the electrodes. Excimer laser ablation has the ability to machine a wide range of polymers with the depth of the ablated structure being controlled by the fluence of the beam and the number of laser pulses received by the workpiece. Therefore, excimer laser ablation can be used to produce via holes only with careful control of the machining process. Figure 4 shows the ablation properties of a 3 $\mu$ m polyimide film. The ablation depth for a single laser pulse is a linear function of the beam fluence. Also shown in figure 4 is the threshold of damage for a thin gold film similar to that used in Biofactory electrode arrays. From the graph it can be seen that using fluences less than 180 mJcm<sup>-2</sup> will allow the polyimide film to be fully ablated whilst preventing any damage to the underlying electrodes. In this work, a fluence of 100 mJcm<sup>-2</sup> was chosen to minimise the chance of damaging the electrodes through either

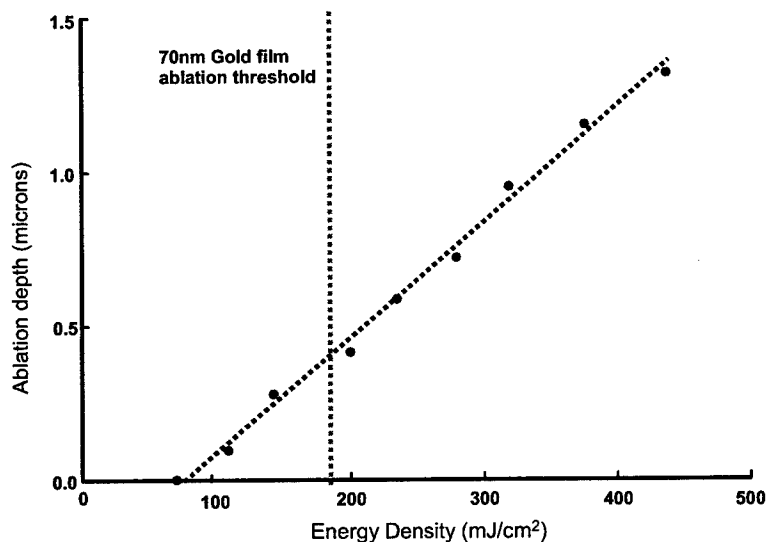


**Figure 4.** The ablation characteristics of a 3μm thick polyimide film

electrodes. To improve the metalisation, the sidewall angle of the via holes had to be increased in a controlled manner to around 70°. To achieve this sidewall angle, the via holes were machined with a series of steps. Having produced a normal 10μm wide via hole using the previously described method, the workpiece was moved by 1.4μm to one side of the via hole and the workpiece was exposed to a further 8 laser pulses. Repeating this a further 6 times produced a wall profile consisting of 7 steps. Due to the 20° wall angle, these steps tended to merge into one continuous slope. Repeating the process on the opposite side of the via hole produced a reliable through connection between bus-bars and the underlying field producing electrodes. Figure 5 shows a demonstration via hole containing 4 sidewall steps on the front and rear walls of the via hole. These faces correspond to the direction of the bus-bar connecting electrodes.

## FLUIDIC CONTROL AND DISTRIBUTION

Microfluidic channel systems form an important role in the encapsulation of Biofactory devices. In general, the modular microelectrode arrays used in Biofactories are planar structures, confinement of a sample to the active regions of these electrode arrays occurs at the encapsulation stage through the use of fluidic channels formed in a rigid, optically transparent, encapsulating layer. Fluidic channel systems in encapsulating layers have been formed using several processes including the direct serial writing of channels using excimer laser ablation. Since fluid motion within

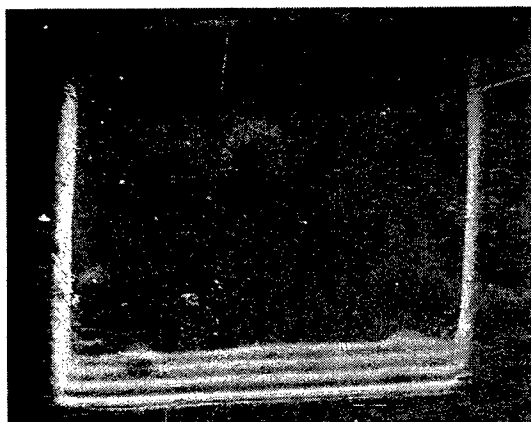


**Figure 5.** A demonstration via hole with 4 sidewall steps on the front and rear walls.

Biofactory devices is limited, such channels can be of simple rectangular cross section without the concern of particle trapping as a result of fluidic flow profiles. However, of more importance is the interconnection of Biofactory devices with external laboratory equipment. In general, laboratory fluidic interconnection employs circular cross section tubing. Therefore, manifold components are required to convert circular cross section inlet and outlet ports to rectangular cross section channels within Biofactories. In addition, such manifolds may also be required for the distribution of particle suspensions to multiple Biofactory devices on a single substrate. To allow easy interconnection of fluidic components with arbitrary cross sections, a process for laser ablation based micromachining using greyscale or grey tone masks has been developed.

Conventional laser patterning processes make use of 'binary' masks. These simple masks consist of regions where light is either fully transmitted through the mask or completely blocked. Since

ablation or thermal stress while maintaining a reasonable rate of machining. Under such conditions, via holes could be produced reliably with 60 laser pulses.

Using either serial writing or scanning machining modes, electrodes via hole arrays were produced with minimal recasting of debris. The excimer laser ablation machining process produced via holes with sidewall angles of approximately 20° from vertical. However, experimental evaluation of electrode arrays fabricated in this manner revealed an unacceptable level of failed or unreliable via hole connections. Following electron beam microscopy investigation, it was found that, due to the near vertical nature of the sidewalls, via holes appeared to be receiving poor metal coatings during the evaporation of the bus-bar connecting

the mask is binary in nature, all exposed regions are illuminated with the same fluence. Therefore, equal amounts of the material are removed in all illuminated regions and the mask pattern is accurately transferred. Greyscale masks, as the name suggests, permit controlled amounts of light to be transmitted allowing a workpiece sample to be exposed to a range of beam fluences. As shown in figure 4, above a threshold of ablation, there is a linear relationship between the depth of ablation and the beam fluence. Therefore, spatially controlling the fluence at a workpiece allows the direct transfer of three-dimensional structures in a simple machining step. Figure 6 illustrates this concept. Here a V-groove structure is to be produced in a polymer workpiece sample. Figure 6b shows the energy profile required to produce the V-groove through the control of ablation depth. At the edges of the groove, no illumination occurs whilst at the centre of the groove, the material is fully illuminated. The V-groove walls are produced using a linear gradient of fluence from the ablation threshold to 100% of the beam fluence. Figure 6c shows schematically the greyscale mask required to produce this fluence gradient. Here it can be clearly seen that zero illumination occurs where the mask is black, 100% illumination occurs where the mask is clear and levels of grey are used to produce a the controlled fluence gradient.

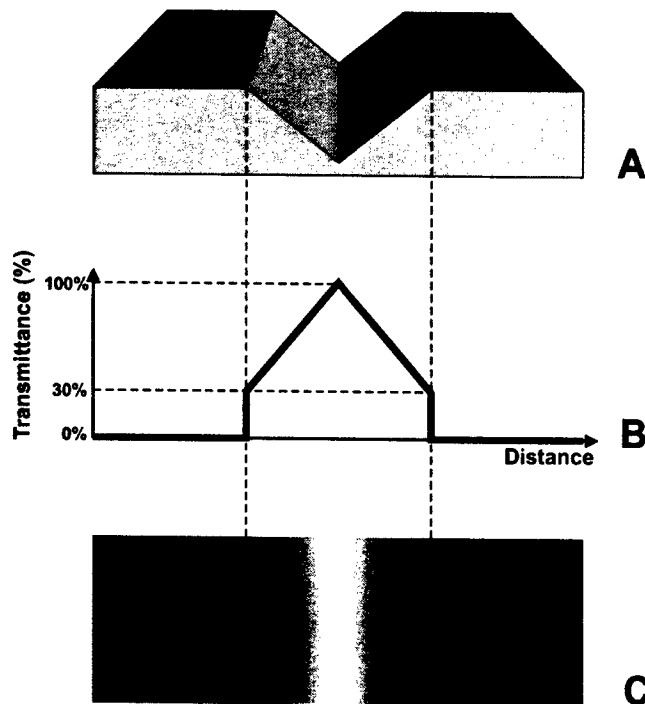
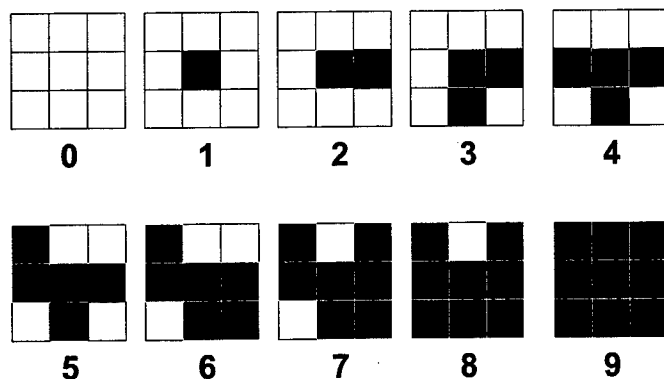


**Figure 6.** An illustration of the function of a greyscale mask. (a) The structure to be machined. In this case a simple V-groove (b) The exposure fluence required to create the V-groove through a single ablation process. At the apex of the groove the material is fully illuminated, whilst at the edges of the groove zero exposure occurs. A linear fluence gradient is required from the ablation threshold to full illumination to create the linear walls to the groove. (c) An illustration of the greyscale mask used to produce the V-groove structure. Where zero illumination is required the mask is black, where full exposure is required the mask is clear. The fluence gradient is achieved by applying a dithering process to produce a reduction in the mask transmittance. With dither pattern elements much smaller in size than the smallest feature resolvable by the beam delivery optics, a smooth wall surface is achieved.

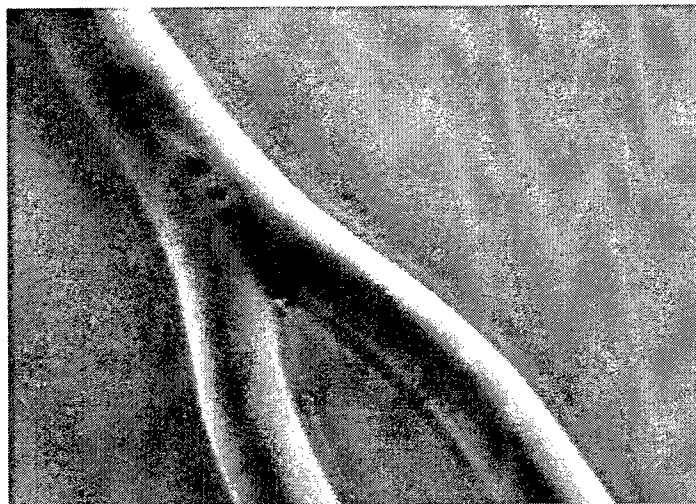
To allow low cost greyscale based laser micromachining, greyscale masks need to be created using conventional binary mask technology. This can be achieved using binary dithering techniques similar to those used in printing and computer graphics applications. The dithering process controls the average transmittance of the mask over a defined unit area by using a series of dot patterns as shown in figure 7. If the dimensions of the unit area are below the maximum resolution of the beam delivery optics, the individual features of the unit will not be reproduced but instead the ablation depth will depend on the average intensity of the light transmitted through each unit of the mask. The expansion of the computer graphics industry in recent years has led to the publication of many dithering algorithms suitable for converting between desired image intensity and binary dot patterns. In this work, the clustered dot ordered dither algorithm<sup>7</sup> has been used.

Figure 7 illustrates the output of this algorithm. In summary, each mask unit area is subdivided into an  $n \times n$  grid. The algorithm determines which elements of this grid are filled and which are left clear with particular attention being paid to the connectivity between filled elements of the grid. A filled area indicates a black (zero transmittance) region of the mask and a clear region indicates a clear (full transmittance) region of the mask. In the case of Figure 7,  $n = 3$  resulting in 10 discrete grey levels in the mask. The number of grey levels can be increased by increasing  $n$ . Using this technique with a binary mask production process, the number of grey levels is given by  $n^2 + 1$ .

Laser greyscale masks for this work were produced in-house either using a standard photolithographic process or using the resist



**Figure 7.** An illustration of the output of the clustered dot ordered dither algorithm used to produce varying transmittance in greyscale masks. The small regions of the mask are subdivided into  $n$  by  $n$  grids, in this case  $n=3$  leading to 10 discrete grey levels, the algorithm determines which elements of the grid are filled and which remain clear. In the algorithm, particular attention is paid to the connectivity between filled elements of the grid.



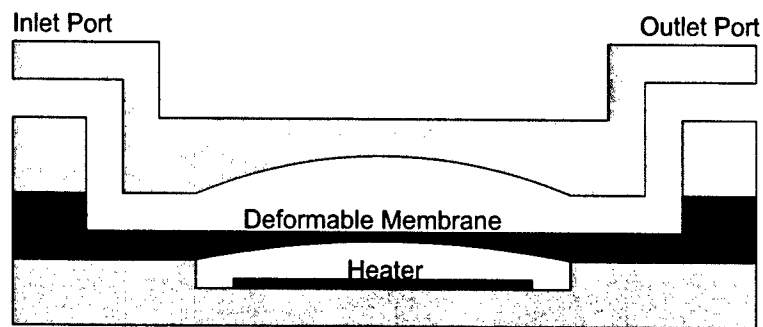
**Figure 8.** Electron micrograph of a  $100\mu\text{m}$  microfluidic manifold moulding tool microfluidic produced in SU-8 using greyscale masking techniques.

channel is a second, fluid filled, chamber containing a thin microelectrode on a rigid, glass, substrate. On passing a current through the electrode, heat is produced which causes the fluid in this lower chamber to expand. The separating layer between the upper channel and lower chamber is graded in thickness to allow controlled deformation of the floor of the upper channel. Pressure from the expanding fluid in the lower chamber causes the floor of the channel to extend until it completely blocks the channel so providing fluidic isolation. To provide a strong seal, the ceiling of the upper channel can also be contoured to match the deformation of the channel floor. The use of flexible, deformable, materials makes this form of valving ideal for use with particulate suspensions. Contouring of the channel floor and ceiling can be achieved either using greyscale masking techniques or by the simple machining of concentric circles increasing the

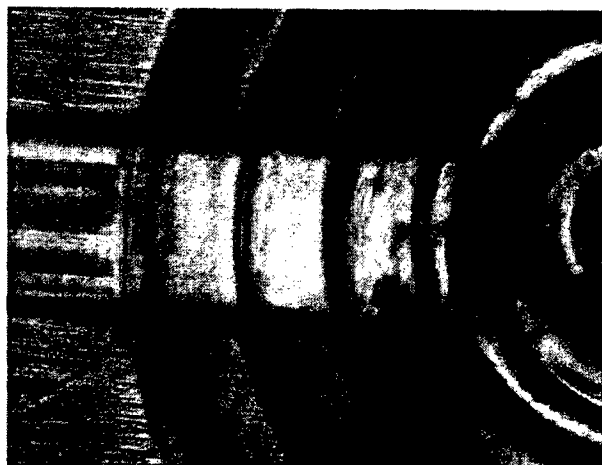
mask production process described previously. In both cases the demagnification factor of the projection lens allowed mask dither features to be larger than the optical resolution of the projection lens. Optimum greyscale reproduction was achieved using a  $10\times$  projection lens with a resolution of  $0.8\mu\text{m}$ .

Greyscale laser micromachining has been used in two ways. The first was for the direct machining of channel and manifold structures in polymers such as polycarbonate and PMMA. Here manifolds were constructed in two symmetrical halves that were bonded together using either adhesive, solvent or thermal bonding processes to form a complete manifold. The second application of greyscale machining was the fabrication of moulding tools for the production of multiple manifold systems using thermal embossing processes. Figure 8 shows a simple manifold moulding tool produced using the photosensitive epoxy-based resist SU-8. The channel structure is shown as a positive, raised, feature in the tool. When embossed into a polymer substrate such as polycarbonate, the tool produces a half channel which can be solvent bonded, using ethylene chloride, to a matching half channel producing a full channel with arbitrary symmetrical cross sectional geometry. It is of interest to note in figure 8 the smooth surface quality of the semicircular manifold mould tool. In this case, the inlet side of the manifold (top) has a cross-sectional area twice that of the outlet channels (bottom).

Associated with fluidic distribution in Biofactory devices is the need to provide fluidic isolation of portions of Biofactory devices. This is achieved through the use of microfabricated valve devices as illustrated in figure 9. These use a structure similar to that proposed by Quake<sup>8</sup>. The sidewalls and floor of a microfluidic channel are fabricated in a flexible, easily deformable, material such as rubber or thin PDMS. Beneath the floor of the



A



B



C

**Figure 9.** Laser micromachined membrane valves. (A) The floor and sidewalls of a fluidic channel are formed from a flexible material such as rubber or PDMS. The ceiling of the fluidic channel contains a dome structure. Below the flexible floor is a fluid filled chamber containing a heater. The flexible floor has a graded thickness over the heater chamber. On energising the heater, fluid in the heater chamber expands and deforms the flexible floor of the upper channel until the upper channel is blocked. Contouring of the ceiling of the upper channel allows the formation of a good fluidic seal. (B) A close up image of the thinned deformable floor. Thinning is achieved by machining concentric circles of decreasing depth in the floor material using a wavelength of 193nm. The fluence of the laser beam determines the depth of ablation. (C) An overall view of a microvalve showing the inlet to outlet channel running left to right with the heater chamber extending to the lower edge of the image.

depth of machining with reducing circle radii. For the valve shown in figure 9, the flexible material was a 100 $\mu\text{m}$  thick rubber film formulated to combine strength and deformability. Machining used a serial writing mode with a wavelength of 193nm. A 200 $\mu\text{m}$  aperture mask was projected through a 10x demagnification lens to provide a 20 $\mu\text{m}$  beam at the workpiece. A beam fluence of 1 Jcm<sup>-2</sup> was used with the depth of ablation being controlled by the number of laser pulses incident per unit area of the workpiece. Figure 9b and 9c show optical micrographs of a sample valve system. The overall thickness of the device is approximately 200 $\mu\text{m}$  with a diameter of 200 $\mu\text{m}$ .

#### EXTERNAL FLUIDIC INTERFACES

The success of many miniaturised Laboratory-on-a-Chip systems will depend on their ability to reliably interface with conventional, larger, laboratory equipment. Laser micromachining has also been successfully applied to the creation of microfluidic interconnection ports for Biofactory devices. Biofactory devices employ low-pressure fluid flow and only at the time samples enter or leave a device. Interconnection ports have been designed to allow low cost single or



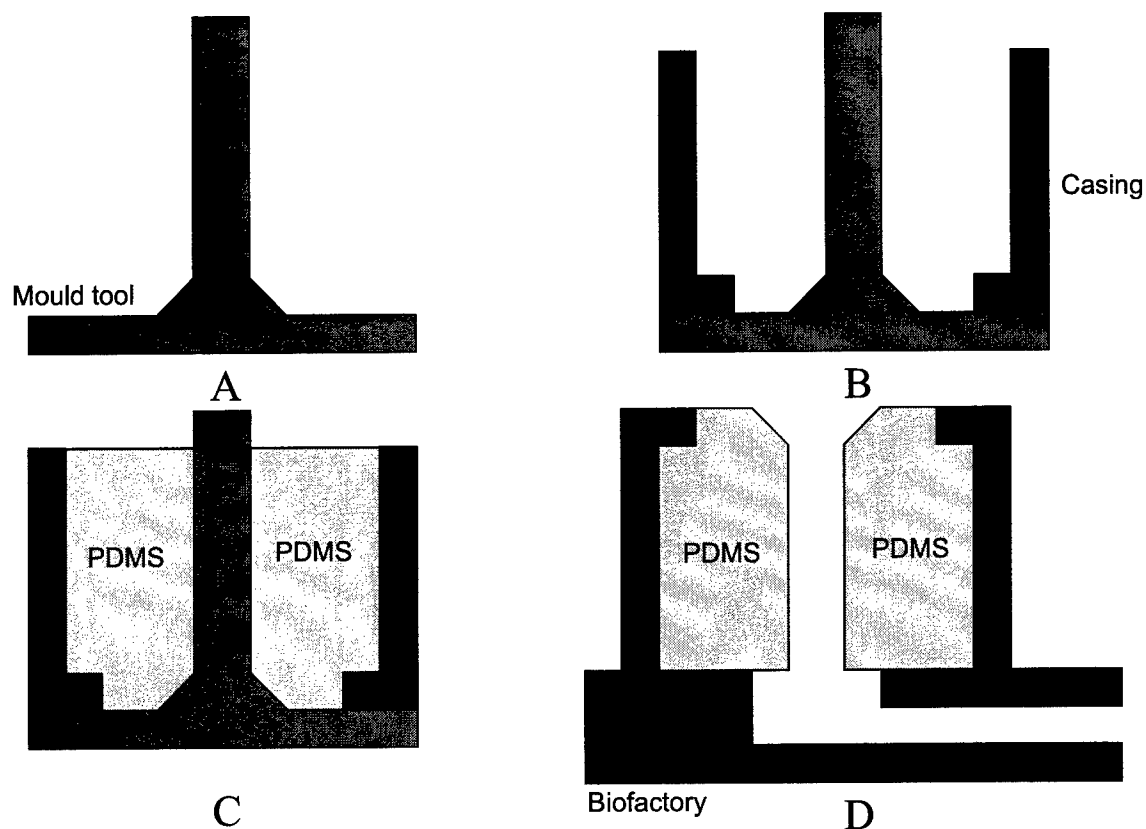


**Figure 10.** Micromoulding for external fluidic interconnects. (A) A substrate is laser micromachined to produce a negative mould tool of the final PDMS structure. (B) The mould tool is mounted on the inverted outer casing of the inlet port component. (C) PDMS is poured into the cavity formed by the tool and casing until the PDMS reaches the level of the upper wall of the casing. (D) When set, the polymer mould tool is removed and the combined casing and PDMS structured port is inverted and bonded to the interconnection region of a Biofactory device.

multiple use connections suitable for use in automated sample distribution equipment. Such equipment typically uses rigid thin-walled metal tubing to deliver known volumes of a sample onto analytical tools such as multi-well plate arrays. To allow these systems to distribute samples to Biofactory devices, interconnection ports must be able to accept and form a seal around the metal tube. Flexible, mouldable materials such as PDMS<sup>9</sup> are ideal for this purpose. Figure 10 illustrates how laser micromachining can be used for the production of micromoulds for structuring PDMS. Excimer laser ablation based micromachining is used to produce a negative of the structure to be imprinted in the PDMS. In this case the structure consists of a vertical pillar with a cone-shaped base. The mould structure is then mounted on the inverted casing of the interconnection port and PDMS in a liquid state is poured into the cavity created from the mould tool and casing. The PDMS is then allowed to cure before the mould tool is removed. The PDMS insert and casing can then be inverted and bonded to the interconnection region of a Biofactory device.

There are several factors to be considered in fabricating the Biofactory interconnection ports. The first is the choice of materials for the mould tool and outer casing. The mould tool material should possess low adhesion to PDMS in its cured form. Experimentation has shown that the epoxy based photoresist SU-8 to be a suitable material for the mould tool. Conversely, the outer casing of the interconnection port should have good adhesion to cured PDMS. This allows a firm bond between the casing and PDMS insert so assisting the sealing of the port whilst providing mechanical strength. The design of the mould tool is also critical for the operation of the interconnection port. The cone shaped base of the tool is intended to provide a tapered entrance to the port and hence assist in guiding a thin-walled metal tube into the

body of the port. The diameter of this cone is controlled by the positioning accuracy of the automated delivery system and the flexibility of the delivery tube. The fluidic seal of the port is formed by the compression of PDMS onto the outer wall of the delivery tube when it is inserted into the body of the port. Therefore, the diameter of the pillar of the mould tool has to be carefully chosen to be slightly smaller than the diameter of the metal tube but allowing both a good seal and easy insertion and removal. A secondary factor in determining the diameter of the pillar is the composition of the PDMS used as the port insert. PDMS is a two part, addition curing, clear potting compound. Mixing the two parts in different ratios allowed control of the flexibility of the cured PDMS. In this work, a range of mix ratios ranging from 3:1 to 30:1 were used depending on the width and material of the automated delivery tube. PDMS curing was achieved by heating the sample at 80°C for 15 minutes.

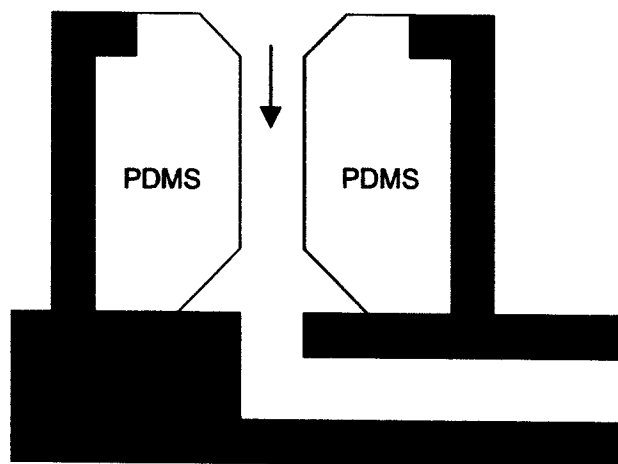


**Figure 11.** Illustration of a single use interconnection port. The flared exit to the body of the port mates with the flared end of a sample delivery tube to lock the delivery tube in position.

In the case of the interconnection port shown in figure 10d, a multiple insertion design is illustrated. By employing a two part mould tool allowing a cone-shaped entrance and exit to be imprinted in the PDMS insert, a single use interconnection port can be fabricated. The design of such a port is shown in figure 11. Here, the delivery tube possesses a flared end that matches the cone-shaped exit of the PDMS insert. When the tube is inserted into the port, the PDMS stretches to allow the tube to pass along the body of the PDMS insert. When fully inserted, the flared end of the tube mates with the flared exit of the PDMS insert to lock the tube in position. In this construction, any backpressure created within the Biofactory device pushes the flared end against the bulk of the PDMS and increases the strength of the fluidic seal.

## CONCLUSIONS

This work has demonstrated that excimer laser ablation based micromachining has a useful role to play in the development of miniaturised Laboratory-on-a-Chip technologies such as the Biofactory devices described here. Examples have been presented to illustrate the use of excimer lasers in the fabrication of complex multilayer microelectrode arrays allowing electrokinetic phenomena such as travelling wave dielectrophoresis to be exploited in micro devices. Of particular importance is the use of laser micromachining to produce accurately profiled electrical via holes in multilayer devices. In addition, the flexible nature of laser micromachining has been demonstrated through examples of fluidic distribution and control components which interface with larger scale production processes such as thermal embossing and injection moulding. This work has culminated in the production of a fully integrated miniaturised Biofactory-on-a-Chip device for the analysis of water borne parasites (figure 2).

## ACKNOWLEDGEMENTS

We acknowledge the UK Engineering and Physical Sciences Research Council (EPSRC) and Biological and Biotechnological Research Council (BBSRC) for supporting this research work over a number of years. We thank R. Pethig, M. S. Talary, J. A. Tame, Xiao-Feng Zhou, J. P. Kerslake, J. Drysdale and C. Dalton for their useful discussions and assistance during this work. We also thank N. Rizvi of Exitech Ltd. (UK) for technical assistance and guidance in excimer laser micromachining.

## REFERENCES

1. R. Pethig, Dielectrophoresis, "*Using Inhomogeneous AC Electrical Fields to Separate and Manipulate Cells.*" *Critical Reviews in Biotechnology* **16** (4) 331-348, 1996
2. A.D. Goater and R. Pethig, "Electrorotation and Dielectrophoresis." *Parasitology* **117** 177-189, 1998
3. R. Pethig, J.P.H. Burt, A. Parton, N. Rizvi, M.S. Talary and J.A. Tame, "Development of Biofactory-on-a-Chip Technology Using Excimer Laser Micromachining." *J. Micromech. Microeng.* **8** 57-63 1998
4. M.S. Talary, J.P.H. Burt, J.A. Tame and R. Pethig, "Electromanipulation and Separation of Cells using Travelling Electric Fields." *J. Phys. D: Appl. Phys* **29** 2198-2203, 1996
5. J. Zhang, K.L. Tan, G.D. Hong, L.J. Yang and H.Q. Gong, "Polymerization Optimization of SU-8 Photoresist and its Application in Microfluidic Systems and MEMS." *J. Micromech. Microeng.* **11** 20-26, 2001
6. N.H. Rizvi, E.C. Harvey, P.T. Rumsby, J.P.H. Burt, M.S. Talary, J.A. Tame and R. Pethig, "An Excimer Laser Micromachining System for the Production of Bioparticle Electromanipulation Devices." *Proc. Int. Soc. Opt. Eng.* **3224** 255-272, 1997
7. C. J. Hayden and J.P.H. Burt, "Fabrication of Fluidic Manifold Systems Using Single Exposure Grayscale Masks." *Proc. SPIE* **4404** 231-237, 2001
8. M.A. Unger, H-P Chou, A. Scherer and S.R. Quake, "Monolithic Microfabricated Valves and Pumps by Multilayer Soft Lithography." *Science* **288** 113-116, 2000
9. B. Xu, F. Arias, S.T. Brittain, X-M Zhao, B. Grzybowski, S. Torquato and G.M. Whitesides, "Making Negative Poisson's Ratio Microstructures by Soft Lithography." *Advanced Materials* **11** 1186-1189, 1999

# Laser Micromachining of Polymeric Mold Inserts for Rapid Prototyping of PMMA-Devices via Photomolding

W. Pflöging, T. Hanemann, W. Bernauer, M. Torge  
Forschungszentrum Karlsruhe, Institut für Materialforschung  
Postfach 3640, D-76021 Karlsruhe, Germany

## ABSTRACT

New technical approaches in biotechnology call for fast, cost efficient and precise patterning techniques in order to realize first polymeric prototypes in a small-scale production. For this purpose a new promising replication procedure was developed: In the first processing step UV-laser radiation is used for direct precision patterning of chemically stable polymer bulk material such as PSU, PEEK and PI. In the second processing step thin metallic layers are deposited onto the polymer surface ("protection layer"). Finally, in the third processing step these laser generated molds are used for replication of PMMA prototypes via UV-light induced reaction injection molding (photomolding). The metallic layers on the polymeric surface have to suppress or to avoid an undesired chemical interaction between the polymer surface and the MMA/PMMA resin which is used in photomolding. The deposition of a thin Pt/Au layer system leads to a significant increase of mold insert lifetime from 1-5 up to 20 replication cycles for structures with high aspect ratios. Structures with aspect ratios of larger than 10 can be achieved with a minimal lateral dimension of about 6µm. For this rapid tooling technique the actual impressive technical performances compared to other mold insert fabrication techniques will be presented with respect to the prototyping of microdevices made of PMMA.

**Keywords:** rapid fabrication technologies, micromolding, mold inserts, laser micromachining, Excimer, frequency quadrupled Nd:YAG, polymer, photomolding

## 1. INTRODUCTION

In the macroscopic world different "rapid"-technologies like Rapid Prototyping, Rapid Manufacturing or Rapid Tooling have been established for a fast prototype or molding tool development. At Forschungszentrum Karlsruhe GmbH different micropatterning techniques are established either to realize a fast fabrication of prototypes via direct patterning, or to enable a large scale production of microcomponents made of polymers, metals or ceramics. Best optical qualities with a surface roughness at the sidewalls of about  $R_a < 50$  nm and high aspect ratios up to 650 are obtained with patterns produced by LIGA<sup>1</sup>. In LIGA the patterning of the polymer surface is performed with synchrotron radiation as illumination source. An alternative LIGA process is the so called "poor-mans LIGA" in which Excimer laser ablation of polymers is used instead of synchrotron illumination. This process only enables small aspect ratios and a surface roughness in the range of  $R_a = 100$  nm. Via electroforming, polymer structures can be transferred into a metallic shape (e.g. nickel) which is used as a mold insert in replication techniques like injection molding<sup>2</sup> and hot embossing<sup>3</sup>. Micromilling is applied for the fabrication of prototype structures and mold inserts using profiled cutting tools or end-mills<sup>4,5</sup>, and laser micromachining represents a versatile method for structuring a broad range of materials. Satisfying the need for smooth surfaces and, if necessary, sloped walls for easy replication, mechanically cut and laser machined structures are manufactured and replicated by hot embossing and injection molding. First promising results have been achieved by combining the microfabrication techniques, e.g. mechanical micromachining and LIGA for the manufacture of an optical multi-fiber connector, demonstrating clearly that interdisciplinary work in a research center is an effective way of realizing complex microstructures and applications. For applications which do not require structural details typical of the LIGA technology mechanical microengineering using micromilling or -cutting devices as well as laser-assisted micromachining allows a cost and time reduced mold insert fabrication. The state of the art of the laser technology concerning the fabrication of metallic mold inserts was described in detail<sup>6</sup>. In this paper we will also give a short technical update of the new capabilities in laser-assisted fabrication of metallic mold inserts developed at Forschungszentrum Karlsruhe GmbH (section 3.1). Excimer laser radiation is a perfect tool for the patterning of polymers with excellent surface qualities. Under optimized laser parameters the laser patterned areas reveal an average surface roughness of about 100-200nm or better. The

\*Correspondence: Email: [wilhelm.pfloging@imf.fzk.de](mailto:wilhelm.pfloging@imf.fzk.de) Fax: ++49-7247-82-7288

sidewall of patterned structures is much better. Furthermore, the steepness of the sidewalls can be of a few degrees or nearly zero. This excellent properties of polymer ablation via Excimer laser radiation is caused by a homogenous laser intensity profile as well as by the nearly "cold" laser ablation of polymers. The mechanism of polymer ablation can be described in most cases as a combination of direct bond breaking and thermal excitations. For high absorbing polymers the non-thermal processes are dominating which results in good surface qualities during laser patterning<sup>7</sup>. With Excimer laser radiation aspect ratios up to 40 are realized in polymer surfaces. The lateral resolution of the structures is in the micrometer range. The aim of this contribution is to realize a fast production (rapid fabrication) of polymeric prototypes of high accuracy. At the start of product development only a small number of prototypes for functional testing is necessary. Therefore, several steps of redesign and subsequent mold insert fabrication will follow. If the functional testing leads to the desired results, then the final metallic mold insert for a large scale production via micro injection molding should be fabricated. If there is a need of redesign, then an additional "processing loop" including CAD/CAM, laser ablation and photomolding will be necessary (see figure 1):

1. definition of an initial design by customer
2. fabrication of polymeric mold insert with initial design (rapid tooling): 1-2 days
3. replication in PMMA with photomolding (rapid prototyping): 0.5 days
4. functional testing of the prototyped microcomponents
5. redesign with subsequent mold insert fabrication and repetition of previous steps until final design achieved followed by mass production with injection molding or hot embossing.

The need of a fast and cheap technology for the fabrication of mold inserts arises. Furthermore, a data sheet including information about accuracy, aspect ratio, steepness, surface quality and ablation rate of the laser fabricated mold insert as well as a first cost-calculation for the process will be necessary. A fast and cheap technology may be the laser-assisted patterning of polymeric mold inserts which will be discussed in this paper. Appropriate polymers are good absorbers for the used 248 nm laser wavelength, and furthermore, the polymers have to be chemical stable against organic solvents and the used feedstock material (PMMA/MMA). The last criteria will be defined as lifetime of mold inserts expressed as maximum possible number of replication cycles without any defects. The replication of polymeric mold inserts is performed with UV-light-induced reaction injection molding (photomolding) process (UV-RIM) which enables a fast production of prototypes made of PMMA. In this paper we focus onto the process sequence "laser patterning" and "replication via photomolding" (dotted area in figure 1). The aim is the optimization of the laser assisted fabrication of polymeric mold inserts with respect to the photomolding technique. After each processing step (laser processing and photomolding) a quality control (q.c.) is performed in order to identify a possible process trouble or to optimize the particular processing steps. The process control is performed ex-situ. For this purpose the laser machined mold inserts as well as the parts demolded by photomolding are characterized by Scanning Electron Microscopy (SEM) and/or with 3D surface imaging. If the laser patterned surfaces reveal a derivation of the initial design, then the process of laser ablation has to be repeated under optimized parameters. If the laser patterned mold insert matches well with the desired design, then photomolding can be performed. The demolded parts are characterized concerning aspect ratio, accuracy and surface quality. If the demolded parts reveal a significant difference caused by the photomolding technique, then the process of demolding under optimized parameters or feedstock composition has to be performed.

Main application fields in which this process sequence may be first established are fluidic and bio-chip technologies. For example Capillary-Electrophoresis (CE)-Chips are commercially made of glass, silicon or quartz<sup>8</sup>. They are used in biological and chemical analysis for the handling of small volumes of liquids ( $10^{-9}$ - $10^{-12}$  l) in order to perform separation and detection ( $\mu$ -TAS). At Forschungszentrum Karlsruhe GmbH and elsewhere<sup>8</sup> the use of polymer materials instead of Si, glass or quartz is investigated, because polymers can easily and economically be replicated in micro injection molding techniques.

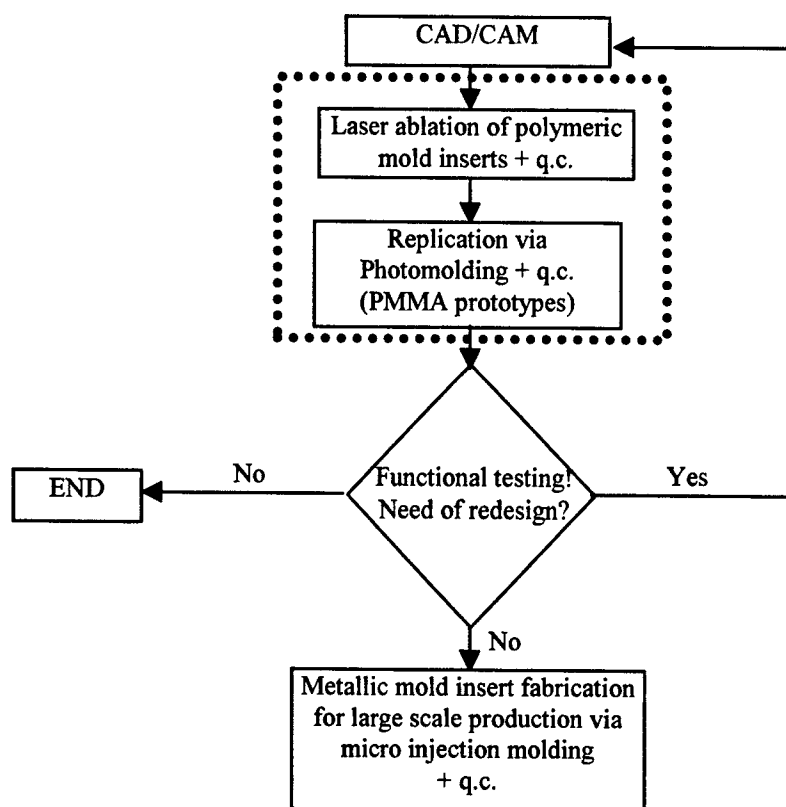


Figure 1: Sequence of processing steps for the development and large scale production of microcomponents with functional design (q.c.: quality control).

## 2. EXPERIMENTAL PROCEDURE

For the UV-laser-assisted prototyping of CE-Chips three different types of polymers as possible materials for the mold inserts are investigated: polyetheretherketone (PEEK), polysulfone (PSU) and polyimide (PI). These materials are selected, because they are chemically stable and they are good absorbers for KrF-Excimer laser radiation (wavelength 248 nm) as well as for frequency quadrupled (4 $\omega$ ) Nd:YAG laser radiation (wavelength 266 nm). The Excimer laser ablation is performed with a laser micromachining system (Exitech PS2000) which operates with a Lambda LPX 210i as radiation source. Different mask techniques are used in order to obtain the desired pattern: Direct optical imaging of complex structures or motorized masks are established. Furthermore, a motorized rotating mask is used which enables us to change complex mask structures with high precision and without stopping the ablation process. This mask technique will be further used for the patterning of large complex structures. Up to 40 different masks can be located on the rotating mask system. Another technical option is the use of a motorized aperture mask: The CAD data can be directly transmitted into the polymeric surface. The aperture consists of four independent shields which can be positioned with  $\mu\text{m}$  accuracy. This is a precise processing technique for the fabrication of well defined groove structures: If steep walls are necessary at the start and at the end of a groove, then this can be realized by opening a closed mask (at the start) and closing an opened mask (at the end) which has to be synchronized with the laser pulses. Another geometry which is possible with a motorized masks is the crossing of two grooves with the same depth in the groove as well as in the crossing area. Furthermore, curved grooves and grooves with a variation of cross section can be fabricated. This "flexible" technology is a scanning technology (laser direct writing) and needs no additional masks, but the processing time may be long compared to a direct optical imaging of a large mask geometry.

If the scanning process is too slow because of the small laser repetition rate (<100 Hz) it may be useful to establish a 4 $\omega$  Nd:YAG laser radiation source where laser repetition rates up to 2000 Hz are possible. This could cause a reduction of processing time of more than one magnitude. First investigations in polymer ablation are carried out with a PowerChip Nano UV (JDS Uniphase) with a pulse width of about 400 ps and a pulse energy of about 10  $\mu\text{J}$ . The high laser fluences of

$>40 \text{ J/cm}^2$  enables polymer ablation as well as ablation and drilling of glass, steel and ceramics. Because of the small pulse width a significant reduction of thermal contribution in the ablation processes is expected. For PC, PSU, PEEK and PI first investigations concerning ablation rate and surface roughness are performed. The fabrication of first polymeric mold inserts with CE-Chip design are carried out.

### 3. LASER MICROMACHINING

#### 3.1 Laser processes for the manufacturing of metallic mold inserts – state of the art

Alloy steel as well as cemented carbide are of interest for laser assisted mold insert fabrication. With these materials we realize a new kind of mold inserts which can endure high mechanical, thermal and chemical abrasions during injection molding of ceramics, metals and composites. The main challenges are to produce defect free and smooth surfaces during laser patterning in order to enable micro injection molding. A significant decrease of debris was obtained via laser-assisted patterning of hard materials such as cemented carbide with frequency-tripled Q-switch Nd:YAG (wavelength 355 nm)<sup>9</sup> and Q-switch Nd:YAG (wavelength 1064 nm)<sup>10</sup>. But the surface roughness as well as the pore formation at the sidewalls disable the replication of micro-parts via micro injection molding techniques.

Alloy steel or carbon steel are not as hard as cemented carbide but due to the higher ductility mechanical tensions will decrease more during injection molding. So we decided to take effort in process development of laser micro caving (LMC). The patterning of metallic mold inserts via LMC enables a "clean" patterning process with only a small amount of debris and melt. Surface qualities with a roughness of about  $R_a=200\text{-}300 \text{ nm}$  can be realized. The ablation rates are in the range of  $10^5\text{-}10^6 \mu\text{m}^3/\text{s}$ . Electropolishing as post-processing step enables the formation of curved shapes with a surface roughness of about  $R_a=100\text{-}200 \text{ nm}$ . Further analytic results in more detail concerning ablation mechanism and reaction layers were achieved<sup>11</sup>. Microstructures composed of polymers or ceramic-composites are successfully demolded by using the UV-RIM technique with aspect ratios up to 10. Fundamental aspects of LMC of steel bulk materials were investigated in detail. CE-Chips made of PMMA are fabricated and their functionality is demonstrated<sup>6</sup>.

The actual research and development is focused on the technical transfer of three dimensional shapes, which are created in CAD modules, into the technical process including CAM, process strategy and laser material processing. For this purpose the desired three dimensional geometry is created in a 3D-CAD tool (figure 2). In dependence on the ablation rate per laser scan the geometry is subdivided into layers with a thickness of about  $3\text{-}20 \mu\text{m}$ . Each of the layer can get an individual filling strategy. One important strategy is the change of scanning direction after each layer. The value of the angle between two scanning directions can be changed as desired. The change of scanning direction should avoid an accumulation of scanning patterns. Furthermore, the steepness of sidewalls as well as their surface quality can be optimized by using appropriate scanning directions. An additional process strategy is the choice of the appropriate scan offset which is in the range of 5 and  $15 \mu\text{m}$  for an optical focus diameter of about  $20 \mu\text{m}$ . This parameter determines the average surface roughness and ablation depth per layer. The best average surface roughness without any post-processing is of about  $R_a=200\text{-}300 \text{ nm}$  while the ablation rate is in the range of  $3\text{-}20 \mu\text{m}/\text{layer}$ .

Furthermore, the processing along the contours within one layer may be important for laser microcaving of steel surfaces. In some cases it is useful to perform a separate ablation-strategy along the contour of a shape. Especially for CE-Chip designs the contour has to be patterned much more frequently than the rest of the layer in order to get an improved steepness of the sidewalls. Up to now, one disadvantage of laser microcaving is the roundness of the bottom of patterned areas. This is mainly caused by the gaussian intensity profile of the laser beam as well as by the reduced laser beam absorption at sloped contours. To overcome this problem a 5 axis position stage will be built up in order to realize a high precise material processing at the contours for different incident angles of the laser beam. It is well known, that this technical measure leads to a significant improvement of the steepness of sidewalls by using Q-switch Nd:YAG laser radiation. Even undercuts are possible, which are not desired for replication techniques but which may be useful for the three-dimensional patterning of metallic prototypes.

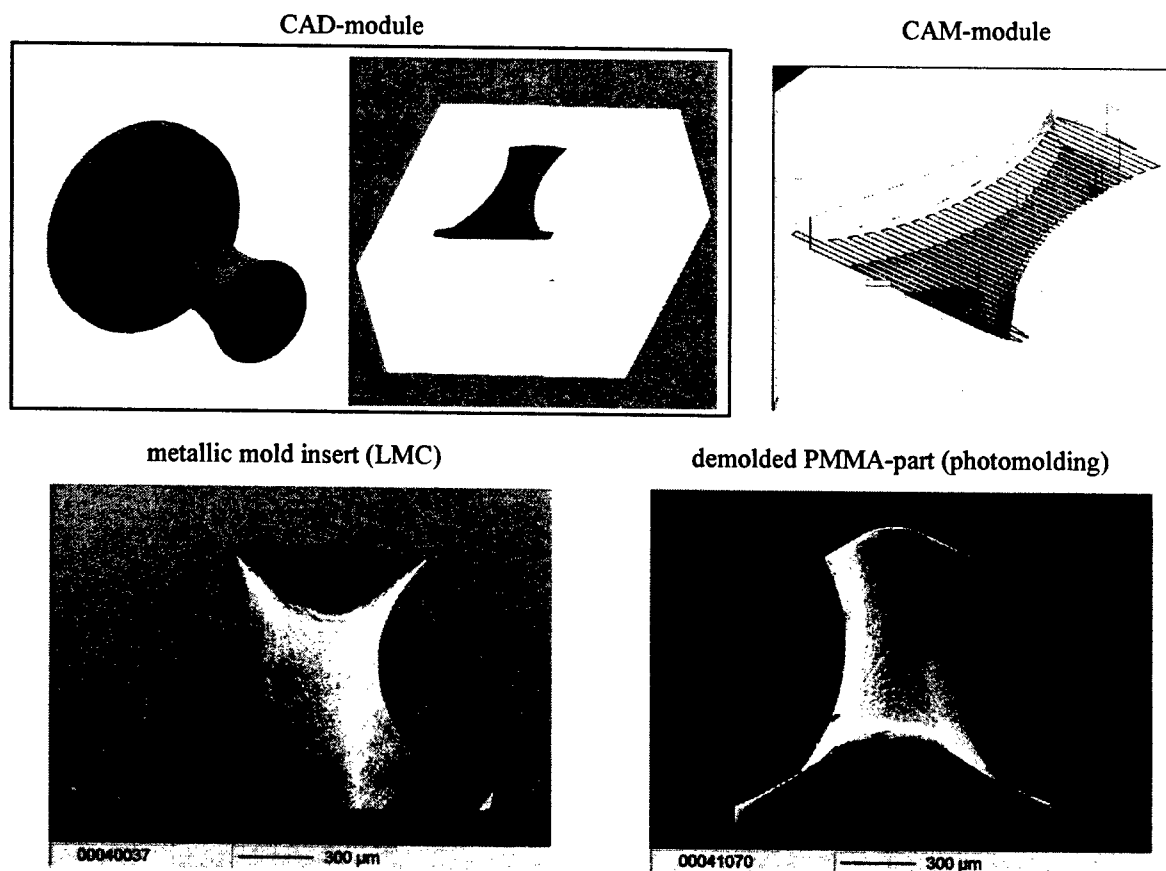


Figure 2: Different stages of prototype fabrication: initial design of a three dimensional part (CAD-module); individual filling strategy for each of the 40 layers (CAM-module); laser patterned steel substrate X16CrNiSi25-20 (LMC) and demolded part made of PMMA (photomolding).

## 2.2 New technical approach: Rapid tooling of polymeric mold inserts

Excimer laser ablation of polymers enables the formation of grooves with nearly rectangular cross section. This effect is caused by mainly two reasons: 1. The intensity profile of the laser beam is nearly rectangular; 2. The ablation rate is nearly constant above the threshold of laser fluence which depends on the material in each case<sup>12</sup>. The last reason causes a constant ablation rate also in the region near the sidewall, where the incident angle of the laser beam differs slightly from 90° (90° means normal incidence of the laser beam). The ablation rate depends on the specific material and is in general in the range of 0.3-1 μm/pulse, while the surface roughness in the patterned area may be of about  $R_a=100-200$  nm. A further significant advantage of Excimer laser processing is the possibility of the patterning of large areas per one laser pulse (several mm<sup>2</sup>/pulse) compared to the small optical focus diameter of Nd:YAG laser radiation (5-50 μm). This means that complex and large mask structures can be directly transferred to the polymer surface via an optical imaging. Because of these properties the desire for polymeric mold inserts was born. Unfortunately the hardness of polymers is low compared to metallic mold inserts. Furthermore, polymers may react with the ambient air, may react with the feedstock material or may be chemically changed because of elevated temperatures. These aspects may strongly influence the functionality of the polymeric mold. Therefore, we have decided to investigate the rapid tooling of polymeric mold inserts only for the small-scale fabrication of prototypes. For further decrease of total processing time and production costs during product development it may be useful to establish polymeric mold inserts for the first prototypes<sup>13</sup>. For the fast fabrication of polymeric micro parts with structures of high aspect ratio a new promising replication procedure is investigated:

1. Polymer bulk material is patterned by UV-laser radiation (KrF-Excimer or 4ω Nd:YAG)
2. Thin metallic films are deposited onto the surface of the polymeric mold insert
3. Finally, replication is performed via photomolding/UV-RIM

KrF-Excimer laser radiation enables the 3D micro structuring of a large number of polymers with high accuracy and high aspect ratios up to 40. Because of a possible chemical interaction during photomolding between the feedstock material



(resin) and the polymeric mold we decided to use chemically stable polymer materials such as PSU, PEEK and PI. Additionally, we investigate the improvement of mold insert lifetime (number of defect-free replications) by the deposition of thin metallic layers onto the polymeric surfaces.

## 2.3 Patterning of PSU, PEEK and PI with UV laser radiation

### 2.3.1 Excimer

The ablation process is mainly influenced by the laser fluence  $\epsilon$ . The etch rate as function of laser fluences for the polymers PSU, PEEK and PI is shown in figure 3. It is obvious for PEEK and PSU that the etch rate increases linearly with increasing  $\epsilon$  for values between 1 J/cm<sup>2</sup> and 5 J/cm<sup>2</sup>. PI reveals the smallest etch rate of all of the selected polymers. Furthermore, the etch rate of PI as function of  $\epsilon$  reveals three regions (see figure 3) which can be referred to <sup>12</sup>:

1. (0.4 J/cm<sup>2</sup> – 1.8 J/cm<sup>2</sup>) saturated Excimer laser absorption with

$$R \propto \frac{1}{\alpha} (\epsilon - \epsilon_0),$$

where  $\epsilon_0$  denotes a characteristic laser fluence usually not equal to the threshold laser fluence and  $\alpha$  is called "effective absorption coefficient",

2. (1.8 J/cm<sup>2</sup> - 3.0 J/cm<sup>2</sup>) plume attenuation of the laser intensity which final results in a
3. (> 3.0 J/cm<sup>2</sup>) saturated ablation rate.

For significant smaller laser fluences one will expect a further region referred to linear Excimer laser absorption which can be described by the Beer's absorption law <sup>12</sup>. For  $\epsilon > 3$  J/cm<sup>2</sup> the ablation rate for PI tends to a saturation. For applications it is suitable to work within this third region in order to guarantee a high accuracy in structure depth. Small variations in pulse energy lead to no significant change of the ablation rate. Furthermore, it is observed that with increasing  $\epsilon$  the contours of side walls become more rectangular. For example the inclination angle of a sidewall in PSU decreases from 17° ( $\epsilon=1$  J/cm<sup>2</sup>) down to 6° ( $\epsilon=5$  J/cm<sup>2</sup>). The inclination angle for PEEK is somewhat smaller (7° for  $\epsilon=2$  J/cm<sup>2</sup> and 5° for  $\epsilon=4$  J/cm<sup>2</sup>). At very high ablation rates a slight rounding is indicated at the bottom of laser patterned walls. With increasing  $\epsilon$  a decrease of debris formation is observed. The size of material fragments as well as the surface roughness of the side walls decrease significantly with increasing  $\epsilon$ . In the case of increasing laser pulse number  $N$  an enhanced deposition of debris is observed and the size of ejected material fragments increases. Rounding of edges on the ground of laser patterned grooves occurs. This effect becomes more important with an increasing number of  $N$ .

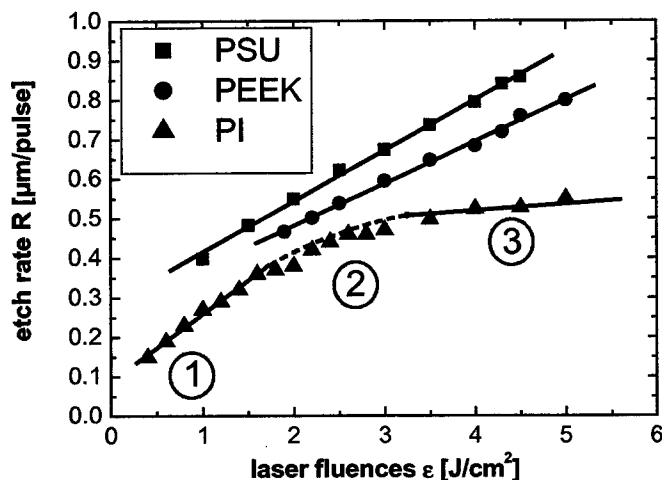


Figure 3: Etch rate for polysulfone (PSU), polyetheretherketone (PEEK) and polyimide (PI) as function of laser fluences (KrF-Excimer, wavelength 248 nm, pulse width 25 ns, laser repetition rate 10 Hz, number of laser pulses 100)

The numerical aperture NA of the objective has a great influence on the cross section of laser patterned trenches. A rectangular cross section is achieved with numerical apertures under 0.25. The appropriate slope of the sidewalls depends on

a suitable laser fluence as described above. High numerical apertures cause significant roundings on the patterned ground. In the case of  $NA > 0.4$ , undercuts of the sidewalls and rounded edges on top of the trenches can hardly be avoided. Steep sidewalls and well defined contours of edges are required for the fabrication of polymeric mold inserts. For this purpose, objectives with  $NA = 0.10$  are used.

The wet-chemical pre-treatment of the polymer and the processing gas was an important aspect for an improved surface quality: The cleaning of PSU and PEEK in the ultrasonic bath and the use of helium as process gas caused a drastic reduction of the debris formations. Thus, the surface roughness could be reduced to  $R_a < 200$  nm. For PSU the effect of wet-chemical pre-treatment is very significant and may be caused by a penetration of organic solvent in the outer polymer surface<sup>6</sup>.

The best attainable surface roughness after Excimer laser patterning of the selected polymers is in the range of  $R_a = 100$ –200 nm for PEEK and PSU. For PI the average surface roughness is significantly lower than 100 nm. The average roughness for PI (figure 3, region 3) is between 50 nm and 60 nm for high laser fluences. This is an excellent condition for the laser-assisted fabrication of polymeric mold inserts and the use of photomolding as replication technique.

### 2.3.2 Frequency quadrupled Nd:YAG

Laser patterning of polymers with  $4\omega$  Nd:YAG Laser radiation is performed with high laser fluences ( $> 40$  J/cm<sup>2</sup>) and high repetition rates (1000 Hz). The ablation depth as function of laser pulse number is determined for the selected chemically stable polymers (see chapter 2) as well as for polycarbonate (figure 4). It is obvious that the laser etch rate is constant for all polymers over a large ablation depth. The etch rates are listed in table 1. Furthermore, the curves of PSU, PEEK and PI in figure 4 reveal nearly the same slope but an offset is indicated which leads to decreasing ablation depth for  $PSU < PEEK < PI$ . This can be explained by a change of etch rate within the first 50 laser pulses. After 50 laser pulses the etch rate is nearly constant for all these polymers, while for a laser pulse number smaller than 50 the etch rates are significantly different between these polymers. The ablation rate for PC is significantly larger than these of the other polymers for all laser pulse numbers, namely PC. The surface roughness for PC varies only between  $R_a = 140$ –400 nm for all laser pulse numbers. PI reveals the smallest etch rate but the surface roughness varies between  $R_a = 0.3$ –1.3  $\mu$ m. The surface roughness largely depends on the pulse overlap during laser scanning as well as on the optical focus diameter, and a further optimization of laser parameters has to be optimized in further investigations. The debris formation is significantly reduced for all polymers compared to the polymer ablation with Excimer laser radiation. We assume that this is caused by the small laser pulse width of 400 ps of the  $4\omega$  Nd:YAG compared to 25 ns of the KrF-Excimer. The small pulse width leads to a significant reduction of thermal contributions during ablation. This is also indicated by the laser structuring of test structures such as very small walls with a width of about 3–5  $\mu$ m and a height of about 100  $\mu$ m.

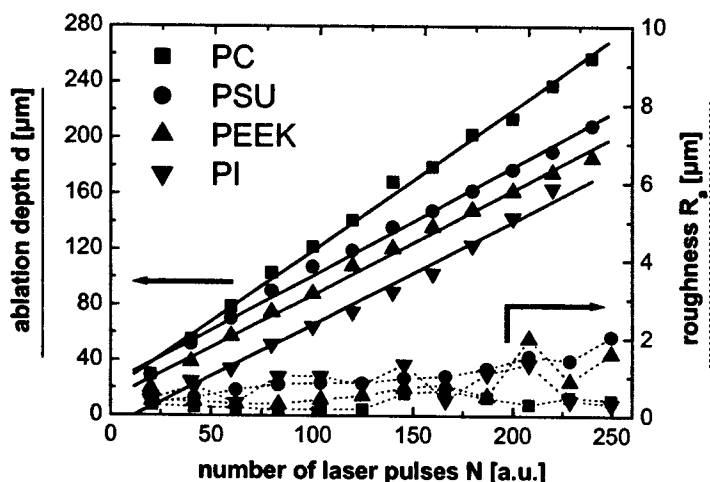


Figure 4: Ablation depth and average surface roughness as function of laser pulse number ( $4\omega$  Nd:YAG, wavelength 266 nm, pulse width 400 ps, laser repetition rate 1000 Hz, focal length 75 mm) for polycarbonate (PC), polyetheretherketone (PEEK), polysulfone (PSU) and polyimide (PI).

laser pulse number N	PC	PSU	PEEK	PI
> 50	1.00 $\mu\text{m}/\text{pulse}$	0.78 $\mu\text{m}/\text{pulse}$	0.75 $\mu\text{m}/\text{pulse}$	0.74 $\mu\text{m}/\text{pulse}$
20	1.48 $\mu\text{m}/\text{pulse}$	1.46 $\mu\text{m}/\text{pulse}$	0.99 $\mu\text{m}/\text{pulse}$	0.55 $\mu\text{m}/\text{pulse}$

Table 1: Etch rates for polycarbonate (PC), polyetheretherketone (PEEK), polysulfone (PSU) and polyimide (PI) (4 $\omega$  Nd:YAG, wavelength 266 nm, pulse width 400 ps, laser repetition rate 1000 Hz, focal length 75 mm) determined by the slope of the linear graphs in figure 4 as well as calculated for the first 20 pulses.

#### 4. LIGHT INDUCED REACTION INJECTION MOLDING (PHOTOMOLDING)

Micro injection molding as well as hot embossing are established microfabrication techniques, the first one suitable for mid and large scale fabrication and the latter one of small-scale fabrication and with some restrictions for prototyping. The installation of a mold insert and the establishing of a stable and defect-free molding process with optimized parameters is time consuming for injection molding and for hot embossing. It takes up to one day in each case. In micro injection molding the molding cycle times are short (depending on the used plastic material and aspect ratio of the surface relief: 2 up to 8 min) but the setup and optimization times can be quite extensive, in case of hot embossing typical cycle times are 10 up to 30 min but accompanied by reduced setup and optimization times down to some hours. The cycle time is mainly determined by the molding tool's heating and cooling procedure, the setup time by the more or less tool complexity. As a consequence the light induced reaction molding was developed using the rapid UV curing instead of the slow thermal curing of reactive resins. In analogy to stereolithography low viscous photocurable resins contains methylmethacrylates or unsaturated polyesters (UP) and the related monomer (MMA or styrene) are used as mold material. In opposite to stereolithography a real 3D shape cannot be realized because of the use of a mold insert as master containing the microstructures on the surface. In order to keep the compatibility with the other micro replication techniques the geometric size of the mold insert cavities was adapted from micro injection molding and hot embossing. The experimental replication setup is similar to a typical reaction injection molding equipment but had to be extended with the technical necessities for photocuring. The replication machinery consist only of a few parts: lower borosilicate glass molding tool facing the UV/Vis source, upper molding tool with mold inserts, ejector pins for demolding, connectors to a vacuum pump and external temperature control as well as the reactive resin reservoir (figure 5). The complete molding cycle proceeds isothermally under ambient conditions. The cycle time is independent from the microstructure's aspect ratio and determined by the photocuring speed of 1 min per mm mold thickness in the given setup. In case of full process automatization cycle times around 1 minute should be possible. The total setup time including the fitting of two mold inserts is smaller than 30 minutes. One molding cycle consist of the following five process steps:

1. Closing of the molding tool
2. Evacuation of the mold cavities
3. Low pressure resin injection (< 1 MPa)
4. Photocuring with applied holding pressure
5. Mold opening and part removal

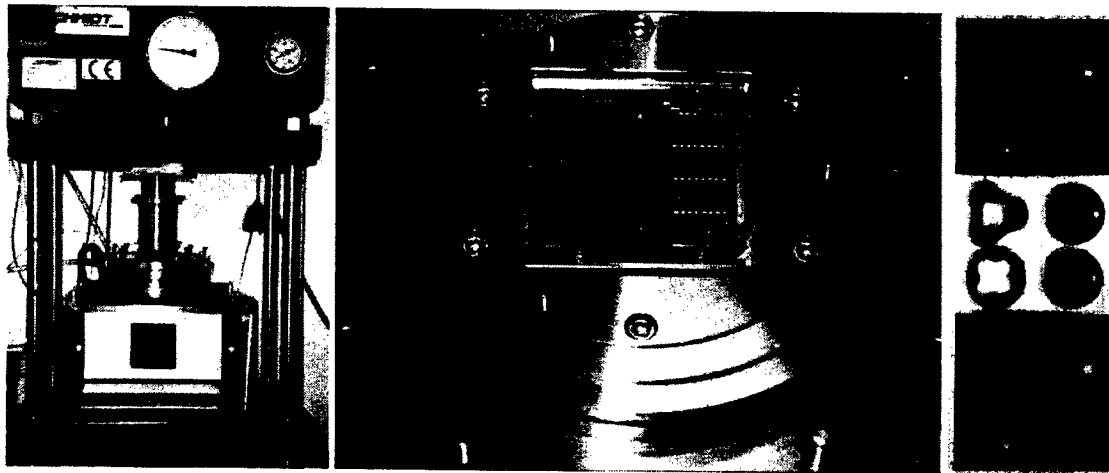


Figure 5: Photomolding machinery, top view on upper molding tool carrying two metallic mold inserts and surface image of a metallic mold insert carrying annular gear wheel system.

Due to the rapid setup and curing times it is possible to obtain first prototypes made of PMMA within one hour. The actual technical limits of the photomolding replication technique using pure polymeric resins are: smallest structural detail: 200 nm, largest aspect ratio: 10 (free standing walls, height 400  $\mu\text{m}$ , width 40  $\mu\text{m}$ ) and 20 (small trenches, height 2 mm, width 0.1 mm) respectively, given by the accessible mold inserts. More experimental details are given in <sup>14, 15</sup>.

## 5. POLYMERIC MOLD INSERTS AND DEMOLDED PARTS MADE OF PMMA

The first demolding experiments reveal that the necessity of a protection layer for the mold inserts still arises (table 2): The surface volume of the polymeric mold inserts made of PSU, PEEK and PI increases. Therefore, an undercut may arise and the replication process via photomolding will be only possible for 1-5 replication cycles. The best results without protection layer reveals PI with 5 cycles. The effect of increasing volume and reduced mold insert lifetime may be caused by a penetration of the resin or monomer in the outer surface of the polymeric mold. We assume that the penetration depth may be in the range of several  $\mu\text{m}$ . A replication of micro-sized structures with high aspect ratio was only possible for one or two replication cycles. Aspect ratios of about 6.6 were achieved with a structure width of the walls of about 10  $\mu\text{m}$ .

First investigations were performed with a Pt/Au layer system with a thickness of about several ten nm. With these protection metallic layers the number of possible replication cycles increases. But after several replication cycles, a reaction between resin and the polymeric mold inserts still occurs. This finally leads to a destruction of the mold insert. In the case of PSU and PEEK only 3 and 5 cycles are possible (table 2). In the case of mold inserts made of PI the protection layer leads to a significant increase of lifetime. We assume that the main problem is still a small adhesion of the metallic layer. This assumption is supported by the fact that repetition of metallic film deposition after several demolding cycles leads to a significant increased mold insert lifetime. Because of chemical interaction between polymeric mold insert and the monomers used in photomolding it is useful to protect the mold insert surface with thin metal films. Future work will be concerned with further improvement of the thin film adhesion onto the polymeric mold inserts.

Lifetime (number of defect-free replications)	PSU		PEEK		PI	
	without	with	without	with	without	with
	protection layer		protection layer		protection layer	
	1	3	3	5	4	> 20

Table 2: Lifetime of polymeric mold inserts with and without protective metallic layer.

In the first investigations different test structures with high aspect ratio and small structure size are patterned with Excimer laser radiation in order to develop the process parameters, to demonstrate the possibilities (compared to conventional

patterning techniques such as micromilling) and to select the appropriate polymer material. Because of the increased lifetime of PI and the good ablation properties concerning constant ablation rate (figure 3) and small surface roughness ( $R_a < 100$  nm) we decided to use PI as material for the mold inserts. Figure 6 shows the mold insert and demolded PMMA part with an array of columns with a diameter of  $8\mu\text{m}$  and a height of about  $61\mu\text{m}$ . The smallest distance we have realized between two columns is  $6\mu\text{m}$  by a column height of about  $190\mu\text{m}$ . This example shows that the surface quality of laser patterned PI is good enough for the replication of structures with high aspect ratio and large surface area.

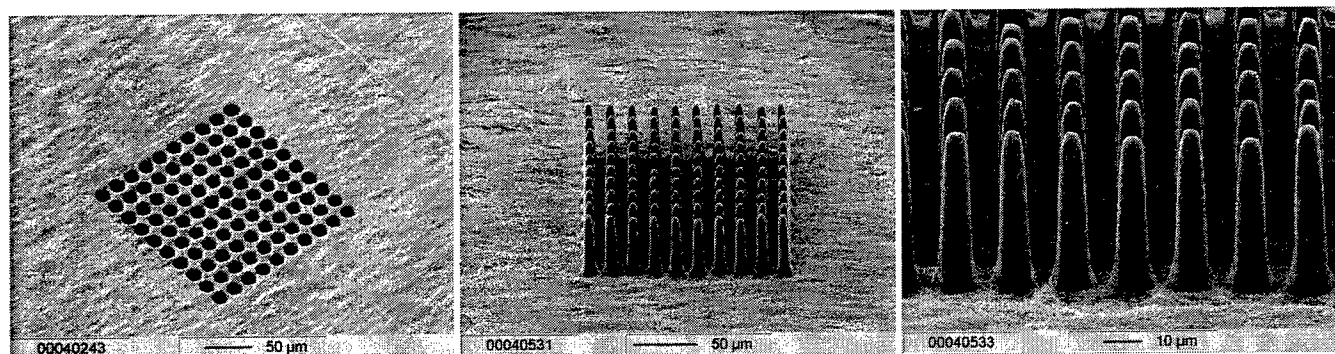


Figure 6: Mold insert made of PI (left) and demolded part made of PMMA (middle, right) with a test design "array of columns" (KrF-Excimer, laser fluence  $2.5\text{ J/cm}^2$ , repetition rate  $10\text{ Hz}$ , number of laser pulses  $N=135$ , depth of drilled holes  $61\mu\text{m}$ )

Excimer laser patterning of grooves in PI leads to well defined and rectangular walls made of PMMA after replication (figure 7). The thickness of the demolded walls is  $10\mu\text{m}$  and the aspect ratio is of about 10. Laser patterning of polymeric mold inserts with Excimer laser radiation can be performed either via laser scanning of a flexible mask aperture or via laser illumination of complex mask structures. In the latter case the quality of the used illumination mask defines the quality of the demolded part. We have used laser cut steel foils as mask structures. Laser cutting of steel foil induces small ripple structures in the cutting trenches, which can be recognized in the micro-sized ripple structure of the side-walls in demolded parts. For further decrease of roughness at the side-walls the use of lithographic chromium-quartz masks will be necessary.

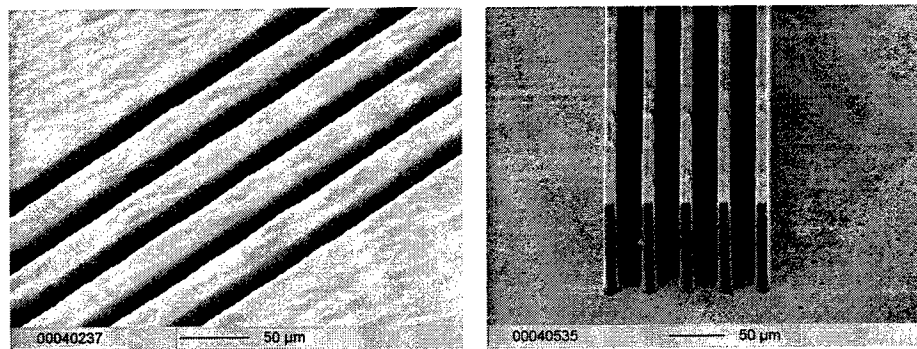


Figure 7: Mold insert made of PI (left) and molded part made of PMMA (right) with a test design "array of walls" (KrF-Excimer, laser fluence  $2.5\text{ J/cm}^2$ , repetition rate  $10\text{ Hz}$ , number of laser pulses  $N=225$ , depth of grooves  $100\mu\text{m}$ )

The next two examples show mold inserts made of PI which are patterned with the aid of  $4\omega$  Nd:YAG laser radiation. The first example (figure 8) reveals the design of an internal rotor of a micro annular gear pump. This component has a height of about  $430\text{ nm}$  which is suitable for the desired application in gear pumps. It is obvious that the very good quality of the sidewalls enables the demolding of such a depth structure. The surface quality of the bottom of the laser patterned area is influenced by the small laser focus diameter as well as by the gaussian intensity profile of the  $4\omega$  Nd:YAG. The shape and roughness of the "microstructure" at the bottom also depends on laser pulse overlap. In this example the pulse to pulse distance is  $1\mu\text{m}$ . The laser patterning is not carried out with a synchronization of laser repetition rate and x,y-stage movement. This may lead to a significant increase of ablation depth at the edges of a pattern, and a usage as mold insert may be restricted. The contour of the molded part in figure 8 reveals a kind of bur which is caused by this non-synchronization.

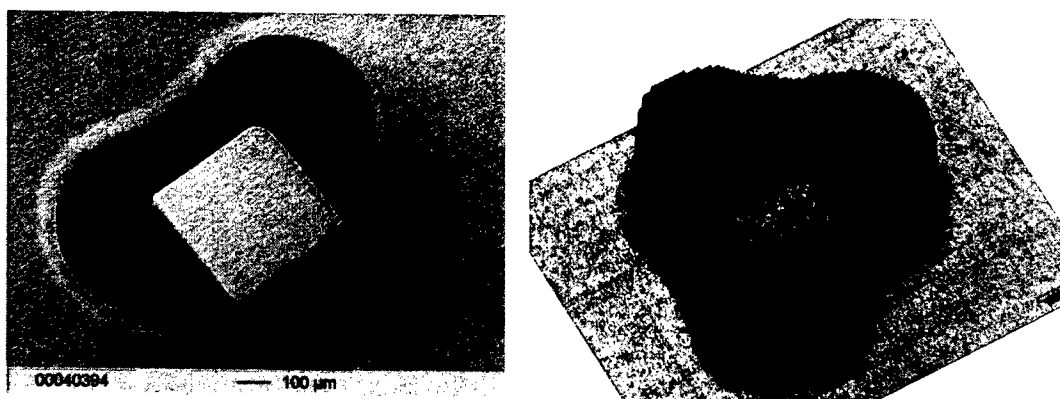


Figure 8: Mold insert made of PI (left) and molded part made of PMMA (right) with a design from an internal rotor of a micro annular gear pump: structure height 430  $\mu\text{m}$  (4 $\omega$  Nd:YAG, repetition rate 1000 Hz, scan offset 5  $\mu\text{m}$ )<sup>16</sup>.

The second example (figure 9) reveals a Capillary-Electrophoresis (CE)-Chip design with a height of about 40  $\mu\text{m}$ . The special requirement of this design is the large area which has to be patterned via scanning of the laser beam. With respect to the processing time, large areas ( $\geq 10 \text{ mm} \times 10 \text{ mm}$ ) should only be patterned with 4 $\omega$  Nd:YAG laser radiation, if the depth of the structures is significantly smaller than 100  $\mu\text{m}$ . In the case of the CE-Chip design it may be more reasonable to fabricate the prototypes directly via UV laser ablation of polymers or to use LMC (see chapter 3.1) for the patterning of metallic mold inserts<sup>6</sup>.

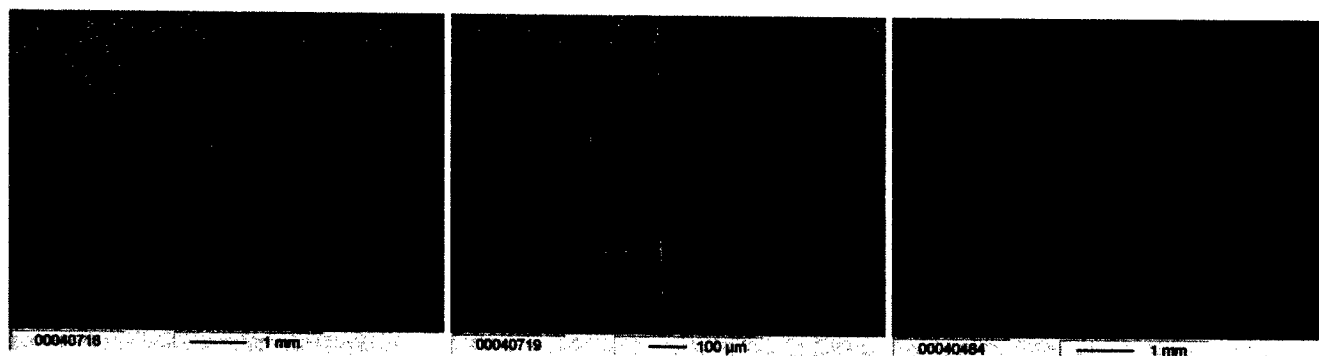


Figure 9: Mold insert made of PI with CE-Chip design. Left: Overview of long separation capillary and small injection/waste capillaries with inlet reservoirs. Middle: Cross area of injection (from left) and separation capillaries (from below), structure height 40  $\mu\text{m}$  (4 $\omega$  Nd:YAG, repetition rate 1000 Hz, scan offset 10  $\mu\text{m}$ ). Right: Molded part made of PMMA.

## 6. CONCLUSION & OUTLOOK

A new technical approach for the fabrication of first prototypes with high aspect ratios by using polymeric mold inserts is presented with respect to photomolding as replication technique. The total processing time starting from the CAD-data until the production of the first prototypes can be reduced to two days, laser processing of polymer mold inserts (1.5 days) and replication via photomolding (0.5 days) included. Future investigations will be focused on the following aspects:

- Further improvement of the thin film adhesion onto the polymeric mold inserts in order to improve the lifetime of the polymeric mold inserts
- Use of lithographic chromium-quartz masks and/or motorized mask systems for the patterning of polymeric mold inserts with Excimer laser radiation
- Synchronization of laser repetition rate (4 $\omega$  Nd:YAG) and x,y-stage movement in order to avoid depth variations at the contours
- Changing of the gaussian intensity profile to a nearly rectangular profile via special masks and/or optics in order to improve the accuracy and reproducibility of the ablation process with 4 $\omega$  Nd:YAG

- Characterisation of the molded polymer modules concerning geometrical, physical and chemical properties which is necessary for bio-analytic applications
- Further prototype molding using highly filled composite systems and fabrication of ceramic and metal prototypes

### ACKNOWLEDGEMENTS

We are grateful to our colleagues M. Beiser, M. Hoffmann and R. Vouriot for their technical assistance in SEM/EDX. We also thank M. Blumhofer for his support in laser profilometry and H. Besser for helpful discussions. We gratefully acknowledge the financial support by the German government (BMBF 03N6018).

### REFERENCES

1. <http://www.fzk.de/pmt/englisch/default.htm>
2. V. Piottter, "Innovative molding technologies for the fabrication of components for microsystems", *SPIE Proc.* **3680**, pp. 456-463, 1999.
3. M. Hecke, K.D. Müller, and W. Bacher, "Microstructured Plastic Foils Produced by Hot Embossing", *Proc. Harmst 99*, pp. 84-85, Kisarazu, 1999.
4. T. Schaller, L. Bohn, J. Mayer, and K. Schubert, "Microstructure grooves width of less than 50  $\mu\text{m}$  cut with ground hard metal micro end mills", *Prec. Eng.* **23**, pp. 229-235, 1999.
5. T. Schaller, M. Hecke, and R. Ruprecht, "Mechanical Micromachining for Mold Insert Fabrication and Replication", *Proc ASPE 1999 Spring Topical Meeting* **19**, pp. 3-8, 1999.
6. W. Pfleging, T. Hanemann, W. Bernauer, M. Torge, "Laser micromachining of mold inserts for replication techniques - State of the art and application", *Proc. of SPIE* **4274**, pp. 331-345, 2001.
7. D. Bäuerle, "Laser Processing and Chemistry", ISBN 3-540-66891-8, Springer Verlag Berlin, Heidelberg, New York, pp. 221-257, 2000.
8. H. Becker, and W. Dietz, "Microfluidic devices for  $\mu$ -TAS applications fabricated by polymer hot embossing", *SPIE Proc. Microfluidic Devices and Systems*, pp. 177-182, 1998.
9. A. Gillner, "Laser Micro Machining", *Proceedings of the International Seminar on Precision Engineering and Micro Technology euspen*, Aachen, Germany, pp. 105-112, 2000.
10. W. Pfleging, T. Hanemann, A. Meier, "Surface Modifications of Metallic Mold Inserts during Laser Treatment", Weinheim, Wiley-VCH, EUROMAT - *Surface Engineering* **11**, pp. 455-460, 1999.
11. W. Pfleging, A. Meier, T. Hanemann, H. Gruhn, K.-H. Zum Gahr, "Laser micromachining of metallic mold inserts for replication techniques", *Mat. Res. Soc. Symp.* **617**, J5.5.1 - J5.5.6, 2000.
12. G. H. Pettit, R. Sauerbrey, "Pulsed Ultraviolet Laser Ablation", *Appl. Phys. A* **56**, pp. 51-63, 1993.
13. T. Shimizu, Y. Murakoshi, T. Sano, R. Maeda, S. Sugiyama, "Fabrication of micro-parts by high aspect ratio structuring and metal injection molding using the supercritical debinding method", *Microsystem Technologies* **5**, pp. 90-92, 1998.
14. T. Hanemann, R. Ruprecht, J. H. Haußelt, "Micromolding and Photopolymerisation", *Adv. Mater.* **9(11)**, pp. 927 - 929, 1997.
15. T. Hanemann, W. Pfleging, J.H. Haußelt, K.-H. Zum Gahr, "Laser Micromaching & Light Induced Reaction Injection Molding as Suitable Process Sequence for the Rapid Fabrication of Microcomponents", *Micro System Technologies*, in press.
16. [http://www.hnp-mikrosysteme.de/hnp-english/prinzip\\_e.htm#](http://www.hnp-mikrosysteme.de/hnp-english/prinzip_e.htm#)

# Bimetallic Thermal Activated Films for Microfabrication, Photomasks and Data Storage

Yuqiang Tu, Glenn Chapman\*, Marinko Sarunic  
School of Engineering Science, Simon Fraser University, BC

## ABSTRACT

Bimetallic thermal resist Bi/In has shown many applications in the areas of microfabrication, photomasks and data storage. Optical modeling shows that this class of thermal resists is wavelength invariant, and Bi/In can perform even better at 13.4 nm than at 248 nm due to the increase of absorption and the reduction of reflection. Images were successfully made on Bi/In films with both proximity (0.5 mm) and projection exposures with Nd-YAG laser running at 2<sup>nd</sup> harmonic wavelength. A new kind of developing solution (HCl:H<sub>2</sub>O<sub>2</sub>:H<sub>2</sub>O=1:1:48) used at room temperature was found to be more effective in descumming than nitric acetic acid solution. Both have the etching selectivity of unexposed area to exposed area >60:1. Developed Bi/In resist shows good conductivity, which can be used as both a metal plating masking and seeding layer. 2 to 10 µm wide Cu and Ni lines and squares were successfully plated on the developed Bi/In patterns on glass slides and silicon wafers. Shelf test shows that the properties of Bi/In film do not change after being kept in a humid temperature-lifted environment for 10 days. Large optical transmission changes (OD>3.5 before laser exposure and <0.3 after exposure) indicate Bi/In can be used for direct-write photomasks and data storage media. Heat-treatment enhances the OD exposed/unexposed OD change.

**Keywords:** Microlithography, Thermal Resist, Inorganic photoresist, Cu plating, photomask.

## 1. INTRODUCTION

Currently microfabrication photolithography is dominated by the use of organic based photoresists. However, as the movement to shorter wavelength (<157 nm) exposures continues organic resists have presented problems connected with the extreme short absorption depth of the light. Furthermore organic photoresists have always involved many wet processes (application, development, and cleans) at a time when most other microfabrication processes are driven towards dry processes.

An alternative is to consider inorganic based resist processes. In recent research [1] a bimetallic inorganic resist was investigated that operates by thermal changes induced by the optical exposure of modern Excimer laser short pulse (4-20 nanosecond) exposure systems. The exposure energy in these laser pulses creates sufficient temperature increases that thermally activated processes can be considered. This opens a whole class of resists with many interesting properties that extend beyond regular resist applications.

Inorganic dry thermal resists have shown several potential advantages over current organic spin-on photoresists. First, inorganic resists can be deposited by a number of dry processes, for example Physical Vapour Deposition (PVD) and Chemical Vapour Deposition (CVD), and are compliant with vacuum based all-dry lithography. Secondly conventional organic photoresists are spin-coated on substrates generating many problems, such as edge bead formation, coating on backside edge. These issues will negatively affect the subsequent processes causing problems such as high particle counts, contaminations. Thirdly switching to inorganic resists may eliminate organic materials in the process flow and effectively reduce the number of cleans required. Lastly since the conversion process of thermal resist uses the heat generated by a laser pulse thermal resist is more wavelength invariant than organic photoresists. Moreover, unlike current photoresists, most thermal resists have the advantage that the conversion process exhibits a threshold behavior. Photoresists follow the law of reciprocity. For example, the energy from multiple low intensity pulses converts the resist exactly as would a single pulse with energy equivalent to the sum of the low intensity pulses. In contrast, many low energy pulses that do not raise the thermal resist temperature above the reaction threshold will have no effect on the thermal resist. Bi/In and its class of bilayer metallic films have shown the potential of being a thermal resist for the next generation of microfabrication technology.

In addition, metallic based resists can enable processes that could never be done by regular organic resists. Consider copper, which has become the major metallization material for Integrated Circuit (IC) fabrication processes

\* glenn@cs.sfu.ca; phone 1-604-291-3814; fax 1-604-291-4951; <http://www.ensc.sfu.ca/people/faculty/chapman/>; School of Engineering Science, Simon Fraser University, 8888 University Drive, Burnaby, BC V5A 1S6, Canada



due to its superior conductivity. The standard copper deposition process involves copper seeding, plating and Chemical Mechanical Polishing (CMP) processes. Since metallic bilayer thermal resists are conductive after development, a novel application is investigated which uses these resists as both patterning and metallization seeding material for electroplating. For regular IC's this could simplify the wafer fabrication process flow, reduce defects, and increase the wafer yield and throughput.

This paper investigates several potential applications of the Bi/In bilayer metallic material. A new acid base solution was found to be an effective developer for Bi/In thermal resist. Bi/In was also researched as a seeding pattern layer for a new laser LIGA process involving metal electroplating. The potential of Bi/In bilayer as a highly sensitive write-once optical recording material, which has much lower melting point (200°C) and lower structural transition temperature (less than 175°C), has been studied. The change in the light absorption of the Bi/In film after exposure has also been investigated with the potential for creating a direct write photomask by exploiting the change in exposure feature.

## 2. BIMETALLIC THERMAL RESIST: A DRY PROCESS

The requirements of a bimetallic alloying thermal resist have been discussed previously [1]. The concept is to choose two thin films whose materials have a phase diagram that contains a eutectic, an alloy with a melting point local minimum less than below the melting point of either metal [1]. The Bi/In phase diagram has a eutectic temperature of 72°C at 22% bismuth and a local temperature minimum of 112°C at 53% bismuth [2]. The composition of the alloy formed is selected by the thickness of the deposited Bi and In layers. For example, to form the 53% Bi alloy, the thickness of the deposited bismuth film will be nearly equal to the indium thickness. While Bi/In bimetallic resists have been the main focus of this research, many other alloy mixtures or ratios have been identified [3] making this a whole class of potential resist alloys. Two particularly promising combinations are Bismuth Tin (BiSn, 43% Bi, with a eutectic point of 139°C) and Indium Tin (InSn, 47% Sn with a eutectic point of 117°C) [4]. Their structure and deposition would in the same manner as the Bi/In films, though their behavior shows some differences.

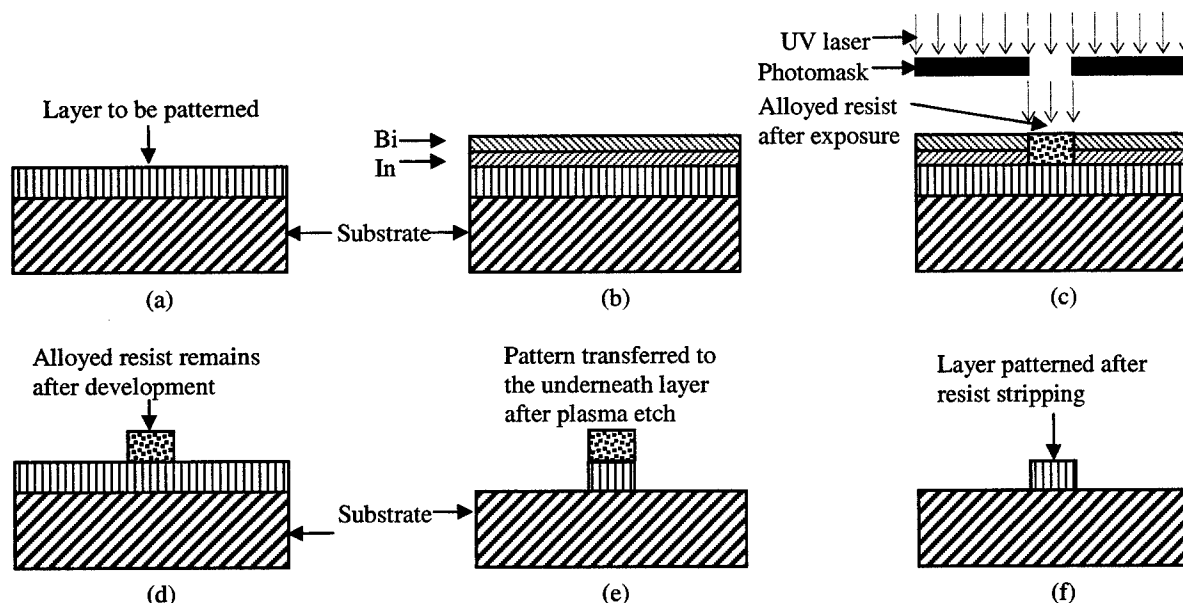


Figure 1. A dry bimetallic thermal resist process. (a) shows the substrate and the layer to be patterned. (b) In and Bi have been sputtered onto the substrate. (c) UV exposure converts the exposed area into alloy, which has different chemical properties from the unexposed area. (d) The development process removes the unexposed and retains the exposed area. (e) The pattern is transferred to the underneath layer by either plasma or wet etch. (f) The whole process is completed by stripping the resist.

Bimetallic thermal alloying resists consist of two thin metal films. In and Bi (see Figure 1(b)), in this case, are RF or DC sputtered to the thickness of 15-150 nm on a thin film layer that is going to be patterned. When exposed to light under a photomask, as shown in Figure 1 (c), the material in the exposed area will absorb the light energy and be heated up to above the Bi/In eutectic temperature. Since the alloy has a lower melting point than either individual film, melting will begin at the interface between the two layers and move outward as the melt pool grows. At the

end of the laser pulse, the resist layers will cool and solidify as the eutectic alloy. The material in the unexposed area, where the light is blocked by the photomask, will remain the same as two-layer structure. Tests show that the alloy have different chemical properties from Bi or In. For the resist development after exposures, two etch solutions have been found (see section 5) which will attack the areas of unexposed resist more aggressively than the exposed areas. After the resist development, the alloyed area remains while the unexposed area is removed, as shown in Figure 1 (d). The pattern is then transferred to the underneath layer to be patterned by plasma etching or wet etching. After the resist stripping, the whole lithography process is completed.

### 3. OPTICAL MODEL: THE CREATION OF WAVELENGTH INVARIANCE

Unlike the current organic photoresists, which operate by photochemical processes, bimetallic thermal resists are activated by the heat that the resist films generate by the absorption of the laser exposure. Reflection, transmission and absorption occur when a laser illuminates the surface of a thin film. Understanding the interaction between the laser beam and the bimetallic thin film will help us analyze and design the thermal resist films. An optical model [5,6,7] was established based on an Airy Summation which is a complete sum of all the electric field vectors traveling into the film and reflected at each interface at the surface and bottom of the absorbing media. The accuracy of the model has been verified by comparing the results with other publications, and our experimental results. The model calculates the total amount of light reflected from the top surface (R), transmitted through the bottom surface (T), and absorbed through the total thickness of the imaging layers (A), which vary with the laser wavelength and the resist thickness. The three plots in Figure 2 are the simulated reflection, transmission and absorption curves versus film thickness at wavelengths of commonly proposed or used exposure systems 248 nm (current exposure systems), 157 nm (follow on from the new 195 nm systems) and 13.4 nm (Extreme UV or EUV systems projected for sub 70 nm exposure systems). The wavelength invariance of the Bi/In resist was demonstrated by calculating the relative change in reflected, transmitted, and absorbed light in the imaging layers when switching from 248 nm to 157 nm exposures. It is noticed that the difference between 157 nm and 248 nm curves is less than 5% of the 248 nm values for 20 nm thick imaging layers or greater. This indicates only modest changes in the energy deposited in the imaging layers, and thus exposure characteristics, as the exposure wavelength moves from 248 nm to 157 nm. It is also interesting to note that below this the reflectivity of the films decline. When wavelength moves from 157 nm to 13.4 nm the absorption increases 24% at the thickness 20 nm of each layer, and reflectivity becomes very small. As absorption is the energy source to convert thermal resists, it is expected that Bi/In thermal resist will perform better at 13.4 nm than at 248 nm.

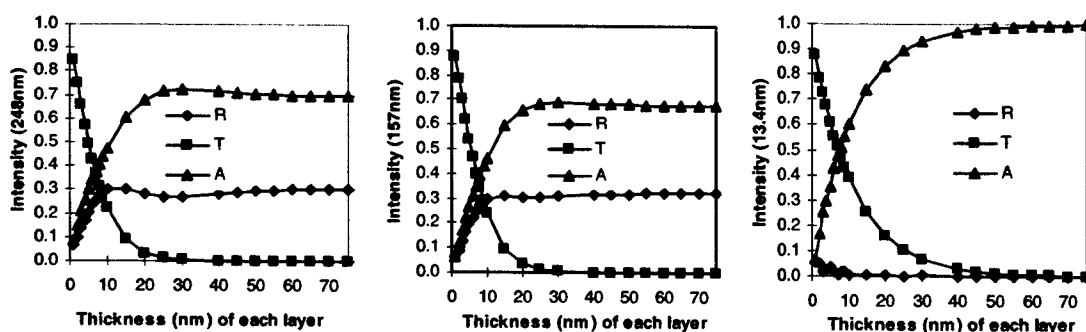


Figure 2. The simulation results from the optical model. The three plots are the reflection, transmission and absorption curves versus film thickness at wavelength 13.4 nm, 157 nm and 248 nm. It is noticed that the absorption, which is the resist activation energy source maintains at about 60% of the incoming light at 20 nm thick of each layer and above, showing the wavelength invariance property.

The charts in Figure 3 are the RAT difference between (a) 248 nm and 157 nm, and (b) 248 nm and 13.4 nm. Plot (a) indicates that the difference between these two wavelengths is very small. The absorption difference is less than 5% of the 248 nm values for 20 nm thick imaging layer. This is only a modest change in the energy deposited in the imaging layer, and thus exposure characteristics, as the exposure wavelength changes from 248 nm to 157 nm. As mentioned previously in this section, plot (b) shows that the light absorption increases when the light wavelength decreases from 248 nm to 13.4 nm.

The Poynting vector for an absorbing medium has been used to calculate the intensity of the light as a function of the depth into the Bi/In films. The light intensity in the film (P curve) and the energy deposited per unit volume (Q curve) are shown in Figure 4. Also notice the interference pattern seen in the Q curves of Figure 4 (b) which occurs because the wavelength of light is significantly smaller than the total thickness of the film. Because of the relatively high transmittance through the bilayer, 33% of the deposited energy is in the bottom layer. This indicates

that the bilayer will heat up quickly, and there will be significant heat generation from the laser pulse at the metal interface, which is surprising for such a thick film.

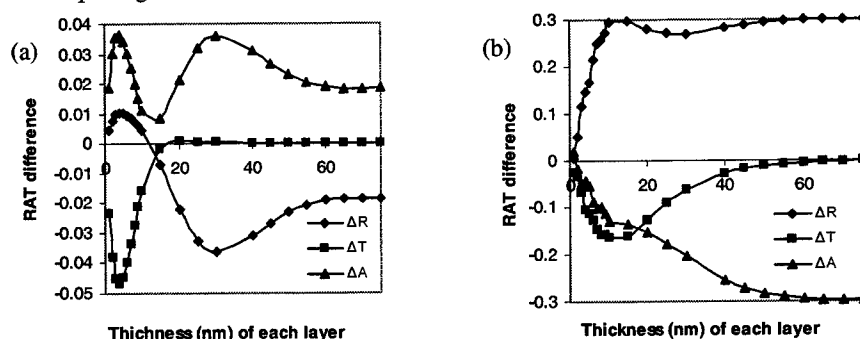


Figure 3. RAT difference between (a) 248 nm and 157 nm and (b) 248 nm and 13.4 nm. The difference between 248 nm and 157 nm is very small showing that the optical property of the Bi/In film does not change so much. It is interesting to notice that the absorption improves when the laser wavelength moves from 248 nm to 13.4 nm.

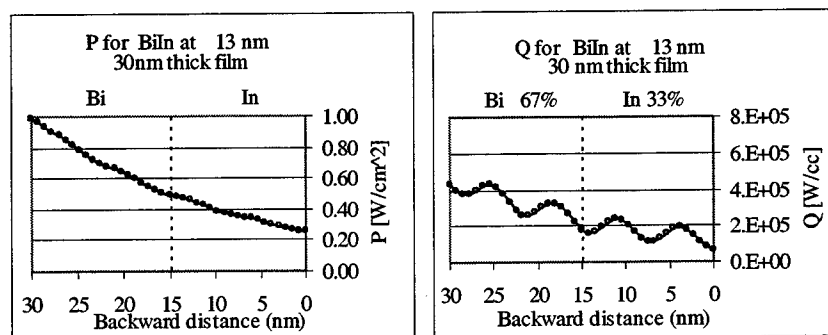


Figure 4. P and Q curves for 30 nm total thick film of Bi on In bilayer exposed with 13 nm EUV. It is interesting to notice the interference pattern in the Q curve, which is similar to the light interference inside a thin film.

#### 4. RESIST EXPOSURE

The Bi/In films were prepared by a single pump down DC/RF sputtering depositions on glass slides, quartz slides, and silicon wafers. The detailed deposition parameters were reported separately [1]. Two laser setups were used to make images on the Bi/In thermal resist. A 5W Ar ion laser in CW mode was used in conjunction with an X-Y table with the positioning accuracy of  $0.01\mu\text{m}$  and an electro-optic shutter to generate pulses of minimum duration  $10\mu\text{s}$ . Large areas ( $1\text{cm}^2$  or larger) were exposed by raster scanning across the surface of the resist. The scanning speed is set to  $10\text{mm/sec}$ . In Ar laser exposures, two objective lenses were used, depending on the application. A 50mm focal length converging lens with a beam waist of  $w_f=5\mu\text{m}$  was mainly used to produce large exposed areas. A 50X microscope objective lens with a beam waist of  $w_f=1\mu\text{m}$  was used to make fine structures such as lines and small squares.

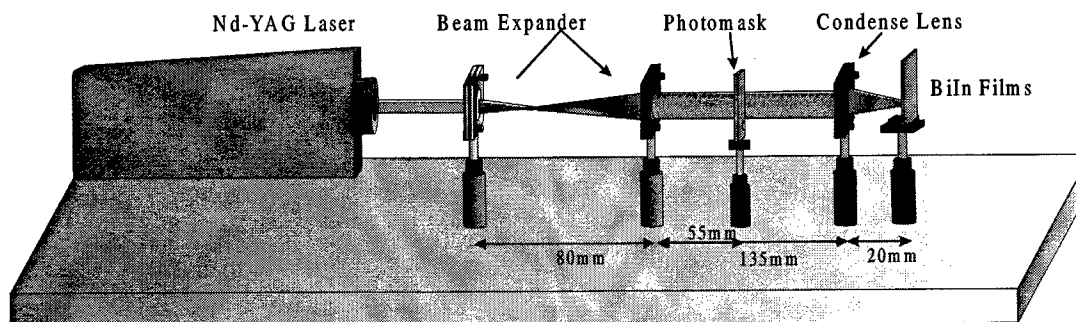


Figure 5. The optical setup for Nd:YAG to make a projected image on the Bi/In thermal resist.

An Nd-YAG laser with non-linear crystal conversion to output laser light at 533 nm (400mJ max), 266 nm (100 mJ max) and 213 nm (40 mJ max) was used to make projected images. The Nd-YAG laser was employed to provide short pulse exposures. Two distinct optical setups were utilized for Nd:YAG laser: (a) a projection system consisting of a beam expander and a condensing lens with photo masks in between as shown in Figure 5, and (b) the laser beam with a diameter of approximately 5mm was used without any additional lenses to focus it. An Nd-YAG laser running at 2<sup>nd</sup> harmonic 533 nm (green) was used as a projecting source, with an energy density of 2.5 mJ/cm<sup>2</sup>, and 2 pulses/sec. 2-10 pulses were used to make an exposure. From the point of conversion the Nd-YAG exposures are similar to those produced in a real stepper exposure system. It is interesting to note that the exposed areas of the thermal resist is more transparent than the unexposed area, and hence the pattern is visible. Figure 6 (a) and (b) are the front and back-lit microscopic pictures of the projected images on 45 nm Bi/In film using the projecting optics. The image was made with the following conditions: laser power of 145mJ/cm<sup>2</sup>, pulse repetition rate of 30Hz, and exposure duration = 12min. It should be noticed that the laser power used here was not the actual power used to make the projected image due to the beam expander. It is estimated that only less than 10% of the energy was used for the exposure. As expected, the exposed area is more transparent than the unexposed area. Also images have been made on Bi/In films as shown in Figure 7 using the unfocused beam. A normal chrome mask with fine structures of various sizes was placed 0.5mm before the Bi/In film.

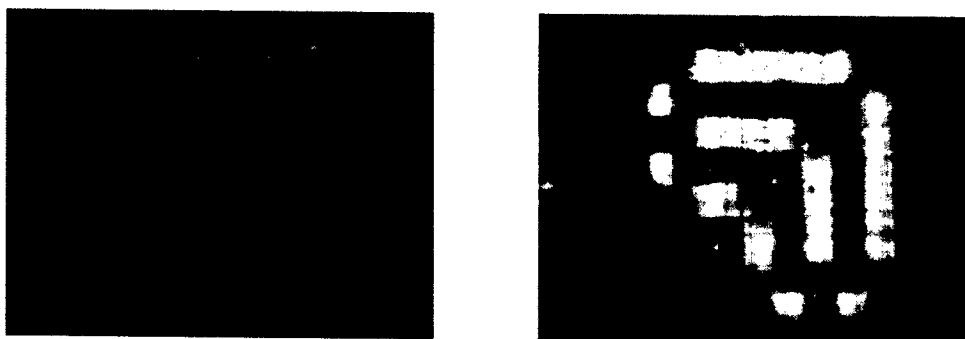


Figure 6. (a) is the front-lit microscopic view of a projected image on Bi/In. (b) is the back-lit microscopic view of the same projected image. The line width is 20  $\mu\text{m}$ .

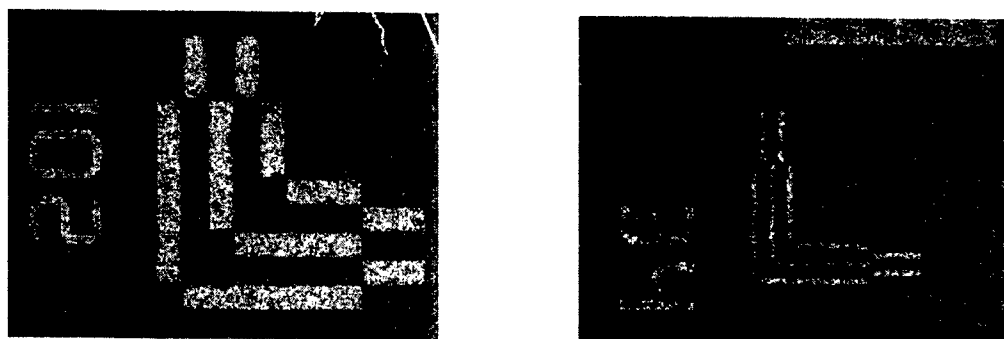


Figure 7. Images were made on a Bi/In 35 nm/35 nm film, using 533 nm unfocused Nd-YAG laser at 2.5 mJ/cm<sup>2</sup>, 3.5 ns/pulse. The line width is 150 $\mu\text{m}$  in (a) and 30 $\mu\text{m}$  in (b). These lines are un-developed and show how clear the exposed image is.

## 5. RESIST DEVELOPMENT

One of the requirements for a working resist is that the laser exposed area and the unexposed area should have different chemical properties so that it can be successfully developed to form a lithographic hard mask after exposure. It was noticed that Bi/In deposited on glass and quartz substrates converted to a significantly less optically-absorbing material when exposed to laser pulses. Such considerable optical change indicates that the converted materials have significantly different physical and chemical characteristics than the unconverted materials. In wafer fabrication industry, an etch selectivity ratio >20:1 (that is the ratio between the etch rate of the unexposed

and exposed layers) is preferred when developing hard masks. It has been found that two kinds of acid based solutions are effective in developing the exposed films to get an image pattern by removing the unexposed area, thus making the resist a negative one. The first is a mixture solution of nitric acid and acetic acid ( $\text{HNO}_3:\text{CH}_3\text{COOH}:\text{H}_2\text{O} = 1:3:6$ ), which gives a very good etching selectivity of exposed to unexposed area of larger than 65:1 (refer to Table 1). The etch rate of unexposed area is about 26 Å/sec. However nitric acid solution has scumming problem: it can not remove trace alloy residue in the unexposed area. To solve this problem, usually 100% over-development is applied.

The second is a solution of  $\text{HCl}:\text{H}_2\text{O}_2:\text{H}_2\text{O} = 1:1:48$ , which was discovered to be a developer with even better performance. It has been reported [1] that Bi/In can be stripped by RCA2 ( $\text{HCl}:\text{H}_2\text{O}_2:\text{H}_2\text{O} = 1:1:6$ ) cleaning after the patterning is done or there is a need for reworking. In stead of using the  $\text{HCl}:\text{H}_2\text{O}_2:\text{H}_2\text{O}$  solution at a much higher concentration and at the temperature of 80°C for stripping, the exposed films are developed in a much diluted formula (1:1:48) and at room temperature. The selectivity is above 60:1, the etch rate is faster than nitric acid solution, and it has good descumming capability. Figure 8 shows the result from an etch comparison experiment. A Bi/In film deposited on  $\text{SiO}_2$  (wet oxide on 4" wafer) with equal thickness of 90 nm Bi and In was used in this test. A series of lines were first made by Ar CW laser scanning. The sample was then dipped in the developing solution for 5 sec to over 15 min and rinsed thoroughly with DI water. A profilometer was used to measure the film thickness at the exposed and unexposed areas. One can notice that the thickness of the unexposed area of the film reduces rapidly, while that of the exposed area changes slowly with time.

Table 1. Development solutions

Solution	Chemical Ratio	pH Value	Etching Selectivity	Etch Rate
Nitric Acid Solution	$\text{HNO}_3:\text{CH}_3\text{COOH}:\text{H}_2\text{O} = 1:3:6$	2	> 65:1	26 Å/sec
$\text{HCl}:\text{H}_2\text{O}_2:\text{H}_2\text{O} @ 25^\circ\text{C}$	$\text{HCl}:\text{H}_2\text{O}_2:\text{H}_2\text{O} = 1:1:48$	2	> 60:1	30 Å/sec

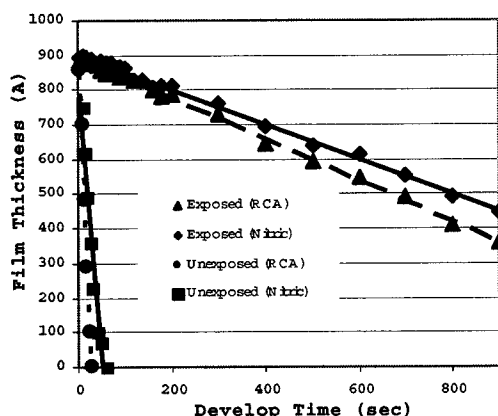


Figure 8. Film thickness vs etching time in Nitric acid and  $\text{HCl}:\text{H}_2\text{O}_2:\text{H}_2\text{O}$  solutions.

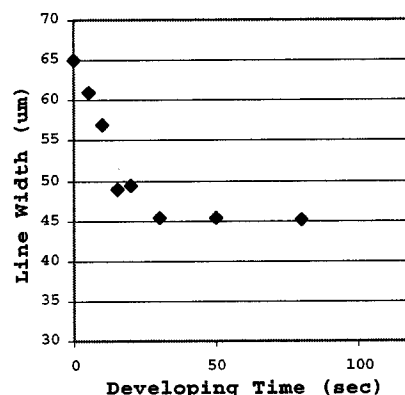


Figure 9. Line width reduces with the developing time. It saturates at certain point.

It is also noticed that the width of the exposed lines decreased with the developing time. A 45 nm/45 nm Bi/In film was exposed with 65 μm wide lines using CW Ar laser scanning. The sample was developed in  $\text{HCl}:\text{H}_2\text{O}_2:\text{H}_2\text{O}$  solution for different duration. The width of the lines was measured using an optical microscope line width system. As shown in Figure 9, the line width dropped quite fast for the first 20 seconds, and then saturated at 45 μm. There are many possible causes to this line width reduction phenomenon. Perhaps the most likely reason is that since the Ar laser intensity across the laser beam follows the Gaussian distribution, the thermal resist exposed to the beam edge is not converted as completely as at the center of the beam. Also the heat dissipation along lateral directions in the resist film could partly convert the film when the film thickness is greater than 30 nm.[8]

Figure 10 is an SEM picture of a developed Bi/In line pattern on  $\text{SiO}_2$  layer on a silicon wafer. These are 2 μm wide lines with 10 μm spacing made by Ar laser (514 nm at 0.05W) raster scanning on a 45 nm/45 nm Bi/In film. The sample was developed in the  $\text{HCl}:\text{H}_2\text{O}_2:\text{H}_2\text{O}$  solution for 60 sec. As the total thickness of the film is only about 850 Å, we could not get a very good cross-section SEM picture. Figure 11 shows a 45° tilted SEM picture of the developed Bi/In lines.

Plasma etching of the bimetallic thermal resist is now under development to make this a completely dry lithographic process.

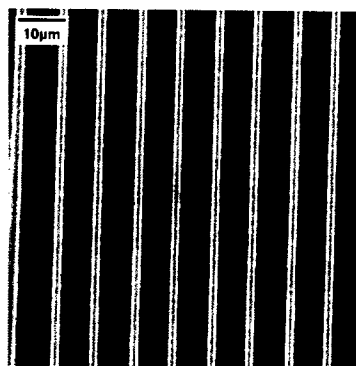


Figure 10. SEM picture of developed 2  $\mu\text{m}$  wide Bi/In lines with 10  $\mu\text{m}$  spacing.

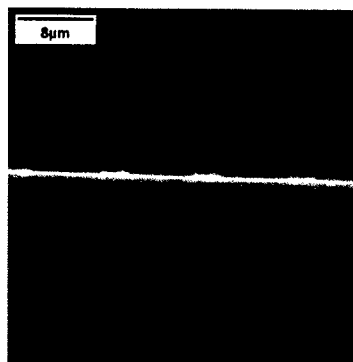


Figure 11. A 45° tilted SEM picture of developed Bi/In lines on  $\text{SiO}_2/\text{Si}$  wafer.

## 6. ELECTRIC PROPERTIES OF Bi/In RESIST

A significant difference from the organic photoresist is that the metallic bilayer thin film thermal resist is conductive both before and after exposure. The electrical conductivity opens the door to many potential applications. The sheet resistance of the exposed and unexposed samples was measured using a Model MP0705A four-point probe from Wentworth Labs, which is connected to an HP 3478A multimeter. The 4 probes are arranged in a line with 1mm spacing between one another. Electric current flows between the outer two probes, and the voltage drop across the film is measured by the inner two probes. The advantage of this method is that it eliminates any contact resistance in the measurement. To ensure the accuracy of the measurement, it is required that the conducting film thickness be less than 40% of the spacing, and the edges of the film be more than 4 times the spacing distance from the measurement point. The sheet resistance measurement was carried out on a series of Bi/In thin film samples. The bilayer film was sputter-deposited on glass slides with 30 nm equal thick Bi on top of the In layer. The sheet resistance was first measured on the unexposed Bi/In film (named as Bi/In 30/30 U in Table 2), and then on the Ar laser raster-exposed areas (as Bi/In 30/30 E in table 2). The laser power was 0.20W. The exposed sample was dipped in  $\text{HCl}:\text{H}_2\text{O}_2:\text{H}_2\text{O}$  solution for 40 second for development, and its sheet resistance was measured after  $\text{N}_2$  blow-dry (as Bi/In 30/30 D in table 2). The resistances of single layer Bi and In films of thickness 15 nm, 30 nm, and 45 nm were also measured.

It is noticed that the resistivity of the thinner Bi and In films is higher than that of bulk materials, dropping significantly as the films get thicker. This can be attributed to the fact that the oxidized part of the film is more significant in thinner films than in thicker films. It is noticed that the exposed films are slightly more conductive than unexposed films. A surprising finding is that the developed resist is conductive. This indicates that the Bi/In thermal resist can not only be used as a patterning material, but also as an electric plating seeding layer. This has the potential to simplify the manufacturing process since separate resist removal and seeding processes are not required. The developed film is more conductive than most of the current barrier layer films and silicide films. For example, the resistivity of the most conductive silicide  $\text{TiSi}_2$  is about  $1.6 \times 10^{-2} \Omega\text{cm}$ , and TaN, the barrier layer used for copper plating, is about  $2.5 \times 10^{-1} \Omega\text{cm}$  [9].

Table 2. Sheet resistance and resistivity

	Bi (15nm)	Bi (30nm)	Bi (45nm)	In (15nm)	In (30nm)	In (45nm)	Bi/In 30/30 U	Bi/In 30/30 E	Bi/In 30/30 D
Sheet resistance ( $\Omega/\text{sq}$ )	484.7 $\pm$ 39	171.0 $\pm$ 13	79.6 $\pm$ 5	32 $\pm$ 3	9.3 $\pm$ 0.9	3.5 $\pm$ 0.2	82.8 $\pm$ 6	80.8 $\pm$ 5	97.5 $\pm$ 7
Film resistivity ( $\Omega\text{cm}$ )	7.27 $\times 10^{-4}$	5.13 $\times 10^{-4}$	3.58 $\times 10^{-4}$	4.91 $\times 10^{-5}$	2.79 $\times 10^{-5}$	1.56 $\times 10^{-5}$	4.97 $\times 10^{-4}$	4.85 $\times 10^{-4}$	5.03 $\times 10^{-4}$
Bulk resistivity ( $\Omega\text{cm}$ )	1.3 $\times 10^{-4}$			8.0 $\times 10^{-6}$			-	-	-

## 7. METAL PLATING ON DEVELOPED Bi/In RESIST

Metallization is an important process in the microfabrication of both chips and MEMS. PVD and CVD metal coating has been the major deposition method in both areas, which has the disadvantage of not being able to deposit thick films (much greater than 1.5  $\mu\text{m}$ ) on the substrate due to film stress. By comparison, metal electroplating can not only put several microns even dozens of microns thick of films on the substrate, but also fill high aspect ratio vias and contacts. Copper plating has been very successful in the wafer fabrication recently for high end microchips.

However current copper plating technique involves many processes, such as seeding, lithography, and plasma etching, which can increase the cycle time and introduce process defects.

Due to its unusual conductive property, Bi/In has demonstrated that it can be used as a direct laser write electroplating resist material. The Bi/In resist can be deposited and directly written on with the laser, and it will act as both a patterning material after development and a seeding layer for plating. By comparison considerable efforts have been made to achieve high-aspect ratio structures in the micromachining area. Using X-ray lithography, standard LIGA process can be used to fabricate very high structures (as high as 1mm) with sub-micron lateral accuracy [10]. However, the high cost using synchrotron X-ray source prevents it from being a common micromachining process. With Bi/In as both patterning and seeding layer, one can easily plate thick films to achieve high aspect ratio structures. Conductive bimetallic thermal resist could be an alternative to LIGA process.

Cu and Ni plating was carried out on developed Bi/In layers on various substrates such as Si wafers, glass slides, wet-oxidized wafers. The Bi/In resist was first exposed to Ar laser by raster-scanning exposure patterns, such as lines and square areas. Laser power varied from 0.05W to 0.35W. The films were then developed in nitric acid or  $\text{HCl}:\text{H}_2\text{O}_2:\text{H}_2\text{O}$  solutions for 40 to 100 seconds to remove those unexposed areas. During the laser scanning period, conductive pads were designed and exposed for plating connection. Table 3 shows the chemical ingredients for the plating. Cu plating was carried out in room temperature and Ni at 55°C. Figure 12(a) shows several Cu lines inside a square Cu window, the space between two Cu lines is 10 $\mu\text{m}$ . To make this pattern on Bi/In, the large window frame was first raster-scanned with Ar laser on the X-Y table. Then the lines were made again by Ar laser by a single scan. As shown here, as copper plating continues, a high aspect ratio structure can be achieved. Figure 12(b) is the SEM picture of a Cu square with an opened window, and 12(c) are the Cu lines. The plated copper layers are 3 $\mu\text{m}$  thick. Figure 13(a) is a Ni mesh plated on Si substrate. Each square is 10 by 10  $\mu\text{m}$ . 13(b) shows a densely plated area. The space between two Ni lines is 5  $\mu\text{m}$ . 13(c) is a small Ni pattern, the thin line is 2  $\mu\text{m}$  wide. The plated nickel layer is 4  $\mu\text{m}$  thick.

Table 3. Cu and Ni plating parameters

	1 liter plating solution	Plating Temperature	Typical Plating Current Density
Cu	$\text{CuSO}_4 \cdot 5\text{H}_2\text{O}=100\text{g}$ , $\text{H}_2\text{SO}_4=10\text{ml}$	25°C	10-50 A/m <sup>2</sup>
Ni	$\text{NiSO}_4 \cdot 6\text{H}_2\text{O}=150\text{g}$ , $\text{NiCl}_2 \cdot 6\text{H}_2\text{O}=60\text{g}$ , $\text{H}_3\text{BO}_3=37.5\text{g}$	55°C	10-50 A/m <sup>2</sup>

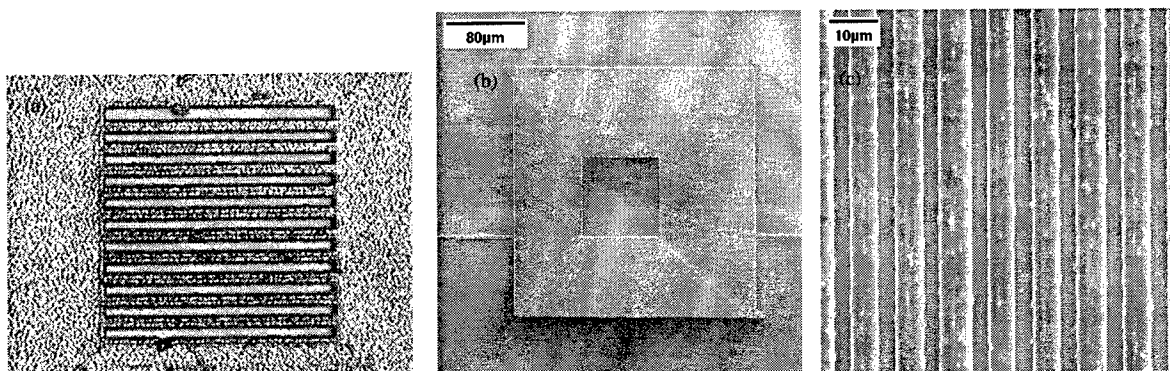


Figure 12. (a) An optical picture of plated Cu on  $\text{SiO}_2$ . The spacing between two lines is 10  $\mu\text{m}$ . (b) SEM picture of a Cu square and (c) SEM picture of Cu lines. The copper layer is 3  $\mu\text{m}$  thick.

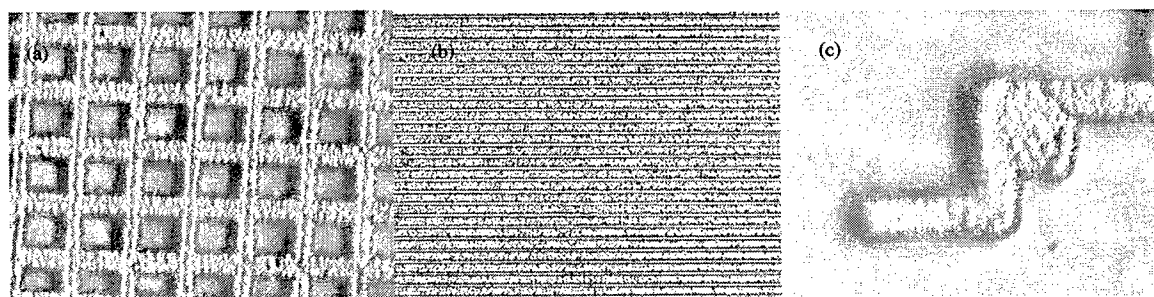


Figure 13. Optical pictures of plated Ni on Si wafer. (a) Ni mesh. The spacing between two lines is 10  $\mu\text{m}$ . (b) densely plated Ni lines with 5 $\mu\text{m}$  spacing and (c) a small pattern of 4  $\mu\text{m}$  square with 2  $\mu\text{m}$  wide line.

## 8. Bi/In RESIST FILM STABILITY TEST (SHELF TEST)

A shelf lifetime test was conducted to investigate the stability of the deposited Bi/In film. A 50 nm/50 nm Bi/In film was deposited on a glass slide which was subsequently cut into 4 pieces. XRD analysis and UV spectrum were carried out on each of the slide pieces before the shelf test. A multi-purpose stainless steel oven was used for the shelf test. The oven temperature was kept at  $50 \pm 1^\circ\text{C}$ ,  $>90\%$  humidity for 10 days (Table 4).

Table 4. Shelf test conditions.

Sample	#1	#2	#3	#4
Bi/In film structure	50 nm / 50 nm	50 nm / 50 nm	50 nm / 50 nm	50 nm / 50 nm
Shelf Test Temperature	$50 \pm 1^\circ\text{C}$	$50 \pm 1^\circ\text{C}$	$50 \pm 1^\circ\text{C}$	$50 \pm 1^\circ\text{C}$
Shelf Test Humidity	$>90\%$	$>90\%$	$>90\%$	$>90\%$
Shelf Test Duration	66 hours	117 hours	158 hours	233 hours

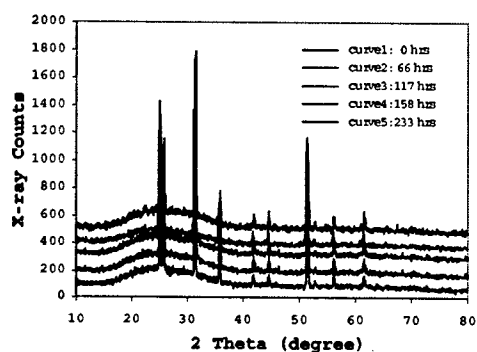


Figure 14. XRD spectrum for shelf test on a 50 nm/50 nm Bi/In film. From the bottom to the top are curves of 1) as-deposited, 2) after 66 hours, 3) 117 hours, 4) 158 hours and 5) 233 hours of shelf time.

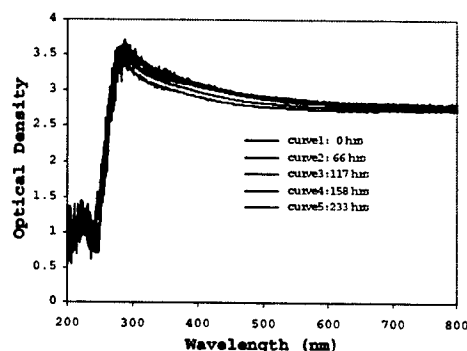


Figure 15. Spectrometer result. From bottom to top are 1) after 233 hours, 2) 0 hours, 3) after 66 hours, 4) after 158 hours and 5) after 117 hours of shelf test.

The 4 samples were taken out of the oven separately according to the time schedule in Table 4, and then XRD and UV spectrum tests were immediately conducted. Figure 14 is the combined result of pre and post shelf test XRD. The film property does not change even after around 10 days under humid and hot environment. Spectrometer measurements on the samples described above also show the same result, as in Figure 15.

## 9. OPTICAL CHARACTERISTICS OF Bi/In FILMS

In the optics information storage industry, alloying and phase change materials are widely used. Due to the prevalent applications of CD-R and CD-RW both at home and in the office, developing new types of recording media with higher sensitivity and better signal to noise ratio has generated a great deal of interest. Optical recording is achieved by changing the optical properties before and after laser irradiation, and optical reading is achieved by taking the advantage of the contrast difference between the laser exposed and non-laser exposed area. There are 2 types of optical storage media: write-once and write many. The basic requirements of thin film media as optical storage media are high laser writing sensitivity, sharp conversion threshold, good optical contrast and stability. The recording mechanism has also been well studied and categorized into following 6 types [11]: 1) ablation, 2) phase/microstructure change, 3) chemical reaction, 4) particle coalescence, 5) topography change and 6) magnetization change. Among all the optical recording materials, Te-based alloys and doped Te oxide films are the most thoroughly studied media [12]. Because of the low melting point ( $452^\circ\text{C}$ ), low thermal diffusivity, and high optical absorption coefficient ( $\alpha \sim 4.9 \times 10^5 \text{ cm}^{-1}$  at 830 nm for Te), Te and its alloys have been considered to be among the most sensitive materials for ablation optical recording. The typical phase/microstructure change media for storage are  $\text{TeO}_{1.1}$ , Ge and Sn doped  $\text{TeO}_{1.1}$ ,  $\text{Sb}_2\text{Se}_3$  on  $\text{Bi}_2\text{Te}_3$ , and some other chalcogenide films. Watanabe et al [14] reported that the optical characteristics of  $\text{Sb}_2\text{Se}_3$  and  $\text{Sb}_2\text{Te}_3$  films were changed due to an amorphous-crystalline phase transition below  $200^\circ\text{C}$ . The respective reflectivity of 400 Å  $\text{Sb}_2\text{Se}_3$  and 300 Å  $\text{Sb}_2\text{Te}_3$  films, each on a Te reflective layer increased from 10% to 30% and from 45% to 65% by laser radiation. Media in chemical reaction category are usually composed of 2 thin layers, such as Pd-Si, Pt-Si and Rh-Si bilayer films [11,15, 16]. The initial reflectivity was first made low by choosing the proper thickness for each layer so that the antireflection condition was achieved. After laser irradiation the reflectivity became significantly higher due to the detuning of the



antireflection condition, and a silicide compound was formed. In some cases ablation also happened during the process.

The large optical property changes before and after the laser exposure on this class of bimetallic thermal resist films put it in this same class of optical storage materials. To characterize the optical properties of Bi/In films before and after laser writing a CARY 3E spectrometer was used to measure the absorption through the raster scan (CW Ar) exposed areas on the film. The absorption spectrum was measured for areas raster scanned with a range of laser intensities from 50mW to 900mW. Figure 16 (a) graphs the Optical Density (OD) of the film versus the exposure wavelength for a 50 nm/50 nm Bi/In film. The Bi/In sample was heat-treated for 72 hours at 50°C before exposure. The OD of the unconverted film is roughly 3.5 – 4.0 from 400 nm to 800 nm. As the power of the laser exposure is increased, the OD of the converted area reaches a minimum corresponding to the energy at which all of the material in the layers is converted. The absorption spectrum for the converted layers in the range from 400 nm to 800 nm reaches a minimum value of roughly 0.25 OD at an exposure intensity of 900mW. This represented a change in the OD of more than 3 orders in terms of transmitted light power. Also notice how smooth and flat the absorption spectra are across a long range in wavelengths. This indicates that Bi/In and its class of bimetallic films can be used as a direct-write photomask material.

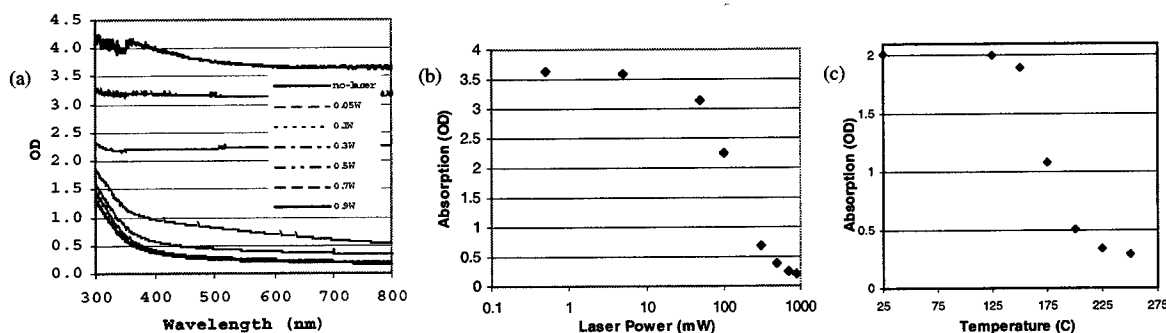


Figure 16. (a) Absorption through 50 nm/50 nm Bi/In exposed with the Ar laser at different intensities. From top to bottom: 0, 50, 100, 300, 500, 700 and 900mW. The sample was heat-treated for 72 hours at 50°C. (b) 50 nm/50 nm Bi/In film optical absorption vs laser power at wavelength 635 nm. Absorption drops drastically at 100 mW laser power and saturates after 300mW. (c) Absorption at 635 nm wavelength vs heat treatment temperature. The 30 nm/30 nm Bi/In film shows a transition threshold temperature around 125°C.

Figure 16 (b) shows a curve of optical absorption versus laser writing power. It is noticed that when the laser is below 50 mW (the laser beam is 20  $\mu$ m in diameter) the OD of the films is above 3. Since 50mW is much higher than typical CD-ROM reading power of 0.2 ~ 0.3 mW, normal laser reading will not change the properties of the bimetallic film, thus the media stability and the data storage reliability. Absorption drops sharply around 100 mW writing power, and it quickly saturates from 300 mW onwards and the optical density stabilizes around 0.25 OD on glass substrates. With thinner films the writing power can be made much lower and the optical density difference (OD ratio between exposed and unexposed area) can still be maintained. Similar to laser exposure, heat treatment gives the same conversion result as shown in Figure 16 (c). The samples were heated up in an oven for 5 minutes. It clearly shows a conversion threshold at around 125°C, which is lower than most other reported data storage media material. The optical absorption saturates around 0.29 OD after 225°C. With this low absorption levels the Bi/In resist is near the needs for a direct write photomask where the converted areas can directly be used as the mask "openings" without development

## 10. CONCLUSIONS

Bi/In is a bimetallic thermally alloy resist with many unique properties. Airy Summation modeling results show that Bi/In and its class of metallic bilayer structure films offers an interesting advantage as a next generation thermal resists as they are wavelength invariant even down to the 13.4 nm planned for the EUV exposure systems. It is predicted that Bi/In will perform even better at 13.4 nm than at 248 nm wavelength. To simulate the conventional stepper, an image projection optical setup has been used to make projected images on Bi/In films with Nd-YAG laser running at 2<sup>nd</sup> harmonic wavelength. Wet etching/developing solution HCl:H<sub>2</sub>O<sub>2</sub>:H<sub>2</sub>O solution has shown good selectivity and descumming performance for Bi/In thermal resists. Etch selectivity larger than 60:1 has been achieved. Due to its electric conductivity, the patterned Bi/In resist was demonstrated as a metal plating seeding layer. Fine structures of Cu and Ni have been successfully plated on various kinds of substrates. Conductive resists could potentially serve as patterning and seeding layers for metallization processes in semiconductor industry. This

all-in-one material could greatly simplify the metallization processes and increase the fabrication yield and throughput. Heat treatment was found to be effective to increase the optical density difference before and after the laser exposure. This shows that Bi/In has the potential to be used as a direct-write photomask material. The sharp drop in optical absorption around 100 mW writing power and the optical density stabilization around 0.25 OD on glass substrates indicate that Bi/In film can also potentially be used as a laser recording material.

## REFERENCES

1. Marinko V. Sarunic, Glenn H. Chapman, Yuqiang Tu, "A Prototype Laser Activated Bimetallic Thermal Resist For Microfabrication", Proc. SPIE Vol. 4274, pp. 183-193, January 2001
2. H. J. Hagemann, W. Gudat and C. Kunz, "Optical Constants from the Far Infrared to the X-Ray Region: Mg, Al, Cu, Ag, Au, Bi, C and  $\text{Al}_2\text{O}_3$ ", Deutsches Elektronen-Synchrotron, May 1974.
3. M.V. Sarunic, Master Thesis "Bi/In: A prototype Bimetallic Laser Activated Thermal Inorganic Resist for Microlithography", Chapter 3, School of Engineering Science, Simon Fraser University, 2001.
4. Max Hansen, Constitution of binary alloys, McGraw-Hill, 1958.
5. M.V. Sarunic, Master Thesis "Bi/In: A prototype Bimetallic Laser Activated Thermal Inorganic Resist for Microlithography", Chapter 2, School of Engineering Science, Simon Fraser University, 2001.
6. Knittl, Zdenek, "Optics of thin films; an optical multilayer theory", London ; New York : Wiley, 1976
7. Heavens, O.S. "Optical properties of thin solid films", London : Methuen, 1970.
8. Dan Gelbart and Valentin A. Karasyuk, "UV thermoresists: sub-100-nm imaging without proximity effects", Proc. SPIE Vol. 3676, p. 786-793, March 1999.
9. G.S. Chen, S.T. Chen, "Diffusion Barrier Properties of Single- and Multilayered Quasi-amorphous Tantalum Nitride Thin Films against Copper Penetration", J. Appl. Phys. 87, 8473 (2000)
10. W. Ehrfeld, F. Gotz, D. Munchmeyer, W. Schelb, and D. Schmidt, "LIGA Process: Sensor Construction Techniques Via Xray Lithography," Tech. Digest of Solid-State Sensor and Actuator Workshop, Hilton Head, SC, pp. 1-4, June 1998.
11. Wen-yaung Lee, "Thin Films for Optical Data Storage", J. Vac. Sci. Technol. A3(3), pp 640-646, May/Jun 1985.
12. W.Y. Lee, et al, "Nanosecond Pulsed Laser-Induced Segregation of Te in  $\text{TeO}_x$  Films", J. Vac. Sci. Technol. A 4 (6), pp 2988-2992, Nov/Dec 1986.
13. W.Y. Lee, et al, "Reactively Sputter-deposited and Coevaporated  $\text{TeO}_x$  Thin Films for Optical Recording", J. Vac. Sci. Technol. A 4 (3), pp 553-557, May/Jun 1986.
14. K. Watanabe, N. Sato and S. Miyaoka, J. Appl. Phys. 54, 1256 (1983).
15. P. Arun, A.G. Vedeshwar, "Potential of  $\text{Sb}_2\text{Se}_3$  Films for Photo-Thermal Phase Change Optical Storage", Thin Solid Films 000 (1998) 1-20.
16. Toshihisa Nonaka, et al, "Crystal Structure of GeTe and  $\text{Ge}_2\text{Sb}_2\text{Te}_5$  Meta-stable Phase", Thin Solid Films 370 (2000) 258-261.

## Cell-by-Cell Construction of Living Tissue

Bradley R. Ringeisen, Heungsoo Kim, H. Daniel Young, Barry J. Spargo, R.C.Y. Auyeung, Alberto Pique, Douglas Chrisey

4555 Overlook Ave. SW, Naval Research Laboratory, Codes 6372 and 6115, Washington, DC  
20375

Peter K. Wu

Southern Oregon University, Ashland, WA

### ABSTRACT

This paper outlines investigations into a potentially revolutionary approach to tissue engineering. Tissue is a complex three-dimensional structure that contains many different biomaterials such as cells, proteins, and extracellular matrix molecules that are ordered in a very precise way to serve specific functions. In order to replicate such complex structure, it is necessary to have a tool that could deposit all these materials in an accurate and controlled fashion. Most methods to fabricate living three-dimensional structures involve techniques to engineer biocompatible and biodegradable scaffolding, which is then seeded with living cells to form tissue. This scaffolding gives the tissue needed support, but the resulting tissue inherently has no microscopic cellular structure because cells are injected into the scaffolding where they adhere at random. We have developed a novel technique that actually engineers *tissue*, not scaffolding, that includes the mesoscopic cellular structure inherent in natural tissues. This approach uses a laser-based rapid prototyping system known as matrix assisted pulsed laser evaporation direct write (MAPLE DW) to construct living tissue cell-by-cell. This manuscript details our efforts to rapidly

and reproducibly fabricate complex 2D and 3D tissue structures with MAPLE-DW by placing different cells and biomaterials accurately and adherently on the mesoscopic scale.

**Keywords:** Tissue Engineering, Direct Write Technology, MAPLE DW, Cell Patterning, Protein Microarray, Laser Processing, Laser-Tissue Interaction.

## 1. INTRODUCTION

The demand and need for arbitrarily engineered tissues is growing, and a great deal of technology envisioned for the future involves highly integrated devices that contain biological components as well as structural and electronic elements. New microfabrication techniques are needed to produce these tissues and devices, which will contain complicated combinations of living cells, biomaterials, polymers, ceramics, metals, and composite mixtures. The next generation of engineered tissues will potentially provide laboratories with an endless supply of living samples to test new drugs, bone-cartilage hybrid structures to treat damaged or aging joints, and surgeons with entire organs for transplant. Other future uses for engineered tissue are tissue-based devices such as an implantable device to remotely monitor a person's health status. These types of hybrid devices will require complex tissue structures to be placed adjacent to miniature electronics needed to gather data and transmit the information via RF communications. The medical community also will benefit from tissue-based devices for automated pathogen monitoring and advanced DNA and protein identification. In order to make these next generation tissue structures and hybrid devices a reality, versatile biocompatible microfabrication techniques will be needed, both to advance the basic research that will enable these technologies and as a rapid method for construction.

We are developing a biological fabrication technique that can arbitrary generate patterns of living cells and other biomaterials. This level of control is currently unavailable to biological researchers and tissue engineers, who are forced to operate in the same manner as a mechanical engineer without access to computer numerically controlled

machining, or an electrical engineer without semiconductor microlithography. Consider the aspects of an ideal 21st century biological microfabrication tool. This single tool can accept a supply of almost any material from a reservoir or holding substrate, and use it to fabricate a structure with micron-resolution features. It can easily switch from one material to another and is compact, rapid, highly automated and relies on a CAD/CAM manufacturing strategy. The primary challenge in constructing such a tool is the actual fabrication method, which must be gentle enough to move a living cell without rupturing its membrane and energetic enough to shape metals and oxides (note that the gentle, low energy end of this range is the most challenging). Manipulation by laser-materials interaction meets all these requirements. A laser spot can be easily focused and positioned at the micron scale. Lasers are readily available throughout the UV/VIS/IR spectrum, and can deliver an enormous range of energy densities. This allows specific laser-materials interactions to be easily selected and controlled at will (e.g. ablation, induced micro-explosions, photon momentum, photochemical, photothermal) and makes it possible to effectively manipulate any material at the micron-level. Furthermore, lasers are reliable, compact and integrate well into automated systems.

The Naval Research Laboratories has developed a laser forward transfer technique termed Matrix Assisted Pulsed Laser Evaporation Direct-Write (MAPLE-DW).<sup>1,2,3,4</sup> This technique uses highly localized laser-induced vaporization (micro-explosions) to transfer material from a coating on a carrier support onto a receiving substrate. Typically the support is a transparent polymer or silica, and focused laser pulses propagate through the support, producing rapid heating near the material/support interface. This heating generates an interfacial pocket of vapor, which then releases and propels material onto a receiving substrate. By scanning and modulating the laser, the transferred material can produce a high-resolution pattern or structure. The MAPLE-DW technique has demonstrated remarkable success with all classes of inorganic materials.

Fragile biomaterials are more difficult to micromanipulate, but in the last year MAPLE-DW has been used to form mesoscopic patterns of living prokaryotic cells (*E. coli* bacteria), living mammalian cells (Chinese hamster ovaries, human osteoblasts, and mouse pluripotent cells), as well as active proteins (anti-BSA, biotinylated BSA). With this laser transfer technique, it is possible to deposit patterns of cells over a surface in an arbitrary pattern, and produce patterns of different cells with close proximity to one another. In the near future this technique may allow easy fabrication of 2D and 3D engineered tissue as well as high-density microarrays for protein identification. Rapid processing of engineered tissue would enable countless experiments on different tissue structures to be run in parallel, allowing experimental

parameters to be explored more quickly than by traditional techniques. Current techniques are also unable to form engineered tissue that contains different cell types. Our approach would allow studies on tissue containing different cell types such as bone/cartilage or muscle/tendon/bone junctions. Also, our technique would give the added benefit of increased reproducibility because we would accurately place cells and biomaterials in a computer-controlled fashion, eliminating the non-uniform and random placement of cells resulting when they are injected into engineered scaffolds (i.e., cells inevitably adhere to different parts of the scaffolding for each new experiment). Constructing tissue cell-by-cell would eliminate this inherent inconsistency.

The ultimate goal is to create a single tool that is capable of fabricating complex living systems with the option of integrating electronic components for detection, transmission, and actuation. Before this is accomplished, however, there are still biological-specific problems associated with the energetic nature of laser forward transfer. Some of our studies have demonstrated near 100% cell viability in transferred samples, but these experiments are difficult to reproduce reliably, preventing the identification of optimal bio-transfer parameter regimes. Cell mortality rates can be high during transfer if laser energy, environmental controls, and substrates are not optimized. The destruction of sensitive biological materials could be caused by photochemical effects, laser-induced heating, or the mechanical compression and shock associated with the transfer process. Shearing forces during separation with the support or impact with the substrate could also rupture cell membranes. Undoubtedly, different effects induce cell death at different laser wavelengths and fluences. This paper presents initial studies to optimize biomaterial transfers, including the materials necessary to construct tissue such as living cells and active proteins.

## **2. TRADITIONAL APPROACHES TO CELL PATTERNING AND TISSUE ENGINEERING**

Fabricating patterns, arrays and structures of living cells is an important research area due to the emerging fields of tissue engineering and living device fabrication, such as tissue-based sensors and microfluidic components.<sup>5,6,7,8</sup> There are two main areas of research related to forming patterns or structures of cells. The first area uses a variety of techniques, ranging from photolithography to microcontact printing and other "soft lithography" approaches, to form 2D cell arrays.<sup>9,10,11,12,13,14,15,16</sup> These techniques have one common theme: surfaces are functionally modified so that cell-specific adhesive patches are presented to a cell solution. These techniques, therefore, form cell arrays not by direct cell placement but by indirectly functionalizing surfaces that are receptive to cell adhesion. Thus far, researchers have

focused on modifying the chemistry of surfaces to produce 2D cell arrays and patterns, and there are no examples of these techniques fabricating 3D cellular or tissue structures.

The second research area focuses specifically on engineering 3D cellular or tissue structures to speed regeneration of damaged tissue by direct *in vivo* implantation. Nearly all current efforts to engineer tissue fall under two categories: a) methods that rely upon seeding living cells into porous, biodegradable scaffolding made from natural and unnatural sources,<sup>17,18,19,20,21</sup> and b) methods that transplant cells without a carrier or matrix.<sup>22</sup> The later approach relies upon transplanted cells to repair damaged tissue by using the damaged tissue itself as a platform for growth. Obvious improvements to this approach can be made if mesoscopic structure that mimics the undamaged tissue can be given to the transplanted cells.<sup>23</sup> In many cases, this allows the tissue to heal faster and stronger because the cells are given a blueprint for proper growth. Current research focused on giving transplanted cells macroscopic structure (i.e., to repair a mm to cm tissue wound) is based on engineered scaffolds from different biocompatible and biodegradable molecules including proteins, extracellular matrix components, hydrogels, and polymers.<sup>24,25</sup> Most tissue engineering, therefore, is actually scaffold engineering, where polymer or protein structures are molded, shaped, and then seeded with cells to fill or repair *in vivo* tissue. This approach is most mature in the area of skin grafts where engineered tissue is routinely used to accelerate healing of burned or damaged skin.<sup>26,27,28</sup> There is currently intense research focused on broadening this approach to tissues for transplantation into the liver, heart, nervous system, urinary system, and the musculo-skeletal system.<sup>29,30</sup>

### 3. EXPERIMENTAL BACKGROUND

MAPLE-DW is a specialized *laser forward transfer* technique which uses focused laser pulses to transfer material from a thin coating on a carrier support, onto a receiving substrate. As shown in figure 1 the support is a transparent polymer or silica, and the focused laser pulse propagates through the support, producing rapid heating near the material/support interface. This generates

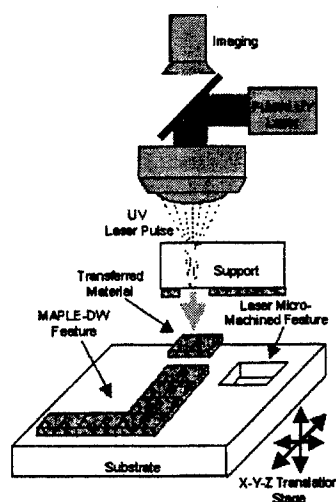


**Figure 1.** Schematic of the MAPLE DW apparatus that is capable of forming mesoscopic patterns of inorganics as well as living cells and active biomaterials.

vapor that releases and propels a pixel of material onto a substrate. By scanning and modulating the laser, the transferred material can produce a high-resolution pattern. The most notable industrial use of laser forward transfer has been in the high-volume printing industry, for platemaking and proofing<sup>31</sup>. These applications are highly developed, but are limited to transfer of visually pigmented ink and ink carrier materials. Recent efforts have centered on extension of laser forward transfer to other materials.

When laser heating explosively generates vapor faster than thermal diffusion can occur, the transfer process is considered to be in the ablation regime. This is known as laser induced forward transfer (LIFT) when a high-power, ablative mechanism is used to transfer patterns of solid-state materials.<sup>32</sup> In these cases the entire volume of transferred material is either vaporized or melted, and this severely limits the phases of materials that can be used for microfabrication. The most sophisticated LIFT work has been performed by Zergioti et al.<sup>33</sup>, who demonstrated sub-micron pixels of a few metal and oxide materials, in air.

Recently our group at the Naval Research Laboratories has extended the LIFT process, using ablation-regime transfer but with lower power sub-microsecond laser pulses, in order to allow direct writing of a wider range of useful materials, without damage during transfer. The result was MAPLE-DW - a high speed, low-energy process that couples the laser power into a volatile matrix material, protecting fragile suspended or solvated components from laser damage. Originally, MAPLE-DW was developed for the direct-writing and rapid prototyping of micron-scale passive electronic devices, and it has been very successful at this application. Using conductive, resistive and dielectric inks, MAPLE-DW has been used for the direct-write fabrication of various high-performance electronic elements<sup>34,35</sup>. However, it was soon discovered that the MAPLE-DW process could produce mesoscopic pixels (a homogeneous continuous spot) of *virtually any UV-absorbing viscous material*<sup>36</sup>, provided that the absorptivity is sufficiently high at the laser wavelength. Furthermore, adjacent pixels usually merge on the substrate to form a pinhole-free pattern with <10 micron edge resolution, making the technique attractive for device fabrication in general. Patterned arrays of other materials such as chemoselective polymers<sup>37</sup> and phosphors<sup>38</sup> have been demonstrated. Most recently MAPLE-DW has been used to deposit patterns of biomaterials such as active proteins and living cells<sup>39,40,41,42</sup>.

As discussed in Section 2, there are several technologies capable of writing adjacent patterns or three-dimensional structures of different biomaterials, but fewer techniques exist that produce patterns that are software generated, have micron resolution, and are written at sub-millisecond times.

#### 4. RESULTS AND DISCUSSION



#### 4.1. Dispensing Picoliter-scale Aliquots of Active Proteins

By uniformly spreading a viscous protein solution over the MAPLE DW quartz support, picoliter-scale droplets of active proteins can be spotted down onto most any substrate. Figure 2 shows an optical micrograph of two anti-BSA/glycerol droplets dispensed onto a silanted glass slide using two different laser energies (2.5 and 7.6  $\mu\text{J}$ ), a laser spot size of  $200 \times 200 \mu\text{m}^2$ , and a support/substrate distance of 75  $\mu\text{m}$ . Other



Figure 2. MDW of Anti-BSA/glycerol on Digene Silanated™ slides as a function of laser energy using a ribbon to substrate distance of 75  $\mu\text{m}$ . The minimum transferred spot size is 75  $\mu\text{m}$  dia. with an estimated volume of 90 pl.

experiments demonstrated that protein solutions could be deposited into microwells and microchannels. Figure 3 is an optical micrograph of several anti-BSA droplets dispensed into a polystyrene microchannel 150  $\mu\text{m}$  wide and 70  $\mu\text{m}$  deep. Similar droplet resolution is achieved for both planar and microchannel substrates.

The uniformity and symmetry of the droplets transferred over 0.075 and 0.15 mm suggests that at laser energies near threshold, pattern resolution is independent of support-substrate distance.



Figure 3. MDW of an array of Anti-BSA/glycerol in a 150  $\mu\text{m}$  wide and 70  $\mu\text{m}$  deep channel in polystyrene

Previous experiments using inorganic materials show that at laser energies above threshold a "cone-shaped" spray of many smaller droplets is formed.<sup>43</sup> This spray results in a rapid loss of line resolution as the distance between the support and substrate is increased. The results presented in this manuscript indicate that the transfer mechanism for protein solutions must involve the formation of a constant diameter jet or droplet of fluid instead of a cone. One possible explanation for these results is that the increased viscosity and homogeneous nature of the protein solution may act to bind the fluid together as it is released from the bulk material on the support. Fast-time imaging studies are currently underway to investigate the material transfer mechanism that is responsible for these observed transfer properties.

The first step in demonstrating that MAPLE DW is capable of creating a protein microarray is to fabricate a single element array that can be assayed with standard fluorescent-tagging procedures. Figure 3a is a fluorescent image of laser-deposited, biotinylated bovine serum albumin (BSA) spots. Droplets of 250  $\mu\text{g/mL}$  biotinylated BSA were first deposited onto a nitrocellulose-coated glass slide (FASTslides, Schleicher&Schuell, Keene, N.H.) by laser transfer. The slide was then exposed to 200  $\mu\text{L}$  of 50  $\text{mg/mL}$  BSA to block the nitrocellulose sites where protein was not dispensed. After washing twice with TBST [10  $\text{mM}$  Tris-HCl (pH 8), 150  $\text{mM}$  NaCl, 0.05% Tween 20<sup>®</sup>], the slide was exposed to 100  $\mu\text{L}$  of 1:100 diluted Cy5-labelled streptavidin in TBST for 30 minutes to enable imaging of the active biotinylated BSA sites by a GenePix 4000B (Axon Instruments, Inc.) reader at 635 nm. This

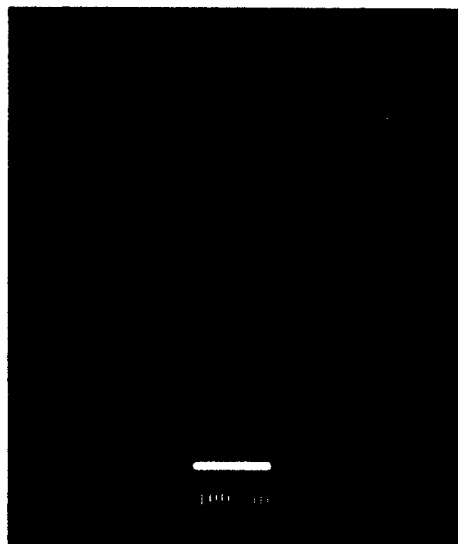


Figure 4. UV micrograph of a biotinylated BSA microarray deposited by laser transfer onto a nitrocellulose-coated glass slide. Fluorescence is due to the binding of Cy5-tagged streptavidin to the biotinylated protein.

laser deposition and fluorescent tagging experiment demonstrates that our approach is able to accurately place biotin-labeled protein onto standard microarray slides and assay the presence of bound protein in 50  $\mu\text{m}$  areas.

The microarray shown in Figure 2 demonstrates that laser transfer is superior to tradition pin arraying techniques for the deposition of antibody microarrays. First, the spot size shown in Figure 2 is five times smaller than the standard spot for a pin arrayer; laser transfer can therefore form 25 times more dense arrays. Laser transfer also uses protein solution more efficiently because each drop contains roughly 65 picoliters of fluid compared to a minimum of 33 nanoliters for standard arraying. Also a minimum of 100 nanoliters of starting material is required compared to tens of microliters for a pin arrayer. Therefore less material is needed for laser transfer and virtually no material is wasted. This increased efficiency enables over 1500 arrays to be fabricated with only 100 nanoliters of starting solution—a 5000 fold decrease in material usage compared to the pin technique. The small amount of starting materials required would also allow dilute antibody solutions to be concentrated to smaller volumes, enabling more molecules to be deposited per area. Because the laser pulse can be focused to spot sizes as small as 10  $\mu\text{m}^2$ , we believe the ultimate resolution of droplets

dispensed by MAPLE DW could be 5  $\mu\text{m}$  or less. This would enable several orders of magnitude more proteins to be assayed per slide than by any other current technology.

#### 4.2. Fabrication of Living Cell Patterns

Laser direct write of living cells was first demonstrated by forming patterns of the bacteria *E. coli*.<sup>40</sup> Post-laser transferred cells were determined to be intact and viable by SEM imaging, green fluorescent protein expression, and cell culturing experiments. In terms of studying tissue engineering, it is more important to study eukaryotic species, such as bone or muscle cells that form cohesive

tissue, rather than prokaryotic cells.

Successful laser-transfer experiments

have also been performed on two species

of eukaryotic cells: Chinese hamster

ovaries (CHO) and human osteoblasts.

Figures 5 and 6 show evidence that these

more fragile and complex cells can also

survive the laser transfer process. Figure

5 (a) and (b) are optical micrographs of transferred CHO cells immediately following laser transfer and after three days of culturing, respectively. Close inspection of panel (a) shows the presence of both CHO cells and the hydrogel used as a matrix to grow the cells on the quartz support. The transferred hydrogel allows the cells to adhere to their new environment and helps to hydrate cells until the pattern is submerged in growth media several minutes after the transfer is complete. The increased number and adherent nature of the transferred cells shown in panel (b) indicate that at least some of the cells remain viable post-transfer.

Similarly, Figure 6 (a), (b), and (c) show fluorescent micrographs of human osteoblasts pre-transfer (cultured on the laser support/ribbon) and immediately post-transfer after exposure to the live/dead assay, respectively. The green and orange fluorescence from different cells is due to the exposure of the cells to a standard live/dead assay where green indicates a live cell (calcein dye) and orange indicates the presence of a dead cell (Ethidium homodimer). Panel (a)

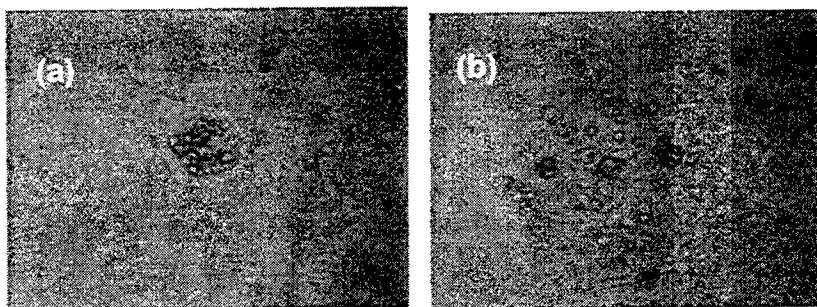
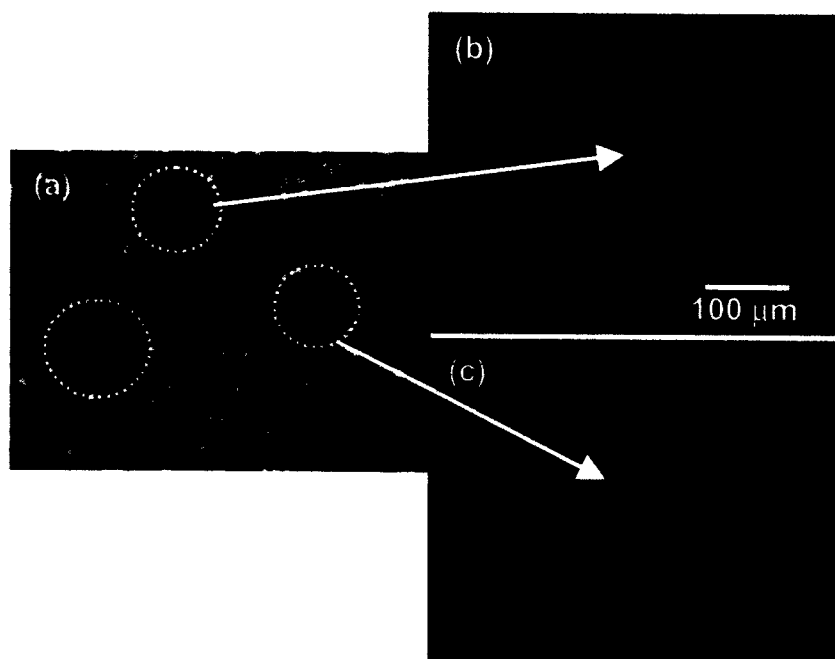


Figure 5. (a) Optical micrograph of CHO cells and hydrogel immediately after laser-transfer. (b) Same transferred CHO cells after three days of culturing.

demonstrates that nearly all cells pre-transfer are viable (osteoblast culture on hydrogel layer on quartz support), while panels (b) and (c) show that nearly 100% of the osteoblasts remain viable immediately after transfer.

Although these results appear very promising, note that we have had some difficulty in reproducibly achieving near 100% viability. Specifically, if the transfers are not performed in a wet environment, with near-threshold laser energies, and with "soft" receiving substrates, cell mortality rates can reach 100%. Therefore, further studies are needed to enhance our understanding of the transfer process. We plan to perform more detailed sets of experiments first using automation to more fully explore the parameter space and then high-speed imaging of the cell transfers to help understand what forces may be causing cell mortality.



**Figure 6.** (a) Micrograph of UV exposed human osteoblasts on the laser transfer support. (b) 100% viability of laser-transferred osteoblasts. (c) 6 out of 7 live osteoblasts post-transfer.

## 5. SUMMARY AND CONCLUSIONS

These results demonstrate that MAPLE DW is a versatile technique capable of forming mesoscopic patterns of active proteins and living cells, two components necessary for the cell-by-cell construction of complex tissue structures.

We have used this approach to dispense 50 micron diameter protein droplets (200 micron diameter laser spot) onto

planar surfaces, microwells, and microarray substrates. By focusing the laser to smaller dimensions (5 micron capabilities), these dimensions could be decreased by at least an order of magnitude, allowing sub-10 micron protein spots to be formed. Previously published results demonstrated the ability to form patterns of living *E. coli*, and here we presented evidence that these capabilities can be extended to living eukaryotic cells such as CHO and human osteoblasts. We therefore believe that this technique may be a general method to form arbitrary patterns and structures of most any living cell type. By controlling these depositions with a computer-aided design/manufacturing system, we hope to extend this technology to fabricate entire tissues, complete with their natural microscopic structure.

- <sup>1</sup> D. B. Chrisey, *Science*, 289, (2000) 879-881.
- <sup>2</sup> D. B. Chrisey, A. Pique, R. Modi, H. D. Wu, R. C. Y. Auyeung, H. D. Young, R. Chung, *Appl. Surf. Sci.*, 6683 (2000) 1-8.
- <sup>3</sup> J. M. Fitz-Gerald, A. Pique, D. B. Chrisey, P. D. Rack, M. Zeleznik, R. C. Y. Auyeung, S. Lakeou, *Appl. Phys. Lett.*, 76 (2000) 1386.
- <sup>4</sup> D. Young, H. D. Wu, R. C. Y. Auyeung, R. Modi, J. Fitz-Gerald, A. Pique, D. B. Chrisey, P. Atanassova, T. Kodas, *J. Mater. Res.*, 16 (2001) 1720-1725.
- <sup>5</sup> Langer, R.; Vacanti, J.P. *Science*, 260 (1993) 920-926.
- <sup>6</sup> Lysaght, M.J. and Reyes, J. *Tissue Eng.*, 7 (2001) 485-93
- <sup>7</sup> Giaever, I.; Keese, C.M. *Nature*, 366 (1993) 591-592.
- <sup>8</sup> Fisherman, H.A.; Orwar, O.; Allbritton, N.L.; Modi, B.P.; Shear, J.B.; Scheller, R.H.; Zare, R.N. *Anal. Chem.*, 68 (1996) 1181-1186.
- <sup>9</sup> Spargo, B.J, et al. *Proc Natl Acad Sci USA*, 91 (1994) 11070-11074.
- <sup>10</sup> Wilbur, J.L, Kumar, A, Biebuyck, H.A, Kim, E, Whitesides, G.M. *Nanotechnology*, 7 (1996) 452-457.
- <sup>11</sup> Kane, R.S, Takayama, S, Ostuni, E, Ingber, D.E, Whitesides, G.M. *Biomaterials*, 20 (1999) 2363-2376.
- <sup>12</sup> Ito, Y. *Biomaterials*, 20 (1999) 2333-2342.
- <sup>13</sup> Folch, A, Jo, B.H, Hurtado, O, Beebe, D.J, Toner, M. *J. Biomed. Mat. Res.*, 52 (2000) 346-353.
- <sup>14</sup> Folch, A and Toner M. *Ann. Rev. Biomed. Eng.*, 2 (2000) 227.
- <sup>15</sup> Takayama, S, et al. *Proc Natl Acad Sci.*, 96 (1999) 5545-5548.
- <sup>16</sup> D.R. Jung, et al. *Critical Reviews in Biotechnology*, 21 (2001) 111-154.
- <sup>17</sup> Temenoff, J.S. and Mikos, A.G. *Biomaterials*, 21 (2000) 431.
- <sup>18</sup> Solchaga, L.A.; Dennis, J.E.; Goldberg, V.M.; Caplan, A.I. *J. Orthop. Res.*, 17 (1999) 205-213..
- <sup>19</sup> Athanasiou, K.; Krovick, D.; Schenck, R. *Tissue Eng.*, 3 (1997) 363-373.
- <sup>20</sup> Caplan, A.I. and Bruder, S.P. In: Lanza, R.P.; Chick, W.L.; Langer, R. eds. *Principles of Tissue Engineering*. Springer, NY: R.G. Landes Co., 1996, pp. 599-618.
- <sup>21</sup> Caplan, A.I.; Fink, D.J.; Bruder, S.P.; Young, R.G.; Butler, D.L. In: Patrick, Jr., C.W.; Mikos, A.G.; McIntire, L.V. eds. *Frontiers in Tissue Engineering*. NY: Elsevier Science, 1998, pp. 471-480.
- <sup>22</sup> Asonuma, K.; Gilbert, J.C.; Stein, J.E.; Takeda, T.; Vacanti, J.P. *J. Pediatr. Surg.* 27 (1992) 298-301.
- <sup>23</sup> Vacanti, J.P. *Cell Transplantation*, 2 (1993) 409-410.
- <sup>24</sup> Kapur, R.; Spargo, B.J.; Chen, M.; Calvert, J.M.; Rudolph, A.S. *J. Biomed. Mat. Res.*, 33 (1996) 205-216.
- <sup>25</sup> Lee, K.Y. and Mooney, D.J. *Chem. Rev.*, 101 (2001) 1869-1879.
- <sup>26</sup> Rennekampff, H.O.; Kiessig, V.; Hansbrough, J.F. *J Surg. Res.*, 62 (1996) 288-95
- <sup>27</sup> Horch R.E.; Debus, M.; Wagner, G.; Stark, G.B. *Tissue Eng.*, 6 (2000) 53-67
- <sup>28</sup> Voigt, M.; Schauer, M.; Schaefer, D.J.; Andree, C.; Horch, R.; Stark, G.B. *Tissue Eng.*, 5 (1999) 563-72
- <sup>29</sup> Zeltinger, J.; Landeen, L.K.; Alexander, H.G.; Kidd, I.D.; Sibanda, B. *Tissue Eng.*, 7 (2001) 9-22
- <sup>30</sup> Takezawa, T.; Inoue, M.; Aoki, S.; Sekiguchi, M.; Wada, K.; Anazawa, H. Hanai, N. *Tissue Eng.*, 6 (2000) 641-50.
- <sup>31</sup> C. DeBoer, *Journal of Imaging Science and Technology*, 42 (1998) 63-69.
- <sup>32</sup> Z. Kantor, Z. Toth, T. Szorenyi, *Appl. Phys. A* 54 (1002) 170-175.
- <sup>33</sup> I. Zergioti, S. Mailis, N. A. Vainos, P. Papakonstantinou, C. Kalpouzos, C. P. Grigoropoulos, C. Fotakis, *Appl. Phys. A*, 66 (1998) 579-582.

- <sup>34</sup> D. B. Chrisey, A. Pique, J. Fitz-Gerald, R. C. Y. Auyeung, R. A. McGill, H. D. Wu, M. Duignan, *Applied Surface Science*, 154-155 (2000) 593-600.
- <sup>35</sup> D. B. Chrisey, A. Pique, R. Modi, H. D. Wu, R. C. Y. Auyeung, H. D. Young, R. Chung, *Appl. Surf. Sci.*, 6683 (2000) 1-8.
- <sup>36</sup> D. B. Chrisey, *Science*, 289 (2000) 879-881.
- <sup>37</sup> A. Pique, D. B. Chrisey, R. C. Y. Auyeung, J. Fitz-Gerald, H. D. Wu, R. A. McGill, S. Lakeou, P. K. Wu, V. Nguyen, M. Duignan, *Appl. Phys. A [Suppl.]*, (1999) S279-S284.
- <sup>38</sup> J. M. Fitz-Gerald, A. Pique, D. B. Chrisey, P. D. Rack, M. Zeleznik, R. C. Y. Auyeung, S. Lakeou, *Applied Physics Letters*, 76 (2000) 1386.
- <sup>39</sup> Ringeisen, B.R.; et al. Proceedings of the Fourth International Conference on Modeling and Simulation of Microsystems, Hilton Head Island, SC, March 2001.
- <sup>40</sup> Ringeisen, B.R.; et al. *Biomaterials*, to be published January 2002.
- <sup>41</sup> Ringeisen, B.R.; et al. *American Biotechnology Laboratory*, May 2001.
- <sup>42</sup> D. B. Chrisey, A. Piqué, J. Fitz-Gerald, B. Ringeisen, R. Modi, *Laser Focus World*, 36 (2000) 113.
- <sup>43</sup> D. Young, R.C.Y. Auyeung, A. Pique, D.B. Chrisey, and D.D. Dlott, *App. Phys. Lett.* 78, 3169 (2001).

# Direct writing of planar ultracapacitors by laser forward transfer processing

Craig B. Arnold<sup>a\*</sup>, Ryan C. Wartena<sup>b</sup>, Bhanu Pratap<sup>a</sup>, Karen E. Swider-Lyons<sup>b</sup>  
and Alberto Piqué<sup>a</sup>

<sup>a</sup>Materials Science and Technology Division, Code 6372

<sup>b</sup>Chemistry Division, Code 6171

Naval Research Laboratory, Washington, DC 20375, USA

## ABSTRACT

We employ a novel laser forward transfer process, Matrix Assisted Pulsed Laser Evaporation Direct Write (MAPLE-DW), in combination with ultraviolet laser micromachining, to fabricate mesoscale ultracapacitors and microbatteries under ambient temperature and atmospheric conditions. Our laser engineering approach enables the deposition of hydrous ruthenium oxide ( $\text{RuO}_x\text{H}_y$  or  $\text{RuO}_2 \cdot x \text{H}_2\text{O}$ ) films with the desired high surface area morphology, without compromising the electrochemical performance of this high specific capacitance material. We compare three different deposition formulations incorporating ethylene glycol, glycerol, or sulfuric acid. The best electrochemical performance is achieved using a mixture of sulfuric acid with  $\text{RuO}_2 \cdot 0.5 \text{H}_2\text{O}$  electrode material. Our ultracapacitors exhibit the expected linear discharge behavior under a constant current drain, and the electrochemical properties of these cells scale proportionately when combined in parallel and series.

**Keywords:** laser direct write, laser micromachining, MAPLE-DW, microbattery, electrochemical capacitor, supercapacitor, pseudocapacitor, hydrous ruthenium oxide,  $\text{RuO}_2$

## 1. INTRODUCTION

High capacitance electrochemical capacitors have been studied for more than 40 years, yet it has only been in last decade that they have gained widespread attention.<sup>1,2</sup> The interest in these systems has arisen mainly from commercial applications, such as electric or hybrid powered vehicles or power backup sources, where there is a need for energy storage systems that can hold relatively large amounts of energy yet deliver it in short pulses leading to high power output.<sup>3,4</sup> Conventional parallel plate capacitors can deliver high power, but are limited in the amount of energy they can store. Electrochemical capacitors provide an intermediate range of power and energy between parallel plate capacitors and conventional batteries. Hydrous ruthenium oxide ultracapacitors are a type of electrochemical capacitor with a high capacitance due to the rapid double insertion and release of protons and electrons in the active material.<sup>2,5,6</sup>

The need for high power pulsed energy sources is also important in the development of micro-power sources for microelectronic and microelectronic mechanical systems (MEMS). Although the maximum power requirements for pulsed operations are typically much less than one watt per square centimeter, this low output power is more than can be delivered by a thin-film microbattery.<sup>7,8</sup> Therefore, the development of hybrid micro-power systems that incorporate a high power ultracapacitor in combination with a microbattery is essential for the future of next generation micro-devices.<sup>9</sup>

The manufacture of thin-film hydrous ruthenium oxide ultracapacitors is difficult due to the complex materials requirements for an effective, high capacitance power source.<sup>5</sup> The most advantageous morphology for a high capacity ultracapacitor is a permeable, porous structure leading to a large effective surface area.<sup>1,2</sup> The  $\text{RuO}_2 \cdot x \text{H}_2\text{O}$  system has the additional limitation that the capacitance of the material depends on the processing temperature.<sup>6,10,11</sup> These aspects of morphological constraints and processing temperature limitations, in addition to the presence of water in the oxide structure have made  $\text{RuO}_2 \cdot x \text{H}_2\text{O}$  incompatible with standard

\*Corresponding author: Email: craig@ccs.nrl.navy.mil; Telephone (202)404-2093; Fax (202)767-5301

vacuum techniques for thin film growth such as physical vapor deposition. Instead, recent studies of thin film ultracapacitors have focused on the development of anhydrous metal oxide systems deposited by sputtering.<sup>12</sup>

We overcome the difficulties associated with the deposition of hydrous metal oxide films by using a laser direct writing technique, Matrix Assisted Pulsed Laser Evaporation-Direct Write (MAPLE-DW).<sup>13,14</sup> In this technique, an "ink" composed of a sacrificial liquid matrix (transfer vehicle) and the material to be deposited (passenger material) is laser forward transferred to a substrate below. The presence of the liquid enable the deposited film to flow and achieve a relatively flat and pinhole-free surface. This technique produces thin-films of the hydrous material with the desired morphological properties without the need for high temperature or lithographic processing following deposition. Ultracapacitor electrodes are shaped from the deposited film using UV laser machining.<sup>15</sup>

A distinct advantage of MAPLE-DW is the ability to operate under ambient conditions to deposit a mixture of  $\text{RuO}_2 \cdot 0.5 \text{H}_2\text{O}$  and a liquid electrolyte. This technique of distributing electrolyte within the electrode is commonly used in the production of larger scale electrochemical power sources, but it is not possible with other thin film techniques such as PVD, CVD, or sol-gel methods. Additionally, the use of liquid sulfuric acid electrolyte, as opposed to solid-state materials, enables higher proton conductivity in the electrolyte and enhances ultracapacitor properties.<sup>16</sup>

In this paper, we describe the use of laser processing to deposit functional planar ultracapacitors with energy and power densities commensurate with larger power sources. We capitalize on the advantage of an ambient process to study the influence of different transfer vehicles and find that sulfuric acid vehicles produces ultracapacitors with the best electrochemical properties. Finally, by combining the ultracapacitors in parallel and series, we are able to achieve proportionately larger capacitance and voltage, respectively.

## 2. EXPERIMENTAL PROCEDURES

Thin film hydrous ruthenium oxide planar ultracapacitors are deposited using the MAPLE-DW technique previously described in detail.<sup>13,14</sup> Figure 1 shows a schematic of the experimental approach. We transfer a wet ink composed of a liquid vehicle (ethylene glycol, glycerol or sulfuric acid) and the passenger material ( $\text{RuO}_2 \cdot 0.5 \text{H}_2\text{O}$ ). Commercially available hydrated ruthenium oxide powder is oven heated to  $150^\circ\text{C}$  for 18 hours to yield a material with the desired water content of 0.5 mol  $\text{H}_2\text{O}$  per mol  $\text{RuO}_2$  for optimal charge storage.<sup>6,17</sup> This ink is dispersed on a quartz plate to form the ribbon depicted in figure 1a. A frequency-tripled Nd:YAG laser ( $\lambda=355 \text{ nm}$ ) is used to irradiate the back of the ribbon inducing a forward transfer of material to a substrate  $100 \mu\text{m}$  below the ribbon.

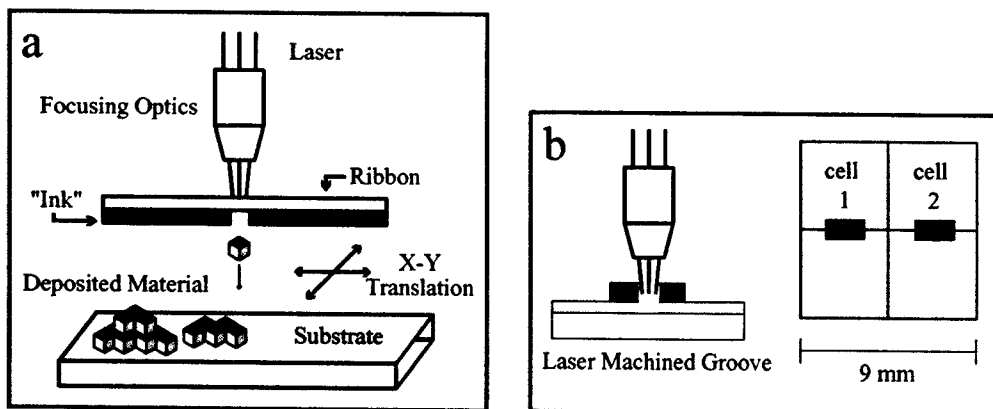


**Figure 1.** Schematic of MAPLE-DW technique (a) laser forward transfer of a wet "ink" layer for film deposition (b) UV laser machining of film to form isolated electrodes. The two ultracapacitor cells are  $1 \text{ mm} \times 2 \text{ mm} \times 10 \mu\text{m}$ .



The substrate is a 1 cm x 1 cm gold-coated quartz wafer that has been laser machined with a 9 mm "window pane" structure to electrically isolate four current collector pads (figure 1b). Hydrated ruthenium oxide films 1 mm x 2 mm x 10  $\mu\text{m}$  are deposited to span across the machined groove in the gold. A line is then laser machined across the film providing a symmetric planar ultracapacitor with 0.5 mm x 2 mm x 10  $\mu\text{m}$  electrodes. Two such ultracapacitors are deposited on each substrate. The volume of each ultracapacitor is  $2 \times 10^{-5}$  mL and the approximate mass is 50  $\mu\text{g}$ .

The excess vehicle deposited in the  $\text{RuO}_2 \cdot 0.5 \text{H}_2\text{O}$  film must be removed prior to laser machining in order to obtain sharp interfaces. When we use organic transfer vehicles, the as-deposited films are dried on a hot plate at 100  $^\circ\text{C}$  for 10 minutes prior to laser machining. After the films are machined, the remaining vehicle is removed from the samples by heating in an oven at 5  $^\circ\text{C}/\text{min}$  to 150  $^\circ\text{C}$  and held for 3 hours. For films deposited with sulfuric acid, the excess vehicle is removed by IR laser irradiation ( $\lambda=1064\text{nm}$ ) and the final bake is not used.

Electrochemical evaluation of capacitance and charge-discharge behavior is carried out using a potentiostat (EG&G PAR Model 263) connected to a probe station. The ultracapacitors are encapsulated in Nafion<sup>®</sup> and submerged in 0.5 M  $\text{H}_2\text{SO}_4$  solution during testing. Multiple chronopotentiometry steps are used to charge and discharge the ultracapacitors between 0 and 1 V in a two-electrode configuration. All cells were charged at a constant current of 50  $\mu\text{A}$  and discharged at 10, 50, or 100  $\mu\text{A}$ .

### 3. RESULTS AND DISCUSSION

Hydrous ruthenium oxide films deposited and processed by our technique exhibit desirable morphologic qualities of a high capacity ultracapacitor. Figure 2 shows optical and electron micrographs of the deposited material. The optical image (figure 2a) shows we are able to deposit uniform films of  $\text{RuO}_2 \cdot 0.5 \text{H}_2\text{O}$  which are laser machined with precision ( $< 20 \mu\text{m}$  groove). Optical examination indicate that under these processing conditions, there is no large scale collateral damage to the area surrounding the groove.

Under higher magnification with SEM (figure 2b,c), the deposited thin films appear highly porous throughout the active material, regardless of the transfer vehicle used. The porous structure remains undamaged by UV laser machining in the region near the machined groove. This morphology is desirable as it provides a large effective surface area and enables the electrolyte to easily permeate the electrode. This provides high ionic transport to the active material where the balance between protonic and electronic conduction mechanisms within the nanostructured material leads to the high capacitance in the  $\text{RuO}_2 \cdot 0.5 \text{H}_2\text{O}$  system.<sup>11</sup> Since  $\text{RuO}_2$  is a metallic conductor, the high level of electrode porosity is not detrimental to the electronic transport.

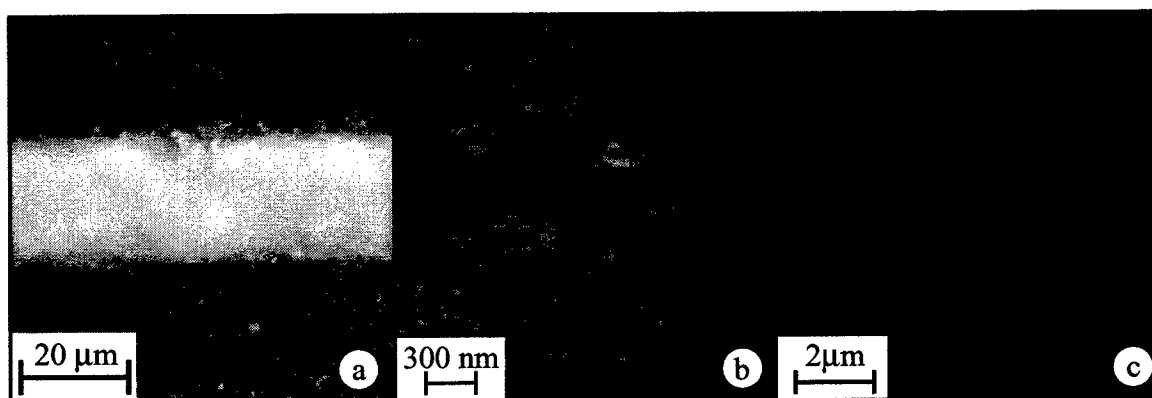


**Figure 2.** Micrographs of deposited  $\text{RuO}_2 \cdot 0.5 \text{H}_2\text{O}$  thin-films (a) Optical image at 50x magnification showing the laser machined groove through a  $\text{RuO}_2 \cdot 0.5 \text{H}_2\text{O}$  film. (b) SEM image of electrode at 20,000x magnification. (c) SEM image of electrode near the laser machined groove (bottom of image) magnified 3000x.

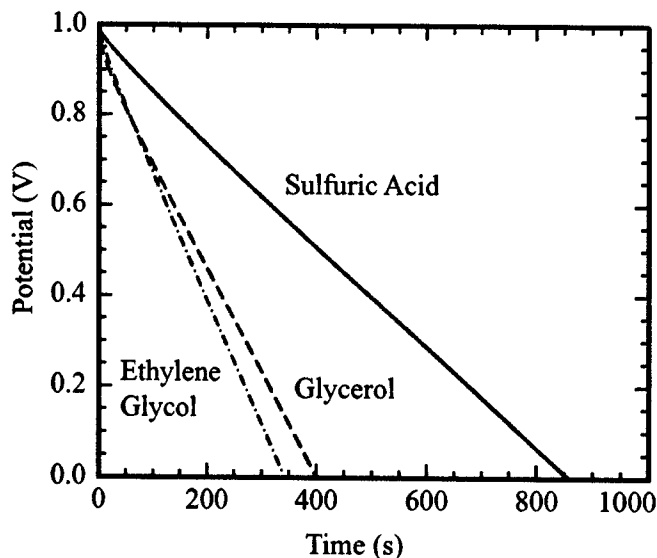


**Figure 3.** 10  $\mu\text{A}$  discharge profile of  $\text{RuO}_2 \cdot 0.5 \text{H}_2\text{O}$  ultracapacitors deposited using three different transfer vehicles; ethylene glycol, glycerol and sulfuric acid. Discharge times are 350, 400, and 850 s respectively.

The ultimate test for any of our ultracapacitors is the electrical response of the power source and its ability to store and deliver charge. Figure 3 shows the 10  $\mu\text{A}$  chronopotentiometric discharge profiles for samples transferred with three different vehicles (ethylene glycol, glycerol and sulfuric acid solutions). In all cases, the discharge is linear as expected for an ideal capacitor. Samples deposited from inks containing  $\text{H}_2\text{SO}_4$  exhibit the longest discharge time, 850 s, as compared to those deposited from glycerol and ethylene glycol based inks that last 400 and 350 s respectively.

A constant capacitance is justified by the linear discharge behavior, so the average specific capacitance of the sample is given by

$$c = \frac{I \Delta t}{m \Delta V}, \quad (1)$$

where  $I$  is the constant discharge current,  $\Delta t$  is the total discharge time,  $\Delta V$  is the maximum potential difference, and  $m$  is the mass of the ultracapacitor, including the electrolyte. The specific energy,  $\epsilon$ , and average specific power,  $p$ , are obtained from the area under the curve by

$$\epsilon = \frac{I}{m} \int V dt \quad (2)$$

$$p = \frac{\epsilon}{\Delta t}. \quad (3)$$

Table 1 shows the calculated values of specific capacitance, specific energy and specific power for the data shown in figure 3.

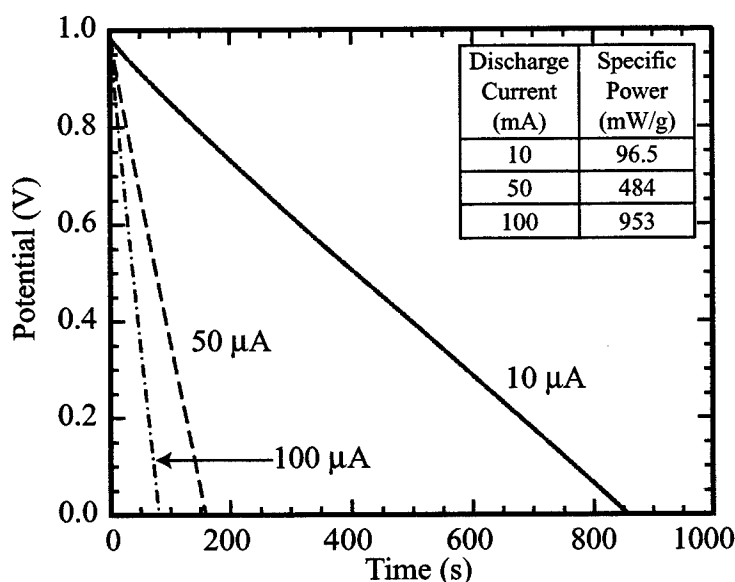
When the discharge current is increased (figure 4), the specific power increases while the specific energy remains unchanged. The discharge time for a ultracapacitor deposited with a sulfuric acid vehicle varies proportionately under 10, 50, and 100  $\mu\text{A}$  discharge currents, and decreases to 80 s at the largest current. This corresponds to a specific power of nearly 1000 mW/g and a specific energy of 21 mW/g. Ultracapacitors prepared using ethylene glycol and glycerol transfer vehicles exhibit a similar scaling behavior with correspondingly lower specific energy.

**Table 1.** Calculated values of specific capacitance, energy density and average power using equations 1-3 and the data shown in figure 3.

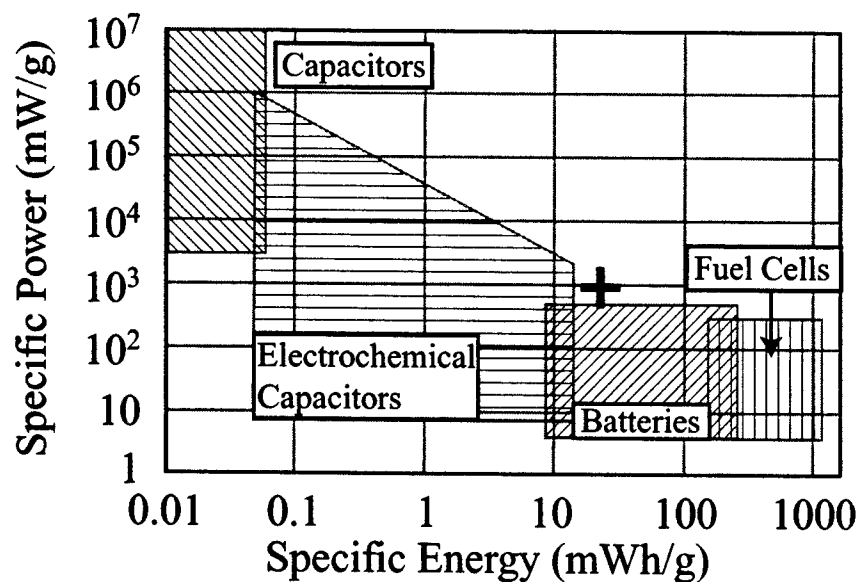
Transfer Vehicle	Specific Capacitance (F/g)	Specific Energy (mWh/g)	Specific Power (mW/g)
H <sub>2</sub> SO <sub>4</sub>	174	23.0	96.5
Glycerol	83.0	10.4	93.5
Ethylene Glycol	69.5	9.15	96.3

Figure 5 shows a Ragone plot with typical values for different types of energy storage devices.<sup>3</sup> The maximum specific power for our RuO<sub>2</sub> · 0.5 H<sub>2</sub>O cells deposited with sulfuric acid is represented by a cross on the plot. Our ultracapacitors exhibit behavior in the region of high specific energy and high specific power for an electrochemical capacitor. It should be noted that the main source of uncertainty in our measured values for specific energy and power arises from the mass determination.

Ultracapacitors transferred using a sulfuric acid vehicle exhibit superior electrochemical characteristics in comparison to those deposited using organic transfer vehicles. Typical MAPLE-DW depositions make use of organic vehicles due to their ease in handling and their ability to make stable ink formulations. Sulfuric acid poses additional challenges to the processing and development of a usable formulation due to its high acidity, but the advantages in energy storage outweigh the handling difficulties. We believe the deleterious effects of oxidation and decomposition of residual organics in the presence of the acidic electrolyte may cause contamination to the electrically active hydrous ruthenium oxide. In contrast, the use of a sulfuric acid transfer vehicle precludes the need for complete removal of the transfer vehicle thus decreasing the possibility for contamination of our active material and enabling a better distribution of electrolyte in the electrode.



**Figure 4.** Chronopotentiometry of RuO<sub>2</sub> · 0.5 H<sub>2</sub>O ultracapacitors for sulfuric acid transfer vehicle at 10, 50 and 100 μA discharge currents. The discharge times of 80, 160, and 850 s respectively convert to the specific power values through equation 3.



**Figure 5.** Ragone plot of various energy storage devices.<sup>3</sup> The cross represent our data from ultracapacitors deposited with a sulfuric acid transfer vehicle and a discharge current of 100  $\mu$ A.

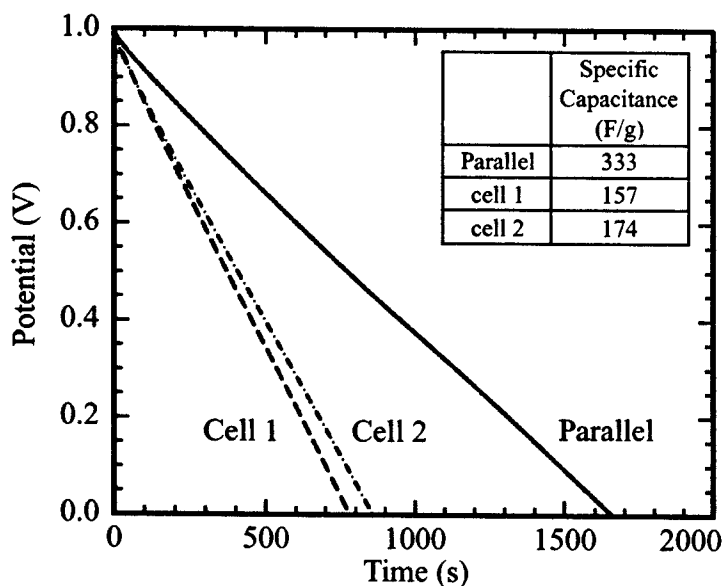


**Figure 6.** Chronopotentiometry of  $\text{RuO}_2 \cdot 0.5 \text{H}_2\text{O}$  ultracapacitors for sulfuric acid transfer vehicle at 10  $\mu$ A discharge currents on two cells and the parallel combination. The values for specific capacitance are given in the table.

Further evidence of process viability is demonstrated when the ultracapacitors are connected in parallel and series. Figure 6 shows 10  $\mu\text{A}$  discharge profiles for two ultracapacitors deposited with sulfuric acid and connected in parallel. Again, the system is charged to 1 V and the discharge curves exhibit linear behavior. However, this parallel configuration has an extended discharge time of 1660 s. Calculations show the specific capacitance of the system is additive, as expected for capacitors in parallel, while the specific energy reflects the average of the two individual cells.

Ultracapacitor cells are also combined in series to increase the voltage of the system. In this case (the data is not shown here), the system is charged to 2 V at 50  $\mu\text{A}$ . Upon discharge at 10  $\mu\text{A}$  to 0 V, we find the specific energy and specific power remain essentially unchanged. The calculation of capacitance from this system exhibits the expected inverse addition rules of series capacitors.

#### 4. SUMMARY

We have demonstrated that a laser engineering approach is a viable method for fabricating mesoscale ultracapacitors. Ultracapacitors of hydrous ruthenium oxide electrodes and sulfuric acid electrolyte are successfully produced using an ambient forward laser transfer technique (MAPLE-DW) in addition to UV laser machining. The evaluation of two different organic transfer vehicles and sulfuric acid transfer vehicle indicates that the choice of sulfuric acid enhances the electrochemical properties of the ultracapacitors. Configurations of  $\text{RuO}_2 \cdot 0.5 \text{H}_2\text{O}$  ultracapacitors in series and parallel exhibit the expected additive behavior.

#### ACKNOWLEDGMENTS

This research is supported by the Office of Naval Research. CBA acknowledges the support of the National Research Council postdoctoral associate program and RCW acknowledges the support of the American Society for Engineering Education.

#### REFERENCES

1. B. E. Conway, V. Birss, and J. Wojtowicz, "The role and utilization of pseudocapacitance for energy storage by supercapacitors," *J. Power Sources* **66**, pp. 1-14, 1997.
2. S. Trasattia and P. Kurzweil, "Electrochemical supercapacitors as versatile energy stores," *Plat. Met. Rev.* **38**, pp. 46-56, 1994.
3. R. Kotz and M. Carlen, "Principles and applications of electrochemical capacitors," *Electrochimica Acta* **45**, pp. 2483-2498, 2000.
4. L. P. Jarvis, T. B. Atwater, and P. J. Cygan, "Fuel cell/electrochemical capacitor hybrid for intermittent high power applications," *J. Power Sources* **79**, pp. 60-63, 1999.
5. S. Sarangapani, B. Tilak, and C. Chen, "Materials for electrochemical capacitors," *J. Electrochem. Soc.* **143**, pp. 3791-3799, 1996.
6. J. P. Zheng, P. J. Cygan, and T. R. Jow, "Hydrous ruthenium oxide as an electrode material for electrochemical capacitors," *J. Electrochem. Soc.* **142**, pp. 2699-2703, 1995.
7. J. N. Harb, R. M. LaFollette, R. H. Selfridge, and L. L. Howell, "Microbatteries for self-sustained hybrid micropower supplies," *J. Power Sources* **104**, pp. 46-51, 2002.
8. J. B. Bates, N. J. Dudney, B. Neudecker, A. Ueda, and C. D. Evans, "Thin-film lithium and lithium-ion batteries," *Solid State Ionics* **135**, pp. 33-45, 2000.
9. K. E. Swider-Lyons, A. Piqué, C. B. Arnold, and R. C. Wartena, "Direct write microbatteries for next-generation microelectronic devices," in *Symposium on Rapid Prototyping Technologies - Tissue Engineering to Conformal Electronics*, Materials Research Society, (Pittsburgh, PA), *In Press*.
10. D. A. McKeown, P. L. Hagans, L. P. L. Carette, A. E. Russell, K. E. Swider, and D. R. Rolison, "Structure of hydrous ruthenium oxides: Implications for charge storage," *J. Phys. Chem. B* **103**, pp. 4825-4832, 1999.

11. K. E. Swider-Lyons, K. M. Bussmann, D. L. Griscom, C. T. Love, D. R. Rolison, W. Dmowski, and T. Egami, "A new nanocomposite model for hydrous  $\text{RuO}_2$ ," in *Solid State Ionic Devices II-Ceramic Sensors*, E. Wachsman, W. Weppner, E. Traveda, P. Vanysek, N. Yamazoe, and M. Liu, eds., **2000-32**, pp. 148-156, Electrochem. Society, 2000.
12. Y. S. Yoon, W. I. Cho, J. H. Lim, and D. J. Choi, "Solid-state thin-film supercapacitor with ruthenium oxide and solid electrolyte thin films," *J. Power Sources* **101**, pp. 126-129, 2001.
13. A. Pique, D. B. Chrisey, J. M. Fitz-Gerald, R. A. McGill, R. C. Y. Auyeung, H. D. Wu, S. Lakeou, V. Nguyen, R. Chung, and M. Duignan, "Direct writing of electronic and sensor materials using a laser transfer technique," *J. Mater. Res.* **15**, pp. 1872-1875, 2000.
14. D. B. Chrisey, A. Pique, J. Fitz-Gerald, R. C. Y. Auyeung, R. A. McGill, H. D. Wu, and M. Duignan, "New approach to laser direct writing active and passive mesoscopic circuit elements," *Appl. Surf. Sci.* **154-155**, pp. 593-600, 2000.
15. C. B. Arnold, R. C. Wartena, B. Pratap, K. E. Swider-Lyons, and A. Piqué, "Laser direct writing of hydrous ruthenium dioxide micro-pseudocapacitors," in *Symposium on Rapid Prototyping Technologies - Tissue Engineering to Conformal Electronics*, Materials Research Society, (Pittsburgh, PA), *In press*.
16. W. G. Pell and B. E. Conway, "Analysis of power limitations at porous supercapacitor electrodes under cyclic voltammetry modulation and dc charge," *J. Power Sources* **96**, pp. 57-67, 2001.
17. K. E. Swider-Lyons, D. W. Weir, C. T. Love, R. Modi, T. Sutto, A. Pique, and D. B. Chrisey, "Direct-write microbatteries as integrated power sources for microelectronic devices," in *Power Sources for the New Millennium*, M. Jain, M. Ryan, S. Surampudi, R. Marsh, and G. Najarjan, eds., **2000-22**, pp. 272-276, Electrochem. Society, 2000.

# Direct-Write of Sensor Devices by a Laser Forward Transfer Technique

A. Piqué<sup>a\*</sup>, D.W. Weir<sup>a</sup>, P.K. Wu<sup>b</sup>, B. Pratap<sup>a</sup>, C.B. Arnold<sup>a</sup>, B.R. Ringeisen<sup>a</sup>,  
R.A. McGill<sup>a</sup>, R.C.Y. Auyeung<sup>a</sup>, R.A. Kant<sup>a</sup> and D.B. Chrisey<sup>a</sup>

<sup>a</sup>Naval Research Laboratory, Washington, DC 20375

<sup>b</sup>Department of Physics, Southern Oregon University, OR 97520

## ABSTRACT

The use of direct-write techniques in the design and manufacture of sensor devices provides a flexible approach for next generation commercial and defense sensor applications. Using a laser forward transfer technique, we have demonstrated the ability to rapidly prototype temperature, biological and chemical sensor devices. This process, known as matrix assisted pulsed laser evaporation direct-write or MAPLE DW is compatible with a broad class of materials ranging from metals and electronic ceramics to chemoselective polymers and biomaterials. Various types of miniature sensor designs have been fabricated incorporating different materials such as metals, polymers, biomaterials or composites as multilayers or discrete structures on a single substrate. The MAPLE DW process is computer controlled which allows the sensor design to be easily modified and adapted to any specific application. To illustrate the potential of this technique, a functional chemical sensor system is demonstrated by fabricating all the passive and sensor components by MAPLE DW on a polyimide substrate. Additional devices fabricated by MAPLE DW including biosensors and temperature sensors and their performance are shown to illustrate the breadth of MAPLE DW and how this technique may influence current and future sensor applications.

**Keywords:** MAPLE Direct-Write, Laser Transfer, Direct-Write of Sensor Materials, Temperature Sensors, Biological Sensors, Chemical Sensors, Chemiresistor.

## 1. INTRODUCTION

Current trends for developing advanced electronic and sensor systems place great emphasis in achieving performance levels generally associated with integrated circuits. This requires further miniaturization, while enhancing the functionality and reliability of existing components. It also requires new strategies in order to eliminate the long lead times required for the fabrication of prototypes and evaluation of new materials and designs. In particular, for chemical and biological sensor development, the trend is toward the fabrication of micron scale devices and dense array platforms<sup>1</sup>.

An individual chemical or biological sensor element consists of a transducer or substrate coated with one of a range of sorbent coating materials that collect the analyte of interest either in a reversible or irreversible binding process. Physicochemical changes in the sorbent coating, as a result of analyte binding events, are monitored and converted to electrical signals for display or recording. The range of sorbent materials covers a plethora of types and properties from simple polymers to higher-ordered biological structures. In order for these materials to perform as expected, their chemical and structural properties must remain uncompromised during the manufacture of the sensor<sup>1</sup>. In addition to the materials constraints, current commercial and military applications for chemical and biological sensors require systems to be portable (hand-held or smaller in size) so that analytical measurements can be made in the field. The above requirements have pushed traditional manufacturing techniques to their limits. Novel fabrication approaches for integrated micron sized sensor elements and systems are required.

---

\* Correspondence: Email: pique@nrl.navy.mil; Telephone: (202) 767 5653; Fax: (202) 767 5301

The use of direct-write techniques, that do not need photolithographic processing, provide a solution to the above constraints. Direct-write technologies do not compete with photolithography for size and scale, but rather add a complementary tool for specific applications requiring rapid turnaround and/or pattern iteration, conformal patterning, or for modeling difficult circuits<sup>2</sup>. Examples of direct-write technologies for fabricating or modifying metallic interconnects and/or other electronic passive elements include ink jet printing<sup>3</sup>, direct-write of ceramic slurries (Micropen©)<sup>4</sup>, laser trimming<sup>5</sup> and laser chemical vapor deposition (LCVD)<sup>6</sup>. However, none of the above techniques is capable of operating in air and at room temperature while maintaining sub-10  $\mu$ m resolution and without requiring *ex situ* processing. Furthermore, multiple techniques are necessary to deposit and process the broad classes of materials employed in electronic and sensor applications.

Over the past decade, various laser-based direct-write techniques have been developed for depositing different types of materials such as metals for interconnects and mask repair. More recently, a new laser-based direct-write technique, called MAPLE DW, for Matrix-Assisted Pulsed-Laser Evaporation Direct-Write, has been used for the direct-write of conformal electronic devices<sup>7-10</sup>, phosphor materials<sup>11</sup>, microbatteries<sup>12,13</sup> and even viable biomaterials<sup>14,15</sup>. In this paper, the use of the MAPLE DW technique for the fabrication of temperature, biological and chemical sensors is described. We compare the performance of chemiresistor gas sensors made by spray coating and by MAPLE DW. Finally, we demonstrate a complete chemical sensor system fabricated by MAPLE DW

## 2. BACKGROUND

MAPLE DW, is a laser-based processing technique that was originally developed to fabricate and rapidly prototype mesoscopic electronic devices utilizing matrices containing metallic, dielectric or resistive materials<sup>6</sup>. This approach, however, is gentle enough to successfully form patterns and three-dimensional structures of a wide variety of organics, including chemically sensitive polymers, active proteins and antibodies as well as viable cells<sup>14,15</sup>.

MAPLE DW involves the forward transfer of materials from a UV transparent support to a receiving substrate. The transfers are performed by mixing the active, or sensitive material in a UV-absorbent matrix to form an "ink". The ink is then applied to the UV-transparent support to form the "ribbon" as shown in Figure 1. A focused UV laser pulse is directed through the backside of the ribbon so that the laser energy interacts with the matrix at the support interface. The UV microscope objective that focuses the laser at the interface also serves as an optical guide to determine the region of the ribbon to be transferred. Layers of matrix near the support interface evaporate due to localized heating from the laser-material interaction. This vaporization releases the remaining ink by gently and uniformly propelling it away from the support. In this manner, MAPLE DW is capable of producing passive electronic devices (i.e., interconnects, resistors, capacitors) with line widths of the order of 10 microns. By removing the ribbon and allowing the laser pulse to interact with the substrate, this approach is also able to micromachine channels and through vias into polymer, semiconductor, and metal surfaces as well as trim deposited structures to meet design specifications. All micromachining and material transfer can be controlled by computer (CAD/CAM), which enables this tool to rapidly fabricate complex structures without the aid of masks or moulds. This technique, therefore, has the potential to fabricate by a single tool, complete prototype systems on a single substrate including the sensor coating, transducer, support electronics and even the microbatteries required to power the whole system.

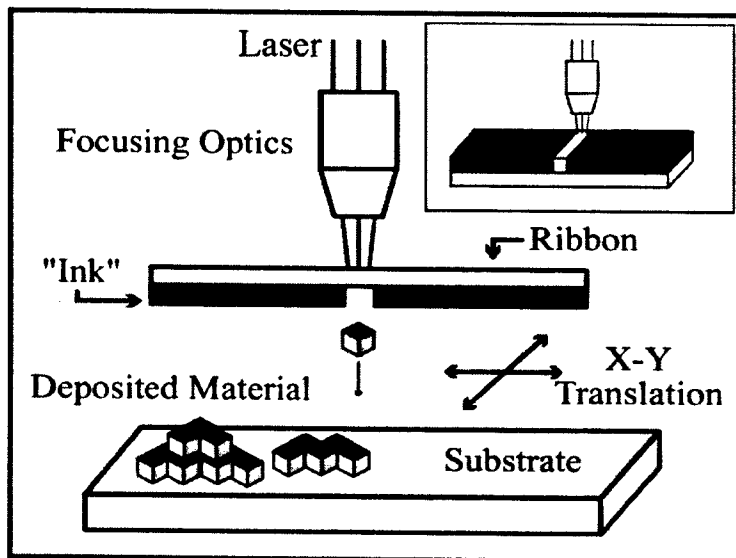


Figure 1. Schematic diagram illustrating the MAPLE DW process. Inset: the same setup can be used for micromachining with the ribbon removed.



### 3. EXPERIMENTAL

#### 3.1 MAPLE DW Ribbon Preparation

Borosilicate glass discs, double side polished, 5.0 cm diameter x 3mm thick were used as ribbon supports. For the fabrication of the temperature sensors, a screen printable silver paste (Parmod RRA-100, from Paralec, Inc.) was applied to one side of the discs using a #4 wire-coater (Gardner, Inc.) to form an ink layer about 15  $\mu\text{m}$  thick. For the fabrication of the biosensor, a paste containing polyphenol oxidase, graphite and mineral oil was applied using the same wire-coater. In the case of the chemical sensors, the ribbons were prepared by spray coating a solution containing 0.1 gm of polyepichlorohydrin (PECH, average  $M_w = 700000$ , Aldrich) and 0.01 gm of acetylene carbon black (Alfa) mixed in 50 ml of chloroform. The coated side of the ribbons was kept at a distance of 100-200  $\mu\text{m}$  from the substrate with a spacer. Both the substrate and the ribbon were held in place using a vacuum chuck over the X-Y substrate translation stage. The third harmonic emission of a Nd:YAG laser,  $\lambda = 355 \text{ nm}$  (Spectra Physics), was directed through a circular aperture and a 10x objective lens, resulting in a 85  $\mu\text{m}$  diameter spot at the ribbon. The laser fluence varied between 0.1 – 1.0  $\text{J}/\text{cm}^2$  depending on the material being transferred, and was estimated by averaging the total energy of the incident beam over the irradiated area.

#### 3.2 Temperature sensor fabrication and testing

Silver conductive lines were transferred by MAPLE DW onto polyimide substrates and used as temperature sensors. The length and layout of the lines was easily modified via computer control in order to achieve  $\sim 10\text{-}\mu\text{m}$  thick and  $\sim 100\text{-}\mu\text{m}$  wide patterns. The silver ink was dried at 100  $^\circ\text{C}$  on a hot plate to remove excess solvent and then cured at 280  $^\circ\text{C}$  in an oven for 10 min to decompose the organic silver precursors in order to form conductive patterns. These patterns in the form of serpentine lines were evaluated as temperature sensors by comparing their response to that of a type K thermocouple. One of the MAPLE DW serpentine patterns and a thermocouple were mounted next to each other and exposed to heat pulses generated by a heat gun over a temperature range of 24 to 60  $^\circ\text{C}$ . The resistance of the serpentine was measured as a function of time using a computer controlled 34401A digital multimeter (Agilent).

#### 3.3 Biosensor fabrication and testing

A 2 mm x 2 mm pad containing the biosensor mixture of polyphenol oxidase/mineral oil/graphite was deposited by MAPLE DW over Pt electrodes on a polyimide substrate. The resulting biosensor was immersed in a catechol/water solution in order to measure the current generated across the Pt electrodes by the electrochemical reaction between the polyphenol oxidase and the catechol. Details of the measurement are provided elsewhere<sup>14</sup>. Cyclic voltammetry measurements were performed using a PAR 263 potentiostat (EG&G) driven with M270 software.

#### 3.4 Chemical sensor fabrication and testing

For the chemical sensors, 1 mm x 4 mm pads of PECH/carbon were deposited by MAPLE DW over silver interdigitated electrodes. To verify the operation of the MAPLE DW sensors, similar pads of PECH/carbon were spray coated onto a second set of silver electrodes. The silver electrodes were deposited by MAPLE DW onto polyimide substrates in the same way as the serpentine lines. The response of the PECH/carbon sensors was evaluated by exposing them to controlled exposures of toluene and dimethylmethylphosphonate (DMMP) vapor streams. The carrier air temperature and humidity were controlled with a Miller Nelson HCS-301 air-humidity generator. An automated Harvard 22 liquid syringe pump system was utilized to generate analyte vapor by injecting the liquid analyte into a heated evaporation plate system. The resulting vapor was mixed with humidified carrier air and passed into a test chamber housing the chemical sensors. The test chamber consisted of a hermetic enclosure with opposite inlet and outlet gas ports, to allow vapor flow over the sensors. The chemical integrity of the PECH polymer transfers was verified by FTIR using a Magna-IR 750 spectrophotometer (Nicolet). The spectra from 4 mm x 4 mm pads of pure PECH (no carbon) deposited by MAPLE DW onto NaCl discs was compared to that of a PECH films spray coated from a solution of PECH in chloroform.

## 4. RESULTS AND DISCUSSION

### 4.1 Temperature sensors

Physical sensors are essential for many aspects of manufacturing, medical and condition-based maintenance applications. These and other uses are pushing the development of physical sensors towards increased miniaturization and their integration within the physical structure of a part or component. However, most manufacturing processes are incapable of fabricating embedded sensors and instead the sensors are attached to the component being monitored. Due to the fragile nature of most sensor transducers, these tend to fail prematurely. Direct-write processes offer the ability to fabricate robust physical sensors embedded within the physical part in order to gather information regarding temperature, pressure, stress, torque, acceleration, wear, humidity, pH, etc. Such types of embedded physical sensors would find numerous uses for applications ranging from determining when a helicopter rotor shaft needs replacement to *in situ* monitoring with a surgical catheter.

Using MAPLE DW, we have demonstrated a simple temperature sensor on a polyimide substrate. A silver serpentine line about 10 cm long, occupying a 5 mm x 5 mm area and with a resistance of about 100 ohms was made by MAPLE DW as shown in Figure 2(a). The variation in resistance as a function of temperature was calibrated against a type K thermocouple resulting on a  $R/T$  of 0.21 ohms/K for the sensor element. The response of the MAPLE DW temperature sensor to a heat pulse from a heat gun mirrored that of an adjacent thermocouple and it is shown in Figure 2(b).

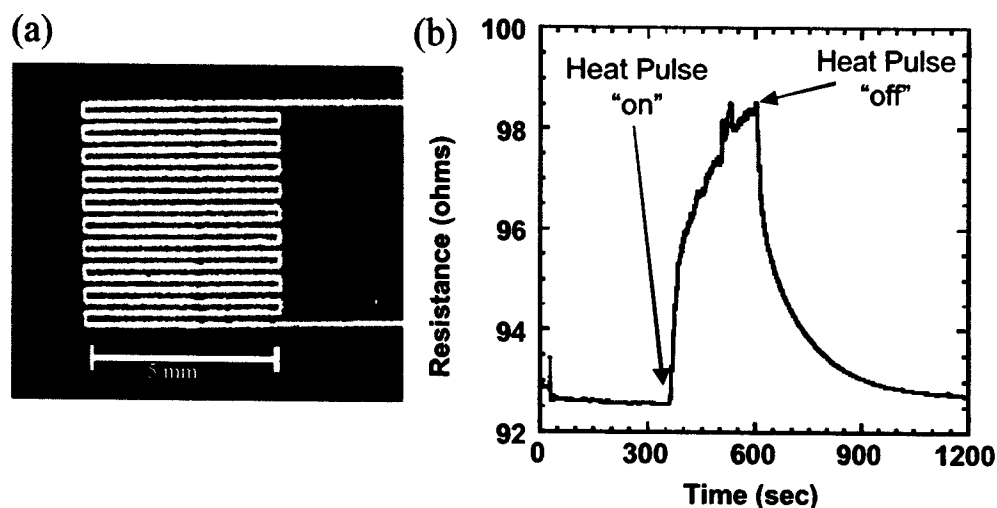


Figure 2. (a) Photograph of a temperature sensor made by MAPLE DW of a silver serpentine line on a polyimide substrate. (b) Response of this sensor to a heat pulse.

### 4.2 Dopamine biosensor

Wu et al.<sup>14</sup> demonstrated the fabrication of a simple amperometric biosensor for the detection of the neurotransmitter dopamine (a catechol derivative) using MAPLE DW. The sensor operates due to the oxidation of dopamine to dopamine quinone in the presence of polyphenol oxidase. The reaction is electrochemically reversible in the presence of a suitable voltage across the electrodes, resulting in a current proportional to the dopamine concentration. The MAPLE DW transferred polyphenol oxidase/mineral oil/graphite pad is robust. The sensor does not show any signs of delamination or dissolution after several hours of operation immersed in an aqueous solution, indicative of good adhesion and immobilization. Figure 3 shows a photograph of the biosensor element.

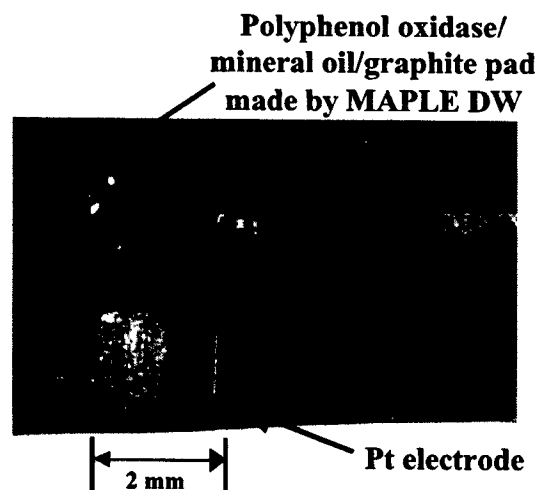


Figure 3. Amperometric biosensor made by MAPLE DW

### 4.3 Chemiresistor gas sensors

By using dispersions of conductive materials such as carbon and non-conductive chemoselective polymers, gas sensors based on conductimetric techniques<sup>16,17</sup> can be fabricated. In the correct ratio, the polymer/carbon composite becomes conductive and its resistance will change when exposed to different vapors, as shown schematically in Figure 4. These types of chemical sensors are known as chemiresistors and are extremely simple to operate and ideally suited for miniaturization and manufacture in array form. For this work, PECH was selected since it is a polymer with a range of solubilities to numerous analytes, making it well suited for the fabrication of chemical gas sensors with broad applicability to a variety of different types of analytes.

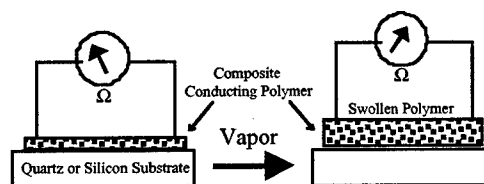


Figure 4. Schematic showing the basic operation of a chemiresistor gas sensor.

In order to determine if the chemical structure of the PECH polymer was affected by the MAPLE DW process, we compared the FTIR spectra of PECH films deposited by MAPLE DW and by spray coating onto NaCl substrates. The FTIR spectra of the spray coated PECH and MAPLE DW PECH are essentially identical with very similar stretching frequencies and absorbance ratios as shown in Figure 5.

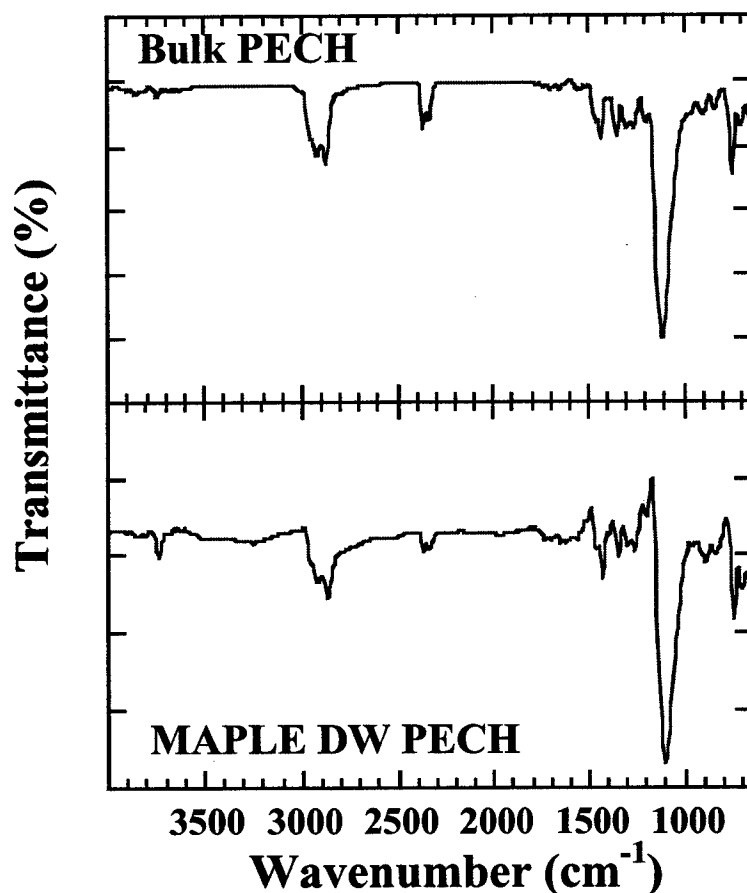


Figure 5. FTIR spectra from PECH films made by spray coating (bulk PECH) and by MAPLE DW on NaCl substrates.

Figure 6 shows a micrograph of a typical PECH/carbon chemoresistive pad fabricated by MAPLE DW across a set of silver interdigitated electrodes also made by MAPLE DW on a polyimide substrate. In order to evaluate the performance of the chemiresistors made by MAPLE DW, similar PECH/carbon pads were fabricated by spray coating and placed side by side and exposed to calibrated concentrations of analyte vapors. Toluene and DMMP were used as analytes. Toluene and DMMP cover a range of solubility properties from a low polarity hydrocarbon to a polar and hydrogen-bond basic phosphonate ester. Toluene is a chemical present in diesel vapor, while DMMP is a simulant and precursor for chemical nerve agents. The results of the vapors tests indicated that the response of the MAPLE DW and that of the spray coated chemiresistors were similar and showed sensitivities of the order of parts per million (ppm). The response of both chemoresistors when exposed to various concentrations of toluene and DMMP vapors are shown in Figure 7.

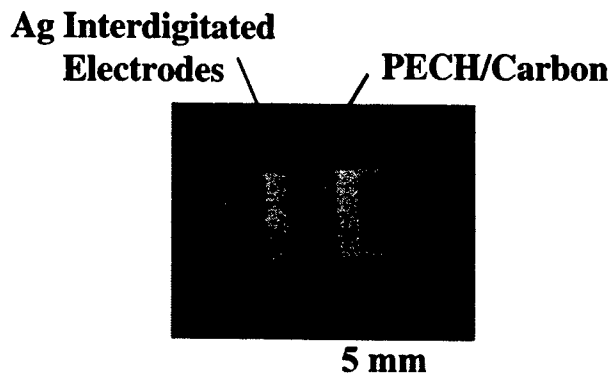


Figure 6. Optical micrograph of a chemiresistor gas sensor element made by MAPLE DW.

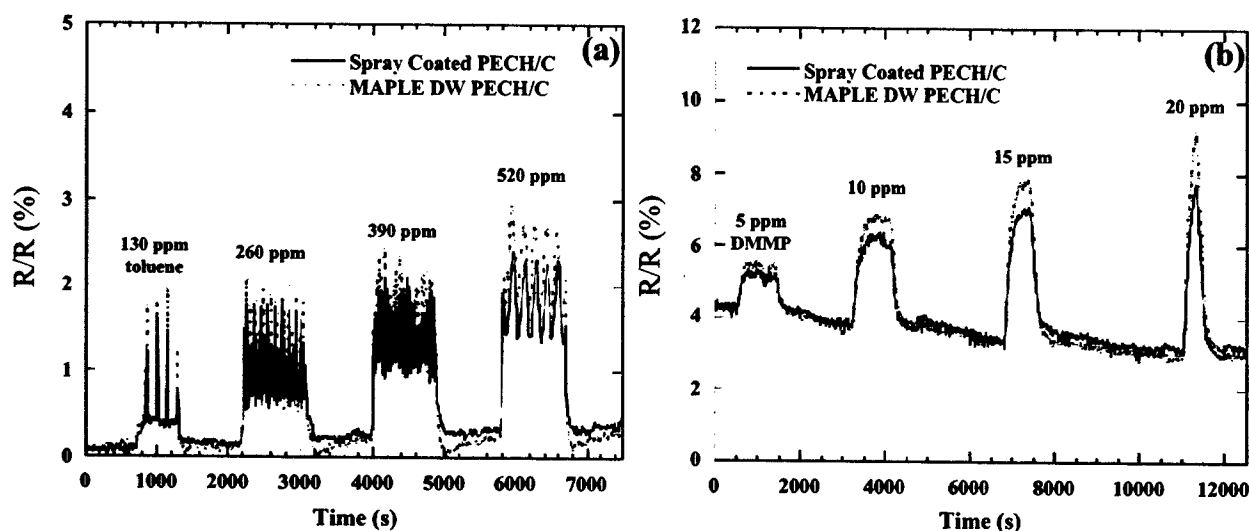


Figure 7. Response of a spray coated and a MAPLE DW PECH/carbon chemiresistor sensors to various concentrations of (a) toluene and (b) DMMP vapors. The spikes on the toluene response signals are due to the syringe pump system used to generate the calibrated vapor exposures.

The real potential of MAPLE DW is made clear when a complete sensor system consisting of a single sensor element, interconnects and passive electronic components is fabricated using this laser direct-write technique. An actual working example is provided in Figure 8 which shows a photograph of a complete self contained chemical sensor system manufactured on a 5cm x 5 cm polyimide substrate. The majority of the components shown on this image, including the chemiresistor, the Ag interconnects and the polymer thick film resistors, but not the LED's and the 4-quad comparator IC (which were soldered to the circuit afterwards), were fabricated by MAPLE DW. Future plans include the fabrication of multiple sensor elements in the form of arrays and the addition of microbatteries all made by MAPLE DW.

## 5. SUMMARY

MAPLE DW is an ideal process for the direct-write of sensors since it operates in air and at low temperatures. It is compatible with many types of substrates and conditions which are ideal for the processing of numerous physical, chemical and biological sensor materials. MAPLE DW has been used for rapid prototyping of custom-engineered physical, biological and chemical sensors in various types of geometries. The versatility and CAD/CAM features of the MAPLE

DW technique allow sensor elements and complete sensor systems to be easily reconfigured and integrated with other components. Furthermore, in the case of chemiresistive gas chemical sensors, this work shows that the performance of the MAPLE DW sensor elements is comparable to that of similar sensors made by traditional manufacturing techniques.

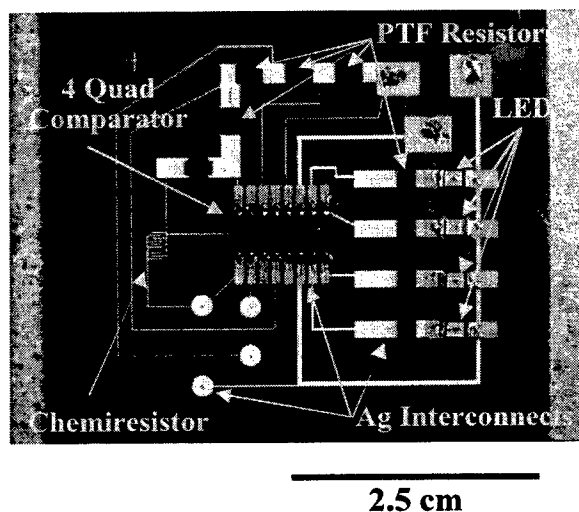


Figure 8. Photograph of a working chemiresistor sensor system made by MAPLE DW. The photograph shows all the elements of the sensor except for the batteries which are mounted on the back.

## 6. ACKNOWLEDGEMENTS

The authors would like to thank S. A. Mathews and M. T. Duignan for their help in the fabrication of the self contained chemical sensor. This work was supported by the Office of Naval Research and DARPA, through the DARPA-MICE program.

## 7. REFERENCES

1. R.A. McGill, B. Ringeisen and P.K. Wu, "The Role of Direct Writing for Chemical and Biological Materials: Commercial and Military Applications", in *Direct-Write Technologies for Rapid Prototyping Applications*, edited by A. Piqué and D.B. Chrisey, p. 93, Academic, San Diego, 2001.
2. A. Piqué and D.B. Chrisey, editors, *Direct-Write Technologies for Rapid Prototyping Applications*, Academic, San Diego, 2001.
3. D.J. Hayes and D.B. Wallace, *SPIE Proceedings*, **2920**, 296, (1996).
4. D. Dimos and P. Yang, *Proc. of 48th Electronic Components and Technology Conf.*, Seattle, Washington, p. 225 (IEEE, New York, 1998).
5. C.P. Christensen, M.T. Duignan and L.R. Rodriguez, *SPIE Proceedings*, **1835**, 128, (1993).
6. D.J. Ehrlich and J.Y. Tsao, editors, *Laser Microfabrication: Thin Film Processes and Lithography*, Academic, Boston, 1989.
7. A. Piqué, D.B. Chrisey, R.C.Y. Auyeung, S. Lakeou, R. Chung, R.A. McGill, P.K. Wu, M. Duignan, J. Fitz-Gerald, and H. D. Wu, *SPIE Proceedings*, **3618**, 330, (1999).
8. A. Piqué, D.B. Chrisey, R.C.Y. Auyeung, J. Fitz-Gerald, H.D. Wu, R.A. McGill, S. Lakeou, P.K. Wu, V. Nguyen and M. Duignan, *Appl. Phys. A*, **69**, S279 (1999).
9. D.B. Chrisey, A. Piqué, J.M. Fitz-Gerald, R.C.Y. Auyeung, R.A. McGill, H.D. Wu and M. Duignan, *Appl. Surf. Sci.*, **154**, 593 (2000).
10. A. Piqué, D.B. Chrisey, J.M. Fitz-Gerald, R.A. McGill, R.C.Y. Auyeung, H.D. Wu, S. Lakeou, V. Nguyen, R. Chung and M. Duignan, *J. Mater. Res.*, **15**, 1872 (2000).

11. J.M. Fitz-Gerald, A. Piqué, D.B. Chrisey, P.D. Rack, M. Zeleznik, R.C.Y. Auyeung and S. Lakeou, *Appl. Phys. Lett.*, **76**, 1386 (2000).
12. K.E. Swider-Lyons, D.W. Weir, C.T. Love, R. Modi, T. Sutto, A. Piqué and D.B. Chrisey, *Power Sources for the Next Millenium*, edited by M. Jain, M.A. Ryan, S. Surampdi, R.A. Marsh and G. Nagrajan, *Electrochem. Soc. Proc.*, **2000-22**, 272 (2000).
13. A. Piqué, K.E. Swider-Lyons, D.W. Weir, C.T. Love, R. Modi, *SPIE Proceedings*, **4274**, 317, (2001).
14. P.K. Wu, B. Ringeisen, J. Callahan, M. Brooks, D.M. Bubb, H.D. Wu, A. Piqué, B. Spargo, R. A. McGill and D.B. Chrisey, *Thin Solid Films*, **398-399**, 607 (2001).
15. B. Ringeisen, D.B. Chrisey, A. Piqué, H.D. Young, R. Modi, M. Bucaro, J. Jones-Meehan and B.J. Spargo, *Biomaterials*, **23**, 161 (2002).
16. J.W. Gardner, M. Craven, C. Dow, E.L. Hines, *Meas. Sci. Technol.*, **9**, 120 (1998).
17. J.V. Hatfield, P. Neaves, P.J. Hicks, K. Persaud, P. Travers, *Sens. Actuators B: Chem.*, **18**, 221 (1994).

# Integrated tool for fabrication of electronic components by laser direct write

Scott A. Mathews\*, Chengping Zhang, Todd Kegresse, David Liu  
Potomac Photonics, Inc.

## ABSTRACT

A prototype workstation has been developed that allows the fabrication of passive electronic components at low temperatures using a laser direct-write process. The work station combines a variety of laser processing techniques onto a single, integrated platform. These techniques include material deposition, laser micromachining, laser sintering, and laser trimming. One particular process, referred to as "mill and fill", combines the laser micromachining ability of the tool with "off-the-shelf" conductor pastes to allow the fabrication of high density metallization at very low temperatures (200°C). The present work describes the details of the "mill and fill" process and shows examples of prototype devices fabricated using this technique.

## 1. INTRODUCTION

This tool was designed primarily for rapid prototyping and small scale production of electronic circuits. To this end, the tool is based entirely on direct write processes that do not require masks, phototools, resists, developers, wet chemical etchants, or electroplating. As a result, this machine not only reduces circuit fabrication time, but also allows circuit design changes to be made through the software and applied immediately to a device under fabrication. A high resolution, "through-the-lens" imaging system guarantees accurate registration of features with respect to pre-existing patterns. In this way, a circuit design can be modified and fabricated in a matter of hours, rather than days.

This tool combines several different laser based functions onto a single, integrated platform. This integrated platform allows both additive and subtractive patterning techniques to be employed with only minor adjustment of the machine. Additionally, a long pulse or CW infrared laser can be delivered to the sample for thermal processing.

The subtractive processes employed are standard laser micromachining techniques. These techniques can be used to trim previously patterned components, pattern continuous layers, drill vias, mill grooves and recesses, and to excise components or complete circuits.<sup>1</sup>

Two additive processes have been widely demonstrated with this machine. The first, "Matrix Assisted Pulsed Laser Evaporation- Direct Write" (MAPLE-DW)<sup>2</sup>, involves dispersing a material on a transparent backing sheet called a "ribbon", holding the ribbon in close proximity to a receiving substrate, and irradiating the ribbon with a short pulse UV laser. The laser vaporizes a small volume of material at the interface, propelling the remaining material toward the receiving substrate. Patterning is accomplished by scanning the laser beam, translating the substrate, or a combination of the two. The details of this process can be found elsewhere.<sup>3</sup> The MAPLE-DW process has been used to pattern a wide variety of materials including silver, copper, high-k dielectric, low loss dielectric, "cermet" resistor, polymer thick film (PTF) pastes, phosphors, and even live cells.<sup>4,5</sup>

A second additive patterning process is referred to as "mill and fill", and is the primary subject of this paper. This process involves the micromachining of an appropriate pattern of grooves and recesses into the surface of the substrate. These features are then filled with a specific material in the form of a paste or "ink". The excess material is then removed using a squeegee. The substrate, with filled features, is then thermally processed, typically by oven baking. This process is illustrated schematically in figure 1.

---

\* smathews@potomac-laser.com; phone (301) 459-3031; fax (301) 459-3034; www.potomac-laser.com;  
Potomac Photonics, Inc, 4445 Nicole Drive, Lanham, MD, USA 20706

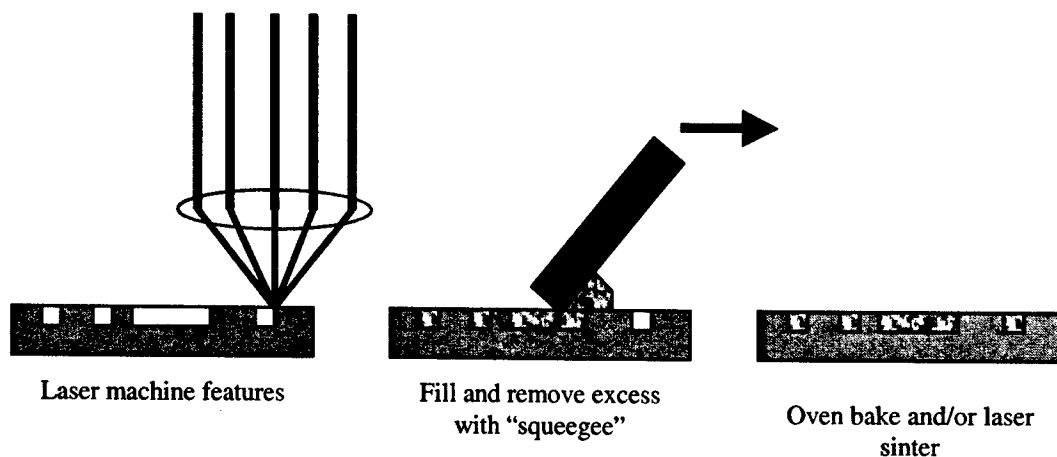


Figure 1. Schematic diagram of the "mill and fill" process.

## 2. RESULTS

The initial work on this process was done using silver inks or pastes deposited on polyimide foils. Polyimide was chosen as the substrate material for several reasons. Polyimide has excellent electrical properties (resistivity, dielectric strength, dielectric constant, etc.) and is widely used in the microelectronics industry, especially in the areas of "flex-circuits" and medical devices. Polyimide ablates easily with a short pulse UV laser<sup>6</sup>. The tool can create micron scale features with relatively smooth and clean surfaces. Micron or even sub-micron scale depth control can be achieved over the entire substrate area. Finally, polyimide substrates can withstand temperatures as high as 400°C, a processing temperature that is compatible with several off-the-shelf paste materials.

A wide variety of samples have been fabricated on polyimide using this process<sup>1,3</sup>. Most of these samples were filled using Parelec Parmod<sup>®</sup> silver, dried at 100°C for 15 minutes, and baked at 350°C for 30 minutes. Silver conductors fabricated in this manner have resistivities as low as 5  $\mu\Omega\cdot\text{cm}$ , or 3.1 times that of bulk silver. Conducting lines baked at 350°C adhered well to the polyimide substrate, passing the "Scotch tape" test and the "#2 pencil test". Because the finished layers are nearly planar, they are easily laminated together. This permits the fabrication of multi-layer structures with both blind and through vias. The view "through-the-lens" capability of the tool simplifies the alignment and registration of subsequent conducting layers and vias. Figure 2 shows an example of such a multi-layer structure. This sample is a "daisy-chain", with conductors on three separate layers, which have been laminated and interconnected with blind vias.

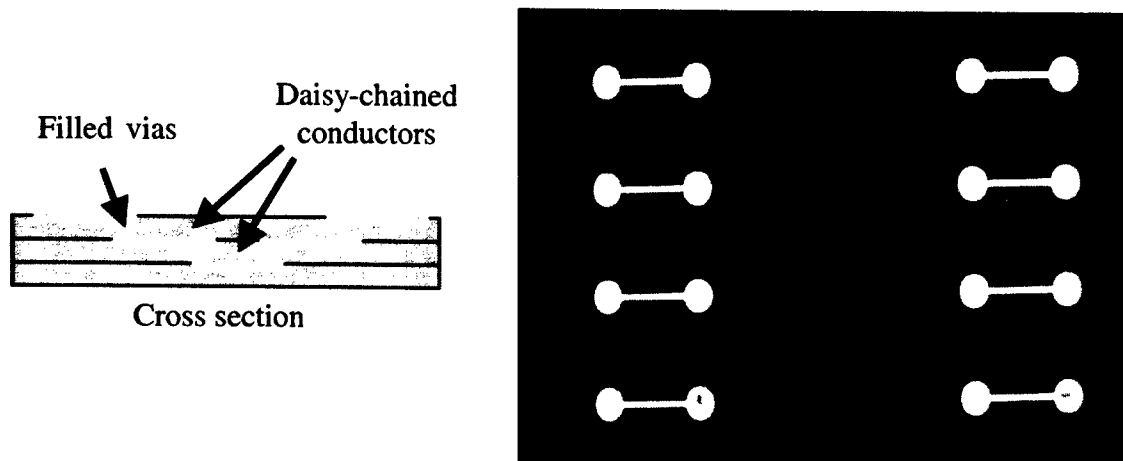


Figure 2. A three layer "Daisy-chain" structure of silver conductor on laminated polyimide.



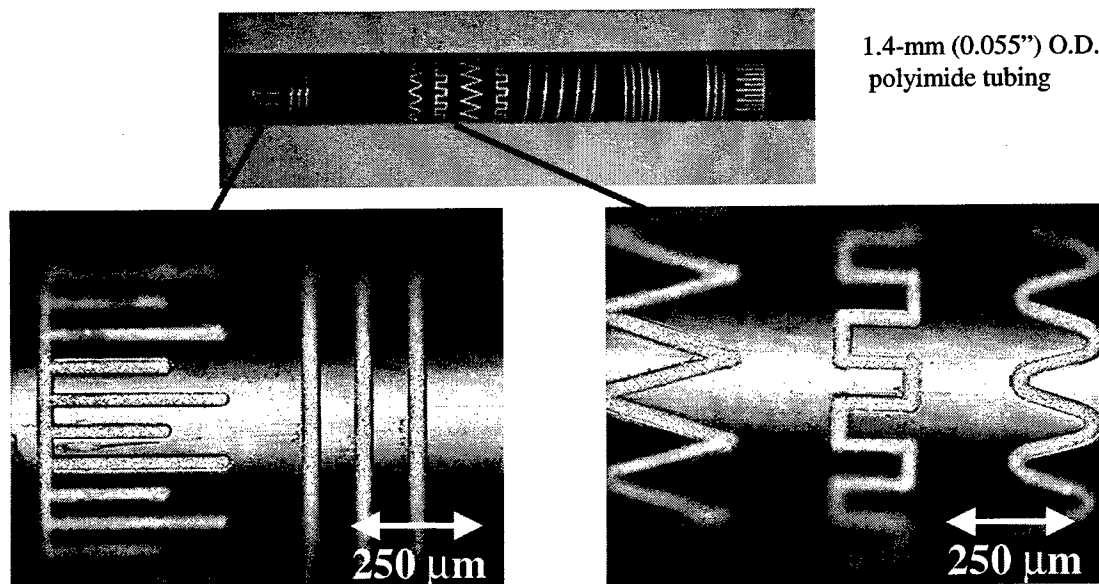


Figure 3. Conformal metallization on a polyimide tube.

One of the advantages of the mill and fill process is its ability to create conformal circuitry. Conformal circuitry can be produced by patterning a planar, flexible substrate which is subsequently bent or rolled into its final shape. However, this process is also capable of creating conformal metallization directly on non-planar surfaces, provided the surfaces are regular and smooth. This conformal ability is demonstrated by the patterned metallization of a 1.4 mm diameter polyimide tube, shown in figure 3. Although more complex three-dimensional surfaces can be patterned using this technique, the squeegee process generally requires creative solutions in order to remove the excess ink from the surface.

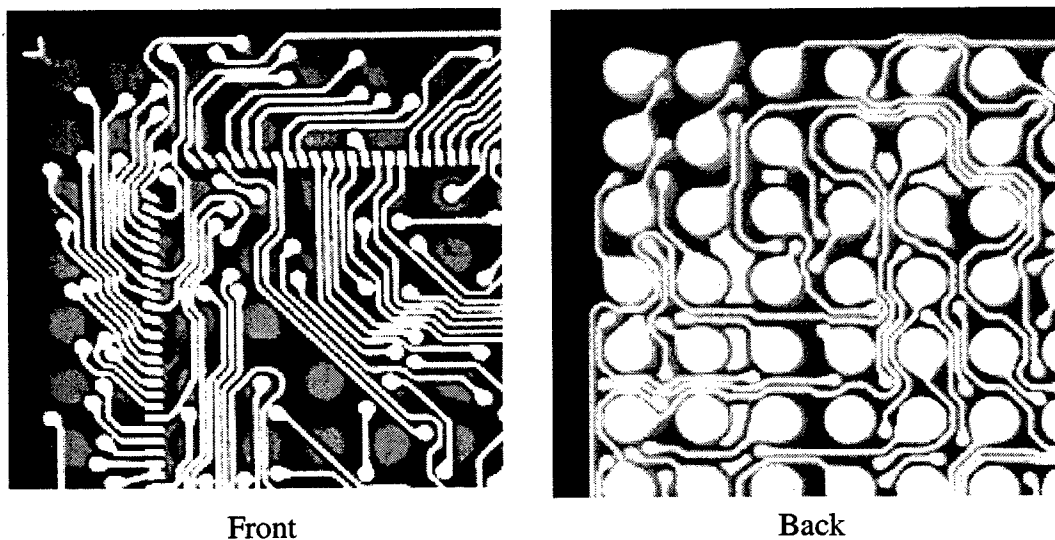


Figure 4. A contact redistribution layer made by "mill and fill" on a polyimide foil.

In order to demonstrate the fabrication of complex conductor patterns at low temperature, we have fabricated contact redistribution layers on polyimide and on a low temperature polymer laminate. Figure 4

shows the front and back sides of one sample on a polyimide foil. The features on the front side of the sample, including vias, were machined first. The conducting traces and vias were then filled with Parelec Parmod® silver, dried at 100°C for 15 minutes, and baked at 200°C for 30 minutes. The sample was then re-mounted on the machine, back side up, and registered using the vision system. The features in the back side were then machined and filled with the same silver composition and subjected to the same baking cycle. The resistivity of the resulting silver lines was approximately  $6.5 \mu\Omega\cdot\text{cm}$ , or 4.1 times that of bulk silver.

The same pattern was then fabricated on a low temperature, laminated, polymer substrate, shown in figure 5. The polymer substrate was such that the maximum processing temperature was limited to 220°C. Normally, the metallization of this type of low temperature substrate would require the use of photo-resists, projection or contact masks, electro-plating, and wet chemical etch. Because this device was still in the prototyping phase, the mill and fill process was considered as an alternative technique in order to minimize "turn around" time and simplify design modifications.

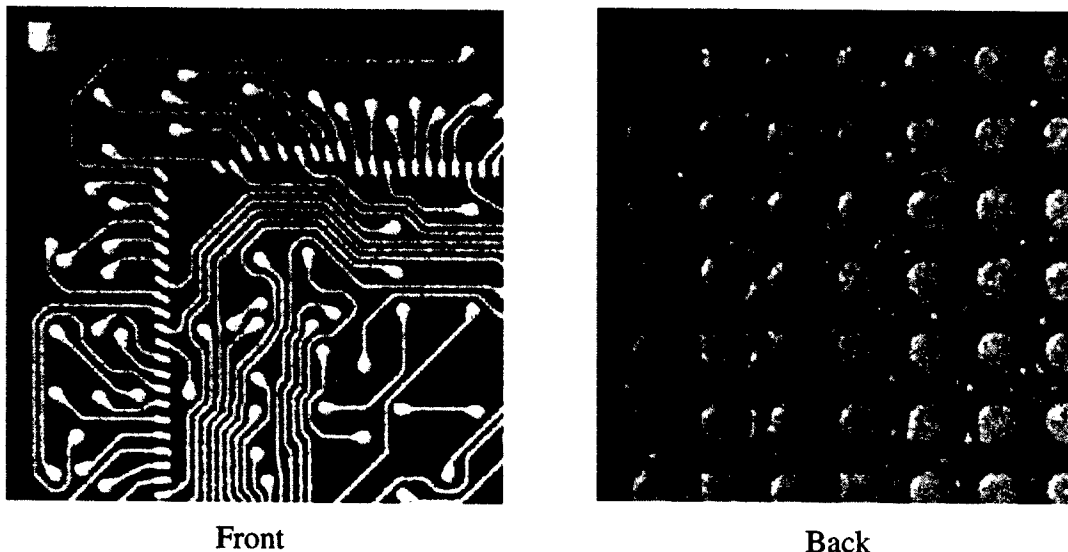


Figure 5. A contact redistribution layer made by "mill and fill" on a polymer laminate.

The substrate consisted of a 2 mil copper layer, with pre-drilled 12 mil vias, sandwiched between two 5 mil layers of polymer. The conductors were 15 to 20  $\mu\text{m}$  deep and 2 mil wide with 2 mil spaces to the closest adjacent line. The through vias were 7 mils in diameter. The via pattern was registered with respect to the pre-drilled 12 mil vias such that the conductors remain electrically isolated from the copper layer. The traces on the front side and the through vias were machined first. The front side pattern and through vias were then filled and dried. The sample was then re-mounted and registered in order to machine the backside pattern. The filling and drying steps were then repeated to complete the backside. The sample baked only once at 200°C in order to minimize any heat effects on the polymer substrate. The resulting silver traces had resistances of several tenths of an ohm and maintained good adhesion to the polymer substrate even when the substrate was flexed to the point that the polymer layers fractured.

### 3. CONCLUSION

The "mill and fill" technique allows the patterning of high density interconnects at very low temperatures and is therefore ideal for the rapid prototyping of circuits on polymer substrates. When combined with the other functions of our tool, such as MAPLE-DW deposition, laser sintering, and laser trimming, it yields a system capable of patterning a wide variety of materials with micron scale resolution, on a wide variety of substrates.

## ACKNOWLEDGMENTS

This work has been supported by the Defense Advanced Research Projects Agency, Defense Sciences Office, under the Mesoscale Conformance Electronics initiative, headed by Dr. Valerie Browning.

## REFERENCES

1. Scott Mathews, Paolina Atanassova, Hugh Denham, Rohit Modi, Ray Auyeung, and Michael Duignan, "An Integrated Tool for Rapid Prototyping of Electronic Circuits Using a Laser Direct Write Technique", *2001 Fall MRS Meeting Proceedings*, Symposium Q, Materials Research Society, Warrendale PA, 2001
2. A. Piquè, D.B. Chrisey, R.C.Y. Auyeung, S. Lakeou, R. Chung, R.A. McGill, P.K. Wu, M.T. Duignan, J.M. Fitz-Gerald, and H.D. Wu, "Laser Direct Writing of Circuit Elements and Sensors", *SPIE Proceedings*, Vol. 3618, p.330, SPIE, Bellingham WA, 1999
3. Scott A. Mathews, Michael T. Duignan, David N. Well, Paolina Atanassova, and Toivo Kudas, "An Integrated Tool for Fabrication of Electronic Components by Laser Direct-Write", *HD International Proceedings 2001*, 183-188, IMAPS, Washington DC, 2001
4. J.M. Fitz-Gerald, A. Piquè, D.B. Chrisey, P.D. Rack, M. Zeleznik, R.C.Y. Auyeung, and S. Lakeou, "Laser direct writing of phosphor screens for high-definition displays", *Applied Physics Letters*, vol. 76 No. 11, 1386-1388, 2000
5. B.R. Ringeisen, D.B. Chrisey, A. Piquè, H.D. Young, R. Modi, M. Bucaro, J. Jones-Meehan, B.J. Spargo, "Generation of mesoscopic patterns of viable *Escherichia coli* by ambient laser transfer", *Biomaterials*, 23, 161-166, 2002
6. Gregory P. Behrmann and Michael T. Duignan, "Excimer laser micromachining for rapid fabrication of diffractive optical elements", *Applied Optics*, Vol. 36 No. 20, 4666-4674, 1997

# Laser-Based Sample Preparation for Electronic Package Failure Analysis

B.M. Frazier, S.A. Mathews, M.T. Duignan  
Potomac Photonics, Inc., Lanham, MD, USA  
L.D. Skoglund, Z. Wang, R.C. Dias  
Intel Corporation, Chandler, AZ, USA

## Abstract

Failure analysis has come to play a key role in ensuring quality and reliability in semiconductor devices, associated packaging and printed wiring boards. Tools are increasingly available to those investigating high-density integrated circuits at the die level, particularly for edit and repair operations. Until recently however, this capability has been limited by the inherent low-resolution mechanical/manual processes used for destructive analysis on electronics packaging. A laser-based tool has been developed to selectively and locally enable access to traces and layers within packages and provide a way to perform edits to an area of interest.

## Introduction

Failure Analysis (FA) serves a number of purposes, including the reduction of in-service failures and the collection of data to form design rules for future products. It is widely noted in the FA industry that current challenges are exceeding the capabilities of available tools [1]. Here we explore the application of laser micromachining to FA sample preparation and destructive evaluation.

## Laser Micromachining System

Laser micromachining offers increased accuracy over mechanical or hand processing, it is typically most useful and cost-effective for features in the 2-200 $\mu$ m range. Further, with innovative optical configurations, the laser beam profile can be altered in-situ to allow low-fluence, fine delayering with micron-level resolution, or high-fluence coarse cutting for package cross-sectioning and other milling operations.

DEPACK is a commercially available Laser Micromachining system designed specifically for failure analysis operations. The system can micro machine, or delayer organic packaging with depth and spatial resolutions of 1-2 $\mu$ m and

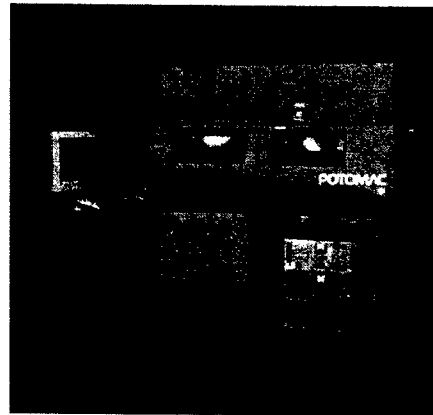


Figure 1 Potomac DEPACK Micromachining System

with its coaxial optics, offers in-situ machine vision feedback of the process. The system accepts CAD inputs, so delayering can be confined to the region immediately around a fault, as opposed to Reactive Ion Etching (RIE) where, unless complex masks are used, the delayering becomes global. With in-situ adjustability, delayering can be either selective or non-selective, allowing preservation of metal traces within a package or penetration through metal to access deeper buried features.

The system is comprised of two lasers, a short pulse (20-30nsec) UV laser and a continuous wave (CW) infrared (IR) laser, beam delivery optics and scanning head, computer controlled stages, and application-specific software [2]. The UV laser enables localized micromachining of organic and ceramic packaging materials, while the IR laser enables precise soldering of fine wires to metal traces within a package for testing and fault isolation. Further, the machine has the capability of directly depositing passive component materials by laser forward transfer [3], for localized editing of circuits.

## Experimental Approach

Several defective flip-chip organic land grid array (OLGA) packages [4], were de-processed using laser micro machining. The goal was to ascertain whether micro machining could enhance the accuracy and efficiency of destructive processing.

## Delayering

Reactive ion etching (RIE) is commonly used for organic package delayering. However, RIE is limited in two ways. Unless masks are employed RIE is a global process, forcing the operator to remove a complete package layer. Also, RIE systems, as typically found in F/A labs are not capable of penetrating planar metal layers without the addition of hazardous gases such as

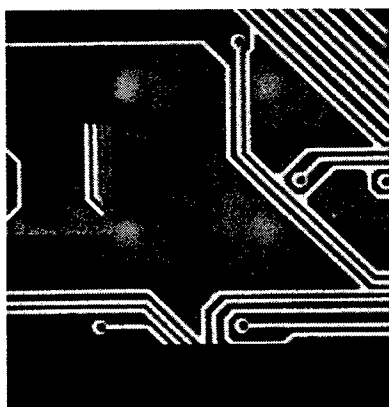


Figure 2 OLGA package with solder mask removed by laser delayering. Trace widths are 25 $\mu$ m.

chlorine, making investigation under such layers very difficult.

Figure 2 shows how laser micro machining techniques developed at Potomac Photonics [2] make possible localized delayering, reducing the

destructive impact of the process. Figures 3 and 4 show how, with minor in-situ adjustments in laser beam profile [5], the machining process will either preserve or remove planar metal layers for localized access to all layers within the multi-layer organic land grid array (OLGA) packages used in this study. For these packages, removal rates on the order of 1-2 $\mu$ m/shot were obtained with a 30 $\mu$ m<sup>2</sup> spot. In delayering mode, laser pulses can be synchronized to stage motion.

Power shorting failure mechanism can occur in flip-chip (and other) devices and packaging [6]. This delayering and editing method can be used to access and repair such shorts. In figure 5, first and second level metallizations were exposed for accessing a plane-to-plane short in the area shown between the two layers. Because the delayering in this case was localized and copper metal traces were preserved, electrical testing could continue on this device after the short was repaired.

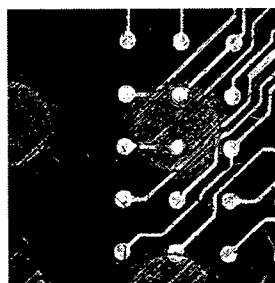


Figure 3 Backside delayering with Cu traces exposed



Figure 4 Backside delayering in similar region with Cu traces milled away to expose the CU plane below.

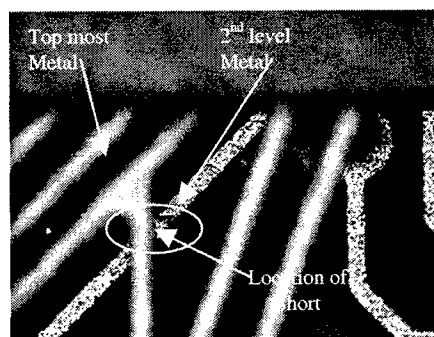


Figure 5 Top metal layer layer accessed with 2<sup>nd</sup> metal layer left intact. Trace widths are 25 $\mu$ m.

## Cross Sectioning

Cross-section cuts allow significantly better access to buried faults, such as delamination, interconnect voids and solder bump defects. Clearly, it is desirable to study these faults in a non-destructive manner. However, in many cases it is necessary to surgically examine the defect of fault to fully understand the root cause of a failure, getting as close as possible to a defect without destroying it [6,7].

Collateral damage associated with the laser cut was also low relative to traditional X-sectioning methods such as diamond saw cuts, mechanical milling or grinding. Cut kerf widths for these 1mm fiber reinforced packages were approximately 50 $\mu$ m. Cuts were within 5 $\mu$ m (in X and Y axes) of the defect region without additional processing. Removal rates in cross-section mode were as high as 100 $\mu$ m/pass. Total processing time was <10min. Once cross-sectioned, the part was turned on edge and using delayer mode, micro machined at 1-2 $\mu$ m per pass to expose the defect region.

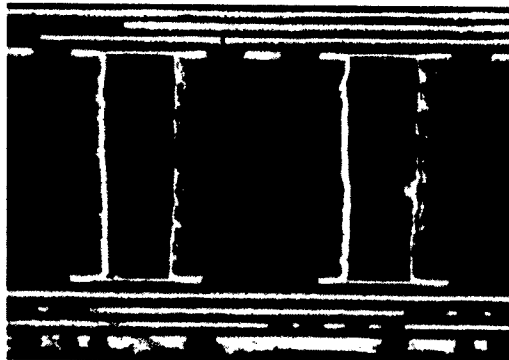


Figure 6 Package cross section cut using typical diamond X-sectioning blade

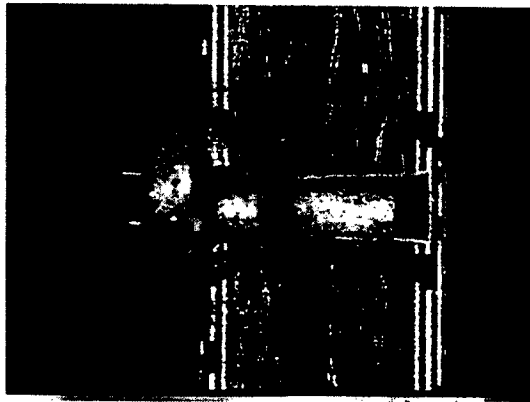


Figure 7 Package cross section cut performed using DEPACK Laser routine

## Edit-Repair

Focused ion beam (FIB) systems are used in product development and yield enhancement to deprocess silicon integrated circuits [8]. The DEPACK system performs the same basic function as FIB except it does it on the packaging, and edits as well by adding metal or dielectric using the laser direct-write capability of the upgraded system. The tool used in our experiments was implemented with an infrared laser to allow laser-assisted soldering of metal wires to points within a package exposed by the micromachining process.

With micromanipulators, a wire was positioned and soldered to a thru-hole connection, as shown in Figure 8. We see this as a first step in duplicating FIB capabilities for IC's at the package level, allowing the repair of open circuits, signal redistribution and simplifying connections to a package for electrical test.



Figure 8 Cu wire laser soldered to PWB via. Via is 400 $\mu$ m DIA.

## Summary

We have shown that Ultraviolet laser micro machining is useful for failure analysis operations, such as organic package delayering and cross-sectioning. When combined with infrared laser-assisted soldering, the tool can be used for circuit edits, including signal redistribution and repair of open circuits. Once faults are localized, laser micro machining provides high-resolution access for any further analysis. This tool is capable of penetrating planar metal layers and lands where current RIE systems cannot. Cross section cutting of 1mm organic/fiber reinforced packages is also possible with 50 $\mu$ m kerf widths, positional accuracy of  $\pm$  5 microns and low collateral damage. The DEPACK system combines several key capabilities, which had previously been unavailable all in one tool.

The standard DEPACK system can be expanded with additional hardware capabilities to duplicate the separate direct-write deposition equipment capabilities outlined here [3].

## References

1. J. Ouellette, The Industrial Physicist, p11, June 1998
2. G.P. Behrmann and M.T. Duignan, "Excimer Laser Micromachining for Rapid Fabrication of Diffractive Optical Elements", Applied Optics, 36(20), 10 July 1997
3. Mathews, et al, "Integrated Tool for Fabrication of Electronic Components by Laser Direct Write", Photonics West Conference Proceedings, 2002 (to be published)
4. R.Shukla, et al., Flip chip CPU package technology at Intel: A technology and manufacturing Overview, 49<sup>th</sup> Electronic components and Technology Conference, 1999, pp 945-949
5. US Patent Application
6. Hsiung, et al, "Failure Analysis Process Flow and Common Failure Mechanisms in Flip-Chip Packaged Devices", ISTFA Conference Proceedings, 2000
7. D. Goyal, "X-ray Tomography for Electronic Packages", ISTFA Conference Proceedings, 2000
8. Herschbein, S.B., L.S. Fischer, A.D. Shore, M.P.Tenney, T.L.Kane, "The challenges of Focused-Ion-Beam Chip Repair and Debug Assistance in the 0.25 micron Copper Interconnect Millenium" ISTFA, 16-20 November 1998.

# **The potential of ultra-short laser pulses (<10 ps) in future material processing: “mode-locked Ti:sapphire” vs. “q-switch Nd:YAG” applications.**

David Ashkenasi,  
Laser- und Medizin-Technologie GmbH, Berlin, Germany;

## **ABSTRACT**

This paper discusses possible potentials of ultra short laser pulses in the pulse width range <10 picosecond from the perspective of laser micro processing. With the problems involved generating ultra short laser pulses at high average power it will be shown, that the most successful applications performed with ultra short pulse technology is associated with problems, where the precise energy localization plays a crucial role. The discussion is based on laser processing examples from the application laboratory at the LMTB GmbH comparing applications using q-switch Nd:YAG lasers with nanosecond pulse widths (and an average power between 10 and 100 W) and mode-locked, amplified Ti:sapphire lasers (average power < 1 W).

**Keywords:** laser processing, micro structuring, short and ultra-short pulses, tungsten, aluminum nitride, transparent dielectrics, thin films.

## **1. INTRODUCTION**

The availability of ultra short, sub-ps, pulsed lasers has stimulated a growing interest in exploiting the enhanced flexibility of femtosecond technology for micro-machining. Ultra short laser pulses (USLP) offer a variety of advantages for precision micro-fabrication. Due to lower energetic thresholds for sub-picosecond ablation and the controllability of individual laser pulses (e.g. by laser pulse duration) the amount of energy deposited into the processed sample can be minimized and highly localized. This leads to a reduction of unwanted thermal effects, a minimization of energy diffusion, so that very clean microstructures can be achieved with optimized pulses. Also non-linear optical effects may be exploited. Self-focusing due to the non-linear optical Kerr effect may be used to induce long, narrow 3d-modification traces into the bulk of wide band-gap materials. Long, micrometer thin channels can be also drilled taking advantage of the high ablation rates and low heat deposition when employing USLP.<sup>1,2</sup>

However, there are a few important drawbacks to be considered presently, trying to implement ultra short pulse technology for wide spread laser processing, such as micro structuring or high aspect hole drilling. Presently, most laser systems capable of generating USLP are accompanied with certain disadvantages compared to industrial q-switch Nd:YAG lasers generating ns pulses: they usually do not allow “turn-key” operation (although this problem is being solved), they have a fairly complicated and costly design (especially during the proto-type stages), and, most importantly, a direct amplification of USLP is very difficult. The damage threshold limit of the optical elements for high peak intensities is a very challenging task to overcome. Present ultra fast laser systems are typically limited to average powers of 1W at a repetition rate of usually 1 kHz, leading to single pulse energy near 1 mJ. For pulse widths above several ps, energy amplification is less difficult because of the comparatively lower peak powers involved. However, even considering the newest commercial laser developments for ps applications with average powers over 20 W,<sup>3</sup> the high repetition rates of 80 MHz or even 160 MHz limit the single pulse energies of the IR laser pulses to 100 to 200 nJ per pulse. A q-switch Nd:YAG laser system generating ns laser pulses with an average power of 10 W to 50 W (or even 200 W) at 10 kHz repetition rate and single pulse energies over 10 mJ is readily available for diffraction limited processing in industrial applications. Based on present laser systems generating USLP at limited average power and relatively high costs, an intensive discussion is to be observed on the question if USLP can manifest itself an important alternative in material processing? This paper discusses this problem by presenting potential applications for ns laser pulses and USLP, at which the energy localization and a minimal heat affected zone will play a crucial role in micro processing.



## 2. MICRO PROCESSING USING Q-SWITCH Nd:YAG LASERS

Micro processing with solid state lasers is typically conducted in a direct writing alignment. The laser beam is focused down to the  $\mu\text{m}$  range to provide optimal spatial energy localization. Diffraction limited processing suggests a very good beam quality, i.e.  $\text{TEM}_{00}$  mode output. This can be easily provided with Nd:YAG laser systems at moderate average powers of 10 W and above. With the implementation of diode lasers pumping the solid state rods, and driven by innovative resonator design, the average power for diffraction limited applications is constantly being shifted to higher levels, even above 200 W. High average power at sufficient single pulse energy is an important factor for industrial applications, since it determines the processing speed and therefore the cost factor for any laser based batch production. However, most applications can be addressed at lower laser average powers. Fig. 1 demonstrates this for laser micro welding and drilling of a thin stainless steel tube, e.g. for medical applications. The micro welding of the tube end was conducted in cw mode of the 10 W Nd:YAG single rod laser in  $\text{TEM}_{00}$  mode. Afterwards, the 100  $\mu\text{m}$  thin wall was laser drilled (single sided) using the 100 ns laser pulses generated in the q-switch technique of the identical laser system, where the laser beam was focused to a spot size of ca. 30  $\mu\text{m}$ .

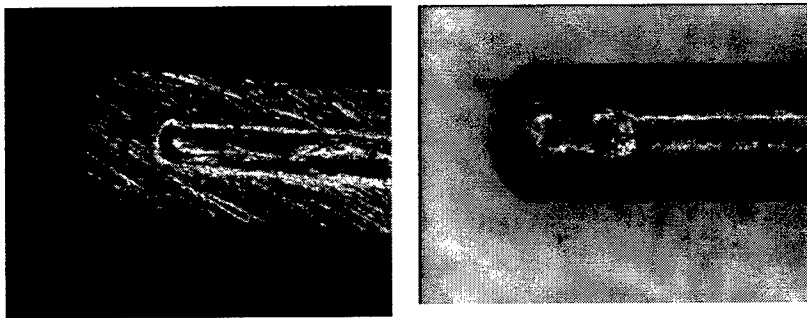


**Fig. 1:** Far left microscope picture depicts the side cut analysis after laser micro welding of a 300  $\mu\text{m}$  thin stainless steel tube (left edge). Other microscope picture illustrates the same tube with a 40  $\mu\text{m}$  hole laser drilled close to the micro welded end.

Another example of laser micro processing is illustrated in Fig. 2. Tungsten foils with a thickness of 150  $\mu\text{m}$  were laser cut using 100 ns laser pulses at an average power below 10 W and a repetition rate of 1.5 kHz. The example shown in Fig. 2 represents the company logo of laser and medical technology LMTB GmbH at a size of 1  $\text{mm}^2$ . The high precision achievable with ns laser pulses is demonstrated in the zoom microscope pictures in Fig. 2b and c. The CAD design is translated into the CNC program for the sample and optical moving stages. Special care was taken in the choice of beam polarization in respect to the direction of sample movement and in the supply of processing gas. The laser cut tungsten foil can be utilized for projection processing, as demonstrated in the result of Fig. 2d. The company logo in Fig. 2a was used as projection mask and illuminated with the light of an excimer laser at a wavelength of 248 nm. The projection scaling was approx. 1:12. The ablated feature on the tungsten sample can be characterized as a micro tag in Fig. 2d and scales only 140x140  $\mu\text{m}^2$ .

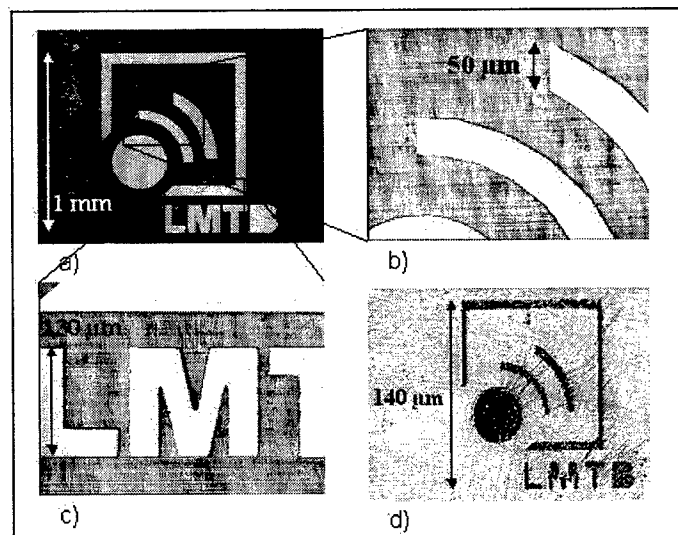


**Fig. 2:** a-c) Tungsten foil with a thickness of 150  $\mu\text{m}$  laser cut in focusing alignment. Laser parameters set as following: wavelength = 1.06  $\mu\text{m}$ , pulse width = 100 ns, repetition rate = 1.5 kHz. d) tungsten foil of fig. 2a) mask projected 1:12 on a different tungsten sample using excimer laser light at 248 nm.

For most processing applications with metals, the wavelength of  $1.06\text{ }\mu\text{m}$  is adequate for micro structuring tasks, such as micro drilling. In the case of copper, for example, the processing at the 2. harmonic yielding a wavelength of  $532\text{ nm}$  ensures an enhanced photon penetration and suggests a higher processing efficiency, even taking the ca. 50 % loss in the average power into account.<sup>4</sup> For the most dielectric materials, glass, crystals, polymers and ceramics, the linear absorption characteristics yield a fairly high penetration depth for laser light in the visible and infrared spectral range. Laser processing of these materials with is usually performed in the ultraviolet, e.g.  $355$  or  $266\text{ nm}$ . For the high aspect drilling of micro holes in aluminum oxide ( $\text{Al}_2\text{O}_3$ ) and aluminum nitride ( $\text{AlN}$ ) the following results demonstrate that a high localization in a shallow depth is not necessarily essential. The laser beam of a master oscillator power amplifier (MOPA) Nd:YAG laser system<sup>5</sup> was focused down to a diameter of  $80\text{ }\mu\text{m}$  ( $1/e^2$ ) onto the surface of the ceramic samples. Laser processing was performed with a burst of 40 laser pulses at a  $100\text{ Hz}$  rate, leading to a average repetition rate of  $4\text{ kHz}$ . The laser pulse width of  $120\text{ ns}$  is comparable to the situation described earlier. Several ceramic plates of  $250\text{ }\mu\text{m}$  thickness each were stacked to receive a total sample thickness of  $20\text{ mm}$ . The laser drilling experiments were performed in normal air. The holes of the front and rear side of every ceramic plate was measured to obtain the drilling performance throughout the channel. Fig. 3 compares the drilling performance in  $\text{Al}_2\text{O}_3$  and  $\text{AlN}$  for different fluence levels. The aspect ratios obtained at an average hole diameter of  $100\text{ }\mu\text{m}$  are 1:100 and higher. The processing time in  $\text{AlN}$  for the first  $10\text{ mm}$  hole depth was only  $8\text{ s}$ . At higher depths the ablation rate falls almost exponentially leading to ca.  $120\text{ s}$  for the  $16\text{ mm}$  hole depth. Similar results were obtained for stainless steel and copper. Further laser micro drilling investigations with the MOPA laser system are performed in our laboratory to determine, if this high aspect ratio can be obtained for smaller hole diameters, such as  $50\text{ }\mu\text{m}$  and smaller.

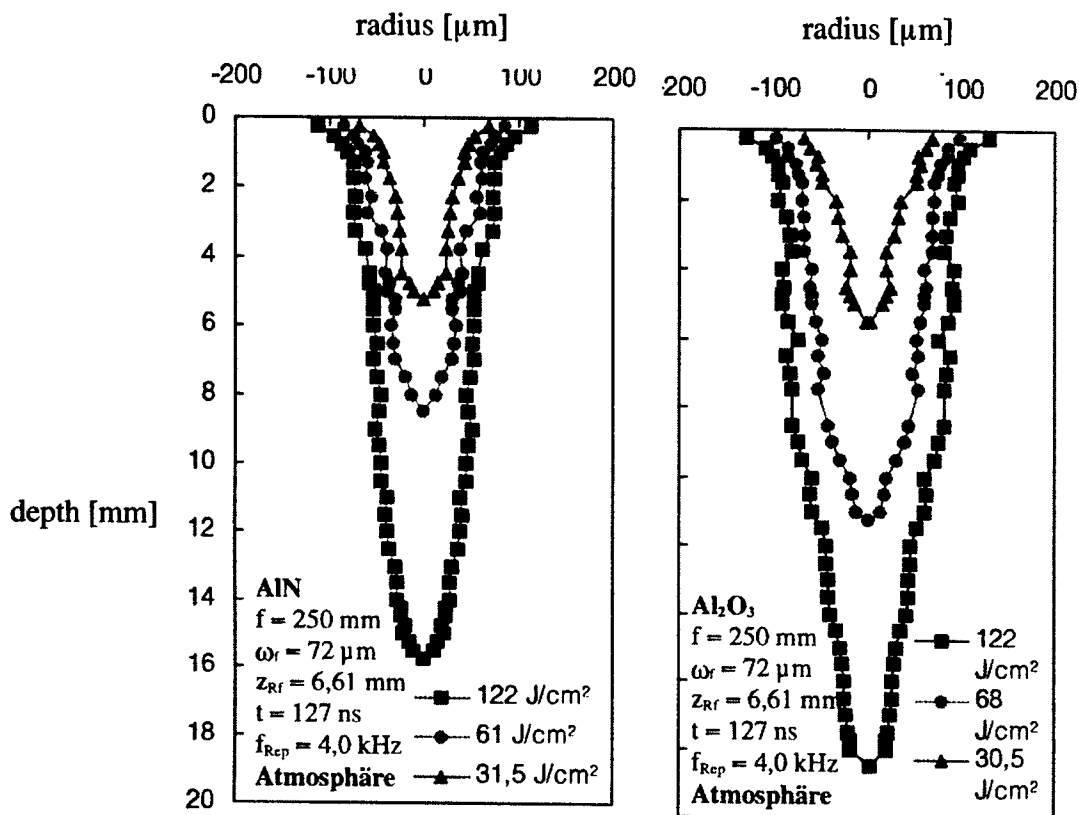


**Fig. 3:** High aspect ratio drilling of long holes in ceramic materials –  $\text{AlN}$  and  $\text{Al}_2\text{O}_3$  - at different fluence levels: 31.5, 61 and  $122\text{ J/cm}^2$ .

### 3. MICRO PROCESSING USING ULTRA SHORT LASER PULSES

The availability of ultra short laser pulses (USLP) has stimulated a growing interest in exploiting the enhanced flexibility of femtosecond technology for micro-machining. USLP offer a variety of advantages for precision micro-fabrication. Due to lower energetic thresholds for sub-picosecond ablation<sup>6,7</sup> and the controllability of individual laser pulses (e.g. by laser pulse duration) the amount of energy deposited into the processed sample can be minimized. This leads to a reduction of unwanted thermal effects, due to a minimization of energy diffusion, that may be exploited for micro processing of materials.

Well defined localization of photon energy is crucial for high quality removal of a thin layers on a substrate. Selective removal of only one layer on a multi-layer system is even more challenging. And this is more true if these layers are transparent. The successful selective laser-induced removal of thin transparent layers is reported in this proceedings.<sup>8</sup> Fig. 4 depicts an example of indium tin oxide (ITO) removed from the glass substrate using 3 ps laser pulses at a wavelength of 800 nm. The fairly well-defined edges of the resulting 150 nm deep groove is outlined by a rim with a curl of only 20 nm. A further improvement in quality was observed after using sub-ps laser pulses at equal wavelength. Using UV laser pulses at a pulse width in the ns range yields a curl of several 100 nm to 1  $\mu\text{m}$ . This is not adequate for most applications, although CO<sub>2</sub> snow cleaning as additional processing step may reduce this problem.

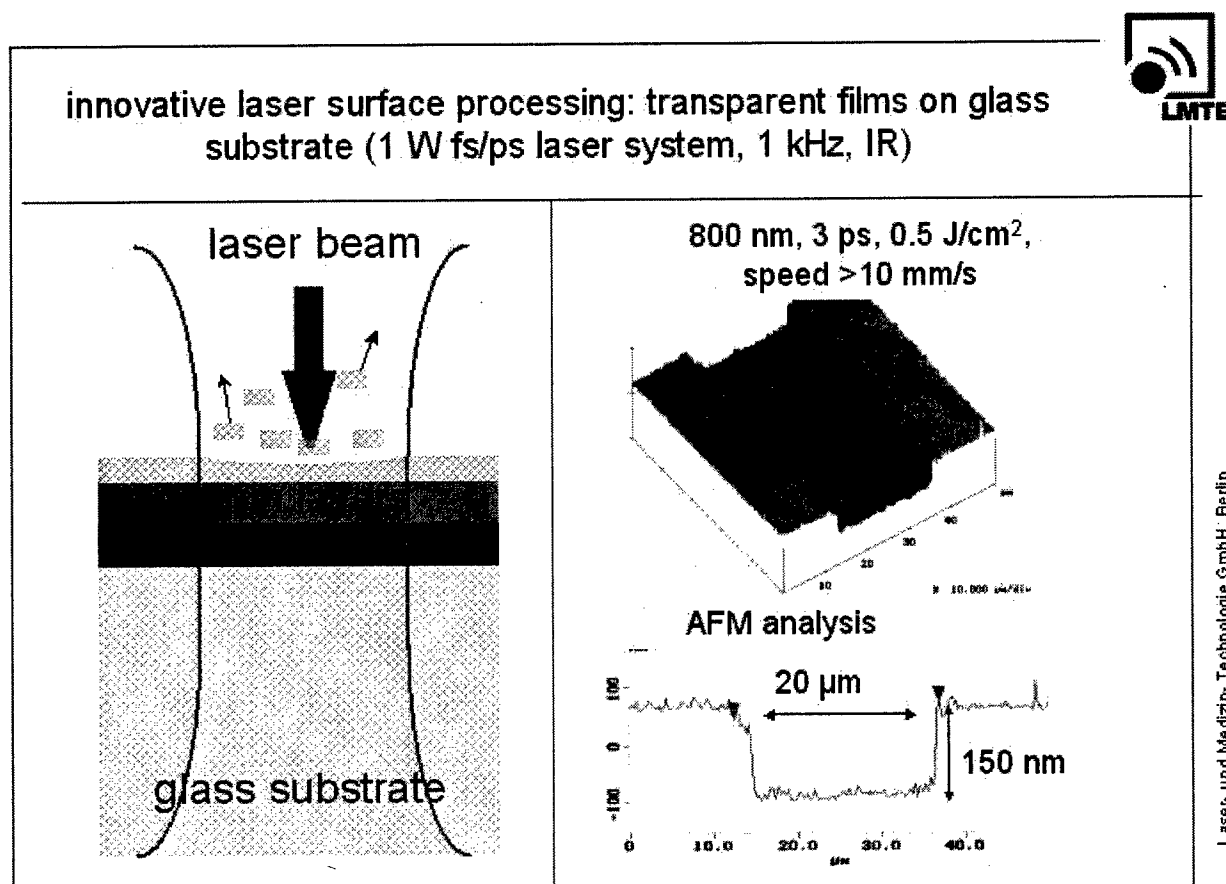


**Fig. 4:** Schematic illustration of the initial condition concerning selective laser-induced removal of single transparent layer in a multi-layer system (left). Atomic force analysis of laser removed ITO layer from the glass substrate using 3 ps laser pulses at 800 nm wavelength (right).

Atomic force analysis of the laser processed ITO layer reveal the following situation: at a fluence of  $< 2 \text{ J/cm}^2$  the first shot roughens the surface. The second shot initiates the ablation, additional shots removes the remaining ITO from the glass surface. The AFM profile analysis suggests a linear increase of ablated volume with increasing fluence. In other words, applying USLP at 800 nm even enables a partial removal of the 150 nm thin ITO layer, and this highly reproducible. Since the linear absorption coefficient for ITO at 800 nm is  $< 1 \%$ , non linear excitation is responsible for the high localizing of photon energy, comparable to metal case.

Bulk micro processing of transparent materials with USLP can differ strongly from similar applications using ns laser pulses, where laser-induced plasma generation is accompanied by macroscopic cracking of the material. Typical applications using ns laser pulses for glass like materials are sub-surface marking or decorative "art-work" inside the bulk, which are easily observable with the naked eye due to the generation of more or less large stray centers.<sup>9</sup> The picture changes completely when USLP are focused inside the bulk of transparent dielectrics. The plasma generation, i.e. the laser-induced concentration of free electrons, can be limited below damage threshold in applications using USLP.<sup>10</sup> In this case multi-photon ionization plays a more dominate role compared to avalanche ionization. Therefore, the energy impact into the material can be controlled in a way without indorsing the traditional dielectric breakdown. This advantage of USLP is utilized to write wave guide like structures inside bulk fused silica and other transparent materials.<sup>11</sup>

The microscope picture in Fig. 5 illustrates an array of micro-traces, each spaced ca.  $5 \mu\text{m}$  inside a thin glass plate, which were generated by (tightly) focused laser pulses of 200 fs pulse duration and  $5 \mu\text{J}$  single energy with a micro-objective at a focal length of 5 mm inside the sample. The micro-traces, which closely resemble the documented wave guide structures, are ca.  $1 \mu\text{m}$  in diameter (top view). Using a less tight focusing arrangement, any form of visible bulk modifications in this glass was not observed, although the fluence in the focus was estimated to be far above bulk damage threshold. For example, using a lens of 30 mm focal length strong super continuum generation at 200 fs laser pulses was observed, however, no sign of irreversible changes inside the material. This changed completely using 2 ps laser pulses at which bulk modifications were located even with lenses of much longer focal length. The traces generated under the ps laser pulses were broader (compared to the example in Fig. 10) and did not remain at a constant depth. Compared to fs laser pulses, laser-induced bulk processing with ps pulses in glass and  $\alpha\text{-SiO}_2$  can be performed using less tight focusing arrangements, however, incubation effects seem to be of higher importance.<sup>12</sup> Laser bulk

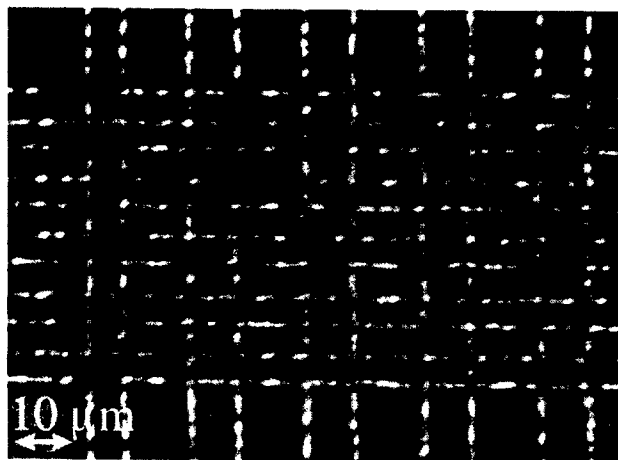


Fig. 5: Top microscope picture of small vertical and horizontal micro-traces 10 and  $5 \mu\text{m}$  apart, respectively, inside a 0.5 mm thick glass substrate. Each „grating line“ was generated by focusing 200 fs laser pulses at  $5 \mu\text{J}$  energy inside the sample with a micro-objective of approximately 5 mm focal length. The processing velocity of the sample in the above case was 0.3 mm/s at a laser repetition rate of 1 kHz.

processing with fs laser pulses demonstrate in most cases visible single-shot modification, if the localization of photon energy inside the material was not hindered by strong defocusing effects, such as super continuum generation.

Even if the laser beam of USLP is focused onto the front surface of the sample damage can develop inside the bulk at laser fluence levels far below the surface damage threshold. Due to the self-focusing of the laser beam inside a media with positive Kerr-coefficient the fluence increases until bulk damage threshold is reached. The depth at which damage occurs can be controlled by adjusting either pulse energy or pulse duration, as discussed in detail for fused silica.<sup>13</sup> This provides the possibility not only to generate three dimensional structures inside the bulk without altering front and rear surface, but also to generate micro holes only on the rear side.<sup>14</sup>

#### 4. DISCUSSION

This paper confined the comparison of applications using q-switch and mode-locked laser systems on a wavelength range in the infrared. In both cases, transformation into shorter wavelengths is of course easily available, yielding a variety of different pulse widths – wavelengths combinations. While for USLP linear optical absorption processes may be of less importance, the choice in wavelength for ns material processing is of greater significance in those cases, where the optical penetration depth is to be minimized. This alone, however, does not ensure the necessary localization of energy in the material due to diffusion processes and phase transformations in the time frame of the laser-material interaction. Fig. 6 outlines some of the most important contributions in laser-material interaction for e.g. laser-induced processing. Basically, a division into three main mechanisms describes the interaction and forthcoming processes in different time domains. Photon excitation of the electronic systems occurs almost instantaneously, leading to generation of “hot” electrons in a “cold” lattice. During interaction with USLP (equaling a pulse width  $< 10$  ps, as defined in this paper) the lattice temperature remains below electron temperature. The electron-phonon coupling strength characterizes the energy transfer dynamics into the lattice. For metals, the electron-phonon coupling is much weaker than for dielectrics, therefore, the energy transfer needs more time to reach an equilibrium stage between electron and phonon system. There are laser-induced effects that are observed with ps and even sub-ps dynamics, much earlier than any thermal reaction is expected to occur. Defect formation in dielectrics such as self-trapped excitons yield transient energy levels in a sub-ps time scale, e.g. only 150 fs for fused silica. Another “non-thermal” effect is the with USLP induced ultra fast phase transformation in sub-ps reaction time for semi-conductors and perhaps also for metals. Recently, it has been demonstrated that a pronounced surface ionization of a dielectric surface leads to “non-thermal” Coulomb explosion with an ablation depth of ca. 3 nm.<sup>15,16</sup> Of course, these “non-thermal” processes are eventually superimposed by thermal material reactions, such as phase explosion, normal boiling and normal vaporization. The significance of each individual “non-thermal” ablation processes, however, can be to some part controlled by the choice of pulse width and other laser parameters such as laser repetition rate. Investigations using pulse shaping technology to provide a train of USLP with THz repetition rate is a very promising approach to control the excitation mechanism and forthcoming effects.<sup>17</sup>

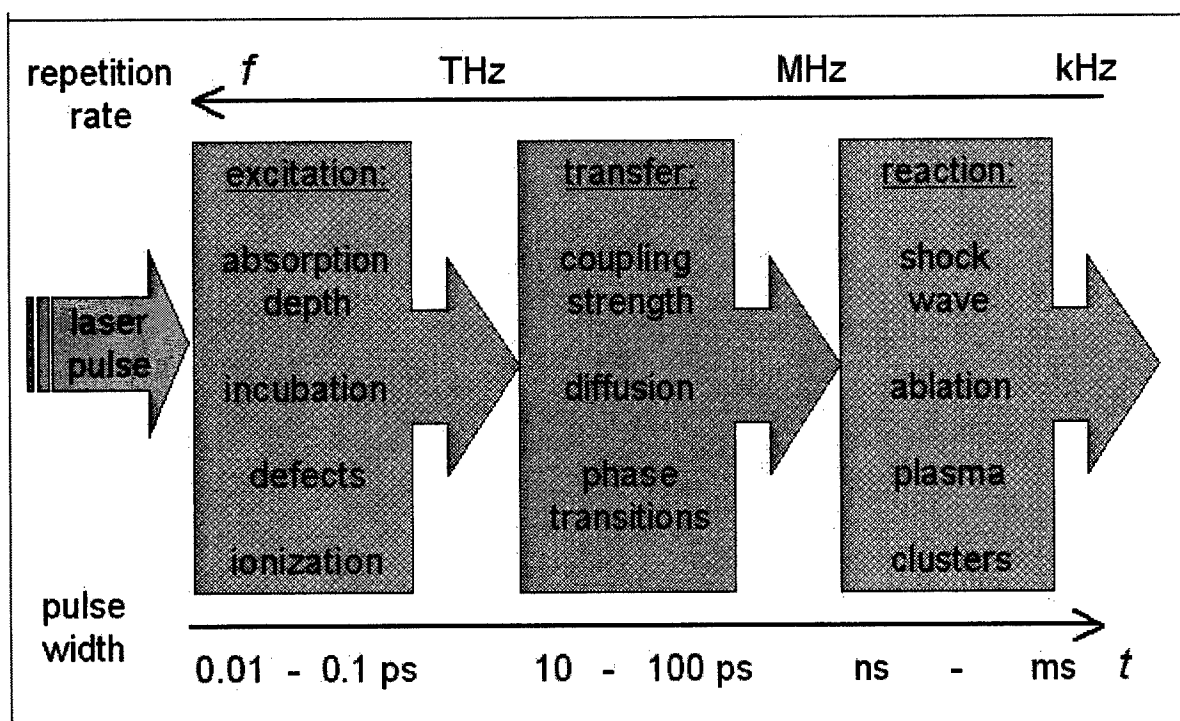


**Fig. 6:** Schematic illustration of the different mechanism involved in laser-material-interaction, electron excitation, energy transfer, and material reaction, relative to the expected dynamic range, taking (theoretical) laser repetition rates into account.

Part of the absorbed laser energy is not carried out by the ablated material but remains within the material. As indicated, diffusion mechanisms play an additional dominant role in defining the actual energy localization in the lattice. This loss mechanism will account for much of the obtained heat affected zone outside the laser irradiated area. In metals, for example, a large energy loss contribution can be attributed to the diffusion of hot and ballistic electrons, reducing the significance of USLP for metal processing. The formation of a liquid phase is important for micro welding applications. However, it is in many cases a very substantial problem in laser-metal interaction with laser pulses in the ns pulse width range and above. Single USLP will not interact with a thermally activated liquid phase. However, processing at high repetition rate this effect may gain in significance, if the liquid phase remains in the zone of irradiance. Another effect contributing to the amount of energy remaining in the material is the development of a shock wave that can have a very negative influence on the processing quality, especially for brittle material. The shock wave contribution gains with reduced pulse width and is especially strong for ns laser pulses. For USLP, however, theoretical and experimental studies suggest that the shock wave introduced in the interaction zone does not couple very well with the environment and therefore remains a very local effect.<sup>18</sup>

In drilling deep holes, plasma and cluster formation can interact with USLP even at a very moderate repetition rate. It is unclear, if the nature of the laser-induced plasma inside a deep laser drilled hole differs in USLP from ns pulse width applications. Investigations in this field are important to access possible advantages of USLP applications, where a massive amount of material has to be removed. Provided USLP can be readily generated at an average power of ca. 100 W (at a high quality spatial beam profile) in the near future, there is still some skepticism, if femtosecond technology will be implemented for this kind of industrial applications.

## 5. SUMMARY

This paper compares material processing using q-switch and mode-locked laser systems based on chosen examples of applications, where ns and ultra short laser pulses demonstrate their highest potential for wide spread industrial applications. The application laboratories for applied laser technology at the LMTB GmbH understands its role as independent service institution for laser micro processing, interfacing between laser system development and industrial production. In near future, q-switch solid state lasers may play a dominate role in micro processing, e.g. micro structuring of metals and for high speed channel drilling applications, where high average powers are essential. On the other hand, certain applications can not be accomplished with ns laser pulses, either due to the peak power necessary to induce intensity relevant effects or based on possible stringent initial conditions concerning the energy localization. The laser processing of thin transparent layers and 3d bulk micro structuring of transparent materials to generate complex functional optical devices are only two examples demonstrating the potential of USLP in present and future applications.

## 6. ACKNOWLEDGMENT

The author would like to thank Thomas Metzger and Alexander Binder for the help with the experiments involving the high aspect drilling in AlN and micro cutting of metals with ns Nd:YAG lasers in our application laboratory. Also, Thomas Riesbeck (Technical University Berlin) is greatly acknowledged for his assistance in applications involving the MOPA Nd:YAG laser. In addition, the author appreciates the aid of Razvan Stoian and Arkadi Rosenfeld (Max Born Institut, Berlin) for the valuable on going discussions and close cooperation.

## REFERENCES

- 1) E.E.B. Campbell, D. Ashkenasi, A. Rosenfeld, *Lasers in Materials Science* (Trans Tech Publications, Switzerland, 1999), pp. 123-144, 1997.
- 2) Y. Li, et al., Three-dimensional hole drilling of silica glass from the rear surface with femtosecond laser pulses, *Appl. Opt. Lett.* **26**, pp. 1912-1914, 2001
- 3) See for example [www.spectra-physics.com](http://www.spectra-physics.com), [www.lumera-laser.com](http://www.lumera-laser.com), and [www.imra.com](http://www.imra.com).
- 4) B. Smandek, B. Klimt, F. Maßmann, T. Metzger, D. Ashkenasi, Mikromaterialbearbeitung mit grünen Nd:YAG-Laser bei kurzen Pulsen“, *LaserPraxis* **2**, pp. 10-12, 2001
- 5) The improvement of the home developed MOPA Nd:YAG laser system is conducted in cooperation with the group of Prof. Eichler at the Technical University Berlin. For details on the laser system address corresponding author: [d.ashkenasi@lmtb.de](mailto:d.ashkenasi@lmtb.de).
- 6) B.C. Stuart, M.D. Feit, A.M. Rubenchik, B.W. Shore, M.D. Perry, *Phys. Rev. Lett.* **74**, pp. 2248 1995.
- 7) D. Ashkenasi, A. Rosenfeld, *SPIE Proc.* **3618**, pp. 102-113, 1999.
- 8) D. Ashkenasi, A. Rosenfeld, *SPIE Proc.* **4637**, in print, 2002.
- 9) See for example: [www.vitro.com](http://www.vitro.com).
- 10) C.B. Schaffer, A. Brodeur, J.F. Garcia, and E. Mazur, “Micromachining bulk glass using femtosecond laser pulses with nanojoule energy”, *Opt. Lett.* **26**, pp. 93-95, 2001.
- 11) For example: A. Marcinkevicius et al., *Opt. Lett.* **26**, 277, 2001; A. M. Streltsov et al., *Opt. Lett.* **26**, 42, 2001; D. Homoelle et al., *Opt. Lett.* **24**, 1311, 1999; S.-H. Cho et al., *Opt. Comm.* **168**, 287, 1999; K. Miura et al., *SPIE Proc.* **3618**, 141, 1999.
- 12) A. Rosenfeld, M. Lorenz, R. Stoian, D. Ashkenasi, „Ultrashort-laser-pulse damage of transparent materials and role of incubation“, *Appl. Phys. A* **69** [Supl.], pp. 373-376, 1999.
- 13) D. Ashkenasi, H. Varel, A. Rosenfeld, S. Henz, J. Herrmann, and E.E.B. Campbell, „Application of self-focusing of ps laser pulses for three dimensional microstructuring of transparent materials“, *Appl. Phys. Lett.* **72**, pp. 1442-1444, 1999.
- 14) D. Ashkenasi, G. Herbst, A. Rosenfeld, H. Varel, M. Lorenz, R. Stoian, E.E.B. Campbell, „Laser ablation and structuring of transparent materials with ultrashort laser pulses“, *SPIE Proc.* **3343**, pp. 400-410, 1998.
- 15) R. Stoian, D. Ashkenasi, A. Rosenfeld, E.E.B. Campbell, *Phys. Rev. B* **62**, pp. 13167, 2000.
- 16) R. Stoian, A. Rosenfeld, D. Ashkenasi et al., Surface charging and impulsive ion ejection during ultrashort pulsed laser ablation, *Phys. Rev. Lett.*, in print, 2002.
- 17) R. Stoian, A. Rosenfeld, et al., Laser ablation of dielectrics with temporary shaped femtosecond pulse, *Appl. Phys. Lett.* **80**, pp. 353, 2002.
- 18) A.M. Rubenchik et al., *Appl. Surf. Science* 127-129, 193, 1998; M. Feit et al., *Appl. Surf. Science* 127-129, 869, 1998; J. Noack et al., *Appl. Optics* **37**, 4092, 1998; J. Noack et al., *J. Appl. Phys.* **83**, 7488, 1998.

---

Corresponding author: [d.ashkenasi@lmtb.de](mailto:d.ashkenasi@lmtb.de); phone: +49 30 67053-6; fax: +49 30 67053-500; <http://www.lmtb.de>; Fabeckstr. 60-62, D-14195 Berlin, Germany; CEO Prof. Dr. G. Mueller.

# Short Pulse Width Micromachining of Hard Materials Using DPSS Nd:YAG Lasers

M. Heglin, S.V.Govorkov, M.Scaggs, H.Theoharidis, T. Schoelzel  
Lambda Physik, Fort Lauderdale, Florida, USA

## ABSTRACT

The material processing results of an industrial, short-pulse duration (~15ns) DPSS YAG laser producing peak powers greater than 0.2MW is discussed in this paper. This peak power provides sufficient materials processing capability to meet the micro machining needs in the automotive, semiconductor, micro-electronic, medical and telecommunication industries. All hard and soft materials including: plastics, metals, ceramics, diamond and other crystalline materials are suitable candidates for the processing capability of this laser. Micron level features can be machined in these materials to a depth in excess of 1mm with high quality results. In most applications feature sizes can be achieved that are not possible or economical with existing technologies. The optical beam delivery system requirements, and overall micro-machining set-up are also described. The drilling and cutting versatility down to feature sizes of less than 7µm, as well as, complex shapes are shown. The wavelength, pulselength, and peakpower are described and related to their effect on recast, micro-cracking and material removal rates. Material removal effects related to progressive penetration into the material will be reviewed. The requirements of this DPSS laser technology to meet the operational requirements for high duty cycle operation in industrial environments is covered along with processing flexibility and lower operating cost.

## INTRODUCTION

The laser was invented in 1960 and ever since a significant effort has been devoted to investigate the materials processing capability of various types of lasers and wavelengths. In recent years the use of UV excimer lasers have demonstrated excellent photo-ablation capability for micro-fabrication applications in a wide range of materials. Lately however, diode pumped solid state Nd:YAG lasers that also operate in the IR at 1064, Green at 532 nm and UV at 355 nm has come on the market. These lasers produce higher pulse rates and superior beam quality ( $M^2 < 1.3$ ) resulting in the ability to drill and cut hard and soft materials like plastics, and Polyamides. The effects of laser parameters such as pulse length, energy density, wavelength and beam quality, have been examined for their effects on the micro-fabrication process, in an effort to find the most efficient conditions<sup>1-3</sup>. As the marketplace sees the introduction of new products, technology continues to expand as these increasingly more complex devices emerge and the challenges for cost effective manufacturing need to be met.

As laser micro processing of hard materials has continued to gain acceptance in the industry, Semiconductor based devices including Micro Electro Mechanical Systems (MEMS), multi-chip modules (MCMs), Chip Scale Packages (CSPs), and Ball Grid Arrays (BGAs) require the drilling and or cutting of micro or smaller holes, slots or trenches. The commercial importance of developing a new low cost method of micro machining is evident from the wide use of sensors, digital cameras, fuel injectors, inkjet printer nozzles, medical, and telecom devices. The materials of particular interest are found mainly in the semiconductor industry including: Si, GaAs, AlN, Al<sub>2</sub>O<sub>3</sub>, Si<sub>3</sub>N<sub>4</sub>. Drilling of fuel injector nozzles is one application in the automotive industry that points to the importance of micro machining of high quality holes typically 50-200 micrometers in diameter machined in metals like stainless and carbon steel beyond 1 mm in thickness. Laser drilling has been in common use for drilling of air-cooling holes for a number of years in nickel and cobalt alloys and refractory metals. The generation of short pulse-width lasers can produce better surface finishes with less recast and to better tolerances. In the medical industry, the requirements for micro-features in components like catheters and stents is growing. Precise machining of diamond, both natural and synthetic, for diverse applications including cutting tools and wire die applications is now easily done.



## MICROMACHINING VARIABLES

Pulsed lasers with high brightness with operational pulse length of 10 to 30 nanoseconds allow high accuracy in micromachining applications. When these pulses are delivered at a pulse repetition rates in the kilohertz range, fast material removal rates are achieved. As shown in Figure 1, when pulse widths are maintained in the short nanosecond level most of the material is removed in a vapor state, as opposed to melt ejection common with long-pulse drilling. In order to maintain high accuracy and minimize heat affected zone, the laser fluence has held to several  $10 \text{ J/cm}^2$ , so as to reduce plasma shielding and post-pulse plasma heating effects<sup>1</sup>. The resultant material removal rate is approximately  $1 \mu\text{m}$  per pulse. To effectively make this a production tool the pulse repetition rate must be in the multi kilohertz range to insure an effective micro machining speed.

Expelled metal vapor and plasma shielding are factors that do become limiting factor in drilling especially when holes with high L/D ratios are involved. As the hole penetrates the material the cloud of vapor, ejected material and plasma is encountered. As the hole approached 1 mm in depth the blockage effect of this cloud further attenuates the beam. In contrast, the thickness of plasma layer at the surface is limited to roughly  $100 \mu\text{m}$  during the pulse. In order to reduce plasma formation it is necessary to employ all means available, such as using shorter laser wavelength or even inert gas coverage.

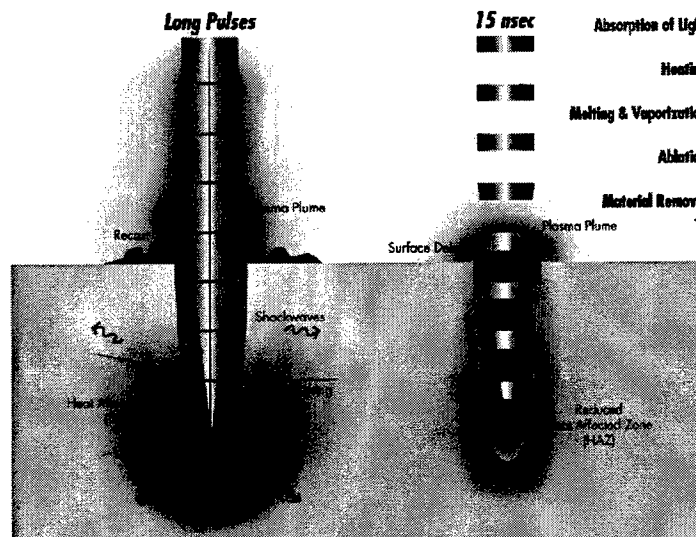


Figure 1. Schematic illustration of the effect of pulse length on micromachining of hard materials.

The set-up requirements for a pulsed laser in a micro machining application involve four sets of interrelated variables that need to be understood and controlled to achieve optimum results. The first set of variables is laser related and includes the proper establishment of laser power, diameter and divergence of the beam, pulse width, mode, and beam profile. The second group applies to focusing parameters and includes shape of lens, depth of focus, depth of field, spot size, mask imaging vs. direct focus. The next set of variables is work piece related and includes type of material, thickness, flatness, surface reflectivity, hardness, melting temperature, and surface roughness. Finally, there are process related variables that include coatings, speed, shape of feature, gas assist, shielding, single or dual side processing, etc.

The process of micro machining involves achieving a controlled explosion at the point where the laser beam energy is focused on the work piece. The shorter the pulse width the higher becomes the peak temperature of the material. In addition, the thermal nature of the process, which results in the generation of recast and a heat-affected zone adjacent to the point of impact, is minimized. In contrast, continuous-wave carbon dioxide lasers or conventional flash-lamp and arc-lamp pumped Nd:YAG lasers produce pulse lengths well over 1 microsecond. To achieve maximum material removal efficiency with these lasers it is necessary to apply an external assist in the form of high-

pressure co-axial gas jet. The purpose of the gas assist is to protect the lens from ejected melted particles, accelerate the cutting speed and depth by the use of an exothermic reaction from a reactive gas like oxygen and finally, the high pressure of the gas flushes out some of the molten material from the cut zone.

## SYSTEM OVERVIEW

This paper shows the unique benefits of DPPS lasers that produce short nanosecond pulses in the order of 15 ns. The short pulse duration of these lasers were found to offer benefits for the end user where the need to achieve high quality, small features and a low cost of ownership. Our application lab has demonstrated successful processing in actual components involving hole drilling (both through and blind), cutting, trenching, coatings ablation. The process range includes but is not limited to the following summary of requirements.

- Dimensions in the 7 - 200 micrometers range.
- Elimination of surface contamination or recast material buildup to reduce the cost of ownership by doing away with post-processing manufacturing steps.
- Eliminate micro-cracking to maintain the integrity of the substrate,
- Achieve high accuracy dimensions of 1 micrometer or better.
- High aspect ratios of up to 50:1.
- High processing speed

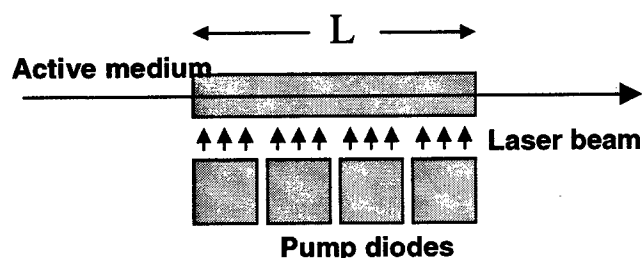
Therefore, the tests covered by this paper involved the use of several diode-pumped Nd:YAG laser models of a product called Gator which is manufactured by Lambda Physik. The full Gator series of DPPS lasers are shown in Figure 2.

Model	Wavelength	Average Power at 10kHz	Pulse Duration	M <sup>2</sup>
GATOR 1064	1064nm	10W	15ns	<1.2
GATOR 532	532nm	5W	15ns	<1.2
GATOR 355	355nm	3W	15ns	<1.2
POWERGATOR 1064	1064nm	28W	15ns	<1.2
POWERGATOR 532	532nm	14W	15ns	<1.2
POWERGATOR 355	355nm	10W	15ns	<1.2

Figure 2. Model and specifications overview of the Gator product line.

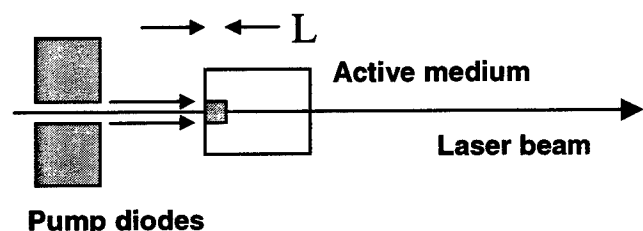
Side-pumped geometry, Figure 3, is used for both the standard Gator and the amplified Power Gator versions of the Lambda Physik DPPS lasers. Side pumping permits the unlimited scaling up of the output power, which is achieved by simply increasing the cross-sectional area of the gain medium in amplifier stages. Necessary small-signal gain is achieved by selecting proper length of the gain medium. This also facilitates generation of short laser pulse in the oscillator. As opposed to this, competitive end-pumped lasers have limited gain per pass, since the gain length (at given ion concentration) is determined by the absorption of the pump radiation. As a general result, these lasers tend to utilize gain materials with greater gain cross-section (e.g. neodymium vanadate), which also have shorter storage time. Such lasers achieve optimum performance at a higher repetition rate (30 to 50 kHz) that, in turn, leads to lower energy per pulse output. Also, limited gain leads to longer pulse length. Since micro machining of hard materials demands high peak intensity, we believe that 10 kHz repetition rate of the Lambda Physik side-pumped Nd:YAG laser, coupled with pulse duration below 20 ns, provides a good balance between micromachining speed (as determined by the number of pulses per unit of time) and precision, as well as feasibility of machining deep, high-aspect ratio structures in hard materials.

### Side-pumping:



Unlimited gain  
 $\text{Gain} = \exp(n\sigma L)$ ,  
 $L$ : Length of the rod,  
 $n$ : ion concentration,  
 $\sigma$ : gain cross-section.

### End-pumping:



Limited gain:  
 $G = \exp(\sigma/\sigma_1)$ ,  
 $\sigma_1$ : pump absorption cross-section.

Figure 3, Side pumping / M.O.P.A. configuration

If the laser is to operate at the second (532nm) or third (355nm) harmonic wavelength, the Gator's design has taken this into consideration with a hands free crystals management system that is part of the laser head and requires no maintenance throughout the entire lifetime of the laser head. The harmonic crystals get replaced along with the laser head about every 20,000 hours further simplifying the maintenance of the system. Replacement of the laser head takes less than an hour and can be performed on site directly by the customer. A trade in program for used laser heads brings down the operating costs from 7 dollars per hour for the PowerGator 1064 down to 4 dollars per hour for the Gator 1064. That equals 20 cents per million pulses for the PowerGator 1064 and 11 cents per million pulses for the Gator 1064 respectively.

### PROCESSING SYSTEM SET-UP AND MICROMACHINED EXAMPLES

As shown in Figure 4, the micromachining optical setup consisted of a shutter, attenuator, quarter wave plate (to create circular polarization) and a focusing lens with the focal length of 50 to 150 mm in the beam path. For the linear cuts, samples were translated with micrometer-accurate XY motion stages operated from a CNC controller. For trepanning, the beam is scanned along a circular path achieved by passing the beam through rotating optical wedges. Other techniques can also be used including a two-axis galvo scanner or using the circular interpolation program on a standard two-axis set of CNC operated motion stages.

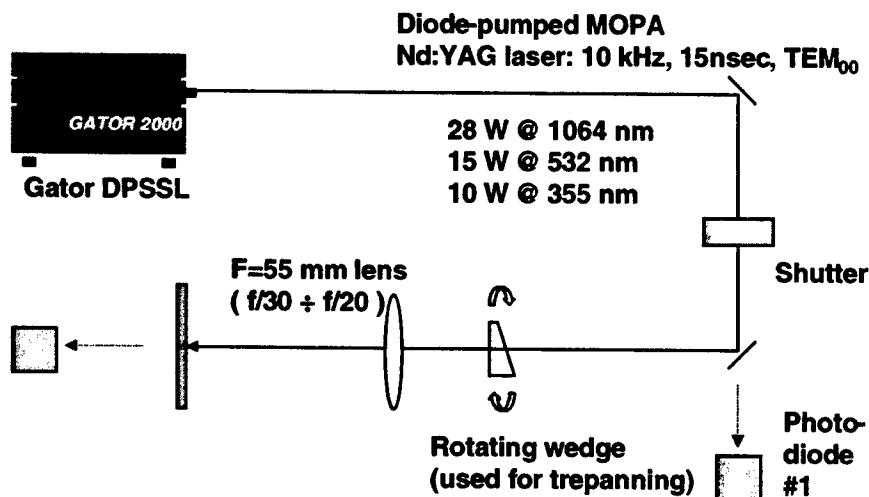


Figure 4. Optical system set-up

Hole drilling can be accomplished by several techniques as shown in Figure 5. The holes in these tests were produced either by percussion drilling or trepanning. With a material removal rate of approximately 1.0 micron per pulse the result is a relatively high ablation rate with a laser pulse rate of 10kHz. For example, 20 micron diameter via holes can be drilled in 625 micron thick silicon wafer at a rate of about 10 holes per second using the "drill on the fly" method. This method uses a trigger signal generated from an encoder attached to the shaft of the servomotor driving the precision X-Y stages. At precise positions the encoder signal causes the laser to fire one pulse. With the high speed stages moving back and forth over the required pattern of holes the drilling rate is increased substantially because the stages do not stop at each hole location.

Peak power is an important processing parameter. Lasers that produce longer pulse lengths will have lower peak power even if the average power is the same. A 15 ns pulse at 10 Watts, 10kHz and higher repetition rates will produce a peak power intensity of about 66kw. Another laser that may be advertised to operate at 10 watts but its pulse width is in the order of 50 ns will only have a peak power of 20 kw. Such a laser can remove the same material but at a rate 3 times slower. A longer pulse width also increases the thermal damage to the substrate by increasing the HAZ (heat affective zone). Using shorter pulses (in the order of 10 ns) allows overcoming these limitations. The optimum condition to achieve proper material ejection is extremely high pressure reached in the vapor plume. Each 10ns-pulse removes a thin layer of material that is typically a few micrometers<sup>1</sup> thick. Heat conduction into parent material is limited to a few micrometers. Therefore, one can increase the intensity of the incident beam for deeper penetration into the material, without the penalty of damaging material at the entrance surface or sidewalls.

Examples of stainless steel and aluminum and copper and diamond materials cut with 355nm, 15 ns and 10kHz laser pulses are shown in Figure 6 and 7. No cutting nozzles or gas assist was used in these tests. Similar results are achieved in other metals such as silver, gold, nickel, steel and aerospace alloys. The hardness of the material or melting temperature seems to have minor effect on the ablation rate.

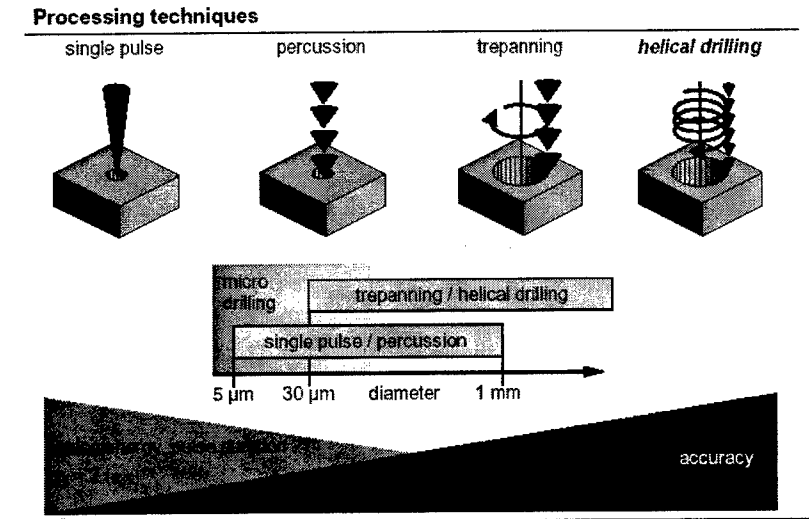
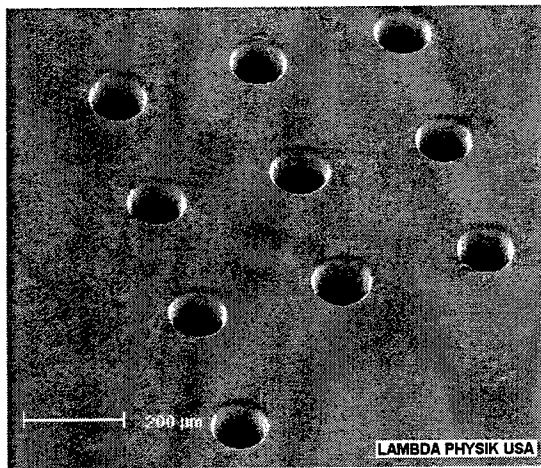
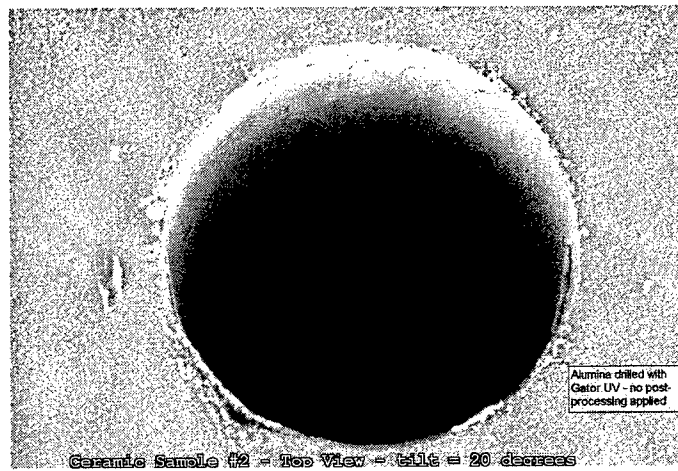


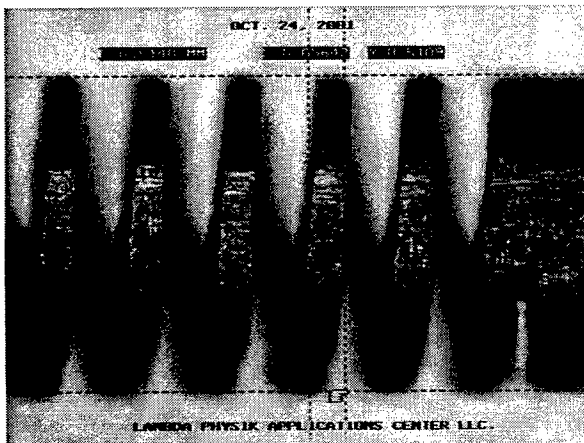
Figure 5. Beam delivery processing options



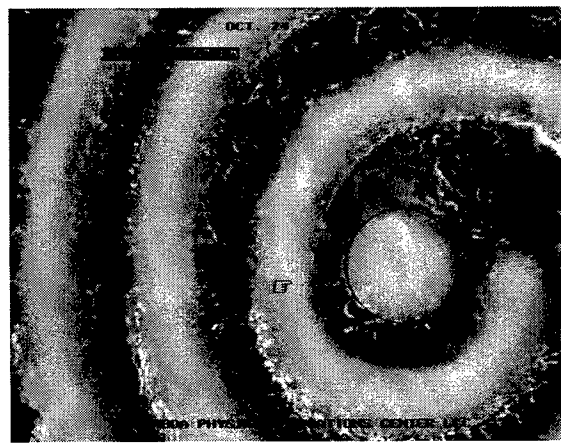
Stainless steel plate 0.55 mm thick



100 micron diameter hole drilled in alumina ceramic



Stainless tube 0.5mm thick



Copper ablated off ceramic - 10 micron line/space

Figure 6. Examples of stainless steel and alumina ceramic parts cut with 355nm, 15 ns and 10kHz pulse rate

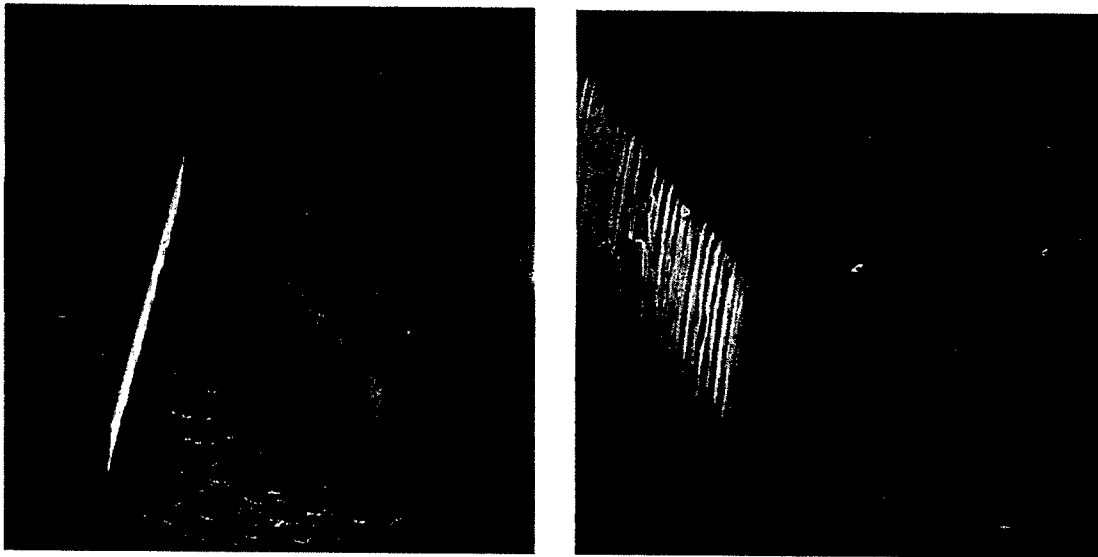


Figure 7. CVD/PCD diamond, 0.31 mm-thick.

### THE EFFECT OF WAVELENGTH ON MICROMACHINING

Selecting the proper laser beam wavelength is important because it can affect the micromachining process as shown in Figure 8. Some materials, like silicon and certain ceramics, are transparent for the conventional Nd:YAG wavelength in the 1  $\mu\text{m}$  region. Although IR lasers can still be used, albeit at higher intensity and with negative effects of larger HAZ, etc. results can be improved by using either 532 or 355 nm wavelength. A second benefit is that at shorter wavelengths the beam attenuation in the plasma and melt droplet "cloud" is reduced. As sample thickness increases it was found that using the shorter wavelength is important especially when high aspect-ratio micromachined features are involved<sup>1</sup>. The geometry of the plume changes when one switch from ablating thin to thick material. The vapor expansion is limited to a narrow channel, whereas at the surface it expands laterally to several times of the beam diameter<sup>6</sup>. Such "single-dimensional" vapor expansion in a deep hole should cause higher particle density and temperature within the plume. An additional source of vapor is caused by the absorption of the laser beam at the walls of the hole. For samples thicker than roughly 0.5 mm it was observed that an increase in minimum fluence was required for drilling, as well as a dramatic wavelength dependence of the average ablation rate.

In summary, for the high aspect ratio holes the wavelength dependence of the average ablation rate is very strong. It becomes clear that shorter wavelengths provides a greater "process window" and much less peripheral damage at the whole entrance for the material thickness approaching 1 mm. The wavelength effect is high because the beam must penetrate a thick layer of dense plasma, which is not present in drilling thin foils.

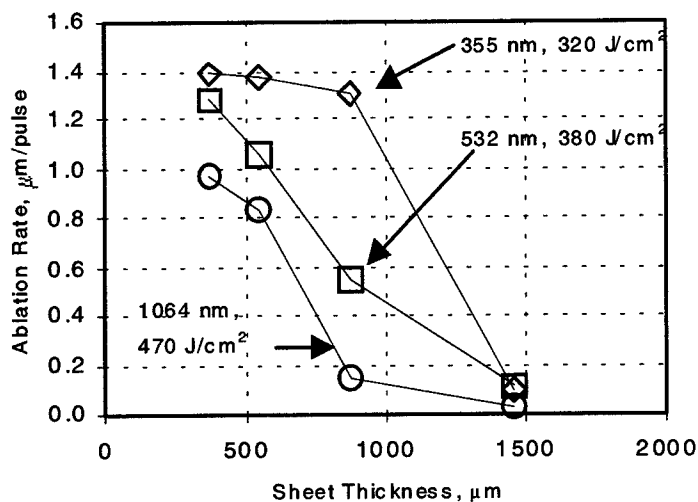


Figure 8. Effect of wavelength in drilling stainless steel.

## PULSE WIDTH CONSEQUENCE ON MICROMACHING

An excellent example showing the advantage of short pulse width ablation is shown in Figure 9 using crystalline silicon with 15-nsec and 25-nsec pulses at the wavelength of 355 nm. The samples were standard commercial available silicon wafers 0.55 mm thick. The laser power used averaged slightly over 2 W, but the repetition rate was fixed at 10 kHz. An  $f=100$  mm lens focused the beam onto the sample surface. The divergence and diameter of the beams for both 15 ns and 25 ns-pulse lasers were equalized and the "best focus" position was established by minimizing the time for percussion drilling. The cross-sections shape is a schematic representation of the holes, as found in the microphotographs. The entrance shape of the hole hints that the plasma plume shapes this part of the hole. This is likely the cause of the extreme tapering off of the holes towards the exit. The amount of taper shown in the holes drilled with longer pulse widths indicates insufficient intensity of the beam as the hole progresses deeper into the silicon. Also the effect of increased laser beam attenuation in the plasma plume is a likely effect. The difference in the thermal diffusion length for these two pulse durations is marginal so a conclusion is that the difference lies in the amount of plasma produced during the pulse. Tests show that the speed of expansion of the plasma plume reach 5 micrometers per nanosecond<sup>5</sup>. This means that the 15 ns pulse penetrates less than roughly 75 micrometer-thick layer of plasma, but the 25 ns pulse passes through up to 125 micrometer-thick layer. The result is that more laser energy is being absorbed in the plasma plume for the longer pulse that further increases its temperature and density. The increase in energy and thickness of the plasma plume causes greater beam attenuation and more material removal via slow melting by the plasma plume after the laser pulse is finished. The tests showed that even relatively small changes in the pulse length (within an order of magnitude) might result in significant difference in the quality of the features.

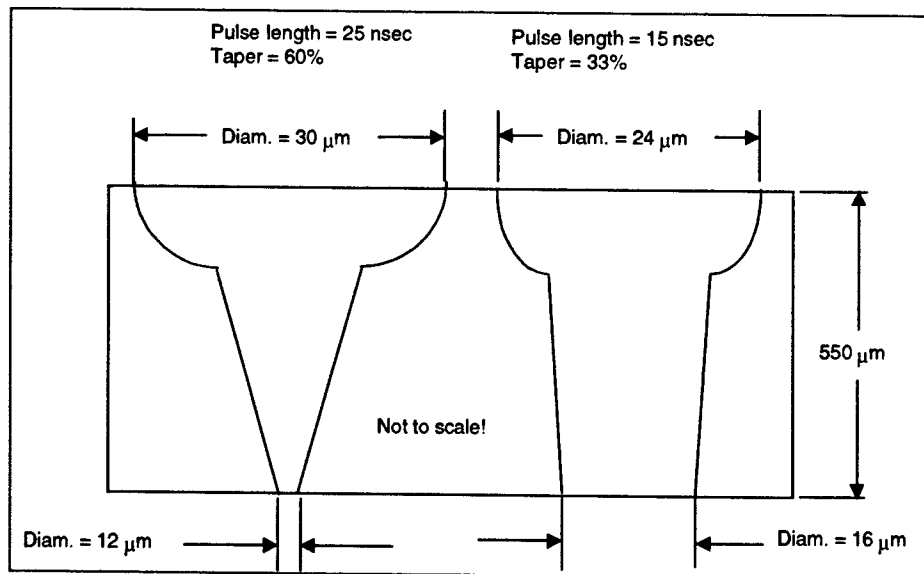


Figure 9. Schematic comparison of percussion-drilled holes drilled at 25 ns and 15nsec pulses at 355 nm.

Pulses in the nanosecond range have an advantage of removing very thin, controllable slices of material with minimum damage to the adjacent areas. Shorter pulses also provide higher peak intensity, which is a major controlling factor in ablating hard materials.

During percussion drilling with longer pulses a greater amount of laser-generated plasma resulted in increased taper and greater amount of silicon oxide being deposited on the sample surface. It was also noted that the exits of the holes were more irregular in shape as compared to almost round exits in holes drilled with shorter pulses.

As shown in Figure 10, one direct commercial benefit of using a laser that produces 15 ns pulse width at 355 nm and 10 kHz results in high quality micromachining of silicon and sapphire. Other hard materials achieve similar high quality results. Holes and slots with minimum to no taper and little to no dross or microcracking can be produced in 670 micron thick silicon at rates over 1.3 mm/second. Sapphire wafers can also be cut with high quality crack and debris free trenches below 25 micron in width.

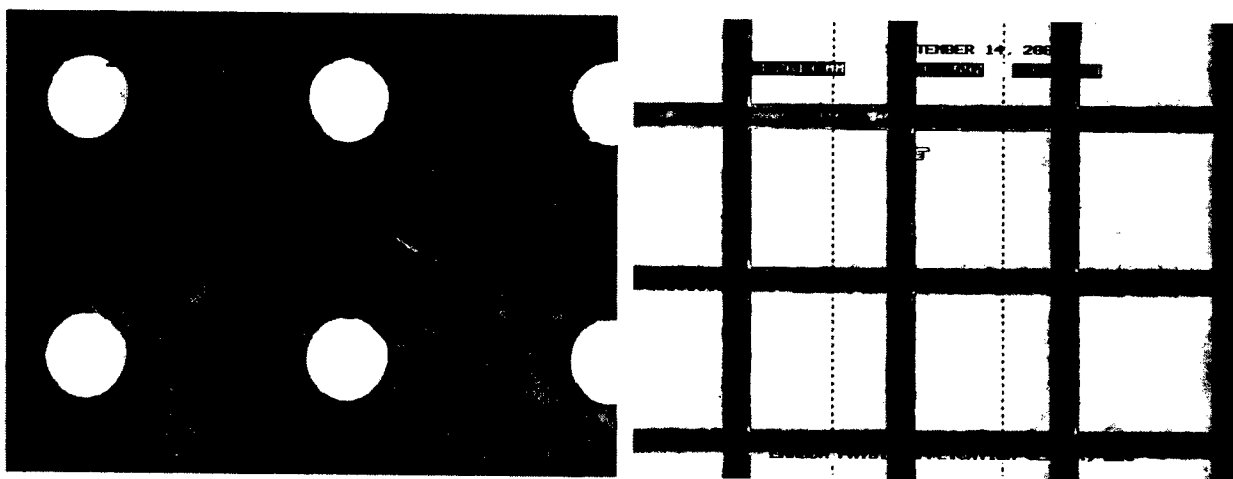


Figure 10. Holes drilled in silicon and trenches cut in sapphire chips are using 355 nm and 15 ns pulse width at 10kHz.



## COMMERCIAL BENEFITS OF AN INDUSTRIAL DPSS LASER

The Gator series of DPSS lasers used to produce the results described in this paper are one of the most compact and reliable nanosecond pulsed industrial lasers on the market. Not only does the Gator offer the industrial customer new level of performance but it also provides a quality of operation not found in current flashlamp or arc lamp pumped Nd:YAG lasers. The main consumable components of these types of lasers are the lamps. The Gator employs the latest state of the art long life diodes to pump the Nd:YAG rod instead of lamps and an advanced harmonic generation crystals management system resulting in a laser that will provide continuous trouble-free operating for over 20,000 hours. The only maintenance required on the laser head throughout its expected lifetime is the periodic exchange of the cooling water and filter plus replacement of the drying cartridge in the laser head which is required about once every 1000 hours of operation.

The PowerGator system is unique in that it can deliver a 10-Watt beam at 355 nm and with a simple program command switch its operation to 1064 nm output at 30 watts.

Since the laser head is assembled in a clean room and hermetically sealed from outside contaminations, the optical components require no maintenance, alignment or tuning during the life of the laser head. This means that in a two-shift operation 5 days per week the laser will continue to provide "on demand" service for up to 5 years. Copper vapor lasers or femto-second lasers which are also advertised for similar micromachining applications are still lab machines without the performance or reliability required to meet the needs for long term industrial service. Complete optical beam delivery systems are simple and can be constructed from available off the shelf components. A typical beam delivery may include a combination of attenuators, fast process shutters, trepanning heads, two axis high-speed galvo scanners, conventional fixed lens focusing lens, zoom telescopes, two wavelength switching capability and combined galvo/fixed focus heads.

## CONCLUSIONS

The market for hard material micromachining lasers with high reliability is quickly growing. This market is driven by the need for a low cost method to perform advanced processing from a wide range of industries including semiconductor, automotive, telecom and microelectronics and medical. Current processing tools are challenged to keep up with new demands from manufacturing and engineering for smaller features and corresponding increase in accuracy and flexibility. Short nanosecond (~10nsec) DPSS lasers can make components that require features to be machined down to a few-micrometers in size, without the unwanted material damage effects associated with the heat transferred from longer-pulse laser sources. This pulse-length effect becomes not only a quality-limiting factor but also limits the processing of certain materials. The high peak-power of the Gator combined with wavelength versatility from IR to UV plus extreme reliability and low maintenance requirements are key to its successful implementation in the most demanding commercial and industrial production environments.

## REFERENCES

1. Govorkov, S.V.; Slobodtchikov, E.V.; Wiessner, A.O.; Basting, D. High-throughput micromachining of steel and ceramics with solid state UV laser, High-Power Laser Ablation III Proceedings of SPIE. Vol. 4065. Editors: Phipps, Claude R. August 2000; pp. 790-800.
2. Govorkov, S.V.; Slobodtchikov, E.V.; Wiessner, A.O.; Basting, D. High-accuracy microdrilling of steel with solid state UV laser at a rate of 10 mm/sec. Laser Applications in Microelectronic and Optoelectronic Manufacturing V. Editors: Helvajian, Henry; Sugioka, Koji; Gower, Malcolm C.; Dubowski, Jan J. Proceedings of SPIE Volume: 3933; June 2000.
3. Abeln, T., Radtke, J., Dausinger, F. High precision drilling with short-pulsed solid-state lasers. Proc. ICALEO'99: November 15-17, 1999, Orlando, FL. Laser Institute of America, Orlando, FL, 1999; pp.195-203.
4. Chang, J.J., Warner, B.E., Dragon, E.P., Martinez, M.W. Precision micromachining with pulsed green lasers. J.Laser Applications. Vol 10: 1998; pp.285-291.
5. Chang, J.J., Warner, B.E. Laser-plasma interaction during visible-laser ablation of metals. Appl.Phys.Letts. Vol. 69: 1996; pp.473-475.

6. Breitling, D., Schittenhelm, H., Berger, P., Dausinger, F., Hugel, H. Shadowgraphic and interferometric investigations on Nd:YAG laser-induced vapor / plasma plumes for different processing wavelengths. Appl. Phys. Vol. A69 [Suppl.]: 1999; pp.S505-S508.
7. Pinho, G.P. Callies, G., Schittenhelm, H., Mueller, R.E., Berger, P., Duley, W.W., Hugel, H. Energy transfer in the laser ablation of metals. Proc. SPIE. Vol. 2991: 1997; pp.21-28.

# Laser Assisted Manufacture for Performance Optimised, Dielectrically Loaded GPS Antennas for Mobile Telephones

Oliver Leisten<sup>\*a</sup>, Jim Fieret<sup>\*\*b</sup>, Ines Stassen<sup>\*\*b</sup>, Phil Rumsby<sup>\*\*b</sup>,  
Patrick McEvoy<sup>\*\*\*c</sup>, Yiannis Vardaxoglou<sup>\*\*\*c</sup>

<sup>a</sup>Sarantel Ltd, <sup>b</sup>Exitech Ltd, <sup>c</sup>Loughborough University

## ABSTRACT

The use of ceramic cores of high dielectric constant is an essential part of a strategy to miniaturise GPS antennas for mobile telephones. The core reduces the guide wavelength of the conducting structures on the antenna, thereby creating a need for high-resolution imaging to maintain very accurate dimensions. It is for this principal reason that a novel laser imaging technology has been developed using a positive electrophoretic photoresist and UV excimer laser mask imaging to produce the conducting features on the surface of the antenna. Furthermore, a significant process challenge in producing this type of antenna concerns the reproducibility of the right-hand circular polarisation performance and the bandwidth over which this can be achieved - which becomes progressively smaller as antenna size is reduced. It is therefore a vital requirement that the antennas have the option to be tuned by a laser trimming process at an automatic RF testing station. A galvanometer controlled Nd:YAG laser spot is used to trim the conductive pattern on the top of the antenna following an RF measurement to characterise the resonant frequencies of the four helical conductors. Results demonstrate the laser imaging and trimming techniques ensure a high-speed method of guaranteeing the antenna performance. The technique is appropriate for other antenna types such as GSM, Bluetooth and Wireless LAN.

**Keywords:** excimer laser, Nd:YAG laser, trimming, resist exposure

## 1. INTRODUCTION

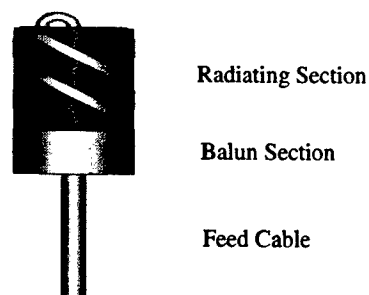
In line with a 1996 US Federal Communications Commission mandate on cellular wireless handset location, manufacturers have turned to integrated Global Positioning System (GPS) receiver solutions to provide the required accuracy resolution. These are the so called "Network Assist" GPS schemes that reduce the time needed to establish a handset position fix by improving the coherence of the tracking process - thereby improving its dynamic range so that it can work in non-open sky environments. However the total time taken remains proportional to the strength of the received satellite signal (preferably >-135 dB) at the antenna. The use of an appropriate antenna for a GPS receiver is very important, as it has to achieve uniform coverage of the satellites in view, reject the cross-polarised multi-path signals and operate efficiently. A sensible choice of antenna for systems, which do not accommodate a large ground plane such as in the case of handsets, is a balanced structure such as the quadrifilar helix antenna [1]. Sarantel has developed a highly dielectrically loaded form [2] of this style to reduce its size with respect to air-loaded antennas. The compact dimensions of contemporary wireless handsets dictate that dielectrically loaded quadrifilar helix antenna must be designed to be small in size, immune to the normal deteriorating effect of holding the handset and resilient to the effects of use in close proximity to the user's head.

This paper describes the characteristics of a novel GPS antenna that is designed to fit into a cellular telephone handset, and also the pivotal contribution of the laser technologies involved in the process to manufacture it. The technical approach that is used in this process is highly innovative because the antenna is a novel product that has been developed and put into commercial production at Sarantel Limited. The imaging and automatic laser trimming tools have been developed and constructed by Exitech Ltd under contract by the owners of the IPR Sarantel Ltd.

\*oleisten@sarantel.com; phone +44 (0) 1933 670560; fax +44 (0) 1933 401155; <http://www.sarantel.com>; Sarantel Ltd, Rutherford Drive, Park Farm I.E. South, Wellingborough NN8 6AQ, UK; \*\*j.fieret@exitech.co.uk; i.stassen@exitech.co.uk; p.rumsby@exitech.co.uk; phone +44 (0) 1933 883324; fax +44 (0) 1933 883334; Exitech Ltd, Hanborough Park, Long hanborough, Oxford OX29 8SL, UK; \*\*\*p.mcevoy@lboro.ac.uk; phone +44 (0) 1509 227081; j.c.vardaxoglou@lboro.ac.uk; phone +44 (0) 1509 222815; fax +44 (0) 1509 227091; Dept. of Electronic and Electrical Engineering, Loughborough University, Loughborough LE11 3TU, UK; <http://www.lboro.ac.uk/departments/el>

## 2. DUAL GPS/MOBILE TELEPHONE OPERATION

The dielectric-loaded quadrifilar helix antenna is designed to receive right-hand circularly polarised energy from the GPS satellite network. Operating at 1.57542 GHz, its non-dielectric-loaded counter part is approximately six times larger. It comprises a zirconium tin titanate (relative permittivity = 36) ceramic puck, 17.75 mm in length and 10 mm in diameter, which acts as a substrate to a thin layer of copper. The image on the right of Figure 1 shows the pair of diagonal resonant loops that are fed at the top of the antenna using a co-axial cable passed through the ceramic.



The lower section of the antenna is a sleeve **balun** (**balanced-unbalanced**). The distance from the cable solder point at the base of the antenna to the balun rim is designed to be  $90^\circ$  in electrical length. While isolating the radiating section of the antenna from surface currents on the application device, it also acts to transition the otherwise inherently unbalanced currents from the cable to a balanced feed for the loop.

Figure 1. dielectric-loaded quadrifilar helix antenna.

The radiating section of the antenna can be considered to be composed of two bifilar resonant loops. Figure 2 shows a plot of the simulated electromagnetic current distribution at the top of the antenna. The labels on each arm indicate the relative angular phase difference of the current from the cable feed point. The current distribution is critical to the antenna receiving the right-hand circularly polarised transmissions from the satellite network, and depends strongly on the precise geometry of the bifilar resonant loops. It is this strong dependence on the geometry that necessitates extraordinary high accuracy on the dimensions of the resonant loops, and necessitates the use of UV laser mask imaging.

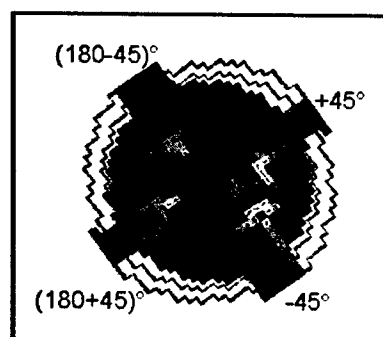


Figure 2. simulated current distribution.

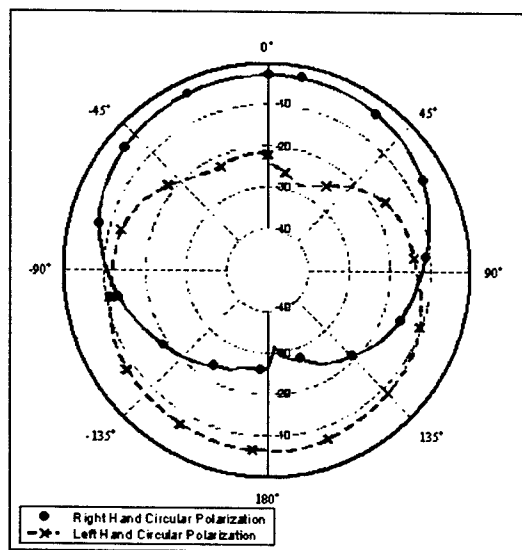


Figure 3. right-hand and left-hand circularly polarised radiation gain pattern of the antenna.

This sensitivity is demonstrated in Figure 3, showing a plot of the right-hand and left-hand circularly polarised radiation gain pattern of the antenna. Both the gain and the broad beam volute shape of the right-hand polarised trace are proportional to the current distribution on the antenna. If the current phase is non-orthogonal between the helices, the gain is reduced and the beam width becomes more directional. Furthermore, the desired 15 dB ratio between the right and left hand polarisations becomes impaired. This can reduce the performance of the antenna to the point where the GPS application receiver could take more time to compute a fix.

The artwork dimensions are referenced to the top surface of the antenna. The required radiating length is proportional to the dielectric constant of the ceramic so that the part handling is manipulated to suit in the laser exposure tool. The performance of the antenna is further guaranteed by using a laser to trim tuning holes in the top artwork to compensate for any current phase distortion.

### 3. ANTENNA MANUFACTURING PROCESSES

#### 3.1 copper/resist coating/resist development

The manufacturing process consists of plating and etching techniques that are well defined industrially for printed circuit board technology but is entirely new when applied to three-dimensional ceramic components. The ceramic pucks are processed in batches (figure 4) through a series of electroless and electrolytic plating baths that deposit a thin layer of copper, which is followed by the application of a UV sensitive electrophoretic photoresist (figure 5). Care is taken to ensure the copper layer is distributed evenly across the ceramic surfaces and that the electrophoretic photoresist is applied with a regulated viscosity. If there is significant uncontrolled variation in the viscosity, the electrophoretic photoresist may not cross-polymerise to a sufficient depth, which can lead to undesired undercut during the etching process.

The parts are then stored in a light safe environment until they are ready to be processed through the UV laser exposure tool. This process is described in more detail below. Once the photoresist pattern has been cross linked in the UV, the parts are developed in bulk through a series of baths. Attention is paid to the process time to ensure that the exposed artwork is sufficiently protected for the etch process.

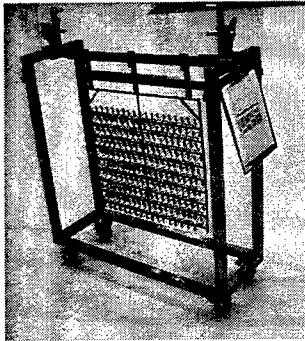


Figure 4. A batch of antenna pucks ready for coating.

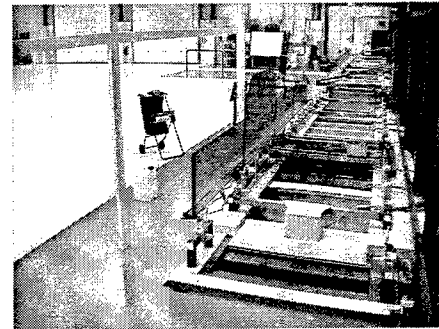


Figure 5. Wet coating line.

#### 3.2 laser exposure tool

The antennas require a copper pattern with extremely tight dimensional tolerances onto a cylindrical surface, with precise match-up with a pattern on the top surface. All pattern dimensions need to be kept to within very tight tolerances, and some dimensions on the cylindrical surface have to be kept to within a few micron (balun height). Various industrial processes, all based on photoresist and etching procedures, have been assessed for their suitability.

Exposure by means of conventional UV light sources such as mercury lamps necessitates the use of a contact mask in the form of a metal sleeve with the required pattern machined into it. The main advantage of this method is the modest capital outlay for the exposure tool, but this is negated by the inadequate accuracy that can be achieved by this method because of the tolerances in antenna dimensions and the requirement for a small gap so as not to damage the photoresist when applying the sleeve. Moreover, the sleeves can be expensive and slow to manufacture, with long lead-time. In order to achieve acceptable cycle times (a few seconds per antenna), multiple sleeves would be required for batch exposure (typical exposure time is a minute or so).

Direct laser machining of the copper is technically possible but extremely slow compared to lithographic techniques, due to the large numbers of photons required for laser ablation compared to cross-linking polymer photoresist molecules. Copper has a high ablation threshold so that the ablation process requires a focussed beam from a fundamental mode Nd:YAG laser together with galvanometer raster scanners. In order to maintain accuracy, the laser will have to operate in TEM<sub>00</sub> mode so that available output power is limited to say 30 W. Such a laser would only process about one antenna per minute. Moreover, the process has a narrow parameter tolerance and is sensitive to even small variations in the thickness of the copper. Excessive exposure of the underlying ceramic to laser radiation can also cause a change in the local dielectric properties which is detrimental to the operation of the antenna. Debris management is also a problem.

Direct ablation of the photoresist is possible, and this process can be made to work considerably faster than copper ablation because the photoresist is much thinner and has a lower ablation threshold. With the highest power industrial excimer laser currently available, the throughput can be an order of magnitude faster compared to copper ablation. The disadvantages of this method are the high capital- and running costs of the excimer laser and, again, debris management.

Exposure on the other hand with a low power UV excimer laser can effectively cross-link the photoresist of one antenna within a very short time (less than one second) so that this process is limited by the efficiency of the robotic handling system and potentially very high throughputs can be achieved. The capital- and running costs of such a laser are modest, and the additional lithographic step that is required (i.e. the removal of the unexposed photoresist) is inexpensive and can easily be integrated into the same bench as the other wet steps of the antenna production. This method was implemented for the antenna production line (figure 6).

The exposure tool therefore uses a high repetition rate UV excimer laser with low pulse energy to expose the photoresist at a radiation dose adequate to expose the photoresist all the way down to the copper and a fluence that is sufficiently low not to cause ablation- or other damage to the photoresist. The thickness of the photoresist and the choice of excimer laser are closely correlated. A program of research was carried out to determine the optimum combination of excimer laser wavelength and resist thickness in order to determine the best compromise between process speed, yield and cost.



Figure 6. From left to right: bare ceramic substrate, copper coating, resist coating, after exposure and development, after copper etching and resist stripping.

A rotary tray containing 24 antenna substrates is manually placed onto an indexing table and a pick-and place robot transfers the antenna substrates onto a spring steel pin which holds the substrate firmly in position through its bore. The base of the pin widens into a cone which, after nickel plating, acts as a mirror to expose the base of the antenna at the same time as the sides. The spring steel pin is mounted on a rotary stage with z-elevator, fixed on top of a high speed linear stage which moves the antenna substrate from the loading to the exposure position. Transfer is via an intermediate position where the height of the antenna top face is accurately measured with an optical sensor and the position of a small notch at the base of the antenna substrate is determined (also with an optical sensor). The notch is necessary because subsequent robotic assembling and soldering operations need alignment to a mechanical feature. The top and side patterns need to be positioned precisely with respect to the notch.

The antenna substrate needs to be exposed to laser radiation on the top and bottom faces and over the whole of its side circumference. In fact it is only the inside of the bore which needs not be exposed. The exposure is done in two steps: one which exposes the top face, and one which simultaneously exposes the side and bottom face. Figure 7 shows the chrome-on-quartz photomask patterns that are used.



Figure 7. Exposed antenna (left), side pattern (middle) and top pattern (right) mask images for GPS antenna.

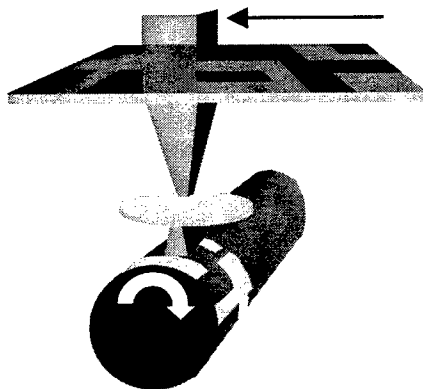


Figure 8. Synchronised mask and antenna motion

The photomask with the side pattern is held on a vertical x-y stage assembly which can be moved in synchronous motion with the rotation stage onto which the antenna substrate is mounted (figure 8). The mask plate is illuminated by a narrow line of laser light which is homogenised along the longer dimension by means of two pairs of cylindrical lenslet assemblies. The mask is imaged onto the side of the antenna by means of a custom-designed high resolution, diffraction limited lens with unity imaging ratio. In order to minimise distortion effects due to eccentricity of the antenna bore this lens has telecentric properties. The antenna is illuminated a few degrees off-axis in order not to expose the photoresist on the top face. The height of the antenna can be adjusted with a z-stage in order to position the pattern at precisely the correct height. The base of the image of the side pattern on the mask plate extends several mm below the base of the antenna in the image plane in order to expose the base of the antenna.

After imaging the side pattern, a pneumatically operated mirror drops into the laser beam which re-directs it through a second optical train for the top face exposure. The top pattern is imaged onto the antenna top face through a separate 1:1 imaging lens with diffraction-limited resolution. Illumination of the mask is achieved by re-sizing the excimer laser beam by means of cylindrical lenses but without homogenisers. The top pattern photomask is held on a linear stage in order to help alignment. Care must be taken to make sure that the side pattern spiral arms match up with the four arms of the top pattern of the antenna. This is done by rotating the antenna by a certain amount after having detected the position of the notch. Small corrections in the rotation on each antenna substrate are automatically carried out according to the measured height of the antenna top surface.

Since both the side and the top pattern photomasks are held on motion stages, the exposure tool can quickly change from one antenna design to another simply by moving to a different pattern in another area of the photomask. Figure 6 shows the various steps in the production process of the antennas, and figure 9 shows the complete laser imaging tool.

After laser exposure, the antenna substrates are dipped into a sodium hydroxide solution to remove the resist from the unexposed areas of the antennas, followed by a copper etching and resist stripping procedures. An automated fabrication line assembles the antennas with a connector pin and matching box (see figure 10).

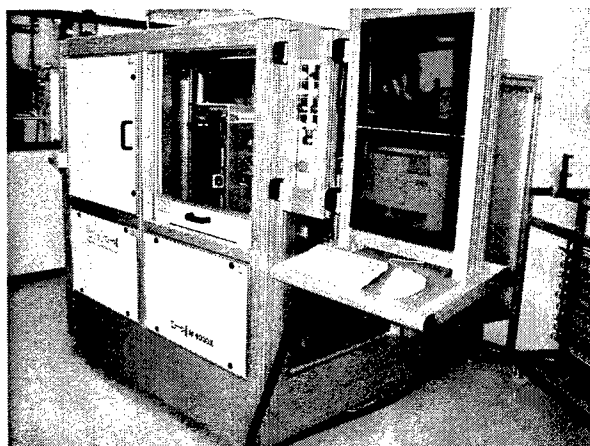


Figure 9. Exitech M4000X excimer laser exposure tool.

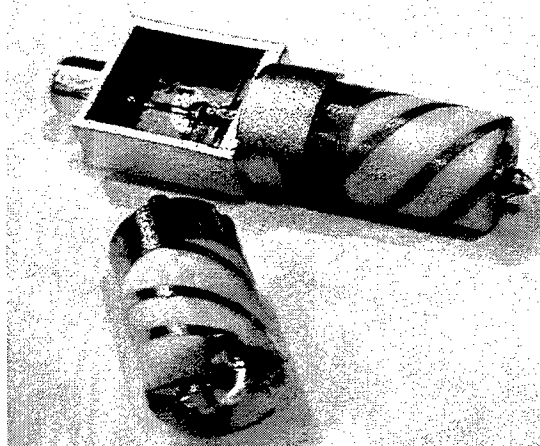


Figure 10. Antennas with (top) and without matching box (bottom).

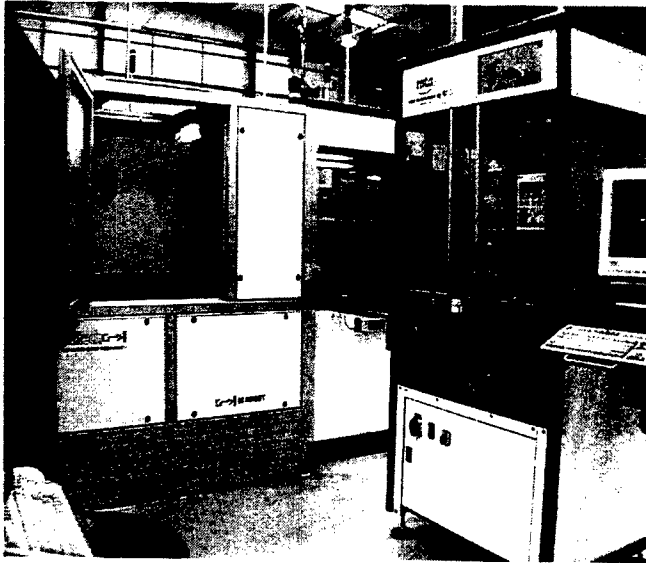


Figure 11. Laser trimming station.

### 3.3 Laser trimming

In order for the antennas to operate at precisely the correct frequency of 1575.42 MHz, within a tolerance of 2 MHz, the majority of antennas produced need small adjustments to the induction loops formed by the copper pattern on the antennas. This trimming requirement exists despite the excellent accuracy which can be achieved with laser imaging of the pattern, and is primarily a consequence of the spread in antenna dimensions, dielectric properties of the ceramic material, and copper thickness and resistivity.

The trimming is carried out with a fundamental mode Nd:YAG laser in TEM<sub>00</sub> mode, resulting in a small laser spot size. The laser beam is focused onto the antenna by means of a flat-field (f-theta) lens, and scanned across the top surface of the antenna by means of an x-y galvanometer in order to ablate small areas of copper.

The laser trimming tool, figure 11, is integrated in a robotic assembly loop which fits the matching boxes to the antennas (this loop is separate from the antenna assembly line). A pick-and-place robot picks up an antenna with fitted matching box and places this in a pneumatically actuated chuck on a high speed linear stage which moves the antenna into the laser-safe trimming tool enclosure through a pneumatically operated door. Once in the trimming position, four RF probes mounted radially around the antenna are moved to close proximity of the antenna perimeter, at the balun level such that each probe is located at the base of each of the four spiral arms. The resonant frequency and balance of the antenna is measured with the probes and a network analyser with specially developed trimming algorithms determines the amount of copper (if any) needed to be removed from each of the four arms of the antenna top pattern. The trimming algorithms were developed by Sarantel specifically for this purpose.

Conventional methods for measuring an antenna pattern require a large screened room with the inner surface of the walls covered in radio frequency absorbing material, in order to simulate free space conditions and to measure the

output from the antenna under test. In the case of the dielectric loaded quadrifilar antenna, this measurement takes about five minutes to rotate the part through 360° in one plane and to plot the measured data for interpretation. While this is the most comprehensive method of measurement, it is not a cost effective solution for a high volume production run. An alternative method for evaluating the antenna performance using capacitive probe measurements to "sniff" the current at the bottom of each of the helices has been developed at Sarantel and implemented in the laser trimming tool. This novel technique is employed to provide a high throughput of parts in a similar fashion to the approach taken to die probing in the integrated circuit industry. Figure 12 shows a schematic section drawing of the probe and where it is pointed at the antenna.

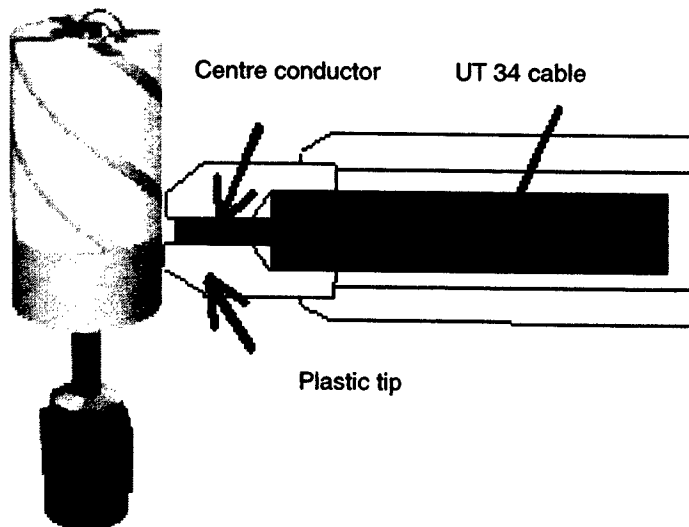


Figure 12. Antenna RF measurement probe.



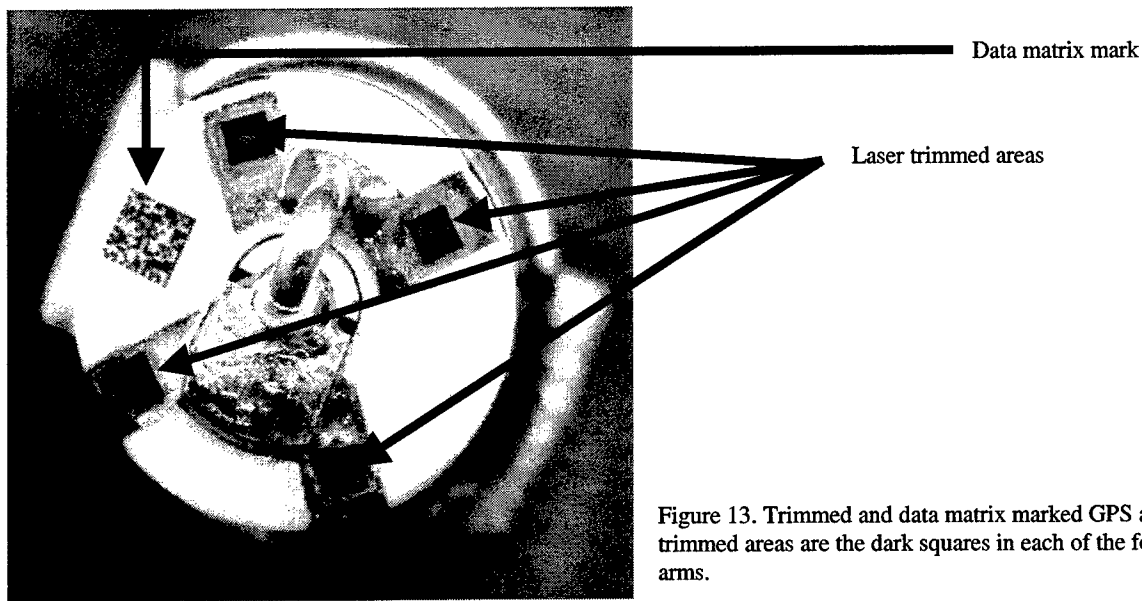


Figure 13. Trimmed and data matrix marked GPS antenna. The trimmed areas are the dark squares in each of the four copper arms.

After the trimming operation, the antenna is measured again with the RF probes and accepted or rejected. All antennas, accepted as well as rejected, are marked with a unique data matrix code that is produced with the same laser as for trimming (figure 13).

## 5. CONCLUSION

We have demonstrated that the laser technology can fulfil a critical role in the high-volume manufacture of small GPS antennas that are suitable for E-911 emergency handset location. The methodology that has been described in this paper is embodied in a manufacturing process that is available for licence from Sarantel Ltd.

## REFERENCES

- [1] Resonant quadrifilar helix design., Kilgus, C.C. Microwave Journal, December 1970
- [2] Miniaturised dielectrically-loaded quadrifilar antenna for Global Positioning System (GPS) Leisten, O.; Vardaxoglou, J. C.; McEvoy, P.; Seager, R.; Wingfield, A. Electronics Letters, v 37, n 22, (Oct 25 2001 2001), p 1321-132

# Effect of Laser Parameters on the Exposure and Selective Etch Rate in Photostructurable Glass

Frank E. Livingston\*, William W. Hansen, Adam Huang and Henry Helvajian

Center for Microtechnology  
The Aerospace Corporation, El Segundo, CA 90245-4691, USA

## ABSTRACT

Photostructurable glass-ceramic materials have received significant attention due to their utility in aerospace engineering and microtechnology. For example, the ability to fabricate structures in glass is important in the design and integration of microscale electronic, optical and fluidic devices. Direct-write pulsed ultraviolet (UV) laser processing techniques have been utilized recently to create patterned three-dimensional (3D) microstructures in a lithium-aluminosilicate glass (Foturan<sup>TM</sup>, Schott Corp.). The direct-write microfabrication process involves the formation of an initial latent image in the glass via UV laser radiation. Thermal-induced ceramization is utilized to develop the latent image into a permanent image. Material removal and microstructure fabrication are then accomplished by preferential isotropic etching of the developed regions.

Precise control of the laser processing parameters is essential to ensure efficient and consistent microstructure fabrication. Unfortunately, detailed information does not exist regarding the influence of the laser characteristics on the exposure and photochemical etch rate in photostructurable glass. The present study investigated the effects of laser power (fluence) on the selective chemical etch rate in Foturan glass. The results will facilitate precise timed-etch procedures for volumetric processing of 3D microstructures in photostructurable glass. Variation of the laser exposure during direct-write patterning affects the etch conditions and permits the concurrent formation of microscale features with markedly different aspect ratios. This direct-write variable exposure processing technique also facilitates the formation of variegated aspect ratio structures on a common substrate following a single batch etch without the need for a complex masking sequence.

**Keywords:** laser microfabrication, 3D fabrication, volumetric patterning, photostructurable glass ceramic, MEMS and microtechnology

## 1. INTRODUCTION

Optical lithography and chemical etching techniques are utilized frequently in the fabrication of traditional microelectromechanical systems (MEMS).<sup>1</sup> These devices require the integration of microscale structures that retain variegated aspect ratios. The aspect ratios of a microfabricated structure depend on numerous optical and chemical properties. For example, the ability to cofabricate large microstructures (>500  $\mu\text{m}$ ) and maximize the processing aspect ratio is influenced critically by the chemical resiliency of the photoresist, the chemical etching rate of the underlying substrate material and the anisotropic character of the etching process. Large aspect ratio structures in MEMS devices are often prepared in bulk silicon using reactive ion etching (RIE)<sup>1</sup> or deep reactive ion etching (DRIE)<sup>2</sup> techniques. These plasma-etching techniques are noteworthy for their effectiveness in reducing undercuts in patterned structures.

However, a major limitation of standard wet chemical and (D)RIE techniques is their inability to cofabricate microstructures with widely different aspect ratios on a common substrate. Variegated aspect ratio structures on a shared substrate may be particularly useful in MEMS fluidic technology and the integration of nanoelectromechanical systems

\* Corresponding author. Phone: 1-310-336-0056; Fax: 1-310-336-5846; E-mail: [Frank.E.Livingston@aero.org](mailto:Frank.E.Livingston@aero.org); The Aerospace Corporation, Mail Station M2/241, 2350 E. El Segundo Blvd., El Segundo, CA 90245-4691, USA.

(NEMS) into MEMS devices. For example, microscopic relief along sidewall and trench structures are incorporated into mesoscopic millimeter- and centimeter-scale MEMS fluidic devices to facilitate mixing and chemistry.

In addition, future complex nanometer-sized sensors, resonators and engineered materials will require the simultaneous integration of NEMS structures within MEMS structures. Developing the capability to adjoin NEMS and MEMS components will provide several system design advantages. One advantage is the ability to isolate physically the NEMS unit from substrate effects. NEMS and MEMS cofabrication will also provide a convenient packaging method to couple adaptively to the larger physical world. Finally, signal amplification from a NEMS device could be enhanced through the localized attachment of a compatible MEMS component.

For MEMS applications requiring concurrent and proximal high aspect ratio and low aspect ratio features, the fabrication solution generally involves the use of an elaborate masking sequence. The sequential masking steps are intended to protect physically the low aspect ratio structures during the long duration etching time needed to form the high aspect ratio structures. An alternative approach concerns the introduction of dopants and impurities into the substrate that selectively alter the local etching rate and permit the concurrent formation of high and low aspect ratio features. A second alternative is to generate the high and low aspect ratio structures on separate substrates. Following preparation, the substrates can be joined or packaged together to merge the variegated aspect ratio structures. Unfortunately, these alternative solutions are time consuming and difficult and expensive to implement.

To address the limitations associated with microprocessing in silicon-based materials, we have focused on patterning and microstructure fabrication in photostructurable glass-ceramics (photosittals or photocerams). Following exposure to ultraviolet (UV) radiation, these photoactive composite materials can undergo controlled devitrification at low temperatures to form a metastable crystalline phase in the amorphous glass.<sup>3</sup> This crystalline phase can then be preferentially and isotropically etched with aqueous hydrofluoric acid (HF) to fabricate microscale structures.<sup>4</sup> Microstructure fabrication in photocerams has typically been achieved using UV lamp lithography with a mask.<sup>5</sup> These photolithographic and masked-etching processing techniques have been utilized to generate 2D patterns and extruded prismatic shapes or 2.5D structures.

The Aerospace Corporation has significantly refined the general processing of photostructurable glass-ceramic materials.<sup>6-8</sup> One major improvement includes the incorporation of pulsed, high repetition rate UV lasers into the patterning process. In contrast to a UV lamp source, the application of pulsed UV lasers has enabled direct-write operations and the fabrication of true 3D microstructures without the need for sequential masking. The UV wavelength of the laser patterning process can also be varied to control the penetration depth within the bulk glass material. Precise control of the optical penetration depth and incident laser fluence has facilitated the fabrication of embedded and interconnected microstructures.<sup>6</sup>

The present study investigated the effects of laser power (fluence) on the selective etch rate in Foturan glass. The results will facilitate precise timed-etch procedures for volumetric processing of 3D microstructures in photostructurable glass. Variation of the laser exposure during direct-write patterning will affect the etch conditions and permit the concurrent formation of microscale features with markedly different aspect ratios. These variegated aspect ratio structures can be realized on a common substrate and released simultaneously following a single batch etch without the need for a complex masking sequence.

## 2. EXPERIMENTAL

### 2.1 General Setup

The direct-write UV laser micromachining experimental setup is shown in Fig. 1a. The micromachining lasers, optical components and sample translation stage were located on a vibrationally-isolated optical table. UV exposure and volumetric processing were accomplished using a diode-pumped, Q-switched Nd:YVO<sub>4</sub> laser (BL6S-106QH, Spectra-Physics). The Nd:YVO<sub>4</sub> laser was equipped with frequency-tripling LBO crystals (HM355-1MMW module) to produce laser radiation at  $\lambda=355$  nm. Typical output power for the Nd:YVO<sub>4</sub> laser operating in Q-switched TEM<sub>00</sub> mode was



**Figure 1.** Photograph of the direct-write UV laser micromachining experimental setup.

~180 mW at a nominal pulse repetition rate of 10.0 kHz and a diode current of 18.0 A. The pulse-to-pulse stability was  $\pm 5.0\%$ . Laser powers were measured using surface absorbing disk calorimeters (PM3 and PM10, Molectron Detector, Inc.). Typical laser pulse durations of  $6.0 \pm 0.5$  ns (fwhm) were achieved in the Q-switched TEM<sub>00</sub> operation mode. The temporal profile of the Q-switched TEM<sub>00</sub> pulse was monitored using a silicon photodetector (ET-2020, Electro-Optics Technology, Inc.).

The incident laser surface power was varied using a computer-controlled circular neutral density (ND) filter (CNDQ-2-2.00, CVI Laser Corp.). The ND filter was coupled to a micropositioning motor that allowed rotation of the filter to  $< 0.1^\circ$ . Consequently, the incident laser surface power could be precisely modulated and dynamically controlled during the direct-write patterning process; i.e., continuously *variable* laser exposure processing. Using the ND filter and microstepper assembly, the laser power delivered to the glass substrate surface could be varied from  $P=0.1$  mW to  $P=30.0$  mW with a resolution of 10  $\mu$ W. The resolution was primarily limited by the sensitivity of the surface absorbing disk calorimeter.

The laser beam was focused on the glass substrate surface using a UV-transparent achromatic 10x microscope objective (LMU-10x-248, OFR). The effective focal length of the microscope objective was  $f=20.0$  mm at  $\lambda=355$  nm. The laser spot diameter was  $\sim 3.0$   $\mu$ m and the confocal parameter was  $\sim 1.0$  mm. The glass substrate sample was positioned on a 10.0 cm diameter vacuum chuck. During direct-write laser patterning, precise translation of the glass sample was accomplished using motorized XYZ microstep positioners under computer control. The XY positioners (310062AT, Daedel/Parker Hannifin) had a total travel range of 15.0 cm and a positional accuracy of  $\pm 0.2$   $\mu$ m/mm of travel distance. The XY bi-directional repeatability was  $\pm 0.02$   $\mu$ m/mm of travel distance. The Z positioner (ZE-10, Danaher Precision Systems) had a total travel range of 25.4 mm and a positional accuracy of  $\pm 0.8$   $\mu$ m/mm of travel distance. The bi-directional repeatability of the Z positioner was  $\pm 0.1$   $\mu$ m/mm of travel distance.

## 2.2 Direct-Write UV Laser Processing

**2.2.1 Photoceramic Material.** The photostructurable glass-ceramic employed in this etch rate study was obtained from Schott Corporation under the trade name Foturan<sup>TM</sup>. This photosensitive material is an alkali-aluminosilicate glass and is comprised of the following admixtures: SiO<sub>2</sub> (75-85%), Li<sub>2</sub>O (7-11%), K<sub>2</sub>O and Al<sub>2</sub>O<sub>3</sub> (3-6%), Na<sub>2</sub>O (1-2%), ZnO (0-2%), Sb<sub>2</sub>O<sub>3</sub> (0.2-0.4%), Ag<sub>2</sub>O (0.05-0.15%) and Ce<sub>2</sub>O<sub>3</sub> (0.01-0.04%). The Foturan glass wafers were 100.0 mm in diameter and 1.0 mm in thickness. Prior to use, the Foturan wafers were cleaned using Liqui-Nox glass detergent (Alconox, Inc.) and deionized water, and rinsed with high-purity acetone (CH<sub>3</sub>COCH<sub>3</sub>, reagent grade >99.6%, J. T. Baker) and methanol (CH<sub>3</sub>OH, anhydrous grade >99.8%, Spectrum Chemical).

**2.2.2 UV Exposure and Latent Image Formation.** The direct-write microfabrication process was initiated via pulsed UV laser irradiation. For Foturan, the photosensitive character is believed to be derived from the oxidation-reduction photochemistry associated with trapped Ce<sup>3+</sup> (admixture Ce<sub>2</sub>O<sub>3</sub>) and Ag<sup>+</sup> (admixture Ag<sub>2</sub>O) ions.<sup>3</sup> These species are stabilized by Sb<sub>2</sub>O<sub>3</sub> in the lithium-aluminosilicate glass host. The UV radiation induces photoionization of the nascent cerium ions ( $\text{Ce}^{3+} + h\nu \rightarrow \text{Ce}^{4+} + e^-$ ). The free electrons can then neutralize nearby silver ions ( $\text{Ag}^+ + e^- \rightarrow \text{Ag}^0$ ) and create a latent image of the absorption event.

To minimize potential contributions from material inhomogeneities and compositional variations, the etch depth and etch rate measurements incorporated a comprehensive and detailed laser exposure pattern. A CAD representation of the laser exposure template employed in this study is shown in Fig. 2. The laser exposure template consisted of eight individual microdiscs for each Foturan wafer. The circular microdiscs were 25.0 mm in diameter and were oriented in a polar array. One microdisc did not contain a laser exposure pattern and was used as a witness sample for the native glass etch rate measurements. The seven additional microdiscs contained an 8x8 laser exposure matrix. This laser exposure matrix was comprised of 64 rectangular regions that were 1000  $\mu\text{m}$  in length and 500  $\mu\text{m}$  in width. These regions were created by rastering the laser beam across the glass sample surface at a constant microstepper velocity of 1.0 mm/s and a laser pulse repetition rate of 10.0 kHz. Each exposed region contained 100 laser raster lines that were spatially offset by 5.0  $\mu\text{m}$ . Each microdisc was also labeled with an identification code and alignment markers. The identification labels were formatted as *Mijk*, where *M* is the glass material (F=Foturan), *i* is the etch time, *j* is the etch trial number and *k* is the exposure wavelength (0=355 nm).

The 8x8 laser exposure matrix corresponded to 16 distinct power levels, where each set of four adjacent rectangular exposed regions received equivalent laser power or exposure. The average incident laser powers used in the present study ranged from  $P=2.0$  mW to  $P=25.0$  mW at a laser pulse repetition rate of 10.0 kHz. These parameters corresponded to an average incident pulse energy of 0.2-2.5  $\mu\text{J}$ . At a microstepper velocity of 1.0 mm/s and a repetition rate of 10.0 kHz, each laser spot area received 30 laser pulses. Incident laser fluences ranged from  $F=0.2$   $\mu\text{J}/\mu\text{m}^2$  at  $P=2.0$  mW to  $F=2.65$   $\mu\text{J}/\mu\text{m}^2$  at  $P=25.0$  mW. Laser powers  $<2$  mW were not used since the native glass etch rate was nearly equivalent to the exposed glass etch rate at lower laser power. Laser powers  $>25$  mW were not employed due to glass fracture and cracking.

**2.2.3 Thermal Processing and Permanent Image Formation.** Development of the latent image into a visible permanent image involved timed heat treatment. Thermal regulation and heat processing was achieved using a programmable furnace (Vulcan 3-550; Ney Corp.). First, the exposed glass substrate was heated from  $T=23.0$   $^{\circ}\text{C}$  to  $T=500.0$   $^{\circ}\text{C}$  at a ramp rate of 5.0  $^{\circ}\text{C}/\text{min}$ . The exposed glass sample temperature was then maintained at  $T=500.0$   $^{\circ}\text{C}$  for 60.0 min. During this heat cycle, silver atoms diffuse and agglomerate to form Ag nanocrystals:  $x\text{Ag}^0 \rightarrow (\text{Ag}^0)_x$ .

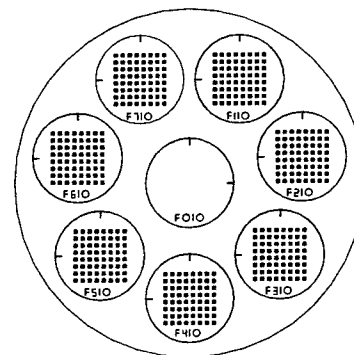


Figure 2. CAD representation of the laser exposure pattern.

Subsequently, the glass substrate temperature was increased from  $T=500.0$   $^{\circ}\text{C}$  to  $T=605.0$   $^{\circ}\text{C}$  at a ramp rate of 3.0  $^{\circ}\text{C}/\text{min}$ . The exposed wafer temperature was then maintained at 605.0  $^{\circ}\text{C}$  for 60.0 min. The pre-formed Ag nanocrystals act as nucleation sites and facilitate the growth of lithium metasilicate ( $\text{Li}_2\text{SiO}_3$ ) crystallites. The size and density of the  $\text{Li}_2\text{SiO}_3$  crystalline phase can be altered significantly by the heat treatment protocol. Preliminary X-ray diffraction (XRD) analysis of the exposed and thermally processed regions suggests that the lithium metasilicate crystallites formed under the present experimental conditions are  $\sim 500$ -1000  $\text{\AA}$  in diameter. Following thermal processing, the Foturan wafers were polished to an optical finish and cut to remove the individual microdiscs.

**2.2.4 Preferential Isotropic Etching.** Material removal and microstructure fabrication are realized by preferential isotropic chemical etching. The three-dimensional exposed pattern is composed primarily of lithium metasilicate crystallites and retains physical and chemical properties (e.g., density, refractive index, expansion coefficient) that are markedly different compared to the native amorphous silicate glass. In particular, the dissolution rate of the crystalline lithium metasilicate phase in dilute aqueous hydrofluoric acid (HF) is  $\sim 20$ -50 times faster compared to the unexposed amorphous phase:  $\text{Li}_2\text{SiO}_3 + 8\text{HF} \rightarrow 2\text{LiF} + \text{H}_2\text{SiF}_6 + 3\text{H}_2\text{O}$ .<sup>3</sup> In the current study, preferential isotropic chemical etching was performed using a 5.0% HF/ $\text{H}_2\text{O}$  solution at room temperature. The aqueous HF etchant was delivered to the glass substrate surface using a high-pressure sprayer assembly. This high-pressure HF sprayer was timer-controlled and contained two eight-nozzle arrays. The nozzle arrays were located above and below the glass sample and could be operated independently to deliver the HF etchant to the desired surface of the glass substrate. The HF sprayer was operated at a nominal flow rate of  $\sim 4.3$  L/min. During the HF etching process, the glass sample was also rotated at  $\sim 20$

revolutions/sec to facilitate uniform HF delivery and efficient removal of the etched products. A new aqueous HF solution was used for each of the seven exposed microdiscs.

### 2.3 Etch Depth and Etch Rate Measurements

Etch depth measurements were performed using a non-contact, white-light optical profiler (NT-2000, Wyko Corp.) equipped with a Mirau interferometric microscope and piezoelectric transducer. The optical profiler was operated in vertical-scanning interferometry (VSI) mode to measure surface feature heights on the glass substrate samples. Vertical resolution of the VSI mode is  $\sim 3$  nm for a single scan measurement and  $<1$  nm for a multiple scan measurement. VSI images were obtained using a 10x microscope objective with an effective field of view of  $1172 \mu\text{m} \times 892 \mu\text{m}$ .

Prior to optical analysis, the native and exposed Foturan microdiscs were coated with a thin gold (Au) or aluminum (Al) metallic film to enhance the surface reflectivity. The Au and Al metallic films were deposited using an evaporative metal source operated under high vacuum ( $\sim 1 \times 10^{-6}$  Torr) conditions. The thicknesses of the Au and Al coatings were 2000 Å and 1700 Å, respectively. A 100 Å chromium (Cr) interlayer was utilized to promote adhesion of the metal film to the underlying Foturan glass substrate. These metal coating thicknesses were negligible compared with the measured etch depths that ranged from  $\sim 3 \mu\text{m}$  to  $\sim 440 \mu\text{m}$ .

The native and exposed etch depths were measured by using VSI scanning techniques to optically profile the witness and processed glass samples as depicted in Fig. 3. The witness sample corresponds to a Foturan microdisc that has undergone thermal treatment, polishing and metal coating. The processed sample corresponds to a Foturan microdisc that was exposed to patterned laser irradiation at  $\lambda=355$  nm, thermally processed and polished, etched chemically with a

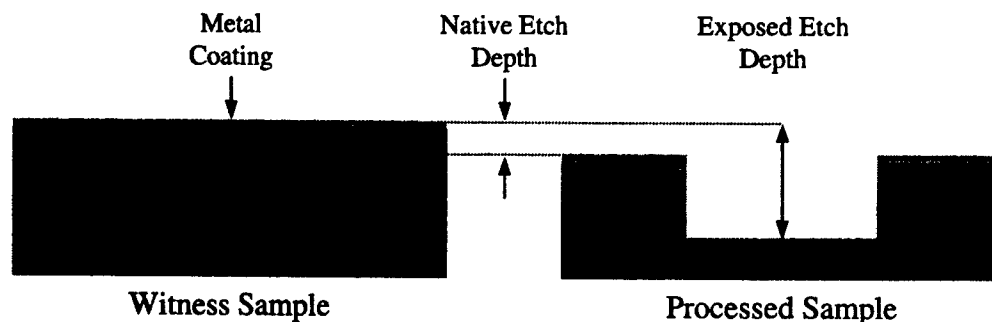


**Figure 3.** Schematic representation of the vertical-scanning interferometry technique used to measure the native and exposed etch depths in Foturan glass.

5.0% aqueous HF solution and coated with a reflective metal film. The native etch depth was measured by simultaneously scanning a witness sample and a processed sample. The native etch depth was then calculated from the height difference between a surface region on the unexposed and unetched witness sample and an unexposed surface region of the processed sample. The exposed etch depth was determined by scanning an exposed rectangular region on a processed sample. The exposed etch depth was then calculated from the height difference between the top surface and the bottom trench surface of the exposed microdisc. The reported exposed etch depth was corrected for the contribution from the native etch depth.

### 3. RESULTS

#### 3.1 Laser Exposure Patterns

Figure 4a shows a photograph of a 100.0 mm diameter Foturan wafer following UV laser exposure and thermal processing. The laser exposure template corresponding to the eight-microdisc array is clearly evident. The 8x8 matrices on each of the seven exposed microdiscs were created using equivalent power or fluence levels. The microdisc located in the center of the polar array was not exposed to laser patterning. This unexposed microdisc was used as witness sample in the native etch depth and native etch rate measurements. An enlarged view of an individual Foturan microdisc following laser exposure and heat treatment is shown in Fig. 4b. The power levels used to create the laser exposure pattern are labeled as P1-P16 in Fig. 4b and ranged from 2.0 mW to 25.0 mW.

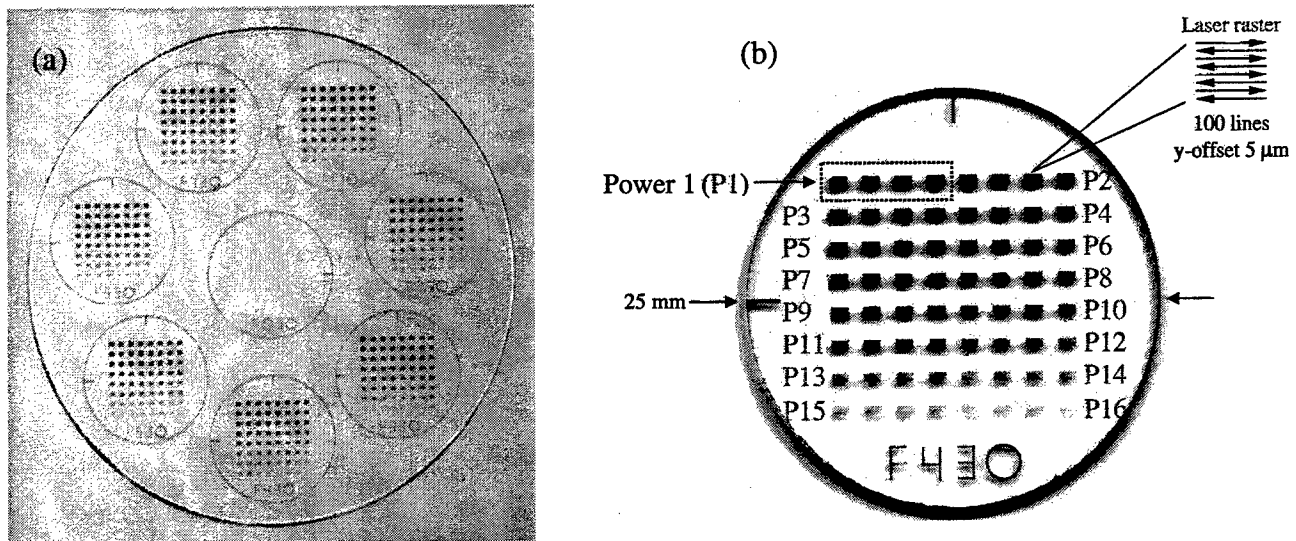


**Figure 4.** (a) Photograph of a Foturan wafer following variable laser exposure and thermal processing. (b) Scanned image of an individual Foturan microdisc extracted from the master wafer.

#### 3.2 Etch Rate Results

Figure 5 shows the etch depth versus etch time for native unexposed Foturan. The unexposed glass samples were etched in 5.0% HF/H<sub>2</sub>O at T=23.5 °C. The native etch depths ranged from ~3.0 μm at t=5.0 min to ~16.0 μm at t=28.0 min. The native etch rate was determined to be  $0.62 \pm 0.06$  μm/min at an etching temperature of T=23.5 °C. Each data point in Fig. 5 represents the average etch depth obtained from the VSI analysis of 30 locations on three separate Foturan microdiscs. The solid line represents a linear least-squares regression fit to the etch depth data.

The etch depth versus etch time for exposed and processed Foturan at selected incident laser powers is displayed in Fig. 6. The incident laser powers ranged from P=2.5 mW to P=25.0 mW at a pulse repetition rate of 10.0 kHz. The etch depths varied from 3.5 μm at t=5.0 min to 25.0 μm at t=23.0 min for a low laser exposure power of P=2.5 mW. In comparison, a high laser exposure power of 25.0 mW produced etch depths that ranged from 96.2 μm at t=5.0 min to 439.5 μm at t=23.0 min. Each data point in Fig. 6 represents the average etch depth derived from 60 VSI measurements. The solid lines in Fig. 6 represent linear least-squares regression fits to the etch depth data.

The data presented in Figs. 5 and 6 can be recast in the form of an etch rate ratio which is defined as: etch rate ratio = (exposed etch rate / native etch rate). Figure 7 shows the etch rate ratio versus incident laser power and reveals two distinct laser processing regimes. For low incident laser powers ranging from P=2.0 mW to P=6.0 mW, the etch rate ratio increased linearly versus power with a slope of  $5.8 \pm 0.4$  mW<sup>-1</sup>. In this low power regime, the etch rate ratio varied from 1.2:1 at P=2.0 mW to 23.3:1 at P=6.0 mW. The second laser processing regime corresponds to incident laser

powers ranging from  $P=10.0$  mW to  $P=25.0$  mW. In this high power regime, the measured etch rate ratio remained constant at  $\sim 30:1$ .

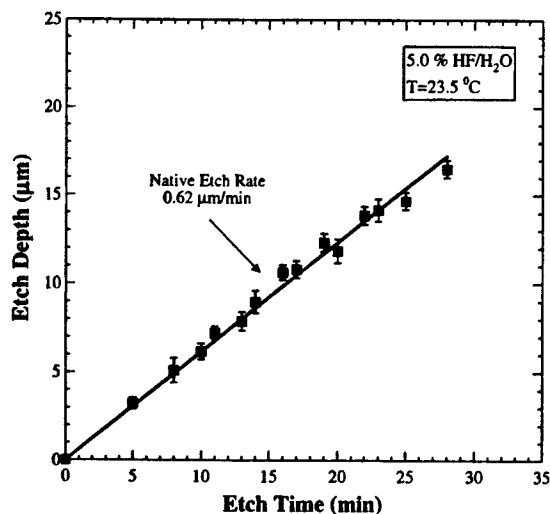


Figure 5. Etch depth versus etch time for native unexposed Foturan.

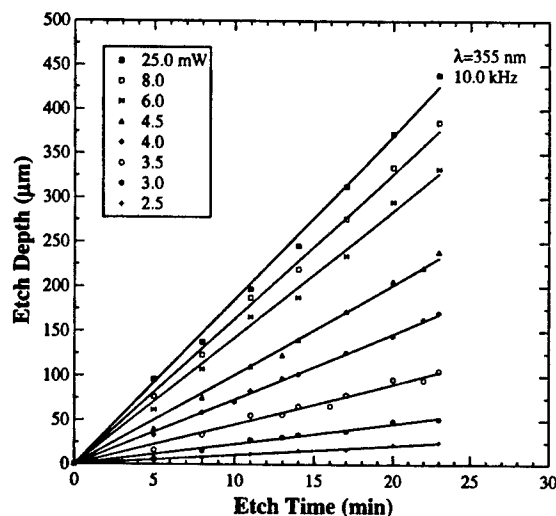


Figure 6. Etch depth versus etch time for exposed and processed Foturan at various incident laser powers.

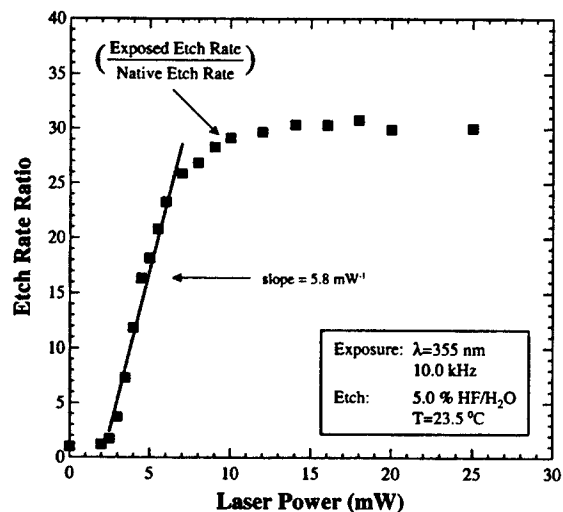


Figure 7. Etch rate ratio versus incident laser power for Foturan. The laser spot diameter was  $3.0 \mu\text{m}$ .

the diameter of each set of circles was increased by  $400 \mu\text{m}$  to yield a total diameter for the Fresnel lens assembly of  $2.10 \text{ mm}$ . The incident laser powers used to generate the permanent image pattern in Fig. 8a varied from  $P=4.5$  mW to  $P=15.0$  mW at a pulse repetition rate of  $10.0 \text{ kHz}$ . These power levels corresponded to etch rates that ranged from  $10.0 \mu\text{m/min}$  to  $18.7 \mu\text{m/min}$ .

## 4. DISCUSSION

### 4.1 Sample Microstructures Realized Using Variable Laser Exposure Processing

To illustrate the utility of the direct-write variable laser exposure technique, the etch rate results presented in Fig. 7 were implemented in the fabrication of several novel microstructures. Figure 8 shows the controlled fabrication of a Fresnel-type lens in Foturan glass. The laser exposure pattern employed to create the Fresnel lens consisted of five sets of concentric circles. Each set of concentric circles was patterned using a different selected laser power level.

A photograph of the developed permanent image pattern in the Foturan substrate prior to chemical etching is provided in Fig. 8a. The center region was comprised of 100 concentric circles that were spatially offset by  $5.0 \mu\text{m}$ . Each of the four outer sets of circular steps consisted of 40 concentric circles that were also spatially offset by  $5.0 \mu\text{m}$ . Consequently,



A photograph of the fabricated Fresnel lens structure following preferential HF etching for  $t=40.0$  min at  $T=23.5^\circ\text{C}$  is displayed in Fig. 8b. The total depth of the inner circular region of the Fresnel structure was  $\sim 700\text{ }\mu\text{m}$  and the ledge heights ranged from  $\sim 60\text{ }\mu\text{m}$  to  $\sim 400\text{ }\mu\text{m}$ . These dimensions were consistent with the incident laser powers and the absolute etch rate and etch rate ratio results shown in Figs. 5-7. The microscale features contained in the Fresnel lens structure were created concurrently utilizing variable laser exposure techniques combined with a single batch etch procedure. In contrast to traditional etching techniques, the fabrication of these features did not require the use of an intricate masking sequence.

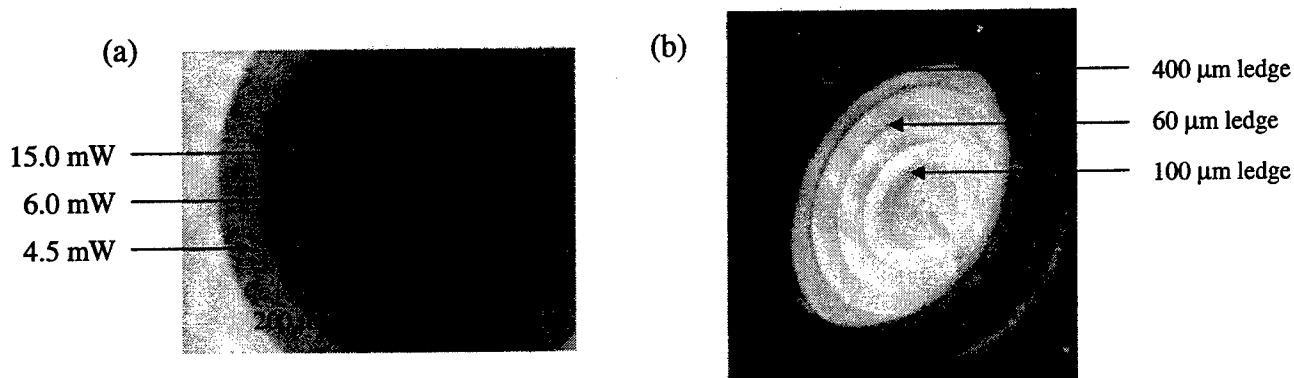


**Figure 8.** Photographs of the Fresnel-type lens structure following (a) variable laser exposure at  $\lambda=355\text{ nm}$  and thermal processing and (b) preferential HF etching for  $t=40.0$  min at  $T=23.5^\circ\text{C}$ .

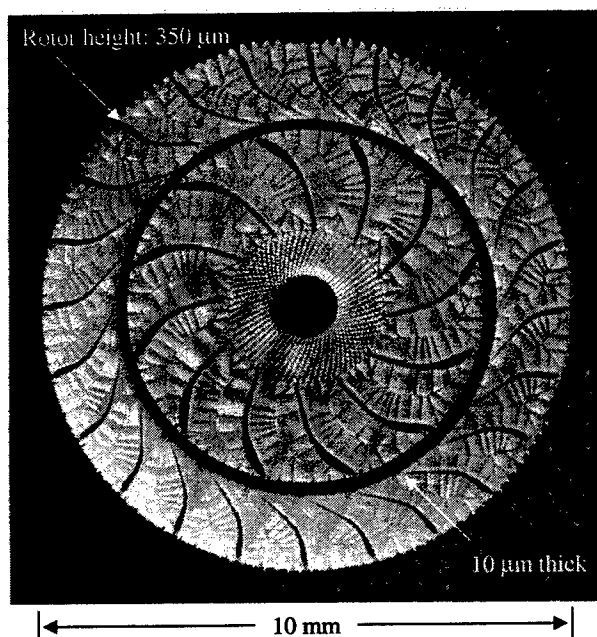


**Figure 9.** Photograph of a complex 3D multi-segment turbine fabricated using direct-write variable laser exposure processing.

The direct-write variable laser exposure technique has also been applied to fabricate microturbine structures for a miniature micropower generator. A photograph of a complex 3D multi-segment turbine prepared in Foturan is shown in Fig. 9. The outer diameter of the microturbine assembly was  $\sim 10.0\text{ mm}$  and the supporting base height was  $\sim 300\text{ }\mu\text{m}$ . The outer and inner microturbine structures contained 24 and 12 rotor vanes, respectively. The vane heights were  $\sim 350\text{ }\mu\text{m}$  and the vane thicknesses varied from  $\sim 10\text{--}20\text{ }\mu\text{m}$ . Figure 9 further reveals that the variable laser exposure technique can be utilized to create simultaneously high aspect ratio ( $\sim 35:1$ ) and low aspect ratio microscale features with complex texturing and multi-faceted surfaces.

## 5. CONCLUSIONS

The selective chemical etch rate of UV laser-exposed and thermally processed Foturan glass was shown to be strongly dependent on the incident laser dose and power. Controlled variation of the laser exposure and etch rate was integrated into a direct-write processing scheme. The unique combination of direct-write volumetric laser patterning and variable exposure techniques provides a powerful analytical tool for creating true 3D microstructures with markedly different heights and aspect ratios. These microscale features can be fabricated concurrently on a common substrate and realized in a single batch etch without a masking sequence. The variable laser exposure method also facilitates rapid prototype processing and pattern and component uniformity.

## ACKNOWLEDGMENTS

The authors gratefully acknowledge the financial support of The Aerospace Corporate Research Initiative and Dr. Howard Schlossberg at AFOSR (MIPR025203553). The authors also thank Mr. Mark E. Ostrander of the Fabrication and Technical Support Department for cutting, polishing and coating the Foturan glass microdiscs and Mr. Paul M. Adams of the Materials Processing and Evaluation Department for performing the XRD analysis.

## REFERENCES

1. M. Madou, *Fundamentals of Microfabrication*, CRC Press, New York, 1997.
2. J. Bhardwaj, H. Ashraf, and A. McQuarrie, "Dry Silicon Etching for MEMS," *Proceedings of the Symposium on Microstructures and Microfabrication*, Montreal, Quebec, Canada, 1997.
3. A. Bereznoi, *Glass-Ceramics and Photo-Sitalls*, Plenum Press, New York, 1970.
4. D. Hulsenberg, R. Brunsch, K. Schmidt, and F. Reinhold, *Micromechanische Bearbeitung von Fotoempfindlichen Glas*, *Silikatechnik*, **41**, 364, 1990.
5. T. R. Dietrich, W. Ehrfeld, M. Lacher, M. Kramer and B. Speit, "Fabrication Technologies for Microsystems Utilizing Photo-Etchable Glass," *Microelec. Eng.* **30**, 497, 1996.
6. P. D. Fuqua, D. P. Taylor, H. Helvajian, W. W. Hansen, and M. H. Abraham, "A UV Direct-Write Approach for Formation of Embedded Structures in Photostructurable Glass-Ceramics," *Mat. Res. Soc. Symp. Proc.* **79**, 624, 2000.
7. W. W. Hansen, S. W. Janson, and H. Helvajian, "Direct-Write UV Laser Microfabrication of 3D Structures in Lithium-Alumosilicate Glass," *SPIE Proc.* **2991**, 104, 1997.
8. J. Brannon, J. Greer, and H. Helvajian, "Laser Processing for Microengineering Applications," *Microengineering Aerospace Systems*, H. Helvajian, Ed., The Aerospace Press, El Segundo, 1999.

# Laser plasma emission of small particles in different gas atmospheres

Alexander Andreev<sup>a,b</sup>, Toshitsugu Ueda<sup>a</sup>, Muneaki Wakamatsu<sup>a</sup>

<sup>a</sup>)Yokogawa Electric Corporation, Tokyo, 180-8750 Japan

<sup>b</sup>)Institute for Laser Physics, St. Petersburg 193232, Russia

## ABSTRACT

The problem of laser pulse interaction with small solid particles (SSP) in a gas atmosphere when detecting its parameters is a serious one in industrial and environmental applications. Previous investigations have shown the possibility of using the laser induced breakdown method. This method is very sensitive, but for a particle size of less than 0.1  $\mu\text{m}$  the damage threshold of the solid target is very close to the breakdown point of pure gas. At breakdown, a small volume of dense hot plasma emits radiation by which the size and material of particles can be detected.

We used an analytical model, simulation code and experiments to analyze this radiation and found that the emitted intensity varied with laser, gas and particle parameters. The increased dependence of SSP plasma emission rate on initial particle volume permits this method to be used for measuring small particle size by using emitted line spectrum at the late time stage.

Keywords: small particle, gas atmosphere, pulse laser, plasma, radiation, measurement

## 1. INTRODUCTION

Laser-induced breakdown (LIB) of gases has been the subject of a number of studies on plasma generation. It has been observed in many studies that the threshold for generating shielding plasma in the presence of a solid is significantly lower than the threshold for clean gases (see for example<sup>1,2</sup>). First, the dependence of aerosol breakdown on its size was predicted<sup>1</sup> and then clarified<sup>3,4</sup>. The particle breakdown threshold value is greatly influenced by particle material, particle diameter, laser wavelength, intensity and pulse duration.

The problem of measuring small solid particle (SSP) size is important for industrial and environmental applications. Previous investigations have shown the possibility of using the laser breakdown method for such detection. The sensitivity of this method is a thousand times higher than that of conventional methods such as ICP and MIT<sup>5</sup>. However, when the size of a particle located in gas is less than 0.1  $\mu\text{m}$ , the damage threshold is very close to the breakdown point of pure gas. After breakdown, there is a small volume of dense hot plasma that emits radiation in lines and continuum. This study set out to determine the threshold intensity required to generate dense plasma when interacting with SSP suspended in gas and its emission. We analyzed this radiation by experiment, analytical model and simulation code, and found that the emission intensity varied depending on the laser type and plasma parameters including initial particle size.

## 2. EXPERIMENTAL SET-UP

Figure 1 shows a block diagram of the prototype particle calibration system<sup>5</sup>. A commercially available flash-lamp excitation Nd:YAG laser was used. The maximum repeated frequency of the laser was about 100 Hz with pulse duration of 5.8 ns and pulse energy of 10 - 50 mJ. We used a 50-mm focal length lens to focus the laser. A commercially available generation device was used for uniformly distributing particles in the atmosphere without condensing them. Standard particles generated by the particle generation device were led through a pipe to the breakdown cell. The pulse laser light was focused in this cell and generated LIB. The light generated by breakdown was led to a monochromator and recorded by a streak camera with timesharing spectrum. The data in the streak camera was read by a computer and processed. The time resolution of the streak camera was less than 10 ps.

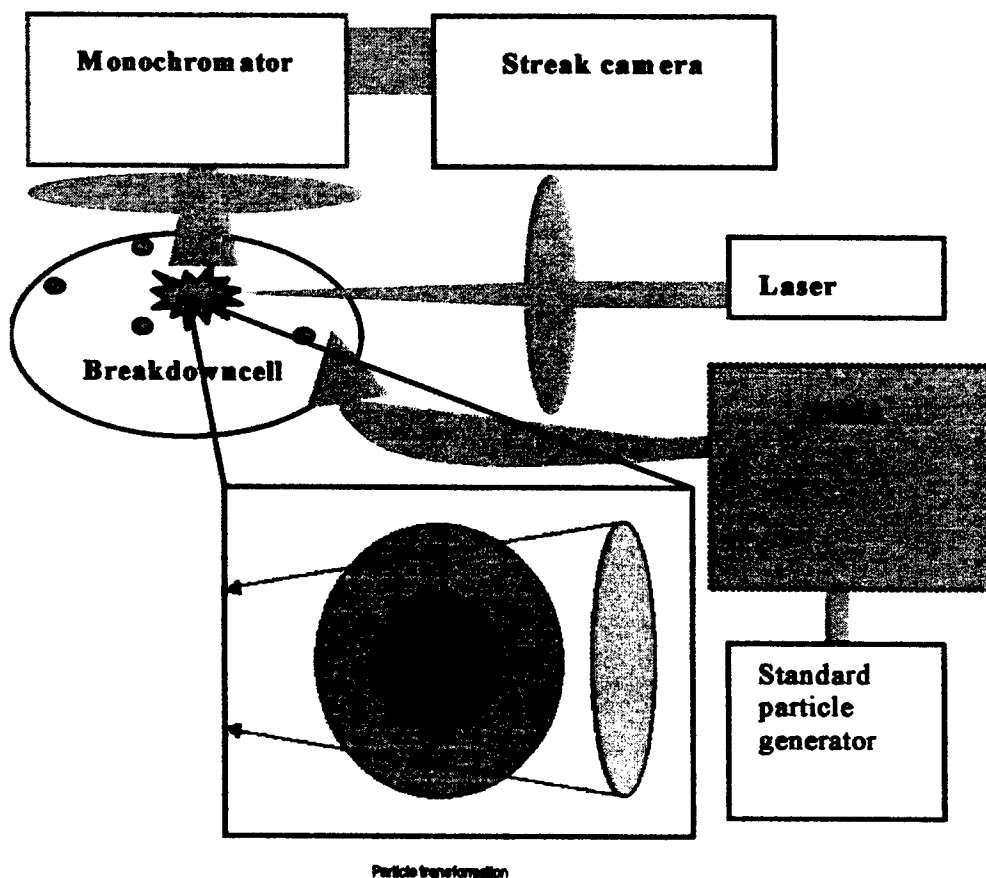


Figure 1. Particle detection system.

### 3. COMPUTER CODE AND NUMERICAL SIMULATIONS

The developed simulation code includes the following physical processes: propagation of a heat wave inside matter, hydrodynamics of gas atmosphere and plasma by two-temperature approximation, thermo heating, absorption of laser radiation, thermal radiation emission and absorption by gas and plasma.

We consider that gas matter consists of two subsystems: the subsystem of heavy particles (molecules, atoms and ions), and the electron-oscillator subsystem which consists of thermal energy of electrons, molecular energy of oscillation and dissociation and energy of electron excitation and ionization of atoms and ions. We suppose that at any moment each subsystem is in equilibrium determined by own temperature and gas density. The energy of heavy particles is the sum of the energies of movement and rotation of its components. The energy of the systems changes due to collisions of electrons with heavy particles and due to movement and rotation channels. We also take into account electron thermo-conductivity and energy transformation by radiation emission and absorption of the electron oscillation subsystem. We used table data for the equilibrium thermodynamic and optics properties of the gas<sup>12</sup>. The equations are solved numerically by the methods of<sup>7,8</sup>.

### 4. PLASMA EMISSION

In paper [9] we considered the main processes of SSP LIB. The first step of laser pulse interaction with SSP is particle heating and evaporation by laser radiation. For a small spherical particle we obtained the laser intensity required to heat and vaporize this particle. The breakdown threshold laser intensity was found also. As our particle is located in gas, we cannot exceed the breakdown threshold of pure

gas. We checked our theory by our and other experimental data. The experiment was done using PSL particles located in air, but simulation of the values was calculated using carbon particles, and the experimental and theoretical results agreed with each other<sup>9</sup>.

During laser breakdown (and after, if the duration of the laser pulse is longer than the breakdown time), the electron concentration in the particle vapor rises rapidly and at some point in time the plasma frequency can reach and even exceed the laser frequency. At some distance from the particle center, there is a resonant point at which the absorption coefficient increases greatly.

After LIB the entire focal volume of the gas and particles breaks down and we must consider radiation from this complex area. From the large initial SSP density, its radiation will be more than air radiation initially, but due to the huge volume difference the Bremsstrahlung radiation of air will increase very fast after the radius of PP has doubled. In this case, we should analyze the line emission of elements other than those of gas. We will consider the late stage of the process when emission from SSP plasma exceeds gas plasma emission, because we investigated the early stage previously<sup>9</sup>.

#### 4.1 Simulation results

To calculate the plasma emission of SSP and gas we used the code described in<sup>10</sup>. From simulations regarding LIB SSP in gas, we obtained the following findings:

- Evaporation through laser irradiation starts from the surface of SSP and the volume increases.
- The evaporated material is quickly ionized if the laser intensity exceeds the breakdown threshold.
- The PP absorbs laser energy while the laser pulse continues and the temperature rises; the temperature then decreases slowly after the pulse.
- Absorption is determined first by absorption of the solid and at that moment the gas is transparent. The PP size is close to that of SSP, and has resonance. There is sufficient growth in absorption if  $T_e$  is high enough.
- After the surrounding particle gas is ionized by particle radiation, it absorbs much laser light in the "light absorption wave" regime<sup>1</sup>.
- In the early stage at time  $< 0.1$  ns, emission from the vapor plasma exceeds air radiation.

An example of the simulation results is shown in Fig. 2, showing the density and temperature distributions of the interaction area at 100 ns for carbon particles of initial size 100 nm in air at 1 atm pressure. We see that even at this moment, a strong shock wave propagates into gas but then attenuates quickly. Most of the radiation is emitted from the area near the contact boundary between the particle gas and air. This area spreads up to the distance of the shock wave head.

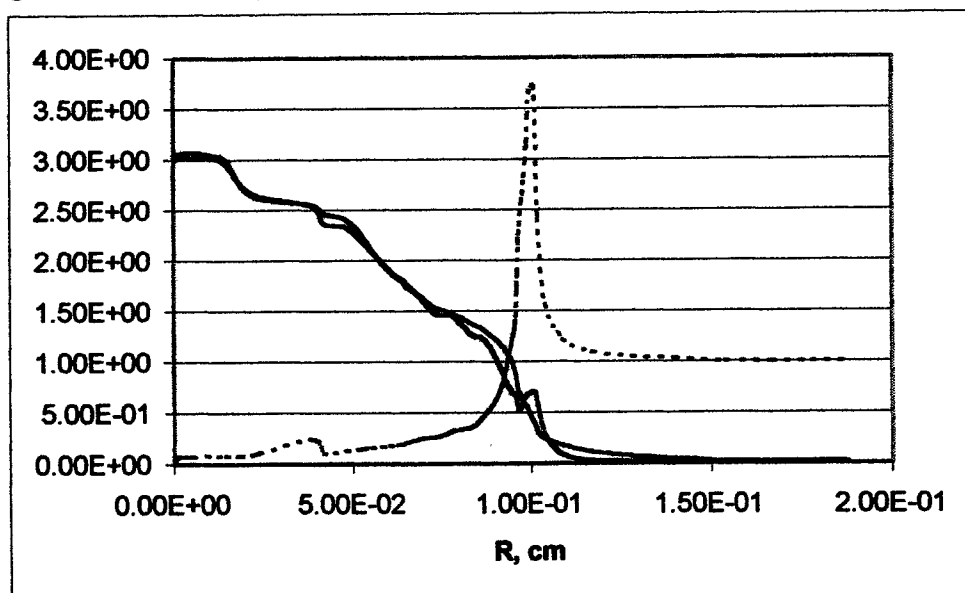


Figure 2. Density (dash line) and electron and ion temperature (solid lines) distributions of interaction area at the moment 100 ns for carbon particle with initial size 100 nm in air at 1 atm pressure; laser intensity 200 GW/cm<sup>2</sup>, pulse duration 5.8 ns.

Main factors influencing the emission produced by the particles and ambient atmosphere are:

- 1) Changes in the vaporized amount by plasma shielding
- 2) Changes in plasma temperature by the absorption of laser radiation
- 3) Changes in the plasma expansion during and after the laser pulse

The increase in the emission intensities in the rarefied atmosphere is related to the first factor. The plasma temperature is higher for denser conditions due to the second factor. The slower decay rate of the temperature is related to the third factor. Plasma confinement by the surrounding atmosphere prevents fast expansion of plasma.

The calculated maximum shown in Fig. 3, in which the line emission intensity changes as a function of the ambient pressure, is explained by the above mechanisms.

The differences in emitted intensities in Ar (red curve) and air (blue curve) can be explained by the differences in densities, thermal conductivities and absorption coefficients of the gases. The line's radiation of energy of quantum  $\epsilon \approx 2$  eV and  $\epsilon \approx 5$  eV has almost 5 times more absorption in air than in Ar<sup>13</sup>. This is related to the molecular structure of air. There is also only vapor cooling by radiation and thermal conductivity after 100 ns when the shock wave has attenuated. Gas thermal conductivity increases with its temperature and pressure, especially after breakdown because of the coefficient of plasma conductivity. Therefore, particle vapor cools faster when ambient gas pressure is higher.

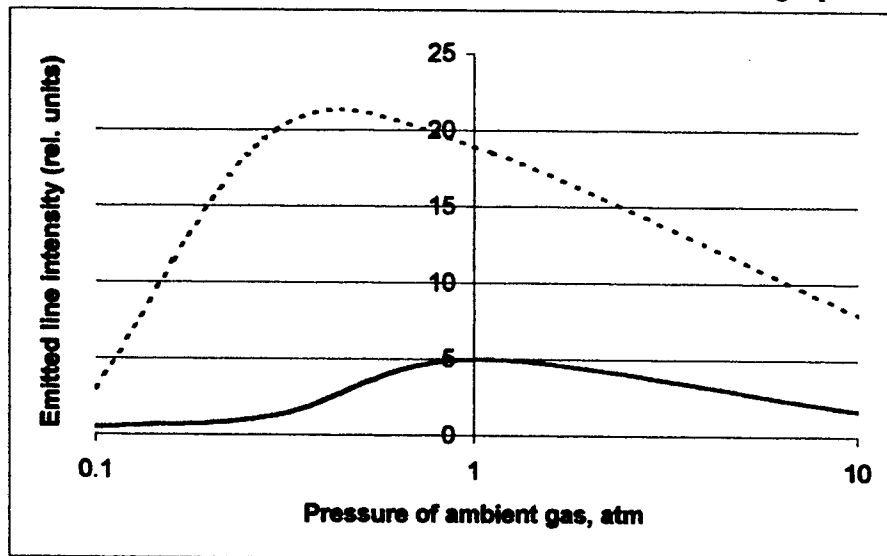


Figure 3. Calculated dependence of emitted line intensity on the pressure of ambient gas (dash curve - Ar, solid curve - air) for PSL particle of diameter 100 nm.

Figure 4 shows the dependence of  $E_r$  on initial particle size  $r_0$ , where  $E_r$  is total energy emitted in the line spectral range [4.7, 5.1 eV] and integrated in space at the moment  $t = 100$  ns.

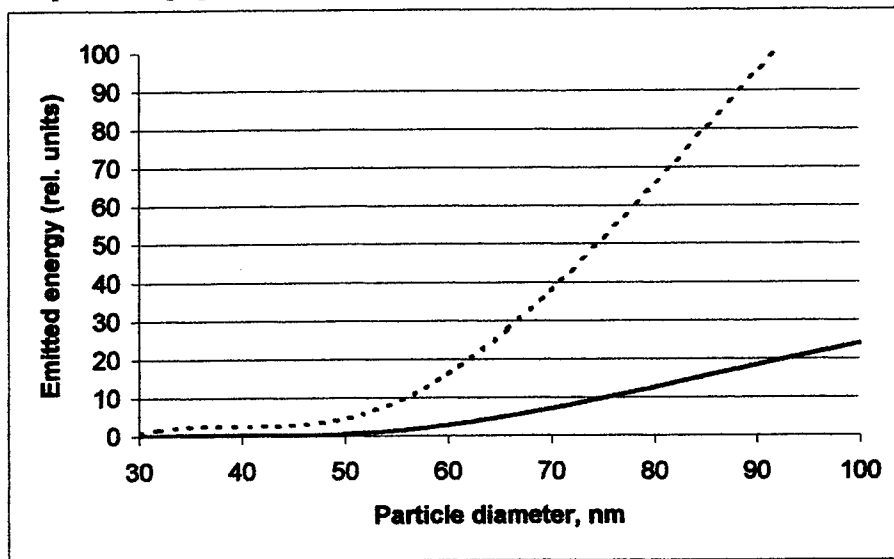


Figure 4. Calculated dependence of  $E_r$  on initial particle size of PSL particle in air of 1 atm (dash curve) and 0.1 atm (solid curve) pressure.

#### 4.2 Experimental results and comparison with theory

In the measurements, we observed the spectral line of Na (D line), a component of salt. Our results proved that the intensity of the line emission is greatly affected by ambient pressure and the type of surrounding gas<sup>9</sup> and the experimental results correlate closely with our simulation and analytical model<sup>10</sup>. Figure 5 shows the results of testing the average diameter of salt particles and the total emission energy of the Na D-line. These results show that the eventual size of particles that can be measured at present is approximately 30 nm. The results of the simulation and model approximation are slightly different due to the limitations of our models.

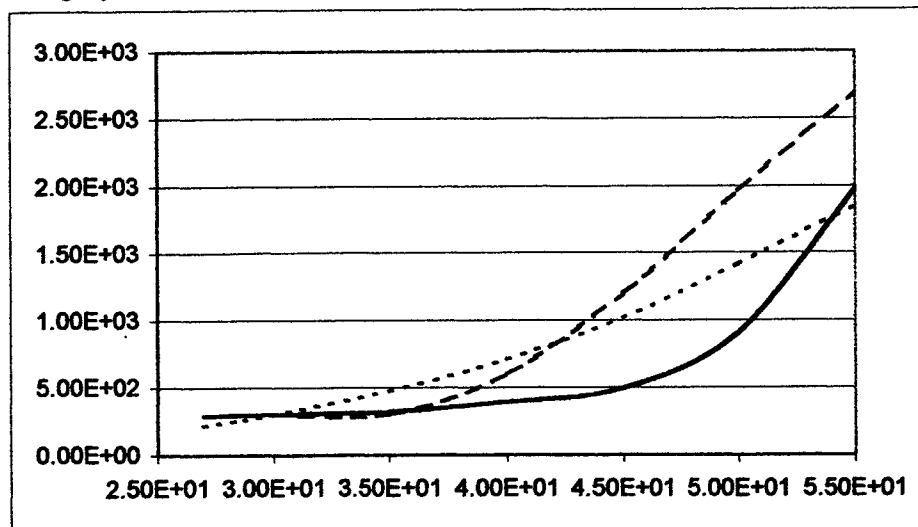


Figure 5. Dependence of  $E_r$  emitted energy, in the spectral range [2.05, 2.15 eV], at the moment  $t = 100$  ns, on initial particle size (in nm) for Na particle in Ar at 0.3 atm pressure. Here: dash curve – experimental data, dots – simulation results, solid – model approximation.

## 5. CONCLUSION

We analyzed the line emission of particle plasma after laser breakdown by experiment, and found that the emission intensity varied depending on the laser type and plasma parameters including initial particle size.

We developed an analytical model and simulation code to calculate laser pulse interaction with small solid particles in a gas atmosphere. During the interaction, the surrounding particle gas was ionized by particle plasma radiation and absorbed much laser light. Thereafter, the total light emission from gas exceeded the emission from plasma particles from a large gas radiated volume, but the line emission from particle plasma permitted the target material to be detected at a late stage of the process. The increased dependence of SSP plasma line emission rate on initial particle size permits this method to be used for measuring particle size for particle diameters of less than 100 nm.

## ACNOLEDGEMENTS

This work was supported by the R&D Institute for Photonics Engineering, the Manufacturing Science and Technology Center, and the New Energy and Industrial Technology Development Organization.

## REFERENCES

1. Yu. P. Raizer, Laser-induced discharge phenomena: "Studies in Soviet Science," NY, 1977.
2. T. Kitamori, K. Yokose, K. Suzuki, T. Sawada, *Jpn. J. Applied Physics*, **27**, No. 6, pp. L983, 1988, S.I. Anisimov, *Sov. Phys. JETP*, **27**, p. 182, 1968.
3. G.H. Canavan and P.E. Nielsen, *Appl. Phys. Lett.*, **22**, p. 40, 1973.
4. D.C. Smith, *Journal of Applied Physics*, **48**, No. 6, p. 2217, 1977.
5. T. Ueda, H. Hayashi, A.A. Andreev, et al., *The 4 Symp. APMT*, p. 142, 2000.
6. A.A. Andreev et al., *Probl. Nauchn. Priborostr.* **3**, p. 884, 1993.
7. A.A. Samarskii, V.G. Popov: "Numerical schemes of gas dynamics," M., Nauka, 1975.
8. A.P. Golub, *Journal Calculation Math. & Math. Phys.*, **23**, p. 142, 1983.
9. A. Andreev, T. Ueda, M. Wakamatsu, *Proc. of SPIE*, **3935**, p. 139, 2000.
10. A. Andreev, T. Ueda, M. Wakamatsu et al., *Proc. of SPIE*, **4350**, p. 161.
11. Y. Iida, *Spectrochimica Acta*, **45B**, p. 1353, 1990.
12. I.B. Kosyrev et al., *Astronom. Vestnik*, **30**, p. 316, 1996.
13. NIST Atomic Spectra Database, 1999.



# Xe(He,Kr)-I<sub>2</sub>(Cl<sub>2</sub>) GLOW, BARRIER AND CAPACITIVE DISCHARGE EXCILAMPS

Victor F. Tarasenko, Mikhail I. Lomaev, Dmitry V. Shitz, Victor S. Skakun  
Institute of High Current Electronics, 4, Akademichesky Ave., Tomsk 634055, Russia  
E-mail: VFT@loi.hcei.tsc.ru

## ABSTRACT

In the present paper, Iodine, XeI\*, XeCl\*, KrCl barrier, glow and capacitive discharge excilamps have been studied. Xe-I<sub>2</sub>, He-I<sub>2</sub> or Xe-He-I<sub>2</sub> excilamps emit at iodine monatomic resonance lines in the range of 180 – 210 nm, and on XeI\* molecule band ( $\lambda_{\text{max}} = 253$  nm). Besides that, by varying pressure and mixture composition, it is possible to control relation between iodine monatomic lines and XeI\* molecule band radiation intensity. The efficiency level is up to 12 %. The lifetime in sealed-off excilamps was more 1000 h. It is shown that at barrier KrCl and XeCl excilamps excitation by short (2÷2,5  $\mu$ s) unipolar or bipolar voltage pulses the efficiency is higher than by sine pulses excitation. Output at  $\lambda \sim 222$  nm up to 100 W and at 308 nm up to 75 W from barrier discharge excilamps was obtained. Presence of filaments occurs to be a necessary condition to obtain high efficiency since in that case a demanded level of excitation specific power is being achieved. Radiation pulse delay relatively to excitation in the conditions of homogeneous discharge probably demonstrates low efficiency of KrCl\* and XeCl\* molecules formation at a low level of excitation power. Output at  $\lambda \sim 222$  nm up to 190 W and at 308 nm up to 91 W from glow discharge excilamps was demonstrated.

**Keywords:** Iodine, XeI\*, XeCl\*, KrCl excilamps; barrier, capacitive and glow discharges; efficiency

## 1. INTRODUCTION

In recent decade, interest in design and development of new types of UV and VUV spontaneous radiation sources, in particular excilamps, has considerably grown. These sources are essentially simpler in design and operation as compared to lasers, and emit in wider range of wavelengths. The most efficient excilamps on transitions of rare gas dimers R<sub>2</sub>\* and rare gas monohalides RX\* can find wide industrial application. Therefore improving of their output parameters is of great importance. An active interest has been expressed in creation of efficient mercury free gas discharge sources of spontaneous radiation in UV and VUV spectrum ranges [1,2]. For the most part the papers of this direction are devoted to study more efficient Xe excilamps radiating in the main at B-X transition of X<sub>2</sub>\* dimer ( $\lambda = 172$  nm) [3-5 and others]. Nevertheless, in a row of applied problems radiation at the range of 180 – 210 nm is demanded which may be obtained using iodine excilamp operating on iodine vapors or mixture of iodine with inert gases [6-9]. In the radiation spectrum of such lamps at low pressure the lines of iodine atomic transitions at  $\lambda = 183, 185, 206$  nm; and at high pressure the bands of molecule I<sub>2</sub> ( $\lambda = 342$  nm) and corresponding exciplex molecules are dominating. In the case of using Xe – I<sub>2</sub> mixture the most intensive B-X band of the molecule XeI\* ( $\lambda = 253$  nm) coincides with the resonance line of mercury atom that is rather promising from the point of view of mercury free luminescent lamps creation.

Barrier discharge excilamps are the most simple and rather promising UV and VUV radiation sources. A great many papers has been devoted to such lamps investigation of these lamps [3,4, 17-24]. Working temperature of excilamp influences on efficiency and is dependent on cooling conditions and average pumping power. Thus, the question concerning the efficiency is rather important both from the point of view of obtaining definite values of specific and integral energy parameters of excilamp and from the lifetime increase viewpoint. For barrier discharge excilamps excitation, the sine voltage generators are traditionally used. Characteristic values of conversion efficiency of the power input into operating media into optical radiation made as 10-15 % [17,18]. This is in correlation with the results obtained for the glow discharge excited excilamps [25-27]. Earlier in [20, 21] we noted the advantage of using sine form of the voltage pulse of 22 kHz frequency in comparison with a short high voltage pulse with 50÷100 ns duration for excitation of Xe<sub>2</sub>, Kr<sub>2</sub>, KrCl and XeCl excilamps by a barrier discharge. According to [21], the main reason to obtain low efficiency in the case of short high voltage pulses formed by a thyatron TGI 10000/25 based generator is first of all decrease of

energy input into gas discharge plasma relatively to the storage one. Secondly, considerable overvoltages occur at the gas discharge gap leading to non-optimal from the viewpoint of forming exciplex molecules values of presented normalized electric field strength  $E/p$  in the gas discharge plasma ( $E$  is electric field strength,  $p$  is pressure). Along with this, in recent papers [3, 4] efficiency increase of  $\text{Xe}_2$ -barrier discharge excilamp at short (risetime is about 250÷750 ns) excitation as compared to sine pulse excitation were demonstrated. To the authors of [3] opinion, increase of efficiency observed occurs owing to forming of optimal function of electron distribution by energy and minimization of elastic and non-elastic energy losses of electrons in the processes not leading to excimer molecule  $\text{Xe}_2^*$  formation. It notes in paper [4] that for  $\text{Xe}_2$  excilamp efficiency increase it is necessary to form a homogeneous (diffuse) discharge with essentially lower electron density as compared to the electron density characteristic for filaments. Discharge homogeneity is being provided due to steep front of voltage pulse. It is known that formation of exciplex and excimer molecules differs [28]. That is why there are grounds to believe that the conditions corresponding to obtain maximal efficiency may also differ, for e.g., for  $\text{Xe}_2^*$  and  $\text{KrCl}^*$  excilamps.

In this paper, output parameters of excilamps with different geometry pumped by continuous glow discharge, capacitive discharge, barrier discharge are presented. The work is devoted to investigate of  $\text{Xe}(\text{He})\text{-I}_2$  excilamps excited by glow and capacitive low-pressure discharges, to study of the form, excitation pulse power and other discharge parameters influence on barrier  $\text{KrCl}$  and  $\text{XeCl}$  excilamps efficiency and to investigate of  $\text{KrCl}$  and  $\text{XeCl}$  excilamps excited by glow discharge.

## 2. EXPERIMENTAL SET-UP AND METHODS

The experiments with iodine were conducted with the excilamps of cylindrical construction made of quartz with transmissivity at  $\lambda = 200$  nm not less than 70%. In a row of cases in order to increase the operating lifetime a special box with iodine in a solid phase connected to the discharge volume was used. The temperature of the box as the most cool zone of the lamp determines the concentration of iodine vapours in the operating mixture. In Figs 1 and 2 the constructions of glow discharge and capacitive discharge excilamps are presented. Electrodes, bulb walls, discharge zone, and the box with crystalline iodine are shown by numerals 1, 2, 3, and 4, correspondingly. The Fig. 1a,b depicts constructions of the glow discharge excilamps, correspondingly, in zones behind electrodes and in the middle part of the bulb. The Fig. 2 shows the capacitive discharge excilamps. For excitation there were used high voltage generators with pulse repetition rates from 10 to 100 kHz for the capacitive discharge excilamps, and the set step-up transformer providing alternating and rectified voltage for the glow discharge excilamps.

In the experiments with barrier discharge, traditionally constructed water cooled coaxial lamps made of quartz were used [19]. Gas gap was 6÷9 mm, excilamp length was varied from 5 to 75 cm. High voltage was applied to external electrode made of metallic grid. Two generators were used for excitation, one of those provided obtaining of sine voltage with frequency of 17 kHz, and the second generator provided unipolar and bipolar voltage pulses with duration at the base about 2  $\mu\text{s}$ , rise- and faltime duration was of about 250 ns or about 1  $\mu\text{s}$  at p.r.r. 10÷100 kHz. Principal electric circuit of the second generator is presented in Fig. 3.

In the experiments with glow discharge coaxial and cylindrical lamps made of quartz were used. Diameter of the tubes was 20, 55 mm and its length was up to 150 cm. The gap between the tubes in coaxial excilamp was from 5 to 20 mm. The electrodes of glow discharge excilamps were coupled to DC power supply providing discharge current up to 1 A and voltage across the discharge gap up to 10 kV. AC power supply voltage was used in some experiments.

Excitation power for barrier and capacitive discharge was determined by two methods, using well-known method of volt-coulomb loops [13, 14] and by determining voltage at gas discharge gap taking into account voltage fall at lamp capacity. In the second case there was a possibility to determine a instantaneous power value and deposited excitation energy for the instant moment of time. For the glow discharge excilamps discharge current ( $I$ ) and voltage across the excilamps ( $U$ ) were monitored using DC or pulsed milliammeters and kilovoltmeter. Input power was calculated as  $P=I \times U$ .

The working mixtures were prepared just in the lamp volume with successive inlet of halogen ( $\text{Cl}_2$ ,  $\text{I}_2$ ) and inert ( $\text{Xe}$ ,  $\text{Kr}$ ,  $\text{Ar}$ ,  $\text{Ne}$ ,  $\text{He}$ ). Registering of current pulses, voltage, and also time behaviour of radiation pulses were realised using, correspondingly, current shunt, voltage divider, FEK-22 and oscilloscope TDS-220. In a row of cases, for the lamp capacity voltage fall determining, an additional capacity was installed in series into circuit. Measurements of radiation intensity in the needed spectral range were made using calibrated photodiode FEK-22 SPU and set of light-filters with definite transmitting coefficients at different spectral ranges using known method [15]. Besides that, the radiation spectrum of the lamp in the range of 200 ÷ 600 nm using special spectral complex including monochromator MDR-23

and FEU-100 was measured. Integral picture of the discharge lighting was photographed using a digital camera.

### 3. EXPERIMENTAL RESULTS and DISCUSSION

#### 3.1 Xe-I<sub>2</sub>, He-I<sub>2</sub> or Xe- He-I<sub>2</sub> excilamps

The radiation intensities in the range  $200 \text{ nm} < \lambda < 255 \text{ nm}$  for operating glow discharge and capacitive discharge excilamps with operating mixtures Xe - I<sub>2</sub>, He - I<sub>2</sub>, He - Xe - I<sub>2</sub> at equal partial pressures of He and Xe, Ar - I<sub>2</sub> and I<sub>2</sub> were estimated. The pressure of the active media of the glow discharge excilamp which the maximum radiation power level was provided was typical for a glow discharge [16] and made  $\sim 0.1 \div 20$  Torr. Pressure increase resulted in decreasing of radiation power and worse discharge operating due to contracting occur. Low pressures as  $< 0.1$  Torr were also non optimal. First, it occurred due to radiation power decrease. Second, at low pressure cathode material sputtering and metal electrode iodide production rate increase resulting in undesirable decrease of the tube transparency. The data obtained on radiation power of excilamp for different operating mixtures in Table 1 are presented. Excitation was performed at equal pressures of buffer gas and iodine vapours (the temperature of the box, the most cool bulb zone of the excilamp with crystal iodine did not changed), and at equal voltage to the lamp's electrodes from the supply source.

Table 1.

Operating mixture	Xe - I <sub>2</sub>	He - I <sub>2</sub>	He-Xe-I <sub>2</sub>	Ar - I <sub>2</sub>
Radiation power, arb. un.	1	0.9	0.85	0.1

It is seen from the Table 1 that the most high values of the radiation power take place for the operating media Xe - I<sub>2</sub>, He - I<sub>2</sub>, He - Xe - I<sub>2</sub>. Maximal output power radiation made up to 14 W. Radiation efficiency made there not less than  $\sim 12$  %. Dependencies of the glow discharge excilamp efficiency and output power on excitation power for the operating media Xe - I<sub>2</sub>, He - I<sub>2</sub> are presented in Fig. 4a, 4b. When using operating medium Ar - I<sub>2</sub> or iodine vapours only the lamp operation is much worse. Efficiency value with this did not exceed  $\sim 2 \div 4$  %. The lifetime of the sealed-off glow discharge excilamp with operating mixture Xe - I<sub>2</sub> made more than 1000 hours. When needed the box could be heat-isolated or warmed, either at the expense of the part of the discharge current flowing to special electrode placed in the box. Current was reduced with use of a resistor placed between the spiral and one of the main electrodes. Maximal output power radiation was obtained up to 12 W.

The similar results have been obtained for the capacitive discharge excilamps. The performance radiation intensities in the range  $200 < \lambda < 255 \text{ nm}$  at filling-in the lamp with operating mixtures Ne - I<sub>2</sub>, Kr - I<sub>2</sub>, Xe - I<sub>2</sub>, He - I<sub>2</sub> and He - Xe - I<sub>2</sub> at equal partial pressures of He and Xe, and also in the mixture Ar - I<sub>2</sub> and iodine vapours were defined. The optimum pressure of operating mixture at which the maximum power level of UV was provided depends on pulsed repetition rate and it did not exceed 15 Torr for the frequency 20 kHz, with this use of more heavy buffer gases decreased the optimum pressure. In Table 2 the data obtained on lamp radiation power determination for different operating mixtures are presented. The excitation was realised at equal pressures of the buffer gas and iodine vapours, and also at equal voltage applied to the lamp electrodes from the supply source at 20 kHz frequency. Maximal output power radiation made up to 14 W. It is seen from the Table 2 that the most high radiation power values take place when using operating mixtures such as He - I<sub>2</sub>, Xe - I<sub>2</sub>, He - Xe - I<sub>2</sub>. The radiation efficiency was not less than  $\sim 9$  %. At use of Ar - I<sub>2</sub> operating mixture the lamp's operation was much worse. Value of efficiency did not exceed  $\sim 1$  %. Excitation of only iodine vapours without addition of buffer gas with listed conditions on supply and geometry demanded preliminary lamp warming up and gave more less radiation powers.

Table 2.

Operating mixture	Xe-I <sub>2</sub>	He-I <sub>2</sub>	He-Xe-I <sub>2</sub>	Ne-I <sub>2</sub>	Ar-I <sub>2</sub>
Radiation power, arb. un.	0.9	1	0.7	0.4	0.1

Radiation spectrum of the capacitive discharge excilamp in the operating mixture Xe-I<sub>2</sub> at pressure of Xe  $\approx$  1 Torr is presented in Fig. 5. It is seen that at this mixture pressure the atomic iodine line  $\lambda = 206.2$  nm dominates in the spectrum. At pressure rise up to 10 Torr and more the radiation spectrum contains not only the line  $\lambda = 206.2$  nm but also the band  $\lambda = 253$  nm of the molecule XeI\* increasing with the mixture pressure rise.

The lifetime of the sealed-off excilamp pumped by a capacitive discharge with the operating mixture Xe - I<sub>2</sub> made more than 1000 hours.

### 3.2. KrCl and XeCl excilamps pumped by a barrier discharge

During the experiments, aiming at checking of different conditions influence on KrCl and XeCl excilamp efficiency, optimization of pressure and mixture composition containing Kr, Xe and Cl<sub>2</sub> was preliminarily made. The best data were obtained for the mixture Kr : Cl<sub>2</sub>  $\approx$  200 : (1+0.5) at total pressure  $\approx$  200 Torr. Output at  $\lambda \sim 222$  nm up to 100 W from barrier discharge excilamps was demonstrated. At decrease of the total pressure or Cl<sub>2</sub> contents, the most homogeneous discharge is still observed in the mixture but radiation power decreases. Pressure increase or Cl<sub>2</sub> contents in the mixture leads to discharge contraction with formation of bright lighting sparks, i.e. contraction channels, that also leads to radiation power decreasing.

As it was noted above, in the present work the generators were used which provided excitation pulses formation of different forms. In Fig. 6 typical oscilloscope traces of current pulses, voltage at the lamp electrodes, radiation pulse at B-X transition of the KrCl\* molecule, calculated excitation power curves for the sine pulse generator used are presented. It is seen that the radiation takes place during the most time of the discharge active phase (after the sharp voltage decrease at the discharge gap). It is also necessary to note radiation intensity modulation, delay ( $\approx 2 \div 2.5$   $\mu$ s) of radiation pulse relatively to initial stage of excitation pulse and their further correlation are demonstrated. The characteristic is a relative constant of the gas discharge voltage fall. That determines the small value of the displacement current  $I_b$  relatively to the total current at the gas discharge gap  $I_\Sigma$ :

$$I_b = S \cdot \frac{\partial D}{\partial t} = S \cdot \frac{\partial(\epsilon_0 \cdot \epsilon \cdot E)}{\partial t} \approx S \cdot \epsilon_0 \cdot \epsilon \cdot \frac{1}{d} \cdot \frac{\partial U_g}{\partial t} = C_g \cdot \frac{\partial U_g}{\partial t} \leq 0.25 \cdot I_\Sigma, \quad (1)$$

where  $D$ ,  $E$ ,  $U_g$  are electric displacement, electric field strength and voltage fall at the gas discharge gap;  $\epsilon_0$ ,  $\epsilon$  are electric constant and plasma dielectric permeability, correspondingly;  $S$ ,  $d$ ,  $C_g$  are area, gap and capacity of the gas discharge gap.

Plasma dielectric permeability value  $\epsilon$  in general case of medium with dispersion could be approximately taken as 1 and its change with can be neglected. The equation for plasma dielectric permeability value dependent on circular frequency of the field applied  $\omega$  in [16] is presented as:

$$\epsilon(\omega) = 1 - \frac{4\pi e^2 n_e}{m(\omega^2 + \nu_m^2)} = 1 - \frac{\omega_p^2}{\omega^2 + \nu_m^2}, \quad (2)$$

where  $\omega_p$  is plasma frequency,  $\nu_m$  is collision frequency of electrons,  $n_e$  is electron density,  $e$  is charge of electron. Estimation of the value  $\epsilon(\omega)$  for the experiment conditions presents, first, practical absence of dependence of  $\epsilon$  on  $\omega$ , since  $\omega < \nu_m \sim 10^{12}$  c<sup>-1</sup>. Second, at electron concentration at the range  $10^{12} \div 10^{14}$  cm<sup>-3</sup>, characteristic for barrier discharge, the value  $\epsilon$  makes about  $1 \div 0.9 \sim 1$ . At lamp operation, a rather homogeneous discharge with diffuse filaments is visually observed. The dependencies of lamp efficiency and radiation specific power via specific power of excitation in optimal operating mixture and sine pulses excitation are presented in Fig. 7 Absolute values of efficiency and tendency of its dependence on excitation power well correlates with the results obtained in [18].

When using single and bipolar excitation pulses with duration in base about 2  $\mu$ s at p.r.r. 17, 33, 60, 93 kHz, the more non-homogeneous discharge combustion with well pronounced filaments is visually observed. Filaments density is approximately about 1.5 times lower ( $\approx 0.4$  cm<sup>-2</sup>) than in the case of sine pulse excitation. In Fig. 8 efficiency dependencies and radiation specific power ones on excitation specific power for the case of unipolar excitation pulses at 93 kHz are demonstrated. It is necessary to note that specific characteristics were defined taking into account the whole discharge volume, though it is obvious that in presence of well-pronounced filaments both volume excitation and radiation are drastically non-homogeneous. That is why the above-mentioned characteristics should be considered in

presence of filaments as average along the discharge volume. Comparison of Fig. 7 and Fig. 8 allows to conclude that, firstly, at increase of input power in the both cases efficiency decreases, that may be related to overexcitation and overheating of medium. Secondly, at short-pulse excitation there is one advantage (for about 20 % for equal values of specific power of excitation). Due to more quick voltage increase at the discharge gap and its variations in time the displacement current occurs to be comparable by amplitude with the total current. This causes strong modulation of excitation power and correlating with the last modulation of the radiation power. (Fig. 9).

As it has been already intimated above in [4], Xe<sub>2</sub> barrier discharge excilamp efficiency is dependent on the discharge homogeneity. In order to check possible influence of the discharge homogeneity on KrCl excilamp efficiency, an additional experiment in absence of visually observed in the gas discharge plasma filaments was conducted, that was realized in Kr : Cl<sub>2</sub> ≅ 200 : 0.5 mixture at total pressure 100 Torr and excitation by short pulses. The results of that check are presented in Fig. 11. The main difference from the above presented data is, first of all, non-monotonous run of the efficiency curve with a maximum at excitation specific power of about 0.45 W/cm<sup>3</sup>. Secondly, the most high value of efficiency in this case occurs to be in 2÷3 times lower relatively to those ones obtained for the mixtures for the conditions of Fig. 10 at the same excitation specific powers. Besides that, in absence of filaments, just as in the case of sine voltage excitation, there is a radiation pulse delay of about 0.5 μs relatively to the excitation pulse beginning. At the same time, in presence of filaments, such a delay is practically not observed (Fig. 9, Fig. 11). The main reason for such a distinction is probably an essentially high excitation specific power in the volume occupied by filaments. This difference can be of 2 orders and more since according to estimations the occupied by filaments volume is so much times smaller than the total gas discharge volume taking into account during excitation specific power determination. A correlation between the values of normalized electric field strength  $E/p$ , excitation specific power for a unit volume unity and per particle, efficiency for the conditions of the experiment conducted, and also for the glow discharge [26] gives the following results. First, at comparable values of efficiency about 10 % in glow and barrier discharges in presence of filaments there are close values  $E/p \approx 8\text{--}10 \text{ V}\cdot\text{cm}^{-1}\cdot\text{Torr}^{-1}$ , excitation specific power for a unit volume  $\approx \text{tens W}\cdot\text{cm}^{-3}$ ,  $\approx (10\text{--}50)\cdot 10^{-18} \text{ W}$  for one particle. For the barrier discharge, the volume occupied by filaments is taken into account. Secondly, at the essentially lower efficiency (2.5–4 %) at homogeneous combustion of the barrier discharge (without visually registered filaments) the excitation specific powers make  $\approx 0.3\div 3 \text{ W}\cdot\text{cm}^{-3}$  and  $\approx (0.2\div 2) \cdot 10^{-18} \text{ W}$  for one particle.  $E/p$  is  $\geq 15 \text{ V}\cdot\text{cm}^{-1}\cdot\text{Torr}^{-1}$ .

Values of plasma energy input during one period for a unit of volume in barrier discharge,  $Q$ , are determined by capacity of dielectric layers of the lamp  $C_d$  (typical values  $C_d \approx 1\text{--}1.5 \text{ pF}\cdot\text{cm}^{-2}$ ), by gas gap  $d$  and voltage amplitude  $U_{\text{MAX}}$ :

$$Q \leq \frac{C_d \cdot U_{\text{MAX}}^2}{2d} \quad (3)$$

In homogeneous discharge, the energy is nearly uniform for a unit volume, and in presence of filaments, all energy is only in unit volume filaments themselves, that does provide excitation specific power increase in the discharge with filaments. Increasing of deposited in plasma energy during one period for a unit volume in barrier discharge, homogeneous combustion including, is possible at increasing of supply voltage, using dielectric with high value  $\epsilon$ , but obvious technical difficulties occur here such as electric strength of dielectrics, difficulties when work with high voltage, etc.

Thus, based on the presented data the following conclusions can be done. Presence of filaments, i.e. spatial zones with high excitation specific power in a barrier discharge is a necessary condition to obtain high efficiency of barrier discharge KrCl excilamp. Uniform distribution of similar excitation power input in the volume in the homogeneous discharge conditions leads to efficiency decrease. At lower excitation power, the rates of plasma chemical reactions providing excited exciplex KrCl\* molecules are low that leads to the observed in the experiment a radiation pulse delay relatively the excitation pulse beginning. Efficiency non-monotonous dependence versus excitation specific power in the discharge without filaments (Fig. 10) with a maximum at  $\approx 0.45 \text{ Wcm}^{-2}$  can be obviously explained by more high values of  $E/p$  and, correspondingly, by non-optimal conditions of KrCl\* molecules formation. Similar dependences were either obtained for XeCl barrier discharged excilamp.

### 3.3. KrCl и XeCl excilamps pumped by a glow discharge

Coaxial excilamps. Excilamp with the gap from 7 up to 18 mm was found to emit the highest average power. Output power at  $\lambda \sim 222 \text{ nm}$  up to 190 W was obtained. Output power about 50 W and efficiency with respect to input power as

high as 14% was demonstrated. Similar results were obtained in Xe-Cl<sub>2</sub> mixture at  $\lambda \sim 308$  nm. Output power of about 91 W was demonstrated. Distribution of the output along the excilamp length was measured. It was found that the UV radiation intensity decreases noticeably only in the cathode region. Operation time of the excilamp is limited due to its overheating and exhaust of chlorine molecules. It is significant that enlargement of excilamp dimensions can substantially increase the operation time. Besides, upgrading of excilamp design, using stable to halogen action materials, cleaning of the original gas components and improvement in water cooling show promise of substantial increase of the mixture lifetime.

Cylindrical excilamps. XeCl- and KrCl- excilamps with the tube diameters  $d=56$  mm and  $L=94$  and 150 cm in length were used in our experiments. The voltage across the tube is defined by chlorine concentration in gas mixture and pressure. In these excilamps, for the fall of the UV output in cathode region to be decreased, we used electrodes with experimentally defined shape. Therewith, the UV output variations along the excilamp were no more than 10-15%, while the fall near cathode was not evident. Output power up to 185 W was obtained at  $\lambda \sim 222$  nm.

#### 4. CONCLUSION

The study of Xe-I<sub>2</sub> and He - I<sub>2</sub> glow and capacitive discharge excilamps was performed. The efficiency up to 12 % and lifetime in sealed-off excilamps more 1000 h were demonstrated. These results can be utilised in developing and use of effective lamps based on glow and high-frequency capacitive discharges radiating in vacuum ultraviolet and ultraviolet ranges of wavelengths.

At excitation of the barrier KrCl and XeCl excilamps by short (about 2  $\mu$ s) unipolar or bipolar voltage pulses the efficiency obtained is somewhat higher (in average it is in 10-30 % for the equal values of specific pumping power) as compared to excitation by the sine pulses. Output at  $\lambda \sim 222$  nm up to 100 W and at 308 nm up to 75 W from barrier discharge excilamps was demonstrated. With homogeneous discharge (in absence of visually observed filaments) the excilamp operating efficiency occurs to be 2-3 times worse as compared with the discharge when the filaments present. The presence of filaments appears to be a necessary condition in order to obtain a high efficiency since at limiting of plasma energy input the excited volume being essentially reduced and accordingly the demanded level of specific excitation power is achieved. Radiation pulse delay relatively to homogeneous discharge excitation is obviously also notes to the low efficiency of KrCl\* and XeCl\* molecules formation at low excitation power level.

Output at  $\lambda \sim 222$  nm up to 190 W and at 308 nm up to 91 W from glow discharge excilamps was demonstrated.

#### 5. ACKNOWLEDGEMENTS

We gratefully acknowledge the ISTC support of the Project No. 1270 on development excilamps.

#### REFERENCES

1. Proc. of the 8<sup>th</sup> Int. Symp. On Science & Technology of Light Sources, Greifswald, Germany, 1998.
2. Proc. of the 9<sup>th</sup> Int. Symp. On Science & Technology of Light Sources, Cornell University, Ithaca, NY, USA, 2001.
3. F. Vollkommmer, L. Hitzschke, Proc. of the 8<sup>th</sup> Int. Symp. LS-8, Greifswald, Germany, pp. 51-60, 1998.
4. R. P. Mildron, and R. J. Carman, "Enhanced Efficiency from a Xe Excimer Barrier Discharge Lamp Employing Short-Pulsed Excitation", *J. Phys. D: Appl. Phys.* **34**, L1-L6, 2001
5. A. Oda, H. Sugawara, Y. Sakai, H. Akashi, "Estimation of the output power and efficiency of Xe barrier discharge excimer lamps using a one-dimensional fluid model for various voltage waveforms", *J. Phys. D: Appl. Phys.* **33**, pp. 1507-1513, 2000.
6. Harteck P., Reeves R.R., Thompson B.A., "The Iodine Lamp: A Light Source for Selective Excitation of CO", *Naturforsch. Z.* **19** a, pp. 2-6, 1964.
7. G. Liuti, J.E. Mentall, "Monochromatic Iodine Lamp", *Rev. Sci. Instr.* **39**, N 11, pp. 1767-1768, 1968.
8. J.-Y. Zhang, I.W. Boyd, "Efficient XeI excimer ultraviolet sources from a dielectric barrier discharge", *J. Appl. Phys.* **84**, N3, pp. 1174-1178, 1998.
9. U. Gross, A. Ubelis, P. Spietz, J. Burrows, "Iodine and mercury resonance lamps for kinetics experiments and their spectra in the far ultraviolet", *J. Phys. D: Appl. Phys.* **33**, pp. 1588-1591, 2000.
10. G.N. Rochlin, *Discharge Light Sources*, Moscow, 1991.

11. M.I. Lomaev, A.N. Panchenko, V.F. Tarasenko. Patent RF, (19) RU (11) 2151442 (13) C1 (51) 7 H 01 J 61/12, 17/20, issued 20. 06. 2000.
12. M.I. Lomaev, V.S. Skakun, E.A. Sosnin, V.F. Tarasenko. Patent RF, (19) RU (11) 2154323 (13) C2 (51) 7 H 01 J 61/16, 17/20, 7/06, issued 10. 08. 2000.
13. T.C. Manley, "The electric characteristics of the ozonator discharge," *Trans. Electrochem. Soc.* **84**, pp. 83-96, 1943.
14. Z. Falkenstein, J.J. Coogan, "Microdischarge behavior in the silent discharge of nitrogen-oxygen and water-air mixtures", *J. Phys. D: Appl. Phys.* **30**, pp. 817-825, 1997.
15. M.M. Gurevich, *Photometry*, S.-Peterburg, 1983.
16. Yu.P. Raizer, *Gas Discharge Physics*, Moscow, 1987.
17. B. Eliasson, and U. Kogelschatz, "Modeling and Applications of Silent Discharge Plasmas," *IEEE Trans. on Plasma Science* **19**, pp. 309-323, 1991.
18. J.-Y. Zhang, and I. W. Boyd., "Efficient excimer ultraviolet sources from a dielectric barrier discharge in rare-gas/halogen mixtures", *J. Appl. Phys.* **80**, pp.633-638, 1996.
19. Kuznetsov A.A, Skakun V.S., Tarasenko V.F., Fomin E.A., "Exsimer elektric - discharge tube with  $\lambda \sim 126, 146$ , or  $172 \text{ nm}$ ", *Tech. Phys. Lett.* **19**, No. 3. pp.133-134. 1993.
20. M.I. Lomaev, V.S. Skakun, E.A. Sosnin and V.F. Tarasenko, "Barrier discharge pumped excilamps", *Atmos. Oceanic Optics.* **11**, N 2-3, pp. 243 - 249, 1998.
21. A. M. Boichenko, V.S. Skakun, E.A. Sosnin, V. F. Tarasenko, S.I. Yakovlenko, "Emission efficiency of exciplex and excimer molecules pumped by a barrier discharge", *Laser Phys.* **10**, N2. pp.540-552. 2000
22. E. Arnold, R. Dreiskemper and S. Reber, *Proc. of the 8th Int. Symp. LS-8*, Graifswald, Germany, 30th August - 3rd September, 90, 1998
23. V.F. Tarasenko, E.B. Chernov, M.V.Erofeev, M.L. Lomaev, A.N. Panchenko, V.S. Skakun, E.A.Sosnin, D.V. Shitz, "UV and VUV excilammps excited by glow, barrier and capacitive discharges", *Appl.Phys.* **69A**. pp. 327-329, 1999.
24. M.V. Erofeev, V.S. Skakun, E.A. Sosnin, V.F. Tarasenko, and E.B. Chernov, "Lifetime of working mixtures of XeCl and KrCl Excilamp", *Atmos. Oceanic. Opt.* **13**, No.3. pp.286-288, 2000
25. A.P. Golovizkii, "Creation Possibility of Effective Light Sources based on inert - halogens mixtures glow discharge", *Tech. Phys. Lett.* **18**, 8, pp.73 - 76, 1992.
26. M.I. Lomaev, A.N. Panchenko, V.S. Skakun, E.A. Sosnin, V.F. Tarasenko, M.G. Adamson, B.R. Myers, F.T. Wang, "Excilamp producing up to 130 W of output power and possibility of its applications", *Laser and Particle Beams*, **15**, 2, pp. 339-345, 1997.
27. A.N. Panchenko, E.A. Sosnin, V.F. Tarasenko, "Improvement of output parameters of glow discharge UV excilamps", *Optics Communications*, **161**, pp. 249-252, 1999
28. E.W. McDaniel, W.L. Nighan, *Applied atomic collision physics. Vol. 3. Gas Lasers*, Academic Press, London, 1982
29. V.G. Samoilovich, V.I. Gibalov, K.V. Kozlov. *Barrier Discharge Physical Chemistry*, Moscow State Univ., 1989.

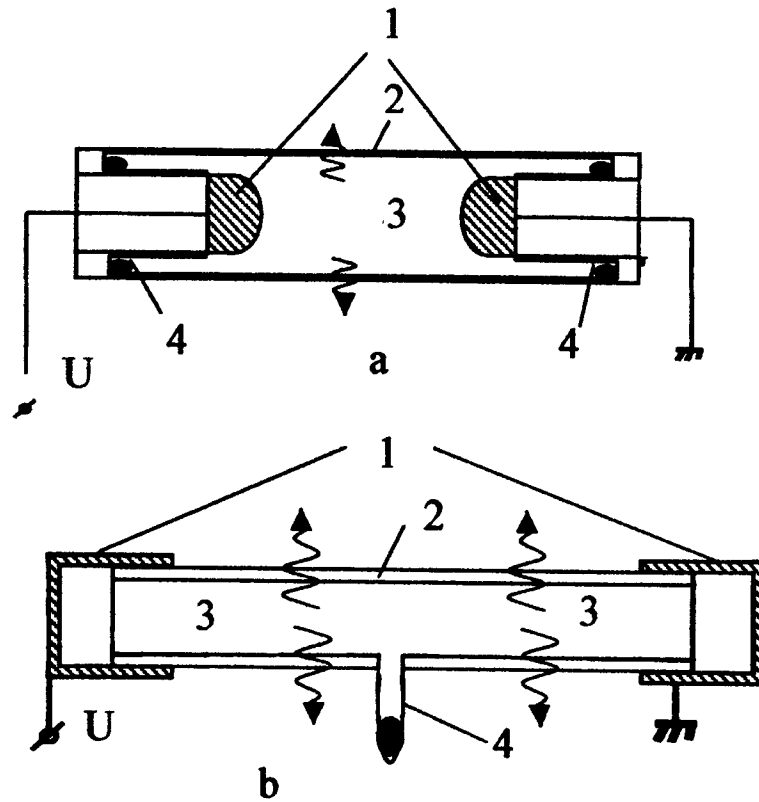


Fig. 1. Design of glow discharge excilamps : 1- electrodes, 2- quartz bulb  
3 - gas-vapour mixture, 4 - iodine in solid state.

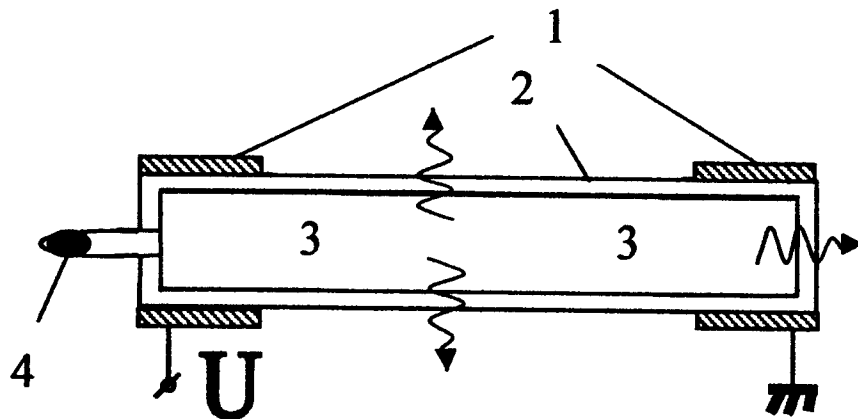


Fig. 2. Design of capacitive discharge excilamps: 1- electrodes, 2- quartz bulb, 3 - gas-vapour  
mixture, 4 - iodine in solid state.



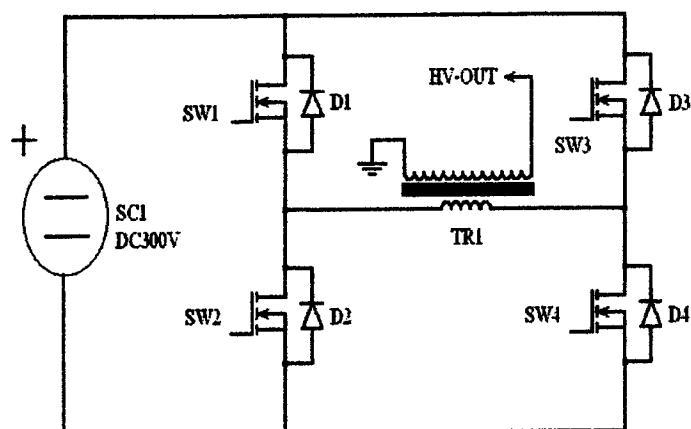


Fig. 3. Principal electric circuit of steep rising bipolar series generator.

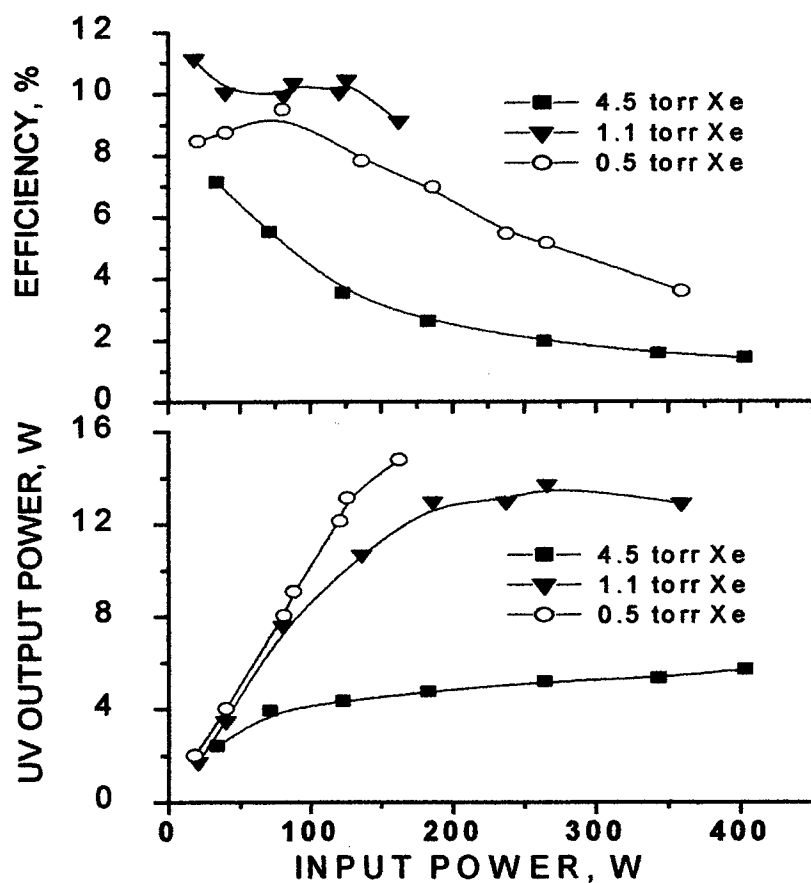


Fig. 4a. Efficiency and UV ( $\lambda = 206$  nm) average output power as a function of input power at various values of Xe pressure. Xe - I<sub>2</sub> glow discharge tube.

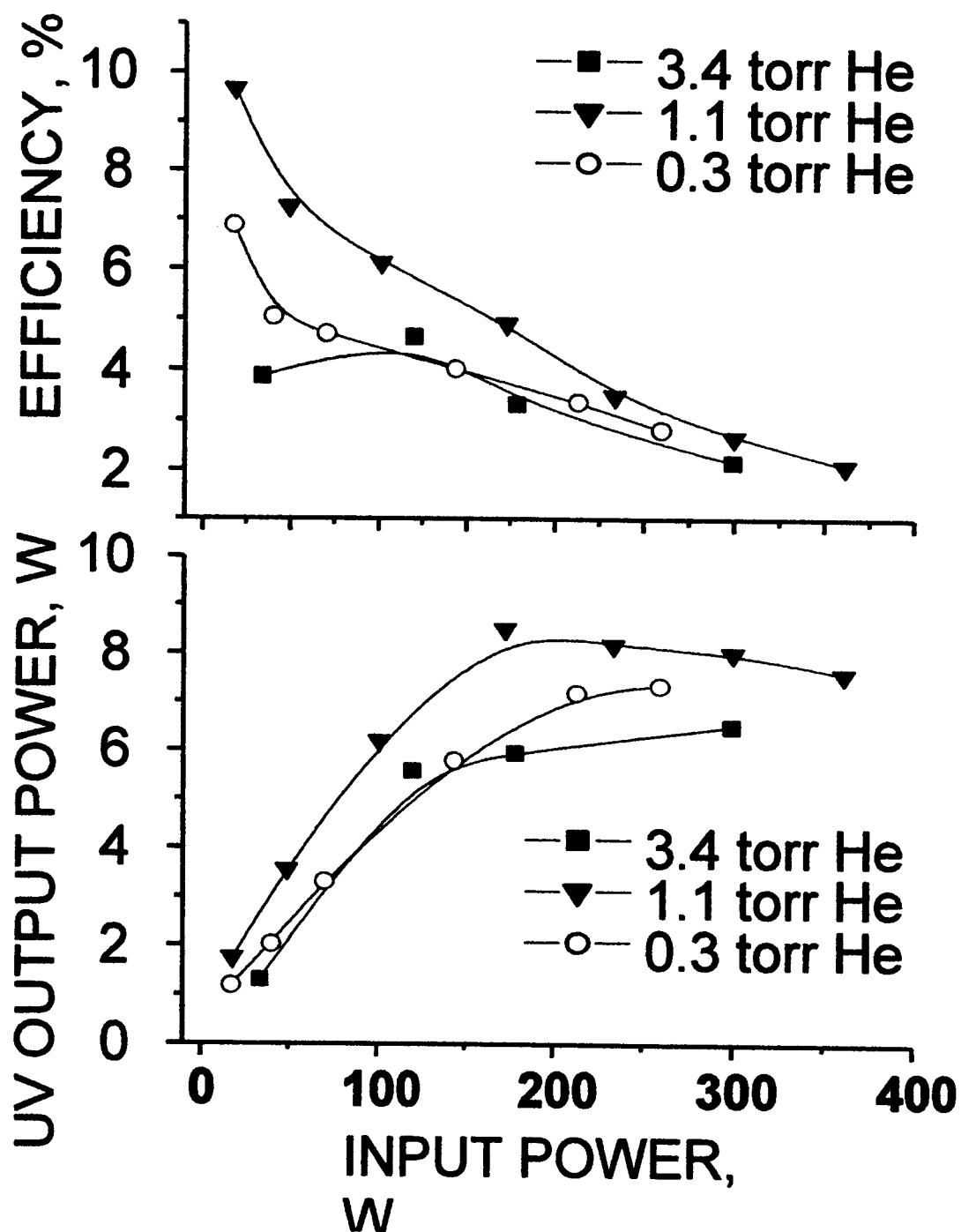


Fig. 4b. Efficiency and UV ( $\lambda = 206$  nm) average output power as a function of input power at various He pressure. He - I<sub>2</sub> glow discharge tube.

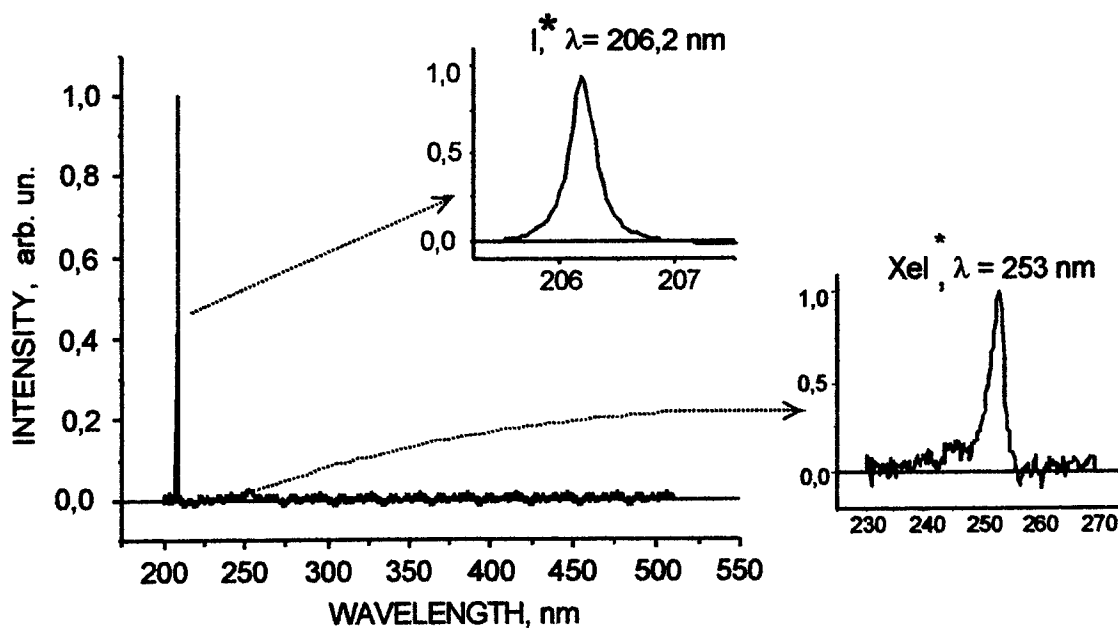


Fig. 5. Spectrum of Xe-I<sub>2</sub> capacitive discharge excilamp.

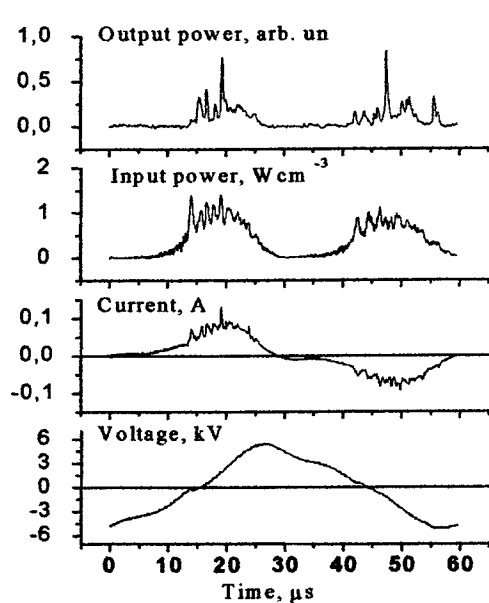


Fig. 6. Oscilloscope traces of UV radiation intensity, total current pulses, excilamp electrodes voltage, and calculated power excitation curve for sine voltage generator.

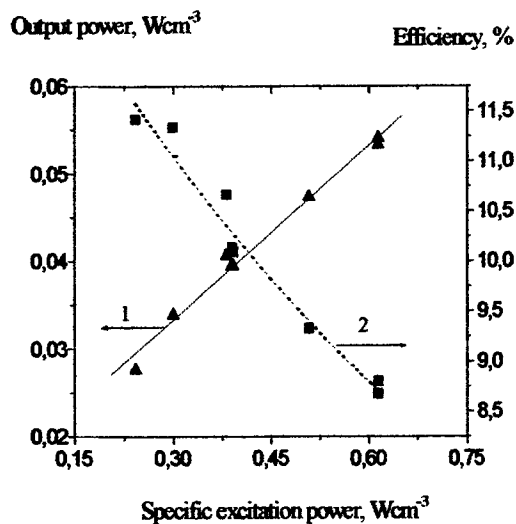


Fig. 7. Dependences of specific radiation power (1) and efficiency (2) on average specific excitation power for sine voltage generator.

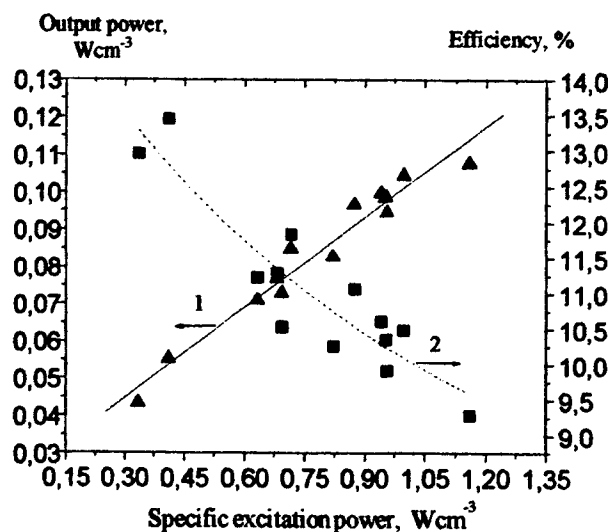


Fig. 8. Specific radiation power (1) and efficiency (2) dependences on average specific excitation power for unipolar excitation pulse at frequency 93 kHz.

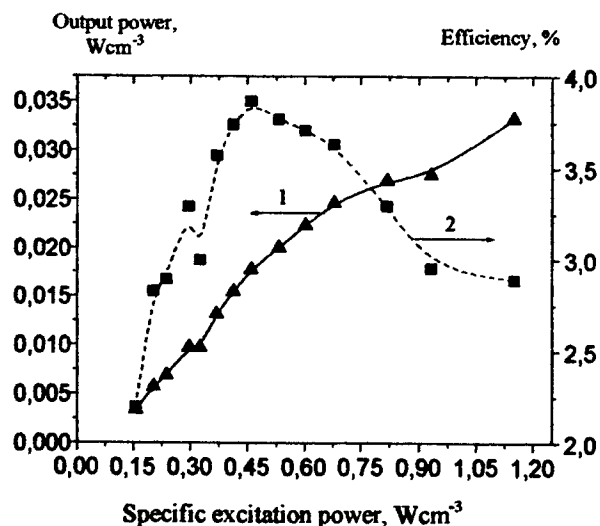


Fig. 10. Specific radiation power (1) and efficiency (2) dependences on average specific excitation power in absence of filaments. Mixture Kr :  $Cl_2 \cong 200 : 0.5$  at total pressure 100 Torr, for steeply rising ( $\sim 1 \mu s$ ) voltage generator.

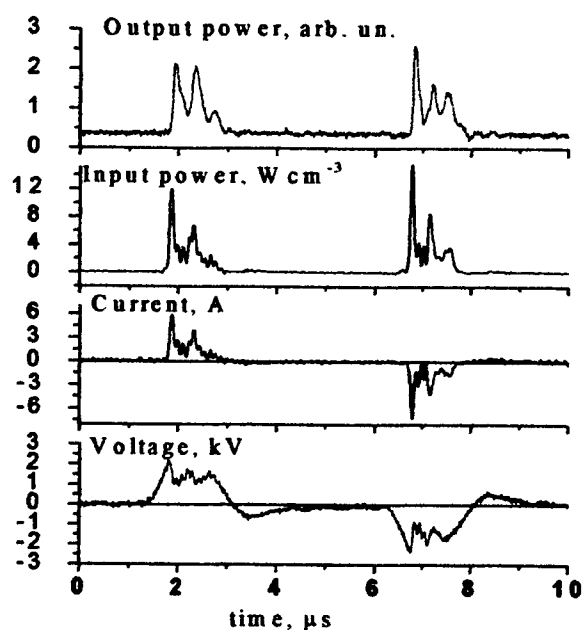


Fig. 9. Oscilloscope traces of UV radiation intensity, total current pulses, calculated power excitation curve, gas discharge gap voltage curve for steeply rising ( $\sim 1 \mu s$ ) voltage generator.

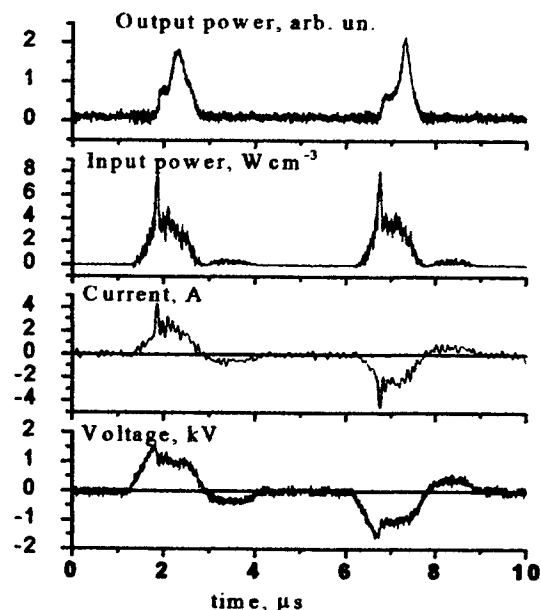


Fig. 11. Oscilloscope traces of UV radiation intensity, calculation curves of power excitation, active part of current, voltage at the gas discharge gap when steeply rising ( $\sim 1 \mu s$ ) voltage generator used. Mixture Kr :  $Cl_2 \cong 200 : 0.5$  at total pressure 100 Torr in the absence of filaments.

# Pulsed laser deposition of silicon dioxide thin films with silicone targets for fabricating waveguide devices

Masayuki Okoshi, Masaaki Kuramatsu, Narumi Inoue  
Department of Electrical and Electronic Engineering, National Defense Academy,  
1-10-20 Hashirimizu, Yokosuka 239-8686, Japan

## ABSTRACT

Silicon dioxide ( $\text{SiO}_2$ ) thin films were deposited at room temperature by 193-nm ArF excimer laser ablation of silicone in oxygen atmosphere. Only the side chains ( $\text{CH}_3$ ) of the target were photo-dissociated during ablation to deposit Si-O bonds on a substrate in high laser fluence at about  $10 \text{ J/cm}^2$ . Oxygen gas worked to oxidize the Si-O bonds ejected from the target to form  $\text{SiO}_2$  thin films at the gas pressure of  $4.4 \times 10^{-2}$  Torr, in addition to reducing the isolated carbon mixed into the films. We also found that the deposition rate could control refractive index of the films. The refractive index of the film deposited at 0.05 nm/pulse is greater than that of the film at 0.1 nm/pulse. Thus, a 0.2- $\mu\text{m}$ -thick  $\text{SiO}_2$  cladding film deposited at 0.1 nm/pulse was firstly formed on the whole surface of a 100- $\mu\text{m}$ -thick polyester film, and then a 0.6  $\mu\text{m}$ -thick  $\text{SiO}_2$  core film at 0.05 nm/pulse was fabricated in a line on the sample. The sample functioned as a waveguide device for a 633-nm line of He-Ne laser.

**Keywords:** pulsed laser deposition (PLD), laser ablation, silicone,  $\text{SiO}_2$  film, ArF excimer laser, oxygen gas, room temperature, refractive index, optical waveguide

## 1. INTRODUCTION

The compositional fidelity of pulsed laser deposition (PLD) is a useful feature for depositing multielement thin films. In fact, the deposition of high-temperature superconductors brought about the first successes with the feature.<sup>1</sup> Also, the thin-film deposition of polymers made use of this compositional fidelity.<sup>2-4</sup>

In PLD, ultraviolet (UV) lasers such as excimer lasers have been used mainly as the excitation source for the ablation of solid target surfaces. One of the merits of UV lasers for PLD is that it reduces the droplets mixed into a film.<sup>5</sup> However, in the case of polymers, the high photon energy of UV lasers affects the fragmentation of polymer targets. Therefore, the composition of polymer films in PLD is sensitive to the wavelength and laser fluence of UV lasers.<sup>6</sup>

In this study, we deposited transparent, carbon-free  $\text{SiO}_2$  thin films at room temperature by PLD with silicone targets.<sup>7-9</sup> In this case, we did not make use of the compositional fidelity of PLD. The high photon energy (6.4 eV) of an ArF excimer laser (193 nm) can dissociate  $\text{CH}_3$  from silicone to eject Si-O bonds selectively by ablation. During the ablation, oxygen gas worked to oxidize the Si-O bonds ejected from silicone target to deposit  $\text{SiO}_2$  thin films. In addition, oxygen gas reduced the isolated carbon mixed into the films. In this paper, we found the refractive index change of the  $\text{SiO}_2$  films by changing the deposition rate, in our PLD. Based on the present result, we fabricated a flexible optical waveguide by depositing the  $\text{SiO}_2$  films with different refractive indices on a 100- $\mu\text{m}$ -thick polyester film.

## 2. EXPERIMENTAL

The experimental arrangement used in the present PLD work was almost identical to the one used in the previous work.<sup>8</sup> A laser beam generated by an ArF laser (Lambda Physik EMG 202MSC) was introduced into a chamber through a quartz window and focused on the silicone target by a 350 mm focal length lens. The laser fluence on the target was approximately  $10 \text{ J/cm}^2$ .<sup>7,9</sup> In order to control the refractive index of the films, the deposition rate was carefully kept at 0.1 nm/pulse and at 0.05 nm/pulse by adjusting the laser pulse energy, maintaining the laser fluence. The pulse repetition rate was 1 Hz. The chamber was evacuated by a turbomolecular pump to less than  $4.4 \times 10^{-5}$  Torr, and oxygen gas was introduced into the chamber at the gas pressure of  $4.4 \times 10^{-2}$  Torr.<sup>7,8</sup> The target was located 25 mm from the substrate. The substrate was 100- $\mu\text{m}$ -thick polyester films. The films were deposited at room temperature.

## 3. RESULTS AND DISCUSSION

### 3.1 Refractive index change

Figure 1 shows the refractive index of the films deposited at the rates of 0.1 nm/pulse and 0.05 nm/pulse. Both films were produced with uniform thickness (about 130 nm). The refractive index of the films deposited on Si was measured at a 633 nm wavelength by the ellipsometer (Mizojiri Optical Co., Ltd, DVA-36LD). In the case of 0.1 nm/pulse, the refractive index of the films was within the region of 1.37 to 1.40. The reason of the noticeable error might be due to the instability of laser pulse energy. When the deposition rate lowered from 0.1 nm/pulse to 0.05 nm/pulse, the refractive index was changed to 1.42 to 1.43. The results suggest that the refractive index of the  $\text{SiO}_2$  films can be controlled by the deposition rate.

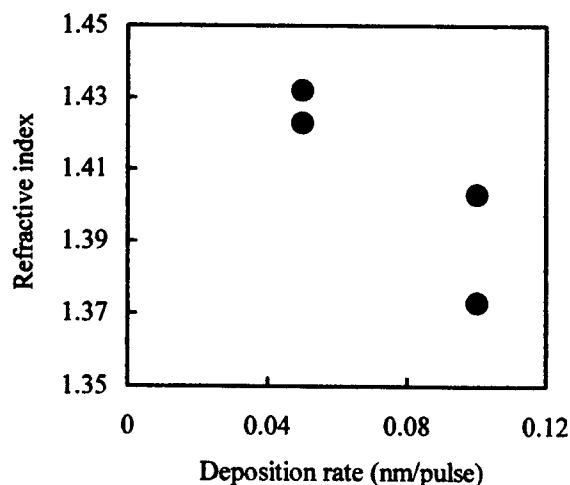


Figure 1: The refractive index of the films deposited at the rates of 0.1 nm/pulse and 0.05 nm/pulse.

### 3.2 A flexible optical waveguide

Based on the above results, we fabricated a  $\text{SiO}_2$  optical waveguide on a polyester film, as shown in Fig. 2. A  $0.2\text{-}\mu\text{m}$ -thick  $\text{SiO}_2$  cladding film deposited at  $0.1\text{ nm/pulse}$  was firstly formed on the whole surface of a  $100\text{-}\mu\text{m}$ -thick polyester film, and then a  $0.6\text{-}\mu\text{m}$ -thick  $\text{SiO}_2$  core film deposited at  $0.05\text{ nm/pulse}$  was fabricated in a line on the sample. A  $633\text{-nm}$  line of He-Ne laser was used for the measurements. The beam of He-Ne laser was coupled to the core film with a BK-7 prism (refractive index of 1.52). Also, the propagating beam in the core film was led out through another BK-7 prism. The single-mode propagation was observed, as shown in the photograph in Fig. 2. Therefore, the samples functioned as an optical waveguide for a  $633\text{-nm}$  line of He-Ne laser.

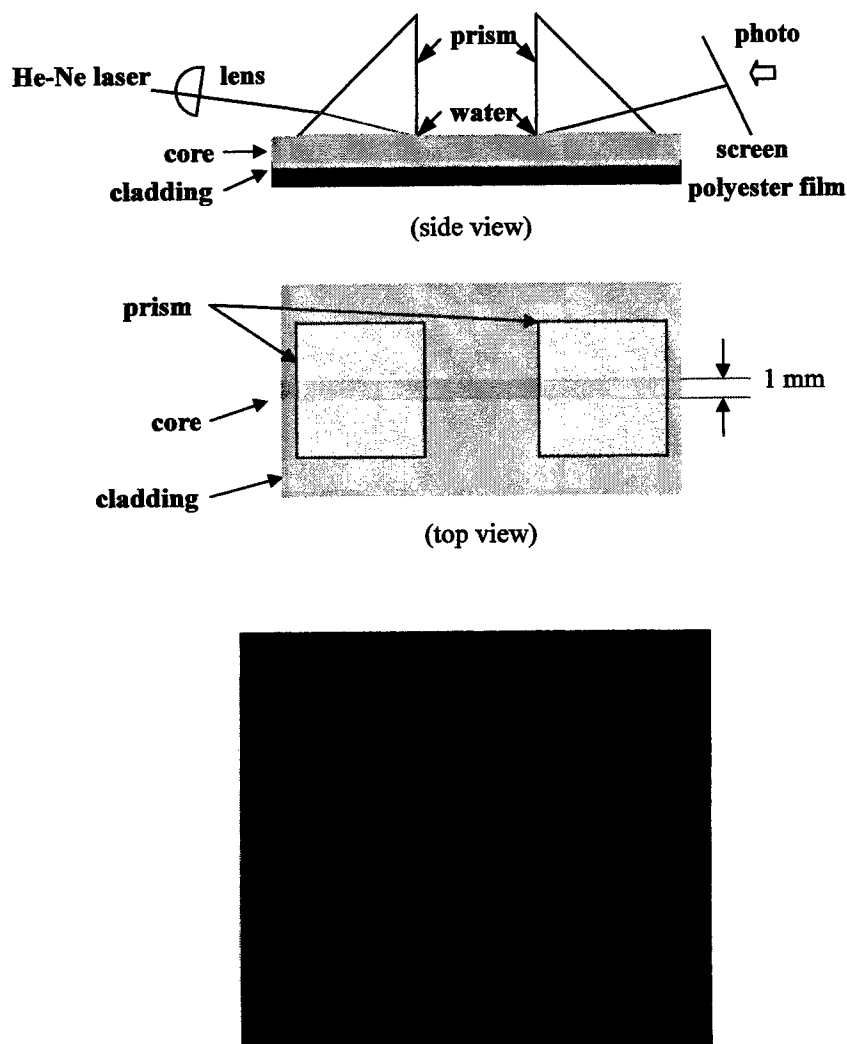


Figure 2: Illustrations of an arrangement for optical waveguiding and the photograph of a screen image of the propagating  $633\text{-nm}$  He-Ne laser beam in the core film led out through a BK-7 prism.

#### 4. CONCLUSIONS

We deposited SiO<sub>2</sub> films with different refractive indices by the PLD with silicone targets. The deposition rate could induce the refractive index change of the SiO<sub>2</sub> films. Based on the present result, a flexible SiO<sub>2</sub> optical waveguide was fabricated on a 100- $\mu$ m-thick polyester film for a 633-nm line of He-Ne laser.

#### ACKNOWLEDGMENTS

The authors are grateful to Mr. Ken-ichi Hayashi, TRDI of Japan Defense Agency, for assistance in ellipsometer measurements, and to Associate Professor Satoshi Tanaka, Department of Communications Engineering, for valuable discussions. One of the authors (M.O.) acknowledges the support by Kanagawa Academy of Science and Technology Research Grants.

#### REFERENCES

1. D. B. Chrisey and G. K. Hubler, *Pulsed Laser Deposition of Thin Films*, Wiley, New York, 1994.
2. S. G. Hansen and T. E. Robitaille, "Formation of polymer films by pulsed laser evaporation," *Appl. Phys. Lett.* **52**, pp. 81-83, 1988.
3. G. B. Blanchet, C. R. Fincher Jr., C. L. Jackson, S. I. Shah and K. H. Gardner, "Laser ablation and the production of polymer films," *Science*, **262**, pp. 719-720, 1993.
4. Y. Ueno, T. Fujii and F. Kannari, "Deposition of fluoropolymer thin films by vacuum-ultraviolet laser ablation," *Appl. Phys. Lett.* **65**, pp.1370-1372, 1994.
5. For instance, M. Okoshi, M. Hanabusa and K. Miyake, "Pulsed laser deposition of corrosion-resistant iron thin films," *Jpn. J. Appl. Phys.* **36**, pp.L801-L804, 1997.
6. S. Nishio, T. Chiba, A. Matsuzaki and H. Sato, "Control of structure of deposited polymer films by ablation laser wavelength," *J. Appl. Phys.* **79**, pp. 7198-7204, 1998.
7. M. Okoshi, M. Kuramatsu, and N. Inoue, "Laser ablation of silicone rubber for fabricating SiO<sub>2</sub> thin films," *Jpn. J. Appl. Phys.* **40**, pp. L41-L42, 2001.
8. M. Okoshi, M. Kuramatsu, and N. Inoue, "Pulsed laser deposition of SiO<sub>2</sub> thin films with dimethylpolysiloxane targets," to be published in *Jpn. J. Appl. Phys.*
9. M. Okoshi, M. Kuramatsu, and N. Inoue, "Thin film deposition by laser ablation of dimethylpolysiloxane," to be published in *Applied Surface Science*.



# Application and Observation of Laser-Induced Forward Transfer Process

Yoshiki Nakata<sup>\*a</sup>, Tatsuo Okada<sup>a</sup>, Mitsuo Maeda<sup>a</sup>

<sup>a</sup>Graduate School of Information Science and Electrical Engineering, Kyushu University,  
6-10-1 Hakozaki, Fukuoka 812-8581, Japan  
Tel:+81-92-642-3965, Fax:+81-92-642-3965  
E-mail: nakata@photon.ees.kyushu-u.ac.jp

## ABSTRACT

Laser-induced forward transfer (LIFT) was applied to eject micron-sized TiO<sub>2</sub> particles on gold thin film on SiO<sub>2</sub> substrate. The behavior of the ejected TiO<sub>2</sub> particles in the gas phase was imaged by light scattering method. The fastest velocity of the particles exceeded 700 m/s. In addition, laser dye film on SiO<sub>2</sub> substrate was transferred by LIFT and deposited on the other SiO<sub>2</sub> substrate, and it emitted fluorescence with excitation by second harmonic wave of YAG laser at 532 nm.

**Keywords:** laser-induced forward transfer (LIFT), laser ablation, process measurement by imaging, TiO<sub>2</sub> particle, laser dye

## 1. INTRODUCTION

Laser-induced forward transfer (LIFT) is a method for the deposition of a small sized thin film. The schematic of LIFT is shown in Fig. 1 (a). In this method, a donor film on a transparent substrate is ablated by a pulsed laser from rear side of the substrate, and the ablated film is ejected by the reaction of plasma expansion of ablation plasma, and then deposited on the surface of the other substrate faced the donor film. LIFT has been applied to many kinds of samples as metals and oxides.<sup>1,2</sup> We have investigated the behavior of atoms, emissive particles in LIFT process by two-dimensional laser-induced fluorescence (2D-LIF) and imaging of emission techniques attached to a long working-distance microscope.<sup>3,4</sup> From the results, the atoms flew with the fastest velocity of more than 2 km/s, whereas emissive particles flew with slower velocity of about 100 m/s. On the other hand, we have applied LIFT to transfer particles, as shown in Fig. 1 (b).<sup>5</sup> In this method, firstly particles are applied on a donor film, then they are ejected by

\* nakata@ees.kyushu-u.ac.jp; phone 81 92 642-3895; fax 81 92 642-3965; <http://photon.ees.kyushu-u.ac.jp/index.html>;  
Graduate school of ISEE, Kyushu university, 6-10-1 Hakozaki, Higashi-ku, Fukuoka, 812-8581 Japan

LIFT process. In the past experiment, we imaged the behavior of the ejected fluorescent particles in gas phase in LIFT process by 2D-LIF, and the fastest velocity was 280 m/s.

In this experiment,  $\text{TiO}_2$  particles applied on gold thin film on  $\text{SiO}_2$  glass substrate was ejected by LIFT. The gold film thickness, intensity of ablation laser and atmospheric gas condition were changed, and the behavior of the ejected particles was imaged by light scattering method. In this method, mie-scattering of blue light scattered by ejected particles was imaged by an image-intensified CCD camera attached to a long working distance optical microscope. In addition, LIFT of laser dye was tried.

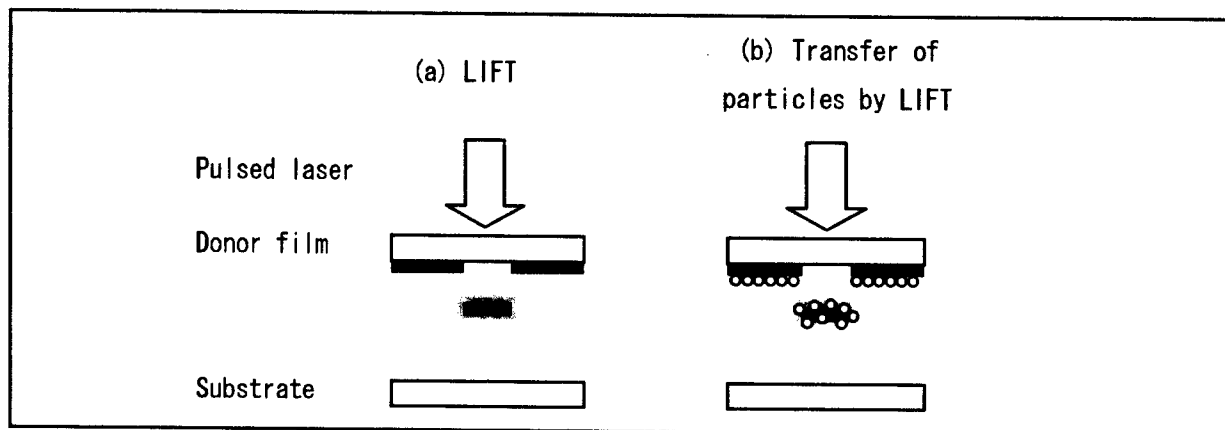


Figure 1: Schematic of LIFT and transfer of particles by LIFT.

## 2. EXPERIMENTAL SETUP

Experimental procedure of the LIFT of  $\text{TiO}_2$  is as follows: The fabrication of sample is explained in Fig. 2.  $\text{SiO}_2$  glass substrate was used, and on which gold thin film was evaporated. The thickness of the gold thin film was 0 to 500 nm, and 0 means no base gold film. Then  $\text{TiO}_2$  particle solution was applied and dried. The gold film was used as a base film which is laser ablated to lift the  $\text{TiO}_2$  particles on the film, but even without base gold film  $\text{TiO}_2$  particles were ejected as shown in the next section. The diameter of  $\text{TiO}_2$  particle was 1 to 2  $\mu\text{m}$ , and the thickness of  $\text{TiO}_2$  layer was about 15  $\mu\text{m}$ . In the case of LIFT of laser dye, ten drops of ethanol solution of Rhodamine 610 laser dye (Exciton corp.) was applied and dried.

The experimental setup of LIFT is shown in Fig. 3. The vacuum chamber was evacuated by a rotary pump, in which a

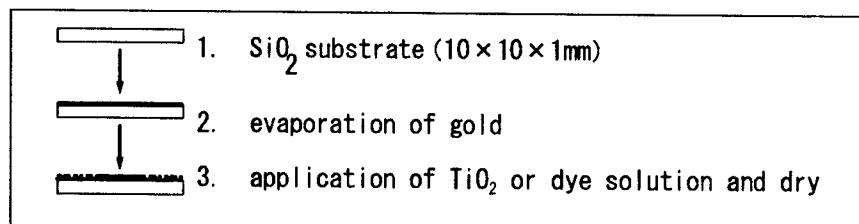


Figure 2: Fabrication of sample.

sample was placed. It was ablated by a SHG of Nd:YAG laser with the wavelength of 532 nm and the pulse width of about 8 ns. The ejected  $\text{TiO}_2$  particles in gas phase were irradiated by a broad emission from ethanol solution of Coumarine 440 laser dye (Exciton corp.) excited by a XeCl excimer laser at the wavelength of 308 nm. The scattered light from  $\text{TiO}_2$  particles was observed by an image-intensified CCD camera attached to a long working distance microscope and through a blue pass filter to cut thermal emission from the ejected particles.

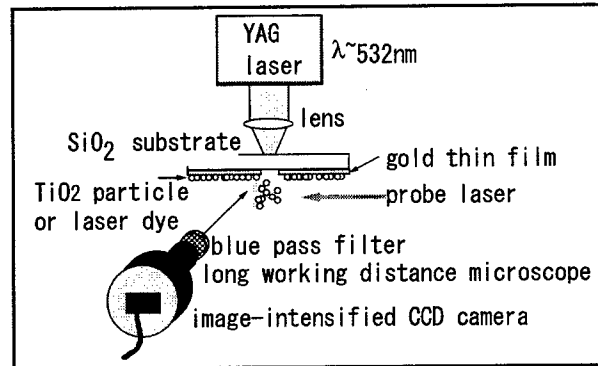


Figure 3: Experimental setup of LIFT.

### 3. RESULTS

#### 3.1 Image of an ablation spot

Fig. 4 shows an example image of ablation spot on donor film observed by an optical microscope. The film thickness of gold was 200 nm, and ablation laser energy was 3.0 mJ. White region in the ablation spot is due to the transformation of  $\text{SiO}_2$  substrate. The etching of transparent material in contact with an opaque material has been reported by Wang et al.<sup>7</sup> The edge of  $\text{TiO}_2$  film is blackened due to adherence of Ti or Au produced by the ablation in LIFT process. From this picture, the fluence is calculated to be about  $1.5 \text{ J/cm}^2$ . The ablation laser energy was changed as a parameter in the following experiments.

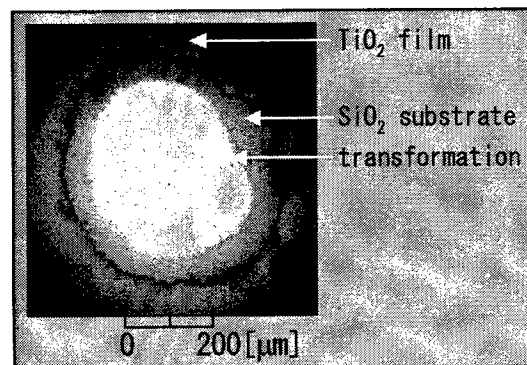


Figure 4: Ablation spot.

### 3.2 Behaviors of $\text{TiO}_2$ particles in LIFT process

Fig. 5 shows the spatial and temporal distributions of particles ejected by LIFT at different delay times. The base gold film thickness was 0 or 50 nm, and atmospheric condition was vacuum and air. The ablation energy was 0.29 mJ. The images of hole left after the LIFT process are also shown. The scales at right hand side shows the distance from the sample film, and dotted lines show the surfaces of the film. The tone in the pictures is inverted, so black regions in the pictures show the scattered probe laser beam, and show the existence of the particles. The signal of the left side in each image is weakened because of the scattering of the probe laser by the particles at the right side in the image.

In all LIFT process conditions in Fig. 5, the ejected particles flew as the delay time and perpendicular to the surface of the film. At later delay time after about 50  $\mu\text{s}$ , large droplets with slow velocity appeared. In both atmospheric conditions of vacuum and air, the velocity seems to be slowed with base gold film with 50 nm thickness. This is due to the reflection of the ablation laser by the gold film, not due to the mass of the film because it is quite lighter compared with that of  $\text{TiO}_2$  layer. So, with a base film which absorb an ablation laser efficiently, the velocity of the particles can be increased. The particles are also slowed with the existence of air, and this is due to drag by air. Similar behaviors of the ejected atoms, emissive particles were reported in the previous papers.<sup>3,4</sup>

The distances of the front edge of the distributions of particles derived from Fig. 5 are plotted as a function of delay time in Fig. 6. The atmospheric condition and base gold film thickness was (a) vacuum and 0 nm, (b) vacuum and 50 nm, (c) air and 0 nm and (d) air and 50 nm, respectively. There is a delay of 0.5 or 1.0  $\mu\text{s}$  before the ejection of particles when the process was done in air or base gold film was used. After the ejection, they flew with almost steady velocity, and the value was (a) 240, (b) 120, (c) 107 and (d) 19 m/s for each LIFT condition in Fig. 6, respectively.

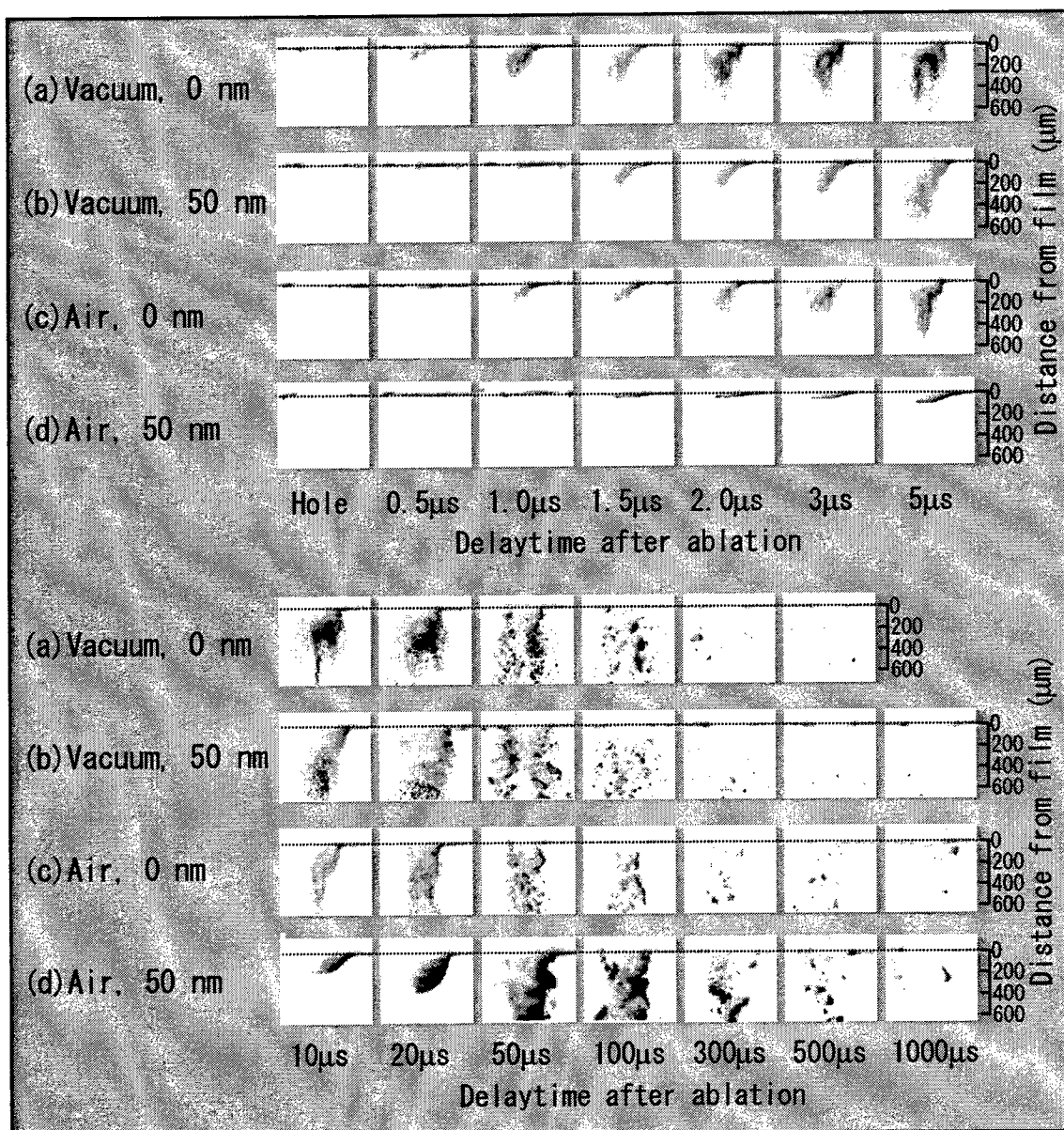


Figure 5: Spatial and temporal distributions of  $\text{TiO}_2$  particles. The thickness of base gold film was 0 or 50 nm, and the atmospheric condition was vacuum or air.

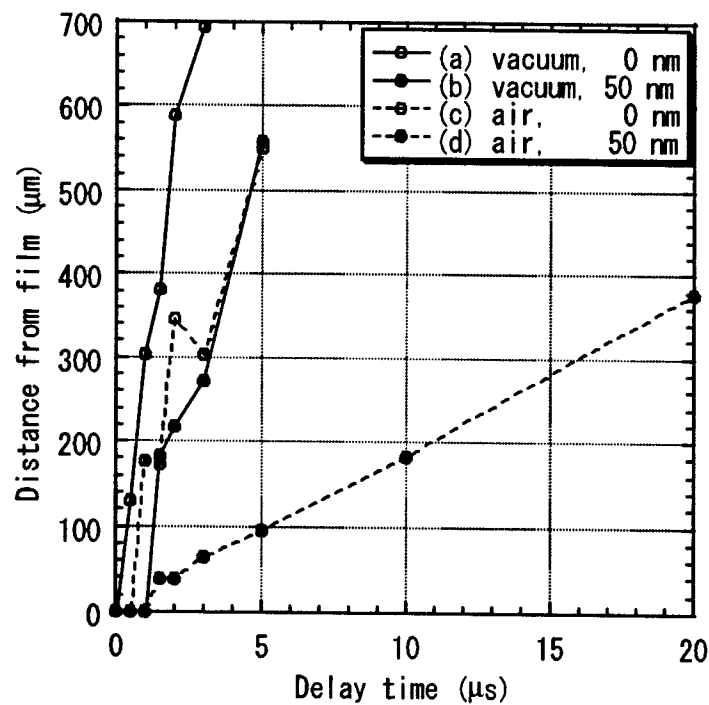


Figure 6: Distances of the propagation front edges of the particles from donor films as a function of delay time.

Fig. 7 shows the ablation energy dependence of the temporal and spatial distributions of ejected particles. The atmospheric condition and film thickness were differed. It seems that in all LIFT conditions the velocity is fast and the amount of ejected particles are abound with higher ablation laser energy. The positions of the front edge of the particles at 2  $\mu\text{s}$  after ablation as a function of ablation laser energy is shown in Fig. 8. It is interesting that the velocity is fastened nonlinearly as the increase of ablation laser energy, and which is different with the behavior of atoms or emissive particles in LIFT process reported in our past paper or other researchers in which the velocity was saturated as the increase of ablation laser energy.<sup>5,6</sup> The velocity was slowed by the existence of gold base film.

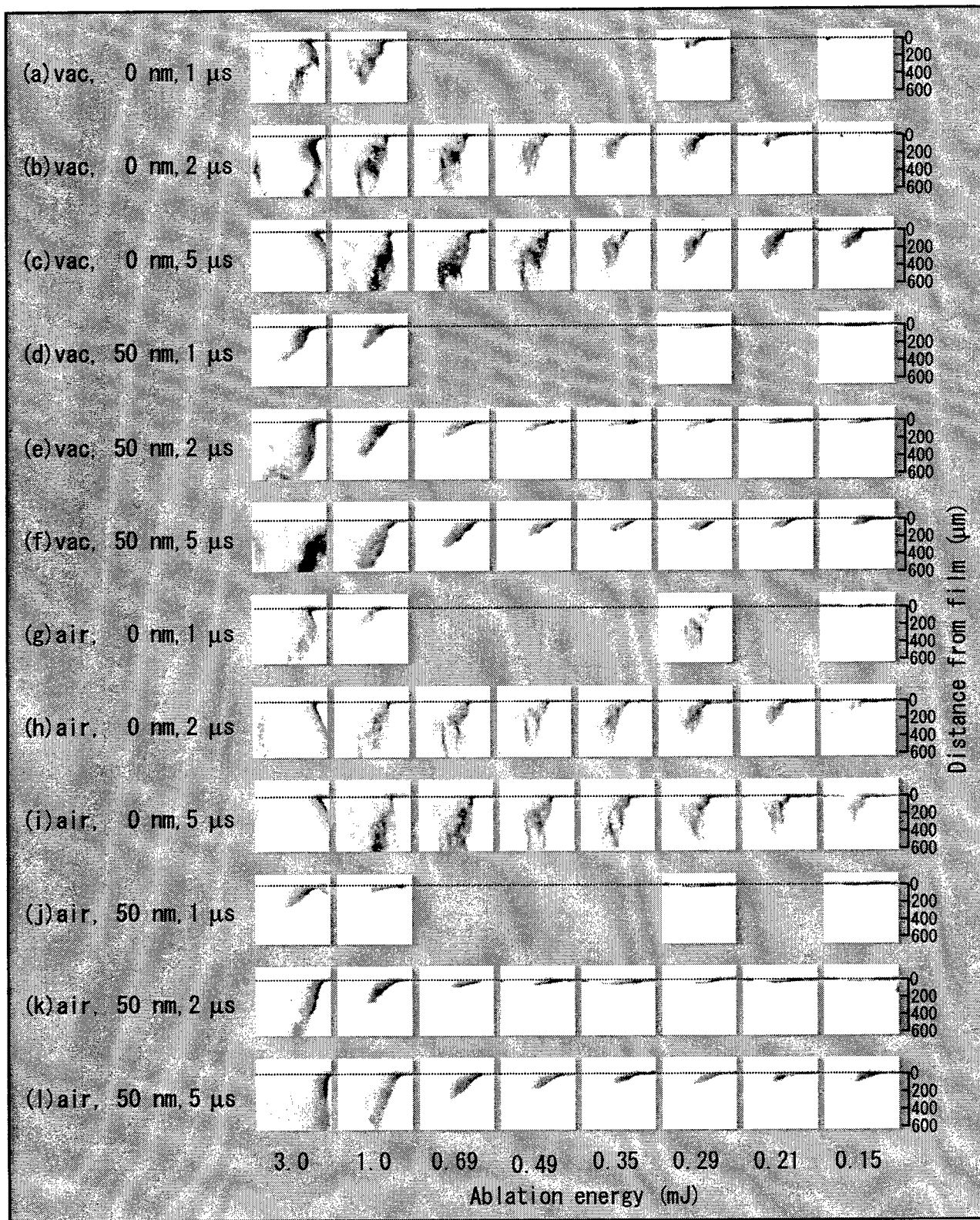


Figure 7: Ablation energy dependence of the spatial and temporal distributions of the  $\text{TiO}_2$  particles.

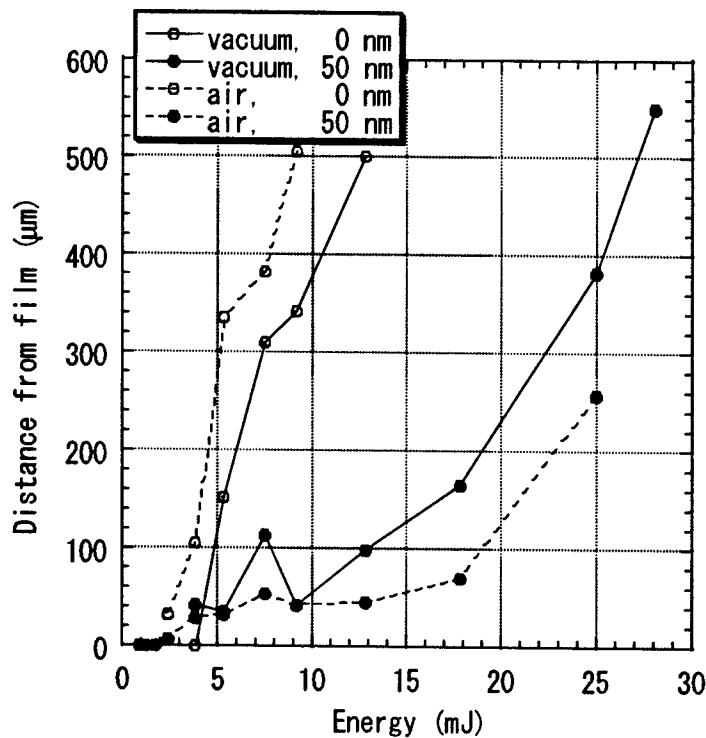


Figure 8: Distances of the propagation front edges from donor films as a function of ablation laser energy.

Fig. 9 shows the temporal and spatial distributions of ejected particles with different base gold film thicknesses observed in vacuum, and the ablation laser energy was 3.0 mJ. It seems that there is no tendency against the difference of the base gold film thickness with this ablation laser energy, which is different with the case in former figures. When no base gold film and the delay time was 1  $\mu$ s, the fastest particles flew beyond the observed area. In this case the velocity of the particles excess 700 m/s. This is quite fast compared with the past experiment<sup>3</sup> observing the velocity of the fluorescent particles on gold base film. The characteristically different conditions in these experiments are the ablation laser energy and ablated area, and they were below 100  $\mu$ J and smaller than 50  $\mu$ m in diameter in the past experiment.



Figure 9: Temporal and spatial distributions of ejected particles with different base gold film thicknesses.



### 3.3 LIFT of laser dye

LIFT of laser dye is useful for marking and doping, and it can emit fluorescence at wavelength longer than excitation light. Fig. 10 shows the transfer of laser dye thin film by LIFT. The distance between the donor and acceptor substrates were about 15  $\mu\text{m}$ . The ablation laser energy was about 0.15 mJ, and the fluence was about 0.20 J/cm<sup>2</sup>. The pictures of donor film and deposited films on SiO<sub>2</sub> observed by CCD camera, and fluorescence from deposited film with excitation light from YAG laser at 532 nm observed by an image-intensified CCD camera with 532 nm cut filter are shown. It is shown that the laser dye was successfully transferred and emitted fluorescence with excitation after transfer by LIFT. This shows that the temperature of the process is low enough to keep the chemical structure of laser dye. In the past experiment, polystyrene particle which has melting point of 115 centigrade was successfully transferred with keeping the shape. So, LIFT is available to deposit materials which are destroyed by heat.

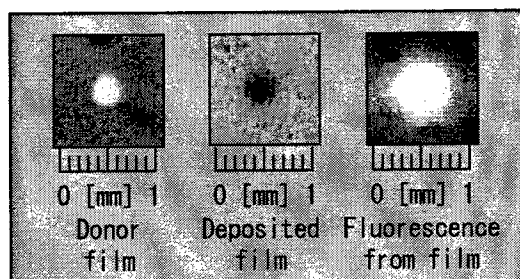


Figure 10: Transfer of laser dye. Pictures of a hole on donor film, deposited film and fluorescence from the deposited film are shown.

## 4. SUMMARY

LIFT was applied to eject micron-sized TiO<sub>2</sub> particles on gold thin film on SiO<sub>2</sub> substrate. The behavior of the ejected TiO<sub>2</sub> particles in the gas phase was imaged by light scattering method attached to an optical microscope. They flew perpendicular to the donor film, and the fastest velocity of particles exceeded 700 m/s. Velocity was slowed with the existence of base gold film and air. In addition, laser dye film on SiO<sub>2</sub> substrate was transferred and deposited on the other SiO<sub>2</sub> substrate by LIFT, and the deposited film emitted fluorescence with excitation by second harmonic wave of YAG laser at 532 nm.

## REFERENCES

1. J. Bohandy, B. F. Kim and F. J. Kim, "Metal deposition from a supported metal film using an excimer laser", *J. Appl. Phys.* **60**, pp. 1538-1539, 1986.
2. G. Koundourakis, C. Rockstuhl, D. Papazoglou, A. Klini, I. Zergioti, N. A. Vainos, C. Fotakis, "Laser printing of active optical microstructures", *Appl. Phys. Lett.* **78**, pp. 868-870.
3. Y. Nakata, T. Okada, M. Maeda, "Microscopic observation of laser-induced forward transfer process by two-dimensional laser induced fluorescence technique", *Proc. SPIE* **3933**, pp. 457-468, 2000.
4. Y. Nakata, T. Okada, "Time-resolved microscopic imaging of the laser-induced forward transfer process", *Appl. Phys. A* **69**, pp. S275-S278, 1999.
5. Y. Nakata, T. Okada, M. Maeda, "Ejection of particles placed on a thin-film by laser-induced forward transfer", *Proc. SPIE* **4274**, pp. 204-211, 2001.
6. A. B. Bullock, P. R. Bolton, "Laser-induced back ablation of aluminum thin films using picosecond laser pulses", *J. Appl. Phys.* **85**, 460-465, 1999.
7. J. Wang, H. Niino, A. Yabe, "Micromachining of transparent materials with super-heated liquid generated by multiphotonic absorption of organic molecule", *Appl. Surf. Sci.* **154-155**, 571-576, 2000.

# Pulsed Laser Ablation of IC Packages for the Device Failure Analyses

M. H. Hong<sup>\*a</sup>, Z.H. Mai<sup>b</sup>, G.X. Chen<sup>a</sup>, T. Thiam<sup>b</sup>, W.D. Song<sup>a</sup>, Y.F. Lu<sup>a</sup>, C.E. Soh<sup>b</sup>, T.C. Chong<sup>a</sup>

<sup>a</sup>Laser Microprocessing Group, Data Storage Institute, DSI Building,  
5 Engineering Drive 1, Singapore 117608

<sup>b</sup>Advanced Micro Devices (S) Pte Ltd, Singapore 469028

## ABSTRACT

Pulsed laser ablation of mold compounds for IC packaging in air and with steam assistance is investigated. It is applied to decap IC packages and expose computer CPU dies for the device failure analyses. Compared with chemical decapping, the laser ablation has advantages of being fast speed, non-contact & dry processing. Laser ablation with the steam assistance results in higher ablation rate and wider ablated crater with much smoother surface morphology. It implies that the steam assisted laser ablation can achieve a faster and better quality laser processing. Audible acoustic wave and plasma optical signal diagnostics are also carried out to have a better understanding of the mechanisms behind. Light wavelength and laser fluence applied in the decapping are two important parameters. The 532 nm Nd:YAG laser decapping at a low laser fluence can achieve a large decapping area with a fine ablation profile. IC packages decapped by the laser ablation show good quality for the device failure analyses.

**Keywords:** Laser ablation, steam assistance, mold compounds and device failure analyses.

## 1. INTRODUCTION

In the early days of semiconductor fabrication, integrated circuit (IC) devices were largely packaged in glass, ceramic or metal. Since 1960s, device manufacturers began to investigate the possibility of encapsulating their products in plastic materials or polymers [1]. The main incentives of the plastic encapsulation were large cost reduction over other material packaging and high compatibility with mass production. It allows several hundred packages to be encapsulated in a single operation, which only takes a few minutes. As IC technology develops, plastic packaging has already received the greatest emphasis and extensively applied in the IC packaging [2]. With major advantages in cost, size, weight, performance and availability, plastic IC packages have attracted 97% of the market share of worldwide microcircuit sales. During the IC device packaging, small wafer die is placed on the wafer die so that it achieves the electric connection of the IC circuits with the outside other function circuits. To ensure the IC packages' resistance abilities to the environment affect (such as heat and humidity), a thin transparent layer of epoxy materials is bonded above the wafer die and completely covers the wafer die. Then the IC circuits are encapsulated inside the black mold compounds. IC package failure analysis is one of the important processes in the industry to trace the roots of the device failure and increase the manufacturing yield. There are many techniques in the device failure analyses [3-4]. For example, electric signal detection is a typical technique to detect the electric failure with the analysis of the electric diagnostic results. However, it is very difficult to get the enough information due to the high integration of the circuits. To have a better understanding of the device failure reasons, it is necessary to unpack the IC packages and remove the black mold compounds on the top of epoxy layer and wafer die. It is called the decapping of IC packages. Chemical decapping technique is currently used in the IC device failure analyses. In the chemical decapping, either sulfuric acid and/or nitride acid are used, depending on mold compounds for different plastic packages. During the chemical decapping, bond pads, solder balls and copper traces in organic die attachment are potentially damaged after dozens of hours in the chemical solution reaction. It is also difficult to protect the leadframe during the chemical decapping. Therefore, it is a

\*dsihmh@dsi.nus.edu.sg; Phone 65-8748707; fax 65-7771349; <http://www.dsi.nus.edu.sg>; DSI Building, 5, Engineering Drive 1, Singapore 117608

high challenge for the industry to find a new solution to unpack the IC packages without any side affect to its internal circuit structures.

Pulsed laser ablation of the solid substrates has been extensively applied in thin film deposition, surface cleaning, structure patterning and chemical composition analyses [5-8]. There is explosive removal of the substrate materials during the high power and short pulse laser irradiation. It is based on the laser photo-ablation by breaking chemical bonds of organic materials or the thermal ablation due to superfluous laser energy irradiated [9-11]. Mold compound is a complex mixture of  $\text{SiO}_2$ , curing agents and accelerators [12]. By irradiating a pulsed laser beam on an IC package, the laser ablation can be used to remove the mold compounds easily, which has been successfully applied in the mold deflashing of the IC packages [13]. In this paper, pulsed laser ablation of the mold compounds in air and with the steam assistance is studied. Acoustic wave and plasma optical signal diagnostics are carried out to get the better understanding of the dynamic laser processing and provide an option for the process real-time monitoring. This technique is then applied to decap the IC packages for the device failure analyses.

## 2. EXPERIMENTAL SETUP

Figure 1 shows the experimental setup of pulsed laser decapping of the IC packages for the device failure analyses in air and with the steam assistance. A KrF excimer laser (Lambda Physik LPX 100,  $\lambda=248$  nm,  $\tau$  (FWHM) =30 ns) or an Nd:YAG laser (B&I 5022 D.NS 10,  $\lambda=532$  nm,  $\tau$  (FWHM) =7 ns) was used as a light source. Laser beam was focussed by a lens at a focal length of 250 mm and irradiated perpendicularly to an IC package surface. Laser fluence was adjusted by changing pulse energy from the laser controller. Substrate morphology was analyzed by an Alpha-Step 200 profilometer (Tencor Instruments) to get the information on the depth and width of the ablated crater. A wide-band microphone (Sony ECM-23F3, frequency response: 20 Hz to 20 kHz) was applied to capture audible acoustic waves generated during the laser ablation. An ultrafast phototube (Hamamatsu R1328U-53) was used to diagnose optical signals from plasma generation and its dynamics. The signals were sent to a fast digital oscilloscope (Tektronix TDS520, 500 MHz) for data storage and analyses. For the steam assisted laser ablation,  $\text{N}_2$  gas carried hot water vapor generated by the heater to the nozzle outlet and formed a steam layer on the substrate surface. Thickness of the steam film was in dozens of microns (estimated from interference patterns). It can be tuned by gas following rate, steam temperature and nozzle position.

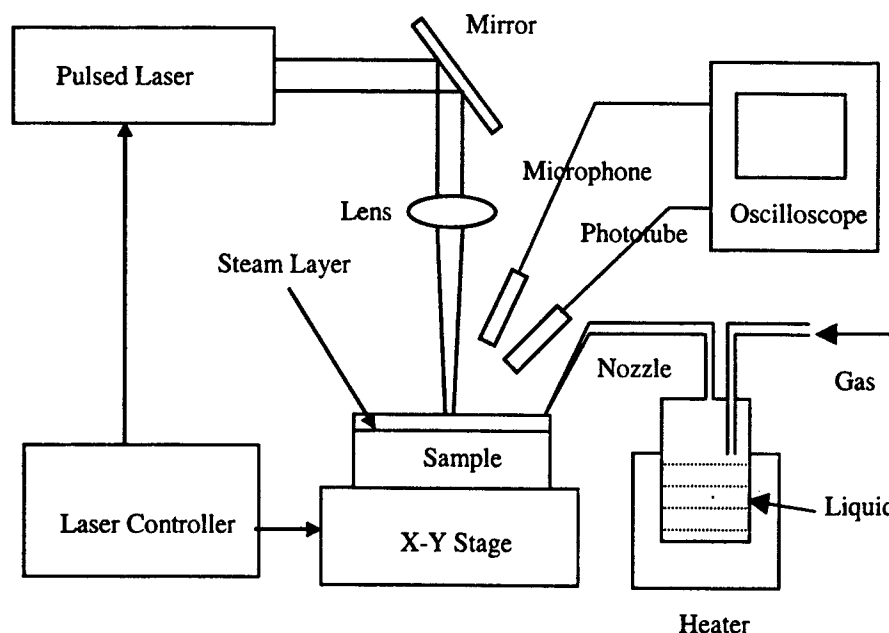


Figure 1 Experimental setup of pulsed laser decapping of the IC packages for the device failure analyses.

### 3. RESULTS AND DISCUSSION

#### 3.1 KrF excimer laser ablation of mold compounds in air and with the steam assistance:

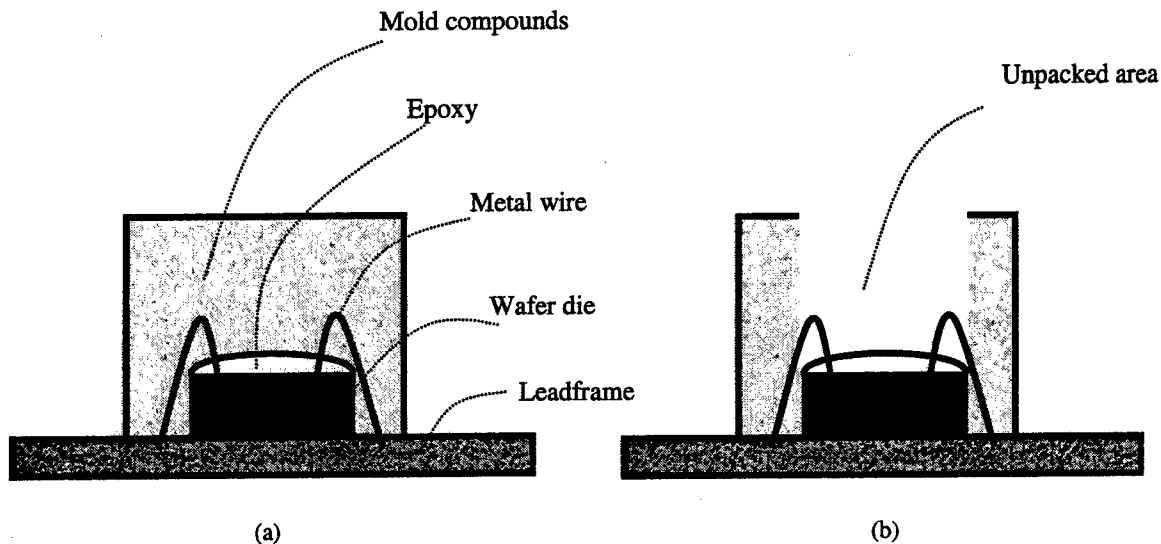
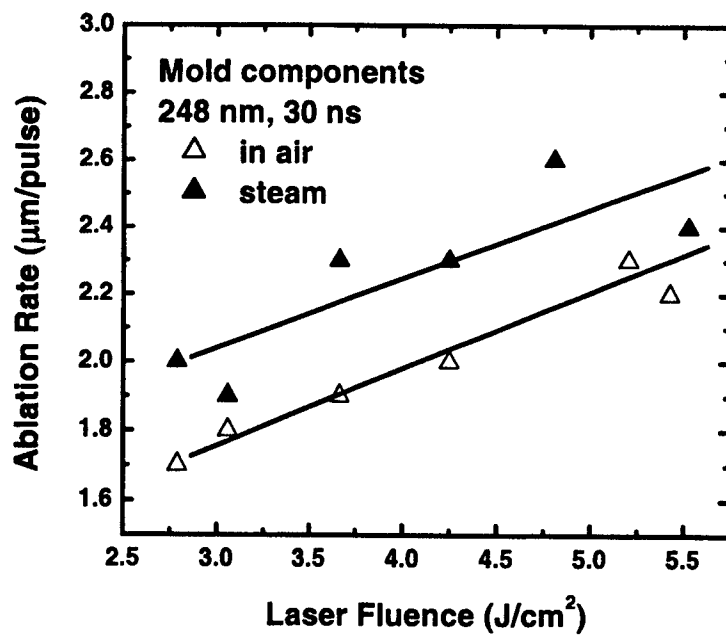
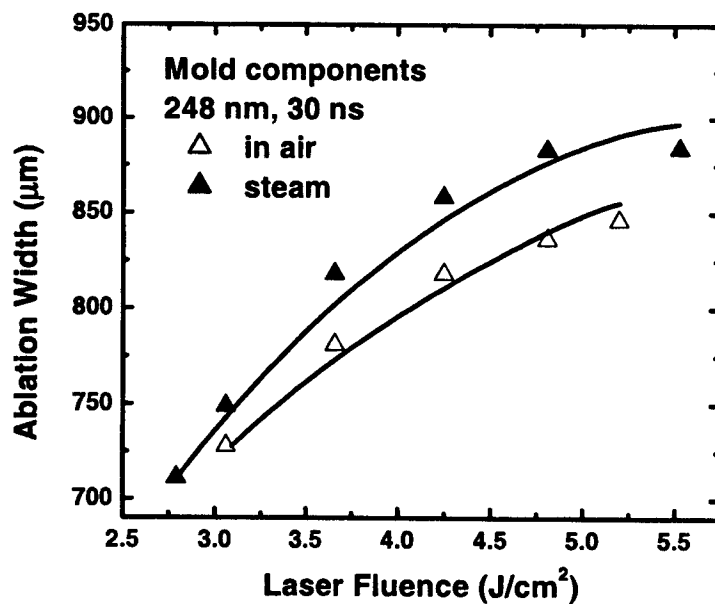


Figure 2 The structures of IC packages before (a) and after (b) the decapping for device failure analyses.

Figure 2 shows the structures of IC packages before (a) and after (b) the decapping for device failure analyses. The objective of the laser decapping is to achieve the complete removal of the mold compounds on the top of the die and epoxy layer so as to expose metal wire and die circuit structures for the failure analyses. Laser irradiation should not damage the epoxy layer and die surface. Therefore, it is very important to know how many materials are removed during the laser decapping so that the process can be properly informed whether and when the laser decapping has reached the epoxy layer. Laser ablation rate is one key parameter to characterize the ablation results. It is defined as the average depth of the ablated crater after one pulse of the laser irradiation and provides the information on the depth profile during the laser ablation. The width and length of the ablated crater are related to the geometry of laser spot on the package surface. Figure 3 shows the dependence of ablation rate and width on laser fluence during the KrF excimer laser ablation of mold compounds in air and with the steam assistance. For a laser fluence of  $5.5 \text{ J/cm}^2$ , the ablation rate is  $2.1 \text{ }\mu\text{m}$  for the ablation in air. If the laser output energy is  $250 \text{ mJ}$  at a repetition rate of  $10 \text{ Hz}$ , it can be estimated that one pulse of the laser irradiation can remove a volume of  $10^{-2} \text{ mm}^3$  mold compounds. It needs about 22500 pulses of the laser irradiation to form a decapping crater in the size of  $15 \text{ mm} \times 15 \text{ mm} \times 1 \text{ mm}$ . The whole process takes about 1 hour including the time for the beam scanning. Comparing with the dozens of hours chemical decapping, the laser ablation has the advantages of fast speed processing. It can also be observed in Fig. 3 that the ablation depth and width from the steam assisted laser ablation are much higher than those in the air. For the laser fluence of  $5.5 \text{ J/cm}^2$ , the ablate rate is increased from  $2.1 \text{ }\mu\text{m}$  to  $2.3 \text{ }\mu\text{m}$  and the width from  $850 \text{ }\mu\text{m}$  to  $875 \text{ }\mu\text{m}$ . It implies that with the steam assistance, the laser ablation can remove about 15 % more volume of the mold compound materials, which provides a faster laser decapping. In our previous study, it is shown that the ablated crater with the steam assistance has a smoother profile, which also provides a better and more uniform laser ablation geometry on the package surface [14]. However, there is one important issue, which should be taken into account during the laser decapping: the epoxy layer and die surface will also be ablated away by the KrF excimer laser at a laser fluence of  $5.5 \text{ J/cm}^2$  (The threshold fluence for the silicon ablation is around  $1.2 \text{ J/cm}^2$ ). Therefore, the laser fluence needs to be tuned down to avoid any damage on the epoxy



(a)



(b)

Figure 3 Ablation rate (a) and width (b) versus laser fluence during the KrF excimer laser ablation of mold compounds in air and with the steam assistance.

layer and die surface when the laser ablation is about to reach the interface layer between the mold compounds and epoxy layer.

### 3.2 Signal diagnostics during the laser ablation of mold compounds in air and with the steam assistance:

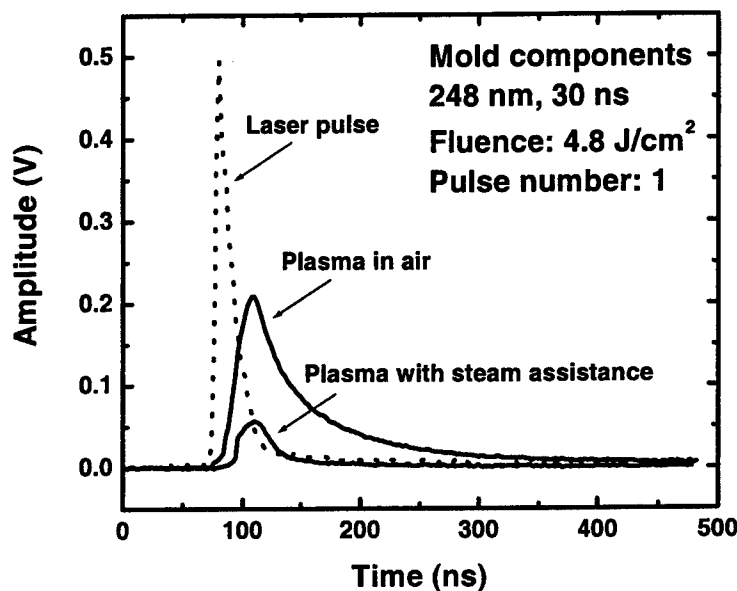


Figure 4 Optical signals detected by the ultrafast phototube during the KrF excimer laser ablation of mold compounds in air and with the steam assistance at a laser fluence of  $4.8 \text{ J/cm}^2$ . For the good view of the signals, the plasma signal in air was enlarged 2 times and the signal with the steam assistance 5 times.

Figure 4 shows the optical signals detected by the ultrafast phototube during the KrF excimer laser ablation of mold compounds in air and with the steam assistance at a laser fluence of  $4.8 \text{ J/cm}^2$  (For the good view of the signals, the plasma signal in air was enlarged 2 times and the signal with the steam assistance 5 times). It is clear that the plasma in air starts at several nanoseconds later than the laser pulse. The plasma optical signal overlaps with the laser pulse. It is attributed to the laser plasma interaction. During the laser ablation, the leading part of the laser pulse energy is absorbed by the substrate surface, which leads to the substrate surface temperature increase, melting, evaporation and plasma generation. The plasma generated is in highly dynamic and will absorb the later part of the incoming laser energy, which limits the laser energy irradiating on the substrate surface. This process is called the plasma shielding effect and results in the saturation of the ablation rate as laser fluence increases. Laser plasma interaction can be characterized from the overlapping area of the laser scattering pulse and the plasma profile [15]. The high overlapping area implies the stronger laser plasma interaction. Compared with the steam assisted laser ablation, it can be informed from Fig. 4 that the peak amplitude of the plasma optical signal for the laser ablation in air is about 10 times higher. Meanwhile, the plasma signal for the laser ablation with the steam assistance starts about 20 ns later than that in the air ablation. It can be concluded that the laser plasma interaction is greatly reduced with the steam assistance. There is more laser energy passing through the plasma to enhance the laser ablation with more substrate materials removal.

Pulsed laser ablation is a rich source for acoustic wave emission in the frequency spectra of both sonic and ultrasonic components [16]. With a microphone nearby the substrate surface to detect the audible acoustic waves, the laser ablation information can be sensed in non-contact mode. In our previous study, it is found that the first peak-to-peak amplitude of the acoustic waves is closely related to the ablation rate [17]. It can provide the information how many substrate materials are removed during the laser irradiation and serve as a real-time monitoring for the laser decapping process. Figure 5 shows the first peak-to-peak amplitude of the acoustic waves versus laser fluence during

the KrF excimer laser ablation of the mold compounds in air and with the steam assistance. It is clear that variation of the peak amplitude with the laser fluence has the same tendency as the ablation rate. The peak amplitude is also higher for the steam assisted laser ablation than that in the air. The audible acoustic wave generation is due to the ablated substrate materials interaction with the surrounding air molecules. During the plasma dynamics, the friction among tiny ablated substrate materials and the air molecules decays the plasma shock wave into the audible acoustic waves. The more ablated substrate materials, the stronger friction and the stronger acoustic waves. It shows that the steam layer on the substrate surface confines the shock wave and induces the more substrate materials removal.

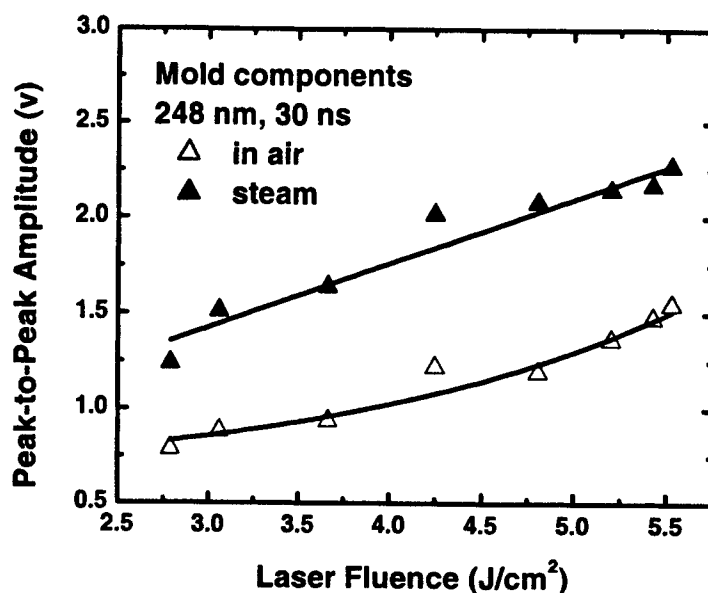


Figure 5 The first peak-to-peak amplitude of the audible acoustic wave versus laser fluence during the KrF excimer laser ablation of mold compounds in air and with the steam assistance.

### 3.3 532 nm Nd:YAG laser ablation of mold compounds in air and with the steam assistance:

Figure 6 shows the curve of ablation rate versus laser fluence during the 532 nm Nd:YAG laser ablation of the mold compounds in air and with the steam assistance. It is clear that the ablation rate increases greatly with the steam assistance. For a laser fluence of 250 mJ/cm², the ablation rate increases from 15 nm to 75 nm. It implies that the steam assistance can enhance the laser ablation much stronger at a lower laser fluence for a shorter pulse duration laser. For the Nd:YAG laser output pulse energy of 600 mJ and repetition rate of 10 Hz, one pulse of the laser irradiation can remove a volume of  $3.6 \times 10^{-3} \text{ mm}^3$  for the laser ablation in air and  $1.8 \times 10^{-2} \text{ mm}^3$  with the steam assistance. It needs 62500 and 12500 pulses of laser irradiation to form an ablated crater with a size of 15 mm x 15 mm x 1 mm, respectively. The whole process takes about 2 hours and half an hour, respectively. Compared with the KrF excimer laser decapping at the high fluence, the Nd:YAG laser decapping covers a large area with much smaller ablation rate, which can achieve the finer removal of the materials and avoid the scanning overlapping problems as well. With the steam assistance, the processing speed is faster. The other advantage is that the epoxy layer is transparent to the green light. The laser irradiation of the KrF excimer laser may induce the chemical modification of the epoxy layer, since its photon energy is 5 eV, which is higher than the chemical bonding energy for the organic materials from 3 to 5 eV. It may affect the protection layer properties and induce the difficulties for the device further failure analyses. Therefore, it can be concluded that low fluence and steam assisted laser ablation with the 532 nm Nd:YAG laser irradiation would be one of the best options for the laser decapping of the IC packages for the device failure analyses. Figure 7 shows the microscopic images of (a) Au lines, (b) solder bonds in lead frame, (c) bond pads on wafer die and (d) circuit structures on the wafer die for the IC packages decapped by the Nd:YAG laser with the steam assistance. It is clear that there is no damage on the package surface. Different device parts and circuit structures on the die can be clearly observed.



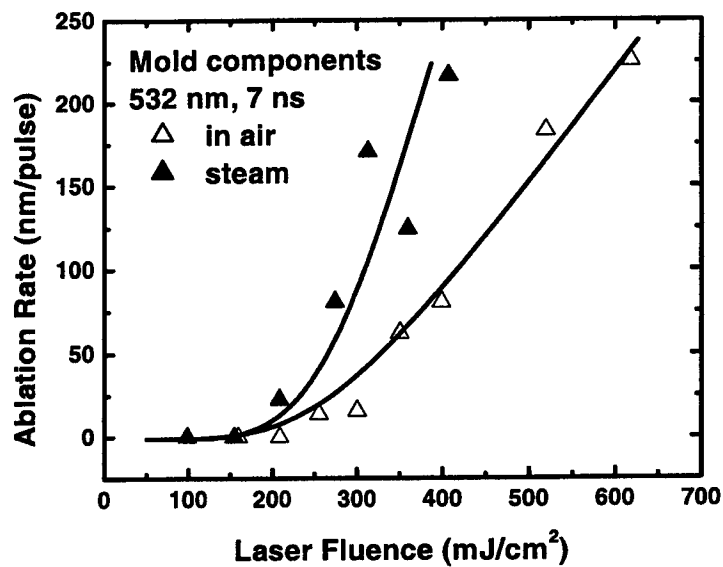
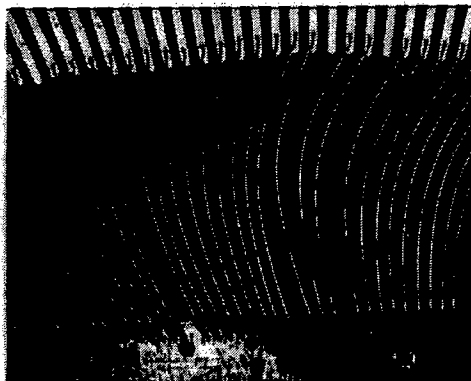
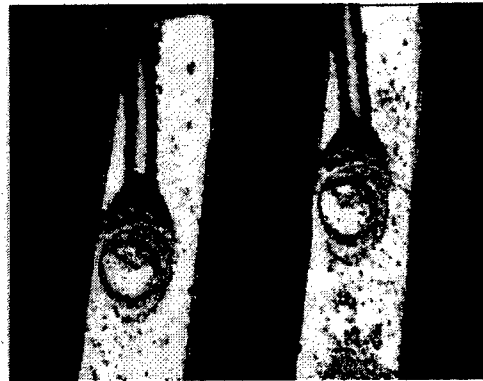


Figure 6 Ablation rate versus laser fluence during the 532 nm Nd:YAG laser ablation of mold compounds in air and with the steam assistance.



(a)



(b)



(c)



(d)

Figure 7 Microscopic images of (a) Au lines, (b) solder bonds in leadframe, (c) bond pads on wafer die and (d) circuit structures on the die for the IC packages decapped by the steam assisted laser ablation.

#### 4. CONCLUSIONS

Pulsed laser ablation of the mold compound materials for the IC packaging by the KrF excimer laser and Nd:YAG laser irradiation is investigated. It is found that the ablation rate increases with laser fluence and the laser ablation result can be enhanced with the steam assistance. Diagnostics of the audible acoustic waves and plasma optical signals shows that the steam assistance results in the weaker laser plasma interaction and stronger confinement of the plasma shock wave, which leads to more laser energy irradiating onto the substrate surfaces and more substrate materials removal. A 532 nm Nd:YAG laser would be the better laser source than the KrF excimer laser for the device decapping. It can avoid the possible chemical property modification for the epoxy layer under the UV light irradiation. Low laser fluence irradiation can provide the large processing area and fine ablation profile. The laser ablation achieves the clear exposure of different device parts and circuit structures on the wafer die without the substrate surface damages.

#### REFERENCES

1. M.T. Goosey, Eds., *Plastics for Electronics* (Elsevier, London, 1985).
2. Norman G. Einspruch, Eds., *VLSI Electronics Microstructure Science*, Vol. 9 (Academic, New York, 1985).
3. C.Y. Chang and S.M. Sze, Eds., *ULSI Technology* (McGRAW-HILL, New York, 1996).
4. Lawrence C. Wagner, Eds., *Failure analysis of integrated circuits : tools and techniques* (Kluwer Academic Publishers, 1999).
5. R.K. Singh and J. Narayan, *Physics Review B*, 41, 8843 (1990).
6. J.H. Brannon, *Circuits and Devices*, Sept., 19 (1990).
7. Y.F. Lu, W.D. Song, M.H. Hong, T.C. Chong and T.S. Low, *J. Appl. Phys.* 80, 499 (1996).
8. A.V. Pakhomov, W. Nichols and J. Borysow, *Appl. Spec.* 50, 880 (1996).
9. B. Luk'yanchuk, N. Bityurin, S. Anisimov, N. Arnold and D. Bauerle, *Appl. Phys. A*, 62, 397 (1996).
10. H. Schmidt, J. Ihlemann, B. Wolff-Rottke, K. Luther and J. Troe, *J. Appl. Phys.*, 83, 5458 (1998).
11. G.H. Pettit, M.N. Ediger, D.W. Hahn, B.E. Brison and R. Sauerbrey, *Appl. Phys. A*, 58, 373 (1994).
12. R. Zecber, *Plastics Engineering* June, 35 (1985).
13. Y.F. Lu, M.H. Hong, D.S.H. Chan and T.S. Low, *Mat. Res. Soc. Proc.* 397, 323 (1996).
14. S. Zhu, Y.F. Lu, M.H. Hong and X.Y. Chen, *J. Appl. Phys.* 89, 2400 (2001).
15. Y.F. Lu, M.H. Hong and T.S. Low, *J. Appl. Phys.*, 85, 2899 (1999).
16. W.P. Leung and A. C. Tam, *Appl. Phys. Lett.*, 60, 23 (1992).
17. M.H. Hong, Y.F. Lu, W.D. Song, D.M. Liu and T.S. Low, *SPIE* Vol. 3184, 148 (1997).

## **Physical and Chemical Aspects of Laser-Materials Interactions Relevant to Laser Processing**

J. T. Dickinson

Surface Dynamics Laboratory, Physics Department  
Washington State University, Pullman, WA 99164-2814

### **ABSTRACT**

The use of lasers in packaging and materials processing is an increasingly attractive choice for high technology manufacturing. As we push for more demanding materials processing tasks and smaller dimensions, an understanding of the underlying physical and chemical aspects of problems becomes important. Here we discuss some of these issues relevant to materials processing.

### **1. INTRODUCTION**

Soon after the development of the first laser it was suggested that it would have uses as a manufacturing tool due to many of the advantages of radiation sources over conventional mechanical and thermal techniques. Today lasers are used for a number of laser processing tasks in advanced packaging and interconnect industry. As the commercial boom in microelectronic and optoelectronic devices and the trend toward miniaturization continues, industrial use of lasers will play an increasingly important role. Materials ranging from ceramics/glasses, metals, semiconductors, polymers, natural and manmade fibers and composites have all been shown to interact with one or more laser types in useful ways. The current arsenal of lasers of current or future industrial interest include both CW and pulsed lasers. The commonly used lasers include the CO<sub>2</sub> laser, Excimer Lasers, Solid State Lasers (including diode pumped YAG and Ti:Sapphire lasers), Metal Vapor Lasers, and for some applications, Diode (semiconductor) lasers.

The microfabrication applications that are potentially well matched to using lasers include:

#### **Use of Lasers in Packaging/Processing**

- |                               |                                  |
|-------------------------------|----------------------------------|
| • <b>Etching</b>              | • <b>Trimming</b>                |
| • <b>Cutting</b>              | • <b>Welding/Soldering</b>       |
| • <b>Stripping</b>            | • <b>Bonding</b>                 |
| • <b>Cleaning</b>             | • <b>Marking/Printing</b>        |
| • <b>Drilling</b>             | • <b>Annealing</b>               |
| • <b>Surface Modification</b> | • <b>Photolithography</b>        |
| • <b>Dry Patterning</b>       | • <b>Mask Fabrication</b>        |
| • <b>Scribing</b>             | • <b>3D Microstructures</b>      |
| • <b>Deposition (PLD)</b>     | • <b>Laser Recrystallization</b> |

Microhole drilling and trimming of resistors and capacitors and laser recrystallization are certainly the most successful applications of lasers in microelectronics.

The "advantages" of using lasers always must be weighed against disadvantages. A typical list of advantages include:

### **"Advantages" of Using Lasers**

- **Close tolerance (resolution; feature size-usually wavelength dependent)**
- **Repeatability (often excellent)**
- **Potential unit cost reductions, cost effectiveness**
- **Material versatility (including fragile, ultrathin, highly reflective materials)**
- **Roughness of Surfaces (Sometimes < nm)**
- **Minimal distortion in heat affected zones**
- **No tooling to wear out or change over**
- **Non-contact processing eliminates unwanted stress on materials**
- **Clean processing: minimal debris, burrs, uplifted recast**
- **Flexibility - fast setups achieved with computer controls**

HOWEVER—in evaluating these "advantages" one must weigh the extent or degree of each, thus the quotation marks around the word advantages. For example, is the resulting roughness tolerable, is a small amount of re-deposited particulates acceptable, is the process truly competitive with traditional methods cost-wise. Regarding costs, always lurking in the background are the expenses for operator training and addressing safety concerns. The "complaints" of a fabrication manager might include:

- *it doesn't work (it breaks it, instead of makes it);*
- *it's UNPREDICTABLE (e.g., no software package to model the entire process);*
- *it's too slow;*
- *it's too BIG (the modified area) or*
- *it's too SMALL;*
- *it's only one at a time;*
- *it messes up (harms, degrades, contaminates) the 'neighborhood';*
- *it's too expensive;*
- *it's only line of sight;*
- *the laser and/or optics need too much maintenance.*

Basic physics and chemistry can help address only a few of these issues. Of course, we note that the university academics state in every research proposal they submit: "*We need to understand the underlying mechanisms so that we can advance the technology.*" In truth, most of the advancements in fabrication and processing are occurring ahead of the science and can't wait. It is often only when a particular process is very promising yet is not quite working, or not optimized, or has too many uncontrolled parameters that fundamental understanding would be a benefit. If the value-added by performing some manufacturing step using lasers is high, this further motivates more basic research on mechanisms and understanding.

## **II. PHYSICAL AND CHEMICAL ASPECTS**

So let us explore a few of the major questions and issues involved in laser materials interactions, particularly those that involve material removal and heat driven processes. Some of the important aspects are:

## Important Aspects of Laser Materials Interactions

- **Light Absorption Processes** (linear; nonlinear – multiphoton, multiple-photon; defects)
- **Absorbed energy density vs. position and time**
- **Emission Mechanisms** (e-, ions, neutrals, clusters, “chunks”)
- **Factors influencing rates of material removal and/or material modification**
- **Photothermal vs. Photoelectronic** (fs, ps, ns)
- **Role of thermal-mechanical phenomena** ( $\nabla T$ , shock)

**Melting/Resolidification**

**Fracture, spallation (particles)**

**Diffusion; Segregation**

**Vaporization**

**Condensation of vapors in gas phase (particles)**

- **Role of external environment** (reactive gases, liquids, pressure)
- **Equilibrium Thermodynamics vs. Non-Equilibrium**
- **Role of laser-plume interactions**
- **Role of Laser Parameters**  
( $\lambda$ ,  $t_{\text{pulse}}$ ,  $I_{\text{peak}}$ ,  $\theta$ , spot size, rep. Rate, no. of pulses)
- **Understanding Dependence on Target Parameters**  
(e.g., optical & thermal properties, defects, morphology, spatial distributions, interfaces)
- **Generating PREDICTIVE MODELS (GRAND CHALLENGE to theorists)**

All of these facets are addressable with today's knowledge and understanding of the underlying physics and chemistry. We want to emphasize that much of what is happening in the use of lasers involves either bond breaking or bond making. Usually it is desired to do this locally (precisely), quickly (to be cost effective; to avoid too much heating), and with “no” collateral damage. The use of lasers in fabrication is similar to the use of lasers in medicine – just like the medical doctor, the fabricator must abide by the constraint: “*Above All, Do No Harm*”. Minimizing this surrounding “damage” is often the biggest challenge. Often the types of bonds being broken (or made) influences the choice of laser parameters which include wavelength, pulse width/CW, peak irradiance, angle of incidence, spot size, repetition rate, and number of pulses. We usually consider four fundamental types of bonding:

- **Covalent Bonding** (diamond, Si, Ge, GaAs, GaN, BN, SiO<sub>2</sub>)
- **Ionic Bonding** (alkali halides, alkaline earth halides, metal oxides such as MgO)
- **Metallic Bonding** (metals in general)
- **Intermolecular Forces** (Hydrogen Bonding (strongest), Dipole-Dipole Forces, London Dispersion Forces (non-polar structures interacting—weakest)).

An example of where intermolecular forces would be important are interfaces which will be (making bonds) or are (breaking bonds) connected via adhesive bonds; another example is the entire range of interactions involving unwanted ‘pesky’ particles adhering to substrates which need to be removed. Using laser cleaning to remove a particle thus requires that these intermolecular forces be overcome

in order to detach the particle. Electrostatic charge, if present, can of course increase the bonding of particles to surfaces considerably. The use of water ("steam cleaning") in laser cleaning would assist in neutralizing this charge along with the advantages of nucleating bubbles to assist lifting particles.<sup>1,2,3</sup> Of course all glassy polymers consist of covalently bonded polymer chains with intermolecular forces interacting between the chains. Thus, the properties of common polymers such as polymethylmethacrylate (PMMA), polycarbonate (PC), and polystyrene (PS), are strongly dependent on these intermolecular forces which lead to interchain friction, entanglements, and free-volume dependent attributes (e.g., thermal properties; gas diffusivity).

Figure 1 shows schematically the interaction of a laser beam with a structure of some complexity. Assuming a reasonable degree of absorption (so we can ignore transmission), the incident photons are absorbed either due to excitation of electrons or for longer wavelengths, excitation of vibrational modes. The reflectivity of the material then dictates how much of the incident beam is absorbed. The 3D distribution of absorption centers exposed to the incident beam and their optical properties in relation to the laser light dictate the energy density distribution in the near surface region. In metals, absorption takes place very near the surface and can occur by excitation of both conduction band (free electron-like) and valance band (interband absorption) electrons are the absorbing entities. These electrons transfer their increased kinetic energy to the lattice via phonon scattering on time scales of ps, resulting in a temperature increase. For long pulses ( $> \text{ps}$ ) heating is occurring during the pulse and so in general one can treat light energy to heat in one step.

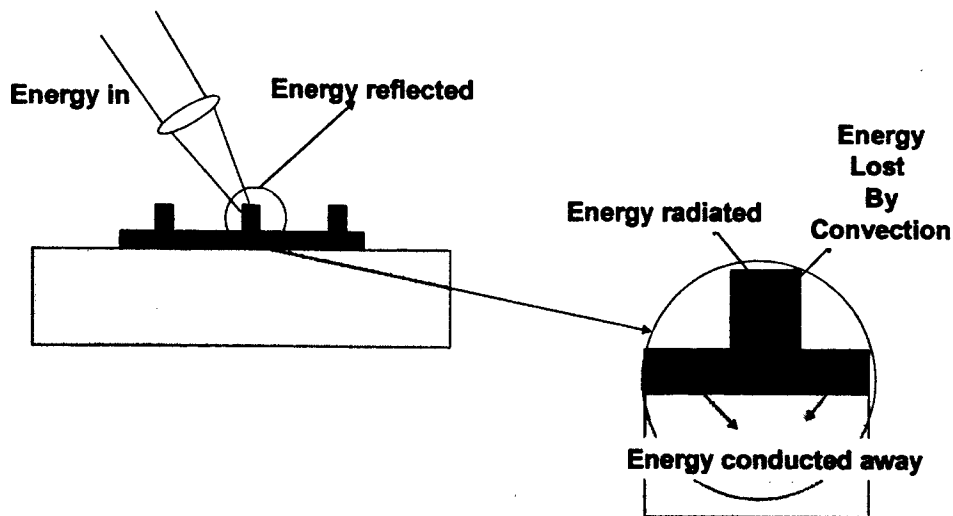


Fig. 1. Schematic of relevant interactions and consequences of energy absorption.

For semiconductors and insulators, absorption is either through vibrational excitation (requiring infrared light matching allowed vibrational transitions of the material) or electronic excitations (e.g., via chromophores, defects, or band-to-band transitions). The electronic energy tends to be more localized than in metals, but in "real materials", the electronic energy is again quickly transformed into thermal energy. Atomic dimension energy localization can assist in the breakdown of materials, particularly in crystalline ceramics and silica-based glasses. For example, electron-hole pairs in an insulator are trapped at a lattice site which then may lead to motion of nuclei – the beginnings of decomposition of the material, all non-thermal in nature. Numerous examples of such phenomena are presented in the book by Itoh and Stoneham.<sup>4</sup> However, many of

the rates of material removal using lasers, even those initiated by electronic processes, are still thermally enhanced or thermally controlled; thus, in general, the practical use of lasers in fabrication is dominated by thermal processes--thus arguing over "photoelectronic" vs. "photothermal" is moot.

**Comments on Thermal Modeling.** In seeking precision in processing, the fate of this deposited energy is highly significant. As seen in Fig. 1, the dispersion of the thermal energy away from the region where it was absorbed can involve radiative, convective, and conductive transport. By far the most important for practical applications is the heat transport by diffusion/conduction away from the higher temperature irradiated region into the cooler surrounding material. The rates and dimensions involved determine the spatial region that reaches high temperatures--the so-called Heat Affected Zone. Many modeling efforts have been focused on predicting the spatial and temporal distribution,  $T(r,t)$ , during and following the laser pulse.<sup>5</sup> One can readily write down the appropriate time and space dependent Heat Equation:

$$\frac{\partial T(r, t)}{\partial t} = \frac{H(r, t)}{C_p} + \frac{1}{\rho C_p} \nabla \cdot (k \nabla T) \quad (1)$$

where  $k = \rho C_p \kappa$  = thermal conductivity with units of Joules / (m K s)

$\kappa$  = thermal diffusivity, in  $m^2/s$

Note that  $\rho$ ,  $C_p$ , and  $\kappa$  are all Temperature Dependent; Therefore,  $k$  is Temperature Dependent.

$H(r, t)$  = Heat input per unit mass in Joule / (Kg s); for linear absorption,  $H$  is proportional to  $\alpha I(r, t)$

where  $\alpha$  = linear absorption coefficient and  $I(r, t)$  = instantaneous power density of the laser irradiation during the pulse.

The methods commonly used to solve analytically or numerically are:

Laplace transforms	}	Analytic
Green's functions		
Fourier transforms		
Stochastic/Monte Carlo	}	Numerical
Finite Differences		

Computer models suffer from two potential difficulties:

- Poor physical description. (The system has been idealized to the point where it no longer describes reality--similar to the physicist's "Spherical Cow").
- Poor algorithm. (The algorithm is not adequate to describe the behavior of the model, let alone reality.) Finite element models of laser absorption and heating generally involve good algorithms, but the computational overhead is high and again only simple models can be studied.

One approach that seems promising is the use of stochastic models. Stochastic models of laser absorption utilize a 'lean and mean' algorithm, allowing for more complex, realistic physical models. The main limitation to the physical models it can describe is that the temperature in each little cell is considered to be uniform. There are tricks to minimize the impact of this assumption (smaller cells, extrapolation etc.). Algorithmically, the output of these models always displays stochastic noise, which can be minimized by raising the number of heat packets and cells. Stochastic models provide an important check on the more well behaved output of finite element and Monte Carlo codes. If simplified physical models employed by these more sophisticated algorithms are adequate, their results will be consistent with properly executed stochastic models (to within the noise limits). An impressive example of a simulation of laser heating of silicon and silver surfaces using a stochastic/Monte Carlo method is described by Houle and Hinsberg,<sup>6</sup> where peak temperatures reached at the center of a Gaussian shaped laser spot vs. laser power and temperature vs. time were compared with experimental data. Fig. 2 shows Houle and Hinsberg's results for Si and Ag

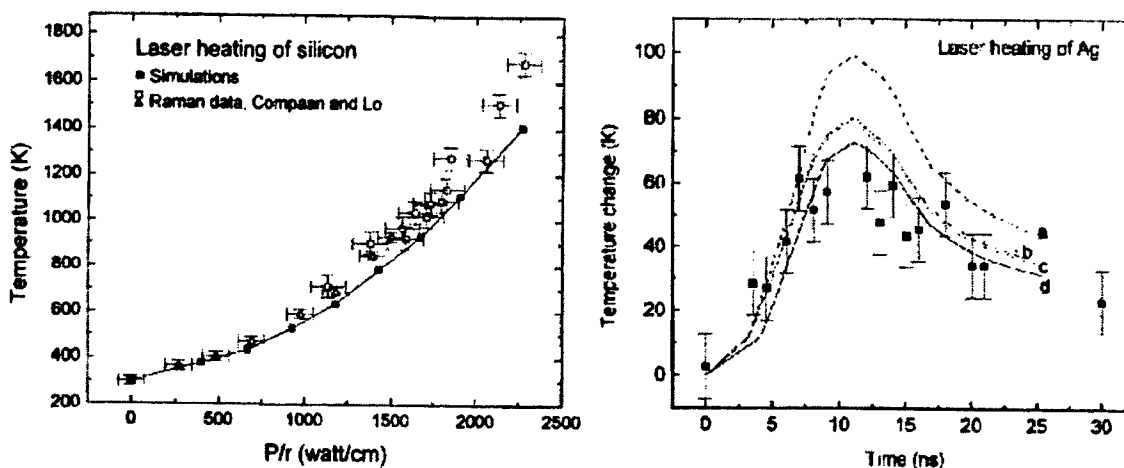


Fig. 2. (a) Simulations and Raman measurements of Si surface temperature at the center of the laser spot under CW laser irradiation as a function of  $P/r$ , where  $P$  is the laser power and  $r$  is the  $1/e$  radius of the laser beam. (b) Simulations of the temperature and 2nd harmonic generation in a silver surface under pulsed IR irradiation (8 ns FWHM, 125 MW/cm<sup>2</sup>). Traces are simulations assuming various optical parameters to determine their effect on the result.<sup>6</sup>

Note that even for a well known material such as Ag, the optical parameters were not sufficiently known to nail the experimental data although the overall time dependence looks very promising.

Which again raises the difficulty in modeling and simulation has to do again with complexity—namely, obtaining the appropriate physical constants. For simple homogeneous materials such as many pure metals and semiconductors, the optical and thermal constants are often available. Si, being the most studied element in the history of science, is very well characterized. As an example of  $T$  dependent thermal constants, we show data taken from the web for crystalline Si in Fig. 3. For more complex materials of use in packaging and fabrication, such information is very difficult if not impossible to obtain. In addition, optical constants may be fluence and time dependent; spatial dependence is often critical, and the influence of scattering cannot be ignored. Thus, surface roughness, the presence of interfaces, and the evolution of sub-micron structures in the irradiated region further complicates quantitative modeling. The temperature dependence of both



optical and thermal constants is often needed over large ranges, including through phase transitions (e.g., melting).

#### Temperature dependence of Thermal Constants of Si

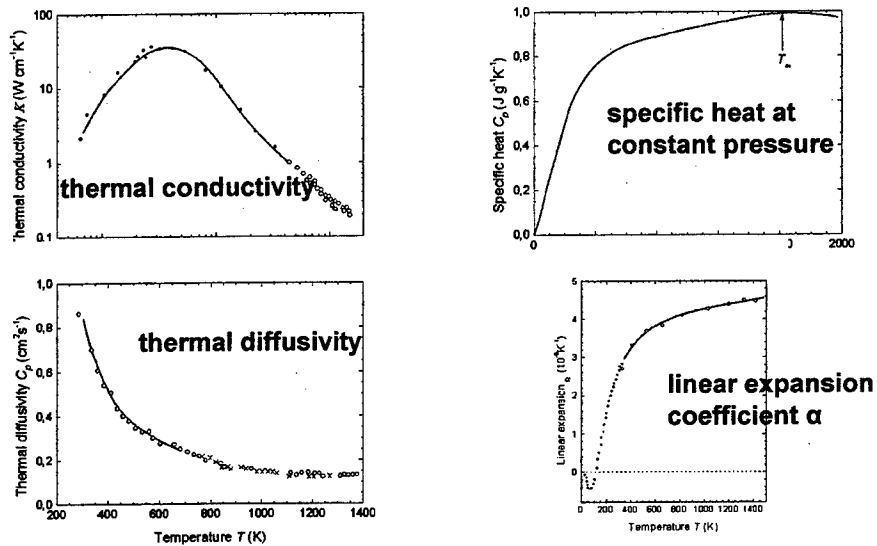


Fig. 3. Temperature dependence of the thermal constants for crystalline silicon.

**Comments on the potential of ultrafast lasers.** A number of studies have shown that femtosecond lasers are capable of producing machined features with a much smaller heat affected zone or re-solidified layer compared to ns pulses.<sup>7-11</sup> Most commercial ultrafast lasers are based on a Ti:Sapphire mode-locked oscillator pumped with a diode laser such as a doubled Nd:YVO<sub>4</sub> (at 532 nm). The oscillator output is tunable from 700 nm to 1000 nm and pulse energies are on the order of tens of nanojoules and a pulse repetition rate of tens of MHz. Much higher pulse energies (and therefore peak power) can be achieved using a regenerative amplifier, with typical outputs of a few mJ/pulse and frequencies up to a few kHz at pulse widths around 100 fs. Focusing the output of such a laser often makes possible exceptionally high quality machining for a wide variety of materials including transparent solids (e.g., silica based glasses), as well as sintered ceramics, metals, and polymers. At low irradiance on transparent materials, for sub bandgap photon energies the absorption behavior shows strong similarity to longer (ns) pulses, namely single photon defect-dominated absorption.<sup>12-14</sup> For strong absorbers (e.g., metals), again, single photon absorption occurs just as it does with longer, lower irradiance pulses. For short pulses, a two temperature model works well in describing the energy density vs. position and time, where only the electrons are heated (to very high  $T_{\text{electron}}$ ) during the laser pulse, followed by ps time scale transfer of the energy to the lattice, resulting in a lagging and lower  $T_{\text{lattice}}$  at a rate determined by the electron-lattice coupling constant usually denoted by  $\gamma$ .<sup>15</sup>

At higher irradiance in all materials, the high peak power of an amplified ultrafast laser can result in multiphoton ionization (MPI) which can lead directly to breakdown of the material. MPI also provides free electrons which can act as "seeds"; if the pulse is greater than  $\sim 40$  fs, these seed electrons can absorb laser energy via inverse bremsstrahlung. If the energy of these "heated" electrons reaches sufficient energy to impact ionize atoms in the solid, avalanche ionization develops and the material breaks down. The thresholds in irradiance for breakdown in either regime are highly stable and give very predictable, reproducible behavior.

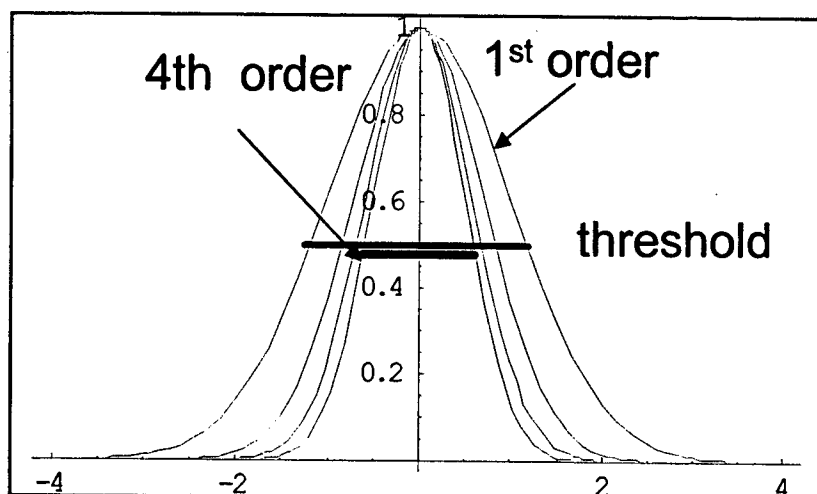


Fig. 4. Energy density distributions vs. position for a Gaussian laser profile where we have normalized the distributions for 1<sup>st</sup> through 4<sup>th</sup> order. For a process with a threshold for each order the width of the active beam decreases. Using FWHM as the relevant distance, a 4<sup>th</sup> order process has ~ half the width.

Most processing studies to date have been carried out above the threshold for plasma formation. Because of the short interaction time, heat diffusion from the focus region of the laser beam into the surrounding area is very limited, thereby minimizing collateral damage. Due to the non-linearity, higher order absorption with for Gaussian beam profiles results in only the central portion of the beam being absorbed. 4<sup>th</sup> order absorption, for example, has a width less than 1/2 the Full Width at Half Maximum (FWHM) of the 1<sup>st</sup> order absorption, as shown in Fig. 4. Thus, ultrafast materials processing allows the machining of sub-wavelength feature size, which is not normally feasible with nanosecond lasers. Furthermore, because the multiphoton interaction with the material does not require direct absorption, ultrafast amplifiers can be used to process a wide spectrum of materials as mentioned above. The amount of material removed/pulse is very constant with ultrafast lasers, although because the energy/pulse is so low, the amount removed can be small. So if one is concerned with precision and small feature size, pulse to pulse reproducibility, and an extremely high degree of control, ultrafast lasers are very attractive. Brute force tasks requiring a few to watts of average energy thus require falling back on the traditional longer pulse or CW laser sources.

**Free Electron Laser (FEL).** Often new laser sources take time to reach full potential and usefulness to the fabrication community. The FEL clearly falls into that category. Nevertheless, the laser-materials community has shown a lot of interest in these sources. There are several FELs in the world; the machine at Jefferson National Accelerator Facility, Newport, has been emphasizing materials processing as one of its major uses.<sup>16</sup> Currently the Jefferson FEL has achieved the highest average power of any such machine at 2.1 kW. It is tunable over the wavelength range of 3-6.2  $\mu\text{m}$ . Laser light is generated by causing bunches of relativistic electrons to "wobble" by passing through a set of alternating oriented north and south pole oriented magnets. The strong and rapid acceleration associated with this motion causes light emission. A pair of resonator mirrors at opposite ends of the wiggler or undulator provide the cavity. The nature of the resulting pulse train is unique, consisting a train of micropulses of length 0.5 to 1.7 ps typically spaced by 50 ns and packaged in a macropulse of lengths ranging from a few  $\mu\text{s}$  to CW. The beam is highly polarized with polarizations exceeding

6000:1. Micropulse energies have reached as high as 70  $\mu\text{J}$ . An upgrade at Jefferson is underway to significantly increase the average power and extend the available light into the UV down to 250 nm. Plans are for 10 kW in the IR and > 2 kW in the UV. Because of the tunability of the FEL, this offers opportunities to determine the benefits of exciting particular transitions in a material such as targeting IR transitions. One interesting result is the observation of significantly enhanced material removal from polymers when certain vibrational modes within the polymer (e.g., polystyrene) were excited with tuned IR.<sup>17</sup> Other materials studies that have been investigated with IR-FEL light include ablation of carbon materials,<sup>18</sup> vaporization of fused silica,<sup>19</sup> as well as studies on texturing and micromachining polymers and metals,<sup>20</sup> and the production of single wall C nanotubes.<sup>21</sup>

**Other areas of interest.** Fundamental studies that focus on improvement, optimization, and extension of the use of lasers for processing are wide ranging and it is impossible to cover them all. I simply want to list a few general areas and examples for the packaging and laser processing community to consider. References given in the cited articles are extensive.

Type of Study	Goal	Example
Wavelength dependence of laser materials interactions.	Determine the mechanisms and understand why different wavelengths behave as they do.	Defects vs. intrinsic absorption; <sup>22</sup> Direct coupling into vibrational modes of polymers, crystalline solids; <sup>17</sup> near surface absorption vs. bulk absorption—mechanical consequences (melting vs. fracture); <sup>23</sup> particulate formation. <sup>24</sup>
Role of Chemical Environment on Material Removal rates; surface modification	Seeking synergisms and understanding of how surrounding reactive gases and liquids can cause enhanced interactions.	The role of water on laser decomposition and desorption; <sup>25</sup> surface microstructuring; <sup>26</sup> reactive etching in liquids. <sup>27</sup>
Adding absorbers to materials	Addition of strong absorption centers and understanding the absorbed energy enhances the sensitivity of the laser material interaction.	Increasing defect densities; <sup>28</sup> adding dyes to polymers to enhance absorption; <sup>29</sup> improved patterning. <sup>30</sup>
Adding exothermicity to solids	Using chemistry to design exothermic decomposing solids to improve rates and quality of ablation.	Use of polymers with functional groups tailored for rapid and energetic decomposition. <sup>31,32</sup>
Interesting simulations and mechanistic studies.	Using basic physics and chemistry to understand processes of interest to ablation and fabrication.	Molecular dynamics studies of ablation; <sup>33</sup> ablation mechanisms; <sup>34</sup> laser cleaning. <sup>35</sup>

Another consideration in the use of lasers for packaging and processing has to do with diagnostics. As more sophistication in terms of characterization and monitoring what is happening during a laser materials process, we point out that there are a number of techniques where (primarily) lasers can be used to probe the material and near surface region, even in real time. These include:

### **Uses of Lasers for Diagnostics**

- **Real time LIBS (Laser Induced Breakdown Spectroscopy)**
- **Photothermal Deflection**
- **Black-Body Analysis**
- **Interferometry**
- **Ellipsometry**
- **Non-linear optical spectroscopy**
- **Plasma resonance spectroscopy**
- **Roughness (laser scattering)**
- **Confocal Microscopy**
- **Spectroscopy (Raman, Reflection, Electron/X-ray, EDAX)**

Often such signals can be used to determine end-points on various material removal applications.

Finally, we point out that the use of lasers in biology and medicine is expanding at an enormous rate. One of the major reasons is that health issues are highly valued by society so that funds for any potential diagnostic tool or cure finds support. The developments in the use of lasers in medicine have relied strongly on previous work on ceramics, polymers, and metals that fall into the traditional laser materials interactions domain. Nevertheless, because of the intensity of their activity, it would be wise to watch developments in the bio-areas and when appropriate, take back any good ideas. Some of the areas that may be relevant include the following:

### **Where Bio and Materials Might Meet**

- **Surgery – cellular; sub-cellular level; ultrafast; MUST minimize damage**
- **Use of Laser Tweezers—particle manipulation**
- **Fluorescent tags (perhaps in polymer composites)**
- **Water (bubbles, jets, shockwaves)—use of other fluids**
- **Optical Diagnostics (non-invasive photodiagnostics)**
- **Use of cryogenics (sprays that cool while laser heats)**
- **Tissue welding (bonding at buried interfaces)**
- **Reshaping Tissue (e.g., cartilage can be molded and shaped at 60 C)**
- **Modeling of Complex Systems (skin, eye, blood vessels)**
- **Field Enhancement techniques (use of metal nanotips to enhance E fields)**

Other areas of technology that are places to watch for new ideas are the Micro-Electro-Mechanical Structures (MEMS) and Nanotechnology arenas. In a variety of applications, processing and packaging will necessarily follow the trends to go to smaller and smaller dimensions. Thus, fabrication in several domains will clearly point in the direction of manipulating and generating features that eventually will challenge our usual approaches involving refractive optics that are limited by the wavelength of light.

### III. CONCLUSIONS

The use of lasers will continue to be increased for processing and packaging applications. As the requirements for precision, quality, and manufacturing rates intensify, physical and chemical understanding will aid in making desired progress. As usual, practical needs are leading our understanding, simulation, and modeling capability. The reason is primarily the complexity of the structures, mix of materials, surface and bulk heterogeneities, and the presence of interfaces that make it challenging. Obtaining all of the needed optical, thermal, and mechanical constants for these models can also be difficult. Motivation is highest (as seen, for example in the use of lasers in medicine) where high value processes are involved. Where high value arises, "the experimentalists and simulators will come."

### ACKNOWLEDGMENTS

The author would like to thank Steve Langford, Washington State University, and Jan Dubowski, National Research Council, Canada, for helpful discussions. This work was supported in part by the U.S. Department of Energy under Grant DE-FG03-98ER14864 and by the National Science Foundation KDI Grant DMR-9980015.

### REFERENCES

1. A. C. Tam, N. Do, L. Klees, P. T. Leung, and P. W. Leung, "Explosion of a liquid film in contact with a pulse heated solid surface detected by the probe-beam deflection method," *Optics Lett.* **17**, 1809 (1992).
2. A. C. Tam, W. P. Leung, W. Zapka, and W. Ziemlich, "Laser-cleaning techniques for removal of surface particulates," *J. Appl. Phys.* **71**, 3515-3523 (1992).
3. A. C. Tam, H. K. Park, and C. P. Grigoropoulos, "Laser Cleaning of surface contaminants," *Appl. Surf. Sci.* **127-129**, 721-725 (1998).
4. N. Itoh and M. Stoneham, *Materials Modification by Electronic Excitation* (Cambridge University, Cambridge, UK, 2000).
5. D. Bäuerle, *Laser Processing and Chemistry* (Springer, Berlin, 1996).
6. F. H. Houle and W. D. Hinsberg, "Stochastic simulations of heat flow with applications to laser-solid interactions," *Appl. Phys. A* **66**, 143 (1998).
7. J. Krüger and W. Kautek, "Femtosecond-pulse visible laser processing of transparent materials," *Appl. Surf. Sci.* **96-98**, 430-438 (1996).
8. X. Liu, D. Du, and G. Mourou, "Laser ablation and micromachining with ultrashort laser pulses," *IEEE J. Quantum Electron.* **33**, 1706-1716 (1997).
9. M. D. Feit, A. M. Rubenchik, B.-M. Kim, L. B. D. Silva, and M. D. Perry, "Physical characterization of ultrafast laser pulse drilling of biological tissue," submitted to *Appl. Surf. Sci.* (1998).
10. P. Rudolph, J. Bonse, J. Krüger, and W. Kautek, "Femtosecond- and nanosecond-pulse laser ablation of bariumaluminumborosilicate glass," *Appl. Phys. A* **69**, S763 (1999).
11. J. Bonse, S. Baudach, J. Krüger, W. Kautek, and M. Lenzner, "Femtosecond laser ablation of silicon-modification thresholds and morphology," *Applied physics. A* **74**, 19 (2002).
12. R. M. Williams, K. M. Beck, A. G. Joly, J. T. Dickinson, and W. P. Hess, in *Pulse-width influence on laser induced desorption of positive ions from ionic solids*, San Jose, CA, 1999 (SPIE), p. 37-44.
13. K. M. Beck, A. G. Joly, and W. P. Hess, "Time-resolved femtosecond laser induced desorption from MgO and LiF single crystals," to appear in *Appl. Phys. A* (2000).
14. W. P. Hess, A. G. Joly, K. M. Beck, R. M. Williams, and J. T. Dickinson, "Femtosecond time-resolved laser induced desorption of positive ions from MgO," *Appl. Physics A* **69**, S389-S393 (2000).
15. B. N. Chichkov, C. Momma, S. Nolte, F. v. Alvensleben, and A. Tünnermann, "Femtosecond, picosecond, and nanosecond laser ablation of solids," *App. Phys. A* **63**, 109-115 (1996).
16. W. B. Colson, E. D. Johnson, M. J. Kelley, and H. A. Schwettman, "Putting Free-Electron Lasers to Work," *Physics Today* **55**, 35 (2002).

17. D. M. Bubb, M. R. Papantonakis, J. S. Horwitz, R. F. Haglund, B. Toftmann, R. A. McGill, and D. B. Chrisey, "Vapor deposition of polystyrene thin films by intense laser vibrational excitation," *Chemical physics letters* **352**, 135 (2002).
18. M. Hanabusa and M. Okoshi, "Ablation of Carbon Materials Using Excimer Lasers, a Free Electron Laser, and Synchrotron Radiation," *Reza kenkyu = The review of laser engineering* **26**, 806 (1998).
19. R. F. Haglund Jr and D. R. Ermer, "Explosive vaporization in fused silica initiated by a tunable infrared laser," *Appl. Surf. Sci.* **168**, 258 (2001).
20. H. F. Dylla, in *Laser Focus World; Vol. August* (2001).
21. A. Loper and others, "Production of Single Walled Carbon Nanotubes using tunable radiation from a Free Electron Laser," APS 2001 March Meeting (2001).
22. T. Lippert, T. Nakamura, H. Niino, A. Yabe, and T. L. i. c. a. p. m. o. p. f. D. o. t. i. wavelength, "Laser induced chemical and physical modifications of polymer films: Dependence on the irradiation wavelength," *Applied surface science* **109-110**, 227 (1997).
23. S. C. Langford, M. L. Alexander, J. S. Young, and J. T. Dickinson, "Production of particles by laser-induced fracture of single crystal  $\text{NaNO}_3$  for chemical analysis by inductively coupled mass spectroscopy," manuscript in preparation (2001).
24. R. L. Webb, J. T. Dickinson, and G. Exarhos, "Characterization of particulates accompanying laser ablation of  $\text{NaNO}_3$ ," *Appl. Spectrosc.* **51**, 707-717 (1997).
25. S. C. Langford, M. L. Dawes, and J. T. Dickinson, "The role of dehydration in excimer laser interactions with a transparent, hydrated mineral- $\text{CaHPO}_4 \cdot 2\text{H}_2\text{O}$ ," *Appl. Surf. Sci.* **127-129**, 81-87 (1998).
26. A. J. Pedraza, J. D. Fowlkes, S. Jesse, C. Mao, and D. H. Lowndes, "Surface micro-structuring of silicon by excimer-laser irradiation in reactive atmospheres," *Applied surface science* **168**, 251 (2001).
27. J. Wang, H. Niino, and A. Yabe, "Micromachining of quartz crystal with excimer lasers by laser-induced backside wet etching," *Applied physics. A* **69**, S271 (1999).
28. J. T. Dickinson, in *Experimental Methods in Physical Sciences; Vol. 30*, edited by J. C. Miller and R. F. Haglund (Academic Press, New York, 1998), p. 139-172.
29. T. Lippert, R. L. Webb, S. C. Langford, and J. T. Dickinson, "Dopant induced ablation of poly(methyl methacrylate) at 308 nm," *J. Appl. Phys.* **85**, 1838-1847 (1999).
30. S. Preuss and M. Stuke, "Single-shot micro-patterning of polymer surfaces by UV incubation/dye laser ablation using photochromism," *Applied surface science* **69**, 253 (1993).
31. T. Lippert, J. Stebani, J. Ihlemann, O. Nuyken, and A. Wokaun, "Excimer-laser ablation of novel triazene polymers - Influence of structural parameters on the ablation characteristics," *J. Phys. Chem.* **97**, 12296-12301 (1993).
32. T. Lippert, S. C. Langford, A. Wokaun, G. Savas, and J. T. Dickinson, "Analysis of neutral fragments from ultraviolet laser irradiation of a photolabile triazeno polymer," *J. App. Phys.* **86**, 7116-7122 (1999).
33. L. V. Zhigilei and B. J. Garrison, "Mechanisms of laser ablation from molecular dynamics simulations: dependence on the initial temperature and pulse duration," *Applied physics. A* **69**, S75 (1999).
34. E. G. Gamaly, A. V. Rode, A. Perrone, and A. Zocco, "Mechanisms of ablation-rate decrease in multiple-pulse laser ablation," *App. Phys. A* **73**, 143 (2001).
35. X. Zhou, K. Imasaki, H. Furukawa, H. Umino, K. Sakagish, S. Nakai, and C. Yamanaka, "Simulation study and experiment on laser-ablation surface cleaning," *Optics and laser technology* **33**, 189-194 (2001).

# Plasma Behavior During High Brightness (DPSS) Laser Materials Interaction

J.Mazumder, Mark Douglass\* and Peng Li  
Center For Laser-Aided Intelligent Manufacturing  
University of Michigan, Ann Arbor, MI-48109-2125

## 1. INTRODUCTION

Diode pumped Nd-YAG lasers are becoming a potentially powerful tool for microelectronics packaging and micro-machining. One of the major advantages of such lasers is high brightness and pulse formatting capability. This offers a tool for controlled materials removal or micro-welding. The recently developed high power diode pumped Nd-YAG laser with Slab geometry opened the door for even higher power density. On the other hand, high brightness poses a challenge for management of laser-induced plasma for process stability and repeatability. In order to develop the fundamental understanding of the role of plasma during the laser micro-machining, one needs to fully characterize the plasma density. Laser Absorption Spectroscopy is a good tool for that purpose since it measures the events near the ground level where population is high and thus measurements are more accurate. This paper describes the technique and presents the results.

## 2. THEORY OF ATOMIC ABSORPTION SPECTROSCOPY

The following formulation for recovering the atomic density and temperature was employed during this study. If a beam of light of frequency  $\nu$  and intensity  $\frac{dI_\nu}{dz} = -\sigma_\nu I_\nu$  passes through a medium of length  $dx$  (Figure 1) then the absorption may be expressed as (Thorne, Litzen et al. 1999):

$$\frac{dI_\nu}{dx} = -\sigma_\nu I_\nu \quad (2.1)$$

where  $I_\nu$  is the frequency dependent intensity and  $\sigma_\nu$  is the frequency dependent absorption coefficient of the medium.

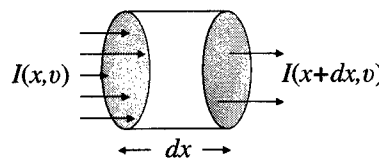


Figure 1. Absorption of light through a medium

Integrating (2.1) with respect to  $x$  over a distance  $l$ ,

$$\ln \left| \frac{I_\nu(l)}{I_\nu(0)} \right| = - \int_0^l \sigma_\nu dx \quad (2.2)$$

Assuming that the population of the upper level of the transition is negligible in comparison to the population of the lower level, the absorption coefficient can be related to the atomic density of the lower level of the absorption transition,  $n_i$ , by (Duffey, McNeela et al. 1993):

$$\int_{line} \sigma_v dv = \frac{\pi e^2}{M_A c} n_i f_{ik} \quad (2.3)$$

where  $e$  is the electron charge,  $M_A$  is the atomic mass,  $c$  is the speed of light and  $f_{ik}$  is the oscillator strength.

If the integral over the frequency is performed on (2.2), and (2.3) is substituted and solved for  $n_i$  then:

$$\int_0^l n_i(x) dx = \frac{M_A c}{\pi e^2 f_{ik}} \int_{line} \ln \left| \frac{I_v(0)}{I_v(l)} \right| dv \quad (2.4)$$

If the absorbing medium is assumed to have a cylindrical shape, then the density as a function of radial position in the plume for various heights can be recovered by the inverse Abel transform (Duffey, McNeela et al. 1995). If the probe laser beam is translated at different positions  $x$ , the distance of closest approach to the axis of symmetry by the probe beam, then the Abel transform yields:

$$N_h(x) = 2 \int_x^\infty \frac{m_i(r, h) dr}{\sqrt{r^2 - x^2}} = \frac{M_A c}{\pi e^2 f_{ik}} \int_{line} \ln \left| \frac{I_v(0)}{I_v(l)} \right| dv \quad (2.5)$$

where  $N_h(x)$  is the Abel transform function,  $r$  is the radius from the axis of symmetry and  $h$  is the height within the plume.

Using an Abel inversion technique developed by Smith et al. (Smith, Keefer et al. 1988),  $n_i$  can be recovered by simultaneously applying an inverse Hankel transform of the Fourier transform of the transform function  $N_h(x)$ :

$$n_i(r) = 2\pi \int_0^\infty q J_0(2\pi r q) \int_{-\infty}^\infty N_h(x) \exp[-j2\pi x q] dx dq \quad (2.6)$$

where  $J_0$  is the zero-order Bessel function of the first kind and  $q$  is the frequency in the Fourier domain.

The atomic density for a particular electronic level as a function of radius can now be found by way of the integrated line intensity:

$$n_i(r) = \frac{2M_A c}{e^2 f_{ik}} \int_0^\infty q J_0(2\pi r q) \int_{-\infty}^\infty \exp(-j2\pi x q) \int_{line} \ln \left| \frac{I_v(0)}{I_v(l)} \right| dv dx dq \quad (2.7)$$

Assuming local thermodynamic equilibrium (LTE) holds, the electronic, or excitation, temperature as a function of plume radius may also be found through the Boltzmann relation using absorption lines originating from different lower states (Duffey, McNeela et al. 1995):

$$\frac{n_i(r)}{n_j(r)} = \frac{g_i}{g_j} \exp \left( -\frac{(E_i - E_j)}{kT(r)} \right) \quad (2.8)$$

where the subscripts  $i$  and  $j$  indicate the upper and lower electronic energy levels,  $g$  is the degeneracy,  $E$  is the energy,  $k$  is Boltzmann's constant and  $T$  is the electronic temperature.

Alternatively, if more than two lines are available then the excitation temperature can be determined from comparing the relative densities for different states. If  $\log(n_i/g_i)$  is plotted against  $E/k$  for several states and is fit by a straight line, the slope of the line is equal to  $-1/T$  and  $T$  can be determined.



### 3. EXPERIMENTAL DESIGN

#### 3.1 Experimental Set Up

The material used in the experiments for plasma characterization was AISI 52100 steel, which can provide several accessible transition lines in visible and near U.V. The alloy composition is given in Table 1. Iron spectra have been well studied and contain an abundance of strong electronic transitions whose wavelengths are easily accessible by dye lasers.

Table 1. Composition of SAE 52100 steel

Element	C	Cr	Mn	Si	Fe
Weight %	1.0	1.45	0.35	0.275	balance

The laser utilized in the experiments was designed by General Electric at their Center for Research and Development in Schenectady, NY. It is a diode-pumped Nd:YAG laser that operates at the fundamental Nd:YAG wavelength of 1.06 $\mu$ m. The solid-state crystal is a slab geometry that is face-pumped by the diode lasers. The stable resonator configuration produced up to 400 W average power and a beam quality, M2, of approximately 10.

The laser was operated in Q-switch "burst" mode. The diodes were pulsed at 300Hz repetition rates and 400 $\mu$ s pulse widths, giving a 12% duty cycle. In the burst mode, a pair of acousto-optic modulators (AOMs) provided Q-switching at 40 kHz repetition rates and 110ns pulse widths to modulate the laser during the pump pulses. This produced, on average, 15 Q-switched pulses per pump pulse. The Q-switching produced peak powers per pulse of about 0.8MW (at 260W average power).

The beam was delivered via a 45° turning mirror down to a 200mm focal length, plano-convex, fused silica lens. The lens, in conjunction with a beam width of 10mm, resulted in an f-number of about 20 and, assuming an M2 of 10, a focused spot size of approximately 270 $\mu$ m.

The processed coupons were 0.5" (13mm) thick, 1.75" (44mm) diameter samples machined from 52100 steel bar stock with both faces milled. The coupons were held with a surface facing up toward the incoming beam and then translated at 2ipm (0.08cm/s) transverse to the beam in straight lines using Aerotech linear motor XY tables.

Argon shield gas was supplied at a flow rate of 25CFH (12lpm) about 0.75" (20mm) from the workpiece surface at an angle of about 80 degrees. The gas nozzle diameter was 0.4" (10mm).

A tunable ring-dye laser was used to produce the probe beam. It was a Coherent 899-29 Autoscan system with the capability of achieving a laser line width of less than 500kHz. The dye was pumped by about 5W in the multi-line UV wavelength range by a Coherent Innova 200-20/4 argon ion laser. The dye used was Stilbene 420 in solution with ethylene glycol, which allowed continuous tuning from 420-450nm.

The dye laser output was about 80mW and was sent through an optical isolator to prevent back reflections into the laser cavity. It was then focused into a 3 $\mu$ m single mode fiber that ran from the dye laser's optic table to the GE laser workstation. The fiber end was held in a Newport F-915T fiber coupler where the beam exiting the fiber was collimated by 10x microscope objective. The output power from the fiber end was about 5mW. The beam was then focused by a 200mm f.l. lens into the plume, re-collimated by another 200mm f.l. lens, passed through an iris, reflected off two turning mirrors, through a 300mm f.l. lens, another iris and finally a bandpass filter (70nm FWHM centered at 450nm) after which an amplified photodetector collected the focused light. The beam was sent along the back of the setup by the two turning mirrors in order to increase the path length and isolate the photodetector from plume emissions. The long path length, irises and bandpass filter were utilized to reduce optical noise from the plume. The fiber coupler and the focusing 200mm f.l. lens were mounted on XZ stages to provide vertical and horizontal movements of the beam relative to the plume while also keeping the beam centered in the optics. The schematic of the setup can be seen in Figure 2 and a photographic image in Figure 3.

The data collection utilized the Autoscan interface box, a pair of boxcar integrators (Stanford Research Systems SR250), a pulse generator (SRS DG535), a photodiode positioned at the exit window of the GE laser (Thorlabs amplified PD), and a digital oscilloscope (Tektronix TDS 3052).

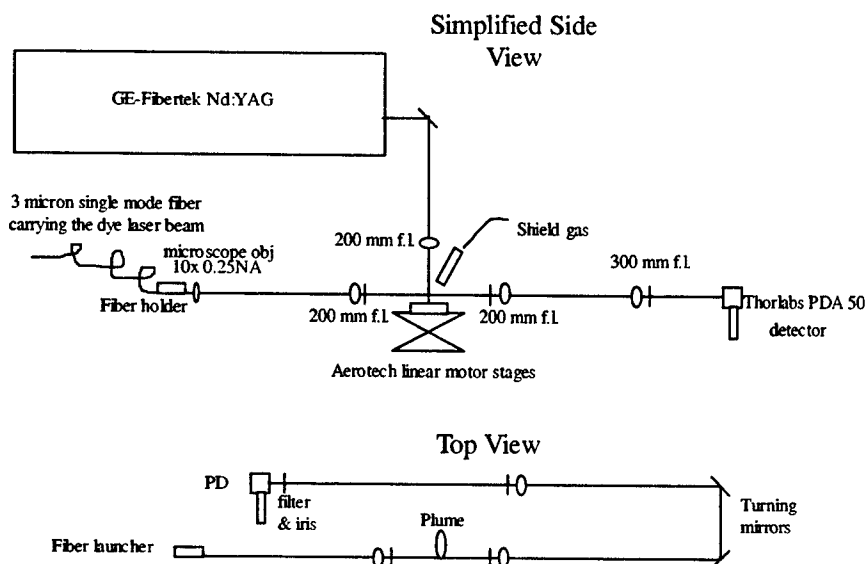


Figure 2. Schematic of the absorption spectroscopy experiment

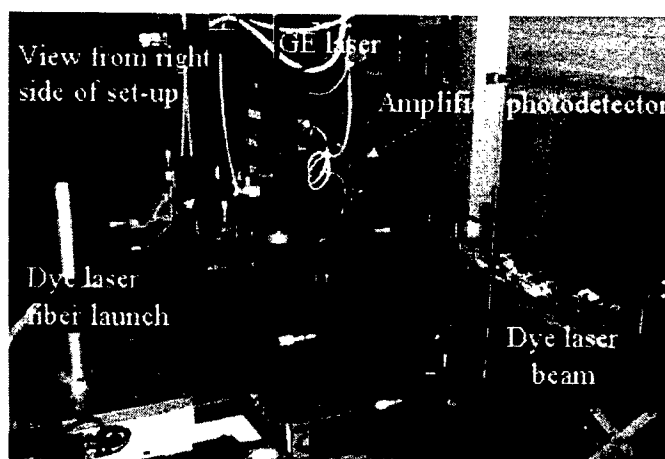


Figure 3. Dye laser beam path and optical components as viewed from the right

### 3.2 Process Conditions and Data Collection

Table 2 gives the independent variables examined in the study. First, three laser powers (average) were used: 80, 150 and 260W. A 390W (maximum power at the time of the experiments) was also attempted. However, the amount of spatter from the workpiece was excessive, resulting in having to replace cover slides often as well as causing damage to the probe beam optics.

Table 2. Independent variables

Independent variable	Conditions
Average laser power	80, 150, 260W
Delay from start of GE laser pulse	3, 6, 9 $\mu$ s
Probe beam height above workpiece	0.8, 1.5, 2.5mm

Second, three different boxcar gate delays relative to the beginning of the GE laser pulse, 3, 6 and 9 $\mu$ s, were used. 12 $\mu$ s was also used at a power of 260W for a simple comparison to the earlier delays. 3 $\mu$ s was the earliest time the plume could be probed without encountering significant plume emission interference. At 1 and 2 $\mu$ s, even with the irises apertured to just barely larger than the dye laser beam, the plume emission was still strong enough that the absorption measurements were not reliable due to emission interference. The plume was also not significantly probed beyond 9 $\mu$ s because the absorption was too weak to measure at the lower laser powers, although at 260W there was still enough absorption at 12 $\mu$ s to take some measurements. Because absorption could not be detected beyond 12 $\mu$ s, interference from the next pulse was not an issue since the pulse spacing was 25 $\mu$ s (40kHz).

Finally, the probe beam height was adjusted starting from 0.8mm above the surface of the substrate to heights of 1.5 and 2.5mm. Heights above 2.5mm demonstrated weak, if any, absorption, particularly at the earliest delay time, 3 $\mu$ s. However, some measurements at 3.5mm could be taken at 260W and a delay of 12 $\mu$ s.

Regarding the atomic iron transitions studied, Table 3 shows the different Fe I transitions investigated and their respective transition probability data. The data was compiled from the NIST Atomic Spectra Database ([http://physics.nist.gov/cgi-bin/AtData/main\\_asd](http://physics.nist.gov/cgi-bin/AtData/main_asd)). The labels noted in the last column of the table are a scheme by which the different transitions could be quickly differentiated during data recording. Many different lines were scanned using the dye laser in order to determine which ones were optimal for the experiments. In some cases, such as lines C, D and E, the absorption was so strong that the detector read 0V (i.e. essentially 100% absorption) for a large portion of the scan resulting in an absorption profiles with flat tops. In another case, G, the line investigated overlapped an adjacent line too much to reliably curve-fit the absorption profile. Thus, these lines were ignored. Also, lines with lower level energies above 23,000cm<sup>-1</sup> were not strong enough to detect.

Table 3. Transitions and probability data (highlighted indicates transitions which were primarily used in the study)

$\lambda_{vacuum}$ (nm)	$E_i$ (cm <sup>-1</sup> )	Lower level electron configuration	Term symbol	$f_{ji}$	$g_i$	Label for exp.
437.7159	0.000	3d <sup>6</sup> 4s <sup>2</sup>	<sup>5</sup> D <sub>4</sub>	0.000104	9	C
438.4776	11,976.234	3d <sup>7</sup> ( <sup>4</sup> F)4s	<sup>3</sup> F <sub>4</sub>	0.176	9	D
441.6362	12,968.549	3d <sup>7</sup> ( <sup>4</sup> F)4s	<sup>3</sup> F <sub>2</sub>	0.0487	5	E
442.3809	22,946.808	3d <sup>7</sup> ( <sup>4</sup> P)4s	<sup>3</sup> P <sub>1</sub>	0.026	3	I
444.3585	17,726.981	3d <sup>7</sup> ( <sup>4</sup> P)4s	<sup>5</sup> P <sub>2</sub>	0.0111	5	J
444.8967	17,927.376	3d <sup>7</sup> ( <sup>4</sup> P)4s	<sup>5</sup> P <sub>1</sub>	0.0152	3	K
<b>446.0369</b>	<b>17,550.175</b>	<b>3d<sup>7</sup>(<sup>4</sup>P)4s</b>	<b><sup>5</sup>P<sub>3</sub></b>	<b>0.00752</b>	<b>7</b>	<b>M</b>
<b>446.2904</b>	<b>704.004</b>	<b>3d<sup>6</sup>4s<sup>2</sup></b>	<b><sup>5</sup>D<sub>2</sub></b>	<b>0.000123</b>	<b>5</b>	<b>F</b>
<b>446.7805</b>	<b>22,838.318</b>	<b>3d<sup>7</sup>(<sup>4</sup>P)4s</b>	<b><sup>3</sup>P<sub>2</sub></b>	<b>0.050</b>	<b>5</b>	<b>N</b>
448.3427	888.129	3d <sup>6</sup> 4s <sup>2</sup>	<sup>5</sup> D <sub>1</sub>	0.000105	3	G

Three lines were chosen for the full study to expedite data collection: F, M and N. These lines were chosen because: (a) they were all close in wavelength (overall separation 0.75nm), (b) their lower energy levels were spaced relatively far apart and (c) their lower energy levels overlapped those that were eliminated from the study, resulting in little loss of information.

Since the dye laser beam was continuous and could not be synchronized with the GE laser pulses, boxcars were necessary for precise timing in detecting the dye laser signal. A gate could be set so the boxcars would read voltages only at specified time periods relative to a trigger and the resulting signal could also be amplified by the boxcars. The boxcars were not used to perform any averaging. Boxcar 1 was used for detecting the absorption signal when the plume was present and Boxcar 2 was used for the baseline dye laser power signal without a plume. The gate delay for Boxcar 1, relative to signal A-B from the pulse generator, was one of the independent variables of the experiment and set to 3, 6, 9 and, in one case, 12 $\mu$ s, and the gate width was set to 0.5 $\mu$ s. The gate delay of Boxcar 2 was 800 $\mu$ s and the width 15 $\mu$ s. This was to ensure that the plume was completely extinct before the signal was acquired.

In order to properly map out the Abel inverted densities and temperatures of the plume, the probe beam had to be used to measure as many points across the width of the plume as possible for each height above the surface, i.e. the Abel inversion becomes more accurate the greater the spatial resolution during measurement. A 200mm f.l. lens was chosen to focus the probe beam into the plume since it offered a reasonable compromise in spot size vs. depth of focus. The focused beam width was about 120 $\mu$ m and the depth of focus about 5mm, which was longer than the plume dimensions.

Data was collected for each transition, the beam was indexed horizontally by 150 $\mu$ m and then data collection taken again for each transition. This process was repeated until no additional absorption could be detected for any one of the lines.

At each point in the plume the absorption profile was collected for each transition. In order to obtain the absorption profile, the dye laser frequency had to be scanned while the signals from the boxcars were acquired, i.e. the dye laser's frequency changed at specified intervals and stopped during each interval to collect the signals from the boxcars. The scan parameters could be set in the Autoscan software. For these experiments the data interval was 100MHz and the total scan distance was 30GHz (three segments of 10GHz) for a total of 300 data points per scan.

The Autoscan data from a sample scan can be seen in Figure 4. Notice that the VET signals are smooth and continuous and that the dye laser power is constant throughout the scan. Any scan that had a poor laser power or VET signal was expunged and the scan repeated.

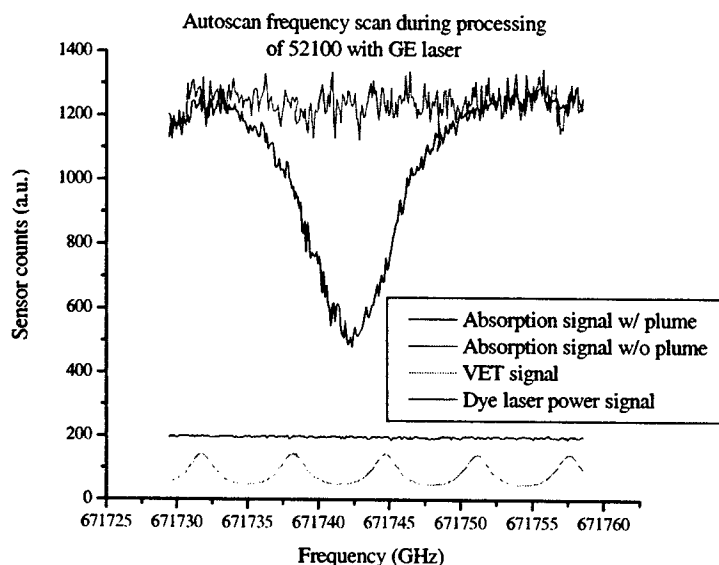


Figure 4. Acquired Autoscan data during absorption spectroscopy experiments

### 3.3 Density and Temperature Calculations

Once the scan files were assembled, the natural log of the ratio of the 100% transmitted beam (no plume) to the transmitted partially absorbed beam (plume present) was calculated:  $\ln(I_0/I)$ .

The next task was to curve fit the absorption profile. Early in the study it was found that the absorption profiles fit neither a pure Gaussian nor a pure Lorentzian profile. Therefore they were fit using a Voigt profile, which is a convolution of Gaussian and Lorentzian profiles. The program used to curve fit the data utilized an algorithm developed by Kuntz (Kuntz 1997).

Next, another program assembled multiple curve fit files for use in an Abel inversion calculation. The data was symmetrized using Smith's technique, centered and truncated at 99.7%. The truncation was simply a window filter applied to the data in the Fourier domain during the Abel inversion that removed high frequency noise. In general, truncations less than 99.7% produced Abel inverted results that contained either high frequency noise or features that could not be reconciled with the general trends of the pre-Abel results. First the Abel-inverted densities were calculated and then used to calculate the temperatures.

## 4. RESULTS AND DISCUSSION

A design of experiments was followed where the DPSSL was operated at powers of 80, 150 and 260W, the data collected at delays of 3, 6 and 9 $\mu$ s and the plume probed from heights of 0.8, 1.5 and 2.5mm above the surface of the workpiece. The resulting absorption profiles from three transitions of Fe I were analyzed using Abel inversion for calculating atomic densities and temperature. Time-of-flight measurements and some time-averaged emission spectral data were also taken. Line broadening of the absorption profiles was considered and the microstructure of the processed steel was examined.

It was found that the peak atomic densities under all conditions were typically on the order of  $10^{16}\text{cm}^{-3}$  for the lower level of 446.29nm (F),  $10^{14}\text{cm}^{-3}$  for the lower level of 446.03nm (M), and  $10^{13}\text{cm}^{-3}$  for the lower level of 446.03nm (N), as shown in Figures 5, 6, and 7. Thus, as the lower energy level of the transition increases, the atomic density at that level decreases, which is consistent with the Boltzmann distribution.

In the design of experiments, different heights in the plume were probed by the dye laser. Although different processing conditions produced different density patterns within the plume, no definitive correlation could be made between the changes in density within the plume with respect to the independent variables, delay and power.

In regard to correlating the densities to the delay, some conclusions can be made. First, the F transition demonstrates significant populations, greater than  $10^{15}\text{cm}^{-3}$ , for all conditions with the exception of the 2.5mm height at 150W and delay of 3 $\mu$ s. At the lowest height, the density generally increased with delay at 80W but decreased with delay at 150 and 260W. At the greater heights, the density peaked early at 80W but peaked at the later delays at 150 and 260W. Also, the density of the lower level of the F transition was not appreciably sensitive to the delay time at which it was probed, that is the density variation was not great between delays up to 9 $\mu$ s.

The M and N transitions demonstrated similar responses in densities to different delays. The plume density decreased with time, except for the extreme case of the 3 $\mu$ s delay at 150W power where the power was not large enough to have built up the populations at the 2.5mm height. Also, unlike the F transition, the M and N transitions' densities were highly sensitive to the time at which they were probed and showed dynamic responses to delay time.

Overall, the lowest lying transition, F, demonstrated significant population up to 12 $\mu$ s and did not vary much between 3-9 $\mu$ s. Since it is a ground level transition it is representative of the entire density of iron atoms, thus the plume still has a considerable density of iron atoms. The M and N transitions obviously showed dramatic decreases in population with time because of the plume cooling.

Regarding density changes with power, as the power increased the densities of all of the transitions increased near the top of the plume and early in the plume lifetime. Also, the density at the bottom of the plume was not very sensitive to power changes whereas the density at the top of the plume shows great sensitivity to changes in laser power.

Overall, the transitions demonstrate similar trends in density changes with power, although the similarities are greatest at the early delays.

Using the density results, some trends in the plume width became evident. At the early delays, 3 and 6  $\mu\text{s}$ , the plume width increases with power but remains relatively constant with power at 9  $\mu\text{s}$ . Second, the plume remained constant with height at 80W but decreased with height at the early delays and then was constant with height by 9  $\mu\text{s}$  for 150 and 260W. Finally, at the lower heights the plume width generally remained constant with delay but increased with delay at 2.5mm.

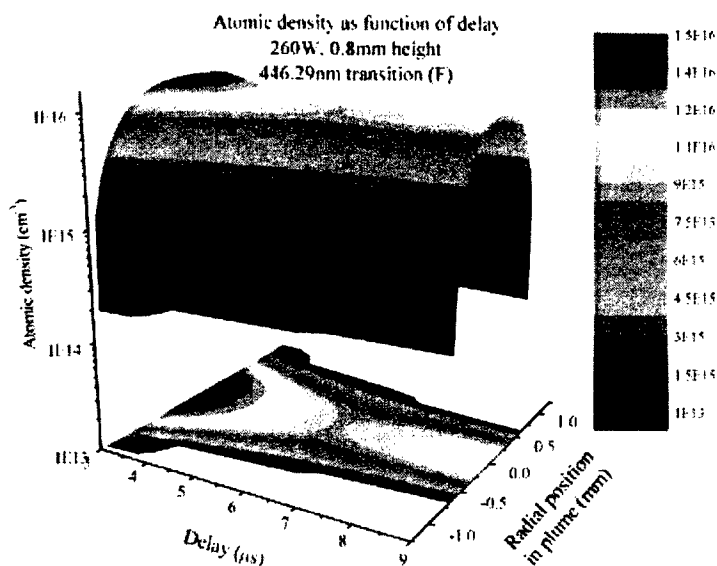


Figure 5. Atomic density of 446.29nm transition (F) vs. delay for 260W power, 0.8mm height

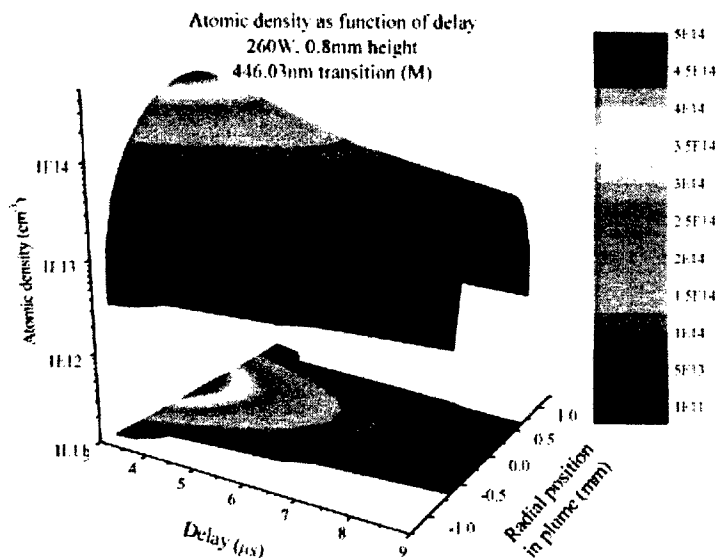


Figure 6. Atomic density of 446.03nm transition (M) vs. delay for 260W power, 0.8mm height

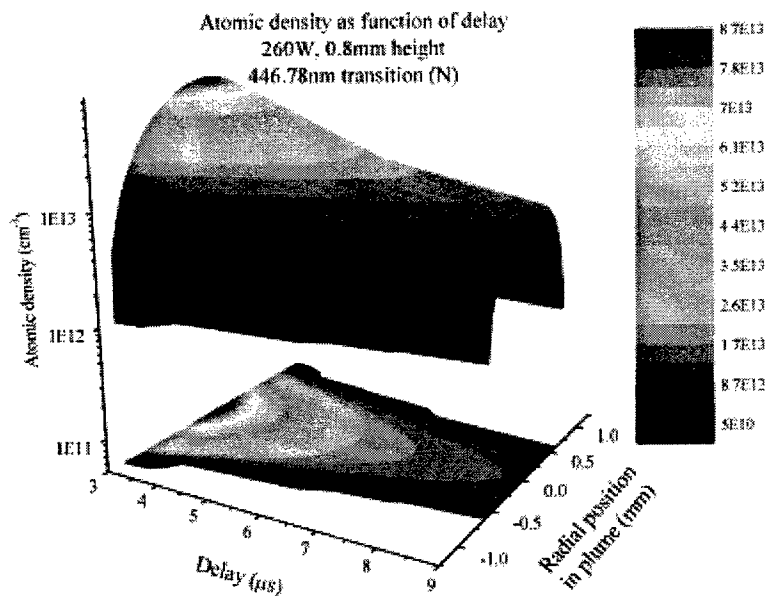


Figure 7. Atomic density of 446.78nm transition (N) vs. delay for 260W power, 0.8mm height

## SUMMARY

Laser atomic absorption spectroscopy using a tunable ring dye laser was successfully implemented in analyzing the vapor plume created during processing of steel with a diode-pumped solid-state laser (DPSSL). This work represents the first comprehensive characterization of atomic species within plasma produced by a high power, DPSSL.

## ACKNOWLEDGEMENTS

This work was made possible by a grant from DARPA TRP Project for Precision Laser Machining Consortium lead by TRW. Dr. Len Marabella was the Program Manager.

## REFERENCES

- Duffey, T. P., T. G. McNeela, et al. (1993). "Absorption spectroscopic measurement of atomic density in laser-induced vapor plume." *Applied Physics Letters* **63**(17): 2339-2341.
- Duffey, T. P., T. G. McNeela, et al. (1995). "Absorption spectroscopic measurements of plume density and temperature in production of nanocrystalline NbAl<sub>3</sub> by laser ablation deposition." *Physical Review B* **51**(20): 14652-14663.
- Kuntz, M. (1997). "A new implementation of the Humlicek algorithm for the calculation of the Voigt profile function." *Journal of Quantitative Spectroscopy & Radiative Transfer* **57**(6): 819-824.
- Smith, L. M., D. R. Keefer, et al. (1988). "Abel inversion using transform techniques." *Journal of Quantitative Spectroscopy & Radiative Transfer* **39**(5): 367-373.
- Thorne, A. P., U. Litzen, et al. (1999). *Spectrophysics: principles and applications*. New York, Springer.

# **Laser material processing: An industrial view of packaging applications**

James Brannon\*  
IBM Storage Technology Division  
San Jose, CA

## **ABSTRACT**

In the past two decades, laser applications in the packaging of microelectronics and photonics have clearly made a mark in industrial processing. With the commercial availability of reliable UV and IR lasers, a wealth of techniques and methods have evolved: generation of vias, high resolution patterning of materials by etching and ablation, laser bonding and microwelding, stripping of insulation and cladding, deposition of conductors, creation of surface microstructures, cleaning of sensitive surfaces, and a variety of drilling, slicing, and dicing processes. The list goes on and on, and what new techniques may evolve is limited only by human ingenuity. In this presentation I will review several of these applications with particular emphasis on those that are industrially useful. Many interesting concepts in laser processing fill the pages of scientific and engineering journals, but few of these ideas are seriously considered for a manufacturing environment. In concluding this talk, I will attempt to answer just what makes an industrially successful laser process.

**Keywords:** laser processing, lasers, microelectronics, packaging, material processing

## **1. INTRODUCTION**

Over the past two decades, the interest in laser-based packaging applications has grown dramatically. Nowhere has the fruition of this interest been more evident than in the for-profit commercial sector. With the shrinking dimensions of current and future electronic circuitry, lasers have provided the necessary pin-point thermal and photochemical activation to permit the accomplishment of both micro- and nano-scale machining processes. The recent advent of high quality solid-state lasers, with pulse durations down to femtoseconds, holds much promise for the increasing use of lasers in the high tech manufacturing environment.

Business and manufacturing strides into the laser arena have grown congruously with the availability of robust, high quality, and reliable lasers and their associated optical components. For example, nearly 20 years ago the first tentative steps into the world of laser ablation of vias for microelectronic packaging structures occurred at a time when industrially-ready excimer lasers were just being conceived.<sup>1</sup> Hand-in-hand with the growing success of this process, improvements in the quality of eximer lasers in turn spawned more applications and interest. Now days, high quality laser machining of packaging vias is routine in many commercial sectors. Similarly, the improvement in optical materials and coatings has proceeded with the growth of industrial laser processes. Optical surface coatings that would once fail after short lifetimes, particularly when operating at intense UV wavelengths, now have vastly improved properties and their long-term operation is taken for granted. It is clear that advances in laser instrumentation and optical techniques is symbiotic with the increased use these devices in the packaging industry.

However, even with the impressive improvements noted above, many potential laser applications never make the "cut" (so to speak) into industrial processing. There are many reasons for this, and I will return to a discussion of this point near the end of this article. For now, it is clearly understood that a particular laser process must be cost-effective. That is to say, the process must provide a significant improvement over competing technologies (which always exist), and must do so in a manner that provides an acceptable financial return for the investment. Returning to the excimer laser via application, a considerable debate occurred within the industry in the mid-1980's as to the competitiveness of laser via



technology versus that of plasma etching. At that time, the investment in and understanding of plasma via technology far exceeded that of laser processing. Nevertheless, the superiority of the fabricated laser vias, their increased speed of production, and the relative simplicity of the laser process, opened the door for a cost-effective excimer laser technology that has enjoyed success ever since.

## **2. A CATALOG OF APPLICATIONS**

Laser applications in microelectronic and photonic packaging involves optical means for integrating micro- and nanoscale components into a complete assembly which will perform a specific function. As geometries of the packaging structures continues to shrink, the system performance becomes limited by the ability of technologies to process on such a small scale. Because of the laser's ability to focus to less than micron spot sizes, it has become a "natural" processing tool in the photonics world. As one might guess, many processing ideas involving lasers have been conceived and used over the years in pursuit of this endeavor. In this section, several of these applications will be discussed.

### **2.1 Vias and hole-drilling**

The packaging structures on which logic chips are mounted contain many layers of electrical circuitry. Each metallization layer, containing copper, aluminum, or other alloys, is separated from other metal layers by a dielectric layer. This dielectric may be composed of organic polymer, glass, or other composite. In order to connect one metallization layer to another, via holes must be created at certain spatial locations in the dielectric. For over a decade, UV excimer lasers have excelled at this technology, particularly with respect to organic polymer ablation.<sup>2</sup> Currently, solid-state and CO<sub>2</sub> lasers are being increasingly used in place of the more costly and complex excimers. For larger vias, > 100  $\mu\text{m}$  or so, IR CO<sub>2</sub> lasers are used, while for smaller micro-vias, frequency tripled or quadrupled solid-state Nd lasers have proven beneficial. The most common vias today are "blind" (as opposed to through-hole) vias which terminate on an exposed metal layer.<sup>3</sup> These serve as a means to connect the outer metal layer of a circuit to the underlying inner layer. Laser drilling is commonly used for high density via applications on printed circuit boards, such as exist in cellular telephones, small video cameras, hand-held computers, and a host of other portable products.

As previously discussed, via drilling is a "success" application in packaging electronics due to its speed, simplicity, and high quality. As such, many manufacturers and companies have gone over to this mode of fabrication. This is particularly true for vias less than 100  $\mu\text{m}$  in diameter - a regime where there are few, if any, competing technologies. The laser nicely fills a manufacturing niche in this case.

### **2.2 Laser etching and patterning**

An intriguing application is the creation of electrical circuitry by subtractive etching or ablation of a metal layer. By any number of techniques, mask image projection for example, a laser beam can be patterned and used to irradiate a metal surface. Depending upon the laser and wavelength used, patterned metal "lines" (circuit wiring) on the order of a micron can be created. The removal process is typically subtractive etching where a gaseous "developer" is used in conjunction with the laser irradiation to form the pattern. As an example, micro-scale patterning of copper lines using a chlorine-based developing gas has been demonstrated.<sup>4</sup>

From an industrial viewpoint, this procedure possesses several problems which has inhibited its widespread use. Since toxic gases are often involved, a means to contain and eliminate the used gas must be provided. This involves costly vacuum equipment and scrubbing devices. Further, due to MTF considerations, it is difficult, if not impossible, to reproduce the mask pattern with very high fidelity during laser irradiation of the metal. As a result, metal lines created may take on a rounded aspect that may lead to imprecision and electrical shorting. This is particularly true in the case of laser ablation without etchant gases. Lastly, metal corrosion due to residual contamination of the etching gas may lead to premature failure of the device. For these reasons, laser patterning of electrical circuitry remains more a laboratory interest than an industrial process.

### **2.3 Insulation stripping**

Compared to mechanical, thermal, electric, or chemical means of removing plastic insulation, laser removal offers precision and speed without the necessity of contacting the underlying wire or optical fiber. This technique has been used for years in the electronic industry, and has only recently been applied to optical fiber stripping. The use of 10.6

$\mu\text{m}$  wavelength  $\text{CO}_2$  laser radiation for insulation stripping has, and continues to be, frequently used for applications that do not demand high precision or for which the underlying substrate is not particularly sensitive. The relatively long pulse duration and weak absorptivity in many plastic insulators results in rather poor stripping characteristics. In contrast, UV laser stripping is necessitated for accurate and high precision use in microelectronics and photonics. The strong UV absorption of most polymers permits layer-by-layer removal, while the short duration minimizes heat flow.

Laser stripping has been used in microelectronics to selectively remove insulation in regions in which circuit taps or wire bonding are to occur. The smaller the circuitry, the higher quality of laser insulation "cut" that is needed in order to precisely locate the bond region. More lately, use of UV stripping for optical fibers has grown.<sup>5</sup> In this application, the polymer insulation is stripped off the optical fiber, exposing the glass cladding for further processing. Optical fiber stripping has been used, for example, in hermetic sealing, strain relief in fiber packages, UV generation of fiber Bragg gratings, and in the "pigtail" or coupling of laser diodes. Further, this process is easily amenable to the automation necessary for widespread use.

#### **2.4 Laser scribing**

Laser scribing of substrates used in microelectronic packaging applications has become fairly routine. Scribing of ceramic substrates such as alumina or aluminum nitride involves drilling a series of blind holes in sequential proximity to each other.<sup>6</sup> The substrate can then be easily separated into smaller pieces by mechanically forcing or snapping it along the line defined by the laser holes. Typically the laser of choice for ceramic scribing operations is the pulsed  $\text{CO}_2$  laser of several hundred watts average power operating with rise and fall times of tens of microseconds. The high power, short pulse nature of the radiation permits rapid and precise ablation of ceramic. The spacing of the holes and their depth prove to be two important parameters for high quality scribing. Experiments have demonstrated that hole depths of approximately 30-40% of the substrate thickness achieve the minimum fracture force required to cleanly break the substrate. Depending on laser wavelength and optical considerations, hole spacing may vary from a center-to-center pitch of 2-4 hole diameters.

Because of the relative simplicity of the scribing process, several manufacturers have incorporated such laser systems into their production line. This process has become cost-effective for several reasons: an efficient, high quality laser can be utilized, the processing is rapid and can be done in ambient air, the system can be automated, and there is minimal down time for maintenance and repair. Overall, laser scribing, similar to its cousin laser cutting, has established itself as a prominent application of laser processing.

#### **2.5 Laser bonding and welding**

Laser bonding, welding, and soldering is used extensively in the microelectronics packaging industry for both component assembly and final case sealing. Tape automated bonding (TAB) has been in use for several decades to connect TAB leads to silicon dies. Historically, TAB has relied on a thermo-compression technique involving relatively large area heating and pressure. This approach has proven problematic due to the high temperatures and pressures - particularly as component dimensions have shrunk. Laser bonding for TAB relies on focused, local heating only to accomplish the bond.<sup>7</sup> Laser radiation is applied in intense msec-duration pulses to melt and reflow the tin-coated tape as it contacts a copper/gold "bump" on the die. This results in a strong bond since tin forms stable alloys with both copper and gold. Similar to laser TAB, laser reflow soldering is growing in importance as device sizes diminish. The fine focus characteristics of laser radiation permit precisely located melting and reflow of solder material (typically tin-lead alloys) between the regions to be bonded. Laser micro-welding is a direct joining of surfaces by precise heating, and is often used in the industry for making glass-to-metal seals, and enclosing of sensitive electronic components.

In a similar vein to laser scribing, laser bonding operations have succeeded in industry because of the relative speed and simplicity of the process. Because lasers can provide precise deposition of heat for controlled periods, it has proved suitable for bonding processes in microelectronics. This type of laser process can only be expected to grow as electronic devices become more complex and intricate.

## 2.6 Laser repair

The use of lasers to repair electronic components and circuitry has become an important operation.<sup>8</sup> This is particularly true in microelectronics where the device size now limits the use of conventional circuit repair techniques. Once a circuit defect has been identified as an "open" (lack of conductivity) or "short" (conductivity existing where it should not), an appropriate laser repair scheme can be utilized. For repair of shorts, precisely located ablation pulses are used to remove the shorting material and thus create a gap in the undesirable conducting line. In the case of opens, at least two technologies are available. The first is laser chemical vapor deposition (LCVD) which utilizes finely focused laser light to deposit gold or copper films from both gas-phase and condensed phase precursors. The second process, known as laser make-link, has been developed in the last few years.<sup>9</sup> This method for open repair works on the principle that two metal lines in proximity can be joined by use of a Q-switched pulse which irradiates the small region between them. During the nsec laser shock, the relatively brittle dielectric between the lines fractures and permits the thermally expanding metal edges to reflow, contact, and join. This process works for metal lines on the same level of metallization in a package structure, or between two levels of metal.

Given the custom and specific nature of this process, laser repair is clearly not a high volume application. Nevertheless, cost-benefit analysis can still be applied to its use, especially given the paucity of other repair methods. Laser repair has found a useful niche in the microelectronics industry since it provides a clear and useful advantage.

## 3. WHAT MAKES AN INDUSTRIALLY USEFUL LASER PROCESS ?

To conclude this paper, a few comments are in order concerning the attributes possessed by industrially successful laser processing methods. Regardless of the process, there appear to be at least five qualities that any laser process for manufacturing should possess:

1. **Utility** - the laser process must provide a clear solution to a manufacturing problem that is not achievable by more conventional techniques. Often, the laser is considered for use because it represents a high-tech solution to a problem, when in fact a more sober analysis may indicate a non-laser method to provide nearly the same benefit at a reduced level of cost and complexity.
2. **Cost-effectiveness** - even if a laser method provides a unique and advantageous manufacturing solution, it must do so without adding significant financial pressure to the cost budget. A laser process that is a little more expensive than a conventional technique, yet provides a huge improvement or advantage, will often become the industrial process of choice.
3. **Simplicity** - this point cannot be emphasized enough. To be successful, a laser process must operate simply and with a minimum of human interaction. If two or three Ph.D. scientists need to be hovering over the top of a laser processing setup in order for it to work properly, this is prescription for failure. If the process cannot be simply operated by someone of minimal intelligence, the process engineering needs to be rethought and/or redone.
4. **Timing** - in order for a process to move into manufacturing, it must be available at the right time. Once the manufacturing design and assembly line is locked-in, few if any changes can be made. A good analogy is to view the manufacturing acceptance time as a window that is open for only short periods. The successful laser process will be timed to go through the window when it is open.
5. **Extendibility** - not only must the laser process do the job it was designed for now, but it should also have utility for future requirements. It thus becomes part of the future planning, and ensures its survival. Those techniques which don't hold much promise for extendibility of often not incorporated into manufacturing schemes.

## REFERENCES

1. J. Lankard and G. Wolbold, "Excimer laser ablation of polyimide in a manufacturing facility," Appl. Phys. A, **54**, p. 355, 1992.

2. J. Brannon and T. Wassick, "Excimer laser ablation of polyimide: a 14-year IBM perspective," *Proc. SPIE*, **2991**, p. 301, 1997.
3. D. Moser, "Lasers tool up for via formation," *Laser Focus*, **37(6)**, p. 213, June 2001.
4. J. Brannon, "Micropatterning of surfaces by excimer laser projection," *J. Vac. Sci. Technol.* **B7(5)**, p. 1064, 1989.
5. G. Ogura, "Laser stripping of optical fibers opens up new applications," *Laser Focus*, **37(6)**, p. 169, June 2001.
6. W. H. Shiner and S. R. Maynard, "Cutting and scribing of substrates," in *LIA Handbook of Laser Material Processing* (J. F. Ready, ed.), Chap. 26.2, Laser Institute of America, Magnolia Publishing, Inc., Orlando, 2001.
7. J. Hayward, "Laser Tape Automated Bonding," in *LIA Handbook of Laser Material Processing* (J. F. Ready, ed.), Chap. 25.2.1, Laser Institute of America, Magnolia Publishing, Inc., Orlando, 2001.
8. T. Wassick, *Proceedings of the 42nd Electronic Component Conference*, p. 759, 1992.
9. J. Bernstein, W. Zhang, and C. Nicholas, "Laser formed metallic connections," *IEEE Trans. Comp. Pack. Mfg. Tech.*, Part B, **21(2)**, p. 194, 1998.

\*jbrannon@us.ibm.com; phone 408-256-4565; fax 408-256-2410; IBM Storage Technology Division, 5600 Cottle Rd., San Jose, CA 95193.

# Water-jet guided laser: possibilities and potential for singulation of electronic packages

Frank R. Wagner<sup>\*a</sup>, Akos Spiegel<sup>\*\*b</sup>, Nandor Vago<sup>\*\*b</sup>, Bernold Richerzhagen<sup>\*a</sup>  
<sup>a</sup>Synova Inc; <sup>b</sup>Dept. of Atomic Physics, Budapest Univ. of Techn. and Economics

## ABSTRACT

Singulation of packages is an important step in the manufacturing of IC devices. Presently, the most widely used technique is abrasive sawing. Due to the combination of different materials used in packages such as copper and mold compound, the saw rapidly blunts and also conventional laser cutting is no alternative.

Since 3 years, a new process is available for high precision material processing: the water-jet guided laser. This process combines the advantages of cold cutting by a water-jet with the high precision and speed of a laser cut and is now applied into electronic package singulation.

We show that complete mold compound removal inbetween the copper contacts in a first step is important. The following step of copper cutting is usually the speed-determining step of the singulation process. The mold compound can be ablated due to the reflected or diffused light. Thus care has to been taken in order not to alter too much the good mold compound edge quality during the copper cutting step. Flipping the sample between the two steps, and using different nozzle sizes for mold compound and copper cutting, give the best results. In all cases however, the copper cut is wear free and without burrs, which is an important advantage compared to mechanical sawing.

Typical cutting speeds for different copper thicknesses will be given and the possibilities for further speed enhancements will be briefly discussed.

**Keywords:** Laser cutting, electronic packages, copper, mold compound, 532nm, CSP, QFN, MLF.

## 1. INTRODUCTION

Electronic packages are generally made out of two compounds. Initially, you have the substrate that will be soldered to the final circuit board. This is usually a copper lead frame or a thin glass fiber enhanced polymer circuit board with solder-balls. Secondly, there is the mold compound that protects the chip itself and the connections of the chip with the substrate. This material is normally a brittle, black polymer (Bakelite) with different filler materials. These electronic packages are produced in ever increasing number by numerous manufacturers and are referred to by different abbreviations. The most general designation is CSP (Chip Scale Package), which comprises the various types like such as BGA, QFN, and MLF<sup>1</sup>. Hereafter, we'll refer to them simply as "electronic packages".

Economic, high quality singulation of these packages is especially difficult in the case of the copper & mold compound version. This type of package is often produced using a Matrix-Array Process, enhancing productivity roughly by a factor of 3<sup>1</sup>. If the packages are produced in this manner, both materials mold compound and copper must be cut during the singulation process. Generally, the reasons for the most important problems arising in package singulation are the very different mechanical, thermal, optical and electrical properties of the materials involved. Nevertheless, the precise, burr free singulation of copper only, in the case of separately molded packages, is still a topic.

Today, mechanical sawing is primarily used to singulate these packages. The main problem with this method is the inherent softness of the copper, leading to important burr formation and rapid wear of the sawing blade due to smearing. The burr formation is a considerable disadvantage, because of too big of burrs, making it impossible to solder the package properly to the final circuit board. Another approach for package singulation is conventional laser cutting, but it leads to poor cut quality, as the thermal and optical properties of the used materials are very different.

Therefore, we propose an alternative, which is based on the process of the water-jet guided laser cutting<sup>2</sup>: With this unique laser cutting method a free, laminar water-jet is used as an optical wave guide in order to guide a high power laser onto the sample. The main advantages of this method compared to conventional laser cutting are: (i) parallel sidewalls (even in thick mold compound layers), (ii) low thermal load of the sample due to the cooling of the sample between the laser pulses exactly at the place where it was heated before, and (iii) an efficient expulsion of the melted copper due to the high momentum of the water-jet. Compared to sawing, burr free cuts of copper can be achieved and the mechanical force on the sample is much lower.

\* [wagner@synova.ch](mailto:wagner@synova.ch); phone +41 21 693 8371; fax +41 21 693 8370; <http://www.synova.ch>; Synova SA, CH-1015 Lausanne, Switzerland; \*\* [Spiegel@phy.bme.hu](mailto:Spiegel@phy.bme.hu); Budapest University of Technology and Economics, Department of Atomic Physics, H-1111, Hungary

We tested several processing possibilities concerning quality and speed of the cut. Further on, we'll give projections on achievable cutting speeds with different equipments.

## 2. EXPERIMENTAL DETAILS

The schematic of the setup is shown in Fig 1. The used lasers are multimode q-switched frequency-doubled Nd:YAG lasers (Corona, Coherent Inc. (US)). We use pure de-ionized and filtered water at 50 to 500 bars. The nozzles are made out of sapphire or diamond in order to generate a long stable water-jet. The laser beam is focused through a quartz window into the nozzle, very much like a usual fiber coupling and is thereafter reflected in the water-jet at the air-water interface due to the index step (Fig 2).

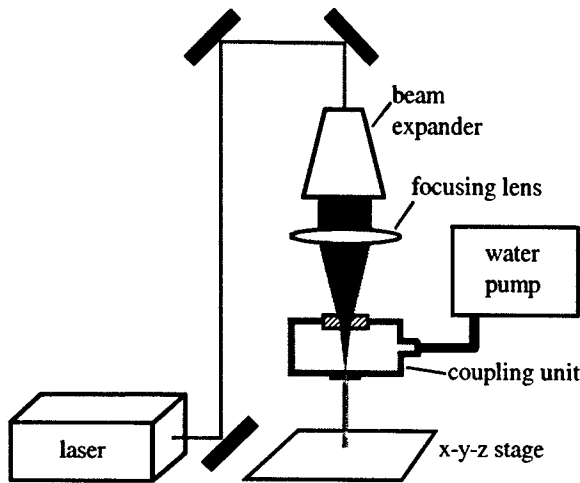


Figure 1: Schematic of the water-jet guided laser setup

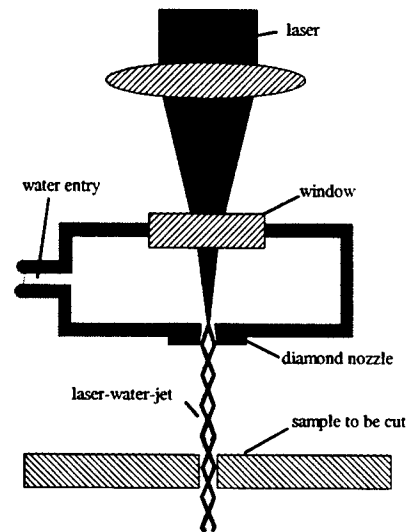


Figure 2: Detailed sketch of the coupling unit

The samples were clamped onto an x-y-z stage, and during the cutting process the samples were moved under the water-jet guided laser beam (laser-water-jet). The z-variation of the stage is only necessary in order to adapt to the different working distances of differently sized nozzles at different water pressures<sup>3</sup> and is not used during the cutting procedure.

## 3. RESULTS AND DISCUSSION

In a first step, optimum laser parameters for mold compound cutting and copper cutting were determined independently (Table 1). These parameters allow high cutting speeds with good edge quality. The absolute values of the cutting speeds naturally depend on the thicknesses of the materials. Examples of cutting speeds will be given in section 3.3. The dependency of cutting speed versus material thickness is exponential in the case of copper (Fig 11).

Material	$\lambda$ / nm	$I_{\text{peak}}$ / MW/cm <sup>2</sup>	$v$ / kHz	$\tau$ / ns	$E_{\text{pulse}}$ / mJ	$P_{\text{av}}$ / W	$D_{\text{nozzle}}$ / $\mu\text{m}$
Mold compound	532	29 – 42	45 – 60	300 – 360	0.4 – 0.9	25 – 38	80, 100
Copper	532	310	30	230	1.7	52	60

Table 1: Optimal processing parameters for copper and mold compound as determined in separate measurements. ( $\lambda$ : wavelength,  $I_{\text{peak}}$ : peak intensity,  $v$ : pulse repetition rate,  $\tau$ : Full Width at Half Maximum (FWHM) pulse length,  $E_{\text{pulse}}$ : energy per pulse,  $P_{\text{av}}$ : average laser power,  $D_{\text{nozzle}}$ : diameters of water-jet nozzles)

It is clear from the parameters given in Table 1, that mold compound and copper cannot be cut simultaneously in one step. Because of the reasons given in Section 3.1, the mold compound needs to be removed first. The copper lead frame is then cut in a second step.

The different cutting procedures and the resulting cut qualities as well as the resulting cutting speeds will be discussed in the following according to the definitions given in Fig. 3.

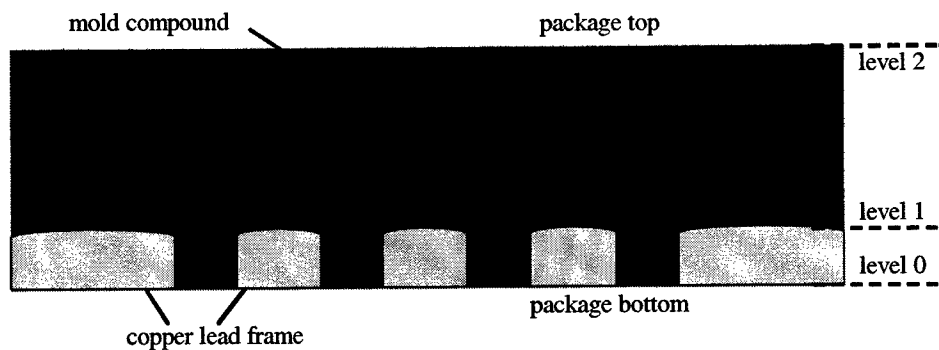


Figure 3: Schematic cross section of a typical cutting track upon electronic package singulation. The definitions will be used for the descriptions of the different cutting procedures.

In all cutting procedures, the mold compound was cut from the top. However, we tried mold compound cutting from level 2 down to level 1 only, and "complete" removal of the mold compound (level 2 down to level 0). For this first step we used water-jet nozzles with diameters of 80 microns and 100 microns. In a second step, the copper cutting was performed, sometimes from the top and sometimes from the bottom of the package. The nozzle sizes used for this step were 60 microns or 80 microns nozzle diameter.

### 3.1. Copper cutting speed and quality optimization

The quality of the copper cutting is always very good compared to mechanical sawing. The burr formation is practically absent at high water pressures, and the cuts are slightly tapered. Fig. 4 shows a side view of a package based on an etched copper lead frame that was singulated with the water-jet guided laser. Burr formation is so small that we can even see the typical cross section generated by the etching process.

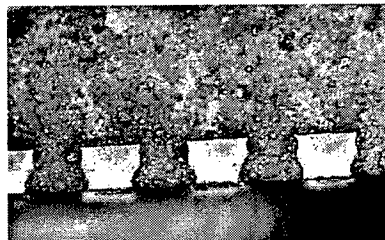


Figure 4: Side view of a singulated QFN. Due to the burr free cut, the typical cross section of the etched holes in the lead frame can be recognized.

The problem during the copper cutting step is much more speed optimization than quality optimization, especially when considering that all other steps are faster. One of the major findings in our work is that the copper cutting speed depends strongly on the presence of well adhering, mold compound residues between the copper contacts.

The speed of the mold compound cutting step is obviously higher if we cut only until level 1 (Fig. 3), but this causes an important disadvantage in the copper cutting step: the possible copper cutting speed is approximately divided by two if the remaining mold compound between the copper contacts adheres well (speed example, see section 3.3). Badly adhering mold compound residues between the copper contacts do not lower the cutting speed.

A possible explanation for this behavior is illustrated in Fig 5. The high peak intensities, which are used for copper cutting (Table 1), generate a strong explosion when the light is absorbed in the mold compound residues. If less mold compound is left between the copper contacts, the explosion will be smaller. But the energy of the explosion is only of minor importance. More important is the expansion direction of the resulting pressure wave: If well adhering mold compound is between the copper contacts, the explosion can only expand towards the top of the package, i.e. towards the incident water-jet, which will be disturbed (Fig. 5 left). When the water-jet is disturbed, it will take a little time for it so settle down again and all light emitted during this time by the laser is lost for the cutting process as it is not guided properly to the sample.

On the contrary, if the mold compound residues are only badly adhering, or the holes between the copper contacts are already opened by the first machining step, the energy of the explosion mostly expands downwards due to the pressure of the water-jet (Fig. 5 right).

With remaining mold compound small water pressure leads to higher cutting speed, because the water jet is more stable at smaller water pressures (90 bars). In the case of the completely removed mold compound, the optimal water pressure is higher, because at higher pressures the expulsion of the molten copper out of the kerf is more efficient (250 bars).

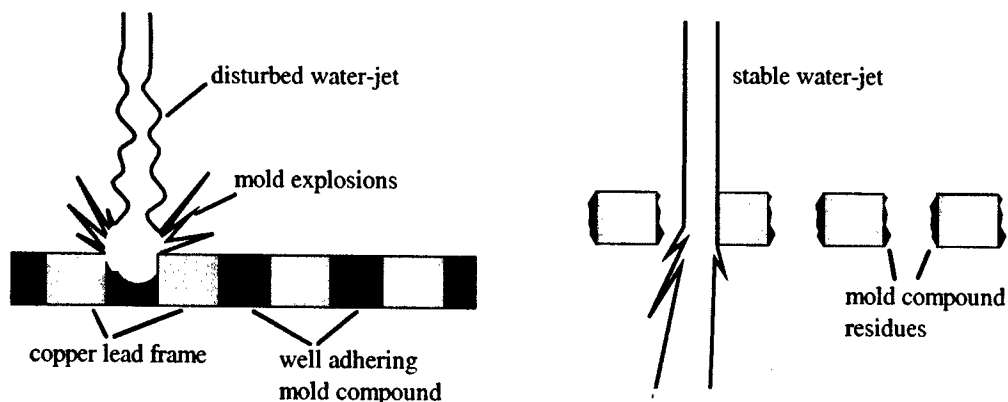


Figure 5: Schematics of the copper cutting process with well adhering mold compound between the copper contacts (left side), and without well adhering mold compound residues (right side).

The regular interruptions of the copper substrate itself do not destabilize the water-jet. Due to the small width of the copper contacts; they can even be cut at slightly higher speeds than a normal copper foil. Fig. 6 shows schematically the situation of a cut, which was performed at a too high translation speed. The sample is only cut through at the very border. Thereafter the melted front approaches its equilibrium angle, and the sample is cut only partially. The cut part at the border of the sample lengthens as a lower translation speed of the laser is chosen. In the case of a multi-pass cut of a thin copper contact; the small cut parts join each other from both sides at a translation speed that is still higher than the equilibrium cutting speed of a foil of the same thickness.

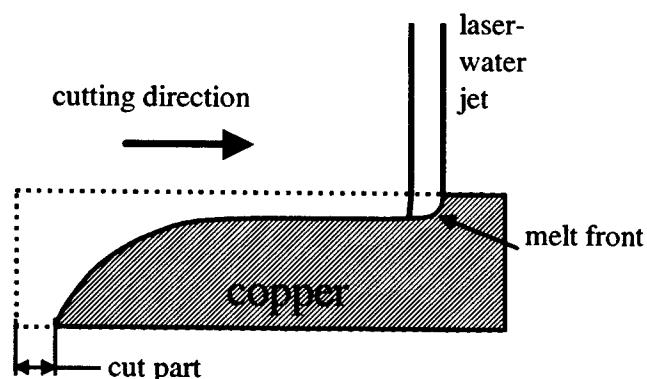


Figure 6: Schematic cross section of a cut close to the border of the foil. The "cut part" is longer and the equilibrium cut depth is higher at lower translation speeds of the laser-water-jet.

### 3.2. Mold compound cutting speed and quality

The mold compound can be cut much faster than the copper lead frame (speed example, see section 3.3). The edge quality after mold compound cutting only is also good (Fig 7 left). The problem is that the diffused light generated during the copper cutting step alters this good edge quality (Fig 7 right).



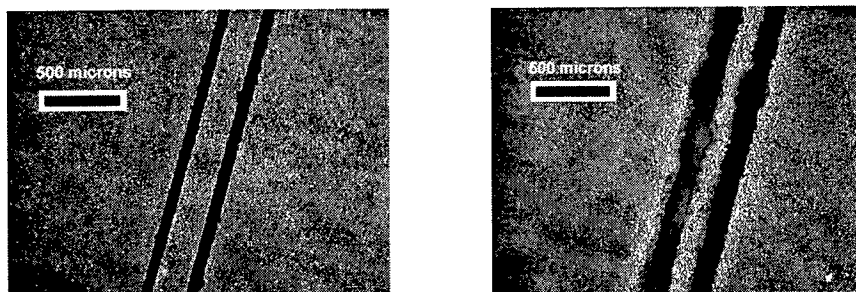


Figure 7: Top view of a cut in the mold compound only (left), and the same cut after copper cutting from the bottom side with the same nozzle, i.e. following procedure B (Fig. 8) (right side).

The aim of the optimization of the cutting procedure is thus to minimize this alterations. For this purpose, we tried the cutting procedures that are schematically depicted in Fig 8.

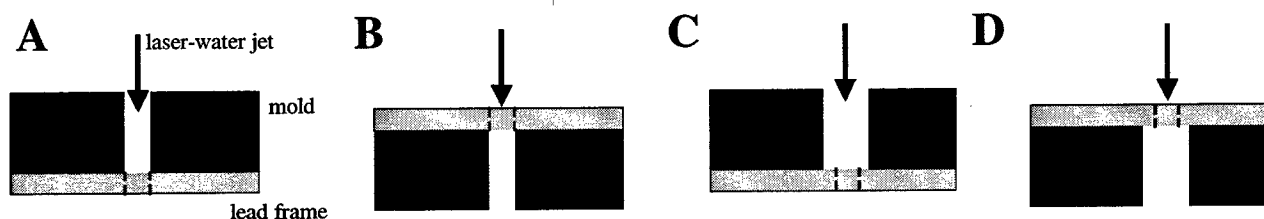


Figure 8: schematic representation of the different cutting procedures, which were tried in order to decrease the alterations of the mold compound cutting quality due to diffuse light during the copper cutting step. .

As a result we can classify the alterations of the mold compound cut quality as follows: When cutting the copper from the bottom (Fig 8 B & D); the water jet is disturbed at the lead frame and diffused light at still very high intensity shines onto the borders of the mold compound, thus ablating the mold compound on the edges leading to an enlargement of the cutting kerf and bad edge quality (Fig 7 right)

If the copper is cut from the top (Fig 8 A & C); diffuse light is generated by reflection on the copper. This causes the mold compound to be ablated just above the lead frame, resulting in an undercut (Fig. 9 left). Both types of alterations can be decreased if the mold is cut with a bigger nozzle than used for the copper cutting (Fig 8 B & D, Fig 9 right).

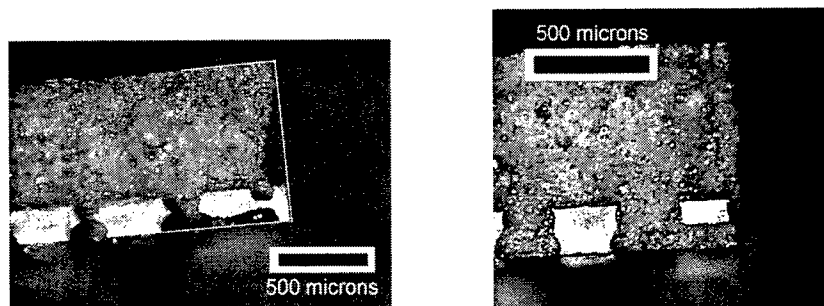


Figure 9: Side view of a cut in the mold compound with strong undercut (left), and side view of an edge after the optimized cutting procedure depicted in Fig 8 D. This means using different nozzle sizes for mold compound and copper, and cutting the copper from the bottom (right).

Another defect, which is caused by the same physical process of ablation of the mold compound by reflected light, is the retraction of the mold compound from the edge of the copper contacts. Fig. 10 shows a typical backside view on the left side. The picture on the right side of Fig 10 confirms that the retraction is caused by ablation due to reflected light. The defect occurs only in the vicinity of the contacts and it is stronger when the jet slides onto the copper contact than when it leaves the copper contact.

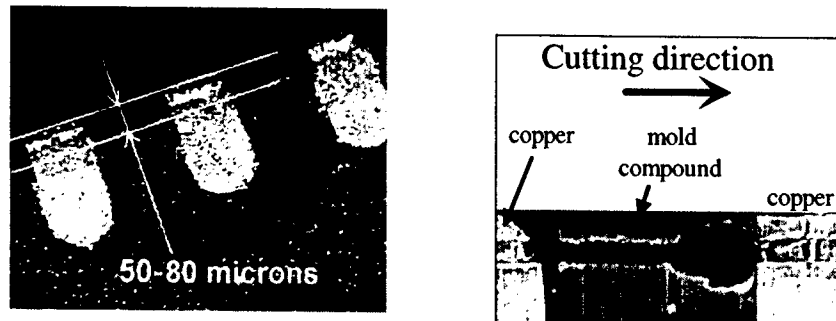


Figure 10: Typical backside view of a singulated copper based chip scale package (left), backside view of a sample where the mold compound was partially removed from cutting from the bottom (right).

This defect can only be decreased if careful precutting of the mold compound is done. Usually the mold compound retraction is between 50 microns and 100 microns, always depending on the particular type of mold compound.

### 3.3. The best cutting procedure with the present equipment

The most successful strategy for singulating electronic packages with the water-jet guided laser is depicted in Fig 8 D. Firstly, the mold compound is cut from the top with a 100-micron nozzle, applying the parameters of Table 1. For a typical package thickness of 900 microns, a cutting speed of  $v_m = 20$  mm/s could be achieved in this first step. The copper lead frame should then be cut from the bottom using a 60-micron nozzle in order not to alter the mold compound quality significantly. The resulting cutting speed in this second step depends greatly on the thickness of the copper lead frame. Approximate values of the copper cutting speed,  $v_c$ , are given in Fig 11. The exact values depend on the surface finish of the lead frame and eventually applied platings.

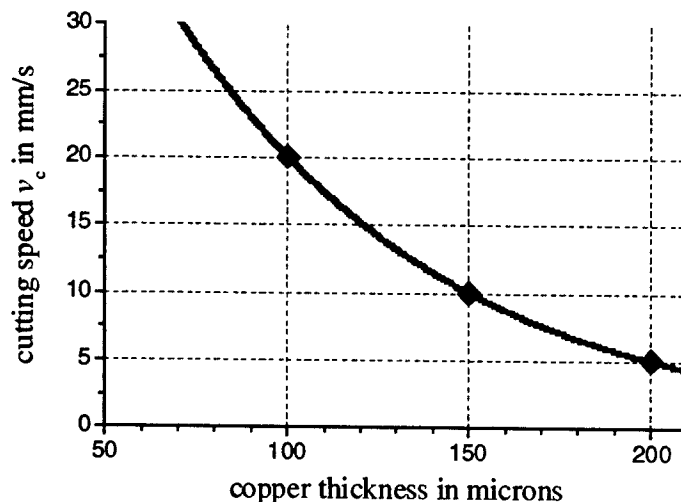


Figure 11: Approximate values for copper cutting speeds using the parameters presented in Table 1.

The resulting, total, cutting speed,  $v$ , of the package is then given by:  $v = (1/v_m + 1/v_c)^{-1}$ . For example a 900-micron thick package with a 200-micron thick copper lead frame is thus singulated burr free with a cutting speed of  $v = 4$  mm/s. A top view of the final result is shown in Fig. 9. A backside view is given in Fig. 8 (left side) and the side view is depicted in Fig. 7 (right side).

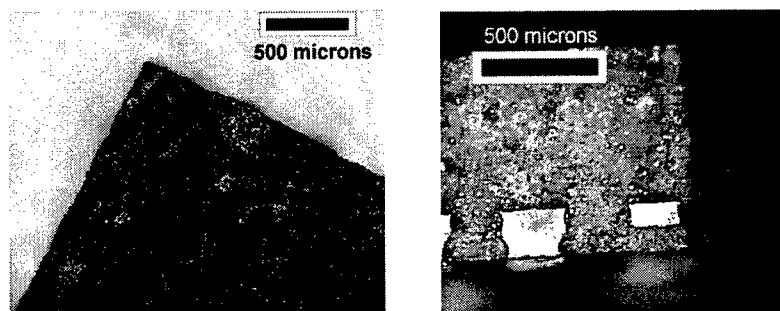


Figure 12: Top side view of a 900-micron thick package (200 micron copper) that was singulated according to the above-described cutting procedure (left). The right image shows the edge of the same package (repeated).

The use of different nozzle sizes in this cutting procedure causes only a very slight deviation of  $1.3^\circ$  from the usual  $90^\circ$  edge angle for a 900-micron thick package.

### 3.4. Speed projection using other equipment

The above-described procedure was until now tested in the lab only. Industrial implementation needs evidently some handling efforts for flipping and aligning the frames between the two cutting steps. These technical problems however can properly be solved using modern inline equipment.

Another question to ask is whether the expensive 532 nm-photons should be used for the mold compound cutting, which can be easily performed by infrared light too. Using the normal Nd:YAG laser based version of the water-jet guided laser the mold compound can be cut much faster and with the same quality. The enhancement of the copper cutting speed is much more critical for a successful industrial application of electronic package singulation by the water-jet guided laser technique and will be discussed now.

The two principal strategies for faster copper cutting are increasing the average laser power and decreasing the lead frame thickness.

Increasing the laser power is undoubtedly possible and recent developments in the industrial laser market (Quantronics, Coherent, Lee Laser) are very positive in this means. Due to the highly polarized nature of the frequency doubled laser light a doubling of the laser power is easily possible by combining two lasers with crossed polarizations. As long as the peak power of the pulses stays constant and the pulses of the two lasers are alternated; we expect a linear relationship between average laser power and copper cutting speed. In other words, using two combined lasers would double the copper cutting speed. Therefore speeds of up to 40 mm/s are feasible.

Nevertheless, the more cost efficient way to increase the copper cutting speed is to decrease the copper thickness in the cutting track. Already the majority of electronic packages is based on 200-micron thick copper lead frames, which is already a reasonable thickness for laser based package singulation. Future developments tend to lean towards smaller packages, based on thinner substrates. Independently of the total lead frame thickness, the copper thickness can be decreased in the cutting tracks of etched lead frames by just a minor design modification. This modification however would lead to a nearly exponential increase of the copper cutting speed as illustrated before (Fig. 11).

Furthermore, both approaches of decreasing the copper thickness in the streets and increasing average laser power can be combined for a higher performing singulation of electronic packages.

## 4. CONCLUSIONS

The presented method of electronic package singulation by the water-jet guided laser technique results in superior cut quality compared to mechanical sawing. In particular, the cuts are burr free, which is critical for the soldering process of the packages on the final electronic board. The difficulties arising from the very different thermal and optical properties of the used materials could be limited using an adapted cutting procedure. Due to the cooling of the sample by the water-jet, the technique allows for high quality cuts in such different materials as mold compound and copper. In contrast to mechanical sawing, the method represents a wear-free possibility to singulate copper based electronic packages. The absence of wear in the presented singulation method is one of the most important cost-of-ownership arguments for the realization of a corresponding production machine. The transposition of these results into a production machine is easily possible because of the already existing fully automated Laser-Dicing System, which are based on the water-jet guided laser technique.

The cutting speeds of packages that are based on thin copper substrates (100 – 150 microns) are already competitive today. Further speeds enhancements will be achieved in the future using more powerful lasers and adapting the lead frame design to the singulation technique.

## 5. SUMMARY

In summary, we present a new solution to resolve one of the important problems related to electronic packages: the singulation of copper lead frame based molded packages. The different aspects of package singulation by the water-jet guided laser technique were discussed in detail.

The importance of complete mold compound removal in between the copper contacts in a first step was pointed out. The following step of copper cutting is usually the speed-determining step of the singulation process. The mold compound can be ablated due to the reflected or diffused light. Thus care has to been taken in order not to alter too much the good mold compound edge quality during the copper cutting step. Flipping the sample between the two steps, and using different nozzle sizes for mold compound and copper cutting, gave the best results. In all cases however, the copper is cut without burrs, a decisive advantage compared to mechanical sawing.

Typical cutting speeds for different copper thicknesses were given and the possibilities for further speed enhancements were briefly discussed.

## 6. ACKNOWLEDGEMENTS

We acknowledge the support of Coherent Inc.. A.S. and N.V. acknowledge the financial support by the Swiss scholarship program.

## 7. REFERENCES

1. G. Kühnlein, *A Design and Manufacturing solution for high reliable non-leaded CSP's like QFN*, in unknown, 2001.
2. B. Richerzhagen, *Entwicklung und Konstruktion eines Systems zur Übertragung von Laserenergie für die Laserzahnbehandlung*, in PhD-thesis No 1207, 1993, EPFL: Lausanne.
3. A. M. Sterling and C. A. Sleicher, "The instability of capillary jets", *Journal of Fluid Mechanics*, **68**, p. 477-495, 1975.

# **Laser Joining of Glass with Silicon**

Reiner Witte, Hans Herfurth, Stefan Heinemann  
Fraunhofer USA, Center for Laser Technology, Plymouth, MI 48170

## **ABSTRACT**

New joining techniques are required for the variety of materials used in the manufacture of microsystems. Lasers are emerging as a useful tool for joining miniaturized devices. The beam can be focused to less than .001" allowing localized joining of very small geometries. There is minimal heat input into the part so distortion and change in material properties is minimal. The high quality of the laser welds and the precise process control enable hermetic sealing.

Glass to silicon bonds are required in a vast array of opto-electronic components, including laser sources, sensors, switches and multiplexers. Typically, adhesives as well as direct and anodic bonding techniques are used to join the different materials. Adhesive residues, low bond strength, heating of entire parts during joining and poor long-term stability are disadvantages of these conventional techniques.

Laser bonding is a promising alternative due to the increased bond strength and high repeatability. Compact and efficient diode lasers equipped with fiber beam delivery in the power range of <50W are applied to the sandwiched glass-silicon structure. During bonding, the laser beam penetrates the upper part and is absorbed at the surface of the bottom part. A clean environment and good part fit-up is required to ensure proper bonding, high bond strength, and hermetic sealing. The process eliminates adhesives; therefore reducing costs due to shorter cycle times, lower maintenance and less inventory. The process requires no handling of toxic liquids and creates no fumes. Furthermore, the bonded parts are free of any residue or contamination, reducing scrap rates. This study investigates the process parameter window and determines the impact on the parts and the stability of the process. The results will lead to the development of several applications in the areas of telecommunications, biomedical devices and MEMS. This includes the encapsulation of MEMS, the covering of sensors and the packaging of biomedical products. The selectivity of the process will be demonstrated on flat coupons.

Keywords: Selective bonding, Glass, Silicon, MEMS

## **1. Introduction**

Typically methods applied in wafer bonding are anodic bonding and room temperature bonding. Anodic bonding is based on the fact that alkali ions move at high temperatures from one wafer to another facilitated by an externally applied electrostatic field. This effect combined with the occurrence of Van der Waals forces results in a very strong connection between the wafers. However, there are some restrictions to this method. Anodic bonding takes place at elevated temperatures up to 500°C and requires an extended processing time of several minutes. In addition, the process cannot be applied locally; typically the entire contact surface between the parts is being bonded. Extremely high demands on cleanliness and flatness must be fulfilled to bond wafers at room temperature by stacking them and applying an initial clamping force.

Laser supported bonding is based on the principle of adhesion of solids. In this case, the heat input by the laser beam initiates the bond. In principle, this method can be selectively applied to very small structures with a laser beam. The minimum size of the bond area is primarily determined by the spot size of the laser beam. This paper includes a general overview on the possibilities of laser-supported bonding and bonding results using different laser sources. An outlook on potential industrial applications will be given.

## 2. Material

The requirements on both parts to be joined, glass and silicon, are very high. As known from anodic bonding in silicon manufacturing, the surfaces must have a high flatness, parallelism and low roughness /1/. The material must also be free of any impurities. The physical properties of the materials such as optical, mechanical and thermal appearance are defined in the following.

### 2.1. Characteristics

#### 2.1.1. Geometrical tolerances and surface quality

In addition to the surface cleanliness there are two main specifications that are important for the mechanical properties in wafer bonding:

- Flatness
- Roughness

The surface flatness is a macroscopic measure of the deviation of the wafer's front surface from a specified reference plane, assuming that the backside of the wafer is ideally flat /2/. The total thickness variation (TTV), also known as waviness, is commonly used to specify the surface flatness and describes the difference between the highest and the lowest elevation of the top surface of the wafer.

During the bonding process, each wafer is elastically deformed to achieve conformity of the two surfaces /3/. Any flatness defects of the glass and silicon wafers can result in periodic strain patterns (contrast fluctuations) corresponding to typical spatial frequencies of a bonded pair that can be detected by X-ray topography. Larger areas of flatness defects may result in a reduced bond quality or a lack of bonding.

The silicon wafer material that was used is a standard material with total thickness variation of less than 1 $\mu$ m. For the glass wafer, a similar value is given referred to as the peak to valley. The glass wafers from Schott have a peak to valley measurement of 0.09mm.

After grinding or lapping, wafers are mounted on a flat plate by vacuum or wax. External pressure is applied to push the wafer against the polishing pad, which is moved across the wafer surface. Polishing slurry of a colloidal dispersion of silica (SiO<sub>2</sub>) powder in an aqueous solution of potassium hydroxide is applied onto the pad to perform the polishing operation. The polishing pad materials are usually poromeric artificial fabrics such as polyester felt or polyurethane. The diameter of the silica particles used is in the range of 40 to 1000 Å, typically 100 Å /4/. The pH-value of the slurry is around 10-11 and the concentration of silica is typically 3-4% /5/.

Today, the polishing technology in wafer processing is able to produce silicon wafers with a roughness in the range of 1 to 2 Å. Chemo-mechanical polishing produces silicon wafer surfaces that exhibit sufficient smoothness and are free of haze and damage.

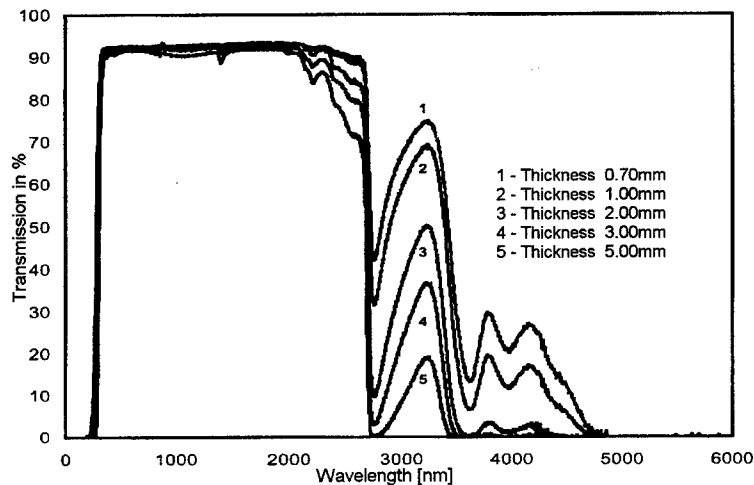
For the silicon wafers, a roughness of 100nm is specified by the customer. The glass wafers did not require special polishing because the surface roughness after manufacturing was better than 3nm.

## 2.1.2. Optical properties

The laser-supported bonding is based on the principle of transmission welding with laser radiation, which is well known from laser welding of plastics /6, 7/. This principle requires that one of the parts to be joined is transparent for the laser radiation and the other material is able to absorb the laser energy. The transmission spectrum of glass (Borofloat® 33) is shown in Figure 1. For wavelengths between 300nm and 2000nm the transmission is approximately 90%, fulfilling the requirements for transmission welding.

Figure 1

Transmission spectrum of Borofloat® glass with different thicknesses/8/.

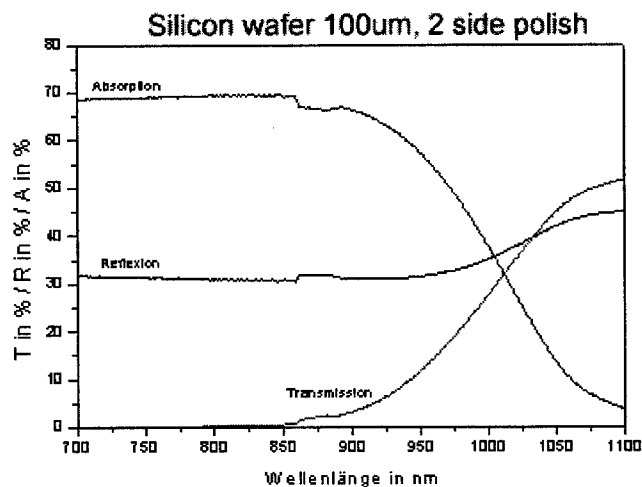


Silicon has high absorption properties for wavelengths up to 900nm [Figure 2]; at longer wavelengths the absorption decreases rapidly and the transmission and the reflection increase accordingly. Based on these characteristics, laser sources with a wavelength of less than 900nm should preferably be applied to conduct laser-supported bonding. High power diode lasers adequately cover this wavelength range.

After heating of the silicon, the absorption at higher wavelengths increases rapidly to nearly 90%. For this reason, the Nd:YAG laser with radiation at 1.06μm is also appropriate, especially considering the better beam quality and the smaller spot size.

Figure 2

Transmission, Absorption and Reflexion of 100μm thick silicon /9/



### 2.1.3. Thermal properties

The laser beam heats both materials during the bonding process. A close match of the thermal expansion coefficient of both materials is necessary to avoid damage during processing or afterward during the cooling phase. Otherwise, the mechanical stress induced during the heat cycle will result in cracks.

Some commercial glass materials exhibit a thermal expansion coefficient that is identical or very close to silicon. Most commonly used in anodic bonding are glasses from Schott GmbH (Borofloat®) and Corning (Pyrex® 7070, 7740). Table 1 includes a brief overview on the material specifications.

Table 1

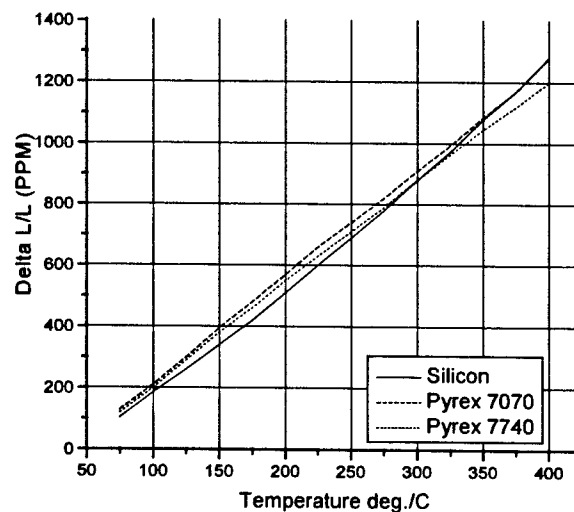
Comparison of different glasses and silicon. /10,11/

Manufacturer	Product Name	Working Point °C	Softening Point °C	Annealing Point °C	Strain Point °C	Thermal Expansion (*10 <sup>-6</sup> *°C <sup>-1</sup> )
Schott	Borofloat 33	1280	820	560	518	3.25
Corning	Pyrex 7740	1252	821	560	510	3.25
Corning	Pyrex 7070	1068	n/a	496	456	3.20
			Melting Point °C	Boiling Point °C		
Diverse	Silicon		1412	3270		2.6

The glass material must have a temperature above the softening point (approximately 820°C) to allow the move of alkali ions into the glass. During processing, the temperature at the interface must be kept below 1400°C to avoid melting of the silicon. Melting of silicon would destroy the single crystal and result locally in a polycrystalline structure that exhibits different properties than the original structure.

Figure 3

Thermal expansion over temperature of Pyrex® glass and silicon. /12/





## 3. Processing

### 3.1. Sample preparation

Commercially available wafer material and glass samples were used for the investigation of laser-supported bonding. The materials meet the requirements for flatness and surface quality, however special treatments are necessary to remove the oxide layer from the silicon and to achieve the needed cleanliness of the sample. The surfaces must be free of particulate, organic, and metallic contamination because the cleanliness has a direct effect on both the structural and optical properties of the bonding interface as well as on the resulting electrical properties of the bonded materials.

#### 3.1.1. Surface cleaning

The cleaning techniques applied must remove all contamination from the surfaces without degrading surface smoothness. Similar to very large scale integration (VLSI) device fabrication, a silicon surface with a high degree of smoothness and flatness is also a key concern in laser-supported bonding. A hydrogen-peroxide-based (RCA) wet cleaning solution (see Table 2) that is typically used for wafer bonding was also found to be appropriate for laser-supported bonding.

Table 2

Cleaning of silicon with hydrogen-peroxide-based solution. 50% unstabilized  $H_2O_2$ , 50%  $NH_4OH$ , 37% HCL /1/

Cleaning step	Compositions by Volume	Operating Temperature (deg. C)	Operating Time (min)	Designed to Remove
Ethanol	$C_2H_5OH$	25	5 (Supersonic)	Dust, fat
RCA 1	$NH_4OH:H_2O_2:H_2O$ 0.25:1:5	70	10 (Supersonic)	Particles, organics, some metals
Rinse	Di $H_2O$	25	5	RCA 1
RCA 2	$HCl:H_2O_2:H_2O$ 1:2:8	75	20	Alkali and heavy metals
Rinse	Di $H_2O$	25	5	RCA 2

The surface of glass is less reactive with its natural ambient. Therefore, it is not necessary to apply the same cleaning schedule as is applied for silicon. After removing the organics and particles with RCA1 and rinsing with DI water, the glass samples are ready for use.

### 3.2. Laser sources

Two different laser types with different wavelengths and output power were investigated: a 30 W diode laser and a 1000 W Nd:YAG. Diode lasers have significantly improved in recent years and represent a promising alternative to conventional laser sources. The system used provides laser radiation at a wavelength of 808 nm and delivers the beam through a 600  $\mu m$  step index fiber to the workpiece. A minimum spot diameter of 750  $\mu m$  is achieved at a focal length of 50mm.

The Nd:YAG laser beam has a wavelength of 1064nm and delivers a maximum power of 1000 W through a 300  $\mu m$  fiber. With this setup, a focus diameter of 150  $\mu m$  can be achieved using a 100 mm focal length.

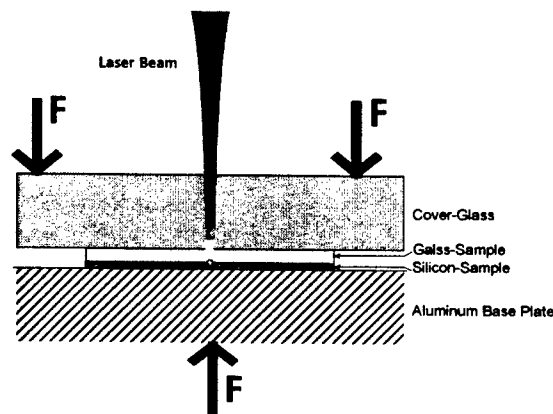
Compared to the diode laser, significantly higher intensities in the focal spot are achievable with the Nd:YAG laser. However, the diode laser radiation is better absorbed by the silicon surface (see Figure 2). The objective for the comparison was to determine if a bonding process still can be established using the highly cost effective diode laser.

### 3.3. Clamping

To achieve intimate contact between the silicon and glass samples, a pneumatic fixture (Figure 4) was used, that can apply pressure between 1MPa and 30MPa. A transparent cover plate made of fused silica applies the clamping pressure to the sample surface and allows access of the laser beam. A three-axis motion system was used to scan the surface of the samples with the laser beam. This set-up offers high flexibility to vary speed, focal position and feed direction.

Figure 4

Schematic drawing of processing glass to silicon wafer bonding



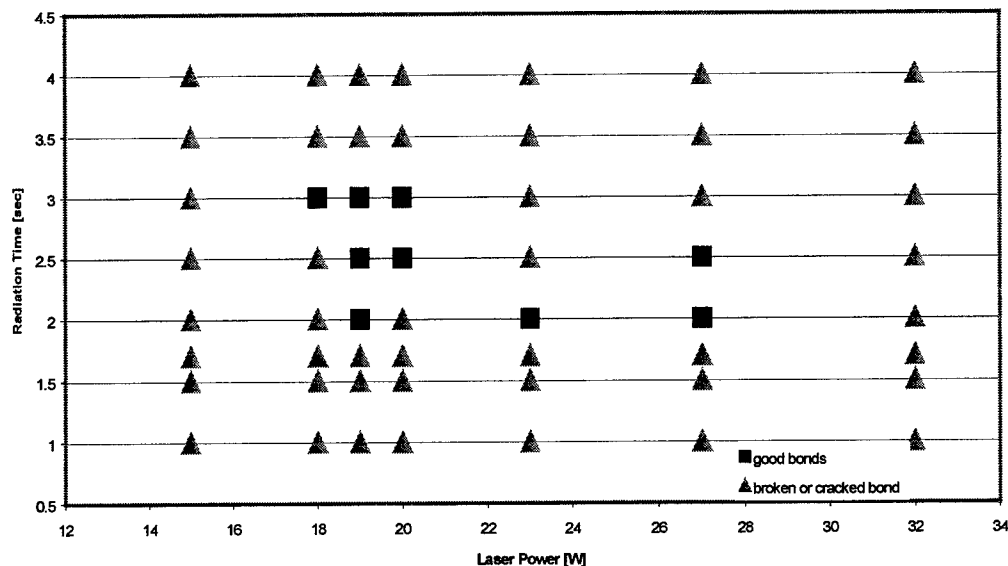
In the investigation using the 30 W diode laser, a layer of polytetrafluorethylene (PTFE) was used to control the heat flow from the silicon into the aluminum base plate. The PTFE layer serves as an insulator that allows sufficient heating of the material even with the low power diode laser. Without the PTFE layer it was not possible to achieve any bonding. During the tests with the Nd:YAG laser, isolation was not necessary due to the higher intensity in the focal spot of this laser.

## 4. Results

The investigation included tests where the samples were stationary relative to the laser beam (static tests) and tests where the samples were moved under the stationary beam (dynamic tests). During the static tests, the laser beam was used to bond a single spot. The heat input was controlled by the laser power and the beam-on-time. Figure 5 shows the matrix of settings for the beam-on-time and the power that was investigated to determine appropriate conditions for bonding. It is distinguished between parameter settings that result in good bonds and settings that lead to defects. Typical bonding defects include lack of bond strength and crack formation during and after processing. The tests using the diode laser show a small parameter window where bonding is possible.

Figure 5

Radiation time vs. laser power for static diode laser tests.



Due to the heat input of the laser beam into the silicon wafer, thermal and mechanical stress results in the bonded parts. In the dynamic experiments, it was found that the duration of the heat input is relevant for producing cracks in the glass. During the process, the average temperature is steadily increasing in the silicon. At the beginning of the bond line, the parts are already connected while the rest of the silicon is expanding because of the heat input. The glass is less subjected to this effect because the absorbed energy in the glass is negligible so that only the connection to the silicon heats up the glass. At the end of the bond line, both materials will cool off with the result that the silicon bulk material is much warmer than the glass during bonding. Since silicon shrinks more than glass, mechanical stress is induced and cracks occur if the stress exceeds the strength of the bond.

Furthermore, the energy input must be well controlled to achieve localized bonding and avoid melting of silicon. Melting of the silicon will result in a poly crystalline structure with changed electrical and mechanical properties. Bonds where melting of silicon occurred also exhibit a rough interface.

Examples of static and dynamic bonding are shown in Figure 6. The left picture is a single pulse with a beam-on-time of 2 sec and a laser power of 27W. The lines in the middle and the circle on the right side are also done with 27W. The speed for the lines is 0.07m/min and for the circle 0.08m/min. The length of the lines is 3mm and the diameter of the circle is 3mm.

Figure 6

Samples after processing with diode laser.

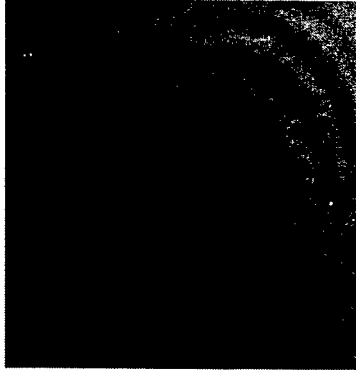


Due to the different beam characteristics and beam quality of the Nd:YAG laser, there are differences in the clamping and the required power. The higher intensity in the focal spot enables bonding without using a PTFE

layer between silicon and the aluminum base plate. The speed can be increased up to 200mm/min at a focal spot diameter of 300 $\mu$ m. The sample in Figure 7 shows a circle with a 3mm diameter that is bonded at a speed of 100mm/min and 47W laser power.

Figure 7

Bonded circle  
with Nd:YAG  
laser at  
100mm/min and  
47W.



## 5. Summary and perspective

Localized laser bonding of glass to silicon has been investigated using a diode laser and an Nd:YAG laser. The main differences between these laser types are the beam quality and the output power. The investigation included the testing of bonds on spots, straight lines and circles. Bonding was successfully established with both laser types, however the tests show that the usable parameter window to achieve good bonds is narrow. Either cracking of the glass wafer or a lack of bonding is observed if the heat input deviates from the appropriate settings. It was also found that cleanliness and surface conditions of samples and appropriate clamping are crucial to bond the materials.

The results exhibit a high potential for laser bonding to address an increasing need for localized joining of materials in the manufacture of miniaturized components. Future work will include the further development and optimization of the bonding process for glass-to-silicon and the characterization of the bond strength, durability and residual stresses.

## 6. References:

- /1/ Q.-Y. Tong, U. Goesele, Semiconductor Wafer Bonding, John Wiley & Son., 1999;
- /2/ T. Takahagi, A. Ishitani and S. Wakao, Chemical structure and reactivity of a silicon single crystal surface fluorinated by xenon fluoride, J. Appl. Phys., 76, 3140, 1994
- /3/ K. Hofmann, G.W. Rubloff and R.A. McCorkle, Defect formation in thermal SiO<sub>2</sub> by high-temperature annealing, Appl. Phys. Lett., 49, 1525, 1986
- /4/ C.C. Payne, Silica sol composition for polishing silicon wafers, U.S. Patent No. 4,462,188 (1984)
- /5/ R.M. Mandle, Process for preparing a polishing compound and product, U.S. Patent No. 3,298,807, 1967]
- /6/ T. Nilsson, C. Lampa, Diode laser welding of plastics, Proceedings of the 7<sup>th</sup> Nordic Conference in Laser Processing of Materials, Acta Universitatis Lappeenrantaensis 84, 1999, 472-481

/7/ H. Puetz, D. Haensch, H.-G. Treusch, S. Pflueger, Laser welding offers an array of assembly advantages, Modern Plastics, September 1997, 121-123]

/8/ Schott AG, Borofloat 33 product information, 2001

/9/ Fraunhofer Institut fuer Laser Technologie (ILT), Aachen, 2000

/10/ Schott AG, product information 2001

/11/ Corning Inc., product information 2001

/12/ Corning, Glass Silicon Constraint Substrates, 1999

# Processing of silicon by Nd:YAG-lasers with harmonics generation

Panzner Michael, Kasper Jörg, Wust Hendrik, Klotzbach Udo, Beyer Eckhard  
(Fraunhofer Institute Material and Beam Technology, Germany, 01277 Dresden,  
Winterbergstraße 28)

## ABSTRACT

Micro structures in silicon are applied in different fields of industry, medicine and research. Examples are micro mechanical sensors for car security systems, nozzle plates for printer, and optical elements for X-ray beam splitting. Wherever the accuracy of etched silicon structures is not required, laser processes with short pulses and small wave length can be an option with the advantage of shorter process time

High quality cutting and drilling of silicon can be achieved by application of diode pumped q-switched Nd:YAG-lasers and harmonics generation. The short pulses (15 ns) and the UV wave length (355 nm) of the Gator UV from Lambda Physik AG, for example, allow a reduction of thermal effects like deposition of molten material and heat effected zones at the edges. Especially in the case of deep structures the ablation plasma causes powerful heating of the walls. An reduction of the plasma temperatures and so the heat influence on the walls can be realized by a small laser wave length with low plasma absorption. Short laser pulse durations are necessary to reduce the heat effected depth or melting due to heat flow from the ablation area into the bulk material. Also the duration and intensity of plasma heating is reduced by short laser pulses.

In this contribution the possibilities and limits of laser machining of Si by diode pumped Nd:YAG-lasers with harmonics generation will be presented by means of structures processed by application of a scanner with f-theta-optic. The results will be discussed concerning the experimental setup and the laser parameters.

**Keywords:** laser processing, laser ablation, laser cutting, microstructure processing, silicon

## INTRODUCTION

Silicon is one of the most thoroughly investigated materials. The vast majority of electronic components is based on semi-conducting mono-crystalline silicon. Polycrystalline and amorphous silicon is used in solar cell technology. Micromechanical components as acceleration sensors in car safety systems and micro-fluidic circuits are made of silicon. Silicon is also used as a substrate for X-ray mirrors, for example.

Every one of the mentioned applications involves some structuring of the bulk material because silicon of the required quality cannot be generated as pre-formed parts. The high accuracy required for micro-mechanical components with their structural dimensions of typically a few micrometers is realized with etching technology. Mechanical cutting with its lower accuracy is applied for separating the chips on the wafer. Also laser induced etching [1] is coming up as a process technology. The laser beam technology has an accuracy intermediate between etching and mechanical cutting, combined with the essential advantage of high flexibility: The beam spot on the material can be rapidly moved by scanning, and/or the sample can be moved below the spot.

The technology applied for a special purpose is chosen according to several quality criteria:

- amount of deposited material along the edges,
- width of damaged material along the edges,
- minimum structural dimensions,
- maximum flank slope,
- smoothness of flanks and bottom.

The accuracy of structuring with pulse laser depends on wavelength, pulse time, pulse repetition rate, and intensity distribution on the beam spot, as well as on the beam guiding technique.

Much effort has been done in application of short pulse laser technology for silicon processing [2,3]. When comparing fs-laser technology and ns-laser technology, it appears that industrial requirements can be more easily satisfied with ns-lasers.

As explained in the following, essentially improved accuracy of silicon structuring can be expected from using harmonics with their shorter wavelength instead of the original IR-beam of the Nd:YAG-laser.

The penetration depth of the beam into the material is usually quantified by a decay length, here denoted as  $x_{opt}$ , which is the inverse of the absorption coefficient  $\alpha(\lambda)$ . Note that its dependence on the wavelength  $\lambda$  may be very strong as seen in Fig. 1 for silicon. In case of very small penetration depth there is a high concentration of deposited power per pulse so that essentially the whole heated layer can be removed while the amount of melt being present can be negligibly small. In case of larger penetration depth and correspondingly lower concentration of deposited power per pulse, a larger amount of melt is present but the rate of removal may be low.

The decay lengths (or optical penetration depth) of the Nd:YAG-laser radiation and its harmonics as derived from Fig. 1 are listed here:

$$\begin{aligned}\lambda = 1064\mu\text{m} &\rightarrow x_{opt} \approx 60 \mu\text{m} \\ \lambda = 532\mu\text{m} &\rightarrow x_{opt} \approx 0.5 \mu\text{m} \\ \lambda = 355\mu\text{m} &\rightarrow x_{opt} \approx 0.01\mu\text{m}\end{aligned}$$

Whether the optical penetration depth is a relevant quantity here depends on the comparison with the thermal penetration depth  $x_{th}$  related to the thermal diffusivity  $\kappa$  of the material:

$$x_{th} = (\kappa\tau)^{1/2}, \quad \kappa = \lambda/(\rho c) \quad \rho = \text{density} \quad c = \text{specific heat} \quad \tau = \text{pulse duration}$$

Obviously, shorter pulses make smaller thermal penetration depth. 15ns pulses from the laser GATOR applied here on silicon at room temperature, for example, make  $x_{th} \approx 4 \mu\text{m}$ .

The accuracy of the generated structure and the quality of its edges are influenced by the ablation plasma. Especially within deep holes, plasma can lead to melt formation at the wall and to removal of material in places where it is not to be removed [4].

To avoid exceedingly high plasma temperature, the absorption by inverse bremsstrahlung should be kept low. As the plasma absorption  $\alpha_p$  goes with the inverse square of the frequency,

$$\alpha_p \approx \frac{n}{\nu^2} \cdot e^{(\Delta E_0)/kT_e}, \quad [5]$$

$n$  = electron density,  $k$  = Boltzmann constant,  $T_e$  = electron temperature,  $\Delta E_0$  = energy gap,  $\nu$  = light frequency

higher frequency or smaller wavelength makes lower absorption and hence lower temperature.

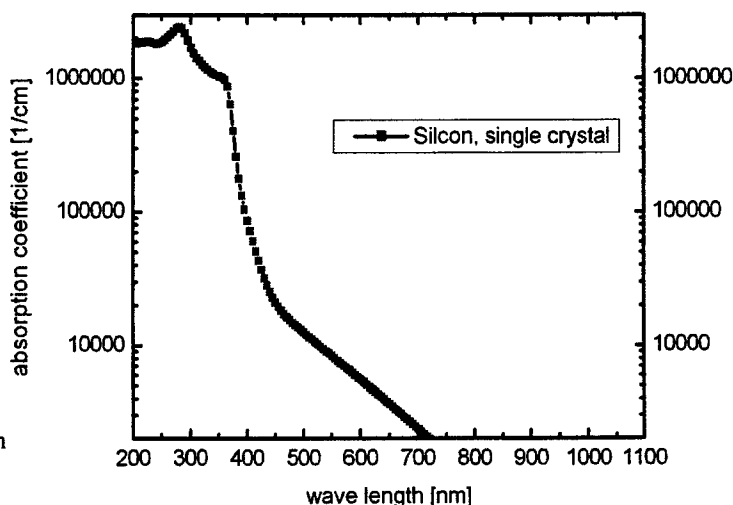


Fig. 1 Absorption coefficient in dependence on wave length [6]

Melt formation may cause a problem as the melt driven out of the hole by the plasma pressure can get stuck to the cooler parts of the borehole wall.

From the above considerations it can be deduced that diode-pumped solid-state lasers with harmonics generation and pulses  $\tau < 30$  ns, which have become commercially available only recently, should be suitable for high-accuracy structuring processes on silicon.

## EXPERIMENTAL

The structuring experiments have been done with a frequency-doubled Nd:YAG-laser of type POWER GATOR GREEN and a frequency-tripled Nd:YAG-laser of type GATOR UV of Lambda Physik. The POWER GATOR has got an integrated beam amplifier. It provides a 532nm-beam of 13.5 W with 10 kHz pulse repetition rate. The GATOR UV, without amplifier, provides 3 W at 355nm and same pulse rate. The pulse shape is seen in Fig. 2.

By expanding the beam diameter of either laser by telescope (10-fold for 532nm and 5-fold for 355nm) the intensity is reduced on the optical elements but increased in the focus. Beam deflection is realized with scanners produced by Arges. Focusing is done with a flat field lens of 10 mm focal distance. After focusing, the remaining beam powers are 11 W (green) and 2.2 W (UV). The beams are linearly polarized but can be transformed into circular-polarized beams by means of a quarter-wave plate. The samples can be moved and adjusted on supports driven by step motors.

The samples were cut from 4" Si-wafers, thickness 550 $\mu$ m with 111 orientation. After structuring, the samples were etched with 20% hydrofluoric acid and rinsed with distilled water to remove deposits of SiO<sub>2</sub> along the edges, then inspected with light and scanning electron microscopy. Some samples were cut at various stages of structuring in order to follow the progress of substance removal. A special etching technique reveals the heat-affected and melt zones. The structural widths and depths were measured with the microscopes supported by suitable software.

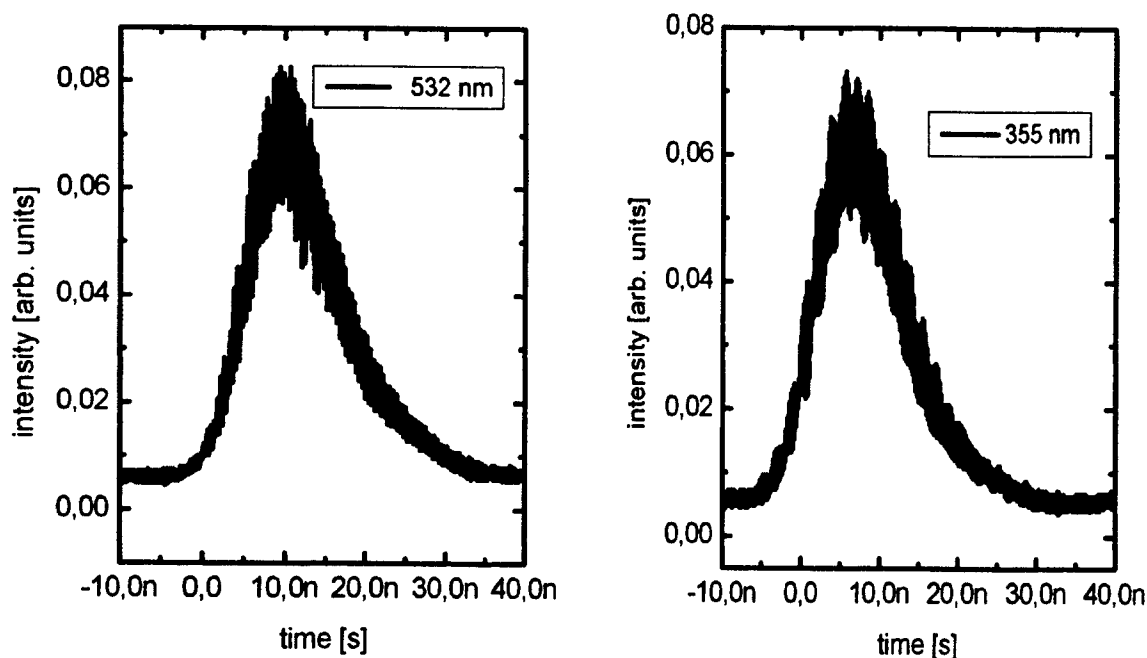


Fig. 2 Temporal intensity profile of 100 laser pulses, POWER GATOR 532 nm left, GATOR UV right



## RESULTS

### Single pulses and percussion holes

The focused laser beam spot was moved over the silicon surface by means of scanner with a path velocity as high as 6.5 m/s so that with 10 kHz repetition rate the effect of the individual pulses was resolved, as seen in the SEM images (Fig. 3, sample slightly tilted). A 15  $\mu\text{m}$  wide crater is formed, surrounded by a 40  $\mu\text{m}$  wide area covered with splashed melt.

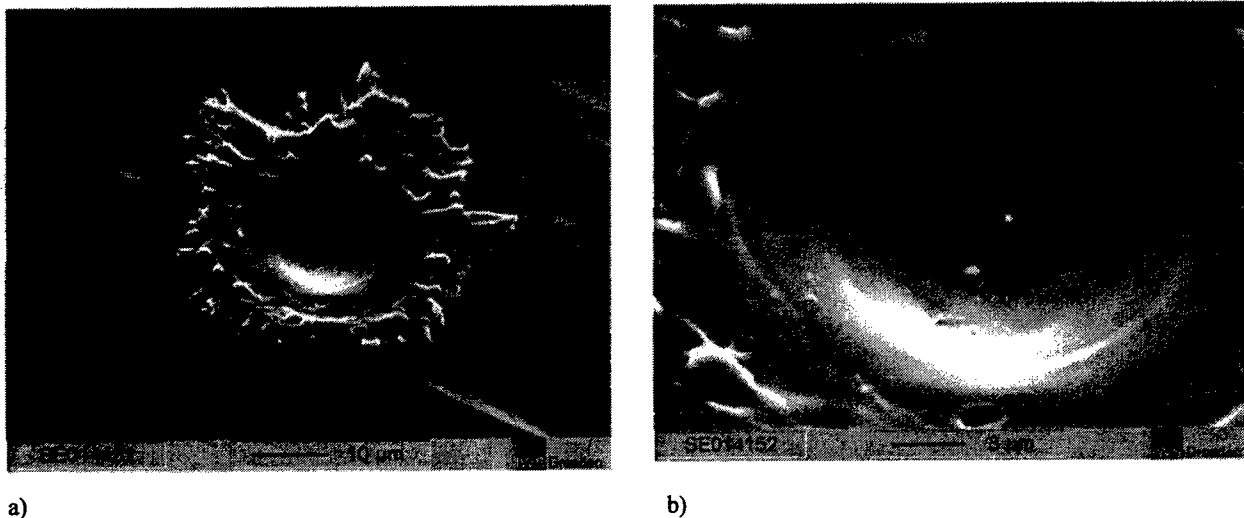


Fig. 3 SEM-Images of the effect of single UV pulses on an unpolished Si 111 surface  
a) overview of the whole spot, b) sector of the image a)

With stationary spot, through holes are formed after 20 000 pulses (Fig. 4). The beam was focused on the surface of the sample. The hole diameter is 25  $\mu\text{m}$  at the entry and 20  $\mu\text{m}$  at the exit, which means a taper ratio of

$$T = \frac{d_{\text{entry}} - d_{\text{exit}}}{\text{thickness}} * 100 \% = 0,9 \%. 0,9 \%$$

The effect of HF-cleaning is distinctly visible: The deposited  $\text{SiO}_2$  is removed. However, the cleaned surface seems to be slightly rough. A molten rim may be formed around the entry edge of the hole. The hole wall and edge quality at the exit is seen in Fig. 5.

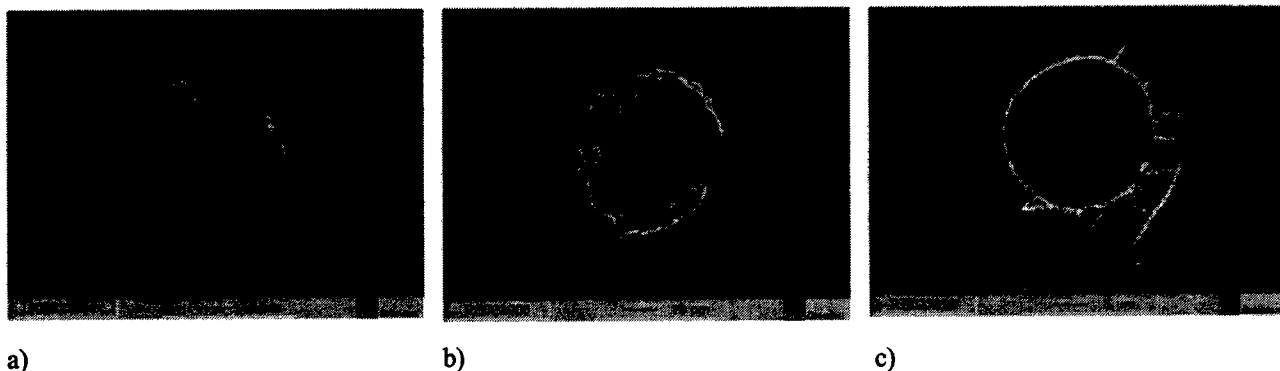
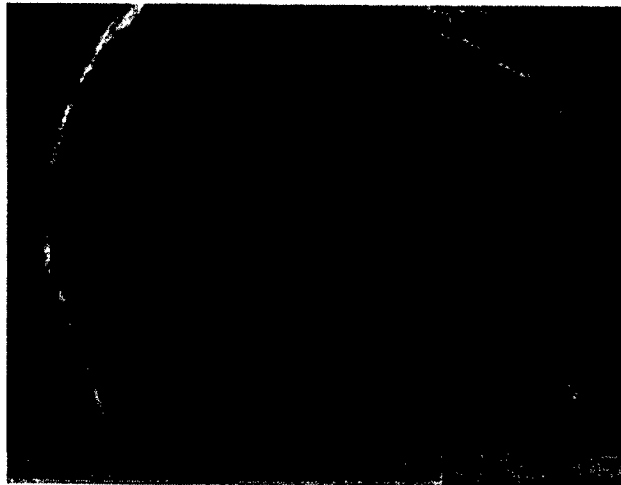


Fig. 4 SEM images of percussion holes in Si 111, thickness 550  $\mu\text{m}$ , 20 000 pulses, 10 kHz  
a) hole entry without HF-cleaning, b) hole entry after HF-cleaning, c) hole exit

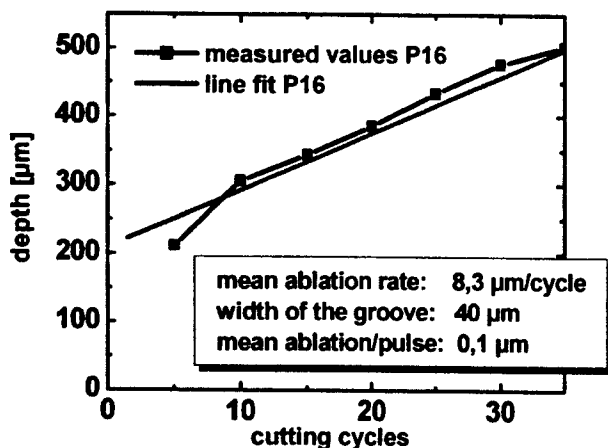
Fig. 5 percussion hole, exit, tilted 30°



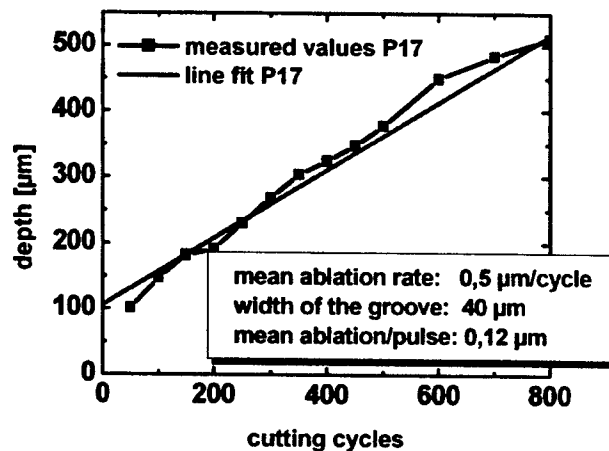
### Si-cutting

With the short wavelengths and short pulses applied here, the laser beam erosion of Si is dominated by sublimation, although it is obvious that transient melting, too, is part of the process.

The depth of trenches obtained with repeated erosion cycles is plotted in Fig. 6, 7. for two beam path velocities for the lasers GATOR UV and POWER GATER 532 nm. The erosion rate has always been found larger at the beginning and becoming nearly stationary, with some fluctuations, at a depth of about 200  $\mu\text{m}$ . In the case of cutting thick samples we found erosion stopping because of enhanced beam reflections at the trench walls for smaller spots. Wider trenches allow deeper cuts.



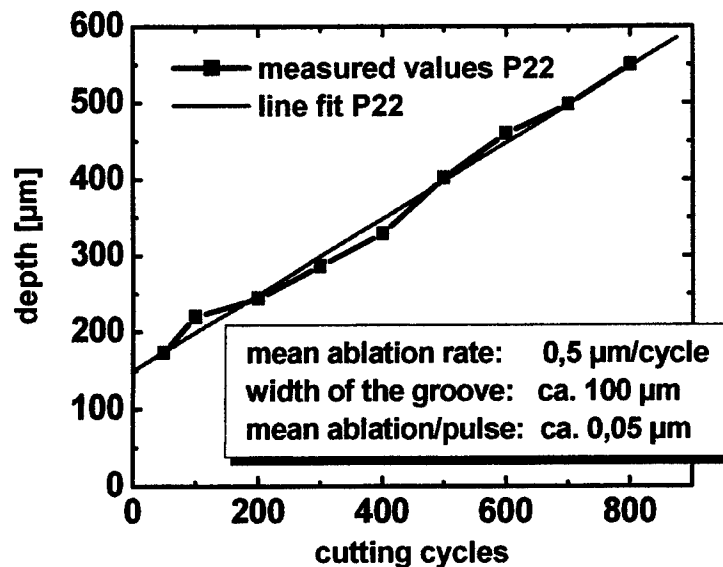
a)



b)

Fig. 6 Cutting depth in dependence on the number of cutting cycles, sample Si 111, thickness 550  $\mu\text{m}$   
a) GATOR UV, cutting velocity 5 mm/s, b) GATOR UV, cutting velocity 100 mm/s

Fig. 7 Cutting depth in dependence on the number of cutting cycles, sample Si 111, thickness 550  $\mu\text{m}$  (POWER GATOR GREEN, cutting velocity 100 mm/s)



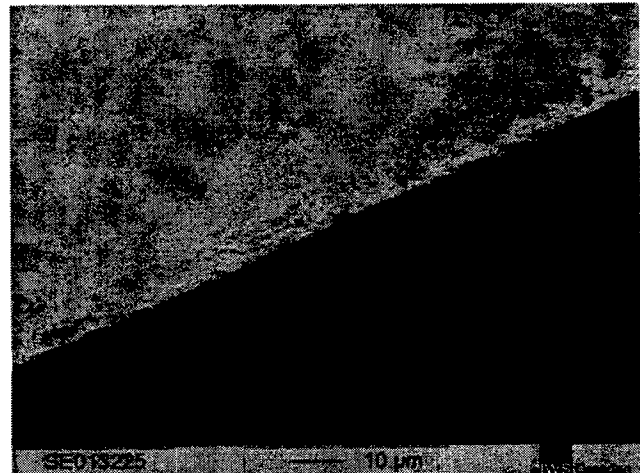
The cause of this trend is not obvious. As expected from Fig.1, the erosion rate is higher with 355 nm. Because of the low accuracy of depth measurement, the difference in the erosion rate for 5 and 100mm/s path velocity seems to be insignificant.

The cross-shaped cut in a 550 $\mu\text{m}$  silicon wafer seen in Fig. 8a gives an impression of the quality, which is even higher for thinner material because of less heat accumulation and melting near the edges during the cutting process.(Fig. 8b). Cutting with 335nm beam produces smaller amounts of melt and hence higher quality than cutting with 532 nm. The obtained gap widths are 40  $\mu\text{m}$  and 100  $\mu\text{m}$ , respectively.

Fig. 8b shows a section through a 550  $\mu\text{m}$  wafer cut with GATOR UV. The taper angle of the gap is 88.3°, and the width is 18  $\mu\text{m}$  below (Fig. 9a), with higher edge quality than above.



a)



b)

Fig. 8: Silicon wafers cut with GATOR UV, 355nm  
a) crossed cuts in 550 $\mu\text{m}$  wafer, beam entry, b) cut in 355 $\mu\text{m}$  wafer, beam entry

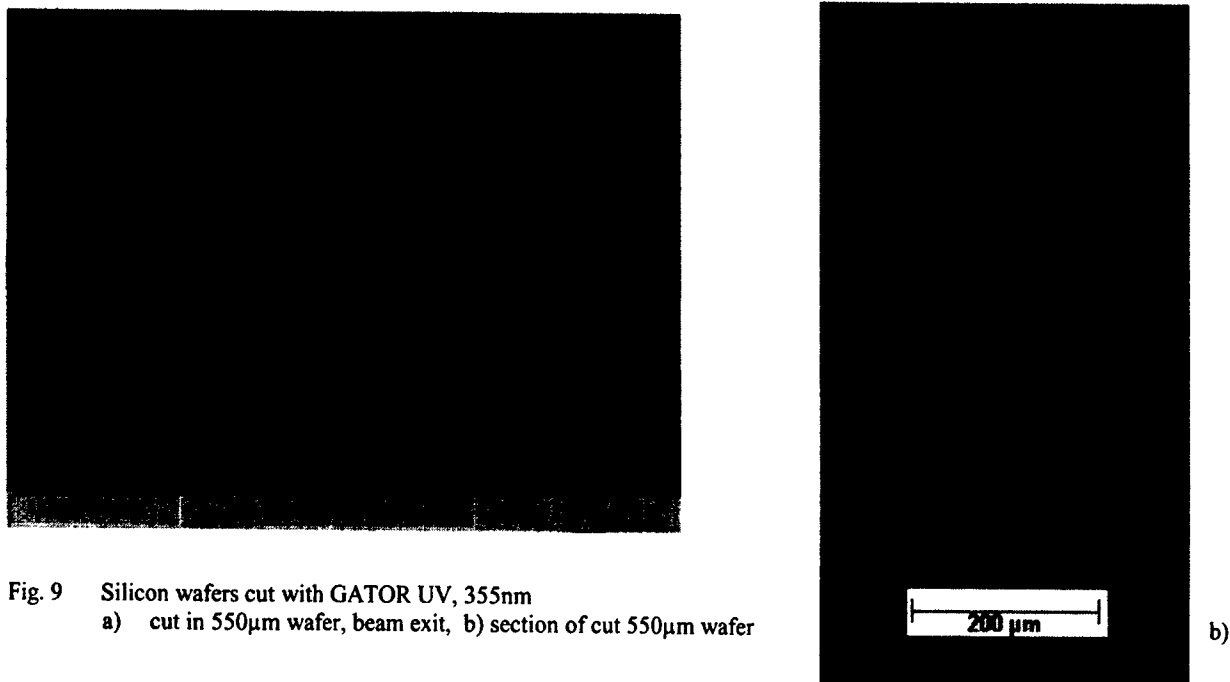


Fig. 9 Silicon wafers cut with GATOR UV, 355nm  
a) cut in 550 $\mu$ m wafer, beam exit, b) section of cut 550 $\mu$ m wafer

### Area ablation of silicon

2.5-D-structures in silicon as applied in micro-fluidics, for example, are usually produced by means of a mask projection technique, with a homogenized excimer laser beam covering the whole area [7]. The alternative technique by scanning a solid state laser beam produces rougher faces because of the localized irradiation. In order to apply this flexible technique nevertheless, quantitative information on the resulting roughness has to be obtained, and ways to minimize this roughness have to be found. The rectangular pit in Fig. 9 has been obtained by line-wise scanning, with the line direction switched by 40° after every coverage of the area, so that with 9 area scans a certain symmetry of the process is realized. Other numbers than 9, with the corresponding angles, have also been tried with the results seen in Fig. 10. The bottom face obtained in this way is fairly well isotropic compared to faces obtained with conventional scanning in two directions.

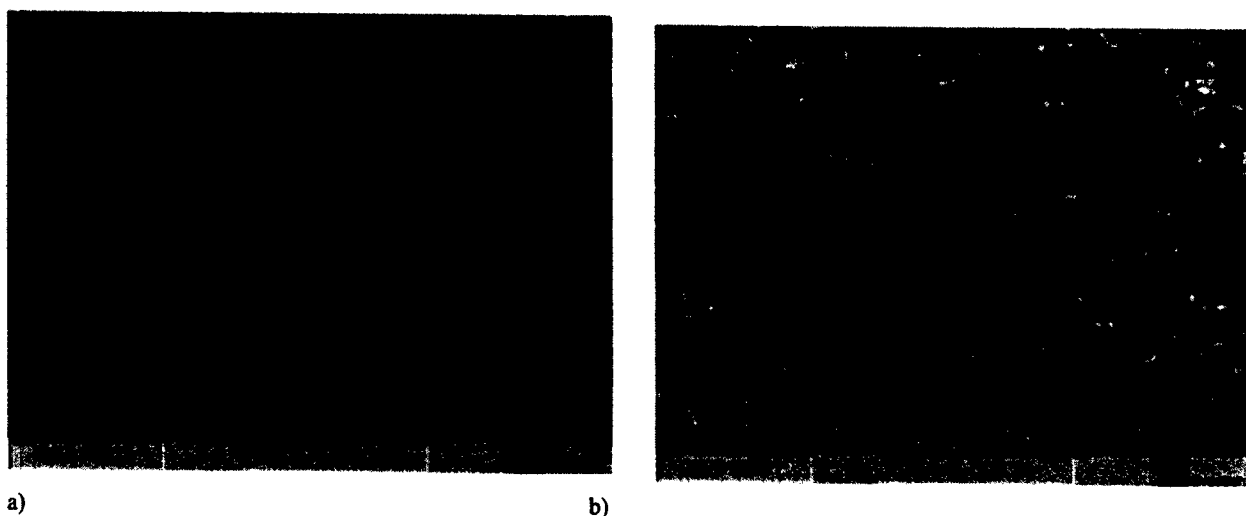


Fig. 9: Erosion of Si 111 face with GATOR UV (335nm), beam power on sample 1.1W, 9 scans differing by 40° line direction, velocity 70mm/s, a) survey, b) bottom face magnified

As expected the erosion rate varies essentially inversely with the scanning velocity (Fig.10).

The micro roughness of about 0.8  $\mu\text{m}$  on average is found to be nearly independent of velocity and number of scans but dependent on line spacing. In these investigations, the optimum spacing of 10  $\mu\text{m}$  was chosen.

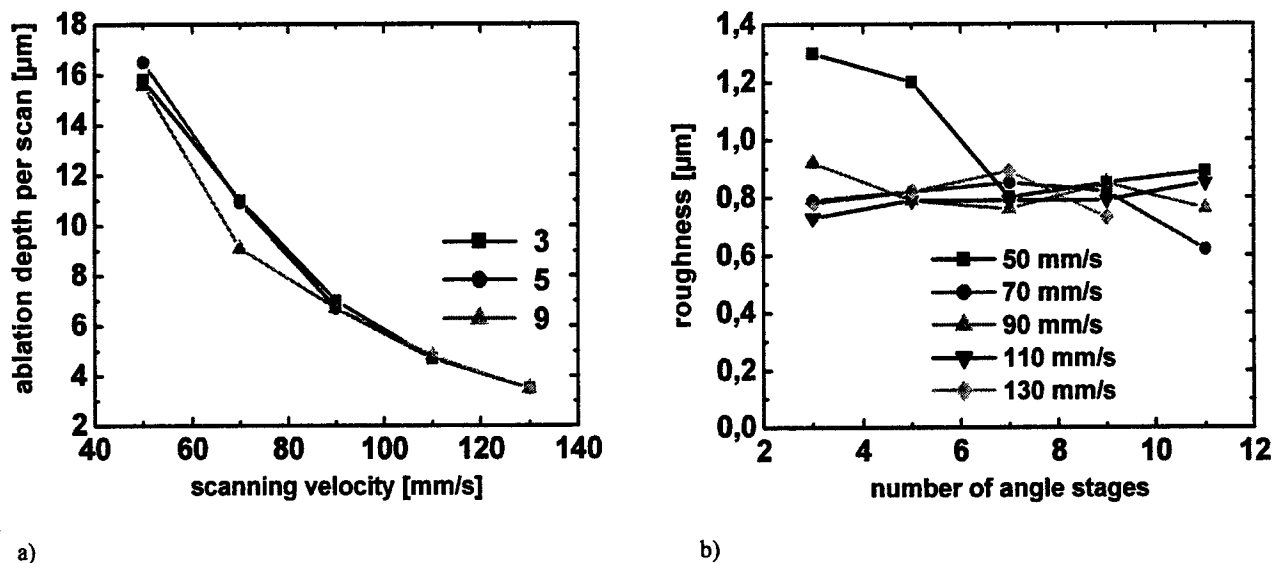


Fig. 10 Processing parameters of scanning with changing direction  
a) average ablation depth per single scan for several numbers of scans  
b) roughness for several velocities and numbers of scans

## Application

With the flexible and well controllable technique combining solid-state laser and scanner, structures suitable for micro-mechanics and micro-fluidics can be easily produced. For demonstration, a toothed gear has been cut from a 550  $\mu\text{m}$  silicon slab. The clean edges have been obtained with hydrofluoric acid etching as described under Experimental.

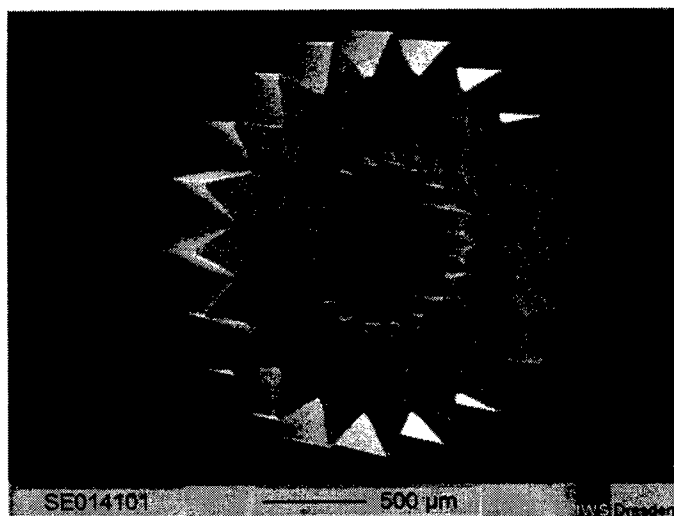


Fig. 10 Toothed gear cut with GATOR UV

## SUMMARY

The presented results demonstrate that solid-state lasers of the GATOR type are suitable for structuring silicon. By judging the obtained accuracy and erosion rate in relation to the effort, the GATOR UV is more favourable than the 532nm version.

Although laser structuring does not reach the accuracy of etching, its flexibility and high rate make it a promising technique, especially in a parameter range where mechanical tooling meets its limits.

This technique is expected to be suitable for producing structures in micro-mechanics, micro-fluidics, and sensorics. In particular, the cutting of irregular-shaped sensor chips might be a promising application.

## ACKNOWLEDGEMENTS

The authors are indebted to Lambda Physik for support in experimenting, and to Dr. Wolf, TU Munich, for roughness and erosion depth measurements.

## REFERENCES

1. B. Shen, R. Izquierdo and M. Meunier, „Laser Fabrication of Three-Dimensional Microstructures, Cavities and Columns”, *SPIE Vol. 2045*, p. 91,
2. P. Lorazo, L.J. Lewis and M. Meunier, “Picosecond pulse laser ablation of silicon: a molecular-dynamics study”, *Applied Surface Sciences* **168**, pp. 276- 279, 2000
3. J. Bonseo, S. Baudach, J. Krüger, M. Lenzner, J.M. Wrobel, W. Kautek, “Femtosecond-pulse laser machining of semiconducting materials”, Conference Digest. “Conference on Laser and Electro-Optics Europe”, Piscataway, NJ, USA, 2000
4. Kaspar, J., Luft, A., „Electron Microscopic Investigation of Structural Changes in Single Crystalline Silicon Induced by Short Pulse Laser Drilling.”, *Proc. of the Micro Materials Conf.*, p. 539, Hrsg. Michel, B., Winkler, T., Druckhaus Dresden GmbH, Dresden, 1997
5. A. Lenk, Dissertation “Komplexe Erfassung der Energie- und Teilchenströme bei der Laserpulse-Anblation von Aluminium”, Department of mathematics and natural sciences, Technical University Dresden, Dresden, 1996
6. E. D. Palik, *Handbook of optical Constants of Solids II*, (Palik, Hrsg.), Academic press, Inc., 1997
7. R.C. Crafer and P.J. Oaklay, *Processing in Manufacturing*, p. 163, Chapman & Hall, London, 1993

# Laser Welding of Polymers Using High Power Diode Lasers

Friedrich G. Bachmann<sup>\*a</sup>, Ulrich A. Russek<sup>\*\*b</sup>

<sup>a</sup>ROFIN-SINAR Laser GmbH; <sup>b</sup>Fraunhofer-Institute for Laser Technology

## ABSTRACT

Laser welding of polymers using high power diode lasers offers specific process advantages over conventional technologies, such as short process times while providing optically and qualitatively valuable weld seams, contactless yielding of the joining energy, absence of process induced vibrations, imposing minimal thermal stress and avoiding particle generation. Furthermore this method exhibits high integration capabilities and automatization potential. Moreover, because of the current favorable cost development within the high power diode laser market laser welding of polymers has become more and more an industrially accepted joining method. This novel technology permits both, reliable high quality joining of mechanically and electronically highly sensitive micro components and hermetic sealing of macro components. There are different welding strategies available, which are adaptable to the current application.

Within the frame of this discourse scientific and also application oriented results concerning laser transmission welding of polymers using preferably diode lasers are presented. Besides the used laser systems the fundamental process strategies as well as decisive process parameters are illustrated. The importance of optical, thermal and mechanical properties is discussed. Applications at real technical components will be presented, demonstrating the industrial implementation capability and the advantages of a novel technology.

## 1. INTRODUCTION

Welding of polymer materials by local heating above the softening temperature by laser radiation and a following joining step is well known since about ten years now [1,2]. CO<sub>2</sub> and preferably Nd:YAG lasers have been used that time. However, the success story for joining of polymers with lasers has begun with the appearance of the high power diode lasers; these lasers are very small, reliable and efficient, which makes them simple to integrate and easy to handle, but also cost efficient, since their high electrical-to-optical efficiency and very little service needs reduces the running costs considerably compared to conventional high power lasers. On the other hand laser polymer welding calls for special requirements beyond those characteristics for the conventional polymer joining technologies, e.g. matching of the melting resp. decomposition temperatures, if different materials shall be joined etc.. Among others laser welding requires suitable optical properties, a special geometrical configuration and laser adapted weld seam design; on the first glance, this may sound as a restriction which limits the applicability of this method, but there are good chances to overcome these limitations, if these requirements can be considered in the product design and the selection of the materials.

## 2. HIGH POWER DIODE LASERS

Diode lasers are well known from their applications in communication and information technology as well as in consumer electronics. In the beginning of the last decade, diode lasers could be scaled up to a power level, which made them attractive for materials processing. This became possible by special semiconductor technology, but especially by the development of sophisticated cooling, mounting and beam forming technologies [3]. High power diode lasers are extremely compact and reliable laser sources, which furthermore show an electrical-to-optical efficiency of about 50%, which makes them also very attractive under an economic point of view. Because of their special construction – high power is achieved by incoherent coupling of several low power sources – the beam quality of high power diode lasers is limited, but by far sufficient for standard polymer welding applications. The wavelength of these diode lasers is in the range between 750 nm and 1050 nm, where 808 nm, 940 nm and 980 nm are the most prominent wavelengths, because of their applicability for solid state laser pumping.

\* f\_bachmann@compuserve.com; phone +49 (0)89 930901-24; fax +49 (0)89 930901-80; <http://www.rofin.com>;  
ROFIN-SINAR Laser GmbH, Umlandstr. 13, D-85609 Aschheim, Germany;

\*\* russek@ilt.fhg.de; phone: +49 (0)241 8906-158; fax +49 (0)241 8906-121; <http://www.fhg.ilt.de>; Fraunhofer Institute for Laser Technology, Steinbachstr. 15, D-52074 Aachen, Germany

## 2.1 The diode laser principle\*

From a traditional diode laser element typically only a few milliwatts can be extracted from a pn-transition; in fact a diode laser is a complex sequence of differently doped GaAlAs layers, which sometimes have only the thickness of a few atomic layers. The light is actually emitted from a layer, which is about a micron in width and also in thickness. From such an element typically a few milliwatts of laser light can be extracted. To increase the power, several of these lasers are positioned side by side or the emitting area is extended to a stripe as schematically shown in Fig. 1 [4]. The special shape of the light generation area leads to special light emitting characteristics, which shows a high divergence in the direction of the pn-transition ("fast axis"), and a lower divergence, but a wide emitting "stripe" in the other ("slow axis"), as also represented in Fig. 1. For electrical and optical reasons, the width of such a stripe is limited to 200 to 300  $\mu\text{m}$ .

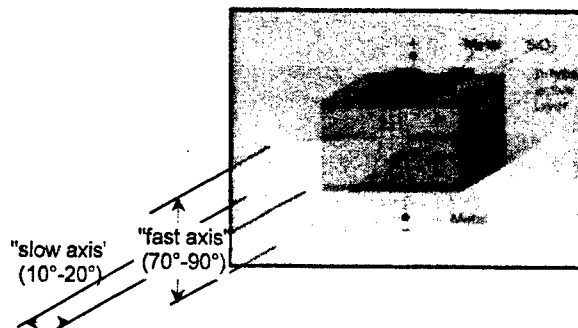


Fig. 1: Scheme of light generation in a pn-transition of a laser diode [after 4]

Further power increase is reached by integration of several such elements into one semiconductor element, which has a size of about 10000  $\mu\text{m}$  x 1000  $\mu\text{m}$  x 115  $\mu\text{m}$ , where 1000  $\mu\text{m}$  is the resonator length in this case. This may be as long as 2 mm in today's high power lasers. This unit is called a "laser bar" and schematically shown in Fig. 2.

## 2.2 Power increase by cooling

Even if these laser bars show electrical-to-optical efficiencies of 40 to even above 50%, considerable amount of heat must be removed through the small footprint if power resp. current is increased further. Therefore, the laser bar must be mounted onto a special water-cooled heat sink, which removes the excess heat and, thus, prevents the bar resp. the mirror facets from thermal destruction. The micro-channel cooling technology was originally based on silicon anisotropic etching [5]; today these heat sinks are typically manufactured from copper. They contain a network of small channels, with a cross section of ca. 300  $\mu\text{m}$  x 300  $\mu\text{m}$ . Water is driven through these microchannels, which are located underneath the laser bar (Fig. 3) for most efficient cooling. Typical flow rates through such a cooler are in the order of 0,5 l/min; a typical heat resistance is in the range of 0,4 K/W. This cooling efficiency allows to use the laser at currents up to 50 A, i.e. to create laser power up to 40 or 50W, or even higher without any damage. The mounting of the laser bars onto the copper cooling unit must be very accurate, so the optical properties of the bar are not affected and the cooling is uniformly and efficient. Actually, positioning accuracy in the micron range is required for all directions; bending of the bar (the so called "smile") must be minimised at any means, since this most severely distorts the beam if fast axis collimation (see sect. 2.3) is performed. The solder material must be sufficiently ductile, so it releases the mechanical stress, caused by the different thermal expansion coefficients of the GaAs based semiconductor material and the copper.

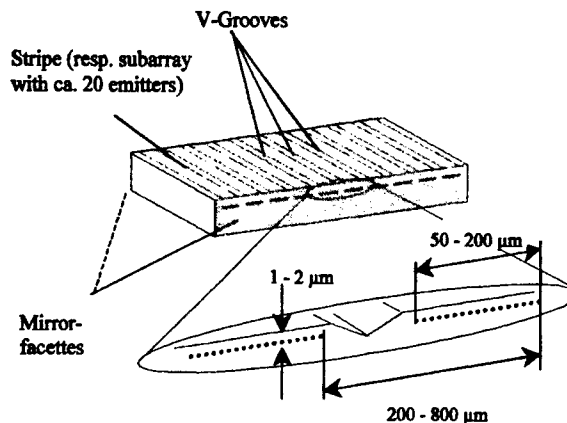


Fig. 2: Integration of several individual diode lasers into one "laser bar"

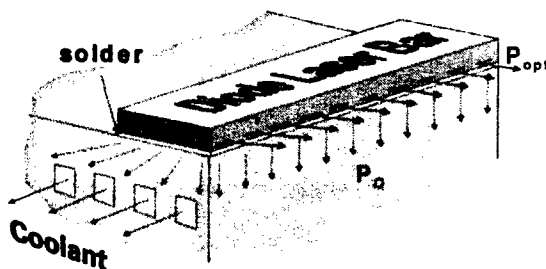


Fig. 3: Scheme of a micro-channel cooler; the bar is precision mounted by a special solder

\* Portions of this section were originally published in ref [3]



### 2.3 Optical considerations and beam forming methods

The beam quality in the "fast axis" is almost diffraction limited and shows a Gaussian intensity distribution with a very narrow beam waist. In the slow axis, i.e. where the stripes or groups of dots are positioned side by side we find a reduced angle, but a wide emitting stripe, i.e. a wide beam width. Thus, the beam quality in the slow axis is much inferior than in the fast axis. This behavior is explained in Fig.4 which summarizes the characteristic numbers of a diode laser bar: A measure for the beam quality is the beam parameter product  $BPP = w_0 \cdot \theta_0$ , i.e. the product of the half beam waist and the half far field divergence angle. With the characteristic numbers shown in Fig. 4 we calculate BPP for the fast axis to about 0.26 to 0.55 mm mrad<sup>1</sup>, whereas we get 4.3 to 21 mm mrad for the single emitter in the slow axis direction and as high numbers as 450 to 700 mm mrad if the entire bar is considered.

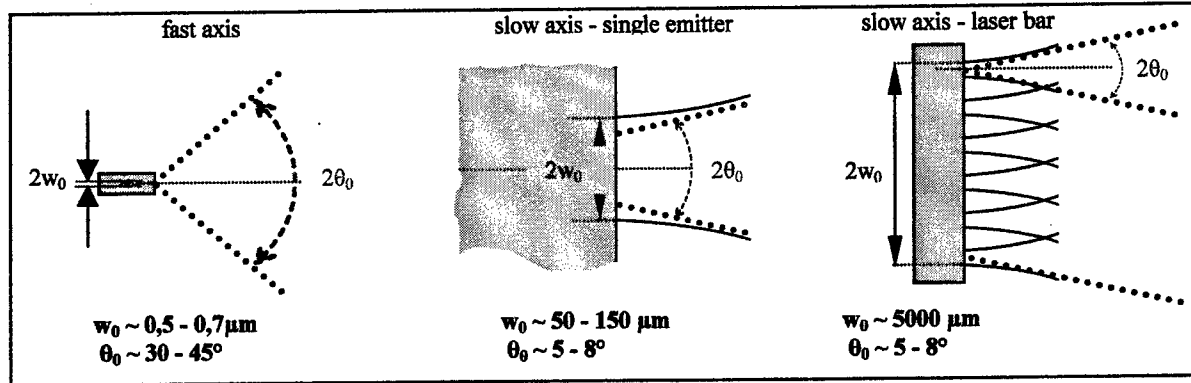


Fig.4: Beam-Parameter-Product consideration for diode laser bars

Because of the large divergence in the fast axis, a cylindrical micro-lens is positioned closely to the front mirror of the diode laser bar, which turns the beam into a collimated parallel beam in this axis (Fig. 5, left). To further increase the power, such units can be stacked on top of each other (Fig. 5, right). The slow axis emission of a single stripe might be collimated by a slow axis collimation lens array [3] to some extent.

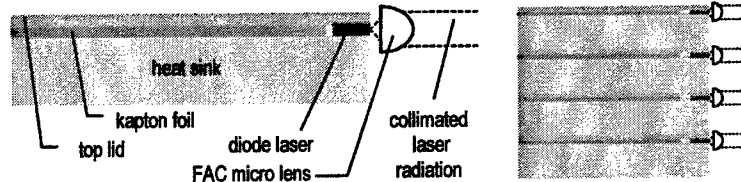


Fig.5: Fast-axis collimation (FAC) by cylindrical lens (schematically, side view, left); stacked units (right)

However, considering the beam parameter products above, in the slow axis, the width of the entire bar has to be considered as the beam waist. In fact, the non-emitting space between the emitting lines is included into the beam waist. Typically the non-emitting area covers between 50 and 75% of the laser bar, which corresponds to a "filling factor" (i.e. "emitting area") of 50 to 25 %. Thus, if beam quality shall be improved, single emitters should be treated and combined. There are certain difficulties to overcome, if slow axis radiation shall be improved. This can be easily seen in the sketch of the radiation of the laser bar (Fig. 4, right), the radiation of the individual emission lines already overlap closely to the output coupler, because of their divergence. Therefore, a special micro-optical element (Fig.6) has been developed [6]. After fast axis collimation (part #4 in Fig. 6) micro prisms (#6) deflect the light from the diode laser bar (#1) resp. the single emitters (#2) into different directions, where they are made parallel by another prism assembly (#7). That way, overlap of the individual emitters is avoided and light is then collimated in the slow axis by a set of cylindrical lenses (#8). Finally, the light is collected by a spherical lens (#9). So the grouping of the emitting stripes has finally changed by this optical element from a lined up sequence to a stacking on top of each other, as schematically represented in the insert box on top of Fig. 6.

<sup>1</sup> the value for a diffraction limited beam is  $\lambda/\pi$ , which is about 0.26 ... 0.31 mm mrad, depending from wavelength

## 2.4 Diode laser systems for polymer welding

With the optical tools, which are described above, high performance diode laser units with a beam quality as good as 40 mrad at 30 W and 60 mrad at 160 W can be realized. This is sufficient for the most cases of polymer welding. Typically, these units are complete units including power supply as well as cooling unit. Such a system (without cooling unit) is shown in fig. 7. 160 W are delivered at a spot size of  $0.6 \times 1.2 \text{ mm}^2$  at a working distance of 84 mm. Also, fiber coupled units are available e.g. the unit presented in Fig. 8, which can deliver 30 W out of a fiber with a core diameter of  $400 \mu\text{m}$  and a numerical aperture of 0,22.

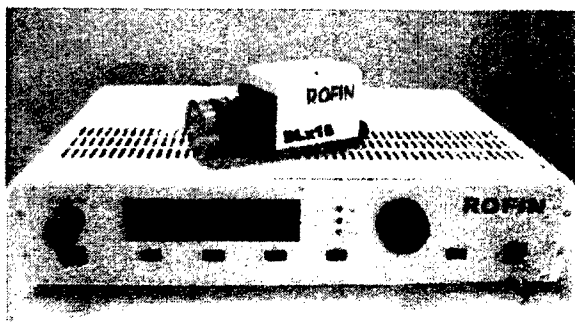


Fig. 7: ROFIN DLx16. 160 W laser for polymer welding; beam size is  $0.6 \times 1.2 \text{ mm}^2$  at a working distance of about 75 mm

## 2.5 On-line process control unit

As we will see in sect. 4 polymer welding processes often take place in a small temperature range of only a few ten degrees. Since on the other hand fluctuations may be caused by change in the absorption properties or by changes in the feed rate, a feedback system for active power control is a very useful tool. A pyrometer is monitoring the actual temperature radiation of the weld area. It is connected with a computer, which controls the laser power by a feedback loop. The process temperature can be maintained constant over a certain range even if the optical properties are changing or if other effects change the amount of absorbed power (e.g. change in feed rate). This could be impressively demonstrated first at the Fraunhofer-Institute for Laser Technology [7], as shown in Fig. 9. The x-y-handling system is decelerating and accelerating if it has to turn around sharp corners. This leads to a local overheating causing decomposition of the material (Fig. 9, left). If the feedback control is activated, the seam can be properly welded without any damage (Fig. 9, right). Additionally, a camera is integrated into the working head, which allows accurate positioning and to some extent visual process inspection.

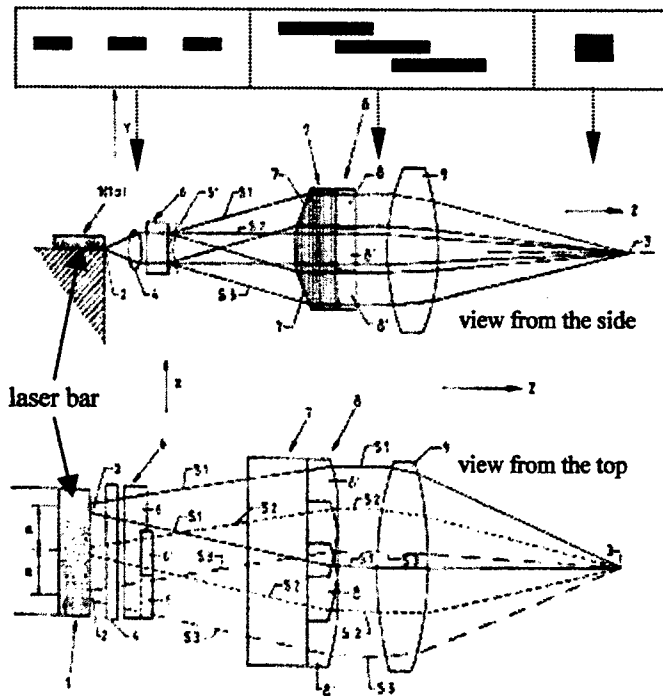


Fig. 6: Micro-optical element for the separation and forming of the single emitters to improve beam quality [6]; insert box top: representation of intensity distribution at different places in the micro-optical element.

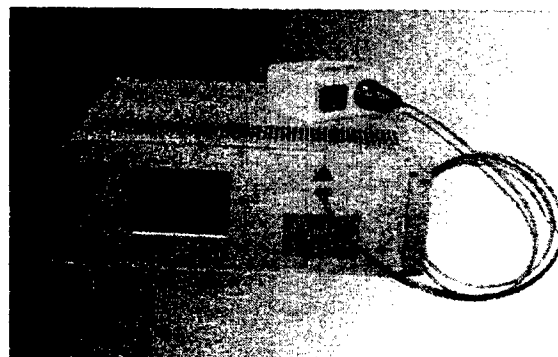


Fig. 8: ROFIN DFx03: 30 W laser for polymer welding with a  $400 \mu\text{m}$ , 0.22 NA fibre and a working head, which contains a pyrometer for active process control

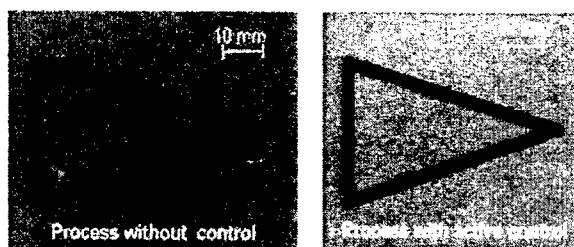


Fig. 9: The effect of pyrometer control [7]

### 3. BASICS OF POLYMER WELDING WITH LASERS

Using laser light as an energy source for welding of materials is well known and applied in industry since a long time. It is state of the art for metal joining. However, welding of polymers must be considered as a totally different process relating to the macroscopic setup as well as to the microscopic processes. Furthermore, if conventional methods for joining of polymers are considered, optical properties and interaction of light with matter do not play any role, contrary to the laser weld, where those processes are the essential steps. Therefore, in the following we will go a little more into the detail of the interaction between light and matter and of the basic processing technology for laser welding of polymers.

#### 3.1 Light-matter interaction

If light is incident to a materials surface it can be either reflected or penetrate into the material. Reflection is represented as R in Fig. 10. As well known, the reflectivity of metals is rather high, very often even above 90% for high quality surfaces and for the wavelength of the CO<sub>2</sub> laser around 10  $\mu\text{m}$ . The situation may improve for Nd:YAG ( $\lambda = 1,06 \mu\text{m}$ ) or diode lasers ( $\lambda = 800 - 1000 \text{ nm}$ ), where normally lower reflectivity can be found, which makes those lasers more efficient related to the process. The part of the light, which is not reflected enters the material. In metals this non-reflected light is absorbed within a length of less than a micron and transferred into heat. This finally may lead to heating, melting, vaporizing or even ionization, which is used for heat treatment, welding or cutting with laser. In polymers, especially in their natural state, at the wavelength of diode lasers no such strong absorption can be found. As light passes through the medium, it will be absorbed (A) according to Lambert-Beer's law,  $I(x) = I_0 e^{-\alpha x}$ , where I

denotes the intensity of the light and  $\alpha$  represents the absorption coefficient, which can also depend on the material, on the wavelength, on temperature and other parameters. The light, which is absorbed by the material is transferred to heat and thus, leading to a temperature increase, which may cause melting or thermal destruction. In fact, the absorption coefficient  $\alpha$  can cover values from zero (fully transparent) over a medium range (volume absorber) up to as high numbers as  $10000 \text{ cm}^{-1}$  (surface absorber). This behavior is schematically shown in the insert in Fig. 10. Scattering (R') is of course only found in volume absorbers and only under certain conditions (see sect.4.2). In this process the light is deflected from its way by the surface of e.g. particles, crystals or grain boundaries, but the energy of the light is not transferred to the material and thus, does not affect the state of the matter. The light, which finally goes straight through the material without being affected and escapes from the material is the transmitted light (T).

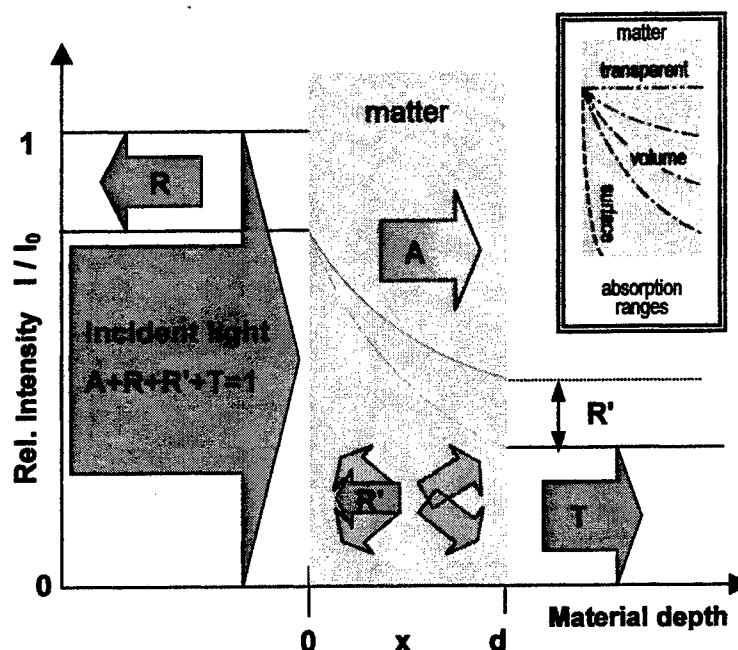


Fig. 10: Light matter interaction (after [1]); insert: intensity curve for transparent (---), volume absorbing (----) and surface absorbing material (—)

#### 3.2 The basic polymer laser welding process

A very prominent geometry for metal welding is butt welding; however, this configuration is difficult to control for polymer welding, as a consequence of the special properties of the polymer material. Contrary to metals, heat conductivity is very small for polymers (see sect. 4.1). This means the heat is preferably generated, where the laser radiation is absorbed in the material. In a rough approximation on a short time-scale the temperature profile follows the absorption profile of the laser radiation, i.e. the polymer can only be melted over its entire depth, if almost uniform absorption is realized over the thickness of the material. This is, however, in conflict with Lambert-Beer's law, or rather requires a low absorption coefficient, as is schematically represented in Fig. 11. As can be easily recognized, a strong absorption, as in case c) generates a high temperature at the surface, but not throughout the entire material, and thus, no strong weld

can be obtained. The weak absorption, as in case a) is definitely advantageous as far as the temperature profile is concerned, but the price for this is, that a large amount of the laser power is transmitted through the material and, thus, not used for the process. Problems also arise from the high viscosity of the molten polymer (see sect. 4.1); i.e. even if the material has been softened it does not necessarily flow together deliberately, i.e. normally pressure has to be applied to mix the molten partners together. Thus, even if demonstrated in some experiments at special material configurations and with a selected laser wavelength [8], butt welding is not an optimal configuration for laser welding of polymers.

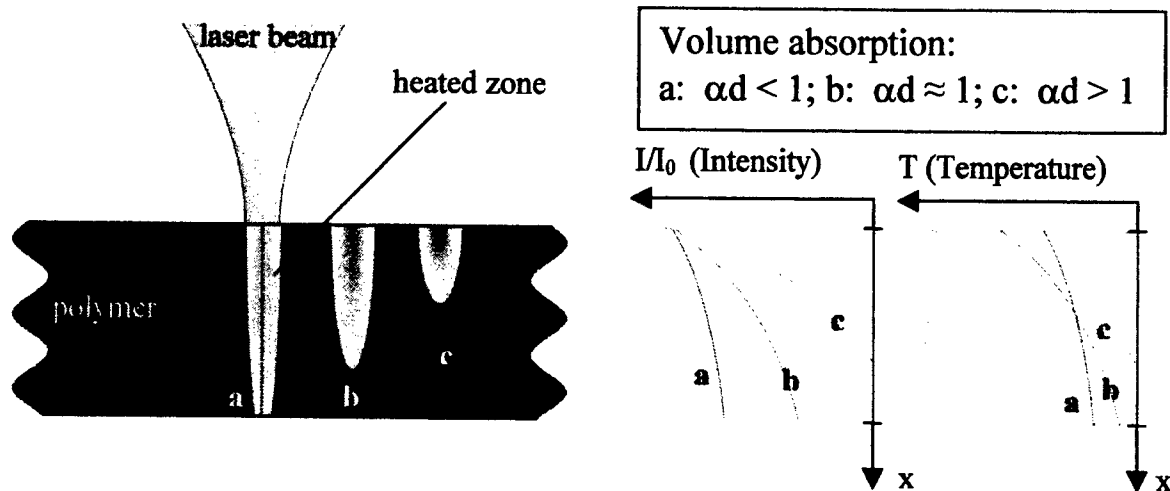


Fig. 11: Schematic representation of a butt welding configuration; intensity and temperature profile

As proven in a wide variety and from several groups working in laser polymer welding, overlap weld is the preferred geometry. Overlap welding is much easier to handle and to control and has a much wider area of application, than the butt weld. However, also here a special configuration is necessary. The top layer (i.e. the first layer, which is penetrated by the laser radiation) must be transparent for the laser radiation, whereas the bottom layer must be sufficiently absorbing, as explained by the sketch in Fig. 12. In this case, the absorbed light generates heating and melting of the bottom layer first. Heat is then transferred via thermal conduction between the joining partners to the non-absorbing part, which

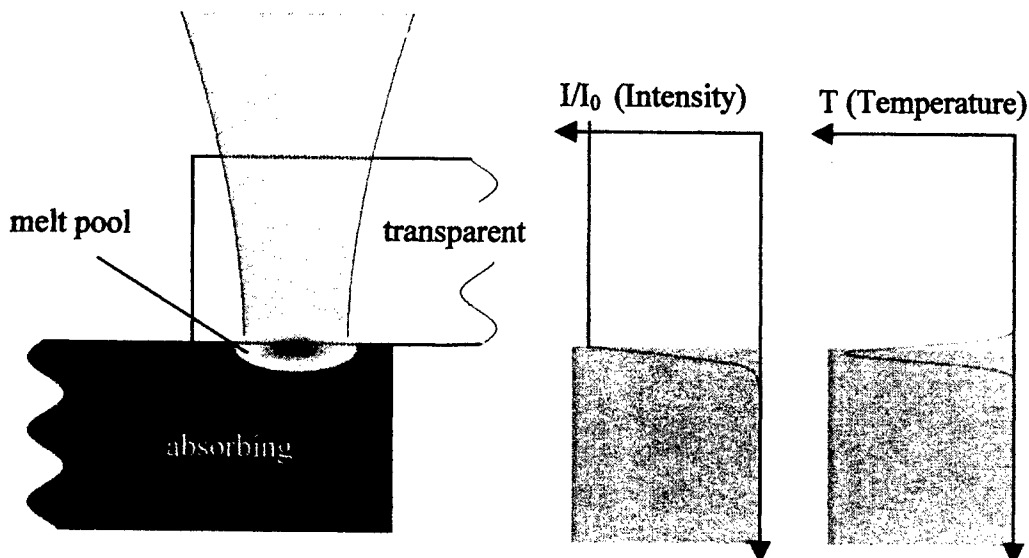


Fig. 12: Schematic representation of overlap configuration; intensity and temperature profile

also starts melting at the interface under certain conditions. By intermixing or diffusion the polymer chains may combine. After cooling and re-solidification a firm connection is formed at the seam. The method is called "laser transmission welding". If properly performed and if the materials resp. material combination is suited for laser welding (see sect. 4.1), laser transmission welding generates a strong and cosmetically perfect, almost invisible, seam with little thermal load to the product. Furthermore, laser welding of polymers is flexible, gentle and environmentally friendly.

#### 4. THE INFLUENCE OF THERMAL, MECHANICAL AND OPTICAL PARAMETERS

In comparison with metals, polymers show a totally different mechanical, thermal and optical behavior. These parameters, however are essential for the success and the understanding of the laser welding process.

##### 4.1 Thermal behavior of polymers

As any material, polymers undergo phase transitions if they are heated up. This is schematically presented in Fig.13 ([1],[9]), where the mechanical strength is shown vs. the temperature. This behavior is clearly different from (pure) metals, where defined phase transition occur. In polymers, the status changes not at a well defined temperature but over a temperature range, which can be explained by the fact that chain length is statistically distributed over a certain range, by different chain structures, side chain effects, molecular and crystallite size and molecular forces. Furthermore, different classes or polymers show totally different characteristics. For realization of a welding process, of course the material must be sufficiently soft or liquid, so the molten phases can flow together; thus, from Fig. 13 we may easily recognize, that thermosets cannot be welded at all and that there are certain limitations for elastomers. Thermoplastic materials are suited for welding from the thermo-mechanical point of view. The viscosity of molten polymers (without filler materials) may go down to a value in the range from  $10^7$  to  $10^9$  cP; however, these values are much higher than those of liquids or molten metals<sup>2</sup> and thus, molten polymer material normally does not flow without an external force, i.e. pressure.

As temperature increases materials normally expand. This is also the case for polymers, as can be easily seen in Fig. 14. In fact, the thermal expansion coefficient of polymers is considerably higher than for metals. Furthermore, the effect is much stronger for the (partially) crystalline materials, than it is for the amorphous. The strong heat expansion coefficient may not only cause pressure at the seam, but also cause mechanical stress after the seam cooled down. This might especially be true if different materials are welded. This stress may cause a separation of the weld even hours after the weld was performed. Tempering might be necessary to avoid this effect.

The heat conductivity of polymers is typically in the range of about 0.1 to 1 W/(m\*K), which is 3 to 4 orders of magnitude less than the heat conductivity of metals (e.g. Cu:  $\lambda \approx 10^3$  W/(m\*K)). This fact together with the large

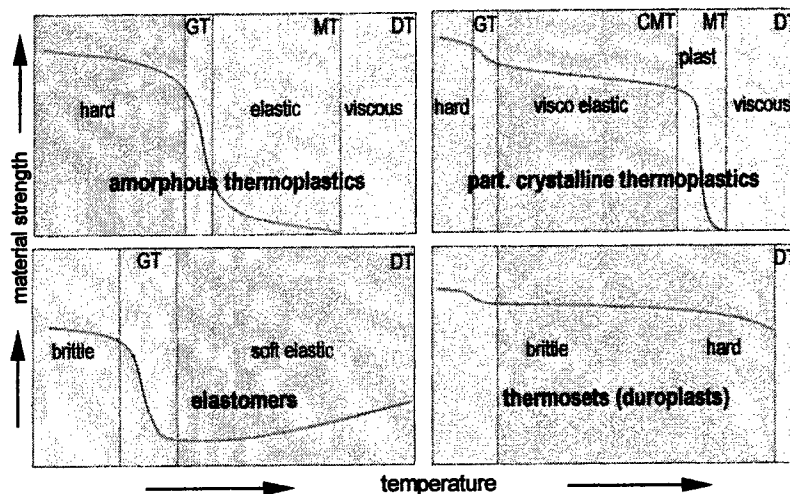


Fig. 13: Mechanical strength as a function of temperature (qualitatively) for different polymer classes (GT=Glass Temperature; MT=Melt Temperature; CMT=Crystal Melt Temperature; DT=Decomposition Temperature. □=applications range [after [1],[9]])

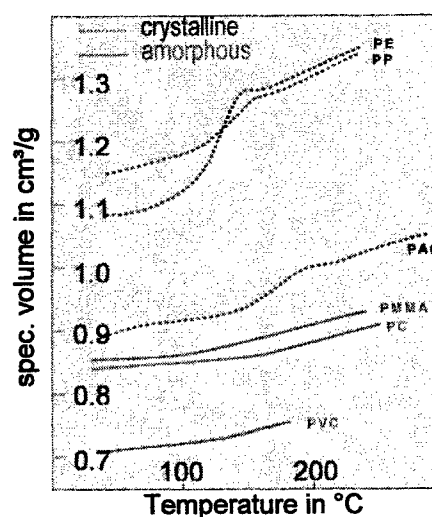


Fig. 14: expansion of polymers during heating (after [9])

<sup>2</sup> as an example: Fe with 2,5%C at 1400 °C:  $\eta=2,2\text{cP}$ ; Na at 100 °C:  $\eta=7 \times 10^{-3}$  cP; water at 20 °C:  $\eta=1\text{cP}$

difference of the viscosity of these materials is one of the key reasons, why polymer welding is so different from metal welding. It also explains, why the absorption must be carefully matched, if butt welding is performed (see §3.2.)

Tab. 1 gives an overview about melt and decomposition temperature ranges for different materials, taken from textbooks or brochures. Of course the temperature during the weld must be kept below the decomposition temperature, but well above the melt temperature, if a joint shall be formed. Thus, the acceptable temperature range for a reliable process sometimes covers only a few ten degrees! Therefore, the use of feedback loops for temperature control as described in sect. 2.5, are mandatory in some cases. The data in table 1 also indicate, even for "identical" materials, the data may differ, depending from the manufacturing process (which influences e.g. chain length or may use certain additives). Welding of different polymer materials is possible under certain circumstances. Nevertheless, the melting range of both materials must be overlapping, since otherwise one partner may decompose, whereas the other one may not be molten at all.

Polymer	Glas- $T_g$ [°C]	flow- $T_f$ [°C]	cryst. melt $T_m$ [°C]	decomp. $T_d$ [°C]	temperature [°C]					
					100	150	200	250	300	350
ABS										
PA6	40		220	~ 327						
PA66										
PC	145	240		325						
HD-PE	- 85		130 - 146	360 - 390						
PEEK	120		340							
PMMA	104	180		226 - 256						
POM										
PP	- 18		160 - 208	336 - 366						
PS	97	180		318 - 348						
PTFE	- 20		327	424 - 513						
PVC	80	175		~250						
SAN										

Table 1: Characteristic temperatures for polymers:  
 melting range  decomposition

#### 4.2 Optical properties of polymers

The optical properties of the material influence the laser welding process considerably. The top layer has to be transparent, as indicated in sect. 3. Reflection and absorption properties of the bottom layer are important parameters for the welding, since these parameters control the incoupling of the radiation to the bulk material, i.e. the initial step for the laser welding. As indicated in Fig. 15, which shows a typical absorption spectrum for a polymer (Poly-Carbonate), most polymers are almost not absorbing for the diode laser radiation in their natural state and thus, fulfil the first requirement. The indicated loss of about 10% may be related to reflection at the surface or some scattering effects. Unfortunately, low absorption does not necessarily mean high transmission. This holds only for amorphous materials. If material is crystalline, the incoming radiation can be easily deflected by scattering effects in the bulk material, as described in fig. 16. Because of the distribution of the laser power due to scattering an increase of the laser spot diameter at the joining interface may occur. As a consequence of this the power density is further reduced and the seam width might be increased. Scattering effects can also be caused by filler material, e.g. glass fibers. The strength of the effect depends very strongly from the grain or particle size. An expansion of the laser beam diameter by a factor of 3 has been observed on a 2 mm thick PBT (Poly-Butylene-Terephthalat) sample [10].

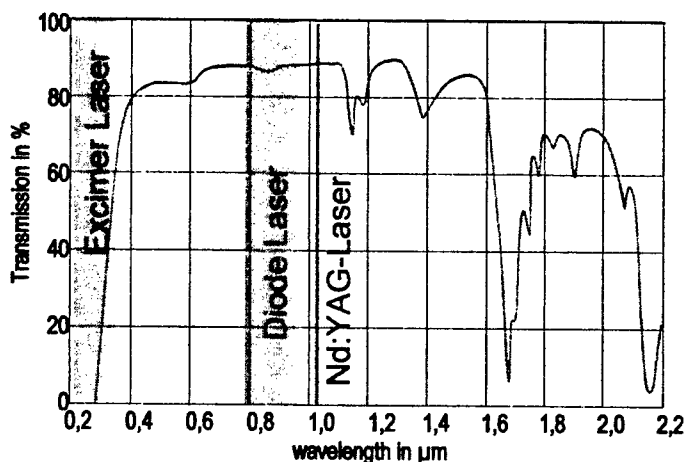


Fig. 15: Characteristic absorption spectrum of polymers: poly-carbonate, thickness is 3.2 mm [11]

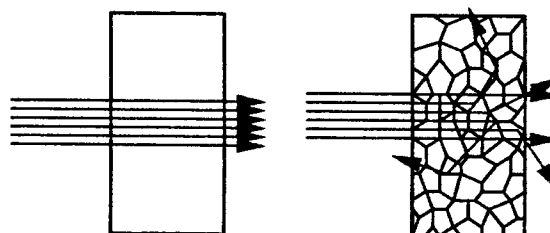


Fig. 16: Effect of light scattering by crystals  
 Left: amorphous, right: crystalline

A prominent feature of polymer parts today is the fact, that there is almost no limitation in the color design. Therefore, influence of colors on the welding process must be analyzed. Colors are generated by special color agents, which influence the optical properties in the visible spectral region. Unfortunately, as indicated in Fig. 17, not only the visible region is influenced, but also the near infrared, where the emission of the diode lasers take place. The spectra of polyamide PA6 in its natural form as well as with pigments for different colors [11] clearly indicate a change in the color, which affects heavily absorption, reflection and transmission in the diode lasers wavelength range! Change of the color means changes in the process parameters! Development of special pigments, which consider the properties in the near infrared spectral range is most probably unavoidable to face up to this challenge. Of course, influence of the color agent on the optical properties depends on its concentration. Black color is commonly realized by "carbon black", i.e. soot. this is the strongest absorber material for diode (and other) laser radiation, but of course only acceptable, if black parts (as absorbing partner) are suitable. At the moment different R&D projects focus on these topics, while promising results are expected already.

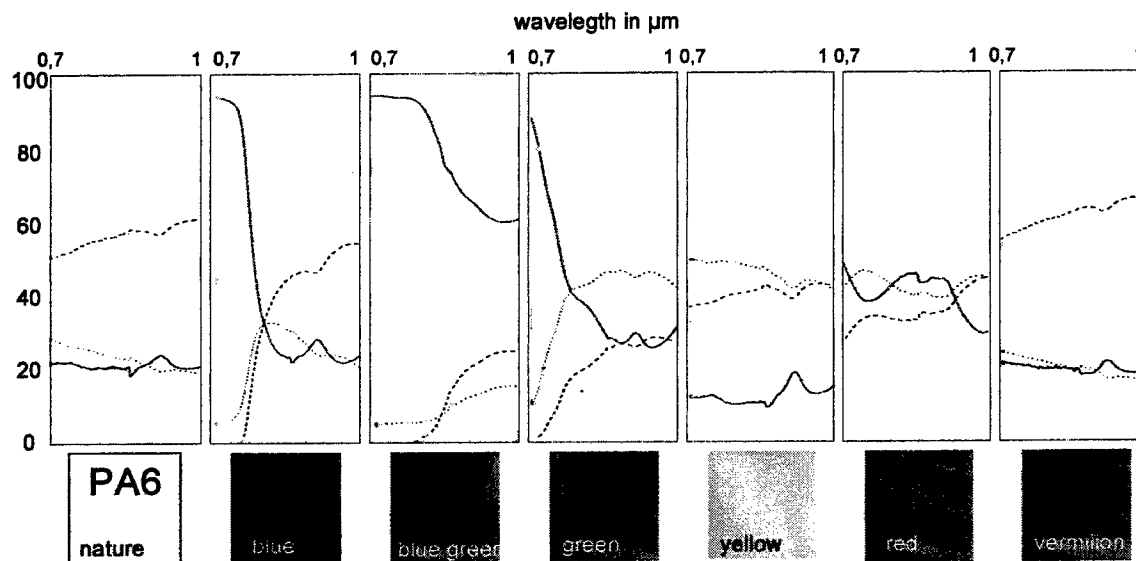


Fig. 17: dependence of transmission (-----), reflection (.....) and absorption (——) from the colour [7]

#### 4.3 Mechanical preconditions for laser polymer welding

If the parts to be welded are put together, a gap may be present between the parts. This is especially true, if large parts and three dimensional seam geometries are considered. On the other hand, referring to sect. 3.2, the heat, which is generated in the absorbing partner must be transferred to the non-absorbing part by heat conduction. Thus no gaps is advantageous for the functionality of the process. If the gap is too large, no heat transfer will take place. This should be considered as early as the parts are designed. A clever designed clamping tool to press the parts together is of course also very helpful. The rather large volume expansion, if the material is melted (see sect. 4.1) is a considerable advantage in this case, since it helps to bridge the gap over a certain range. It is rather hard to give a clear number for an acceptable gap. This depends very much from the materials properties (see Fig. 14), from the weld geometry and from the absorption properties. It must be taken into account the volume expansion is the more efficient the larger the volume of the melt actually is. Therefore, controlling the melt volume by seam width and by absorption length, i.e. pigment or absorber concentration, provides also an opportunity to optimize the gap bridging and improve the welding [10, 12].

### 5. CONFIGURATIONS OF LASER POLYMER WELDING

Contrary to the well established metal welding technology, where a standard set-up is employed for almost all laser welding applications, different approaches are found for the polymer laser weld technology [13, 14]. This is caused by the special properties of the polymers on the one hand, but especially by the special properties and chances of the diode laser technology on the other hand.

### 5.1 "Vector" or "contour" weld

The standard welding set-up, as very well known from metal weld, is the so called "vector weld" or "contour weld". In this case, the focussed laser beam is moved over the materials surface, following the weld seam geometry (see Fig. 18). The laser source might be a diode laser, either with or without fiber coupling or also NdYAG laser, with or without fiber, dependent on the application. Typically, the laser power is in the range of 10 to 100 W and an xy-handling system or a robot is used for moving the part. Welding speeds typically range from 2 to 5 m/min, in some cases up to 20 m/min. This method provides a simple, very flexible, easy controllable and cost efficient method for laser polymer welding. Most examples for polymer welding, which are known so far, have been performed according to this method. Of course optimal weld strength depends from the welding parameters as can be easily understood. If at a constant power the velocity is too low, overheating resp. burning and decomposition of the material may occur. Increasing speed improves the process to an optimum but leads to insufficient melting, if speed is too high. The opposite is the case, if velocity is kept constant whereas power is changed. insufficient melting occurs if power is too low, whereas, after an optimum, burning and decomposition take place, if power is increase to too high values. It should be noted there is no movement of the parts against each other during the weld process, since the material is hard, except at the place, where the laser beam is melting the material. For process reliability the online temperature measurement and power control feedback as described in sect. 2.5 can be very well applied in this configuration.

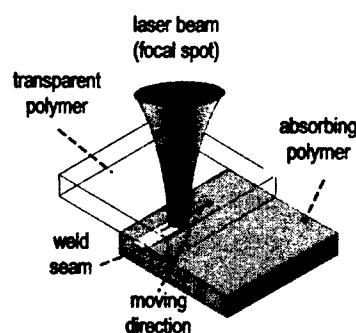


Fig. 18: Sketch of vector weld set-up

### 5.2 Simultaneous weld

The compact and modular set-up of high power diodes lasers offers the possibility realizing a novel method for generating high quality welds, the simultaneous welding process. Several high power diode lasers are arranged in a way that they irradiate as a whole the entire weld seam contour. The joining of the entire contour is obtained with only one single-short-time irradiation. The number of employed diodes depends on the dimension of the work piece resp. the seam, the required power as well as the employed simultaneous welding strategy. The homogeneity of the intensity distribution over the entire weld seam contour has to be guaranteed within a certain frame, otherwise areas of no weld, soft joining, good weld and decomposition alternate. The size of the acceptable frame of deviations within the intensity distribution depends on material properties as well as weld seam geometry and design. Realising the simultaneous process appropriate laser beam guiding as well laser beam forming have to be performed. There lies the challenge in establishing the simultaneous laser process. There are different strategies possible to realise simultaneous welding, such as direct irradiation of the weld seam contour, using classic optical components, employing mask technology (see sect. 5.4) or application of fibre bundles. At the moment, direct irradiation is the most common method, since the handling of sophisticated laser beam guiding and laser beam forming systems is not well matured, so far. Applying direct radiation, the challenge consists in positioning the single high power diode laser modules. Additionally, the untreated intensity distribution of the single diode laser modules has to allow lining up the single intensity distributions, while avoiding inhomogeneities in the intensity distribution. Employing direct radiation offers also the possibility not generating an closed weld seam contour but several single joints at a time (simultaneous tacking), such as for large parts in automobile industry. The advantages of the simultaneous welding process are: (i) very short cycle times compared to contour welding; (ii) no dynamic motion system guiding the laser beam required, (iii) longer interaction times than contour welding possible at still a much higher throughput and (iv) a marked gap bridging capability, since a slight movement of the parts becomes now possible. Of course these advantages have to be paid off by higher total laser power, by less flexibility compared to contour weld and eventually by marked expenditure for special beam shaping components if complex, round shaped parts are considered.

First systematic basic investigations have proven the supposition simultaneous welding offers larger process windows, an increased gap bridging capability as well as slightly higher weld strength than contour welding [12,15].

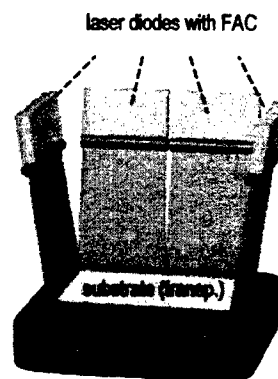


Fig. 19: sketch of simultaneous weld



### 5.3 Quasi-simultaneous weld

The same effect as described in 5.2 can be reached, if a focused laser in conjunction with a fast galvo-scanning mirror system is used (Fig. 20). If the power is sufficiently high and scanning speed is fast enough, in fact so fast that the heat loss is so little, that no re-solidification occurs, the entire seam is softened as well, so that a quasi-simultaneous weld procedure is realized. Compared to the simultaneous weld as described in sect. 5.2, obviously this set-up offers higher flexibility, since arbitrary two-dimensional contours, i.e. curved seams, can be covered. The scanning device, however, limits the area size to about  $200 \times 200 \text{ mm}^2$ . Parts, which are obstructing the beam may also cause a problem.

### 5.4 Mask weld configuration

Another way to circumvent the limitation in simultaneous welding regarding the seam geometry is to put a mask between the laser and the work piece. This mask is conformal with the seam, so those places, which shall not be exposed to the laser radiation are protected. The lasers may be assembled, so all open areas in the mask are filled simultaneously or a line scan can be performed as shown in the sketch in Fig. 21. The process efficiency, however is reduced by the fact, that power is blocked from the mask and thus, not used for the process.

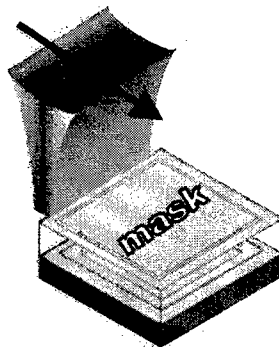


Fig. 21: Mask weld configuration

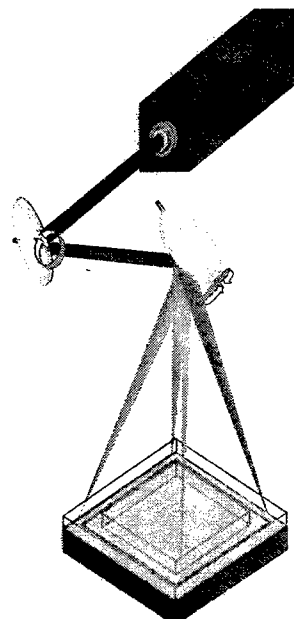


Fig. 20: Sketch of quasi-simultaneous weld set-up

## 6. EXAMPLES FOR LASER POLYMER WELDING

Even laser welding of polymers is still a young joining technology, several application have already found transfer into industrial production. In the following, real, technical components are presented, while proofing the industrial implementation capability as well as the advantages of a novel technology.

### 6.1 Filter housing

Polymeric filter components in automotive industry are sometimes small and contain several mechanical parts. After implementing the parts into a housing, it has to be hermetically sealed, while guaranteeing water tightness as well as no sticking or squeezing of the mechanical parts. In this case, overlap joint geometry is applied for the welding, while the laser penetrates the circulating collar of the transparent joining partner. The joining takes place within an automatic assembly cell consisting mainly of a robot, a high power diode laser system, a clamping device, a process monitoring system as well as a joining parts reservoir. Within the arm of the robot the grabbing device and the laser head are integrated. The laser radiation is coupled into a glass fibre and focused onto the work piece area by means of an optical system. The robot guides the focus spot along the joining contour. Application of pyrometer technology permits process monitoring guaranteeing a reproducible process, while adapting laser power or feed rate to weld seam properties avoiding high temperatures causing decomposition. A pneumatic clamping device is automatically loaded and unloaded by means of the grabbing device. The gentle laser welding process takes about 2 seconds and results in a form fitting as well as high-grade welding quality.

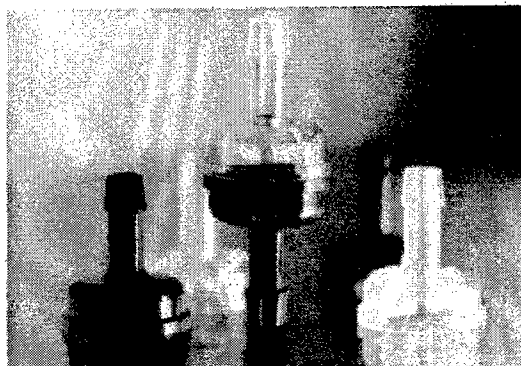
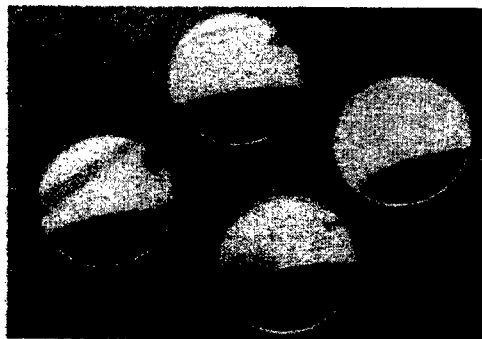


Fig. 22: Filter cases of motor vehicle  
(Material: Polyamide (PA))

## 6.2 Polymeric spectacles

Polymers replace commonly applied materials because of several advantages such as low weight and less costs. For instance, glasses of spectacles which are made of highly transparent polymers, such as PMMA or PC. Joining the polymeric glasses and bridge or ear piece can be realized by laser polymer welding.

**Fig. 23:** Laser welded polymer spectacles  
(Material: Poly-carbonate (PC))



## 6.3 Key-less go-card

Due to the increasing implementation of electronics in automobiles, also electronic locking and security systems have entered automotive industry. For example, the key-less go-card, which is a kind of electronic key in check card format. Within this card sensitive electronic components are implemented. These would be either mechanically or thermally destroyed by employing conventional welding technologies. Therefore, it has been the goal welding the joining partners water tight, while avoiding any damage of the inherent components. The process of overlap laser welding allows a defined local and temporal energy input. It should be mentioned here, both parts are black for the human eye. However, whereas the bottom (absorbing) part is made black conventionally by carbon black, special "black" pigments are used, which are transparent in the spectral range of the diode laser. The laser energy is absorbed within a layer of about 100  $\mu\text{m}$  within the joining area. Both joining partners are placed in their final position before the process starts. They are not influenced by any uncontrolled heat or mechanical vibrations. Additionally, both joining partners appear black to the human eye. However, by using a black but laser transparent pigmentation, the overlap process has been realized. Both halves of the card could be joined absolutely water tight, with no harm to the electronic components, while meeting the mechanical demands [14].

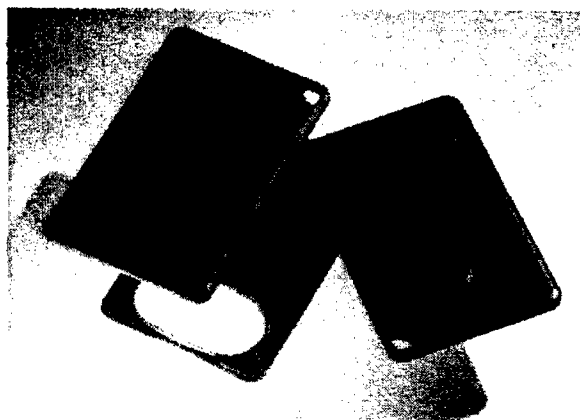


**Fig. 24:** key-less go-card with integrated electronic components  
(Material: Polyamid (PA))

## 6.4 Simultaneously welded test samples

The simultaneous welding process is still in an early stage, but investigated in research projects intensively; among other potential diode laser applications this technology is also part of the work in the German national research project

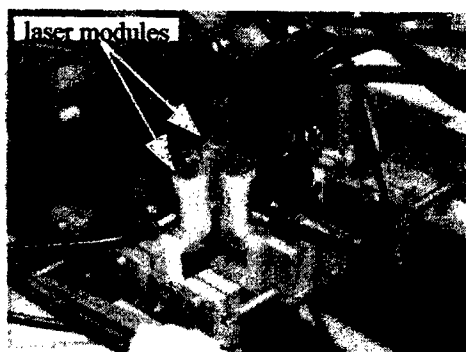


**Fig. 25:** Setup for simultaneous polymer welding of rectangular boxes

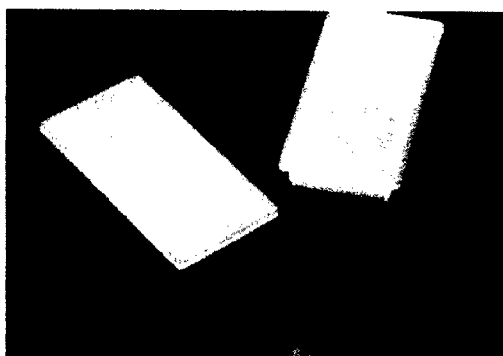


**Fig. 26:** Simultaneously welded water tight boxes  
(Material: poly-propylene (PP))

MDS<sup>3</sup> (= **M**odulare **D**iodenlaser **S**trahlwerkzeuge). Employing direct irradiation using six individually controllable high power diode laser modules, as shown in Fig. 25 the depicted test sample could be hermetically welded. The weld seam length is about 120 mm in total, while the welding takes place within 0,5 seconds. The weld has been water tight and withstands a burst pressure of 8 bars [15]. The test sample is just a dummy for initial investigation, while obtaining first systematic results of the simultaneous process. However, the test sample is acting as a representative for similar applications in electronics, automotive, communication technologies.

#### 6.5 Welding of large parts: Polymeric pump housing, polymeric windows

Besides small parts also middle size as well as large parts can be welded. Fig. 26 shows a polymeric pump or turbine housing of POM (Poly-oxymethylene) joined by contour welding. A larger product is represented by a laser welded polymer window (Fig. 27). The entire weld seam length is about 180 cm. Within the frame two transparent window screens are welded by laser radiation. Employing a 100 W line-shaped laser spot feed rates up to 20 m/min were realized. Former, the joint has been realized by gluing, which has had several disadvantages such as, higher number of manufacturing processes, contamination of the work place, cleaning of polluted air, costs. Furthermore, the welded windows can be directly shipped to the customer after joining, while glued windows needs several hours of setting time, which corresponds to additional store room [12].

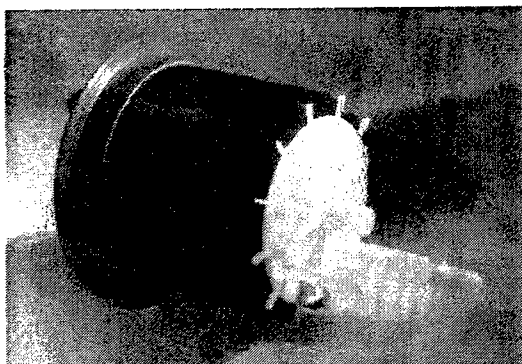


Fig. 27: Polymeric pump or turbine housing  
(Material: Poly-Oxy-Methylene (POM))

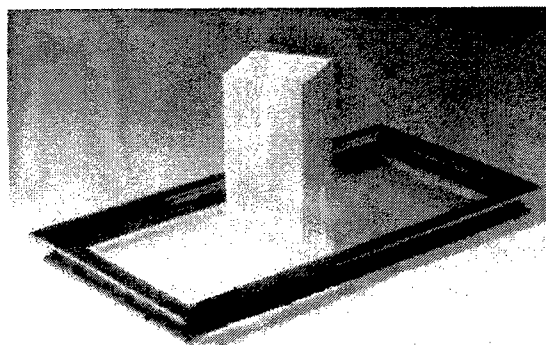


Fig. 28: Diode laser welded plastic window  
(Material: Acryl-Butyl-Styrol (ABS) /  
Poly-Methyl-Methacrylat (PMMA))

## 7. CONCLUSION

Polymer welding with diode lasers is an emerging technology, which offers several advantages over existing technologies and which has a high potential as a supplemental method, especially in those cases, where sensitive electronic parts, fine structures or the necessity of absolute cleanliness prohibits conventional ultrasonic or vibration methods. However, considerable work has still to be done, especially in polymer and pigment technology to develop materials, which are optimized for the laser welding process.

## ACKNOWLEDGEMENT

Part of this work was performed in frame of International European and National German Research and Development projects:

The "MDS" Project<sup>3</sup> "Modulare Diodenlaser- Strahlwerkzeuge – optische Schweißzange - optische Schere" [16] is a project founded by the BMBF (German Ministry for Education and Research), while focusing on novel high power diode laser devices as well as their application within the German industry. The BMBF is gratefully acknowledged for financial support under the BMBF number 13N7367 and 13N7377/2. The project has been started in 1998 and ends in 2003.

<sup>3</sup> Modular Diode Laser Beam Tools [16]

The EC-project "POLYWELD" is a BRITE EURAM project aiming at the development of laser welding as a new joining technique for polymer materials. The European Commission is acknowledged for financial support under "IMT/SMT" programs (1994-1998). The POLYWELD Project started in 1998 as BRITE EURAM project BE 97-4625, contract number: BRPR-CT-0634. It has been finished in 2001.

The funding of these institutions is gratefully acknowledged.

## REFERENCES

- [1] R.Klein, Thesis RWTH Aachen, Germany, (1990)
- [2] W.W.Duley, Polym. Eng.. Sci. 32 (9) 582, (1992)
- [3] F.Bachmann, "Advanced Laser Technologies Conference 2001", Constanta,, Romania, Sep. 11-14, 2001; To be published in Proc. SPIE (2001)
- [4] B.R.Marx; *Laser Focus World*, Sept. 1998, p. 104
- [5] B.D.Tuckerman, Thesis, Stanford University (1984)
- [6] Patent No. DE 195 00 513 C1; Dilas Diodenlaser GmbH, Mainz, Germany (1996)
- [7] H.Pütz U.-A.Russek, A.Gillner; Fachkatalog "Kunststoffverarbeitung in Deutschland", Sept. 2000, p.21 (2000)
- [8] M.May, *Laser-Praxis*, April 2001, pp 19-24 (2001)
- [9] G.Menges, *Werkstoffkunde Kunststoffe*, Hanser Verlag (1999)
- [10] U.-A.Russek; Proceedings ICALEO 2001, Oct 2001. Jacksonville FL, USA (2001)
- [11] Spectra were taken by Fraunhofer-Institute for Laser Technology, Aachen, Germany
- [12] U.-A.Russek; F.Lupp, B.Palfelt; results gained in frame of EC-funded R&D-project "POLYWELD"
- [13] F.Bachmann, 3<sup>rd</sup> EUROFORUM Conference "Polymers in Automotive Industry", Freising, Germany, Oct 2000
- [14] U.-A.Russek, G.Otto, M.Poggel; *Laser-Praxis* April 2001, p.14-16, (2001)
- [15] U.-A.Russek; F.Lupp, B.Friedrich; results gained in frame of nationally-funded R&D-project "MDS"
- [16] F.Bachmann, Proceedings of the 4<sup>th</sup> Symposium on Advanced Photon Processing and Measurement Technologies, Tokyo, Nov 22<sup>nd</sup>, 2000, p.94 (2000)

# **Laser Micro Welding of Electronic Components**

H. K. Tönshoff, K. Körber, C. Kulik, K. Schäfer

Laser Zentrum Hannover e.V.

30419 Hannover, Germany

## **ABSTRACT**

This paper presents results on machine and process development for laser welding of surface mounted devices (SMD) on thermal resistant polymer based molded interconnect devices (MID) with copper layers of 35  $\mu\text{m}$  and 70  $\mu\text{m}$  thickness. Characteristics, advantages and problems of this technology are shown and possibilities to achieve reproducible results are discussed. The investigations are carried out with pulsed Nd:YAG-lasers with a maximum average power of 300 W. Additionally, a process control concept evaluating the reflected process radiation is discussed.

## **1. INTRODUCTION**

In many fields of automotive and measurement technology there is an increasing trend to integrate electronic functions in sensor and actuator systems, which are exposed to environment temperatures of more than 150 °C. This integration generates the need for components which combine complex mechanical functions with electronic ones. Here, the MID technology is a very suitable way to generate such parts (Figure 1). Polyimide with its long term temperature resistance of 270 °C is therefore a suitable substrate material [3]. Moreover, polyimide has a sufficient adhesion for copper. The three-dimensional shape however causes problems using conventional soldering processes.

For all this reasons, selective joining processes like laser welding provides an effective and promising solution [1,2]. Laser welded contacts present high mechanical and thermal strength [4,5]. Moreover, the heat affected zone is minimized and even positions on the MID, that are not accessible with conventional soldering processes can be processed by laser welding. Since the laser welding process requires no solder, there is no need for an additional work cycle and the pollution of the environment is avoided.

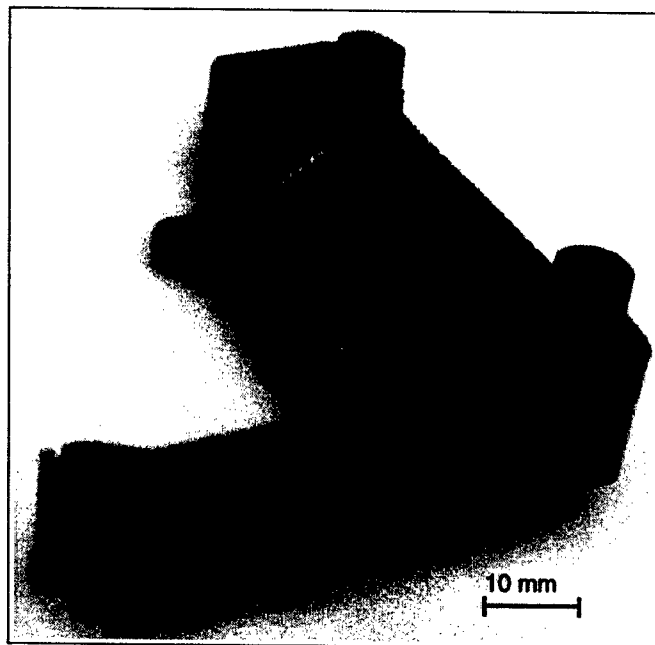


Figure 1: Example of a 3-dimensional molded interconnect device (3-D MID) /10/

## 2. MACHINE DESCRIPTION

To meet the requirements of laser welding processes, a flexible machine set up (Figure 2) was chosen and realized at the Laser Zentrum Hannover e.V. Three infrared lasers with an average power from 10 W up to 300 W were integrated in the system. For the investigations, a fiber coupled, pulsed Nd:YAG laser with a maximum average power of 220 W is used. The optical path consists of two main components: The working head, that includes a precise focussing optic and a coaxial gas supply, enables even micro-welding processes such as laser bonding due to a minimum beam diameter of less than 20  $\mu\text{m}$ . The scanner optic with a 100 mm f-theta focussing lens provides a very fast and flexible machining of devices which do not require a positioning accuracy of less than 10  $\mu\text{m}$ . The changing between working head and scanner and even the selection of the laser source is realized by motor driven flip mirrors.

The workpiece is moved by a high precision x-y-z stage with an accuracy of  $\pm 1 \mu\text{m}$  and an optional rotation stage. The travel of the x-axis allows the machining of workpieces under the scanner as well as under the precision working head in the same fixture.

The monitoring systems are used for positioning and assessment of the workpieces. The scanner system has an off-axis camera for positioning the samples. The working head is equipped with a coaxial monitoring system that provides a high accuracy. Additional to the camera system, a binocular is adapted.

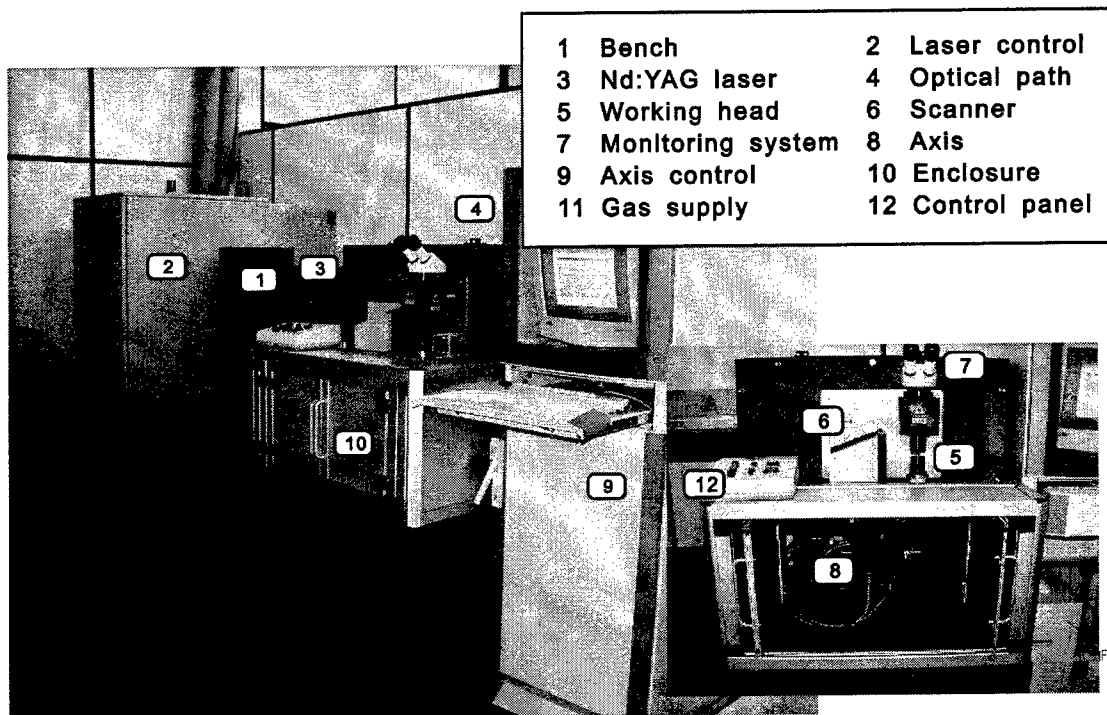


Figure 2: Machine set-up for micro welding

### 3. INVESTIGATIONS

The emphasis of the investigations is laid on laser welding of surface mounted devices on circuit boards. The SMDs consist of a polymer housing and leads of  $\text{CuFe}_2\text{P}$ . Due to the required temperature resistance, polyimide is chosen as substrate material for the circuit boards. The thickness of the copper layers is 35 and 70  $\mu\text{m}$ .

Characteristics and problems of laser welding of electronic components are shown in Figure 3. As mentioned, laser welding is an adequate process due to high mechanical and thermal strength of the joint and low thermal stress on the components because of the local heat supply.

On the other hand, problems using laser welding of SMD are caused by geometrical and material properties. Inaccuracies in SMD fabrication entail gaps and angles between the lead of the SMD and the copper layer. This causes varying thermal conditions in the contact zone during welding. Another point is the high reflection and the variable absorption due to oxidation or surface irregularities.

The high thermal conductivity of the copper layer of only 35  $\mu\text{m}$  thickness and the high melting point of copper of 1083  $^{\circ}\text{C}$  require local process temperatures that are higher than the short term temperature resistance of the polyimide substrate of only 400  $^{\circ}\text{C}$ . For this reasons, the reproducibility of the process is limited to a narrow process window.

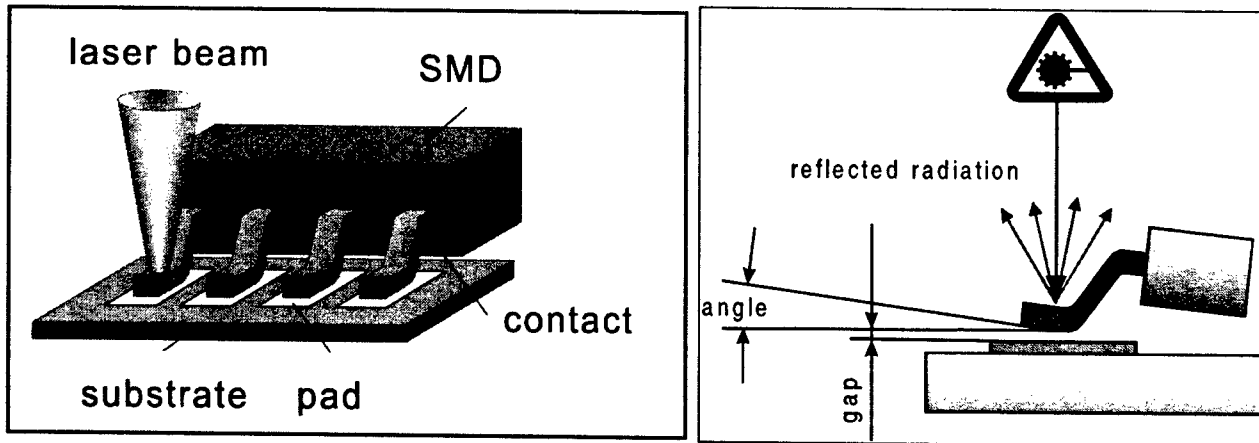


Figure 3: Characteristics and problems of laser welding of electronic components

A successful joining process requires a certain amount of energy to be absorbed by the surface of the lead. The way the energy is brought into the material can be influenced by the laser parameters like pulse duration, pulse shape, number of pulses, pulse repetition rate and focal position.

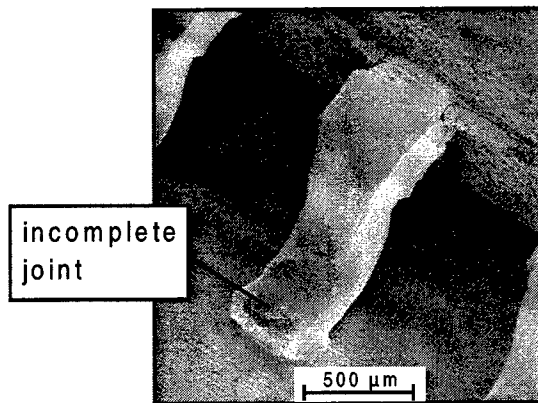
In dependence of the losses due to heat conduction, the welding depth is proportional or slightly degressive with increasing pulse duration at constant laser power. At a short pulse duration of 1 ms, the pulse power has to be increased in order to provide the required energy. This leads to deep welding or drilling. At a pulse duration of 10 ms with the same pulse energy, a proper joint between the lead and the copper layer can be realized, but the polyimide substrate is damaged. The high heat conductivity causes process temperatures, higher than the thermal resistance of the substrate. The optimization of the process results in a pulse duration in the range of 5 ms.

The pulse shape shows minor influence on this process during the investigations. This can be explained by the dominating effects of varying absorption caused by surface irregularities or changing thermal conditions due to gaps. In order to achieve a more constant absorption the number of pulses and the pulse repetition rate were varied. But by this, no improvement could be reached. The high amount of energy that is brought into the material leads to ablations of the copper layer from the polyimide.

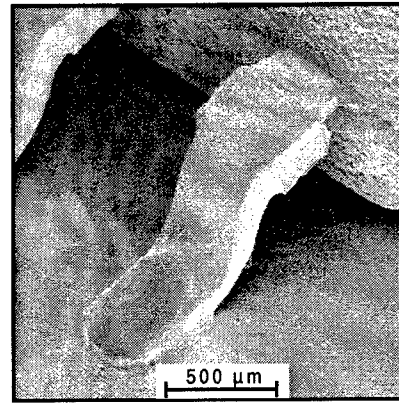
The influence of the pulse energy on the quality of a laser welded contact is shown in Figure 4. Both contacts are single pulse welded. The focal plane is at the surface of the lead. Thus, there results a spot diameter of 200  $\mu\text{m}$ . The left joint shows an incomplete connection due to an insufficient pulse energy. The right lead is very good connected to the copper layer. Peel tests have also shown that the adhesion of the copper layer and the polyimide is still as high as of the basic material.



laser	: Nd:YAG	material	: CuFe <sub>2</sub> P on Cu
beam guidance	: 400 $\mu$ m fibre	thickness	: 35 $\mu$ m Cu
optics	: $f_k = 100$ mm, $f_f = 50$ mm	geometry	: overlap joint
pulse duration	: 5 ms, single pulse	focal pos.	: 0.0 mm
pulse energy	: Q = 3.3 / 4.3 J		



a) Q = 3.3 J



b) Q = 4.3 J

Figure 4: Influence of pulse energy on joint quality of SMD

This undamaged contact zone is shown in the cross section of the laser welded components in Figure 5. The structure of the copper layer shows a good mixture with the components of the lead material.

laser	: Nd:YAG	material	: CuFe <sub>2</sub> P/Cu/PI
beam guidance	: 400 $\mu$ m fibre	thickness	: 35 $\mu$ m Cu
optics	: $f_c = 100$ mm, $f_f = 50$ mm	geometry	: overlap joint
pulse duration	: 5 ms, single pulse	focal pos.	: 0.0 mm
pulse energy	: E = 4.3 J		

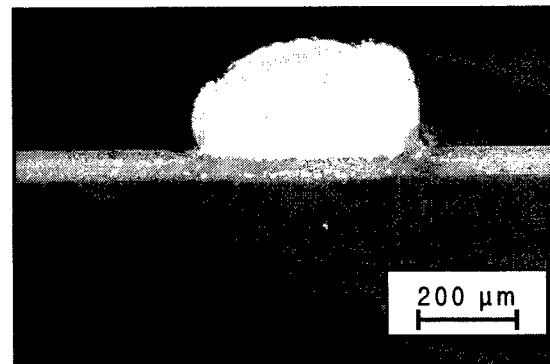
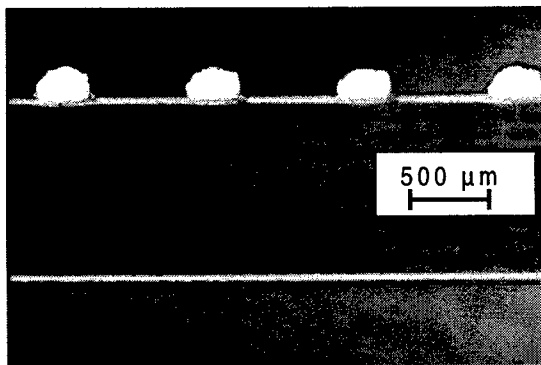


Figure 5: Cross section of laser welded SMD on circuit board

The previous results show, that one of the most essential need is to increase the reproducibility of the welding process. Therefore, a process control system is used. The set up of the system is shown in Figure 6. The process radiation emitted by the welding process, is measured by a photoelectric sensor. Process radiation is emitted in several directions from the welding zone. A part of this radiation is reflected and emitted through the lens system and the optical fiber. A beam splitter reflects a defined part of the radiation onto the optical sensor [8,9].

The measured signal is influenced by several process parameters such as laser power, optical components, focal position, material and gap width. If the welding process is optimized, a reference signal is recorded. Welding defects can be detected by differences between the process signal and the reference signal.

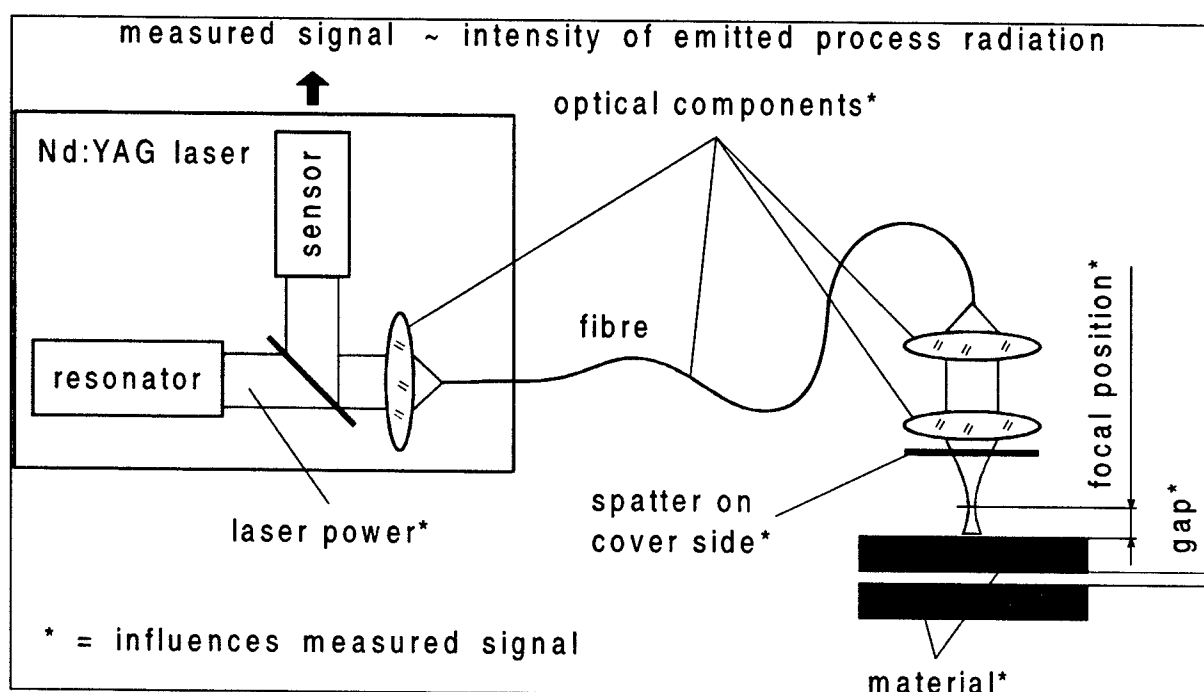


Figure 6: Set up of the process control system ProWatcher Pulse

The process signal during laser welding of a lead on a circuit board is shown in Figure 7. All process parameters that influence the measured signal, like laser power or focal position are constant. Only the gap width between the lead and the copper surface is varied from 0  $\mu\text{m}$  to 100  $\mu\text{m}$  in steps of 20 and 30  $\mu\text{m}$ . The diagram shows a similar characteristic for gap widths of 50  $\mu\text{m}$  and less. With increasing gap width, a significant peak in the process signal is measured for the values of 70  $\mu\text{m}$  and 100  $\mu\text{m}$ .

The sudden increase of signal is caused by the increasing heat radiation of the process. Due to the increasing gap, the thermal conditions have changed and the heat transfer is reduced. This results in higher process temperatures and the destruction of the substrate material.

laser	: Nd:YAG	material	: CuFe <sub>2</sub> P on Cu
beam guidance	: 400 µm fibre	thickness	: 0.07 mm Cu
optics	: f <sub>k</sub> = 100 mm, f <sub>f</sub> = 50 mm	geometry	: overlap joint
pulse duration	: 5 ms	focal pos.	: 0.0 mm
pulse energy	: Q = 4.3 J	sensor	: ProWatcher

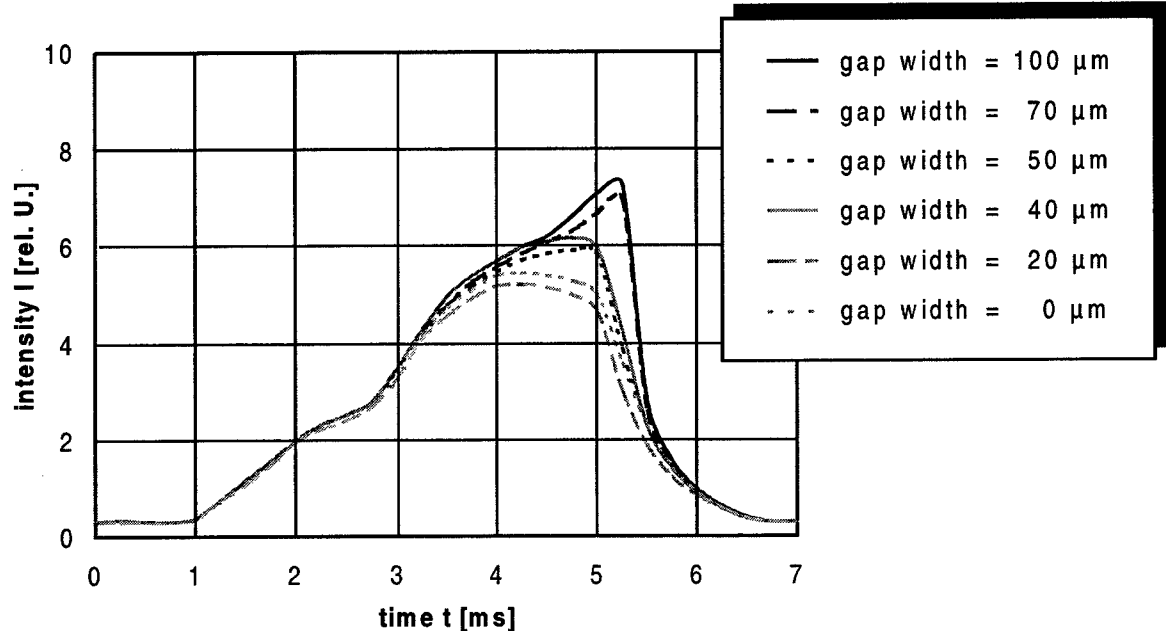


Figure 7: Process radiation signal with respect to gap with

To avoid these gaps between lead and copper layer, an appropriate clamping device has been developed (Figure 8). Furthermore, the geometry is designed to allow a better heat transfer from the lead into the clamp. This leads to a more homogeneous thermal situation and helps avoiding that the thermal resistance of the substrate material is exceeded.

Investigations have shown that contact forces from 8 to 10 N are necessary with this set up to optimize clamping conditions. Before clamping, all leads were pre-bended to an angle of 3 to 5 degrees in order to achieve regular results. Due to the reduction of gaps it will now be possible to focus on the of influence of absorption on the laser welding process. In further investigations this influence has to be determined and measured by process control in order to improve the process reliability.

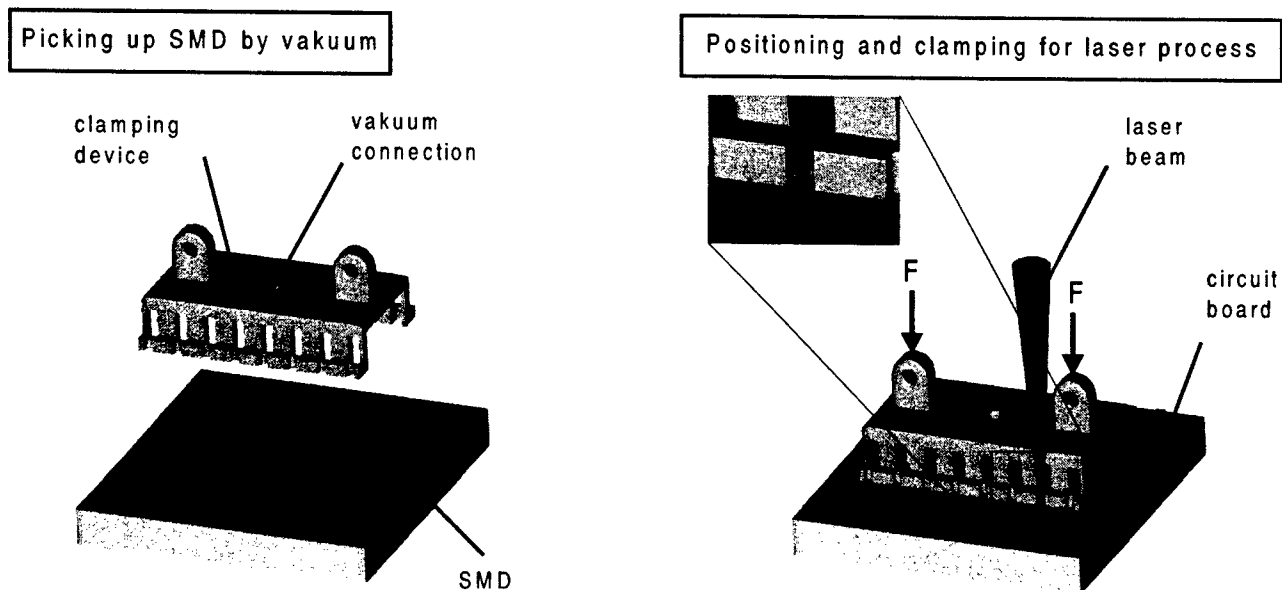


Figure 8: Clamping device for laser welding of SMD

#### 4. CONCLUSIONS

Laser welding is a suitable technique for joining electronic components. Temperature resistant contacts with high mechanical strength can be realized. Even positions on MIDs, that are not accessible with conventional soldering processes can be processed. Since the laser welding process requires no solder, there is no need for an additional work cycle and pollution of environment is avoided.

Problems of laser welding of SMD are caused by geometrical and material properties. Gaps between the leads of the SMD and the copper layer as well as the high reflection and the variable absorption due to oxidation or surface irregularities result in a non-stable process.

The detection of welding defects with a process control system that measures the emitted radiation has shown promising results. Nevertheless, reproducibility has to be increased and guaranteed by improved closed-loop process control systems.

#### 5. ACKNOWLEDGEMENT

The authors would like to thank the AIF (Proj. No. 12784 / N 2) for financial support.

## 6. REFERENCES

- 1 A. Gillner; L. Bosse; T. Kramer; et al.: Laser Micro Joining of Advanced Micro Systems, Proceedings of ICALEO'01, October 2-5, 2000, Dearborn (MI) USA
- 2 Tönshoff, H. K.; Ostendorf, A.; Schäfer, K.: Fiber Laser – Compact Source for Micro Welding, Proceedings of ICALEO'98, November 16-19, 1998, Orlando (FL) USA
- 3 Krauthaim, T.; Pöhlau, F.; Lorenz, W.; Forschungsvereinigung 3-D MID e. V.: Herstellungsverfahren, Gebrauchsanforderungen und Materialkennwerte räumlicher elektronischer Baugruppen, 11/99 - Handbuch
- 4 Schneider, R.: Untersuchung der Einflussgrößen beim Schweißen von Kupferwerkstoffen mit dem Nd:YAG-Laser, Dissertation, April 1994, Technische Universität Braunschweig
- 5 M. Geiger, M. Schmidt, Temperature-resistant contacts, Laser Praxis, October 1998, Carl Hanser Verlag, München, pp. 27 – 30
- 6 F. von Alvensleben, M. Stürmer, K. Kreutzburg, Joining of Materials of poor weldability with Nd:YAG Laser Radiation, BMFT 13 N 6048, December 1995
- 7 M. Glasmacher, H.-J. Pucher, J. Hutfless, Schweißen statt Löten, Laser 6-1994, pp. 24–26, AT-Fachverlag, Stuttgart
- 8 Tönshoff, H. K.; Ostendorf, A.; Güttler, R.; Specker, W.: Online monitoring and closed loop control of laser welding processes, Proceedings of ICALEO'00
- 9 Kawahito, Y; Okada, T.: In-Process Monitoring in Laser Micro Welding and Laser Micro Drilling, Proceedings of ICALEO'00
- 10 Krauthaim, T., Pöhlau, F., Lorenz, W., et al.: Herstellungsverfahren, Gebrauchsanforderungen und Materialkennwerte Räumlicher Elektronischer Baugruppen, Forschungsvereinigung Räumliche Elektronische Baugruppen 3-D MID e.V., November 1999, Erlangen

# Laser welding of plastics transparent to near-infrared radiation

Kimitoshi Sato<sup>\*a</sup>, Yasuo Kurosaki<sup>\*a</sup>, Takushi Saito<sup>\*\*b</sup> and Isao Satoh<sup>\*\*b</sup>

<sup>a</sup>University of Electro-Communications; <sup>b</sup>Tokyo Institute of Technology

## ABSTRACT

This paper deals with a development of laser welding of colored plastics. Welding of thermoplastics using near-infrared lasers has been seen in wide industrial application. Most of thermoplastics are transparent to near-infrared laser. Particular characteristic of near-infrared laser radiation has the ability to heat the interface between the transparent part and absorbent one colored with pigments. However, it is difficult to weld a pair of transparent materials by a laser beam, since there is no absorption region within them. In this paper, the influence of near-IR-transparent plastics on the yield strength of their weldments has been studied: various colored plastics transparent to diode laser radiation were tested as the welding material. The heat transfer within a welding system was also analyzed and assessed the appropriate absorptivity and transmittance of overlapping colored plastic.

## 1. INTRODUCTION

Laser welding of plastics is now important in many industrial applications [1,2]. Some feasibility studies of welding for plastics have been conducted theoretically and experimentally so far [3-8]. Laser welding of plastics has a few advantages to compare with friction welding with ultrasonic vibration such as a rapid and accurate weld bonding with a well controlled movement of laser beam, a hygienic clean process by non-contact heating and an appropriate process for sensitive electrical devices [6]. The CO<sub>2</sub> laser [output wavelength= 10.6μm], Nd:YAG laser [1.06μm] and diode laser [800~950nm] are mainly used in polymer welding. The prerequisite condition for laser welding is that a thermoplastic workpiece absorbs an irradiated energy, and it generates heat. Most thermoplastics have high absorption bands in far-infrared wavelength region like CO<sub>2</sub> laser beam, but tend to be transparent to near-infrared radiation. Therefore, in order to utilize a diode laser for welding, some dye or pigments absorbing near-infrared radiation are necessary to be added to polymers. These radiation properties of polymer are able to be applied to a remarkable welding for polymers. Two polymer substrates, one of which is transparent to and another of which is opaque to a radiation beam, are overlapped, and the laser beam is radiated from the transparent one. The radiated energy is converted into heat, and welding is achieved. Further, most plastic have a characteristic of high transparency for near-infrared radiation, but not always transmit visible ray. Therefore, a use of a colored plastic that is opaque to visible-ray for the transparent part of near-infrared laser welding is realized. In this paper, by using the pigments those are transparent to the near infrared radiation, the characteristics of overlapping welding of thermoplastics of various colors and the influence of the transmittance of colored and clear plastics on the yield strength of their weldments have been studied experimentally. Moreover, the influence of not only the transmittance but also absorptance of overlapping colored plastics was discussed by numerical calculated temperature distributions within the weldments; the degree of possible allowing absorption of transparent plastics was confirmed.

## NOMENCLATURE

- $c$  : specific heat [J/kgK]
- $d$  : laser beam diameter [mm]
- $F$  : yield strength of weldment [MPa]
- $H$  : thickness [mm]

$I$  : irradiation intensity [ $\text{W}/\text{mm}^2$ ]  
 $k$  : thermal conductivity [ $\text{W}/\text{mK}$ ]  
 $q_r$  : heat generation due to the radiation absorption [ $\text{W}/\text{m}^2$ ]  
 $T$  : temperature [ $^{\circ}\text{C}$ ]  
 $U$  : welding speed [ $\text{mm}/\text{s}$ ]  
 $W$  : width [ $\text{mm}$ ]  
 $x,y$  : coordinate [ $\text{mm}$ ]  
 $\beta$  : absorption coefficient [ $\text{m}^{-1}$ ]  
 $\lambda$  : wavelength [ $\text{nm}$ ]  
 $\rho$  : density [ $\text{kg}/\text{m}^3$ ]

#### Subscripts

$0$  : initial  
 $i$  : laminur number of weldment  
 $p$  : weldment  
 $t$  : transparent plate for clamping

## 2. EXPERIMENTAL SETUP AND PROCEDURE

The principles and setups of the welding process employed in this study are illustrated in Fig.1. In the first case, a welding procedure in Fig.(a) belongs to the conventional welding for the combination of "transparent" and "opaque with pigment" substrates (Type-A, the base material of work piece: Polystyrene(PS)). An additive-free transparent plastic plate is placed on the top and three kinds of opaque plastic substrates colored with some pigments (white, gray and black) are placed as the bottom in different three experiments (Table I pigments loading: 1 wt.%). They are set under a constant clamping pressure. The laser beam transmitted through the upper substrates is absorbed within the thin surface layer of the pigmented one.

Second, Fig.1 (b) shows the case of welding of "colored transparent" and "opaque" parts (Type-B, the base materials of workpiece: PS). The upper part is a colored plastic substrate with some pigments those are transparent to a near infrared beam and the second part is an infrared-absorbing black-pigmented plastic one (with carbon-black). The former is nearly visibly opaque but transparent to diode-laser wavelength radiation. Therefore overlap joints can be realized like the Type-A welding. Using above pigments, thermoplastics of various colors were tested.

A diode laser system was used in the polymer welding experiments. It consisted of a 35W diode laser (JOL-S 35, Jenoptik), a beam-condensing unit connected to laser by an optical-fiber cable and a numerically controlled X-Y table as shown in Fig.2. The wavelength of the diode laser used in this study is 808nm.

The sizes and shapes of the welded workpieces are shown in Fig.3. The PS substrate, 10mm in width, 100mm in length and 2mm thickness was used in the Type-A and Type-B welding shown in Fig.3. The optical characteristics of polymer used in the experiment near-infrared wavelength were measured for each specimen.

The welding possibility of each combination was evaluated with the yield strength test. The yield strengths of welded parts were measured using a tensile strength test machine. The shear stress is loaded in the welded part in the strength test as shown in Fig.4. When welding is not completely pursued, separation at the interface of weld part must occur. But when

welding is completely done, the welded part is some times stronger than the base polymer substrates; in this case, the base substrates are broken.

### 3. RESULTS AND DISCUSSION

Figure 5 shows the transmittance of polymeric substrates, 0.2mm in thickness vs. the wavelength used in the Type-A welding. An additive-free transparent PS substrate has high transmittance at near-infrared region. On the other hand, the pigmented (white, gray and black) plastics do not transmit a near-infrared radiation at all. Both black and gray pigments contain fine carbon black particles; therefore the materials colored with them have high absorption for infrared radiation. The white-pigmented plastic sheet almost scatters the near-infrared radiation.

Welding tests were conducted by the workpieces as shown in Fig.3. Welding took place at the interface between welded plastic parts, and no unfavorable phenomena took place at all in the other part of substrate in the case of gray or black absorbing ones. But no welding was carried out in the case using white-pigmented work piece; it was due to absence of the absorbing constituents within white pigment. Figure 6 shows the influence of irradiation intensity on the yield strength of weldments and welding conditions. The result shows that the welded part in the case of gray pigment is somewhat less strength than the one in black one, because the latter includes  $\text{TiO}_2$  that scatters the infrared laser radiation. It is seen from Fig.6 that the yield strength increases in proportional to irradiation intensity. Referring to the case of black pigment, the intensity of the yield strength increases with increasing the radiation intensity until  $I=4.88[\text{W}/\text{mm}^2]$  but decreases over that point. This is considered as degradation of polymer material caused by overheating.

Next, the welding experiments were carried out using not the substrates those are transparent to visible ray but the parts colored with pigments. Since there are many colorants of which the dispersion and deposition are bad for amorphous polymers, it was difficult to color the transparent material like PS using the pigments which show the transparency to the near-infrared radiation. In this paper, with the aim of making laser transmission welding wide and applicable for various resin material, the pigments as the three primary colors (blue: phthalocyanine, red: perylene and yellow: azo) which have the sufficient characteristic of near-infrared transparency were used to overcome such problem. The white pigment ( $\text{TiO}_2$ ) was also used as another colorant. By the mixture of these pigments, the substrates of nine colors were prepared. The transmittance of tested workpieces (2mm thickness) at  $\lambda=808\text{nm}$  are shown at Table 2. The light-colored workpieces showed high transmittance but the dark-colored workpieces showed low transmittance. However, it is possible for the upper transparent workpiece to weld them with the infrared absorbing workpiece if it posses the transmittance of at least 5[%] (See Table 2).

### 4. NUMERICAL SIMULATION

Temperature distribution in a model welding system is numerically estimated. We consider a semi-infinite workpiece subjected to laser irradiation  $I$  of radius  $a$ . The geometry of laser welding system is shown in Fig.8. The weldments: a pair of transparent and absorbing (black colored) PS workpieces are pressed between the transparent PMMA plates. In this simulation, we consider that the laser beam remains stationary while the workpiece travels at a constant velocity  $U$  in the negative  $x$  direction. The origin of the stationary coordinates coincides with the point heat source.

After heat has been emitted for a long time, the heat transfer in welding adopted in our experiment can be considered as a two-dimensional steady conduction problem. Most polymer materials have very low heat diffusivities, and no effect of heat conduction from the welding spot to the other part where laser beam is not radiated is considered.



In this simulation, we adopted two kinds of semitransparent body: one reflects and transmits a radiation beam without any absorption (Type-1:  $T=20.1, 30.1$  and  $45.0$  [%];  $\beta=0$ ); another one reflects, absorbs and transmits it as the upper PS workpiece for welding (Type-2:  $T=20.1, 30.1$  and  $45.0$  [%];  $\beta=800, 600$  and  $400$ , respectively). The influence of absorptivity of the upper workpiece on the heating at the interface between the weldments was examined.

The governing equations can be written as:

Conservation of thermal energy in the top and bottom transparent PMMA plates;

$$\rho_T c_T U \frac{\partial T}{\partial x} = k_T \left( \frac{\partial^2 T}{\partial y^2} + \frac{\partial^2 T}{\partial y^2} \right) \quad (1)$$

Conservation of thermal energy in the welded workpieces;

$$\rho_p c_p U = k_p \left( \frac{\partial^2 T}{\partial x^2} + \frac{\partial^2 T}{\partial y^2} \right) - \frac{\partial q_{rpi}}{\partial y} \quad (2)$$

$$q_{rpi} = I_0 \exp(-\beta_p y) \quad (3)$$

The boundary conditions at the contact interface are as follows:

Inlet of the welding system

$$T = T_0, \text{ at } x=0, -(H_p+H_t) = y = (H_p+H_t)$$

The outer surface of each clamping transparent PMMA plate;

$$k \frac{\partial T}{\partial y} = h(T_w - T_\infty), \text{ at } 0=x=L; y=\pm(H_p+H_t)$$

The boundary between the clamping PMMA plate and the welded PS workpiece;

$$k_T \frac{\partial T}{\partial y} = k_p \frac{\partial T}{\partial y}, \text{ at } 0=x=L; y=\pm H_p$$

The governing equations were solved with a finite-difference method. They were subjected to the influence of material properties (Table 1), the welding condition (Table 3) and the size of control volume (Table 4).

Primarily, the heat transfer in the case of the welding of transparent workpiece without absorbing element and black colored one was simulated. Figure 9 shows the temperature distribution within the welded plastics in the vertical direction at  $x=0$ . The maximum temperature emerges in the black colored a little apart from the interface. In the upper workpiece, the temperature rise was observed only in the vicinity in the interface and was proportional to the transmittance of it.

Secondary, the influence of absorption within the upper workpiece on the temperature rise at the interface was examined.

The temperature distribution within the welded plastics in this case is shown in Fig.10. The maximum temperature emerges in the black colored a little apart from the interface, too; meanwhile, the temperature at around the irradiated surface rose being proportional to the absorption coefficient. In the case of the application of the upper workpiece having too much absorptivity, the temperature rise occurs excessively there then the surface of it melts before welding is performed at the interface. There seems to be the adverse effect for welding, but this result also has the useful aspect. If the upper workpiece has moderate absorptivity to near-infrared radiation not showing melting at the surface, it can be heated at the interface in advance for welding (See Fig.11).

## 5. CONCLUSION

The characteristics of overlapping welding of thermoplastics of various colors and the influence of the transmittance of colored and clear plastics on the yield strength of their weldments have been studied experimentally and numerically. The effect of radiant heating on the temperature profile within the welded plastics was numerically estimated, and it was confirmed that each procedure examined is feasible as laser transmitting welding. The influence of not only the transmittance but also absorptivity of overlapping colored plastics was discussed by numerical calculated temperature distributions within the weldments; the degree of possible allowing absorption of transparent plastics was confirmed.

## ACKNOWLEDGMENTS

This work is supported in part by a grant of Encouragement of Engineering Research from The Foundation of Hattori-Hokokai. The authors thank Sumika Color Corporation for supplying the pigments used in the experimental work.

## REFERENCES

1. H. Puetz, D. Haensch, H.G. Treusch and S. Pflueger, "Laser Welding Offers Array of Assembly Advantages", *Modern Plastics International*, **9**, pp.127-130, 1997.
2. M. Kalpana, "Plastics Welding Technology for Industry", *Assembly Automation*, **17-3**, pp.196-200, 1997.
3. I. A. Jones and N. S. Taylor, "High Speed Welding of Plastics Using Lasers", *ANTEC '94*, pp. 1360-1363, 1994.
4. P. A. Atanasov, "Laser Welding of Plastics: Theory and Experiments", *Optical Engineering*, **34-10**, pp.2976-2980, 1995.
5. H. Potente, J. Korte and F. Becker, "Laser Transmission Welding of Thermoplastics: Analysis of the Heating Phase", *ANTEC '98*, pp.1022-1025, 1998.
6. V. A. Kagan, R. G. Bray and W. P. Kuhn, "Laser Transmission Welding of Semi-Crystalline Thermoplastics – Part1: Optical Characterization of Nylon-Based Plastics", *ANTEC '2000*, pp.1171-1181, 2000.
7. V. A. Kagan and G. P. Pinho, "Laser Transmission Welding of Semi-Crystalline Thermoplastics – Part2: Analysis of Mechanical Performance of Welded Nylon", *ANTEC '2000*, pp. 1183-1190, 2000.
8. I. A. Jones, N.S. Taylor, R. Sallavanti and J. Griffiths, "Use of Infrared Dyes for Transmission Laser Welding of Plastics", *ANTEC '2000*, pp. 1166-1170, 2000.

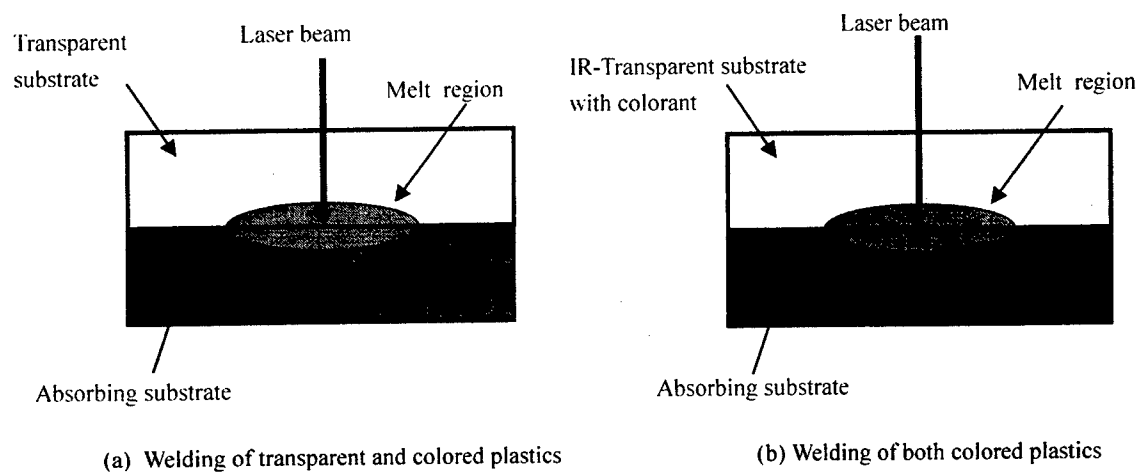


Fig.1 Schematics of laser transmission welding

Table 1 Physical properties of welded plastics

	PS	PMMA
$\rho$ [kg/m <sup>3</sup> ]	1200	1190
$c$ [J/kgK]	1470	1900
$k$ [W/mK]	0.18	0.21

Table 2 Constituent of pigments (Type-A welding)

Color	Constituent
White	TiO <sub>2</sub>
Gray	TiO <sub>2</sub> , C, Fe <sub>2</sub> O <sub>3</sub> , PbCrO <sub>4</sub> -nPbSO <sub>4</sub>
Black	C

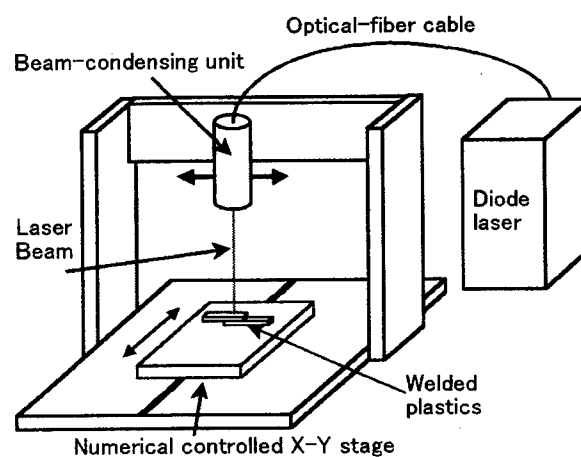


Fig.2 Diode laser welding facility

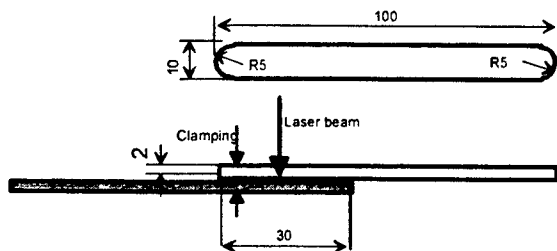


Fig.3 Shape and size of welded workpiece

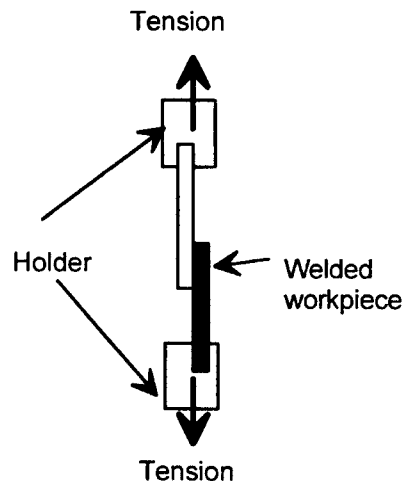


Fig.4 Tensile stress measurement

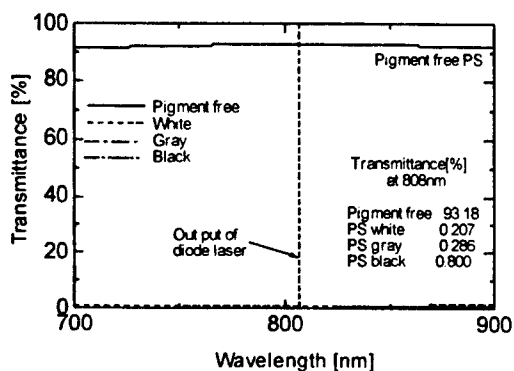


Fig.5 Transmittance of the pigmented PS substrates

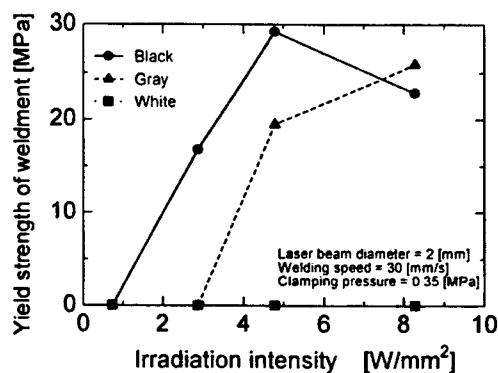


Fig.6 Yield strength of Type-A weldments

Table 2 Transmittance and Welding ability of pigmented workpieces

Color	Transmittance [%]at 808nm	Welding
White	1.7	o
Red	36.9	o
Yellow	90.3	o
Blue	24.3	o
Violet	9.6	o
Green	28.5	o
Brown	17.1	o
Black-1	7.2	o
Black-2	2.4	x

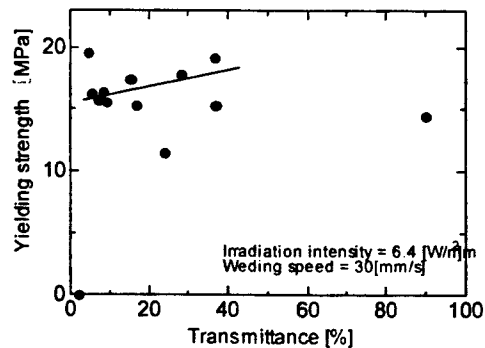


Fig.7 Influence of transmittance of upper workpiece on welding

Table 3 Welding conditions for numerical simulation

Initial temperature [C]	27
Irradiation intensity [W/mm <sup>2</sup> ]	3.2
Laser beam diameter [mm]	2.0
Thickness of plastic substrates [mm]	2
Welding speed [mm/s]	30
Length of weldment [mm]	40
Absorption coefficient of Absorbing workpiece (at 808nm) [m <sup>-1</sup> ]	40000

Table 4 Dimensions of the computational domain and size of control volumes

	x direction	y direction
Top PMMA plate	L=40mm, 200div.	H=7mm, 50div.
Transparent PS workpiece	L=40mm, 200div.	H=2mm, 50div.
Absorbing PS workpiece	L=40mm, 200div.	H=2mm, 50div.
Bottom PMMA plate	L=40mm, 200div.	H=7mm, 50div.

Fig.8 A model of numerical calculation of heat transfer within the welded plastics

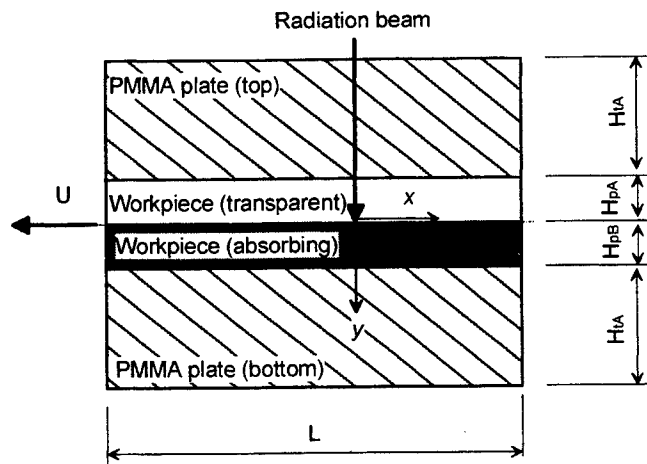
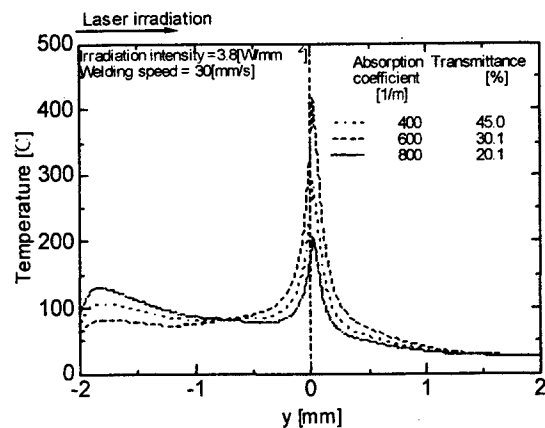


Fig.9 Temperature profile within the welded plastics (Type-1)



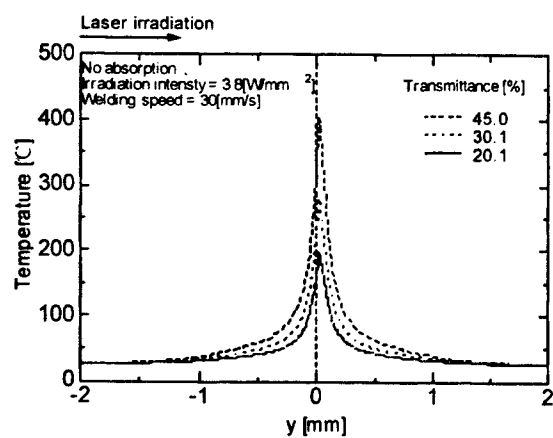


Fig.10 Temperature profile within the welded plastics (Type-2)

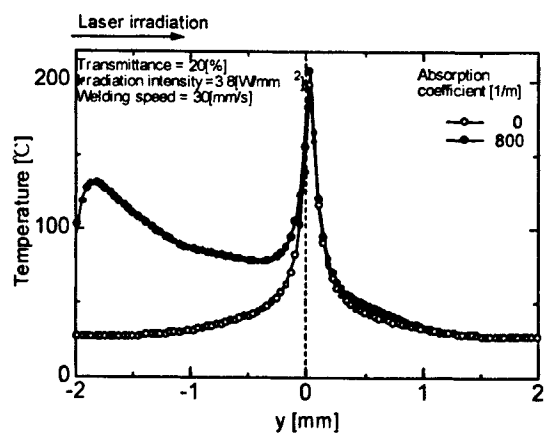


Fig.11 Influence of absorption of upper workpiece on the temperature rise at the interface

# Study and process control in laser conduction welding for millisecond pulse duration range.

Laurent Berthe<sup>a\*</sup>, Delphine Delage<sup>a</sup>, Didier Lepretre<sup>a</sup>, Leonard Bacinello<sup>a</sup>, Wolfgang Knapp<sup>a</sup>, Nicolas Dumont<sup>b</sup>, Friedrich Durand<sup>c</sup>,

<sup>a</sup>Coopération Laser Franco-Allemande/Laboratoire pour l'Application des Laser de Puissance;

<sup>b</sup>Laser Cheval; <sup>c</sup>SMH Automation

## ABSTRACT

A system has been built for the fast control of the laser welding process in conduction regime. Based on a traditional Proportional Integral Derivative (PID) analysis, the system can regulate millisecond laser pulse (its response time is 90 microseconds). Besides, the interaction in this regime has been monitored with different diagnostics. Visible signal above target, IR signal from surface and visualization from CCD camera have been correlated as function of laser power density to distinguish the different phases of interaction (pure conduction, vaporization and/or plasma). With this experimental set up, the detector used for control process could be calibrated. The integration of the system is shown for watch parts assembly.

**Keywords :** laser, welding, conduction, process control, assembly, watch parts.

## 1.INTRODUCTION

For many micro-parts in electronics and mechanics, a high quality level is required for assembly. In the case of laser welding in conduction regime, the interaction laser matter is the main source of defects which can be due to local impurities in material (inclusion, surface state, laser absorption) and/or instabilities in process setup ( geometry defects, gas, laser, focus). Only a real time control process can compensate these disturbances and ensure a recurrent production. So, the aim is the preservation of surface temperature below the material vaporization level.

This paper presents our recent investigations on the process control of laser welding in conduction regime. Based on a traditional Proportional Integral Derivative (PID) regulation of temperature, we show a system which can regulate process for millisecond pulse duration range. Part 2 presents the experimental setup including diagnostics (Camera, visible photodiode, IR photodiode) for a complete monitoring of the laser interaction. Part 3 shows results with the objective of diagnostics correlation and process control system demonstration.

## 2. EXPERIMENTAL SETUP

Figure 1 presents experimental setup.

### 2.1 Laser

Experiments have been performed with a pumped lamp flash Nd:YAG Laser Cheval laser. This one delivers continuous and pulsed (from  $\mu$ s to ms duration) irradiation from 0 to 300W. Its power can be controlled by an analogic input during processes. The response time of the laser from the input command to the irradiation output is 100  $\mu$ s. A Silicium photodiode measures the temporal profile of the laser intensity (Figure 4a). The laser is focused with plano-convex lens which the focal is 75 mm. The spot diameter is 450  $\mu$ m.

\* 16 bis avenue Prieur de la C te d'Or, 94114 Arcueil cedex France  
lberthe@clfa.fr

## 2.2. CDD camera

CCD camera visualizes events above the target. Acquisition is triggered on the signal itself and the exposure time is 33 ms. So, for typical pulse duration used in this study (1-10 ms), images integrate any luminous phenomena. This diagnostic detects the occurrence of vapor and/or low ionized plasma during the interaction. Typical image in conduction regime (see part 3) is presented in Figure 4b. Target is on the top of the picture and laser comes from the bottom.

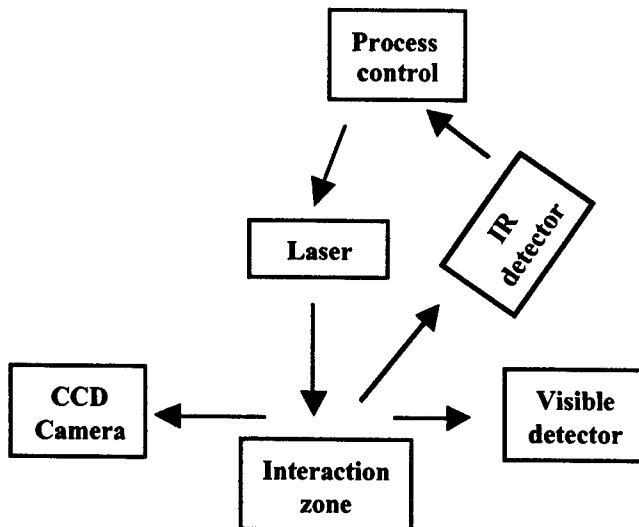
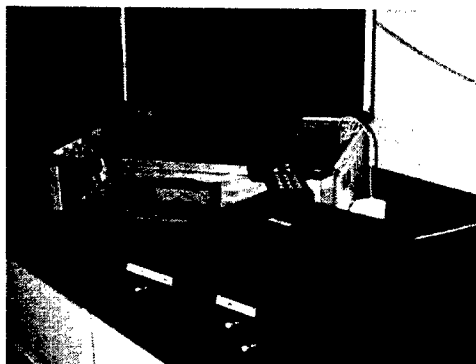
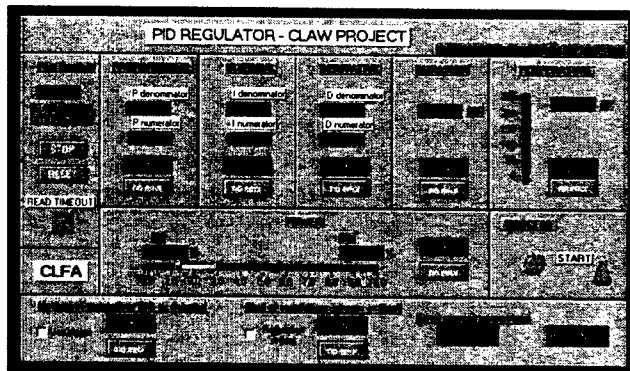


Figure 1 : experimental setup.



(a)



(b)

Figure 2 : presentation of regulation system can be controlled by PC or other system like MEDUSA (©SMH Automation), (b) interface allowing the adjustment of any parameters.

## 2.3 Visible photodiode.

Visible detector is a Silicium photodiode with a 1 ns response time. A doublet of achromatic lens makes the image of the zone above the target on the detector. Schott heat-absorbing glass KG3 transmits visible light from the interaction in rejecting IR emission from laser and interaction. This diagnostic detects luminous events above the target as the CDD camera and measures these temporal variations during the interaction. In production, this cheap diagnostic could replace camera.



## 2.4. IR detector

IR detector is a InGasAs (spectral response: 600-1700nm) photodiode with 50 ns response time which is negligible for millisecond laser pulse. A doublet of achromatic lens makes the image of the surface of the target on the detector with a magnification of 10. So, the surface of detector being 2 mm, the measurement concerns only the centre of laser spot for which the temperature can be considered homogeneous. In this configuration, edges of laser spot which correspond to the highest temperature gradient are eliminated.

Besides, an interferential filter at 1300 nm (10 nm band width) is used in front of detector to distinguish thermal emission surface from laser irradiation which could be closed. Indeed, wavelength of emitted light from a surface in liquid state is in near IR. For example, the maximum intensity emitted by liquid Iron is in 1-1.6  $\mu\text{m}$  wavelength range (surface considered as a blackbody).

Clearly, this light emission measurement is representative of surface temperature in the case of conduction regime without vaporization. Figure 4a presents typical signal of this thermal detector. Part 3 shows that this diagnostic can be calibrated in term of absolute temperature.

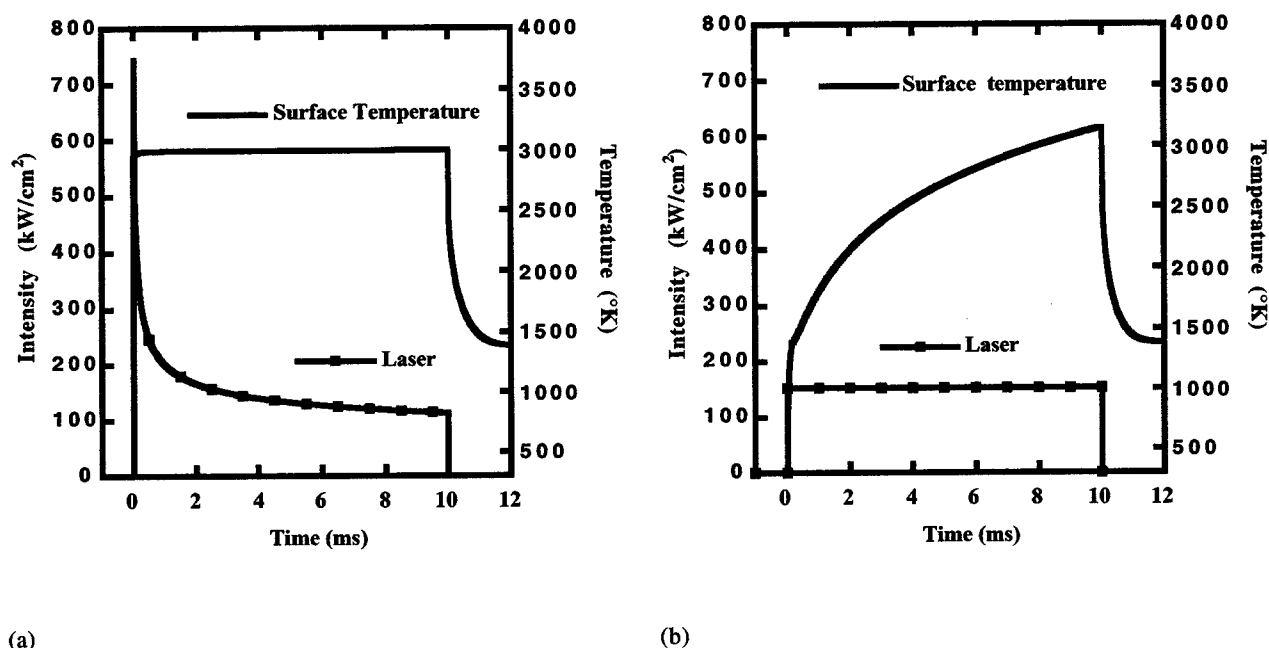


Figure 3 : surface temperature calculated by the code resolving the Fourier's law for a laser heating source and 316L stainless steel (a) simulation of PID regulation: temperature is constant at the temperature order 3000°K. (b) without regulation: vaporization temperature is reached (3100°K). In both cases, total energy deposited on surface by laser is the same (1524 J/cm<sup>2</sup>) during 10 ms pulse duration.

## 1.4. Process control

The process control system is based on a traditional PID analysis. This kind of regulation is commonly used in thermal laser processes<sup>1,2</sup>. However, according to our knowledge, no effort has been done on the response time for millisecond pulse duration.

Experiments have been performed with special system which response time (from the IR detector to laser power command) is 90  $\mu\text{s}$ . Built from micro-controller, the regulator has been tested with different lasers (Cheval and Haas lasers). Besides, any parameters concerning laser and regulation can be modified easily by a simple interface (Figure 2) and system is also

adaptive and can work independently in a line production. In part 3, such example of integration in a machine of watch parts assembly is presented.

### 1.5. Simulation

Simulation of the interaction in conduction regime has been made with a traditional 1D (finite difference) code resolving the Fourier's law for a laser heating source (any loss is taken into account, Laser absorption and thermal-physics properties are constant ). This simple code gives only the typical temporal profiles of surface temperature and laser intensity.

## 3. RESULTS AND DISCUSSION.

### 3.1. Simulations

Figure 3 gives examples of simulation with (a) and without (b) PID regulation for 316L steel. The surface temperature is constant with PID regulation. The corresponding laser power profile is a strong peak to reach the temperature order followed by a slow decrease to sustain the constant level of surface temperature. Figure 3b presents the surface temperature with a square laser pulse which the total energy equals to that one of the simulation with regulation, pulse duration being the same. In this case surface temperature increases with time and exceeds vaporization temperature (3100 °K) from 8 ms. This simple calculation shows the interest of process control even without defects. Indeed, the regulation limits the vaporization surface which could induce high pressure plasma and uncontrolled material ejection.

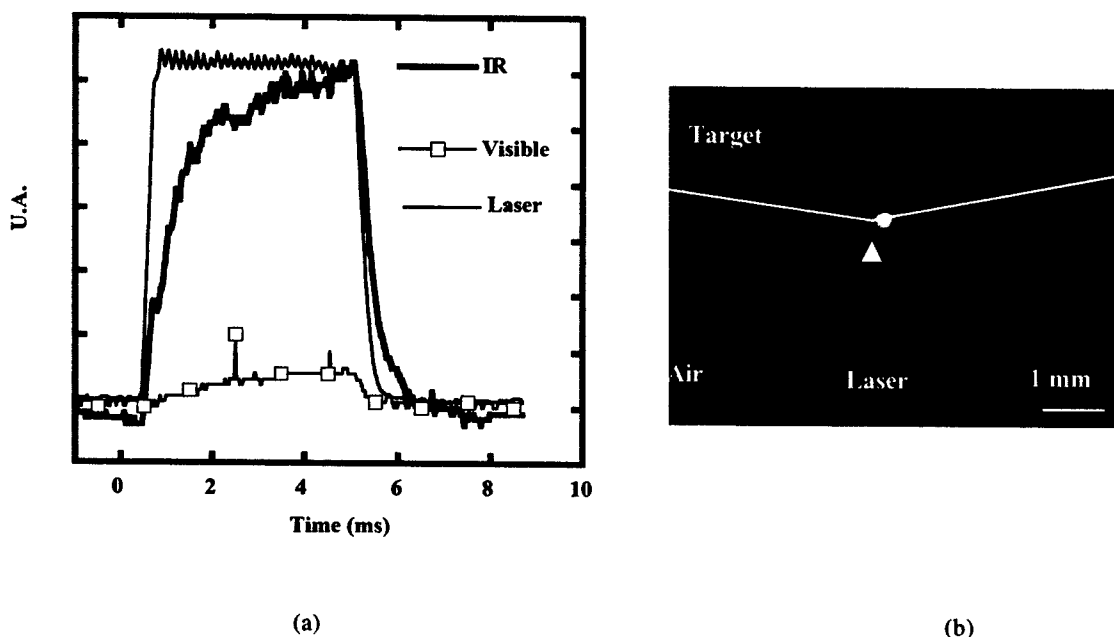


Figure 4 : typical records in conduction regime for a laser pulse duration of 6 ms on massive 316L ( $188 \text{ KW/cm}^2$ ), (a) IR signal at 1300nm (see text), (b) Visible signal (see text) and laser intensity profile, (b) visualization above the target by CCD camera.

### 3.2. Interaction monitoring.

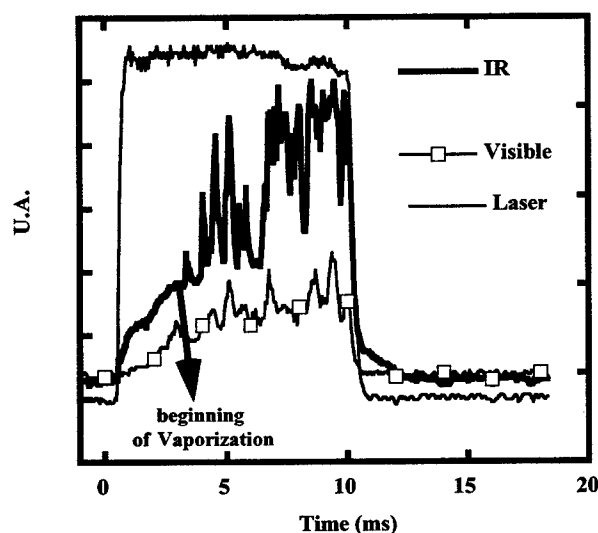
Figure 4 presents records of the different diagnostics for a square laser pulse of 6 ms irradiating 316L steel. In Figure 4a, during the laser irradiation, IR signal increases with time like a typical profile in conduction regime. Indeed, general trend is similar to simulation presented in Figure 3b. Visible detector is very low and seems to follow the temperature signal.

However, the signal to noise rate is too low to use this signal for temperature monitoring. Corresponding CDD camera image (Figure 4b) shows only a weak luminosity at the surface of target. According to visible and temperature signals, no vaporization occurs in these irradiation conditions. Luminosity comes from the surface target which emits in a wide wavelength band (maximum intensity being in IR (see Part2)). After laser irradiation, temperature decreases until complete cooling of material.

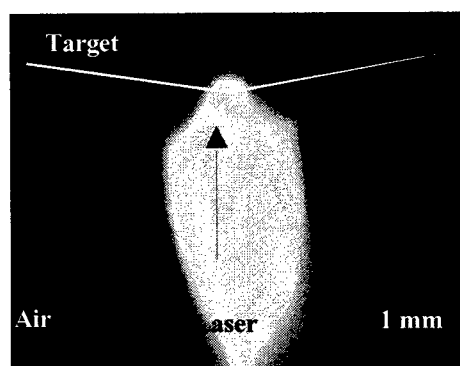
Figure 5 presents records of the different diagnostics for a square pulse of 10 ms irradiating 316L. In Figure 5a, IR detector signal increases with time. However, it may be separated in two phases. The first from the beginning of the laser pulse (time 0 ms) to 3 ms, the profile looks like a conduction signal as shown in Figure 3a. The second until the end of laser pulse, signal is higher with important oscillations. Visible signal follows same variations. Corresponding CDD camera image (Figure 5b) shows a strong luminosity above the target due to hot vapor and/ or plasma emission. The time transition between the two phases is very short. Indeed, time between the end of the first phase and the maximum of the first oscillation is near 200  $\mu$ s. This time depends on material, its state of surface and the experimental conditions. For example, preliminary experiments with Copper seem to show that monitoring is different and time reaction is shorter. However, for present experiments with 316L, the results are reproducible.

Clearly, these irradiation conditions are not optimal for applications because surface state could be pollute by vaporized particles or ejected liquid. For the best quality, interaction process has to remain in conduction regime. A fast process control can only sustain it for milliseconds pulse duration range as Figure 5 shows it.

Besides, these results confirm that IR detector allows an accurate monitoring of laser interaction. Indeed, signal is representative of surface temperature and threshold between pure conduction heating and vapor/plasma regime is detected by the IR photodiode.



(a)



(b)

Figure 5 : typical records in conduction regime for a laser pulse duration of 5 ms on massive 316L ( $188 \text{ KW/cm}^2$ ) , (a) IR signal at 1300nm (see text), (b) Visible signal (see text) and laser intensity profile, (b) visualization above the target by CCD camera.

### 3.3. Calibration

Calibration of the IR detector has been made by using these diagnostics. Vaporization transition of pure material (isolated sheets of Fe, Ta, Mo) has been detected on typical records as shown in Figure 5. Experiments have been repeated on the same material to ensure statistical measurements. Figure 6 presents such calibration. Minimum and maximal values for each material have been reported. Curves show that the response of detector could be linear in 0-4500 °C temperature range. However, for industrial application this procedure is not required. Indeed, signal calibration is too sensitive to experimental conditions. Procedure has to be reproduced after any modification of configuration.

### 3.4. Regulation

Regulation has been performed from IR detector signal in millisecond laser pulse range on 316L. Figure 7 presents an example of regulation for 10 ms pulse duration. Laser intensity profile and temperature signal are also reported. During the laser irradiation, temperature signal can be separated in two main phases. In the first, the signal increases with time, up to the order level which is reached at 2 ms after the beginning of irradiation. In the second phase, IR signal remains at the order level until the end of the pulse. The regulation generates a laser intensity which decreases constantly during the laser pulse. The profile is similar to the one calculated in Figure 3a. However, the first phase is shorter with simulation because the maximum of laser intensity is not limited compared to the experiment. Thus, the laser with the highest possible peak intensity is required for a better initial regulation.

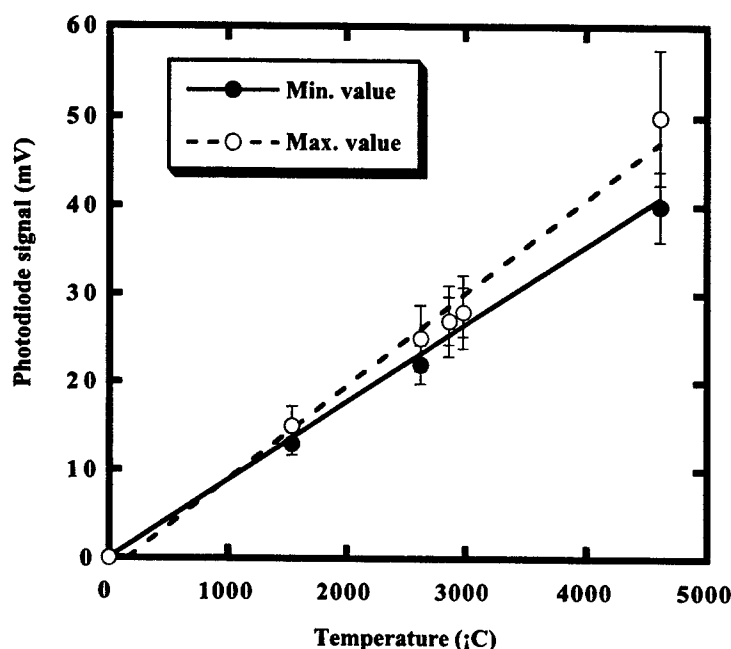


Figure 6 : IR detector calibration with melting and boiling point of pure materials.

Besides, a brutal increase of IR signal occurs 5 ms after the beginning of the pulse. Regulation corrects this defect and IR signal decreases to the order after about 200  $\mu$ s. This could be considered as the experimental total reaction time of the system (regulation + laser). This value is in accordance with the one of each part : 90  $\mu$ s for the regulation, 100  $\mu$ s for the laser.

This reaction time corresponds also to the time transition between conduction regime and vaporization determined on Figure 5(Part 3.2). In fact, to ensure no pollution, the response time of the process control system should be rather lower than this time transition. However, these results shows the effectiveness of the system with a closed response time.

### 3.5. Integration in a machine

Process control system (IR detector and PID system) has been integrated in a machine assembling watch parts by laser welding. Figure 8a shows a photograph of the whole system.

In these applications, the state of surface must be conserved during the process. According to the high quality required and the dimensions of the parts (0.1-2 mm), the laser welding in conduction regime is applied. Then, the aim of the process control is a constant quality for mass production.

IR Detector has been integrated in a special head built by Laser Cheval. Robot, mechanics, automatism, gas, supports and process control system are controlled by the master machine MEDUSA (©SMH Automation). Tests concerned axis-crowns in steel welded with millisecond laser pulse duration. An example of assembled parts is shown on Figure 8b. White arrows fixe the welded zone. Results show that process control does not improve the quality of the assembly but ensures a better reproducibility.

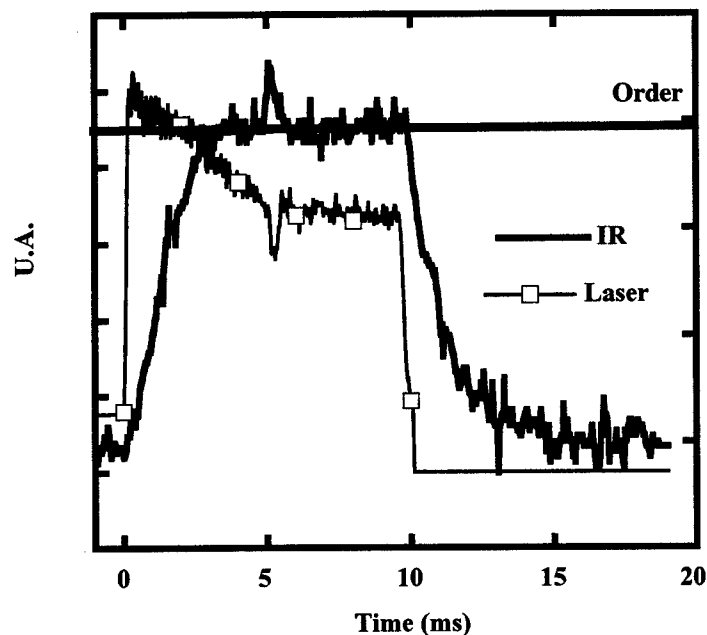


Figure 7 : example of control by the system for 10 ms pulse duration on 316L steel.

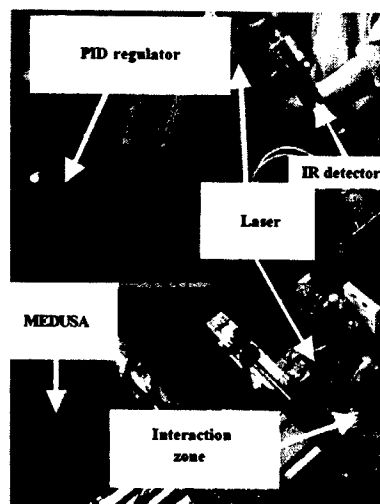
## 4. CONCLUSIONS AND PERSPECTIVES

A control process system has been built for laser welding in conduction regime. For millisecond pulse duration, process monitoring with CDD camera and photodiode confirms the validity of the temperature measurement by simple IR photodiode. Vaporization of material and /or plasma occurrence has been also evidenced on signals. In this way, IR detector has been calibrated in terms of temperature. The effectiveness of process control has been shown in the case of steel and validated for watch assembly application. The measured response time of the system (laser + Process control system) is 200  $\mu$ s in accordance with responses time of each device of the system. In the case of steel, this performance is sufficient for a

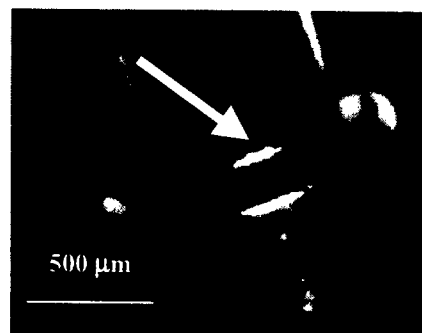
good process control. Further works could concern other materials like Copper, for which the interaction with laser in this regime seems to be very different.

### ACKNOWLEDGEMENT

This work is a part of a BRITE/EURAM Contract BRPR-CT98-0634 - project BE-4855-CLAW called Clean and Low distortion Accurate Welding of micro-parts (CLAW).



(a)



(b)

Figure 8 : Integration of control process system in a machine of laser welding of watch parts. (a) Image of the machine (b) image of the axial parts assembled (white arrow fixes the position of the welded zone)

### REFERENCES

- <sup>1</sup> F. Bataille, C. Pawlavsky, D. Kechemair, "Thermal regulation Applied to CO<sub>2</sub> laser surface treatments", Meas. Sci. Technol., **3**, pp. 50-57, 1992.
- <sup>2</sup> G. Backes, E. W. Kreutz, A. Gasser, "Process monitoring and control during alloying with CO<sub>2</sub> laser radiation", Eclat, 1998, Hanover, Germany, pp.227-236, edited by B.L. Morbike.

# SHADOW – A New Welding Technique

Thorsten Kramer<sup>\*a</sup>, Alexander M. Olowinsky<sup>\*\*a</sup>, Friedrich Durand<sup>\*\*\*b</sup>

<sup>a</sup> Fraunhofer Institute for Laser Technology ILT, Aachen, Germany

<sup>b</sup> SMH Automation, Grenchen, Switzerland

## ABSTRACT

The new welding technique "SHADOW – Stepless High Speed Accurate and Discrete One Pulse Welding" is introduced. SHADOW means the use of a single pulse to generate a quasi continuous weld of several millimeters in length. The processing time is defined by the pulse duration of the pulsed laser. At present, a state-of-the-art laser is capable of a maximum pulse duration of 20 ms. The variation of the laser power depending on time is a vital capability of the pulsed laser to adapt the energy deposition into the workpiece (pulse shaping).

Laser beam welds of several watch components were successfully performed (for further information see paper 4637-77 "New Applications of Laser Beam Micro Welding in Watch Industry"). Similar metals like crowns and axes made out of stainless steel have been welded using pulsed laser radiation. Applying a series of about 130 single pulses for the crown-axis combination the total energy accumulates to 19.5 J. The use of the SHADOW welding technique reduces the energy to 2.5 J.

While welding dissimilar metals like stainless steel and brass, the SHADOW technique has even more advantages. Gearwheels made out of brass have been joined to axes made out of stainless steel. Common pulse mode welding generates a considerable amount of contamination but SHADOW welding reduces drastically the contamination as well as the distortion.

Laser beam welding of copper has a low process reliability due to the high reflection and the high thermal conductivity. SHADOW welds of 3.6 mm length were performed on 250  $\mu$ m thick copper plates with very high reproducibility. As a result, a pilot plant for laser beam welding of copper plates has been set up.

The work to be presented has partly been funded by the European Commission in a project under the contract BRPR-CT-0634.

**Keywords:** Laser Beam Micro Welding, Pulsed Nd:YAG laser, Pulse shaping, Industrial Application, Micro Application, Micro Technology, Micro-Parts, Dissimilar Metals, Copper, Brass

## 1. INTRODUCTION

### 1.1. CLAW

The ongoing trend of miniaturization challenges manufacturers on the one hand to downsize the space required for joining parts and to enhance the flexibility of the manufacturing techniques on the other. The size and the thickness of the micro components to be joined demand small weld geometries which means that only heat conduction joining is applicable. But more and more materials combinations need to be joined to take advantage of the different materials properties such as electrical conductivity or stiffness. The thermo-physical properties of the component's materials and their mutual solubility have therefore to be taken into account. Since some metals generate brittle alloys which have a poor tensile strength welding such a materials combination may technically not be feasible. In respect of their high electrical conductivity copper and brass are of particular interest for the electronics industry and the feasibility to join copper and brass is vital for creating new compact components and products.

Common joining techniques reach their limits in flexibility, reproducibility, preparation and cycle time. Continuous wave laser beam welding ensures a consistent low energy input into the workpiece but the lasers are expensive and not

\* thorsten.kramer@ilt.fraunhofer.de; phone +49 241 8906 -407; fax +49 241 8906 -121;

Fraunhofer Institute for Laser Technology ILT, Steinbachstr. 15, 52074 Aachen, Germany

\*\* alexander.olowsky@ilt.fraunhofer.de; phone +49 241 8906 -491; fax +49 241 8906 -121;

Fraunhofer Institute for Laser Technology, Steinbachstr. 15, 52074 Aachen, Germany

\*\*\* friedrich.durand@eta.ch; phone +41 32 655 -7238; fax +41 32 655 -8389;

SMH Automation a Division of ETA SA Fabrique d'Ebauches, Maienstr. 11, 2540 Grenchen, Switzerland

economical for micro applications. Even pulsed laser beam welding with a typical overlap of 70% to 90% is restricted for seam welding because of a high processing time and a high distortion risk on the base of high energy input into the workpiece.

Since pulsed lasers have a good beam quality their radiation can be focused down to a spot diameter of 50  $\mu\text{m}$  for micro welding applications. In spite of the low average power of pulsed lasers the peak power reaches up to 3 kW. Furthermore pulse shaping is a standard capability of modern pulsed lasers.

The work and results presented have been funded by the European Commission in a project called CLAW under the contract BRPR-CT-0634, where CLAW means Clean and Low Distortion Accurate Welding of Micro-Parts. The objectives of the Claw-project can be summarized as follows:

- Eliminating the contamination
- Reducing the distortion due to handling and joining
- Enhancing the application of laser beam micro welding in industry

The watch industry at present uses joining techniques such as screwing, gluing, press fitting or crimping, but none of these joining techniques is able to guarantee the low tolerances needed for mounting the watch movements. Moreover dissimilar materials like steel and brass come into operation in respect of tribologic aspects. The welding tasks within the CLAW-project were thus to join thin membranes or foils with a thickness down to 5  $\mu\text{m}$  and small watch components such as gearwheels with a thickness of about 100  $\mu\text{m}$  and axes with a diameter of down to 200  $\mu\text{m}$ .

## 1.2. A Bright Idea

In general the beam quality of a laser depends on its average output power. A flash lamp pumped continuous wave laser with an average output power of at least 1 000 W and a beam quality of 25 mm-mrad can be coupled into an optical fiber of 600  $\mu\text{m}$  diameter, see Table 1. If the beam quality can be reduced to 12 mm-mrad either with flash lamp or diode laser pumping the laser radiation can be coupled into a 300  $\mu\text{m}$  optical fiber. The laser radiation of a pulsed laser which has a beam quality of 8 mm-mrad can be delivered to the processing optics via a 200  $\mu\text{m}$  optical fiber at a maximum pulse power  $P_H = 3\,000\text{ W}$ , which can easily be pulse shaped with a typical response time of 50  $\mu\text{s}$ .

**Table 1:**  
Properties of state-of-the-art continuous wave and pulsed lasers

	Maximum Laser Power $P_{\text{max}} / \text{W}$	Average Laser Power $P_{\text{av}} / \text{W}$	Maximum Pulse Power $P_H / \text{W}$	Beam Quality $q / \text{mm-mrad}$	Diameter of Optical Fiber $d / \mu\text{m}$
HL 1006 D	1 400	1 000	-	25	600
HL 1003 D	1 400	1 000	-	12	300
HLD 1003	1 300	1 000	-	12	300
HLD 3504	4 500	3 500	-	16	400
HL 304 P	400	300	8 000	16	400
HL 62 P	75	60	3 000	8	200

www.haas-laser.de

The commonly used laser beam welding techniques, continuous wave welding and pulse mode welding, are not unrestrictedly applicable to all micro welding tasks. In many cases continuous wave lasers may not be used because of their poor beam quality, thus resulting in minimum spot sizes of 600  $\mu\text{m}$  compared to pulsed lasers that can be focused down to minimum spot sizes of down to 50  $\mu\text{m}$  even with fiber coupled systems.

Furthermore, continuous wave lasers are more expensive than pulsed lasers regarding the average output power versus the maximum pulse power and are therefore not economical for micro applications. In industrial applications welding seams of up to 5 mm in length are obtained by using pulsed laser radiation with a typical overlap of 70% to 90%. Pulsed mode welding deposits up to ten times more energy into the workpiece than is required for the recommended tensile strength. High speed video imaging of the welding process revealed that every single pulse melts the material which quickly solidifies at the end of the pulse. The feed rate is limited by the repetition rate and the average output power of the pulsed laser and the required overlap of the pulses. All this results in a high risk of contaminating and distorting the micro-part.

State-of-the-art pulsed lasers are capable of pulse shaping, which is required for welding highly reflective difficult-to-weld materials such as brass or copper. Since the absorbed energy on that account may change up to 20% the low absorption of untreated copper (approximately 5%) and slight fluctuations in reflectance (in the range of 1%) lead to a poor reproducibility of single spot or pulsed mode seam welding. In addition, the reflectivity and the thermal conductivity of copper changes during laser beam treatment. In the temperature range between room and evaporating temperature the absorption coefficient of stainless steel increases with a factor of two whereas the absorption coefficient



of copper increases with a factor of four. The thermal conductivity of stainless steel at room temperature is only half of that at melting temperature, but the thermal conductivity of copper at room temperature is doubled compared to that at melting temperature.

All the above mentioned facts and considerations lead to the conception to apply quasi continuous wave laser beam welding to micro-parts with a part geometry smaller than 500  $\mu\text{m}$  and a weld width smaller than 100  $\mu\text{m}$ . Particularly difficult-to-weld materials and materials combinations such as brass and copper or steel on brass ought to be welded by a new welding technique. To obtain a cycle time as short as possible the processing time should not exceed 20 ms, that is the maximum pulse duration of a state-of-the-art pulsed laser. The pulse shaping capability may be used to adapt the pulse power to the changing reflectivity of copper as discussed above. The main objective in succeeding to apply a new technique or process into industrial manufacturing is the cost effectiveness. In the presented case this means to deploy a low-priced laser with low maintenance costs and that is a pulsed laser.

### 1.3. SHADOW turns to Light

The abbreviation SHADOW stands for **Stepless High Speed Accurate and Discrete One Pulse Welding**. That is the use of a single pulse for quasi continuous wave welding of micro-parts at a high feed. The SHADOW-welding technique introduced in this paper combines the advantages of continuous and pulsed laser beam welding. SHADOW-Welding means seam welding up to 10 mm length at a high feed rate of up to 30 m/min with a pulsed laser for micro applications. The pulse shaping capability of the pulsed laser ensures an effective energy deposition into the workpiece.

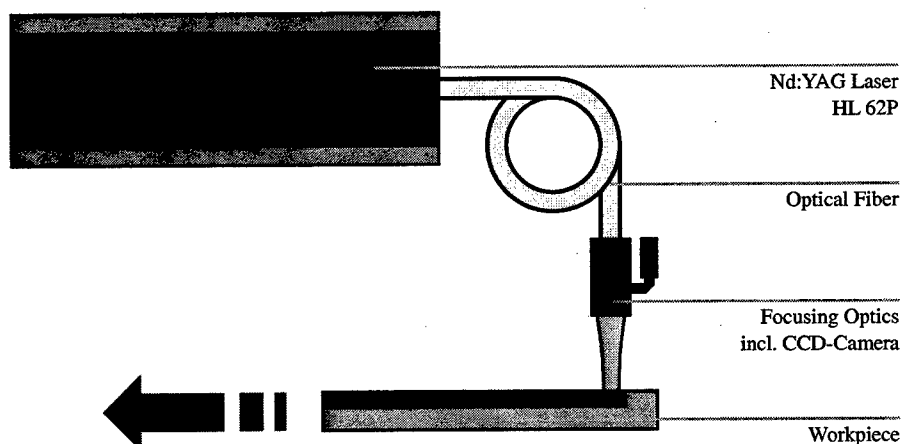
## 2. HARDWARE DEVELOPMENT

### 2.1. Preparation

The principal set-up for testing the SHADOW-technique on stainless steel plates is shown in Figure 1. The laser radiation of the pulsed laser is delivered to the focusing optics by means of an optical fiber and focused to a spot diameter of  $2w_f = 200 \mu\text{m}$ . The workpiece is moved at a feed rate of  $v_f = 10 \text{ m/min}$  such that a single pulse of  $\tau_H = 20 \text{ ms}$  pulse duration creates a weld seam of  $l = 3.6 \text{ mm}$  in length.

$$l = v_f \cdot \tau_H + 2w_f = 167 \frac{\text{mm}}{\text{s}} \cdot 0.020 \text{ s} + 0.2 \text{ mm} = 3.6 \text{ mm} \quad (1)$$

**Figure 1:**  
Schematic Drawing  
of the Set-up



The easiest way to achieve a high feed rate is to rotate the workpiece which should finish a whole turn within  $\tau_H = 20 \text{ ms}$ , leading to a rotational speed of  $(20 \text{ ms})^{-1}$  or 3 000 rpm. A linear feed rate of about  $v_f = 20 \text{ m/min}$  corresponds to a part diameter of  $d = 2.2 \text{ mm}$  or a length of  $l = 6.7 \text{ mm}$ .

$$l = 2\pi \cdot w_f = 2\pi \cdot 1.1 \text{ mm} = 6.7 \text{ mm} \quad (2)$$

$$v_f = \frac{l}{\tau_H} = \frac{6.7 \text{ mm}}{0.02 \text{ s}} = 334 \text{ mm/min} \quad (3)$$

## 2.2. Experimental Set-up

The experimental set-up is represented in Figure 2. The focusing optics includes a CCD-Camera for monitoring. High speed imaging was used to visualize the fast process. Tests of position control have been performed requiring a fast CMOS-camera and a zoom objective.

**Figure 2:**  
Experimental Set-up

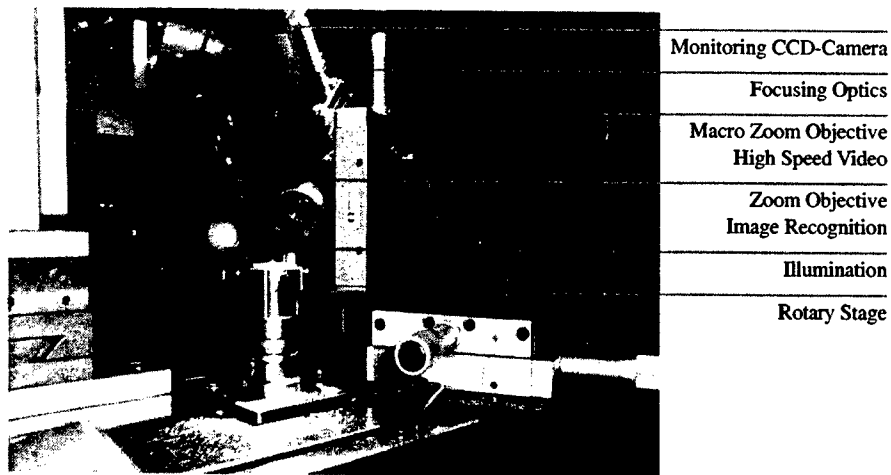


**Figure 3:**  
High Speed Spindle  
and Workpiece  
Holder



Due to the small parts and the large magnification of both objectives, the illumination demanded particular attention. Diode laser radiation ( $\lambda = 806 \text{ nm}$ ) diffusely scattered illuminated the parts and an appropriate band pass filter with a peak wavelength of  $\lambda = 806 \text{ nm}$  and a FWHM of 10 nm was used to protect the camera from back scattered Nd:YAG laser radiation. The rotary stage which was built by SMH Automation was capable of rotating the part at a rotational speed of up to 18 000 rpm with a concentric running of 2  $\mu\text{m}$ . The workpiece holders contained holes for extraction such that the parts were held in place by vacuum as shown in Figure 3.

## 3. PROCESS DEVELOPMENT

### 3.1. Preliminary Tests

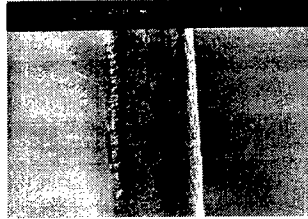
There are four different materials combinations of interest for the watch industry. In addition, copper plates are important for the automotive and electronics industry and their component suppliers, see Table 2. The filled circles indicate a good weldability, whereas the hollow circles indicate a poor weldability.

**Table 2:**  
Materials to be  
welded

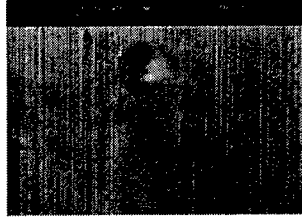
	Stainless Steel	ARCAP	Brass	Copper
Stainless Steel	●	○	○	○
ARCAP		●	○	-
Brass			○	-
Copper				○

Test welds on stainless steel plates (thickness 250  $\mu\text{m}$ ) have been carried out at a maximum feed rate of  $v_f = 10 \text{ m/min}$ . Both top view and cross-section indicated a consistent and robust weld process with a very high reproducibility. The picture in Figure 4, left hand side, shows a top view of a SHADOW weld on stainless steel X8 Cr Ni 1812. Neither contamination nor distortion is observable. The picture on the right hand side of Figure 4 illustrates a clean SHADOW weld on brass Ms 63. The pit indicates the end of the weld.

**Figure 4:**  
Metal Plates  
SHADOW Welds



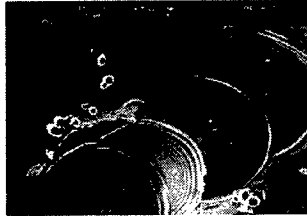
Stainless Steel Plates  
 $Q = 6.2 \text{ J}$ , Pulse Shaped  
 $\tau_H = 20 \text{ ms}$   
 $v_f = 10 \text{ m/min}$   
 $\alpha = 0^\circ$   
Material  
X8 Cr Ni 1812  
 $t = 250 \mu\text{m}$



Stainless Steel Plates  
 $Q = 6 \text{ J}$ , Block Pulse  
 $\tau_H = 20 \text{ ms}$   
 $v_f = 10 \text{ m/min}$   
 $\alpha = 0^\circ$   
Material  
Brass Ms 63  
 $t = 150 \mu\text{m}$

During the welding of thin stainless steel membranes to tubes the pulse mode technique generates a considerable amount of contamination and particle fallout originating from the rapid heating and melting process at the beginning of each pulse as illustrated in Figure 5 (picture on the left). Using the SHADOW technique the surface of the membranes stays clean, no particles or droplets can be detected as shown in Figure 5 (picture on the right).

**Figure 5:**  
Membranes  
Material  
X5 Cr Ni 1810  
 $t = 25 \mu\text{m}$



Pulse Mode  
 $P_H = 300 \text{ W}$ ,  $Q_{\text{tot}} = 27 \text{ J}$   
 $\tau_H = 5 \text{ ms}$ ,  $f_p = 25 \text{ Hz}$   
 $v_f = 300 \text{ mm/min}$



SHADOW  
 $Q = 9 \text{ J}$ , Pulse Shaped  
 $\tau_H = 20 \text{ ms}$   
 $v_f = 30 \text{ m/min}$

The pulse energy for the SHADOW amounts to  $Q = 9 \text{ J}$  which is only one third of the accumulated energy for pulsed welding  $Q_{\text{tot}} = 27 \text{ J}$ . The weld seam of  $l = 10 \text{ mm}$  length required 50 single pulses at a repetition rate of  $f_p = 25 \text{ Hz}$  resulting in a processing time of  $t = 2.0 \text{ s}$  whereas the SHADOW weld can be generated within  $t = 20 \text{ ms}$  using the same pulsed laser.

### 3.2. SHADOW Welding of Watch Components

After the feasibility of welding crowns to the axis by means of pulsed laser radiation has successfully been verified the SHADOW-technique was able to minimize the contamination and discoloration. Figure 6 shows SHADOW welded crowns and axes from Laser Cheval. The discoloration can be eliminated completely by using Argon as protection gas. When the melt pool has been created the laser power has to be reduced to avoid particles ejecting from the melt. During laser treatment the components are heated by the absorbed and distributed laser energy. The laser power should therefore further be reduced. The end of the weld seam overlaps the beginning to smoothen the surface at the start of the weld and the laser power fades out. The variation of the laser power depending on time is illustrated in Figure 7.

**Figure 6:**

Crown - Axis  
SHADOW Weld

$Q = 2.5 \text{ J}$

$\tau_H = 20 \text{ ms}$

$v_f = 8.5 \text{ m/min}$

$\alpha = 20^\circ$

Material

Axis S 20 AP

$d = 0.9 \text{ mm}$

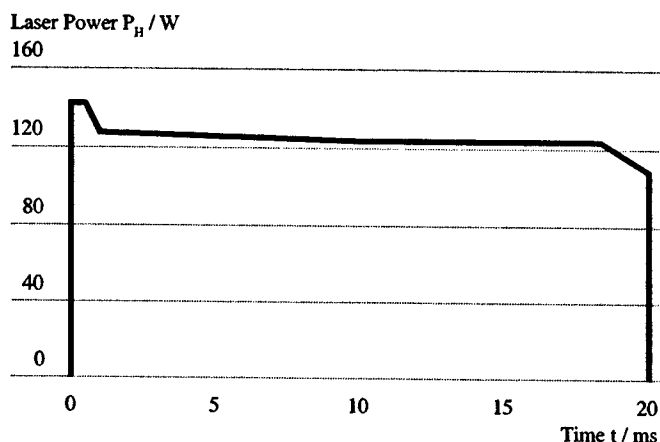
Crown 316 L

$d = 5.0 \text{ mm}$

courtesy of

**Figure 7:**

Variation of the Laser  
Power Depending on  
Time for SHADOW  
Welding of the  
Crown to the Axis



Welding the crowns to the axis by means of pulsed laser radiation takes  $t = 0.65 \text{ s}$  at the maximum repetition rate of the deployed laser ( $f_p = 200 \text{ Hz}$ ) which means that 130 pulse ( $P_H = 300 \text{ W}$ ,  $\tau_H = 0.5 \text{ ms}$ ) were necessary. The total Energy thus amounts to  $Q_{\text{tot}} = 19.5 \text{ J}$  and is about 8 times the pulse energy necessary for SHADOW welding. The tractive force reaches 100 N for a SHADOW weld as well as for a pulsed weld, which satisfies well the specification of 50 N.

The gearwheels from Swatch are made out of brass and ought to be joined to the stainless steel axes. Joining dissimilar metals is known to be difficult due to their different materials (see Table 3). Welding stainless steel to copper is feasible but the welds tend to generate cracks and voids. The difference in melting temperature causes the main difficulties for welding stainless steel to brass.

**Table 3:**

Thermo-Physical  
Properties of  
Different Materials

	Melting Temperature $T_m / ^\circ\text{C}$	Thermal Expansion Coefficient $\alpha_{\text{thermal}} / 10^{-6}/\text{K}$	specific Heat Capacity $c_p / \text{J/kg}\cdot\text{K}$	Thermal Conductivity $\lambda_{\text{thermal}} / \text{W/m}\cdot\text{K}$
AISI 316	1 398	17.5	500	15
E-CU 58	1 083	17.7	380	390
CuZn37	920	20.2	427	120

SHADOW welds on stainless steel and brass plates revealed the origin of the joint. The steel and brass melts do not fuse in the common sense of forming one melt. The joint strength has to be ascribed to the interlocking of the mixed re-solidified material as illustrated in Figure 8. In consequence of the interlocking joint effect, large joints cannot be generated, but small joints for micro applications are realizable.

**Figure 8:**  
Metal Plates  
SHADOW Weld

$Q = 7.5 \text{ J}$

$\tau_H = 20 \text{ ms}$

$v_f = 10 \text{ m/min}$

$\alpha = 0^\circ$

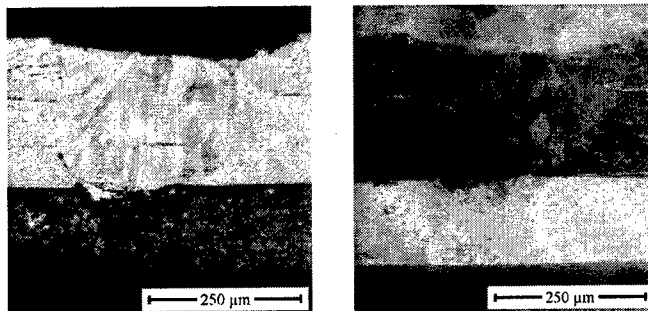
Material

Top CrNi 18 12

$t = 250 \mu\text{m}$

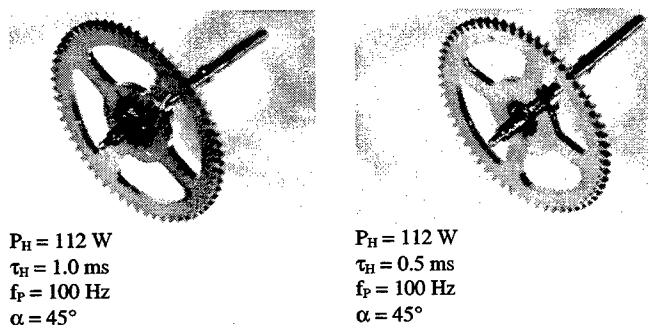
Bottom Ms63

$t = 150 \mu\text{m}$



The investigation of joining gearwheels made out of brass to axes made out of stainless steel started with pulse mode welding as illustrated in Figure 9. Joints with a tractive force of 30 N could be produced, but grime evaporated during the laser treatment contaminated the gearwheel surface. By shortening the pulse duration by half the contamination can be minimized, whereby the tractive force drops to 10 N and below the acceptance level.

**Figure 9:**  
Gearwheel - Axis  
Pulse Mode Weld



courtesy of  
**swatch**

**Figure 10:**  
Gearwheel - Axis  
SHADOW Weld

$Q = 1.3 \text{ J}$

$\tau_H = 20 \text{ ms}$

$v_f = 3.3 \text{ m/min}$

$\alpha = 45^\circ$

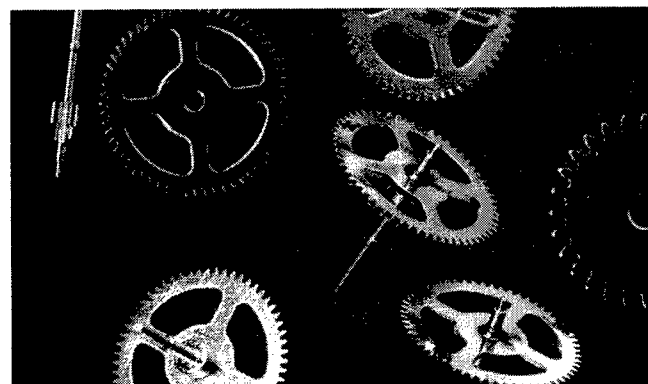
Material

Axis S 20 AP

$d = 0.3 \text{ mm}$

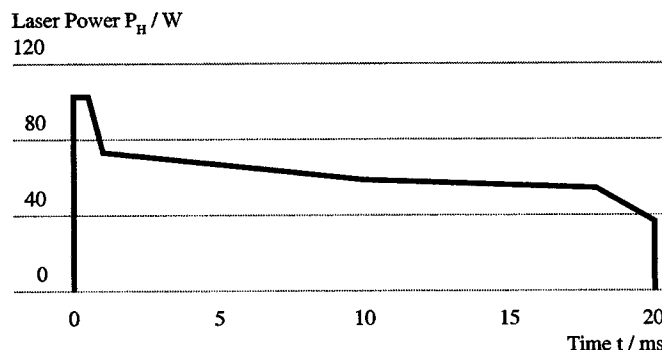
Wheel Ms61Pb

$d = 3.0 \text{ mm}$



courtesy of  
**swatch**

**Figure 11:**  
Variation of the Laser  
Power Depending on  
Time for SHADOW  
Welding of the  
Gearwheel to the  
Axis



FEM Simulation visualized the distortion of the gearwheel and the axis due to the high energy deposition of pulse mode welding. Applying the SHADOW technique the tractive force achieves 30 N and the contamination and distortion can

be kept low. Figure 10 illustrates the SHADOW welding of the gearwheel to the axis. The occurrence of contamination is limited to the start of the weld seam. This can be compared to one of the pulses for pulse mode welding shown in the picture on the left in Figure 9.

The variation of laser power depending on time is shown in Figure 11. The SHADOW pulse starts with a laser power of 112 W that is held for 1.0 ms but then rapidly drops to 70 W. After 10 ms the laser power reaches 60 W and after 18 ms it starts decreasing to 40 W till the end of the pulse.

**Table 4:**  
Comparison  
Pulsed Mode  
versus  
SHADOW

		Pulse Mode A	Pulse Mode B	SHADOW
Pulse Power	$P_H / W$	112	112	shaped
Pulse Duration	$\tau_H / ms$	1.0	0.5	20
Repetition Rate	$f_p / Hz$	100	100	-
Number of Pulses	$N / -$	130	130	1
Energy	$Q_{tot} / J$	14.6	7.3	1.3
Processing Time	$t / s$	1.30	1.30	0.02

Again the pulsed laser source must not be changed when switching from pulse mode welding to SHADOW welding so that almost every pulse mode welding process can easily be changed to the SHADOW technique. Table 4 sums up the important process parameters for welding the gearwheel to the axis. The main objective is to minimize the processing time per part. Changing from pulse mode welding to SHADOW welding the processing time and the energy deposition into the component can drastically be reduced. Regarding the pulse energy, up to six parts can be welded using the SHADOW technique while welding only one part in common pulse mode technique.

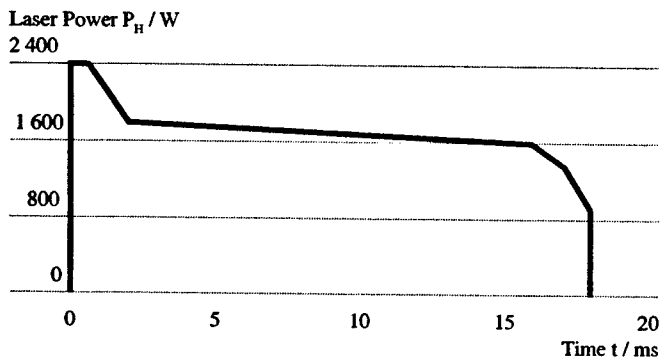
### 3.3. SHADOW Welding of Copper

Furthermore SHADOW possesses advantages for the welding of difficult-to-weld materials such as copper. Figure 12 illustrates SHADOW welding of 250  $\mu m$  thick copper plates. The welds possess a length of  $l = 3.3 mm$  and a width of  $b = 0.6 mm$ . Despite the high and changing reflectivity of the copper surface the welds look uniform and consistent. The reproducibility of the SHADOW welds is considerably higher than that of comparable pulse mode welds.

**Figure 12:**  
Difficult-to-Weld  
Copper Plates  
 $Q = 30 J$   
 $\tau_H = 18 ms$   
 $v_f = 10 m/min$   
 $\alpha = 30^\circ$   
 $t = 250 \mu m$



**Figure 13**  
Variation of the Laser  
Power Depending on  
Time for SHADOW  
Welding of Copper  
Plates



As long as no online control system for laser power regulation with suitable short response time is available the variation of the laser power depending on time needs to be determined by testing. Taking into account the thermo-physical properties of copper the laser pulse melts the copper with a peak power of 2 400 W and then is reduced to 1 800 W. To avoid the broadening of the weld seam, the laser power has to be reduced to 1 500 W before it is smoothly decreased to 900 W at the end of the pulse.

SHADOW welding additionally means increasing or even optimizing the process reliability. A pilot plant for manufacturing electronic components for the automotive industry using the SHADOW technique to weld copper plates has already been set up. Every component consists of about 300 individual parts that have to be welded at two positions. The number of welds per ready mounted component therefore comes up to 600. If a single weld has a defect, the whole component is scrap. The high number of welds requires a fast and reliable welding process to manufacture the number of units needed in the automotive industry and if the component should become a mass product the manufacturing has to be cost effective, too.

**Table 5:**  
Process Capability  
VDI Guideline 3258,  
80% Operation Time,  
One Shift,  
1 280 Hours per Year

	Pulse Mode	Continuous Wave Mode	SHADOW
<b>Invest</b>			
Nd:YAG-Laser	82 000 €	160 000 €	92 000 €
Clamping	40 000 €	40 000 €	40 000 €
Motion System	30 000 €	35 000 €	35 000 €
Handling System	55 000 €	55 000 €	55 000 €
Controlling Systems	50 000 €	50 000 €	50 000 €
	<b>272 000 €</b>	<b>355 000 €</b>	<b>287 000 €</b>
<b>Machine Cost per Hour</b>			
Fixed Machine Costs	53.13 €/h	69.34 €/h	56.05 €/h
Variable Machine Costs	13.28 €/h	17.33 €/h	14.01 €/h
	<b>66.41 €/h</b>	<b>86.67 €/h</b>	<b>70.06 €/h</b>
<b>Operation Costs per 1 m Weld Seam</b>			
Machine Costs	66.41 €/h	86.67 €/h	70.06 €/h
Maximum Feed Rate	1 m/min	20 m/min	30 m/min
	<b>1.11 €</b>	<b>0.07 €</b>	<b>0.04 €</b>

Table 5 compares pulse mode, continuous wave mode and SHADOW welding in respect of the operation costs per 1 m weld seam. The laser for pulse mode welding is supposed to be slightly less expensive than a pulsed laser for SHADOW welding, whereas the price of a continuous wave laser is doubled. The motion system for continuous wave welding as well as for SHADOW welding is more expensive due to the higher feed rate required. The listed fixed machine cost are calculated from the invest and the specifications of the VDI guideline 3258 and the variable machine cost are estimated to 25% of the fixed machine costs. Finally, the operation costs per 1 m weld seam equals the machine costs per hour divided by the maximum feed rate.

Because of the lowest feed rate pulse mode welding is the most expensive welding technique at 1.11 €/m. Continuous wave welding is less expensive (0.07 €/m) than pulse mode welding but rare in micro applications due to the poor beam quality of continuous wave lasers. The operation costs per meter weld seam for SHADOW welding are about half of that for continuous wave welding. Furthermore, most applications using pulse mode welding can be converted to SHADOW welding easily and well-priced.

#### 4. CONCLUSION

SHADOW welding reduces distortion as well as contamination due to low and accurate energy deposition into the components. Even difficult-to-weld materials such as copper or brass can be welded at a high reproducibility. SHADOW welding generates a stable and robust process. The high feed rate leads to a low processing time. Deploying a well-priced pulsed laser for quasi continuous wave welding results in low operation costs. SHADOW welding is a cost effective process for the mass production of micro-parts.

Table 6:

	Pulse Mode	Continuous Wave Mode	SHADOW
Operation Costs per 1 m Weld Seam	1.11 €	0.07 €	0.04 €
Minimum Spot Diameter	50 $\mu\text{m}$	300 $\mu\text{m}$	50 $\mu\text{m}$
Maximum Feed Rate	1 m/min	20 m/min	30 m/min
Processing Time	1.5 s	0.5 s	0.1 s
Contamination	high	low	low
Distortion	high	low	low
Process Control (Monitoring)	yes	yes	yes
Online Power Control	limited	yes	expected
Micro Applications	yes	limited	yes

Table 6 sums up the characteristics of all three welding techniques. SHADOW welding combines all the advantages of both, pulse mode welding as well as continuous wave welding. High speed and low cost processing of micro-parts without contaminating or distorting the components.

### ACKNOWLEDGEMENTS

The work presented has partially been funded by the European Commission in a project under the contract BRPR-CT-0634. The authors want to thank the partners within in the consortium which have strongly contributed to these results. Most of the samples are shown by courtesy of the Swatch Group and Laser Cheval.

### REFERENCES

1. "Laser beam micro welding as a new interconnection technique", *Microelectronics International*, No.39, pp. 44 ff January 1996
2. I. Miyamoto, H. Maruo, Y. Arata, "Beam absorption mechanisms in laser welding", Proc. SPIE, *Laser Processing: Fundamentals, Applications and Systems Engineering*, 3-6 June 1986
3. A. Olowinsky, T. Kramer, N. Dumont, H. Hanebuth, "New applications of laser beam micro welding" Proc. ICALEO 2001, Jacksonville, Florida USA
4. M. Glasmacher, *Prozeß- und Systemtechnik zum Laserstrahl-Mikroschweißen*, Meisenbach Verlag, Bamberg, 1998
5. F. Dausinger, *Strahlwerkzeug Laser: Energieeinkopplung und Prozeßeffectivität*, Teubner Verlag, Stuttgart, 1995
6. G. Fontana and L. Zhang, "Autogenous Laser Welding of Austenitic Stainless Steel to Copper Alloy", *Science and Technology of Welding and Joining*, 1998, Vol. 3 No. 2
7. S. Gopinathan, "Microstructural Evaluation of Laser Welded Copper-Stainless Steel Welds", Proc. ICALEO 97
8. M. Hiraishi, "Laser Lap-Welding of Stainless Steel to Copper Alloy", *Quarterly Journal of Welding Society* 1999, Vol 17
9. W. Kalita, "Structural and Mechanical Properties of CO<sub>2</sub>-Laser Welded Joints in Difficult-To-Weld Metals", *Welding International* 1996, Vol. 10
10. C. Lampa, "Laser Welding of Copper to Stainless Steel", Proc. ICALEO 97
11. E. Schubert, "Lasergestütztes Fügen von Werkstoffkombinationen", *Bleche, Rohre, Profile* 1999, Vol. 46
12. K. Shimizu, "Laser Welding of Copper and Copper Alloy", *Fujitsu Scientific & Technical Journal* 1992, Vol. 28
13. J. F. Lancaster, *Metallurgy of Welding*, Chapman & Hall, 1993



# **Laser penetration spike welding.**

## **A welding tool enabling novel process and design opportunities.**

**D.K. Dijken<sup>a</sup>, W. Hoving<sup>a</sup>, J. Th. M. De Hosson<sup>b</sup>**

**<sup>a</sup>Philips Electronics, Centre for Industrial Technology, The Netherlands**

**<sup>b</sup>University of Groningen, Materials Science Centre, The Netherlands**

### **Abstract**

A novel method for laser welding for sheet metal is presented. This laser spike welding method is capable of bridging large gaps between sheet metal plates (gaps of more than 100% of the top plate thickness). Novel constructions can be designed and manufactured. Examples are light weight metal epoxy multi-layers and constructions having additional strength with respect to rigidity and impact resistance. Its capability to bridge large gaps allows higher dimensional tolerances of parts and positioning equipment. Furthermore higher yields can be obtained in view of the larger tolerances in production. The required laser systems are commercially available and are easily implemented in existing production lines. The lasers are highly reliable, the resulting spike welds are quickly realised and the cost price per weld is very low.

**Keywords:** Laser welding, spike, spot, penetration, gap, pulse shape, rivet, multi layer

## **1 Introduction**

With conventional laser penetration spot welding of sheet metal, process engineers often apply a relatively high laser power and short pulse time. Within a few milliseconds the weld spot is at vapour temperature and metal vapour or a plasma plume is created. When the recoil pressure from the plasma plume is above certain limits, a keyhole is created in the melt.

One of the objectives of the EU sponsored project CLAW (Clean and low distortion accurate welding of micro parts; see acknowledgement) is to develop a clean laser penetration spot welding process. A lower laser power and a longer pulse time leads to a heat conduction welding process. The melt stays just below the metal boil temperature and contamination of the product and the equipment is reduced by more than 90%.

During welding the specific volume of the melt increases by approximately 20%. In this way, using the heat conduction welding process, the maximum gap that can be bridged is limited to typically 30% (of the top plate thickness). Subsequently a new welding method was developed with which larger gaps can be bridged. The idea is to firstly create a quiet melt in the top plate. At the end of the laser pulse the melt is pushed towards the opposing plate. This is achieved with a 'spike', added to the heat conduction pulse (high laser power  $P > 1\text{kW}$ ; short pulse time,  $t < 0.3\text{ms}$ ). It was found that gaps of up to 100% and more of the top plate thickness can be bridged.

In production, parts with larger dimensional tolerances can be welded using this novel method. Further, it gives possibilities for mechanical engineers to create novel product designs in which large gap constructions are chosen for functionality reasons.

## **2 Equipment and materials**

### **2.1 APPLIED LASER**

A commercially available pulsed Trumpf Nd:YAG 124p laser was used for the experiments. The maximum laser power is 6kW, the maximum pulse time is 20ms and the minimum sector time is 0.1ms.

The generated laser light, with a wavelength of 1064nm, is transported through a 400 $\mu\text{m}$  diameter fibre. At the end of the fibre the intensity distribution is homogeneous or 'top hat'. With a standard optical system the laser spot size is imaged and enlarged to a 600 $\mu\text{m}$  spot diameter on the work-piece. A typical laser spike weld pulse-shape is shown in Figure 1, where a  $P=1.7\text{kW}$ ,  $t=0.2\text{ms}$  spike is added to a  $P=300\text{W}$ , 20ms basic pulse.

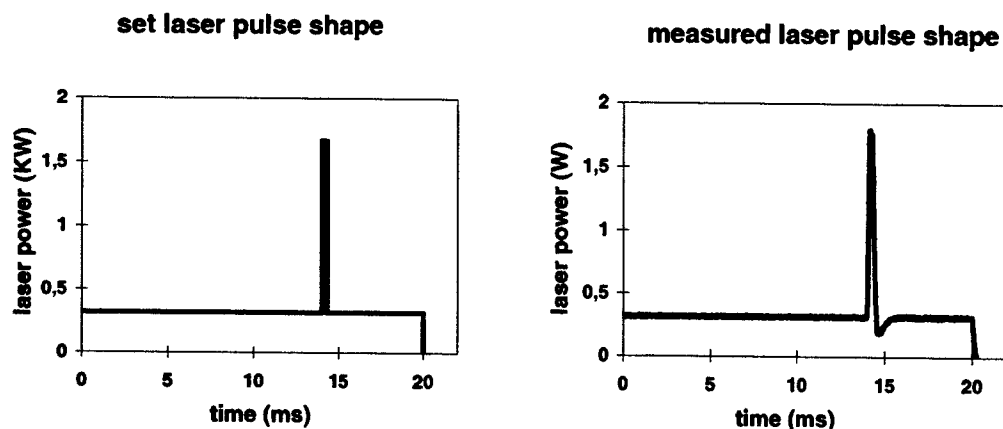


Figure 1 Typical spike weld profile: set profile (left) and measured profile (right) for the Trumpf HL124P laser.

## 2.2 MATERIALS

X8CrNi1812 stainless steel has been used for the experiments. The for this article relevant material properties for this material are: specific mass  $\rho(0)=7900\text{kg/m}^3$  and surface tension coefficient  $\gamma=1.87\text{N/m}$  (iron value).

Sheet metal spacers were applied to obtain the required gaps between the plates. In this study the distance between the edge of the spacer and the centre of the laser weld is approximately 1mm at maximum. The laser penetration spot weld geometry is shown in Figure 2 (cross section view).

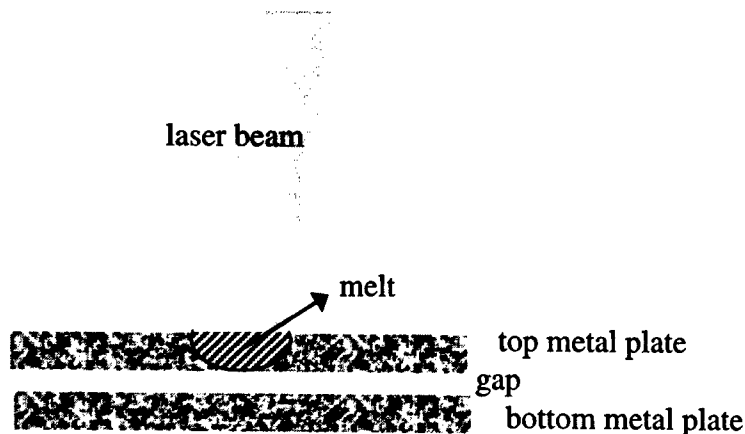


Figure 2 Geometry for laser penetration spot welding.

## 3 Spike pulse time estimation

### 3.1 INTRODUCTION

With spike-welding, a quiet heat conduction melt is first created throughout the top plate. Once the melt is obtained a metal vapour plume is created by applying a short, high power laser pulse. With high speed camera analysis it was determined that the resulting vapour plume height increases approximately linearly with time. This leads to a constant recoil pressure on the melt, pushing the molten material towards the opposite plate.

High speed camera recordings were performed with a Kodak EKTAPRO system. Illumination was done with an ILT Dioweld 50 laser. Figure 3 shows four high speed camera frames of a spike weld, being formed (laser beam comes from the left). At first a heat conduction melt is made in the top plate, after which the melt is pushed down on the bottom plate. The molten droplet wets the bottom plate as can be seen in the fourth frame.

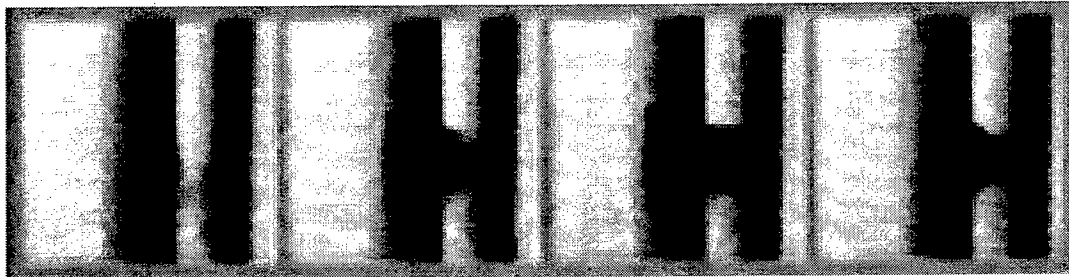


Figure 3 High speed camera recording showing how a spike weld is being made.

### 3.2 RESONANCE FREQUENCY

In order to estimate the required spike time, the resonance frequency of the melt is calculated. If the time constant of the melt is  $T$ , then the spike time  $t_s$ , should be typically equal to  $1/4 \cdot T$  to be fully efficient.

The surface melt contact area,  $A_m$  [ $m^2$ ], between melt and air is given by:

$$A_m = 2\pi \cdot (r_m^2 + a^2). \quad (1)$$

where:

$r_m$  [m] radius of the melt  
 $a$  [m] amplitude of the melt

The surface free energy of the melt is given by:

$$E_\gamma = A_m \gamma = 2\pi \cdot \gamma \cdot (r_m^2 + a^2). \quad (2)$$

where:

$\gamma$  [N/m] surface tension

The force constant  $K_m$  [N/m], of the melt is given by:

$$K_m = \frac{\delta^2 E}{\delta a^2} = 4\pi \cdot \gamma. \quad (3)$$

The mass of the melt  $m_m$  [kg], is given by:

$$m_m = \rho_0 \cdot V_0 = \pi \cdot \rho_0 \cdot h \cdot r_m^2. \quad (4)$$

where:

$\rho_0$  [ $kg/m^3$ ] stainless steel specific mass at room temperature  
 $V_0$  [ $m^3$ ] volume of metal to be molten  
 $h$  [m] plate thickness

Combining of equations 3 and 4 finally leads to:

$$f_m = \frac{1}{2\pi} \sqrt{\frac{K_m}{m_m}} = \frac{1}{\pi \cdot r_m} \sqrt{\frac{\gamma}{\rho_0 \cdot h}}. \quad (5)$$

For a laser pulse of  $P=300W$ ,  $t=16ms$ , the resulting melt radius at the bottom side of the top plate is typically  $r=275 \cdot 10^{-6}m$ . When  $h=250 \cdot 10^{-6}m$ , this leads to  $f_m=1033Hz$ , so the oscillation period of the melt is  $T_m=0.97ms$ . With a  $P=1500W$ ,  $t=0.2ms$  spike, the values  $T_m$  and  $f_m$  are determined with a high speed camera:  $T_m=0.87ms$  and  $f_m=1149Hz$ . So for an effective spike weld, the pulse length of the spike should be 0.2-0.3ms at maximum.

## 4 Process and design opportunities

The above described laser spike weld technique will increase process as well as product design opportunities.

### 4.1 PROCESS OPPORTUNITIES

With the laser penetration spike-welding method, very large gaps can be bridged in production. Variable gaps are the result of dimensional tolerances of parts and tool positioning equipment. Figure 4 shows cross sections of spike welds in 250 $\mu$ m thick X8CrNi1812 stainless steel.

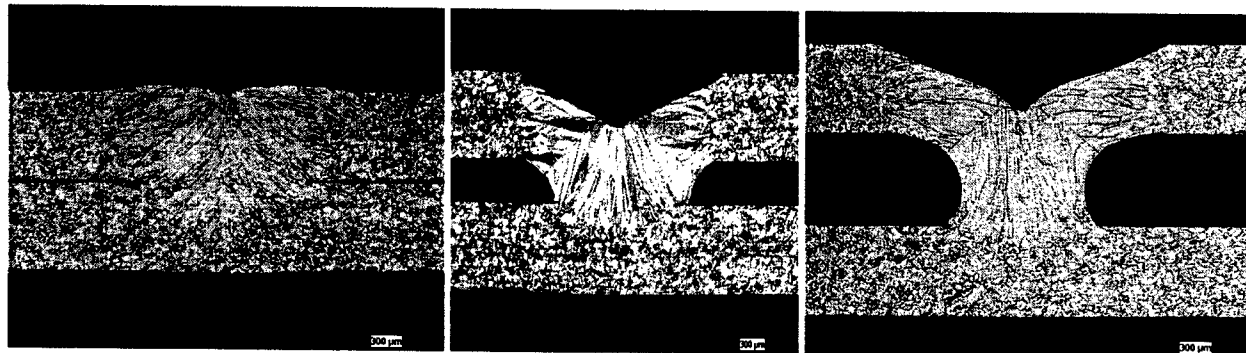


**Figure 4** Cross-sections of laser penetration spike welds in 250 $\mu$ m thick sheets of X8CrNi1812 stainless steel. All welds have been made with the same laser pulse-shape.

The gaps are 0% (20 $\mu$ m), 50% (125 $\mu$ m) and 100% (250 $\mu$ m) of the top layer thickness. The yield strengths are 98N, 75N and 53N respectively. All welds have been made with the same energy  $E=6.7$ J. The pulse-shape is:  $t=0-14$ ms,  $P=325$ W;  $t=14-14.3$ ms,  $P=1650$ W;  $t=15.3-20$ ms,  $P=325$ W, laser spot diameter is 600 $\mu$ m. The spike creates a narrow, approximately 10mm high plasma plume

If the largest gap expected in production circumstances is only 50%, the spike power can be reduced to approximately  $P=825$ W. In this way, the plasma plume contamination from the spike is reduced by a factor of 2. If the largest gap expected is 20% or less, the spike can be omitted, resulting in a zero plasma plume.

It was found that spike welding is a very robust process. The observation is that once the melt touches the bottom plate, it will always wet the bottom plate repeatably and create a repeatable weld strength, depending only on the gap. The spike can be set a few ms earlier or later in the pulse-shape without causing problems. The spike height and width can also be altered by typically 10% and 30% and still create a reliable weld. The optimum ratio of laser spot diameter to sheet metal plate thickness is determined to be 1.5 to 2.5. However, 600 $\mu$ m sheet metal has been spike welded with a 600 $\mu$ m laser spot diameter, leading to a ratio of 1. In that case a longer 40ms basic pulse time is necessary to firstly create the through melt in the top plate. The spike can then be given at 39ms. For this experiment a modified Trumpf laser was applied which can produce pulses up to 40ms.

### 4.2 DESIGN OPPORTUNITIES

A first example is a sheet metal multi-layer, see Figure 5. The plates are welded on top of each other, one by one. With a temporary sheet spacer the gap width is set prior to welding. This is important since, when the spacer is omitted, the gap in between the plates shrinks by roughly 20% during cooling. No costly spacer parts have to be left inside the product and the spacers can be reused for the next weld.

Application possibilities are ridged and light weight constructions, where the multi-layer can be filled with epoxy. This can be of relevance for the aviation industry. The multi-layer construction could also serve as an active heat shielding plate in generators or car engines. A multi-layer construction can also be applied for quick cooling of liquids in the food process industry.

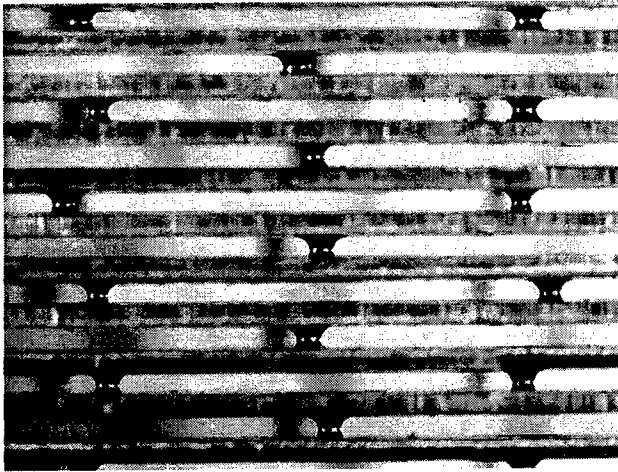


**Figure 5** Lightweight, rigid and impact resistant multi layers can easily be obtained. Stiffness is increased when the space in between the plates is filled with epoxy.

A second example is shown in Figure 6. Here the spike weld serves as an axis in a hinge or sliding plate construction. It was determined experimentally that the tolerances between hinge and middle plate is about 100 $\mu$ m at minimum. The construction is cheap since no additional screws and spacers are required.

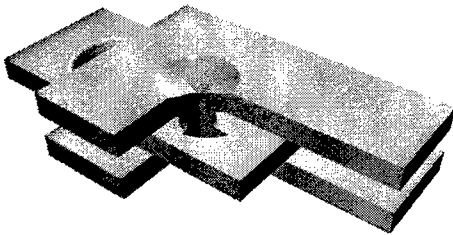
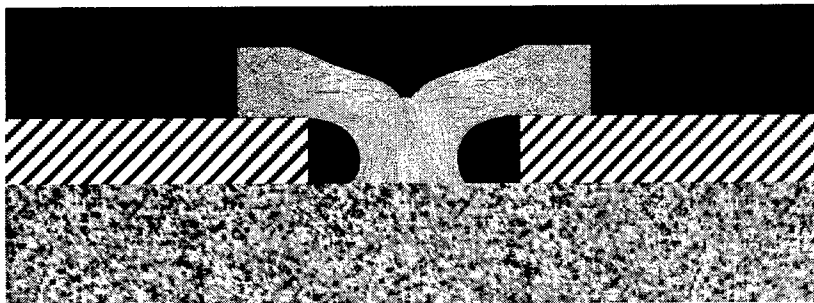


**Figure 6** The spike weld serves as an *axis* in a hinge or a sliding plates construction.

A third example is shown in Figure 7. One or more 'laser rivets' can be applied to connect sheets of plastic or ceramic to a metal base. The metal rivet is simply a cheap metal disc, spike welded to the metal base.



- metal rivet disc
- plastic / ceramic / metal
- metal base

**Figure 7** A metal rivet, obtained with spike weld technique, connecting a sheet (ceramic / plastic / metal) to a metal base.

## 5 Conclusions

A novel laser penetration spot weld method is presented. With this so called 'spike-welding', welds can be made even if the gap in between the metal plates is up to 100% of the top plate thickness. Compared to conventional keyhole laser penetration welding this is an increase by a factor 2.5-5.

Laser spike weld technology offers new and cheap process and product design opportunities:

- 1) *Process opportunities*: Parts with larger dimensional tolerances can be spike welded with less accurate parts positioning equipment (more robust weld processes and process cost reduction).
- 2) *Design opportunities*: Novel and cheap designs can be realised a) connection of sheet plastic or ceramic to a metal base with a spike weld rivet. b) a hinge construction can be made where the spike weld serves as an axis. c) ridged and impact resistant multi-layers can be realised.

## Acknowledgement

The authors wish to thank J.W. Weekamp, N.J.A. van Veen and S.B.J. Flury of Philips CFT for useful discussions. Further the authors would also like to thank H.J. Bos, F.C. Horstmeier and D. Trajkovic, former students of the University of Groningen, Materials Science Centre for heat flow calculations and experiments. Finally the authors thank A. Olowinsky and T. Kramer of the Fraunhofer Institute fur Laser Technology, Aachen for using their high speed camera.

This research was part of the EU funded Brite EuRam project CLAW, 'Clean and Low distortion Accurate Welding of micro parts', 1998 to 2001, Contract No. BRPR-CT98-0643, Project No. BE-4855.

Laser spike-welding is a patent pending technology.

## References

- [1] Laser penetration spike welding, D.K. Dijken, W. Hoving, J.Th.M. De Hosson, Journal of Laser Applications, to be published, 2002.

<sup>a</sup> [d.k.dijken@philips.com](mailto:d.k.dijken@philips.com), [w.hoving@philips.com](mailto:w.hoving@philips.com); phone +31 40 273 3845; <http://www.cft.philips.com>; Philips Electronics, Centre for Industrial Technology, Glaslaan 2, P.O. Box 218, 5600 MD Eindhoven, The Netherlands.

<sup>b</sup> [hossonj@phys.rug.nl](mailto:hossonj@phys.rug.nl); phone +31 50 363 48981; <http://www.phys.rug.nl/mk/index.html>; University of Groningen, Department of Applied Physics, Materials Science Centre, Nijenborgh 4, 9747 AG Groningen, The Netherlands.

# Overview and Future Prospects of the Use of Lasers for Packaging by Microelectronics and Photonics Industry in Japan

Kunihiko Washio<sup>\*a</sup> and Hikaru Kouta<sup>\*\*b</sup>

<sup>a</sup> Control Systems Operations Unit, NEC Corporation

<sup>b</sup> Functional Materials Research Laboratories, NEC Corporation

## ABSTRACT

This paper presents an overview and future prospects of the use of lasers for packaging by the microelectronics and photonics industry in Japan. Various kinds of lasers and material processing technologies have been developed and applied for manufacturing electronic and photonic devices to meet the strong demands for high-performance, lightweight, low energy-consumption mobile digital consumer electronics, broadband optical fiber communications, low-emission and fuel-efficient, easy-to-steer smart cars, etc. This paper emphasizes solid-state lasers as convenient and versatile light sources for packaging advanced compact devices with sensitive passive or active components having small feature sizes. Some of the representative material processing applications using solid-state lasers for electronic and photonic devices are, opaque and clear defects repairing of LCDs, trimming of functional modules, fine-tuning of optical characteristics of photonic devices, forming of various micro-vias for high-density interconnection circuits, laser patterning of amorphous solar-cells, and high-precision laser welding of electronic components such as optical modules, miniature relays and lithium ion batteries. The recent progress in high-power ultra-short pulse solid-state lasers seems to be rapidly increasing their processing capabilities such as for fine adjustment of optical filters, etc.

**Keywords:** packaging, welding, trimming, drilling, patterning, marking, annealing, repairing, photonic devices, lasers

## 1. INTRODUCTION

Laser materials processing has several excellent features, which are increasingly satisfying industry's requirements such as for high-speed, high-precision, clean and flexible processing technologies for swift delivery of high-value added innovative products with minimized or reasonable costs.

Various laser materials processing technologies have been developed and been applied for manufacturing electronic and photonic devices, because of their widely different requirements for treating thin-films, thick-films, metals, polymers, ceramics, optical glasses, etc<sup>1</sup>. Owing to the recent increased demands for light-weight, broad-band and mobile electronic appliances with high-speed internet access capability, such as advanced cellular phones, digital still cameras, note PCs (personal computers), portable digital assistants (PDAs), fine laser materials processing based on compact and highly-stabilized pulsed lasers are becoming vital and indispensable technologies for the development and manufacturing leading-edge products in electronics and photonics industry. High-precision welding is used for fabrication of parts or assembling of wide variety of electric and photonic components. Compact and highly efficient diode-pumped and Q-switched solid-state lasers in second or third harmonic operation mode as well as in fundamental wave mode are now being increasingly incorporated in various laser materials processing systems such as for repairing, marking, drilling and patterning. Excimer lasers are being extensively utilized in lithography and annealing. Emerging technologies based on ultra-short pulse lasers seems to be very promising for fabrication or fine-tuning of novel optical waveguide devices for broadband optical communications.

This paper briefly summarizes what parts or devices are utilizing what kinds of laser materials processing and what kinds of lasers are currently preferably utilized. Detailed explanation will be given on the technological state of the arts and trends in the use of lasers for packaging by microelectronics and photonics industry in Japan.

\* k-washio@az.jp.nec.com; phone +81-3-3798-8461; fax: +81-3-3798-6339; Control Systems Operations Unit, NEC Corporation, 5-7-1 Shiba, Minato-ku, Tokyo, 108-8001, Japan; \*\* h-kouta@bu.jp.nec.com; phone +81-44-856-2167; fax +81-44-856-2245; Functional Materials Research Laboratories, NEC Corporation, 4-1-1 Miyazaki, Miyamae-ku, Kawasaki, 216-8555, Japan

## 2. SUMMARY OF REPRESENTATIVE APPLICATIONS

Some representative applications of laser materials processing used for packaging by electronics and photonics industry are summarized in Table 1. With a glance at Table 1, it can be safely said that almost all present-day leading-edge broad-band and mobile or multimedia electronic appliances are at least utilizing some devices treated with laser material processing. For example, key devices such as LSIs, thin-film transistor (TFT)-LCDs, multi-layer build-up circuit boards, lithium ion batteries, optical modules, are increasingly utilizing some kinds of laser materials processing.

Table 1. Representative applications of laser materials processing used for packaging by electronics and photonics industry

Classification	Components or devices	Applications of laser materials processing	Typical lasers used
Semiconductor devices	LSIs (DRAMs) Optical modules IC Packages CSP IC packages	Memory repairing High precision spot welding IC package marking Interposer micro-via drilling	Q-switched solid-state lasers Pulsed Nd:YAG lasers Q-switched solid-state lasers Q-switched solid-state lasers
Display devices	TFT-LCDs Color filters for LCD Poly-Si TFT-LCD TV tubes	TFT-LCD repairing Color filter repairing Low temperature excimer laser annealing High precision electron-gun spot welding	Q-switched solid-state lasers Q-switched solid-state lasers XeCl excimer lasers Pulsed Nd:YAG lasers
Electric and photonic circuit components	Chip resistors Capacitors Quartz oscillators Printed circuit boards Relays Component packages Optical waveguide devices	Resistor trimming Electrode terminals welding Quartz oscillator tuning Build-up circuit board via drilling Assembling by laser spot welding Component package marking Refractive index modification	Q-switched solid-state lasers Pulsed Nd:YAG lasers Q-switched solid-state lasers Pulsed CO <sub>2</sub> lasers Pulsed Nd:YAG lasers Nd:YAG or CO <sub>2</sub> lasers UV or ultra-short pulse lasers
Peripheral devices	Micro-motors Hard disk sliders Ink-jet printer heads Key boards, key pads	Magnetic-core thin-plates seam welding HD slider suspension spot welding Ink-jet printer nozzle drilling Laser marking	Pulsed Nd:YAG lasers Pulsed Nd:YAG lasers KrF or ArF excimer lasers Q-switched solid-state lasers
Energy devices	Lithium ion batteries  Amorphous silicon solar-cell modules	Seam welding of battery cases and electrode terminal spot welding Laser patterning of amorphous silicon solar cell modules	Pulsed Nd:YAG lasers  Q-switched solid-state lasers

## 3. TYPICAL LASERS USED IN ELECTRONICS AND PHOTONICS INDUSTRY

As shown in Table 1, various kinds of lasers in the wavelength range from deep UV to mid infra-red (IR) are used in electronics and photonics industry depending on the applications. Typical lasers used in the electronics and photonics industry have average powers in the range from one-tenth of watts to several hundred watts. For micro-welding applications, pulse-pumped Nd:YAG lasers with fiber beam delivery with pulse widths in the range from one-tenth of milliseconds to tens of milliseconds are commonly utilized. However, for processing thin-film or thick-film devices, high-peak power and short pulse Q-switched solid-state lasers having peak power exceeding 10kW and pulse widths below 100 ns are most frequently used to reduce heat-affected zone and attain highly precise material removal or surface treatment. Typical solid state lasers used are either Nd:YAG, Nd:YLF, or Nd:YVO<sub>4</sub> lasers. They are used either in fundamental (IR) operation mode or in second harmonic (green), or third and higher harmonic (UV) operation mode. For Q-switched laser applications, compact and highly efficient diode-pumped solid-state lasers in second or third harmonic operation mode as well as in fundamental wave mode are now being preferably utilized than lamp-pumped lasers. UV or deep UV excimer lasers are extensively used for low-temperature annealing of poly-silicon devices, ink-jet printer nozzle drilling, etc. Short pulsed CO<sub>2</sub> lasers are increasingly used for build-up circuit board via drilling, plastic package or paper label marking, etc. For low power application of CO<sub>2</sub> lasers, RF-excited waveguide type lasers are predominantly utilized. For novel optical waveguide device fabrication by refractive index modifications, deep UV excimer lasers or ultra-short pulsed lasers are emerging as promising candidates.



## 4. REPRESENTATIVE APPLICATIONS AND TECHNOLOGICAL TRENDS

### 4.1 Laser welding

#### 4.1.1 Laser spot welding

Laser spot welding is well suited for assembling precise electronic or photonic components accurately with high throughput. Laser spot welding is useful not only for miniaturization but also for accurate and secure connection. Laser spot welding has been extensively utilized for assembling electronic guns for TV tubes, fiber-optical devices such as LD (laser diode) modules<sup>2,3</sup> and polarization beam combiners<sup>4</sup>, etc., miniature power relays<sup>5</sup> and signal relays<sup>6</sup>, ultra-light and thin suspensions for hard-disk head sliders, etc. Figure 1 shows an example of miniature power relays<sup>5</sup> for automotive motor control application assembled by laser spot welding. About 40% volume reduction has been obtained as compared with the conventional model. As for miniature signal relays, the productivity and reliability were remarkably improved by introducing laser welding as a joining method for the coil terminal and hinge spring<sup>6</sup>. Further application of laser welding technology to contact points, coil winding terminals, high-conductive materials are being examined for further miniaturization and higher reliability of the relays. Laser spot welding is also applied for joining terminal tabs or leads to lithium batteries as shown in Fig. 2, double-layer capacitors, etc. to attain enough joining strength with minimized heating effects to the internal compounds. In order to miniaturize tantalum chip capacitors down to 1608-size, face down terminals tantalum chip capacitors as shown in Fig. 3, have been developed by introducing laser spot welding for joining the anode terminal and anode lead wire<sup>7</sup>. An average joint strength of laser-welded parts has been measured to be more than two-fold higher as compared with that obtained by conventional resistance welding method.

Owing to the rapid progress in information technology, requirements for optical modules to be used in optical fiber telecommunication systems are appreciably becoming sophisticated and demanding. To meet the stringent requirements for highly reliable and stable optical modules, an advanced mini-laser welder, M800C, specially designed for low post-weld shift, high precision spot welding<sup>8</sup>, has been developed. This laser equipment has features in highly-stabilized laser output power, digital pulse shape control and highly-balanced beam dividing for simultaneous three-point welding as shown in Fig. 4. It can deliver equally divided three beams with less than  $\pm 1.0\%$  error for the typical output range used for spot welding.

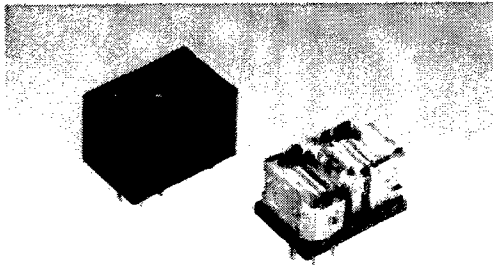


Fig. 1 Miniature power relays for automotive application.

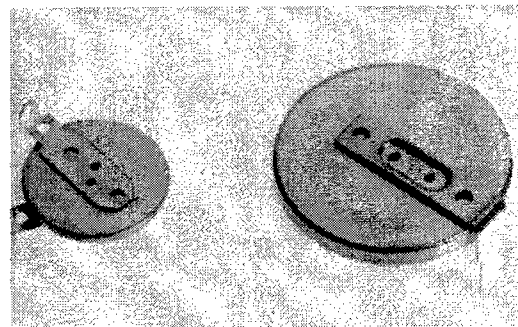


Fig. 2 Lithium batteries with laser-welded terminal tabs.

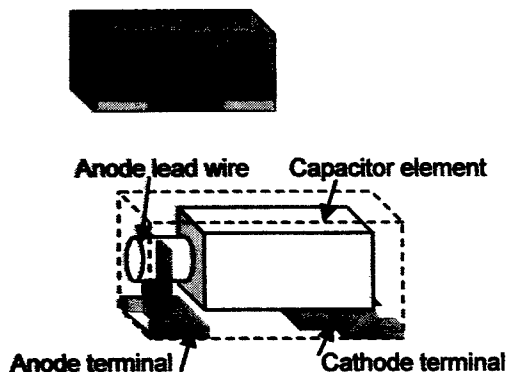


Fig. 3 Structure of novel small tantalum capacitor

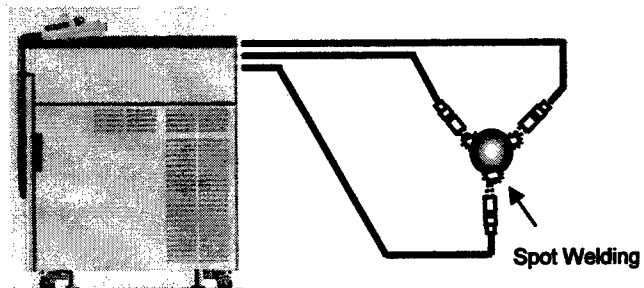


Fig.4 Simultaneous three-point spot welding for optical modules.

#### 4.1.2 Laser seam welding

Pulsed Nd:YAG laser based seam welding has been extensively utilized in assembling prismatic lithium-ion battery cells, fuel injectors, pressure sensors, magnetic cores for miniature motors, etc. High-power, high-repetition rate pulsed laser enables high-precision and high speed seam welding. For seam welding for joining various electronic parts, Nd:YAG lasers, having average power in the range from 200W to 1200W, peak power in the range from 5 kW to 20 kW and maximum pulse repetition rate up to 500 pps, are dominantly utilized. Figure 5 shows an example of prismatic lithium-ion battery seam welded by pulsed Nd:YAG laser. Leak-free, excellent welding quality has been obtained with good surface bead appearance, without causing any serious deterioration of heat sensitive chemical components. Methods for penetration instability prevention have been investigated for seam welding of A3003 aluminum alloy<sup>9-10</sup>. Pulse shaping has been found very effective to improve the quality of aluminum welding in suppression of cracks and imperfect joining. Miniature thin-plate stacked parts such as micro-motor cores, magnetic head cores, etc. have been mass produced by FASTEC® technology (Fastening and Skewing TECHNOlogy of KURODA), utilizing Nd:YAG laser seam welding in a high-speed automatic press system<sup>11</sup>. Micro-motor cores with diameter as small as 2 mm have been manufactured as shown in Fig. 6.

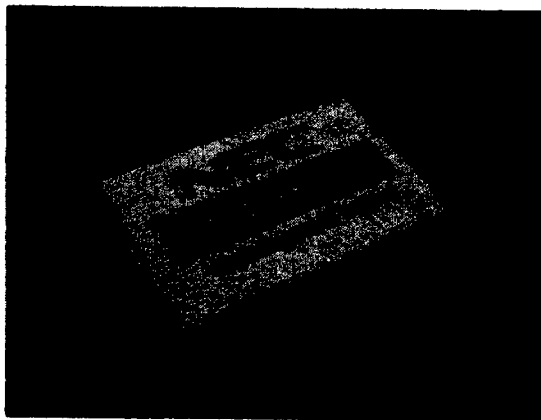


Fig.5 External view of battery seam welded by laser.

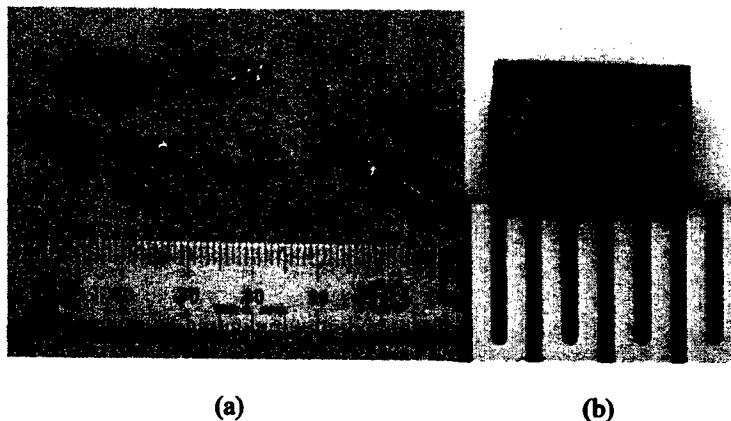


Fig.6 Micro-motor cores fabricated by laser seam welding of stacked thin plates. (a) External view; (b) Magnified view. (Photo: courtesy of KUDADA).

#### 4.2 Laser Trimming

Owing to the increased demands for portable and compact electric appliances such as cellular mobile phones, digital cameras, notebook PCs, etc. laser trimming markets such as for smaller chip size resistors, ultra-low resistance chip resistors for current monitoring, and voltage controlled oscillators (VCOs) have expanded. Currently, dominantly mass-produced thick-film resistor chip size seems to be shifting from 1608 (1.6mm×0.8mm) to 1005 (1.0mm×0.5mm) size and the production share of novel 0603 (0.6mm×0.3mm) size is noticeably increasing. A high speed and high precision laser trimmer NEC SL436H, equipped with 6W average-power diode-pumped Nd:YAG laser having pulse width control function, has recently been developed for small chip size resistors<sup>12</sup>. Figure 7 shows a scanning electron microscope (SEM) photograph of laser trimmed thick-film 0603 type resistor. Figure 8 shows an example of copper film cutting on glass epoxy substrate with 532-nm, frequency-doubled Nd:YAG laser for inductance adjustment of a high-frequency circuit.



Fig. 7 SEM photograph of laser trimmed thick-film 0603 type chip resistor. Kerf width: ca. 20  $\mu$ m.

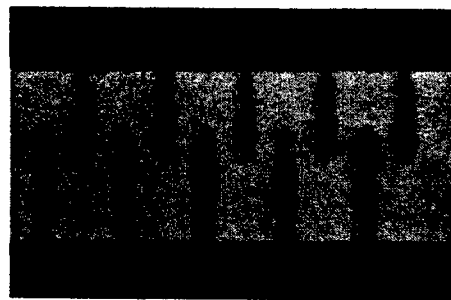


Fig. 8 Cutting of Cu-film on glass epoxy substrate. Thickness: 40  $\mu$ m.

For applications of field trimming after packaging, especially designed trimmable chip resistors and chip capacitors have been developed by several manufacturers. As for thin film trimmable chip resistors, the resistive metal thin film is oxidized by Nd:YAG laser and turns into insulation material. The passivation coat material over the resistive film is 99 % transparent for Nd:YAG laser. Therefore there is no damage on passivation material and no further process is required<sup>13</sup>.

#### 4.3 Laser via drilling

Build-up printed circuit boards are extensively utilized in portable and personal digital electronic appliances such as cellular mobile phones, PDAs, digital video cameras (DVCs) and digital still cameras (DSCs). Laser via drilling is increasingly and preferably utilized with pulsed CO<sub>2</sub> lasers for drilling smaller vias in the range 70-150  $\mu$ m in diameter. Efforts are being made to expand the capability of pulsed CO<sub>2</sub> lasers toward drilling with lesser residue on the via bottom, direct drilling of copper layer, drilling very small-diameter vias below 50  $\mu$ m, or drilling very large-diameter vias exceeding 500  $\mu$ m, etc. By utilizing recently developed high-peak power, short-pulse CO<sub>2</sub> lasers, large-diameter drilling of epoxy resin up to 700  $\mu$ m, direct copper layer drilling and small via drilling as small as 40  $\mu$ m in diameter have been demonstrated<sup>14</sup>.

Micro-via drilling with repetitively pulsed UV lasers such as frequency-tripled (THG) Nd:YAG Q-switched lasers is particularly interesting for smaller via drilling and excellent via shape without bottom layer residue problem, owing to the excellent focusability and higher absorption coefficients of metal and organic materials. A production process consisting of full-additive process for narrower-pad pitch, ultra-high density build-up printed wiring board has been developed by utilizing the Nd:YAG THG laser<sup>15</sup>. Fig. 9 shows the cross sectional view of the 50- $\mu$ m diameter via fabricated using 355nm Nd:YAG THG laser. Corresponding design rule for the ultra-high density build-up substrates are, minimum via/land diameter of 50/75  $\mu$ m and circuit line and space of 25/25  $\mu$ m. Since UV Nd:YAG THG lasers are capable of micro-via drilling down to below 25  $\mu$ m in diameter, they will be increasingly utilized in the near future.

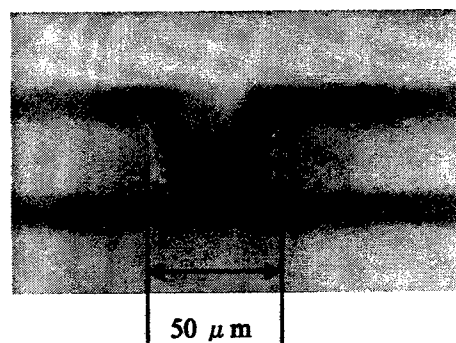


Fig.9 Cross sectional view of 50- $\mu$ m diameter size via fabricated using 355nm Nd:YAG THG laser<sup>15</sup>.

#### 4.4 Laser marking

Laser marking seems to be the largest application segment in electronics industry, if installed numbers of laser systems are compared among various laser material processing applications. Continuously pumped and Q-switched Nd:YAG lasers are preferably utilized for marking various IC molded packages than CO<sub>2</sub> lasers because of their capability of fast and flexible marking with good visibility. Diode-pumped Nd:YAG lasers are preferably utilized for high precision marking because of their excellent beam quality, reliability, controllability and compactness. For marking silicon wafers, there are two types of laser marking technologies, i.e., hard marking and soft marking. Fig. 9 shows an example of hard marking with 1.06  $\mu$ m fundamental Nd:YAG laser<sup>16</sup>. Maximum hard marking depth is about 150  $\mu$ m in practice. Soft marking without splash and debris, as shown in Fig. 10, is performed by using frequency-doubled Nd:YLF lasers<sup>16</sup>.

Figure 11 shows an external view of diode-pumped, general-purpose scanning-type laser marker SL577A having average power of 20W at 10kHz Q-switch repetition rate. With a new type beam scanner, this compact Nd:YAG laser marker can do high-definition marking up to 300 characters/s<sup>17</sup>.

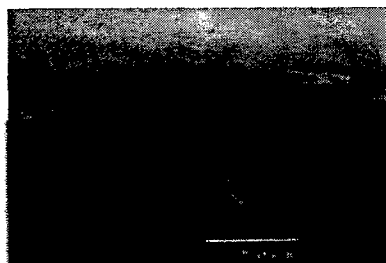


Fig. 9 Cross sectional view of hard marking. Marking depth: 60  $\mu$ m.

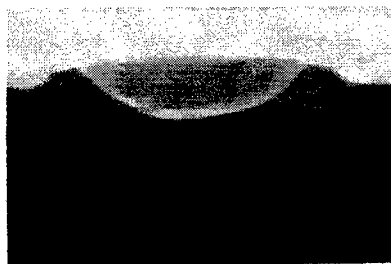


Fig.10 Cross sectional view of soft marking. Marking depth: 6  $\mu$ m.

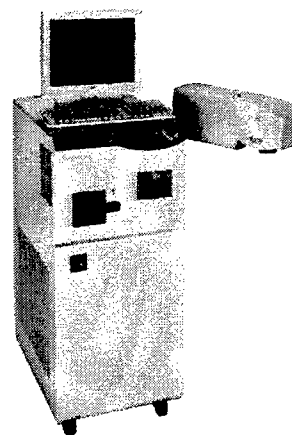


Fig.11 Diode-pumped laser marker SL577A (NEC).

#### 4.5 Laser annealing of TFT

Low-temperature poly-Si (LTPS) TFT LCD has several advantages such as capability of integrating a peripheral driver circuit, achieving higher pixel density and realizing larger aperture ratio as compared with amorphous silicon TFT LCD, owing to its higher electron and hole mobilities realized by excimer laser annealing (ELA) process. ELA can convert amorphous Si layer to polycrystalline Si at low substrate temperature under  $430^{\circ}\text{C}$ , much lower than high-temperature poly-Si (HTPS) technology which requires quartz substrates, thus enabling use of inexpensive, large-size glass substrates. LTPS TFT LCD has initially found rapid and wide spread applications for digital still cameras and digital video camcorders. Now, applications of LTPS TFT LCD have much more diversified, including applications to notebook PCs with larger display size<sup>18-19</sup> and applications to mobile equipment with higher display resolution and lower power consumption<sup>20</sup>. Recently, world's largest class 14.1-class XGA ( $1024 \times 768$ ) LTPS TFT LCD has been developed by Toshiba for commercial notebook PCs<sup>19</sup>. Since most LCD drivers can be integrated directly on the display panel, LTPS TFT LCD can reduce the number of components in the LCD module by 40 % and also reduce the number of connections between drivers IC's and electrodes on the panel by 95%<sup>19</sup>. NEC has developed an ultra high-resolution (230ppi) LTPS TFT reflective LCD for mobile applications<sup>20</sup>. It has  $360 \times 480$  pixels for the 2.6-inch display size. The LCD-module power consumption was about 15 mW at a frame frequency of 30Hz and it was reduced to 1.7 mW with the newly developed partial driving method.

To further decrease the process temperature below  $300^{\circ}\text{C}$  for LTPS for next generation poly-Si based applications, sputtering technology of Si films has been investigated<sup>21</sup>. TFT mobility characteristics of excimer-laser annealed poly-Si TFTs fabricated with sputtering technology at substrate temperature as low as  $100^{\circ}\text{C}$  have been investigated.

#### 4.6 Laser repairing of LCD

General trends of LCD fabrication technologies are oriented toward larger-size display with smaller pixel feature sizes for higher resolution. In the LCD fabrication processes, various kinds of specially designed LCD repairing systems have been developed for TFT-array-fabrication-, cell-assembly- and module-assembly stages<sup>22</sup>. There are two kinds of basic repairing technologies, namely, zapping (material removal) for repairing short-circuit defects or foreign particle inclusion defects and CVD (chemical vapor deposition) for repairing open-circuit defects or transparent bright defects in color filters, etc.

Figure 12 shows general technological trends and an NEC's road map of LCD repairing systems<sup>22</sup>. Owing to the rapid increase in the LCD glass substrate sizes, the accommodation capability of repairing systems are also increasing rapidly. Furthermore, to meet the strong demands for finer high-precision processing, irradiation wavelengths are shifting toward shorter laser wavelength to UV region, around 355 nm, for example. In Fig. 12, standard SL455 series are for zapping function without CVD repairing function. On the other hand, standard SL465 series have both zapping and CVD functions.

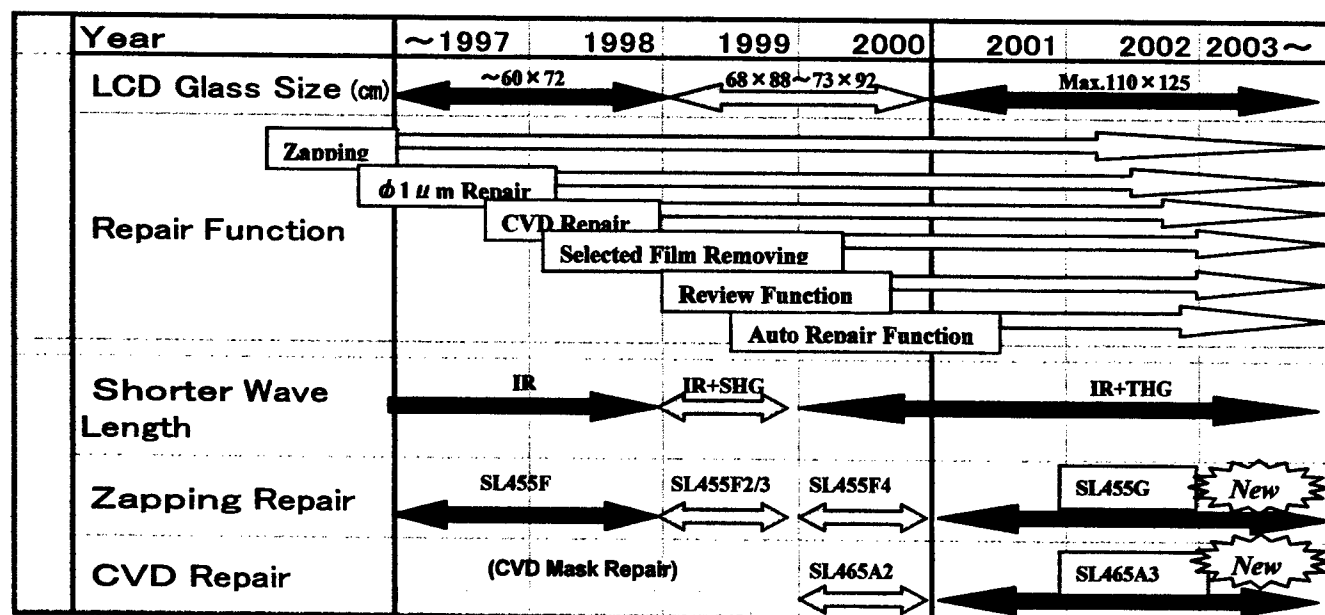


Fig. 12 Road map of LCD repairing systems (NEC)

For CVD processing for large-size glass substrates, elimination of bulky gas chamber and reduction of equipment size, weight and time-consuming large-volume gas evacuation are prerequisite for increasing throughput with lower cost. To meet the requirement of the high throughput for repairing by laser CVD, NEC has developed a unique gas-curtain type processing unit as shown in Fig.13<sup>23</sup>. Deposited films having good electrical conductivity and adhesion for repairing LCD substrates have been obtained. Fig. 14 shows an example of about 5  $\mu$ m width deposited tungsten thin-film by laser CVD for circuit wiring<sup>24</sup>.

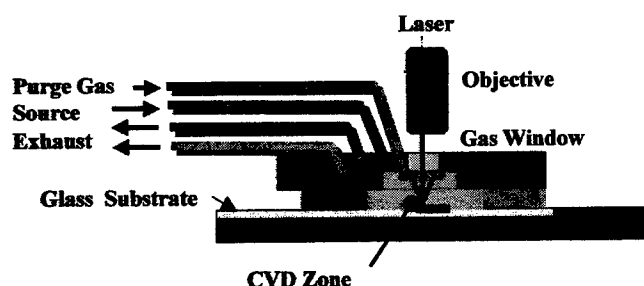


Fig. 13 Sectional structure of gas-curtain-type processing unit.

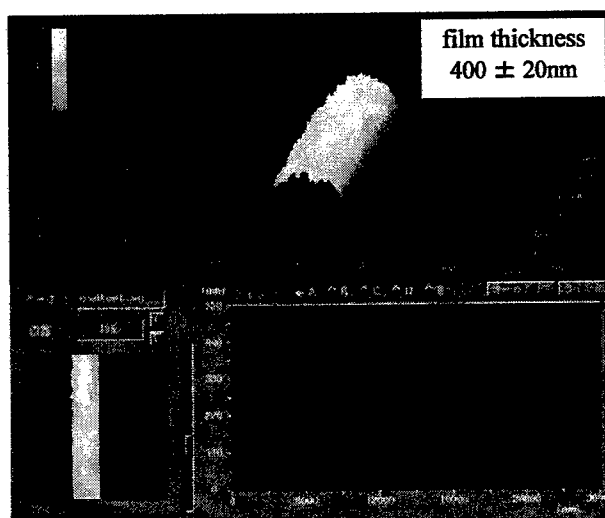


Fig. 14 Deposited tungsten thin-film thickness measurement result by AFM.

#### 4.7 Laser processing of optical waveguide devices

Glass or silica-based planar lightwave circuits (PLC) provide various important devices for both optical wavelength-division multiplexing networks and optical access networks<sup>25</sup>. Nowadays, applications of femtosecond lasers processing to transparent materials for localized two- or three-dimensional refractive-index modification have attracted wide interests for advanced photonic device fabrication<sup>26</sup>. In the following, two kinds of recently made experimental studies on direct writing of optical waveguides and precise tuning of refractive index in an optical waveguides are briefly introduced.

##### 4.7.1 Laser direct-writing of waveguide in silica glass

Figure 15 shows an example of two curved waveguides directly written in silica glass by using 800nm wavelength Ti:sapphire laser having 50 fs pulse width and 400 nJ pulse energy at 250 kHz repetition rate<sup>27</sup>. The laser beam was focused by using a microscope objective lens with NA of 1.3 and  $\times 63$  magnification. The writing speed is about 1mm/s. Figure 16 shows an example of Y-branch written by using the same femtosecond laser. Transmission loss of directly-written optical waveguides as low as 0.2 dB~0.3dB/cm at wavelengths for optical communications have so far been obtained<sup>27</sup>. Such direct-writing of optical waveguides seems to have a variety of applications for optical device customization.

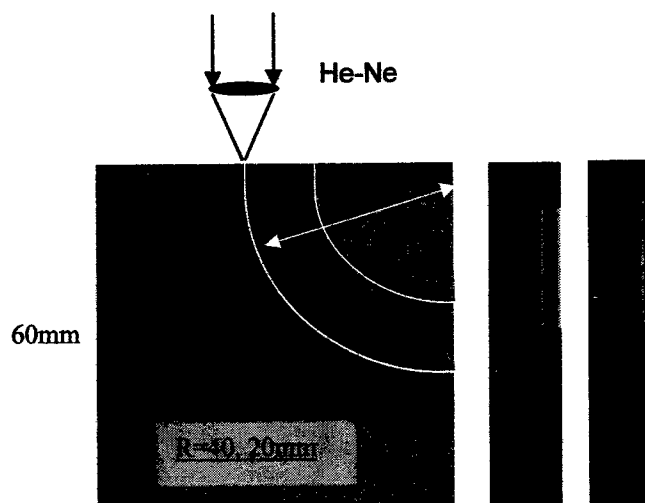


Fig. 15 Light transmission through directly-written waveguides.



Fig. 16 Directly-written optical waveguide Y-branch

##### 4.7.2 Refractive indices adjustment in optical waveguides

There are various optical devices such as optical filters utilizing Mach-Zehnder (MZ)-type interferometers in which precise optical length adjustment and subsequent stabilization of phase-shift are vitally important for obtaining high performance. Use of focused beam of infrared ultra-short pulse laser having 150 fs pulse width, 200 kHz repetition rate, and 800nm wavelength, has been investigated to controllably increase the refractive index of germanium-doped silica planar waveguides<sup>28</sup>, with particular attention to the questions of resultant occurrence of any-induced insertion loss and the thermal stability of the refractive index after ultra-short laser pulse irradiation.

Figure 17 shows a schematic of a portion of MZ PLC device to measure the optical phase shift and the refractive change due to the laser pulse irradiation. The laser irradiated length  $\Delta l$  is about 2mm. The PLC (width 32 mm) has two ports and a 3dB directional coupler on each ends. The amplified spontaneous emission (ASE) light from an Er-doped fiber (1530-1580 nm) was used as a broadband light source and the transmission spectra of the output light was measured with an optical spectrum analyzer at a resolution of around 0.05 nm. Figure 18 shows an example of transmission spectra with and without femtosecond laser pulse irradiation. The laser beam was focused through a microscope objective lens having either x10 or x20 magnification. The writing speed was kept at 100  $\mu$  m/s.

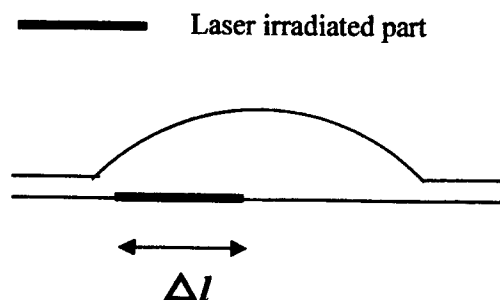


Fig. 17 Schematic of the portion of MZ PLC device.

The refractive index change  $\Delta n$  (increase) was calculated from the optical phase shift. The refractive index change was measured for both TE and TM modes by changing the average laser power from several tens of up to over 300 mW as shown in Fig. 19. For a x20 lens,  $\Delta n$  quickly increased to  $1.6 \times 10^{-3}$  (at 135mW) and then, at a reduced rate of increase, to a saturated value of  $1.8 \times 10^{-3}$  (325mW). The difference in  $\Delta n$  between TE and TM modes was found small and is less than 2%, when the laser power was higher than 260 mW, as shown in Fig. 19.

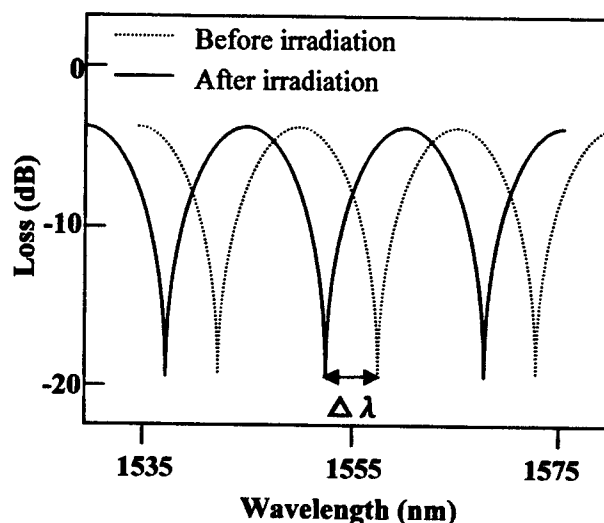


Fig. 18 Change of transmission spectra in MZ PLC.

Change of insertion loss was measured to be negligibly small and within an experimental error of  $\pm 0.1$  dB in the separately made experiment using a straight waveguide. Therefore, the increase in refractive index appears to have occurred within the core area alone. Effects of annealing at 200°C for 10 hours on the increase of refractive indices produced by the irradiation was studied. While the increase of refractive indices produced at 65mW decreased by 10-20%, indices produced at 130mW and above showed negligible decay, indicating that saturated  $\Delta n$  values offer high stability with respect heat. The reason for the robustness with respect to annealing of the saturated  $\Delta n$  values seems to be that any Ge-related, thermally unstable centers initially present in the core had already been eliminated during the femtosecond laser beam irradiation time and no unstable centers remains that later create decay in refractive index values. This is in marked contrast to the thermal instability of UV-induced refractive index increases, which will occur even at temperature below 100°C. This result shows that ultra-short pulse laser is superior to UV laser as a light source for adjusting refractive indices or optical lengths for high precision and highly temperature-robust optical devices such as for AWGs (Arrayed waveguide grating) to be used in the next generation high-performance DWDM optical fiber communications.

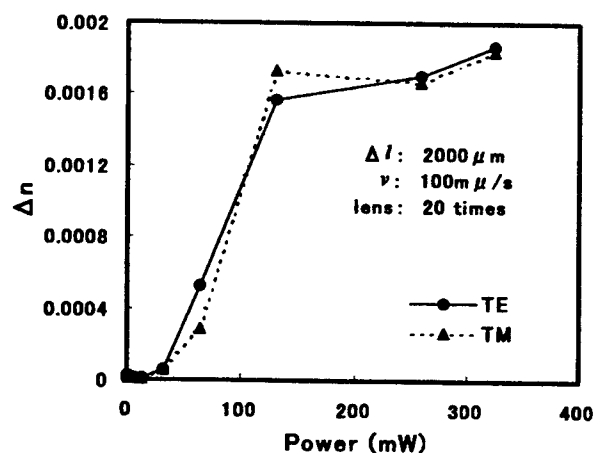


Fig. 19 Increase in refractive index of Ge-doped waveguide by femtosecond ultra-short pulse laser irradiation.

## 5. CONCLUSION

This paper presented an overview and future prospects of the use of lasers for packaging by the electronics and photonics industry in Japan. Various kinds of laser systems based on solid state lasers or gas lasers such as excimer lasers or CO<sub>2</sub> lasers have been developed and applied in manufacturing electronic and

photonic devices to meet the strong demands for high-performance, lightweight, low energy-consumption mobile digital consumer electronics, broadband optical fiber communications, low-emission and fuel-efficient, easy-to steer smart cars, etc. Short-pulse width, high peak power CO<sub>2</sub> lasers are increasingly utilized for drilling various vias for build-up circuit boards. High average power UV excimer lasers are increasingly utilized for low-temperature laser annealing of poly-silicon for advanced TFT LCDs. Emphasis was placed on the use of various solid-state lasers as convenient and versatile light sources for packaging advanced compact devices with sensitive passive or active components having small feature sizes. Some of the representative material processing applications using solid-state lasers for electronic and photonic devices are, short and open circuit defects repairing of LCDs, trimming of functional modules, fine-adjustment of optical characteristics of photonic devices, forming of various micro-vias for ultra-high-density interconnection circuits, laser patterning of amorphous solar-cells, and high-precision laser welding of electronic components such as optical modules, miniature relays and lithium ion batteries. The recent progress in high-peak-power, ultra-short-pulse solid-state lasers seems to be rapidly increasing their processing capabilities such as for fine adjustment of optical filters, etc.

Progress in high-average power light-sources capable of generating high-repetition-rate, short wavelength or short optical pulses, together with advancement in optics for high-precision materials processing, is expected to increasingly play a vital role for electronic and photonic device performance improvement and manufacturing technology innovation.

### ACKNOWLEDGMENT

The authors would like to thank K. Hirao of Kyoto University and S. Fujiwara et al. of Central Glass Co., Ltd for helpful discussions on the use of infrared ultra-short pulsed lasers for fabrication of optical waveguide devices. The authors also would like thank various companies in Japanese electronics industry and colleagues of NEC Corporation for lot of valuable information on the practical applications of laser materials processing and stimulating discussions.

### REFERENCES

1. K. Washio, "Laser applications in electronics and optoelectronics industry in Japan," *Laser Applications in Microelectronic and optoelectronic Manufacturing IV*, J. J. Dubowski, H. Helvajian, E. W. Kreutz and K. Sugioaka eds., Proc. SPIE, **3618**, pp.230-232, 1999.
2. T. Shibuya, T. Shiga, K. Sato, K. Matsumoto and K. Hara, "Highly reliable LD modules," *NEC Res. & Develop.*, **32**, No.1, pp.76-81, 1990.
3. K. Fukuda, M. Shimaoka, T. Ishikawa, H. Kuwano and S. Kaneko, "Precision bonding technology of highly reliable 2.5 Gbit/s optical transmission modules," *Journal of the Japan Society for Precision Engineering*, **67**, pp.1223-1226, 2001 (in Japanese).
4. H. Matsuura, T. Aoki, Y. Watanabe, D. Yoon, M. Tsuyuki, H. Kagiwada, M. Abe and T. Ohta, "Production engineering of polarization beam combiner," *Furukawa Review*, No. 20, pp. 11-14, 2001.
5. T. Ide, A. Kaito, K. Ichikawa, and K. Chiba, "Miniaturization of twin relay for automotive applications," *Proc. 42<sup>nd</sup> relay conference*, pp.23-1~23-6, Boston, May 9-11, 1994.
6. F. Oikawa, H. Yamaguchi and T. Shinoduka, "Development of laser welding technology for mass production of signal relays," *NEC Res. & Develop.*, **41**, No.2, pp. 193-197, 2000 (in Japanese).
7. M. Sano, T. Kouno, O. Yamashita, H. Takata, T. Nagasawa and K. Takahashi, "Development of small undersurface electrode tantalum chip capacitors," *NEC Technical Journal*, **54**, No.11, pp.53-56, 2001 (in Japanese).
8. H. Morita, A. Masago, T. Nakajima, T. Ishida, A. Kuramoto and S. Murayama, "High-performance, digitally power controlled mini-laser welder, specially designed for high precision spot welding of optical modules," *Proc. ICALEO*, paper 208, Laser Institute of America, 2001.
9. N. Nakamura, T. Togawa, K. Okino, S. Watanabe and K. Washio, "Seam welding of A3003 aluminum alloy using high-brightness pulsed slab YAG laser," *Proc. Laser Materials Processing Conference, Section G-ICALEO'97*, pp.130-139, 1997.
10. N. Okada, T. Takase, H. Yusa and N. Nishida, "Welding of aluminum for battery cases using shaped pulses with Nd:YAG lasers", presented at the Lasers in Manufacturing WLT Meetings, June 17-22, 2001.
11. <http://www.kuroda-precision.co.jp/products/kanagata/press/kana01.htm> (in Japanese).
12. K. Ohta, K. Nagamatsu, S. Kudo, K. Iwase, K. Matsushashi and S. Fujii, "Development of laser trimmer SL436H," *NEC Technical Journal*, **54**, No.9, pp. 23-26, 2001 (in Japanese).
13. "Thin film trimmable chip resistors," *Thin Film Components Data Book*, Susumu Co. Ltd., [www.susumu.co.jp](http://www.susumu.co.jp).

14. T. Yazaki and T. Hirotsaki, "CO<sub>2</sub> laser drilling system for PWB," *Denshi Zairyo*, pp. 230-233, Oct. 2001 (in Japanese).
15. O. Futonagane, M. Oda and M. Ishibashi, "Ultra high density build-up PWB," *NEC Technology Journal*, **53**, No. 10, pp.38-41, 2000 (in Japanese).
16. "Trends and technologies of laser markers," *Automation Review*, January 31, 2001 (In Japanese).
17. M. Shibuya, K. Iwase, K. Kitano, M. Kamijo, Y. Murakawa and Y. Baba, "Development of laser diode pumped laser marker SL 577A," *NEC Technology Journal*, **54**, No. 9, pp.19-22, 2001 (in Japanese).
18. T. Nishibe and N. Ibaraki, "Low-temperature p-Si TFT-LCD," *Toshiba Review*, **55**, No.2, pp.32-34, 2000 (in Japanese).
19. [http://www.toshiba.co.jp/about/press/2001\\_10/pr0201.htm](http://www.toshiba.co.jp/about/press/2001_10/pr0201.htm).
20. K. Shiota, K. Sera, N. Takada, N. Ikeda, T. Ootose and H. Haga, "Ultra high-resolution (230ppi) low temperature p-Si TFT reflective LCD for mobile application," *NEC Technology Journal*, **54**, No. 11, pp.16-19, 2001 (in Japanese).
21. H. Nishiki, M. Atkinson, J. Hartzell, and Y. Nakata, "Sputtering technology of Si films for low-temperature poly-Si TFTs," *Sharp Technology Journal*, No. 80, pp. 36-42, 2001 (in Japanese).
22. K. Takei, K. Yakabayashi and S. Watanabe, "Laser repair," *LCD Technology 2001, Supplement for Denshi Zairyo*, pp.173-177, Kogyo Chosakai Publishing Co. Ltd., Tokyo, 2001 (in Japanese).
23. T. Torigoe, "Development of laser CVD repair SL458C," *NEC Technology Journal*, **54**, No. 9, pp.35-38, 2001 (in Japanese).
24. M. Yonekawa, "Development of laser CVD repair for LCD substrate using gas curtain method," *NEC Technology Journal*, **54**, No. 9, pp.31-34, 2001 (in Japanese).
25. A. Himeno, K. Kato and T. Miya, "Silica-based planar lightwave circuits," *IEEE J. Selected Topics in Quantum Electron.*, **4**, pp. 913-924, 1998.
26. C. B. Shaffer and E. Mazur, "Micromachining using ultrashort pulses from a laser oscillator," *Optics & Photonics News*, pp. 20-23, April, 2001.
27. S. Fujiwara, K. Miura, S. Sakaguchi and K. Hirao, "Optical waveguides in glasses written by ultra-short pulse laser," *Extended Abstracts of the 62<sup>nd</sup> Autumn Meeting, 2001*, No. 3, p. 855, paper 14a-ZM-5, The Japan Society of Applied Physics, 2001 (in Japanese).
28. H. Kouta, Y. Urino, T. Hanada and K. Hirao, "Trimming of refractive index in glass waveguide by ultra-short pulse laser," *Extended Abstracts of the 62<sup>nd</sup> Autumn Meeting, 2001*, No. 3, p. 855, paper 14a-ZM-6, The Japan Society of Applied Physics, 2001 (in Japanese).



# Laser Beam Micro Welding in Watch Industry

A. Olowinsky<sup>\*a</sup>, T. Kramer<sup>\*\*a</sup>, F. Durand<sup>\*\*\*b</sup>,

<sup>a</sup> Fraunhofer Institute for Laser Technology ILT Aachen, Germany;

<sup>b</sup> SMH Automation, Grenchen, Switzerland

## ABSTRACT

After the invention of the laser principle and its first application for drilling of jewels in watch movements, the laser was only used for marking. The still ongoing trend of miniaturisation and automation opened a new field of application: laser beam micro welding. This paper gives an overview of the new application of laser beam welding in watch industry. The combination of dissimilar materials like brass and stainless steel is often needed in watch movements due to tribologic aspects. Here, laser beam micro welding offers an alternative to conventional joining techniques like press fit or gluing. Since the watch components are very small the locally limited heat input of the laser beam offers the possibility of weld seam widths  $<200\text{ }\mu\text{m}$ . The depth and the width of the closed weld seam as well as the surface quality can be influenced especially at the end of the seam using the pulse forming capability of a pulsed Nd:YAG laser. Several watch components could be joined by means of laser beam micro welding. The width of the seam could be reduced to  $100\text{--}200\text{ }\mu\text{m}$ . The joining geometries of an axis/wheel combination are in the range of  $100\text{ }\mu\text{m}$  to  $1\text{ mm}$  diameter of the axis and about  $200\text{ }\mu\text{m}$  wheel thickness. The process of laser beam micro welding could be integrated in a fully automated assembly machine for watch movement parts.

This paper will give an overview about some results of a European research project where the welding of microparts was investigated. The aim was to decrease contamination and distortion of the parts during the welding process. The work to be presented has been funded by the European Commission in a project under the contract BRPR-CT-0634.

**Keywords:** Laser beam micro welding, pulsed Nd:YAG laser, pulse shaping, microtechnology, industrial application, watch making industry, dissimilar materials, brass

## 1. INTRODUCTION

The question of friction between two parts is crucial to the movement within a watch. Lubricants can normally not be used because of the tendency of gumming. Therefore two different materials are often chosen for parts getting in contact. Three main combinations are commonly used:

- \* Stainless steel and brass
- \* Stainless steel and copper
- \* Stainless steel and argentan (german silver)

The coefficient of friction is very low compared to equal combinations. Up to now there are conventional joining techniques which are mainly deployed:

- \* Gluing
- \* Press fit
- \* Crimping

\* alexander.olowinsky@ilt.fraunhofer.de; phone +49 241 8906 -491; fax +49 241 8906 -121;  
Fraunhofer Institute for Laser Technology, Steinbachstr. 15, 52074 Aachen, Germany

\*\* thorsten.kramer@ilt.fraunhofer.de; phone +49 241 8906 -407; fax +49 241 8906 -121;  
Fraunhofer Institute for Laser Technology, Steinbachstr. 15, 52074 Aachen, Germany

\*\*\* friedrich.durand@eta.ch; phone +41 32 655 -7238; fax +41 32 655 -8389;  
SMH Automation a Division of ETA SA Fabrique d'Ebauches, Maienstr. 11, 2540 Grenchen, Switzerland

Gluing requires an additional processing step: The glue has to be dispensed. The time between dispensing the glue and the assembly of the two parts to be joined is crucial to this process. The forces strongly depend on the ambient conditions like temperature and pressure. Gluing normally is used to join polymers. In the press fit situation both parts are slightly conical. They are assembled and pressed to each other. Doing this in a specially designed tool delivers either the force which the joint can withstand or the position of the parts with respect to each other. In the majority of cases, the position is therefore controlled and the forces are assumed to be sufficient. For crimping again the position tolerances are fairly high. Here laser beam micro welding with the new SHADOW technique is a solution to overcome the contradiction of accuracy in force and position at a time.

Laser beam welding is a well established manufacturing technology in macro technology. The development of new laser sources with increased beam quality enables small spot sizes down to 50 to 100  $\mu\text{m}$  with pulse power about 100 to 200 W. The small spots sizes are needed since the parts to be welded are often very small. One of the requirements in watch industry is that the weld seam should not be seen. A seam width less than 100  $\mu\text{m}$  therefore should be achieved.

Within the last years the laser beam welding has been extended to welding of micro parts. The still ongoing trend of miniaturization strengthened this development. The combination of dissimilar materials like brass and stainless steel is often needed in watch movements due to tribologic aspects. Here laser beam micro welding offers an alternative to conventional joining techniques.

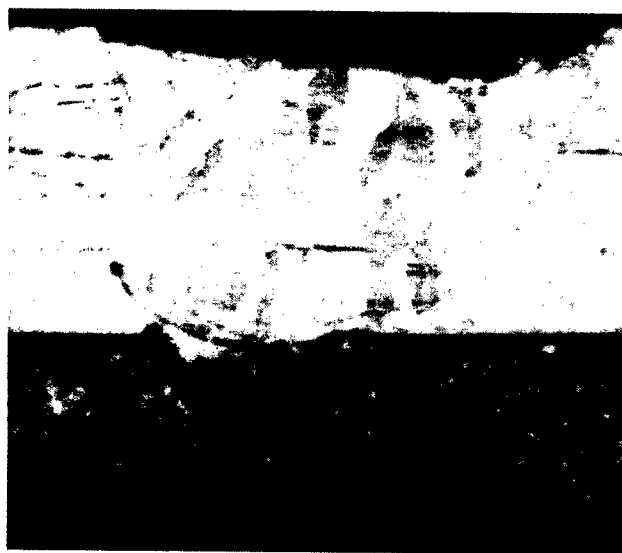
## 2. PROCESS DEVELOPMENT

### 2.1. Joining of Dissimilar Metals

The combination brass and stainless steel is one of the standard packages used in watch movements. The friction coefficient between these two materials is very low. Furthermore brass can easily be stamped. Most of the axes are therefore made of stainless steel (S20AP) and the wheels are stamped of brass (CuZn37). With this materials combination, no lubricants are needed. However, the axes and wheels have to be joint. Up to now, they are mostly assembled in a press fit joint where the geometrical tolerances of the single parts influence the joining forces. The introduction of the laser beam micro welding solves the contradiction of accurate joining position and sufficient joining force: The axes are slightly conical and therefore either the position is correct and the forces are unknown or the forces are correct and the position depends on the manufacturing tolerances of the parts. For laser beam micro welding the two parts are accurately positioned. The remaining gap between the parts can be bridged using appropriate laser parameters. Gaps of up to 20  $\mu\text{m}$  can be accepted. This leads to a reduction of the manufacturing tolerances of the single parts.



Fig. 1 Joining of dissimilar metals  
upper material: X8 CrNi 18 12, 250  $\mu\text{m}$  thick  
lower material: CuZn37, 150  $\mu\text{m}$  thick  
etched on stainless steel, bright field image



darkfield image  
No thoroughly mixing of stainless steel and brass can be observed.

The combination of stainless steel and brass can be achieved using laser beam micro welding. Since the absorption of brass is very low (approx. 10 %) the laser radiation is coupled into the stainless steel. The melting of the brass occurs due to heat conduction through the steel part. Fig. 1 shows the cross section of a 250  $\mu\text{m}$  stainless steel sheet on a 150  $\mu\text{m}$  brass plate. The melted and resolidified stainless steel can easily be seen. The joint is formed just in the interface between the two parts. The two materials are not mixed. However the samples are connected. The zone of interaction is very thin.

## 2.2. New joining technology SHADOW

During the above mentioned project, a new joining technology was developed. This technique is called SHADOW: **STEPLESS HIGH SPEED ACCURATE AND DISCRETE ONE PULSE WELDING**. It is developed to weld small axially symmetric parts which can be turned fast during one single laser pulse. This technique combines the advantages of continuous wave welding (a smooth surface and a high process speed) with the possibilities of the pulsed laser systems (lower costs and the capability of pulse forming). Since the parts are small, the latter advantage of pulse forming reduces the overall energy input which is related to distortion and deformation of the parts.

Up to now continuous wave (cw) laser welding is used only for longer weld seams and for larger parts. A high average laser power,  $P_{av} > 500 \text{ W}$ , and a high processing velocity,  $v > 5 \text{ m/min}$  are required for cw laser welding. Above all, cw laser sources are more expensive than pulsed laser sources. Nevertheless, the joints obtained by cw laser welding show a smooth surface and an optimized microstructure nearly without any pores. The energy per length is less for cw laser welding than for pulsed laser welding.

Pulsed laser sources at present are able to generate a maximum pulse duration of  $\tau_{H,max} = 20 \text{ ms}$ . To weld parts on a length of 2 mm a processing velocity of  $v = 6 \text{ m/min}$  therefore is required. Comparing the energy input ( $Q_{H,SHADOW} = 6 \text{ J}$ ) to the energy input for a similar joint using the multi pulse technique where ten pulses without overlap are needed ( $Q_{H,p} = 10 \times 2.4 \text{ J} = 24 \text{ J}$ ) it is less by a factor of 4. Moreover, the joined parts show less debris or contamination on the surface. Neglecting the time needed to accelerate the parts, the processing time is dramatically reduced.

Fig. 2 shows a comparison of a conventional weld seam with a pulsed Nd:YAG laser and the SHADOW technique. In pulsed mode 130 pulses with a pulse energy  $Q = 0.1 \text{ J}$  are applied. The total energy amounts to 14 J. In comparison the SHADOW technique only uses one pulse with an energy  $Q = 1.3 \text{ J}$ . The reduction of the energy results in a smooth surface without any ejection of particles on the part and a negligible distortion.

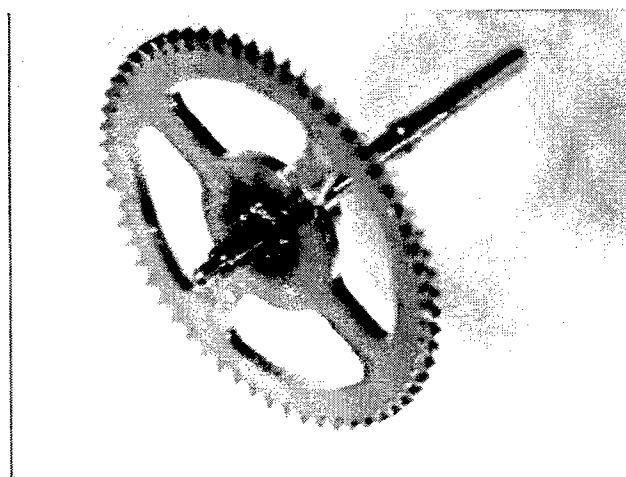
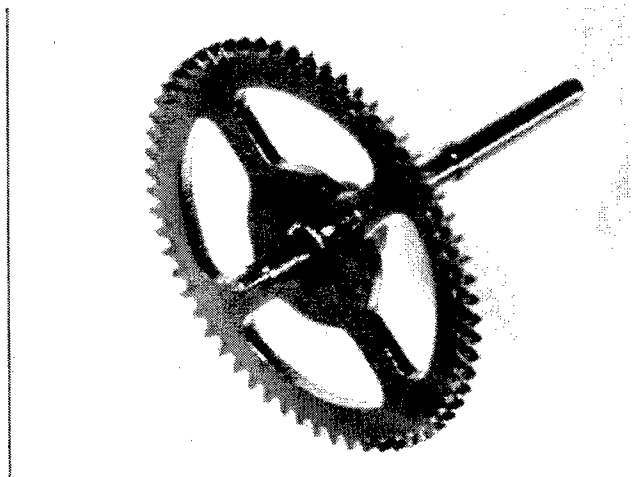


Fig. 2 Welding with conventional pulsed Nd:YAG laser  
 $P_H = 112 \text{ W}$ ,  $\tau_H = 1.0 \text{ ms}$ ,  $f_p = 100 \text{ Hz}$ , 130 pulses  
**Material**  
 Axis S20AP  
 Wheel CuZn37  
 $\varnothing 0,3 \text{ mm}$



Advantage of SHADOW  
 $Q = 1.3 \text{ J}$ ,  $\tau_H = 20 \text{ ms}$ ,  $v = 3.3 \text{ m/min}$   
 Low contamination of the bright and shiny surface

Welding speeds up to 10 m/min can be achieved by applying a 20 ms pulse of a Nd:YAG laser to a workpiece. The speed is realized either by moving the workpiece or the laser beam by means of a scanner or a robot. The used pulse power is normally very low but can be increased to several kW depending on the application. The parts in watch industry are very small therefore only small amounts of energy are needed. The realization of this relative movement for axially symmetrical parts like most of the parts in a watch movement is shown in Fig. 3.

### 3. HARDWARE DEVELOPMENT FOR ASSEMBLY

#### 3.1. Mechanical setup for simple geometries

For basic investigations a simple experimental set-up was built up with a rotating handling and adaptable holders for the different parts. The fibre guided laser beam of a pulsed Nd:YAG laser (HL 62 P) is focussed onto the part. By means of a CCD-camera, the positioning of the laser spot can be observed. Two other imaging systems are used for process monitoring such as High Speed Video Imaging.

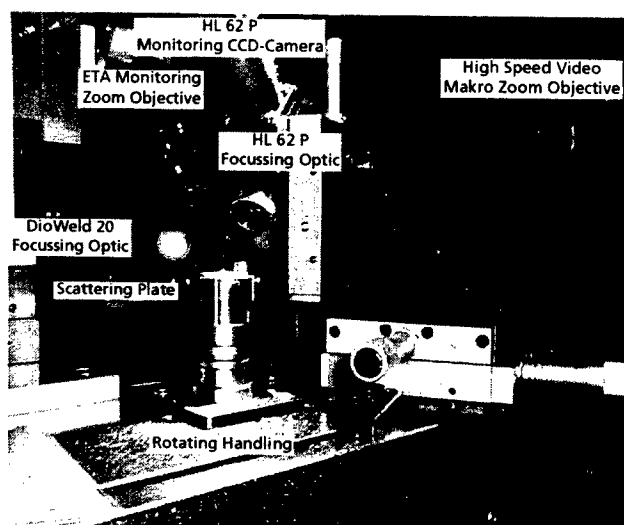


Fig. 3 Mechanical setup for manual assembly



Semi-automated welding system for axes and crowns

With this setup the following axes and crowns are welded in a manually loaded process. The process parameters are as follows:

One single laser pulse with a pulse energy  $Q = 2.5 \text{ J}$  and a pulse duration  $\tau_H = 20 \text{ ms}$  is used to create a rotational weld seam. The part is rotating with 3000 rpm which leads to a welding speed of  $v = 8.5 \text{ m/min}$ . The angle of incidence was  $\alpha = 20^\circ$ .

The mechanical setup with manual loading and unloading is shown in Fig. 3. The complete machine comprises a high speed rotating axis and a holder which can be adapted to the parts to be joined. The laser spot can be positioned on a 3-axes translation stage with respect to the rotating part.

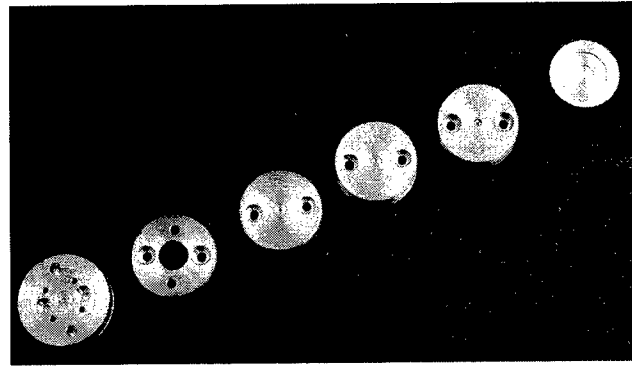
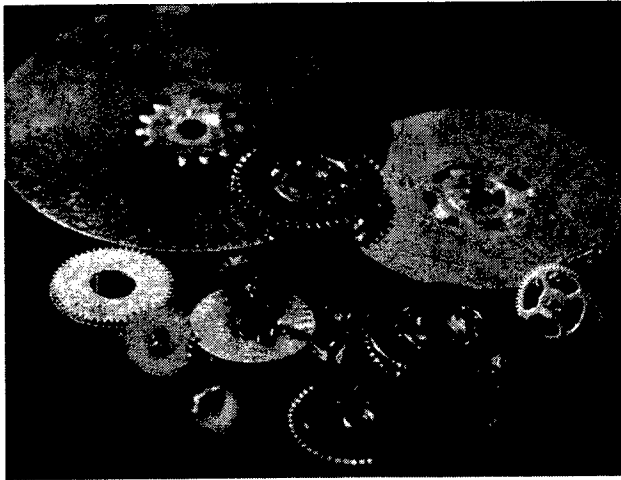


Fig. 4 Various watch components welded with SHADOW technique Inserts for sample holder

On this machine investigations with real-world samples could be carried out. Several components with different materials have been tested.

### 3.2. Semi-automated Pick and place

A first step of automation was made with the introduction of a 4-axes-robot to pick and place axes and crowns

A vacuum gripper is mounted on a -manipulation system. The tip of the gripper is adapted to both the crown and the axis. The four major steps of the manufacturing process are illustrated in Fig. 5.

1. Pick and place of the crown
2. Pick and place of the axis
3. Welding with the SHADOW technique
4. Unloading of the welded sample.

The subsequent steps of storage and material transfer to the following assembly processes are not yet implemented.

The cycle time measures 5 s which is limited by the used manipulation system. A faster system with a higher velocity was already tested and installed. One pick and place operation is made within 0.5 s.

Table 1 gives an estimation of the cycle time for both conventional pulsed laser beam welding and the SHADOW technique.

	Conventional pulsed mode	SHADOW
Pick and place Crown	0.5 s	0.5 s
Pick and place Axis	0.5 s	0.5 s
Welding	130 Pulses @ 200 Hz = 0.65s	1 pulse = 0.02 s
Pick and place for unloading	0.5 s	0.5 s
Cycle time	2.15 s	1.52 s

Table 1 Comparison of the cycle time with conventional pulsed welding system and SHADOW technique. The time for a single pick and place operation is given for a Mitsubishi RP-1AH 4-axes scara robot.

Since the loading and unloading times summarize to 1.5 s in both cases the welding time mainly determines the total cycle time. This is one of the potentials of SHADOW.



Pick and place of the crown      Pick and place of the axis      Welding of the crown to the axis      Unload  
Fig. 5 Robot assisted assembly of axis and crowns

### 3.3. Fully automated assembly cell for watch components

The final aim of the project CLAW was the development of an industrial fully automated assembly cell to demonstrate the capability of the joining process. Two wheels of a watch had to be assembled and welded.

The manufacturing process was divided into several steps:

1. pick and place of the small wheel (étoile) of the date disc which is responsible for the rotational movement
2. pick and place of the larger wheel (disc jour)
3. welding of the two parts in an overlap joint hitting the large wheel on the edge of the inner diameter.
4. unloading the joined parts and packaging on a tray

Additionally the trays were stacked in a LIFO storage system. The sketch of the machine is shown in Fig. 6.

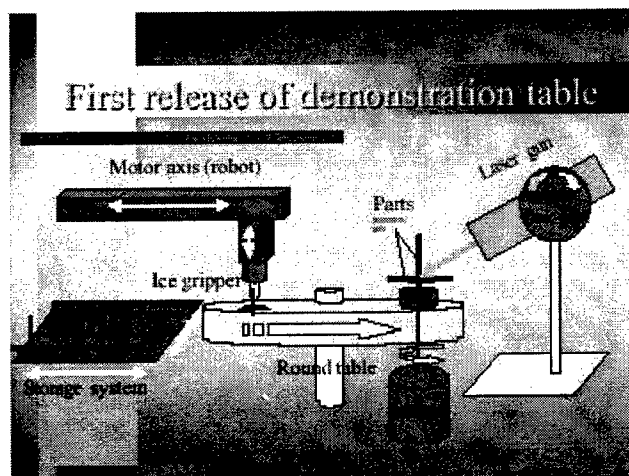


Fig. 6 Fully automated assembly cell for watch components

Laser with Focusing Optics

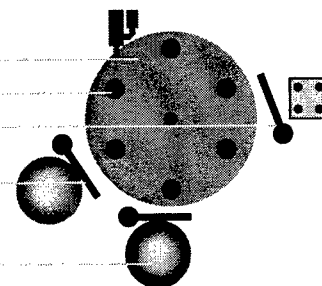
Rotating Table

High Speed Rotating Spindle

Unloading Pick and Place with Storage System

Vacuum Gripper

Part Feeder with Pick and Place



Standard pick and place systems have been used. The complete system is controlled by means of a PLC controller and several motor controllers. No process control system for the welding process was implemented since the process is not sensitive to slight changes in the parts. Only the mechanical positioning of the parts in the holder has to be assured.

#### 4. WELDING OF WATCH COMPONENTS

The experiences of the basic research led to the implementation and validation of the welding process for various watch components. The different materials combinations are listed in Table 2.

Sample	Materials		Pulse energy	Pulse power	Part diameter	Welding speed	Line energy
			[J]	[W]	[mm]	[m/min]	[J/mm]
Crown / Axis	S20AP	S20AP	2.5	125	0.9	8.48	0.88
Gear Wheel	S20AP	S20AP	4.2	210	1.1	10.37	1.22
Bearing	S20AP	S20AP	5.0	250	1.7	16.02	0.94
Date disc	CuZn37	CuZn37	6.0	300	2.5	23.56	0.76
Axis / Wheel	S20AP	CuZn37	1.5	75	0.8	7.54	0.60
Real Axis	S20AP	CuZn37	1.3	65	0.3	2.83	1.38
Intermediate gear wheel	S20AP	CuZn37	4.2	210	1.9	17.91	0.70

Table 2

As shown in the table above, the pulse energy is very moderate since the samples are small. The welding speed depends on the diameter of the parts to be welded as the rotational speed was held constant throughout all experiments. The comparability of the different samples is therefore not given. Only the feasibility of the welding was to be proven.

The line energy applied for the different applications measures from 0.6 to 1.38 J/mm. The energy needed to weld the two parts strongly depends on the diameter and the volume of the parts. The heat capacity and the heat losses into the surrounding material influence the required laser power.

#### 4.1. Joining of similar materials

SHADOW technique creates smooth weld seams with high strength as shown in the following pictures:

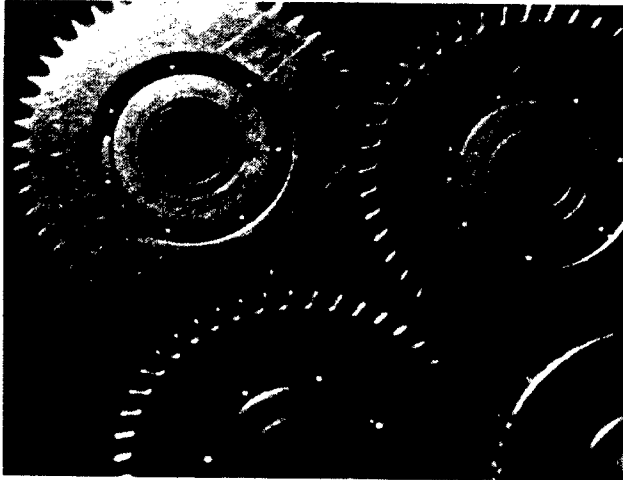


Fig. 7 Bearings for automatic watches

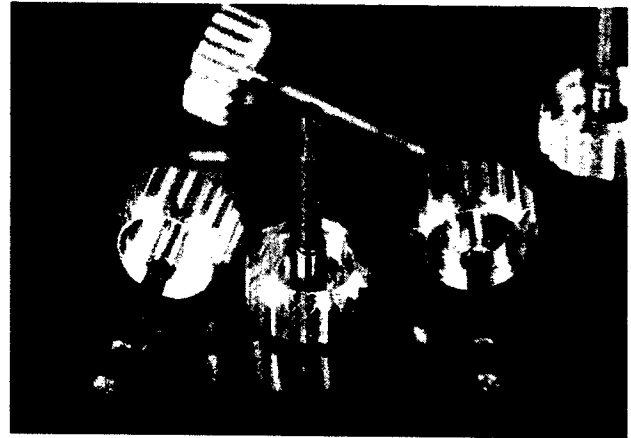


Fig. 8 Axes and crowns of mechanical watches welded with the SHADOW technique.

courtesy of  LASER CHEVAL

In an automatic watch the oscillating mass is mounted on a precision bearing as shown in Fig. 7. The inner ring is adjusted precisely to guarantee a movement free of clearance. After the adjustment process, the two rings are fixed to each other. The conventional process of crimping was now replaced by laser beam micro welding with SHADOW. The diameter of the weld seam is 1.7 mm. The welding speed is 16 m/min. The strength of the joint is increased compared to bearings which are conventionally crimped.

Most of the applications in watch industry are axis/wheel combinations. Since the parts are often stamped out of sheet metal the axis has to be added and joined. The stamped contour in the left picture in Fig. 9 is a kind of hexagon. The gap between the wheel and the axis to be joined is thus not constant. Nevertheless, the weld seam shows a rather smooth surface. The right picture shows the welding of two stamped brass parts (CuZn37) with a thickness of 150  $\mu\text{m}$  for the date disc and 200  $\mu\text{m}$  for the wheel. The task is to weld in a fillet weld. The inner diameter of the weld seam is 2.5 mm. The welding speed measures 23.56 m/min related to the rotational speed. The small wheel is used to turn the large disc within the movement. Both wheels have to be strictly concentric and the tolerances in height deviation are very narrow. The two parts have been welded with the SHADOW technique. The parameters are as follow: With the standard pulse duration of  $\tau_H = 20$  ms the pulse energy was  $Q = 6$  J.4 with an appropriate pulse forming (temporal lapse of power).



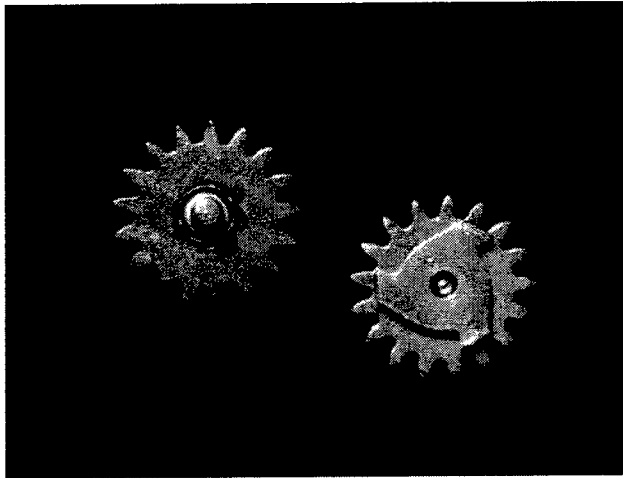


Fig. 9 Small watch components

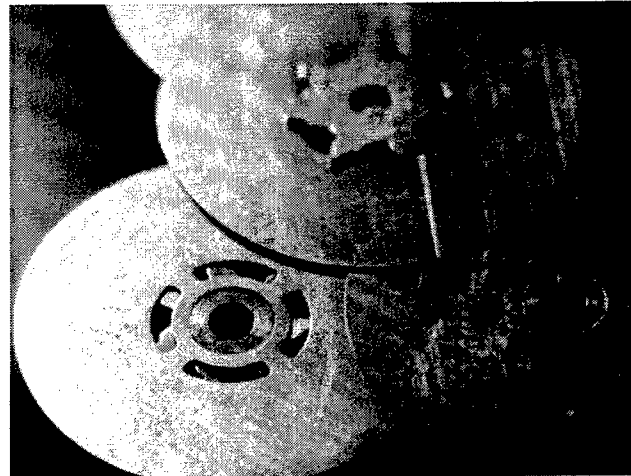


Fig. 10 Date disc

The welding of brass shows up with the problem of ejection of particles and the evaporation of zinc. The liquidus point of CuZn37 ( $T_m = 920^\circ\text{C}$ ) is higher than the evaporation temperature of zinc ( $T_{\text{evap., zinc}} = 900^\circ\text{C}$ ). The application of the SHADOW technique prevents the evaporation of the zinc due to the fast interaction period which is determined by the diameter of the laser spot  $d_{\text{beam}}$  and the welding speed  $v_{\text{welding}}$ :  $t_{\text{interaction}} = \frac{d_{\text{beam}}}{v_{\text{welding}}} = \frac{200 \mu\text{m}}{23.56 \text{ m/min}} = 0.5 \text{ ms}$ . However no evaporation of zinc could be observed.

#### 4.2. Joining of dissimilar materials

As mentioned above the liquidus point of brass (CuZn37) is at about  $920^\circ\text{C}$  whereas the stainless steel S 20AP melts at a much higher temperature (about  $1400^\circ\text{C}$ ). Hence, the process has to be controlled in a way that the steel part reaches first the melting temperature and the energy is transferred by means of heat conduction to the brass. This is shown in Fig. 1. Due to the lower absorption coefficient of brass this effect is achieved by positioning the laser spot slightly on the steel axis. Most of the energy is absorbed in the steel and the brass is heated by heat conduction only.

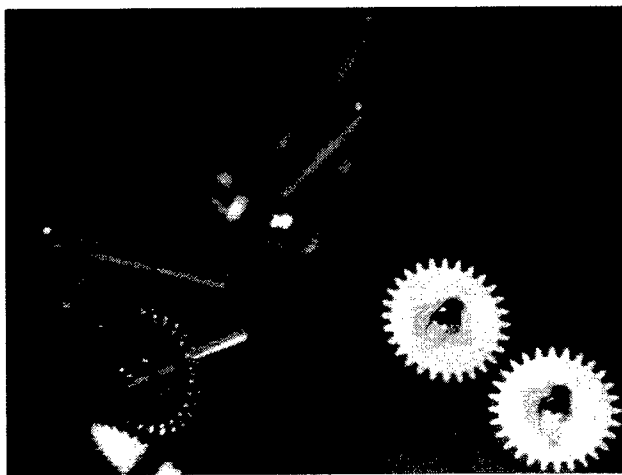


Fig. 11 Simple geometry for axis/wheel combination

##### Material

Axis S20AP  
 $\varnothing 0.3 \text{ mm}$

Wheel CuZn37

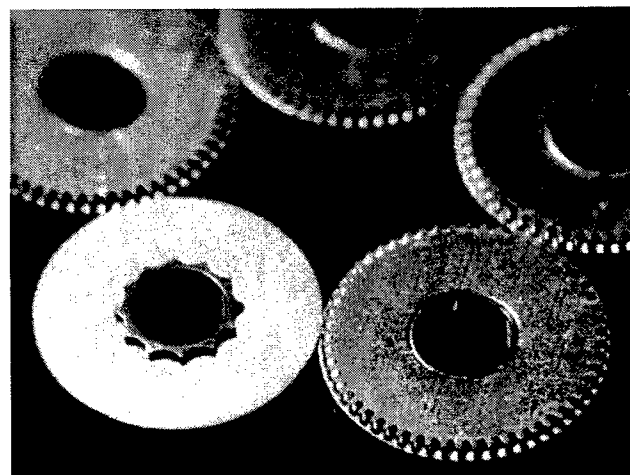


Fig. 12 Intermediate gear wheel

##### Material

Inner wheel S20AP  
 $\varnothing 1.9 \text{ mm}$

Wheel CuZn37

Table 3 summarizes the results in a more qualitative manor since the weldability depends strongly on the geometry of the parts, the volume and the mass of the parts, thus the heat capacity. Thus it appears that the feasibility of laser beam micro welding has to be verified for every single application. However the introduction of the SHADOW technique broadened the field of application as this paper shows.

Material combinations	Application	Feasibility
Steel / steel	Crown / axis	Very good
Steel / brass	Wheel / axis	Feasible
Brass / Brass	Date disc	Good
Arcap / arcap	Wheel / axis	Very good
	Date disc	
Arcap / steel	Wheel / axis	Good

Table 3 Summary of investigated materials combination

## 5. CONCLUSION

With the introduction of SHADOW a new welding technique for „difficult“ materials combinations has been shown. The advantages of low energy input and high processing speed lead to new applications for laser beam micro welding especially in the watch industry. Here first promising results for simple geometries enabled the transfer of the process know-how to real production lines. The implementation of a semi-automated system for axis / crown assembly with manual part feeding showed the capability of the SHADOW process. The energy input could be reduced by a factor of 10 compared to conventional pulsed seam welding. The intention was to introduce laser beam micro welding as an alternative to gluing or crimping.

The stand-alone fully automated assembly cell is a first step towards the industrialization of the process. The watch industry now has to be convinced by the results shown in several applications both for similar as well as for dissimilar materials combinations. Further work will be done in the field of automation and industrialisation of the SHADOW welding technique.

## ACKNOWLEDGEMENTS

The work presented has partially been funded by the European Commission in a project under the contract BRPR-CT-0634. The authors want to thank the partners within in the consortium which have strongly contributed to these results. Most of the samples are shown by courtesy of the Swatch Group and Laser Cheval.

## REFERENCES

1. W.Hoving, "Laser Micro-welding in the Electronics Industry", Proc. Of the 6th International Welding Symposium of the Japan Welding Society, 19-21 November 1996, Nagoya, Japan, pp. 267-272
2. "Laser beam micro welding as a new interconnection technique", *Microelectronics International*, No.39, pp. 44 ff January 1996
3. I. Miyamoto, H. Maruo, Y. Arata, "Beam absorption mechanisms in laser welding", Proc. SPIE, *Laser Processing: Fundamentals, Applications and Systems Engineering*, 3-6 June 1986
4. A. Olowinsky. T. Kramer. N. Dumont. H. Hanebuth. "New applications of laser beam micro welding" Proc. ICALEO 2001, Jacksonville, Florida USA
5. M. Glasmacher, *Prozeß- und Systemtechnik zum Laserstrahl-Mikroschweißen*, Meisenbach Verlag, Bamberg, 1998
6. F. Dausinger, *Strahlwerkzeug Laser: Energieeinkopplung und Prozeßeffectivität*, Teubner Verlag, Stuttgart, 1995

# **LASER APPLICATIONS IN INTEGRATED CIRCUIT PACKAGING**

Y.F. Lu, W.D. Song, Z.M. Ren, C.W. An, K.D. Ye, D.M. Liu,  
W.J. Wang, M.H. Hong and T.C. Chong

Laser Microprocessing Laboratory,  
Department of Electrical Engineering and Data Storage Institute,  
National University of Singapore, 10 Kent Ridge Crescent, Singapore 119260,  
Tel: (65)8742118, Fax: (65)779-1103 , Email: [elcluyf@nus.edu.sg](mailto:elcluyf@nus.edu.sg)

## **ABSTRACT**

Laser processing has large potential in the packaging of integrated circuits (IC). It can be used in many applications such as laser cleaning of IC mold tools, laser deflash to remove mold flash from heat sinks and lead wires of IC packages, laser singulation of BGA (ball grid array) and CSP (chip scale packages), laser reflow of solder ball on GBA, laser marking on packages and on Si wafers. During the implementation of all these applications, laser parameters, material issues, throughput, yield, reliability and monitoring techniques have to be taken into account. Monitoring of laser-induced plasma and laser induced acoustic wave has been used to understand and to control the processes involved in these applications.

**Keywords:** Laser packaging, laser mold cleaning, laser deflash, laser singulation, laser reflow, laser tagging, laser bumping

## **INTRODUCTION**

Laser material processing demonstrated its significance in many areas such as microelectronics, data storage, photonics and nanotechnology, since versatile laser sources provide flexible and unique energy source for precise control of material processing. With current laser technology, a short wavelength down to X-ray range and a short pulse duration down to femtosecond range can be achieved. The extreme conditions created by laser irradiation have provided strong impact on material research. This paper will summarize a few research topics related to laser applications in the packaging of microelectronics devices: laser surface cleaning for IC molding tools, laser removal of mold flash from IC packages (laser deflash), real-time monitoring in laser packaging applications, laser reflow of solder balls for BGA (ball grid array) packages, laser singulation of dies and packages, laser tagging and laser bumping for magnetic disks.

## **RESEARCH RESULTS**

### **1. Laser Cleaning of IC Molding Tools**

Laser surface cleaning is a newly developed technology. It has strong applications in IC and semiconductor industries. This laser-based dry cleaning method was recently developed. Since the new process is chemical free and noise free, it is therefore environmentally friendly. It is also cost effective since there is no consumables and no need to treat the used chemicals in conventional cleaning processes. Laser cleaning can also remove a wide spectrum of contaminants, including those unable to be cleaned in conventional cleaning systems (such as embedded particles and thick organic films). This technology is also area selective, flexible to various kinds of substrates and applicable to on-line processing, etc. This technology has been studied thoroughly and systematically [1,2]. A complete set of theoretical model including laser steam cleaning [3,4] has been developed based on experimental results. The model fits the experimental results well and has been successfully used to predict some new cleaning results in complex chemical and physical environments. Laser surface cleaning has been demonstrated as a new technology to remove small particles and organic contamination from solid surface. It has the advantages of high efficiency, high selectivity, being chemical free and environmentally friendly. It can be used for surface cleaning in different industries such as magnetic recording industry

and semiconductor industry. Research works have been carried out to clean magnetic media surfaces, magnetic heads, and semiconductor wafers. Laser cleaning of IC mold tools is one of the recent research results which shows great potential in industrial applications.

The mechanism of laser cleaning involves many aspects of laser-material interactions. Laser cleaning of particles involves laser-induced fast thermal expansion of substrate or particles, and laser ablation of particles which has small ablation threshold. The laser cleaning of organic contaminants is considered due to laser photo-ablation and thermal-ablation of the contaminants.

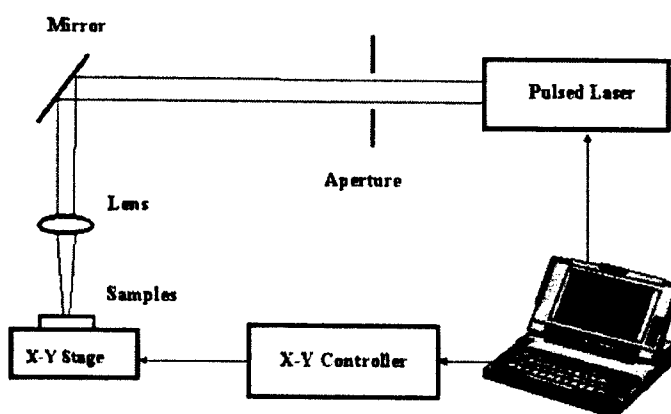


Fig. 1. The schematic diagram of laser cleaning system.

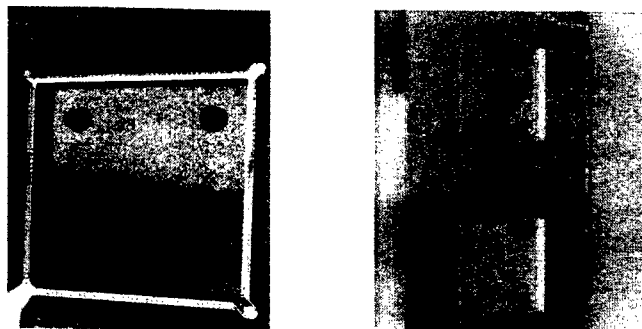


Fig. 2. Some mold surfaces before and after 248 nm excimer laser cleaning with fluence of  $250 \text{ mJ/cm}^2$  and repetition rate of 30 Hz for 30 minutes. The mold surfaces are partially shined during laser cleaning to produce comparable patterns.

The schematic diagram of laser cleaning system is shown in Fig. 1. A KrF excimer laser or a YAG laser is used as a light source for laser cleaning. The experimental results show that grease and wax contaminants on IC mold surfaces can effectively be removed by laser irradiation. It was found that the cleaning threshold is about  $50 \text{ mJ/cm}^2$  and damage threshold is about  $750 \text{ mJ/cm}^2$ . At laser fluence of  $250 \text{ mJ/cm}^2$  with a good cleaning efficiency, no damage was found to the mold surface after 30 min irradiation. An optical microscope was used to observe the mold surfaces before and after laser cleaning. In Fig. 3, the upper half surfaces of the molds are processed by excimer laser cleaning, whilst the lower ones retain the contaminated originals. The efficiency of excimer laser cleaning is obviously high. No damage on the mold surfaces is observed. A commercial system was developed for this purpose (Fig. 3)

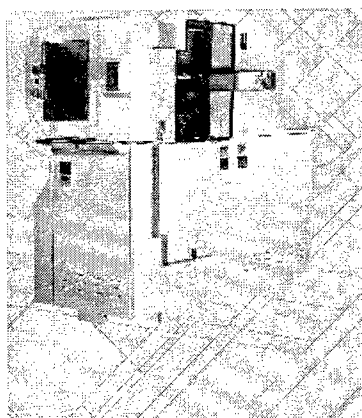


Fig. 3. Laser mold cleaning system

## 2. Laser Removal of Mold Flash from IC Packages

During the molding process of IC packaging, molding compound leaks out and forms flashes on IC package surfaces. It will greatly influence next packaging processes, such as plating and bending. In the worst case, it will even cause scrap of the whole IC package. Therefore, deflash of the IC packages is one of the critical processes in the manufacturing. Medium blasting, water jet shooting and chemical etching are conventional techniques in IC packaging lines. However, these methods have some disadvantages especially when the package sizes shrink. For example, medium blasting applies strong force on the packages, causing strong mechanical stress and even bending and cracks. water jet deflash also has the same drawbacks. Additionally, it requires subsequent drying process. Chemical etching requires subsequent rinse and drying. Sometimes, chemicals can enter the packages and cause reliability issues. Laser deflash [5] was developed to solve these problems. As shown in Figs. 4 and 5, it was developed from laser surface cleaning and is specially designed to serve the IC industry. It plays an important role in IC packaging and can solve some intrinsic problems that were formerly unsolvable.

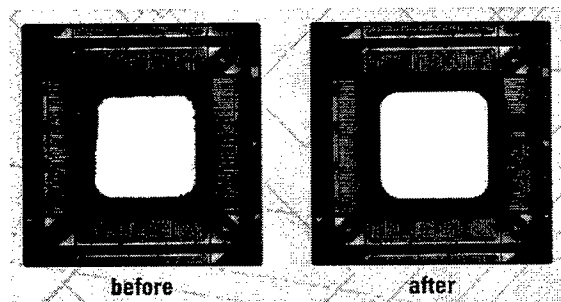


Fig. 4 IC packages before and after laser deflash

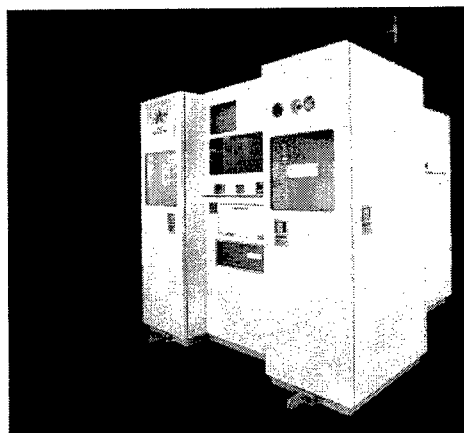


Fig. 5 Laser deflasher system

For laser fluence above a threshold value, pulsed laser ablation can cause explosive removal of the substrate materials with an illuminating plasma generated. By irradiating a laser beam on an IC package, it can be used to remove the molding flashes. Compared with the conventional techniques, pulsed laser deflash has the advantages of being dry process, high efficiency and capability of on-line control. To monitor the laser deflash in real time, it is very important to capture signals generated during the laser ablation and correlate the signals with processing parameters to build up databases for a control loop. Optical multichannel analyzer (OMA) is a non-contact plasma detection technique. By analyzing spectral line positions and the line profiles, chemical compositions and ionization degree during the laser

ablation can be identified. Quantity of the substrate materials removed can also be obtained from the intensity of the spectral lines. Optical emission spectra from excited atoms, ions and molecules are measured as a function of laser fluence and delay time after the laser irradiation. A Nd:YAG laser with the light wavelength of 1064 nm and pulse duration of 7 ns (FWHM) was used as a light source to deflash the molding compound in air. Laser fluence was adjusted from 0 to 10 J/cm<sup>2</sup>. Plasma plume generated during the laser deflash was imaged by two convex lenses (focal lengths: 300 and 100 mm) to an optical fibre which was coupled onto a slit of an optical multichannel analyzer system (Oriel Multispec). A grating with 2400 lines/mm was selected to scan the plasma emission spectrum with a spatial resolution of 0.04 nm. This system is fitted with a gate intensified charge coupled detector (ICCD) array.

Temporally integrated plasma emission spectrum for the molding compound is shown in Fig. 6. It was captured during Nd:YAG laser ablation in air with detection probe at 1 mm from the substrate surface. Laser fluence applied was 9.6 J/cm<sup>2</sup>. The plasma emission spectrum was recorded in a wavelength range from 260 to 640 nm. There are abundant spectral lines and bands in the spectrum. It can be found that there are many emission spectral lines from neutral excited atoms Si I and C I, singly ionized atoms Si II, O II and C II, doubly ionized atoms Si III. There are also emission spectral bands from CN, C<sub>2</sub> and SiO molecules. The most prominent lines and bands observed during the laser ablation are attributed to electronic transitions of neutral excited atoms Si I (288.2, 390.9 and 576.4 nm), molecules CN violet band  $\Delta v=0$  (B<sup>2</sup> $\Sigma^+$  - X<sup>2</sup> $\Sigma^+$ , 385.1-388.3 nm), molecules SiO (422.8, 424.4 nm heads of a <sup>3</sup> $\Sigma$  - <sup>3</sup> $\Pi$  band) and singly ionized atoms CII (393.4 and 396.9 nm). Since about 90% of the molding compound is SiO<sub>2</sub> the spectrum analyses are focused on the spectral lines for SiO, Si I, Si II and Si III. It can also be observed from Fig. 6 that the spectral lines and bands are superimposed on a background continuum. The continuum spectrum is resulted from free-free (bremsstrahlung) and free-bound (recombination) transitions at the early stage of the laser ablation.

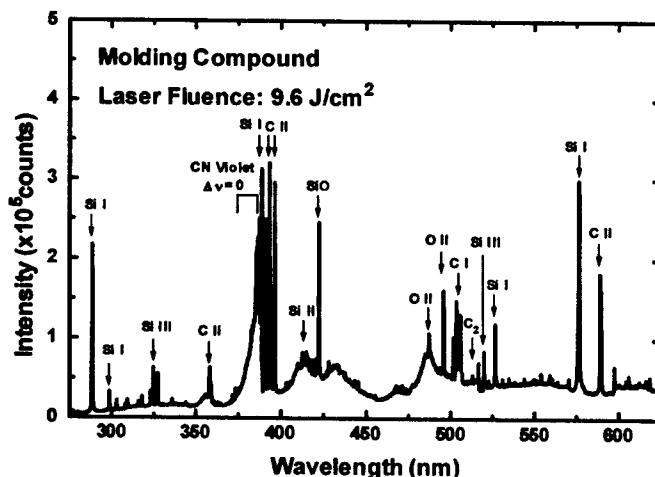


Fig. 6. Temporally integrated optical emission spectrum for detection probe at 1 mm from the substrate surface during Nd:YAG laser ablation of molding compound for a laser fluence of 9.6 J/cm<sup>2</sup>.

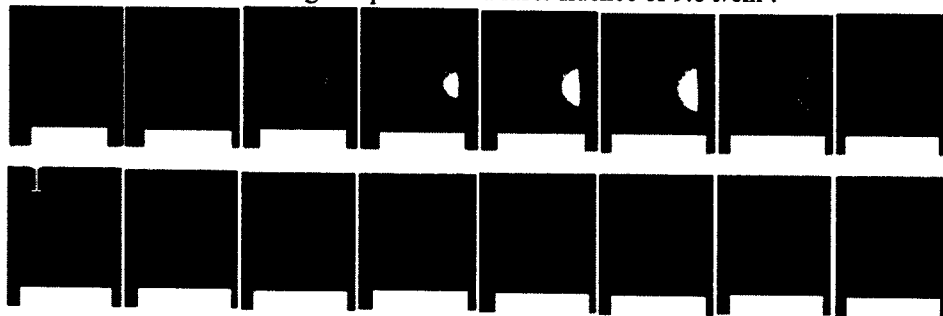


Fig. 7 In laser deflash, the plasma plume evolves as a function of time lapsed.

Figure 7 shows the plasma plume generated during laser deflash which evolves as a function of time. After laser pulse (7 ns), the plasma is generated and the plume grows with brighter light emission. The optical emission is the strongest at

time delay of around 80 to 100 ns. The plasma is then being cooled down by air and becomes smaller and weaker. The plasma plume disappear at a time delay of 50  $\mu$ s.

### 3. Laser Texturing, Laser Disk Tagging and Laser Bumping

Laser texture [6] is another typical application of laser microprocessing technology in magnetic recording industry. Laser texturing has been used in laser disk tagging, laser bumping, laser buffing, etc. In the case of disk tagging, as shown in Figs. 8 and 9, a new technology is developed for the advantages over conventional laser marking. Since current magnetic disk manufacturing does not have disk-identification, traceability becomes very difficult when failures happen at media or drive levels. Laser tagging is well known to enhance the traceability of product and be necessary in modern mass production. However, conventional laser tagging technique employs laser to ablate the product surface to form visual contrast. Due to the stringent cleanliness requirement and multilayered structure of finished disk, conventional laser tagging technique is no longer available. The researchers can employ precisely controlled and nearly perfect  $TEM_{00}$  laser beam to induce deformation of NiP layer on multilayered disk surface. The research results showed that the coupling of excellent beam symmetry and multilayered structure resulted in only surface deformation to form visual contrast. The process is ablation-free and cleanliness is ensured. The developed disk tagging machine in Fig. 10 is fully automatic and meets the requirement of mass production. Typical tagging character size is in the range of 0.5 to 2 mm and user selectable. Besides, a new generation laser bumping technology as shown in Fig. 11 has been developed. Laser bumping machine, BumpMaker as shown in Fig. 12, has been developed and commercialized..

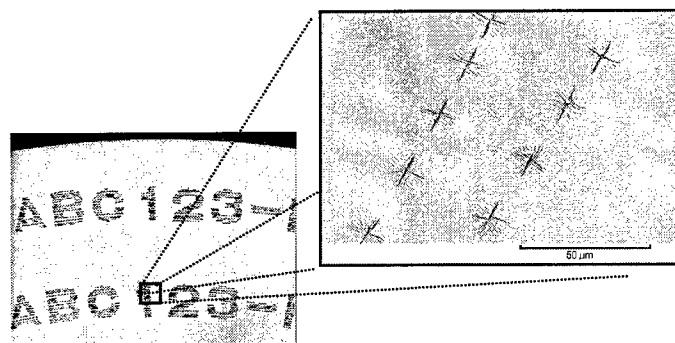


Fig. 8 Laser disk tagging: marking formation

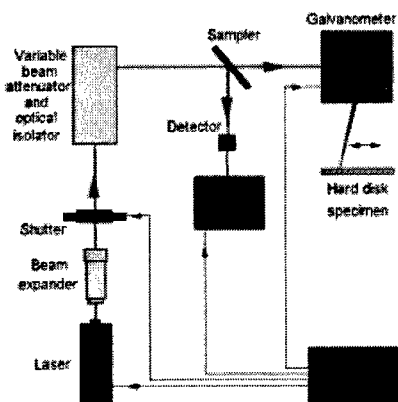


Fig. 9 Laser disk tagging: system configuration

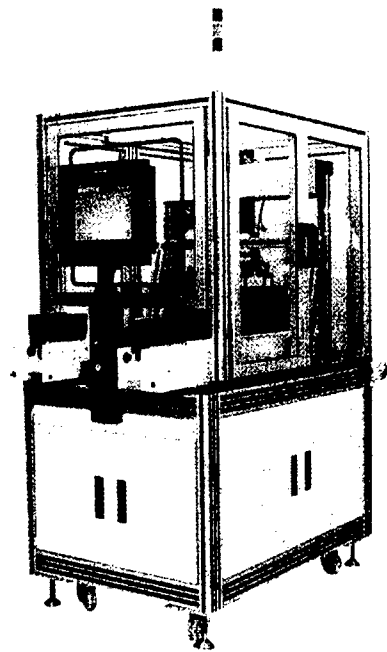


Fig. 10 Laser tagging machine.

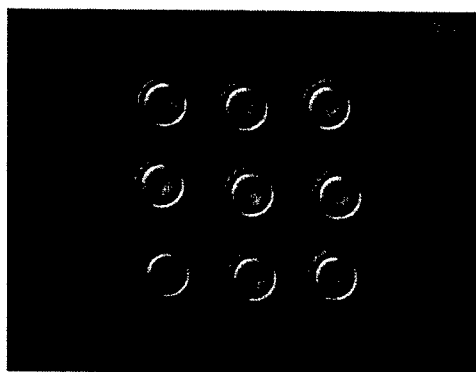


Fig. 11. Laser bumping

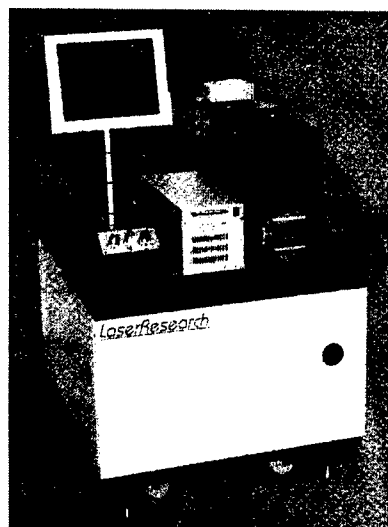


Fig. 12 Laser BumpMaker



#### 4. Plastic ball grid array reflow using a fast-modulated CW laser

Laser soldering in electronics manufacturing has drawn considerable attention over passed ten years [7-9], because of its merits to accurately and quickly deliver laser energy onto a localized area which will greatly reduce the thermal effect to electronic components and substrates. The unique ability of laser soldering had been applied to solder fine pitch surface mount technology (SMT) [10] devices. The results showed that the heat levels applied could be suited to the requirements of individual solder joints with an accuracy superior to other soldering techniques. Very short heat exposure times with an order of magnitude of a tenth of second could be obtained with laser soldering, causing the lowest possible thermal load of components and substrate.

Plastic ball grid array reflow using a fast-modulated CW laser is studied. A CW/Q-switched Nd:YAG laser is modified to work in the fast-modulated CW mode. The Sn-Pb eutectic solder balls with a diameter of  $760\text{ }\mu\text{m}$  and a kind of Au-Ni-Cu solder pads are used in the study. Varying the laser power and the laser-on time respectively, the solderable parameter region of laser reflow for the solder balls and solder pads is obtained. Shear strength tests are also performed to finding out the optimal reflow parameters. The measured shear strength is higher than 1500 gf, with the maximum value over 1900 gf. An energy equilibrium model is proposed to compare the solderable region predicted theoretically with the experimental results and to estimate the average temperatures of solder joint under the performed experiment conditions.

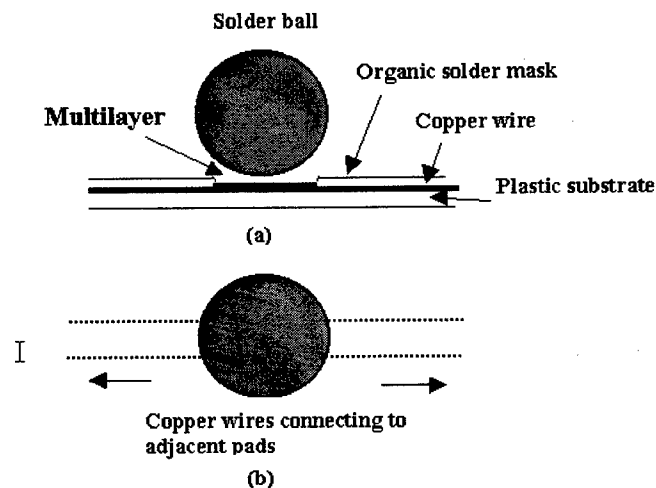


Fig. 13. Layout of solder ball and PBGA substrate, (a) cross section, (b) top view

The Sn-Pb eutectic solder balls with a diameter of  $760\text{ }\mu\text{m}$  are used in the experiments. Their composition is 63Sn/37Pb. The schematic layout of the solder ball and the PBGA substrate, which is specially designed for R&D purpose, is shown in Fig. 13. The solder pad has a multilayered structure, copper under-layer, nickel middle-layer and gold top-layer with the thickness around 23, 12 and  $0.2\text{ }\mu\text{m}$  respectively. It is surrounded and partially covered by an organic solder mask, and is supported by plastic substrate. The pad diameter is the same as that of the solder ball. Nevertheless, the solderable part of the pad, which is bared out of the solder mask, is about  $635\text{ }\mu\text{m}$  in diameter. Each pad is connected to the adjacent pads in two directions by built-in copper wires with a pitch of 1.5 mm. The cross section of the wire is about  $215 \times 35\text{ }\mu\text{m}^2$ .

If the combination of the laser power and the laser-on time provides sufficient solder wetting on the pad, soldered bump with strong shear strength can be obtained. It means that, within the solderable region, each laser power is corresponding to a laser-on time to form a set of optimal reflow parameters, and vice versa. Here only the sufficient wetting is concerned. If the facts of throughput, thermal effects to substrate and circuit and others are taken into account, some more limitations should be introduced. In this experiment, the laser power is set at 22 W and the laser-on time is

increased from 80 to 140 ms to find the optimal reflow condition. The shear strength tests are carried out to measure shear strengths of the soldered bumps. For easy test, the balls are soldered on skip lines, as shown in Fig. 14. Each condition is used to solder four balls and the average shear strength is taken into account. The results show that the shear strength increases as the laser-on time increases from 80 to 110 ms. Above 110 ms, the shear strength tends to saturate at about 1900 gf. It is probably due to the fact that the laser-on time of 110 ms at the laser power of 22 W already provides sufficient wetting time.

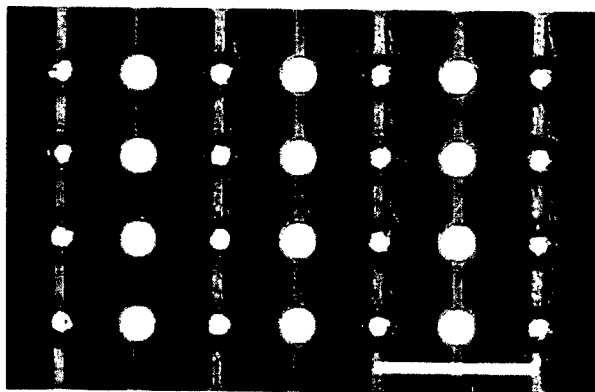


Fig. 14. Skip lines of reflowed bumps for shear strength tests, the bar representing 3 mm

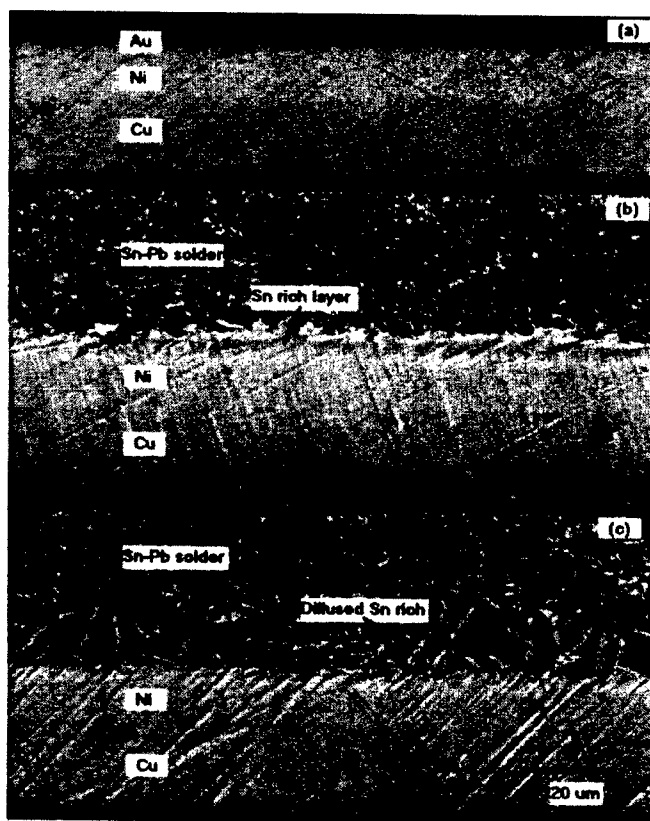


Fig. 15. Optical micrographs of sectioned samples, (a) Au/Ni/Cu pad before reflow, (b) interface reflowed at laser-on time of 80 ms and laser power of 22 W, (c) interface reflowed at laser-on time of 110 ms and laser power of 22 W.

The minimum shear strength of the soldered bump at the laser-on time of 80 ms is 1525 gf, which is about the same as the average shear strength of the same size bumps reflowed by oven [11]. It is 26% lower than the maximum shear strength of the laser-reflowed bump. Comparing parameters used during laser reflow and oven reflow, there are two significant differences, reflow time and reflow temperature. During oven reflow of the Sn-Pb eutectic solder balls, the total wetting time is about 30 – 50 s when the temperature is above the solder's liquids or melting temperature, which is much longer than that during laser reflow, about 100 ms. On the other hand, the laser reflow temperature should be much higher in order to get enough wetting. These significant differences may result in different structure formation on solder-pad interface. Figure 15 shows cross-section micrographs of the Au/Ni/Cu pad before reflow and the solder-pad interfaces after reflow using the laser-on times of 80 and 110 ms and the same laser power of 22 W. Composition analyses are carried out using Auger electron spectroscopy and X-ray photoelectron. The results illustrate that there is a Sn rich layer with a thickness of about 5  $\mu\text{m}$  formed on Ni pad surface when the laser-on time is 80 ms. When the laser-on time increases to 110 ms, such Sn rich layer starts to diffuse to solder material. There is no  $\text{Ni}_3\text{Sn}_4$  compound found over the solder-pad interface, while it is an intermetallic compound usually formed during oven reflow. Such composition difference probably is the reason why the bump shear strength reflowed by laser is stronger than that reflowed by oven, due to the brittle feature of this kind of intermetallic compound.

### 5. Laser singulation and ink-jet laser marking

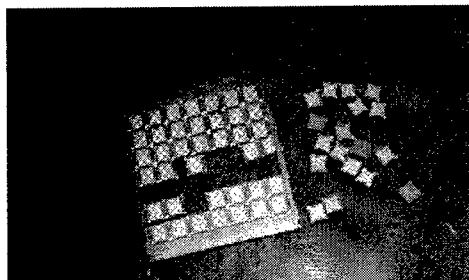


Fig. 16. Laser isolation and singulation of BGA packages.



Fig. 17. Laser isolation and singulation of BGA packages.

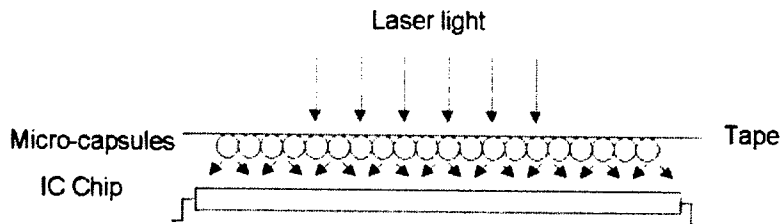


Fig. 18. Schematic diagram of ink-jet laser marking.

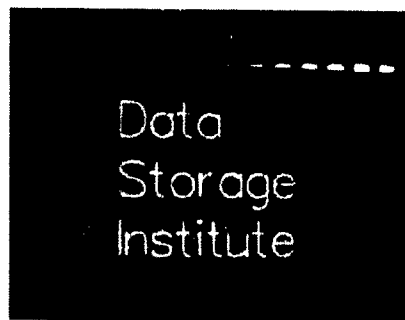


Fig. 19. High-contrast characters produced by of ink-jet laser marking.

There are many other applications. Among them, laser isolation and singulation of BGA packages (Fig. 16) and dies (Fig. 17), and ink-jet laser marking (Figs. 18 and 19) will have good potential in applications.

## CONCLUSIONS

In summary, laser microprocessing technology has been successfully applied in microelectronics packaging. Among the various applications, laser cleaning of IC mold tools, laser deflash of IC packages, laser texturing, tagging and bumping for magnetic disks, laser reflow of BGA, laser isolation and singulation of packages and dies, and ink-jet laser marking have demonstrated their advantages and capabilities.

## REFERENCES

1. Y.F. Lu, W. D. Song, B.W. Ang, D.S.H. Chan and T.S. Low, "A Theoretical Model for Laser Removal of Particles from Solid Surface", *Appl. Phys.* A65, pp. 9-13, 1997.
2. Y.F. Lu, W.D. Song, K.D. Ye, Y.P. Lee, D.S.H. Chan and T.S. Low, "A Cleaning Model for Removal of Particles due to Laser-Induced Thermal Stress in Substrate", *Jpn J. Appl. Phys.* 36(10A), pp. L1304-L1306, 1997.
3. Y.F. Lu, Y. Zhang, W.D. Song and D.S.H. Chan, "A Theoretical Model for Laser Cleaning of Microparticles in a thin liquid layer", *Jpn. J. Appl. Phys.*, 37(11A), pp. L1330-L1332, 1998.
4. Y.F. Lu, Y. Zhang and W.D. Song, "Laser cleaning of tiny particles in a thin liquid layer and its theoretical model", *Appl. Surf. Sci.*, 139, pp. 140-144, 1999.
5. M.H. Hong, Y.F. Lu, and Q. Chen, "Optical emission spectrum analyses during pulsed laser deflash of Integrated Circuit packages", *Jpn J. Appl. Phys.* 1, 38(12A), pp. 6750-6753, 1999.

6. D.M. Liu, Y.F. Lu, Y. Yuan, W.J. Wang, T.S. Low, T.S. Wee, K.T. Chang, and R.J.K. Goh, "Laser Induced Deformation on Hard Disk Surface", *Appl. Surf. Sci.*, 139, pp. 482-488, 1999.
7. M. Greenstein, "Optical absorption aspects of laser soldering for high density interconnects", *Applied Optics*, 28(21), 4595-4603 (1989)
8. D. G. Whitehead, A. V. Polijanczuk and P. M. Beckett, "Reflow soldering by laser", *ASME Heat Transfer Division*, 143, 47-56 (1990)
9. W. Yang, R. W. Messler, JR. and L. E. Felton, "Laser Beam soldering behavior of eutectic Sn-Ag solder", *Welding Research Supplement I*, 224-229 (1995)
10. J. Nicolics, L. Musiejovsky, and E. Semerad, "Optimization of process parameters for laser soldering of surface mounted devices", *IEEE Trans. Comp., Hybrids, Manuf. Technol.*, 15(6), 1154-1159 (1992)
11. H. Z. Chong and Y. Sung, "Solder joint reliability of plastic ball grid array packages", *Soldering & Surface Mount Technology*, 11(1), 44-48 (1999)

## Addendum

The following papers were announced for publication in these proceedings but have been withdrawn or are unavailable.

- [4637-01]      **Mechanisms and effects in the UV laser ablation of molecular solids**  
S. K. Georgiou, A. Koubenakis, A. Athannassiou, D. Anglos, C. Fotakis,  
V. Tornari, Foundation for Research and Technology-Hellas (Greece)
- [4637-13]      **Nanothin coatings on fluidized powders for engineering and pharmaceutical applications**  
J. D. Talton, Nanosphere, Inc. (USA); G. Hochhaus, Univ. of Florida (USA)
- [4637-14]      **Resonant IR-pulsed laser deposition of polymer films**  
D. M. Bubb, J. S. Horwitz, J. H. Callahan, R. A. McGill, E. J. Houser,  
D. B. Chrisey, Naval Research Lab. (USA); M. R. Papantonakis,  
R. F. Haglund, Jr., Vanderbilt Univ. (USA); M. Galicia, A. Vertes,  
George Washington Univ. (USA); B. Toftmann, Risø National Lab. (Denmark)
- [4637-17]      **Production of solar cells from  $A_2B_6$  compounds by MAPLE technology on polymer substrates**  
N. Electronov, V. S. Serbezov, E. Dimitroff, N. Zlatanov, Solaris Nano  
Technology Industries Inc. (Bulgaria)
- [4637-22]      **Controlled modification of the refractive index of dielectrics with femtosecond pulses**  
P. B. Corkum, National Research Council Canada
- [4637-53]      **Laser technology for micro via formation, structuring, and cutting**  
D. J. Meier, J. Kickelhain, LPKF Laser & Electronics AG (Germany)
- [4637-56]      **Femtosecond laser action on solid dielectric surface: from thermal to nonthermal effects**  
V. E. Gruzdev, A. S. Gruzdeva, S.I. Vavilov State Optical Institute (Russia)
- [4637-57]      **Physical limits for formation of laser craters in semiconductor materials by nanosecond UV pulses**  
A. R. Novoselov, A. G. Klimenko, E. V. Fedosenko, Institute of Semiconductor  
Physics (Russia)
- [4637-58]      **Fabrication of water-soluble evaporative models by laser scanning**  
T. Kamitani, O. Yamada, Y. Marutani, Osaka Sangyo Univ. (Japan)
- [4637-59]      **Electrophysical behavior of PZT ceramics synthesized by selective laser sintering method**  
E. Y. Tarasova, I. V. Shishkovsky, A. L. Petrov, P.N. Lebedev Physical Institute  
(Russia)

- [4637-60]     **Researching conditions of the selective laser sintering in the powdered system Al-Ti**  
A. S. Panin, A. L. Petrov, I. V. Shishkovsky, Y. G. Morozov, S. A. Nefedov,  
P.N. Lebedev Physical Institute (Russia)
- [4637-69]     **Laser bonding for packaging of microfluidic devices**  
X. Xu, J. Kim, Purdue Univ. (USA)
- [4637-81]     **Laser forward transfer using a rheological fluid layer**  
D. A. Young, R. C. Y. Auyeung, A. Piqué, D. B. Chrisey, Naval Research Lab.  
(USA); D. D. Dlott, Univ. of Illinois/Urbana-Champaign (USA)

## Author Index

- Aden, Mirko, 54  
 Akane, Toshimitsu, 235, 243  
 An, Cheng Wu, 581  
 Ando, Nobuo, 111  
 Andreev, Alexander A., 413  
 Anglos, Dmitris, Addendum  
 Arnold, Craig B., 353, 361  
 Asano, Taishi, 197  
 Ashkenasi, David, 169, 378  
 Athannassiou, Athanasia, Addendum  
 Audouard, E., 148  
 Auyeung, Raymond C. Y., Addendum, 341, 361  
 Bachmann, Friedrich G., 505  
 Bacinello, Leonard, 537  
 Baubeau, E., 148  
 Ben-Yakar, Adela, 212  
 Bernauer, W., 318  
 Berthe, Laurent, 537  
 Beyer, Eckhard, 496  
 Brannon, James H., 474  
 Bubb, Daniel M., Addendum  
 Burghardt, Berthold, 228  
 Burt, Julian P. H., 305  
 Byer, Robert L., 212  
 Cadotte, Maxime, 75  
 Callahan, John H., Addendum  
 Chapman, Glenn H., 330  
 Chen, G. X., 445  
 Chen, Kevin P., 228, 251  
 Chichkov, Boris N., 188  
 Chimmalg, Anant, 204  
 Choi, Tae Y., 204  
 Chong, Tow Chong, 270, 445, 581  
 Chrisey, Douglas B., Addendum, 341, 361  
 Constantinide, Dan, 90  
 Coric, Dragan, 251  
 Corkum, Paul B., Addendum  
 Dausinger, Friedrich, 31, 127  
 Dawes, Mary L., 1  
 De Hosson, J. Th. M., 555  
 Delage, Delphine, 537  
 Dias, Rajen C., 374  
 Dickinson, J. Thomas, 1, 453  
 Dijken, Durandus K., 555  
 Dimitroff, Emil, Addendum  
 Dlott, Dana D., Addendum  
 Douglass, Mark, 465  
 Dubowski, Jan J., 82  
 Ducharme, Mathieu, 75  
 Duignan, Michael T., 374  
 Dumont, Nicolas, 537  
 Durand, Friedrich, 537, 545, 571  
 Dyer, Peter E., 218  
 Electronov, Nasko, Addendum  
 Fedosenko, Evgeny V., Addendum  
 Fieret, Jim, 397  
 Fotakis, Costas, Addendum  
 Frazier, Brandon M., 374  
 Gagnon, Yves, 75  
 Galicia, M., Addendum  
 Garnov, Serge V., 31  
 Georgiou, Savas K., Addendum  
 Ghandour, Osman A., 90  
 Goater, Andrew D., 305  
 Govorkov, Sergei V., 386  
 Grigoropoulos, Constantine P., 204  
 Gruzdev, Vitali E., Addendum  
 Gruzdeva, Anastasia S., Addendum  
 Haglund, Richard F., Jr., Addendum  
 Hanemann, Thomas, 318  
 Hansen, William W., 297, 404  
 Hato, Yukinori, 111  
 Hayden, Christopher J., 305  
 Heglin, Michael, 386  
 Heinemann, Stefan, 487  
 Helvajian, Henry, 297, 404  
 Herfurth, Hans, 487  
 Herman, Peter R., 228, 251  
 Hochhaus, Gunther, Addendum  
 Hong, Ming Hui, 270, 445, 581  
 Horn, Alexander, 258  
 Horwitz, James S., Addendum  
 Houser, Eric J., Addendum  
 Hoving, Willem, 555  
 Huang, Adam, 297, 404  
 Huot, Nicolas, 148  
 Husmann, Andreas, 54  
 Ihlemann, Jürgen, 228  
 Inoue, Narumi, 431  
 Itoh, Kazuyoshi, 197  
 Jacquorie, Michael, 258  
 Janson, Siegfried W., 297  
 Jonin, Christian, 148  
 Juodkazis, Saulius, 159  
 Kamitani, T., Addendum  
 Kant, Richard A., 361  
 Kasper, Jörg, 496  
 Kawaguchi, Yoshizo, 13, 135  
 Kawahara, Kosuke, 180  
 Kegresse, Todd, 369  
 Kickelhain, Joerg, Addendum  
 Kim, Heungsoo, 341  
 Kim, Joohan, Addendum  
 Kitahara, Junko, 111  
 Klimenko, Anatoly G., Addendum  
 Klotzbach, Udo, 496  
 Knapp, Wolfgang, 537  
 Konov, Vitali I., 31  
 Körber, Klaus, 519  
 Koubenakis, Antonis, Addendum



Kouta, Hikaru, 561  
 Kramer, Thorsten, 545, 571  
 Krauß, Hans-Joachim, 102  
 Kreutz, Ernst W., 54, 258  
 Kulik, Christian, 280, 519  
 Kuramatsu, Masaaki, 431  
 Kuroda, Daisuke, 197  
 Kurogi, Yasunobu, 180  
 Kurosaki, Yasuo, 528  
 Kurosawa, Kou, 180  
 Lacourse, Alain, 75  
 Langford, Steve C., 1  
 Laporte, Pierre, 148  
 Le Harzic, Ronan, 148  
 Leisten, Oliver, 397  
 Lepretre, Didier, 537  
 Li, Jianzhao, 228, 251  
 Li, Peng, 465  
 Li, Zhong Li, 43  
 Liu, Da Ming, 581  
 Liu, David, 369  
 Livingston, Frank E., 404  
 Lomaev, Mikhail I., 419  
 Lu, Yong F., 270, 445, 581  
 Lui, Lena, 43  
 Maeda, Mitsuo, 21, 435  
 Mai, Zhi Hong, 445  
 Makino, Toshiharu, 119  
 Malyutin, Alexander A., 31  
 Marowsky, Gerd, 228  
 Marutani, Y. Addendum  
 Maswadi, Saher M., 218  
 Mathews, Scott A., 369, 374  
 Matsuo, Naoyuki, 180  
 Matsuo, Norihide, 180  
 Matsuo, Shigeki, 159  
 Matsuzaki, Akiyoshi, 111  
 Mazumder, Jyotirmoy, 465  
 McEvoy, Patrick, 397  
 McGill, Robert A., Addendum, 361  
 Meier, Dieter J., Addendum  
 Meunier, Michel, 75  
 Midorikawa, Katsumi, 235, 243, 270  
 Misawa, Hiroaki, 159  
 Moran, Peter M., 43  
 Morozov, Yuriy G., Addendum  
 Murata, Jun, 111  
 Nakata, Yoshiki, 21, 435  
 Narazaki, Aiko, 13, 135  
 Nefedov, Sergey A., Addendum  
 Niessen, Markus, 54  
 Niino, Hiroyuki, 13, 135  
 Ninomiya, Takahumi, 180  
 Nishii, Junji, 159, 197  
 Nishio, Satoru, 111  
 Nolte, Stefan, 188  
 Novoselov, Andrew R., Addendum  
 Nwe, Khin Hla, 1  
 Obata, Kotaro, 243  
 Oesterlin, Peter, 228  
 Okada, Tatsuo, 21, 435  
 Okoshi, Masayuki, 431  
 Okumura, Motoyoshi, 111  
 Olowinsky, Alexander M., 545, 571  
 Ostendorf, Andreas, 280  
 Otto, Andreas, 102  
 Panin, Anton S., Addendum  
 Panzner, Michael, 496  
 Papantonakis, Michael R., Addendum  
 Petrov, Alexei L., Addendum  
 Pfleging, Wilhelm, 318  
 Piqué, Alberto, Addendum, 341, 353, 361  
 Placzek-Popko, Ewa, 82  
 Poprawe, Reinhart, 54, 258  
 Pratap, Bhanu, 353, 361  
 Ren, Zhong Min, 581  
 Richerzhagen, Bernold, 479  
 Ringeisen, Bradley R., 341, 361  
 Rosenfeld, Arkadi, 169  
 Rumsby, Phil, 397  
 Ruschin, Shlomo, 235  
 Russek, Ulrich A., 505  
 Saito, Takushi, 528  
 Sarunic, Marinko V., 330  
 Sato, Kimitoshi, 528  
 Sato, Tadatake, 13, 135  
 Satoh, Isao, 528  
 Sawada, Hiroshi, 180  
 Scaggs, Michael J., 386  
 Schäfer, K., 519  
 Schoelzel, T., 386  
 Serbezov, Valery S., Addendum  
 Sheets, Ron E., 90  
 Shinagawa, Taishi, 197  
 Shishkovsky, Igor V., Addendum  
 Shitz, Dmitry V., 419  
 Skakun, Victor S., 419  
 Skoglund, Lars D., 374  
 Snelling, Howard V., 218  
 Soh, Chye E., 445  
 Song, Wen D., 445, 581  
 Spargo, Barry J., 341  
 Spiegel, Akos, 479  
 Stassen, Ines, 397  
 Stute, Uwe, 280  
 Sugioaka, Koji, 235, 243, 270  
 Suzuki, Nobuyasu, 119  
 Swider-Lyons, Karen E., 353  
 Talkenberg, Marc, 258  
 Talton, James D., Addendum  
 Tame, John A., 305  
 Tamura, Kazuyuki, 111  
 Tang, Haipeng, 82  
 Tarasenko, Victor F., 419  
 Tarasova, Ekaterina Y., Addendum  
 Theoharidis, Haris, 386  
 Thiam, Thomas, 445  
 Toftmann, Bo, Addendum  
 Tönshoff, Hans K., 519  
 Torge, Maika, 318  
 Tornari, Vivi, Addendum  
 Toyoda, Koichi, 243

Tsarkova, Olga G., 31  
Tu, Yuqiang, 330  
Tünnermann, Andreas, 188  
Ueda, Toshitsugu, 413  
Vago, Nandor, 479  
Valette, Serge, 148  
Vardaxoglou, Yiannis, 397  
Veiko, Vadim P., 64  
Vertes, Akos, Addendum  
Wagner, Frank R., 479  
Wakamatsu, Muneaki, 413  
Walton, Christopher D., 218  
Wang, Wei Jie, 581  
Wang, Zhiyong, 374  
Wartena, Ryan C., 353  
Washio, Kunihiro, 561  
Watanabe, Mitsuru, 159  
Watanabe, Wataru, 197  
Webb, James B., 82  
Wei, X. Midori, 228, 251  
Weir, David W., 361  
Will, Matthias, 188  
Witte, Reiner, 487  
Wong, L. L., 270  
Wrobel, Jerzy M., 82  
Wu, Ding J., 270  
Wu, Peter K., 341, 361  
Wust, Hendrik, 496  
Xu, Xianfan, Addendum, 291  
Yabe, Akira, 13, 135  
Yakovlev, Nikolai L., 43  
Yamada, Kazuhiro, 197  
Yamada, O., Addendum  
Yamada, Yuka, 119  
Yarom, G., 235  
Ye, Kaidong D., 581  
Yokotani, Atsushi, 180  
Yoshida, Takehito, 119  
Young, Donald A., Addendum  
Young, H. Daniel, 341  
Yow, Soh Zeom, 43  
Zhang, Chengping, 369  
Zhang, Richard X., 291  
Zlatanov, Nick, Addendum